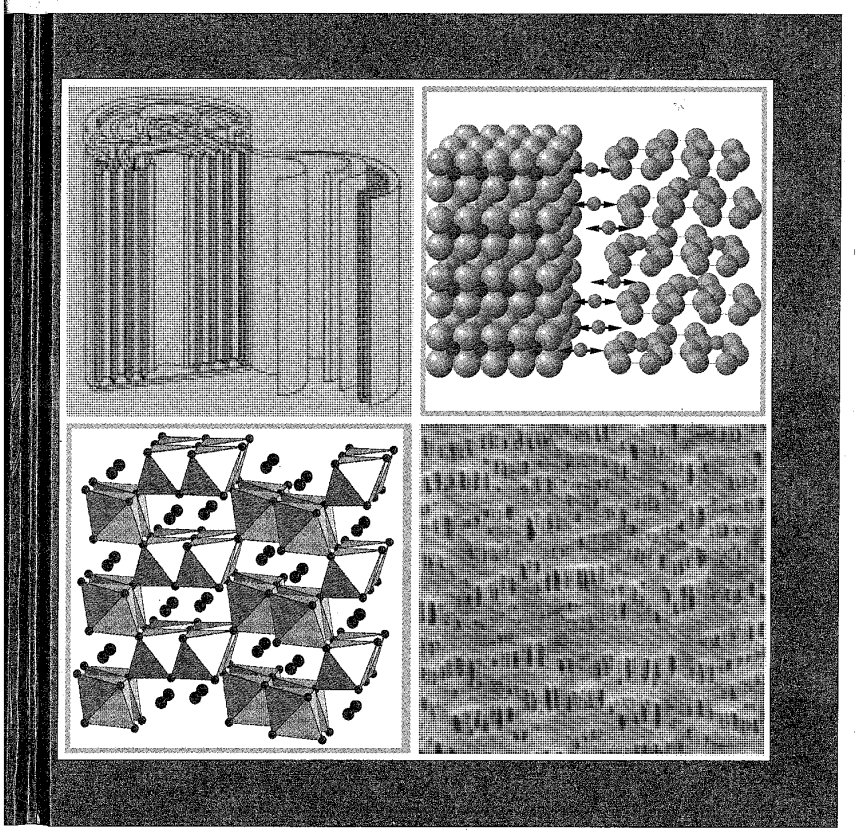
WILEY-VCH

Handbook of Battery Materials

Edited by Jürgen O. Besenhard



Jürgen O. Besenhard (Ed.)

Handbook of Battery Materials

WILEY-VCH

CosMX Exhibit 1008, Page 2 of 633

Further Titles of Interest

K. Kordesch, G. Simader
Fuel Cells and Their Applications
ISBN 3-527-28579-2

M. Wakihara, O. Yamamotu (Eds.)
Lithium Ion Batteries
Fundamentals and Performance
ISBN 3-527-28566-0

Jürgen O. Besenhard (Ed.)

Handbook of Battery Materials

WILEY-VCH Weinheim · New York · Chichester
Brisbane · Singapore · Toronto

Prof. Dr. J. O. Besenhard
Institut für Chemische Technologie Anorganischer Stoffe
Technische Universität Graz
Stremayrgasse 16/III
A-8010 Graz
Austria

This book was carefully produced. Nevertheless, authors, editors and publisher do not warrant the information contained therein to be free of errors. Readers are advised to keep in mind that statements, data, illustrations, procedural details or other items may inadvertently be inaccurate.

Library of Congress Card No. applied for.

A catalogue record for this book is available from the British Library.

Deutsche Bibliothek Cataloguing-in-Publication Data

Handbook of battery materials / ed. Jürgen O. Besenhard. -
Weinheim ; New York ; Chichester ; Brisbane ; Singapore ; Toronto :
Wiley-VCH, 1999
ISBN 3-527-29469-4

© WILEY-VCH Verlag GmbH. D-69469 Weinheim (Federal Republic of Germany), 1999
Printed on acid-free and chlorine-free paper.
All rights reserved (including those of translation in other languages). No part of this book may be reproduced in any form - by photoprinting, microfilm, or any other means - nor transmitted or translated into machine language without written permission from the publishers. Registered names, trademarks, etc. used in this book, even when not specifically marked as such, are not to be considered unprotected by law.
Composition: Data Source Systems, 1900 Timisoara, Romania. Printing: betz-druck gmbh, D-64291 Darmstadt. Bookbinding: J. Schäffer GmbH & Co. KG., D-67269 Grünstadt.
Printed in the Federal Republic of Germany.

Preface

At present batteries worth more than 30 billion USD are produced every year and the demand is still increasing rapidly as more and more mobile electronic end electric devices ranging from mobile phones to electric vehicles are entering into our life. The various materials required to manufacture these batteries are mostly supplied by the chemical industry. Ten thousands of chemists, physicists and material scientists are focusing on the development of new materials for energy storage and conversion. As the performance of the battery system is in many cases a key issue deciding the market success of a cordless product there is in fact a kind of worldwide race for advanced batteries.

Unfortunately, the chemistry of batteries is usually dealt with in a fairly superficial manner in common textbooks of inorganic or solid state chemistry. On the other hand, there are many books specialising on batteries, however, concentrating mostly on their basic electrochemistry, performance and construction. The intention of this book is to fill the gap and to provide deeper insight into chemical as well as electrochemical reactions and processes related with the discharging and charging of batteries. The Handbook of Battery Materials is a comprehensive source of detailed information written by leading experts. I believe it will be a valuable tool for all those who are teaching inorganic chemistry, polymer chemistry or materials science at a graduate or higher level and, of course, for all those who are doing research in the fields of materials for energy storage and conversion.

There are countless materials which have been proposed and investigated for battery applications. The Handbook of Battery Materials concentrates on those materials which have already found real and considerable practical applications and I hope that colleagues who do not find their "babies" included will understand.

The organization of the Handbook of Battery Materials is simple, dividing between aqueous electrolyte batteries and alkali metal batteries and further in anodes, cathodes, electrolytes and separators. There are also three more general chapters about thermodynamics and mechanistics of electrode reactions, practical batteries and the global competition of primary and secondary batteries.

Finally I would like to express my thanks to all the authors who contributed to this volume, to colleagues who supported this work by their advise and to Karin Scholze who managed all the practical problems related with the collection and compilation of 23 articles in due term.

Graz, October 1998

Jürgen O. Besenhard

3 1211 01102637 0

Contents

List of Contributors XXIII

Part I: Fundamentals and General Aspects of Electrochemical Power Sources

1 **Thermodynamics and Mechanistics** 1
Günther Hambitzer, Karsten Pinkwart, Christiane Ripp, Christian Schiller

1.1 Electrochemical Power Sources 1
1.2 Electrochemical Fundamentals 2
1.2.1 The Electrochemical Cell 2
1.2.2 The Electrochemical Series of Metals 4
1.2.3 Discharging 6
1.2.4 Charging 7
1.3 Thermodynamics 7
1.3.1 Electrode Processes at Equilibrium 7
1.3.2 Reaction Free Energy ΔG and Equilibrium Cell Voltage $\Delta\varepsilon_{00}$ 8
1.3.3 Concentration Dependence of the Equilibrium Cell Voltage 9
1.3.4 Temperature Dependence of Equilibrium Cell Voltage 10
1.3.5 Pressure Dependence of the Equilibrium Cell Voltage 11
1.3.6 Overpotential of Half-Cells and Internal Resistance 12
1.4 Criteria for the Assessment of Batteries 13
1.4.1 Terminal Voltage 14
1.4.2 Current–Voltage Diagram 14
1.4.3 Discharge Characteristic 14
1.4.4 Characteristic Line of Charge 15
1.4.5 Overcharge Reactions 15
1.4.6 Coulometric Efficiency and Energy Efficiency 15
1.4.7 Cycle Life 16
1.4.8 Specific Energy and Energy Density 16
1.5 References 17

2 **Practical Batteries** 19
Koji Nishio and Nobuhiro Furukawa

2.1 Alkaline–Manganese Batteries 19
2.2 Nickel–Cadmium Batteries 21
2.3 Nickel–Metal Hydride Batteries 26
2.4 Lithium Primary Batteries 31

2.4.1 Lithium–Manganese Dioxide Batteries 32
2.4.2 Lithium–Carbon Monofluoride Batteries 38
2.4.3 Lithium-Thionyl chloride batteries 39
2.5 Coin-Type Lithium Secondary Batteries 40
2.5.1 Secondary Lithium–Manganese Dioxide Batteries 40
2.5.2 Lithium-Vanadium Oxide Secondary Batteries 44
2.5.3 Lithium–Polyaniline Batteries 44
2.5.4 Secondary Lithium-Carbon Batteries 45
2.5.5 Secondary Li–LGH–Vanadium Oxide Batteries 45
2.5.6 Secondary Lithium–Polyacene Batteries 45
2.5.7 Secondary Niobium Oxide–Vanadium Oxide Batteries 46
2.5.8 Secondary Titanium Oxide–Manganese Oxide Batteries 46
2.6 Lithium-Ion Batteries 47
2.6.1 Positive Electrode Materials 47
2.6.2 Negative Electrode Materials 50
2.6.3 Battery Performances 54
2.7 Lithium Secondary Battery with Metal Anodes 56
2.8 References 58

3 Global Competition of Primary and Secondary Batteries 63
Karl Kordesch and Josef Daniel- Ivad

3.1 Introduction 63
3.1.1 Estimate of Battery Market Trends and Expansions, 1995 to 2001 65
3.1.2 The Small-Format Alkaline Battery Market in the USA and Europe, and Internationally 66
3.1.3 Who Buys Batteries ? 67
3.1.4 The Lithium Primary Market 67
3.1.5 Primary Zinc–Air Batteries 67
3.2 Rechargeable Batteries (Consumer and OEM Markets) 68
3.2.1 Ni–Cd Batteries 69
3.2.2 Progress in Ni–Metal Hydride Batteries 69
3.2.3 Lead–Acid Batteries 70
3.2.4 Li Secondary Batteries: Status and Future Projections 70
3.2.4.1 The Advances in Anodes 70
3.2.4.2 Li Cells with Metallic Anodes 70
3.2.4.3 The Advances in Cathodes 71
3.2.4.4 Electrolytes 71
3.2.4.5 Separators 72
3.2.4.6 Competitors Among Li Ion Battery Manufacturers 72
3.2.5 Competition from Rechargeable Zinc–Air Batteries 72
3.3 Li batteries as Power Sources for Electric Vehicles? 73
3.4 Rechargeable Alkaline $MnO_2 - Zn$ (RAM™) Batteries 73
3.4.1 History and Present Situation 73

CosMX Exhibit 1008, Page 8 of 633

3.4.2 The Advantages of RAM Batteries 74
3.4.3 Typical RAM Applications 74
3.4.4 Characteristics of RAM Batteries 75
3.4.5 RAM Battery Charging 77
3.4.5.1 External or Internal Chargers 77
3.4.5.2 Series Charging for OEM Applications 79
3.4.5.3 Power Packs 79
3.4.5.4 Solar Panel Charging 79
3.4.5.5 RAM Safety 81
3.5 Summary and Outlook 81
3.6 References 82

Part II: Materials for Aqueous Electrolyte Batteries

1 Structural Chemistry of Manganese Dioxide and Related Compounds 85
Jörg H. Albering

1.1 Introduction 85
1.2 Tunnel Structures 86
1.2.1 $\beta - MnO_2$ 86
1.2.2 Ramsdellite 88
1.2.3 $\gamma - MnO_2$ and $\varepsilon - MnO_2$ 89
1.2.4 $\alpha - MnO_2$ 94
1.2.5 Romanèchite, Todorokite, and Related Compounds 96
1.3 Layer Structures 98
1.3.1 Mn_5O_8 and Similar Compounds 98
1.3.2 Lithioporite 101
1.3.3 Chalcophanite 102
1.3.4 $\delta - MnO_2$ materials 103
1.3.5 10 Å Phyllomanganates of the Buserite Type 107
1.4 Reduced Manganese Oxides 107
1.4.1 Compounds of Composition MnOOH 108
1.4.1.1 Manganite ($\gamma - MnOOH$) 108
1.4.1.2 Groutite ($\alpha - MnOOH$) 108
1.4.1.3 $\delta - MnOOH$ 109
1.4.1.4 Feitknechtite $\beta - MnOOH$ 109
1.4.2 Spinel-type Compounds Mn_3O_4 and $\gamma - Mn_2O_3$ 109
1.4.3 Pyrochroite, $Mn(OH)_2$ 110
1.5 Conclusion 110
1.6 References 110

CosMX Exhibit 1008, Page 9 of 633

2 Electrochemistry of Manganese Oxides 113
Akiya Kozawa, Kohei Yamamoto and Masaki Yoshio

2.1 Introduction 113
2.2 Electrochemical Properties of EMD 115
2.2.1 Discharge Curves and Electrochemical Reactions 115
2.2.2 Modification of Discharge Behavior of EMD with $Bi(OH)_3$ 115
2.2.3 Factors Which Influence MnO_2 Potential 115
2.2.3.1 Surface Condition of MnO_2 115
2.2.3.2 Standard Potential of MnO_2 in 1 mol L^{-1} KOH 118
2.2.4 Three Types of Polarization for MnO_2 118
2.2.5 Discharge Tests for Battery Materials 120
2.3 Physical Properties and Chemical Composition of EMD 123
2.3.1 Cross-Section of the Pores 124
2.3.2 Closed Pores 124
2.3.3 Effective Volume Measurement 124
2.4 Conversion of EMD to $LiMnO_2$ or $LiMnO_4$ for Rechargeable Li Batteries 129
2.4.1 Melt-Impregnation (M–I) Method for EMD 129
2.4.2 Preparation of $Li_{0.3}MnO_2$ from EMD [25] 130
2.4.3 Preparation of $LiMn_2O_4$ from EMD [25, 27] 131
2.5 Discharge Curves of EMD Alkaline Cells (AA and AAA Cells) 131
2.6 References 132

3 Nickel Hydroxides 135
James McBreen

3.1 Introduction 135
3.2 Nickel Hydroxide Battery Electrodes 136
3.3 Solid State Chemistry of Nickel Hydroxides 137
3.3.1 Hydrous Nickel Oxides 137
3.3.1.1 $\beta - Ni(OH)_2$ 137
3.3.1.2 $\alpha - Ni(OH)_2$ 139
3.3.1.3 $\beta - NiOOH$ 142
3.3.1.4 $\gamma - NiOOH$ 143
3.3.1.5 Relevance of Model Compounds to Electrode Materials 143
3.3.2 Pyroaurite-Type Nickel Hydroxides 144
3.4 Electrochemical Reactions 145
3.4.1 Overall Reaction and Thermodynamics of the $Ni(OH)_2$/NiOOH Couple 145
3.4.2 Nature of the $Ni(OH)_2$/NiOOH Reaction 147
3.4.3 Nickel Oxidation State 148
3.4.4 Oxygen Evolution 148
3.4.5 Hydrogen Oxidation 148
3.5 References 149

CosMX Exhibit 1008, Page 10 of 633

4 Lead Oxides 153
Dietrich Berndt

4.1 Introduction 153
4.2 Lead / Oxygen Compounds 154
4.2.1 Lead Oxide (PbO) 154
4.2.2 Minium (Pb_3O_4) 155
4.2.3. Lead Dioxide (PBO_2) 155
4.2.4. Nonstoichiometric PbO_x Phases 156
4.2.5. Basic Sulfates 156
4.2.6. Physical and Chemical Properties 156
4.3 The Thermodynamic Situation 156
4.3.1 Water Decomposition 157
4.3.2 Oxidation of Lead 158
4.3.3 The Thermodynamic Situation in Lead–Acid Batteries 159
4.3.4. Thermodynamic Data 162
4.4 PbO_2 as Active Material in Lead–Acid Batteries 163
4.4.1 Planté Plates 164
4.4.2. Pasted Plates 165
4.4.2.1 Manufacture of the Active Material 165
4.4.2.2 Tank Formation 167
4.4.2.3 Container Formation 168
4.4.3 Tubular Plates 168
4.5 Passivation of Lead by its Oxides 169
4.5.1 Disintegration of the Oxide Layer at Open-Circuit Voltage 171
4.5.2 Charge Preservation in Negative Electrodes by a PbO Layer 171
4.6 Ageing Effects 172
4.6.1 The Influence of Antimony, Tin, and Phosphoric Acid 173
4.7 References 173

5 Bromine–Storage Materials 177
Ch. Fabjan and J. Drobits

5.1 Introduction 177
5.2 Possibilities for Bromine Storage 179
5.2.1 General Aspects 179
5.2.2 Quaternary Ammonium-Polybromide Complexes 180
5.3 Physical Properties of the Bromine Storage Phase 184
5.3.1 Conductivity 184
5.3.2 Viscosity and Specific Weight 186
5.3.3 Diffusion Coefficients 187
5.3.4 State of Aggregation 188
5.4 Analytical Study of a Battery Charge Cycle 188
5.5 Safety, Physiological Aspects, and Recycling 189

CosMX Exhibit 1008, Page 11 of 633

5.5.1 Safety 189
5.5.2 Physiological Aspects 191
5.5.3 Recycling 191
5.6 References 192

6 Metallic Negatives 195
L. O. Binder

6.1 Introduction 195
6.2 Overview 195
6.3 Battery Anodes ("Negatives") 196
6.3.1 Aluminum 196
6.3.2 Cadmium 196
6.3.3 Iron 197
6.3.4 Lead 197
6.3.5 Lithium 198
6.3.6 Magnesium 198
6.3.7 Zinc 199
6.3.7.1 Zinc Electrodes for "Acidic" (Neutral) Primaries 200
6.3.7.2 Zinc Electrodes for Alkaline Primaries 200
6.3.7.3 Zinc Electrodes for Alkaline Storage Batteries 202
6.3.7.4 Zinc Electrodes for Alkaline "Low-Cost" Reusables 203
6.3.7.5 Zinc Electrodes for Zinc-Flow Batteries 205
6.4 References 206

7 Metal Hydride Electrodes 209
James J. Reilly

7.1 Introduction 209
7.1.1 Thermodynamics 209
7.1.2 Electronic Properties 212
7.1.3 Reaction Rules and Predictive Theories 212
7.2 Metal Hydride–Nickel Batteries 212
7.2.1 Alloy Activation 214
7.2.2 AB_5 Electrodes 214
7.2.2.1 Chemical Properties of AB_5 Hydrides 215
7.2.2.2 Preparation of AB_5 Electrodes 216
7.2.2.3 Effect of Temperature 217
7.2.3 Electrode Corrosion and Storage Capacity 217
7.2.4 Corrosion and Composition 218
7.2.4.1 Effect of Cerium 220
7.2.4.2 Effect of Cobalt 222
7.2.4.3 Effect of Aluminum 222

CosMX Exhibit 1008, Page 12 of 633

7.2.4.4 Effect of Manganese 224
7.3 AB_2 Hydride Electrodes 225
7.4 XAS Studies of Alloy Electrode Materials 227
7.5 Summary 227
7.6 References 228

8 Carbons 231
K. Kinoshita

8.1 Introduction 231
8.2 Physicochemical Properties of Carbon Materials 232
8.2.1 Physical Properties 232
8.2.2 Chemical Properties 234
8.3 Electrochemical Behavior 235
8.3.1 Potential 235
8.3.2 Conductive Matrix 236
8.3.3 Electrochemical Properties 238
8.3.4 Electrochemical Oxidation 238
8.3.5 Electrocatalysis 239
8.3.6 Intercalation 242
8.4 Concluding Remarks 243
8.5 References 243

9 Separators 245
Werner Böhnstedt

9.1 General Principles 245
9.1.1 Basic Functions of the Separators 245
9.1.2 Characterizing Properties 246
9.1.2.1 Backweb, Ribs, and Overall Thickness 246
9.1.2.2 Porosity, Pore Size, and Pore Shape 247
9.1.2.3 Electrical Resistance 248
9.1.3 Battery and Battery Separator Markets 250
9.2 Separators for Lead–Acid Storage Batteries 251
9.2.1 Development History 251
9.2.1.1 Historical Beginnings 251
9.2.1.2 Starter Battery Separators 252
9.2.1.3 Industrial Battery Separators 254
9.2.2 Separators for Starter Batteries 258
9.2.2.1 Polyethylene Pocket Separators 258
9.2.2.2 Leaf Separators 263
9.2.2.3 Comparative Evaluation of Starter Battery Separators 269
9.2.3 Separators for Industrial Batteries 272

CosMX Exhibit 1008, Page 13 of 633

9.2.3.1 Separators for Traction Batteries 272
9.2.3.2 Separators for Open Stationary Batteries 276
9.2.3.3 Separators for Sealed Lead–Acid Batteries 278
9.3 Separators for Alkaline Storage Batteries 281
9.3.1 General 281
9.3.2 Primary Cells 282
9.3.3 Nickel Systems 283
9.3.3.1 Nickel–Cadmium Batteries 283
9.3.3.2 Nickel–Metal Hydride Batteries 284
9.3.4 Zinc Systems 285
9.3.4.1 Nickel–Zinc Storage Batteries 285
9.3.4.2 Zinc–Manganese Dioxide Secondary Cells 285
9.3.4.3 Zinc–Air Batteries 286
9.3.4.4 Zinc–Bromine Batteries 286
9.3.4.5 Zinc–Silver Oxide Storage Batteries 286
9.3.5 Separators Materials for Alkaline Batteries 287
9.4 References 289

Part III: Materials for Alkali Metal Batteries

1 The Structural Stability of Transition Metal Oxide Insertion Electrodes for Lithium Batteries 293
M. M. Thackeray

1.1 Introduction 293
1.2 Tunnel Structures: MnO_2 Compounds 295
1.2.1 $\alpha - MnO_2$ 295
1.2.2 $0.15\ Li_2 \cdot \alpha - MnO_2$ 296
1.2.3 $\beta - MnO_2$ 297
1.2.4 $\gamma - MnO_2$ and Ramsdellite $- MnO_2$ 297
1.2.5 Lithiated Ramsdellite $- MnO_2$ 298
1.2.6 Orthorhombic $Na_{0.44}MnO_2$ 299
1.3 Layered–Structures 299
1.3.1 $LiCoO_2$ 300
1.3.2 $LiNiO_2$ 301
1.3.3 Li–Mn–O Compounds 301
1.3.3.1 $LiMnO_2$ from $NaMnO_2$ 301
1.3.3.2 $Li_{2-x}MnO_{3-x/2}$ and Lithiated Derivatives 302
1.3.3.3 Orthorhombic $LiMnO_2$ 303
1.3.4 Orthorhombic $LiFeO_2$ 303
1.3.5 Li–V–O Compounds 304
1.3.5.1 $LiVO_2$ 304
1.3.5.2 $\alpha - V_2O_5$ and its Lithiated Derivatives 304

CosMX Exhibit 1008, Page 14 of 633

1.3.5.3 $Li_{1.2}V_3O_8$ 305
1.3.5.4 $Li_{0.6}V_{2-\delta}O_{4-\delta} \cdot H_2O$ and $Li_{0.6}V_{2-\delta}O_{4-\delta}$ 306
1.4 Framework Structures: The Family of Spinel Compounds 307
1.4.1 Fe_3O_4, Mn_3O_4 and Co_3O_4 308
1.4.2 Li–Mn–O Spinels 309
1.4.2.1 $Li[Mn_2]O_4$ 310
1.4.2.2 $Li_4Mn_5O_{12}$ 312
1.4.2.3 $Li[Mn_{1.5}Ni_{0.5}]O_4$ 313
1.4.2.4 Oxygen-Rich and Oxygen Deficient Spinels, $LiMn_2O_{4\pm\delta}$ 313
1.4.2.5 Thin-Film $LiMn_2O_4$ 313
1.4.3 Li–V–O Spinels 314
1.4.3.1 The Normal Spinel, $Li[V_2]O_4$ 314
1.4.3.2 The Inverse Spinels, $V[LiM]O_4$ (M=Ni Co) 315
1.4.4 Li–Co–O Spinels 315
1.4.4.1 $Li[Co_2]O_4$ and $Li_2Co_2O_4$ (LT-$LiCoO_2$) 315
1.4.5 Li–Ti–O spinels 316
1.4.5.1 $Li[Ti_2]O_4$ and $Li_4Ti_5O_{12}$ 316
1.5 Concluding Remarks 317
1.6 References 317

2 Overcharge-Protected Oxide Cathodes 323
Tsutomu Ohzuku

2.1 Introduction 323
2.2 Candidate Materials for Advanced Lithium Batteries 323
2.3 Specific Problems in Designing High–Volume, High–Energy, Reliable Lithium–Ion Batteries 326
2.4 Reaction Mechanism of $Li_{1-x}NiO_2$ and Its Thermal Behaviour with Organic Electrolyte 326
2.5 Possible Haystack-Type Reaction Associated with Thermal Runaway in a Closed Reaction Vessel 329
2.6 Characteristic Features of Solid-State Redox Reactions in $Li_{1-x}NiO_2$ 330
2.7 Synthesis and Characterization of the Solid Solution of $LiNiO_2$ and α-$LiAlO_2$ 332
2.8 An Innovative $LiAl_{1/4}Ni_{3/4}O_2$ Insertion Material for Lithium-Ion Batteries 333
2.9 Concluding Remarks 335
2.10 References 336

3 Rechargeable Lithium Anodes 339
Jun-ichi Yamaki and Shin-ichi Tobishima

3.1 Introduction 339
3.2 Surface of Uncycled Lithium Foil 341

CosMX Exhibit 1008, Page 15 of 633

3.3 Surface of Lithium Coupled With Electrolytes 341
3.4 Cycling Efficiency of Lithium Anode 342
3.4.1 Measurement Methods 342
3.5 Reasons for The Decrease in Lithium Cycling Efficiency 343
3.6 Morphology of Deposited Lithium 343
3.7 The Amount of Dead Lithium and Cell Performance 345
3.8 Improvement in the Cycling Efficiency of a Lithium Anode 346
3.8.1 Electrolytes 346
3.8.2 Electrolyte Additives 347
3.8.2.1 Stable Additives Limiting Chemical Reaction Between the Electrolyte and Lithium 347
3.8.2.2 Additives Modifying the State of Solvation of Lithium Ions 348
3.8.2.3 Reactive Additives Used to Make a Better Protective Film 348
3.8.3 Stack Pressure on Electrodes 351
3.8.4 Composite Lithium Anode 352
3.8.5 Influence of Cathode on Lithium Surface Film 352
3.8.6 An Alternative to the Lithium-Metal Anode (Lithium-Ion Inserted Anodes) 352
3.9 Safety of Rechargeable Lithium Metal Cells 353
3.9.1. Considerations Regarding Cell Safety 353
3.9.2. Safety Test Results 354
3.9.2.1 External Short 354
3.9.2.2 Overcharge 354
3.9.2.3 Nail Penetration 354
3.9.2.4 Crush 354
3.9.2.5 Heating 354
3.10 Conclusion 354
3.11 References 355

4 Lithium Alloy Anodes 359
Robert A. Huggins

4.1 Introduction 359
4.2 Problems with the Rechargeability of Elemental Electrodes 360
4.3 Lithium Alloys as an Alternative 361
4.4 Alloys Formed in Situ from Convertible Oxides 362
4.5 Thermodynamic Basis for Electrode Potentials and Capacities under Conditions in which Complete Equilibrium can be Assumed 363
4.6 Crystallographic Aspects and the Possibility of Selective Equilibrium 365
4.7 Kinetic Aspects 366
4.8 Examples of Lithium Alloy Systems 368
4.8.1 Lithium–Aluminium System 368
4.8.2 Lithium–Silicon System 368
4.8.3 Lithium–Tin System 370
4.9 Lithium Alloys at Lower Temperatures 371

CosMX Exhibit 1008, Page 16 of 633

4.10 The Mixed-Conductor Matrix Concept 374
4.11 Solid Electrolyte Matrix Electrode Structures 379
4.12 What About the Future ? 379
4.13 References 379

5 Lithiaded Carbons 383
Martin Winter and Jürgen Otto Besenhard

5.1 Introduction 383
5.1.1 Why Lithiated Carbons? 385
5.1.2 Electrochemical Formation of Lithiated Carbons 386
5.2 Graphitic and Non Graphitic Carbons 386
5.2.1 Carbons: Classification, Synthesis, and Structures 387
5.2.2 Lithiated Graphitic Carbons (Li_xC_n) 390
5.2.2.1 In-Plane Structures 390
5.2.2.2 Stage Formation 391
5.2.2.3 Reversible and Irreversible Specific Charge 392
5.2.3 Li_xC_6 vs. $Li_x(solv)_yC_n$ 394
5.2.4 Lithiated Nongraphitic Carbons 398
5.2.5 Lithiated Carbons Containing Heteroatoms 404
5.2.6 Lithiated Fullerenes 405
5.3. Lithiated Carbons vs. Competing Anode Materials 406
5.4 Summary 408
5.5 References 409

6 The Anode/Electrolyte Interface 419
E. Peled, D. Golodnitsky and J. Pencier

6.1 Introduction 419
6.2 SEI Formation Chemical Composition, and Morphology 420
6.2.1 SEI Formation Processes 420
6.2.2 Chemical Composition and Morphology of the SEI 422
6.2.2.1 Ether-Based Liquid Electrolytes 422
6.2.2.2 Carbonate-Based Liquid Electrolyte 424
6.2.2.3 Polymer (PE), Composite Polymer (CPE), and Gelled Electrolytes 426
6.2.3 Reactivity of e^-_{sol} with Electrolyte Components – a Tool for the Selection of Electrolyte Materials 427
6.3 SEI Formation on Carbonaceous Electrodes 429
6.3.1 Surface Structure and Chemistry of Carbon and Graphite 430
6.3.2 The First Intercalation Step in Carbonaceous Anodes 432
6.3.3 Parameters Affecting Q_{IR} 436
6.3.4 Graphite Modification by Mild Oxidation and Chemically Bonded (CB) SEI .. 437
6.3.5 Chemical Composition and Morphology of the SEI 439

CosMX Exhibit 1008, Page 17 of 633

6.3.5.1 Carbons and Graphites 439
6.3.5.2 HOPG 441
6.3.6 SEI Formation on Alloys 443
6.4 Models for SEI Electrodes 443
6.4.1 Liquid Electrolytes 443
6.4.2 Polymer Electrolytes 446
6.4.3 Effect of Electrolyte Composition on SEI Properties 447
6.4.3.1 Lithium Electrode 447
6.4.3.2 Li_xC_6 Electrode 451
6.5 Summary and Conclusions 452
6.6 References 453

7 Liquid Nonaqueous Electrolyte 457
J. Barthel and H.J. Gores

7.1 Introduction 457
7.2 Components of the Liquid Electrolyte 458
7.2.1 The Solvents 458
7.2.2 The Salts 461
7.2.3 Purification of Electrolytes 464
7.3 Intrinsic Properties 465
7.3.1 Chemical Models of Electrolytes 465
7.3.2 Ion-Pair Association Constants 465
7.3.3 Triple-Ion Association Constants 468
7.3.3.1 Bilateral Triple-Ion Formation 468
7.3.3.2 Unilateral Triple-Ion Formation. 468
7.3.3.3 Selective Solvation of Ions and Competition Between Solvation and Ion Association. 471
7.4 Bulk Properties 473
7.4.1 Electrochemical Stability Range 473
7.4.2 Chemical Stability of Electrolytes with Lithium and Lithiated Carbon 479
7.4.3 Conductivity of Concentrated Solutions 485
7.4.3.1 Introduction 485
7.4.3.2 Conductivity-Determining Parameters 486
7.4.3.3 The Role of Solvent Viscosity, Ionic Radii, and Solvation 486
7.4.3.4 The Role of Ion Association 488
7.4.3.5 Effects of Selective Solvation and Competition Between Solvation and Ion Association 488
7.4.3.6 Optimization of Conductivity 490
7.5 References 491

8 Polymer Electrolytes 499
Fiona Gray and Michel Armand

CosMX Exhibit 1008, Page 18 of 633

8.1 Introduction 499
8.2 Solvent-Free Polymer Electrolytes 501
8.2.1 Technology 501
8.2.2 The Fundamentals of a Polymer Electrolyte 502
8.2.3 Conductivity, Structure, and Morphology 503
8.2.4 Second-Generation Polymer Electrolytes 504
8.2.5 Structure and Ionic Motion 506
8.2.6 Mechanisms of Ionic Motion 507
8.2.7 An Analysis of Ionic Species 510
8.2.8 Cation-Transport Properties 510
8.3 Hybrid Electrolytes 512
8.3.1 Gel Electrolytes 513
8.3.2 Batteries 516
8.3.3 Enhancing Cation Mobility 518
8.3.4 Mixed-Phase Electrolytes 518
8.4 Looking to the Future 520
8.5 References 520

9 Solid Electrolytes 525
P. Birke and W. Weppner

9.1 Introduction 525
9.2 Fundamental Aspects of Solid Electrolytes 526
9.2.1 Structural Defects 526
9.2.2 Migration and Diffusion of Charge Carriers in Solids 531
9.3 Applicable Solid Electrolytes for Batteries 533
9.3.1 General Aspects 533
9.3.2 Lithium-, Sodium-, and Potassium-Ion Conductors 536
9.3.3 Capacity and Energy Density Aspects 537
9.4 Design Aspects of Solid Electrolytes 537
9.5 Preparation of Solid Electrolytes 540
9.5.1 Monolithic Samples 540
9.5.1.1 Solid-State Reactions 540
9.5.1.2 The Pechini Method 540
9.5.1.3 Wet Chemical Methods 540
9.5.1.4. Combustion Synthesis and Explosion Methods 541
9.5.1.5 Composites 542
9.5.1.6 Sintering Processes 542
9.5.2 Thick Film Solid Electrolytes 542
9.5.2.1 Screen Printing 542
9.5.2.2 Tape Casting 542
9.5.3 Thin-Film Solid Electrolytes 543
9.5.3.1 Sputtering 543
9.5.3.2 Evaporation 543

CosMX Exhibit 1008, Page 19 of 633

9.5.3.3 Spin-On Coating and Spay Pyrolysis 544
9.6 Experimental Techniques for the Determination of the Properties of Solid Electrolytes 544
9.6.1 Partial Ionic Conductivity 544
9.6.1.1 Direct-Current (DC) Measurements 544
9.6.1.2 Impedance Analysis 545
9.6.1.3 Determination of the Activation Energy 545
9.6.2 Partial Electronic Conductivity 546
9.6.2.1 Determination of the Transference Number 547
9.6.2.2 The Hebb–Wagner Method 547
9.6.2.3 Mobility of Electrons and Holes 548
9.6.2.4 Concentration of Electrons and Holes 549
9.6.3 Stability Window 549
9.6.4 Determination of the Ionics Conduction Mechanism and Related Types of Defects 550
9.7 References 551

10 Separators for Lithium-Ion Batteries 553
R. Spotnitz

10.1 Introduction 553
10.2 How a Battery Separator is Used 553
10.3 Microporous Separator Materials 554
10.4 Gel Electrolyte Separators 557
10.5 Polymer Electrolytes 558
10.6 Characterization of Separators 558
10.7 Mathematical Modeling of Separators 561
10.8 Conclusions 562
10.9 References 562

11 Materials for High Temperature Batteries 565
H. Böhm

11.1 Introduction 565
11.2 The ZEBRA System 566
11.2.1 The ZEBRA Cell 566
11.2.2 Properties of ZEBRA Cells 567
11.2.3 Internal Resistance of ZEBRA Cells 568
11.2.4 The ZEBRA Battery 569
11.3 The Sodium Sulfur Battery 571
11.3.1 The Na / S System [11] 571
11.3.2 The Na / S Cell 572
11.3.3 The Na / S Battery 574

CosMX Exhibit 1008, Page 20 of 633

11.3.4 Corrosion-Resistant Materials for Sodium/Sulfur Cells 575
11.3.4.1 Glass Seal 575
11.3.4.2 Cathode and Anode Seal 575
11.3.4.3 Current Collector for the Sulfur Electrode 576
11.4 Components for High-Temperature Batteries 576
11.4.1 The Ceramic Electrolyte β'' –Alumina 576
11.4.1.1 Doping of β'' - Al_2O_3 577
11.4.1.2 Manufacture of β'' –Alumina Electrolyte Tubes 577
11.4.1.3 Properties of β'' –Alumina Tubes 581
11.4.1.4 Stability of β'' –Alumina and β'' –Alumina 581
11.4.2 The Second Electrolyte $NaAlCl_4$ and the $NaCl - AlCl_3$ System 582
11.4.2.1 Phase Diagram 582
11.4.2.2 Vapor Pressure 583
11.4.2.3 Density 583
11.4.2.4 Viscosity 583
11.4.2.5 Dissociation 584
11.4.2.6 Ionic Conductivity 584
11.4.2.7 Solubility of Nickel Chloride in Sodium Aluminum Chloride 585
11.4.3 Nickel Chloride $NiCl_2$ [41] and the $NiCl_2 - NaCl$ System 586
11.4.3.1 Relevant Properties of $NiCl_2$ 586
11.4.3.2 $NiCl_2 - NaCl$ System 586
11.4.4 Materials for Thermal Insulation 587
11.4.4.1 Multifoil Insulation 587
11.4.4.2 Glass Fiber Boards 588
11.4.4.3 Microporous Insulation 588
11.4.4.4 Comparison of Thermal Insulation Materials 589
11.4.5 Data for Cell 589
11.4.5.1 Nickel [46] 589
11.4.5.2 Liquid Sodium [47] 590
11.4.5.3 NaCl [46] 590
11.4.5.4 Sulfur and Sodium Polysulfides 590
11.5 References 591

List of Symbols 593

Index 605

CosMX Exhibit 1008, Page 21 of 633

List of Contributors

Albering, Jörg H. (II: 1)
Institute for Chemical Technology
of Inorganic Materials
Graz University of Technology
Stremayrgasse 16/III
8010 Graz
Austria

Armand, Michel (III:8)
Departement de Chimie
Université de Montréal
C.P. 6128, Succursale Centre-Ville
Montréal
Québec H3C 3J7
Canada

Barthel, J. (III:7)
Institut für Physikalische und
Theoretische Chemie
der Universität Regensburg
93040 Regensburg
Germany

Berndt, Dietrich (II:4)
Am Weißen Berg 3
61476 Kronberg
Germany

Besenhard, Jürgen Otto (III:5)
Institute for Chemical Technology
of Inorganic Materials
Graz University ofTechnology
Stremayrgasse 16/III
8010 Graz
Austria

Binder, L. O. (II:6)
Institute for Chemical Technology
of Inorganic Materials
Graz University of Technology
Stremayrgasse 16/III
8010 Graz
Austria

Birke, P. (III:9)
Christian-Albrechts University
Technical Faculty
Chair for Sensors and Solid State Ionics
Kaisestr. 2
24143 Kiel
Germany

Böhm, H. (IV)
AEG Anglo Batteries GmbH
Söflinger Straße 100
89077 Ulm
Germany

Böhnstedt, Werner (II:9)
Daramic, Inc.
Erlengang 31
22844 Norderstedt
Germany

Daniel-Ivad, Josef(I:3)
Battery Technologies,Inc.
Richmond Hill
Ontario L4B 1C3
Canada

Drobits, J. (II:5)
Institut für Technische Elektrochemie
Technische Universität Wien
Getreidemarkt 9/158
1060 Wien
Austria

Fabjan, Ch. (II:5)
Institut für Technische Elektrochemie
Technische Universität Wien
Getreidemarkt 9/158
1060 Wien
Austria

Furukawa, Nobuhiro (I:2)
Electrochemistry Department
New Materials Research Center
Sanyo Electric Co., Ltd.
1-18-13 Hashiridani
Hirakata City
Osaka 573-8534
Japan

Golodnitsky, D. (III:6)
Department of Chemistry
Tel Aviv University
Tel Aviv 69978
Israel

Gores, J. (III:7)
Institut für Physikalische und
Theoretische Chemie
der Universität Regensburg
93040 Regensburg
Germany

Gray, Fiona (III:8)
School ofChemistry
University of St Andrews
The Purdie Building
North Haugh
St Andrews
Fife KY16 9ST
UK

Hambitzer, Günther (I: 1)
FORTU BAT
Batterien GmbH
Wöschbacherstr. 37
76327 Pfinztal
Germany

Hoffmann, D. (III: 10)
Hoechst Celanese Corp.
Separations Products Division
Charlotte
North Carolina 28273
USA

Huggins, Robert A. (III:4)
Technical Faculty
Christian-Albrechts-University
Kaiserstr. 2
24143 Kiel
Germany

Kinoshita, K. (II:8)
Energy and Environment Division
Lawrence Berkeley Laboratory
Berkeley
California 94720
USA

Kozawa, Akiya (II:2)
ITE Battery Research Institute
39 Youke, Ukino
Chiaki-cho
Ichinomiyashi
Aichi-ken 491
Japan

Kordesch, Karl (I:3)
Institute for Chemical Technology
ofInorganic Materials
Graz University of Technology
Stremayrgasse 16/III
8010 Graz
Austria

McBreen, James (II:3)
Department of Applied Science
Brookhaven National Laboratory
Upton
New York 1 1973
USA

CosMX Exhibit 1008, Page 23 of 633

Nishio, Koji (I:2)
Electrochemistry Department
New Materials Research Center
Sanyo Electric Co., Ltd.
1-18-13 Hashiridani
Hirakata City
Osaka 573-8534
Japan

Ohzuku, Tsutomu (III:2)
Department of Applied Chemistry
Faculty of Engineering
Osaka City University
Sugimoto 3-3-138
Sumiyoshi
Osaka 558-8585
Japan

Peled, Emanuel (III:6)
Department of Chemistry
Tel Aviv University
Tel Aviv 69978
Israel

Penciner, J. (III:6)
Department ofChemistry
Tel Aviv University
Tel Aviv 69978
Israel

Pinkwart, Karsten (I: 1)
Institut für Chemische Technologie
J.-v.-Frauenhofer-Str. 7
76327 Pfinztal
Germany

Reilly, James J. (II:7)
Department of Applied Science
Brookhaven National Laboratory
Upton
New York 1 1973
USA

Ripp, Christiane (I: 1)
Institut für Chemische Technologie
J.-v.-Frauenhofer-Str. 7
76327 Pfinztal
Germany

Schiller, Christian (I: 1)
Institut für Chemische Technologie
J.-v.-Frauenhofer-Str. 7
76327 Pfinztal
Germany

Schuster, Peter (II: 5)
Institut für Technische Elektrochemie
Technische Universität Wien
Getreidemarkt 9/158
1060 Wien
Austria

Shirai, H. (III: 10)
Hoechst Celanese Corp.
Separations Products Division
Charlotte
North Carolina 28273
USA

Spotnitz, R. (III: 10)
Hoechst Celanese Corp.
Separations Products Division
Charlotte
North Carolina 28273
USA

Thackeray, Michael M. (III: 1)
Electrochemical Technology Program
Chemical Technology Division
Argonne National Laboratory
Argonne
Illinois 60439
USA

CosMX Exhibit 1008, Page 24 of 633

Tobishima, Shin-ichi (III: 3)
NTT Integrated Information &
Energy Systems Laboratories
Tokai-mura
Ibaraki-ken 3 19-1 1
Japan

Weppner, W. (III:9)
Christian-Albrechts University
Technical Faculty
Chair for Sensors and Solid State Ionics
Kaisestr. 2
24143 Kiel
Germany

Winter, Martin (III: 5)
Institute for Chemical Technology
of Inorganic Materials
Graz University of Technology
Stremayrgasse 16/III
8010 Graz
Austria

Yamaki, Jun-ichi (III: 3)
NTT Integrated Information &
Energy Systems Laboratories
Tokai-mura
Ibaraki-ken 3 19-1 1
Japan

Yamamoto, Kohei (II:2)
Fuji Electrochemical Co.
Washizu, Kosai-shi
Shizuoka-Ken 431
Japan

Yoshio, Masaki (II:2)
Saga University
Faculty of Science & Engineering
Dept. of Industrial Chemistry
Honjyo-cho, Saga 840
Japan

CosMX Exhibit 1008, Page 25 of 633

Part I:
Fundamentals and General Aspects of Electrochemical Power Sources

1 Thermodynamics and Mechanistics

G. Hambitzer, K. Pinkwart, C. Ripp, C. Schiller

1.1 Electrochemical Power Sources

Electrochemical power sources convert chemical energy into electrical energy. At least two reaction partners undergo a chemical process during operation. The energy of this reaction is available as electric current at a defined voltage and time [1].

Electrochemical power sources differ from others, such as thermal power plants, by the fact that the energy conversion occurs without any intermediate steps; for example, in the case of thermal power plants fuel is first converted in thermal energy, and finally electric power is produced using generators. In the case of electrochemical power sources this otherwise multistep process is achieved directly in only one step. As a consequence, electrochemical systems show some advantages, such as energy efficiency.

The various existing types of electrochemical storage system differ in the nature of the chemical reaction, structural features and form, reflecting the large number of possible applications.

The single system generally consists of one electrochemical cell — the so-called galvanic element [1]. This supplies a relatively low cell voltage of 0.5–4V. To reach a higher voltage the cells can be connected in series with others, and for a higher capacity it is necessary to link them parallel. In both cases the resulting ensemble is called a battery.

Depending on the principle of operation, cells are classified in the following three groups.

(1) *Primary cells* are non rechargeable cells, in which the electrochemical reaction is irreversible. They contain only a fixed amount of the reacting compounds and are discharged only once. If the educts are consumed by discharging, the cell cannot, or should not, be used again. A well-known example of a primary cell is the Daniell element, consisting of zinc and copper.

(2) *Secondary cells* (accumulators) are rechargeable several times [1]. Only reversible electrochemical reactions offer such a possibility. After the cell is discharged, externally applied electrical energy forces a reversal of the electrochemical process; as a consequence, the reactants exist in their original form again and the stored electrochemical energy can be used again by the consumer. The process should be reversible hundreds or even thousands of times, so that the lifetime is lengthened. This is a fundamental advantage, especially with regard to the important aspect

CosMX Exhibit 1008, Page 27 of 633

of the purchasing costs, which are normally much higher than those of primary cells. Furthermore, the resulting environmental friendliness should also be taken into account.

(3) *Fuel cells* [2], in contrast with the previous cells described above, operate in a continuous process. The reactants — nowadays often hydrogen and oxygen — must be fed continuously into the cell from outside.

Typical fields of application for electrochemical systems are SLI batteries (starter–light–ignition) in cars and electric devices for providing emergency current or, in the future, powering for vehicles. A growing number of other new areas of application is also accessible, e.g., as current sources for portable devices such as cellular phones, notebooks, cordless tools, etc. These new applications are often related to the necessity for low weight. In addition, they should have a large storage capacity and high specific energy densities. Most of the applications mentioned could be covered by primary batteries, but economic and ecological reason lead to the use of secondary systems.

Apart from the improvement and scaling up of known systems such as the lead accumulator or the nickel/cadmium cell, new types of cells have also been developed. Here, rechargeable lithium batteries and nickel–systems seem to be the most promising; the reason for this will be apparent from the following sections [3].

To judge which battery systems are reasonable for a possible application, a wide knowledge of the principles of functioning and the different materials utilized is necessary. The following sections therefore present a short introduction on this topic and on the basic mechanisms of batteries [4]. Finally, an initial view of some important criteria for comparing different systems is given.

1.2 Electrochemical Fundamentals

1.2.1 The Electrochemical Cell

A characteristic feature of an electrochemical cell is that the electronic current, which is the movement of electrons in the external circuit, is generated by the electrochemical processes at the electrodes. In contrast to the electronic current, the charge is transported between the positive and the negative electrode in the electrolyte by ions. Generally the current in the electrolyte consists of the movement of negative and positive ions.

The simplified electrode processes are shown schematically in Fig. 1. Starting with an open circuit, when a metal A is dipped into the solution, it partly dissolves and electrons remain at the electrode until a characteristic electron density has been built up. For metal B, which is more noble than A (see Sec. 1.2.2), the same process takes place, but the amount of dissolution and therefore the resulting electron density are lower.

If these two electrodes are connected by an electronic conductor, the electron flow starts from the negative electrode (with higher electron density) to the positive electrode. The electrode A/electrolyte system tries to keep the electron density constant. As a consequence additional metal A dissolves at the negative electrode, forming A^+ in solution and electrons e^-, which are located on the surface of metal A:

$$A \rightarrow A^+ + e^- \qquad (1)$$

CosMX Exhibit 1008, Page 28 of 633

At the positive electrode the electronic current results in an increasing electron density. The electrode B/electrolyte system compensates this process by the consumption of electrons for the deposition of B^+ ions:

$$B^+ + e^- \rightarrow B \qquad (2)$$

The electronic current stops if one of the following conditions is fulfilled:

- the base metal A is completely dissolved, or
- all B^+ ions are precipitated

It is therefore necessary to add a soluble salt to the positive electrode compartment to maintain the current for a longer period. This salt consists of B^+ ions and corresponding negative ions. The two electrode compartments are divided by an appropriate separator to prevent the migration and the deposition of B^+ ions at the negative electrode A. Since this separator blocks the exchange of positive ions, only the negative ions are responsible for the charge transport in the cell.

This means that, for each electron flowing in the outer circuit from the negative to the positive electrode, a negative ion in the electrolyte diffuses to the negative electrode compartment.

Generally, the limiting factor for the electronic current flow is the transport of these ions. Therefore the electrolyte solution should have a low resistance.

An electrolyte may be characterized by resistance $\rho[\Omega\,\mathrm{cm}]$, which is defined as the resistance of the solution between two electrodes at a distance of 1 cm and an area of $1\,\mathrm{cm}^2$. The reciprocal value is called the specific conductivity $\kappa\,[\Omega^{-1}\,\mathrm{cm}^{-1}]$ [5]. For comparison the values of κ for various materials are given in Fig. 2; Here is a wide spread for different electrolyte solutions. The selection of a suitable, high-conductivity electrolyte solution for an electrochemical cell depends on its compatibility with other components, such as the positive and negative electrodes.

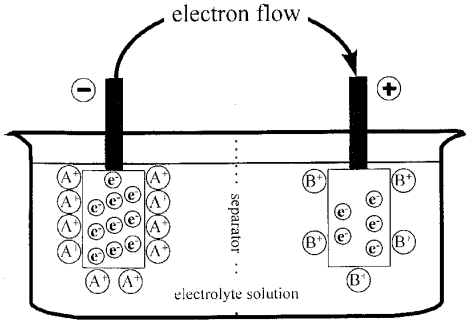


Figure 1. Electrochemical cell with negative and positive electrodes

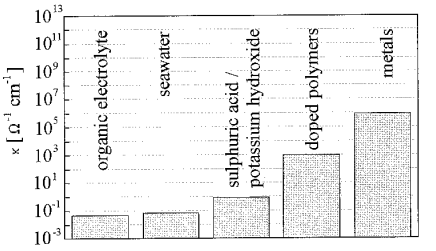


Figure 2. Comparison of the specific conductivity of different materials.

From the chemical viewpoint, the galvanic cell is a current source in which a local separation of oxidation and reduction process exists. This is explained below by the example of the Daniell element (Fig. 3). Here the galvanic cell contains copper as the positive electrode, zinc as the nega-

CosMX Exhibit 1008, Page 29 of 633

tive electrode, and their corresponding ion sulfates as the aqueous electrolyte.

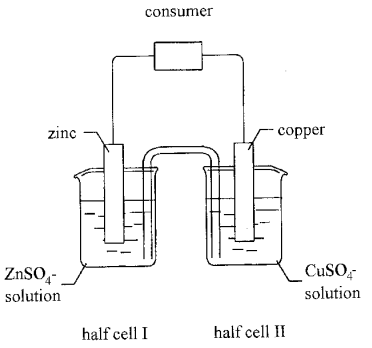


Figure 3. Daniell element

A salt bridge serves as an ion-conducting connection between the two half-cells. When the external circuit is closed, the oxidation reaction starts with the dissolution of the zinc electrode and the formation of zinc ions in half-cell I. In half-cell II copper ions are reduced and metallic copper is deposited. The sulfate ions remain unchanged in the aqueous solution. The overall cell reaction consists of an electron transfer between zinc and copper ions:

oxidation/half-cell I:

$$Zn \rightarrow Zn^{2+} + 2e^- \quad (3)$$

reduction/half-cell II:

$$Cu^{2+} + 2e^- \rightarrow Cu \quad (4)$$

overall cell reaction:

$$Zn + Cu^{2+} \rightarrow Zn^{2+} + Cu \quad (5)$$

A typical feature of a redox reaction is an exchange of electrons between at least two reaction partners. It is characterized by the fact that oxidation and reduction always occur at the same time. For the Daniell element the copper ions are the oxidizing agent and the zinc ions the reducing agent. Both together form the corresponding redox pair:

$$Red_1 + Ox_2 \rightarrow Ox_1 + Red_2 \quad (6)$$

$$CuSO_4 + Zn \rightarrow ZnSO_4 + Cu \quad (7)$$

The electrode where the oxidation dominates during discharge is called the anode (negative pole); the other electrode where the reduction predominates, is the cathode (positive pole).

1.2.2 The Electrochemical Series of Metals

The question arises as to which metal is dissolved, and which one is deposited, when combined in an electrochemical cell. The electrochemical series indicates how easily a metal is oxidized or its ions are reduced, i.e., converted into positively charged ions or metal atoms respectively. The standard potential serves for the comparison of different metals.

In galvanic cells it is only possible to determine the potential difference as a voltage between two half-cells, but not the absolute potential of the single electrode. To measure the potential difference it has to be ensured that an electrochemical equilibrium exists at the phase boundaries, e.g., at the electrode/electrolyte interface. At the least it is required that there is no flux of current in the external and internal circuits.

To compare the potentials of the half-cells a reference must be defined. For this reason it was decided, arbitrarily, that the

CosMX Exhibit 1008, Page 30 of 633

potential of the hydrogen electrode in a $1\,mol\,L^{-1}$ acidic solution is equal to 0 V at a temperature of 25°C and a pressure of 101.3 kPa. These are called standard conditions [6].

The reaction of hydrogen in acidic solution is a half-cell reaction and can therefore be handled like the metal/metal salt solution system:

$$H_2 + 2H_2O \rightarrow 2H_3O^+ + 2e^- \quad (8)$$

An experimental set-up for the hydrogen half-cell is illustrated in Fig. 4.

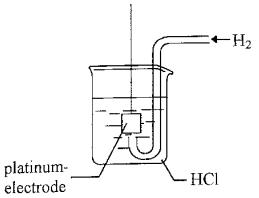


Figure 4. Hydrogen electrode with hydrogen-saturated platinum electrode in hydrochloric acid.

The potentials of the metals in their $1\,mol\,L^{-1}$ salt solution are all related to the standard or normal hydrogen electrode (NHE). For the measurement, the hydrogen half-cell is combined with another half-cell to form a galvanic cell. The measured voltage is called the normal potential or standard electrode potential, E^0 of the metal. If the metals are ranked according to their normal potentials, the resulting order is called the electrochemical series of metals (Fig. 5). Depending on their position on this potential series, they are known as base ($E^0 < 0$) or noble ($E^0 > 0$) metals.

$$Zn \rightarrow Zn^{2+} + 2e^- \quad E^0 = -0.76\,V_{NHE} \quad (9)$$

$$Cu \rightarrow Cu^{2+} + 2e^- \quad E^0 = +0.34\,V_{NHE} \quad (10)$$

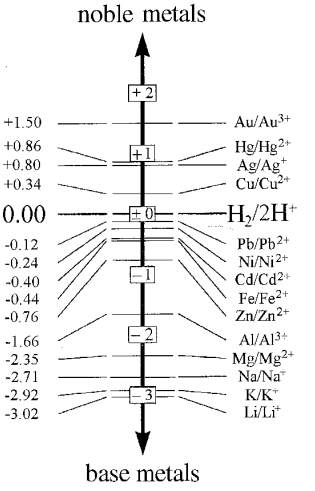
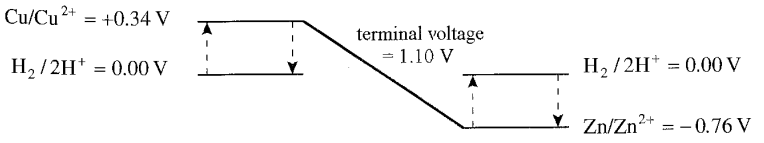


Figure 5. Electrochemical series of metals and their standard potentials in volt (measured against NHE).

For the Daniell element in Fig. 3, a potential difference $\Delta\varepsilon_{00}$ is obtained by calculation from the values in Fig. 5 according to Eq. (11); under equilibrum conditions the potential difference corresponds to the terminal voltage of the cell.

$$\Delta\varepsilon_{00} = E^0(Cu/Cu^{2+}) - E^0(Zn/Zn^{2+}) \quad (11)$$



CosMX Exhibit 1008, Page 31 of 633

If there are no standard conditions or in the case where it is not be possible to measure the standard potential, the value can be determined by thermodynamic calculations (see Sec. 1.3.2).

For the application of a galvanic cell as a power source, the half-cells are chosen in such a way that their potentials $\varepsilon_{I,II}$ are spread as far apart as possible. It is thus clear why alkaline metals, especially lithium or sodium, are interesting as new materials for the negative electrode. Besides having a strongly negative standard potential, with their relatively low density, a high specific energy can be realized by combination with a positive electrode.

Comparison of the Daniell element, the nickel/cadmium accumulator, and, the lithium/manganese dioxide primary cell, as examples, shows the influence of the electrode materials on different cell parameters (Table 1).

1.2.3 Discharging

During the discharge process electrons are released at the anode from the electrochemical active material, which is oxidized. At the same time cathodic substances are reduced by receiving electrons. The transport of the electrons occurs through an external consumer.

At the anode, a relationship, known as Faraday's first law, exists between the electronic current I and the mass m of the substance which donates electrons [7]:

$$m = \frac{M}{zF} \cdot It \tag{12}$$

where m = active mass, M = molar mass, z = number of electrons exchanged, and F = Faraday constant = 96485 C mol^{-1} = 26.8 Ah mol^{-1}.

The Faraday constant is the product of the elementary charge e (1.602×10^{-19} C) and the Avogadro constant N_A (6.023×10^{23} mol^{-1}):

$$F = \frac{It}{n} = \frac{Q}{n} = N_A e \tag{13}$$

where Q = quantity of electricity (electric charge) and n = number of moles of electrons exchanged.

Table 1. Comparison of the cell parameters of various cells [4]

Cell type	Cell reaction	Standard potential (V)	Terminal voltage, $\Delta\varepsilon_{00}$ (V)	Capacity (Ah kg^{-1})	Specific energy (Wh kg^{-1})
Daniell primary	$Zn + CuSO_4 \rightarrow ZnSO_4 + Cu$	$E^0(Zn/Zn^{2+}) = -0.76$ $E^0(Cu/Cu^{2+}) = 0.34$	1.10	238.2	262
Ni/Cd accumulator	$Cd + 2NiOOH + 2H_2O \rightarrow$ $Cd(OH)_2 + 2Ni(OH)_2$	$E^0(Cd/Cd^{2+}) = -0.81$ $E^0(Ni^{2+}/Ni^{3+}) = 0.49$	1.30	161.5	210
Li/MnO_2 primary	$Li + MnO_2 \rightarrow LiMnO_2$	$E^0(Li/Li^+) = -3.04$ $E^0(Mn^{3+}/Mn^{4+}) = 0.16$	3.20	285.4	856.3

CosMX Exhibit 1008, Page 32 of 633

For the Daniell element the electron-donating reaction is the oxidation of zinc. The active mass m which is necessary to deliver a capacity of 1 Ah, is calculated as follows:

$$Zn \rightarrow Zn^{2+} + 2e^-$$

$$M = 65{,}4\ \text{g mol}^{-1},\ z = 2,$$
$$F = 26.8\ \text{Ah mol}^{-1},\ Q = 1\ \text{Ah}$$

$$m = \frac{M}{zF} \cdot Q$$
$$= 1.22\ \text{g}$$

Of course, the Faraday's first law applies for cathodic processes as well. Therefore the deposition of 1 Ah of copper ions results in an increase in the electrode mass of $m = 1.18$ g.

In addition Faraday recognized that, for different electrode reactions and the same amount of charge, the ratio of the reacting masses is equal to the ratio of the equivalent masses:

$$\frac{m_A}{m_B} = \frac{M_A|z_B|}{M_B|z_A|} \qquad (14)$$

The ratio in Eq. (14) expresses the fact that 1 mol of electrons discharges

- 1 mol of monovalent ions,
- 0.5 mol of bivalent ions, or
- $1/z$ mol of z-valent ions

1.2.4 Charging

The charging process should only be applied for secondary cells, because the electrochemical reactions are reversible, in contrast to primary cells. Charging of primary cells, may lead to electrochemical side reactions, e.g., the decomposition of the electrolyte solution with possibly dangerous follow-up reactions which may even result in explosions [8].

Generally ions are reduced at the negative electrode during charging, an oxidation process takes place at the positive electrode. The voltage source must deliver a charge voltage which is at least equivalent to the difference, $\Delta\varepsilon_{00}$, between the equilibrium potentials of the two half-cells. Generally the charge voltage is higher than $\Delta\varepsilon_{00}$.

1.3 Thermodynamics

1.3.1 Electrode Processes at Equilibrium

Similarly to chemical reactions, it is possible to treat electrochemical reactions in equilibrium with the help of the thermodynamics.

Besides measuring the potential in the standard conditions, it is possible to calculate its value from thermodynamic data [9]. In addition one can determine the influence of changing pressure, temperature, concentration, etc.

During the determination of standard electrode potentials an electrochemical equilibrium must always exist at the phase boundaries, e.g. that of the electrode/electrolyte. From a macroscopic viewpoint no external current flows and no reaction takes place. From a microscopic viewpoint or a molecular scale, a continuous exchange of charges occurs at the phase boundaries. In this context Fig. 6 demonstrates this fact at the anode of the Daniell element.

CosMX Exhibit 1008, Page 33 of 633

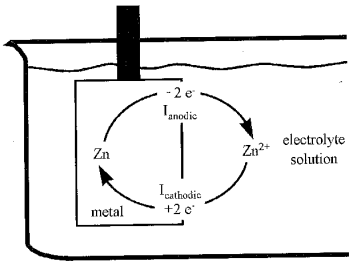


Figure 6. Metal (zinc)/ electrolyte solution (zinc sulfate) phase boundary in the equilibrium state.

The exchange of charge carriers in the molecular sphere at the zinc/electrolyte solution phase boundary corresponds to equal anodic and cathodic currents. These compensate each other in the case of equilibrium.

Three kinds of equilibrium potentials are distinguishable.[1] A metal-ion potential exists if a metal and its ions are present in balanced phases, e.g., zinc and zinc ions at the anode of the Daniell element.[2] A redox potential can be found if both phases exchange electrons and the electron exchange is in equilibrium: for example, the normal hydrogen half-cell with an electron transfer between hydrogen and protons at the platinum electrode. In the case where a couple of different ions are present, of which only one can cross the phase boundary — a situation which may exist at a semipermeable membrane — one obtains a so called membrane potential. Well-known examples are the sodium/potassium ion pumps in human cells.

1.3.2 Reaction Free Energy ΔG and Equilibrium Cell Voltage $\Delta\varepsilon_{00}$

Instead of the possibility of directly measuring the equilibrium cell voltage $\Delta\varepsilon_{00}$ in standard conditions, it can be calculated from the reaction free energy ΔG for one formula conversion. In this context one of the fundamental equations is the Gibbs-Helmholtz relation, Eq. (15) [7].

$$\Delta G = \Delta H - T\Delta S \tag{15}$$

For the electrochemical cell reaction, the reaction free energy ΔG is the utilizable electrical energy. The reaction enthalpy ΔH is the theoretical available energy, which is increased or reduced by an amount $T\Delta S$. The product of the temperature and the entropy describes the amount of heat consumed or released reversibly during the reaction. With tabulated values for the enthalpy and the entropy it is possible to obtain ΔG.

Using the reaction free energy ΔG, the cell voltage $\Delta\varepsilon_0$ can be calculated. At first, the number n of moles of electrons exchanged during an electrode reaction must be determined from the cell reaction. For the Daniell element (see example), two moles of electrons are released or received, respectively:

$$1\,\text{mol Zn} \rightarrow 1\,\text{mol Zn}^{2+} + 2\,\text{mol e}^- \tag{16}$$

$$1\,\text{mol Cu} \rightarrow 1\,\text{mol Cu}^{2+} + 2\,\text{mol e}^- \tag{17}$$

With the definition of the Faraday constant (Eq. 13) the amount of charge for the cell reaction for one formula conversion is given by Eq. (18):

$$Q = It = nF \tag{18}$$

This quantity of charge results in the electrical energy:

$$\Delta\varepsilon_{00} \cdot Q = \Delta\varepsilon_{00} \cdot nF \tag{19}$$

Thermodynamic considerations require the

CosMX Exhibit 1008, Page 34 of 633

cell reaction to be reversible during one formula conversion. This means that all partial processes in a cell remain in equilibrium. The current is kept infinitely small, so that the cell voltage $\Delta\varepsilon_0$ and the equilibrium cell voltage $\Delta\varepsilon_{00}$ are equal. Furthermore, inside the cell no gradient in the concentration in the electrolyte should exist, i.e., the zinc- and copper-ion concentrations must be constant throughout the Daniell element. For these conditions the utilizable electrical energy $\Delta\varepsilon_{00} \cdot zF$ per mol corresponds to the reaction free energy ΔG of the galvanic cell, which during the cell reaction anoints to

$$\Delta G = -zF\Delta\varepsilon_{00} \tag{20}$$

For the Daniell element under standard conditions (T = 298 K),

$$Zn + CuSO_4 \longrightarrow ZnSO_4 + Cu$$

reaction enthalpy: $\Delta H = -210.1\,\mathrm{kJ\,mol^{-1}}$

entropy: $\Delta S = -7.2\,\mathrm{J\,K^{-1}\,mol^{-1}}$

reaction free energy: $\Delta G = \Delta H - T\Delta S$

$\Delta G = -208\,\mathrm{kJ\,mol^{-1}}$

Faraday constant: $F = 96485\,\mathrm{C\,mol^{-1}}$

number of exchanged electrons: $z = 2$

cell voltage:

$$\Delta\varepsilon_{00} = -\frac{\Delta G}{zF}\left[\frac{\mathrm{kJ\,mol^{-1}}}{\mathrm{C\,mol^{-1}}}\right] = 1.1\,\mathrm{V}$$

1.3.3 Concentration Dependence of the Equilibrium Cell Voltage

It is established by chemical thermodynamics that the sum of the chemical potentials μ_i of the substances ν_i involved in the gross reaction are equal to the reaction free energy.

$$\Delta G = \sum \nu_i \cdot \mu_i \tag{21}$$

Here ν_i the stoichiometric factors of the i the compound used in the equation for the cell reaction, having a plus sign for the substances formed and a negative sign for the compounds consumed.

As a result of the combination of Eqs. (20) and (21), the reaction free energy, ΔG, and the equilibrium cell voltage, $\Delta\varepsilon_{00}$, under standard conditions are related to the sum of the chemical potentials μ_i of the substances involved:

$$-\frac{\Delta G}{zF} = \Delta\varepsilon_{00} = \frac{1}{zF}\sum \nu_i \cdot \mu_i \tag{22}$$

It was mentioned earlier that the equilibrium cell voltage $\Delta\varepsilon_{00}$ is equal to the difference between the equilibrium potentials of its half-cells; e.g., for the Daniell element,

$$\Delta\varepsilon_{00} = E^0(\mathrm{Cu/Cu^{2+}}) - E^0(\mathrm{Zn/Zn^{2+}}) \tag{11}$$

The chemical potential of one half-cell depends on the concentration c_i of the compounds which react at the electrode:

$$\mu_i = \mu_{i,0} + RT \ln c_i \tag{23}$$

where R = universal gas constant = 8.3 $\mathrm{J\,mol^{-1}\,K^{-1}}$

As a consequence, the equilibrium potential of the single half-cell also depends on the concentrations of the compounds involved. The Nernst equation [Eq. (24)], which is one of the most important electrochemical relations, explains this context

CosMX Exhibit 1008, Page 35 of 633

[10]. It results if Eq. (23) is inserted into Eq. (22) with regard to one half-cell:

$$\Delta\varepsilon_0 = \Delta\varepsilon_{00} + \frac{RT}{zF} \cdot \sum \nu_i \cdot \ln c_i \qquad (24)$$

For a metal-ion electrode, the Nernst equation is:

$$\Delta\varepsilon_0 = \Delta\varepsilon_{00} + \frac{RT}{zF} \ln\left(\frac{c_{Me^{2+}}}{c_{Me}}\right) \qquad (25)$$

which may be used, for example, for the calculation of the concentration dependence of the zinc electrode.

For one half-cell of the Daniell element at a temperature of T = 298 K,

$$Zn \longrightarrow Zn^{2+} + 2e^-$$

concentration: $c_{Zn^{2+}} = 0.1\,mol\,L^{-1}$
universal gas constant: $R = 8.3\,J\,mol^{-1}\,K^{-1}$
Faraday constant: $F = 96485\,C\,mol^{-1}$
number of exchanged electrons: $z = 2$
standard potential vs. NHE:

$$\Delta\varepsilon_{00}(Zn/Zn^{2+}) = -0.76\,V$$

$$\Delta\varepsilon_0 = \Delta\varepsilon_{00} + \frac{RT}{zF} \ln\left(\frac{c_{Zn^{2+}}}{c_{Zn}}\right)$$
$$= -0.79\,V$$

The variation of the concentration from 1 $mol\,L^{-1}$ (standard condition) to 0.1 $mol\,L^{-1}$ is related to a change in the potential of –0.03 V.

If the concentrations of the copper and zinc ions within a Daniell element are known, the cell voltage $\Delta\varepsilon_0$ results as follows:

$$\Delta\varepsilon_0 = \varepsilon_0(Cu/Cu^{2+}) - \varepsilon_0(Zn/Zn^{2+}) \qquad (26)$$

1.3.4 Temperature Dependence of Equilibrium Cell Voltage

The temperature dependence of the equilibrium cell voltage forms the basis for determining the thermodynamic variables ΔG, ΔH, and ΔS. The values of the equilibrium cell voltage $\Delta\varepsilon_{00}$ and the temperature coefficient $d\Delta\varepsilon_{00}/dT$, which are necessary for the calculation, can be measured exactly in experiments.

The temperature dependence of the cell voltage $\Delta\varepsilon_0$ results from Eq. (20) by partial differentiation at constant cell pressure:

$$\left(\frac{\partial\Delta\varepsilon_0}{\partial T}\right)_p = -\frac{1}{zF}\left(\frac{\partial\Delta G}{\partial T}\right)_p \qquad (27)$$

The temperature coefficient of the reaction free energy follows, through thermodynamic relationships [7], by partial differentiation of Eq. (15):

$$\left(\frac{\partial\Delta G}{\partial T}\right)_p = -\Delta S \qquad (28)$$

$$\left(\frac{\partial\Delta\varepsilon_0}{\partial T}\right)_p = -\frac{1}{zF}(-\Delta S)_p \qquad (29)$$

The reversible reaction heat of the cell is defined as the reaction entropy multiplied by the temperature [Eq. (15)]. For an electrochemical cell it is also called the Peltier effect and can be described as the difference between the reaction enthalpy ΔH and the reaction free energy ΔG. If the difference between the reaction free energy ΔG and the reaction enthalpy ΔH is below zero, the cell becomes warmer. On the other hand, for a difference larger than zero, it cools down. The reversible heat W of the electrochemical cell is therefore:

CosMX Exhibit 1008, Page 36 of 633

$$W = \Delta G - \Delta H = -T\Delta S \quad (30)$$

For the Daniell element in standard conditions, T = 298 K:

$$Zn + CuSO_4 \longrightarrow ZnSO_4 + Cu$$

reaction enthalpy: $\Delta H = -210.1\,kJ\,mol^{-1}$
reaction free energy: $\Delta G = -208\,kJ\,mol^{-1}$
heat: $W = \Delta G - \Delta H = 2.1\,kJ\,mol^{-1}$

The reversible amount of heat $2.1\,kJ\,mol^{-1}$ is consumed by charging, and released by discharging.

The relation between reaction free energy, temperature, cell voltage, and reversible heat in a galvanic cell is reflected by the Gibbs–Helmholtz equation [Eq. (31)].

$$\Delta H = \Delta G - T\left(\frac{\partial \Delta G}{\partial T}\right)_p \quad (31)$$

Insertion of Eq. for ΔG results in

$$\Delta H = zF\left[\Delta\varepsilon_{00} + T\left(\frac{\partial \Delta\varepsilon_0}{\partial T}\right)_p\right] \quad (32)$$

Earlier it was deduced for ΔS and ΔG:

$$\Delta S = zF\left(\frac{\partial \Delta\varepsilon_0}{\partial T}\right)_p \quad (33)$$

$$\Delta G = -zF\Delta\varepsilon_0 \quad (34)$$

From experiments it is possible to obtain the temperature coefficient for the Daniell element, $\Delta\varepsilon_0 / T = -3.6 \times 10^{-5}\,V\,K^{-1}$:

temperature: $T = 298\,K$
equilibrium cell voltage: $\Delta\varepsilon_{00} = 1.1\,V$
Faraday constant: $F = 96485\,C\,mol^{-1}$
number of exchanged electrons: $z = 2$

reaction enthalpy:

$$\Delta H = zF\left[\Delta\varepsilon_{00} + T\left(\frac{\partial \Delta\varepsilon_0}{\partial T}\right)_p\right] = 212.2\,kJ\,mol^{-1}$$

reaction entropy:

$$\Delta S = zF\left(\frac{\partial \Delta\varepsilon_0}{\partial T}\right)_p = -2.1\,kJ\,K^{-1}$$

reaction free energy:

$$\Delta G = -zF\Delta\varepsilon_0 = 208\,kJ\,mol^{-1}$$

The calculation of the reaction free energy is possible with Eq. (34) and the determination of the reaction entropy ΔS follows from Eq. (33).

1.3.5 Pressure Dependence of the Equilibrium Cell Voltage

It is clear that the cell voltage is nearly independent of the pressure if the reaction takes place between solid and liquid phases, where the change in volume is negligibly low. On the other hand, in reactions involving the evaluation or disappearance of gases this volume has to be considered [11].

The pressure dependence of the reaction free energy is equivalent to the volume change resulting from one formula conversion:

$$\left(\frac{\partial \Delta G}{\partial p}\right)_T = \Delta V \quad (35)$$

CosMX Exhibit 1008, Page 37 of 633

With $\Delta G = -nF\Delta\varepsilon_0$ and $\Delta V = -RT/p$, Eq. (36) results

$$\left(\frac{\partial\Delta\varepsilon_0}{\partial p}\right)_T = -\frac{RT}{nF}\cdot\frac{1}{p} \tag{36}$$

By integration the dependence of the equilibrium cell voltage on the partial pressure of the dissolved gas (with the integration constant K equivalent to $\Delta\varepsilon_{00}$ [10]) is obtained.

$$\Delta\varepsilon_0 = K - \frac{RT}{nF}\ln p \tag{37}$$

The example of a hydrogen/oxygen fuel cell illustrates this relationship.

For a hydrogen/oxygen fuel cell at standard conditions, T = 298 K and p = 101.3 kPa, an increase of the pressure to 1013 kPa results in:

Cell reaction:

$$2H_2 + O_2 \rightarrow 2H_2O$$

standard potential (oxygen):

$$E^0 = +1.23\ \text{V}$$

standard potential (hydrogen):

$$E^0 = 0\ \text{V}$$

standard cell voltage:

$$\Delta\varepsilon_{00} = +1.23\ \text{V}_{\text{NHE}}$$

For the anode,

$$\varepsilon_0 = E^0 + \frac{RT}{nF}\ln p_{O_2}$$
$$= 1.23\ \text{V} + 0.03\ \text{V}$$
$$= 1.26\ \text{V}$$

For the cathode,

$$\varepsilon_0 = E^0 - \frac{RT}{nF}\ln p_{H_2}^2$$
$$= 0\ \text{V} - 0.06\ \text{V}$$
$$= -0.06\ \text{V}$$

$$\Delta\varepsilon_0 = 1.26\ \text{V} - (-0.06\ \text{V}) = 1.32\ \text{V}$$

The increase in the standard cell voltage is 0.09 V at the higher pressure.

1.3.6 Overpotential of Half-Cells and Internal Resistance

The potential of the electrode surface is determined by the Nernst equation introduced in Sec. 1.3.3. In an equilibrium, the currents in anodic and cathodic directions are equal. If they are related to an electrode area, they are called exchange-current densities, j_0:

$$j_a = |j_c| = j_0 \tag{38}$$

where j_a and j_c are the anodic and cathodic current densities (A cm^{-2}), respectively.

If a current flows, for example while discharging a battery, a shift in the potential of the single half-cell is measured. This deviation is called over-potential, η [12]. Thus, the real potential $\Delta\varepsilon_{\text{real}}$ has to be calculated with Eq. (39):

$$\Delta\varepsilon_{\text{real}} = \Delta\varepsilon_0 - \sum|\eta| \tag{39}$$

It is clear that for a half-cell the sum of the overpotentials should be as low as possible. Depending on their origin, a distinction has to be made between few different types:

- *Charge-transfer overpotential.* The charge-transfer overpotential is caused by

CosMX Exhibit 1008, Page 38 of 633

a limitation on the speed of the charge transfer through the phase-boundary electrode/electrolyte that is generally dependent on the nature of the substances that are reacting, the conditions in the electrolyte, and the characteristics of the electrode (for example, the kind of metal). The formulas which deal with this form of overpotential are the Butler–Volmer equation and the Tafel equation [10].

- *Diffusion overpotential.* When high current densities j exist at electrodes (at the boundary to the electrolyte), an impoverishment of the reacting substances is possible. In this case the reaction kinetics are determined only by diffusion processes through this zone, the so-called Nernst layer. Without dealing with the derivation in detail, the following formula is obtained for the diffusion overpotential that occurs (with j_{limit} as the maximum current density):

$$\eta_{\text{diff}} = \left| \frac{RT}{zF} \ln\left(1 - \frac{j}{j_{\text{limit}}}\right) \right| \tag{40}$$

As expected, the value η_{diff} increases with higher current densities.

- *Reaction overpotential.* Both overpotentials mentioned above are normally of higher importance than the reaction overpotential. It may happen sometimes, however, that other phenomena, which occur in the electrolyte or during electrode processes, such as adsorption and desorption, are the speed-limiting factors.
- *Crystallization overpotential.* This exists as a result of the inhibited intercalation of metal ions into their lattice. This process is of fundamental importance when secondary batteries are charged, especially during metal deposition on the negative side.

Corresponding to the charge in the potential of single electrodes which is related to their different overpotentials, a shift in the overall cell voltage is observed. Moreover, an increasing cell temperature can be noticed. Besides Joule-effect heat losses W_{J}, caused by voltage drops due to the internal resistance R_{i} (electrolyte, contact to the electrodes, etc.) of the cell, thermal losses W_{K} (related to overpotentials) are the reason for this phenomenon.

$$W_{\text{J}} = I^2 R_{\text{i}} t \tag{41}$$

$$W_{\text{K}} = I \sum \eta_{\text{i}} t \tag{42}$$

1.4 Criteria for the Assessment of Batteries

The demand for electrically operated tools or devices that can be handled independently of stationary power sources led to a variety of different battery systems which are chosen depending on the field of application. In the case of rare usage, e.g., for household electric torches or for long-term applications with low current consumption, such as watches or heart pacemakers, primary cells (zinc–carbon, alkaline-manganese or lithium-iodide cells) are chosen. For many applications such as starter batteries in cars, only rechargeable battery systems, e.g., lead accumulators, are reasonable with regard to costs and the environment.

The different applications led to an immense number of configurations and sizes, for example small round cells for hearing aids or large prismatic cells for the lead accumulators used in trucks. Here the great variety of demands has the consequence

CosMX Exhibit 1008, Page 39 of 633

that nowadays no battery system is able to cope with all of them. The choice of the "right" battery system for a single application is therefore often a compromise.

The external set-up of different battery systems is generally simple and differs in principle only little from one system to another. A mechanically stable cell case bears the positive and negative electrodes, which are separated by a membrane and are connected with electron-conducting poles. Ion conduction between the electrodes is guaranteed usually by fluid or gel-like electrolyte [13].

For the assessment of different battery systems, a comparison of the most important features has to be done.

1.4.1 Terminal Voltage

During charging and discharging of the cell, the terminal voltage U is measured between the poles. It should also be possible to calculate directly the thermodynamic terminal voltage from the thermodynamic data of the cell reaction. This value often differs slightly from the terminal voltage measured between the poles of the cell because of an inhibited equilibrium state or side reactions.

1.4.2 Current–Voltage Diagram

An important experimentally available feature is the current–voltage characteristic, from which the terminal voltage ($U_{t.v.}$) supplied by the electrochemical cell at the corresponding discharge current may be determined. The product of current I and the accompanying terminal voltage is the electric power P delivered by the battery system at a given time.

$$P = IU \tag{43}$$

The power density P_S (W kg^{-1}) of the element results if the power is related to the battery weight. Figure 7 shows the current–voltage characteristic of a Leclanché element.

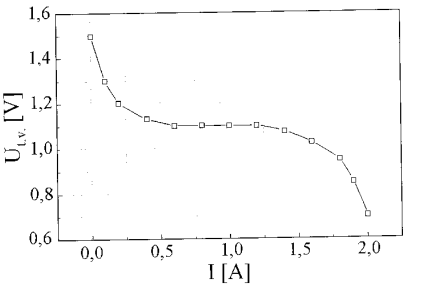


Figure 7. Current–voltage characteristic of a Leclanché element.

1.4.3 Discharge Characteristic

The discharge curve (Fig. 8) is another important feature of battery systems: therefore the terminal voltage is plotted against the discharge capacity. For an ideal battery the terminal voltage drops to zero in a single step when the stored energy is completely consumed.

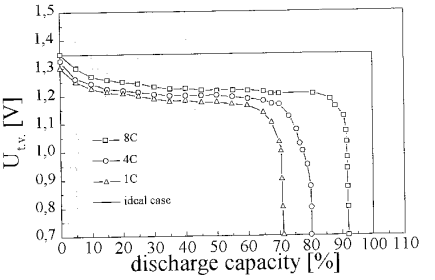


Figure 8. Ideal discharge characteristic, and discharge characteristic of a nickel/cadmium system.

CosMX Exhibit 1008, Page 40 of 633

The discharge rate C is defined by the discharge current and the nominal capacity of the secondary cell. It is equal to the reciprocal value of the discharging time:

$$C = \frac{\text{discharge current}}{\text{nominal capacity}} \qquad (44)$$

The nominal capacity of every system is defined by a specific value of C; for example, for the nickel–cadmium system, it is $C/20$. By discharging with a higher current, the final capacity obtainable becomes lower.

1.4.4 Characteristic Line of Charge

During charging, the accumulator receives the electrical energy — previously released — in the form of storable chemical energy. Terminal voltage, charging time, number of cycles, and other parameters are influenced by the charging procedure in a single battery system. Figure 9 shows how the cell voltage varies with the charge capacity for the nickel/cadmium system at different currents.

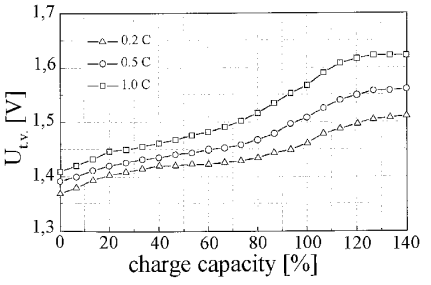


Figure 9. Dependence of the cell voltage on the charge capacity for three different currents in the nickel/cadmium system.

1.4.5 Overcharge Reactions

Nearly all electricity consumers demand a high voltage, which is realized by connecting cells in series. Since the single cells have different capacities, it is impossible to maintain the optimal charge voltage in the weakest cell at the end of the charge process. As a consequence the cell voltage increases and, besides the main charging reaction, chemical or electrochemical side reactions are possible. A well-known problem is the decomposition of the electrolyte solution (for example, water to hydrogen at the negative electrode, or to oxygen at the positive electrode). In some battery systems these evolved gases react back with formation of the educts. For example, in the nickel/cadmium cell oxygen is formed at the positive electrode and reacts back at the negative electrode, warming up the cell [8].

To avoid this problem for lithium-ion batteries consisting out of non-overchargeable cells, computer-controlled charging systems regulate the voltage for each single cell.

1.4.6 Coulometric Efficiency and Energy Efficiency

The efficiency during an energy conversion is defined as the ratio of the energy converted relative to the energy consumed. This parameter is only decisive for secondary systems. The charge Q_{charge} which is necessary to load an accumulator is always higher than the charge ($Q_{\text{discharge}}$) released during discharge. This is caused by incomplete conversion of the charging current into utilizable reaction products. Useless side reactions with heat production may occur. Here, numerous parameters are im-

CosMX Exhibit 1008, Page 41 of 633

portant, e.g., the current density, the temperature, the thickness and the porosity of the separator, and the age of the cell.

There are two possible ways to describe the efficiency of batteries — the coulometric efficiency and the energy efficiency.

- *Coulometric efficiency:*

$$q_{Ah} = \frac{Q_{discharge}}{Q_{charge}} \tag{45}$$

The reciprocal value, $f = 1/q_{Ah}$ of the coulometric efficiency is called the charging factor. The coulometric efficiency for electrochemical energy conversion is about 70–90 percent for nickel/cadmium and nearly 100 percent for lithium-ion accumulators [14].

- *Energy efficiency:*

$$q_{Wh} = q_{Ah} \cdot \frac{\bar{U}_{discharge}}{\bar{U}_{charge}} \tag{46}$$

Here, $\bar{U}_{discharge}$ and $\bar{U}_{charge}$ are the average terminal voltages during discharge and charge. The discharge voltage is normally lower than the charge voltage because of the internal resistance and overpotentials. For this reason the coulometric efficiency is always higher than the energy efficiency. It is influenced by the same terms as the charge efficiency, but in addition by the discharge current and the charging procedure. The efficiencies of different accumulator systems are compared in Table 2.

1.4.7 Cycle Life

Another important parameter for describing a secondary electrochemical cell is the achievable number of cycles or the lifetime. For economic and ecological reasons, systems with a high cycle life are preferred. The number of cycles indicates how often a secondary battery can be charged and discharged repeatedly before a lower limit (defined as a failure) of the capacity is reached. This value is often set at 80 percent of the nominal capacity. To compare different battery systems, besides the number of cycles, the depth of discharge must be quoted.

1.4.8 Specific Energy and Energy Density

Regarding the specific energy, i.e., the electric energy per mass, a major distinction can be made between today's aqueous and nonaqueous battery systems [15]. Apart from batteries for some special applications, there are

- aqueous batteries with 100 Wh kg^{-1} for primary systems, and about 60 Wh kg^{-1} for secondary systems; and
- nonaqueous batteries with about 400 Wh kg^{-1} for primary systems and about 120 Wh kg^{-1} for secondary systems.

Table 2. Comparison of the efficiencies of different accumulators

System	Coulometric efficiency	Energy efficiency
Lead-acid accumulator	0.80	0.65 – 0.70
Nickel/cadmium accumulator	0.65 – 0.70	0.55 – 0.65
Nickel/metal hydride accumulator	0.65 – 0.70	0.55 – 0.65

CosMX Exhibit 1008, Page 42 of 633

For comparison, the utilizable electrical or mechanical energy of a gasoline engine is 3000 Wh kg^{-1} gasoline.
Zinc/carbon and alkaline/manganese cells are primary battery systems; lead, nickel/cadmium, and nickel/metal hydride accumulators are secondary batteries with aqueous electrolyte solutions. Their performances are compared in Table 3. The aqueous battery systems generally show only limited operation at low temperatures. Because of the decomposition of the water, the voltage of a single cell is limited. For this reason, more and more systems, such as lithium-ion batteries, use organic or polymer electrolytes.

Table 3. Comparison of primary and secondary battery systems

System	Specific energy (Wh kg^{-1})		Energy density (practical) (Wh L^{-1})
	Theoretical	Practical	
Alkaline(zinc)/ manganese cell	336	50–80	120–150
Zinc/ carbon	358	60–90	140–200
Lead–acid	170	35	90
Nickel/ cadmium	209	50	90
Nickel/metal hydride	380	60	80
Lithium ion/metal oxide	500–550	150	220

1.5 References

[1] D. Linden, *Handbook of Batteries*, 2nd ed., McGraw-Hill, New York, **1995**.

[2] K. Kordesch, G. Simader, *Fuel Cells and Their Applications*, VCH, Weinheim, **1996**.

[3] H.A. Kiehne, *Battery Technology Handbook*, Marcel Dekker, New York, **1989**.

[4] H.D. Jaksch, *Batterielexikon*, Pflaum Verlag, München, **1993**.

[5] Hamann, W. Vielstich, *Elektrochemie*, VCH, Weinheim, **1997**.

[6] D.T.Sawyer, A. Sobkowiak, J.L. Roberts, *Electrochemistry for Chemists*, John Wiley, New York, **1995**.

[7] R.A. Alberty, R.J. Silbey, *Physical Chemistry*, John Wiley, New York, **1996**.

[8] S.C. Levy, P.Bro, *Battery Hazards and Accident Prevention*, Plenum, New York, **1994**.

[9] D.R. Lide, *Handbook of Chemistry and Physics*, 72nd ed., CRC Press, Boca Raton, **1992**.

[10] A.J. Bard, L.R. Faulkner, *Electrochemical Methods*, John Wiley, London, **1980**.

[11] J.O'M. Bockris, A.K.N. Reddy, *Modern Electrochemistry*, vols. 1–2, John Wiley, New York, **1970**.

[12] Southampton Electrochemistry Group (Ed.), *Instrumental Methods in Electrochemistry*, Ellis Horwood, Chichester, **1985**.

[13] M.Z.A. Munshi, *Handbook of Solid State Batteries and Capacitors*, World Scientific, Singapore, **1995**.

[14] J.-P. Gabano, *Lithium Batteries*, Academic Press, London, **1983**.

[15] V. Barsukov, F. Beck, *New Promising Electrochemical Systems for Rechargeable Batteries*, Kluwer Academic Publishers, Dordrecht, **1996**.

CosMX Exhibit 1008, Page 43 of 633

2 Practical Batteries

Koji Nishio and Nobuhiro Furukawa

Batteries can be roughly divided into primary and secondary batteries. Primary batteries cannot be electrically charged, but these batteries have high energy density and good storage characteristics. Lithium primary batteries, which have been commercialized about 20 years ago, exist in many forms: for example lithium–manganese dioxide, lithium–carbon monofluoride, and lithium–thionyl chloride batteries. They are used with the other batteries such as carbon–zinc, alkaline–manganese, zinc–air, and silver oxide–zinc batteries.

Secondary batteries can be electrically charged, and these batteries can offer savings in costs and resources. Recently, lithium–ion and nickel–metal hydride batteries have been developed, and are used with the other secondary batteries, such as nickel–cadmium, lead–acid, and coin–type lithium secondary batteries.

The variety of practical batteries has increased during the last 20 years. Applications for traditional and new practical battery systems are increasing, and the market for lithium–ion batteries and nickel–metal hydride batteries has grown remarkably. This chapter deals with consumer–type batteries, which have developed relatively recently.

2.1 Alkaline–Manganese Batteries

Batteries using an alkaline solution for electrolyte are commonly called alkaline batteries. They are high-power owing to the high conductivity of the alkaline solution. Alkaline batteries include primary batteries, typical of which are alkaline–manganese batteries, and secondary batteries, typical of which are nickel–cadmium and nickel–metal hydride batteries. These batteries are widely used.

The dry cell was invented by Leclanché in the 1860s. This type of battery was developed in the 19th century. In the 1940s, Rubel achieved significant progress in alkaline–zinc batteries, and manufactured zinc powder with high surface area to prevent zinc passivation.

The discharge of alkaline–manganese batteries comes from the electrochemical reactions at the anode and cathode. During discharge, the negative electrode material, zinc, is oxidized, forming zinc oxide; at the same time, MnO_2 in the positive electrode is reduced (MnOOH):

Cathode reaction:

$$2MnO_2 + H_2O + 2e^- \rightarrow 2MnOOH + 2OH^-$$

0.12 V vs. NHE (1)

CosMX Exhibit 1008, Page 44 of 633

Anode reaction:
$Zn + 2OH^- \rightarrow ZnO + H_2O + 2e^-$ −1.33 V vs. NHE (2)

Overall reaction:
$Zn + 2MnO_2 \rightarrow ZnO + 2MnOOH$ 1.45 V (3)

The initial voltage of an alkaline–manganese dioxide battery is about 1,5 V. Alkaline–manganese batteries use a concentrated alkaline aqueous solution (typically in the range of 30–45 % potassium hydroxide) for electrolyte. In this concentrated electrolyte, the zinc electrode reaction proceeds, but if the concentration of the alkaline solution is low, then the zinc tends to passivate.

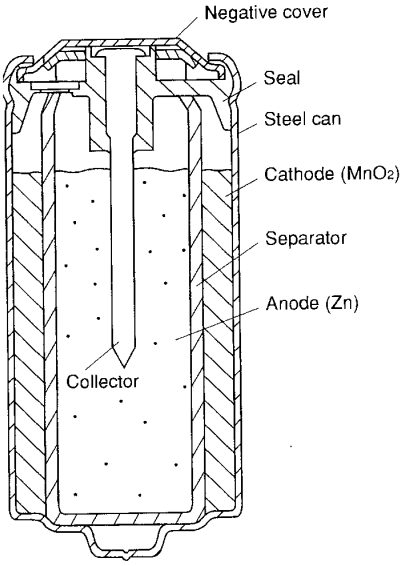


Figure 1. Cell construction of an alkaline–manganese battery

The cell construction of an alkaline–manganese battery is shown in Fig. 1. The steel can serves as a current collector for the manganese dioxide electrode. Inside the can is a cathode containing manganese dioxide and graphite powder. Zinc powder is packed inside the separator together with the electrolyte solution and a gelling agent. An anode collector is inserted into the zinc powder. The battery is hermetically sealed, which is contributes to its good shelf life.

Figure 2 shows a comparison of the discharge characteristics between alkaline–manganese batteries and Leclanché batteries. The capacity of the alkaline–manganese batteries is about three times as large as that of the Leclanché batteries.

Amalgamated zinc powder has been used as the negative material to prevent zinc corrosion and zinc passivation. Recently, from the viewpoint of environmental problems, mercury-free alkaline–manganese batteries were developed by using zinc powder with indium, bismuth and other additives [2–4]. Adding indium to zinc powder is the most effective way to improve the characteristics of the cells [3]. Figure 3 shows the variation in the internal impedance of the cells according to the additive content of the zinc powder.

Today's battery performance has greatly improved. The capacity of newly developed alkaline–manganese batteries is about 1.5 times higher than that of conventional batteries [5]. Figure 4 shows a comparison of the discharge characteristics of cells between newly developed and conventional types. Therefore, alkaline–manganese batteries have become more suitable requiring high current than they once were.

CosMX Exhibit 1008, Page 45 of 633

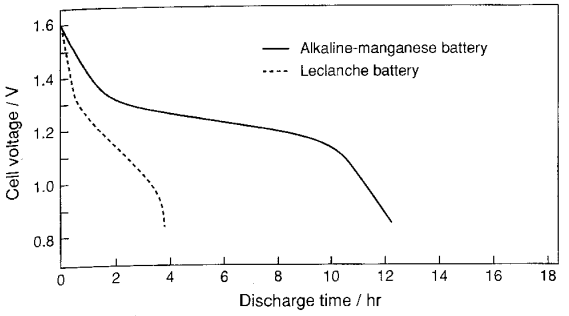


Figure 2. Comparison between the discharge characteristics of alkaline–manganese and Leclanché batteries (load 7.5 Ω ; temperature 20 °C)

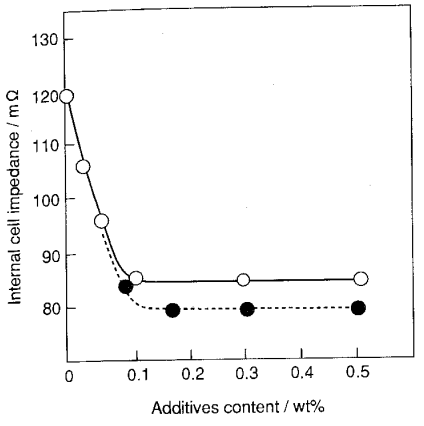


Figure 3. Variation of internal impedance of alkaline–manganese cells with the additives content of the zinc powder: ○, Hg additive;●, In additive.

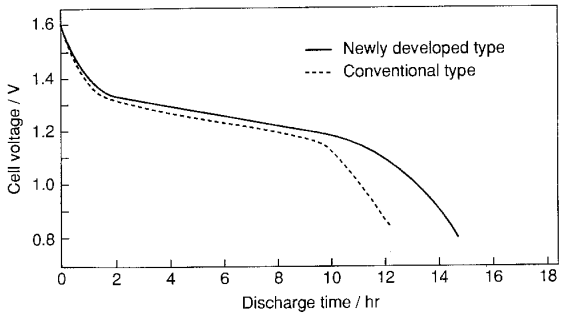


Figure 4. Comparison between the discharge characteristics of newly developed and conventional alkaline–manganese cells (load 7.5 Ω ; temperature 20 °C)

2.2 Nickel–Cadmium Batteries

The nickel–cadmium battery [6] has a positive electrode made of nickel hydroxide and a negative electrode in which a cadmium compound is used as the active material. Potassium hydroxide is used as the electrolyte. During charge and discharge, the following reactions take place:

CosMX Exhibit 1008, Page 46 of 633

Positive electrode reaction:

$$NiOOH + H_2O + e^- \underset{\text{Charge}}{\overset{\text{Discharge}}{\rightleftharpoons}} Ni(OH)_2 + OH^- \qquad 0.52 \text{ V vs. NHE} \qquad (4)$$

Negative electrode reaction:

$$Cd + 2OH^- \underset{\text{Charge}}{\overset{\text{Disharge}}{\rightleftharpoons}} Cd(OH)_2 + 2e^- \qquad -080 \text{ V vs. NHE} \qquad (5)$$

Overall battery reaction:

$$2NiOOH + Cd + 2H_2O \underset{\text{Charge}}{\overset{\text{Discharge}}{\rightleftharpoons}} 2Ni(OH)_2 + Cd(OH)_2 \qquad 1.32 \text{ V} \qquad (6)$$

Reactions take place at the positive electrode between nickel oxyhydroxide and nickel hydroxide, and at the negative electrode between cadmium metal and cadmium hydroxide. In addition, the H_2O molecules, which are generated during charging, are consumed during discharging. Therefore, variations in electrolyte concentration are insignificant. Because of this reaction, the nickel–cadmium battery excels in temperature characteristics, high-rate discharge characteristics, durability, etc. [7]. Most significant is the fact that the amount of electrolyte in the cell can be reduced enough to allow the manufacture of completely sealed cells.

The nickel–cadmium battery was invented by Jungner in 1899. The battery used nickel hydroxide for the positive electrode, cadmium hydroxide for the negative electrode, and an alkaline solution for the electrolyte. Jungner's nickel–cadmium battery has undergone various forms of the development using improved materials and manufacturing processes to achieve a superior level of performance.

In 1932, Shlecht and Ackermann invented the sintered plate. In those days, conventional plates involved a system in which the active materials were packed into a metal container called a pocket or tube. However, with the sintered-plate method, the active materials are placed inside a porous electrode formed of sintered nickel powder. In 1947, Neumann achieved a completely sealed structure. This idea of protection against overcharge and overdischarge by proper capacity balance is illustrated in Fig. 5.

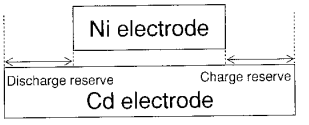


Figure 5. Electrode capacity balance of a sealed Ni–Cd battery.

Focusing on the concept of the completely sealed system, the Sanyo Electric Co. developed sealed-type nickel–cadmium batteries in 1961. This type of battery enjoys a wide application range that is still expanding; a large variety of nickel–cadmium batteries has been developed to meet user needs ranging from low-current uses like emergency power sources and semiconductor memories to high-power applications such as cordless drills.

Figure 6 shows the typical structural design of a cylindrical nickel–cadmium

CosMX Exhibit 1008, Page 47 of 633

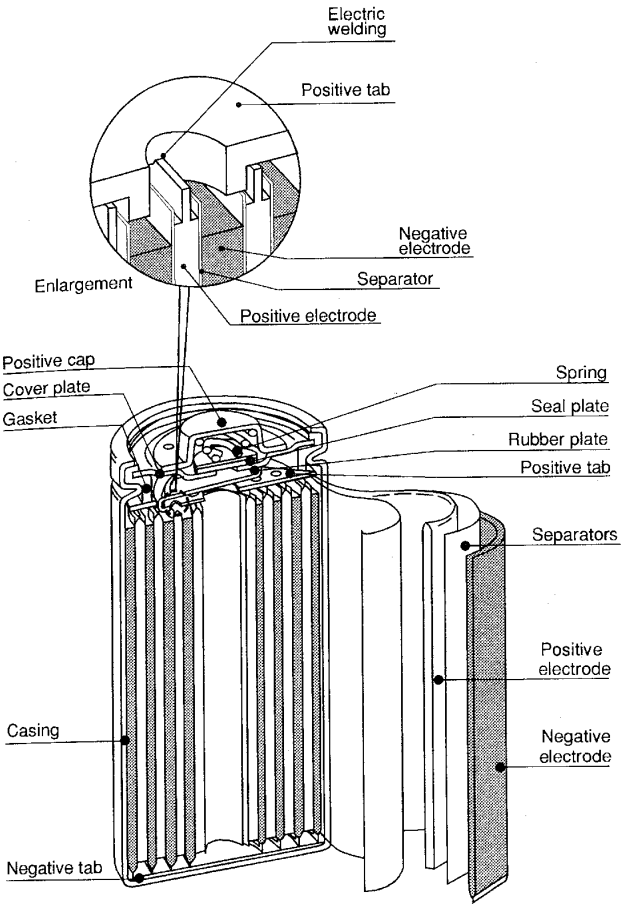


Figure 6. Structural design of a cylindrical Ni–Cd battery

battery. It has a safety vent, as illustrated in Fig. 7, which automatically opens and releases excessive pressure when the internal gas pressure increases. Formation of hydrogen is avoided by "extra" $Cd(OH)_2$, oxygen is removed by reaction with Cd.

Figure 8 shows the charge characteristics when charging is performed at a constant current. In nickel–cadmium batteries, characteristics such as cell voltage, internal gas pressure, and cell temperature vary during charging, depending on the charge current and ambient temperature. Figure 9

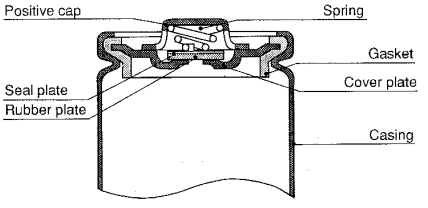


Figure 7. Safety vent of an Ni–Cd battery

shows the discharge characteristics at various discharge rates. The discharge capacity of the cell decreases as the discharge cur-

CosMX Exhibit 1008, Page 48 of 633

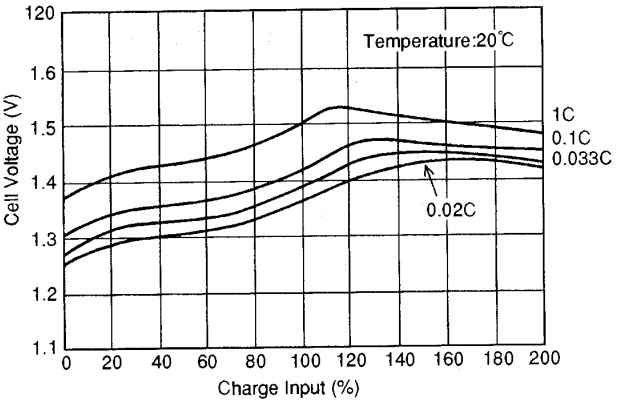


Figure 8. Charge characteristics of an Ni–Cd battery at a constant current (cell type 1200SC; temperature 20 °C).

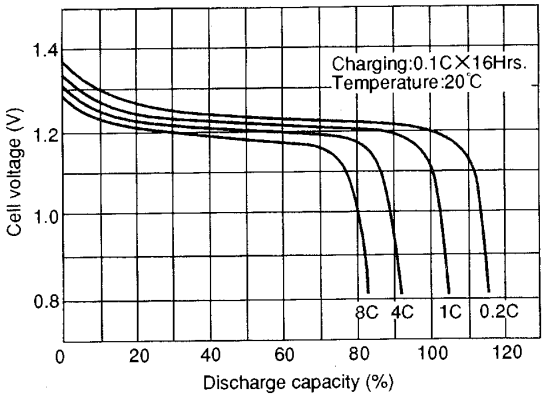


Figure 9. Discharge characteristics of an Ni–Cd battery at various discharge currents (cell type 1200SC)

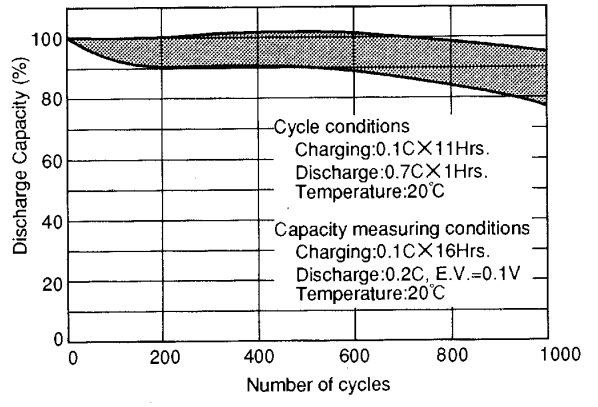


Figure 10. Charge–discharge cycle characteristics of an Ni–Cd battery (cell type 1200SC).

rent increases. However, compared with other batteries, nickel–cadmium batteries have excellent high-current discharge characteristics. A continuous, high-current discharge at 4 C or, in some types, over 10 C is possible.

Figure 10 shows the charge–discharge cycle characteristics. As shown in this fig-

CosMX Exhibit 1008, Page 49 of 633

ure, nickel–cadmium batteries exhibit excellent cycle characteristics and no noticeable decline is observed after 1000 charge–discharge cycles.

The significant features of nickel–cadmium batteries can be summarized as follows:

(i) Outstanding economy and long service life, which can exceed 500 charge–discharge cycles
(ii) Low internal resistance, which enables a high-rate of discharge, and a constant discharge voltage, which provides an excellent source of DC power for any battery-operated appliance.
(iii) A completely sealed construction which prevents the leakage of electrolyte and is maintenance-free. No restrictions on mounting direction enable use in any appliance.
(iv) Ability to withstand overcharge and overdischarge.
(v) A long storage life without deterioration in performance and recovery of normal performance after recharging.
(vi) Wide operating-temperature range.

Recent advances in electronics technologies have accelerated the trend towards smaller and lighter devices. For the secondary batteries that serve as power supplies for these devices, there is also an increasing demand for the development of more compact, lighter batteries with high energy density and high performance. Improvements have been made possible mainly because of progress in the nickel electrode.

For many years, sintered-nickel electrodes have been used as the positive electrodes for sealed-type nickel–cadmium batteries. With an increase in the demand for high energy density, this type of electrode has been improved. Figure 11 shows an improved sintered substrate with high porosity. In addition, a new type of manufacturing process has been developed for a nickel electrode, which is made by pasting nickel hydroxide particles (Fig. 12) into a three-dimensional nickel substrate (Fig. 13). To increase the energy density of nickel electrode, it is important to put as many nickel hydroxyde particles as possible into a given substrate, and improve its utilization. Such new electrodes are used for high–capacity nickel–cadmium batteries.

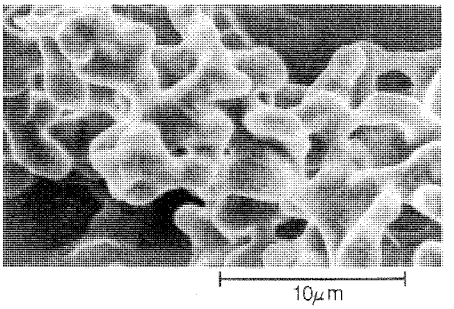


Figure 11. Improved sintered substrate with high porosity.

As mentioned above, nickel–cadmium batteries have excellent characteristics and

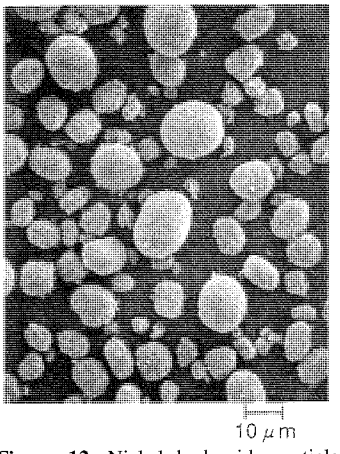


Figure 12. Nickel hydroxide particles for active materials.

CosMX Exhibit 1008, Page 50 of 633

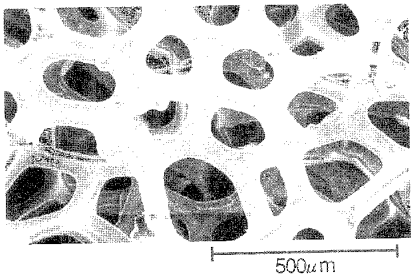


Figure 13. Three-dimensional nickel substrate.

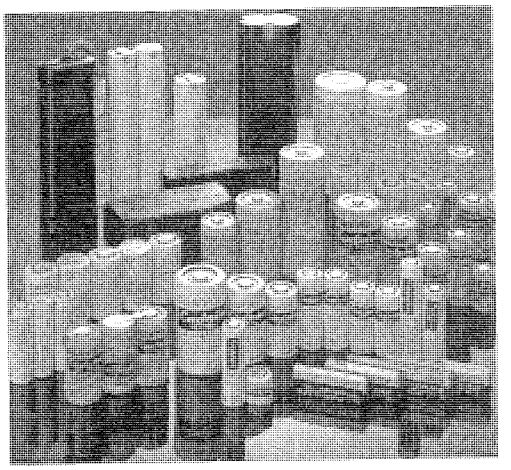


Figure 14. Various Ni–Cd batteries. • • • •

are used in diverse fields. Special-purpose batteries (Fig. 14) comply effectively with the requirements for improvement of various devices, for example high-capacity, fast-charge, high-temperature, heat–resistant, memory backup.

2.3 Nickel–Metal Hydride Batteries

Nickel–metal hydride batteries contain a nickel electrode similar to that used in nickel–cadmium batteries as the positive electrode, and a hydrogen-absorbing alloy of electrode for the negative electrode. This has made the development of a hydrogen-absorbing alloy electrode important.

Hydrogen-absorbing alloy can reversible absorb and desorb a large amount of hydrogen. Hydrogen gas is rapidly absorbed in the gas phase, then desorbed on the alloy (gas–solid reaction). In the electrode reaction, the alloy electrochemically absorbs and desorbs hydrogen in an alkaline solution (electrochemical reaction):

Positive electrode reaction:

$$NiOOH + H_2O + e^- \underset{\text{Charge}}{\overset{\text{Discharge}}{\rightleftharpoons}} Ni(OH)_2 + OH^- \qquad 0.52\ \text{V vs NHE} \qquad (7)$$

Negative electrode reaction:

$$MH + OH^- \underset{\text{Charge}}{\overset{\text{Discharge}}{\rightleftharpoons}} M + H_2O + e^- \qquad -0.80\ \text{V vs. NHE} \qquad (8)$$

Overall battery reaction:

$$NiOOH + MH \underset{\text{Charge}}{\overset{\text{Discharge}}{\rightleftharpoons}} Ni(OH)_2 + M \qquad 1.32\ \text{V} \qquad (9)$$

where M=hydrogen-absorbing alloy and MH=metal hydride

CosMX Exhibit 1008, Page 51 of 633

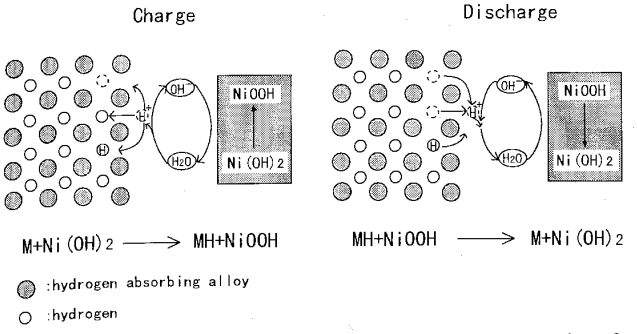


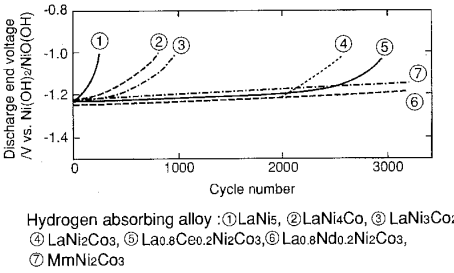
Figure 15. Reaction mechanism of the charging–discharging reaction of an MH electrode.

Figure 15 shows a typical mechanism of the charge–discharge reaction. During charging, the electrolytic reaction of water causes the hydrogen, which is present in atomic form on the surface of the hydrogen-absorbing alloy in the negative electrode, to disperse into and be absorbed by the alloy (discharge reaction). During discharge, the absorbed hydrogen reacts with hydroxide ions at the surface of the hydrogen-absorbing alloy to become water once again (charge reaction). In other words, the active material of the electrode reaction is hydrogen, and the hydrogen-absorbing alloy acts as a storage medium for the active material.

Hydrogen-absorbing alloys were discovered in the 1960s [8]. Metal hydride electrode materials were studied in the 1970s and 1980s [9–12]. To be suitable as the negative electrode material for a high-performance cell, a hydrogen-absorbing alloy must allow a large amount of hydrogen to be absorbed and desorbed in an alkaline solution, its reaction rate must be high, and it must have a long charge–discharge cycle life.

Much of this study was conducted on $LaNi_5$-based alloys [13–20] and $TiNi_x$-based alloys [21–23]. Sanyo Electric, Matsushita Battery and most other battery manufacturers have been using $LaNi_5$-based rare earth–nickel-type alloys [24, 25]. Some manufacturers are using a $TiNi_x$-based alloy [23].

It was though that rare earth–nickel-type alloys had a large exchange current density and that they absorbed a large amount of hydrogen, thereby enabling the construction of high-energy-density batteries. The first step in this development was to obtain a sufficient cycle life for their use as an electrode material.



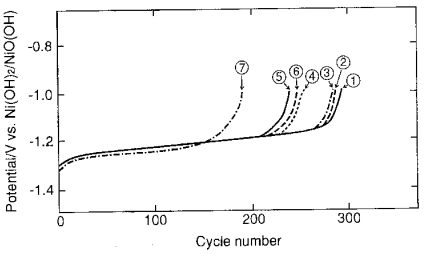
Hydrogen absorbing alloy :①$LaNi_5$, ②$LaNi_4Co$, ③$LaNi_3Co_2$, ④$LaNi_2Co_3$, ⑤$La_{0.8}Ce_{0.2}Ni_2Co_3$, ⑥$La_{0.8}Nd_{0.2}Ni_2Co_3$, ⑦$MmNi_2Co_3$

Figure 16. Charge-discharge cycle characteristics of various MH alloy electrodes.

Figure 16 shows the charge–discharge cycle characteristics of alloys in which part of the nickel component was replaced with cobalt. Misch metal (Mm), which is a mixture of rare earth elements such as lanthanum, cerium, praseodymium, and neodymium, was used in place of lanthanum. It was found that the partial replacement of nickel with cobalt and the substi-

CosMX Exhibit 1008, Page 52 of 633

tution of the lanthanum content with Mm was very useful in improving the charge–discharge cycle life. However, such alloys have insufficient capacity, as shown in Fig. 17 [19]. From study of the effect that their compositions had on the charge–discharge capacity, it was concluded that the best alloy elements were $Mm(Ni-Co-Al-Mn)_x$. This alloy led to the commercialization of sealed nickel–metal hydride batteries. All the battery manufacturers who use a rare earth–nickel-type alloy for the negative electrode material employ similar alloys with slightly different compositions.



Hydrogen absorbing alloy :①$LaNi_5$, ②$LaNi_4Co$, ③$LaNi_3Co_2$, ④$LaNi_2Co_3$, ⑤$La_{0.8}Ce_{0.2}Ni_2Co_3$, ⑥$La_{0.8}Nd_{0.2}Ni_2Co_3$, ⑦$MmNi_2Co_3$

Figure 17. Discharge characteristics of various MH alloy electrodes.

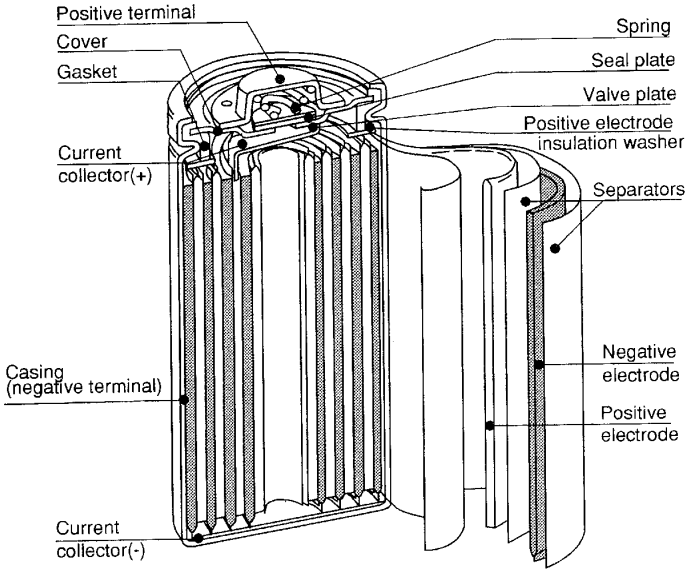


Figure 18. Internal structure of the cylindrical Ni–MH battery.

The nickel–metal hydride battery comes in two shapes: cylindrical and prismatic. The internal structure of the cylindrical battery is shown in Fig. 18. It consists of positive and negative electrode sheets wrapped within the battery, with separators between. Figure 19 shows the internal structure of the prismatic battery: it consists of layered positive and negative electrode sheets, interlayered with separators. These structures are similar to that of the nickel–cadmium battery.

CosMX Exhibit 1008, Page 53 of 633

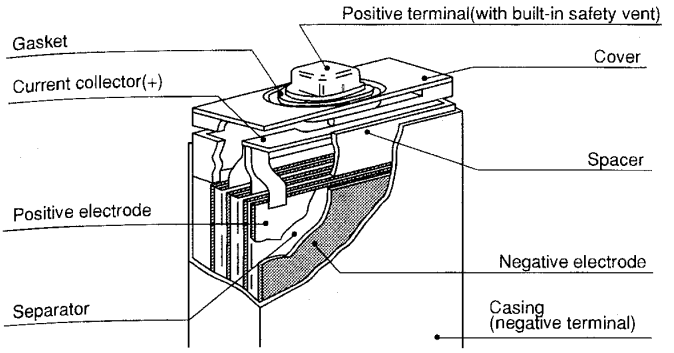


Figure 19. Internal structure of the prismatic Ni–MH battery.

Figure 20 shows the charge–discharge characteristics of the AA-size nickel–metal hydride battery in comparison with the nickel–cadmium battery produced by Sanyo Electric. Its capacity density is 1.5 to 1.8 higher than that of nickel–cadmium batteries.

Charging is the process of returning a discharged battery to a state in which it can be used again. The nickel–metal hydride battery is normally charged with a constant current. This method has the advantage of allowing an easy calculation of the amount of charging based on the charging time. The standard for determining discharge capacity is a charging time of 16h using a 0.1 C current at 20±5 °C. Battery voltage increases as the charging current increases,

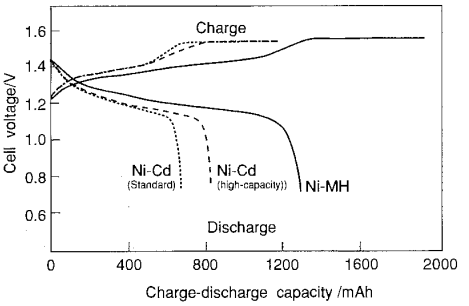


Figure 20. Charge–discharge characteristics of an Ni–MH battery (cell type AA).

and decreases as the battery temperature increases. The general charging characteristics of a nickel–metal hydride battery are shown in Fig. 21. The battery voltage, gas pressure within the battery, and battery

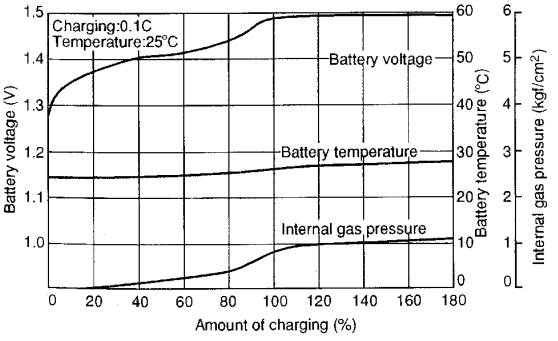


Figure 21. General charging characteristics of an Ni–MH battery (cell type 4/3A).

CosMX Exhibit 1008, Page 54 of 633

temperature change as time elapses under continued charging.

The discharge voltage of nickel–metal hydride batteries is almost the same as that of nickel–cadmium batteries.

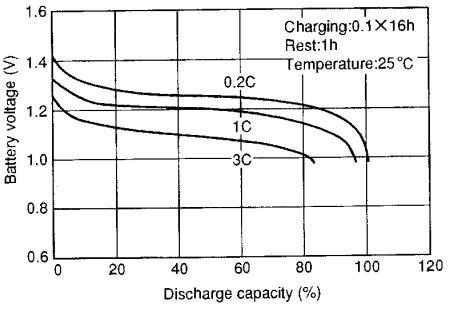


Figure 22. Discharge characteristics of an Ni–MH battery at various rates (cell type 4/3A).

Figure 22 shows the discharge characteristics at the 0.2 C, 1 C and 3 C rate. The high-rate discharge characteristics of a nickel–metal hydride battery compare unfavorably with those of a nickel–cadmium battery, because the specific surface area of the metal hydride electrode is smaller than that of the cadmium electrode. Since the battery voltage drops dramatically if the discharge current exceeds 3 C, it is better to use a current under 3 C. Figure 23 shows the charge–discharge characteristics. A life of 1000 cycles was obtained.

The outstanding characteristics of the nickel–metal hydride battery are as follows:

(i) The discharge capacity is 80% higher than that of the standard nickel-cadmium battery;
(ii) A low internal resistance, which enables high-rate discharge;
(iii) A long charge-discharge cycle life, which can exceed 1000 cycle, and cell materials which are adaptable to the environment.

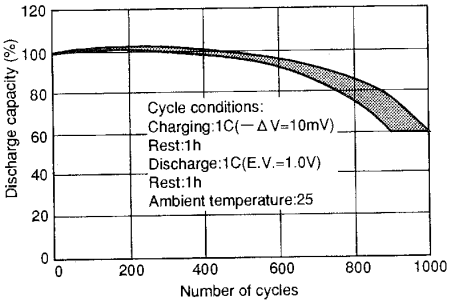


Figure 23. Charge–discharge characteristics of an Ni–MH battery (cell type 4/3AA).

Since nickel–metal hydride batteries were commercialized in 1990, they have become increasingly popular as a power source for computers, cellular phones, electric shavers, and other products.

The high capacity of the nickel–metal hydride battery, which is approximately twice that of a standard nickel–cadmium battery, is possible because a hydrogen-absorbing alloy is used for the negative electrode. This alloy absorbs a large amount of hydrogen and features excellent reversibility of hydrogen absorption and desorption; thus the batteries' characteristics mainly depend on the physical and chemical properties of the hydrogen-absorbing alloy used for the negative electrode.

Improvement of Mm(Ni - Co - Al - Mn)$_x$ type alloys has been achieved in various ways. It was reported that alloys with a nonstoichiometric composition [Mm(Ni - Co - Mn - Al)$_x$: $4.5 \leq x \leq 4.8$] had a larger discharge capacity than those with stoichiometric alloys [26-27]. Using X-ray diffraction analysis, it was found that the larger capacity is dependent on an increase in the unit cell volume of alloys with x=4.5–4.8. It was also reported that annealing treatment improved the durability of this type of alloy.

CosMX Exhibit 1008, Page 55 of 633

The effects of both chemical compositional factors and the production process on the electrochemical properties of MH alloy electrodes were investigated [28]. Figure 24 shows the P–C isotherms of $Mm(Ni-Co-Al-Mn)_{4.76}$ alloys prepared by a rapid quenching and/or annealing process. The P–C isotherms of an induction-melted and as-cast alloy showed no plateau region, while the others, particularly the rapidly quenched and annealed alloy, showed clear plateau regions between 0.2 H/M and 0.6 H/M, indicating that the rapid quenching and/or annealing process succeeded in homogenizing the microstructure. It was concluded that this process provides a larger hydrogen storage capacity in an alloy with a nonstoichiometric composition, $AB_{4.76}$.

Figure 25 shows nickel–metal hydrides batteries that have been improved by using the technique mentioned above.

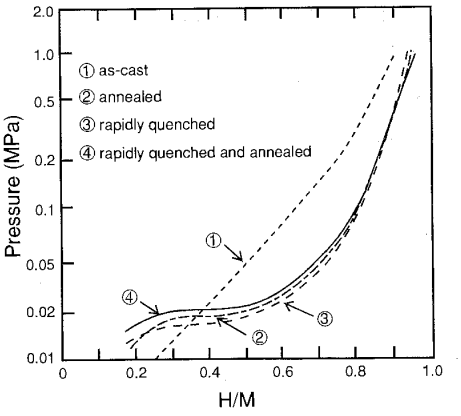


Figure 24. P–C isotherms of $Mm(Ni-Co-Al-Mn)_{4.76}$ alloys prepared through a rapid quenching and/or annealing process.

These techniques are useful for improving cell characteristics such as cell capacity and charge–discharge cycle life.

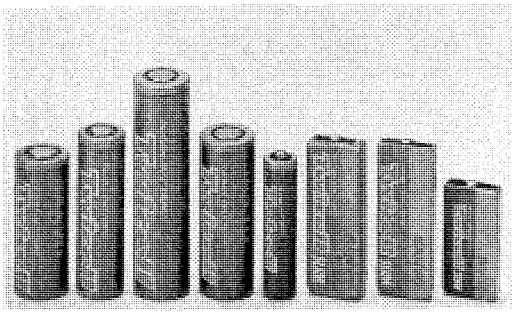


Figure 25. Nickel-metal hydride batteries manufactured by new technology.

2.4 Lithium Primary Batteries

The electrode potential of lithium is –3.01 V vs. NHE, which is the lowest value among all the metals. Lithium has the lowest density ($0.54 g cm^{-3}$) and the lowest electrochemical equivalent ($0.259 g Ah^{-1}$) of all solids. As a result of these physical properties, nonaqueous electrolyte batteries using lithium offer the possibility of high voltage and a high energy density. Organic and inorganic solvents which are stable with lithium are selected as the electrolytes for lithium batteries.

Primary lithium batteries offer these advantages as well as good low-temperature characteristics. There are many kinds of primary lithium batteries, with

CosMX Exhibit 1008, Page 56 of 633

various cathode active materials; the main ones are lithium–manganese dioxide, lithium–carbon monofluoride, and lithium–thionyl chloride batteries [29].

2.4.1 Lithium–Manganese Dioxide Batteries

MnO_2 is used for the same purpose as the cathode active material in lithium–manganese dioxide ($Li-MnO_2$) batteries; it has been used for a long time in zinc–carbon and alkaline–manganese dioxide batteries, which are aqueous-electrolyte systems.
In 1975, the Sanyo Electric Co. identified a novel reaction between lithium and MnO_2 and succeeded in exploiting this as the $Li-MnO_2$ battery. Sanyo has also granted the manufacturing technology for $Li-MnO_2$ batteries to major battery manufacturers around the world, and more than 15 companies are now producing it worldwide.

The following reaction mechanism is suggested to occur in $Li-MnO_2$:

Anode reaction:

$$Li \rightarrow Li^+ + e^- \qquad (10)$$

Cathode reaction:

$$MnO_2 + Li^+ + e^- \rightarrow MnO_2^-(Li^+) \qquad (11)$$

Overall battery reaction:

$$MnO_2 + Li \rightarrow MnO_2^-(Li^+) \qquad (12)$$

where $MnO_2^-(Li^+)$ signifies that the lithium ion is introduced into the MnO_2 crystal lattice.

Figure 26 shows a schematic presentation of the solid phase during the discharge of the MnO_2 crystal lattice, where tetravalent manganese is reduced to trivalent manganese.

In $Li-MnO_2$ batteries, lithium perchlorate ($LiClO_4$) or lithium trifluoromethanesulfonate ($LiCF_3SO_3$) is widely employed as an electrolytic solute, and mainly propylene carbonate (PC) and 1,2-dimethoxyethane (DME) are employed as a mixed solvent. The PC–DME–$LiCLO_4$ electrolyte shows high conductivity ($>10^{-2}\,\Omega^{-1}\,cm^{-1}$) and low viscosity (< 3 cP).

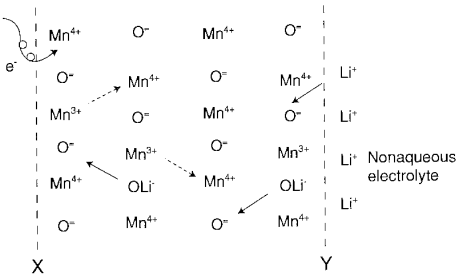


Figure 26. Schematic presentation of the solid phase during the discharge of MnO_2. The arrows show directions of movement of the electrons and lithium ions: ——▶, lithium–ion movement; - - - - - ▶, electron movement; X, MnO_2–electronic conductor interface; Y, MnO_2–solution interface.

The requirements for the MnO_2 active material in $Li-MnO_2$ batteries are as follows:

(i) It must be almost anhydrous.
(ii) It must have an optimized crystal structure suitable for the diffusion of Li^+ ions into the MnO_2 crystal lattice.

Although it is important that no water should exist in the cathode materials of nonaqueous batteries, the presence of a little water is unavoidable when MnO_2 is used as the active material. It is believed that this water is bound in the crystal structure, and that it has no effect on the storage characteristics, as shown in Fig. 27, where the relationship of the MnO_2

CosMX Exhibit 1008, Page 57 of 633

heat-treatment temperature to the residual capacity ratio after 11 months of storage at 60 °C is plotted.

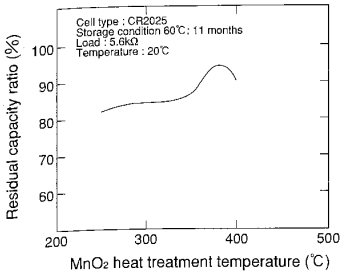


Figure 27. Relation of MnO_2 heat treatment temperature and residual capacity ratio after 11 months at 60 °C.

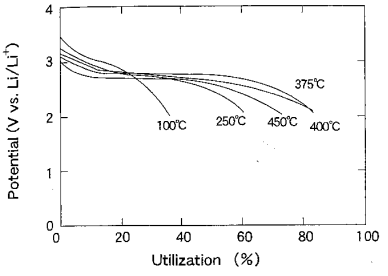


Figure 28. Discharge characteristics at a current density of 1.2 mA cm^{-2} of electrolytic MnO_2 heat-treated at various temperatures.

Figure 28 shows the discharge characteristics at a current density of 1.2 mA cm^{-2} of electrolytic MnO_2 heat-treated at various temperatures. From the characteristics shown, it may be concluded that the optimum heat-treatment temperature range for stable discharge is between 375 and 400 °C, which agrees with the data of Fig. 27.

The general advantages of the $Li-MnO_2$ battery system are as follows:

(i) High voltage and high energy density. $Li-MnO_2$ batteries are capable of maintaining a stable voltage of 3 V, which is about twice that of conventional dry-cell batteries. Because of this advantage, a single $Li-MnO_2$ battery can be used to replace two, and in practice even three, conventional dry-cell batteries.

(ii) Excellent discharge characteristics. Since $Li-MnO_2$ batteries are capable of maintaining stable voltage levels throughout long periods of discharge, a single battery can be used as the internal power source throughout the operational lifetime of a given item of equipment, eliminating the need for battery replacement. In addition, batteries using a crimp-sealed system with a spiral electrode can be used to provide high current discharge for a wide variety of applications.

(iii) Superior leakage resistance. The use of an organic solvent rather than an alkaline aqueous solution for the electrolyte results in significantly reduced corrosion and a much lower possibility of electrolyte leakage.

(iv) Superior storage characteristics. $Li-MnO_2$ batteries employing MnO_2, lithium and a stable electrolyte exhibit a very low tendency towards self-discharge. The degree of self-discharge exhibited by $Li-MnO_2$ batteries stored at room temperature is as follows:
- Crimp-sealed batteries: 1% per annum
- Laser-sealed batteries: 0.5% per annum

(v) A wide operating-temperature range. Because they use an organic electrolyte with a very low freezing point, lithium batteries operate at extremely low temperatures. Moreover, they demonstrate superior characteristics over a wide temperature range from cold to hot, as follows:

CosMX Exhibit 1008, Page 58 of 633

- Crimp-sealed batteries: –20 to +70 °C
- Laser-sealed batteries: –40 to +85 °C

(vi) A high degree of stability and safety. Since $Li-MnO_2$ batteries do not contain toxic liquids or gases, they pose no major pollution problems.

$Li-MnO_2$ batteries are classified according to their shape and construction, which are shown in Fig. 29.

The cathode of coin-type batteries consists of MnO_2 with the addition of a conductive material and binder. The anode is a disk made of lithium metal, which is pressed onto the stainless steel anode can. The separator is nonwoven cloth made of polypropylene, which is places between the cathode and the anode.

Cylindrical batteries can be classified into two basic types: one with a spiral structure, and one with an inside-out structure. The former consists of a thin, wound cathode and the lithium anode with a separator between them. The latter is constructed by pressing the cathode mixture into a high-density cylindrical form. Batteries with the spiral construction are suitable for high-rate drain, and those with the inside-out construction are suitable for high energy density.

The sealing system can also be classified into two types: crimp sealing and laser sealing. A comparison of these sealing methods is shown in Fig. 30, the degree of airtightness with laser sealing being equivalent to a ceramic-based hermetic seal.

Figure 31 shows the construction of the 2CR5 $Li-MnO_2$ battery, which is used as the central power source for fully automatic cameras. The 2CR5 is composed of two CR15400 batteries connected in series. It is encapsulated in a plastic material and designed in shapes that will prevent misuse. The nominal voltage of the 2CR5 is 6 V.

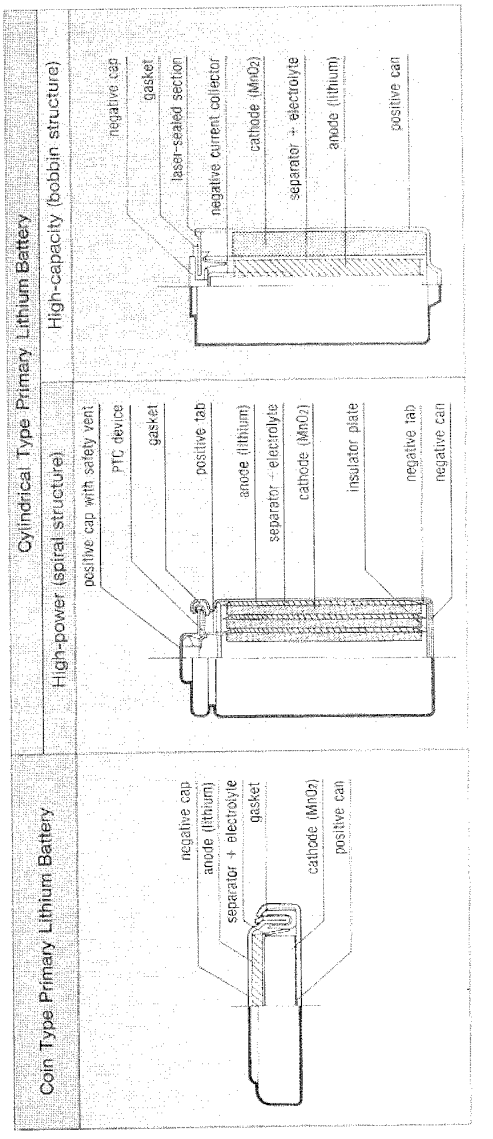


Figure 29. Shapes and construction of lithium–manganese dioxide batteries.

CosMX Exhibit 1008, Page 59 of 633

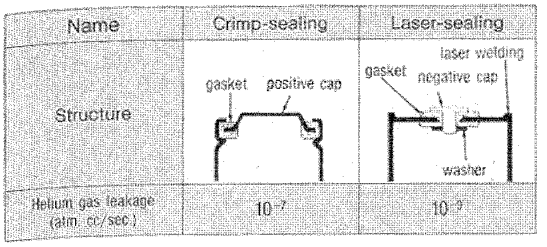


Figure 30. The relationship of the seal type to the leak rate of helium for cylindrical lithium–manganese dioxide batteries.

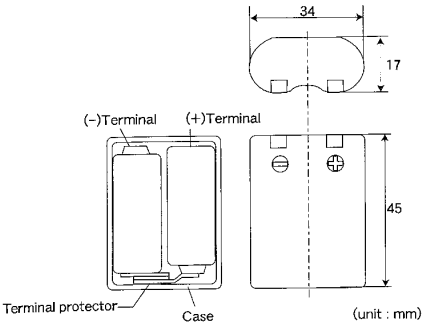


Figure 31. The construction, shape and dimensions of the 2CR5 lithium–manganese dioxide battery for fully automatic cameras.

When the 2CR5 is short-circuited, a thermal protector prevents the battery from overheating by substantially increasing the protector resistance. When the short circuit is removed, the 2CR5 operates normally. The thermal protector does not impede the ability of the 2CR5 to deliver high current. When the discharge current is depleted, the user can easily remove the 2CR5 from the camera and replace it with a new one.

$Li-MnO_2$ batteries are available in a variety of shapes and construction [30] in accordance with their particular use. Figure 32 shows various applications of lithium batteries based on their drain current. Coin-type batteries are generally used for low-rate drain. Cylindrical batteries with the inside-out construction can serve as a memory backup power source. Cylindrical batteries with the spiral construction, as mentioned above, are suitable for high-rate drains such as strobe light sources and camera autowiding systems, and will spread to various other fields, as high-power sources for cassette tape recorders, high-performance lights, 8 mm VTRs, LCD TVs, mobile telephones, transceivers, and other highly portable electronic equipment. Tables 1, 2, 3, and 4 show the specifications of coin-type, cylindrical inside-out construction, cylindrical spiral construction and user-replaceable batteries, respectively.

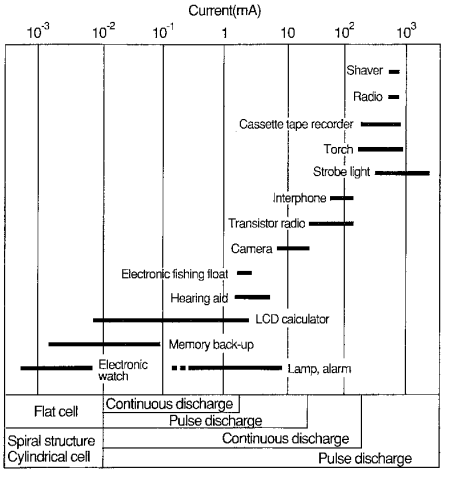


Figure 32. Various applications of lithium-manganese dioxide batteries, based of their drain currents.

CosMX Exhibit 1008, Page 60 of 633

Table 1. Specifications of coin-type manganese dioxide–lithium batteries

Model	Nominal voltage (V)	Nominal capacity (mAh)	Standard discharge current (mA)	Discharge current (mA)		Dimensions (mm)		Weight (g)
				Max.	Standard	Diameter	Height	
CR1220	3	35	0.1	2	10	12.5	2.0	0.8
CR1620	3	60	0.2	3	20	16.0	2.0	1.2
CR2016	3	80	0.3	5	50	20.0	1.6	1.7
CR2025	3	155	0.3	6	50	20.0	2.5	2.7
CR2032	3	220	0.3	4	40	20.0	3.2	3.2
CR2430	3	280	0.3	6	50	24.5	3.0	4.0
CR2450	3	560	0.3	3	50	24.5	5.0	6.2

Table 2. Specifications of cylindrical, inside-out construction, manganese dioxide-lithium batteries

Model	Nominal voltage (V)	Nominal capacity (mAh)	Standard discharge current (mA)	Discharge current (mA)		Dimensions (mm)		Weight (g)
				Max.	Standard	Diameter	Height	
CR4520SE	3	850	0.5	7	70	14.5	25.0	9
CR12600SE	3	1500	1.0	15	250	12.0	60.0	15
CR17335SE	3	1800	1.0	8	100	17.0	33.5	17
CR17450SE	3	2500	1.0	9	150	17.0	45.0	22
CR23500SE	3	5000	1.0	10	200	23.0	50.0	42

Table 3. Specifications of cylindrical, spiral construction, manganese dioxide–lithium batteries

Model	Nominal voltage (V)	Nominal capacity (mAh)	Standard discharge current (mA)	Discharge current (mA)		Dimensions (mm)		Weight (g)
				Max.	Standard	Diameter	Height	
CR–1/3N	3	160	2	60	80	11.6	10.8	3.3
2CR–/3N	6	160	2	60	80	13.0	25.2	9.1
CR15270	3	750	10	1000	2500	15.5	27.0	11
CR15400	3	1300	10	1500	3500	15.5	40.0	17
CR17335	3	1300	10	1500	3500	17.0	33.8	16
CR17450E–R	3	2000	5	1000	2500	17.0	45.0	22

Table 4. Specifications of cylindrical, spiral construction, user-replaceable, manganese dioxide-lithium batteries

Model	Nominal voltage (V)	Nominal capacity (mAh)	Standard discharge current (mA)	Discharge current (mA)		Dimensions (mm)		Weight (g)
				Max.	Standard	Diameter	Height	
CR2	3	750	10	1000	2500	15.6	27.0	3.3
CR123A	3	1300	10	1500	3500	17.0	34.5	9.1
CR-P2	6	1300	10	1500	3500	$34.8(L)\times 19.5(W)\times 35.8(H)$		11
2CR5	3	1300	10	1500	3500	$34\ (L)\times 17(W)\times 45(H)$		17

CosMX Exhibit 1008, Page 61 of 633

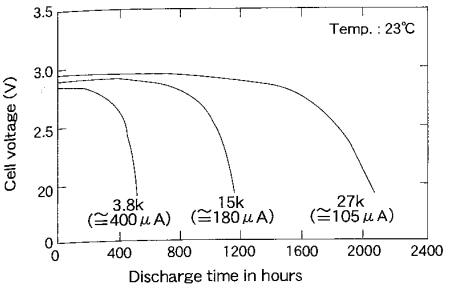


Figure 33 Load characteristics of the CR2032 lithium–manganese dioxide battery.

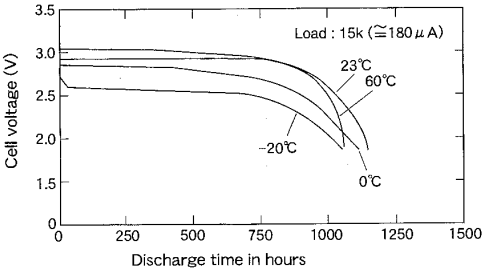


Figure 34. Temperature characteristics of the CR2032 lithium–manganese dioxide battery.

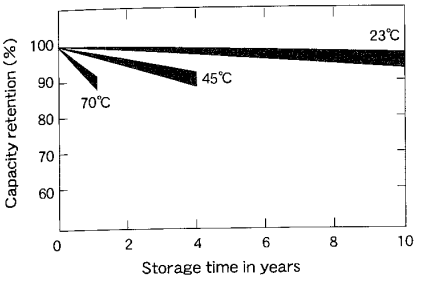


Figure 35. Self-discharge characteristics of the CR17335SE lithium–manganese dioxide battery.

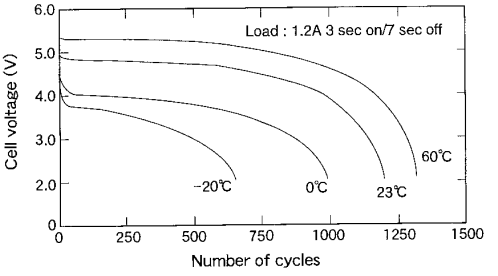


Figure 36. Pulse discharge characteristics of the 2CR5 lithium–manganese dioxide battery.

Figure 33 shows the load characteristics of the coin type CR2032. The cell voltage of the battery is approximately 3 V. Figure 34 shows the temperature characteristics of the CR2032. The battery discharges at a stable voltage over the wide temperature range of –20 to 70 °C.

Figure 35 shows the storage characteristics of the cylindrical inside-out construction CR17335SE. This battery demonstrates extremely good storage characteristics; storage for 100 days at 70 °C is equivalent to 10 years at room temperature. Figure 36 shows the pulse discharge characteristics of the user-replaceable 2CR5. The operating voltage is stable over the wide temperature range of –20 to 60 °C. It can be used as a power source for tape recorders, LCD TVs, camera motors

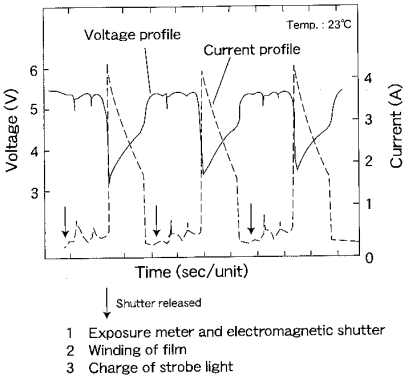


Figure 37. Practical test results of a 2CR5 lithium–manganese dioxide battery in a fully automatic camera at 23 °C.

for film rewinding, and camera flash systems. Figure 37 shows practical tests of the

CosMX Exhibit 1008, Page 62 of 633

2CR5 in a fully automatic camera at 23 °C. When the shutter is released, the discharged current powers the exposure meter and the electromagnetic shutter, and it is also used for winding the film and charging the strobe light for the next photograph. Since the strobe light can be charged within 2 s, continuous photographs can be taken with the strobe light at short time intervals, as the figure shows. Continuous photographs can be taken with the strobe light even at –40 °C. Moreover, there is no voltage delay during the initial discharge stage, even at low temperatures at high pulse rates [31–35].

2.4.2 Lithium–Carbon Monofluoride Batteries

The world's first $Li-(CF)_n$ battery was developed by Matsushita Battery Industrial Co., and several types are being manufactured.

$(CF)_n$ is prepared by the reaction of carbon powder with fluorine gas at an elevated temperature. The properties of $(CF)_n$ are similar to those of polytetrafluoroethylene (PTFE) which is prepared by organic synthesis.

The discharge reaction of $(CF)_n$ is generally considered to be as follows:

Anode reaction:

$$n\mathrm{Li} \rightarrow n\mathrm{Li}^+ + n\mathrm{e}^- \quad (13)$$

Cathode reaction:

$$(\mathrm{CF})_n + n\mathrm{e}^- \rightarrow n\mathrm{C} + n\mathrm{F}^- \quad (14)$$

Overall battery reaction:

$$n\mathrm{Li} + (\mathrm{CF})_n \rightarrow n\mathrm{C} + n\mathrm{LiF} \quad (15)$$

The general advantage of the $Li-(CF)_n$ batteries are the same as those of $Li-MnO_2$ batteries.

They may be classified by their structure, as coin, cylindrical and pin types. Table 5, 6, 7 respectively show their specifications. Applications of $Li-(CF)_n$ batteries as power sources are spreading from professional and business uses, such as in wireless transmitters and integrated circuit (IC) memory preservation, to consumer uses in electronic watches, cameras, calculators, and the like. Pin-type batteries are used for illumination–type fishing floats with a light-emitting diode. Coin-type batteries, which have a stable packing insulation, separator, and electrolyte for high

Table 5. Specifications of coin-type lithium–carbon monofluoride batteries

Model	Nominal Voltage (V)	Nominal capacity (mAh)	discharge current (mA)		Dimensions (mm)		Weight (g)
			Max.	Standard	Diameter	Height	
BR1216	3	25	5	0.03	12.5	1.60	0.6
BR1220	3	35	5	0.03	12.5	2.00	0.7
BR1225	3	48	5	0.03	12.5	2.50	0.8
BR1616	3	48	8	0.03	1.60	1.60	1.0
BR1632	3	120	8	0.03	16.0	3.20	1.5
BR2016	3	75	10	0.03	20.0	1.60	1.5
BR2020	3	100	10	0.03	20.0	2.00	2.0
BR2032	3	190	10	0.03	20.0	3.20	2.5
BR2320	3	110	10	0.03	23.0	2.00	2.5
BR2325	3	165	10	0.03	23.0	2.50	3.2
BR2330	3	255	10	0.03	23.0	3.00	3.2
BR3032	3	500	10	0.03	30.0	3.20	5.5

CosMX Exhibit 1008, Page 63 of 633

Table 6. Specifications of cylindrical lithium–carbon monofluoride batteries

Model	Nominal voltage (V)	Nominal capacity (mAh)	Discharge current (mA)		Dimensions (mm)		Weight (g)
			Max.	Standard	Diameter	Height	
BR-2/3A	3	1200	250	2.5	17.0	33.5	13.5
BR-A	3	1800	250	2.5	17.0	45.5	18.0
BR-C	3	5000	300	150.0	26.0	50.5	42.0

Table 7. Specifications of pin-type lithium–carbon monofluoride batteries

Model	Nominal voltage (V)	Nominal capacity (mAh)	Discharge current (mA)		Dimensions (mm)		Weight (g)
			Max.	Standard	Diameter	Height	
BR425	3	25	4	0.5	4.2	25.9	0.55
BR435	3	50	6	1.0	4.2	35.9	0.85

Table 8. Specification of coin-type lithium–carbon monofluoride batteries for high-temperature range

Model	Nominal voltage (V)	Nominal capacity (mAh)	Dimensions (mm)		Operating temperature range (°C)
			Diameter	Height	
BR1225A	3	48	12.5	2.5	–40 to 150
BR1632A	3	120	16.0	3.0	–40 to 150

temperature usage, are applicable at temperatures as high as 150 °C. The packing insulation and separator are made of special-use engineering plastics. Table 8 shows the specifications of coin-type batteries for high-temperature usage [36].

2.4.3 Lithium-Thionyl Chloride Batteries

The $Li-SOCl_2$ battery consists of a lithium-metal foil anode, a porous carbon cathode, a porous non-woven glass or polymeric separator between them, and an electrolyte containing thionyl chloride and a soluble salt, usually lithium tetrachloroaluminate. Thionyl chloride serves as both the cathode active material and the electrolytic solvent. The carbon cathode serves as a catalytic surface for the reduction of thionyl chloride and as a repository for the insoluble products of the discharge reaction.

Although the detailed mechanism for the reduction of thionyl chloride at the carbon surface is rather complicated and has been the subject of much controversy, the battery reactions are described as follows:

Anode reaction:

$$4Li \rightarrow 4Li^+ + 4e^- \quad (16)$$

Cathode reaction:

$$2SOCl_2 + 4Li^+ + 4e^- \rightarrow 4LiCl + S + SO_2 \quad (17)$$

Overall battery reaction:

$$4Li + 2SOCl_2 \rightarrow 4LiCl + S + SO_2 \quad (18)$$

CosMX Exhibit 1008, Page 64 of 633

Sulfur dioxide is soluble in the electrolyte. Sulfur is soluble up to about 1 mol dm^{-3}, but it precipitates in the cathode pores near the end of discharge. Lithium chloride is essentially insoluble and precipitates on the surfaces of the pores of the carbon cathode, forming an insulating layer which terminates the operation of cathode-limited cells [37].

The battery, which features a high (3.6 V) operating voltage and wide operating temperature range (–55 to 85 °C) can serve as a memory backup power source. Table 9 shows their specifications [38].

Table 9. Specifications of cylindrical lithium–thionyl chloride batteries

Model	Nominal voltage (V)	Nominal capacity (mAh)	Dimensions (mm)		Weight (g)
			Diameter	Height	
ER3V P	3.6	1,000	19.5	24.5	8.5
ER4V P	3.6	1,200	19.5	24.5	10
ER6V P	3.6	2,000	19.5	47.0	16
ER6LV P	3.6	1,800	19.5	47.0	16
ER17330V P	3.6	1,700	20.5	29.5	13
ER17500V P	3.6	2,700	20.5	47.0	19

2.5 Coin-Type Lithium Secondary Batteries [39]

2.5.1 Secondary Lithium–Manganese Dioxide Batteries

It has been reported that MnO_2 has poor rechargeability [12,13]. However, most investigations were on $\gamma, \gamma/\beta$, and $\beta-MnO_2$, which are similar to the MnO_2 used in primary $Li-MnO_2$ batteries. In $\gamma/\beta-MnO_2$, an expansion of the crystal lattice occurs when Li^+ ions are inserted into its crystal structure. However, the degree of expansion does not increase much after a large initial change at quite a low level of discharge. It was considered that, if MnO_2 contained a small amount of Li in its crystal structure beforehand, the reversibility of its crystal structure would be improved.

In order to improve the rechargeability of $\gamma/\beta-MnO_2$, two types of lithium containing manganese oxides, spinel $LiMn_2O_4$ and heat-treated $LiOH_3 \cdot MnO_2$ (composite dimensional manganese oxide: CDMO), were prepared. First, the discharge and charge curves of $\gamma/\beta-MnO_2$, spinel $LiMn_2O_4$, and CDMO were measured. The cycle tests and discharge tests were carried out with flat–cells, with Li–Al alloy as the negative electrode; the electrolyte was 1 mol L^{-1} $LiClO_4$ – PC/DME . The results are shown in Fig. 38 : when spinel $LiMn_2O_4$ capacity and CDMO were discharged to 2 V, both showed stable curves.

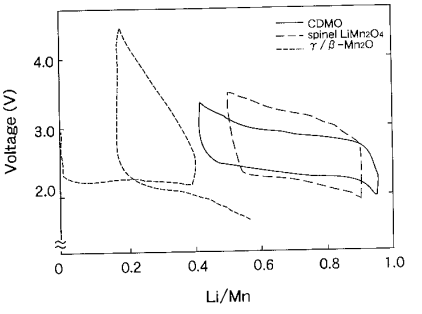


Figure 38. Discharge and charge curves for $\gamma/\beta-MnO_2$, spinel $LiMn_2O_4$ and CDMO electrodes.

CosMX Exhibit 1008, Page 65 of 633

CDMO showed a 0.2 e/Mn larger capacity than spinel $LiMn_2O_4$, but $\gamma/\beta-MnO_2$ could not be fully charged to the 0.4 e/Mn level; in the second discharge, the discharge voltage of $\gamma/\beta-MnO_2$ was lower than that in the first discharge. Figure 39 shows the results of cycle tests on coin-type cells at a depth of 0.14 e/Mn. It was found that spinel $LiMn_2O_4$ and CDMO had better rechargeability than $\gamma/\beta-MnO_2$. No deterioration was observed in spinel $LiMn_2O_4$, or CDMO.

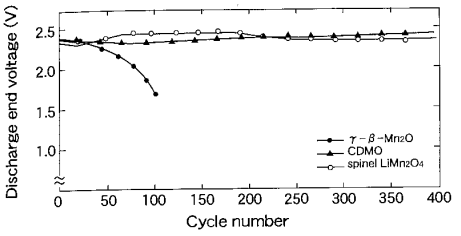


Figure 39. Cycling performance of various manganese oxide electrodes.

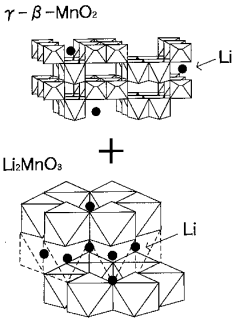


Figure 40. Proposed structure of CDMO

The crystal structure model of heat-treated $LiOH-MnO_2$ is considered to be as shown in Fig. 40. It is composed of $\gamma/\beta-MnO_2$ which includes some Li, and Li_2MnO_3. $\gamma/\beta-MnO_2$ has one-dimensional channels, whereas Li_2MnO_3 has a structure in which Li atoms reside as layers, which accounts for its being named composite dimensional manganese oxide (CDMO).

An Li–Al Alloy was investigated for use as a negative electrode material for lithium secondary batteries. Figure 41 shows the cycle performance of a Li–Al electrode at 6% depth of discharge (DOD). The Li–Al alloy was prepared by an electrochemical method. The life of this electrode was only 250 cycles, and the Li–Al alloy was not adequate as a negative material for a practical lithium battery.

In order to clarify the reason for the deterioration in the Li–Al alloy electrode, morphological changes in it were investigated by scanning electron microscopy (SEM) after electrochemical alloying and cycling. The Li reacted with the Al nonuniformly during electrochemical alloying, and after the cycling fine particles were observed. It was though that the pulverization resulted from the nonuniform reaction of Li and Al.

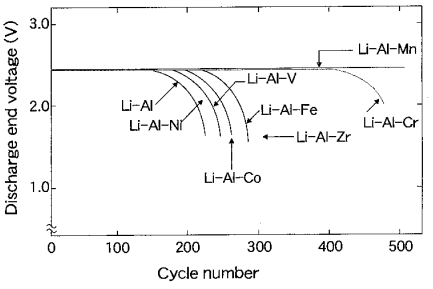


Figure 41. Cycling performance of several Li–Al alloy electrodes (discharge end 6% of total Li in Li–Al alloy; current density 1.1 mA cm^{-2}).

Several metal additives were investigated to improve this nonuniform reaction. Figure 41 shows the cycle performance of several Li–Al alloy electrodes. It was found that Li–Al–Mn and Li–Al–Cr alloys had better rechargeability than Li–Al alloy; in the Li–Al–Mn alloy, particularly no de-

CosMX Exhibit 1008, Page 66 of 633

terioration was observed even at the 500th cycle. It was confirmed by SEM that the Li–Al–Mn alloy did not turn to powder after cycling. Based on these results, Li-Al-Mn alloy was chosen as the negative electrode material for coin-type secondary lithium batteries.

Figure 42 shows the structure of the ML series of secondary lithium-manganese dioxide batteries, and Fig. 43 shows the discharge curves of the ML2430 cell (diameter 24.5 mm, height 3.0 mm). The nominal voltage and capacity of the ML2430 are 3 V and 90 mAh, respectively, and the energy density is 160 Whl^{-1}. Figures 44 and 45 show the pulse characteristics and the dependence of discharge capacity on load; the discharge capacity is 90 mAh, even with a 1 kΩ load.

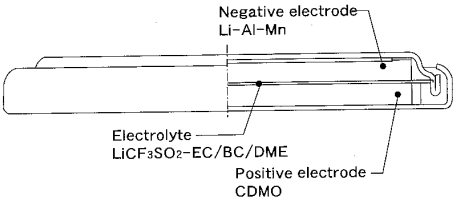


Figure 42. Cell structure of the Li–Al–CDMO cell (ML2430). EC, ethylene carbonate; BC, butylene carbonate

As regards the cycle performance, the ML2430 exhibits 3000 cycles at 5% depth and 500 cycles at a 20% depth of charge (Fig. 46). It can be used over a wide range of temperatures, from –20 to 60 °C. The discharge capacity at –20 °C is 90% of the discharge capacity at 23 °C (Fig. 47). The storage characteristics of the ML2430 were also measured (Fig. 48); storage for 60 days at 60 °C is considered to be equivalent to storage for three years at room temperature. The loss of discharge capacity is less than 5% per year [42–47].

Finally, Table 10 shows the specifications of secondary lithium–manganese dioxide batteries. Recently, the use of these batteries as sources for memory backup has expanded remarkably [47].

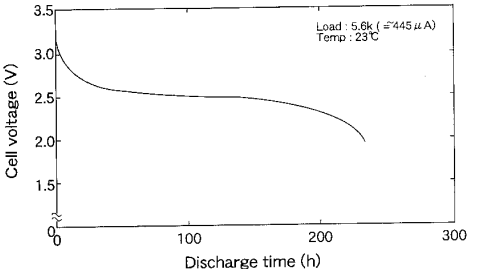


Figure 43. Discharge characteristics of the Li–Al–CDMO cell (ML2430).

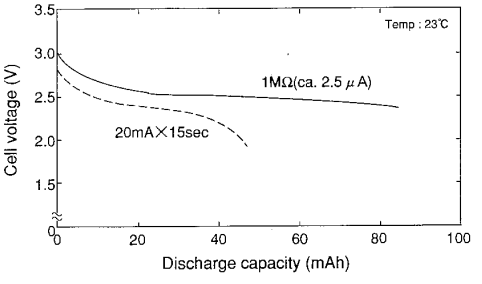


Figure 44. Pulse characteristics of the Li–Al–CDMO cell (ML2430).

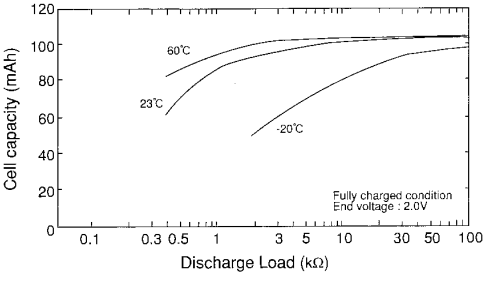


Figure 45. Dependence of discharge capacity on load (ML2430)

CosMX Exhibit 1008, Page 67 of 633

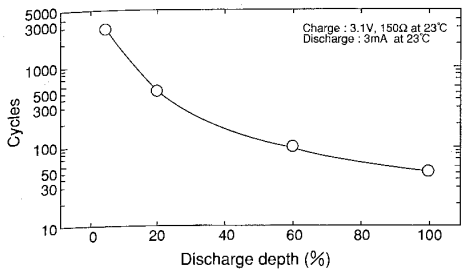


Figure 46. Cycling performance of the Li–Al-CDMO cell (ML2430). The number of 100% charge–discharge cycles is calculated until the capacity drops to 100% of the nominal value (end voltage 2.0 V). The number of 5%, 20% and 60% charge–discharge cycles is calculated until an end voltage of 2.0 V.

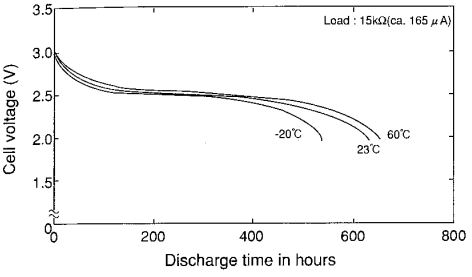


Figure 47. Discharge characteristics of the Li–Al-CDMO cell (ML2430) at several temperatures.

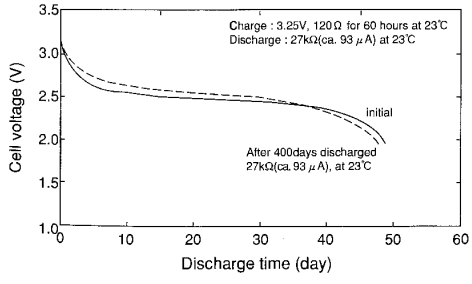


Figure 48. Storage characteristics of the Li–Al-CDMO cell (ML2430).

Table 10. Specifications of secondary lithium-manganese dioxide batteries

Model	Nominal voltage (V)	Nominal capacity (mAh)	Standard charge–discharge current (mA)	Max. discharge current (mA)		Charge–discharge cycle characteristics	Charging method	Dimensions (mm)		Weight (g)
				Continuous	Puls			Diameter	Height	
ML1220	3	12	0.1	2	5		Constant-voltage charging at 3.1±0.15 V	12.5	2.0	0.8
ML2016	3	25	0.3	8	20	3,000 cycles (discharge depth of 0.5%)		20.0	1.6	1.8
ML2430	3	90	0.5	10	20	500 cycles (discharge depth of 20%)	2.95±0.15 V (continuous charging at high temperature)	24.5	3.0	4.1

CosMX Exhibit 1008, Page 68 of 633

2.5.2 Lithium-Vanadium Oxide Secondary Batteries

Lithium–vanadium oxide rechargeable batteries were developed as memory backup power sources with high reliability and high energy density.

The active material of the positive electrode is vanadium pentoxide, and that of the negative electrode is a lithium–aluminum alloy. The electrolyte contains an organic solvent. The operating voltage is high, flat 3 V. The energy density is 100-140 $Wh l^{-1}$. The batteries have excellent overcharge-withstanding characteristics. They can serve as a memory backup power source, and they are applicable to various types of microcomputer equipment, because they can be installed in a small space. Table 11 shows the specifications of these batteries [48, 49].

2.5.3 Lithium–Polyaniline Batteries

This battery is a completely new system with a conductive polymer of polyaniline for the positive electrode, a lithium alloy for the negative electrode and an organic solvent for the electrolyte. The battery features an operating voltage of 2–3 V. The energy density of the AL920 (diameter 9.5 mm, height 2.0 mm) is 11 $Wh l^{-1}$. It can serve as a memory backup power source. Table 12 shows the specifications of these batteries [50]. Chemically synthesized conductive polyaniline which is suitable for mass production has been investigated by Sanyo; conductive polymers of this type will be used as nonpollution materials in the future [51].

Table 11. Specifications of secondary lithium–vanadium oxide batteries

Model	Nominal voltage (V)	Nominal capacity (mAh)	Discharge current (mA)		Dimensions (mm)		Weight (g)
			Max.	Standard	Diameter	Height	
VL621	3	1.5	–	0.01	6.8	2.1	0.3
VL1261	3	5	–	0.03	12.5	1.6	0.7
VL1220	3	7	–	0.03	12.5	2.0	0.8
VL2020	3	20	–	0.07	20.0	2.0	2.2
VL2320	3	30	–	0.10	23.0	2.0	2.8
VL2330	3	50	–	0.10	23.0	3.0	3.7
VL3032	3	100	–	0.20	3.2	3.2	6.3

Table 12. Specifications of secondary lithium-polyaniline batteries

Model	Nominal voltage (V)	Nominal capacity (mAh)	Standard discharge current (mA)	Cycling characteristics	Dimensions		Weight (g)
					Diameter	Height	
Al920	3	0.5 (3–2 V)	0.001–1	0.1 mAh >1000 cycles	9.5	2.0	0.4
Al2016	3	3 (3–2 V)	0.001–5	1 mAh >1000 cycles	20.0	1.6	1.7
Al2032	3	8 (3–2 V)	0.001–5	3 mAh >1000 cycles	20.0	3.2	2.6

Table 13. Specifications of secondary lithium–carbon batteries

Model	Nominal voltage (V)	Nominal capacity (mAh)	Dimensions (mm)		Weight (g)	Recommended discharge current
			Diameter	Height		
CL2020	3	1.0 (3–2 V)	19.7–20.0	2.0 ± 0.2	1.9	1 μA–5 mA

CosMX Exhibit 1008, Page 69 of 633

2.5.4 Secondary Lithium-Carbon Batteries

Some fusible alloys composed of Bi, Pb, Sn, and Cd exhibit good characteristics as material for the negative electrode of secondary lithium batteries. The alloy can absorb the lithium into the negative electrode during charge and it can release the absorbed lithium into the electrolyte as ions during discharge. Dendritic deposition does not occur and the coulombic efficiency is high, because lithium metal is not deposited.

The active material of the negative electrode is an alloy which contains 50% Bi, 25% Pb, 12.5% Sn, and 12.5% Cd. The active material of the positive electrode is an activated carbon in which the specific surface area is about 1000 $m^2 g^{-1}$, and it has an electrical capacity through the large electric double layer. Table 13 shows the specifications of the batteries [52]. The operating voltage is 2–3 V. The energy density of the CL2020 (diameter 20 mm, height 2 mm) is 4.0 $Wh l^{-1}$. Long-term charge and discharge are possible. The batteries are used as a memory-backup supply for microcomputerized equipment and as maintenance-free power sources for solar–battery hybrid clocks, watches, and pocket calculators [53, 54].

2.5.5 Secondary Li–LGH–Vanadium Oxide Batteries

The active material of the negative electrode is a newly produced linear-graphite-hybrid (LGH) as the supporting carrier of lithium and the active material of the positive electrode is made of amorphous $V_2O_3 - P_2O_5$. By use of these active materials, the short cycle life of the charge-discharge characteristics due to lithium dendrite can be improved and the capacity decrease due to overdischarge can be reduced.

The battery features an operating voltage of 1.5-3 V. The energy density of the VG2025 (diameter 20.0 mm, height 2.5 mm) is 96 $Wh l^{-1}$. It can serve as a memory backup power source. Table 14 shows the specifications of the batteries [55].

2.5.6 Secondary Lithium–Polyacene Batteries

These batteries incorporate a polyacenic semiconductor (PAS) for the active material of the positive electrode, lithium for that of the negative electrode and an organic solvent for the electrolyte. PAS is essentially amorphous with a rather loose structure of molecular-size order with an interlayer distance of 4.0 Å, which is larger than the 3.35 Å of graphite [56, 57].

The batteries feature a high operating voltage of 2.0–3.3 V. The energy density of SL621 (diameter 6.8 mm, height 2.1 mm) is 6.5 $Wh l^{-1}$. It is applicable to various types of small, thin equipment requiring backup for memory and clock function. Table 15 shows the specifications of lithium–polyacene batteries [58].

Table 14. Specifications of secondary Li–LGH–amorphous V_2O_5 batteries

Model	Nominal voltage (V)	Nominal capacity (mAh)	Dimensions (mm)		Weight	Recommended discharge temperature
			Diameter	Height		
VG2025	3	25	20.0	2.5	2.5	–20°C–60°C
VG2430	3	50	24.5	3.0	4.3	–20°C–60°C

CosMX Exhibit 1008, Page 70 of 633

Table 15. Specifications of secondary lithium–polyacene batteries

Model	Electrical characteristics (at room temperature)						Dimensions (mm)		Weight
	Nominal Voltage (V)	Nominal capacity (mAh)	Internal Resistance (Ω)	Standard charging current (mA)	Standard charging method	Cycle time (min)	Diameter	Height	
SL414	3	0.013	800	0.01–0.2	Constant–voltage charging	1000	4.8	1.4	0.06
SL614	3	0.07	160	0.001–0.5			6.8	1.4	0.16
SL621	3	0.15	190	0.001–1			6.8	2.1	0.2
SL920	3	0.30	90	0.001–3			9.5	2.1	0.4

2.5.7 Secondary Niobium Oxide–Vanadium Oxide Batteries

These batteries have vanadium oxide as the active material of the positive electrode, niobium oxide for the active material of the negative electrode, and an organic solvent for the electrolyte. Lithium ions enter the vanadium oxide from the niobium oxide during discharge, and lithium ions enter the niobium oxide from the vanadium oxide during charge.

The energy density of the VN1616 (diameter 16 mm, height 1.6 mm) is 37 Whl^{-1}. The discharge voltage is 1.0–1.8 V. The charge–discharge cycle life is in excess of 700. These batteries can be charged relatively fast and withstand overdischarging (0 V). They can serve as power sources for memory backup and for compact equipment in place of Ni–Cd button batteries. They are also applicable to medical equipment, solar clocks, solar radios, and pagers. Table 16 shows the specifications of the batteries [59].

Table 16. Specifications of secondary niobium oxide–vanadium oxide batteries

Model	Nominal voltage (V)	Nominal capacity (mAh)	Dimensions (mm)		Weight (g)
			Diameter	Height	
VN621	1.5	1.2	6.8	2.1	0.3
VN1616	1.5	8	16	1.6	1.2

2.5.8 Secondary Titanium Oxide–Manganese Oxide Batteries

These batteries are new systems which use a lithium–manganese composite oxide for the active material of the positive electrode a lithium–titanium oxide with a spinel structure for that of the negative electrode, and an organic solvent for the electrolyte. Lithium ions enter the manganese oxide from the titanium oxide during discharge and lithium ions enter the titanium oxide from the manganese oxide during charge.

The lithium–titanium oxides are prepared by heating a mixture of anatase (TiO_2) and LiOH at a high temperature. The product heated at 800–900 °C has a spinel structure of $Li_{4/3}Ti_{5/3}O_4$. When the charge and discharge cycles are performed

CosMX Exhibit 1008, Page 71 of 633

Table 17. Specifications of secondary titanium oxide–manganese oxide batteries

Model	Nominal voltage (V)	Nominal capacity (mAh)	Discharge current (mA)		Dimensions (mm)		Weight (g)
			Max.	Standard	Diameter	Height	
MT621	1.5	1.2	–	0.1	6.8	2.1	0.3
MT920	1.5	3	–	0.2	9.5	2.0	0.3
MT1620	1.5	11	–	0.5	16.0	2.0	0.3

between 2.5 and 0.5 V versus a lithium electrode, good cyclability (> 400 cycles) is obtained in the plateau region. The open-circuit potential in the charge plateau is 1.58 V relative to lithium electrode and polarization during charge and discharge is small. The capacity density in the plateau is about 147 $mAhg^{-1}$, which corresponds to a 0.84-electron transfer for $Li_{4/3}Ti_{5/3}O_4$ [60, 61].

The batteries feature a 1.5 V operating voltage. The energy density of the MT920 (diameter 9.5 mm, height 2.0 mm) is 45 Whl^{-1}. It is applicable to watches in which the power source is rechargeable with a solar battery, and it can serve as a memory backup power source. Table 17 shows the specifications of $TiO_2 - MnO_2$ batteries [62].

2.6 Lithium-Ion Batteries

Lithium-ion batteries are generally composed of lithium containing a transition-metal oxide as the positive electrode material and a carbon material as the negative electrode material. Figure 49 illustrates the principle of the lithium-ion battery. When the cell is constructed, it is in the discharge state. Then charged, lithium ions move from the positive electrode through the electrolyte and electrons also move from the positive electrode to the negative electrode through the external circuit with the charger. As the potential of the positive electrode rises and that of the negative electrode is lowered by charging, the voltage of the cell becomes higher. The cell is discharged by the connection of a load between the positive and negative electrodes. In this case, the lithium ions and electrons move in opposite directions while charging. Consequently, electrical energy is obtained.

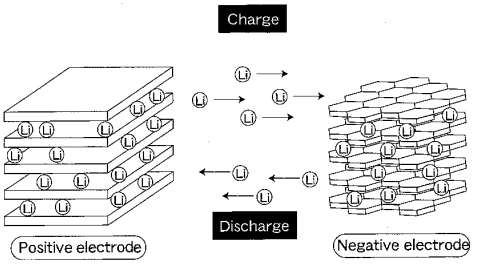


Figure 49. Principle of the lithium-ion battery

2.6.1 Positive Electrode Materials

Many studies have been done on complex oxides of lithium and a transition metal, such as $LiCoO_2$, $LiNiO_2$, and $LiMn_2O_4$. $LiCoO_2$ and $LiNiO_2$ have $\alpha - NaFeO_2$ structure. These materials are in space group *r*3*m*, in which the transition metal and lithium ions are located at octahedral 3(a) and 3(b) sites, respectively, and oxygen ions are at 6(c) sites. The oxygen ions form cubic close packing. This structure can be described as layered, giant,

CosMX Exhibit 1008, Page 72 of 633

with alternating lithium-cation sheets and CoO_2 / NiO_2 -anion sheets.

In contrast, $LiMn_2O_4$ has a spinel structure. This material has the space group *Fd3m* in which the transition-metal and lithium ions are located at octahedral 8(a) and tetrahedral 16(d) sites, respectively, and the oxygen ions are at 32(e) sites. There are octahedral 16(c) sites around the 8(a) sites and lithium ions can diffuse through the 16(c) and 8(a) sites. As this structure contains a diffusion path for the lithium ions, these ions can be deintercalated and intercalated in these compositions.

The research on $LiCoO_2$ is more advanced because of the simplicity of sample preparation [63]. Figure 50 shows the first charge–discharge curves of $LiCoO_2$. The sample was prepared from Li_2CO_3 and $CoCO_3$. Lithium and cobalt salts were mixed well, and reacted at 850 °C for 20 h in air. The reaction conditions were such that the sample could show the maximum rechargeable capacity.

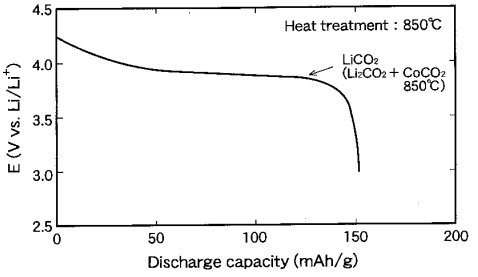


Figure 50. Discharge characteristics of $LiCoO_2$ (current density 0.25 mA cm^{-2})

The electrolyte was a mixture of ethylene carbonate and diethyl carbonate containing 1 mol L^{-1} $LiPF_6$. In order to attain a high-voltage charge, an aluminum substrate was used. The data in Fig. 50 were taken at the charge cutoff potential of 4.3 V (versus Li/Li^{+1}). The working voltage is extremely high, so an oxidation-resistant electrolyte is necessary in the development of 4 V secondary batteries.

As can be seen in Fig. 50, the average working potential is about 3.6 V and rechargeability is reasonably good. The capacity of $LiCoO_2$ was 150 mAh g^{-1}.
The conditions for synthesizing $LiNiO_2$ are said to be more complicated than those for $LiCoO_2$, but $LiNiO_2$ offers an advantage in terms of the availability of natural resources and cost [64–67]. Suitable conditions for synthesizing $LiNiO_2$, such as raw materials, heat-treating temperature and atmosphere, have been investigated [68].

Lithium–nickel oxides form various lithium compounds, lithium hydroxides (LiOH), Li_2CO_3, nickel hydroxide ($Ni(OH)_2$), nickel carbonate ($NiCO_3$) and nickel oxide (NiO). Figure 51 shows the discharge characteristics of lithium-nickel oxides synthesized from these compounds. They were heat-treated at 850 °C for 20 h in air. Although the lithium nickel oxides showed a smaller discharge capacity than that of $LiCoO_2$, LiOH and $Ni(OH)_2$ were considered to be appropiate raw materials.

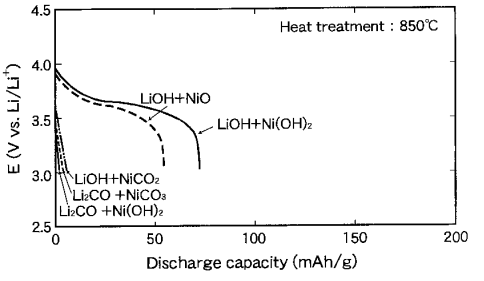


Figure 51. Discharge characteristics of some lithium–nickel oxides (current density 0.25 mA cm^{-2}).

CosMX Exhibit 1008, Page 73 of 633

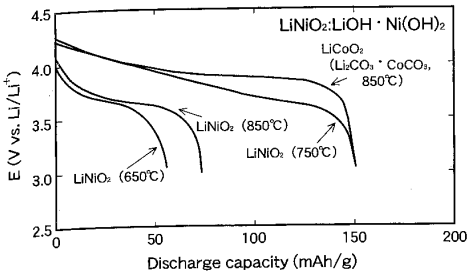


Figure 52. Discharge characteristics of some lithium–nickel oxides and $LiCoO_2$ (current density 0.25 mA cm^{-2}).

Figure 52 shows the discharge characteristics of $LiCoO_2$ and lithium–nickel oxides prepared from LiOH and $Ni(OH)_2$ at 650, 750 and 850 °C. Lithium–nickel oxide heat-treated at 750 °C showed nearly the same discharge capacity as $LiCoO_2$ while the discharge potential was lower than that of $LiCoO_2$. Composition of these oxides was determined by chemical analysis. The compositions of lithium–cobalt oxide prepared at 850 °C and lithium–nickel oxides prepared at 650 and 750 °C were very close to $LiCoO_{2.0}$ and $LiNiO_{2.0}$, respectively. On the other hand, the composition of lithium–nickel oxides prepared at 850 °C was $LiNiO_{1.8}$, and the decrease in their discharge capacity was caused by oxygen defects in their structure.

In order to examine the influence of the heat-treatment atmosphere, $LiCoO_2$ and $LiNiO_2$ were synthesized in an oxygen atmosphere. As a result, $LiNiO_2$ heat-treated in oxygen showed much better discharge characteristics than that in the air or oxygen. $LiNiO_2$ heat-treated in oxygen showed a discharge capacity of more than 190 mAh g^{-1}, which was greater than that of $LiCoO_2$, as shown in Fig. 53. From these results, LiOH and $Ni(OH)_2$ were found to be appropiate raw materials, and the most suitable conditions were 750 °C in oxygen, which produced a greater discharge capacity (more than 190 mAh g^{-1}) than $LiCoO_2$.

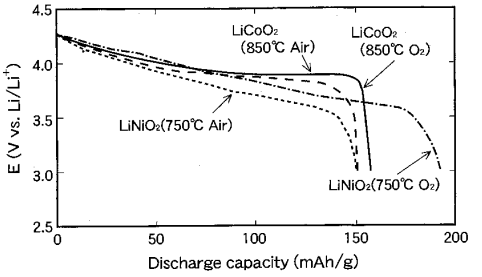


Figure 53. Discharge characteristics of $LiNiO_2$ and $LiCoO_2$ synthetized in air or oxygen (current density 0.25 mA cm^{-2}).

As $LiMn_2O_4$ offers an advantage in terms of the availability of natural resources and cost, many studies were made concerning charge–discharge characteristics and structure [60–71]. Figure 54 shows the discharge curve of $LiMn_2O_4$.

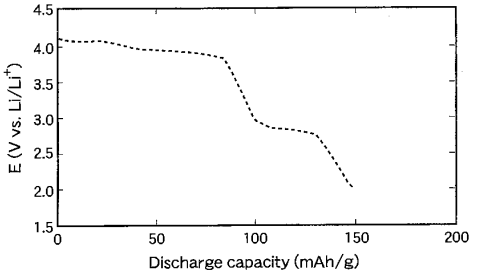


Figure 54. Discharge characteristics of $LiMn_2O_4$.

The operating voltage is extremely high, so an oxidation-resistant electrolyte is necessary for developing 4 V secondary batteries. As can be seen in Fig. 54, the average operating potential is about 3.6 V and rechargeability is reasonably good. However, the discharge capacity of

CosMX Exhibit 1008, Page 74 of 633

$LiMn_2O_4$ is less than 150 $mAh\,g^{-1}$. Consequently, the main feature of $LiMn_2O_4$ is its low cost, but the discharge capacity is also lower than $LiCoO_2$ and $LiNiO_2$.

$LiCo_{1-x}Ni_xO_2$ composite oxides consisting of $LiNiO_2$ and $LiCoO_2$ have also been studied; the influence of the Co/Ni ratio in these materials (x=0.1– 0.9) was examined. Figure 55 shows their discharge characteristics. The highest discharge capacity was obtained in the case of x=0.7. The discharge capacity of $LiCo_{0.3}Ni_{0.7}O_2$ was more than 150 $mAh\,g^{-1}$; as it has almost the same capacity as $LiCoO_2$ and $LiNiO_2$, this material is desirable as the positive electrode material for lithium-ion batteries.

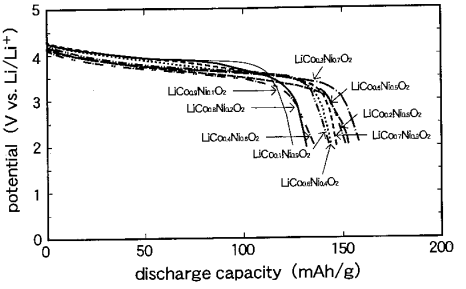


Figure 55. Discharge characteristics of $LiCo_xNi_{1-x}O_2$.

2.6.2 Negative Electrode Materials

Carbon materials which have the closest-packed hexagonal structures are used as the negative electrode for lithium-ion batteries; carbon atoms on the (0 0 2) plane are linked by conjugated bonds, and these planes (graphite planes) are layered. The layer interdistance is more than 3.35 Å and lithium ions can be intercalated and deintercalated. As the potential of carbon materials with intercalated lithium ions is low, many studies have been done on carbon negative electrodes [72–75].

There are many kinds of carbon materials, with different crystallinity. Their crystallinity generally develops due to heat-treatment in a gas atmosphere ("soft" carbon). However, there are some kinds of carbon ("hard" carbon) in which it is difficult to develop this cristallinity by the heat-treatment method. Both kinds of carbon materials are used as the negative electrode for lithium-ion batteries.

Soft carbon is also classified by its crystallinity. For example, acetylene black and carbon black are regarded as typical carbon materials with low crystallinity. Coke materials are carbon materials with intermediate crystallinity. It is easy to obtain these materials because they are made from petroleum and coal and they were actively studied in the 1980s. In contrast , there are some graphite materials which have high crystallinity; their capacity is greater than that of coke materials, and these materials have been studied more recently, in the 1990s [76–80].

Coke materials are generally made by heat-treatment of petroleum pitch or coal-tar pitch in an N_2 atmosphere. Coke made from petroleum is called "petroleum coke" and that from coal is called "pitch coke". These materials have the closest–packed hexagonal structures. The crystallinity of coke materials is not so high as that of graphite. The crystallite size of coke along the c-axis (L_c) is small (about 10-20 Å) and the interlayer distance (d value; about 3.38–3.80 Å) is large.

Figure 56 shows the charge–discharge characteristics of coke materials such as petroleum coke and pitch coke in propylene carbonate containing 1 $mol\,L^{-1}$ $LiPF_6$. The discharge capacity of the coke electrodes was from 180 to 240 $mAh\,g^{-1}$. The initial efficiency (charge–discharge effi-

CosMX Exhibit 1008, Page 75 of 633

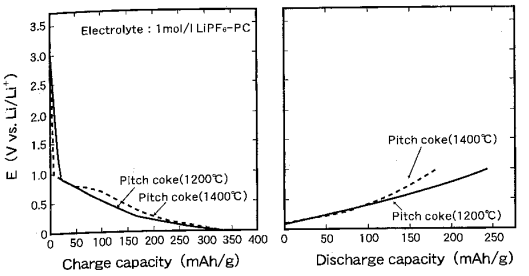


Figure 56. Charge–dicharge characteristics of some carbon material electrodes (1st cycle current density 0.2 mA cm^{-2}).

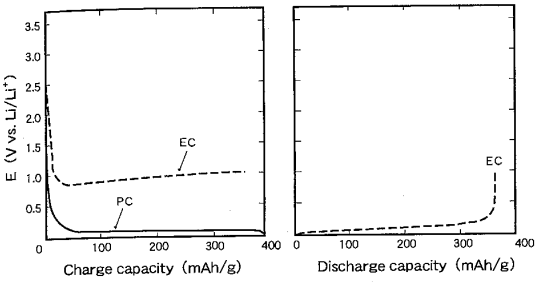


Figure 57. Charge–dicharge characteristics of some carbon material electrodes (1st cycle current density 0.2 mA cm^{-2}).

ciency coulombic efficiency) of the coke electrodes was 75–82%, and the efficiency after the second cycle was 100%. The charge-discharge characteristics in different electrolytes, such as butylene carbonate, γ – butyrolactone, sulfolane and ethylene carbonate, were also tested. The results are almost the same as those for propylene carbonate. It was found that the charge–discharge characteristics are not strongly influenced by the nature of the electrolyte.

The cycling characteristics of coke materials were also tested: the deterioration ratio of the charge–discharge efficiency after 500 cycles was small, and coke materials showed sufficiently good cycling performance to be used as negative electrode materials for lithium–ion batteries. The performance of coke materials does not depend very much on the electrolyte, but their disadvantage is low discharge capacity.

Graphite materials with high crystallinity are further classified by their production method. Graphite materials made by heat-treating coke materials at temperatures higher than about 2000 °C are called "artificial graphite". On the other hand, there are also natural graphite materials which have the highest crystallinity of all carbon materials. These materials have the ideally closest-packed hexagonal structure. The L_c of natural graphite is more than 1000 Å and the d value is 3.354 Å, values which are close to the ideal graphite crystal structure [81, 82].

The crystallinity of artificial graphite can generally be controlled by the heat-treatment temperature, but it is lower than that of natural graphite. The L_c of artificial graphite is less than 1000 Å and the d value is more than 3.36 Å.

Figure 57 shows the charge-discharge characteristics of a natural graphite electrode in typical electrolytes such as propylene carbonate and ethylene carbonate containing 1 mol L^{-1} $LiPF_6$. Natural graphite could not be charged in propylene carbonate; the gas evolved during the attempt to charge was identified as propyl-

CosMX Exhibit 1008, Page 76 of 633

ene by gas chromatography, and it is believed that its evolution was caused by the decomposition of the solvent. No gas evolution was observed in ethylene carbonate.

The discharge capacity of the natural graphite electrodes was 370 $mAh\,g^{-1}$. The initial efficiency of the coke electrodes was 92%, and the efficiency after the second cycle was 100%. The theoretical capacity of C_6Li is 372 $mAh\,g^{-1}$ and it is gold, as is charged natural graphite. These results suggest that C_6Li was produced by the electrochemical reduction of natural graphite, and the formation of C_6Li was confirmed. Figure 58 shows the X-ray diffraction pattern of natural graphite during charge: the peak was shifted to a lower angle by charging. In the case of full charging, the peak was 24°, which indicates the formation of C_6Li. The discharge capacity of natural graphite is close to that of C_6Li. Its charge–discharge curves are very flat and the charge–discharge potential is very low. These features are advantageous for lithium-ion batteries because it is anticipated that the voltage of a lithium-ion battery using natural graphite as the negative electrode is high and its charge–discharge curve is flat.

The charge–discharge characteristics of artificial graphite were also tested; artificial graphite could not be charged in propylene carbonate for the same reason as natural graphite, but it could also undergo charge–discharge in ethylene carbonate. Figure 59 shows the charge–discharge characteristics of some graphite electrodes in ethylene carbonate containing 1 mol L^{-1} $LiPF_6$. Those of the artificial graphite electrode are also very flat, and the charge–discharge potential is also very low as for the natural graphite electrode.

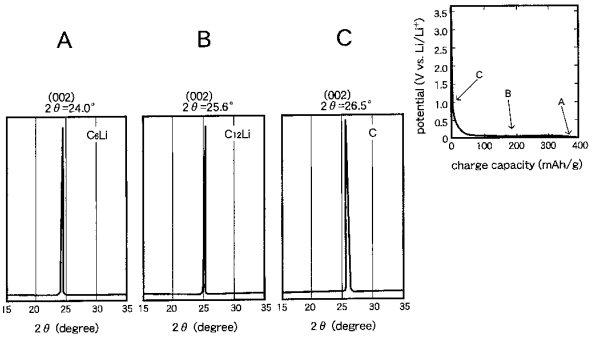


Figure 58. X-ray diffraction patterns of natural graphite.

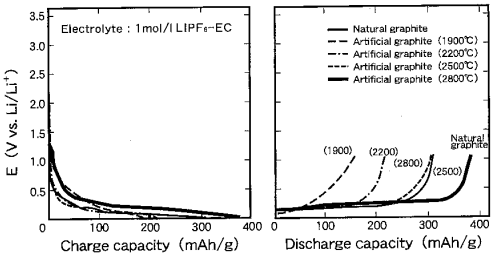


Figure 59. Charge–discharge characteristics of some graphite material electrodes (1st cycle current density 0.2 mA cm^{-2}).

CosMX Exhibit 1008, Page 77 of 633

However, the discharge capacity of artificial graphite is smaller than that of natural graphite, and depended on the heat-treatment temperature. Artificial graphite made by heat-treatment at a higher temperature showed a higher discharge capacity; as it has higher crystallinity, it is suggested that the discharge capacity of the graphite electrode may be related to the crystallinity of the graphite material.

The cycling characteristics of graphite electrodes were also tested. The deterioration ratio of the charge–discharge efficiency after 500 cycles was small and the graphite materials showed good cycling performance. The crystal structures of charged and discharged natural graphite electrodes at the fifth and 100th cycles were measured by the X-ray diffraction method; the results are shown in Fig. 60. For both cycles, the peak shifted to a lower angle after charging, and 2θ of the peak was 24°, which indicates the formation of C_6Li. By discharging, the 2θ of the peak became 26.5°, which indicates the extraction of lithium. No change was observed in the crystal structure of natural graphite up to 100 cycles.

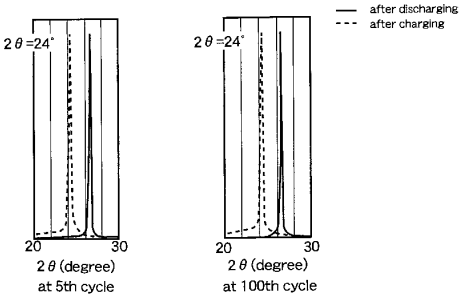


Figure 60. X-ray diffraction of natural graphite.

Figure 61 shows the relationship between the discharge capacity, the initial efficiency, and the L_c of some soft carbon materials when ethylene carbonate was used as a solvent. Figure 62 shows the relationship between the discharge capacity, the initial efficiency, and the d value in the same conditions. The carbon materials with longer L_c and smaller d values showed a higher discharge capacity and a higher initial charge–discharge efficiency. Natural graphite had the highest discharge capacity and the highest initial efficiency.

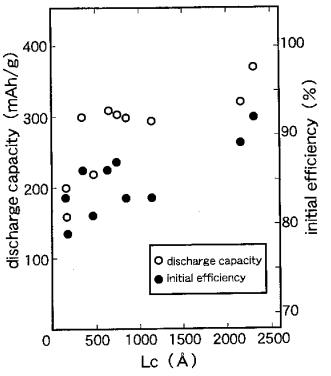


Figure 61. Relationship between discharge capacity, initial efficiency, and L_c of soft carbon materials.

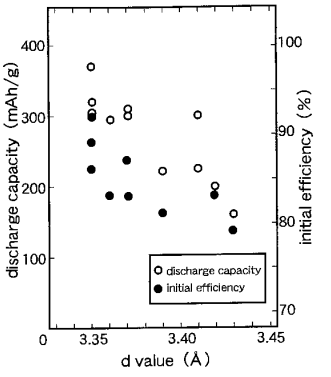


Figure 62. Relationship between discharge capacity, initial efficiency, and d value of soft carbon materials (O , discharge capacity; • , initial efficiency).

Both hard and soft carbons are used as negative electrode materials for lithium-ion batteries. Hard carbon is made by heat-treating organic polymer materials such as phenol resin. The heat-treatment tempera-

CosMX Exhibit 1008, Page 78 of 633

ture of these materials is the same as that of petroleum and coal when making coke materials.

Good charge–discharge characteristics have been reported [83], and the cycle characteristics were as good as soft carbon. The discharge capacity was strongly influenced by the charge–discharge conditions. There are some reports that the discharge capacity is larger than that of C_6Li as measured by the best charge–discharge method, but this method is difficult to use for practical lithium-ion batteries. The discharge capacity of hard carbon is expected to be smaller than that of soft carbon electrodes as measured by a practical charge–discharge method.

Polyacene is classified as a material which does not belong to either soft or hard carbons [84]. It is also made by heat-treatment of phenol resin. As the heat-treatment temperature is lower than about 1000 °C, polyacene contains hydrogen and oxygen atoms. It has a conjugated plane into which lithium ions are doped. It was reported that the discharge capacity of polyacene is more than 1000 $mAh\,g^{-1}$. However, there are no practical lithium-ion batteries using polyacene.

2.6.3 Battery Performances

Figure 63 shows the structure of a commercialized cylindrical-type lithium-ion battery. The lithium-ion battery is generally constructed with a spiral structure which serves as the separator between the positive and negative electrodes. An organic electrolyte containing lithium salts of which the conductivity is smaller than that of an aqueous electrolyte is used for this battery, but the short distance between the positive and negative electrodes and the large area of the electrode confer good characteristics.

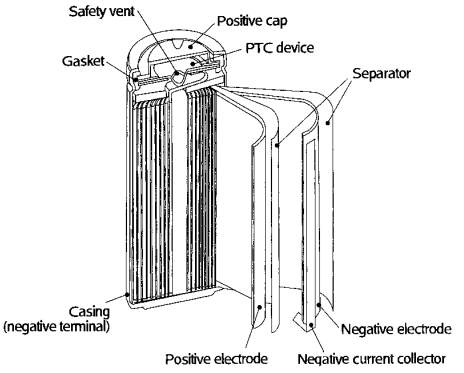


Figure 63. Structure of a lithium–ion battery. PTC, positive thermal coefficient device.

As mentioned above, the typical positive electrode material is $LiCoO_2$, and there are typically two types of negative electrode materials, such as coke and graphite. The characteristics of lithium-ion batteries constructed using these electrode materials are discussed below.

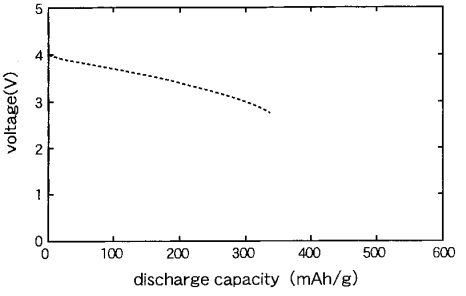


Figure 64. Discharge characteristics of an $LiCoO_2$ / coke cell.

Figure 64 shows the discharge characteristics of a cylindrical type $LiCoO_2$-coke cell. The discharge capacity is 350 mAh, the average discharge voltage is 3.6 V, and the energy density of this battery is 164 $Wh\,l^{-1}$ or 66 $Wh\,kg^{-1}$. The cell voltage of this battery decreased greatly during

CosMX Exhibit 1008, Page 79 of 633

discharge. This feature is not favorable from the viewpoint of total energy density, but it is easy to determine the residual capacity from the cell voltage [85].

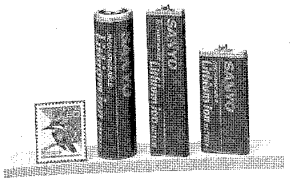


Figure 65. $LiCoO_2$ – natural graphite cells.

Figure 65 shows commercialized $LiCoO_2$–natural graphite cells and Table 18 shows the specification of these batteries. There are two types of batteries: cylindrical and prismatic. The cylindrical-type battery in Fig. 65 is called 18650 because its diameter is 18 mm and its length is 65 mm.

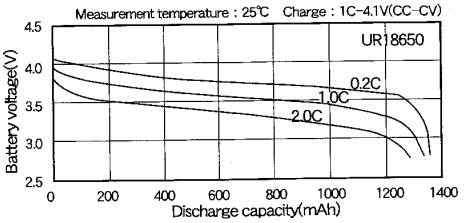


Figure 66. Discharge characteristics of the $LiCoO_2$ - natural graphite cell.

Figure 66 shows the discharge characteristics of the 18650-type cell. The discharge capacity is 1350 mAh, the average discharge voltage is 3.6 V, and the energy density of this battery is 294 $Wh\,l^{-1}$ or 122 $Wh\,kg^{-1}$. The energy density of this battery is higher than that of the $LiCoO_2$–coke cell, and its decrease in cell voltage was small during discharge, which is favorable from the viewpoint of total energy density.

Table 18. Specifications of $LiCoO_2$ – natural graphite cells

Model	Nominal voltage (V)	Nominal capacity* (mAh)	Standard charging method	Dimensions (mm)				Weight (g)
				Diameter	Thickness	Width	Height	
Cylindrical								
UR18650	3.6	1350	1 C–4.1 V	18	–	–	65	~40
UR18500	3.6	900	constant	18	–	–	50	~30
Rectangular			current–					
UF812248		550	constant	–	8.1	225	48	~18
UF102248	3.6	750	voltage	–	10.5	22.5	48	~24
UF611958	3.6	400	2.5/h	–	6.1	19.5	58	~15

Operating temperature: charge at 0 to 40 °C, discharge at –20 to 60 °C
*Guaranteed discharge capacity at 0.2 C (E_v = 2.75 V).

These features are caused by the graphite negative electrode. The $LiCoO_2$–graphite system is superior to $LiCoO_2$–coke in energy density and charge–discharge characteristics [86].

As the cost of $LiCoO_2$ is high, other positive electrode materials will eventually take the place of $LiCoO_2$. $LiNiO_2$ and $LiMnO_2$ are often mentioned as positive electrode materials instead of $LiCoO_2$ [87]. $LiNiO_2$ is desirable because it offers a larger capacity and lower cost than $LiCoO_2$, and it is expected that a $LiNiO_2$–graphite cell will be commercialized in the near future.

CosMX Exhibit 1008, Page 80 of 633

2.7 Lithium Secondary Battery with Metal Anodes

Secondary lithium–metal batteries which have a lithium–metal anode are attractive because their energy density is theoretically higher than that of lithium-ion batteries. Lithium–molybdenum disulfide batteries were the world's first secondary cylindrical lithium—metal batteries. However, the batteries were recalled in 1989 because of an overheating defect. Lithium–manganese dioxide batteries are the only secondary cylindrical lithium—metal batteries which are manufactured at present. Lithium–vanadium oxide batteries are being researched and developed. Furthermore, electrolytes, electrolyte additives and lithium surface treatments are being studied to improve safety and rechargeability.

$Li-MoS_2$ batteries were developed by Moli Energy; lithium is intercalated into the positive MoS_2 material. The value of x can vary from about 0.2 for a fully charged battery to about 1.0 for a fully discharged battery in accordance with reaction:

$$xLi + MoS_2 \rightarrow Li_xMoS_2 \qquad (19)$$

Products include an AA—size battery, a C—size battery, and a developmental BC—size (diameter 66 mm, height 152 mm) battery with a nominal 65 Ah capacity. The features of these batteries are a long charge-retention time, a direct state-of-charge indicator based on a variable open-circuit voltage, a high energy density relative to that of other rechargeable batteries, and a high power density [88].

A new rechargeable $Li-Li_xMnO_2$ 3 V battery system was developed by Tadiran Ltd. The active material of the negative electrode is lithium metal, and that of the positive electrode is lithiated manganese dioxide. These batteries have an organic electrolyte and separator, and exhibit excellent performance and safe behavior. The capacity of the AA— size battery is 800–750 mAh, and the energy density is 125–145 $Wh\,kg^{-1}$ or 280–315 $Wh\,l^{-1}$. At charging regimes around C/10, more than 350 cycles at 100% DOD could be obtained. An accumulated capacity of about 200 Ah can be achieved under cycling [89].

The system can prevent explosion, fire, and venting with fire under conditions of abuse. These batteries have a unique battery chemistry based on $LiAsF_6$/1,3–dioxolane/tributylamine electrolyte solutions which provide internal safety mechanism that protect the batteries from short-circuit, overcharge and thermal runaway upon heating to 135 °C. This behavior is due to the fact that the electrolyte solution is stable at low-to-medium temperatures but polymerizes at a temperature over 125 °C [90].

The active material of the negative electrode is lithium metal, and that of the positive electrode is amorphous V_2O_5 $(a-V_2O_5)$. A prototype AA–size battery has an energy of 2 Wh (900 mAh), an energy density of 110 $Wh\,kg^{-1}$ or 250 $Wh\,l^{-1}$, and a life of 150 to 300 cycles depending on the discharge and charge currents.

One of the most important factors determining whether or not secondary lithium metal batteries become commercially viable is battery safety, which is affected many factors: insufficient information is available about safety of practical secondary lithium metal batteries [91]. Vanadium compounds dissolve electrochemically and are deposited on the lithium anode during charge–discharge cycle. The

CosMX Exhibit 1008, Page 81 of 633

low reactivity of the vanadium-deposited lithium anode has been observed by calorimetry; a chemical-state analysis and morphological investigation of the lithium anode suggest that the improvement in stability is primarily due to a passivation film [92].

Films on lithium play an important part in secondary lithium metal batteries. Electrolytes, electrolyte additives, and lithium surface treatments modify the lithium surface and change the morphology of the lithium and its current efficiency [93].

Various cyclic ethers are reported to be superior solvents for secondary lithium metal batteries. 1,3-Dioxolane [94, 95] and 1,2-dimethoxyethane [95] show good cyclic characteristics. 1,3-Dioxolane–$LiB(CH_3)_4$ is highly conductive and has shown utility as an electrolyte in ambient temperature secondary lithium battery systems wherein a high rate of current drain is a desirable feature [96]. Researchers at Exxon used 1,3-dioxolane or 1,2-dimethoxyethane–$LiClO_4$ or $LiB(C_6H_5)_4$ and 2-methyltetrahydrofuran–$LiAsF_6$ in a lithium–titanium disulfide system [97]. 1,3-Dioxolane–1,2-dimethoxyethane–$Li_2B_{10}Cl_{10}$ exhibited chemical stability towards the components of a lithium–titanium disulfide cell and showed promise as an electrolyte in such cells [98]. Among various systems composed of an ether-based solvent and a lithium salt, THF–$LiAsF_6$ was the least reactive to lithium at elevated temperature and gave the best cycling efficiency [99, 100]. Tetrahydrofuran-diethyl ether–$LiAsF_6$ afforded lithium electrode cycling efficiency in excess of 98% [101].

2-Methyltetrahydrofuran (2MeTHF) showed good cycling characteristics [102–104], and 2MeTHF–$LiAsF_6$ showed promise of yielding high energy density and cycle life [105]. In an investigation of tetrahydrofurans methylated in the α-position: 2MeTHF–$LiAsF_6$ and 2,5-dimethyltetrahydrofuran–$LiAsF_6$ showed good cycling characteristics [106].

Several solvents other than ethers have also been reported to be superior solvents for secondary lithium batteries. Ethylene carbonate showed good cycling characteristics [107, 108].

The addition of 2-me-thylfuran, thiophene, 2-methylthiophene, pyrrole, and 4—methylthiazole to propylene carbonate–$LiPF_6$ or propylene carbonate–THF–$LiPF_6$ improved the cycling efficiency [109]. THF–2MeTHF–$LiAsF_6$ with an additional of 2-methylfuran showed the longest cycle life [110, 111].

The addition of some metal ions, such as Mg^{2+}, Zn^{2+}, In^{3+}, or Ga^{3+}, and some organic additives, such as 2-thiophene, 2-methylfuran, or benzene, to propylene carbonate–$LiClO_4$ improved the coulombic efficiency for lithium cycling [112]. Lithium deposition on a lithium surface covered with a chemically stable, thin and tight layer which was formed by the addition of HF to electrolyte can suppress the lithium dendrite formation in secondary lithium batteries [113].

The dendritic growth of lithium was suppressed on a lithium electrode surface modified by an ultrathin solid polymer electrolyte prepared from 1,1—difluoroethane by plasma polymerization [114].

A high rate discharge led to the recombination of isolated lithium which resulted in an increase in cycle life, and the cycle life decreased with an increase in the charge current density [115].

While the initial surface species formed on lithium in alkyl carbonates consist of $ROCO_2Li$ compounds, these species react with water to form Li_2CO_3, CO_2, and ROH. This reaction gradually changes the composition of the surface films formed on

CosMX Exhibit 1008, Page 82 of 633

lithium in these solvents, and Li_2CO_3 becomes the major component [116]. A film of Li_2CO_3 was formed on lithium by the direct reaction of propylene carbonate with lithium [117]. Diethyl carbonate was found to react with lithium to form lithium ethyl carbonate [118]. The main reaction products in the surface film on lithium were CH_3OLi in 1,2-dimethoxyethane, and C_4H_9OLi in tetrahydrofuran [119]. A surface film which contained ROLi, $ROCO_2Li$, and Li_2CO_3 was formed on lithium in 1.3-Dioxolane–$LiClO_4$ [120].

A lithium electrode is reported to show high rechargeability in solutions containing $LiAsF_6$. A brown film composed of an $(-O-As-O)_n$ polymer and LiF was formed on lithium in THF–$LiAsF_6$ [121]; elsewhere, a film on lithium was determined to be As_2O_3 and $F_2AsOAsF_2$ in THF–$LiAsF_6$ [122]. Another film had a probable two-layer structure consisting of Li_2O covered by an outer Li_2O-CO_2 adduct in 2MeTHF–$LiAsF_6$ [123]. A film of reduction product $ROCO_2Li$ was formed on lithium in ethylene carbonate–$LiAsF_6$ or propylene carbonate–$LiAsF_6$ [124].

As the cycling efficiency of metallic lithium is always significantly below 100% (~ 99%), the lithium anode has to be overdimensioned (200–400%) in practical cells.

2.8 References

[1] R. W. Graham, *Secondary Batteries*, **1978**.

[2] Sanyo Electric Co., Ltd. *Alkaline Manganese Battery Catalogue*, **1995**.

[3] M. Yano, M. Nogami, *Denki Kagaku*, **1997**, *65*, 154.

[4] A. Miura, *Denki Kagaku*, **1989**, *57(6)*, 459.

[5] T. Akazawa, W. Sekiguchi, J. Nakagawa, *Proc. 28th Battery Symp., Tokyo, Japan*, **1987**.

[6] *Engineering Handbook of Sealed Type Nickel–Cadmium Batteries*, Sanyo Electric Co., Ltd., Osaka, **1988**.

[7] C. D. S. Tuck, *Modern Battery Technology*, Sanyo Electric Co., Ltd., Osaka; **1991**, p. 244–289.

[8] J.H.N. van Vucht, F.A. Kuijpers, H.C.A.M. Brunning, *Philips Res. Rep.*, **1970**, *25*, 133.

[9] M. A. Gutjahr, H. Buchner, K. Beccu, *Proc. 8th Int. Symp. of a new reversible negative electrode for alkaline storage batteries based on metal alloy hydrides*, **1974**, p. 79.

[10] R. L. Cohen, J. H. Wernick, *Science*, **1981**, *214*, 1081.

[11] S. Suda, *Int. J. Hydrogen Energy*, **1987**, *12*, 323.

[12] J. J. G. Willimes, *Philips J. Res.*, **1984**, *39*, 1.

[13] J. R. van Beek, H. C. Donkersloot, J. J. G. Willimes, *Power Sources*, **1985**, *10*, 317.

[14] M. Ikoma, Y. Kawano, N. Yanagihara, N. Ito, I. Matsumoto, *Proc. 27th Battery Symp., Osaka, Japan*, **1986**, p. 89.

[15] N. Furukawa, Y. Inoue, T. Matsumoto, *Proc. 28th Battery Symp., Tokyo, Japan*, **1987**, p. 107.

[16] Y. Sato, M. Kanda, E. Yagasaki, K. Kanno, *Proc. 28th Battery Symp., Tokyo, Japan*, **1987**, p. 109.

[17] M. Ikoma, Y. Ito, H. Kawano, M. Ikeyama, K. Iwasaki, I. Matsumoto, *Proc. 28th Battery Symp., Tokyo, Japan*, **1987**, p. 112.

[18] H. Ogawa M. Ikoma, H. Kawano, I. Matsumoto, *Power Sources*, **1988**, *12*, 393.

[19] I. Yonezu, M. Nogami, K. Inoue, T. Matsumoto, T. Saito, N. Furukawa, *Proc. Hydrogen Energy Systems Society of Japan*, Publication 14-1, **1989**, p. 21.

[20] M. Nogami, M. Tadokoro, N. Furukawa, *176tn Meet. Electrochem. Soc. FL, USA*, **1989**, p. 130.

[21] S. Wakao, H. Sawa, H. Nakao, S. Chubachi, M. Abe, *J. Less-Common Met.*, **1987**, *131*, 311.

[22] M. A. Fetcenko, S. Venkatesan, S. R. Ovshinsky, *Proc. 34th Int. Power Sources Symp., NJ, USA*, **1990**, p. 305.

[23] R. Nagai, S. Wada, H. Hrista, K. Kajita, Y. Uetani, *Proc. 23th Battery Symp., Kyoto, Japan*, **1991**, p. 175.

[24] M. Nogami, Y. Morioka, Y. Ishikura, N. Furukawa, *Denki Kagaku*, **1993**, *61*, 997.

[25] M. Nogami, N. Furukawa, *J. Chem. Soc. Jpn.*, **1995**, 1.

CosMX Exhibit 1008, Page 83 of 633

[26] M. Nogami, M. Tadokoro, M. Kimoto, Y. Chikano, T. Ise, N. Furukawa, *Denki Kagaku*, **1993**, *61*, 1088.

[27] Y. Chikano, M. Kimoto, R. Maeda, M. Nogami, K. Nishio, T. Saito, S. Nakahori, S. Murakami, N. Furukawa, *Proc. Electrochem. Soc.*, Publication 94-27, **1994**, p. 403.

[28] I. Yonezu, M. Nogami, *Proc. 7th Canadian Hydrogen Workshop, Quebec, Canada*, **1995**, p. 171

[29] H. V. Venkatasetty, *Lithium Battery Technology* (Ed: H. V. Venlakasetty), John Willey & Sons, New York, **1990**, p. 61.

[30] *Catalogue of lithium-manganese dioxide batteries*, Sanyo Electric Co., Ltd., **1997**.

[31] S. Narukawa, N Furukawa, *Modern Battery Technology*, (Ed: C. V. Stuck), Ellis Horwood, New York, **1993**, p. 348.

[32] H. Ikeda, *Lithium Batteries* (Ed.: J. P. Gabano), Academic Press, New York, **1983**, p. 169.

[33] T. Nohma, S. Yoshimura, K. Nishio, T. Saito, *Lithium Batteries* (Ed.: G. Pistoia), Elsevier, Amsterdam, **1994**, p. 417.

[34] M. Takahashi, S. Yoshimura, I. Nakane, T. Nohma, K. Nishio, T. Saito, M. Fujimoto, S. Narukawa, M. Hara, N. Furukawa, *J. Power Sources*, **1993**, *43–44*, 253

[35] K. Nishio, S. Yoshimura, T. Saito, *J. Power Sources*, **1995**, *55*, 115.

[36] *Catalogue of lithium-carbon monofluoride batteries*, Matsushita Battery Industrial Co., Ltd., **1996**.

[37] M. Fukuda, T. Iijima, *Lithium Batteries* (Ed.: J. P. Gabano), Academic Press, New York, **1983**, p. 211.

[38] F. Gibbard, T. B. Reddy, *Modern Battery Technology* (Ed.: C. V. Stuck), Ellis Horwood, New York, **1993**, p. 287.

[39] *Catalogue of lithium-thionyl chloride batteries*, Toshiba Battery Co., Ltd., **1996**.

[40] S. B. Brummer, *Lithium Battery Technology* (Ed.: H. V. Venkatasetty), John Willey & Sons, New York, **1989**, p. 159.

[41] D. W. Dampier, *J. Electrochem. Soc.*, **1974**, *121*, 656.

[42] G. Pistoia, *J. Electrochem. Soc.*, **1982**, *129*, 1861.

[43] T. Nohma, S. Yoshimura, K. Nishio, T. Saito, *Lithium Batteries* (Ed.: G. Pistoia), Elsevier, Amsterdam, **1994**, p. 417.

[44] T. Nohma, T. Saito, N. Furukawa, *J. Power Sources*, **1989**, *26*, 389.

[45] T. Nohma, Y. Yamamoto, K. Nishio, I. Nakane, N. Furukawa, *J. Power Sources*, **1990**, *32*, 373.

[46] T. Nohma, Y. Yamamoto, I. Nakane, N. Furukawa, *J. Power Sources*, **1992**, *39*, 51.

[47] H. Watanabe, T. Nohma, I. Nakane, S. Yoshimura, K. Nishio, T. Saito, *J. Power Sources*, **1990**, *32*, 373.

[48] *Catalogue of secondary lithium-manganese dioxide batteries*, Sanyo Electric Co., Ltd., **1997**.

[49] N. Koshiba, T. Ikehata, K. Takata, *National Technical Report*, **1991**, *37(1)*, 64.

[50] *Catalogue of lithium-vanadium oxide secondary batteries*, Matsushita Battery Industrial Co., Ltd., **1996**.

[51] *Catalogue of lithium-polyaniline batteries*, Seiko Instruments Inc., **1996**.

[52] K. Nishio, M. Fujimoto, N. Yoshinaga, N. Furukawa, O. Ando, H. Ono, T. Murayama, *J. Power Sources*, **1991**, *34*, 153.

[53] *Catalogue of secondary lithium-carbon batteries*, Matsushita Battery Industrial Co., Ltd., **1996**.

[54] N. Koshiba, H. Hayakawa, K. Momose, *Proc. Symp. Battery Assoc. Japan*, **1985**, p. 145.

[55] Y. Toyoguchi, J. Yamaura, T. Matui, N. Koshiba, T. Shigematsu, T. Ikehata, *National Technical Report*, **1986**, *32(5)*, 116.

[56] *Catalogue of secondary Li-LGH-vanadium oxide batteries*, Toshiba Battery Co., Ltd., **1996**.

[57] S. Yata, *Proc. 60th Electrochem. Meeting Japan*, **1993**, p. 184.

[58] S. Yata, Y. Hata, H. Kinoshita, N. Ando, T. Hashimoto, K. Tanaka, T. Yamabe, *Proc. Symp. Battery Assoc. Japan*, **1993**, p. 63.

[59] *Catalogue of secondary lithium-polyacene batteries*, Seiko Instruments Inc., **1996**.

[60] *Catalogue of secondary niobium oxide-vanadium oxide batteries*, Matsushita Battery Industrial Co., Ltd., **1996**.

[61] N. Koshba. K. Takata, M. Nakanishi, E. Asaka, Z. Takahara, *Denki Kagaku*, **1994**, *62*, 870.

[62] T. Ohzuku, A. Ueda, *Solid State Ionics*, **1994**, *69*, 201.

[63] *Catalogue of secondary titanium oxide-manganese oxide batteries*, Matsushita Battery Industrial Co., Ltd., **1996**.

[64] J. N. Reimers, J. R. Dahn, *J. Electrochem. Soc.*, **1992**, *139*, 2091.

[65] J. R. Dahn, *Solid State Ionics*, **1990**, *44*, 87.

CosMX Exhibit 1008, Page 84 of 633

[66] R. Kanno, H. Kubo, Y. Kawamoto, *J. Solid State Chem.*, **1994**, *110*, 216.
[67] T. Ohzuku, A. Ueda, M. Nagayama, *J. Electrochem. Soc.*, **1993**, *140*, 1862.
[68] T. Ohzuku, H. Komori, M. Nagayama, K. Sawai, T. Hirai, *Chemistry Express*, **1991**, *16*, 161.
[69] T. Nohma, H. Kurokawa, M. Uehara, M. Takahashi, K. Nishio, T. Saito, *J. Power Sources*, **1995**, *54*, 522.
[70] A. Momchilov, V. Manev, A. Nassalevska, A. Kozawa, *J. Power Sources*, **1993**, *41*, 305.
[71] T. Ohzuku, M. Kitagawa, T. Hirai, *J. Electrochem. Soc.*, **1990**, *137*, 769.
[72] T. Ohzuku, H. Komori, K. Sawai, T. Hirai, *Chemistry Express*, **1991**, *5*, 733.
[73] N. Imanishi, S. Ohashi, T. Ichikawa, T. Takeda, O. Yamamoto, *J. Power Sources*, **1992**, *39*, 185.
[74] R. Kanno, Y. Takeda, T. Ichikawa, K. Nakanishi, O. Yamamoto, *J. Power Sources*, **1989**, *26*, 535.
[75] M. Mohri, N. Yanagisawa, Y. Tajima, H. Tanaka, T. Mitate, S. Nakajima, M. Yoshida, Y. Yoshimoto, T. Suzuki, H. Wada, *J. Power Sources*, **1989**, *26*, 545.
[76] Y. Mori, T. Iriyama, T. Hashimoto, S. Yamazaki, F. Fawakami, H. Shiroki, T. Yamabe, *J. Power Sources*, **1995**, *56*, 205.
[77] H. Fujimoto, A. Mabuchi, K. Tokumitsu, T. Kasuh, *J. Power Sources*, **1995**, *54*, 440.
[78] K. Tatsumi, N. Iwashita, H. Sakaebe, H. Shioyama, S. Higuchi, A Mabuchi, H. Fujimoto, *J. Electrochem. Soc.*, **1995**, *142*, 716.
[79] N. Takami, A. Satoh, M. Hara, T. Ohsaki, *J. Electrochem. Soc.*, **1995**, *142*, 371.
[80] S. Komatsu, T. Fukunaga, M. Terasaki, M. Mizutani, M. Yamachi, T. Ohsaki, *33rd Battery Symp. Japan*, **1992**, p. 89.
[81] T. Tamaki, M. Tamaki, *Proc. 36th Battery Symp. Japan*, **1992**, p. 105.
[82] M. Fujimoto, K. Ueno, T. Nouma, M. Takahashi, K. Nishio, T. Saito, *Proc. Symp. on New Sealed Rechargeable Batteries and Supercapacitors*, **1993**, p. 280.
[83] M. Fujimoto, Y. Kida, T. Nouma, M. Takahashi, K. Nishio, T. Saito, *J. Power Sources*, **1996**, *63*, 127.
[84] N. Sonobe, M. Ishikawa, T. Iwasaki, *35th Battery Symp. Japan*, **1994**, p. 47.
[85] S. Yata, Y. Hato, H. Kinoshita, A. Anekawa, T. Hashimoto, K. Tanaka, T. Yamabe, *35th Battery Symp. Japan*, **1994**, p. 59.
[86] K. Ozawa, *Solid State Ionics*, **1994**, *69*, 212.
[87] T. Saitoh, T. Nohma, M. Takahashi, M. Fujitomo, K. Nishio, *Proc. on New Sealed Rechargeable Batteries and Supercapacitors*, **1993**, p. 355.
[88] D. Guyomard, J. M. Tarascon, *J. Electrochem. Soc.*, **1992**, *139*, 937.
[89] A. R. Stiles, *New Materials and New Processes*, **1985**, *3*, p. 89.
[90] P. Dan, E. Mengeritski, Y. Geronov, D. Aurbach, I. Weismann, *J. Power Sources*, **1995**, *54*, 143.
[91] E. Mengeritski, P. Dan, I. Weismann, A. Zaban, D. Aurbach, *J. Electrochem. Soc.*, **1996**, *143*, 2110.
[92] S. Tobishima, Y. Sakurai, J. Yamaki, *8th Int. Meeting on Lithium Batteries*, **1996**, p. 362.
[93] M. Arakawa, Y. Nemoto, S. Tobishima, M. Ichimura, *J. Power Sources*, **1993**, *43–44*, 517.
[94] D. Aurbach, A. Zaban, Y. Gofes, V. E. Ely, I. Weismann, O. Chusid, O. Abranzon, *7th Int. Meeting on Lithium Batteries*, **1994**, p.97.
[95] G. H. Newmann, *Proc. Workshop on Lithium Non-Aqueous Battery Electrochemistry*, Publication 80-7, The Electrochemical Society, NJ, **1980**, p. 143.
[96] W. N. Olmstead, *Proc. Symp. Lithium Batteries*, Publication 81-4, The Electrochemical Society, NJ, **1981**, p. 150.
[97] L. O. Klemann, G. H. Newmann, *J. Electrochem. Soc.*, **1981**, *128*, 13.
[98] K. M. Abraham, *J. Power Sources*, **1981/2**, *7*, 1.
[99] J. W. Johnson, M. S. Whittingham, *J. Electrochem. Soc.*, **1980**, *127*, 1653.
[100] V. R. Koch, J. H. Young., *J. Electrochem. Soc.*, **1978**, *125*, 1371.
[101] V. R. Koch, *J. Electrochem. Soc.*, **1979**, *126*, 181.
[102] V. R. Koch, J. L. Goldman, C. J. Mattos, Mulvaney, *J. Electrochem. Soc.*, **1982**, *129*, 1.
[103] V. R. Koch, *US Parent 4*, **1978**, *118*, 550.
[104] K. M. Abraham, *J. Electrochem. Soc.*, **1981**, *128*, 2493
[105] M. S. Whittingham, *J. Electroanal. Chem.*, **1981**, *118*, 229.
[106] S. P. S. Yen, D. Shen, R. P. Vasquez, F. J. Grunthaner, R. B. Somoano., *J. Electrochem. Soc.*, **1981**, *128*, 1434.
[107] J. W. Goldman, R. M. Mank, J. H. Young, V. R. Koch., *J. Electrochem. Soc.*, **1980**, *127*, 1461.
[108] M. Watanabe, M. Kanba, K. Nagaoka, I. Shi-

CosMX Exhibit 1008, Page 85 of 633

nohara, *J. Appl. Polym. Sci.*, **1982**, *27*, 4191.
[109] L. Heermann, J. Van Baelen, *Bull. Soc. Chim. Belg.*, **1972**, *81*, 379.
[110] T. Iizima, *National Technical Report*, **1974**, *20(1)*, 35.
[111] Y. Matsuda, M. Morita, *Prog. Batteries and Solar Cells*, **1988**, *9*, 266.
[112] S. Surampudi, D. H. Shen, C. K. Huang, S. R. Narayan, A. Attia, G. Halper, *J. Power Sources*, **1993**, *43–44*, 27.
[113] Y. Matsuda, *J. Power Sources*, **1993**, *43*, 1.
[114] Z. Takehara, *7th Int. Meeting Lithium Batteries*, **1994**, p. 37.
[115] Z. Takehara, Z. Ogumi, Y. Utimoto, K. Yasuda, H. Yoshida, *J. Power Sources*, **1993**, *43–44*, 377.
[116] M. Arakawa, S. Tobishima, Y. Nemoto, M. Ichimura, *J. Power Sources*, **1993**, *43–44*, 27.
[117] D. Aurbach, A. Zaban, Y. E. Ely, I. Weissman, O Chusid, O. Abramzon, *7th Int. Meeting Lithium Batteries*, **1994**, p. 97.
[118] R. Fong, M. C. Reid, R. S. McMillan, J. R. Dahn, J. Electrochem. Soc., 1987, 134, 516.
[119] D. Aurbach, M. L. Daroux, P. W. Faguy, E. Yeager, J. Electrochem. Soc., 1987, 134, 1611.
[120] D. Aurbach, M. L. Daroux, P. W. Faguy, E. Yeager, *J. Electrochem. Soc.*, **1988**, *135*, 1863.
[121] Y. Gofer, M. Ben-Zion, D. Aurbach, *J. Power Sources*, **1992**, *39*, 163.
[122] A. V. R. Koch, *J. Electrochem. Soc.*, **1979**, *39*, 163.
[123] M. Odziemkowski, M. Krell, D. E. Irish, *J. Electrochem. Soc.*, **1992**, *139*, 3052.
[124] S. P. S. Yen, D. Shen, R. P. Vasquez, F. J. Grunthaner, R. B. Somoano, *J. Electrochem. Soc.*, **1981**, *128*, 1434.
[125] D. Aurbach, O. Chusid, *J. Electrochem. Soc.*, **1993**, *140*, L1.

CosMX Exhibit 1008, Page 86 of 633

3 Global Competition of Primary and Secondary Batteries

Karl Kordesch and Josef Daniel Ivad

3.1 Introduction

The invention of many systems (primary cells of the zinc/manganese-dioxide type or rechargeable such as lead–acid or zinc/bromine batteries and H_2–air fuel cells, to list just a few), dates back to the late decade of the 19th century; some of these have been developed to commercial levels in the mid-20th century. A "cyclic" repetition of the basic concepts is noticeable, with the combination of old and new ideas leading to an incremental progress. However, there are some completely new technologies, such as the use of alkali metals in nonaqueous electrolytes, which have opened different perspectives. They were enthusiastically received, but they must somehow blend into the total picture, with involvement of economic aspects, also, and they are subjected to the "test of time". The demands of the electronic age, electrical power needs, and human mobility requirements are the driving forces, but in many cases the cost picture and the environment provide urgent reasons for changes in the existing battery technology.

It is not possible to survey the presently existing battery technology here, but much recent information is contained in Ref. [1], and extensive basic literature is contained in Ref. [2], also scheduled to be re-issued in the near future.

Figure 1 shows the principal Zn–carbon (Leclanché) cell and Figure 2 shows the basic construction of a cylindrical AA-size alkaline $Zn - MnO_2$ cell.

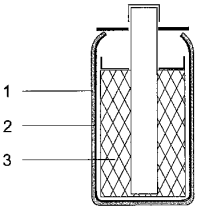


Figure 1. The design principle of a cylindrical Zn–carbon (Leclanché) cell [2]. 1, Zinccan; 2, separator; MnO_2 bobbin (Reproduced by courtesy of Varta Battery AG).

It should be noted that the rechargeable cells discussed later have the same construction and differ only in separator type, electrode composition and cathode / anode balance. For comparison, Fig. 3 shows the design of an AA-size lithium cell. The construction with a spirally rolled electrode increases the power output.

Marketing forecasts for batteries have been compiled from the Annual Reports published by several battery companies. Information based on the trade journals and investor's brochures, which surveyed and evaluated the present and future global distribution of battery types, was collected. Points of interest were the availability of batteries and their performance/cost ratios, but also geographical usage in connection with social considerations, such as per-

CosMX Exhibit 1008, Page 87 of 633

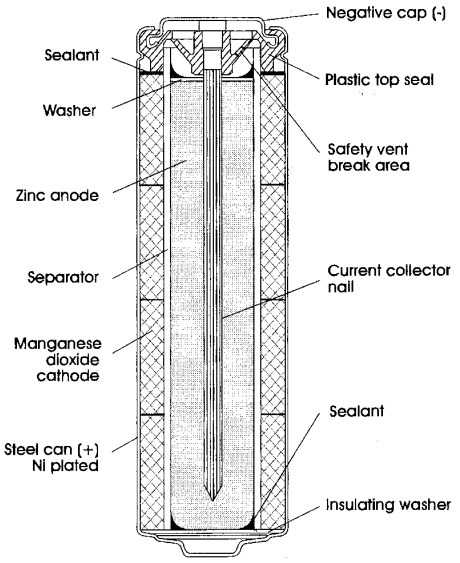


Figure 2. Section through a cylindrical AA-size alkaline $MnO_2 - Zn$ cell. Primary cells and the rechargeable cells discussed later have same construction and differ only in separator type, electrode compositions, and cathode / anode balance. (Reproduced by courtesy of Battery Technologies, Inc.).

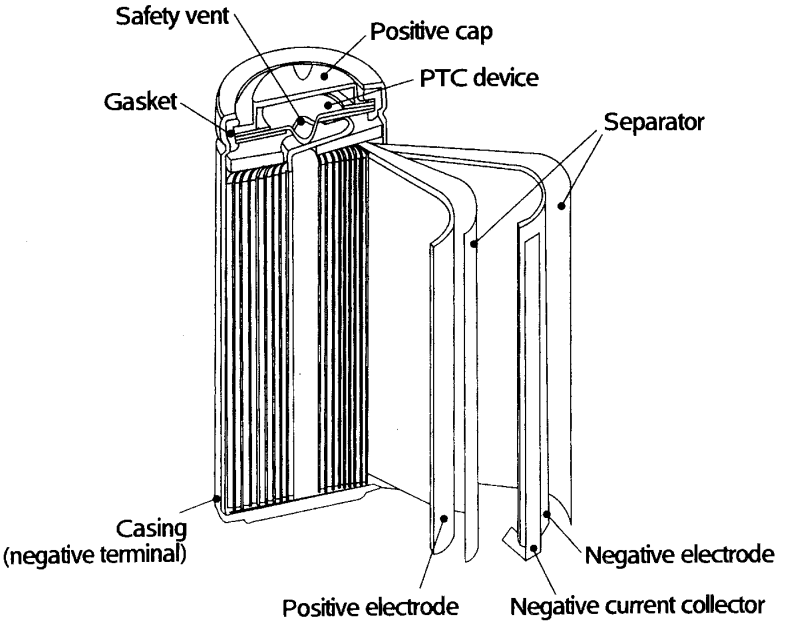


Figure 3. The design of a lithium battery with spirally rolled (large-surface) electrodes. This construction is needed to increase the power output (reproduced by courtesy of Hoppecke, Germany).

CosMX Exhibit 1008, Page 88 of 633

capita income on a regional or country basis [3, 4].

This screening effort does not differ from the way in which other product manufacturers judge their chances of profits and advancements. It implies progress of technology in a different sense, not always depending on the results of studies, which are presented in scientific meetings.

3.1.1 Estimate of Battery Market Trends and Expansions, 1995 to 2001

$Zn - MnO_2$ batteries [2] dominate the world's small-format battery industry. In 1995 Zn–carbon batteries (the carbon rod in the center of Leclanché cells is the reason for this name) comprised 67 percent of the world market, and the other 33% belonged to alkaline cells (Table 1).

Table 1. Distribution between Zn–carbon and alkaline primaries [billion (10^9)] batteries

Battery type	1995	1997	2001
Zn–carbon	18 (67%)	18 (51%)	18 (39%)
Alkaline	9 (33%)	17 (48%)	28 (61%)
Total	27	35	46

Alkaline batteries were introduced in the early 1960s; they last two to five times longer than Zn–carbon cells on continuous discharge and command two or three times the price in the USA (far more in Europe and the East). Alkaline cells became a necessary invention and they succeeded as a result of the requirements of the electronic devices. The essential improvement was the change from ammonium chloride and/or zinc chloride electrolyte to alkaline (KOH) electrolyte, the steel can construction, the outside cathode, and the zinc powder (large surface) anode. A main low-cost feature is that they use pressed cathodes and do not need to follow "jellyroll" designs. Cylindrical cells are manufactured mainly in AAA, AA, C, and D sizes.

Duracell, Eveready, and Rayovac are at present the main producers in the USA. In 1987 Kodak tried to enter the alkaline market, but failed in spite of its strong brandname and top technology. Kodak's ineffectual advertising was blamed for their failure. A contrasting and enterprising example was Duracell, which spent more than any other company on promotions (more than $2 billion on advertising from 1988 to 1994). This is certainly a barrier to the entry of any new competitor.

There was a belief in the 1980s that the battery market had reached a certain stability, but the proliferation of electronics led to a significant growth. Table 2 indicates that the total battery market will continue to increase tremendously until 2001. However, it shows clearly that the proportion of rechargeable batteries will rise by 75 percent and single-use primaries will actually lose 2 percent but will nevertheless stay dominant by a factor of 10.

Table 2. Primary and secondary battery market forecast [billion batteries]

Battery type	1995	1997	2001
Primary*	27 (93%)	35 (93%)	46 (91%)
Rechargeable†	2 (7%)	3 (7%)	5 (9%)
Total	29	38	51

*Zn–carbon plus alkaline
†Without large-format and SLI batteries
Sources: several 1995 market surveys.

Table 1 showed that the growth in the primary (single-use) $Zn - MnO_2$ battery market will be entirely in the alkaline field because in the less-developed countries there will be the strong trend toward alkaline batteries. Zn–Carbon batteries will certainly not disappear, but their poor quality in some regions is an area for improvements (Table 2).

There is also a distant future possibility

CosMX Exhibit 1008, Page 89 of 633

of making high-quality Zn–carbon batteries rechargeable by manufacturing hybrid systems. Zn–carbon–air / MnO_2 and Zn–carbon Br_2 / complex systems are other examples of rejuvenation cycles of old systems when new materials are found [3]. Nowadays, "instant availability and reliability" are the main reasons why many people decide to use disposable alkaline primary cells instead of rechargeable Ni–Cd batteries with a poor shelf-life.

3.1.2 The Small-Format Alkaline Battery Market in the USA and Europe, and Internationally

Table 3 shows that the distribution of alkaline batteries correlates with the statistics of per–capita income. Zn–carbon batteries can be afforded more easily, alkaline batteries cost at least twice as much. However, the electronic "push" for high-quality batteries with good continuous load performance required alkaline cells.

The market indications are clear: China and India are the number-one target countries for building mega-sized manufacturing plants for alkaline $Zn-MnO_2$ batteries of the disposable type. Japan is a historical exception to alkaline cell introduction. This high-technology country uses only about 30 percent alkaline cells. In 1970, when US alkaline technology was maturing, Japan stores could only sell US alkaline batteries through an Eveready-Sony agreement. At present, alkaline primaries in Japan are steadily improving in quality, to serve the electronic market, but in addition Japanese manufacturers are shifting to metal-hydride (MeHy) and lithium batteries for high-power equipment. This does not deter companies from pursuing profitable transfer of alkaline technology to less developed countries. Germany is an exception: the proportion of rechargeable batteries in the consumer market is 20 percent at present, (mostly Ni–Cd), compared with 2 percent in the

Table 3. Geographic sampling of alkaline cell penetration

Region/Country	Population [millions]	Income [10^3 $ per capita]	Batteries per capita	No. of batteries [millions]	Alkaline cell penetration [%]
North America					
USA	260	24.8	10.9	2.843	86.5
Canada	29	13.2	5.5	158	74.7
Europe					
UK	58	17.8	6.8	395	62.0
Germany	81	22.9	5.9	482	51.7
Italy	57	20.5	6.6	377	59.4
Spain	39	14.0	7.4	292	39.4
France	58	22.3	8.9	515	58.4
Russia (parts of)	149	2.7	3.5	525	26
International					
India	870	0.23	1.5	1.300	0.3
Middle East†	110	3.6	3.6	401	14.3
China	1.200	0.43	3.1	3.750	3.2
Latin America‡	348	3.4	5.4	1.890	30.2

†Egypt, Israel, Marocco, S. Arabia
‡Argentina, Brasil, Chile, Colombia, Mexico, Venezuela.
Source: Barney Smith (Duracell Rep.).

CosMX Exhibit 1008, Page 90 of 633

USA. In Europe the technical challenge of recharging but also saving money, continues to be stronger than elsewhere [4].

3.1.3 Who Buys Batteries ?

The average US household uses 30 batteries per year, and 30 percent of US households fall into the heavy-user group, which buys 75 percent of all consumer batteries sold. The heavy-user group comprises young married couples with children in the age range 4 to 12 years, young adults between the ages 16 and 24. The main use is toys (with up to 10 cells!) and electronic gadgets. Purchasing is mostly done on impulse at the check-out counters of supermarkets. More highly priced rechargeable cells are usually kept next to the "better electronics" shelves. The environmental awareness of school children is a good omen for the trend to recharging. School Experiments on solar charging are exciting. It is still not widely known that the production of high-grade batteries uses about 10 times more electrical energy than they contain. The reason is that most of the components (MnO_2, KOH, Zn) are produced electrolytically.

Alkaline primary batteries have recently been introduced to the US Military for cost saving during maneuvers and in offices. At elevated temperature (over 45 °C) and especially in vehicle cargo compartments (up to 70 °C), all other batteries discharge rapidly. To keep rechargeable Ni–Cd, Ni-MeHy, or lead–acid batteries in charged conditions turns out to be a very costly maintenance procedure. The use of rechargeable alkaline MnO_2 (RAM™)* batteries is a simple low–cost solution (see below, Sec. 3.4).

*RAM™ is a Trademark of Battery Technologies, Inc., Canada.

3.1.4 The Lithium Primary Market

The demand for Li coin-type cells (now estimated at one-tenth of alkaline MnO_2 cells) is growing. Matsushita, a major producer in Japan and Malaysia, has opened a plant for camera batteries in the USA. The Advanced Photographic System introduced in 1996 uses such cells. Most of the Li primary batteries are of the $Li-MnO_2$ type. Ultralife is offering D-size cells with 10 Ah-capacity and high-current (4 A) capability. Applications in cellular phones are expected (Sanyo). Thin $Li-MnO_2$ cells are fabricated as "smart" credit cards, for security, phone devices and other related general consumer uses. Eveready still tries to sell its 1.5 V AA cylindrical Li–iron sulfide cell for high-current uses. Also $Li-CF_x$ batteries are on the market; they excel through long life and high–temperature stability. Applications in the medical field use Li-vanadium oxide cells. Military orders for small $Li-SO_2$ cells (Ballard Battery Systems Corp.) and large batteries have fallen, because of budget cuts. Li-thionyl and -sulfuryl cells for missile silos have been eliminated. The current densities in lithium batteries are low, and therefore all small-format cylindrical systems which require higher performance use rolled electrode designs. Figure 3 showed the construction principle for a lithium battery.

3.1.5 Primary Zinc–Air Batteries

The capacity of single-use alkaline zinc-air cells is twice that of manganese dioxide-zinc cells. They cost less than silver oxide-Zn batteries or Li batteries. The best example of consumer usage is the hearing-aid button cell. In sealed condition it can be

CosMX Exhibit 1008, Page 91 of 633

stored for years; once opened, it performs for several weeks or even months on relatively low drains. The design allows only a restricted access of air, so drying-out at low humidity, carbonate formation due to the carbon dioxide from the air, and the wetting-up at high humidity (causing leakage) are minimal. Improvements with gas-selective membrane separators are still envisioned. Most of the air–zinc cells are hybrid cells, and some contain about 15 percent MnO_2, addition of which allows short-term overloading; a certain air-recharging of the MnO_2 is also observed. There is a trend towards manufacture of Zn-air cells in a larger coin-cell format.

3.2 Rechargeable Batteries (Consumer and OEM Markets)

Table 4 shows predictions for the world-wide use of different types of rechargeable batteries, covering consumer and original equipment manufacturer (OEM) markets.

Table 4. World-wide use of consumer-rechargeable batteries [million batteries]

Battery type	1995	1997	2001
Nickel–cadmium	1590 (81%)	1710 (65%)	1940 (42%)
Nickel–metal hydride	310 (16%)	600 (23%)	1716 (37%)
Lithium	30 (2%)	250 (9%)	700 (15%)
Rechargeable alkaline*	20 (1%)	70 (3%)	284 (6%)
Total	1950	2360	4640

*The production of RAM™ batteries by Rayovac started in 1993 in the USA and reached over 50% of the (2%) market of rechargeable cells in the USA by 1995 [43].

Table 5. Comparison of secondary batteries

		PbO_2/Pb	NiO_x/Cd	NiO_x/MH	NiO_x/Zn	Li-ion	MnO_2/Zn
Specific energy [$Wh\,kg^{-1}$]		30	50	60	75	100	75*
Energy density [$Wh\,l^{-1}$]		50	100	180	150	200	180*
Open-circuit voltage [V]		2.1	1.3	1.3	1.75	4.1	1.6
Operating range [V]		2.0–1.8	1.2–1.0	1.2–1.0	1.7–1.1	3.8–3.0	1.4–0.8
Peak charge/discharge rate [C]		6	10	5	3	1	1
Temp. operating range [°C]		–30 to +50	–20 to +45	–10 to +40	–10 to +50	–20 to +60	–10 to +65
Temp. charge range [°C]		0 to +45	0 to +45	0 to +40	0 to +45	0 to +45	–10 to +60
Final charge voltage [V]		2.4	1.5	1.5	1.95	4.5	1.7
Charging time range [h]		2–20	1–3	2–5	3–10	3–20	3–20
Overcharge permitted		Limited	Yes	No	Limited	No	Controlled
Overdischarge (reversal)		No	Yes	Limited	Limited	No	Controlled
Charge efficiency, W [%]		90	85	80	80	90	90
Cycle life	30% DOD	500	2000	800	500	2000 ?	500
	80% DOD	200	800	600	200	800	40
	100% DOD	20–50	500	200	500	200	25
Calendar life [years]		3	5	3	3	3–5	5
Discharge	At 20 °C	3–5	15–20	20–30	15–20	8–15	2
[% / month]	At 45 °C	50	60	80	50	30	5
	At 65 °C	100	100	100	100	100	20
Component toxicity		High	High	Medium	Medium	Medium	None
Relative cost (1997) [Wh]		2	4				
		PbO_2/Pb	NiO_x/Cd	NiO_x/MH	NiO_x/Zn	Li-ion	MnO_2/Zn

*These capacity values are obtained at the initial discharge of AA-size cells.

CosMX Exhibit 1008, Page 92 of 633

The estimated data are again based to a large extent on affordable cost figures, not necessarily on the best suitability for certain performance requirements.

Table 5 presents a comparison of secondary battery performance data.This table reflects the battery situation as reported from different sources, for instance [5, 6], but tries to accommodate several recent changes.

3.2.1 Ni–Cd Batteries

Ni–Cd batteries were the small-format power sources traditionally used since their development in the early 1960s. Due to the Cd–oxygen–gas recombination overcharge cycle, gas-tight hermetically sealed Ni–Cd cells could be used connected in series. Vented or resealable-vent lead-acid batteries could not be used in electronic devices. This resulted in a nearly exclusive use of Ni–Cd cells in consumer and OEM devices. This overcharge possibility also assured the equalization of cells of different capacities and made the use of low-cost chargers possible. The charge current has to be limited to *C*/10 to avoid damage by heating or starting a run-away condition which would discharge the cells completely. However, after prolonged cycling at a low depth of discharge, a "memory effect" develops. The high self-discharge of Ni–Cd cells at temperatures over 45 °C and the impossibility of charging at high summer temperature constitute reliability problems.

3.2.2 Progress in Ni–MeHy Batteries

Environmental objections to cadmium dissipation, and the possibility of increasing the capacity of nickel oxide-based rechargeable batteries by using metal hydrides as anodes, led to the rapid development of Ni–MeHy batteries in the early 1990s. Incorporating many improvements in materials and separators, these batteries have now about 30% more capacity than Ni–Cd batteries and also deliver high currents in the rolled-electrode construction. Their applications include portable, cellular phones and tools. Unfortunately, the price tag has increased by nearly 100 percent. Additional cost increases are due to the requirement for sophisticated charger, avoiding reversal and assuring precise regulations at end of charge. The elevated–temperature self-discharge is even worse than that of the Ni–Cd battery. Charging above 45 °C is not allowed.

A technology agreement was made by Duracell/Toshiba/Varta in 1992, strategically aimed at the portable computer field. In 1994 a joint venture, "The 3 C Alliance" was formed. Standardization of the inventory was the main point. The benefits were seen to be easier replacement and lower cost per unit ($170 for 6 h ?). One of the first commercial partners was Compaq Computer Co.

Matsushita, Gold Peak and Toshiba have announced the production of Ni–MeHy batteries with 300 $Wh\,l^{-1}$ and 90 $Wh\,kg^{-1}$ capacity. Compared with data published in 1990, the values have doubled. Ni – MeHy batteries with hydrophobic separators were improved by application of a wetting coating. The change in this case is based on the reduction of the gas transfer through pores. A change to half the separator thickness can improve the capacity by 30 percent upwards, but it may increase the self-discharge considerably. Zinc addition to MeHy anodes has been studied at Texas A&M University.

CosMX Exhibit 1008, Page 93 of 633

3.2.3 Lead–Acid Batteries

Small-format lead–acid batteries with immobilized electrolyte are still used in some applications such as hand lanterns. Low-cost six or twelve-volt batteries (e.g. 6 Ah size) are used in child-driven toy cars and other sizes in emergency-light or alarm systems, kept on trickle-charge. Efforts are being made to produce bipolar systems which give 30 percent improvements.

3.2.4 Li Secondary Batteries: Status and Future Projections

Rechargeable lithium batteries have dominated the technical developments of recent years [7]. The demand for high-capacity batteries has increased with the proliferation of electronic equipment, portable computers, and cellular phones. The main objection to rechargeable Li batteries was based on safety considerations. Redeposited lithium is far more active than the metal itself and side–reactions or thermal run-aways in the case of shorts were feared. A big advance was the discovery that lithium could be intercalated into carbon materials: thereby it became safer and was used more efficiently. These Li anodes were then combined with Li-containing metal oxides of formula $LiMeO_2$, whereby Me stands for Co, Ni, or Mn. Later, $LiMn_2O_4$ cathodes could also be prepared. The charge and discharge reactions then became only transfer processes and a minimum of electrolyte was required. This way, there is never any metallic Li in the cell, unless the cells are overcharged (over 4.5 V) or reversed, which could be prevented by designing special charger circuits for cells connected in series (e.g., 6 V OEM applications). At the Fall 1996 Meeting of the Electrochemical Society among the ca. 100 papers on Li cells that were presented, many discussed $Li-MnO_2$ structures [8].

3.2.4.1 The Advances in Anodes

The theoretically maximum capacity corresponds to the formula LiC_6 with a theoretical capacity of 372 mAh per g of graphite. Typical actual numbers are $300\,mAh\,g^{-1}$ for graphite and $200\,mAh\,g^{-1}$ for coke. Industrially, various carbons are used: artificial and natural graphites (Sanyo), or petroleum coke, highly graphitized pitch or (3000 °C-treated) carbon fibers (Asahi–Toshiba). "Hard carbon" is the name given to randomly graphitized materials with a turbostratic structure. It can be made by medium-temperature heating of certain plastics, woods, sugars, or other cheap materials (with a spiral molecular structure); therefore the economy is improved. In addition, the voids in these structures take up more lithium and the capacities can go up to 500 $mAh\,g^{-1}$. Adding ultrafine silver powder can raise the values by 20 percent (Hitachi) and the incorporation of silica gives a capacity as high as 750 $mAh\,g^{-1}$. (Simon Fraser University). Fuji Film announced that it will make Li-ion batteries, replacing carbon with amorphous SnO, and reaching a level of 380 $Wh\,l^{-1}$ (see also Chapter III, Secs. 3–6).

3.2.4.2 Li Cells with Metallic Anodes

Such cells are still produced by Tadiran, and the safety aspects are said to be solved using an electrolyte mixture of polyethylene oxide–methylene oxide which polymerizes with the HF released by hot $LiAsF_6$: at 135 °C the electrolyte turns

CosMX Exhibit 1008, Page 94 of 633

into an almost isolating material, increasing the internal resistance [9].

3.2.4.3 The Advances in Cathodes

In this case the metal oxides contain the Li, at a higher positive potential; on charge, only Li ions are travelling via the electrolyte (liquid, polymer, or plastic) into the (–) graphite anode [10]. The cycle numbers are high (up to 1000) for both anodes and cathodes, because the dimensional changes are small. However, only ca. 0.5 Li per Me can be delithiated reversibly (without electrolyte damage due to a voltage increase over 4 V) from oxides like $LiCoO_2$ and $LiNiO_2$. These have a layer structure and $LiMn_2O_4$ has a spinel structure. In a search for higher cell capacities, another structure variation was found in a specially prepared $LiMnO_2$. This type can take up 0.95 Li per Mn. it was produced recently as a stoichiometric layer structure via $NaMnO_2$ [11]. The usual direct synthesis via compounds of Li and of manganese did not succeed. Optimization is still needed because a high cycle life is not established and some shuttle mechanisms exist with the electrolytes. Recent advances have been reported from the National Research Council of Canada [12]. Various Mn oxides have also been studied at the University of Waterloo, fluor-anion substitution by Bellcore, Ni insertion by Moli Energy, and Li–Cr spinels at Fraser University. Cathodes with Cr additions can be cycled up to 1.5 Li per Mn [13], but we must consider large structural changes which lower the cycle life [14].

$LiCoO_2$ is used in most of the Li batteries in production, in spite of its limited availability and cost. It gives the highest capacity and cycle numbers. Lithiated Ni oxide is next in capacity and has been selected by SAFT for small and large batteries. The cycle life is lower than with $LiCoO_2$. There are numerous "3 V" and "4 V" lithiated manganese oxides. Compared with lithiated Co and Ni oxides they have lower capacity and lower cycle life, but they are nontoxic, stable, and most importantly, of low cost. Japan Storage Battery Co. uses a material in which nickel replaces 85 percent of the cobalt. In another formulation (by Ohzuku) aluminum is present in the Ni oxide, causing the mass to become an insulator on overcharge at 4.8 V (see also Chapter III, Secs. 1 and 2).

3.2.4.4 Electrolytes

Liquid organic electrolytes consist of a solvent and a salt: propylene carbonate (PC) for carbon electrodes, ethylene carbonate and dimethyl carbonate (EC and DMC) for graphite electrodes. $LiPF_6$ is the usual conductivity salt. A poorly understood process is the formation of a solid electrolyte interface (SEI) on the anode, starting the intercalation process, probably via Li carbonate. Efficiency losses during the formation depend on the carbons or graphites; gas is the result of decomposition reactions. To reduce the hazards of flammability "solid polymer electrolytes" originally polyethylene oxide —PEO— and "doped polymer" electrolyte with some "plasticizers" were introduced. Valence first used irradiation for additional crosslinking.

Solvated polymers are approaching "gels" in properties, depending on the mobility of the molecules. In some cases the action of a binder and of a separator are combined. By extraction of one of the components and refilling the voids with a liquid, a two-phase system can be created (Bellcore). There are irreversible and re-

CosMX Exhibit 1008, Page 95 of 633

versible losses. In the case of $LiMn_2O_4$ a self-discharge dependence on the surface area of the cathodes was found. It was improved by selecting larger particle sizes and coating with silicates [15] (see also Chapter III, Secs. 7–9).

3.2.4.5 Separators

A great variety of polyolefin separator types are now used in Li ion batteries. They must be stable in the organic electrolytes. Typically they may not be properly wetted by the electrolytes of the optimized composition, e. g., mixtures with PC, PE, and others. Therefore some proprietary treatments are needed to provide hydrophilic behavior. Generally, a microporous nonwoven morphology with a large surface gives a good wettability.

As a safety specialty, polyethylene separators are used to shut down run-away (shorting) Li cells by simply melting and creating a high-resistance barrier. The speed of resistance gains increases, approaching the melting point. Bilayers of polyethylene (PE) and polypropylene (PP) are even faster (Hoechst) (see also Chapter III, Sec.10).

3.2.4.6 Competitors Among Li Ion Battery Manufacturers

Currently (1997) the principal competitors in world markets are the following:

Japan:

A–T Battery Co. is a joint venture between Asahi and Toshiba, to produce Li ion batteries. Fuji Electric and Fuji Film, Hitachi–Maxell (Li-thionyl cells, and now also Li ion cells), Japan Storage Battery Co. (prismatic cells), and Matsushita Battery Co. cover most systems. Mitsubishi Electric, Mitsui, and Sanyo are major producers of the $Li-MnO_2$ system. Sony Energy Tec. produces Li ion batteries. Yuasa works with Hydro–Quebec on polymer systems.

USA:

The only actual producer of Li ion batteries in North America is Moli Energy, Ltd. It started first with metallic Li/molybdenum disulfide cells and failed. Now there are plans for all three big primary companies, Valence Technology/Eveready/AV Delco, to go into production. The first two intend to supply portable electronics, the third will look at automotive applications. Li ion solid polymer rechargeables are produced by Ultralife, which acquired Dowty Batteries (UK). Duracell, which planned a strong Ni–MeHy future, will also go into the US production of Li ion batteries. Rayovac is already involved in Li battery developments. Bellcore belongs to the group of Bell operating companies; it is licensing "plastic" Li technology.

Canada:

Hydro–Quebec (with Yuasa) and 3M were awarded a $33 million development contract from USABC for electric vehicles.

Europe:

Varta Batterie A. G. and Duracell, together plan small-format Li batteries, but also work for USABC to build electric vehicle batteries. Hoppecke also produces $Li-MnO_2$ batteries.

3.2.5 Competition from Rechargeable Zinc–Air Batteries

EAR Energy Resources, which develops Zn–air batteries for portable computers, claims about 250 Wh for a computer unit. The price (in 1994) was $600, including the charger. For the first discharge, ten operating hours are claimed. However, it must be realized that the subsequent cycle behavior is not well established. Sony's Li

CosMX Exhibit 1008, Page 96 of 633

ion batteries promise 5 h of intensive and 15 h of light use, with a high cycle life at one-quarter of the cost.

3.3 Li Batteries as Power Sources for Electric Vehicles?

Li ion batteries are heavily advertised as the future power sources for electric vehicles. This seems premature because the technology of heat management and many questions of safety are not solved. Fuel cells and several types of secondary batteries have a long history in the field of electric vehicle propulsion, with successes and failures. For information on electric vehicle batteries, see [16–22].

3.4 Rechargeable Alkaline MnO_2 – Zn (RAM™) Batteries

The design of a AA-size alkaline manganese dioxide cell is shown in Fig. 1 (Sec. 3.1). Primary and secondary alkaline batteries are constructed in the same way and can be manufactured on essentially the same machinery. The separator material, electrode formulation, and the MnO_2 – Zn balance are different. Rechargeable cells are zinc-limited to prevent a discharge beyond the first electron–equivalent of the MnO_2 reduction. The electrolyte is 7–9 mol L^{-1} KOH. The electrode reactions are:

Cathode:

$$MnO_2 + H_2O + e^- \Leftrightarrow MnOOH + OH^-$$

Anode:

$$Zn + 2OH^- \Leftrightarrow ZnO + H_2O + e^-$$

Overall cell reaction:

$$Zn + 2MnO_2 + H_2O \Leftrightarrow ZnO + 2MnOOH$$

3.4.1 History and Present Situation

In the mid-1970s Eveready (at that time Union Carbide Corp.) produced rechargeable alkaline MnO_2 –zinc batteries for 6 V lanterns and portable TV sets. It did not turn out to be a lasting success; this was because the cells were not strictly zinc-limited and the cathodes discharged too deeply, but there was also no catalytic recombination of H_2 gas of cell-reversal limitation for series–connected cells. OEM applications, when customers forgot to turn the load off, were plagued by leakage problems. The development was continued at the Technical University of Graz, Austria, and later, in 1986, Battery Technologies, Inc. (BTI) was established in Canada. Since then the improved RAM system was licensed to Rayovac Corp. in the USA, producing Renewal™ batteries, to Pure Energy Corp. making Pure Energy™ cells in Canada, to Young Poong Corp. in Korea producing Alcava™ batteries and to Grand Battery Technologies of Malaysia, making Grandcell™ batteries. In Europe the rechargeable batteries are sold as "BIG" by the Battery Innovation Group GmbH and under the name "Accu Cell" by Müller, Germany. The Technology of the RAM battery system is described in [1, 2, 22–39]. Table 6 shows the performance data of RAM cells, sizes AAA, AA, C, and D. The initial discharge of these cell types is within 80 percent of the corresponding primary alkaline cells.

CosMX Exhibit 1008, Page 97 of 633

Table 6. Performance of RAM™ cell sizes AAA, AA, C and D

	AAA	AA	C	D
Open-circuit voltage [V]	1.5	1.5	1.5	1.5
Internal ohmic resistance of fresh cells, [Ω] (approx.)	0.3	0.2	0.15	0.1
Expected Capacity*, [mAh]				
30 mA to 0.9	800	1800	5500	13000
125 mA to 0.9	650	1500	5300	11000
300 mA to 0.9	500	1200	5000	9500
500 mA to 0.9	n/a	800	3500	7200
1000 mA to 0.9	n/a	n/a	2500	5000
Charging pulse/taper				
Charge voltage [V]	1.65±0.03	1.65±0.03	1.65±0.03	1.65±0.03
Max. charge current [A]	1	1	2	2
Dimensions				
Average height [inches/mm]	1.740/44.2	1.965/49.9	1.950/49.5	2.372/60.2
Average diameter [inches/mm]	0.402/10.2	0.553/14.0	1.003/25.5	1.313/33.4
Average weight [g]	10	21	65	135
Operating temperature† [°C]	–20 to +60	–20 to +60	–20 to +60	–20 to +60
Storage temperature [°C]				
Recommended	+15 to +35	+15 to +35	+15 to +35	+15 to +35
Tested	Up to 70	Up to 70	Up to 70	Up to 70
Shelf-life of fresh cells [years]	4 to 5	4 to 5	4 to 5	4 to 5
Cycle life‡ [cycles]	25 to 500 +	25 to 500 +	25 to 500 +	25 to 500 +

*Continuous discharge of fresh cells at room temperature of 22 °C
†Capacity from cells will be lower at lower temperature
‡Cycle life will depend strongly on factors such as rate of discharge, end-point (cut-off) voltage, and depth of discharge

3.4.2 The Advantages of RAM Batteries

These may be summarized as follows:

- Ready to use when purchased, no need to charge before first use
- Low initial cost and excellent charge retention, up to five years
- High capacity for long life between recharges
- Rechargeable many times for economy of operation
- No memory problem when repeatedly partially discharged
- Excellent performance in intermittent use
- Sloping discharge curve allows simple low-battery warning circuitry
- Standard sizes easily replaced when new cells are needed
- Environmentally friendly, and safely disposed of in household waste

3.4.3 Typical RAM Applications

RAM batteries are suitable for all applications served by single-use alkaline cells, such as:

- Toys and games, personal compact disk or cassette players, tape recorders
- Transistor radios, cameras, lighting, and some applications served by Ni–Cd, Ni–MeHy or lithium–ion rechargeables.
- Lower current-rate portable and cellular phones and pagers
- Lower current-rate portable computers and other portable digital equipment

CosMX Exhibit 1008, Page 98 of 633

3.4.4 Characteristics of RAM Batteries

Rechargeable alkaline manganese dioxide–zinc batteries have practically the same discharge characteristics as primary batteries. Figure 4 shows how the discharge curves from the initial discharge voltage level to lower voltages, until a pre-set cut-off voltage is reached.

Figure 5 shows the performance of RAM AA cells as a function of the depth of discharge (DOD) during cycling. The cumulative capacity (in Ah) allows the calculation of the economy of battery usage. If a primary AA cell under a comparable load regime is reckoned to have a capacity in the region of 1.6 Ah (as an average at 4 Ω), the cumulative capacity gives the number of primary cells replaced during the life-time of the rechargeable cell. A replacement factor of 20 to 25 is chosen in advertisements as representing a general consumer usage with deep cycling (80 percent DOD).

If it is desired to optimize RAM battery usage, the examples in Fig. 5 should be considered. A 0.62 Ah cycling at 4 Ω (50 percent DOD of 1.25 Ah initial capacity) results in 80 cycles with a cumulative capacity of nearly 50 Ah. Recharging is done after each discharge. A 0.38 Ah cycling at 10 Ω (25 percent DOD of 1.5 Ah initial capacity) results in over 300 cycles, with a cumulative capacity over 100 Ah. The replacement of 60 alkaline cells and about

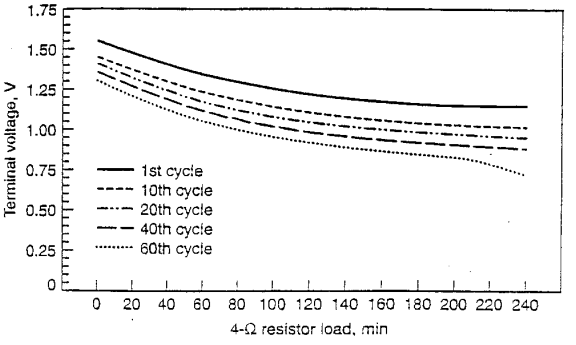


Figure 4. Discharge characteristics of RAM AA cells when cycled at 20 °C. The cells are discharged for 4 h per day at 4 Ω, and charged overnight with a constant voltage charger at 1.7 V.

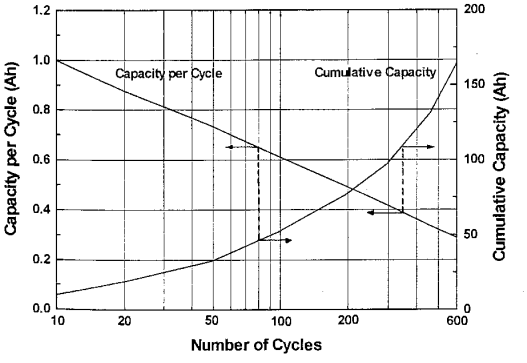


Figure 5. Performance of RAM AA cells as a function of the depth of discharge (DOD); recharging is done after each discharge. For an explanation of these example, see the text.

CosMX Exhibit 1008, Page 99 of 633

100 Leclanché cells can be assumed. The accuracy of the total capacity calculations is not better than ±10 percent due to temperature and other variations, but the economy of recharging is clear.

Effects of Temperature

At low temperatures down to –20 °C RAM cells function but their performance is decreased; the decrease is more severe for higher rates. At higher temperatures up to 50 °C the low-rate performance is unchanged but performance at moderate and especially high rates is much improved.

Self-Discharge

Compared with nickel–cadmium and nickel-metal hydride systems RAM cells exhibit very low self-discharge, making them ideal for intermittent or periodic use without the need to recharge before using, even in hot climates. Figure 6 shows a comparison of the temperature characteristics, for various battery systems in the form of Arrhenius diagrams.

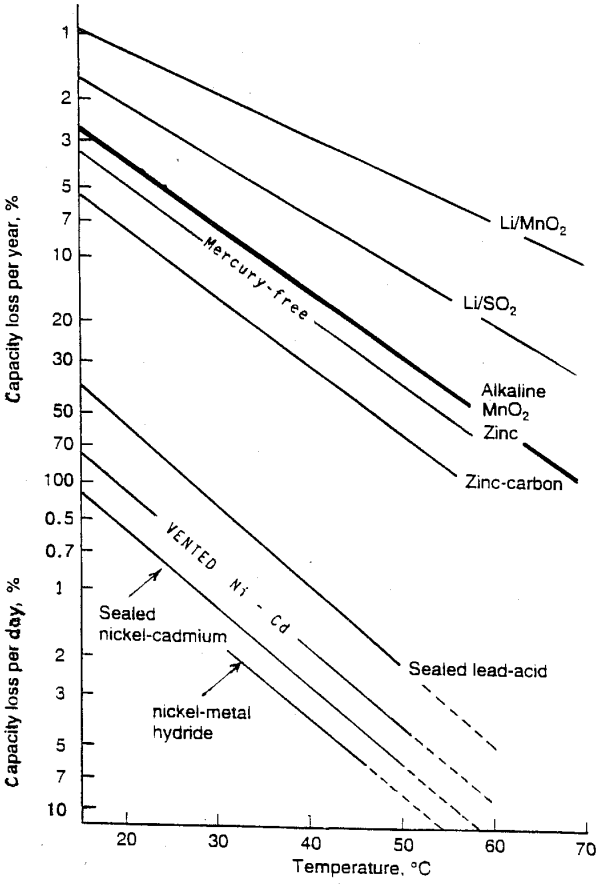


Figure 6. Arrhenius plots for various battery systems. The percentage capacity losses per year and per day are given on a logarithmic scale. The $Li-MnO_2$ cell, which has excellent shelf-life characteristics, is a primary cell, not a rechargeable Li cell

CosMX Exhibit 1008, Page 100 of 633

However, even at room temperature, the shelf-life of batteries with nickel oxide cathodes (Ni-Cd, Ni-MeHy, and Ni-Zn batteries) is a source of difficulties for the consumer who relies on the state of charge of his power source when he needs it–without charging time available. Figure 7 compares the self-discharge of RAM cells with Ni–Cd and Ni–MeHy cells at 20 °C.

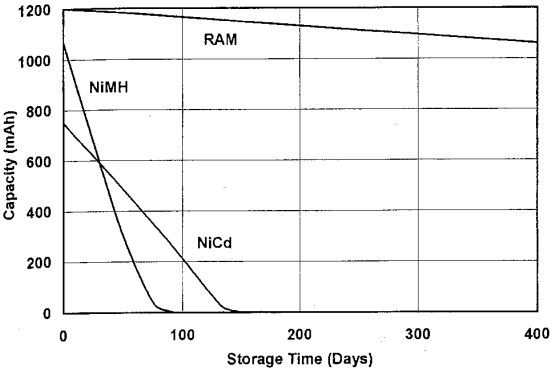


Figure 7. Comparison of the self-discharge of RAM cells vs. Ni–Cd and Ni–MeHy cells at 20 °C.

3.4.5 RAM Battery Charging

RAM cells can be charged by means of voltage-controlled circuits to the 1.65–1.72 V range in order to avoid overcharging. Four cells are usually charged in parallel, overnight. Pulse chargers reduce the charging time considerably. They use the "resistance-free voltage" between the pulses as the reference voltage for the state charge. Examples are Rayovac "Power Station" and Pure Energy "Charge Station". Fast chargers (e.g., Lytron–Accu Cell) are able to charge cells in 3h. No overcharge of RAM cells takes place in approved RAM charges, so cells could be forgotten for several weeks without harming their performance.

3.4.5.1 External or Internal Chargers

Using external chargers, the discharged cells are removed from the battery-operated device and placed in an approved RAM charger where the cell terminals make proper contact for charging. This is the appropriate method when RAM cells are used in applications designed also for operation by single-use alkaline cells. It is also possible to use a multi-cell battery pack and remove it for recharging.

Using built-in chargers, the single-cell or the battery pack are recharged in the battery-operated device, usually in series. For series arrangements of three or more cells, in order to avoid overcharging, special circuits are required to provide overflow of the charging current to individual cells. Also recommended for these series arrangements in the use of diodes for protection against deep cell voltage reversal.

After years of testing, we realized that far simpler and quite inexpensive chargers can be used, especially when the charging is done more slowly, mainly overnight. Reliable chargers made from low–cost components are imperative for a world-wide market penetration. It was found that

two diodes in series or one red LED allow an increasing current overflow when the cells approach and finally reach the fully charged state [30]. Figure 8 shows a low-cost diode-overflow charger for four RAM AA cells [30, 35]. The wide range of the charge end-voltage from 1.65 to 1.75 V makes possible variations in components, temperature and line voltage without affecting performance of the charged cells, as long as sufficient time is allowed. A requirement which we set for any of the low-cost chargers is that the recharging of second- or third-cycle cells with a capacity of about 1.4–1.6 Ah (AA cells) must be achievable within 8–16 h (overnight).

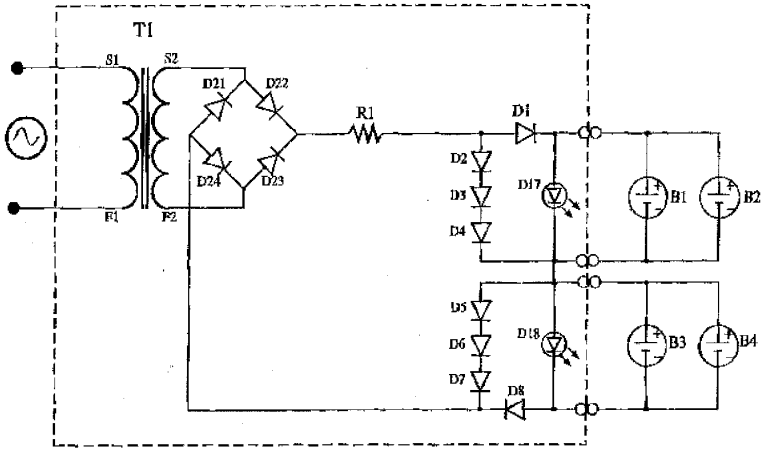


Figure 8. Low-cost diode-overflow charger for four RAM AA cells [30,35].

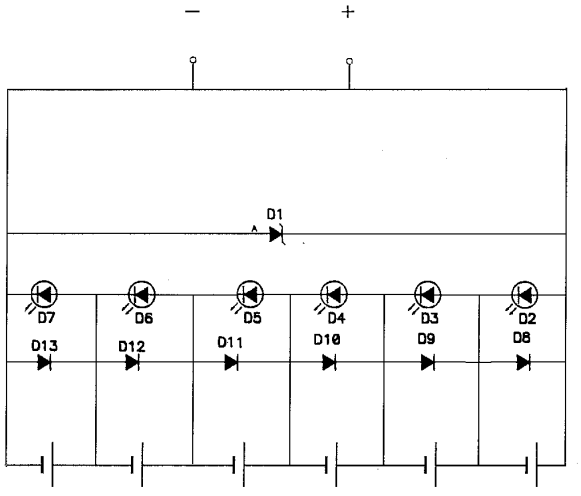


Figure 9. In a Motorola-type cellular phone handset, the six AA cells in series are protected by reversal-limiting diodes, and the overflow at 1.7 V is determined by the six red LEDs [38].

CosMX Exhibit 1008, Page 102 of 633

3.4.5.2 Series Charging for OEM Applications

For many applications it is required that the cells are permanently arranged in series connections, often in packages of different configurations, fitting various devices they are supposed to power (OEM usage). Because RAM batteries without Hg additions are not required to be recycled, the batteries could stay in the device and could be charged from the outside. Such a requirement is typical for a cellular phone handset; for example one of the Motorola versions contains six AA cells. Ni–Cd battery packages are in use at present. A company in New Jersey sells a package with six AA (removable) primary cells for "sure communication in emergencies". Consequently, Porta-Power (S), Pte. Ltd., Singapore, is selling this package with six AA "Renewal" cells. The charging is accomplished by a rectified AC supply and the overflow and equalization requirements on charge are satisfied with six red LEDs, one across each cell, as reported already in [6]. A state-of-charge indicator warns the user against a deep discharge, which could result in a cell- or LED-damaging reversal. We have improved that circuit with the addition of a reversal-limiting diode (conductive at –0.4 V) on each cell (Fig. 9). Now, the user can safely forget to turn off the set !

3.4.5.3 Power Packs

For power packs with parallel/series-connected cells an overflow charger was designed, in which each LED is replaced by one diode and one transistor. There is no back-discharge when the charger is turned off (Patent Pending) [38]. Figure 10 shows a diode/Darlington-transistor circuit of a series (OEM) charger [39]. This low-cost charger is especially suitable for battery bundles.

The connection of AA-size cells in parallel can replace larger cells (e.g., D-size cells). Four AA cells fit into a D-size can, and six AA-cells are in equivalent weight to a D-cell [27]. The utilization of the MnO_2 cathode is considerably improved because the cathode thickness is only 2 mm in a AA cell, but 5 mm in a D-cell. The internal resistance is also lower by a factor of 4 to 6. Figure 11 depicts a 5 Px10 S bundle battery: five AA cells in parallel = 1 bundle, 10 bundles in series make a (nominal) 12 V battery. It is used as the power source for a transmitter/receiver service. A typical load profile is 2 A for 1 min, 0.33 A for 9 min; average load, 0.5 A per bundle or 0.1 A per cell; service, about 15 h. Smaller bundle batteries (with 2×9 cells) are very suitable for notebook-computers: 18 AA cells weight 0.36 kg, and the total initial capacity is 32 Wh.

Benchmarq Microelectronics, Inc., designed a special (more expensive) charging chip for RAM cells, connected in series [40]. The advantage is a complete disconnection of the load when the first cell reaches the predetermined cut-off voltage. Cell reversal is thereby eliminated.

3.4.5.4 Solar Panel Charging

The excellent high-temperature charge retention and charge acceptance of RAM cells allow an effective use of solar energy for recharge. Note that solar charging of nickel–cadmium and nickel–metal hydride cells is not very successful due to the poor high-temperature charge retention of these battery chemistries. The cellular-phone circuit shown in Fig. 9 is also a good example for solar charging.

CosMX Exhibit 1008, Page 103 of 633

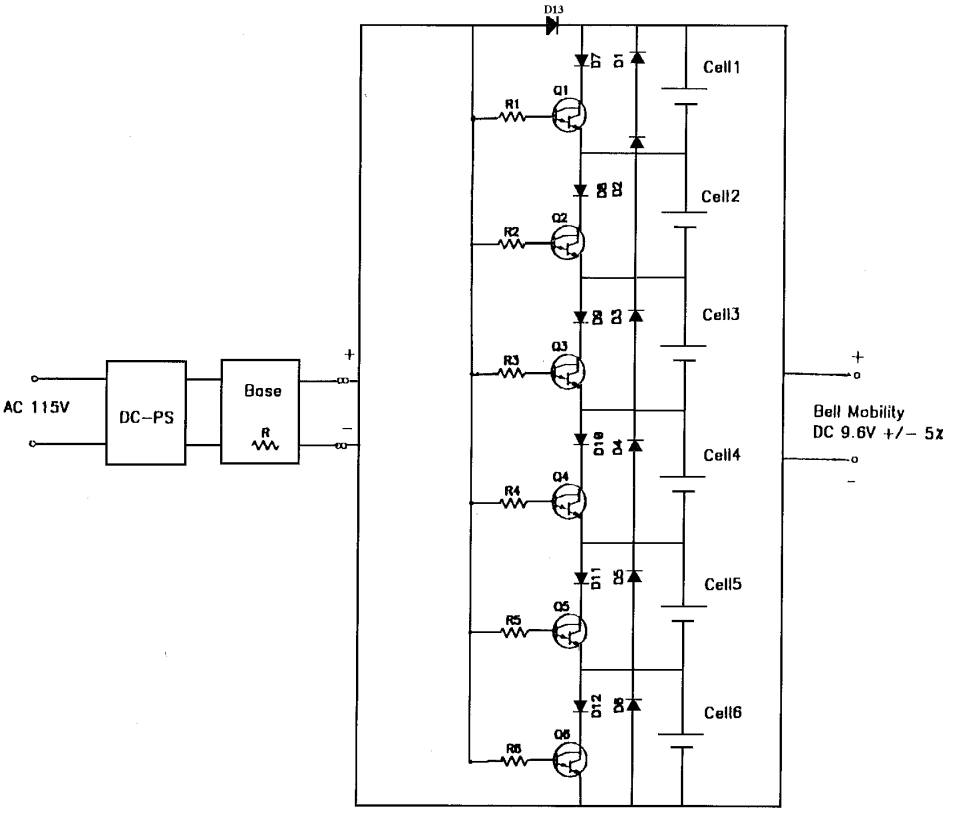


Figure 10. Diode/Darlington-transistor circuit of a series (OEM) charger [39].

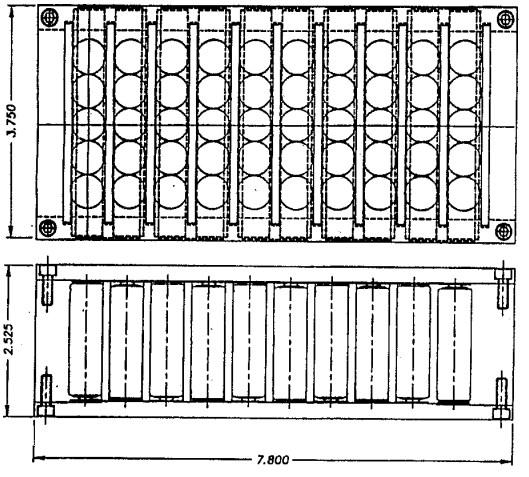


Figure 11. P_x 10 S bundle battery: details are given in the text. Dimensions are in inches.

CosMX Exhibit 1008, Page 104 of 633

3.4.5.5 RAM Safety

Rechargeable alkaline manganese cells made according to BTI's RAM technology meet the requirements of the electrical abuse tests as described in the IEC 86-1 International Standard [41].

Chargers for nickel–cadmium and nickel–meal hydride cells usually use a constant-current charging method in which the constant current continues even after the cells are fully charged. Charging of RAM cells in these chargers result in a rupture of the safety vent, leakage, and therefore loss of cell performance. However, Ni–Cd and Ni–MeHy cells can be charged in RAM overflow-chargers.

Various claims have been made about charging of single-use cells, which, however, are not designed to be recharged. They tend to short, exhibit very limited rechargeability, and develop several other deficiencies, e.g., bulging and leakage, when recharged.

3.5 Summary and Outlook

The primary manganese dioxide–Zn battery industry still controls the small-battery market. The ratio between batteries and rechargeable batteries is still about 10:1, and although the global battery market will nearly double by the year 2001, this ratio will stay practically the same, because the primary market is estimated to grow by 70 percent (actually stealing only 2–3 percent from the primary market).

The most important area of R&D is currently the development of secondary lithium batteries for consumers. The reason is the focus on smaller and lighter batteries with high drain capabilities for an increasingly large number of cellular phones, camcorders, and computers. The next important push is related to the replacement of the cadmium in Ni–Cd batteries.

Technologically it is important that smart battery packages, featuring power management by electronic devices within the battery package, are becoming a necessity due to the sensitive charging characteristics of Li and Ni–MeHy batteries. it should be noted that the same principles at a fraction of the cost have been successfully applied realized by simple reversal protection and overflow components by the low-cost RAM batteries.

Primary-battery manufacturers participate in battery R&D with different goals. Improvement of the existing product is logically continuing, but strategically the change from Zn–carbon batteries to alkaline primary batteries is of the highest importance world-wide. It provides a huge income potential using existing technology without risky investments. However, a radical improvement of Zn–carbon cells is technically possible [42]. Whether it will be successfully applied is questionable.

The dangerous outcome of too conservative an attitude is at present either not recognized or not admitted. Independent manufacturers (financially strong "outsiders") who provide new rechargeable batteries and solar power devices may overtake existing battery manufacturer if they are too conservative. Such a conservative philosophy was the reason for the disappearance of large battery companies at the time of the change from Zn–carbon batteries to alkaline batteries in the 1970s and 1980s.

However, a smart management of one of the large primary alkaline battery producers may do both, i.e., accelerate the alkaline conversion of the Zn–carbon batteries and at the same time supply the con-

CosMX Exhibit 1008, Page 105 of 633

sumer electronic and communications market with "reusable" alkaline manganese dioxide–zinc batteries. They can be produced at only slightly higher cost on the same production lines and the consumer would save money by a factor at least 10, and up to 50. This would be independent of the high-priced rechargeable batteries, which will occupy their own special markets. Forecasting conservatively, without relying on such a "revolutionary" event, the RAM battery market is expected to rise from the 1 percent global rechargeable market portion in 1995 (20 million cells produced only in USA) to 6 percent (280 million cells world-wide) by 2001. This prediction only takes into account licensee production on newly installed turnkey manufacturing lines.

Acknowledgment. We thank and give due credit to our colleagues Courtney McLaughlin and Lorna Eaton-Serbert at BTI, who compiles the battery forecasting information from trade journals, market research, and broker surveys.

3.6 References

[1] D. Linden, McGraw-Hill, *Handbook of Batteries*, 2nd ed., New York, **1994**, Chapters: 8 (Zn–carbon); 10 (alkaline MnO_2); 13 (Zn–air primary); 14 (Li–primary); 24 and 25 (lead–acid); 26 and 27 (Ni–Cd); 29 (Ni–Zn); 33 (Ni-MeHy); 34 (RAM); 36 (Li rechargeable); 37 (Zn–Br); 38 (metal–air rechargeable).

[2] K. Kordesch, (Ed.), *Batteries*, Vol. 1, Manganese Dioxide, Dekker, New York, **1974**, Chapter 2.

[3] Goldman, Sachs & Co., Securities Broker, Alkaline business leads the charge, *U.S. Research*, October 13, **1995**, re: Household Product News: "Duracell joins Gillette".

[4] Smith Barney, *Batteries, Cosmetics, Household Products*, July 24, **1995**.

[5] R. A. Powers (Power Associates, Westlake, OH), D. M. MacArthur (CHEMAC Int., Troy, MI), *Lithium and Lithium Ion Batteries* **1996**, A Report and Analysis.

[6] S. Megahed, B. Scrosati, Li-ion rechargeable batteries, *J. Power Sources*, **1994**, *51*, 79–104.

[7] Proc. 8th Int. Meeting on Lithium Batteries, Nagoya, Japan, June 16–21, 1995, in *J. Power Sources*, **1997**, *68*, 1–742.

[8] *190th Meeting of the Electrochemical Society* San Antonio, TX, October **1996**.

[9] E. Mengerihky, P. Dan, H. Xamm, I. Weissman, E. Zinigrad, D. Aurbach, New $Li-MnO_2$ Technology by Tadiran, *190th ECS Meeting*, Abstract, 115.

[10] J. O. Besenhard, *Chem. Ing. Techn.* **1995**, *67*, 1312.

[11] A. R. Armstrong, P. G. Bruce, *Nature (London)*, **1996**, 381, 499; also P. G. Bruce, A. R. Armstrong, R. Citzendannes, H. Huang, *190th ECS Meeting*, Abstr. 815.

[12] I. J. Davidson, R. S. McMillan, J. J. Murray, Rechargeable $Li_2Cr_xMn_{2-x}O_4$, *J. Power Sources*, **1995**, *54*, 205–208 and 232–235 about $LiMnO_2$.

[13] Z. X. Shu, R. S. McMillan, J. J. Murray, I. J. Davidson, *J. Electrochem. Soc.*, **1995**, *143*, 2230–2235.

[14] W. F. Howard, S. H. Lu, W. H. Averill, A. D. Robertson (Covalent Associates, Inc.), Cr-dope $LiMn_2O_4$ in $LiPF_6$ and Li–methide electrolytes, paper presented at 37th *Power Sources Conference*, Cherry Hill, NJ, June **1996**.

[15] G.G. Amatucci et al. Bellcore, A. Blyr (University ofAmiens, France) Higher temperature performance of $LiMn_2O_4$ after surface reduction and treatments, Ref. [8], Abstract 870.

[16] K. Kordesch, G. Simader, *Fuel Cells and Their Applications*, VCH, Weinheim, **1995**.

[17] K. Kordesch, (Ed.), *Batteries*, Vol. 2, Electric Vehicles, Marcel Dekker, New York, **1977**.

[18] W. A. Adams, A. R. Landgrebe, B. Scrosati, (Eds.), Exploratory research and development of batteries for electric and hybrid vehicles, *ECS Proc.*, **1996**, *96-14*.

[19] J. L. Sudworth, $Na-NiCl_2$ (zebra) batteries, *J. Power Sources*, **1994**, *51*, 105–114.

[20] G. Tomazic, Zn–Br System for EVs, advances and future outlook, *Electrochem. Soc. Proc.*, **1996**, *96-14*, 212–220.

[21] J. McBreen, Ni–Zn batteries, a survey, *J. Power Sources*, **1994**, *51*, 37–44.

[22] K. Kordesch, J. Gsellman, M. Peri, K. Tomantschger, R. Chemelli, The rechargeability

CosMX Exhibit 1008, Page 106 of 633

of manganese dioxide in alkaline electrolyte, *Electrochim. Acta.*, **1981**, *26*(10), 1495–1504.

[23] A. Kozawa, K. V. Kordesch, Silver-catalysed MnO_2 as hydrogen absorber, *Electrochim. Acta.*, **1981**, *26*(10), 1489–1493.

[24] J. Gsellmann, W. Harer, K. Holzleitner, K. Kordesch, Improved rechargeability of manganese dioxide in alkaline electrolytes, *166th Meeting of the Electrochemical Society, October 1984, MnO_2 Symp. Proc.*, **1985**, *85-4*, 567–578.

[25] K. Kordesch, W. Harer, Y. Sharma, R. Uji, K. Tomantschger, D. Freeman, Rechargeable, alkaline zinc manganese dioxide batteries, *33rd Int. Power Sources Symp.*, Cherry Hill, NJ, June 13–16, **1988**, 440–451.

[26] K. Kordesch, L. Binder, J. Gsellmann, E. Kharaman, G. Winkler, Manganese dioxide–hydrogen rechargeable battery, *Power Sources 13* (Eds.: T. Teily, B. W. Baxter), **1991**, 273–284.

[27] K. Kordesch, J. Daniel-Ivad, Ch. Faistauer, High power rechargeable alkaline manganese dioxide–zinc batteries, *182nd Meeting of the Electrochem. Soc.*, Toronto, Oct., **1992**, Extended Abstract 92-2, p. 18-18 (6 AA-bundle battery replacement of single D-cell).

[28] K. Kordesch, L. Binder, W. Taucher, C. Faistauer, J. Daniel-Ivad, The rechargeable alkaline–zinc manganese dioxide system, *Power Source* 14, (Eds.: Attewell, T. Keily), Internatl Power Sources Committee, **1993**.

[29] J. Daniel-Ivad, K. Tomantschger, Charge retention of Hg-free RAM cells, *Proc. 184th Meeting of the Electrochem. Soc.*, Oct. **1993**.

[30] K. Kordesch, C. Faistauer, J. Daniel-Ivad, RAM batteries for consumer applications and the proper selection of chargers, *IBA, 8th Int. Battery Symp.*, Brussels, May **1993**; *Prog. Batteries Batt. Mater.*, **1994**, *13*, 88–213.

[31] L. Binder, K. Kordesch, Production of thin sheet manganese dioxide electrodes for high energy batteries, *IBA, 8th Int. Battery Material Symp.*, Brussels, May **1993**; *Prog. Batteries Batt. Mater.*, **1994**, 256–265.

[32] K. Kordesch, M. Weissenbacher, Rechargeable alkaline manganese dioxide–zinc batteries, *J. Power Sources*, **1994**, *51*, 61–78.

[33] K. Kordesch, L. Binder, J. Gsellmann, W. Taucher, C. Faistauer, Rechargeable alkaline zinc–manganese dioxide batteries, *36th Int. Power Sources Symp.*, Cherry Hill. NJ, June 6–9, **1994**, 266–269.

[34] K. Kordesch, S. Yuwei, Technology process of rechargeable alkaline zinc manganese dioxide batteries in *Battery Bimonthly*, **1995**, *25*, (Dianchi Support: Human Light Industry Research Institute).

[35] D. Gribble, Low-cost chargers for RAM cells, in *Batteries Int.* (Ed.: D. Gribble), July **1995**, 76–77

[36] L. Binder, K. Kordesch, P. Urdl, Improvements of the RAM cell, *J. Electrochem. Soc*, **1996**, **143**, 13–17.

[37] M. Weissenbacher, J. O. Besenhard, K. Kordesch, Bonded rechargeable zinc anode, Electrochem. Soc. Meeting, Chicago, Oct. **1995**: *Proceedings, Rechargeable Zinc Batteries* (Eds.: A. J. Salkind, F. R. McLarnon, V. S. Bagotzki), The Electrochem. Soc., **1996**, *95-14*, 121–134.

[38] K. Kordesch, J. Daniel-Ivad, Rechargeable manganese dioxide batteries (recent chargers), *Proc. 37th Power Sources Conf.*, Cherry Hill, NJ, June 17–20, **1996**, pp. 436–439; K. Kordesch, C. Faistauer, D. Zhang (Patent Pending).

[39] J. Daniel-Ivad, K. Kordesch, In-application use of rechargeable alkaline manganese dioxide/zinc RAM batteries, *Portable by Design Conference*, Santa Clara, CA, March 24–27, **1997**.

[40] P. Nossaman, J. Parvareshi, *RAM In-System Charging*, Benchmarc Microelectronics, Inc., Brochure, January **1996**.

[41] IEC 86-1 International Standard for Primary Batteries. Nickel–Cadmium or Nickel–Metal Hydride Chargers, 1986.

[42] K. Kordesch, C. Fabjan, J. Daniel-Ivad, J. Oliveira, Zinc–carbon-hybrid systems, *Power Sources* Conf. Brighton, April **1997**.

[43] Source: 1995 Nielsen Report.

CosMX Exhibit 1008, Page 107 of 633

Part II:
Materials for Aqueous Electrolyte Batteries

1 Structural Chemistry of Manganese Dioxide and Related Compounds

Jörg H. Albering

1.1 Introduction

In this section the structural properties of the most common manganese dioxide modifications and closely related compounds will be presented and briefly compared. A huge number of compounds are designated as "*Braunstein*" (i.e., manganese dioxide). This term includes all natural and synthetic manganese oxides of composition $MnO_{1.7}-MnO_{2.0}$, regardless of the presence of foreign cations, hydroxide anions, or water molecules in the structure. All the known — and more or less structurally characterized — materials of that composition cannot be reviewed here. The main purpose is to give an overview of the variety of features in the chemistry of manganese oxides and to point out the structural correlations of various modifications within the large family of manganese oxide minerals and synthetic compounds. The occurrence of MnO_2 in natural ores and some methods of synthesizing the different modifications in the laboratory will be briefly described. Details of its electrochemical behavior in Leclanché cells and alkaline Zn/MnO_2 cells, and of its use as a lithium storage material in lithium-ion cells are given in Sec. II/2, and III/1 respectively.

In general, it is very difficult to obtain well-developed single crystals of any modification of MnO_2 in the laboratory [1]. Hence most of the structural data on manganese dioxide are obtained either from single crystals selected from natural ores (e.g., crystals up to 30 cm in length are reported for α-MnO_2 [2]) or by X-ray (XRD) or neutron powder diffraction techniques combined with Rietveld refinements [3]. Most manganese oxides are usually fine-grained and the crystallites may contain many defects, twin domains, superstructures, and partially occupied crystallographic sites. Therefore the XRD technique — although it is the most commonly used and successful method for the determination of the structural properties — is often limited by the poor crystallinity of the materials. Consequently, the effects of structural disorder (e.g., selective reflex broadening, preferred orientation, and the presence of indistinct, overlapping Bragg reflections) on the X-ray powder diffraction patterns can lead to incomplete or false interpretations of the diffraction data and subsequently to incorrect structural models. Thus other methods have to be applied to overcome this problem. The most powerful tool is high-resolution transmission electron microscopy (HRTEM) [4 – 6]. Other methods, e.g., IR spectroscopy [7] and extended X-ray absorption fine structure (EXAFS) measure-

CosMX Exhibit 1008, Page 109 of 633

ments [8], give additional information about the near-neighbor environment, the connection scheme of $Mn(O,OH)_n$ polyhedra, and the different oxidation states of–the manganese atoms in the structure.

The most obvious structural feature in all oxides containing manganese in the oxidation states II, III, or IV is the more or less distorted octahedral oxo- (O^{2-}) or hydroxo- (OH^-) coordination. The $Mn(O,OH)_6$ octahedra can be connected to each other by sharing common corners or edges. Face-sharing (as it is known from Nb cluster compounds containing close Nb–Nb bonds) does not usually occur, since in this case the central atoms of the polyhedra would come into too close contact. So far, a metal cluster is unknown in the structural chemistry of manganese dioxide and related compounds. The closest Mn–Mn distance in the various modifications of MnO_2 usually occurs along the shortest crystallographic axis. Many compounds contain a short translation period ranging approximately from 280 to 290 pm, which represents the distance between the central atoms of two edge-sharing octahedra. The octahedral unit is the fundamental building element for manganese oxides. How the octahedra are connected together can be used to classify the crystal structures. Similarly to silicate chemistry, the large family of manganates (II, III, or IV) can be divided in subgroups which contain characteristic building blocks of edge/corner-sharing $Mn(O,OH)_6$ octahedra [9].

A common structural feature is the formation of one-dimensionally infinite strings of edge-sharing octahedra, which extend along the shortest translation period. Two or three of these strings can be connected to one another by further edge-sharing, thus forming double or triple chains. Four such MnO_6 strings, connected by corner-sharing, enclose, a one–dimensionallly infinite tunnel of various dimensions. This category of compounds is generally described as *chain* or *tunnel* structure. The other frequently occurring structural element is formed from two-dimensionally infinite layers of edge-sharing $Mn(O,OH)_6$ octahedra. The stacking sequence of the octahedral layers and the kind/number of the interlayer atoms or molecules (metal cations, water, hydroxide anions) are further criteria for a structural classification of these *layer* or *sheet* structures ("phyllomanganates").

1.2 Tunnel Structures

1.2.1 $\beta - MnO_2$

The crystal structure of pyrolusite, or $\beta - MnO_2$, is the simplest one within the family of compounds with tunnel structures. The manganese atoms occupy half of the octahedral voids in the hexagonal close packing of oxygen atoms in an ordered manner, thus forming a rutile-type structure. The distorted MnO_6 units build up strings of edge-sharing octahedra extending along the crystallographic *c*-axis. These chains are crosslinked with neighboring chains by sharing common corners, resulting in the formation of narrow [1 × 1] channels in the structure. The voids within the channels are too small for larger cations, but there is enough space for an intercalation of hydrogen or lithium ions. The crystallographic data for $\beta - MnO_2$ and other tunnel structures are summarized in Table 1. The crystal structure of $\beta - MnO_2$ is shown in Fig. 1(a).

The β-modification is the thermodynamically stable form of MnO_2. Hence,

CosMX Exhibit 1008, Page 110 of 633

Table 1. Crystallographic data for manganese oxides with tunnel structures

Compound or mineral	Approximative formula	Symmetry	Space group	Lattice constants						Reference	Tunnel size
				a (pm)	b (pm)	c (pm)	α (°)	β (°)	γ (°)		
Pyrolusite,	MnO_2	Tetragonal	$P4_2/mnm$	440.4	440.4	287.6	90	90	90	[10]	[1 × 1]
$\beta - MnO_2$	MnO_2	Orthorhombic	Pnma	446	932	285	90	90	90	[11]	[1 × 2]
Ramsdellite	$MnO_{2-x}OH_x$	Orthorhombic		446.2	934.2	285.8	90	90	90	[12]	[1 × 1]/[1 × 2]
$\gamma - MnO_2$	$MnO_{2-x}OH_x$	Hexagonal		278.3	278.3	443.7	90	90	120	[12]	[1 × 1]/[1 × 2]
$\alpha - MnO_2$ group											
Kryptomelane	$K_{2-x}Mn_8O_{16}$	Tetragonal	$I4/m$	986.6	986.6	287.2	90	90	90	[13]	[2 × 2]
	$(K,Ba)_{2-x}Mn_8O_{16}$	Monoclinic	$C2/m$	979	288	994	90	90.37	90	[14]	[2 × 2]
Hollandite	$(Ba,K,Pb)_{2-x}(Mn,Fe,Al)_8O_{16}$	Tetragonal	$I4/m$	980.0	980.0	286.0	90	90	90	[15]	[2 × 2]
	$(Ba,K)_{2-x}Mn_8O_{16}$	Monoclinic	$C2/m$	1002.6	287.8	972.9	90	91	90	[16]	[2 × 2]
	$Ba_{2-x}(Mn,Fe)_8O_{16}$	Monoclinic	$P2_1/c$	1003	576	990	90	90.42	90	[17]	[2 × 2]
Coronadite	$Pb_{2-x}Mn_8O_{16}$	Tetragonal	$I4/m$	988.7	988.7	284.2	90	90	90	[18]	[2 × 2]
	$Pb_{1.34}Mn_8O_{16}$	Monoclinic	$C2/m$	991.3	286.5	984.3	90	90.2	90	[19]	[2 × 2]
Manjiroite	$(Na,K)_{2-x}Mn_8O_{16}$	Tetragonal	$I4/m$	991.6	991.6	286.4	90	90	90	[20]	[2 × 2]
	$Na_{2-x}Mn_8O_{16}$	Monoclinic	$C2/m$	991	286	962	90	90.93	90	[21]	[2 × 2]
Larger tunnel structures											
Romanèchite	$BaMn_9O_{10} \cdot 2H_2O$	Orthorhombic		1340	286.4	925.4	90	90	90	[22]	[2 × 3]
	$(Ba,H_2O)_xMn_5O_{10}$	Orthorhombic		1390	572	945	90	90	90	[23]	[2 × 3]
	$Ba_{1.6}Mn_5O_{10} \cdot 1.5H_2O$	Monoclinic	$C2/m$	1393.1	284.6	967.6	90	90.24	90	[24]	[2 × 3]
Rb manganate	$Rb_{16.64}Mn_{24}O_{48}$	Monoclinic	$C2/m$	1419.1	285.1	2432.3	90	91.3	90	[26]	[2 × 4]
Rb manganate	$Rb_{0.27}MnO_2$	Monoclinic	$C2/m$	1464.0	288.6	1504.0	90	92.4	90	[27, 28]	[2 × 5]
Todorokite	$(Mg,Ca,K)_x(Mn,Mg)_6O_{12} \cdot xH_2O$	Orthorhombic		951.6	1031	297	90	90	90	[6]	[3 × 3]
	$(Na,Ca,K)_{0.59}(Mn,Mg)_6O_{12} \cdot 3.1H_2O$	Monoclinic	$P2/m$	978.9	283.4	955.1	90	93.7	90	[25]	[3 × 3]

CosMX Exhibit 1008, Page 111 of 633

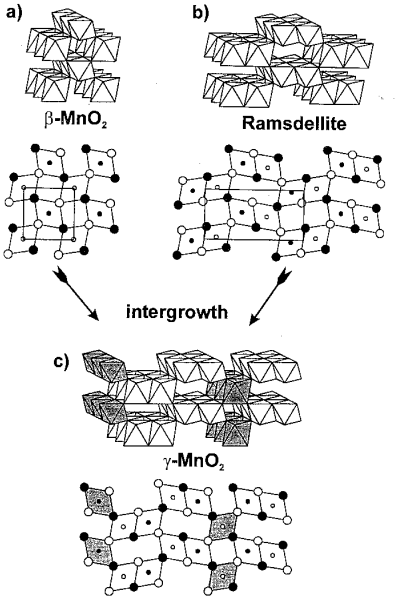


Figure 1. Crystal structure of (a) $\beta-MnO_2$, (b) ramsdellite and (c) the intergrowth structure of these two compounds, $\gamma-MnO_2$. The structures are shown as three-dimensional arrangements of the MnO_6 octahedra and as projections along the short crystallographic *c*-axis , respectively. (Small circles, manganese atoms,- large circles, oxygen atoms,- open circles, height z = 0; filled circles, height z = ½). The shaded octahedra in (c) represent the $\beta-MnO_2$ parts of the intergrowth structure of $\gamma-MnO_2$.

pyrolusite frequently occurs in natural ores and it is easily prepared in a high-purity form by thermal decomposition of manganese nitrate, $Mn(NO_3)_2 \cdot nH_2O$ [29 – 30]. Another method for the synthesis of $\beta-MnO_2$ is by heating $\gamma-MnO_2$ in closed reaction vessels in the presence of strong acids (H_2SO_4 or HNO_3) at 130 – 150°C [11, 32] or under hydrothermal conditions within a wide range of temperature and pressure [11, 33]. Naturally occurring $\beta-MnO_2$ as well as the synthetic materials with a rutile-type structure usually have a stoichiometry very close to the ideal ratio of Mn:O = 1:2. The stability region of MnO_{2-x} is assumed to be in the range of x = 0 – 0.1 [34 – 36]. Pyrolusite is the only modification in which the ideal composition MnO_2 can be reached. Hence, the β-modification can be regarded as a *true* MnO_2 compound.

1.2.2 Ramsdellite

The manganese and oxygen atoms in the ramsdellite modification of MnO_2 occupy the same crystallographic sites as the aluminum and oxygen atoms in the diaspore (AlOOH) structure and may thus be considered to be *isopointal* (according to Parthé and Gelato the term "isotypic" should be reserved for compounds in which the occupancy of the same sites results in identical coordination polyhedra and the same stoichiometry [37]) with this aluminum oxide hydroxide. The crystal structure of ramsdellite is very similar to that of pyrolusite except that the single chains of octahedra in $\beta-MnO_2$ are replaced by double chains in ramsdellite. Consequently, the tunnels extending along the short *c*-axis of the orthorhombic structure (a = 446 pm, b = 932 pm, c = 285 pm; see also Table 1) have a larger dimension ([1 × 2]) compared with those of $\beta-MnO_2$. The cell volume of ramsdellite is approximately double the cell volume of $\beta-MnO_2$. Similarly to pyrolusite, the [1 × 2] channels are too small to allow the presence of cations other than protons or Li^+. However, the transport properties of the ramsdellite crystal structure for protons or lithium ions as well as the structural integrity of the protonated or lithiated compounds are extremely important for the performance of electrochemical cells. As has already been pointed out for pyrolusite, the oxygen atoms in ramsdellite occupy the

CosMX Exhibit 1008, Page 112 of 633

positions of a hexagonally close-packed lattice. The manganese atoms are located in every second pair of neighboring octahedral voids, which share a common edge. One-half of the oxygen atoms has more or less ideal trigonal planar coordination of manganese; the other half is located at the apex of a flat trigonal pyramid formed by one oxygen and three manganese atoms. The crystal structure is shown in Fig. 1(b).

Ramsdellite is thermodynamically unstable toward a transformation into the stable β-modification. Hence, it is rarely found in natural deposits. Natural ramsdellite has a stoichiometry close to the composition of MnO_2 and can be considered another true modification of manganese dioxide. Attempts to synthesize ramsdellite in the laboratory usually lead to materials of questionable composition and structural classification. It is very likely that synthetic "ramsdellite" materials are more or less well-crystallized samples of the γ-modification that will be described in more detail below.

1.2.3 $\gamma-MnO_2$ and $\varepsilon-MnO_2$

For a long time there was uncertainty about the crystal structure of $\gamma-MnO_2$ or the naturally occurring species nsutite. Single-crystal material could be taken neither from natural deposits nor from synthetic manganese oxides prepared by various methods in the laboratory. Powder diffraction patterns of only a very poor quality with diffuse peaks, a high background and a selective peak broadening made the structure determination very complicated. Additionally, a large number of significantly different patterns could be observed, depending strongly on the preparation conditions. Some XRD patterns resembled the diffractograms of pyrolusite, others were similar to the line-rich patterns of ramsdellite samples, and many showed only a few broad peaks, that could be indexed on the basis of hexagonal close packing. A typical XRD pattern of an electrolytically prepared manganese dioxide (EMD sample from "Chemetals") is shown in Fig. 2.

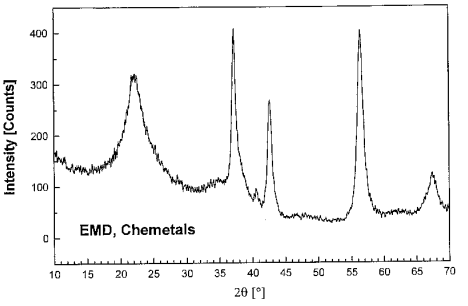


Figure 2. XRD pattern of an EMD sample (Chemetals). The diffractogram is taken with a Bruker AXS D5005 diffractometer using CuKα radiation and a scintillation counter. The step width is 0.02° with a constant counting time of 10 s / step.

In the early literature this wide variety of different powder patterns led to the distinction between $\gamma, \gamma', \gamma''$, and $\varepsilon-MnO_2$ [38]. De Wolff [39, 40] was the first to propose a plausible structural model for these phases. The De Wolff model is based on the assumption that the oxygen atoms in $\gamma-MnO_2$ are hexagonally close packed. The manganese atoms occupy half of the octahedral voids in this matrix, as in pyrolusite or ramsdellite. The only difference between these two modification is the crystallographic *b*-axis of the *Pnma* setting of ramsdellite (see Table 1). The atomic arrangements in the *a*- and *c*-directions are very similar. $\beta-MnO_2$ and ramsdellite differ only in the arrangement of the manganese atoms, which form single chains of edge-sharing octahedra in the β-modification and double chains in ramsdellite.

CosMX Exhibit 1008, Page 113 of 633

Therefore De Wolff proposed in his model that the crystal structure of $\gamma-MnO_2$ intergrowth of pyrolusite and ramsdellite domains. An idealized section of the $\gamma-MnO_2$ intergrowth structure is shown in Fig. 1(c) together with the parent structure of $\beta-MnO_2$ and ramsdellite. Depending on the relative fraction of the two parent components contributing to the crystal structure, the XRD patterns may resemble either one or the other component. The De Wolff model of $\gamma-MnO_2$ was confirmed by HRTEM investigations [4, 5, 41]. In this study the [1 × 1] and [1 × 2] tunnel domains in the structure could be visualized. Additionally, a large number of discontinuities and structural faults were observed. Even larger tunnels (e.g., [2 × 2]) exist in the real lattice of $\gamma-MnO_2$. These findings explain the relatively large amount of water in the compounds and the presence of foreign cations and anions (e.g., sulfate), incorporated during the chemical or electrochemical synthesis.

As described above, the XRD patterns of most $\gamma-MnO_2$ samples differ significantly. Some patterns can be indexed on the basis of the orthorhombic ramsdellite lattice according to the De Wolff model. In these samples the intergrown $\beta-MnO_2$ slices in the structure clearly do not destroy the orthorhombicity of the lattice. With an increasing number of defects and a decreasing order within the domains, the distribution of manganese in the octahedral voids of the hexagonally close packed oxygen atoms becomes more and more statistical. In this case the contribution of the manganese atoms to the coherent scattering of X-rays becomes very small and is sometimes only indicated by the presence of the very broad reflection around 21° (in 2θ, or at about 3.9 – 4.2 Å). Ignoring this peak, all other reflections of such a diffraction pattern can be indexed with a small hexagonal cell (e.g., a = 278.3 pm, 443.7 pm [12]), describing the close packing of the oxygen matrix. These samples with a high degree of disorder at the manganese sites are called $\varepsilon-MnO_2$ (see Fig. 3).

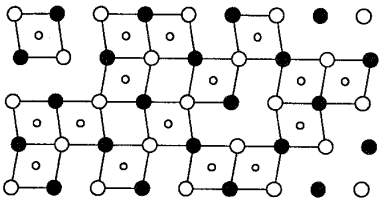


Figure 3. Schematic drawing of the crystal structure of $\varepsilon-MnO_2$. The manganese atoms are randomly distributed in the octahedral voids of the hexagonal close packing of oxygen atoms (adapted from [47]).

This modification contains tunnels of irregular shape and a statistical distribution in the structure. The only limitation for the distribution of the manganese atoms, and thus for the shape and size of the tunnels, is that no face-sharing voids can be occupied by manganese atoms, since in this case the interatomic distance of the Mn^{4+} ions would become too small. Usually, it is quite difficult to distinguish between the XRD patterns of $\gamma-$ and $\varepsilon-MnO_2$. This can only be done by careful analysis of the diffractograms using effective profile-fitting routines and an accurate determination of the orthorhombic or hexagonal lattice parameters [12].

The De Wolff disorder model has been extended to the cation vacancy model for $\gamma-MnO_2$ and $\varepsilon-MnO_2$ by Ruetschi [42]. In this model the occurrence of manganese cation vacancies and the non stoichiometry of electrochemical MnO_2 have been taken into account. Furthermore, the vacancy model deals with the explanation of the different water contents of manganese dioxide. Ruetschi makes some simple assumptions:

CosMX Exhibit 1008, Page 114 of 633

(1) The manganese atoms are distributed in a more or less ordered manner at the slightly distorted octahedral voids in the hexagonally close-packed oxygen atoms (as described above).
(2) A fraction x of the Mn^{4+} ions is missing in the manganese sublattice. For charge compensation, each Mn^{4+} vacancy is coordinated by four protons in the form of OH^- anions at the sites of the O^{2-} ions.
(3) A fraction y of the Mn^{4+} ions are replaced by Mn^{3+}. This fraction determines the average valence of the manganese atoms. For each Mn^{3+} there is a further OH^- ion in the lattice, replacing an O^{2-} anion in the coordination sphere of the Mn^{3+} cation. A schematic drawing of the Ruetschi model is shown in Fig. 4.
(4) Therefore the crystal structure is composed of Mn^{4+}, Mn^{3+}, O^{2-}, OH^-, and vacant sites. The water in the structure is present in the form of OH^- anions and Mn^{4+} vacancies.
(5) Chemisorbed water is considered to be present in the form of surface OH^- groups.
(6) Electronic conductivity arises from delocalized electrons, tunneling or hopping processes.

Therefore, Ruetschi proposes a general formula for $\gamma - MnO_2$:

$$Mn_{1-x-y}{}^{4+}Mn_y^{3+}O_{2-4x-y}^{2-}OH_{4x+y}{}^{-}$$

which replaces the formerly widely accepted, but unsatisfactory, formula:

$$MnO_n \cdot (2-n+m)H_2O$$

The terms x, y, n, and m can easily be transformed into one another by applying Eq. (1) - (4):

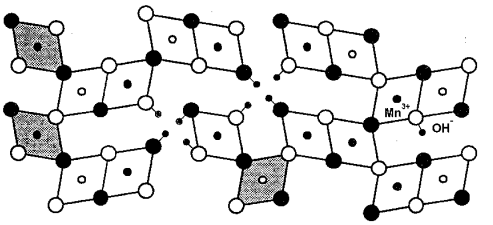


Figure 4. Vacancy (Ruetschi) model for the crystal structure of $\gamma - MnO_2$. The shaded octahedra represent the $\beta - MnO_2$ parts of the lattice. The small gray circles represent protons attached to oxygen atoms.

$$x = \frac{m}{2+m} \tag{1}$$

$$y = \frac{4(2\text{-}n)}{2+m} \tag{2}$$

$$n = \frac{4(1\text{-}x)\text{-}x}{2(1\text{-}x)} \tag{3}$$

$$m = \frac{2x}{1\text{-}x} \tag{4}$$

which allowed Ruetschi to predict the density, proton-transfer rates, electronic behavior, theoretical (maximum) electrochemical capacities, and electrode potentials for a wide range of x and y.

Further improvements on the previously discussed models were proposed in the latest model for $\gamma -$ and $\varepsilon - MnO_2$ by Chabre and Pannetier [12, 43, 44]. Starting from De Wolff's model they developed a structural description of manganese dioxides that accounts for the scattering function of all $\gamma -$ and $\varepsilon - MnO_2$ materials and provides a method of characterizing them quantitatively in terms of structural defects. All $\gamma -$ and $\varepsilon - MnO_2$ samples can be described on the basis of an ideal ramsdellite lattice affected by two kinds of defects:

CosMX Exhibit 1008, Page 115 of 633

(A) A stacking disorder (*De Wolff disorder:* intergrowth of ramsdellite- and pyrolusite- type units, as already described above). This kind of disorder can be quantified by two parameters:

- the probability P_r of occurrence of rutile-like slabs in the crystal structure; the probability of the presence of ramsdellite building blocks is $P_R = 1 - P_r$.
- the junction probability, which describes, e.g., the probability $P_{r,r}$ that a rutile-like layer r is followed by a similar layer. Analogous $P_{R,R}$, $P_{r,R}$, and $P_{R,r}$ parameters can be defined for the three other possibilities of conjunctions.

Starting from the four general possibilities that can occur (completely ordered, partly ordered, segregated, and completely random), Chabre and Pannetier found that the commercially available samples are best described by a truly random sequence of rutile and ramsdellite slabs. Furthermore, an extended simulation study of different rutile and ramsdellite fractions in the structure led to the findings that, e.g., even a small amount P_r of rutile changes the diffraction pattern of ramsdellite significantly. The reflection with an odd value of k are shifted and broadened significantly, while the reflection with $k/2+1$ (e.g., (0 2 1), (1 2 1), (2 4 0), (0 6 1)) are not affected by De Wolff disorder. If starting with $P_r = 1$ (from a pure rutile-type structure) the typical (1 1 0) peak of pyrolusite disappears even at low values of P_r. When a value of 0.5 was reached, a broad peak at about 20° (in 2θ) appeared in the simulated patterns. On the basis of these simulations Pannetier developed a method to estimate the pyrolusite concentration in orthorhombically indexable lattices. After a careful refinement of the lattice constants by profile refinements, the expected (theoretical) d value for the (1 1 0) reflection of ramsdellite is calculated from the lattice constants:

$$d_{(110),\text{expected}} = [1/a^2 + 1/b^2]^{1/2} \qquad (5)$$

Subsequently, the difference $\Delta d_{(110)}$ (in Å) is calculated from the theoretical value and the measured d value of the (1 1 0) reflection. Using the empirical calibration curve (a second– order polynomial, Eq.(6)), the pyrolusite concentration can be calculated or it may be taken from a diagram, as shown in Fig. 5.

$$P_r = 2.471\Delta d - 2.332\Delta^2 d \qquad (6)$$

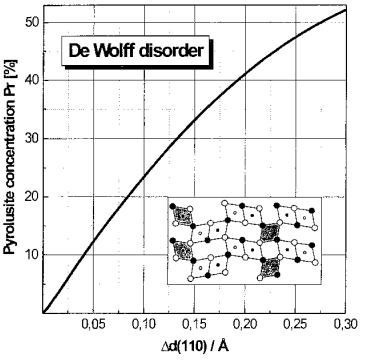


Figure 5. Calibration curve for the determination of the pyrolusite concentration of orthorhombically indexed $\gamma - MnO_2$ samples by comparison of the calculated with the observed $d_{(110)}$ value.

(B) The model of De Wolff disorder gives no explanation for the line broadening of reflections which are not affected by this type of lattice disorder. Chabre and Pannetier ascribed this effect to a micro twinning of the ramsdellite/rutile lattice on the planes [0 2 1] and [0 6 1]. These faces are believed to be growth planes of EMD [45, 46].

CosMX Exhibit 1008, Page 116 of 633

It is well known that in rutile-like structures the planes [0 1 1] and [0 3 1] are twinning planes. Hence, Chabre and Pannetier concluded that twinning faults in the planes [0 2 1] and [0 6 1] (the equivalent planes in the ramsdellite doubled unit cell) are the explanation for some features in the diffraction patterns of $\gamma-MnO_2$: e.g., the lineshift of the (1 1 0) reflection toward lower angles or the merging of the reflection groups (h 2 1)/(h 4 0) and (h 6 1)/(h 0 2).

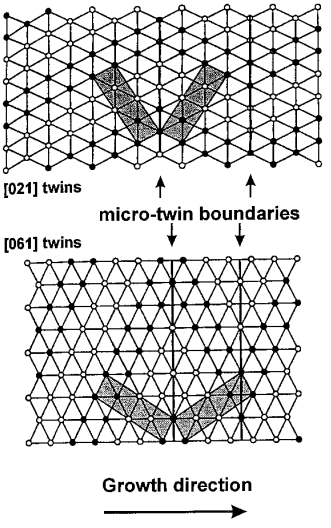


Figure 6. Projection of the manganese atoms in the ramsdellite lattice onto the *bc*-plane. The oxygen atoms are not shown. The twinning planes [021] (above) and [061] (below) are marked with arrows. The twins at these planes are generated by rotating the shaded ramsdellite cells by either 60° or 120° around the *a*-axis. (Adapted from Ref. [47].)

In Fig. 6 the arrangement of the manganese atoms is shown in a projection along the *a*-axis. The unit cells are marked by the shaded regions. It can easily be seen, that no lattice distortion is necessary to form the [0 2 1] and [0 6 1] twins. The very low activation energy for the twinning usually results in a very high number of micro twin boundaries in the crystal structure. The exact number of micro twin domains is difficult to estimate from the diffraction patterns and according to Chabre and Pannetier it is difficult to distinguish between the effects of the two kinds of disorder in the lattice, particularly when there is a large amount of micro twinning. Although the model of Chabre and Pannetier seems to be very close to reality, there might be some features in the structural chemistry of $\gamma-MnO_2$ which still have to be integrated into an optimized model such as the vacancies at the Mn^{4+} sites, the presence of Mn^{3+}, and the presence of larger tunnels (e.g., [1 × 3] or [2 × 2]) in the real lattice.

As already mentioned above the $\gamma-MnO_2/\varepsilon-MnO_2$ modification is usually obtained by electrochemical deposition at graphite, lead, or titanium anodes from a solution of Mn^{2+} salts in strong acids (usually H_2SO_4) (for references see Ref. [48]). Electrochemically prepared manganese dioxide (EMD) usually grows with a fibrous texture along the [0 2 1] and [0 6 1] faces, as described above. Nsutite, the naturally occurring modification of $\gamma-MnO_2$, shows a similar, needle-shaped, crystallite morphology. The fibrous habit can best be seen in chemically prepared samples of $\gamma-MnO_2$. These materials typically consist of bundles and small balls of tiny needles with an average length of about 1 – 4 μm an average width of about 100 – 200 nm and an average thickness of 20 – 100 nm. In contrast to EMD, which usually has a compact but porous consistency, the chemically prepared manganese dioxides (CMDs) have a very low volumetric density and are poorly compressible. The degree of oxidation in

CosMX Exhibit 1008, Page 117 of 633

EMD and in CMD is lower than in pure pyrolusite or ramsdellite. Depending on the (chemical)preparation method, the value of x in $\gamma-MnO_x \cdot nH_2O$ ranges between 1.7 and 1.98; the ideal value of $x = 2$ cannot be reached. Many methods are known for the preparation of $\gamma-MnO_2$ samples. In general, most syntheses can be modified in the way, in which $\gamma-MnO_2$ is obtained. Samples of a good quality can be synthesized by oxidation of Mn (II) salts with peroxodisulfates, permanganates, halogens, chlorates, bromates, and hypohalogenates. Another preparation method is the reaction of permanganates with organic or inorganic reducting agents (for a good collection of further references, see Ref. [46]). More than 100 years of research on MnO_2 led to a huge variety of reaction types, suitable for the production of manganese dioxide samples of widely differing properties. Some CMD materials can be used as active battery components for Leclanché cells or as catalysts; other samples may have ideal properties for organic synthesis. However, the $\gamma-$modification of MnO_2, regardless of by the preparation method (EMD or CMD), is one of most important basic, inorganic chemicals.

1.2.4 $\alpha-MnO_2$

The crystal structure of $\alpha-MnO_2$ consists of a series of [2 × 2] and [1 × 1] tunnels extending along the short crystallographic *c*-axis of the tetragonal unit cell. These tunnels are formed by double chains of edge-sharing Mn_6 octahedra cross linked by sharing corners. A three–dimensional view of the linked octahedra in the $\alpha-MnO_2$ structure as well as a projection of the structure onto the *ab* plane is shown in Fig. 7(a). In contrast to the $\beta-MnO_2$, ramsdellite, and $\gamma-MnO_2$ chain structures discussed above, the larger [2 × 2] tunnel allow various cations to be located in the middle of the cavity.

Hence, it is not surprising that a large number of different minerals with more or less ideal $\alpha-MnO_2$ types of structure are known. Minerals containing sodium (manjiroite), potassium (cryptomelane), barium (hollandite), and lead (coronadite) have been structurally characterized in detail. The crystallographic data for some $\alpha-MnO_2$ compounds are summarized in Table 1, from which it can be seen that the members of the structural family with [2 × 2] tunnels can be described either by an ideal tetragonal or by a monoclinic cell with very similar dimensions, but an angle slightly differing from $\beta = 90°$. Generally, $\alpha-MnO_2$ type compounds have a stoichiometry of $A_{2-y}B_{8-x}O_{16}$ (A = large cations, e.g., K^+, NH_4^+, Ba^{2+}, or water; B = small cations, Mn^{4+}, Mn^{3+}, V^{4+}, Fe^{3+}, Al^{3+}). Each large cation is surrounded by eight oxygen atoms forming a slightly cubic environment and additionally by four oxygen atoms outside the lateral faces of the cube. The octahedrally coordinated manganese atoms can be replaced by other small transition-metal cation with a similar ionic radius. Natural $\alpha-MnO_2$ samples usually contain one large cationic species as the major component (e.g., Ba^{2+} in hollandite) and the other possible elements (e.g., K^+) in minor amounts. Water molecules have similar dimensions to the large ions mentioned above and therefore they can replace these cations the tunnels. The crystallographic *c*-axis of the tetragonal description of $\alpha-MnO_2$ or the *b*-axis of the monoclinic setting, respectively, has a dimension of about 280 – 290 pm. Hence, the shortest distances between the large cation A would be in the same range if their respective sites were completely filled. Since such a short distance does not

CosMX Exhibit 1008, Page 118 of 633

usually occur in oxides (in contrast, in intermetallic compounds or the elemental structures such distances *can* be observed), the A site has an occupancy factor of about 50 percent or lower. This does not mean that a superstructure due to cation ordering will necessarily be observed, although some examples are known in the literature (see Table 2, $Ba_{2-x}(Mn,Fe)_8O_{16}$, with a but significant, amount of water or foreign cations is necessary to prevent the collapse of the lattice. Otherwise submicro heterogenities are formed, in which pyrolusite, ramsdellite, and intergrowth domain of these two structural elements coexist with the [2 × 2] tunnel structure of $\alpha-MnO_2$ within the real lattice.

An interesting property of the sieve-like

Table 2. *T(m,n)* nomenclature scheme for manganese oxides, according to Turner and Buseck [4]

Common dimension	Variable dimension					
	$n=1$	$n=2$	$n=3$	$n=4$	$n=5$	$n=\infty$
$m=1$	$T(1,1)$	$T(1,2)$	$T(1,3)$	$T(1,4)$	$T(1,5)$	$T(1,\infty)$
Examples	$\beta-MnO_2$	Ramsdellite				Birnessite
$m=2$	$T(2,1)$	$T(2,2)$	$T(2,3)$	$T(2,4)$	$T(2,5)$	$T(2,\infty)$
Examples		$\alpha-MnO_2$	Romanèchite	$Rb_{16.64}Mn_{24}O_{48}$	$Rb_{0.27}MnO_2$	Buserite
$m=3$	$T(3,1)$	$T(3,2)$	$T(3,3)$	$T(3,4)$	$T(3,5)$	$T(3,\infty)$
Examples			Todorokite			

doubled monoclinic *b*-axis). Usually the ordered domains of the cations in the $\alpha-MnO_2$ are too small to be detected by the occurrence of superstructure reflections. Thus, the $\alpha-MnO_2$ structure is mostly described by the tetragonal, pseudotetragonal (all angles 90°, true symmetry respective to the atomic arrangement is monoclinic), or monoclinic cell.

The presence of the foreign cation stabilizes the crystal structure of $\alpha-MnO_2$ compounds. This manganese dioxide modification (more exactly it is *not a real* MnO_2 *modification*, since the structure contains a considerable proportion of foreign atoms) can be heated to relatively high temperatures (300 – 400 °C) without destruction of the lattice. Although Thackeray et al. reported the synthesis of cation- and water- free $\alpha-MnO_2$ [49, 50], which is reported to be stable up to 300 °C without destruction of the [2 × 2] tunnel structure, it is commonly believed that a small, structure of $\alpha-MnO_2$ is that it shows pronounced cation exchange. For example, an $\alpha-MnO_2$ with a high barium content is easily prepared by stirring a sample of $(NH_4)_{2-x}Mn_8O_{16}$ (obtained from oxidation of $MnSO_4$ with a concentrated solution of $(NH_4)_2S_2O_8$ in the presence of additional NH_4^+ ions) in an acidified solution of barium nitrate at elevated temperatures. Consequently, the crystal structure of $\alpha-MnO_2$ must contain OH^- groups, cation vacancies, and/or a proportion of manganese with an oxidation state below Mn^{4+} in order to maintain the charge balance. This is reflected in the significantly longer Mn–O distances in the MnO_6 ocathedra in $\alpha-MnO_2$ (198 pm) compared with those in $\beta-MnO_2$ (188 pm).

The wide variety of natural minerals with [2 × 2] tunnels already indicates that a huge number of different compounds of the $\alpha-MnO_2$ type can be obtained by a laboratory synthesis. Most chemical syn-

CosMX Exhibit 1008, Page 119 of 633

thesis can be modified by working with concentrated solutions of the chosen foreign cations or by adding larger quantities, e.g., of potassium salts or ammonium salts during the reaction in order to produce the α-modification as the major product (for references, see Ref. [48]). Similarly, it is possible to produce samples with a controlled $\alpha-MnO_2/\gamma-MnO_2$ ratio by electrolysis in the presence of various amounts of K_2SO_4 or $CaSO_4$ [51].

filled by potassium cations or barium cations and by water molecules. Both an orthorhombic setting [22] and a monoclinically distorted structure [24] have been described in the literature (Table 1). Mukherjee found a doubling of the short *b*-axis of an orthorhombic subcell [23] due to cation/water ordering within the [2 × 3] tunnels. The most reliable and realistic structure determination seems to be the monoclinic structure refinement from sin-

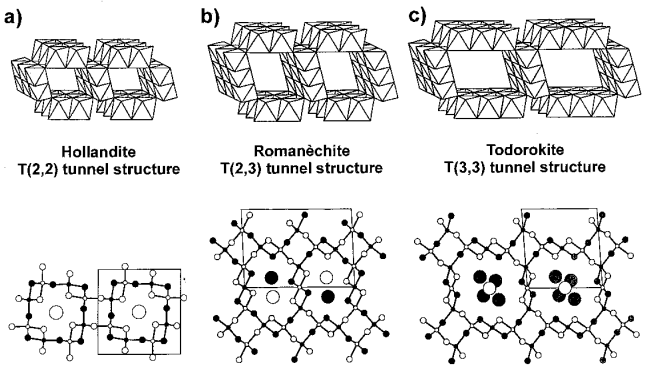


Figure 7. Crystal structures of (a) hollandite, (b) romanèchite (psilomelane), and (c) todorokite. The structures are shown as three-dimensional arrangements of the MnO_6 octahedra (the tunnel-filling cations and water molecules, respectively, are not shown in these plots) and as projections along the short axis. Small, medium, and large circles represent the manganese atoms, oxygen atoms, and the foreign cations or water molecules, respectively. Open circles, height $z = 0$; filled circles, height $z = ½$.

1.2.5 Romanèchite, Todorokite, and Related Compounds

The crystal structure of romanèchite (or psilomelane) is closely related to that of $\alpha-MnO_2$. Where as the α-modification of manganese dioxide consists of corner-sharing double chains of MnO_6 octahedra connected trough common edges, the romanèchite structure is build up by crosslinking of chains of double and triple octahedra, as shown in Fig. 7(b). The resulting [2 × 3] tunnels, extending in the *b* direction of the monoclinic cell, are partially

gle crystal X-ray data collected from a natural romanèchite crystal [24]. The presence of water, Ba^{2+}, and K^+ ions in the structure was found to be essential for the stability of romanèchite. After being heated to higher temperatures the crystal structure collapses and forms the much more stable hollandite-type compound $(Ba,K)_{2-x}Mn_8O_{16}$. Furthermore, in order to account for the charge balance of a romanèchite of the typical composition $Ba_{0.66}Mn_5O_{10}\cdot 1.5\,H_2O$, a certain fraction of the manganese atoms in the structure must have a lower oxidation state than

CosMX Exhibit 1008, Page 120 of 633

Mn(IV), or manganese vacancies must occur. In contrast to the other MnO_2 modification described above, romanèchite contains three nonequivalent manganese sites. Two of these sites have average Mn – O distances of about 191 pm, where as the third Mn octahedral position has a significantly larger Mn – O distance of 199 pm. This indicates that manganese species with a lower valence accumulate at this crystallographic site.

Investigation of the rubidium – manganese – oxygen ternary systems revealed the existence of two manganates (III, IV) with tunnel structures comparable with the mineral romanèchite. $Rb_{16.64}Mn_{24}O_{48}$ [26] contains [2 × 4] tunnels formed by cross linking (through common corners) of double chains with a building element consisting of four edge-sharing MnO_6 octahedra chains. A similar compound, $Rb_{0.27}MnO_2$ [27, 28], consists of MnO_6 octahedra chains, which are connected in a way that [2 × 5] tunnels are formed. The rubidium atoms occupy ordered positions within the tunnels. Although it may be considered speculative, it seems likely that compounds with larger tunnels (e.g., [2 × 6] or [2 × 7]) might exist.

For a long time the structural classification of the mineral todorokite was uncertain, until Turner and Buseck [4] could demonstrate by HRTEM investigations that the crystal structure of that mineral consists of triple chains of edge-sharing octahedra, which form [3 × 3] tunnels by further corner-sharing. These tunnels are partially filled by Mg^{2+}, Ca^{2+}, Na^{+}, K^{+}, and water (according to the chemical analysis of natural todorokites). In 1988 Post and Bish could perform a Rietveld structure determination from XRD data taken for a sample of natural todorokite [25]. This diffraction study confirmed the results of Turner and Buseck. The cations and water molecules in the [3 × 3] tunnels show a high degree of disorder, as could be expected. The mineral itself is rarely found in natural deposits [52]. A reliable laboratory synthesis was not reported until Shen et al. [6] demonstrated by HRTEM and XRD investigations that synthetic todorokite can be obtained by mild hydrothermal synthesis in alkaline solutions in the presence of Mg^{2+} ions. These samples show pronounced ion exchange and have been tested as absorbing agents for organic molecules (i.e., cyclo-C_6H_{12}, CCl_4). The authors found that relatively large amounts (18 – 20 g/100 g todorokite) of the organic compounds can be absorbed. The tunnels in todorokite have a typical diameter of ~690 pm, which seems — similarly to zeolites — to be well suited for the incorporation of small organic molecules.

The intensive investigation of manganese oxides during recent decades led to the discovery of a large number of closely related tunnel structures. The various ways in which the one dimensionally infinite $Mn(O,OH)_6$ octahedra strings in these compounds can be linked to each other resulted in the occurrence of manganese oxides with tunnel sizes ranging from [1 × 1] (pyrolusite) to the very large [3 × 3] channels present in todorokite. The latest investigations of the rubidium manganese oxides $Rb_{0.27}MnO_2$ and $Rb_{16.64}Mn_{24}O_{48}$ [26 – 28] demonstrated that even [2 × 4] and [2 × 5] channel structures do exist. Furthermore, the HRTEM investigations of Turner and Buseck [4, 5] confirmed the intergrowth model of De Wolff for $\gamma-MnO_2$ and it could also be shown that an intergrowth of larger tunnel structures may occur. The authors reported the occurrence of intergrown todorokite [3 × 3] with [3 × 7] structures as well as random arrangements of hollandite ([2×2], $\alpha-MnO_2$) with romanèchite units ([2 ×

CosMX Exhibit 1008, Page 121 of 633

3] tunnels). Therefore they proposed a classification scheme (see Table 2) which describes the crystal structures as a system of tunnels $T(m, n)$ with a common dimension m and a variable dimension n. For example, pyrolusite, which contains only - [1 × 1] tunnels, is denoted as $T(1, 1)$, and a compound that contains [2 × 2] (hollandite-like) and [2 × 3] (romanèchite-type) tunnels can be considered as an intergrowth of $T(2, 2)$ and $T(2, 3)$ types. With increasing n the structures approach the layered compounds (e.g., $T(2, 4)$ and $T(2, 5)$ structures with broad channels). Finally, structural features denoted as $T(1, \infty)$ and $T(2, \infty)$ can be regarded as representatives of phyllomanganates.

1.3 Layer Structures

Similarly to the tunnel structures of $\beta - MnO_2$, ramsdellite, and $\gamma - MnO_2$, the layered manganese dioxides and many related compounds are based on a more or less distorted hexagonal close packing of oxygen atoms. In layer manganates or phyllomanganates, the manganese atoms occupy the octahedral voids in such a way that two-dimensionally infinite sheets of edge-sharing MnO_6 groups are formed. In the direction perpendicular to the layer plane, the empty and filled layers alternate. In general, the structure of layered manganese oxide is similar to the C6 type (CdI_2 or $Mg(OH)_2$ (brucite) structure). A schematic drawing of this lattice type, consisting of stacked layers formed by edge-sharing octahedra, is shown in Fig. 8.

The enormous variety of manganese oxides with structures similar to the one shown in Fig. 8 arises from the different cation and water content of the space between the MnO_6 octahedra sheets, from the various ways the layers may be stacked, and from a large number of possible defects and superstructures in this family of crystal structures. Table 3 gives an overview of the crystallographic properties of some manganese oxides with a layer structure.

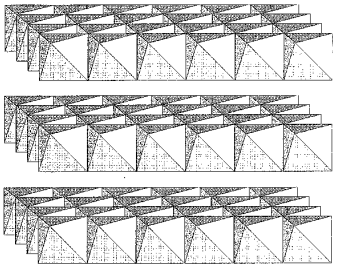


Figure 8. Schematic drawing of the layered manganese oxides. The structure consists of a stacking of empty and Mn(III, IV)-filled layers of edge-sharing octahedra.

1.3.1 Mn_5O_8 and Similar Compounds

The compoud Mn_5O_8 was first described in 1934 by Le Blanc and Wehner [68]. At that time the compound was believed to be a modification of Mn_2O_3. About 30 years later Oswald and Wampetich correctly determined the crystal structure of Mn_5O_8 and the isotypic compound $Cd_2Mn_3O_8$ [69] from single-crystal data. These two manganese oxides, as well as the isotypic copper- and zinc- containing phases $Cu_2Mn_3O_8$ [54] and $Zn_2Mn_3O_8$ [70], crystallize monoclinically. Mn_5O_8 represents a mixed- valence compound containing manganese in the oxidation states Mn^{2+} and Mn^{4+}. Hence, the formula can written as $(Mn^{2+})_2(Mn^{4+})_3O_8$, suggesting that in the isotypic compounds Zn^{2+}, Cu^{2+}, and Cd^{2+} replace the Mn(II) atoms

CosMX Exhibit 1008, Page 122 of 633

at their respective sites. The crystal structure (see Fig. 9) is best described as a strongly distorted pseudohexagonal layer structure, derived from the CdI_2-type structure. The lattice is build up of wave-like sheets of heavily distorted MnO_6 octahedra, in which every fourth manganese atom is missing. The Mn – O distances in the octahedral units range from 185 to 192 pm. The Mn^{2+} cations are placed below and above the Mn^{4+} vacancies, occupying distorted trigonal-prismatic voids. Riou and Lecerf [55] found that the cobalt compound $Co_2Mn_3O_8$ crystallizes with the higher-symmetry space group $Pmn2_1$ compared with Mn_5O_8 (space group $C2/m$). The authors suggested that this might be due to the finding that the cobalt atoms occupy two kinds of sites with differing coordination polyhedra, where as in structures of the Mn_5O_8 type only one coordination occurs for the Mn^{2+} site. The relatively short interlayer distances of 472 pm ($Cu_2Mn_3O_8$), 488 pm (Mn_5O_8), and 510 pm ($Cd_2Mn_3O_8$) indicate a strong interaction between the layers and the interlayer atoms. None of the compounds occurs in natural deposits; they can only be prepared in the laboratory, either by classical solid state chemical methods (e.g., [54, 55]) or by soft-chemical reaction paths under mild conditions. Mn_5O_8 can be obtained by hydrothermal oxidation of MnO in the temperature range 120 – 910 °C at a water pressure of up to 1 kbar and at oxygen partial pressures ranging from 1 to 100 bar [71]. Another method is the oxidation of manganese oxide hydroxides in air or in oxygen at moderate temperatures [72 – 74].

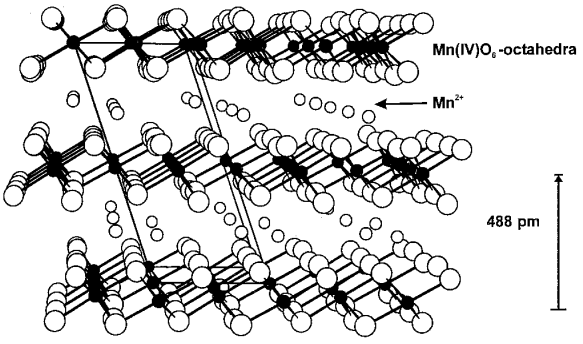


Figure 9. Perspective drawing of the crystal structure of Mn_5O_8. Small, filled balls represent the Mn^{4+} ions; small, open circles mark the positions of the Mn^{2+} ions. The oxygen atoms are shown as large, open circles.

A manganate (III, IV) similar to Mn_5O_8 is known in the literature: ternary lead manganese oxide $Pb_3Mn_7O_{15}$. In this compound the sheets of MnO_6 octahedra contain defects at the manganese sites. Four out of 14 manganese atoms are missing within the layer and are positioned in an octahedral environment above and below the vacancy in the sheets. Additionally, the structure contains Pb – O layers that separate the Mn – O sheets. Thus the stacking sequence in $Pb_3Mn_7O_{15}$ is: MnO_6 (main layer) – MnO_6 (interlayer) – PbO – MnO_6 (interlayer) – MnO_6 (main layer). The distance between the main MnO_6 sheets is larger (678 pm) than in Mn_5O_8 (488 pm), due to the insertion of a PbO layer. The crystal structure is described in the hexagonal space group $P6_3/mcm$ [61] and in its orthorhombic subgroup $Cmcm$ [60] (Table 3).

CosMX Exhibit 1008, Page 123 of 633

Table 3. Crystallographic data of layered manganese(IV,III) oxides

Compound or mineral	Approximate formula	Symmetry	Space group	Lattice constants						Interlayer distance (pm)	Reference
				a (pm)	b (pm)	c (pm)	α (°)	β (°)	γ (°)		
Mn_5O_8 type	Mn_5O_8	Monoclinic	$C2/m$	1034.7	572.4	485.2	90	109.4	90	488	[53]
	$Cd_2Mn_3O_8$	Monoclinic	$C2/m$	1080.6	580.8	493.2	90	109.4	90	510	[53]
	$Cu_2Mn_3O_8$	Monoclinic	$C2/m$	969.5	563.5	491.2	90	103.3	90	472	[54]
	$Co_2Mn_3O_8$	Orthorhombic	$Pmn2_1$	574.3	491.5	936.1	90	90	90	468	[55]
Lithiophorite	$Al_{0.58}Li_{0.32}MnO_2(OH)_2$	Monoclinic	$C2/m$	506.0	291.6	955.0	90	100.5	90	939	[56]
	$Al_{14}Li_6Mn_{21}O_{42}(OH)_{42}$	Rhombohedral	$P3_1$	1337.0	1337.0	2820.0	90	90	120	940	[57]
	$Al_{0.65}Li_{0.33}MnO_2(OH)_2$	Rhombohedral	$R\bar{3}m$	292.5	292.5	2816.9	90	90	120	939	[58]
$Na_2Mn_3O_7$	$Na_2Mn_3O_7$	Triclinic	$P1$	663.6	685.4	754.8	105.8	106.9	111.6	490	[59]
$Pb_3Mn_7O_{15}$	$Pb_3Mn_7O_{15}$	Orthorhombic	$Cmcm$	1728	998	1355	90	90	90	678	[60]
	$Pb_3Mn_7O_{15}$	Hexagonal	$P6_3/mcm$	998	998	1355	90	90	120	678	[61]
Chalcophanite	$ZnMn_3O_7 \cdot 3H_2O$	Rhombohedral	$R\bar{3}$	753.3	753.3	2079.4	90	90	120	693	[62]
$\delta - MnO_2$ group											
	$Na_4Mn_{14}O_{27} \cdot 9H_2O$	Orthorhombic		854	1539	1426	90	90	90	713	[63]
	$Mn_{14}O_{27} \cdot 5H_2O$	Hexagonal		284	284	727	90	90	120	272	[64]
	$K_{0.27}MnO_2 \cdot 0.54H_2O$	Rhombohedral	$R\bar{3}m$	284.9	284.9	2153.6	90	90	120	718	[65]
Synth. birnessite	$Na_{0.58}Mn_2O_4 \cdot 1.5H_2O$	Monoclinic	$C2/m$	517.4	285.0	733.6	90	103.2	90	714	[66]
	$K_{0.46}Mn_2O_4 \cdot 1.4H_2O$	Monoclinic	$C2/m$	514.9	284.3	717.6	90	100.8	90	705	[66]
Buserite	$Mg_{0.29}Mn_2O_4 \cdot 1.7H_2O$	Monoclinic	$C2/m$	505.6	284.6	705.4	90	96.6	90	700	[66]
	$(Na,Mn)Mn_3O_7 \cdot nH_2O$	Hexagonal		841	841	1010	90	90	120	1010	[67]

CosMX Exhibit 1008, Page 124 of 633

A third compound of comparable stoichiometry and atomic arrangement has been described by Chang and Jansen [59]. The author prepared the sodium manganate (IV) $Na_2Mn_3O_7$ and determined the crystal structure from single-crystal data. The lattice is built up by two-dimensionally infinite sheets of $[Mn_3O_7]^{2-}$ Similarly to Mn_5O_8 and chalcophanite (see section 1.3.3) a certain fraction of manganese atoms (one in seven) is missing in the layers. The sodium atoms are located above these vacancies in a distorted octahedral coordination. The distance between the MnO_6 main layers in $Na_2Mn_3O_7$ [490 pm] is comparable with the interlayer spacing in Mn_5O_8 and in isotypic compounds (472 – 510 pm).

1.3.2 Lithiophorite

The mineral lithiophorite, $(Al,Li)MnO_2(OH)_2$, can be found in natural deposits together with other manganese oxides. It is somewhat unusual within the family of manganese oxides containing foreign cations or anions, since it has been found that only small amounts of other transition metals and *no* larger alkaline metals (e.g., Na^+ or K^+) can replace the manganese and lithium atoms, respectively, in the crystal structure [75–78]. Lithiophorite has a layer structure (see Fig. 10), in which sheets of edge-sharing MnO_6 octahedra alternate with very similar layers of $(Al,Li)(OH)_6$ octahedra. The two layer types in the crystal structure are connected by O – H bridging bonds between the OH^- groups of the $(Al,Li)-OH$ sheet and the oxygen atoms in the Mn – O layers. The distance between two Mn – O layers is in the region of 940 pm. The sheets are stacked in a way that each OH group is located directly above or below of an oxygen atom of a neighboring MnO_6 layer

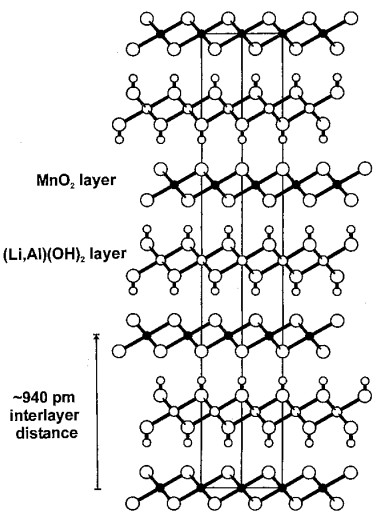


Figure 10. Projection of of the crystal of lithiophorite, $(Li,Al)MnO_2(OH)_2$, along the [110] direction of the hexagonal cell [58]. The connections within the MnO_6 and $(Li,Al)(OH)_6$ octahedra layers are emphasized. For a better understanding the O – H bridging bounds between the two layer types are not shown.

Since the first structure determination by Wadsley [56] in 1952 there has been confusion about the correct cell dimensions and symmetry of natural as well of synthetic lithiophorite. Wadsley determined a monoclinic cell (for details see Table 3) with a disordered distribution of the lithium and aluminium atoms at their respective sites. Giovanoli et al. [75] found, in a sample of synthetic lithiophorite, that the unique monoclinic *b*-axis of Wadsley's cell setting has to tripled for correct indexing of the electron diffraction patterns. Additionally, they concluded that the lithium and aluminum atoms occupy different sites and show an ordered arrangement within the layers. Thus, the resulting formula given by Giovanelli et al.

CosMX Exhibit 1008, Page 125 of 633

is $LiAl_2Mn_3O_6(OH)_6$. Another structure determination was performed by Pauling and Kamb [57]; the large superstructure unit cell that they deduced has a trigonal symmetry. A model for the ordering of lithium and aluminium atoms has been proposed and the authors suggested that one of 21 octahedra in the $(Al, Li) - OH$ layer remain vacant. The latest structure model was suggested by Post and Appleman [58] in 1994. They refined the crystal structure with a trigonal unit, which has a similar c-axis (c = 2816.9 pm) to the cell proposed by Pauling et al. (2820 pm), but a very short a-axis of only 282.5 pm. In the structural model of Post and Appleman the lithium and aluminum atoms are statistically distributed at their respective crystallographic sites (this model is shown in Fig. 10).

All the structure models discussed above describe generally the same structural feature: the alternation of Mn – O and $(Al, Li) - OH$ sheets. The only difference is that each model deals with a slightly different atomic arrangement in terms of ordering at the Al/Li site and the commensurability of the layer stacking in the various superstructures of the simple monoclinic model proposed by Wadsley. Since all of these authors investigated different samples with possibly slightly differing structural properties, none of the models is necessarily.

1.3.3 Chalcophanite

The crystal structure of the mineral chalcophanite, $ZnMn_3O_7 \cdot 3H_2O$ (see Fig. 11), was one of the first layer structures of manganese oxides that has been determined.

Wadsley [79] described the crystal structure with a triclinic unit cell ($a = b$ = 754 pm. c = 822 pm, α = 90°, β = 117.2°, γ = 120°), while Post and Appleman [62] found a trigonal symmetry (a = 753.3 pm, c = 2079.4 pm). However, the general features of the crystal structure of chalcophanite are described by both symmetries, although the latter might considered the more reliable one. The crystal lattice consists of single sheets of edge-sharing MnO_6 octahedra, which are separated by layers of water molecules. The zinc atoms are located in octahedral coordination spheres between the water and the MnO_6 layer. The distance between two Mn – O sheets was found to be 717 pm. One in seven of the manganese sites in

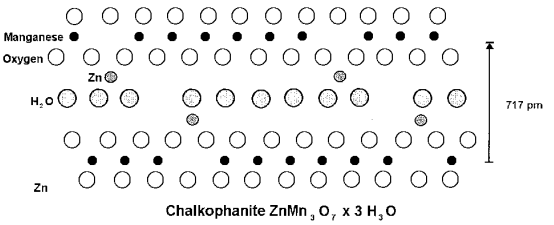


Figure 11. Projection of the chalcophanite ($ZnMn_3O_7 \cdot 3H_2O$) structure along the crystallographic b-axis. The structure consists of layers of edge-sharing MnO_6 octahedra, a separating water layer and single zinc ions which are octahedrally coordinated by three oxygen atoms from the Mn – O sheets and three oxygen atoms from the water layer.

CosMX Exhibit 1008, Page 126 of 633

each layer is unoccupied, so the composition, of the layers is $[Mn_3O_7]^{2-}$ and not MnO_2. Associated with each Mn – O layer and directly above and below the unoccupied Mn position, the Zn^{2+} ions are located in a somewhat distorted octahedral void, formed by three oxygen atoms of the Mn – O layer and three oxygen atoms from the water layer. The two kinds of sheets in the structure are held together by H – O bridging bonds between the water molecules and the oxygen atoms of the Mn–O layer. Natural chalcophanites differ quite significantly from the ideal composition. Not only can the water content be variable, but there are some Mn^{4+} defects in the lattice and the sum of the cations usually exceeds four per formula unit. This indicates that some additional interlayer atoms are present and that some Mn^{4+} ions must be replaced by manganese atoms with a lower oxidation state, e.g., Mn^{2+} and Mn^{3+}.

Similarly to Mn_5O_8 and related compounds, the chalcophanite structure can be interpreted as a "filled" CdI_2-type structure. The space in the octahedral layer is filled by an additional layer of water molecules and some foreign cations. A comparable situation is found in several hydroxozincates, e.g., $Zn_5(OH)_8Cl_2 \cdot H_2O$ or $Zn_5(OH)_6(CO)_3$. In these compounds the layers are formed by edge-sharing zinc hydroxide octahedra, $Zn(OH)_6$, and the space between the layers is filled with chloride and carbonate anions and some Zn^{2+} cations, which are located above and below vacancies in the Zn – OH layers.

1.3.4 $\delta - MnO_2$ materials

A large number of natural mineral and synthetic materials with a layered structure and strongly varying water and foreign-cation content have been collected in the $\delta - MnO_2$ group. Most of these materials have a very poor crystallinity and a wide range of existence. Therefore many authors have described "subgroups" of the layered (III, IV) manganates and named them in a mostly confusing way [80 – 86], e.g., manganous manganates, δ- manganese dioxide, 7 Å phyllomanganates. Giovanoli et al. [87] suggested that all these compounds belong to only one group so only the name $\delta - MnO_2$ should be used to describe these layered manganates. The differences in the XRD patterns arise from the strongly differing composition and crystallinity, but the general arrangements of the structural units for the $\delta - MnO_2$ compounds are the same. The crystal structure is built up from layers of edge – sharing MnO_6 octahedra with a certain number of water molecules and foreign cations between the layers. Hence, the chalcophanite type structure might be considered as a well-crystallized prototype for the structural chemistry of $\delta - MnO_2$ materials. In 1956 Jones and Milne [88] described a mineral of composition $(Na_{0.7}Ca_{0.3})Mn_7O_{14} \cdot 2.8\,H_2O$ that was found in a deposit near Birness in Scotland. Since no mineralogical name had been given to the ore, they called this mineral "birnessite"; this name is now used synonymously for the designation $\delta - MnO_2$. A number of additional studies have revealed that a relatively large number of natural manganese oxide deposits contain materials of the birnessite type [89 – 92]. Additionally, it has been shown that layered manganese oxides of birnessite-type compounds are the major components in the manganese nodules found on the sea floor [92 – 95].

Because of the low crystallinity of $\delta - MnO_2$ and birnessite samples, Giovanoli et al. used high-resolution diffraction

CosMX Exhibit 1008, Page 127 of 633

techniques, XRD powder methods, and chemical analyses in order to study a number of synthetic layer manganates [1, 63, 64]. The crystal structures of the sodium–manganese- (II, III) manganate- (IV) hydrate ($Na_4Mn_7O_{27} \cdot 9H_2O$) and the manganese- (III) manganate- (IV) hydrate $Mn_7O_{13} \cdot 5H_2O$ have been modeled on the basis of the structure of chalcophanite. It could be shown that the lattice of the sodium–manganese manganate (IV) is built up by a stacking of alternating sheets of water and hydroxide ions and layers of edge-sharing MnO_6 octahedra with a distance of about 713 pm between two Mn – O layers. One of every six manganese sites in these layers is unoccupied, and Mn^{2+} and Mn^{3+} are considered to lie above and below these vacancies in a distorted octahedral arrangement formed by three oxygen atoms of the Mn – O layer and three hydroxide ions or water molecules of the intermediate layer. The position of the sodium atoms in this layer remained uncertain. The orthorhombic lattice constants for $Na_4Mn_7O_{27} \cdot 9H_2O$ determined by Giovanoli et al. [63] can be taken from Table 3. The sodium-free compound $Mn_7O_{13} \cdot 5H_2O$ is obtained by leaching of $Na_4Mn_7O_{27} \cdot 9H_2O$ with HNO_3. The structure of the main Mn – O layer (including the Mn^{3+} ions above and below the Mn^{4+} vacancies) is the same as in the sodium-sheets of containing sample. The sodium ions are missing in the water/hydroxide layer separating the MnO_6 octahedra. The distance between the main Mn – O layers is slightly larger (727 pm) than that in the sodium-containing compound (713 pm). For $Mn_7O_{13} \cdot 5H_2O$ a small hexagonal cell of $a = 284$ pm and $c = 727$ pm was found. Recently Chen et al. [65] described a potassium-containing birnessite, $K_{0.27}MnO_2 \cdot 0.54H_2O$, with a similar rhombohedral symmetry ($R\ 3m$), but a tripled c-axis with $c = 2153.6$ pm as compared with 727 pm in $Mn_7O_{13} \cdot 5H_2O$, while the a lattice parameters are quite similar (see Table 3). The distance between two Mn–O layers in $K_{0.27}MnO_2 \cdot 0.54H_2O$ (718 pm) is comparable with that in $Na_4Mn_7O_{27} \cdot 9H_2O$ (713 pm). Giovanoli found that the "pure" $Mn_7O_{13} \cdot 5H_2O$ compounds are less stable than the samples containing foreign ions. Hence, one can conclude that foreign ions (e.g., sodium or potassium) have a stabilizing effect on the layer structure [64]. Additionally, the presence of water in layered manganates might assist in stabilizing the layered arrangement. Figure 12(a) shows a schematic drawing of the crystal structures of a birnessite-type material. Generally, according to Stouff and Boulègue [8], the foreign cations can occupy two different positions: between the water and the Mn – O layer (above an Mn^{4+} vacancy, position B1) or directly between the two main Mn – O layers (at the same height as the water molecules or hydroxide ions, position B2).

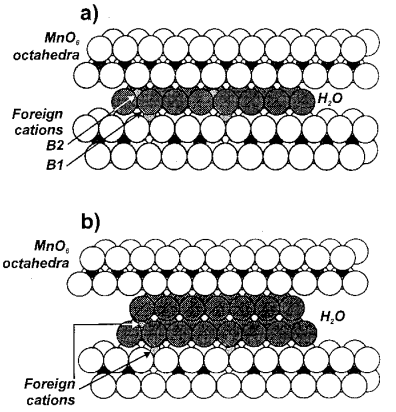


Figure 12. Schematic drawing of the theoretical positions of the foreign metal ions in (a) 7 Å phyllomanganates and (b) 10 Å phyllomanganates. The foreign ions can be located above a manganese vacancy (between the Mn – O layer and the sheet of water molecules) and within the layer, respectively (adapted from [47]).

CosMX Exhibit 1008, Page 128 of 633

Post and Veblen [66] investigated the crystal structures of several synthetic sodium, potassium, and magnesium birnessites by electron diffraction methods and Rietveld refinements of XRD patterns. Starting from the crystal structure of chalcophanite they determined the atomic arrangement in these compounds. The materials of the composition $A_xMnO_2 \cdot yH_2O$ (A = Na, K, Mg) have monoclinic symmetry (see Table 3). Post and Veblen reported a number of detailed structural features for these layered manganates. The average Mn – O bond length of 194 pm is significantly greater than in chalcophanite with a Mn – O distance 190.6 pm. This might be due to a substitution of Mn^{4+} by Mn^{3+} in the MnO_6 octahedra. In contrast to the findings of many other authors, they detected only few manganese vacancies in the Mn – O layer. According to chemical analyses Post and Veblen found that water was the predominant species in the separating layer between the MnO_6 octahedra. The positions of the foreign metal ions depend strongly on the chemical nature of the ions themselves. Figure 13 is a schematic drawing of the atomic arrangement in $Na_{0.58}MnO_2 \cdot 1.5H_2O$ and $Mg_{0.29}MnO_2 \cdot 1.7H_2O$. In the sodium compound the alkaline metal ions occupy sites within the

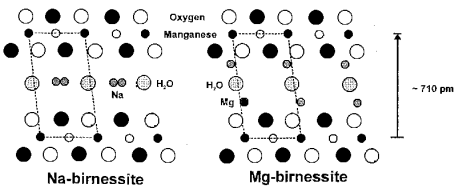


Figure 13. Schematic drawing of the crystal structures of $(Na_{0.58}MnO_2 \cdot 1.5H_2O)$ and $(Mg_{0.29}MnO_2 \cdot 1.7H_2O)$.

layer, whereas the magnesium atoms are located in an octahedral environment between the Mn – O layer and the sheet of water molecules. These two positions correspond to the sites B1 and B2 for foreign metal ions, as proposed by Stouff and Boulègue in Fig. 12(a).

It has been mentioned above that birnessite-type samples can show a wide variety of different XRD patterns. Mostly, the samples show only XRD peaks around 240 pm ($2\theta \approx 37°$ for CuKα radiation) and 142 pm ($2\theta \approx 66°$). These peaks correspond to the (1 0 0) and (1 1 0) reflections of the simple hexagonal setting of the $\delta - MnO_2$ unit cell. Additionally, in some natural as well in synthetic materials the basal plane (0 0 l) reflections (0 0 1) and (0 0 2) do occur at about 700 pm ($2\theta \approx 12°$) and 350 pm ($2\theta \approx 25°$), respectively.

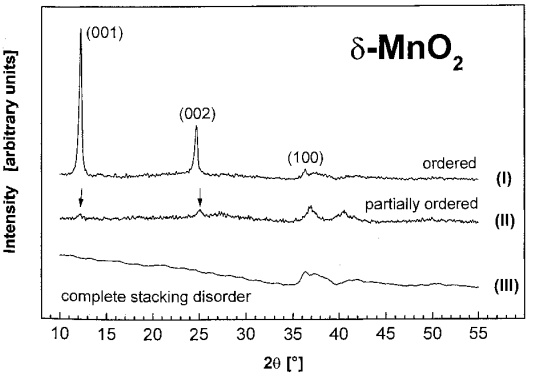


Figure 14. XRD patterns of various $\delta - MnO_2$ samples.

CosMX Exhibit 1008, Page 129 of 633

Figure 14 shows the XRD patterns of three different $\delta - MnO_2$-type samples. Sample I has been prepared by thermal decomposition of $KMnO_4$ at 450 °C for 24 h. Subsequently the resulting dark brown powder was leached with water and dried at 80 °C. The birnessite-type compound II was obtained by synproportionation of $Mn(OH)_2$ with $BaMnO_4$ in an alkaline solution, and sample III is the reaction product of the disproportionation of K_2MnO_4 into $KMnO_4$ and an Mn (IV) compound, which occurs during dilution of a slightly alkaline solution of this manganate–(VI). Sample I shows (0 0 *l*) reflections as well as the (1 0 0) peak, which indicates a high degree of order in the crystal lattice, whereas sample II only shows a very weak (0 0 *l*) reflection. In the XRD pattern of sample III the basal (0 0 *l*) peaks are completely missing. Giovanoli [3] has developed a model that explains this somewhat extraordinary behavior of different $\delta - MnO_2$ materials. In the model of birnessite-type materials proposed by Giovanoli, several arrangements of the Mn – O layer and the interlayer cations or water molecules are possible. The ideal is the perfect ordering of both types of sheets in the structure (see Fig. 15(a)), thus building up a fully commensurate crystal lattice such as is realized in chalcophanite. The XRD pattern of sample I in Fig. 14 may be of a structure type with a high degree of order. In the second case a certain kind of disorder appears within the cation or water layer in terms of an inhomogeneous distribution of the interlayer species, while the distance between the main layers is constant (Fig. 15(b)). A very similar situation is demonstrated in Fig. 15(c): a disorder of the interlayer species is combined with a shift of the main Mn – O layer within its own plane. This results in an incommensurate arrangement of the layers in the direction perpendicular to the layers. As a result the XRD patterns show only weak and broadened (0 0 *l*) peaks, because of the imperfection of the crystal lattice or (in other words) because of the very small homogeneously scattering domains in the crystallites. Sample II in Fig. 14 may be of this kind. The highest degree of disorder is described by the model in Fig. 15(d).

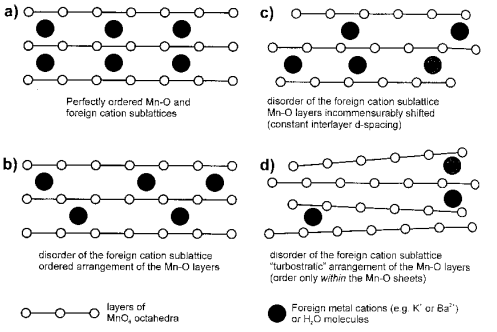


Figure 15. Arrangement of the Mn – O layers and separating sheets according to Giovanoli [3]. The layer structure can be (a) completely ordered or (d) completely disordered (turbostratic disorder). The cases (b) and (c) represent situation between the two extremes. (b) Disorder of the interlayer atoms or molecules but an ordered stacking of the Mn – O layers with constant layer distance. (c) Disorder of the interlayer atoms and an incommensurate shift of the complete Mn – O sheet within the layer plane, resulting in an incommensurate superstructure along the *c*-direction (perpendicular to the layer) and in a diffuse distribution of the electron density in this layer, resulting in a lower contribution of this layer to the 0 0 *l* reflections. (Adapted from Ref. [47]).

In this case the foreign cations and water molecules are inhomogeneously distributed and the Mn – O layers are stacked with no periodicity. In some regions of the lattice, where no foreign cations or water molecules are present, the distance between the layers becomes quite small (comparable with Mn_5O_8), while in regions with separating cations or water molecules the Mn – O sheets are at a

CosMX Exhibit 1008, Page 130 of 633

regular distance from one another. The XRD spectra of such compounds show only the (1 0 0) and (1 1 0) peaks because of a relatively high degree of order within the Mn – O layers, as is also the case for Fig. 15(a) – 15(c). The situation for birnessites is similar to that found in another layer compound with different degrees of crystallinity, namely *graphite* in comparison with its disordered species *carbon black*. Graphite has a high crystallinity and a more or less perfect and commensurate order of the carbon layers, while the hexagonal nets of carbon atoms in the structure of carbon black exhibit a large number of different interlayer distances and stacking faults, also called a *turbostratic* disorder.

1.3.5 10 Å Phyllomanganates of the Buserite Type

Buserite is structurally closely related to the 7 Å manganates discussed above. The crystal structure is built up by slabs of edge-sharing MnO_6 octahedra, which are separated by two layers of water molecules or hydroxide anions. The latter layer contains various amounts of foreign cations (e.g., Na^+, or Mn^{2+}, Mn^{3+}). The main Mn – O layers are at a distance of about 1000 pm. Buserite-type materials were found to be one of the major components of marine manganese deposits. Synthetic buserites of the composition (Na,Mn) $Mn_3O_7 \cdot xH_2O$ have been studied by Wadsley [67]. The symmetry of this hygroscopic material was found to be hexagonal with the lattice constants a = 841 pm (see Table 3). Additionally, Wadsley found that this 10 Å manganate contains not only various amounts of water, part of which can be reversibly extracted and reintroduced into the crystal lattice without destruction of the structure, but also of a significant amount of sodium atoms, which can be easily exchanged within the water and hydroxide layer. In further experiments Giovanoli et al. [96] observed that even bivalent metals (Ca^{2+} or Mg^{2+}) can be incorporated into the buserite structure. In acidic solution the stability of the 10 Å manganates decreases with increasing valence of the interlayer ions and with decreasing number of foreign cations in the structure. On complete dehydration the 10 Å manganates decompose irreversibly to the 7 Å manganates. Hence, the 10 Å phase can be interpreted as a hydrated form of the 7 Å phase, as shown in the schematic drawing of Fig. 12(b). Due to the ion-exchange properties of sodium-rich buserites it is possible to replace sodium by large organic cations (e.g., *n*-dodecy ammonium cations) as Paterson did [97]. This ion exchange increases the layer distance from 1000 pm to about 2600 pm.

1.4 Reduced Manganese Oxides

The reduced manganese oxides and oxide – hydroxides will also be considered briefly in this section, since many of them are of interest for the performance of aqueous manganese dioxide electrodes (e.g., in primary cells), but also in rechargeable alkaline manganese dioxide / zinc cells (RAM cells; e.g., Ref. [98]). Compounds of the composition MnOOH are the reaction product of the electrochemical reduction of manganese dioxides, the electrochemically inactive spinel-type compounds (e.g., Mn_3O_4 or Mn_2O_3) are formed during cycling of a MnO_2 cathode, and the manganese hydroxide $Mn(OH)_2$ is the manganese compound

CosMX Exhibit 1008, Page 131 of 633

with the lowest oxidation state occurring in aqueous systems. The lattice constants and symmetry data of several reduced manganese oxides are summarized in Table 4.

in the laboratory. It also occurs as the reaction product during electrochemical reduction of $\beta - MnO_2$ in batteries.

Table 4. Crystallographic data for reduced manganese oxides and manganese oxide–hydroxides

Compound or mineral	Approximate formula	Symmetry	Space group	Lattice constants						Reference
				a (pm)	b (pm)	c (pm)	α (°)	β (°)	γ (°)	
Groutite	$\alpha - MnOOH$	Orthorhombic	*Pnma*	1076.0	289.0	458.0	90	90	90	[99]
Feitknechtite	$\beta - MnOOH$	Trigonal	*P3m1*	332	332	471	90	90	120	[100]
Manganite	$\gamma - MnOOH$	Orthorhombic	$B2_1/d^*$	880.0	525.0	571.0	90	90	90	[101]
Hausmannite	Mn_3O_4	Tetragonal	$I4_1/amd$	814.0	814.0	942.0	90	90	90	[102]
	$\alpha - Mn_2O_3$	Cubic	*Ia3*	943.0	943.0	943.0	90	90	90	[103]
	$\gamma - Mn_2O_3$	Tetragonal	$I4_1/amd\ P$	815	815	944	90	90	90	[104]
Pyrochroite	$Mn(OH)_2$	Trigonal	*P3m1*	332.2	332.2	473.4	90	90	120	[105]

* Non standard setting of this space group.

1.4.1 Compounds of Composition MnOOH

1.4.1.1 Manganite ($\gamma - MnOOH$)

The crystal structure of manganite is closely related to that of pyrolusite in that it consists of single chains of edge- and corner-sharing $Mn(O,OH)_6$ octahedra. The coordination polyhedra of the Mn^{3+} ions in the structure are strongly distorted due to the Jahn–Teller effect of the trivalent manganese ions and the substitution of O^{2-} counter-ions by OH^- ions. This results in the formation of four short equation Mn – O bonds (with Mn – O distances ranging from 188 to 198 pm) and two longer apical Mn – OH bonds (220 – 233 pm). The formation of hydrogen bridging bonds leads to a pseudo-orthorhombic (or monoclinic) superlattice of the tetragonal $\beta - MnO_2$ parent structure. Manganite is the thermodyamically stable modification of MnOOH; therefore it can found in natural deposits as well as being easily prepared

1.4.1.2 Groutite ($\alpha - MnOOH$)

In the same way as manganite may be regarded as the structurally closely related reduction product of $\beta - MnO_2$, groutite or $\alpha - MnOOH$ was found to be isostructural with ramsdellite. The arrangement of the $Mn(O,OH)_6$ octahedra in $\alpha -$ MnOOH is very similar to that of the ramsdellite modification of MnO_2. The structure consists of double chains of octahedra. As has already been described for manganite, the protons occupy positions in the crystal structure which allow them to build up a hydrogen-bound network within the [2 × 1] tunnels. The situation for MnOOH is comparable with that of the compounds Li_xMnO_2, in which the lithium ions occupy sites in the tunnel of a ramsdellite host lattice. In both compounds the Mn – O octahedra are strongly distorted because of the insertion of foreign cations into the lattice and the resulting reduction from Mn^{4+} to Mn^{3+}. A schematic drawing of the protonated ramsdel-

CosMX Exhibit 1008, Page 132 of 633

lite or $\alpha-MnOOH$ structure (diaspore type) is shown in Fig. 16. The lattice parameters for $\alpha-MnOOH$ are significantly larger that those of ramsdellite, but the symmetry of the parent structure is maintained.

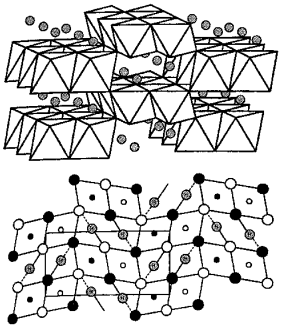


Figure 16. Crystal structure of $\alpha-MnOOH$. The structure is shown as a three-dimensional arrangement of the $Mn(O,OH)_6$ octahedra with the protons filling the [2 × 1] tunnels, and as a projection along the short crystallographic *c*-axis. Small circles, manganese atoms; large circles, oxygen atoms; open circles, height $z = 0$; filled circles, height $z = ½$. The shaded circles represent the hydrogen ions.

1.4.1.3 $\delta-MnOOH$

It can be easly realized that an intergrowth structure of $\beta-MnO_2$ and ramsdellite (i.e., $\gamma-MnO_2$) is protonated (reduced) in a very similar way. By analogy with the De Wolff model for $\gamma-MnO_2$, the crystal structure of $\delta-MnOOH$ can be interpreted as an intergrowth of manganite and groutite [106] domains. $\delta-MnO_2$ is believed to be the reaction product of $\gamma-MnO_2$ during single-electron discharge in alkaline solutions. The unit cell of $\delta-MnOOH$ can be described in terms of an orthorhombic cell, as is the case for many $\gamma-MnO_2$ samples.

1.4.1.4 Feitknechtite $\beta-MnOOH$

The reduced manganese oxide–hydroxides described above are based on tunnel structures. The layered manganates- (III, IV) can be reduced as well. The respective product is best described by a stacking of two-dimensionally infinite sheets of edge-sharing $Mn(O,OH)_6$ octahedra, which are held together by hydrogen bridging bonds between the layers. The crystal structure is very closely related to that of $Mn(OH)_2$ (see Section 1.). The symmetry is hexagonal with unit cell parameters (a = 332 pm, c = 471 pm) which are very close to these of the brucite-type $Mn(OH)_2$ (a = 332.2 pm, c = 473.4 pm). $\delta-MnO_2$ samples are topotactically reduced via $\beta-MnOOH$ to $Mn(OH)_2$ and reoxidized without the need for significant change in the crystal structure.

1.4.2 Spinel-type Compounds Mn_3O_4 and $\gamma-Mn_2O_3$

Both compounds Mn_3O_4 (i.e., hausmannite) and $\gamma-Mn_2O_3$ crystallize with a tetragonally distorted spinel-type structure (see Fig. 17).

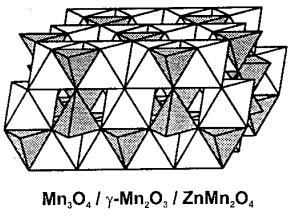


Figure 17. Schematic drawing of the spinel-type structure of Mn_3O_4 and $\gamma-Mn_2O_3$. The structure is built up of MnO_6 octahedra (white) and MnO_4 tetrahedra (shaded).

Hausmannite has the composition $(Mn^{2+})(Mn^{3+})_2O_4$. In this tetragonal

CosMX Exhibit 1008, Page 133 of 633

spinel the bivalent cations are coordinated tetrahedrally, while the Mn^{3+} ions have an octahedral environment. The Mn^{2+} ion can be replaced by other divalent ions with nearly the same radius (e.g., Zn^{2+}; in zinc-containing manganese dioxide batteries heterolyte ($ZnMn_2O_4$), which is isotypic with Mn_3O_4 and may form a solid solution with it, can be observed). If the synthesis of Mn_3O_4 is performed under oxidizing conditions, materials with XRD patterns very similar to that of Mn_3O_4 can be found, but the oxidation state is significantly higher than that of hausmannite. Verwey and De Boer [107] proposed the name of $\gamma - Mn_2O_3$ for samples of the composition $MnO_{1.39}$ – $MnO_{1.5}$. Goodenough and Loeb [108] found that $\gamma - Mn_2O_3$ crystallizes with the tetragonally distorted spinel-type structure of Mn_3O_4 but with significant defects (1/3) at the tetrahedrally coordinated Mn^{3+} site.

1.4.3 Pyrochroite, $Mn(OH)_2$

Pyrochoite, $Mn(OH)_2$, is isotypic with brucite, $Mg(OH)_2$. The crystal structure consists of layers of edge-sharing $Mn(OH)_6$ octahedra. The layers are held together by hydrogen bonding, as shown in Fig. 18. $Mn(OH)_2$ represents the manganese compounds with the lowest valence occurring in aqueous systems. Pyrochroite is easily oxidized in the presence of oxygen, even at ambient condition, and therefore it does not occur in natural ores. The instability towards oxidation might be due to the easy topotactical transformation to the thermodynamically more stable MnOOH and birnessite-type materials containing manganese in the oxidation states III and IV, respectively.

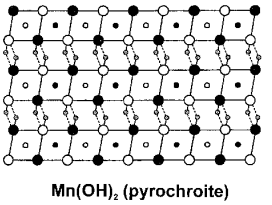


Figure 18. Crystal structure of $Mn(OH)_2$, shown as a projection along the crystallographic a-axis. Small circles, manganese atoms; large circles, oxygen atoms; open circles, height $z = 0$; filled circles, height $z = ½$. The shaded circles represent the hydrogen ions.

1.5 Conclusion

More than 100 years of research on manganese dioxides has resulted in an enormous body of knowledge on the subtle structural details of a huge variety of crystalline materials. This detailed information about the structural chemistry of manganese dioxides and the related physical properties is important for further development of electrochemical systems based on manganese oxides, such as RAM cells or lithium-ion cells, and to enable us to elaborate systematic reaction paths toward the synthesis of new materials with improved properties. The crystal structure, morphology, composition, and physical properties of various manganese oxides still have to be optimized for a large number of different application.

1.6 References

[1] R. Giovanoli, E. Stähli, *Chimia (Aarau)* 1970, *24*, 49 – 61.
[2] P. Ramdohr, G. Frenzel, *Congr. Geol. Int.*,

CosMX Exhibit 1008, Page 134 of 633

Mexico City 1958, *1*, 19 – 73.
[3] R. Giovanoli, 'Natural and synthetic manganese nodules', in: '*Geology and Geochemistry of Manganese*', Vol. 1 (Eds.: I. M. Varentsov, G. Grassely), Akadémiai Kiadó, Budapest, 1980.
[4] S. Turner, P. R. Buseck, *Science* 1981, *2.12*, 1024.
[5] S. Turner, P. R. Buseck, *Science* 1983, *304*, 134.
[6] Y. F. Shen, R. P. Zerger, R. N. DeGuzman, S. L. Suib, L. McCurdy, D. I. Potter, C. L. O'Young, *Science* 1993, 260, 511 – 515.
[7] R. M. Potter, G. R. Possman, *Am. Mineral.*, 1979, *64*, 1199.
[8] P. Stouff, J. *Boulègue, Am. Mineral.*, 1988, *73*, 1162.
[9] R. G. Burns, V. M. Burns, *Proc. MnO_2 Symp.*, Vol. 1 (Eds.: A. Kozawa, R. J. Brodd), 1975, p. 306.
[10] A. A. Bolzan, C. Fong, B. J. Kennedy, C. J. Howard, *Austral. J. Chem. 1993*, 46, 939 – 944.
[11] A. M. Byström, *Acta Chem. Scand.* 1949, *3*, 163 – 173.
[12] J. Pannetier, *Prog. Batt. Batt. Mater.* 1992, *11*, 51 –55.
[13] J. Vicat, E. Fanchon, P. Strobel, P. Tran Qui, *Acta Crystallogr. Sect. B* 1986, *42*, 162 – 167.
[14] A. M. Mathieson, A. D. Waldsley, *Am. Mineral.* 1950, *35*, 485 – 499.
[15] A. Byström, A. M. Byström, *Acta Crystallogr.* 1950, *3*, 146 – 154.
[16] J. E. Post, R. B. von Dreele, P. R. Buseck, *Acta Crystallogr. Sect. B* 1982, *38*, 1056 – 1065.
[17] B. Mukherjee, *Acta Crystallogr.* 1960, *13*, 164 – 165.
[18] M. Faller, University of Berne, 1989, in JCPDS Database Coll. No. 42 – 1347.
[19] J. E. Post, D. L. Bish, *Am. Mineral.* 1989, *74*, 913 – 917.
[20] Y. Nambu, T. Tanida, *J. Jap. Assoc. Mineral. Petrol. Ecom. Geol.* 1967, *58*, 39.
[21] M. Faller. University of Berne, 1989, in JCPDS Database Col. No. 42 – 1349.
[22] B. Mukherjee, *Mineral. Mag.* 1959/60, *32*, 166 – 171.
[23] B. Mukherjee, *Mineral. Mag.* 1965, *35*, 643.
[24] S. Turner, J. E. Post, *Am. Mineral.*, 1988, *73*, 1055 –1061.
[25] J. E. Post, D. L. Bish, *Am. Mineral.*, 1988, *73*, 861 – 869.
[26] T. Rziha, H. Gies, J. Rius, *Eur. J. Mineral.* 1996, *8*, 675 – 686.
[27] N. Yamamoto, O. Tamada, *J. Crystal Growth* 1985, *73*, 199.
[28] O. Tamada, N. Yamamoto, *Mineral. J.* 1986, *13*, 130 – 140.
[29] J. J. Berzelius, *Ann Chem. Phys.* 1817, *6*, 204 – 205.
[30] E. S. Nossen, *Ind. Eng. Chem.* 1951, *43*, 1695 – 1700.
[31] H. Peters, K.–H. Radeke, L. Till, *Z. Anorg. Allg. Chem.* 1966, *346*, 1 –11.
[32] Yu. D. Kondrashev, *Russ. J. Inorg. Chem.* 1957, *2*, 9 – 18.
[33] C. Klingsberg, R. Roy, *J. Am. Ceram. Soc.* 1960, *43*, 620 – 626.
[34] H. Bode, *Angew. Chem.* 1961, *73*, 553 – 560.
[35] A. D. Wadsley, in *Non stoichiometric Compounds* (Ed.: L. Mandelkorn), New York, 1964, 98 – 209.
[36] L. Pons, J. Brenet, *Compt. Rend.* 1965, *260*, 2483 – 2486.
[37] E. Parthé, L. M. Gelato, *Acta Crystallogr. Sect. A* 1984, *40*, 169.
[38] O. Glemser, G. Gattow, H. Meisiek, *Z. Anorg. Allg.* Chem. 1961, *309*, 1.
[39] P. M. De Wolff, *Acta Crystallogr.* 1959, *12*, 341.
[40] P. M. De Wolff, J. W. Visser, R. Giovanoli, R. Brutsch, *Chimia* 1978, *32*, 257.
[41] S. Turner, P. R. Buseck, *Science* 1979, *203*, 456.
[42] P. Ruetschi, *J. Electrochem. Soc.* 1984, *131*, 2737 – 2744.
[43] M. Ripert, J. Pannetier, Y. Chabre, C. Poinsignon, *Mater. Res. Soc. Symp. Proc.* 1991, *210*, 359 –365.
[44] Y. Chabre, J. Pannetier, *Prog. Solid State Chem.* 1995, *23*, 1.
[45] E. Preisler, *J. Appl. Electrochem.* 1976, *6*, 301.
[46] E. Preisler, *J. Appl. Electrochem.* 1976, *6*, 311.
[47] S. W. Donne, Doctoral Thesis, University of Newcastle, Australia 1996
[48] Part 56C1 in: *Gmelins Handbook of Inorganic Chemistry Manganese*, 1973, pp. 157 – 166.
[49] M. H. Roussow, D. C. Liles, M. M. Thackeray, W. I. F. David, S. Hull, *Mater Res. Bull.* 1992, *27*, 221.
[50] C. S. Johnson, D. W. Dees, M. F. Mansuetto, M. M. Thackeray, D. R. Vissers, D. Argyriou, C.–K. Loong, L. Christensen, *J. Power Sources* 1996, in press.
[51] Hoechst AG (E. Preisler, H. Harnisch, G. Mietens), German Patent 2 026 597, 1971.
[52] K. E. Anthony, J. Oswald, *Proc. 14th Int. Power Sources Symp.* 1984, pp. 199 – 215.
[53] H. R. Oswald, M. J. Wampetich, *Helv. Chim.*

CosMX Exhibit 1008, Page 135 of 633

Acta 1967, *50*, 2023 – 2034.
[54] A. Riou, A. Lecerf, *Acta Crystallogr., Sect. B* 1977, *33*, 1896 – 1900.
[55] A. Riou, A. Lecerf, *Acta Crystallogr., Sect. B* 1977, *31*, 2487 – 2490.
[56] A. D. Wadsley, *Acta Crystallogr.* 1952, *5*, 676 – 680.
[57] L. Pauling, B. Kamb, *Am. Mineral.* 1982, *67*, 817 – 821.
[58] J. E. Post, D. E. Appleman, *Am. Mineral.* 1994, *79*, 370 – 374.
[59] F. M. Chang, A. Simon, *Z. Anorg. Allg. Chem.* 1985, *531*, 177 – 182.
[60] R. E. Marsh, F. H. Herbstein, *Acta Crystallogr., Sect. B* 1983, *39*, 280 – 287.
[61] Y. Le Page, L. D. Calvert, *Acta Crystallogr., Sect. B* 1983, *40*, 1787 – 1789.
[62] J. E. Post, D. E. Appleman, *Am. Mineral.* 1988, *73*, 1401 – 1404.
[63] R. Giovanoli, E. Stähli, W. Feitknecht, *Helv. Chim. Acta* 1970, *53*, 209.
[64] R. Giovanoli, E. Stähli, W. Feitknecht, *Helv. Chim. Acta* 1970, *53*, 453.
[65] R. Chen, P. Zavalij, M. S. Wittingham, *Chem. Mater.* 1996, *8*, 1275 – 1280.
[66] J. E. Post, D. R. Veblen, *Am. Mineral.* 1990, *75*, 477 – 489.
[67] A. D. Wadsley, *J. Am. Chem. Soc.* 1950, *72*, 1781.
[68] M. Le Blanc, G. Wehner, *Z. Phys. Chem. A* 1934, *168*, 59 – 78.
[69] H. R. Oswald, M. J. Wampetich, *Helv. Chim. Acta* 1967, *50*, 2023 – 2034.
[70] A. Lecerf, *C.R. Seances Acad. Sci. Paris, Sér. C*, 1974, 279, 879.
[71] C. Klingsberg, R. Roy, *J. Am. Ceram. Soc.* 1960, *43*, 620 – 626.
[72] R. Giovanoli, U. Leuenberger, *Helv. Chim. Acta* 1969, *52*, 2333 – 2347.
[73] R. J. Davis, *Mineral. Mag.* 1967, *36*, 274 – 279.
[74] L. S. Dent Glasser, I. B. Smith, *Mineral. Mag.* 1967, *36*, 976 – 987.
[75] R. Giovanoli, H. Bühler, K. Sokolowska, *J. Microscop.* 1973, *18*, 97.
[76] J. Oswald, *Mineral. Mag.* 1984, *48*, 383.
[77] A. Manceau, S. Llorca, G. Calas, *Geochim. Cosmochim. Acta* 1987, *51*, 105.
[78] A. Manceau, P. R. Buseck, D. Miser, J. Rask, D. Nahon, *Am. Mineral.* 1990, *75*, 90.
[79] A. D. Wadsley, *Acta Crystallogr.* 1955, *8*, 165.
[80] H. F. McMurdie, *Trans. Electrochem. Soc.* 1944, *86*, 313 – 326.
[81] W. F. Cole, A. D. Wadsley, A. Walkley, *Trans. Electrochem. Soc.* 1947, *92*, 133 – 158.
[82] A. Gorgeu, *Ann. Chim. Phys.* 1862, *66*, 153 – 161.
[83] P. Dubois, *Ann. Chim. Phys.* 1936, *5*, 411 – 482.
[84] W. Feitknecht, W. Marti, *Helv. Chim. Acta* 1945, *28*, 149 – 156.
[85] O. Glemser, G. Gattow, H. Meisick, *Z. Anorg. Allg. Chem.* 1961, *309*, 1 – 19.
[86] W. Buser, P. Graf, W. Feitknecht, *Helv. Chim. Acta* 1954, *37*, 2322 – 2333.
[87] R. Giovanoli, E. Stähli, W. Feitknecht, *Chimia* 1969, *23*, 264 – 266.
[88] L. H. P. Jones, A. A. Milne, *Mineral. Mag.* 1956, *31*, 283.
[89] M. Fleischer, W. E. Richmond, *Econ. Geol.* 1943, *381*, 269.
[90] R. B. Finkelman, H. T. Evans, J. J. Matzko, *Mineral. Mag.* 1974, *39*, 549.
[91] S. Park, D. Nahon, Y. Tardy, P. Vieillard, *Am. Mineral.* 1989, *74*, 466.
[92] R. G. Burns, *Geochim. Cosmochim. Acta* 1976, *40*, 95.
[93] D. A. Crerar, H. L. Barnes, *Geochim. Cosmochim. Acta* 1974, *38*, 279.
[94] E. D. Glover, *Am. Mineral.* 1977, *62*, 278.
[95] F. V. Chukhrov, A. I. Gorshkov, V. V. Beresovskaya, A. V. Sivtsov, *Mineralum Deposita* 1979, *14*, 249.
[96] R. Giovanoli, P. Bürki, M. Guiffredi, W. Stumm, *Chimia* 1975, *29*, 517.
[97] E. Paterson, *Am. Mineral.* 1981, *66*, 424.
[98] K. Kordesch, M. Weissenbacher, *J. Power Sources* 1994, *51*, 61 – 78.
[99] R. L. Callin, W. N. Libscomb, *Acta Crystallogr.* 1949, *2*, 104 – 106.
[100] R. Meldau, H. Newelesy, H. Strunz, *Naturwissenschaften* 1973, *60*, 387.
[101] H. Dachs, *Z. Kristallogr.* 1963, *118*, 303 – 326.
[102] G. Aminoff, *Z. Kristallogr.* 1926, *64*, 475 – 490.
[103] S. Geller, *Acta Crystallogr. Sect. B* 1971, *27*, 821 – 828.
[104] K. P. Sinha, A. P. B. Sinha, *J. Phys. Chem.* 1957, *61*, 758 – 761.
[105] A. N. Christensen, G. Ollivier, *Solid State Commun.* 1972, *10*, 609 – 614.
[106] W. C. Maskell, J. E. A. Shaw, F. L. Tye, *Electrochim. Acta* 1981, *26*, 1403.
[107] E. J. W. Verwey, J. H. De Boer, *Recl.Trav. Chim.* 1936, *55*, 531.
[108] J. B. Goodenough, A. L. Loeb, *Phys. Rev.* 1955, *98*, 391.

CosMX Exhibit 1008, Page 136 of 633

2 Electrochemistry of Manganese Oxides

Akiya Kozawa, Kohei Yamamoto and Masaki Yoshio

2.1 Introduction

Most primary dry cells nowadays use MnO_2 as a cathode. The total annual world consumption of MnO_2 for dry cells exceeds 600.000 tons; about 50% being EMD (electrolytic Manganese Dioxide). The total world population was about 5.5 billion in 1997, 5.5×10^9 of whom 640 million (about 12%) were in the developed areas (USA, Japan, Western Europe). They consume 10–15 dry cells per person in a year. In the developing areas (China, South-East Asia, India, Africa, South America), which contain is 88% of the

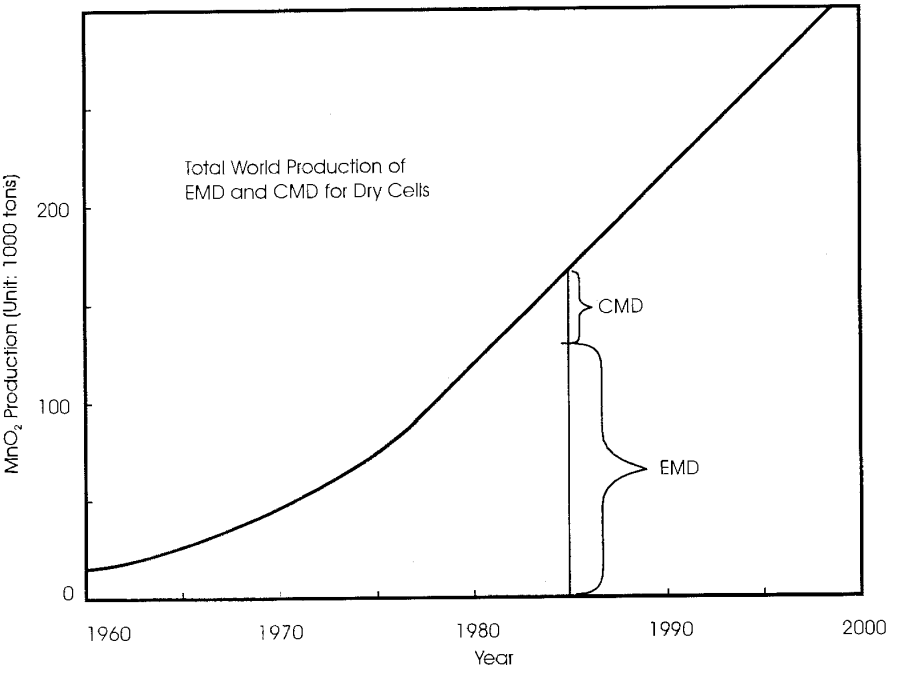


Figure 1. Total world production of EMD and chemical manganese dioxide (CMD).

Table 1. Capacity of primary AA-size cells

	Capacity (mAh)
Regular carbon/Zinc Cells using natural MnO_2 one	500 ± 50
Zinc chloride-type cells using EMD	850 ± 85
Alkaline MnO_2 cells using EMD	2200 ± 220
Li–FeS_2 cells	3000 ± 300

world population, they use only 2–3 cells per person per year. In the USA, Japan, and Western Europe, 60–80% of the dry cells are now alkaline MnO_2 (EMD) cells and $ZnCl_2$ cells using EMD. Therefore, the use of EMD has been increasing, as shown in Fig. 1, and in the future, for dry cells it will grow to at least 2–3 times the current production, since the use of alkaline MnO_2 cells will increase steadily in the developing countries. The most popular dry cell sizes are AA and AAA, since portable electronic devices are becoming smaller. Table 1 compares the capacity of the 1.5 V AA-size cells on the market today. In the developed countries, a rapid growth in rechargeable cells is taking place for various devices such as portable telephones, camcorders and portable computers. One big future application of rechargeable batteries is for EVs (electric vehicles). The most promising rechargeable cells and batteries for small portable devices are Ni–MH cells, alkaline MnO_2 cells and Li-ion batteries using L:CoO_2, $LiMn_2O_4$, or $Li_{0.33}MnO_2$. In this section, we describe the important properties of EMD and new methods determination of these properties.

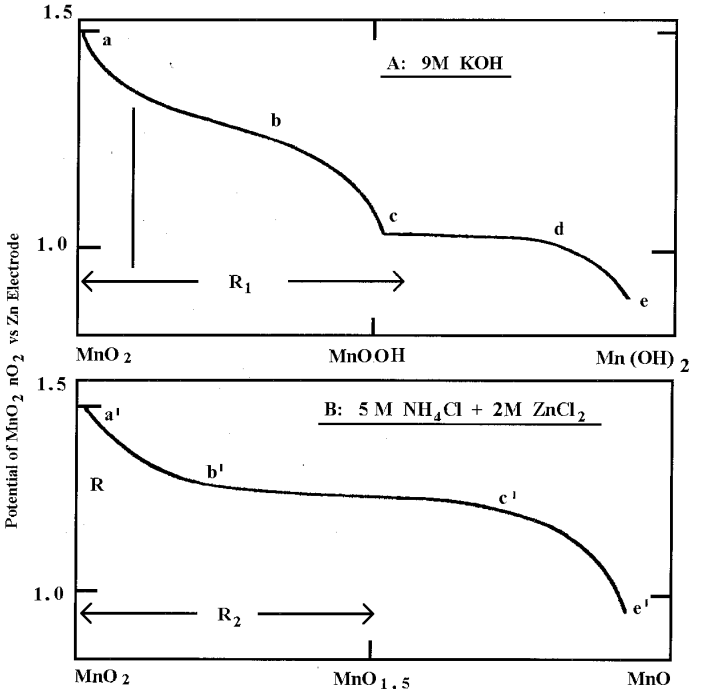


Figure 2. Schematic semi-ideal discharge curves of MnO_2 in 9 mol L^{-1} and 5 mol L^{-1} NH_4Cl_2 + 2 mol L^{-1} $ZnCl_2$ solutions. R_1, range of discharge capacity of commercial alkaline $MnO_2 - Zn$; R_2, range of discharge capacity of commercial Leclanché or zinc chloride cells.

CosMX Exhibit 1008, Page 138 of 633

2.2 Electrochemical Properties of EMD

2.2.1 Discharge Curves and Electrochemical Reactions

The basic electrochemical properties of EMD are summarized schematically in Fig. 2 [1] based on the original work by Kozawa et al. [2–5]. The electrolytic MnO_2 discharges in two steps in 9 mol L^{-1} KOH. The reaction during each step is shown below.

1st step (curve abc in Fig. 2A) in 9 mol L^{-1} KOH:

$$MnO_2 + H_2O \rightarrow MnOOH + OH^- \quad (1)$$

2nd step (curve cde in Fig. 2A) in 9 mol L^{-1} KOH:

$$MnOOH + H_2O \rightarrow Mn(OH)_2 + OH^- \quad (2)$$

In $ZnCl_2$ solutions (with or without NH_4Cl), MnO_2 discharges as shown in Fig. 2(B). The first 25% (from a′ to b′) is essentially the same Eq. (1) and the essential part of curve b′c′ is Eq. (3):

$$MnO_2 + 4H^+ \rightarrow Mn^{2+} + 2H_2O \quad (3)$$

R_1 and R_2 indicate the actual discharge ranges in practical cells.

Under certain conditions, MnO_2 shows a four-step discharge curve [6], as shown in Fig. 3, because MnO_2 can recrystallize during the discharge. Such a recrystallization takes place easily when the discharge is stopped at a deeper stage and at a high temperature (45 °C), as seen in Figs. 3(B)–(D). Even when MnO_2 is continuously discharged, if the current is low (10 mA), MnO_2 recrystallizes during the discharge showing a four-step curve (see Fig. 3A), since there is enough time for recrystallization. This structural change in MnO_2 is very critical (unfavorable) for using MnO_2 in rechargeable batteries, since the recrystallized oxide is not rechargeable. In practical primary dry cells (D, C, and AA sizes) we do not see these four-step curves even when the cell is left at a deep discharge stage. This is probably because of the very limited amount of KOH electrolyte in the cell. This structure change probably occurs through the dissolved Mn(III) ions, as Mn(III) oxide and Mn(II) oxide significantly dissolve when the KOH concentration is high (see Fig. 4). To minimize this structure change, 2–4 mol L^{-1} KOH solution would be a better choice.

2.2.2 Modification of Discharge Behavior of EMD with $Bi(OH)_3$

Both Swinkels et al. [7] and Chabre and Pannetier [9] described the process of EMD reduction as three overlapping processes. Recently Donne et al. reported [9] that the presence of $Bi(OH)_3$ on the EMD surface modified the discharge curve considerably and the rechargeability was increased. Formation of the birnessite structure from EMD and $Bi(OH)_3$ or Bi_2O_3 (mechanically mixed with EMD) [11] is the cause of the increase in rechargeability.

2.2.3 Factors Which Influence MnO_2 Potential

2.2.3.1 Surface Condition of MnO_2

The electrode potential should be a reflection of the ΔF value of the oxide, representing its total energy. However, Kozawa and Sasaki reported [12] that surface con-

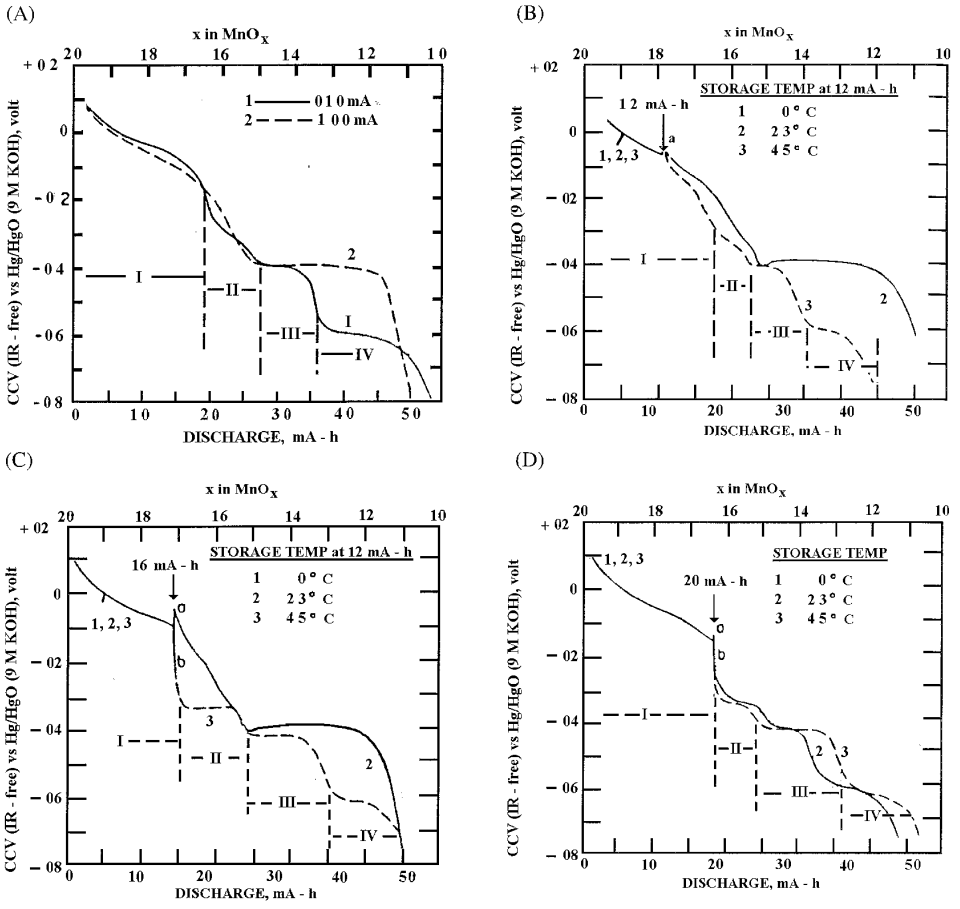
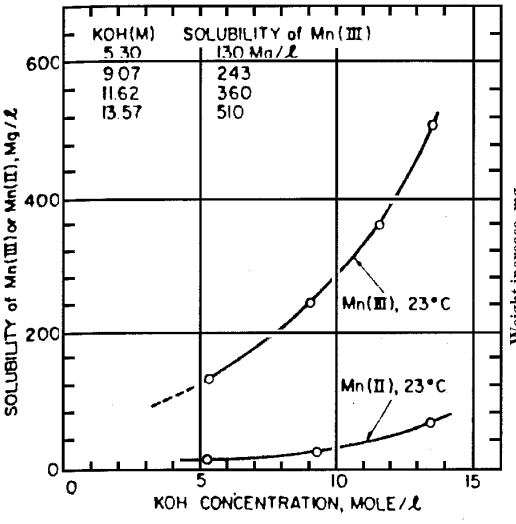


Figure 3. Four step discharge curves of MnO_2 [2]: 100 mg of EMD was discharged continuously in 9 mol L^{-1} KOH (A) and the discharged MnO_2 was stored at the 12 mAh (B), 16 mAh (C), and 20 mAh (D) stages for 96 h. Three cells containing 100 mg of $\gamma - MnO_2$ were discharged at 23 °C at 1mAh to 12, 16 and 20mAh. The cells were kept on open circuit at the temperature shown for 96 h, then the discharge was continued at 1 ma at 23 °C. The cathode potential for the cells stored at 0 °C and 23 °C recovered to point "a" but that of the cell stored at 45 °C decreased to point "b".

ditions of the battery active MnO_2 have some effect on the measured potential. A stable β-MnO_2 was prepared by heating EMD at 400 °C for 10 days. Using the structurally stable oxide, a surface equilibrium with O_2 gas in air was obtained at various temperatures between 100 and 400 °C, based on the weight change (Fig. 5). As seen in Fig. 5, the surface oxide layer decomposes (with release of O_2) and reversibly absorbs O_2 between 300 and 400 °C. When the heated oxide at 400 °C is quickly cooled, the surface condition of 400 °C is maintained (no weight change). When the heated oxide is cooled slowly for 2–3 h at 300 °C, oxygen is adsorbed.

The potential of β-MnO_2 samples which were heated at various temperatures

CosMX Exhibit 1008, Page 140 of 633



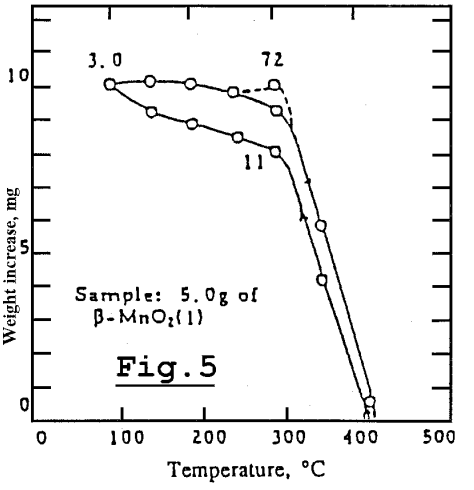


Figure 4. Solubilities of Mn(III) and Mn (II) in KOH [10].

Figure 5. Thermogravimetric equilibrium study of $\beta - MnO_2$. The weight change of the sample was measured in air between 100 and 400 °C, by changing from one temperature to another after attaining a constant weight at each temperature. The reference point of the weight was initial steady-state weight at 400 °C in air. In a few cases, the sample was kept for 3–72 h at the same temperature to see whether the weight changed further or not. It was found that the weight essentially reached in equilibrium at each temperature with 3 H. The number by the points (3, 11, 72) indicate the extra hours waited for this purpose.

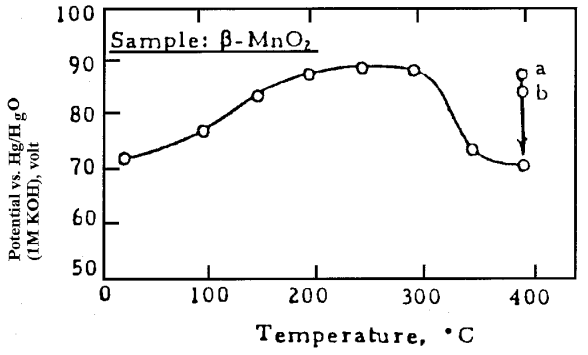


Figure 6. Static potential of $\beta - MnO_2$ after heating in air between 100 and 400 °C. All the samples were heated at each temperature for 2 h and cooled quickly to 25 °C, The potential was measured in 1 mol L^{-1} KOH solution. Point "a" and "b" are the values obtained with the β-MnO_2 samples which were cooled slowly (allowing samples to reach room temperature overnight).

and quickly cooled were determined in 1 mol L^{-1} KOH (Fig. 6). The potential of the β-MnO_2 which was heated at 400 °C and cooled slowly (exposing the oxide surface at 300 °C for sufficient time) is higher (note the potential of points a and b). These results indicate that the potential of MnO_2 can change, depending on the surface condition, by as much as 18 mV. This is important for obtaining the ΔF value.

CosMX Exhibit 1008, Page 141 of 633

2.2.3.2 Standard Potential of MnO_2 in 1 mol L^{-1} KOH

Two types of redox systems (Fig. 7) are used for batteries [14]. The standard potential ($E°$) of MnO_2 should be a good representation of the total energy of the oxide. For two-phase systems such as PbO_2, Ag_2O, HgO, etc., the initial potential (E_i) and middle potential (E_m) are equal to $E°$, from which we can calculate ΔF ($=nFE°$). For MnO_2, a one-phase system, as shown in Fig. 7(A), the E_i (initial potential) cannot be used as $E°$. Kozawa proposed the middle potential (E_m) of the S-shaped curve to be used as the $E°$ value since it can be a fairly good representation of the system to calculate the ΔF value. We need to obtain $E°$ ($=E_m$) of MnO_2 in 1 mol L^{-1} KOH. In our attempt to obtain a repeatable static potential of MnO_2 in 0.1–1 mol L^{-1} KOH solutions, we found that the potential of MnO_2 changes slowly and, it is difficult to reach a steady value. This is probably due to the high porosity and presence of a large amount of fine cavities in the EMD; therefore we still do not have a good $E°$ value for EMD and other MnO_2 samples.

2.2.4 Three Types of Polarization for MnO_2

As shown in Fig. 8, three types of polarization exist during the discharge of porous MnO_2. The battery active EMD or CMD (chemical manganese dioxide) is highly porous and the concentration polarization due to the pH change, $\eta(\Delta pH)$, is very important. Kozawa studied the three types of polarization for ten (IC) MnO_2 samples in 9 mol L^{-1} KOH and 25% $ZnCl_2$ (+5% NH_4Cl) solutions [15] and found $\eta(\Delta pH)$ is much smaller for CMDs. Tables 2 and 3 show the polarization values at 7, 14, and 21 mAh for a 1.0 mA continuous discharge of 100 mg MnO_2 sample having 27 mAh for one–electron reaction. The total polarization, η_T, is the sum of the three polarizations.

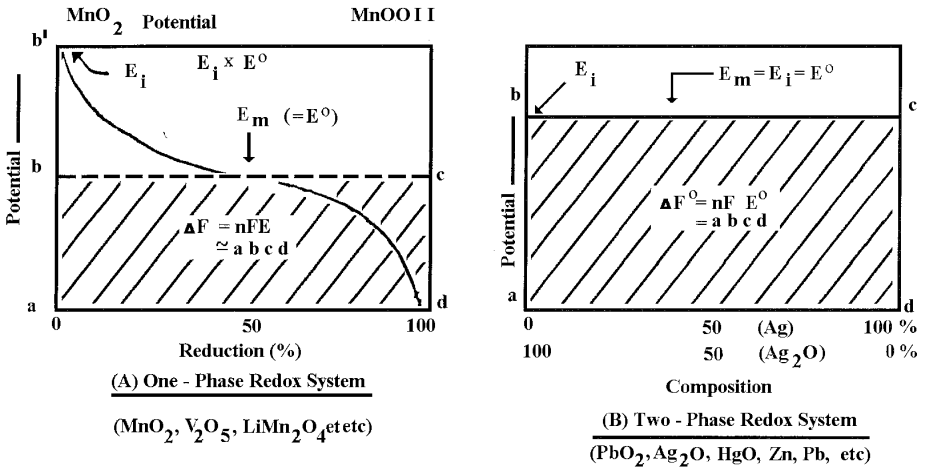


Figure 7. Two types of redox systems [14]: (A) one–phase (MnO_2, V_2O_5, $LiMn_2O_4$, etc.) ; (B) two–phase (PbO_2, Ag_2O, HgO, Zn, Pb, etc.)

CosMX Exhibit 1008, Page 142 of 633

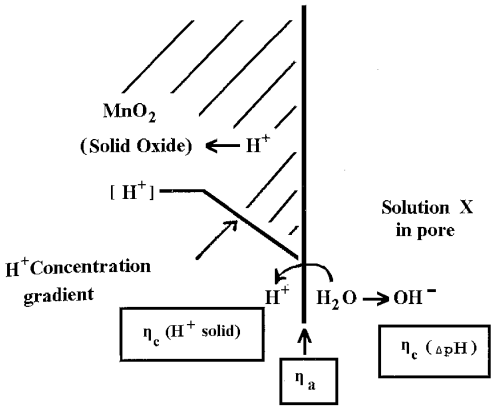


Figure 8. Three types of polarization of MnO_2: (1) η_c (H^+ solid), due to proton diffusion in solid; (2) η_a, due to the solution–solid interface; (3) $\eta_c(\Delta pH)$, due to a pH change of the electrolyte in the pores.

$$\eta_T = \eta_a + \eta_c(\text{solid}) + \eta(\Delta pH)) \quad (4)$$

$$\eta(\Delta pH) = \eta_T - (\eta_a + \eta_c(\text{solid})) \quad (5)$$

Since the pH change $\eta(\Delta pH)$ is practically zero for the discharge in 9 mol L^{-1} KOH solution, we can assume that $\eta_a + \eta_c(\text{solid})$ is the same for the two solutions (9 mol L^{-1} KOH and 25% $ZnCl_2$). Therefore, the difference in the polarization values (in Tables 1 and 2) is

$\eta(\Delta pH)$, where

Table 4 shows $\eta(\Delta pH)$ at the 7 mAh stage. We can see that $\eta(\Delta pH)$ is very small for CMD and nonporous manganese dioxide (NMD). This is very reasonable since the pore diameter of CMD and NMD is much bigger than that of EMD. This is why EMD for $ZnCl_2$ cells is usually produced at high current, in order to increase its pore dimensions.

Table 2. Open-circuit voltage (OCV) and polarization (P) at 1.00 mA per 100 mg sample in 9 mol L^{-1} KOH solution*

IC	MnO_2 sample+	7mAh		14mAh		21mAh	
		OCV (V)	P (V)	OCV (V)	P (V)	OCV (V)	P (V)
1	EMD (Ti anode)	0.022	0.052	−0.050	0.060	−0.261	0.021
2	EMD (Pb anode)	0.023	0.053	−0.048	0.061	−0.250	0.028
3	EMD (C anode)	0.021	0.048	−0.060	0.049	−0.264	0.046
4	EMD	0.013	0.054	−0.080	0.043	−0.272	0.059
5	CMD	−0.047	0.101	−0.170	0.042	−0.249	0.100
7	Natural ore	−0.077	0.188	−0.183	0.168	−0.292	0.119
8	CMD	−0.033	0.090	−0.149	0.047	−0.282	0.068
9	EMD	0.014	0.054	0.065	0.075	−0.241	0.100
10	EMD	0.013	0.052	−0.083	0.054	−0.314	0.016
11	CMD (chlorate process)	0.025	0.085	−0.026	0.119	−0.158	0.157

* Polarization: Voltage different between OCV and *IR*-free CCV (closed-circuit voltage) vs. Hg/HgO (9 mol L^{-1} KOH).

+ EMD: electrolytic MnO_2, CMD: MnO_2 made by chemical process.

CosMX Exhibit 1008, Page 143 of 633

Table 3. OCV and polarization (P) at 1.00 mA per 100 mg sample in 25% $ZnCl_2$ +5% NH_4Cl solution*

IC	MnO_2 sample	7mAh		14mAh		21mAh	
		OCV (V)	P (V)	OCV (V)	P (V)	OCV (V)	P (V)
1	EMD (Ti anode)	0.458	0.127	0.411	0.122	0.431	0.182
2	EMD (Pb anode)	0.443	0.093	0.411	0.108	0.424	0.177
3	EMD (C anode)	0.452	0.086	0.412	0.102	0.422	0.162
4	EMD	0.462	0.112	0.428	0.126	0.441	0.178
5	CMD	0.408	0.097	0.397	0.110	0.432	0.155
7	Natural ore	0.389	0.188	0.383	0.175	0.420	0.231
8	CMD	0.415	0.095	0.393	0.092	0.415	0.134
9	EMD (coarse particles)	0.460	0.096	0.414	0.094	0.442	0.172
10	EMD	0.453	0.093	0.407	0.095	0.431	0.163
11	CMD (chlorate process)	0.476	0.266	0.463	0.204	0.488	0.248

* Polarization voltage different between OCV and *IR*-free CCV. OCV vs. SCE.

Table 4. Polarization and $\eta_c(\Delta pH)$ (in mV)

IC	MnO_2 sample	(a) 9 mol L^{-1} KOH	(b) η_T $ZnCl_2$ *	(b − a) $\eta_c(\Delta pH)$
1	EMD (Ti)	52	127	75
2	EMD (Pb)	53	93	40
3	EMD (C)	48	86	38
4	EMD	54	112	58
5	CMD	101	97	−4
7	NMD	188	188	0
8	CMD	90	95	5
9	EMD	54	96	42
10	EMD	52	93	41

* Measured in 25% $ZnCl_2$ +5% NH_4Cl.

2.2.5 Discharge Tests for Battery Materials

Testing various battery materials (MnO_2, MH, $LiCoO_2$, etc.) requires a simple and repeatable electrochemical test using 0.1–0.5g of sample. Kozawa proposed a plastic cell test [4] using a 100 mg MnO_2 sample mixed with a large amount of graphite and discharging it at 1.0 mA. This method provides reproducible results for open-circuit voltage (OCV), closed-circuit voltage (CCV), polarization, and capacity (mAh) if the mixing and packing technique is practiced thoroughly and the same graphite is used. However, the measured voltage has a considerable effect on the *IR* drop [16]. In 1992, Kozawa et al. [17] proposed an easy, repeatable test method using TAB (Teflonized acetylene black) developed by the Bulgarian laboratory [18]. The three useful TABs available today are shown in Table 5.

TABs are a mixture of a Teflon emulsion and acetylene black, which is prepared by a special vigorous mixing technique.

They are very useful not only for testing. They are being used in practical commercial cells. Figure 9 shows electrode preparation with TAB. Figures 10, 11 and 12 show the test results for a MnO_2 sample (IC No. 17) in 9 mol L^{-1} KOH and 25% $ZnCl_2$ (+5% NH_4Cl) solutions.

Table 5. Composition and application of TABs available

	Teflon (%)	Acetylene black (%)	Surfactant (%)	Applications*
TAB-1	34	66	0	Gas-diffusion electrodes
TAB-2	33	66	1	Lithium battery electrodes
TAB-3	32	64	4	Aqueous battery electrodes

* All three are available for research, in 100g bag, from ITE, Aichi, Japan (Fax: (81) 586-81-1988).

CosMX Exhibit 1008, Page 144 of 633

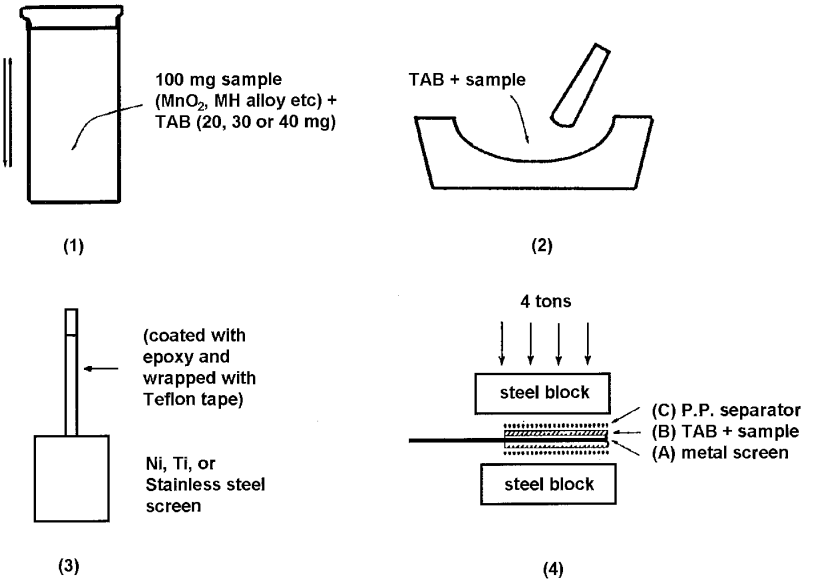


Figure 9. Procedure for the preparation of the test electrode for aqueous electrolytes (9 mol L^{-1} KOH or $ZnCl_2$ solution). (1) the sample is mixed by shaking in a plastic container 20 mm (diam.) × 40 mm (height); (2) the mixture is made into a thin film by grinding with a pestle in a ceramic mortar; (3) the metal screen is prepared; (4) the three layers (A, B, C) are pressed between the steel blocks.

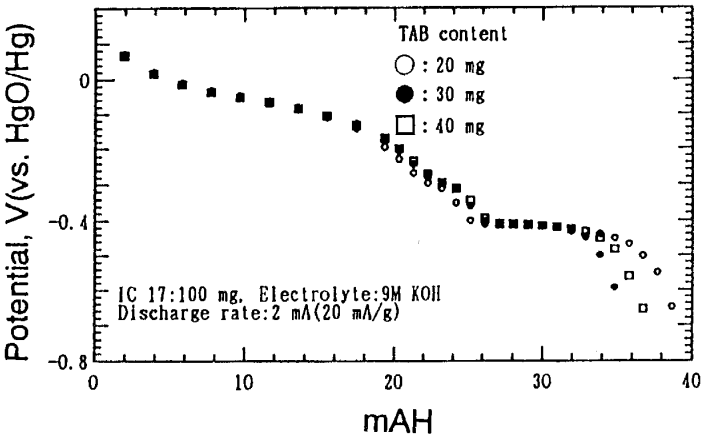


Figure 10. Effect of the amount of TAB on the discharge behavior of IC No. 17 (EMD) in a mol L^{-1} KOH.

Figure 12 shows discharge tests of MnO_2 in 3, 6, and 9 mol L^{-1} KOH solutions with and without O_2. With the 9 mol L^{-1} KOH solution, the effect of dissolved O_2 gas is very small, but the effect is significant with 3 and 6 mol L^{-1} KOH solutions since the O_2 solubility increases. Figure 13 shows that this test method is useful for

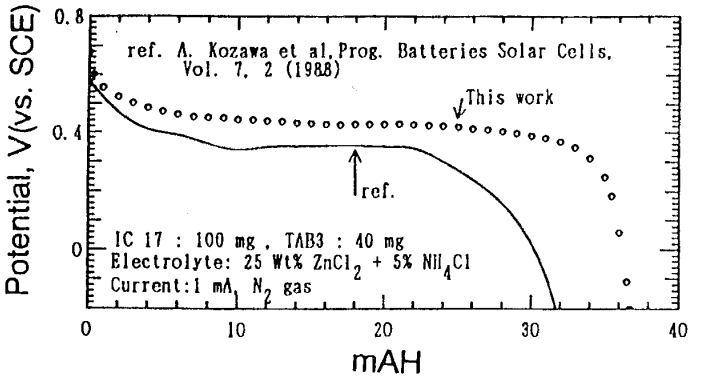


Figure 11. Comparison of discharge behavior of IC No. 17 (EMD) for currently proposed method and a previously published method.

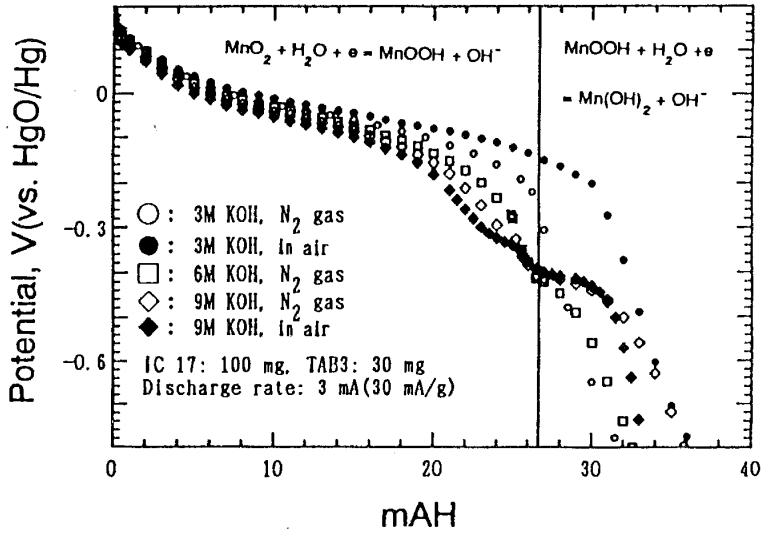


Figure 12. Effect of KOH concentration and dissolved oxygen on the discharge behavior of IC No. 17 (EMD) in 3–9 mol L^{-1} KOH.

MH alloys. $LiCoO_2$ and other materials have also been successfully tested with TAB [17].

Recently, Tachibana et al. [19] used a nickel mesh electrode containing a mixture of Teflon emulsion, graphite (or acetylene black) and oxides (MnO_2, $LiCoO_2$, etc.). In this method the electrode is very thin, and there is no *IR* drop within the electrode. Therefore, measurements can be made by a simple, direct method (no potentiostat is needed).

CosMX Exhibit 1008, Page 146 of 633

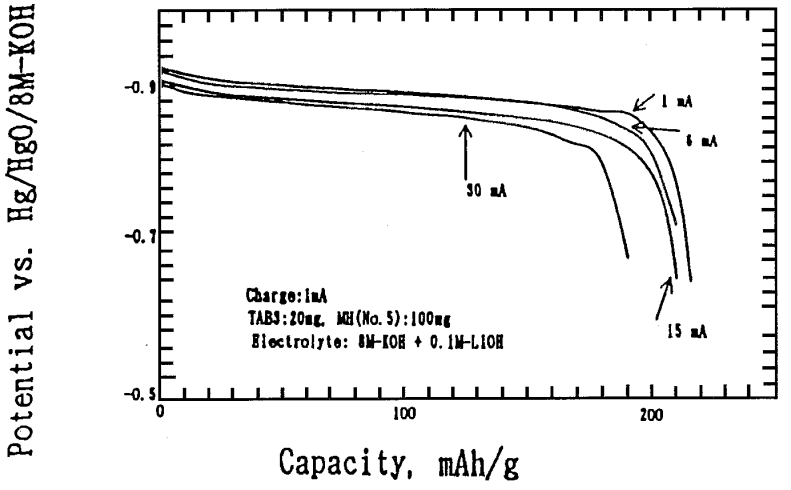


Figure 13. Application of TAB-3 to metal hydride (IBA No. 5) electrode.

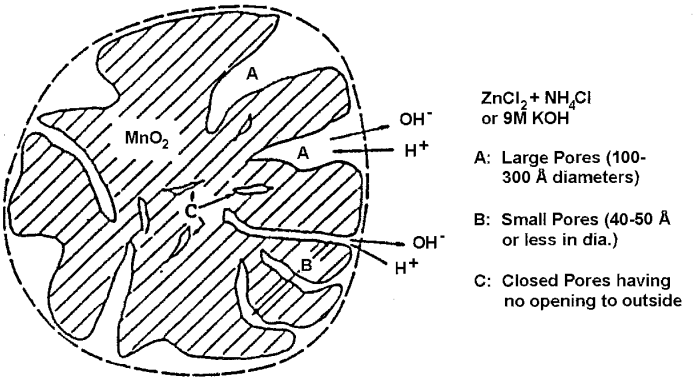


Figure 14. Porous MnO_2 particle with three of pores: A, large pores, 100–300 Å diam.; B, small pores, 40–50 Å or less diam.; C, closed pores with no outside opening; ----- superficial surface; —— true surface including the pore walls.

2.3 Physical Properties and Chemical Composition of EMD

Table 6 shows the physical properties and chemical composition of typical battery active EMDs, and Table 7 shows a typical chemical analysis of EMD. Figure 14 shows a schematic model of an EMD particle showing three types of pores. Figure 15 shows the calculated surface area of non-porous solid cubes having a specific granty (SG) of 1.0, 4.0, and 5.0 $g\,mL^{-1}$. As the measured SG of EMD is 4.3 $g\,mL^{-1}$ and the surface area is 25–35 $m^2\,g^{-1}$, the superficial surface area is less than 0.1 $m^2\,g^{-1}$. Therefore, most of the

CosMX Exhibit 1008, Page 147 of 633

Table 6. Physical properties and chemical composition of EMD

-Physical properties	
Electrical resistivity*	50–100 Ωcm
BET surface area	40–50 m^2g^{-1}
Pore diameter	40–60Å
Pore volume (<150 Å pores)	0.032–0.035 mL/g^{-1}
Density	
• True density	4.0–4.3 g/mL^{-1}
• Apparent density	2.2–2.3 g/mL^{-1}
Average particle size	10–45 ìm
Chemical composition	
MnO_2	92%
H_2O	2–4%
Mn_2O_3 and MnO	3–4%
SO_4^{2-}	~1%
Metallic impurity	Very low

* Measured with powder sample in tablet from under high pressure

Table 7. Specification and typical analysis.

Component	Specification	Typical analysis
MnO_2	91.0% min.	92.0%
Mn	60.0% min.	60.4%
H_2O	2.0% min.	1.8%
HCI Insoluble	0.2% min.	0.02%
SO_4	1.3% min.	1.20%
Fe	150ppm max.	80ppm
Pb	5 ppm max.	<1ppm
Cu	5 ppm max.	1ppm
Ni	10 ppm max.	3ppm
Co	15 ppm max.	3ppm
Sb	1 ppm max.	<1ppm
As	1 ppm max.	<1ppm
Mo	5 ppm max.	1ppm
Cr	15 ppm max.	5ppm
V	2 ppm max.	<1ppm
K	0.15% max.	0.08%
PH		
• JIS method	5.0–5.6	5.2
• USA method	8.0–9.0	8.5

* Neutralization with NH_4OH or NaOH. JEC Sample, 1997, available from ITE Japanese Office.

electrochemical reaction takes place on the pore wall of the fine pores and cavities since the pore diameter is 50–100 Å.

The ideal battery material should be highly porous, but should have a high density in order to pack as much as possible in to the limited space of the cell. EMD is almost the ideal MnO_2 since it is dense and has fine pores (actually cavities).

2.3.1 Cross-Section of the Pores

Based on the gas adsorption behavior, Kozawa and Yamashita proposed a hypothesis [20, 21] that the cross—section of the fine pores of EMD is a cavity shape as shown in Fig. 16. The cross-section of the pore by computer calculation is a circle (Fig. 16A). Nobody knows the real shape of the cross-section as yet. Kozawa's belief in the cavity shape (Fig. 16B) is based on the results of experiments involving the oxygen adsorbed and desorbed from the pore walls [20].

2.3.2 Closed Pores

The presence of closed pores was demonstrated by Kozawa [22] by measuring the BET surface area of EMD samples of various particle sizes. Kozawa's new method for the determination of the closed pore is based on the relationship of the BET surface area and the particle size, by extrapolating the surface area value to zero particle size (Fig. 17). Table 8 shows the percentage of closed pores of various EMD samples.

2.3.3 Effective Volume Measurement

A new, simple, and practical method for pore volume measurement was proposed

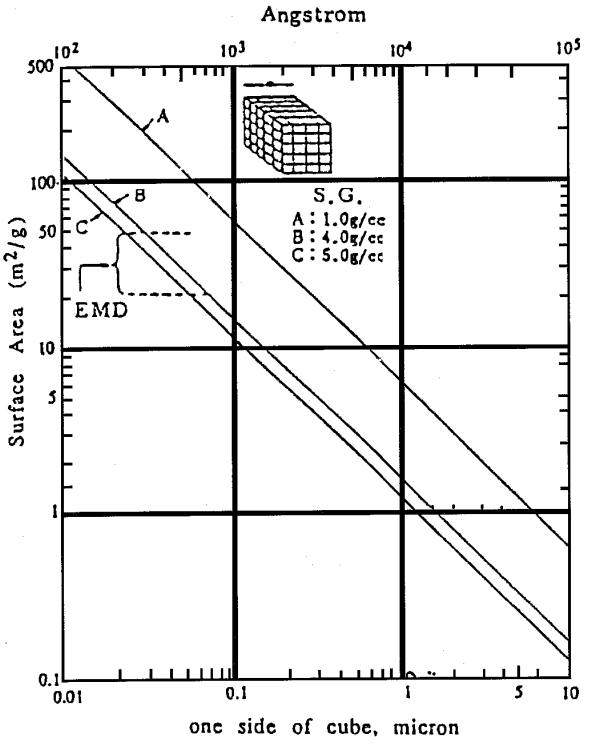


Figure 15. Surface area of solid cubes of various specific gravities.

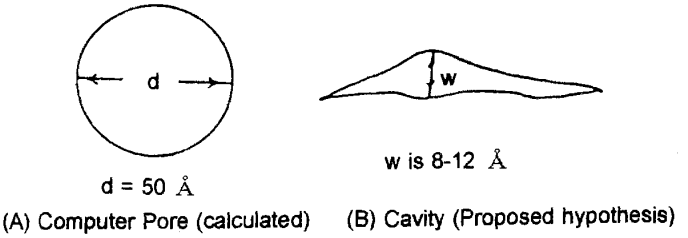


Figure 16. Cross-section of pore and cavity in EMD.

by Kozawa [23]. The method requires only a 100 mL graduated cylinder as explained in Fig. 18. The principle is illustrated in Fig. 19. In the method, water is added to an MnO_2 sample (50g) in an 100 mL cylinder. For each water addition (0.5 mL), the MnO_2 sample and water are mixed as shown in Fig. 18 step (3). Water vapor is adsorbed very quickly on the pore walls or condensed in the cavities. Therefore, shaking the mixture ten times is sufficient. The volume of the sample is measured after tapping 5 or 10 times. As soon as the pores are completely filled with water, the water level in the cylinder begins to rise, as shown in Fig. 19.

CosMX Exhibit 1008, Page 149 of 633

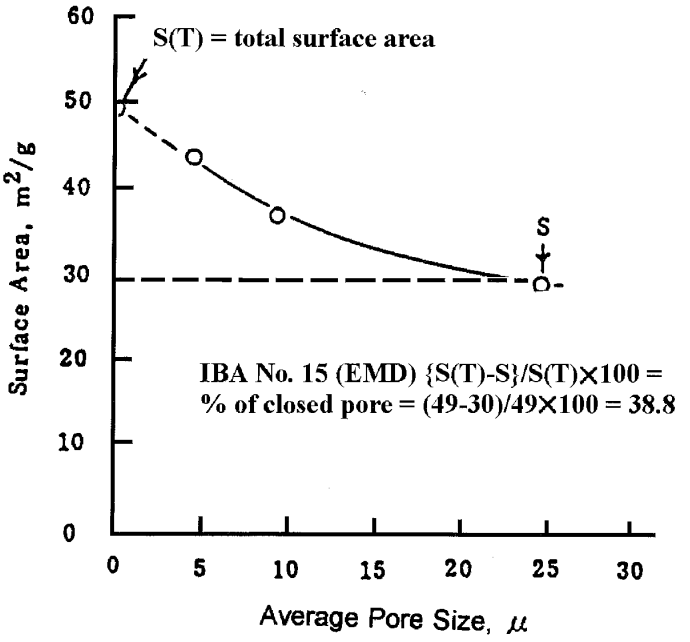


Figure 17. Example of BET surface area vs average particle size (APS).

Table 8. Percentage of closed pores (CP) in MnO_2 samples*

MnO_2 Sample	Description	APS (50%) (μM)	S (m^2g^{-1})	S(T) (m^2g^{-1})	CP (%)
IC No. 1 (EMD)	Regular EMD made by the electrodeposition on a Ti anode from $MnSO_4 + H_2SO_4$ solution (pore diameter is 50Å)	45.0	48.2	58.0	16.9
IC No. 8 (CMD)	Chemical MnO_2 prepared by the thermal decomposition of $MnCO_3$ with additional process to deposit $\gamma - MnO_2$ (pore diameter is 70Å)	45.0	92.8	94.3	1.6
IC No. 9 (EMD)	Coarse EMD sample	77.0	66.0	72.0	8.3
IC No. 13 (NMD)	A typical natural MnO_2 for dry cells	25.0	24.0	30.0	20.0
IBA No. 15 (EMD)	Dense EMD deposited from a suspension bath of $MnSO_4$ solution; the pore size is considerably finer than regular EMD, such as IC No. 1	25.0	30.0	48.0	37.5
IBA No. 17 (EMD)	Regular EMD deposited on Ti anode	25.7	48.0	57.0	15.8
IBA No. 20 (EMD)	EMD deposited on Ti anode with a medium particle size	24.0	42.5	50.0	15.0
IBA No. 22 (CMD)	A CMD made by thermal decomposition of $MnCO_3$ around 320°C in oxygen with steam	77.0	52.0	59.0	13.4
IBA No. 27 (NMD)	Natural ore from Mexico; excellent for carbon–zinc cells	17.5	27.0	30.0	10.0

* Summary of closed pore percentages: EMD, 16.9–37.5%; CMD, 1.6–13.4%; NMD, 10–20%.
+ Abbreviations: APS, average particle size of the original sample at 50wt.%; S, BET surface area of original sample; S(T), total BET surface area obtained by extrapolation.

CosMX Exhibit 1008, Page 150 of 633

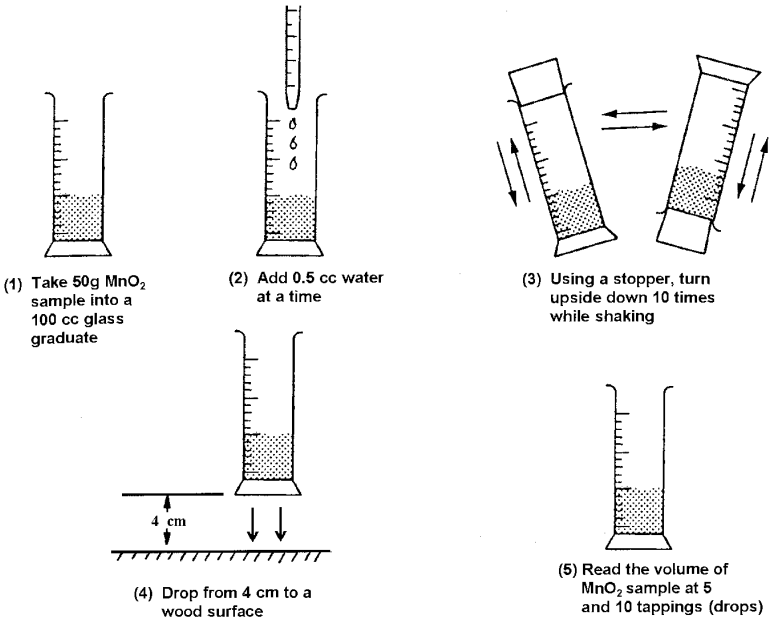


Figure 18. Procedure for EPV (effective pore volume) measurement: (a) a 50 g MnO_2 sample is placed in a 100 mL graduated cylinder;(2) water is added gradually in 0.5 mL portions; (3) with a stopper in place, the cylinder is turned upside down 10 times while being shaken; (4) the cylinder is droppes 4 cm onto a wooden surface; (5) the MnO_2 sample volume is read after 5 and 10 taps (i.e., drops).

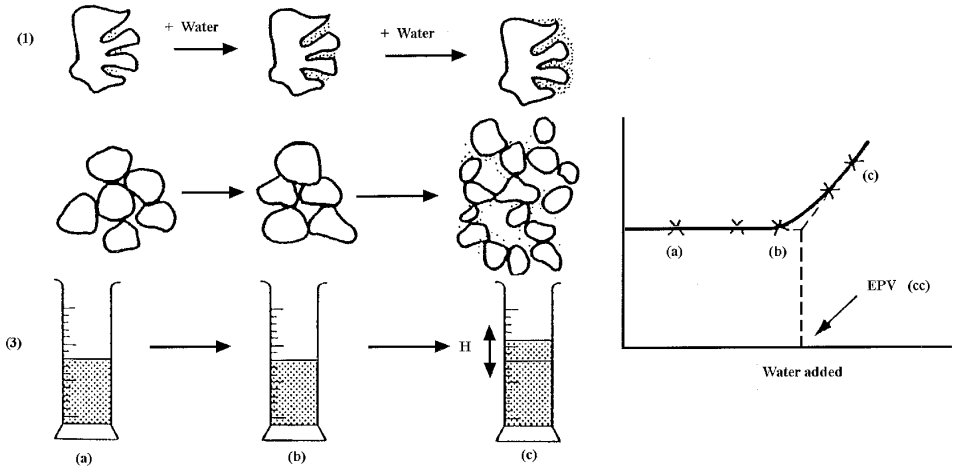


Figure 19. Model fo the sudden volume increase of MnO_2 powder sample at EPV (effective pore volume) point. (a) water fills 50% of the pores; (b) water fills almost 100% of the pores; (c) when excess water (1–2 mL more than the pore volume) is added, the MnO_2 volume suddenly increases by 5–10 mL since the particles stick to each over. The sudden increase (far more than the amount of water added) is shown as *H* in (3), stage (c), above.

CosMX Exhibit 1008, Page 151 of 633

From the variation of the volume of the EMD vs. the amount of added water, the EPV (effective pore volume) is obtained as shown in Fig. 19.

This method is practical and useful for battery engineers. As seen in Fig. 20, when the MnO_2 (EMD) sample (IC No. 9) was heated to 120 and 230 °C, the effective pore volume (EPV) increased from 1.55 mL (for 25 °C) to 3.2 mL (for 120 °C) and to 3.5 mL (for 230 °C), confirming our previous results. Table 9 shows pore volume values measured by this method.

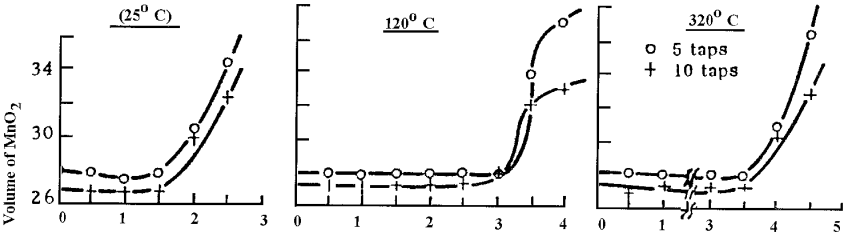


Figure 20. Volume of 50 g MnO_2 (IC No. 9)uppon addition of water (the volume was measured after 5 and 10 taps).

Table 9. EPVs (effective pore volumes) IC and IBA MnO_2 samples

MnO_2 sample	Heat treatment temp. (°C)	Initial volume of 50g (mL)	Pore volume by N_2 desorption (mL/g^{-1})	EPV (mL/g^{-1})	%based on N_2 pore volume	Remarks*
IC No. 1	(25)	24.0	—	0.024	—	
(EMD, Ti)	120	23.5	0.0416	0.044	105.8	0
	230	23.0	0.0539	0.050	92.8	0
IC No. 2	(25)	25.5	—	0.026	—	
(EMD, Pb)	120	24.0	0.0332	0.040	120.5	0
	230	26.0	0.0449	0.044	98.0	0
IC No. 3	(25)	26.0	—	0.032	—	
(EMD, C)	120	27.0	0.0407	0.044	108.1	0
	230	26.5	0.0524	0.064	122.1	0
IC No. 4	(25)	32.0	—		(No clear step)	
(EMD)	120	31.0	0.0367			
	230	30.5	0.0479			
IC No. 5	(25)	38.0	—	0.208	—	
(CMD)	120	38.0	0.408	0.240	170.5	x
	230	40.0	0.1515	0.244	161.1	x
IC No. 7	(25)	27.0	—	0.010	—	
(NMD)	120	27.5	0.0242	0.014	58.3	x
	230	27.0	0.0284	0.014	50.0	x
IC No. 8	(25)	33.0	—	0.164	—	
(CMU)	120	33.5	0.177	0.170	96.1	0
	230	34.0	0.183	0.170	93.0	0
IC No. 9	(25)	27.0	—	0.032	—	
(EMD)	120	27.5	0.0545	0.062	113.7	0
	230	27.5	0.0664	0.072	108.4	0

CosMX Exhibit 1008, Page 152 of 633

Table 9. Continued

IC No. 10	(25)	27.0	—	0.046	—	
(EMD)	120	27.0	0.0490	0.060	122.4	0
	230	27.0	0.0571	0.062	108.8	0
IC No. 11	(25)	20.0	—	0.010	—	
(CMD)	120	20.5	0.0062	0.026	419.4	x
	230	20.5	0.0089	0.016	179.7	x
IBA No. 14	(25)	22.5	—	0.020	—	
(EMD)	120	22.0	0.036	0.030	83.3	0
IBA No. 15	(25)	26.0	—	0.020	—	
(EMD)	120	26.0	0.038	0.046	121.0	0
IBA No. 16	(25)	24.5	—	0.024	—	
(EMD)	120	25.0	0.037	0.034	91.9	0
IBA No. 17	(25)	26.0	—	0.040	—	
(EMD)	120	26.0	0.043	0.034	79.1	0
IBA No. 18	(25)	23.0	—	0.024	—	
(EMD)	120	24.0	0.040	0.040	100.0	0
IBA No. 19	(25)	22.5	—	0.024	—	
(EMD)	120	22.0	0.041	0.038	92.7	0
IBA No. 20	(25)	25.0	—	0.038	—	
(EMD)	120	26.0	0.055	0.054	98.2	0
IBA No. 21	(25)	42.5	—		(No clear step)	
(EMD)	120	42.5	0.099			
IBA No. 22	(25)	26.0	—	0.174	—	
(CMD)	120	26.5	0.181	0.182	100.6	0
IBA No. 23	(25)	23.0	—	0.036	—	
(EMD)	120	23.5	0.042	0.056	133.3	Δ
IBA No. 24	(25)	24.0	—	0.040	—	
(EMD)	120	23.0	0.058	0.052	123.8	0
IBA No. 25	(25)	25.0	—	0.062	—	
(EMD)	120	25.5	0.084	0.078	92.8	0
IBA No. 26	(25)	24.5	—	0.040	—	
(EMD)	120	25.0	0.058	0.062	106.9	0

* Remarks: 0, difference is within 25% (75–125%); Δ, difference is within 50% (50–150%); x, difference is over 50%.

2.4 Conversion of EMD to $LiMnO_2$ or $LiMn_2O_4$ for Rechargeable Li Batteries

An industrial quantity of high-purity EMD is now being produced for alkaline MnO_2 – Zn cells. Therefore, EMD is an excellent source of future cathode materials ($Li_{0.3}MnO_2$ and $LiMn_2O_4$) for rechargeable lithium batteries. Electric vehicles need large batteries using inexpensive electrode materials. $LiMn_2O_4$ or $Li_{0.3}MnO_2$ would be a potential cathode material for EV batteries. Today's rechargeable Li batteries mostly use $LiCoO_2$, since these small batteries are for portable telephones, camcorders, and other portable electronic devices. $Li_{0.3}MnO_2$ will be for 3 V systems and $LiMn_2O_4$ for 4 V systems. Both oxides can be easily produced from EMD.

2.4.1 Melt-Impregnation (M–I) Method for EMD

Since EMD is highly porous, having 50-

CosMX Exhibit 1008, Page 153 of 633

100 Å pores, we can use the M–I method developed by Yoshio [24]. This process consists of a two-step heating. In the first step, a thorough mixture of a Li salt ($LiNO_3$ or LiOH) and EMD powder is heated at a temperature which is slightly above the melting point of the salt in order to allow the molten salt to penetrate into the pores of the EMD. The mixture is then heated at 350 °C or 650–800 °C, depending on the intended material, $LiMnO_4$ or $LiMn_2O_4$ respectively. The melting point of $LiNO_3$ is 260 °C and that of LiOH is 420 °C. When a nonporous MnO_2 is used to produce $LiMn_2O_4$, the MnO_2 must be ground to fine particles with the Li salt before heating. The heated product must be ground 5 to 10 times after each repeated treatment. The entire process is very time consuming.

2.4.2 Preparation of $Li_{0.3}MnO_2$ from EMD [25]

An EMD and $LiNO_3$ mixture (molar ratio 3:1) is heated at 260 °C (the melting point of $LiNO_3$) and then further heated to 350 °C for 5 h.

The MnO_2 for this purpose can be CMD such as IC No.12 or Cellmax, but an EMD which was prepared at a high current density of 1.5–5 $A\,dm^{-2}$ during the electrolysis of a $MnSO_4$–H_2SO_4 bath (95 °C) is very suitable since the high-current-density EMD has much larger pores and high surface area (60 $m^2\,g^{-1}$ or higher). The $Li_{0.3}MnO_2$ produces 150–180 $mAh\,g^{-1}$. An AA-size 3 V Li cell using this oxide has 300 $Wh\,L^{-1}$ and 140 $Wh\,kg^{-1}$, which is larger than the 4 V cells of 225 $Wh\,L^{-1}$ and 95 $Wh\,kg^{-1}$. The discharge curves are shown in Fig. 21.

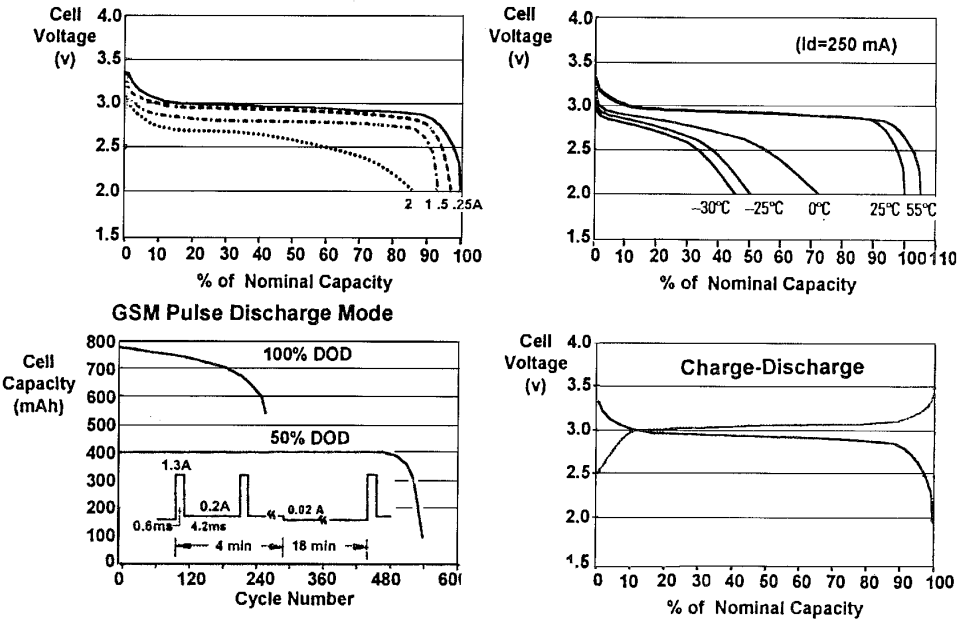


Figure 21. Cell performance of $LiMnO_2$ oxide. The anode is metallic Li [26].

CosMX Exhibit 1008, Page 154 of 633

2.4.3 Preparation of $LiMn_2O_4$ from EMD [25, 27]

A mixture of LiOH and EMD is heated at 420 °C for 2–3 h in order to allow molten LiOH to penetrate into the pores of the EMD. The mixture is then heated from 650 to 800 °C to produce $LiMn_2O_4$. The amount of LiOH and EMD in the mixture must be stoichiometric (LiOH : MnO_2 = 1:2). The product, $LiMn_2O_4$, is usually tested by cyclic voltammetry (Fig. 22): a good $LiMn_2O_4$ does not have peaks at a and b.(peak a (3.3 V) would be due to the oxygen deficiency and peak b (4.5 V) to replacement of the Li ion sites by Mn^{4+} ion). Since EMD has many fine pores and the Li salt and MnO_2 are mixed intimately in the M–I method, an excellent $LiMn_2O_4$ is produced which does not show peaks a and b.

2.5 Discharge Curves of EMD Alkaline Cells (AA and AAA Cells)

Figure 23 shows discharge caves of a new type of alkaline cells, which is able to discharge at a very high rate.

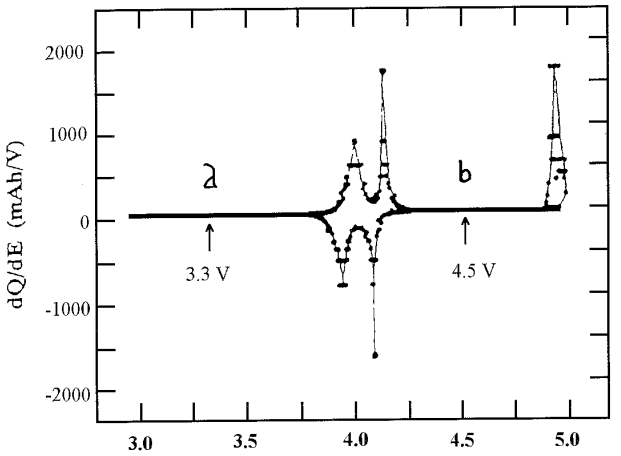


Figure 22. Cyclic voltammogram of $LiMn_2O_4$

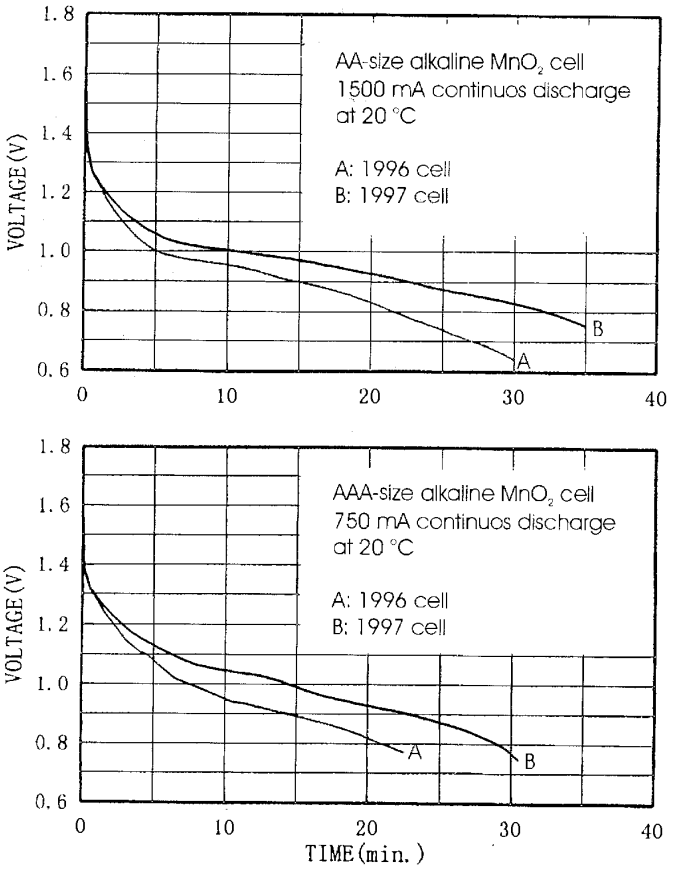


Figure 23. New japanese alkaline cells using expanded graphite and other recent improvement

2.6 References

[1] A. Kozawa, *Power Sources* **1979**, *7*, p. 485.

[2] A. Kozawa, J.F. Yeager, *J. Electrochem. Soc.* **1965**, *112*, 959.

[3] A. Kozawa, R.A. Powers, *J. Electrochem. Soc.* **1966**, *113*, 870.

[4] A. Kozawa, R.A. Powers, *J. Electrochem. Tech. no.1* **1967**, *5*, 535.

[5] A. Kozawa, R.A. Powers, *J. Electrochem. Soc.* **1968**, *115*, 122, 1003.

[6] A. Kozawa, R.A. Powers, *J. Electrochem. Soc. Jpn* **1969**, *37*, 31.

[7] D.A.J. Swinkels, K.E. Anthony, P.M. Fredericks, P.R. Osborn, *J. Electroanal. Chem.* **1984**, *168*, 433.

[8] Y. Chabre, J. Pannetier, *Prog. Solid State Chem.* **1995**, *23*, 1.

[9] S.W. Donne, G.A. Laurance, D.A.J. Swinkels, *Prog. Batteries Batt. Mater.* **1997**, *16*, 79.

[10] A. Kozawa, T. Kalnoki-Kis, J.F. Yeager, *J. Electrochem. Soc.* **1966**, *113*, 405.

[11] K. Tschikawa, K. Matsuki, A. Kozawa, *Paper presented at IBA Singapore Meeting, Sept. 5–12*, **1997**.

[12] A. Kozawa, K. Sasaki, *Denki Kagaku* **1954**, *22*, 569, 571.

[13] A. Kozawa, *Proc. Symp. on MnO_2 Electrode*

CosMX Exhibit 1008, Page 156 of 633

85-4, **1985**, US Electrochemical Society, Pennington, PA, **19xx**.
[14] A. Kozawa, R.A. Power, *J. Chem. Educ.* **1972**, *49*, 587.
[15] A. Kozawa, *Denki Kagaku* **1982**, *50*, 763.
[16] A. Kozawa, G. Kana, K. Horiba, Y.Takeuchi, *Denki Kagaku* **1988**, *7*, 2.
[17] A. Kozawa, M. Yoshio, H. Noguchi, G. Piao, A.Uchiyama, *Prog. Batteries Batt. Mater.* **1992**, *11*, 235.
[18] V. Manev, A. Momchilov, K. Tagawa, A. Kozawa, *Prog. Batteries Batt. Mater.* **1993**, *12*, 157.
[19] K. Tachibana, K. Matsuki, A. Kozawa, *Prog. Batteries Batt. Mater* **1997**, *16*, 322.
[20] (a) A. Kozawa, *Handbook of MnO_2* (Eds.: D. Glover, B. Schumm Jr., A. Kozawa), IBA Inc., **1989**, p. 295, *idem Prog. Batteries Batt. Mater.* **1988**, *7*, 59.
[21] M. Yamashita, M. Ida, H. Takemura, A. Kozawa, *Prog. Batteries Batt. Mater.* **1993**, *12*, 19.
[22] A. Kozawa, *Handbook of MnO_2* (Eds.; D. Glover, B. Schumm Jr., A. Kozawa), IBA Inc., p. 287, **1989**, *idem, Prog. Batteries Batt. Mater.* **1988**, *7*, 320.
[23] A. Kozawa, *Prog. Batteries Batt. Mater.* **1988**, *7*, 327.
[24] M. Yoshio, S. Inoue, M. Hyakutake, G. Piao, H. Nakamura, *J. Power Sources* **1991**, *34*, 147.
[25] M. Yoshio, A. Kozawa, *Prog. Battery Batt. Mater.* **1995**, *14*, 87.
[26] Tadiran, *ITE Battery Newsletter* **1997**, 2,45.
[27] Y.Xia, H. Zhou, M. Yoshio, *J. Electrochem. Soc.* **1997**, *144*, 2593.

CosMX Exhibit 1008, Page 157 of 633

3 Nickel Hydroxides

James McBreen

3.1 Introduction

Nickel hydroxides have been used as the active material in the positive electrodes of several alkaline batteries for over century [1]. These materials continue to attract much attention because of the commercial importance of nickel–cadmium and nickel–metal hydride batteries. In addition to being the cathode active material in nickel–metal hydride batteries, $Ni(OH)_2$ is an important corrosion product of the anode during cycling. There are several reviews of work in the field [2–10].

Progress in understanding the reactions of nickel hydroxide electrodes has been very slow because of the complex nature of the reactions. Exercises which are normally trivial for most battery electrodes, such as the determination of the open- circuit potential, the overall reaction, and the oxidation state of the charged material, have required much effort and ingenuity. The materials have been studied by an enormous array of spectroscopic, structural, and electrochemical techniques. The most significant advance in the understanding of the overall reaction was made by Bode and his co-workers [11]. They established that both the discharged material ($Ni(OH)_2$) and the charged material (NiOOH) could exits in two forms. One form of $Ni(OH)_2$, which was designated as $\beta - Ni(OH)_2$, is anhydrous and has a layered brucite ($Mg(OH)_2$) structure. The other form, $\alpha - Ni(OH)_2$, is hydrated and has intercalated water between brucite-like layers. Oxidation of $\beta - Ni(OH)_2$ on charge produces $\beta - NiOOH$ and oxidation of $\alpha - Ni(OH)_2$ produces $\gamma - NiOOH$. Discharge of $\beta - NiOOH$ yields $\beta - Ni(OH)_2$ and discharge of $\gamma - NiOOH$ yields $\alpha - Ni(OH)_2$. On discharge stand the $\alpha - Ni(OH)_2$ can dehydrate and recrystallize in the concentrated alkaline electrolyte to form $\beta - Ni(OH)_2$. Bode et al. also found that $\beta - NiOOH$ could be converted to $\gamma - NiOOH$ when the electrode is overcharged. Their overall reaction scheme is shown schematically in Fig. 1.

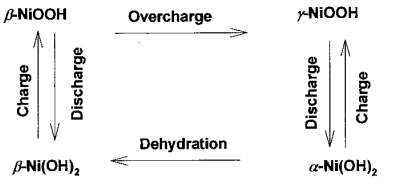


Figure 1. Reaction scheme of Bode [11].

All subsequent work has in general validated these conclusions. The two reaction schemes are often referred to as the β/β and the α/γ cycles.

This section gives a brief overview of the structure of nickel hydroxide battery electrodes and a more detailed review of the solid-state chemistry and electrochemistry of the electrode materials. Emphasis is on work done since 1989.

3.2 Nickel Hydroxide Battery Electrodes

Conventional nickel hydroxide battery electrodes are designed to operate on the β/β cycle, to accommodate the volume changes that occur during cycling, and to have adequate electronic conductivity to yield high utilization of the active material on discharge. The β/β cycle is preferred because there is less swelling of the active material on cycling. The conductivity of $\beta-NiOOH$ is more than five orders of magnitude higher than that for $Ni(OH)_2$ [12]. As a result there is usually no problem in charging the electrode because the $NiOOH$ that forms increases the conductivity of the active material. However, on discharge the charged material can become isolated in a resistive matrix of the discharged product and cannot be discharged at useful rates [13]. Operation on the β/β cycle is ensured by control of the electrolyte composition and the use of a combination of additives such as Co and Zn. Provisions have to be made for electronic conduction to the active material and confinement of the active material on cycling. Over the years several electrode designs have been used. These include incorporation of the active material in pocket plates, perforated metal tubes, sintered nickel plaques, plastic-bonded electrodes with graphite as the conductive diluent, nickel foams, and fibrous nickel mats.

Pocket and tubular electrodes have been described in detail by Falk and Salkind [1]. McBreen has reviewed work on both sintered plate and plastic-bonded electrode technology [9]. More recent work is on the use of nickel foams and nickel mats.

Early work on the use of foams and mats has been reviewed [9]. Nickel fiber, nickel-plated steel fiber or nickel-plated graphite fiber mats are preferred because they have smaller pores (~50 μm) [14]. The most recently developed mats can have porosities as high as 95% [13], and are much lighter than the sintered nickel plaques, which typically have porosities between 80 and 90%. Initially, standard cathodic impregnation methods were used to load the active material into the foam [9]. More recently, the preferred method is to incorporate the $Ni(OH)_2$ in the form of a slurry into the mat [13, 14]. This has been called the "suspension impregnation method" [14]. Considerable improvement in the $Ni(OH)_2$ has been achieved by the addition of divalent Co compounds to the slurry. The best results were achieved with the addition of 10% CoO [13, 15]. The following mechanism has been proposed for this improvement [13]. In the alkaline electrolyte CoO dissolves to form the blue cobaltite ion. The ion precipitates on the $Ni(OH)_2$ particles to form insoluble $\beta-Co(OH)_2$. On charge the $\beta-Co(OH)_2$ is oxidized to a highly conductive $\beta-CoOOH$ which is not reduced on subsequent discharges. The $\beta-CoOOH$ provides interparticle contact and access of electrons to the active material.

Considerable increases in the capacity density of the electrodes have been achieved through the use of high-density $\beta-Ni(OH)_2$ with a uniform particle size, a narrow range of pore sizes, and a high tapping density (1.9–2.0 gcm^{-3}) [15, 16].

CosMX Exhibit 1008, Page 159 of 633

Conventional $\beta-Ni(OH)_2$ consists of irregular particles with 30% inner pore volume, a large range of pore sizes, and a tapping density of ~1.6g cm^{-3}. With the new material it is possible to increase the active material filling by 20%. Using this material it was possible to make electrodes with capacity densities exceeding 550 mAh cm^{-3}. Conventional sintered plates have capacity densities of ~400mAh cm^{-3}.

A major problem with pasted-plastic-bonded and fiber mat electrodes is swelling of the electrode on cycling. This is due to the formation of $\gamma-NiOOH$. This causes comminution of the active material and an increase in the pore volume. This problem can be largely avoided by the use of $\beta-Ni(OH)_2$ containing ~7% of co-precipitated Cd or Zn. The co-precipitation of one of these additives along with 7% Co also greatly improves the charge acceptance of the electrode at elevated temperatures (up to 45°C) [15]. This additive combination also greatly improves the charge retention at elevated temperatures [15]. Zinc is preferred over Cd as an additive because of its lower toxicity, and the detrimental effect of Cd on metal hydride electrodes. These advances in the nickel hydroxide electrode represent considerable progress, and have increased the capacity of sealed nickel–cadmium AA cells, at the C rate, from 500 to 800mAh [15].

3.3 Solid State Chemistry of Nickel Hydroxides

3.3.1 Hydrous Nickel Oxides

$\beta-Ni(OH)_2$, $\alpha-Ni(OH)_2$, $\beta-NiOOH$ and $\gamma-NiOOH$ are considered to be the model divalent and trivalent materials for the nickel hydroxide electrode.

3.3.1.1 $\beta-Ni(OH)_2$

$\beta-Ni(OH)_2$ can be made with a well-defined crystalline structure and is many ways similar to the active material in chemically prepared battery electrodes that are made by the method described by Fleischer [17]. Several methods of preparation have been reported. One is to precipitate the hydroxide at 100°C from a nickel nitrate solution by addition of a KOH solution. Further enhancement in the crystallinity of this material has been obtained by hydrothermal treatment in an aqueous slurry containing NH_4OH,,KOH [18], or NaOH [19]. A method which produces good crystals has been described by Fievet and Figlarz [20]. The hydroxide is prepared in two steps. First an ammonia solution is added to a nickel nitrate solution at room temperature. The precipitate is washed, and then hydrotermally treated at 200°C. Another method is to precipitate the hydroxide by dropwise addition of 3 mol L^{-1} $Ni(NO_3)_2$ to hot (90°C) 7 mol L^{-1} KOH with constant stirring. The precipitate is washed and dried. The $Ni(OH)_2$ is then dissolved in 8 mol L^{-1} NH_4OH and the resulting blue solution of $Ni(NH_3)_6(OH)_2$ is transferred to a desiccator containing concentrated H_2SO_4 and kept there for several days. Slow removal of the NH_3 by H_2SO_4 yields well-formed glassy flakes of $\beta-Ni(OH)_2$ [21]. $\alpha-Ni(OH)_2$ can be prepared electrochemically. This can be converted to $\beta-Ni(OH)_2$ by heating in 6–9 mol L^{-1} KOH at 90°C for 2–3 h [11].

The definitive structural determination of the β-hydroxide is the powder neutron diffraction work of Greaves and Thomas on $\beta-Ni(OD)_2$ [22]. They did neutron

CosMX Exhibit 1008, Page 160 of 633

diffraction studies on well-crystallized deuterated $Ni(OD)_2$ that had been prepared by a hydrothermal method. They also investigated a high-surface-area $Ni(OH)_2$ that was prepared by precipitation on addition of KOH to an $NiSO_4$ solution. The X-ray and neutron diffraction results indicate that $\beta - Ni(OH)_2$ has a brucite C6-type structure that is isomorphous with the divalent hydroxides of Ca, Mg, Fe, Co, and Cd. The structure is shown in Fig.2.

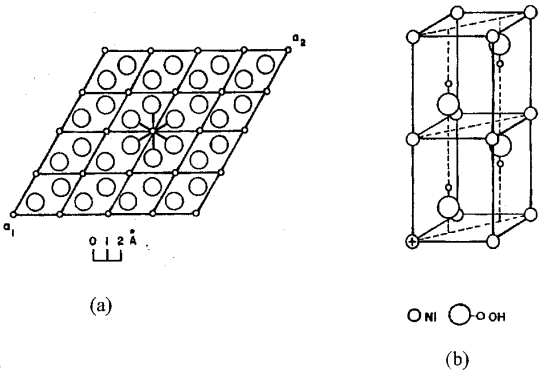


Figure 2. The brucite structure of $Ni(OH)_2$: (a) hexagonal brucite layer, in which the small circles are the Ni atoms and the large circles the O atoms and alternate O atoms are below and above the plane of the Ni atoms; (b) stacking of the planes showing the orientation of the O–H bonds.

The crystal consists of stacked layers of nickel–oxygen octahedra. The nickels are all in the (0 0 0 1) plane and are surrounded by six hydroxyl groups, each of which is alternately above and below the (0 0 0 1) plane. The fractional coordinates are 0, 0, 0 for nickel and 1/3, 2/3, z and 2/3, 1/3, z for oxygen. Values for the crystallographic parameters of well-crystallized $\beta - Ni(OD)_2$ are given in Table 1.

Table.1. Crystallographic Parameters for $\beta - Ni(OD)_2$ [22]

Parameter	(Å)
a_0	3.126
c_0	4.593
Ni–O bond length	2.073
O–H bond length	0.973
Ni–Ni bond length	3.126

Because of anomalous scattering by H the results for the as-precipitated $Ni(OH)_2$ could not be refined. Nevertheless, cell constants and the O–H bond distance could be determined. The results showed that the as-precipitated material was different from the well-crystallized material. The unit cell dimensions were $a_0 = 3.119$ and $c_0 = 4.686$ Å. Also the O–H bond length was 1.08Å, a value similar to that previously reported by Szytula et al. in a neutron diffraction study of $Ni(OH)_2$ [23]. The O–H bond is both well crystallized and as precipitated materials is parallel to the c-axis. The difference between well-crystallized and as precipitated material is important since the well-crystallized material is not electrochemically active. The differences between the materials are attributed to a defective structure that accrues from the large concentration of surface OH^- ion groups in the high-surface-area material [22]. These are associated with absorbed water. This is a consistent with an absorption band in the infrared at $1630\,cm^{-1}$. This is not seen in the well-crystallized material.

CosMX Exhibit 1008, Page 161 of 633

Infrared spectroscopy has also confirmed the octahedral coordination of nickel by hydroxyl groups [24, 25]. No evidence has found for hydrogen bonding. In battery materials, evidence was also found for a small amount of absorbed water [24, 26]. Even though these materials contain small amounts of water they are still classified as $\beta-Ni(OH)_2$ because of an (0 0 1) X-ray reflection corresponding to a d spacing of 4.65Å. Thermogravimetric analysis (TGA) indicates that the water is removed at higher temperatures [26–28]. Kober [24, 26] has proposed that this water is associated with nickel ions in the lattice and suggested the formula $[Ni(H_2O)_{0.326}](OH)_2$ for the chemically prepared battery material. A similar formula was proposed by Dennsted and Loser [27]. However, this has been disputed [29]. The evidence is that well crystallized $\beta-Ni(OH)_2$ does not contain absorbed water [22, 29]. However, the high-surface-area material that is use in batteries does. This is consistence with the expansion in the c-axis of the crystal from 4.593 to 4.686Å, the increase in the average O–H bond distance from 0.973 to 1.08Å [22] and the presence of broad absorption bond in the infrared spectrum at $1630\,cm^{-1}$ [22, 24, 26]. TGA results indicate that this water is removed in a single process over a temperature range of 50–150°C [30].

The Raman spectroscopic work of Jacovitz [31], Cornilsen et al. [32, 33], and Audemer et al. [34] is the most direct spectroscopic evidence that the discharge product in battery electrodes, operating of the β/β cycle, is different from well-crystallized $\beta-Ni(OH)_2$. The O–H stretching modes and the lattice modes in the Raman spectra are different from those found for well-crystallized $Ni(OH)_2$, prepared by recrystallization from the ammonia complex, and are more similar to those found for the initial material prepared by Barnard et al. [21] by precipitation of the $Ni(OH)_2$ by adding $3\,mol\,L^{-1}$ $Ni(NO_3)_2$ to hot $7\,mol\,L^{-1}$ KOH. In discharged electrodes a Raman band at $3605\,cm^{-1}$ is observed. This has been as described to absorbed water molecules on the surface of the $Ni(OH)_2$ [34]. There have been discrepant results in the Raman evidence for adsorbed water. However, some water cannot be ruled out since the O–H modes are very poor Raman scatterers. Infrared spectroscopic is much better at detecting water and Jackovitz has seen water-stretching modes in both the nondeuterated and deuterated material after discharge [31]. Audemer et al. have also seen this band at $1630\,cm^{-1}$. Furthermore, they have confirmed that both the Raman band at $3605\,cm^{-1}$ on the IR band at $1630\,cm^{-1}$ decrease at temperatures above 100°C and completely vanish and 150°C. Neutron diffraction work on $Ni(OH)_2$ and Raman and IR spectroscopy clearly show that discharge product in battery electrodes is closely related, but is not identical, to well-crystallized. $\beta-Ni(OH)_2$ It probably has a defect structure, which facilitates water adsorption and the electrochemical reactions.

3.3.1.2 $\alpha-Ni(OH)_2$

$\alpha-Ni(OH)_2$, which has a highly hydrated structure, was first identified by Lotmar and Fectknecht [35]. $\alpha-Ni(OH)_2$ is a major component of the active material in battery electrodes when nickel battery plaques are cathodically impregnated from an aqueous $Ni(NO_3)_2$ solution at temperatures below 60°C [36]. $\alpha-Ni(OH)_2$ can be prepared chemically by precipitation from dilute solutions at room temperature. One method is simply to add an ammonia solution to a nickel

CosMX Exhibit 1008, Page 162 of 633

nitrate solution [20]. Another method is to add 0.5 or 1 mol L^{-1} KOH to 1 mol L^{-1} $Ni(NO_3)_2$ [21]. In both cases the precipitate is filtered and washed. Methods for electrochemical preparation of $\alpha-Ni(OH)_2$ films on nickel substrates have been described [37, 38]. One method consists of cathodically polarizing a cleaned nickel sheet in a quiescent 0.1 mol L^{-1} $Ni(NO_3)_2$ solution at 8mA cm^{-2}. There is reduction of nitrate and a concomitant increase in pH at the electrode surface. This causes precipitation of an adherent coating of $\alpha-Ni(OH)_2$ on the nickel. A 100 s period of deposition will produce 0.5mg cm^{-2} of $\alpha-Ni(OH)_2$.

Determination of the structure of $\alpha-Ni(OH)_2$ has been difficult, since sometimes it exhibits no diffraction pattern [39]. After washing with water a diffuse pattern develops. Hydrothermal treatment eventually leads to well-crystallized $\beta-Ni(OH)_2$ [39, 40]. The evolution of the X-ray diffraction patterns is shown Fig. 3. Bode proposed a layered structure for $\alpha-Ni(OH)_2$ similar to that for $\beta-Ni(OH)_2$ [11]. His suggested structure was essentially identical to that shown for $\beta-Ni(OH)_2$ in Fig. 2, except that between the (0 0 0 1) planes there are water molecules that result in an expansion of the *c*-axis spacing to about 8Å. Bode proposed a $3Ni(OH)_2 \cdot 2H_2O$ unit cell and assigned definite positions to the intercalated water molecules in which two-thirds of the available nickel sites were occupied with water molecules [39]. The model gives unit cell dimensions of $a_0 = 5.42$ Å and $c_0 = 8.05$ Å. In addition to the increase in *c*-axis spacing, Bode reported a small contraction in the lattice parameters within the layer planes of $\alpha-Ni(OH)_2$. Later work by Figlarz and Le Bihan, using the X-ray diffraction line profiles, showed that $\alpha-Ni(OH)_2$ was turbostratic and that it

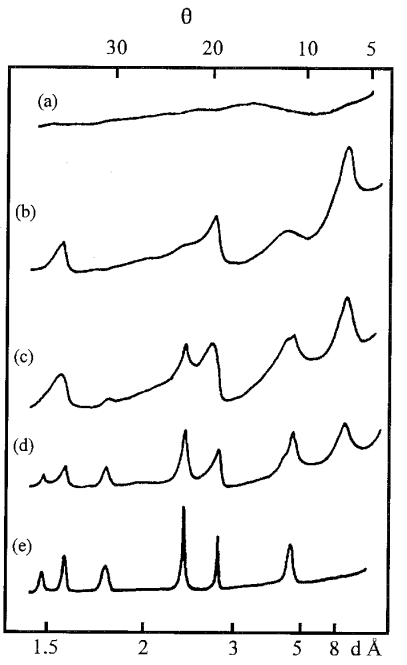


Figure 3. X-ray diffraction patterns (Co K_α) for $\alpha-Ni(OH)_2$: (a) as-precipitated (b)–(d) increasing in crystallinity with time when aged in water. The pattern (e) for $\beta-Ni(OH)_2$ eventually develops (42).

consisted of brucite-like layers randomly oriented along the *c*-axis [41]. Subsequently McEwen [19], too, used line profile analysis to arrive at the same conclusion. He also concluded that the intercalated water layer was not ordered. He disputed the contraction in the basal plane that was proposed by Bode, and ascribed the diffraction peak shifts to disorder and particle size effects. Le Bihan and Figlarz use a combination of X-ray diffraction, electron microscopy, and infrared spectroscopy to study, $\alpha-Ni(OH)_2$ as-prepared and after repeated washing in water [42]. They confirmed that in the α-structure the $Ni(OH)_2$ planes are essentially identical to those shown for $\beta-Ni(OH)_2$ in Fig. 2. The layers are

CosMX Exhibit 1008, Page 163 of 633

stacked with random orientation. The *c*-axis spacing is constant but the layers are randomly oriented. The layers, are separated by water molecules that are hydrogen-bonded to the Ni–OH groups in the basal planes. In electron micrographs turbostratic nickel hydroxide appears as thin crumpled sheets. The crystallites have a mean size of 30Å along [0 0 1 1], which corresponds to a stacking of five layers. The basal plane dimensions are about 80Å [42]. Because of the high degree of division, $\alpha-Ni(OH)_2$ retains adsorbed surface water and a small amount (<3%) of nitrate ions [43]. Thermogravimetric analysis indicates that the adsorbed water is removed between 50 and 90°C, whereas the intercalated water is removed between 90 and 180°C [30].

Pandya et al. have used extended X-ray ascription fine structure (EXAFS) to study both cathodically deposited $\alpha-Ni(OH)_2$ and chemically prepared $\beta-Ni(OH)_2$ [44]. Measurements were done at both 77 and 297 K. The results for $\beta-Ni(OH)_2$ are in agreement with the neutron diffraction data [22]. In the case of $\alpha-Ni(OH)_2$ they found a contraction in the first Ni–Ni bond distance in the basal plane. The value was 3.13Å for $\beta-Ni(OH)_2$ and 3.08Å for $\alpha-Ni(OH)_2$. The fact that a similar significant contraction of 0.05Å was seen at both 77 and 297K when using two reference compounds (NiO and $\beta-Ni(OH)_2$) led them to conclude that the contraction was a real effect and not an artifact due to structural disorder. They speculate that the contraction may be due to hydrogen bonding of OH groups in the brucite planes with intercalated water molecules. These ex-situ results on $\alpha-Ni(OH)_2$ were compared with in-situ results in $1\,mol\,L^{-1}$ KOH. In the ex-situ experiments the $\alpha-Ni(OH)_2$ was prepared electrochemically, washed with water and dried in vacuum. In the in-situ experiment the hydroxide film after preparation, was simply rinsed without drying, and immediately immersed in the cell containing $1\,mol\,L^{-1}$ KOH. The coordination numbers for Ni–O for the in-situ samples were consistently higher. The significance of this is not clear: it might suggest some water association with nickel as was postulated by Kober [24, 27].

Raman spectroscopy results indicate that the structure of $\alpha-Ni(OH)_2$ is very dependent on how it is prepared [32, 33, 45]. Data on chemically prepared [32, 33], cathodically deposited [32, 33, 45] and electrochemically reduced $\gamma-NiOOH$ have been obtained [32, 33, 45]. There are differences in all the spectra, both in the lattice modes and the O–H stretching modes. The shifts in the lattice modes for the reduced $\gamma-NiOOH$ may be due to this material having an oxidation state higher than two. The changes in the O–H stretching modes may be due to changes in water content and hydrogen bonding.

Figlarz and his co-workers have suggested that the formula $Ni(OH)_2 \cdot nH_2O$ is not the correct one for $\alpha-Ni(OH)_2$ [46, 47]. They studied $\alpha-Ni(OH)_2$ materials made by precipitation of the hydroxide by the addition of NH_4OH to solutions of various nickel salts. In addition to $Ni(NO_3)_2$ and $NiCO_3$ they used nickel salts with carboxylic anions of various sizes. They found that the interlaminar distance in the $\alpha-Ni(OH)_2$ depended on the nickel salt anion size. For instance, when the nickel adipate was used the interlaminar distance was 13.2Å. Infrared studies of $\alpha-Ni(OH)_2$ precipitated from $Ni(NO_3)_2$ indicated that NO_3^- was incorporated into the hydroxide and was bonded to Ni. They suggested a model based on hydroxide vacancies and proposed a formula $Ni(OH)_{2-x}A_yB_z \cdot nH_2O$

CosMX Exhibit 1008, Page 164 of 633

where A and B are mono or divalent anions and $x = y + 2z$. Chemical analysis of $\alpha - Ni(OH)_2$ precipitated from $Ni(NO_3)_2$ indicates OH vacancies in the range of 20–30%.

$\alpha - Ni(OH)_2$ is unstable in water and is slowly converted to $\beta - Ni(OH)_2$. Transmission electron micrographs of the reactants and products indicate that the reaction proceeds through the solution [42, 45]. In concentrated KOH the reaction is much more rapid and the product has a smaller particle size. For instance, the $\alpha - Ni(OH)_2$ in an electrochemically impregnated battery electrode is completely converted to $\beta - Ni(OH)_2$ 30 min after immersion in 4.5 mol L^{-1} KOH [36].

Infrared studies of the reaction product in water indicate that the $\beta - Ni(OH)_2$ that is initially formed also contains anions and adsorbed water. As the particle size of the product increases, the amount of anions and adsorbed water decreases [45].

Delmas and co-workers have proposed the existence of an intermediate phase between $\alpha -$ and $\beta - Ni(OH)_2$ [48]. This phase consist of interleaved α and β material and can be formed on ageing of $\alpha - Ni(OH)_2$. Recent Raman results confirm the existence of such a phase [49].

3.3.1.3 β – NiOOH

$\beta - Ni(OH)_2$ has been identified as the primary oxidation product of electrodes containing $\beta - Ni(OH)_2$ [11, 50, 51]. Glemser describes a method for preparation of $\beta - NiOOH$ [52, 53]. A solution of 100g of $Ni(NO_3)_2 \cdot 6H_2O$ in 1.5 l H_2O was added dropwise to a solution of 55g KOH and 12ml Br_2 in 300ml H_2O, while keeping the temperature at 25°C. The black precipitate was washed with CO_2 free water until both K^+ and NO_3^- were removed and then dried over H_2SO_4. Structural determinations of the higher oxides of nickel are complicated because of their amorphous nature [53]. However, it appears that $\beta - Ni(OH)_2$ is oxidized to the trivalent state without major modifications to the brucite structure. The unit cell dimensions change from $a_0 = 3.126$ Å and $c_0 = 4.605$ Å for $\beta - Ni(OH)_2$ to $a_0 = 2.82$ Å and $c_0 = 4.85$ Å for $\beta - NiOOH$. X-ray diffraction clearly indicates expansion along the *c*-axis. Asymmetry in the *h k* lines indicates the turbostratic nature of $\beta - NiOOH$. Even after correcting the a_0 values for this, McEwen found that there was a real contraction in the basal plane [19]. Transmission EXAFS has been used to investigate the oxidation products of $\beta - Ni(OH)_2$ [54, 55]. In-situ measurements plastic-bonded electrodes showed that in the charged state a two-shell fit was necessary for the first Ni–O coordination shell. This suggests that the oxygen coordination in $\beta - NiOOH$ is a distorted octahedral coordination with four oxygens at a distance of 1.88Å and two oxygens at a distance of 2.07Å. The distorted coordination is consistent with the edge features of the X-ray absorption spectra [55, 56]. The overall reaction for the electrochemical formation of $\beta - NiOOH$ is usually given as

$$\beta - Ni(OH)_2 + \beta - NiOOH + H^+ + e^- \quad (1)$$

During the reaction, protons are extracted from the brucite lattice. Infrared spectra [24, 25, 31] show that during charge the sharp hydroxyl band at 3644 cm^{-1} disappears. This absorption is replaced by a diffuse band at 3450 cm^{-1}. The spectra indicate a hydrogen-bonded structure for $\beta - NiOOH$ with no free hydroxyl groups. $\beta - NiOOH$ probably has some adsorbed and absorbed water. However, TGA data

CosMX Exhibit 1008, Page 165 of 633

on charged materials are very limited [57, 58] and it is not always clear that the material is pure $\beta-NiOOH$. Unless electrochemical experiments are done very carefully there is always the possibility of the presence of $\gamma-NiOOH$ [13].

3.3.1.4 $\gamma-NiOOH$

$\gamma-NiOOH$ is the oxidation product of $\alpha-Ni(OH)_2$. It is also produced on overcharge of $\beta-Ni(OH)_2$, particularly when the charge is carried out at high rates in high concentrations of alkali [11, 59]. Use of the lighter alkalis (LiOH and NaOH) favor the formation of $\gamma-NiOOH$ whereas use of RbOH inhibits its formation [60]. The material was first prepared by Glemser and Einerhand [52] by fusing one part Na_2O_2 with three parts NaOH in a nickel crucible at 600°C. Hydrolysis of the product yields $\gamma-NiOOH$. They gave cell dimensions for a rhombohedral system with $a = 2.8$ Å and $c = 20.65$ Å. The material has a layer structure with a spacing of 7.2Å between layers. $\gamma-NiOOH$ always contains small quantities of alkali metal ions and water between the layers, whereas $\beta-NiOOH$ does not. The X-ray diffraction patterns have more, and much sharper, lines than those of either $\alpha-Ni(OH)_2$ or $\beta-NiOOH$ [19, 53]. $\gamma-NiOOH$ prepared by the method of Glemser and Einerhand has the formula $NiOOH \cdot 0.51H_2O$. TGA analysis shows that this water is lost between 50 and 180 °C [58].

3.3.1.5 Relevance of Model Compounds to Electrode Materials

The reaction scheme of Bode [11] was derived by comparison of the X-ray diffraction patterns of the active materials with those for the model compounds. How the $\beta-Ni(OH)_2$ in battery electrodes differs from the model compound is discussed in sec.3.3.1.3. In recent years the arsenal of in-situ techniques for electrode characterization has greatly increased. Most of the results confirm Bode's reaction scheme and essentially all the features of the proposed α/γ cycle. For instance, recent atomic force microscopy (AFM) of $\alpha-Ni(OH)_2$ shows results consistent with a contraction of the interlayer distance from 8.05 Å to 7.2 Å on charge [61–63]. These are the respective interlayer dimensions for the model $\alpha-Ni(OH)_2$ and $\gamma-NiOOH$ compounds. Electrochemical quartz crystal microbalance (ECQM) measurements also confirm the ingress of alkali metal cations into the lattice up on the conversion of $\alpha-Ni(OH)_2$ to $\gamma-NiOOH$ [45, 64, 65]. However, in-situ Raman and surface enhanced Raman spectroscopy (SERS) results on electrochemically prepared $\alpha-Ni(OH)_2$ in 1 mol/L^{-1} NaOH show changes in the O–H stretching modes that are consistent with a weakening of the O–H bond when compared with results for the model α and $\beta-Ni(OH)_2$ compounds [66]. This has been ascribed to the delocalization of protons by intercalated water and Na^+ ions. Similar effects have been seen in passive films on nickel in borate buffer electrolytes [67].

Recent ECQM work and X-ray diffraction have confirmed the conversion of the α/γ cycle to the β/β cycle up on electrochemical cycling in concentrated alkali. Earlier ECQM studies of $\alpha-Ni(OH)_2$ films had shown a mass inversion in the microgravimetric curve after prolonged cycling [64]: there is a mass decrease in charge instead of a mass increase. More recent work has confirmed that this mass

CosMX Exhibit 1008, Page 166 of 633

inversion is due to conversion of the α/γ cycle to the β/β cycle [65].

3.3.2 Pyroaurite-Type Nickel Hydroxides

Allmann found that when suitable trivalent ions were introduced during the precipitation of the hydroxides of Mg, Zn, Mn, Fe, Co, and Ni, these were incorporated in the lattice and the structure changed from the brucite ($Mg(OH)_2$) to the pyroaurite ($[Mg_6Fe_2(OH)_{16}]\cdot[CO_3\cdot\sim 4H_2O]$) type of structure [68]. One of the nickel materials he prepared was an Ni/Al hydroxide. Axmann et al. [69–71] have given the nickel compounds the general formula

$$\underset{K^{x+}}{[Ni^{II}_{1-x}M^{III}_x(OH)_2]^{x+}}\underset{A^{x-}}{[(X^{n-})_{x/n}(H_2O)_z]^{x-}}$$

where $0.2 \le x \le 0.4$ and X^{n-} are the anions of the precursor salts. The resultant structure consists of brucite cationic layers intercalated with anions and water molecules. The cationic nature of the brucite layers is due to the higher valence of the substituent cations, and the anions in the intercalated anion layers provide electroneutrality. As a result the interlayer distance increases from 4.68 to 7.80Å when compared with $\beta-Ni(OH)_2$. The structure is shown schematically in Fig. 4. Electrochemical and chemical oxidation transforms the pyroaurite structure to a product that is isostructural with $\gamma-NiOOH$ [72]. In the early work the pyroaurite compounds were prepared by precipitation. Buss et al. report on the preparation of $Ni_4Al(OH)_{10}NO_3$ prepared in a computer-controlled apparatus wherein a solution of 0.4 mol L^{-1} $Ni(NO_3)_2 6H_2O$+1 mol L^{-1} $Al(NO_3)_3 9H_2O$ in doubly distilled water with the pH adjusted to 2 with 1 mol L^{-1} HNO_3 was simultaneously sprayed with a carbonate-free 1 mol L^{-1} KOH solution into a receptor solution maintained at pH 11.5 and a temperature of 32°C [70, 71]. The precipitate was filtered, washed and dried at 50°C for three days at 0.01 bar and carbon dioxide was excluded at all stages of the preparation.

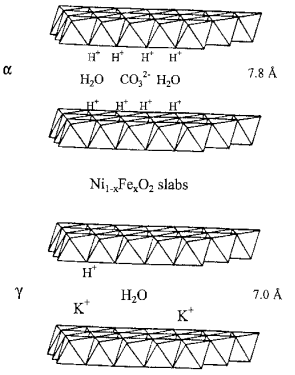


Figure 4. Structure of the Fe(III) substituted pyroaurite phase in the discharged (α) and charged (γ) state. The edge-shared NiO_6 and FeO_6 octahedra are shown. Also shown is the incorporation of anions and water in the galleries of the discharged material. On charging the anions are replaced by cations [77].

Delmas and his co-workers have done extensive work on pyroaurite-type materials which has recently been reviewed [73]. In addition to precipitation methods, they have prepared the materials by mild oxidative hydrolysis of nickelates that were prepared by thermal methods similar to those used for the preparation of $LiNiO_2$ [74]. A cobalt-substituted material $NaCo_x(Ni_{1-x}O_2)$ was prepared by the reaction of Na_2O, Co_3O_4 and NiO at 800 °C under a stream of oxygen. The material was then treated with a 10 mol L^{-1} NaClO +4 mol L^{-1} KOH solution for 15h to form the oxidized γ-oxyhydroxide. The pyroau-

CosMX Exhibit 1008, Page 167 of 633

rite phase was prepared by subsequent reduction in a solution of 0.1 mol L^{-1} H_2O_2 in 4 mol L^{-1} KOH [75]. These mild chemical treatments are referred to as "chemie douce" reaction [69]. The thermally prepared nickelates have a layered R3*m* structure. The "chemie douce" treatments essentially leave the covalently bonded $Co_xNi_{1-x}O_2$ layers intact, as a result of which more-crystalline materials with larger particle sizes can be made by this method.

Most of the work on pyroaurite materials has been done on materials with Fe [68–72, 76, 77], Co [68, 75, 78], Mn [72, 79], or Al [68, 70, 72] substitutions. When at least 20% on the Ni atoms are replaced by the trivalent substituent, the materials are stable in concentrated KOH. In many ways the pyroaurite phase is similar to $\alpha - Ni(OH)_2$. Thus substitution of 20% of the Ni with these trivalent ions stabilize the operation of the electrode in the α/γ cycle in concentrated KOH.

Because of the possibility of applying Mössbauer spectroscopy the solid-state chemistry of the Fe- substituted material is best understood [69, 72, 77]. Mössbauer spectroscopy confirms that the Fe in the pyroaurite type material is Fe(III). Glemser and co-workers have found that electrochemical oxidation of the material converts about 30% of the Fe(III) to Fe(IV) [69, 72]. The results were consistent with a high-spin configuration with the Fe(IV) in FeO_6 octahedra with O_h symmetry. The O_h symmetry can only occur if the surrounding NiO_6 octahedra also have an O_h symmetry. Hence the Fe(IV) ions in the layer must be surrounded by six NiO_6 octahedra with the Ni in the Ni(IV) state. Delmas and coworkers found evidence for Fe(IV) in both high- and low-spin states for oxidized materials prepared by the "chemie douce" method [77]. The difference in the results may be due to the effect of the platelet size on the pyroaurite structure.

In the pyroaurite structure the brucite layers are cationic. However, on oxidation the resultant brucite layers in $\gamma - NiOOH$ are anionic. To preserve electroneutrality, cations and anions are exchanged in the intercalated layer during the oxidation–reduction process. This is illustrated in Fig. 4. In the case of Mn-substituted materials, some Mn can be reduced to Mn(II). This neutralizes the charge in the brucite layer; this part of the structure reverts to the $\beta - Ni(OH)_2$ structure and the intercalated water and anions are expelled from the lattice. With this there is a concomitant irreversible contraction of the interlayer spacing from 7.80 to 4.65Å [72].

3.4 Electrochemical Reactions

3.4.1 Overall Reaction and Thermodynamics of the $Ni(OH)_2/NiOOH$ Couple

In normal battery operation several electrochemical reactions occur on the nickel hydroxide electrode. These are the redox reactions of the active material, oxygen evolution, and in the case of nickel–hydrogen and nickel–metal hydride batteries, hydrogen oxidation. In addition there are parasitic reactions such as the corrosion of nickel current collector materials and the oxidation of organic materials from separators. The initial reaction in the corrosion process is the conversion of Ni to $Ni(OH)_2$.

Because of the complexity of the redox reactions, they cannot be conveniently pre-

CosMX Exhibit 1008, Page 168 of 633

sented in a Pourbaix pH–potential diagram. For battery applications the revised diagram given by Silverman [80] is more correct than that found in the Pourbaix *Atlas* [81]. The diagram is shown in Fig. 5.

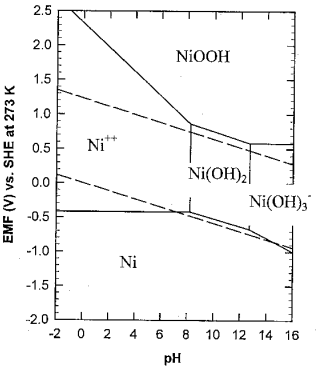


Figure 5. The modified Pourbaix diagram for Ni [80].

The respective literature values for the free energy of formation of $Ni(OH)_2$, NiOOH, H_2O, and HgO are -78.71, -109.58, -56.69, and -13.98 kcal mol^{-1} [80]. The calculated $Ni(OH)_2$/NiOOH reversible potential is 0.41V vs. Hg/HgO. The reversible oxygen potential is 0.30V vs. Hg/HgO. Unlike other battery positive electrode materials, such as AgO or PbO, the nickel hydroxide electrode is a good catalyst for oxygen evolution. Towards the end of charge, oxygen evolution occurs in all nickel batteries, and during charge stand self-discharge occurs via a couple involving the reduction of NiOOH and the oxidation of water to oxygen.

The self-discharge process has made experimental determination of the reversible potential of the $Ni(OH)_2$/NiOOH couple very difficult. A major advance was the realization by Bourgault and Conway that the open-circuit potential of a charged nickel oxide electrode was a mixed potential, not a true equilibrium potential [82], and was the result of two processes: the discharge of NiOOH, and oxygen evolution. They devised an extrapolation technique for the determination of the open-circuit potential of $Ni(OH)_2$ as a function of charge state. Later the work was expanded by Barnard and his co-workers to include oxidation of both α/γ and the β/β couples [83]. The open-circuit potentials depended on pretreatment, such as formation cycles and ageing in concentrated KOH electrolytes. The β/β couples had open-circuit potentials in the range of 0.44–0.47V vs. Hg/HgO whereas the α/γ couples had values in the range of 0.39–0.44V. In cyclic voltammetry experiments the respective anodic and cathodic peaks for the α/γ couple occur at 0.43 and 0.34V. For the β/β couple the peaks are at 0.50 and 0.37V. The reversible potentials of the β/β couple are essentially invariant with KOH concentration whereas those of the α/γ couple vary with OH^- concentration and ageing of $\alpha-NiOH)_2$ reduces the OH^- dependence of the reversible potential [84]. This is due to the conversion to the β/β couple. The reactions for both the β/β and the α/γ couples are highly reversible. Barnard and Randell, in a simple experiment, showed that $\beta-NiOOH$ could oxidize $\alpha-Ni(OH)_2$ to $\gamma-NiOOH$ [85]. This reaction is possible during cyclic voltammetry on $\alpha-Ni(OH)_2$ thin film electrodes in KOH electrolyte, and some of the α material gets transformed to the β form. This could account for the negative drift that is seen in the anodic peaks in the early stages of cycling [66]. Reactions of this type can introduce distortions and features in cyclic volammograms that are difficult to interpret.

CosMX Exhibit 1008, Page 169 of 633

3.4.2 Nature of the $Ni(OH)_2$/NiOOH Reaction

The $Ni(OH)_2$/NiOOH reaction is a topochemical type of reaction that does not involve soluble intermediates. Many aspects of the reaction are controlled by the electrochemical conductivity of the reactants and products. Photoelectrochemical measurements [86, 87] indicate that the discharged material is a p-type semiconductor with a bandgap of about 3.7eV. The charged material is an n-type semiconductor with a bandgap of about 1.75eV. The bandgaps are estimates from absorption spectra [87].

The simple experiments of Kuchinskii and Ershler have provided great insights into the nature of the $Ni(OH)_2$/NiOOH reaction [88, 89]. They investigated oxidation and reduction of a single grain of $Ni(OH)_2$ with a platinum point contact. On charge, the $Ni(OH)_2$ turned black and oxygen was evolved preferentially on the black material and not on the platinum. This implies that NiOOH is conductive and has a lower oxygen overvoltage than platinum oxide. They found that discharge started at the point contact and that formation of resistive $Ni(OH)_2$ at this interface could stop current flow and result in an incomplete discharge. These results provide a good macroscopic picture of how the electrode works.

This type of mechanism has been considered by Barnard et al. [83]. They postulate the initiation of the charging reaction at the $Ni(OH)_2$/current collector interface with the formation of a solid solution of Ni_3^+ ions in $Ni(OH)_2$. With further charging when a fixed nickel ion composition $(Ni^{2+})_x \cdot (Ni^{3+})_{1-x}$ is reached, phase separation occurs with the formation of two phases, one with the composition $(Ni^{2+})_{1-x} \cdot (Ni^{3+})_x$ in contact with the current collector, the other with the composition $(Ni^{2+})_x \cdot (Ni^{3+})_{1-x}$ further out into the active mass. This scheme is consistent with the observations of Briggs and Fleischman on thick $\alpha - Ni(OH)_2$ films [90]. In microscopic observations of cross-sections of partially charged electrodes, they observed a green layer of uncharged $Ni(OH)_2$ in front of the electrode. The central part of the electrode was coated with a black material, and a thin layer in contact with the current collector had a yellowish metallic luster. On discharge the reverse process occurred. It is possible for some of the NiOOH to be isolated in the poorly conducting matrix of $Ni(OH)_2$ and not to be discharged. This has been confirmed in recent in Raman spectroscopy studies in-situ [66].

Sometimes two discharge voltage plateaus are seen on nickel oxide electrodes. Early observations are documented in previous reviews [2, 9]. Normally, nickel oxide electrodes have a voltage plateau on discharge in the potential range of 0.25–0.35V vs. Hg/HgO. The second plateau, which in some cases can account for up to 50% of the capacity, occurs at -0.1 to -0.6 V. At present there is a general consensus that this second plateau is not due to the presence of a new, less-active, compound [91–94]. Five interfaces have been identified for a discharging NiOOH electrode [93]. These are

(a) the Schottky junction between the current collector and the n-type NiOOH, polarized in the forward direction,
(b) the p–n junction between $Ni(OH)_2$ and NiOOH, polarized in the forward direction,
(c) the NiOOH/electrolyte interface,
(d) the $Ni(OH)_2$/electrolyte interface, and

CosMX Exhibit 1008, Page 170 of 633

(e) the Schottky junction between the current collector and $Ni(OH)_2$, polarized in the forward direction.

At the beginning of discharge only junctions (a) and (c) are present. As discharge progresses, junction (e) develops. The passage of current shifts the electrode potential to more-negative values. The hole conductivity of the $Ni(OH)_2$ increases and a second discharge plateau appears. A quantitative modeling effort by Zimmerman [94] supports this hypothesis.

3.4.3 Nickel Oxidation State

Like all other facets of the electrode, determination of the overall redox process has been difficult and many aspects are still disputed. The presence of Ni(IV) species in charged materials has been proposed by many authors. The early work has been reviewed [9]. The evidence for Ni(IV) is based mostly on coulometric data [95] or determinations of active oxygen by titration with iodide or arsenious oxide. Active oxygen contents corresponding to a nickel valence of 3.67 have been reported for $\alpha - Ni(OH)_2$ films charged in 1 mol L^{-1} KOH [95] and values of 3.48 were found for overcharged $\beta - Ni(OH)_2$ battery electrodes in 11 mol L^{-1} KOH [96]. When these electrodes of high active oxygen content are discharged, or even overdischarged, an appreciable amount of active oxygen remains (57). Cycling between a nickel valence of 2.5 and 3.5 has been proposed [97]. X-ray absorption has been used to study the problem [98, 99]. In one case, results consistent with an Ni oxidation state of 3.5 were found for a charged electrode [99]. In the case of the α/γ couple, indications are that a nickel oxidation state of at least 3.5 can be reached on charge. It is not clear that this is the case with the β/β couple. In-situ experiments with simultaneous X-ray diffraction and X-ray absorption measurements should be done on the β/β couple to check for the presence of $\gamma - NiOOH$. Experiments on materials stabilized with both Co and Zn additives are also necessary.

The existence of these high nickel oxidation states offers the possibility of a "two-electron" electrode. This is one of the incentives for stabilizing the α/γ cycle through the use of the pyroaurite structures [73]. With this approach it has been possible to achieve a 1.2 electron exchange for the overall reaction. However, none of the pyroaurite structures is satisfactory for battery electrodes. The Co- and Mn- substituted materials are unstable with cycling [72, 73]. The end-of-charge voltages for both the Fe- and Al- substituted materials are high and the charging efficiencies are low [72, 73]. However, the use of mixed substitution, such as combinations of Co and Al, can lower the charging voltage [73].

3.4.4 Oxygen Evolution

Oxygen evolution occurs on nickel oxide electrodes throughout charge, on overcharge, and on standby. It is the anodic process in the self-discharge reaction of the positive electrode in nickel–cadmium cells. Early work in the field has been reviewed [9]. No significant new work has been reported in recent years.

3.4.5 Hydrogen Oxidation

The reaction of hydrogen at the nickel electrode determines the rate of self-discharge in nickel–hydrogen batteries.

CosMX Exhibit 1008, Page 171 of 633

Under the typical operating pressures (30–50 atm) a nickel-hydrogen battery will loose 50% of its capacity in a week. The self-discharge rate is about five times that encountered in sealed nickel–cadmium batteries, where the rate-determining step is oxygen evolution [100]. Tsenter and Sluzhevskii [101] developed a set of kinetic equations to describe the self-discharge process; in their model its rate depends on the hydrogen pressure and the amount of undischarged NiOOH in the cell. Experimental results of Srinivasan and co-workers confirm many aspects of this model [102]. They used a combination of microcalorimetry, open-circuit voltage measurements, and capacity measurements to study the problem. By doing measurements on the active material and substrate, separately and combined, they were able to establish that hydrogen oxidation occurs predominantly on the charged active material with simultaneous reduction of the oxide.

3.5 References

[1] S.U. Falk, A.J. Salkind, *Alkaline Storage Batteries*, Wiley, New York, **1969**.

[2] P.C. Milner, U.B. Thomas, in *Advances in Electrochemistry and Electrochemical Engineering* (Ed.: C.W. Tobias), Wiley, New York, **1967**, p. 1.

[3] G.W.D. Briggs, in *Electrochemistry,* Vol. 4, Specialist Periodical Reports, The Chemical Society, London, **1974**, p. 33.

[4] A.J. Arvia, D. Posadas, in *Encyclopedia of Electrochemistry of the Elements,* Vol. III (Ed.: A.J. Bard), Marcel Dekker, New York, **1975**, p. 212.

[5] J.L. Weininger, in *Proc. Symp. on the Nickel Electrode* (Eds.: R.G. Gunther, S. Gross), The Electrochemical Society, Pennington, NJ, **1982**, p. 1

[6] P. Oliva, J. Leonardi, J.F. Laurent, C. Delmas, J.J. Bracconier, M. Figlarz, F. Fievet, A. de Guibert, *J. Power Sources* **1982**, *8*, 229.

[7] G. Halpert, *J. Power Sources* **1984**, *12*, 177.

[8] G. Halpert, *Proc. Symp. on Nickel Hydroxide Electrodes* (Eds.: D. A. Corrigan, A. H. Zimmerman), The Electrochemical Society, Pennington, NJ, **1990**, pp. 3–17.

[9] J. McBreen, in *Modern Aspects of Electrochemistry*, Vol. 21 (Eds.: R.E. White, J. O'M. Bockris, B.E. Conway), Plenum Press, New York, **1990**, pp. 29–64.

[10] A. H. Zimmerman, in *Proc. Symp. on Hydrogen and Metal Hydride Batteries* (Eds.: P. D. Bennett, T. Sakai), The Electrochemical Society, Pennington, NJ, **1994**, pp. 268–283.

[11] H. Bode, K. Dehmelt, J. Witte, *Electrochim. Acta* **1966**, *11*, 1079.

[12] A. H. Zimmerman, A. H. Phan, *Proc. Symp. on Hydrogen and Metal Hydride Batteries* (Eds.: P. D. Bennett, T. Sakai), The Electrochemical Society, Pennington, NJ, **1994**, pp. 341–352.

[13] M. Oshitani, H. Yufu, K. Takashima, S. Tsuji, Y. Matsumaru, *J. Electrochem. Soc.* **1989**, *136*, 1590.

[14] W. A. Ferrando. *J. Electrochem. Soc.* **1985**, *132*, 2417.

[15] H. Watada, M. Ohnishi, Y. Harada, M. Oshitani, in *Proc. 25th IECEC Meeting*, IEEE, Piscataway, NJ, **1990**, pp. 299–304.

[16] M. Oshitani, H. Yufu, US. Patent 4 844 999, **1989**.

[17] A. Fleischer, *Trans. Electrochem. Soc.* **1948**, *94*, 289.

[18] M. Aia, *J. Electrochem. Soc.* **1966**, *113*, 1045.

[19] R.S. McEwen, *J. Phys. Chem.* **1971**, *75*, 1782.

[20] F. Fievet, M. Figlarz, *J. Catal.* **1975**, *39*, 350.

[21] R. Barnard, C.F. Randell, F.L. Tye, in *Power Sources 8* (Ed.: J. Thompson), Academic Press, London, **1981**, p. 401.

[22] C. Greaves, M.A. Thomas, *Acta Crystallogr.* Sect. B **1986**, *42*, 51.

[23] A. Szytula, A. Murasik, M. Balanda, *Phys. Stat. Sol.* **1971**, *43*, 125.

[24] F.P. Kober, *J. Electrochem. Soc.* **1965**, *112*, 1064.

[25] F.P. Kober, *J. Electrochem. Soc.* **1967**, *114*, 215.

[26] F.P. Kober, in *Power Sources 1966* (Ed.: D.H. Collins), Pergamon, Oxford **1967**, p. 257.

[27] W. Dennstedt, W. Loser, *Electrochim. Acta* **1971**, *16*, 429.

[28] B. Mani, J.P. deNeufville, *Mater. Res. Bull.*

CosMX Exhibit 1008, Page 172 of 633

1984, *19*, 377.
[29] S. Le Bihan, M. Figlarz, *Electrochim, Acta* **1973**, *18*, 123.
[30] B. Mani, J.P. deNeufville, *J. Electrochem. Soc.* **1988**, *135*, 801.
[31] J.F. Jackovitz, in *Proc. Symp. on the Nickel Electrode* (Eds.: R.G. Gunther, S. Gross), The Electrochemical Society, Pennington, NJ, **1982**, p. 48.
[32] B.C. Cornilsen, P.J. Karjala, P.L. Loyselle, *J. Power Sources* **1988**, *22*, 351.
[33] B.C. Cornilsen, X.-Y. Shan, P.L. Loyselle, *J. Power Sources* **1990**, *29*, 453.
[34] H. Audemer, A. Delahaye, R. Farhi, N. Sac-Epée, J-M. Tarascon, *J. Electrochem. Soc.*, **1997**, *144*, 2614.
[35] Lotmar, W. Fectknecht, *Kristallogr. Mineral. Petrogas Abt. Z* **1936**, *A93*, 368.
[36] F. Portemer, A. Delahaye-Vidal, M. Figlarz, *J. Electrochem. Soc.* **1992**, *139*, 671.
[37] D. M. MacArthur, *J. Electrochem. Soc.* **1970**, *117*, 422.
[38] D.A. Corrigan, *J. Electrochem. Soc.* **1987**, *134*, 377.
[39] H. Bode, *Angew. Chem.* **1961**, *73*, 553.
[40] S. Le Bihan, J. Guenot, M. Fialarz, *C.R. Acad. Sci. Ser. C* **1970**, *270*, 2131.
[41] M. Figlarz, S. Le Bihan, *C.R. Acad. Sci. Ser. C* **1971**, *272*, 580.
[42] S. Le Bihan, M. Figlarz, *J. Cryst. Growth* **1972**, *13/14*, 458.
[43] A Delahaye-Vidal, M. Figlarz, *J. Appl. Electrochem.* **1987**, *17*, 589.
[44] K.I. Pandya, W.E. O'Grady, D.A. Corrigan, J. McBreen, R.W. Hoffman, *J. Phys. Chem.* **1990**, *94*, 21.
[45] S. I. Cordoba-Torresi, C. Gabrielli, A. Hugot-Le Goff, R. Torresi, *J. Electrochem. Soc.* **1991**, *138*, 1548.
[46] P. Genin, A Delahaye-Vidal, F. Portemer, K. Tekkia-Elhsissen, M. Figlarz, *Eur. J. Solid State Inorg. Chem.* **1991**, *28*, 505.
[47] A Delahaye-Vidal, B. Beaudoin, N. Sac-Epée, K. Tekkia-Elhsissen, A. Audemer, M. Figlarz, *Solid State Ionics* **1996**, *84*, 239.
[48] C. Faure, C. Delmas, M. Fouassier, *J. Power Sources* **1991**, *35*, 279.
[49] M. C. Bernard, P. Bernard, M. Keddam, S. Senyarich, H. Takenouti, *Electrochim. Acta* **1996**, *41*, 91.
[50] G.W.D. Briggs, W.F.K. Wynne-Jones, *Trans. Faraday Soc.* **1956**, *52*, 1273.
[51] S.U. Falk, *J. Electrochem. Soc.* **1960**, *107*, 661.
[52] O. Glemser, J. Einerhand, *Z. Anorg. Chem.* **1950**, *261*, 26.
[53] C.A. Melandres, W. Paden, B. Tani, W. Walczak, *J. Electrochem. Soc.* **1987**, *134*, 762.
[54] J. McBreen, W.E. O'Grady, K.I. Pandya, R.W. Hoffman, D.E. Sayers, *Langmuir* **1987**, *3*, 428.
[55] K.I. Pandya, R.W. Hoffman, J. McBreen, W.E. O'Grady, *J. Electrochem. Soc.* **1990**, *137*, 383.
[56] J. McBreen, W.E. O'Grady, G. Tourillon, E. Dartyge, A. Fontaine, K.I. Pandya, *J. Phys. Chem.* **1989**, *93*, 6308.
[57] M. Aia, *J. Electrochem. Soc.* **1965**, *112*, 418.
[58] C. Greaves, M.A. Thomas, M. Turner, *Power Sources 9* (Ed.: J. Thompson), Academic Press, London, **1983**, p. 163.
[59] J.P. Harivel, B. Morignat, J. Labat, J.F. Laurent, in *Power Sources 1966*, (Ed.: D.H. Collins), Pergamon Oxford, **1967**, p. 239.
[60] H. S. Lim, S. A. Verzwyvelt, S. K. Clement, *Proc. 23rd IECEC Meeting*, Vol. 2, American Society of Mechanical Engineers, New York, **1988**, pp. 457–463.
[61] R.-R. Chen, Y. Mo, D.A. Scherson, *Langmuir*, **1994**, *10*, 3933.
[62] P. Häring, R. Kötz, *J. Electroanal. Chem.* **1995**, *385*, 273.
[63] A. Kowal, R. Niewiara, B. Pero• czyk, J. Haber, *Langmuir* **1996**, *12*, 2332.
[64] Y. Mo, E. Hwang, D. A. Scherson, *J. Electrochem. Soc.* **1996**, *143*, 37.
[65] M. S. Kim, T. S. Hwang, K B. Kim, *J. Electrochem. Soc.* **1997**, *144*, 1537.
[66] R. Kostecki, F. McLarnon, *J. Electrochem. Soc.* **1997**, *144*, 485.
[67] L. J. Oblonsky, T. M. Devine, *J. Electrochem. Soc.* **1995**, *142*, 3677.
[68] R. Allmann, *Chimia* **1970**, *24*, 99.
[69] P. Axmann, C. F. Erdbrügger, D. H. Buss, O. Glemser, *Angew. Chem. Int. Ed. Engl.* **1996**, *35*, 1115.
[70] D. H. Buss, W. Diembeck, O. Glemser, *J. Chem. Soc., Chem. Commun.* **1985**, 81.
[71] O. Glemser, D. H. Buss, J. Bauer, US Patent 4 735 629, **1988**.
[72] P. Axmann, O. Glemser, *J. Alloys and Compounds*, **1997**, *246*, 232.
[73] C. Delmas, C. Faure, L. Gautier, L. Guerlou-Demourgues, A. Rougier, *Phil. Trans. R. Soc. Lond.* **1996**, *354A*, 1545.
[74] T. Ohzuku, A. Ueda, Nagayama, *J. Electrochem. Soc.* **1993**, *140*, 1862.
[75] C. Delmas, J. J. Braconnier, Y. Borthomeiu, P.

CosMX Exhibit 1008, Page 173 of 633

Hagenmuller, *Mater. Res. Bull.* **1982**, *17*, 117.
[76] L. Demourges-Guerlou, C. Delmas, *J. Electrochem. Soc.* **1994**, *141*, 713.
[77] L. Demourges-Guerlou, L. Fournès, C. Delmas, *J. Solid State Chem.* **1995**, *114*, 6.
[78] C. Delmas, C. Faure, Y. Borthomeiu, *Mater. Sci. Eng.*, **1992**, *B13*, 89
[79] L. Guerlou-Demourgues, C. Delmas, *J. Electrochem. Soc.* **1996**, *143*, 561.
[80] D.C. Silverman, *Corrosion* **1981**, *37*, 546.
[81] E. Deltombe, N. de Zoubov, M. Pourbaix, in *Atlas of Electrochemical Equilibria in Aqueous Solutions* (Ed.: M. Pourbaix), NACE, Houston, TX, **1974**, p. 330.
[82] P.L. Bourgault, B.E. Conway, *Can. J. Chem.* **1960**, *38*, 1557.
[83[R. Barnard, C.F. Randell, F.L. Tye, *J. Appl. Electrochem.* **1980**, *10*, 109.
[84] R. Barnard, C.F. Randell, F.L. Tye, *J. Electroanal Chem.* **1981**, *119*, 17.
[85] R. Barnard, C.F. Randell, *J. Appl. Electrochem.* **1983**, *13*, 97.
[86] M.J. Madou, M.C.H. McKubre, *J. Electrochem. Soc.* **1983**, *130*, 1056.
[87] M.K. Carpenter. D.A. Corrigan, in *Papers presented at the Atlanta Meeting of the Electrochem. Soc.*, May 15–20, **1988**, Abstract No. 490, p. 700.
[88] E.M. Kuchinskii, B.V. Erschler, *J. Phys. Chem. (U.S.S.R.)* **1940**, *14*, 985.
[89] E.M. Kuchinskii, B.V. Erschler, *Zh. Fiz. Khim.* **1946**, *20*, 539.
[90] G.W.D. Briggs, M. Fleischman, *Trans. Faraday Soc.* **1971**, *67*, 2397.
[91] B. Klapste, J. Mrha, K. Micka, J. Jindra, V. Maracek, *J. Power Sources* **1979**, *4*, 349.
[92] R. Barnard, G.T. Crickmore, J.A. Lee, F.L. Tye, *J. Appl. Electrochem.* **1980**, *10*, 61.
[93] B. Klapste, K. Micka, J. Mrha, J. Vondrak, *J. Power Sources* **1982**, *8*, 351.
[94] A. H. Zimmerman, *Proc. 29th IECEC Meeting*, American Institute of Aeronautics and Astronautics, **1994**, pp. 63–68.
[95] J. Desilvestro, D.A. Corrigan, M.G. Weaver, *J. Electrochem. Soc.* **1988**, *135*, 885.
[96] D. Tuomi, *J. Electrochem. Soc.* **1965**, *112*, 1.
[97] D. A. Corrigan, S. L. Knight, *J. Electrochem. Soc.* **1989**, *136*, 613.
[98] A. N. Mansour, C. A. Melandres, M. Pankuch, R. A. Brizzolara, *J. Electrochem. Soc.* **1994**, *141*, L69.
[99] W. E. O'Grady, K. I. Pandya, K. E. Swider, D. A. Corrigan, *J. Electrochem. Soc.* **1996**, *143*, 1613.
[100] S. Font, J. Goulard, in *Power Sources 5* (Ed.: D.H. Collins), Academic Press, London, **1975**, p. 331.
[101] B.I. Tsenter, A.I. Sluzhevskii, *Elektrokhimiya* **1980**, *54*, 2545.
[102] Y. J. Kim, A. Visintin, S. Srinivasan, A. J. Appleby, *J. Electrochem. Soc.* **1992**, *139*, 351.

CosMX Exhibit 1008, Page 174 of 633

4 Lead Oxides

Dietrich Berndt

4.1 Introduction

Lead oxides play an important role in lead–acid batteries.

- Lead dioxide (PbO_2) forms the charged state of the active material in the positive electrode.
- Lead oxide (PbO) (also called litharge) is formed when the lead surface is exposed to oxygen. Furthermore, it is important as a primary product in the manufacturing process of the active material for the positive and negative electrodes. It is not stable in acidic solution but it is formed as an intermediate layer between lead and lead dioxide at the surface of the corroding grid in the positive electrode. It is also observed underneath lead sulfate layers at the surface of the positive active material.
- Minium (Pb_3O_4) represents a more highly oxidized form of lead oxide that enhances the electrochemical oxidation of lead oxide to lead dioxide.

The history of the lead–acid battery goes back to 1854 when Sinsteden published performance data on this battery system for the first time (cf. Ref. , [1]). The practical importance of the lead–acid battery system was detected, in 1859, independently of Sinsteden's work, by Planté, who produced a rechargeable battery by alternately charging and discharging lead sheets immersed in sulfuric acid [2]. Lead dioxide (PbO_2) as the "active material" is thereby directly generated from lead that is used as the conducting substrate. Planté plates are still in use, and are in principle produced by this method [3]. Separate production of the active material was introduced by Fauré in 1881. It is the basis of the pasted-plate design, mainly used today.

Since those early days, the lead–acid battery has always been the most important rechargeable electrochemical storage system, maintaining its prime position unchallenged now for more than a century. This seems surprising, because the fundamental data concerning the amount of energy that can be stored are rather modest on account of the high weight of the reacting substances. One main reason is the comparatively moderate price of lead–acid batteries. But besides that, there are many features that favor this system, which to a large extent are due to the substances that form the reacting components in the electrodes, e. g.:

- The same chemical element forms the active material in both electrodes:

lead as metal (Pb) in the negative and as lead dioxide (PbO_2) in the positive electrode.

- The reactants are solids of low solubility, and the reactions are highly reversible.
- The reactants compounds lead (Pb), lead sulfate ($PbSO_4$), and lead dioxide (PbO_2) are well-defined chemical compounds, and there are no intermediate states of oxidation. As a consequence, any voltage above the open circuit voltage results in complete charge, and equalizing charges are not required when the battery is used under continual charging in standby applications.
- The electronic conductivity of lead dioxide is comparatively high; thus there is no need for conducting additives.
- Due to the high potential of the $PbO_2 / PbSO_4$ electrode, the cell voltage of 2 V is fairly high, and a comparatively small number of cells is sufficient for a certain battery voltage.
- The high potential of the positive electrode, on the other hand, does not allow the use of conducting metals like copper within the positive electrode. Lead can be used instead due to its passive properties caused by a (PbO_2) layer that largely protects the underlying material, but conducts the electronic current and so allows electrochemical reactions at its surface.

This list could be extended (cf.. Ref. [4]). It simultaneously indicates the large number of parameters that influence the properties of a battery.

4.2 Lead / Oxygen Compounds

Lead forms two types of chemical compounds: lead (II), and lead (IV) compounds based on Pb^{2+} and Pb^{4+} ions, where those based on Pb^{2+} ions are the more stable. The metal is oxidized even at room temperature to lead oxide (PbO) and also by water that contains oxygen and forms lead hydroxide ($Pb(OH)_2$). In the lead–acid battery, the (less stable) lead (IV) oxide (lead dioxide, PbO_2), is of greatest importance. Beside these two, a number of oxides are observed in the battery that are mostly mixtures. A brief survey will now be given of those compounds that are of interest for lead–acid batteries.

4.2.1 Lead Oxide (PbO)

Lead oxide is formed by oxidation of a lead surface according to Eq. (1).

$$2Pb + O_2 \rightarrow 2PbO \qquad (1)$$

One technical process involves blowing air above the surface of molten lead. (cf. The Barton process in Sec. 4.2.1), but also, at room temperature, reaction (1) soon covers any piece of lead exposed to air with a dull gray layer of lead oxide (cf. The milling process in Sec. 4.2.1).

Two modifications are known:

(1) red PbO, the tetragonal modification (litharge);
(2) yellow PbO, the rhombic modification (massicot).

The crystallographic structure is described in Ref. [5], p. 11.

Red PbO is stable at low temperatures,

CosMX Exhibit 1008, Page 176 of 633

whereas yellow PbO is the high-temperature modification. The temperature of conversion is 488 °C:

$$\text{Red PbO} \rightarrow 488\,^{\circ}\text{C} \rightarrow \text{Yellow PbO} \quad (2)$$

At low temperatures the conversion is a slow reaction, and yellow PbO also exists at room temperatures as a metastable modification.

4.2.2 Minium (Pb_3O_4)

Minium, also called red lead, is formed when lead oxide is exposed to air at about 500 °C according to Eq. (3). Roasting ovens are used for the technical process.

$$3PbO + \tfrac{1}{2}O_2 \rightarrow Pb_3O_4 \quad (3)$$

Minium contains Pb^{2+} and Pb^{4+} ions, but it is not simply a mixture of PbO and PbO_2. According to its composition and structure it can be regarded as a lead (II) salt of the lead (IV) acid ($Pb_3O_4 = 2PbO \cdot PbO_2$) (cf. [5], Fig. 2.4, p. 17). In the technical process, the stoichiometric composition Pb_3O_4 is usually not attained and the (fictive) percentage of PbO_2 is often used to specify the grade of oxidation. Stoichiometric Pb_3O_4 contains 34% PbO_2 (239.2g of PbO_2 per 685g Pb_3O_4, cf. Table 2), and the technical products contain PbO_2 in the range between 25 and 30%.

When minium comes in to contact with sulfuric acid it is converted into lead sulfate and lead dioxide according to Eq. (4).

$$Pb_3O_4 + 2H_2SO_4 \rightarrow 2PbSO_4 + PbO_2 + 2H_2O \quad (4)$$

4.2.3. Lead Dioxide (PBO_2)

Lead dioxide exists in two modifications:

(1) a rhombic modifications called $\alpha - PbO_2$;
(2) a tetragonal modification called $\beta - PbO_2$;

Beside the crystalline material, a certain portion of amorphous lead dioxide is always observed. In the working electrode such amorphous material is apparently hydrated and forms a gel structure at the phase boundary between the solid material and the electrolyte (cf. Ref. [6]).

In battery electrodes, the stoichiometric composition is usually not accomplished, and oxidation ends at a composition of about $PbO_{1.98}$ [7].

$\alpha - PbO_2$ is formed in an alkaline environment, whereas $\beta - PbO_2$ is produced in an acidic medium. Both modifications can be prepared by chemical and electrochemical methods (for detailed descriptions of preparations methods and structure see Ref. [5], p. 19, and [8]). In the positive electrodes of lead–acid batteries, a certain portion of $\alpha - PbO_2$ is formed during the electrochemical conversion of the electrode (cf. Secs. 4.4.2.2 and 4.4.2.3). When the battery has been discharged and is charged again, only $\beta - PbO_2$ is formed on account of the acidic environment. For this reason, the content of $\alpha - PbO_2$ decreases with the number of discharge/charge cycles, especially for a high initial $\alpha - PbO_2$ content (cf. Ref. [5], p. 267, esp. Figs. 3.27 and 3.28). Plates containing much $\alpha - PbO_2$ show a reduced initial capacity, which increases gradually on account of the conversion of $\alpha - PbO_2$ to $\beta - PbO_2$. There was some indication that plates with high $\alpha - PbO_2$ content would outperform other plates in standby appli-

CosMX Exhibit 1008, Page 177 of 633

cations. Therefore, the $\alpha / \beta - PbO_2$ ratio has occasionally been specified for stationary lead–acid batteries, but these observations have not been confirmed in general [6]. Other experiments indicate that the structure of lead dioxide agglomerates, which can be influenced by the formation process, is important for cycle stability [9] (cf. also the description of "paste mixing" in Sec. 4.4.2.1).

Under normal conditions $\beta - PbO_2$ is the more stable modification. Under a high pressure (> 8500 bar) the β modification can be transformed to $\alpha - PbO_2$.

4.2.4. Nonstoichiometric PbO_x Phases

PbO_x phases with x between 1.42 and 1.58 can be formed by oxidation of PbO (cf. Ref. [5], p. 18). It is assumed that such compounds are formed underneath the protecting PbO_2 layer at a corroding lead surface (cf. Fig. 8).

4.2.5. Basic Sulfates

Basic sulfates are intermediate compounds that contain lead oxide and lead sulfate and to some extent also water (Table 1). They are stable only in alkaline environment.

Basic sulfates are important intermediates during the manufacturing process, since they determine the structure of the active material in the positive electrode, which again is decisive with respect to the performance data and service life of the battery (cf. Ref. [9]).

4.2.6. Physical and Chemical Properties

Some physical and chemical properties of the lead oxides are compiled in Table 2.

Table 2. Molecular weight, density (cf. [5], Table VII) and electrical resistance of the chemical compounds used in lead–acid batteries.

Substance	Molecular weight ($g\,mol^{-1}$)	Specific weight ($g\,cm^{-3}$)	Electrical resistance (Ωm^{-1})
Pb	207.2	11.34	2×10^{-7}
PbO (red)	232.2	9.35	$10^{13} - 10^{14}$
PbO (yellow)	223.2	9.64	10^{12}
Pb_3O_4	685.6	9.1	9.6×10^{9}
$\alpha - PbO_2$	239.2	9.1–9.4	$10^{-5} - 10^{-6}$
$\beta - PbO_2$	239.2	9.1–9.4	$10^{-5} - 10^{-6}$
$PbSO_4$	303.25	6.1–6.4	
H_2O	18.02	0.997	$\approx 10^{4}$ *

The specific resistance of the oxides depends on pressure (cf. [5], Table 2.3).
* Distilled water.

4.3 The Thermodynamic Situation

The exchange of energy connected with a chemical or electrochemical reaction is described by thermodynamic laws and data, as shown in Chapter 1 of this book. Since these laws apply only to the state of

Table 1. Basic sulfates that are formed as intermediate compounds when lead oxide is mixed with sulfuric acid.

Compound	Formula	pH range	Remark
Monobasic sulfate	$PbO \cdot PbSO_4$	6.28–7.31	
Dibasic sulfate	$2PbO \cdot PbSO_4$		
Tribasic sulfate	$3PbO \cdot H_2O \cdot PbSO_4$	7.31–8.99	
Tetrabasic sulfate	$4PbO \cdot PbSO_4$		$T > 50$ °C

CosMX Exhibit 1008, Page 178 of 633

equilibrium, all reactions are balanced. In an electrochemical cell, these data can only be measured when no current flows through the cell or its electrodes. On account of this balance, the thermodynamic parameters do not depend on the reaction path; they only depend on different energy levels between the final and initial components (the "products" and the "reactants" of the chemical or electrochemical reaction). For the same reason, the laws of thermodynamics describe the possible upper limit of energy that can be delivered by a reaction, or the minimum of energy that is required for its reversal. Thermodynamic data only indicate whether a reaction is possible at a given electrode potential or not; the actual rate of a reaction is largely determined by the laws of electrode kinetics.

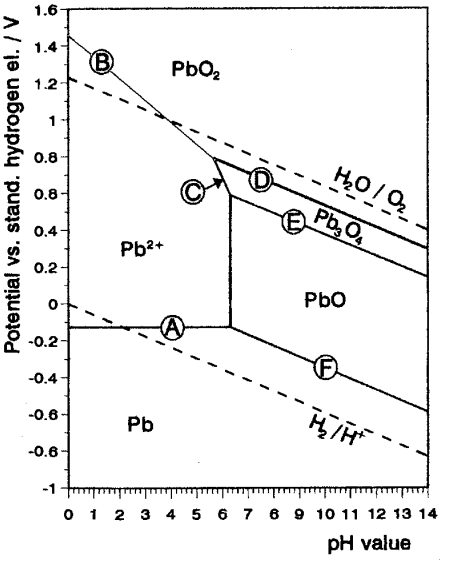


Figure1. Equilibrium potential / pH diagram of the Pb/H_2O system at 25 °C, according to Pourbaix [10], but simplified for $a = 1\,mol\,L^{-1}$. The pH value is used to express the acidity of the solution. Its definition is $pH = -\log(a_{H^+})$; pH stands for the negative logarithm of the activity of the H^+ ions.

A survey of the thermodynamic situation is provided by so-called Pourbaix diagrams [10], which show equilibrium potentials versus the pH value. Figure 1 shows such a diagram for lead and its oxides in a very simplified form that considers only the standard concentrations of the dissolved components. The complete diagram contains a great number of parallel lines that express the various concentrations.

4.3.1 Water Decomposition

The electrolyte in lead–acid batteries is dilute sulfuric acid that contains the component "water". Its stability is an important factor since it can be decomposed into hydrogen and oxygen, and the two broken lines in Fig. 1 represent the borderlines of this stability. They show the equilibrium potentials of hydrogen and oxygen evolution and their dependence on the pH value.

The H_2/H^+ line in Fig. 1 represents the equilibrium potential $E°$ of the hydrogen evolution according to Eq. (5)

$$H_2 \leftrightarrow 2H^+ + 2e^- \tag{5}$$

and its dependence on the pH is described by the Nernst equation [Eq. (6)],

$$E^0 = E^{0.S}_{H^+/H_2} + \frac{RT}{2F} \ln \frac{a^2_{H^+}}{a_{H_2}} \tag{6}$$

with E^0 = equilibrium potential, $E^{0,S}$ = standard value of the equilibrium potential (when a_{H^+} and a_{H_2} are $1\,mol\,L^{-1}$, and a_{H^+}, a_{H_2} = activities (i. e. effective concentrations) of H^+ and H_2 respectively.

Using the definition of the pH value, $pH = -\log(a_{H^+})$, and the relation between the gas pressure (p_{H_2}) and the concentra-

CosMX Exhibit 1008, Page 179 of 633

tion of dissolved gas (a_{H_2}) (Henry's law), Eq. (6) can be written:

$$E^0 = E^{0,S}_{H^+/p_{H_2}} - 2.303\frac{RT}{F}\left\{pH + \frac{1}{2}\log(p_{H_2})\right\} \quad (7)$$

with $-2.303\frac{RT}{F} = -0.0592\,\mathrm{V}$.

This is the curve H_2/H^+ in Fig. 1 for $p_{H_2} = 1\mathrm{atm}$. The standard value of this equation (proton activity $a_{H^+} = 1\,\mathrm{mol\,L^{-1}}$; $p_{H_2} = 1\mathrm{atm}$)

$$E^{0,S}_{H^+/p_{H_2}} = 0 \quad (8)$$

[Eq. (8)] represents by definition the zero point of the electrochemical potential scale (standard hydrogen electrode, often denoted SHE).

The corresponding relation for oxygen evolution:

$$H_2O \rightarrow \frac{1}{2}O_2 + 2H^+ + 2e^- \quad (9)$$

has the equilibrium potential

$$E^0_{O_2} = E^{0,S}_{O_2} + \frac{RT}{2F}\ln\frac{a^{1/2}_{O_2}a^2_{H^+}}{a_{H_2O}} \quad (10)$$

with the standard value

$$E^{0,S}_{O_2} = 1.229\,\mathrm{V} \quad (11)$$

In Fig 1, this is represented by the H_2O/O_2 curve.

$E^0_{O_2}$ is the decomposition voltage of water. Above this value, water is not stable but decomposes with formation of oxygen (O_2).

In Fig. 1, H_2O/O_2 and H_2/H^+ curves are straight lines which have the same slope of $-0.059\mathrm{V}$ per pH unit.

4.3.2 Oxidation of Lead

Curve A in Fig. 1 corresponds to the oxidation of lead to its divalent ion, described by the reaction

$$Pb \leftrightarrow Pb^{2+} + 2e^- \quad (12)$$

with the dependence on activities

$$E^0_{Pb/Pb^{2+}} = E^{0,S}_{Pb/Pb^{2+}} + \frac{RT}{2F}\ln(a_{Pb^{2+}}) \quad (13)$$

and the standard value

$$E^0_{Pb/PbSO_4} = -0.126\,\mathrm{V} \quad (14)$$

$E^0_{Pb/Pb^{2+}}$ does not depend on the pH value. In Fig. 1, the activity of SO_4^{2-} equals $1\,\mathrm{mol\,L^{-1}}$.

At small pH values, the curve A is below the H_2/H^+ curve, which means that lead is not stable in an aqueous solution under these conditions, but is converted into Pb^{2+} ions, and simultaneously water is decomposed with formation of hydrogen H_2.

Curve B describes the corresponding relation for the oxidation of divalent lead ions $Pb^{2+} \rightarrow Pb^{4+}$, which implies the formation of lead dioxide since Pb^{4+} does not exist alone:

$$Pb^{2+} + 2H_2O \rightarrow PbO_2 + 4H^+ + 4e^- \quad (15)$$

The dependence on H^+ concentration (activity) is given by

CosMX Exhibit 1008, Page 180 of 633

$$E^0_{Pb^{2+}/PbO_2} = E^{0,S}_{Pb^{2+}/PbO_2} + \frac{RT}{2F}\ln\frac{a_H^4}{a_{H_2O}^2} \quad (16)$$

and leads to a slope of $2 * 0.0592 = 0.1184$ V per pH unit.

The standard value is:

$$E^0_{Pb^{2+}/PbO_2} = 1.459\,\text{V} \quad (17)$$

At small pH values, the curve B is above the H_2O/O_2 curve, which means that lead dioxide (Pb^{4+} ions) is not stable in such an acidic aqueous solution, but is reduced to Pb^{2+} ions, and simultaneously water is decomposed with formation of oxygen (O_2).

PbO and Pb_3O_4 are oxides of lead that are important primary products. Under certain circumstances, PbO is also observed in lead–acid batteries (cf. Sec. 4.4.5.1). Fig. 1 shows that these oxides are only stable in a neutral or alkaline environment. Their equilibrium potentials are represented by curves C–F and their standard values are compiled in Table 3.

Table 3. Equilibrium potentials shown by the curves C-F in Fig. 1, their standard values and dependences on pH (cf. also Ref. [5], p.36)

Curve	Equilibrium	Standard value, ($E^{0,S}$) (V)	pH dependence (V / pH unit)
C	Pb^{2+}/Pb_3O_4	2.094	–0.2368
D	Pb_3O_4/PbO_2	1.124	–0.0592
E	PbO/Pb_3O_4	0.972	–0.059
F	Pb/PbO	0.248	–0.059

4.3.3 The Thermodynamic Situation in Lead–Acid Batteries

In the lead–acid battery, sulfuric acid has to be considered as an additional component of the charge–discharge reactions. Its equilibrium constant influences the solubility of Pb^{2+} and so the potential of the positive and negative electrodes. Furthermore, basic sulfates exist as intermediate products in the pH range where Fig. 1 shows only PbO (cf. corresponding Pourbaix diagrams in Ref. [5], p. 37, or in Ref. [11]; the latter is cited in Ref. [8]). Table 2 shows the various compounds.

The charge–discharge reaction of the negative electrode corresponds to curve A in Fig. 1, but the Pb^{2+} ion activity is now determined by the solubility of lead sulfate ($PbSO_4$). Thus Eq. (12) has to be modified into

$$Pb + H_2SO_4 \rightarrow PbSO_4 + 2H^+ + 2e^- \quad (18)$$

The dependence of the equilibrium potential on the activities of hydrogen and sulfuric acid is given by the corresponding Nernst equation:

$$E^0_{Pb/PbSO_4} = E^{0,S}_{Pb/PbSO_4} + \frac{RT}{2F}\ln\frac{a^2_{H^+}}{a_{H^+}a_{HSO_4^-}} \quad (19)$$

with the standard value

$$E^{0,S}_{Pb/PbSO_4} = -0.295\,\text{V} \quad (20)$$

The charge–discharge equation of the positive electrode corresponds to curve B in Fig. 1 and the corresponding Eq. (15). But here also the Pb^{2+} activity is now determined by the solubility of lead sulfate, and Eq. (15) has to be modified into:

CosMX Exhibit 1008, Page 181 of 633

$$PbSO_4 + 2H_2O \rightarrow PbO_2 + H_2SO_4 + 2H^+ + 2e^- \quad (21)$$

with the corresponding Nernst equation

$$E^0_{PbO_2/PbSO_4} = E^{0,S}_{PbO_2/PbSO_4} + \frac{RT}{2F} \ln \frac{a^2_{H^+} a_{HSO_4^-}}{a^2_{H_2O}} \quad (22)$$

and the standard value

$$E^{0,S}_{PbO_2/PbSO_4} = 1.636\,V \quad (23)$$

Note: *Here the calculations of the standard potentials are referred to the dissociation of H_2SO_4 into H^+ and HSO_4^- which fairly closely corresponds to the actual situation. Sometimes such calculations are based on the assumption of completely dissociated sulfuric acid,*

$$H_2SO_4 \rightarrow 2H^+ + SO_4^{2-} \quad (24)$$

This causes different standard values, but the results are identical (cf. e.g., Ref. [12]).

Figure 2 illustrates the resulting situation. Due to the strong acidic solution in the battery, it corresponds to Fig. 1 for small pH values, but here the electrode potential is drawn on the vertical axis. The values are referred to the above-mentioned standard hydrogen electrode. To enlarge the scale, the range between 0 and 1.2 V is omitted.

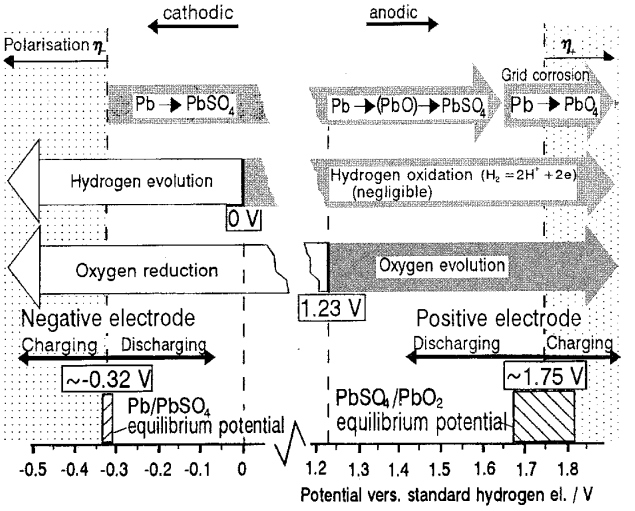


Figure 2. Reactions that occur in lead–acid batteries versus electrode potential (thermodynamic situation). Their equilibrium potentials are inserted as boxed numbers. Equilibrium potentials of the charge–discharge reactions ($Pb/PbSO_4$ and $PbSO_4/PbO_2$) are represented by hatched columns, to indicate their dependence on acid concentration. The inserted equilibrium potentials (−0.32 and +1.75 V) of the charge–discharge reactions correspond to an acid density of 1.23 g cm^{-3}.

CosMX Exhibit 1008, Page 182 of 633

The columns just above the potential scale represent the equilibrium potential of the charge–discharge reaction, given by Eqs. (19) and (22) for the negative and positive electrode, respectively. The width of each column expresses the dependence on acid concentration. The column that represents the $PbSO_4/PbO_2$ equilibrium potential corresponds to line B in Fig. 1. Its standard value is shifted to the more positive potential $E^0 = 1.636\,V$, since the Pb^{2+} concentration amounts to only about 10^{-6} $mol\,L^{-1}$ due to the low solubility of lead sulfate ($PbSO_4$). Above this equilibrium potential, lead dioxide (PbO_2) is formed.

Water decomposition is not directly influenced by sulfate formation and occurs as described in Fig. 1. Thus, in the strong acid hydrogen and oxygen evolution occurs below 0 V and above 1.23 V respectively, as shown in Fig. 2. It means that for thermodynamic reasons, oxygen evolution and hydrogen oxidation (the reversal of hydrogen evolution) are possible at an electrode potential far below that of the positive electrode. The same applies to the corrosion of lead, also indicated by the corresponding arrow in Fig. 2. Thus couples of reactions are to be expected that reduce lead dioxide and so cause self-discharge of the active material:

(1) **Oxygen evolution** according to Eq. (5) is possible above 1.23 V and forms the couple with the discharge reaction (the reversal of Eq.(21)):

Discharge of the positive electrode

$$PbO_2 + H_2SO_4 + 2H^+ + 2e^- \rightarrow PbSO_4 + 2H_2O$$

and oxygen evolution

$$H_2O \rightarrow \tfrac{1}{2}O_2 + 2H^+ + 2e^-$$

with the result

$$PbO_2 + H_2SO_4 \rightarrow \tfrac{1}{2}O_2 + PbSO_4 + H_2O \qquad (25)$$

(2) **Hydrogen oxidation** according to Eq. (5) is possible above 0 V. If hydrogen evolution occurs at the negative electrode and the H_2 evolved reaches the positive electrode, from the thermodynamic situation the reaction that is to be expected is:

Discharge of the positive electrode

$$PbO_2 + H_2SO_4 + 2H^+ + 2e^- \rightarrow PbSO_4 + 2H_2O$$

and hydrogen oxidation

$$H_2 \rightarrow 2H^+ + 2e^-$$

with the result

$$PbO_2 + H_2SO_4 + 2H^+ \rightarrow PbSO_4 + 2H_2O \qquad (26)$$

In practice, however, this reaction can be neglected since its rate is extremely low at the PbO_2 surface.

(3) **Corrosion of lead** starts at the equilibrium potential of the negative electrode. It induces self-discharge of the positive electrode on account of the following couple of reactions:
Discharge of the positive electrode

$$PbO_2 + H_2SO_4 + 2H^+ + 2e^- \rightarrow PbSO_4 + 2H_2O$$

and grid corrosion

$$Pb + H_2O \rightarrow PbO + 2H^+ + 2e^-$$

with the result

CosMX Exhibit 1008, Page 183 of 633

$$PbO_2 + H_2SO_4 + 2H^+ + 2e^- \rightarrow PbSO_4 + 2H_2O \quad (27)$$

Above the potential given by line F in Fig. 1, the formation of PbO is possible, but this is stable only in an alkaline environment. As soon as it comes to contact with sulfuric acid, it is converted into lead sulfate. For this reason PbO is in parentheses in Fig. 2. The final result of these reactions is:

$$PbO_2 + Pb + 2H_2SO_4 \rightarrow 2PbSO_4 + 2H_2O \quad (28)$$

Above the equilibrium potential of the positive electrode, lead is oxidized to PbO_2.

Fortunately, the kinetic parameters reduce the rates of these reactions so far that the gradual self-discharge of the PbO_2 is such a slow reaction that it usually does not affect the performance of the battery.

- Self-discharge by oxygen generation (Eq. (25)) occurs equivalent to a current in the range of 0.5 mA/100Ah, which means $\approx 0.4\,\%$ of nominal capacity per month (starting at higher values).
- Corrosion of the positive grid [Eq. (28)] occurs equivalent to about 1 mA/100Ah at open-circuit voltage and intact passivation layer. It depends on electrode potential, and is at minimum about 40–80mV above the $PbSO_4/PbO_2$ equilibrium potential. The corrosion rate depends furthermore to some extent on alloy composition and is increased with high antimonial alloys.
- As already mentioned, hydrogen oxidation can be neglected.

Although the rate of these reactions is slow, according to its thermodynamic situation the lead dioxide electrode is not stable. Since a similar situation applies to the negative electrode, the lead–acid battery system as a whole is unstable and a certain rate of water decomposition cannot be avoided.

4.3.4. Thermodynamic Data

The thermodynamic data for the substances employed in lead–acid batteries are compiled in Table 4.

Table 4. Standard values (T =25°C) of the thermodynamic data for the chemical compounds in the active material of lead–acid batteries (cf. Ref. [5], p. 366) In older Tables, the energy often is given in calories: 1cal = 4.187J.

Substance	Enthalpy of formation $H^{0,S}$ ($kJ\,mol^{-1}$)	Free enthalpy of formation $G^{0,S}$ ($kJ\,mol^{-1}$)	Entropy, $S^{0,S}$ ($J\,K^{-1}\,mol^{-1}$)
Pb	0	0	64.8
Pb^{2+}	1.67	–24.39	10.5
PbO (red)	–219.0	–199.0	66.5
PbO (yellow)	–217.3	–187.9	68.7
Pb_3O_4	–718.4	–601.2	211
$\alpha - PbO_2$	–265.8	–217.3	92.5
$\beta - PbO_2$	–276.7	–219.3	76.4
$PbSO_4$	–919.9	–813.2	149
H^+	0	0	0
H_2O	–219.0	–237.2	189

CosMX Exhibit 1008, Page 184 of 633

4.4 PbO_2 as Active Material in Lead–Acid Batteries

The active material comprises the substances that constitute the charge–discharge reaction. In the positive electrode of lead–acid batteries, the active material in the charged state is lead dioxide (PbO_2), which is converted into lead sulfate ($PbSO_4$) when the electrode is discharged. The active material is the most essential part of a battery, and battery technology has to aim at optimum constitution and performance for the expected application. This does not only concern the chemical composition but also the physical structure and its stability. Specialized methods have been developed to fulfill these requirements, and the primary products as well as the manufacturing process are usually specified by the individual battery manufacturer.

It is characteristic for battery manufacture is that lead dioxide (PbO_2) as the charged state of the active material is always generated by electrochemical oxidation. Thus electron-conducting bridges are established between the fine particles and a matrix is formed of comparatively low electronic resistance. Three general types of positive electrodes are mainly used today: Planté, pasted, and tubular plates which vary not only in their design but also in the way they are manufactured.

The charge–discharge reactions occur at the phase boundary between the active material and the electrolyte. To make sure that a sufficient rate of reaction is achieved, the surface of the reacting materials has to be large. Otherwise, the kinetic parameters would reduce the reaction rate too much. Table 5 shows the surface areas of the active materials in the positive and the negative electrode.

Figure 3 shows the typical microscopic appearance in the charged and discharged states. Although certain features are characteristic, microscopic pictures of this kind vary considerably, because of the different parameters that influence the formation of the crystals when a substance is precipitated. Furthermore, the charge–discharge

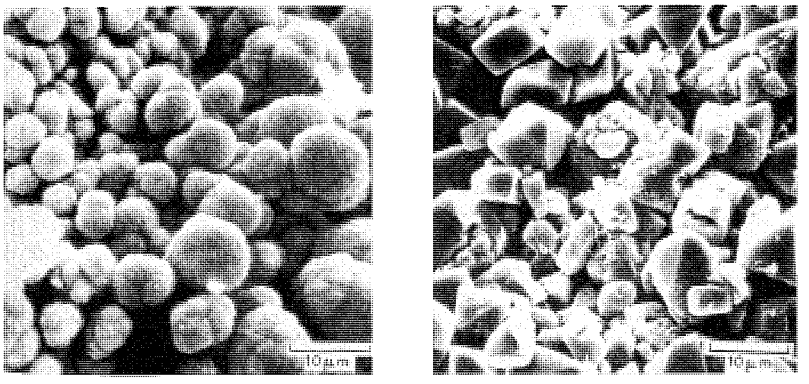


Figure 3. Active material of a lead dioxide electrode, charged on the left, discharged on the right. The charged state shows the typical "lump" structure; in the discharged state lead sulfate crystals dominate [15].

CosMX Exhibit 1008, Page 185 of 633

conditions and the age of the battery influence the morphology of the active material (cf. e.g., Refs. [8], [14]). The "lump" structure is typical of the charged active material of the positive electrode, at least for a fairly new electrode. These "lumps" are porous agglomerates. About 50% of their volume is occupied by lead dioxide; the other 50% is pores. A large share of micropores produces the high surface area shown in Table 5.

Table 5. Surface areas of the active materials in lead–acid batteries

Substance	BET surface (m^2g^{-1})
Lead dioxide PbO_2	4–6
Lead, Pb	0.3–0.6

In the lead–acid battery, the reactions at both electrodes include the dissolved state, which means that the reacting species are dissolved in the course of the reaction. The new chemical compounds formed during the reaction are precipitated again as solid matter. This explains the completely different appearance of the material in the charged and discharged states.

The discharge reaction is the reversal of Eq. (21):

$$PbO_2 + H_2SO_4 + 2H^+ + 2e^- \rightarrow PbSO_4 + 2H_2O \qquad (29)$$

In this reaction at the positive electrode bivalent lead ions are formed by tetravalent lead ions acquiring two electrons according to $Pb^{4+} + 2e^- \rightarrow Pb^{2+}$. The Pb^{2+} ions dissolve but immediately form lead sulfate ($PbSO_4$) on account of the low solubility. Eq. (28) shows that water is formed in addition, since oxygen ions are released from the lead dioxide (PbO_2) and combine with the protons (H^+) to form H_2O molecules. When the battery is being charged, these reactions occur in the opposite direction. Lead dioxide (PbO_2) is formed from lead sulfate ($PbSO_4$) and water, while electrons are released.

The charge–discharge process can be repeated quite often, since the decisive parameters, solubility and dissolution rate of the various compounds, are well matched in the lead–acid battery system. The chemical conversions occur close to each other, and most of the material transport takes place in the micrometer range. Nevertheless, a gradual disintegration of the active material is observed.

The required amount of lead dioxide can be calculated with the aid of Eq. (29), as shown in Table 6. The amount of electricity, required per multiple of this reaction is $2F = 192970As = 53.61Ah$.

Table 6. Molar weight of lead dioxide, required quantity, and utilization

Molar weight (g)	Required quantity ($g\,Ah^{-1}$)	Utilization		
		Theory		Practice
		($Ah\,kg^{-1}$)	($Ah\,lb^{-1}$)	($Ah\,kg^{-1}$)
239.2	4.462	224.1	101.7	60–130

*Utilization in theory derived from Eq. (29); utilization in practice mainly depends on electrode thickness (cf. Ref. [12]).

4.4.1 Planté Plates

In positive Planté plates the lead dioxide is generated by direct oxidation of lead that forms the conducting substrate. Figure 4 shows a cross-section of such a plate. The plate is cast from pure lead. Its surface is enlarged by lamellas that can be seen in Fig. 4. Planté formed the dioxide layer by a large number of charge–discharge cycles. Nowadays, the electrochemical oxidation is enhanced by the addition of perchloric acid ($HClO_4$) during the "formation process". It increases the solubility of lead and increases the corrosion rate so far that a

CosMX Exhibit 1008, Page 186 of 633

single charging cycle is sufficient. The precisely controlled process results in a layer of active material that is about 220 μm thick.

An advantage of this plate design is the short distance that has to be passed by electrons to reach the current conducting core; disadvantage is the weight of this thick core made of pure lead.

Negative electrodes in Planté batteries are of the pasted type.

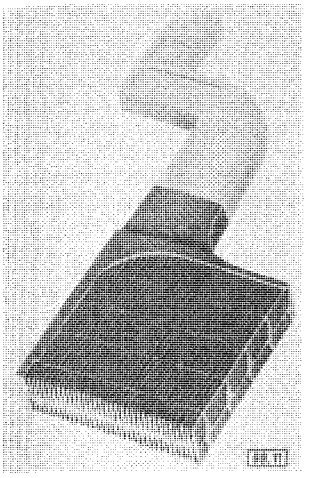


Figure 4. Cross-section of a Planté plate. The fine lamellas of the casting enlarge its surface area by a factor of 8–12. On the top, the current collector, the plate lug, is to be seen.

4.4.2. Pasted Plates

The plate support in lead-acid batteries is usually called the "grid". In most batteries the grid has to provide both mechanical support for the active material and electronic conductivity for the collected current.

Figure 5 shows the design of a grid and its horizontal and vertical cross-sections. This Figure indicates the origin of term "grid" for this kind of plate support.

The network of lead wires must provide optimum mechanical support to the pellets of active material that fill the void space. Sufficient conductivity has also to be provided by the grid. Grids for positive and negative electrodes are usually similar. In batteries designed for extended service life, the positive grid is made heavier to provide a corrosion reserve. For very thin electrodes, a lead foil is used as the substrate and current conductor.

The mechanical support of the active material is of minor importance when additional support is provided, e.g., by envelopes or tubes (cf. Sec. 4.4.3).

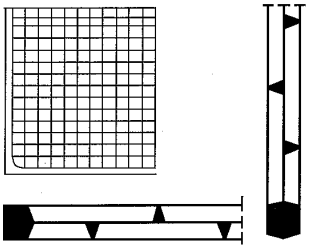


Figure 5. Grid of a lead–acid battery with thicker walls and a rectangular mesh. One corner and cross-sections in vertical and horizontal directions (from [15]).

4.4.2.1 Manufacture of the Active Material

The production of the active material for positive and negative electrodes starts with the same substance, a mixture of lead oxide (PbO) and metallic lead called gray oxide or lead dust. It is a fine powder that contains 20–30 wt.% of lead (Pb). The size of the primary particles is in the range of 1–10 μm . Larger agglomerates are usually formed.

Gray oxide can be produced by a **milling process**, which, strictly speaking, does not mill the material. A rotating drum is filled with solid balls or ingots of lead.

CosMX Exhibit 1008, Page 187 of 633

Flakes are shared, crushed, and at the same time partly oxidized by an airstream that flows through the drum. Temperature and airflow rate are used to control the process to achieve the desired powder. At the end the oxidized material is carried away by an airstream and classified. Particles that are too coarse are fed back into mill.

Another process, the **Barton process**, is based on molten lead. The core of such a device is the "Barton reactor", a heated pot that is partly filled with molten lead. It is continuously refilled by a fine stream of molten lead. Fine droplets of lead are produced by a fast rotating paddle that is partly immersed under the surface of the molten lead within the "Barton reactor". The surface of each droplet is transformed by oxidation into a shell of PbO by an airstream that simultaneously carries away the oxidized particles if they are small enough; otherwise, they fall back into the melt and the process is repeated. Thus the airstream acts as a classifier for particle size.

A short description of both processes is given in Ref. [16]. Nowadays, the Barton process is preferred for a number of reasons: it can more easily be installed in small units and it can be controlled faster [17]. (In a mill it takes a number of hours for the material to run through the drum, so controlling actions are slow).

Paste mixing means the addition of sulfuric acid and water. The result is a fairly stiff paste with a density between 1.1 and $1.4\,g\,cm^{-3}$ containing 8–12wt% of lead sulfate. The water content of thus mix determines the porosity of the active material achievable later (cf. "curing" below). In the paste, a mixture of lead sulfate and basic lead sulfate is formed (cf. Table 1). In the usual mixing process between room temperature and 50 °C, tribasic lead sulfate is formed. The generation of the tetrabasic modification ($4PbO \cdot PbSO_4$) is favored at temperatures above 70 °C [18].

To a certain extent, the formation of the tetrabasic variant is desired, because $4PbO \cdot PbSO_4$ forms fairly large crystals when transformed into lead dioxide (PbO_2). This results in a mechanically stable active material, but there are disadvantages, because it is more difficult to transform this material into lead dioxide, i.e., the formation process (see below) is more expensive (and takes longer) and the initial capacity is slightly reduced (cf., e.g., Ref. [19]. For "long-life batteries" (Bell systems cell), a special process has been developed to produce pure tetrabasic material [20].

Sometimes red lead or minimum (Pb_3O_4) is added to the paste. The addition is usually 5–10wt. %, and is mainly made for easier formation of the final compound lead dioxide (PbO_2) (cf. "curing" and "formation", below).

A general problem in open mixing machines is that the exothermic process

$$PbO + H_2SO_4 \rightarrow PbSO_4 + H_2O \quad (30)$$

causes a temperature increase of the mix ($\Delta H = -173\,kJ\,mol^{-1}$). In mixing machines the evaporation of water is often used for cooling, but then water is lost and the composition of the mix changes. For this reason a certain surplus of water is scheduled in the paste recipe. However, evaporation rate depends on environmental parameters like temperature and humidity, and this limits the possibility of keeping the specified water content of the paste, which is important in regard to the porosity of the active material (as mentioned below).

For accurate mixing, independent of environmental conditions, vacuum mixers are used as shown in Fig. 6.

CosMX Exhibit 1008, Page 188 of 633

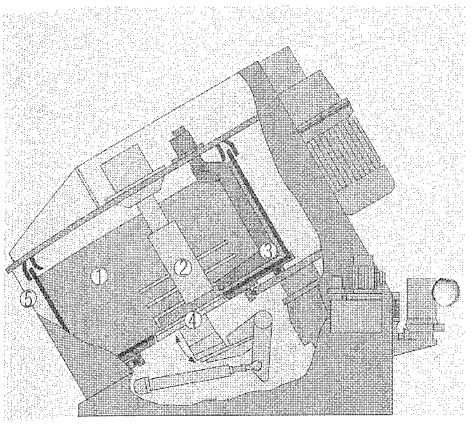


Figure 6. Vacuum mixer for lead paste:1, mixing compartment; 2, fast-rotating mixing tools; 3, material-deflecting plate; 4, discharge opening; 5, static, vacuum-sealed enclosure [21].

In the vacuum mixer, water evaporation is also used for the temperature control, since the evaporation rate can be influenced by the grade of the vacuum. The water vapor, however, does not escape from the mixer, but is condensed and returned into the mix, the composition of which is thus not changed.

At the end of the mixing process, the paste contains about 10wt% of metallic lead and about 50vol.% of water. The water is evaporated during the subsequent production steps, and the resulting void space represents the pore volume of the dried active material.

Pasting means that the paste and the grids are supplied to a machine that smears the mix into the grid. Single plates are superficially dried after pasting, to prevent sticking when they are stacked afterwards. Continuously cast grids leave the pasting machine as an endless ribbon, usually enveloped by paper. Pasting of flat elements or foils is achieved with a slurry instead of a stiff paste (cf. e.g., Ref. [22].

The subsequent production step, the "curing", is especially important for the positive plate, because the structure of the active material can be influenced by environmental conditions such as temperature and humidity [23]. During the curing step, the lead content in the active material is reduced by gradual oxidation from about 10 to less than 3wt%. Furthermore, the water (about 50vol%) is evaporated. This evaporation must be done quite carefully, to ensure that the volume occupied by the water actually gives rise to porosity and is not lost by shrinkage, which again might lead to the formation of cracks. As in the paste-mixing process, the transformation into tetrabasic lead oxide ($PbO \cdot PbSO_4$) is favored at curing temperatures above 70°C [24], which is of prime interest for the later mechanical stability of the positive active material.

Single plates are usually cured in special devices (curing ovens or curing chambers, cf., e.g., [25]) that control humidity as well as temperature. In continuous plate production, the drying of the pasted ribbon is correspondingly controlled. Furthermore, in continuous manufacture final curing can occur after the plates are separated and inserted into the containers.

4.4.2.2 Tank Formation

Tank formation means that the cured positive and negative "raw plates" are inserted alternately in special tanks filled with fairly dilute sulfuric acid (generally in the range 1.1 to $1.15\,g\,cm^{-3}$) and positive and negative plates are connected, a number of each, in parallel with a rectifier. The formation process means that the active material of the plates is electrochemically transformed into the final stage, namely:

- lead dioxide (PbO_2) in the positive electrode and

CosMX Exhibit 1008, Page 189 of 633

- spongy metallic lead (Pb) in the negative electrode.

A survey of formation techniques is given in Ref. [26].

Because of the porous material in the raw plate, both substances are produced in a spongy state with a porosity of about 50 vol%. Tank formation takes between 8 and 48 h, depending on the plate thickness and formation schedule. When the formation process is finished, the plates are washed and dried. They can be stored and later assembled in batteries.

4.4.2.3 Container Formation

The fundamental difference from tank formation is that the battery is assembled first, then filled with electrolyte, and finally the formation process is carried out with the complete battery.

During the **formation process**, the battery is considerably overcharged and generates both hydrogen and oxygen, with resulting water loss. The concentration of the filling acid is adjusted in such a way that the desired final acid concentration is approximated at the end of the formation, and only minor corrections are required; another method includes dumping of the acid and refilling of the battery during the formation step. These methods are known as "one-shot formation" and "two-shot formation", respectively (cf., e.g., Ref. [26], p. 17).

4.4.3 Tubular Plates

The tubular-plate design for the positive electrodes, shown in Fig. 7, is common mainly in European countries for batteries with larger capacities. In this plate design, the conducting elements are separated from the components that contribute mechanical support. The grid consists of vertical lead rods in the centers of tubes that are formed by woven, braided, or nonwoven fabrics.

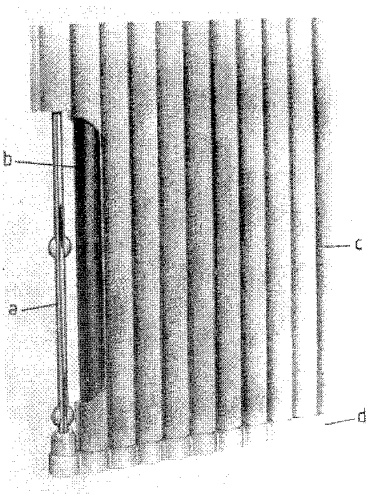


Figure 7. Section of a tubular plate: a, lead-alloy spine (grid); b, active material (PbO_2); c, tube, (in this example, fabric of polyester fibers); d, bottom seal of plastic caps.

The advantage of tubular plates is the comparatively high utilization of the active material which results in a rather low weight in relation to capacity. These features have two causes, namely:

- The central current-collecting spine produces uniform current flow across the active material.
- The mechanical support by the tube allows the use of fairly light active material. This means high porosity and a high utilization factor.

A disadvantage for tubular plates is the fact that a minimum tube diameter between 6 and 8 mm is required for economic production, but the tube diameter corresponds

CosMX Exhibit 1008, Page 190 of 633

with plate thickness, and lead–acid batteries with such thick plates are inferior for high-rate discharge.

The production of tubular positive plates is in principle similar to that of pasted plates. A number of manufacturers use the same gray oxide as the basic filling substance. Sometimes the share or red lead or minium (Pb_3O_4) is increased above 25 or even to 100wt.%. The latter is more economic when the manufacturer runs his own minium plant; then the expense of the chemical oxidation of lead oxide (PbO) to minium (Pb_3O_4) may be compensated by reduced formation cost. Furthermore, curing is not required, because of the high oxidation state, and the battery starts with full capacity when formed.

Different methods are in use for plate filling. The material can be filled as a powder with the aid of vibrators. Other techniques use a slurry of lead oxide or even a paste, as described above [27].

When dry material or a slurry has been filled, "pickling" is required, which means that the plate is stored in sulfuric acid for a short time. The material is soaked by the acid and transformed, at least partly, into lead sulfate ($PbSO_4$), as in the paste-mixing process (Section 4.4.2.1). When minium is used, during the "pickling" process lead dioxide is also formed according to Eq. (4).

The subsequent procedures, formation, washing, drying, and battery assembly are similar to those described above.

4.5 Passivation of Lead by its Oxides

Corrosion of the current-conducting elements in the positive electrode, as of the plate support (grid), bus bars, and terminals, is a side-effect of the high cell voltage of this battery system, which implies a high potential of the positive electrode. Metals that are usually applied as current conductors, and even noble metals like gold, would be dissolved by oxidation when connected to the positive electrode of the lead–acid battery.

Lead can be used, because the corrosion itself forms a rather dense passivating layer of lead dioxide that protects the underlying material against fast corrosion [28]. If foreign metals like copper are used they have to be covered thoroughly by a dense layer of lead.

However, the protecting PbO_2 layer does not establish a stable situation at the phase boundary between metal and oxide layer. Rather, the corrosion process gradually penetrates into the bulk material, and the corrosion of the positive grid represents a restriction of the lead–acid battery that finally limits the useful life, if no other reasons cause earlier failure. Figure 8 illustrates the situation: the active material is represented by the area on the left; the grid is shown on the right. Underneath the porous lead dioxide that constitutes the active material, a dense layer, also of lead dioxide, covers the grid surface. This layer is formed by corrosion and protects the grid. On account of acid depletion a rather stable oxide layer (mainly of $\alpha - PbO_2$) is formed [29]. However, lead dioxide and lead cannot exist beside each other for thermodynamic reasons, and a thin layer of less-oxidized material is always formed between the grid and the lead dioxide (PbO_x in Fig. 8) [30]. The existence of lead oxide (PbO) in this layer has been determined; the existence of higher oxidized species is assumed (PbO_x phases: cf. Ref. [5], p. 18), but their structure is not yet known exactly [31].

CosMX Exhibit 1008, Page 191 of 633

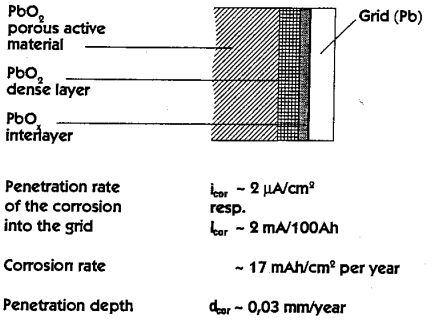


Figure 8. Structure of the corrosion layer at the grid surface. Penetration and corrosion rates are approximated for room temperature and normal float voltage (2.23–2.25 V/cell) (see text).

The PbO_2/PbO_x border slowly penetrates into the metal, but only at a very slow rate as a solid-state reaction. Cracks are formed when the oxide layer exceeds a given thickness, on account of the growth in volume when lead becomes converted into lead dioxide (Table 7). Underneath the cracks the corrosion process starts again and again. As a whole, the corrosion proceeds at a fairly constant rate. It never comes to a standstill, and a continually flowing anodic current, the corrosion current is required to re-establish the corrosion layer.

When the grid material (Pb) is converted into lead dioxide (PbO_2), the basic electrochemical reaction is

$$Pb \rightarrow Pb^{4+} + 4e^- \qquad (31)$$

Table 7. Density and volume ratio af corrosion products related to lead.

	Density ($g\,cm^{-3}$)	Volume ratio relative to Pb
Pb	11.34	1
$PbO_{(red)}$	9.64	1.26
$\alpha - PbO_2$	9.87	1.32
$\beta - PbO_2$	9.3	1.40
$PbSO_4$	6.29	2.64

Twice the amount of electricity is required compared with the discharge reaction at the negative electrode according to Eq. (18), since corrosion involves four valences, which means $4F = 107.21\,Ah$ per multiple of Eq. (31). Consequently, for the corrosion reaction according to Eq. (31) the equivalent values are:

$$\frac{207.19}{107.21} = 1.9326\,g\,Pb/Ah$$

$$\text{or } 517.4\,Ah/kg\,Pb \qquad (32)$$

This value means that $1\,cm^3$ of lead (11.34g; cf. Table 2) is equivalent to 5.89Ah.

A current of $1\,\mu A\,cm^{-2}$ means $8760\,\mu Ah\,cm^{-2}$ per year. Referred to $5.89\,Ah\,cm^{-3}$, a penetration rate of $1.49 \cdot 10^{-3}$ cm/year results, assuming that the corrosion attack occurs uniformly and progresses at a constant rate. Thus the value in Fig. 8 means that a corrosion current of $2\,\mu A\,cm^{-2}$ implies a penetration rate of about $0.03\,mm/year$.

Figure 9 illustrates the consequences for battery practice. The above penetration rate would reduce the cross—section of a grid spine in a tubular electrode by about 50% within the usual service life of 15 years. This result is confirmed by field experience and shows that long-life batteries must have a corresponding "corrosion reserve" in their positive grids.

Since grid material is converted into lead dioxide, a slight increase in the actual capacity is often observed with lead–acid batteries. The reduced cross-section in Fig. 9 does not affect the performance of batteries that are used for discharge durations in the order of one hour or more. Attention must, however, be paid to batteries that are loaded with high currents, because the conductivity of the grid gains importance with increased current flow.

CosMX Exhibit 1008, Page 192 of 633

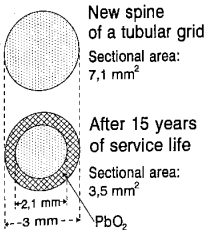


Figure 9. Conversion of grid material into lead dioxide (PbO_2) by corrosion: spine of a positive tubular plate. New plate: 3mm diameter means $7.1\,mm^2$ cross-section (πr^2 with $r = 1.5mm$). Aged plate: reduction of r by $0.03 \times 15 = 0.45mm$ means $\pi r^2 = 3.5\,mm^2$.

The "corrosion capacity of the positive grid" can be estimated from the above figures. The positive grid in lead–acid batteries for stationary and traction applications contains about 10 g of lead / Ah^{-1} (usually slightly more). This means a positive-grid weight of about $1kg/100Ah$. With the values of Eq. (32), the "corrosion capacity" is $500Ah/100Ah$ of battery capacity. The corrosion rate of 1 or $2mA/100Ah$ means 8.76 and $17.52Ah/100Ah$ per year respectively. Related to the 500 Ah of the total "corrosion capacity", 2–4% of the grid material would converted into lead dioxide per year under these assumptions.

4.5.1 Disintegration of the Oxide Layer at Open-Circuit Voltage

In Sec. 4.3.3 it has been shown that corrosion is one or the reactions that cause self-discharge of the positive electrode. In connection with Fig. 8 it has been mentioned that an anodic current, the **corrosion current**, must flow continuously to stabilize the lead dioxide layer at the grid surface. Then the PbO_x layer remains thin because PbO_x is always converted into PbO_2 by further oxidation.

At open-circuit voltage, no anodic current flow through the positive electrode occurs that can oxidize the PbO (or PbO_x) layer, but the corrosion reaction

$$Pb + PbO_2 \rightarrow 2PbO \qquad (33)$$

continues between grid and passivating layer. Consequently the PbO (or PbO_x) layer grows between the grid and PbO_2.

However, as mentioned in Sec. 4.3.3, PbO and PbO_x are not stable against sulfuric acid, and react very fast according to

$$PbO + H_2SO_4 \rightarrow PbSO_4 + H_2O \qquad (34)$$

as soon as these substances come in contact with it. The protecting lead dioxide layer, shown in Fig. 8, would be destroyed by this reaction, and severe grid corrosion is one of the problems that occur when the battery stands for prolonged periods without any charging. Battery manufacturers therefore recommend recharging a lead-acid battery filled with electrolyte within regular periods, which must be shortened when the battery is stored at elevated temperatures.

4.5.2 Charge Preservation in Negative Electrodes by a PbO Layer

The drying of negative plates is not possible without precautions, because of the tendency to spontaneous oxidation. This oxidation reaction is much ac-celerated by water, and the active material of a moist negative electrode is spon-taneously converted into lead oxide when exposed to air. When, on the other hand, the charged plate is dry, a thin layer of oxide covers the surface of the active material, and prevents

CosMX Exhibit 1008, Page 193 of 633

further oxidation. So, prevention of access of oxygen as long as the plates are wet, is a common feature of various methods to achieve **dry charged negative plates**. As a result of the superficial oxidation, a loss of about 10% of capacity is always incurred with the dry charge process, regardless of the method applied.

The dried plates can be stored for a practically unlimited time without losing capacity or ageing. This is true also for complete batteries that are assembled but not yet filled with electrolyte.

4.6 Ageing Effects

The active material of the positive electrode is prone to lose its mechanical strength when repeated discharge/charge cycles occur, because the alternating dissolution and precipitation processes, convert the agglomerate structure into an accumulation of fine crystals [32]. So, the active material suffers degradation and part of it may fall off the plate as fine particles. This process is called **"shedding"**. Shedding of the positive active material is a characteristic feature of ageing conventional lead–acid batteries when they are charged and discharged frequently. It is likewise also described as **"soft positives"**. Shedding is only the outward appearance of a more general ageing process which means that the active material is prone to disintegration of its electronic conductivity and mechanical strength. This causes the so-called **"premature capacity-loss"** [33] (a survey with references is given in Ref. [34]). It becomes evident as a decreasing utilization factor with increasing cycles.

In a model that considers the active material as an aggregate of spheres (*"Kugelhaufen"*) it is explained by a gradual increase in the ohmic resistance, mainly in the connecting region of the individual particles of the active material. They connecting regions establish the electrical contact between the individual particles of the active material. They are decisive for the ohmic resistance because of the minimized cross-sectional areas in these bridging zones. The structure of the connecting regions between the particles of active material is largely influenced by the conditions when these regions are re-established during the charging process. For this reason, it is understandable that the charging conditions are important for the stability of the active material and that in many cases, after a premature decay, full capacity can be regained with suitable charge/discharge procedures [36]. For this reason, the premature capacity loss sometimes is called "reversible capacity decay".

Another model assumes that gel zones are formed by hydrated lead dioxide ($PbO(OH)_2$) and act as bridging elements between the crystallite particles. Electrons can move along the polymer chains of this gel and so cause electronic conductivity between the crystalline zones [37].

Quite often, simultaneously with the capacity decay, the formation of a barrier layer of lead sulfate ($PbSO_4$) is observed between the grid and the active material [38]. In view of the explanation given above, this layer may be the final stage of the process. When the ohmic resistance of the active material is increased, the charge/discharge reaction is restricted to the area close to the grid surface. Then, deep discharge must happen to this part of the active material, causing a high concentration of sulfate.

CosMX Exhibit 1008, Page 194 of 633

4.6.1 The Influence of Antimony, Tin, and Phosphoric Acid

Antimony (Sb) and tin (Sn) are usually not added to the active material, but both are alloying components of the grid. They are gradually released from the grid by corrosion, and permeate the active material by dissolution and diffusion.

The "premature capacity loss" described above, i.e., a decay of the utilization factor, became especially evident when antimony-free alloys were introduced and such batteries were operated in charge/discharge cycle regimes. For this reason, this effect is likewise called the **"antimony-free effect"**, although it is also observed with grids containing antimony. The mechanism of this effect has not yet been explained in detail, but antimony has a strong influence on the stability of the active material that cannot be compensated by special pretreatment or design of the electrodes [39].

When specimens of pure lead and a 5% antimony alloy were periodically oxidized and reduced, lead oxide layers were observed with different structures:

- coarse and insulating with antimony-free electrode,
- fine and low resistance with the antimony alloy [40].

The origin of such insulating layers may explain the high resistance also established within the active material when antimony is not present.

The *"Kugelhaufen"* model mentioned in the preceding section explains the beneficial influence of antimony by improved conductivity of the zones that connect the spheres. According to the gel model, antimony decreases the crystallinity of PbO_2 and so increases the conductivity by the gel zones [41], and especially influences the structure of the corrosion layer intermediate between the grid and active material [42].

Addition of tin to the positive-grid alloy also has a capacity-stabilizing effect, but this apparently concerns only the boundary between the grid and active material. **Phosphoric acid** (H_3PO_4) is added in small amounts to the electrolyte. A beneficial effect on cycle stability has long been known for this acid, which has been used as an additive in conventional lead–acid batteries for many years to improve cycle stability, although the disadvantage of a slightly reduced capacity had to be accepted [43]. Addition of phosphoric acid to the electrolyte improves long-term capacity and reduces the formation of sulfate layers around the grid [44]. The addition of 20–35 $g\,dm^{-3}$ phosphoric acid was protected by patent for valve-regulated lead–acid batteries with gelled electrolyte [45]. Extensive experiments [46] showed that, at low H_3PO_4 concentrations, $Pb_3(PO_4)_2$ acts as an intermediary in the corrosion of Pb to PbO_2. Clearly , the phosphoric acid influences the formation of lead dioxide (PbO_2) on account of its strong adsorption and leads to a fine grain structure of the positive active material [47]. However, in spite of the repeated use of phosphoric acid in lead–acid batteries, some questions on its interaction are still to be elucidated [48].

4.7 References

[1] K.R. Bullock in *Proc. Symp History of Battery Technology* (Ed.: A. J. Salkind), Electrochem. Soc. Proc. Vol. 87—14, Pennington, NJ, **1987**, p. 106; The Electrochemical Society J. Garche, *J. Power Sources*, **1990**, *31*, 401.

[2] G.W. Vinal, *Storage Batteries*, John Wiley,

CosMX Exhibit 1008, Page 195 of 633

New York, **1955**, p. 2ff.
[3] K.V. Kordesch, *Batteries*, Marcel Dekker, New York, **1955**, p. 419.
[4] K.R. Bullock, in *Proc. Symp. Advances in Lead–Acid Batteries*, The Electrochemical Society, Pennington, NJ, **1984**, p. 1.
[5] H. Bode, *Lead Acid Batteries-ohn*, J. Wiley, New York, **1977**, p. 366.
[6] J. Burbank, A.C. Simon, E. Willihnganz, The lead acid cell, in *Advances in Electrochemistry and Electrochemical Engineering, Vol. 8*, John Wiley, New York, **1971**, p. 170.
[7] J. Pohl, H. Rickert, *Power Sources 5, Proc. 9th Int. Symp. Brighton, 1974*, Ed. D.H. Collins Academic Press, **1975**, p. 15.
[8] J.P. Carr, N.A. Hampson, The lead dioxide electrode, in *Chem Rev.*, **1972**, *72*, 679–703.
[9] D. Pavlov, E. Bashtavelova, V. Iliev in *Advances in Lead–Acid Batteries*, Eds.: K.R. Bullock, D. Pavlov, Electrochem. Soc. Proc. Vol. 84-14, The Electrochemical Society, Pennington, NJ, **1984**, p. 16.
[10] M. Pourbaix, *Atlas of Electrochemical Equilibria in Aqueous Solution*, Pergamon, New York, **1966**, p. 485.
[11] S.C. Barnes, R.T. Mathieson in *Batteries*, Ed. D.H. Collins, Pergamon, New York, **1963**, p. 41.
[12] D. Berndt, *Maintenance-Free Batteries*, Research Studies Press, Taunton, UK John Wiley, New York, **1993**, 1st ed., p. 40, **1997**, 2nd ed, 102.
[13] S. Brunauer, P.H. Emmet, E. Teller, *J. Am. Chem. Soc.*, **1938**, 60, 309.
[14] J. Yamashita, H. Yufu, Y. Matsumaru *J. Power Sources*, **1990**, 30, 13.
[15] VARTA Battery AG (Editor), *Bleiakkumulatoren*, 11th ed., VDI-Verlag, Düsseldorf, **1986**, p. 79 (in German).
[16] *Batteries International*, October **1994**, *21*, 84.
[17] E.A. Busdieker, K.W. Maurer, *Batteries International*, July **1993**, *16*, 56.
[18] D. Pavlov, G. Kapazov, *J. Appl. Electrochem.*, **1976**, *6*, 339.
[19] D. Pavlov, N. Kapkov, *J. Electrochem. Soc.*, **1970**, *137*, 1305.
[20] R.V. Biagetti, M.C. Weeks, *Bell Syst. Tech. J.*, **1970**, *49*, 1305.
[21] *Processing Technology for Lead Acid Battery Paste*, Maschinenfabrik Gustav Eirich, Postfach 1160, D-74732 Hardheim, Germany; H.J. Vogel, *Power Sources*, **1994**, *48*, 71.
[22] H. Tamura, *Prog. Batteries Solar Celli, 1988*, 7, 205.
[23] L.T. Lam, D.A.J. Rand, *Batteries International*, **1990**, *137*, 21.
[24] D. Pavlov, N. Kapkov, *J. Electrochem. Soc.*, **1990**, *137*, 21.
[25] G. Clerici, *J. Power Sources*, **1991**, *33*, 67, Fig. 11.
[26] R. Kiessling, *Lead Acid Battery Formation Techniques*, **1992**, Digatron/Firing circuits, Digatron, Industrie Elektronik GmbH, Tempelhofer Str. 12, D-5100 Aachen, Germany; Firing Circuits Inc., Box 2007, Norwlk, CT 06852, USA.
[27] W. Lüdecke, *Batteries International*, October **1990**, 60; F.X. Mittermaier, *Ibid.*, July **1996**, *28*, p. 43.
[28] D. Pavlov, *Ber. Bunsenges Phys. Chem.*, **1967**, *71*, 398; D. Pavlov in *Advances in Lead–Acid Batteries*, Electrochem. Soc. Proc. Vol. 84-14, The Electrochemical Society, Pennington, NJ, **1984**, p. 110.
[29] P. Ruetschi, R.T. Angstadt, *J. Electrochem. Soc.*, **1964**, *111*, 1323.
[30] D. Pavlov, Z. Dinev, *J. Electrochem. Soc.*, **1980**, *127*, 855.
[31] K.R. Bullock, G.M. Trischan, R.G. Burrow, *J. Electrochem. Soc.*, **1980**, *130*, 1283.
[32] S. Atlung, B. Zachau-Christiansen, *J. Power Sources*, **1990**, *30*, 131.
[33] A.F. Hollenkamp, K.K. Constati, A.M. Huey, M.J. Koop, L. Aputeanu, *J. Power Sources*, **1992**, *40*, 125.
[34] E. Meissner, H. Rabenstein, *J. Power Sources*, **1992**, *40*, 157
[35] A. Winsel, E. Voss, U. Hullmeine, *J. Power Sources*, **1990**, *30*, 209; esp. p. 220, Fig. 12.
[36] U. Hullmeine, E. Voss, A. Winsel, *J. Power Sources*, **1989**, *25*, 27.
[37] D. Pavlov, *J. Electrochem. Soc.*, **1992**, *139*, 3075; D. Pavlov, B. Monahov, *J. Electrochem. Soc.*, **1996**, *143*, 3616.
[38] S. Tudor, A. Wesstuch, S.H. Davang, *Electrochem. Techn.*, **1965**, *4*, 406; esp. 408, Fig. 2.
[39] T.G. Chang, *Advances in Lead–Acid Batteries*, Proc.Electrochem. Soc. Vol. 84-14, The Electrochemical Society, Pennington, NJ, **1984**, p. 86.
[40] J. Burbank, *Power Sources 3*, Oriel Press, Newcastle upon Tyne, UK, **1971**, p. 13.
[41] D. Pavlov, A. Dakhouche, T. Rogachev, *Power Sources*, **1993**, *42*, 71.
[42] B. Monahov, D. Pavlov, *J. Electrochem. Soc.*, **1994**, *141*, 2316; D. Pavlov, *Power Sources*,

CosMX Exhibit 1008, Page 196 of 633

1994, *48*, 179.
[43] C. Drotschmann, *Bleiakkumulatoren*, Verlag Chemie, Weinheim, **1951**, p. 161.
[44] S. Tudor, A. Weisstuch, S.H. Davang, *Electrochem. Techn.*, **1967**, *5*, p. 21; esp. 23, Fig. 3.
[45] Accumulatorenfabrik Sonnenschein GmbH, Büdingen, German Patent 1671693, January 12, **1967**.
[46] K. R. Bullock, D.H. McClelland, *J. Electrochem. Soc.*, **1977**, *124*, 1478
[47] J. Garche, H. Döring, K. Wiesener, *J. Power Sources*, **1991**, *33*, 213.
[48] E. Voss, *J. Power Sources*, **1988**, *24*, 171.

CosMX Exhibit 1008, Page 197 of 633

5 Bromine–Storage Materials

Christoph Fabjan, Josef Drobits

5.1 Introduction

As a positive active material for rechargeable cells, bromine offers various attractive properties such as high voltage and specific energy and power. The main difficulty encountered with the operation of a battery using bromine/bromide electrode is the necessity to develop a suitable method technically simple and efficient for the storage of the aggressive and toxic elemental halogen.

Several systems using different negative materials such as Zn [1–3], Li [4], and Al [5] were investigated but at present practical success has been achieved only with the zinc–bromine battery. A satisfactory approach for bromine storage was the formation of organic nonaqueous polybromine complex phases by the reaction of quaternary ammonium salts, dissolved in the aqueous electrolyte solution, with elemental bromine generated in the charge process reducing energy losses due to self–discharge to extraordinary low values.

A variety of complexes exists in solid or liquid state at ambient temperature, in the range required for battery operation. Liquid polybromine phases are preferred since they enable storage of the active material externally to the electrochemical cell stack in a tank, hence enhancing the storage capacity of the system and reducing energy losses in standby periods to very low values. This design requires electrolyte circu-lation and application of the flow battery concept, utilizing its characteristic advan-tages and accepting the drawbacks associated with this type of storage system.

The operating principle and the conceptional design of a multicell bipolar zincflow battery are presented in Fig. 1.

From an aqueous $ZnBr_2$ solution zinc is plated at the cathode during charge whereas bromine is generated at the anode, forming the water immiscible polybromine phase with the complexing agents. In the discharge process zinc metal is dissolved anodically, and the active bromine is consumed from an emulsion of the complex phase and aqueous solution pumped over the electrode surface in the cathodic reac tion. Hence the active materials are reconverted to form aqueous $ZnBr_2$ solution. The net reaction, $Zn^s + Br_2^{naq} \leftrightarrow ZnBr_2^{aq}$, provides a cell voltage of approximately 1.82 V and a theoretical specific energy of 430 Wh kg^{-1}.

The system consists of three essential components.

(1) The cell stack with the bipolar electrodes.
(2) The electrolyte flowing in two inde-

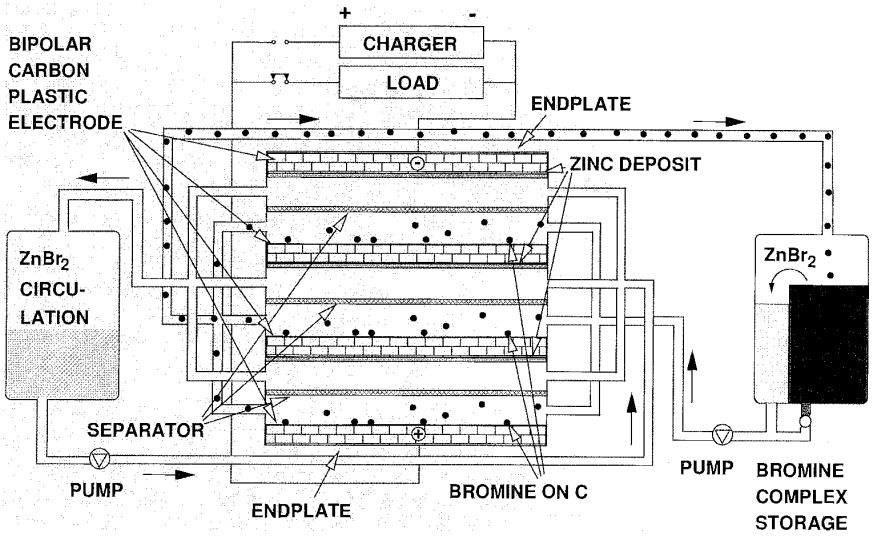


Figure 1. Operating principle of a zinc-flow battery

pendent streams through the electrochemical module and the individual cell compartments, which are divided by microporous separators. In the discharged state the electrolyte is a homogeneous aqueous solution whereas during charge a two–phase electrolyte is produced in the bromine loop.

(3) Auxiliary equipment, such as two pumps, tubing valves and electrolyte reservoirs is also necessary.

The bromine-storing complex phase, as an essential component of the systems has to meet various requirements to ensure the practical success of the battery:

(1) a decrease in the concentration of active bromine in the aqueous solution, which is in equilibrium with the organic bromine–rich phase, to very low values (0.01 mol L^{-1}) to minimize self–discharge;

(2) a decisive reduction in bromine vapour pressure to a few percent of the values obtained with elemental bromine over the full range of operating temperatures from approximately -10 °C to 50 °C;

(3) provision of the liquid state under the conditions described above;

(4) satisfactory electrochemical reactivity in the emulsion with the aqueous electrolyte phase, to minimize polarization and voltage losses;

(5) higher specific density than the aqueous solution to enable fast separation of the two phases;

(6) longterm stability against oxidation or bromination of organic substituents by bromine;

(7) minimization of health and safety risks and environmental impact in the case of battery failure (electrolyte leakage) or damage;

The ionic conductivities of the polybromide complexes are considerable, ap-

CosMX Exhibit 1008, Page 199 of 633

proaching the values of ordinary aqueous salt solutions due to their "fused–salt" nature. This property means an additional advantage since the electrolyte resistivity, the ohmic voltage drop, and polarization effects remain low.

The properties and behavior of the bromine storing polybromide complexes will now be treated in detail from the fundamental and technological viewpoints, including economic and ecological (safety risks, recyclability, disposal, etc.) aspects.

5.2 Possibilities for Bromine Storage

5.2.1 General Aspects

Previously studied possibilities for bromine storage systems are listed in Table 1. The widely known reduction of the Br_2 vapor pressure by formation of adducts with various carbon materials results from strong chemisorption interactions and has been investigated for activated carbon [4]. Adducts containing up to ~ 85 wt. % Br_2 were reported to be stable at ambient temperature; however, considerable equilibrium bromine vapor pressures were found.

Intercalation of molecular Br_2 into graphite yields compounds with higher thermal stabilities [6,7] forming so–called residual compounds which do not quantitatively release all the included Br_2 even at temperatures of ~ 2000 °C [26-31]. Bromine is fixed in the graphitic lattice, bound in two different ways: (i) chemisorption on structural crystalline defects and layer edges; and (ii) intercalation, thus producing separated islands without contacting the crystal edges. Repeated intercalation and extraction of intercalant species leads to exfoliation and destruction of the graphite material. Formation of bromine adducts with zeolites has been reported [8]. A considerable number of crystalline organic compounds containing polyiodide and polybromide anions such as

Table 1. General possibilities for bromine storage

Chemical stabilization	Examples and references
Storage in inorganic solid matrix	Intercalation into graphite [6,7]
	Carbon–bromine adduct [4]
	In zeolites [8]
Polymetric matrix	Polydiallyldimethylammonium bromide [9]
	Polypyrrole [10]
	Poly (*N,N*-dimethyl)-3,4-pyrrolidinium bromide [11]
	Styrene–divinyl benzene copolymers [4]
	Polyacrylamide [12]
Ion-excharger resins	De-acidite FF anion exchange resin [13]
Charge-transfer complexes	Dioxane, pyridine, polyvinyl, pyrrolid one, poly-2-vinvyl pyridine, polyethyleneoxide [4]
Further organic storing materials	Phenyl bromide [14], pyridine, 1-picoline, 2,6-lutidine [15–17]
	Arsonium salts [18, 19]
	Phosphonium salts [20]
	Pyridinium bromides [21]
	Aromatic amines [22]
	Urotropin–bromine adduct [23]
	Pyridinium and sulfonium salts [24]
	Propionitril [25]

CosMX Exhibit 1008, Page 200 of 633

$TMA \cdot 0.7H_2O \cdot xHal_5H$ (TMA= trimesic acid, $x = 0.09$ for Hal = I and $x = 0.103$ for Hal = Br) [32] or $M(dpq)_2Hal$ (M=Ni ; Pd ; dpg = diphenylglyoxime) [33] have been tested with the intention of modeling new conducting materials. Electrical conductance was reported to depend only negligibly on the nature of the anions. Infinite linear chains of essentially Hal_5^- units were found in XRD analyses [32].

As early as 1888 Horton reported the formation of stable urotropin–bromide adducts [23].The storage of bromine in organic solids and particularly as a liquid complex phase stabilized by quaternary ammonium salts is of outstanding importance for modern battery applications. In conjunction with polymeric and porous carbon matrices, these species were used in investigations aiming at the development of solid state batteries [12]. However, high self–discharge rates have remained an unsolved problem for this cell type until today. The zinc–flow battery using liquid polybromide phase from the reaction with quaternary ammonium salts are currently of practical importance in the field of alternative systems of energy storage.

5.2.2 Quaternary Ammonium-Polybromide Complexes

The tendency of the halogens to form chain–like polyanions that are stabilized by delocalization of the negative charge [15,34] is a basic chemical principle. Donor–acceptor interactions between Lewis–acidic Br_2 and halide anions, but also with polyhalides acting as Lewis bases, give rise to the formation of a variety of homo and heteroatomic adducts. The maximum number of atoms in these chains increases with the atomic weights of the halogens (i.e., Cl < Br < I). Stabilities of the predominant species, Br_3^- and Br_5^-,in aqueous [35,36] and organic solvents [36,37] were studied by means of IR, Raman and UV spectroscopy. Within Br_3^- a substantial elongation of bond distances occurs compared with the Br_2 molecule (2.55 vs. 2.28 Å). The asymmetric and symmetric Br–Br stretching modes at ~201–210 and 160–170 cm^{-1} of dissolved tribromide ions in various solvents were found in Raman spectroscopic studies [36] to be approximately 100 cm^{-1} lower than the characteristic value for elemental Br_2 [38]. While theoretical studies predict that the free Br_3^- ion has a linear symmetric structure [39–43], a broad scattered variety of linear and nonlinear symmetric and asymmetric Br_3^- ions were reported to exist in crystalline environment [44, 45, 46, 52] and solution [35,36], according to the size and shape of the corresponding countercations.

Br_5^- forms v-shaped planar species [42,43] with relatively strong terminal and weak central bonds. Raman spectra in aqueous solution and acetonitrile [36] exhibit terminal stretching modes of 250 and 257 cm^{-1} which are essentially higher than in Br_3^-. Structural data from experimental studies exist only for crystalline compounds in which the Br_5^- ions adopt linear geometry. In a theoretical study using density functional theory [43], a central bond angle of 114.6° and a central terminal bond ratio of ~1.111 were obtained; the latter is somewhat smaller than the 1.181 estimated from XRD experiments on linear Br_5^- units in $TMA \cdot 0.7H_2O \cdot xHal_5H$ [32].

It is evident that the shapes and relative stabilities of the polybromide anions depend to a large extent on the nature of the countercations. The tendency to form

CosMX Exhibit 1008, Page 201 of 633

nonaqueous phase is determined by the chemical environment, and depends particularly on the degree of hydratation of the ions. Hence, important properties of bromine storing phases can be varied over a wide range by adjusting the type and composition of the quaternary ammonium salts used. Additional parameters, such as pH, concentration of supporting salts (i.e., Cl^-) also producing heteroatomic polyhalide ions [47], and temperature effects, enhance the difficulties of a systematic investigation of the polybromide structure in practical battery electrolytes.

An overview of the most important quaternary ammonium salts tested for possible applicability in zinc–bromine batteries is presented in Table 2. A rough classification has been applied according to the substance classes of the substituents attached to the nitrogen.

Table 2. Complexation of Br_2 with quaternary ammonium salts

Substance class	Examples and references
Aliphatic	$Me_2Et_2N^+ Br^-$ [48, 49], $MeEt_3N^+ Br^-$ [48, 49]
	$Me_2EtPrN^+ Br^-$ [48–49], $Me_2Et_2PrN^+ Br^-$ [48, 49, 51]
	$Et_3PrN^+ Br^-$ [49]
	$Bu_4N^+ Br^-$ [14, 33, 51–54]
	$Et_4N^+ Br^-$ [14, 51, 52, 55, 56], $Et_4N^+ Cl^-$ [14, 56]
	$Me_4N^+ Br^-$ [51, 52, 54, 57–59]
	$Oct_4N^+ Br^-$ [52]
	$Me_3EtN^+ Br^-$ [49, 60], $Me_3PrN^+ Br^-$ [49]
	$MeEt_2CMN^+ Br^-$ [48]
	$Me_3CMN^+ Br^-$ [49], $Et_3CMN^+ Br^-$ [49]
	$Me_2EtCMN^+ Br^-$ [49], $MeEt_2CMN^+ Br^-$ [49]
	$Oct_3MeN^+ Cl^-$ [59]
	$(isoamyl)_3NHCl$ [53]
	$Me_3NH\,Br$ [53, 61], Me_3NHCl [53]
	$NH_4^+ Br^-$ [62]
	$Et_3hexadecN^+ Br^-$ [63], $Me_2hexadec_2N^+ Br^-$ [63]
	Me_2 dodec - 2 - hydoxy - $EtN^+ Br^-$ [63]
Aromatic	$Et_3PhN^+ Br^-$ [56, 63]
	$Me_3PhN^+ Br^-$ [54, 64, 65]
	Benzyldimethyl-(3-isobutoxy-2-hydroxy propyl)- $N^+ Br^-$ [63]
Heterocyclic	*N*-Methyl-*N*-ethyl pyrrolidinium bromide (MEP) [3, 14, 48–51, 66–74]
	N-methyl-*N*-ethyl morpholinium bromide (MEM) [3, 14, 48–51, 56, 59, 66–75]
	N-chloromethyl-*N*-methyl pyrrolidinium bromide (C-MEP) [48, 49, 75]
	N-chloromethyl-*N*-methyl morpholidinium bromide (C-MEM) [49]
	2-Bromo-cyclohexylpyridinium bromide [50, 56, 63, 76]
	2-Chloro- cyclohexylpyridinium bromide [56, 63]
	N-Bromo-*t*-butyl pyridinium bromide [63]
	N-Methoxymethyl-*N*-methyl piperidinium bromide [75]
Tenside-like	$[PhCH_2NMe_2(CH_2)_6NMe_2CH_2Ph]^{2+}\,2Br^-$ [56, 63]
	$[C_{16}H_{33}NMe_2(CH_2)_4NMe_2C_{16}H_{33}]^{2+}\,2Br^-$ [63]
	$[C_{12}H_{25}NMe_2(C_2H_4O)_3H]^+ Cl^-$ [56]

CosMX Exhibit 1008, Page 202 of 633

The two basic requirements for efficient bromine storage in zinc–bromine batteries, which need to be met in order to ensure low self–discharge and more over a substantial reduction of equilibrium vapor pressure of Br_2 of the polybromide phase in association with low solubillity of active bromine in the aqueous phase. As mentioned by Schnittke [4] the use of aromatic *N*–substituents for battery applications is highly problematic due to their tendency to undergo bromination. Based on Bajpai's pioneering work on vapor pressures [59] (see Fig. 2) and Eustace's [75] study of Br_2 distribution between the complex phase and overstanding aqueous solution in combination with stability considerations *N*–methyl, *N*–ethylmorpholinium bromide (MEM) and *N*–chloromethyl *N*–methylpyrrolidinium bromide (C–MEP) and analogous aliphatic heterocyclic compounds have confirmed their advantages for possible application in zinc–flow batteries.

Eustace noticed the correlation between asymmetric *N*–substitution and low melting points (at temperatures ≥ 15 °C) of the substances [75] observed in this study. The importance of sufficiently high specific densities of the "fused salts" for an efficient separation of the complex phase and the aqueous solution was emphasized. Mixtures of various quaternary ammonium bromides were tested subsequently [49, 51, 68, 77], aiming particularly at the avoidance of crystallization in the temperature range [0–50 °C], which is required for successful operation of flow batteries. No single compound was able to fulfill this demand. From tests of various ratios of MEP, MEM, and aliphatic ammonium bromides at 0, 50 and 100%

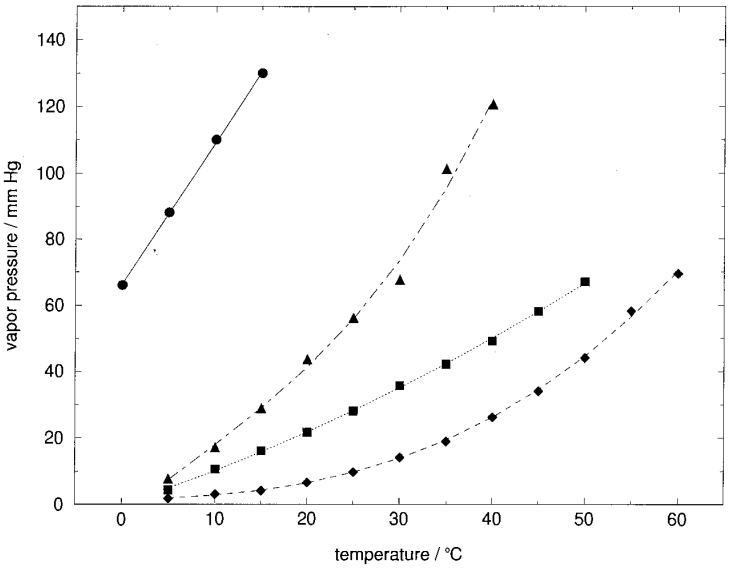


Figure 2. Vapor pressures of bromine/quaternary ammonium salt complexes: elemental Br_2, $Me_4N^+ Br^-$, MEMBr, $Oct_3MeN^+ Cl^-$. From Ref. [59].

CosMX Exhibit 1008, Page 203 of 633

state of charge (SOC) and different temperatures, mixtures of MEP and MEM were found to be particularly useful for bromine storage. The highly efficient potential of MEP for reducing the concentration of free Br_2 in the aqueous phase was pointed out. This fact was also mentioned by Bellows et al. [78] in their study of possibilities for improving the battery electrolyte. Table 3 [49] illustrates the results of that work.

Table 3. Equilibrium bromine concentrations in the aqueous electrolyte phase (taken from Ref. [49])

SOC	QBr	Br_2 concn. (mol L^{-1})		
		0 °C	25 °C	50 °C
0% SOC	MEM	0.095	0.187	0.270
	MEP	0.043	0.065	0.143
50% SOC	MEM	0.049	0.080	0.174
	MEP	0.033	0.037	0.123
100% SOC	MEM	0.115	0.141	0.174
	MEP	0.077	0.054	0.123

Kawahara [66] studied the influence of the molar ratio MEP:MEM on the rate of self–discharge in model batteries. This effect is strongly enhanced by high concentration of bromine in the aqueous electrolyte phase. As suggested by the curves in Fig.3, the ratio 3:1 seems to be the most effective among the mixtures under consideration over one complete charge process, which is represented here by the percentage of electrochemical deposition of the available Zn^{2+}. An evident decrease in the aqueous bromine concentration is a direct consequence of the high storage capacity of the complex phase. A small series of zinc–flow batteries using this MEP:MEM ratio are produced at present by the Powercell Co (Austria).

It should be kept in mind that not only are quaternary ammonium salts useful as complexing agents for bromine storage, but

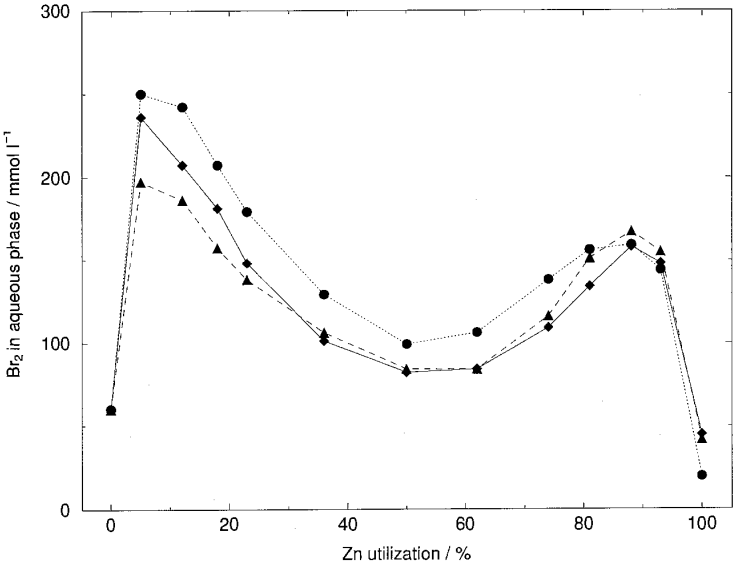


Figure 3. Bromine concentration in the aqueous phase in equilibrium with complexes of different MEP:MEM ratios: 1:1; 3:1, 9:1. Taken from Ref. [66]

CosMX Exhibit 1008, Page 204 of 633

they provide further advantages, in particular concerning the electrochemical deposition of zinc. Their behavior as leveling agents [79] and their dendritic growth inhibiting properties [80,81] are well known. Positive effects on the elimination of hydrogen evolution during the charge process by adding $NH_4^+Cl^-$ (~1:3 $NH_4Cl : ZnBr_2$) to the electrolyte have been reported [82].

5.3 Physical Properties of the Bromine Storage Phase

5.3.1 Conductivity

The conductivity of a number of bromine containing complexes with different quaternary ammonium cations was studied by Gerold (see Ref. [56]) with respect to the dependence on temperature and bromine content. Most of the substances yielded phases that were crystalline at ambient temperature but that could liquefied by addition of large amounts of Br_2.

Electrical conductivities of polybromide complexes containing MEP and MEM were studied by Arbes [73]. Pure MEPBr complexes always show higher conductivity than those containing only MEM, as long as equal amounts of Br_2 are added. According to these investigations the conductivities of the fused polybromide salts increase exponentially with the concentration of Br_2 reaching values typical for the aqueous electrolyte phases (11–20 Ω/cm) at very high bromine contents such as 3 mol Br_2/mol complexing agent.

The dependence on the temperature of the specific resistance (Ω/cm) of the pure MEPBr and MEMBr complexes, and a 1:1 mixture there of , as obtained in Ref. [73], is listed in Table 4. It is remarkable that within the complex phases consisting of Br_2 and either pure MEP or MEM the change of specific resistance at the liquid → solid phase transition amounts to about one order of magnitude, where as the value is only doubled in the 1:1 mixture. The table also indicates that MEMBr complexes possess higher melting temperatures.

Table 4. Specific resistance and states of aggregation of pure MEMBr and MEPBr complexes and a 1:1 mixture (taken from Ref. [73])

Temp (°C)	MEMBr		MEPBr		MEMBr/MEPBr (1:1)	
	Sp. resist. (Ω/cm)	State	Sp. resist. (Ω/cm)	State	Sp. resist. (Ω/cm)	State
0	287	s	194	s	180	s
10	173	s	113	s	93.4	l
20	124	s	28.7	l	43.1	l
30	43.1	l	24.2	l	33.3	l
40	32.3	l	19.3	l	25.6	l
50	24.3	l	16.2	l	21.1	l
60	20.1	l	14.1	l	17.5	l

Cathro et al. determined conductivity data of aqueous electrolyte phases containing MEP and MEM, varying the concentrations of $ZnBr_2$ and of the complexing agents as well as the temperature conditions [68]. Tables 5 and 6 contain a compilation of the results obtained at concentrations close to those occuring during operation of zinc-flow batteries. Aqueous

CosMX Exhibit 1008, Page 205 of 633

phases containing MEM were found to provide better conductivity than those containing MEP.

Table 5. Specific resistance (Ω/cm) of aqueous electrolyte containing MEM and 3 mol L^{-1} $ZnBr_2$ (taken from Ref. [68])

MEM (mol/L^{-1})	3 mol L^{-1} $ZnBr_2$		
	0 °C	25 °C	50 °C
0.0	17.2	9.9	7.4
0.5	22.5	12.7	9.0
0.7	24.5	14.0	11.4
1.0	30.8	15.9	11.6

Table 6. Specific resistance of aqueous electrolyte containing MEM or MEP at 25 °C (taken from Ref. [68])

Concn. (mol L^{-1})		Specific resistance (Ω/cm)	
$ZnBr_2$	QBr	QBr=MEP	QBr=MEM
1	0.3	11.4	9.8
2	0.65	12.1	11.2
3	1.0	16.5	15.9

Eustace [75] studied the specific resistance of samples of bromine–fused salt phase produced by electrolysis of 3.0 mol L^{-1} $ZnBr_2$ and 1.0 mol L^{-1} MEM at 23 °C. As is shown in Fig. 4, a considerable resistance is observed in the initial phase of the charge process, dropping to approximately one-third at 30% Zn utilization. At higher states of charge the increase in the conductivity is significantly slower.

Table 7. Conductivity λ of the polybromide phase at 50% SOC and various contents of Zn^{2+} (taken from Ref. [72])

$[Zn^{2+}]$ (mol L^{-1})	λ (S/cm^{-1})	Temp (°C)
0.00	3.42×10^{-2}	20
0.07	3.53×10^{-2}	20
0.60	2.76×10^{-2}	20
0.95	2.07×10^{-2}	20
2.05	0.58×10^{-2}	21

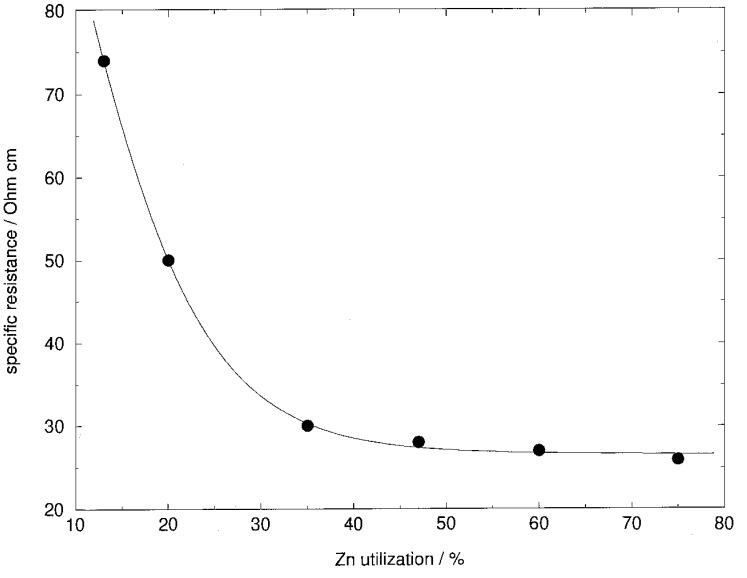


Figure 4. Specific resistance of a pure MEM-polybromide complex phase at 23 °C at various states of charge (represented by zinc utilization). Taken from Ref. [75].

CosMX Exhibit 1008, Page 206 of 633

Corresponding to the state of charge, variable concentrations of Zn-containing complex anions ($[ZnX_n(OH)_m]^{q-}$ with X being Cl or Br, q=1,2 and integers n,m ranging from 0 to 4) were detected in the complex polybromide phase. As is evident from Table 7 compiled by Hauser [72], the electrical conductivity decreases with increasing amounts of zinc. This effect is associated with a rise in the concentration of Br_2 in the equilibrated aqueous phases. The increase in specific conductivity of the complex phase with temperature shown in Table 4 was confirmed by Hauser [72] and Niepraschk [50]; however, the latter reported essentially higher values for the polybromide phase than for the aqueous phase of the electrolyte. He estimated the maximum conductivity to be achieved at ~9 mol Br_2/L complex phase. Figure 5 shows the conductivity of MEM and MEP at different temperatures and Br_2 concentrations. From the temperature dependence of the conductivity the activation energy for the transport of charge can be obtained applying Arrhenius' equation,

$$k = k_0 e^{-\frac{E_A}{RT}} \quad (1)$$

Niepraschk [50] found 23.4 kJ mol^{-1} for pure MEMBr complex and 16.5 kJ mol^{-1} for pure MEPBr complexes at 3 mol Br_2/mol complexing agent. These values increase slightly with decreasing concentration of Br_2. A value of E_A of 11.5 kJ mol^{-1} for a complex phase containing MEP:MEM in the ratio 3;1 at comparable contents of Br_2 was reported by Hauser [72].

5.3.2 Viscosity and Specific Weight

The kinematic viscosity of MEM containing aqueous electrolytes at different concentrations of MEM and $ZnBr_2$ and at different temperatures has been studied [68] (see Table 8).

Kinematic viscosities of aqueous electrolyte phases containing $Et_4N^+Br^-$ and $Bu_4N^+Br^-$ and various concentrations of $ZnBr_2$ were studied by Cedzynska [77]. Ionic conductivity of bromine storing phases was estimated [56] by applying the

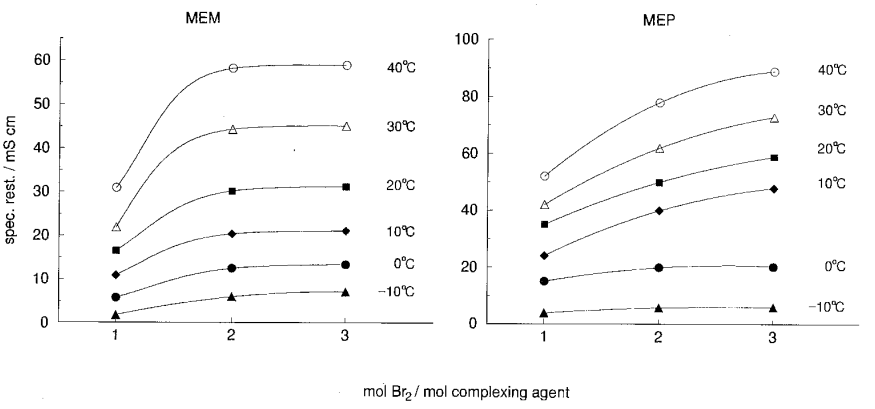


Figure 5. Isotherms for the conductivity of pure MEM and MEP-complex phases (mS/cm^{-1}) versus degree of added Br_2. Taken from Ref. [50].

CosMX Exhibit 1008, Page 207 of 633

Pisarzhevski–Walden equation to measured values of the dynamic viscosity. However, use of this relation is only correct for solutions in the limit of zero concentration and no change in solution mechanism.

Table 8. Kinematic viscosity ($m^2 s^{-1}$) of aqueous electrolyte containing MEM and 3 mol L^{-1} $ZnBr_2$ (taken from Ref. [68])

MEM	3 mol L^{-1} $ZnBr_2$		
(mol/L^{-1})	0 °C	25 °C	50 °C
0.0	2.786	1.371	0.786
0.5	3.722	1.665	0.960
0.7	4.153	1.809	1.048
1.0	4.996	2.175	1.215

Eustace [75] reported a dynamic viscosity of 25 cP a pure MEMBr complex phase at 23 °C. (The specific weight was 2.3 g cm^{-3}).

Typical specific weights of bromine storing complex phases between 10 and 70°C at bromine concentrations in the range of 1–4 mol/mol complexing agent lie around 2.45 ± 0.1 g cm^{-3}. Densities as a function of temperature at various bromine contents of a number of quaternary ammonium salts were given by Gerold [56].

Viscosities and specific weights of complexes and the corresponding aqueous phases, with the aim of simulating realistic battery conditions with MEP:MEM ratio of 1:1, 3:1 and 6:1 in the electrolyte at 50, 75 and 100% states of charge, were studied in a temperature range between ~10 and 50 °C [83]. Kinematic viscosities between $5 \cdot 10^{-6}$ and $30 \cdot 10^{-6}$ $m^2 s^{-1}$ of the complex phases were found. MEP–rich ones.

5.3.3 Diffusion Coefficients

From the value of the diffusion coefficient of Br_2 in electrolyte solutions, conclusions can be draw concerning mass transport in the diffusion layer on the anode surface. Cathro et al. [68] used the rotating disc electrode in order to determine the diffusion coefficients of bromine in aqueous electrolyte phases containing various concentrations of MEM,MEP and $ZnBr_2$. The results are listed in Table 9. It was found that aqueous electrolytes containing MEP exhibit diffusion coefficients higher by ~6% compared with those with MEM. A compilation of diffusion coefficients of Br_2 in various electrolytes is given in Table 10.

Table 9. Diffusion coefficients of Br_2 in the aqueous electrolyte phase at 25 °C (taken from Ref. [68])

Concn. (mol L^{-1})		Specific resistance (Ω/cm)	
$ZnBr_2$	QBr	QBr=MEP	QBr=MEM
1	0.3	1.00	0.95
2	0.65	0.61	0.59
3	1.0	0.38	0.35

Table 10. Diffusion coefficients of Br_2 in the aqueous electrolytes at 25 °C

Diff. coeff. (10^{-9} m^2 s^{-1})	Electrolyte	Ref
0.99	1.0 mol L^{-1} $ZnBr_2$	[84]
1.23	1.0 mol L^{-1} $ZnBr_2$	[68]
1.21	0.1 mol L^{-1} KBr	[85]
1.44	2.2 mol L^{-1} KCl	[86]
2.00	Not reported	[87]

Karigl [71] defined a format diffusion coefficient for bromine transport through a polythylene separator of a zinc–flow battery by considering the separator a diffusion layer. A value of $D_{sep}(Br_3^-) = 2.77 \cdot 10^{-10}$ m^2 s^{-1} was obtained.

Diffusion coefficients of Br_2 in aqueous electrolyte phases containing $Et_4N^+Br^-$, $Bu_4N^+Br^-$ were studied by Cedzynska [77] at various concentrations of $ZnBr_2$. Attempts towards finding an ideal modified (MOD) electrolyte consisting of MEM, MEP, $MeEt_2PrN^+Br^-$ and $Bu_4N^+Br^-$ were made[51].

CosMX Exhibit 1008, Page 208 of 633

5.3.4 State of Aggregation

An indispensable requirement for an efficient complexing agent usable in a zinc–flow battery is a sufficiently low melting point of the corresponding complex phase. By this criterion the application of a vast number of quaternary ammonium cations is ruled out. Low melting points of the bromine-storing phase can commonly be achieved by combinations of two or more different complexing agents. As was anticipated by Gibbard [88], asymmetric substitution of the tendency of the complex crystallize.

Cathro et al. [49] found that the use of mixtures of QBr-compounds (Q = quaternary ammonium) may give a liquid polybromide phase, even though the individual components form solid or highly viscous polybromides. With the two chloro compounds C–MEM and C–MEP white precipitates were formed at 0 °C upon mixing with an aqueous solution of 1 mol/L^{-1} $ZnBr_2$. Symmetrically substituted QBr compounds such as $Me_4N^+Br^-$ and $Et_4N^+Br^-$ yielded solid polybromide phases over wide ranges of temperature and composition [49]. A pronounced influence not only of the temperature but also of the bromine contents of the complex phases is reviewed. Results for the corresponding aqueous phases of the electrolyte can be found in the original paper, which also contains studies of a number of electrolyte phases made up of MEM:MEP mixtures.

5.4 Analytical Study of a Battery Charge Cycle

In order to improve the bromine storing capacity and hence the battery efficiency of a zinc-flow cell, knowledge of the structure and consistency of the complex phase during the entire charge–discharge cycle is an essential requirement.

Until today the only available data obtained by direct sampling of a prototype battery system concerning mass flow of the complexing agents as well as the Br_2 produced in both the aqueous and non-aqueous electrolyte phases have been gained by application of Raman spectroscopy [89, 90].

The most interesting results of a study of a real 12 V/1 kWh zinc-flow battery (Powercell Lda.) with a charge capacity of 92 Ah are reviewed in Figs. 6 and 7.

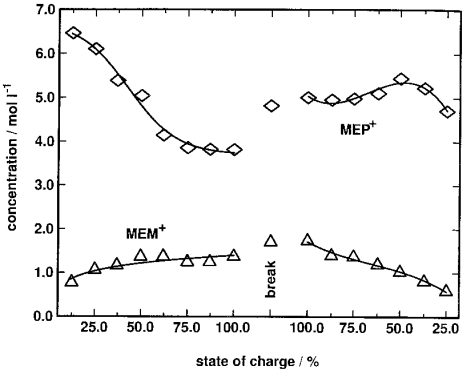


Figure 6. Concentration of the complexing cations MEP^+ (Δ) and MEM^+ (◊) in the complex electrolyte phase during one total charge–discharge cycle of a model zinc-flow battery. Taken from Ref. [90].

phase of the charging procedure shows a very high MEP:MEM ratio (~8:1), reaching the value 3:1 only after 50% SOC. This effect is determined by reaction kinetics and availability of the complexing An electrolyte composition of 3:1 MEP:MEM was used from Fig. 6 it is evident that the complex formed in the initial agents in the cell compartment. During the discharge process, when complex of es-

CosMX Exhibit 1008, Page 209 of 633

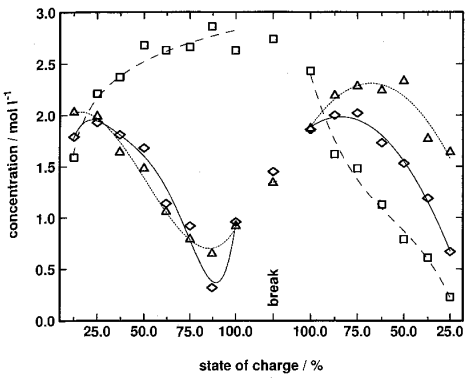


Figure 7. Concentration of Br_2 (◊), Br_3^- (Δ) and Br_5^- (□) in the complex electrolyte phase during one total charge–discharge cycle of a model zinc-flow battery. Taken from Ref. [90].

sentially similar composition was delivered to the anode, MEM was found to be released from the complex more easily then MEP. From these results higher stability of MEP–rich complex phases under the battery operation conditions can be deduced.

An estimate of the concentrations of the individual polybromide anions and of Br_2 in the complex phase during the same charge–discharge cycle, derived from spectral data, is plotted in Fig. 7. The curves indicate a pronounced tendency toward Br_5^- formation during the charge period, but domination of Br_3^- and Br_2 species while the battery is discharging. Highest concentrations of pentabromide seem to be correlated with low contents of complexing agents. Further conclusions from these data must be drawn with extreme caution due to the sensitivity of the equilibrium between the bromine species to thermal effects, influences of the electric fields, and the uncertainties inherent in the underlying mathematical model used for data analysis.

The authors suggested testing of the application of higher MEP:MEM ratios zinc–flow batteries. It should be noticed that the results from a study of the mass flow in the aqueous parts of the system [89] correlated favorably with the findings described above.

5.5 Safety, Physiological Aspects, and Recycling

5.5.1 Safety

Safety risks and the environmental impact are of major importance for the practical success of bromine storage system. The nonaqueous polybromide complexes in general show excellent physical properties, such as good ionic conductivity (0.1–0.05 $\Omega\,cm^{-1}$), oxidation stability (depending on the nature of the ammonium ion), and a low bromine vapor pressure. The concentration of active bromine in the aqueous solution is reduced by formation of the complex phase up to 0.01–0.05 mol/L^{-1}, hence ensuring a decisive decrease of self–discharge.

Figure 2 demonstrates that the bromine vapor pressure over a complex phase remains remarkably low with increasing temperature and is not a critical factor restricting battery operation. Even at ~60 °C, vapor pressures of Br_2 reaching only a few percent of the atmospheric pressure and that of elemental bromine are obtained.

Moreover, calculations on the evaporation rate of bromine from the complex phase were carried out assuming a worst–case scenario, namely a complete spill age of the total bromine inventory (as polybromide complex) of a fully charge (100% SOC) 15 kWh module which means ~32.5 kg of available Br_2, forming a 10 m^2

CosMX Exhibit 1008, Page 210 of 633

pool on the ground as a consequence of battery damage. The rates of bromine evaporation from the complex phase in air were measured in laboratory tests [91] under various conditions (flow, temperature). The results are presented in Fig. 8.

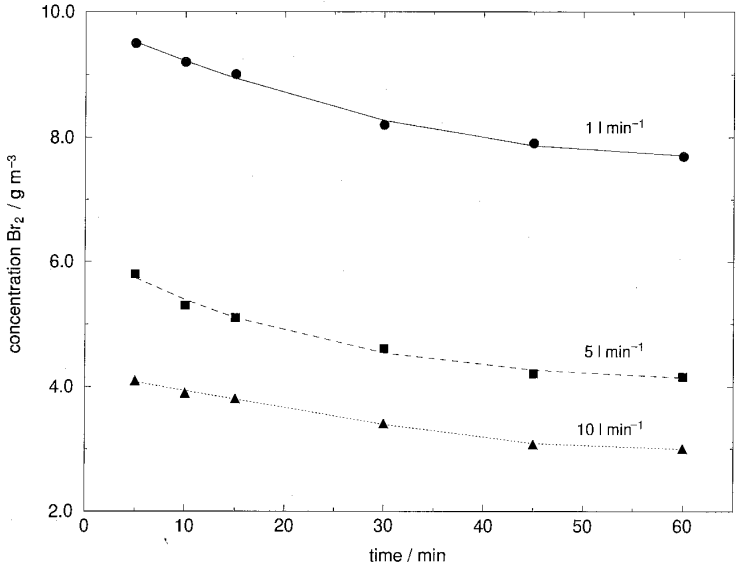


Figure 8. Evaporation rate of bromine from the complex phase at 100% SOC in air. is shown on each curve. Taken from Ref. [69].

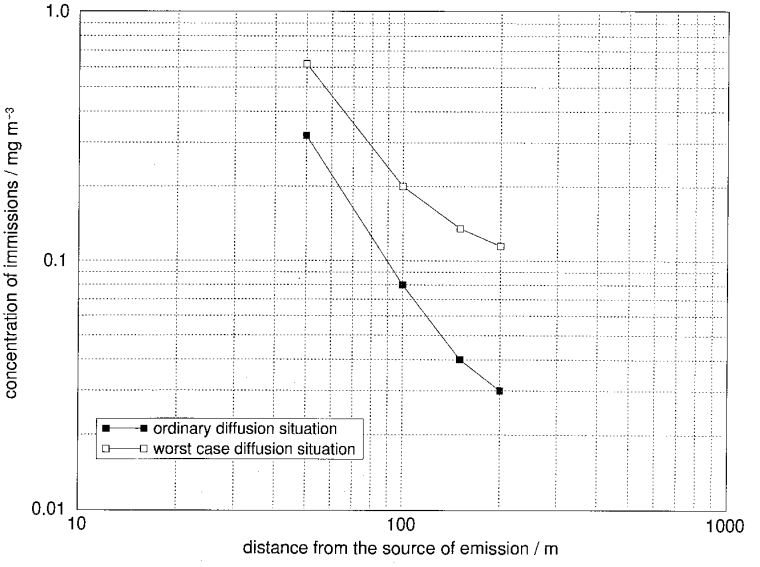


Figure 9. Diffusion of bromine after evaporation from a pool of complex phase at 20 °C. Taken from Ref. [69].

CosMX Exhibit 1008, Page 211 of 633

Figure 9 shows the distribution of bromine emissions (concentrations) as a function of distance from the source of emission, assuming various atmospheric conditions (air flow) at 20 °C. The maximum admissible concentration (MAK value) of 0.7 mg m^{-3} (0.01 ppm) is reached within about 50 m under worst-case atmospheric condition, whereas higher and dangerous values are observed close to the place of complex spillage. However, the assumptions serving as the basis for these estimates and calculations appear rather unrealistic, considering the low probability of a complete release of the complex phase at 100% SOC from the reservoir and of the distribution on the ground, and moreover neglecting the role of the aqueous electrolyte solution which is also present and tends to spread on the complex surface due to its lower density.

The most important safety-relevant measures involving automatic control during battery operation are:

- thermal management, at a maximum of 42 °C;
- automatic pumps and flow control, leakage sensor and pumps that stop automatically in the case of bromine escaping from the stack;
- overcharge control.

As shown by several investigations [91], the bromine-rich polybromide phase by itself is hardly flammable and fire-extinguishing properties have been reported occasionally. The formation of polybrominated dibenzo-dioxins (PBrDD) and furans (PBrDF) due to the plastic-containing housing of a zinc-flow battery cannot be totally neglected in the case of a fire, but their concentrations are far away from the tetrachloro dibenzodioxine (TCDD) toxic equivalents even in a worst-case scenario.

5.5.2 Physiological Aspects

Elemental bromine is a readily evaporating liquid (p_{Br} at 1 °C = 0.23 bar) with high reactivity. Because of the good solubility of Br_2 in lipids, its aggressive and toxic properties affect skin and mucous membranes (bronchi). The MAK value of elemental Br_2 is defined as 0.1 ppm (0.7 mg m^{-3}), while the sense of smell is affected at a value of 0.01 ppm. The lethal concentration (around 100–200 ppm) is reached for example, by twice the MAK value, 5 min, eight times per working unit [91, 92].

Storage of bromine by formation of a polybromide phase with a lowering of the vapor pressure by more than one magnitude, to at least 10% of the value of Br_2 at maximum, is the basic requirement for safe application in zinc-flow batteries [91, 92]. No information is available concerning negative health effects of the complexing agents MEM and MEP.

5.5.3 Recycling

Recycling of the major valuable battery components is an important factor influencing the introduction into the market and the economic development of the system. Figure 10 shows a breakdown of the materials and components, their weight fractions and recyclability.

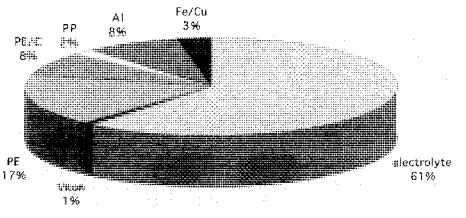


Figure 10. Materials used in a battery, and their recyclability. Taken from Ref. [69].

CosMX Exhibit 1008, Page 212 of 633

Recycling of the electrolyte from used, damaged, or faulty batteries and reuse in new stacks have gained considerable attention. The electrolyte is an essential constituent from the technical and economic viewpoint, showing extraordinary stability and no ageing effects.

5.6 References

[1] R. Zito, US Patent 3 382 105, 3 640 770, 3 640 771, 3 642 738, 3 719 526, **1968–1973**.

[2] M. Eskra, P. Eidler, R. Miles, Zinc–bromine battery development for electric vehicle applications, *Proc. 24th Int. Symp. Automotive technology and Automation, Florence,* **1991**.

[3] EXXON Research Cooperation, *Monthly Progress Report*,April **1980**.

[4] A. Schnittke, Ph. D. Thesis, Ernst-Moritz-Arndt-Univ. Greifswald, (in German), **1992**.

[5] R. Movahedi, Ph. D. Thesis, TU Vienna (in German), **1977**.

[6] A. H• rold, Crystallo-chemistry of carbon intercalation compounds, in *Intercalated Materials* (Ed. F. Levy), D. Reidel, Dordrecht, **1979**, pp. 323–421.

[7] J. C. Rubim, O. Sala, *J. Raman Spectrosc.* **1980**, *9*, 155.

[8] J. C. Rubim, O. Sala, *J. Raman Spectrosc.* **1981**, *11*, 320.

[9] M. Mastragostino, S. Valcher, *Electrochem. Acta* **1983**, *28(4)*, 501–505.

[10] G. Mengoli, M. M. Musiani, R. Tomat, S. Valcher, D. Pletcher, *J. Appl. Electrochem* **1985**, *15*, 697–704.

[11] R. M. Ottenbrite, *Polym. Bull.* **1981**, *6*, 225–228.

[12] J. Manassen, I. Cabasso, *J. Electrochem. Soc.* **1989**, *136*, 578.

[13] H. Irving, P. D. Wilson, *J. Inorg. Nucl. Chem.* **1964**, *26*, 2235.

[14] I. Vogel, Ph. D. Thesis, TU Dresden, Sektion Chemie (in German) **1990**.

[15] A. I. Popov, in *Halogen Chemistry* (Ed. V. Gutmann), Academic Press, New York, **1967**, pp. 225–264.

[16] T. Surles, A. I. Popov, *Inorg. Chem.* **1969**, *8(10)*, 2049.

[17] D. B. Scaife, H. J. V. Tyrell, *Chem. Soc.* **1958**, *386*, as reported by A. Gerold, Master's Thesis, TU Dresden, Sektion Chemie (in German), **1991**.

[18] M. P. Bogaard, J. Peterson, A. D. Rae, *Cryst. Struct. Commun* **1979**, *8*, 347.

[19] J. Ollis, V. J. James, D. Ollis, M. P. Bogaard, *Cryst. Struct. Commun* **1976**, *5*, 39.

[20] M. P. Bogaard, A. D. Rae *Cryst. Struct. Commun* **1982**, *11*, 175.

[21] W. Gabes, D. J. Stufkens, H. Gerding, *J. Mol. Struct.* **1973**, *17*, 329.

[22] K. Fries, *Ann. Chem.* **1906**, *346*, 217.

[23] H. E. L. Horton, **1888**, *Chem. Ber. 21*, 2000.

[24] A. M. Ajami et al.,US Patent **1977**.

[25] P. Singh, K. White, A, J. Parker, *J. Power Sources* **1983**, *10*, 309.

[26] G. Henning, J. D. McClelland, *J. Chem. Phys.* **1975**, *23*, 1431.

[27] J. C. Rouillon, A. Marchand, *C.R. Acad. Sci. Paris* **1972**, *112*, 274.

[28] K. Aoki, *J. Mater. Sci.* **1971**, *6*, 140.

[29] C. Mazieres, G. Colin, J. Jegoudez, R. Setton, *Carbon* **1975**, *13*, 289.

[30] K. Miyauchi, Y. Kakahashi, *Carbon* **1976**, *14*, 35.

[31] F. Bloc, Ph. D. Thesis, Nancy **1964**.

[32] F. H. Herbstein, M. Kapon, G. M. Reisner, *Proc. R. Soc Lond., Ser. A* **1981**, *376*, 301.

[33] D. W. Kalina, J. W. Lyding, M. T. Ratajack, C. R. Kannewurf, T. J. Marks, *J. Am. Chem. Soc.* **1980**, *102*, 7854.

[34] K. F. Tebbe, in *Homoatomic Rings, Chains and Macromolecules of Main-Group Elements* (Ed. A. L. Rheingold), Elsevier, Amsterdam, **1977**, pp. 551–606.

[35] W. B. Person, G. R. Anderson, J. N. Fordemwalt, H. Stammreich, R. Forneris, *J. Chem. Phys.* **1961**, *35*, 908.

[36] J. C. Evans, G. Y-S. Lo, *Inorg. Chem.* **1967**, *6*, 1483.

[37] G. Bellucci, R. Bianchini, C. Chiappe, R. Ambrosetti, *J. Am. Chem. Soc.* **1989**, *111*, 199.

[38] N. N. Greenwood, A. Earnshaw, *Chemie der Elemente*, VCH, Weinheim, Germany, **1990** (in German).

[39] G. A. Bowmaker, P. D. Boyd, R. J. Sorrenson, *J. Chem. Soc., Faraday Trans.2* **1984**, *80*, 1125.

[40] J. Bertelot, C. Guette, P. -L. Desb• ne, J. -J. Basselier, P. Chaquin, D. Masure, *Can. J. Chem.* **1990**, *68*, 464.

[41] G. L. Gutsev, *Russ. J. Phys. Chem.* **1992**, *66*,

CosMX Exhibit 1008, Page 213 of 633

1596.
[42] Z. Lin, M. B. Hall,*Polyhedron* **1993**, *12*, 1499.
[43] P. Schuster, G. Bauer, H. Mikosch, C. Fabjan, J. Drobits, to be published.
[44] G. L. Breneman, R. D. Willet, *Acta Crystallogr. Sect. C* **1986**, *42*, 1614.
[46] G. R. Burns, R. M. Renner, *Spectrochim. Acta Sect. A* **1991**, *47*, 991.
[47] T. X. Wang, M. D. Kelley, J. N. Cooper, R. C. Beckwith, D. W. Margerum, *Inorg. Chem.* **1994**, *33*, 5872.
[48] P. M. Hoobin, K. J. Cathro, J. O. Niere, *J. Appl. Electrochem.* **1989**, *19*, 943–945.
[49] K. J. Cathro, K. Cedzynska, D. C. Constable, P. M. Hoobin, *J. Power Sources* **1986**, *18*, 349.
[50] H. Niepraschk, Master's Thesis, TU Dresden, **1988** (in German).
[51] K. Cedzynska, *Electrochim. Acta* **1995**, *40(8)*, 971.
[52] G. R. Burns, R. M. Renner, *Spectrochim. Acta Sect. A*, **1991**, *47*, 991.
[53] P. L. Mercier, C. A. Kraus, *Proc. Nat. Acad. Sci.* USA **1956**, *42*, 487.
[54] F. Rallo, P. Silvestroni, *Gazz. Chem. Ital.* **1973**, *103*, 1011; idem, *J. Electrochem. Soc.* **1972**, *119(11)*, 1471.
[55] I. Rubinstein, M. Bixon, E. Gileadi, *J. Phys. Chem.* **1980**, *84*, 715.
[56] A. Gerold, Master's Thesis, TU Dresden, Sektion Chemie, **1991** (in German).
[57] G. Clerici, M. Rossi, M. Marcheto, D. H. Collins, *Power Sources 5* Academic Press, London, **1974**, p. 167.
[58] R. Bloch, US Patent 2 566 114, **1951**.
[59] S. N. Bajpai, *J. Chem. Eng. Data* **1981** *26(1)*, 2.
[60] K. Kinoshita, S. C. Leach, C. M. Ablow, *J. Electrochem. Soc.* **1982**, *129(11)*, 2397.
[61] G. W. M• esen, C. A. Kraus, *Proc. Nat. Acad. Sci.* USA **1952**, *38*, 1023.
[62] I. Vogel, A. M• bius, *Electrochim. Acta* **1991**, *36(9)*, 1403.
[63] G. Jacob, Master's Thesis, TU Dresden Sektion Chemie, **1986** (in German).
[64] F. D. Chattaway, G. Hoyle, *J. Chem. Soc.* **1923**, 654.
[65] Y. Kume, D. J. Nakamura, *J. Magn. Reson.* **1976**, *21*, 235.
[66] K. Kawahara, 4th *Int. Zinc–bromine Battery Symp. Perth, Australia*, Toyota Central R&D Inc. Handout, Feb. **1987**.
[67] C. Fabjan, G. Hirss, *Dechema Monographie* 102, VCH Weinheim, **1986**, p. 149 (in German).
[68] K. J. Cathro, K. Cedzynska, D. C. Constable, *J. Power Sources* **1985**, *16*, 53.
[69] C. Fabjan, H. Kronberger, • *sterreich. Z. Energiewirt.* (• ZE) **1993**, *46(9)*, 451 (in German).
[70] W. St• ckl, Ph. D. Thesis TU Vienna **1988**, (in German).
[71] B. Karigl, Ph. D. Thesis TU Vienna **1993**, (in German).
[72] R. Hauser, Ph. D. Thesis TU Vienna **1993**, (in German).
[73] G. Arbes, Ph. D. Thesis TU Vienna **1984**, (in German).
[74] C. Fabjan, K. Kordesch, *Studie und Vorprojekt: Zink–Halogen Batterie / Elektrofahrzeug*, VEW AG Wien, **1982**, *54*, 1 (in German).
[75] D. J. Eustace, *J. Electrochem. Soc.* **1980**, *127*, 528.
[76] A. M• bius, J. Vogel, G. Jakob, K. Grosser, J. Beger, R. Jacobi, C. P• schmann, Word Patent 308 178, **1987**.
[77] K. Cedzynska, *Electrochim. Acta* **1989**, *34(10)*, 1439.
[78] R. J. Bellows *First Int. Zinc–Bromine Battery Symp., Jan 1985*, Final Progress Report, at S.E.A. M• rzzuschlag, Austria, **1985**.
[79] G. Bauer, J. Drobits, C. Fabjan, H. Kronberger, H. Mikosch, P. Schuster, *Elektrochemie der Elektronenleiter, GDCh-Monographie 3*, pp. 121–135, **1996** (in German).
[80] Meidensha Electric Mfg. Co. Ltd., Japan, Japanese Patent 82-129626 820727, **1982** (in Japanese).
[81] Meidensha Electric Mfg. Co. Ltd., Japan, Japanese Patent 82-88911 820527, **1982** (in Japanese).
[82] Ando, Y. (Meidensha Electric Mfg. Co. Ltd., Japan), Japanese Patent 87–209151 870825, **1987** (in Japanese).
[83] J. Drobits, P. Schuster, C. Fabjan, in preparation.
[84] J. Lee, R. Selman, *J. Electrochem. Soc.* **1983**, *130*, 1237.
[85] O. R. Osipov, M. A. Novitskii, Y. M. Povarov, P. D. lukovtsev, *Sov. Electrochem.* **1972**, *8*, 317.
[86] G. N. Voloshina, V.I. Ksenzenko, S. Abdyev, T. Chemleva, *Isv. Akad. Nauk Turkm. SSR, Ser. Fiz.-Tekh. Khim. Geol. Nauk*, **1978**, 64, as reported in Ref. [68].
[87] R. J. Bellows, D. J. Eustace, P. Grimes, J. A.

CosMX Exhibit 1008, Page 214 of 633

Shropshire, H. S. Tsien, A. F. Venero, *Power Sources 7*,(Ed. J. Thompson), Academic Press, London, **1979**, p. 301.
[88] H. F. Gibbard, UK Patent Application Great Britain, **1979**.
[89] G. Bauer, J. Drobits, C. Fabjan, H. Mikosch, P. Schuster, *Chem. Ing. Tech.* **1996**, *68*, 100 (in German).
[90] G. Bauer, J. Drobits, C. Fabjan, H. Mikosch, P. Schuster, *J. Electroanal. Chem.* **1997**, *427*, 123.
[91] Steininger, T• V-Bayer, G3-UTM50, November 25 **1991** and 1 October **1992** (in German).
[92] K. O. Schallaböck, E. Lichtl, *Vorausschauende Umweltverträglichkeitsprüfung für Zink-Brom-Batterien, inst. für Umweltforschung, Forschungsgesellschaft Johanneum, Graz, Austria*, **1984** (in German).

CosMX Exhibit 1008, Page 215 of 633

6 Metallic Negatives

L. O. Binder

6.1 Introduction

Although many different abbreviations for primary and secondary (or storage) batteries are used, the correct form of displaying a battery system is the following:

(–) *Anode material / Electrolyte / Cathode material* (+)

Therefore, being the negative electrode in the system, the anodes are frequently called "negatives". When the battery is ready for use (discharge) the typical battery anode consists of a metal in the form of either sheet, powder, or an electrolytic deposit. The last version is usually found in some of the secondary (storage) batteries. During discharge the metal is oxidized to metal ions delivering a number of electrons corresponding to the positive charge of the cation:

$$M \rightarrow M^{n+} + ne^- \qquad (1)$$

The electrons sustain the current via external load and are used to reduce the active material of the cathode (positive). In the case of storage batteries, the ideal anodic and cathodic reactions are completely reversible.

6.2 Overview

Since numerous metals are used as anodes (negatives) in a variety of battery systems with aqueous electrolyte, there are different ways of arranging them in groups to obtain easier access to the required information. Useful selection categories may be:

(A) the chemical elements (iron, zinc, lead, etc.);
(B) battery types (primary, storage, etc.);
(C) method of anode preparation (metal, metal oxide, or hydroxide + subsequent reduction, other metal compounds + reduction, etc.).

The most suitable way to organize the different metallic negatives in groups seems to be by a combination of these three classifications, using one as the main criterion and the others to create subdivisions. Such a system is demonstrated in the following example:

1st parameter:
(A) Element name (in alphabetical order)
2nd parameter:
(B) Battery type:

CosMX Exhibit 1008, Page 216 of 633

(AB1) primary;
(AB11 ..., AB1*n*) cathodes;
(AB2) storage;

3rd parameter:

(C) Method of preparation:
(AB2C1) introduced in metallic form;
(AB2C2) introduced as metal oxide or hydroxide;
(AB2C3) introduced as other metal compound.

The categories (AB2C1) to (AB2C3) may be similarly subdivided by considering the different cathode materials and thus defining a particular battery system.

6.3 Battery Anodes ("Negatives")

6.3.1 Aluminum

Aluminum is directly applied in its metallic form when it serves as battery anode. The battery concepts considered are in general single-use types (primary batteries). The most developed systems belong to the "metal–air" batteries, using the reduction of atmospheric oxygen as the cathode reaction, e.g., (–) Al / KOH / O_2 (+) or (–) Al / seawater / O_2 (+). The main discharge reactions are:

Anode:

$$4Al \rightarrow 4Al^{3+} + 12e^- \quad (2)$$

Cathode:

$$3O_2 + 6H_2O + 12e^- \rightarrow 12OH^- \quad (3)$$

Overall cell reaction:

$$4Al + 3O_2 + 6H_2O \rightarrow 4Al(OH)_3 \quad (4)$$

In principle all these reactions may be run in pure water but, in order to obtain sufficiently high currents, electrolytes with better conductivity (aqueous solutions of KOH or seawater [1]) are necessary. The latter is found only in naval applications. Although high-purity aluminum (up to 99.999%) is used in science and research dealing with the main discharge reactions and battery design concepts, most prototypes and batteries are built with aluminum alloys. Such materials are Alcan AB, ERC 3–4, Alcan BDW [2, 3] or S1–S6 (binary aluminum–tin alloys) [4]. Aluminum/air batteries with their high specific energy and energy density will find particular applications today and in the near future. The aluminum anode contributes significantly by its outstanding electrochemical equivalent of 2980 Ah/kg. The open-circuit voltage (OCV) of 2.73 V is another argument for the choice of this battery system.

6.3.2 Cadmium

Although one of the most common storage batteries is called the "nickel/cadmium" system ("NiCad"), correctly written (–)Cd/KOH/NiO(OH)(+), cadmium is not usually applied as a metal to form a battery anode. The same can be said with regard to the silver/cadmium [(–) Cd / KOH / AgO (+)] and the "MerCad" battery [(–)Cd/KOH/HgO(+)]. The "metallic negative" in these cases may be formed starting with cadmium hydroxide, incorporated in the pore system of a sintered nickel plate or pressed upon a nickel-plated steel current collector (pocket plates), which is subsequently converted to cadmium metal by electrochemical reduction inside the cell (type AB2C2). This operation is done by the customers when they start the application of these (storage)

CosMX Exhibit 1008, Page 217 of 633

batteries according to the users' manual by inserting them into the appropriate charger for a certain time (e.g., overnight). Cadmium hydroxide for anode formation usually contains some additives (e.g., iron, nickel, graphite) and — in some cases — polymer binding agents [5, 6].

The other method is cadmium electrodeposition on a nickel-plated steel foil (serving as current collector) using a plating bath containing acidified cadmium sulfate (type AB2C3). In this case the user is supplied with a battery in charged ("ready for use") condition.

The reversible anodic charge–discharge reaction is:

$$Cd(OH)_2 + 2e^- \leftrightarrow Cd + 2OH^- \qquad (5)$$

Due to a high hydrogen overvoltage of cadmium in the caustic electrolyte, no amalgamation is needed. The electrochemical equivalent of about 480 Ah/kg is one of the lowest for all metallic anodes and the open circuit voltage of 1.35 V for the "NiCad" is not favorable for many applications. Additionally, people want to restrict the use of cadmium for environmental reasons. The replacement of nickel/cadmium batteries by nickel/metal hydride cells may have been seen in this light. The better performance of the latter (about 30%) is not such a strong argument for paying the much higher price. The advantages are only the flat discharge curve and the extremely good cycle life.

6.3.3 Iron

Probably the best-known battery system using an iron anode is called the nickel/iron battery. It should be written: (–) Fe / KOH / NiO(OH) (+), having its merits as a heavy-duty accumulator [7]. By far less famous and much more recent are the applications of iron anodes in (rechargeable) iron/air cells [(–)Fe/KOH/O_2(+)] [8, 9] and in iron/silver oxide batteries (–) Fe / KOH(+LiOH) / AgO (+) [10, 11].

The composition of an iron anode includes Fe_3O_4 (produced by partial reduction of Fe_2O_3 with hydrogen), iron powder, and additives (e.g., sulfur, FeS, HgO). One group of inventors claims 2000 cycles for an iron electrode containing ZnS as main additive [12]. This mixture is converted to the active iron anode either by internal reduction (AB2C2) or by high-temperature external reduction (AB2C1) [13, 14].

The discharge–charge reaction of this electrode will be done in two steps but only the first step ($Fe \leftrightarrow Fe^{2+} + 2e^-$) is of practical use. For the iron/nickel oxide–hydroxide system these steps (or voltage plateaus) may be written as:

$$Fe + 2NiO(OH) + 2H_2O \leftrightarrow 2Ni(OH)_2 + Fe(OH)_2 \qquad (6)$$

$$3Fe(OH)_2 + 2NiO(OH) \leftrightarrow 2Ni(OH)_2 + Fe_3O_4 + 2H_2O \qquad (7)$$

The overall reaction is:

$$3Fe + 8NiO(OH) + 4H_2O \leftrightarrow 8Ni(OH)_2 + Fe_3O_4 \qquad (8)$$

The electrochemical equivalent of iron (if only the first step is taken into account) is 960 Ah/kg and the open-circuit voltage of the "nickel/iron" cell is 1.4 V.

6.3.4 Lead

The lead electrode used as anode in the well-known lead–acid battery is a rather

CosMX Exhibit 1008, Page 218 of 633

complex structure consisting of a metallic grid (lead–antimony, lead–calcium, or other alloys [15]) filled with a paste made from particles of the active mass, sulfuric acid, and various additives (e.g., expanders). The active mass originally consists of oxidized lead grains with a residual metal content of about 30%. These grains come either from a Barton reactor or from a ball mill. Their particular properties are described in Chapter II, Sec.4. The pasted and cured anode plates have to pass through the formation process, which is nothing else than an external electrochemical reduction done in sulfuric acid (AB2C1). The regular discharge reaction follows a dissolution/precipitation mechanism as follows:

$$Pb \leftrightarrow Pb^{2+} + 2e^- \qquad (9)$$

$$Pb^{2+} + SO_4^{2-} \leftrightarrow PbSO_4 \downarrow \qquad (10)$$

Some attempts have been made to transform the conventional lead accumulator into a "dissolution" accumulator by replacing sulfuric acid with tetrafluoroboric acid (HBF_4) but the highly corrosive and toxic acid was not finally accepted [16].

The electrochemical equivalent of the lead is the lowest of all metallic anodes (260 Ah/kg) but in many applications the high open-circuit voltage of 2.1 V per cell compensates for this disadvantage.

6.3.5 Lithium

Most battery systems in which lithium is applied as anode material belong to the group using nonaqueous electrolytes, but there is one system that works with water serving as solvent and reactant as well. This is only possible because lithium forms a passive layer in solutions containing higher amounts of caustic [17, 18].

Nevertheless, water is decomposed with evolution of hydrogen but under controlled conditions and with a reasonable reaction rate. With water as the active cathode material, the battery system—used in military underwater applications—can be designed as: (–) Li / KOH / H_2O (+) [19]. The regular discharge reactions are:

Anode:

$$Li \rightarrow Li^+ + e^- \qquad (11)$$

Cathode:

$$H_2O + e^- \rightarrow OH^- + \tfrac{1}{2} H_2 \uparrow \qquad (12)$$

Overall reaction:

$$Li + H_2O \rightarrow LiOH + \tfrac{1}{2} H_2 \uparrow \qquad (13)$$

The electrochemical equivalent of 3860 Ah/kg is the highest among all metal anodes and the open-circuit voltage of 2.7–2.8 V (depending on electrolyte concentration) is rather high too.

6.3.6 Magnesium

Magnesium alloys as anode materials are found in (at least) three types of primary cells: the "dry-cell" type, (–) Mg / KOH / MnO_2 (+); magnesium/air batteries, (–) Mg /KOH/ O_2 (+); and water-activated reserve batteries, (–) Mg / KOH / K (+), with K= AgCl, CuCl, $PbCl_2$, Cu_2I_2, CuSCN and again MnO_2. All of these cells are primaries (AB1) using the advantage of a high electrochemical equivalent (2200 Ah/kg) and relatively high open-circuit voltages (e.g., 2.8 V for the Mg/MnO_2 system). The dominating discharge re-

CosMX Exhibit 1008, Page 219 of 633

actions (for the Mg/air system as an example) are:

Anode:

$$Mg \rightarrow Mg^{2+} + 2e^- \quad (14)$$

Cathode:

$$\tfrac{1}{2}O_2 + H_2O + 2e^- \rightarrow 2OH^- \quad (15)$$

Overall reaction:

$$Mg + \tfrac{1}{2}O_2 + H_2O \rightarrow Mg(OH)_2 \quad (16)$$

Side reaction:

$$Mg + 2H_2O \rightarrow Mg(OH)_2 + H_2 \uparrow \quad (17)$$

The most important anodes for battery use are ternary Mg/Al/Zn alloys (AZ 61, AZ 63—Norsk Hydro), an alloy containing 1% of lithium (AZ21), and the rather complex alloy AZ31 (Mg –3 Al –1 Zn –0.2 Mn – 0.15 Ca) [20].

6.3.7 Zinc

The zinc electrode is probably the most widely used metallic negative. The material is relatively cheap, has a good electrochemical equivalent (820 Ah/kg), and shows high open-circuit voltages (OCVs) in most systems (Table 1).

Table 1. Open-circuit voltages of battery systems with zinc anodes

Open-circuit voltage (V)	Cathode material
1.6	MnO_2, acidic
1.5	MnO_2, alkaline
1.73	NiOOH
1.85	AgO
1.65	O_2/air
2.12	Cl_2
1.85	Br_2
1.84	$K_3[Fe(CN)_6]$

It is so universally applied that it may be found in combination with metal oxide cathodes (e.g., HgO, AgO, NiOOH, MnO_2), with catalytically active oxygen electrodes, and with inert cathodes using aqueous halide or ferricyanide solutions as active materials ("zinc-flow" or "redox" batteries). The cell (battery) sizes vary from small button cells for hearing aids or watches up to kilowatt-hour modules for electric vehicles (electrotraction). Primary and storage batteries exist in all categories except that of flow-batteries, where only storage types are found. Acidic, neutral, and alkaline electrolytes are used as well. The (simplified) half-cell reaction for the zinc electrode is the same in all electrolytes:

$$Zn \leftrightarrow Zn^{2+} + 2e^- \quad (18)$$

This reaction may be followed by others (complex formation and/or precipitation) which are independent of the electrode potential but determined by the nature and concentration of the electrolyte. It is impossible to discuss all the problems relating to zinc electrodes without looking at the electrolyte system and the kind of cell operation (primary or rechargeable). The only way to cover all the possible combinations is by another mode of characterization or categorization, which is used in the subsequent sections:

- zinc electrodes for "acidic" (neutral) primaries;

$$[(-)\ Zn/NH_4Cl, ZnCl_2/MnO_2\ (+)] \quad (19)$$

- zinc electrodes for alkaline primaries;

$$[(-)\ Zn/KOH/HgO, MnO_2, air\ (+)] \quad (20)$$

- zinc electrodes for alkaline storage batteries;

$$[(-)\ Zn/KOH/NiOOH, AgO\ (+)] \quad (21)$$

CosMX Exhibit 1008, Page 220 of 633

- zinc electrodes for alkaline "low-cost" reusable;

$$[(-)\,Zn/KOH/MnO_2, air\,(+)] \quad (22)$$

- zinc electrodes for flow batteries;

$$[(-)Zn/H^+ or\,OH^-/\,Br_2, Cl_2, ferricyanide\,(+)] \quad (23)$$

6.3.7.1 Zinc Electrodes for "Acidic" (Neutral) Primaries

The "classical" Leclanché cell uses zinc sheet formed into a cylindrical can serving simultaneously as the anode and as the cell container (AB1C1). The cathode is a mixture of MnO_2 and graphite wrapped into a piece of separator and contacted by a central carbon rod. The can dissolves slowly when the cell is not in use and faster when the cell delivers electrical energy. The reaction following the primary electrochemical zinc dissolution [Eq. (19)] leads, in the case of an ammonium chloride electrolyte, to a zinc diammine cation:

$$Zn^{2+} + 2NH_4^+ + 2OH^- \rightarrow [Zn(NH_3)_2]^{2+} + 2H_2O \quad (24)$$

The (similar) corrosion reaction is:

$$Zn + 2NH_4^+ \rightarrow [Zn(NH_3)_2]^{2+} + H_2\uparrow \quad (25)$$

If aqueous zinc chloride solution serves as electrolyte ("heavy-duty" types), the hydrate of a basic zinc chloride is formed instead of the product in Eq. (24):

$$5Zn^{2+} + 2Cl^- + 8OH^- + H_2O \rightarrow ZnCl_2 \cdot 4ZnO \cdot 5H_2O\downarrow \quad (26)$$

The construction of the anode (sheet, cell container) is responsible for two major problems:

- the relatively small specific surface (cm^2g^{-1}) does not allow higher currents;
- the corrosion reactions usually proceed until the can starts leaking and the electrolyte spillage corrodes the electrical or electronic device powered by the cell.

The corrosion reactions may be slowed down by using zinc alloys (with lead and cadmium, also improving the mechanical properties of zinc to simplify the production process) instead of the pure metal, or by amalgamating the inner surface of the can by adding a small amount of a mercury compound to the electrolyte.

Other ("leakproof") cells use an additional steel can on the outside to prevent any electrolyte loss caused by perforation of the inner zinc beaker when the cell is exhausted.

The problem of low specific surface (which, however, has a beneficial effect on the corrosion rate) cannot be solved so easily. This was one important reason for the development of the alkaline MnO_2 / zinc cell known as "alkaline" or "PAM" (primary alkaline manganese dioxide).

6.3.7.2 Zinc Electrodes for Alkaline Primaries

The alkaline version of the MnO_2 / zinc cell follows a different concept because it turns the construction of the Leclanché cell completely around: now the cathode (MnO_2 + carbon) forms a hollow cylinder contacting the inner wall of the cell container (steel) along its outer surface. The inner cavity has to accommodate anode, electrolyte, separator, and current collector. Usually, the separator forms a basket, which is automatically inserted and pre-

CosMX Exhibit 1008, Page 221 of 633

vents direct contact of the anode material with the cathode and the bottom of the cell container. Anodic active species and electrolyte are provided as a gel consisting of zinc powder, aqueous KOH solution (7–9 mol L^{-1}), gelling agents, and additives. Finally the current collector (a brass nail spot-welded to the metallic part of the cell top) is introduced when the cell top is positioned and the can is crimped to give a gas-tight closure.

Cells of cylindrical geometry are produced mainly in four sizes: D (LR-20), C (LR-14), AA (LR-6), and AAA (LR-03). The two other alkaline cells in this section (using HgO or an oxygen electrode as cathode) are almost exclusively produced as small button cells.

The change from zinc sheet to zinc powder improved the high-current performance of the cell significantly but it increased the corrosion problems (a larger specific surface means a higher corrosion rate).

The discharge reactions now include formation of hydroxo complexes, preferably:

$$Zn^{2+} + 4OH^- \rightarrow [Zn(OH)_4]^{2-} \qquad (27)$$

Depending on electrolyte saturation and KOH concentration, subsequent precipitation reactions may follow:

$$[Zn(OH)_4]^{2-} \rightarrow Zn(OH)_2 \downarrow + 2OH^- \qquad (28)$$

or:

$$[Zn(OH)_4]^{2-} \rightarrow ZnO \downarrow + 2OH^- + H_2O \qquad (29)$$

In competition with the electrochemical discharge reaction and consequently diminishing the shelf life of the cell, chemical dissolution (corrosion) of zinc is more or less active:

$$Zn + 2OH^- + 2H_2O \rightarrow [Zn(OH)_4]^{2-} + H_2 \uparrow \qquad (30)$$

The loss of active zinc and the evolution of hydrogen, causing an intolerable rise of internal pressure, were retarded by amalgamation of zinc particles. For quite long time (up to about 1982) mercury contents of 6% (in some cases up to 8%) were regarded as normal [21]. Then a rapid decrease in the mercury content took place (Fig. 1).

The first step was a reduction of Hg to 3%, which was made possible by the application of new amalgamation methods (surface amalgamation instead of or in addition to volume amalgamation [22, 23]. This first step was followed by a further decrease in the mercury content to 1% when the amalgamation techniques were regarded as suitable for achieving this goal [24]. In the meantime it was found out that extremely pure zinc powder (made from selected raw material by a gas atomization process) which is surface amalgamated might contain far less than 1% mercury without losing corrosion stability [21].

For a couple of years 0.25% Hg became the technical standard. It has to be pointed out that the mercury content of the metallic zinc has to be divided by a factor of roughly 10 to give the mercury content based on the total cell weight of an AA (LR-6) cell. These values are sometimes indicated on the cell labels. With decreasing amalgamation, other corrosion inhibitors had to take over the role of mercury. There are numerous papers and patents claiming corrosion-inhibiting activities of elements like Al, In, Tl, Cd, Ga, Na,

CosMX Exhibit 1008, Page 222 of 633

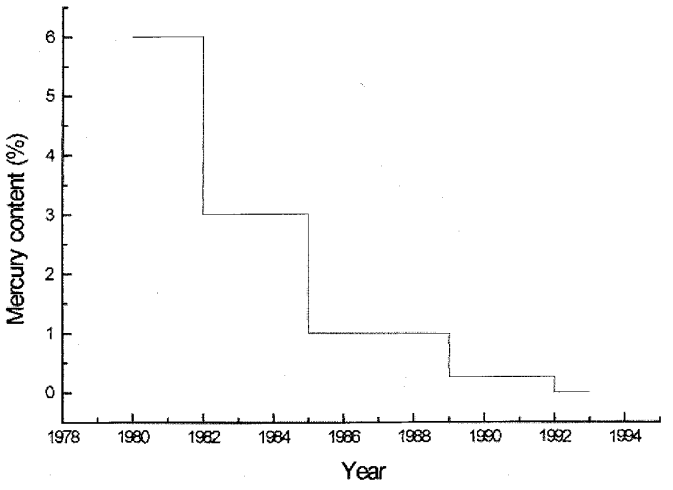


Figure 1. Decrease in mercury content of zinc powders within about ten years

Ca, Co, Ni, Pb, and Bi in single or combined application, with or without small amounts of mercury. The probably most important patents are cited in Ref. [21]. Finally, the research and development activities led to a zinc quality, which is specified as "no mercury added" (nobody dares to claim "zero mercury"). Commercial zinc powders frequently contain a combination of indium, lead, and bismuth in variable concentrations up to 500 ppm each [25].

Some battery-producing companies prefer purchasing pure, nonamalgamated zinc powder to apply their own proprietary corrosion protection system. The general trend is to keep the anodes of all the consumer cells mercury-free (usually indicated by a "green" label) and to make them disposable with the regular household trash. The exceptions to this rule are those cells where this makes no sense, such as cells with a mercuric oxide cathode.

This trend also applies to the "reusable" version of the manganese dioxide/zinc cell, which came onto the consumer market in 1993 (Rayovac, USA). This type is discussed in the next-but-one section.

6.3.7.3 Zinc Electrodes for Alkaline Storage Batteries

Battery systems of complex design and structure using—at least for one electrode—expensive materials are (for economic reasons) mainly conceived as storage batteries. Primary (and "reserve") versions of the zinc/silver oxide battery [(−) Zn/KOH/AgO (+)] — as a first example—are only used in particular cases where the question of cost is not crucial, e.g., for marine [26–28] and space applications [29].

The other example, called the nickel/zinc battery [(−Zn)/KOH/NiOOH(+)], has attracted more attention in two different versions from the "application" and "cell design" viewpoints: one is the small cylindrical consumer cell [30], the other one is the flat-plate module for electrotraction [31]. A very interesting review with an extended collection of references was pub-

CosMX Exhibit 1008, Page 223 of 633

lished in 1992 [32]. Recently, an improved bipolar construction of this battery was presented [33]. The problems related to the zinc electrode grew significantly with the change to a rechargeable (reversible) system. Whereas the discharge of a zinc electrode in a primary cell is a simple electrochemical dissolution with no concern about the oxidation products, these may be of particular importance in a secondary (or storage) cell. The fact of starting with zinc oxide or hydroxide instead of metallic zinc had only a minor influence (AB2C2). In any case, the solubility of zinc oxide or hydroxide in the KOH electrolyte was found to be a key parameter in a reversible zinc electrode [34]. The result of zinc migration ("shape change") was obvious when the electrodes of a flat-plate battery were inspected after a series of charge/discharge cycles. The active material was removed from the electrode edges and agglomerated towards the plate center. If the number of cycles was sufficiently high, the edge areas of the current collector were completely denuded of zinc.

Usually, this phenomenon limits the lifetime of a battery because the storage capacity falls below a reasonable lower limit. One reason for this zinc migration was identified by McBreen [35]: an inhomogeneous current distribution makes the zinc move away from high current density areas. Another mechanism seems to be active as well: an electrolyte convection induced by electro-osmosis through the separator [36].

The consequences of shape change are densification and loss of electrode porosity, increased current density caused by loss of zinc surface area, and finally earlier passivation. Two different forms of pasivation can stop the discharge of a zinc electrode before the active material is exhausted. "Spontaneous" passivation occurs at high current densities within a few seconds. "Long-term" passivation may be observed after hours of continuous discharge in a current density range of 15–35 $mA\,cm^{-2}$. The effects are explained by the existence of supersaturated solutions of ZnO in KOH, which are normally quite stable, but if precipitation is induced by any means (nucleation) solid products form immediately and block the electrodes.

In rechargeable nickel/zinc and silver/zinc batteries this problem is partly compensated for by provision of a massive zinc reserve. The cells are cathode-limited and the amount of anode material exceeds the theoretically required mass by a factor between two and three.

Another complication had to be matched when the zinc electrode was made reversible: in a battery with unstirred electrolyte or an electrolyte gel, dendritic growth of the electrolytically deposited metal takes place. The formation of dendrites cannot be fully suppressed by the use of current collectors with large surface areas (grids, wire fabrics). However, by using improved separators combined in multi layer arrangements, the danger of short-circuiting is reduced.

6.3.7.4 Zinc Electrodes for Alkaline "Low-Cost" Reusables

It was a reasonable idea to use the intensive research work in the fields of zinc, manganese dioxide, and oxygen electrode on one hand, and on rechargeable metal oxide/zinc cells (the preceding section) on the other, to develop "rechargeable" versions of the cells described in Sec. 6.3.7.2. The manganese dioxide/zinc system (by reason of low cost) and the zinc/air system (low cost and high energy density) were the most fascinating ones.

The specification "rechargeable" is

CosMX Exhibit 1008, Page 224 of 633

controversial: for many battery experts it requires the possibility of—at least—some hundreds to a thousand full cycles to call a system "rechargeable". As a compromise, cells designed for 20 to about 200 cycles are designated "reusable" or "renewable" (e.g., RENEWAL™ of Rayovac, USA, for zinc/manganese dioxide; general name RAM™ of BTI Inc., Canada).

In the early stages of development the most stringent difficulties seemed to come to from the cathode side: it took a long time to convince people of the principal rechargeability of manganese dioxide [37, 38] and to find suitable catalysts for the oxygen electrode showing a sufficiently high oxidation stability in the charging procedure [39, 40].

Soon it became evident that the zinc anode, working in both cases under capacity-limiting conditions, causes severe troubles too. Whereas in the zinc/air system the anode automatically limits the discharge (because access to oxygen from the air is practically unlimited), the anode limitation in zinc/manganese dioxide cells has another reason: Kordesch and co-workers showed that the rechargeability of manganese dioxide (i.e., the number of available cycles) depends strongly on the depth of discharge (DOD) (Fig. 2) [41].

It is possible to design a RAM cell either for high initial (first discharge) capacity (up to 1.8 Ah for the AA size, close to the alkaline primary version) and a low cycle number, or for lower initial capacity (that means shallower discharge of MnO_2) but significantly higher cycle number. The commercially available products of today (RENEWAL™ USA, PURE ENERGY™ Canada, ALCAVA™ Korea) follow the first principle. Fortunately, shape-change effects are not important in cells of cylindrical geometry, which are preferred for making RAM products that are exchangeable with primaries. All flat-plate test cells and research batteries showed the same behavior as the nickel/zinc or silver/zinc batteries but without the possibility of oversizing the anode. Although small cylindrical cells cannot be manufactured economically with current collectors made form grid or mesh, it turned out that dendrite formation is not

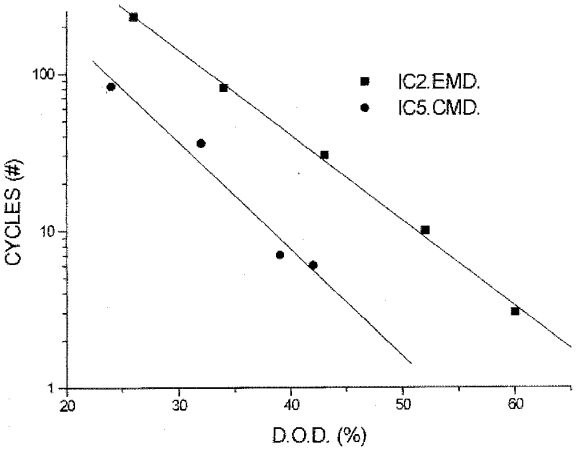


Figure 2. Influence of the DOD on the number of achievable cycles for CMD end EMD samples

CosMX Exhibit 1008, Page 225 of 633

a critical feature if a laminated separator including a "barrier" layer of regenerated cellulose is applied.

Most difficulties arose when—following the general trend—the RAM cell had to be made mercury-free. The final step, especially from about 0.15% mercury to "no added mercury", was quite challenging [42]. Many compounds, although evidently inhibiting zinc corrosion in primary cells, did not work so perfectly with the deposited zinc after the first charge and were only insufficient substitutes for mercury. However, some electrical properties of the first mercury-free test cell after shock or drop tests were inferior compared with those of cells using amalgamated zinc [43]. Apparently, the presence of mercury in the anode mixture had a positive effect on the adhesion of the zinc gel to the current collector, and on the discharge efficiency.

In connection with this observation, it should be noted that only a fraction (usually between 60 and 70%, depending on the discharge current and on the cut-off voltage) of the zinc powder provided in the anode gel could be used as active mass. The rest only acts as a metallic conductor or extension of the brass nail, which forms the current collector. With primary cells the disposal of the remaining fraction of the zinc powder, or its collection for recycling, with the used battery is not troublesome. Zinc powder is not expensive and the rejected material has done its work as an electronically conductive component of the anode mass. By contrast, the rechargeable (reusable) version of the zinc/manganese dioxide cell requires—as stated before—a capacity-limiting anode with good and reproducible(!) discharge process efficiency. For this purpose it is necessary to establish a conductive matrix in the anode space of the cell by admixing lightweight materials with good surface conductivity (and not taking part in the redox reactions of the discharge and charge processes) to the anode gel. This conductive matrix is able to prevent the formation of isolated zinc particles out of contact with the current collector during discharge (a function of particular importance in mercury-free cells), but also serving as a three-dimensional substrate for the zinc deposition on charge[44].

For OEM (original equipment manufacturing) applications, i.e., recharging strings of series-connected cells mounted inside the device, the possibility of utilizing the chemical oxygen–zinc reaction (to provide a certain overcharge capability) has been demonstrated in a modified version of the RAM cell [45]. The efforts made to obtain a rechargeable (reusable) version of the zinc/air battery had to overcome a series of other restrictions. This is not surprising because, in addition to the chemical differences, this system had to deal with a scale-up to sizes applicable to electric vehicle applications. One of the first attempts was called "mechanical recharge". It was a simple exchange of flat-plate anodes at a certain degree of oxidation (discharge) for new ones [46]. The next step was provision of the zinc electrode as a pumpable slurry as well as on-board and central recharge schemes [47]. Finally, the development of stable ("bifunctional") air electrodes favored the construction of real "in-cell" recharge systems [48] (see also Refs. [39, 40]).

6.3.7.5 Zinc Electrodes for Zinc-Flow Batteries

There are three types of zinc-flow batteries (belonging in general to the group of flow or redox batteries) which have been studied intensively: two of them are similar with respect to the reactants involved, the

CosMX Exhibit 1008, Page 226 of 633

zinc/chlorine [(−) Zn/HCl, $ZnCl_2/Cl_2$ (+)] and the zinc/bromine [(−) Zn/HBr, $ZnBr_2/Br_2$ (+)] batteries; the third one uses an alkaline electrolyte and potassium ferricyanide as active cathode material [(−) $Zn/NaOH/K_3[Fe(CN)_6]$ (+)] . The anodes of all three start with zinc provided as aqueous halide solutions (AB2C3).

While the zinc/chlorine battery is preferred for utility load-leveling applications [49], the zinc/bromine system is the more promising one for electric vehicle requirements [50, 51].

Both share more or less the same merits but also the same disadvantages. The beneficial properties are: high OCV (2.12 and 1.85 V respectively); flexibility in design (because the active chemicals are mainly stored in tanks outside the (usually bipolar) cell stack); no problems with zinc deposition in the charging cycle because it works under nearly ideal conditions (perfect mass transport by electrolyte convection, carbon substrates [52]); self-discharge by chemical attack of the acid on the deposited zinc may be ignored because the stack runs dry in the standby mode; and use of relatively cheap construction materials (polymers) and reactants.

The most unpleasant drawbacks are: tanks, tubes, and pumps are required for the electrolyte storage and transport system, increasing the volume of the battery and consuming energy (in the case of the zinc/chlorine battery an extra cooling device had to be provided); highly corrosive electrolytes; public distrust of storing halogens in any form (though it is frequently stated that organic polybromide complexes are quite harmless); and a certain imbalance of the electrochemistry involved (zinc ions form halide complexes of the type $[ZnX_4]^{2-}$ which behave—due to their charge—as anions in the electrical field.

Despite the fact that the zinc/ ferricyanide system employs an alkaline electrolyte, the electrode reactions are quite similar to those in zinc/halogen batteries and battery constructions are usually bipolar too.

Zinc is electrodeposited from the sodium zincate electrolyte during charge. As in the zinc/bromine battery, two separate electrolytes loops ("posilyte" and "negalyte") are required. The only difference is the quality of the separator: The zinc/ bromine system works with a microporous foil made from sintered polymer powder, but the zinc/ferricyanide battery needs a cation exchange membrane in order to obtain acceptable coulombic efficiencies. The occasional transfer of solid sodium ferrocyanide from the negative to the positive tank, to correct for the slow transport of complex cyanide through the membrane, is proposed [54].

All in all, this system is more complicated than the other flow batteries and this handicap postpones wider application.

6.4 References

[1] P. K. Shen, A. C. C. Tseung, C. Kuo, *J. Appl. Electrochem. 24*, **1994**, 145–148.
[2] J. T. Reding, J. J. Newport, *Mater. Protect. 5*, **1996**, 15.
[3] T. Sakans et al., *Mater. Protect. 5*, **1996**, 45.
[4] J. Hunter et al., *Power Sources 13*, (Eds: T. Keily, W. Baxter), Int. Power Sources Symp. Committee, Leatherhead, UK, **1991**, p. 193.
[5] J. Jindra, J. Mrha, K. Micka, Z. Zabransky, V. Koudelka, J. Malik, *J. Power Sources 4*, **1979**, 227–237.
[6] H. N. Seiger, *Proc. Electrochem. Soc. 84(8)*, **1984**, 50.
[7] C. Chakkaravarthy, P. Periasamy, S. Jegannathan, K. I. Vasu, *J. Power Sources 35*, **1991**, 21–35.

CosMX Exhibit 1008, Page 227 of 633

[8] L. Carlsson, L. Ojefors, *J. Electrochem. soc. 127*, **1980**, 525.
[9] L. Ojefors, L. Carlsson, *J. Power Sources 2*, **1977/78**, 287.
[10] E. S. Buzelli, *Proc. 28th Power Sources Symp., ECS, Princeton, NJ*, **1978**, p. 160.
[11] G. A. Bayles, E. S. Buzzelli, J. S. Lauer, *Proc. 34th Power Sources Symposium, IEEE, New York*, **1990**. p. 312.
[12] G. Berger, F. Haschka, US Patent 4,250,236; German Patent 283 7980, **1978**.
[13] E. Soragni, G. Davolio, G. Tarzia, *Power Sources 14*, (Eds.: A. Attewell, T. Keily) Power Sources Symp. Committee, Leatherhead, UK, **1993**, p. 15.
[14] K. W. Lexow, G. Krämer, V. A. Oliapuram, *Power Sources 8*, (Ed.: J. Thompson), Academic Press, New York, **1995**, p. 389.
[15] N. E. Bagshaw, *J. Power Sources 53*, **1995**, 25–30.
[16] F. Beck, BMFT Forschungsbericht No. T79–142, **1979**.
[17] E. L. Littauer, K. C. Tsai, *Proc. 26th Power Sources Conference, ECS, Pennington, NJ*, **1974**, p. 570.
[18] E. L. Littauer, K. C. Tsai, *J. Electrochem. Soc. 123*, **1976**, 964.
[19] N. Shuster, *Proc. 34th Power Sources Symposium, IEEE, New York*, **1990**. p. 118.
[20] M. Sahoo, J. T. N. Atkinson, *J. Mater. Sci. 17*, **1982**, 3564.
[21] W. Glaeser, *Power Sources 12*, (Eds.: T. Keily, W. Baxter), International Power Sources Symp. Committee, Leatherhead, UK, **1989**, p. 265.
[22] K. Myazaki et al., European Patent Application, 0 162 411, **1984**.
[23] M. Meeus et al., US Patent 4 632 699, **1984**.
[24] M. Meeus, Y. Strauven, L. Groothaert, *Power Sources 11*, (Ed.: L. J. Pearce), International Power Sources Symp. Committee, Leatherhead, UK, **1986**, p. 281.
[25] T. Uemura et al., European Patent Application 0 500 313 A2, **1992**.
[26] L. J. Giltner, *Proc. 37th Power Sources Conference, Cherry Hill, NJ*, **1996**, p. 27.
[27] St. Dallek, W. G. Cox, W. P. Kilroy, *Proc. 37th Power Sources Conference, Cherry Hill, NJ*, **1996**, p.31.
[28] St. D. James, R. Serenyi, *Proc. 37th Power Sources Conference, Cherry Hill, NJ*, **1996**, p. 389.
[29] Z. Adamedes, *Proc. 37th Power Sources Conference, Cherry Hill, NJ*, **1996**, p. 390.
[30] M. Kanda et al., *Toshiba Review 124*, **1979**, 3.
[31] F. R. McLarnon, E. J. Cairns, *J. Electrochem Soc. 138*, **1992**, 645.
[32] J. Jindra, *J. Power Sources 37*, **1992**, 297
[33] N. Tassin, G. Bronoel, J. F. Fauvarque, A. Millot, *Proc. 37th Power Sources Conference, Cherry Hill, NJ*, **1996**, p. 378.
[34] R. Jain, T. C. Adler, F. R. McLarnon, E. J. Cairns, *J. Appl. Electrochem. 22*, **1992**, 1039.
[35] J. McBreen, *J. Electrochem. Soc. 119*, **1972**, 1620.
[36] K. W. Choi, D. Hamby, D, N. Bennion, J. Newman, *J. Electrochem. Soc. 123*, **1976**, 1628.
[37] K. Kordesch, J. Gsellmann, *Power Sources 7*, (Ed.: T. Thompson, Academic Press, New York, **1979**, p. 557.
[38] K. Kordesch, J. Gsellmann, M. Peri, K. Tomantschger, R. Chemelli, *Electrochem. Acta 26*, **1981**, 1495.
[39] S. Müller, F. Holzer, O. Haas, C. Schlatter, Ch. Comninellis, *Chimia 49*, **1995**, 27.
[40] S. Müller, F. Holzer, O. Haas, C. Schlatter, Ch. Comninellis, *Electrochem. Soc. Proc. 95–14*, **1996**, 135.
[41] R. Chemelli, J. Gsellmann, G. Körbler, K. Kordesch, Rechargeability of manganese dioxide I. C. samples, *in 2nd Int.* MnO_2 *Symp., Tokyo*, I. C. MnO_2 Sample Office, Cleveland, OH, **1981**.
[42] J.-Y. Huot, *Power Sources 14*, (Eds.: A. Attewell, T. Keily), Int. Power Sources Symp. Committee, Leatherhead, UK, **1993**, p. 177.
[43] M. J. Root, *J. Appl. Electrochem. 25*, **1995**, 1057.
[44] W. Taucher, L. Binder, K. Kordesch, *J. Appl. Electrochem. 22*, **1992**, 95.
[45] L. Binder, K. Kordesch, P. Urdl, *J. Electrochem. Soc. 143*, **1996**, 13.
[46] R. R. Witherspoon, *Proc. Automotive Engineering Conference, SAE, Detroit, MT*, **1969**, Paper No. 690 204.
[47] P. C. Foller, *J. Appl. Electrochem. 16*, **1986**, 527.
[48] G. L. Holleck, A. B. Kon, E. A. Morin, *Proc. 37th Power Sources Conference, Cherry Hill, NJ*, **1996**, p. 432.
[49] P. Carr, C. J. Warde, A. Lijoi, B. D. Brummet, *Proc. 30th Power Sources Symp.*, Electrochem. Soc., Pennington, NJ, **1982**, p. 99.
[50] K. Kordesch, C. Fabjan, *Dechema Monographie 97*, **1984**, p. 255.

CosMX Exhibit 1008, Page 228 of 633

[51] G. Tomazic, *Österreich. Z Elektizitätsw. 1*, **1987**, 13.
[52] C. D. Iacovangelo, F. G. Will, *J. Electrochem. Soc. 132*, **1985**, 851.
[53] R. P. Clark, J. L. Chamberlin, H. J. Saxton, P. C. Symons, *Power Sources 9*, (Ed.: J. Thompson), Academic Press, New York, **1983**, p. 271.
[54] G. B. Adams, R. P. Hollandsworth, E. L. Littauer, *Proc. 4th US D.O.E. Battery Electrochem. Contractors Conference*, **1981**, p. 311.

CosMX Exhibit 1008, Page 229 of 633

7 Metal Hydride Electrodes

James J. Reilly

Many metals and alloys reversibly absorb large quantities of hydrogen to form metal hydride phases. In most cases the volumetric hydrogen density in the hydride phase exceeds that of liquid hydrogen. Although almost all binary hydrides (phases consisting of the elemental metal and hydrogen) are not suitable for hydrogen storage, there is a wide variety of metal alloys which form hydrides, many of which have properties that make them practical, convenient, and safe energy-storage media.

For many years the focus of research was on the storage of hydrogen for use as a gaseous fuel, although the possibility of electrochemical applications was also recognized. Now that focus has dramatically shifted towards electrochemical applications where a metal hydride (MH_x) electrode is used to replace the cadmium electrodes in Cd/Ni batteries. The driving force for such replacement is the environmental problems associated width cadmium. An additional benefit is the higher energy density of the MH_x electrode. This section is concerned primarily width the electrochemical, thermodynamic, and structural properties of metal hydrides that pertain to their use in $Ni - MH_x$ batteries.

7.1 Introduction

A hydrogen–metal system may be defined as consisting of an amorphous or crystalline metal phase containing dissolved hydrogen in interfacial contact with molecular, atomic, or ionized hydrogen. In many cases, depending on temperature and pressure, a metal hydride phase will form of which there are three general categories: ionic, covalent and metallic. Intermetallic hydrides are, of course, a subgroup of the latter class, where hydrogen occupies interstitial sites in the metal lattice and the hydride phase is crystalline. There are a large number of intermetallic compounds, many of which form a hydride by direct and reversible reaction with hydrogen. Consequently, even though most may not be of interest for practical applications, the shear number of intermetallic–H systems constitutes a great advantage over binary systems with respect to the formulation of attractive energy-storage materials.

7.1.1 Thermodynamics

Flanagan and Oates [1] have extensively reviewed the thermodynamics of intermetallic hydrides; also recommended are the classic work of Libowitz [2] and the com-

prehensive text of Müller et al. [3] which treats the properties of binary hydrides. The properties of a metal-hydrogen system can be conveniently summarized by a pressure-temperature-composition (*PCT*) diagram, of which an idealized version is shown in Fig. 1.

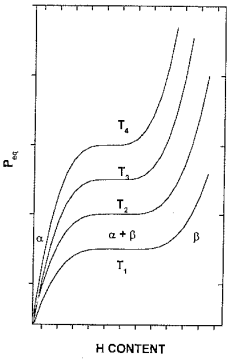


Figure 1. Ideal pressure–composition isotherms showing the hydrogen solid-solution phase, α, and the hydride phase, β. The plateau marks the region of coexistence of the α and β phases. As the temperature is increased the plateau narrows and eventually disappears at some consolute temperature

It is essentially a phase diagram which consists of a family of isotherms that relate the equilibrium pressure of hydrogen to the H content of the metal. Initially the isotherm ascends steeply as hydrogen dissolves in the metal to form a solid solution, which by convention is designated as the α phase. At low concentrations the behaviour is ideal and the isotherm obeys Sievert's Law, i.e.,

$$H_{\text{solid}} = K_s P^{1/2} \tag{1}$$

where H_{solid} is the concentration of hydrogen in metal, K_s is Sievert's constant and P is the equilibrium hydrogen pressure. As the H content of the solid increases, the system departs from ideal behaviour due to H–H attractive interactions primarily caused by elastic strain in the metal; this is reflected by a decreasing slope in the isotherm. When the terminal solubility of hydrogen in the α phase is exceeded, the hydride phase precipitates and is designated the β phase. Upon the appearance of the β phase, the hydrogen pressure will remain constant and the isotherm forms a plateau as more hydrogen is added. The plateau is a consequence of the phase rule and will persist as long as the two solid phases coexist. When the phase conversion is complete the system regains a degree of freedom and the pressure again rises as a function of the hydrogen content. In this region of the diagram electronic factors become dominant as the limiting hydrogen concentration is approached. It is also possible that more than one hydride phase exists, in which case a second plateau will appear. In many systems there is a significant hysteresis effect in the phase conversion process, which is reflected by a higher isotherm plateau pressure for the $\alpha \rightarrow \beta$ conversion then the reverse $\beta \rightarrow \alpha$ process. The effect of increasing temperature is shown by the higher-temperature isotherms T_2, T_3 and T_4. Usually, the miscibility gap narrows as the temperature increases, eventually disappearing as the consolute temperature is reached.

The reaction of a metal with hydrogen gas may be written as:

$$\mathrm{M} + \frac{x}{2}\mathrm{H}_2 \leftrightarrow \mathrm{MH}_x \tag{2}$$

Thermodynamic quantities for a system may be determined from the van't Hoff equation Eq.(3), which defines the equilibrium constant, K, in terms of the reaction enthalpy, ΔH and the temperature, T.

$$\frac{\partial \ln K}{\partial T} = \frac{\Delta H}{RT^2} \tag{3}$$

CosMX Exhibit 1008, Page 231 of 633

For reaction (2),

$$K = \frac{a_{MH_x}}{a_M (f_{H_2})^{x/2}} \tag{4}$$

where a_x is the activity of reactant x and f_{H_2} is the fugacity of hydrogen. Under ideal conditions the activity of a solid may be taken as unity and fugacity as the pressure: then Eq.(3) may be rewritten as

$$\frac{\partial(\ln P_{H_2})^{-x/2}}{\partial T} = \left(\frac{\Delta H}{RT^2}\right) \tag{5}$$

which upon integration yields

$$\ln P_{H_2} = \frac{2}{x}(\Delta H/RT) + C \tag{6}$$

The enthalpy of the phase conversion can be determined from Eq.(6) by plotting the log of the absorption or desorption plateau pressure, $P_{plateau}$, against the reciprocal temperature as indicated in Fig. 2. When the solubility of hydrogen in the metal (α) phase is small, then $\Delta H_{plat} \approx \Delta H_f$, where ΔH_f is essentially the enthalpy of formation of the hydride from the metal [4]; the intercept, C, is equal to $2/x(\Delta S/R)$ where ΔS is the corresponding difference in entropy. Equation (6) is commonly presented as

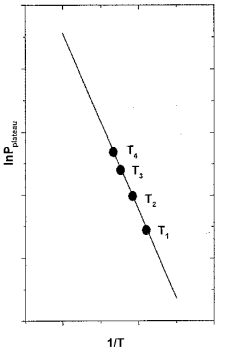


Figure 2. The enthalpy, ΔH, of the phase transformation can be calculated from the variation of $\ln P_{plateau}$ with reciprocical temperature in a van't Hoff plot.

$$\ln P_{plateau} = \frac{A}{T} + B \tag{7}$$

where constants A and B are specified. Thermodynamic data for some representative compounds are given in Table 1.

Table 1. Thermodynamic data

Alloy	Phase conversion	ΔH (kJ mol^{-1}H$_2$)	ΔS (JK^{-1}mol^{-1}H$_2$)	Ref.
MgH_2	$\beta \rightarrow \alpha$	77.1	137	[13]
TiH_2	$Ti \rightarrow TiH_2$	–123	–125	[3]
LaH_2	$\alpha \rightarrow \varepsilon$	–206	–147	[3]
$PdH_{0.6}$	$\beta \rightarrow \alpha$	40.9	91.1	[4]
Mg_2NiH_4	$\beta \rightarrow \alpha$	64.2	122	[13]
$FeTiH_x$	$\gamma \rightarrow \beta$	33.3	104	[14]
$FeTiH_x$	$\beta \rightarrow \alpha$	28.1	106	[14]
$LaNi_5H_x$	$\beta \rightarrow \alpha$	30.0	108	[25]
$LaNi_5H_x$+	$\alpha \rightarrow \beta$	–29.4		[1]
$LaNi_{4.6}Al_{0.4}H_x$	$\beta \rightarrow \alpha$	36.3	109	[7]
$MmNi_5$	$\beta \rightarrow \alpha$	20.9	96	[12]
$MmNi_{355}Co_{0.75}Mn_{0.4}Al_{0.3}$	$\beta \rightarrow \alpha$	29.7	100	[39]
$Mm*Ni_{3.55}Co_{0.75}Mn_{0.4}Al_{0.3}$	$\beta \rightarrow \alpha$	41.5	117	[39]

+ Calorimetric measurement

CosMX Exhibit 1008, Page 232 of 633

7.1.2 Electronic Properties

Switendick was the first to apply modern electronic band theory to metal hydrides [5]. He compared the measured density of electronic states with theoretical results derived from energy band calculations in binary and pseudo-binary systems. Recently, the band structures of intermetallic hydrides including $LaNi_5H_x$ and $FeTiH_x$ have been summarized in a review article by Gupta and Schlapbach [6]. All exhibit certain common features upon the absorption of hydrogen and formation of a distinct hydride phase. They are:

(1) the density of states versus energy function is changed;
(2) new low-lying states having an s-like character appear and are associated with hydrogen;
(3) to the extent that the hydrogen electrons cannot be accommodated in the new low-lying states, they are inserted into empty states near the Fermi level, which in turn shifts.

7.1.3 Reaction Rules and Predictive Theories

There have been numerous studies with the objective of gaining an understanding of the factors that influence the stability, stoichiometry, and H-site occupation in hydride phases. Stability has been correlated with cell volume [7] or the size of the interstitial hole in the metal lattice [8] and the free energy of the $\alpha \leftrightarrow \beta$ phase conversion. This has been widely exploited to modulate hydride phase stability, as discussed in Sec. 7.2.2.1.

Westlake developed a geometric model which is fairly successful in predicting site occupation in AB_5 and AB_2 hydride phases [9]. It involves two structural constraints: that the minimum hole size necessary to accommodate an H atom has a radius of 0.40 Å, and that the minimum distance between two H-occupied sites is 2.10 Å. The former criterion was derived empirically from a survey of known hydride structures, and the latter was suggested by Switendick on the basis of electronic [10] band structure calculations.

A relatively simple set of rules have been found to hold for all intermetallic hydrides useful for hydrogen storage [11]. They may be stated as follows:

(1) In order for an intermetallic compound to react directly and reversibly with hydrogen to form a distinct hydride phase, it is necessary that at least one of the metal components be capable of reacting directly and reversibly with hydrogen to form a stable binary hydride.
(2) If a reaction takes place at a temperature at which the metal atoms are mobile, the system will assume its most favored thermodynamic configuration.
(3) If the metal atoms are not mobile (as is the case in low—temperature reactions) only hydride phases can result in which the metal lattice is structurally very similar to the starting intermetallic compound because the metal atoms are essentially frozen in place. In effect the system may be considered to be pseudo-binary as the metal atoms behave as a single component.

7.2 Metal Hydride–Nickel Batteries

The half-cell reactions taking place in a MH_x / Ni battery may be written as follows:

CosMX Exhibit 1008, Page 233 of 633

$$MH_x + xOH^- \leftrightarrow M + xH_2O + xe^- \quad (8)$$

$$Ni(OOH) + H_2O + e^- \leftrightarrow Ni(OH)_2 + OH^- \quad (9)$$

It is in effect a rocking-chair type of battery in which hydrogen is transferred from one electrode to the other. It is also most convenient that the voltage is essentially the same as the conventional NiCad batteries. It is worthwhile nothing that the NiOOH cathode has a maximum energy density, based on Eq.(9), of 289 $mAhg^{-1}$. This may be compared with 300–400 $mAhg^{-1}$ for current MH_x electrodes and >400 $mAhg^{-1}$ projected for high-capacity MH_x electrodes which, though not yet developed, are certainly conceivable.

Two types of metal hydrides electrodes, comprising the AB_5 and AB_2 classes of intermetallic compounds, are currently of interest. The AB_5 alloys have the hexagonal $CaCu_5$ structure where the A component comprises one or more rare earth elements and B consists of Ni, or another transition metal, or a transition metal combined with other metals. The paradigm compound of this class is $LaNi_5$, which has been well investigated because of its utility in conventional hydrogen-storage applications. Unfortunately $LaNi_5$ is too costly, too unstable, and too corrosion—sensitive for use as a battery electrode. Thus commercial AB_5 electrodes use mischmetal, a low-cost combination of rare earth elements, as a substitute for La. The B_5 component remains primarily Ni but is substituted in part with Co, Mn, Al, etc. The partial substitution of Ni increases the thermodynamic stability of the hydride phase [12] and corrosion resistance. Such an alloy is commonly written as MmB_5 where Mm represents the mischmetal component. The compositions of normal and cerium-free mischmetal are given in Table 2.

The other electrode type, which is not yet in common use in batteries, is usually referred to as the AB_2 or Laves phase electrodes and is discussed in Sec. 7.3. These electrodes are complicated, multiphase alloys with as many as nine metal components. Alloy formulation is primarily an empirical process where the composition is adjusted to provide one or more hydride—forming phases in the particle bulk, but in which the surface is presumed to be corrosion-resistant because of the formation of semi-passivating oxide layers. Unlike the AB_5 alloys, there are few systematic guidelines which can be used to predict alloy properties. Eventually AB_2 alloy electrodes may be more attractive than AB_5 electrodes in terms of cost and energy density, but currently that potential is far from realized. There are also other intermetallic hydrides that have largely been ignored for battery applications because they are, or are perceive to be, too stable, electrochemically inactive, or– most importantly – subject to severe corrosion in the battery environment. Alloys such as Mg_2Ni [13] and FeTi [14] have substantially greater hydrogen/storage capacity than the conventional AB_5 and AB_2 alloys and are less costly. Unfortunately both are passivated rapidly in the electrochemi-

Table 2. Composition of mischmetal *

Rare earth or trace element	Content (wt.%)	
	Normal	Ce-free
Ce	56.9	0.13
La	20.5	58.2
Nd	14.7	29.9
Pr	5.5	7.6
Fe	0.42	0.07
O	0.058	0.47
C	0.032	0.104
N	0.002	0.162
Y	<0.01	0.04
Ca	0.13	0.27

* Analysed at Materials Preparation Center, Ames Laboratory, Ames, IA, USA

CosMX Exhibit 1008, Page 234 of 633

cal environment [15]. High Mg content amorphous alloys, produced by mechanical alloying, have been demonstrated to have initial storage capacities of >400 $mAhg^{-1}$ but they rapidly deteriorate upon cycling [16]. A novel vanadium—based electrode, $TiV_3Ni_{0.56}$, has also been shown to have a high initial storage capacity, 400–500 $mAhg^{-1}$, but also corrodes rapidly upon electrochemical cycling [17].

7.2.1 Alloy Activation

Essentially all metals and alloys which form metallic hydrides require an activation process before the metal will cycle readily between the hydride and the metal phase. All the AB_5 and AB_2 alloys are quite brittle and during the activation procedure are pulverized to fine particles. This greatly enhances subsequent reaction rates. The activation process is considered to take place in two stages: the formation of a reactive surface, and pulverization of the bulk solid to form fine particles. The surface composition of $LaNi_5$ after activation has been defined by x-ray photoemision spectroscopy, Auger electron spectroscopy and magnetic susceptibility studies [18]. There is a surface enrichment of La to give an La:Ni ratio of ≈ 1; the La is associated with oxygen but Ni remains metallic and is present on the surface as clusters containing about 6000 atoms. Thus, the surface of cycled $LaNi_5$ appears to consist of islands of La associated with oxygen and Ni clusters. This is the mechanism by which catalytic metal surface sites are formed for chemical or electrochemical reactions. The activation procedure is straightforward; in gas–solid systems it merely consists of repeated formation and decomposition of the hydride phase [19]. Electrochemical activation also consists of repeated charge and discharge cycles; it sometimes requires extended cycling periods. Alloys may be activated via the gas–solid reactions and then used as an electrode; this can significantly shorten the period required for electrochemical activation.

7.2.2 AB_5 Electrodes

The use of $LaNi_5$ as an electrode was first reported by Justi et al. in 1973 [20]. However, the capacity was less than one-third of 372 $mAhg^{-1}$, which corresponds to the discharge of six hydrogens from $LaNi_5H_6$. This was primarily due to the fact that the dissociation pressure of $LaNi_5H_6$ exceeds 1 atm at 298 K. Thus, in an open cell most of the hydrogen is lost as H_2 gas. A few years later Percheron—Guegan and coworkers [21] substituted Al and Mn in part for nickel, thereby increasing the hydride stability and charge capacity. However, this did not significantly affect the rapid corrosion of the electrode as observed with $LaNi_5$. In 1984 Willems [22] prepared the first multicomponent AB_5 electrode that had an acceptable cycle life. He also reported the positive correlation between lattice expansion and electrode corrosion. Finally, in 1987 an alloy of composition $MmNi_{3.55}Co_{0.75}Mn_{0.4}Al_{0.3}$ was shown to meet the minimum requirement for a practical battery with respect to cost, cycle life, and storage capacity [23]. Indeed, this composition is very similar to those currently used in commercial Ni–MH batteries with AB_5 hydride anodes. Ikoma et al.[24] describe an experimental EV (electric vehicle) battery having an energy density of 70 $Wh\,kg^{-1}$ using an anode of composition $Mm(Ni, Co, Mn, Al)_5$. The electrochemical behavior of this alloy and its relation to small changes in alloys composition are of great practical interest and will be discussed at length in the following sections.

CosMX Exhibit 1008, Page 235 of 633

7.2.2.1 Chemical Properties of AB_5 Hydrides

In order to fully understand the electrochemical behaviour of AB_5 hydrides, a knowledge of their chemical properties is required. Van Vucht et al. [25] were the first to prepare $LaNi_5$ hydride and it is arguably the most thoroughly investigated H—storage compound. It reacts rapidly with hydrogen at room temperature at a pressure of several atmospheres above the equilibrium plateau pressure. *PC* isotherms for this system are shown in Fig. 3.

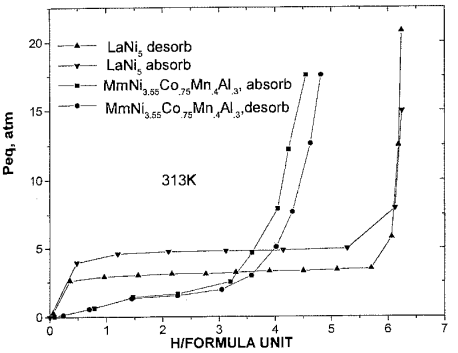


Figure 3. *PC* isotherms for $LaNi_5$ and $MmNi_{3.55}Co_{0.75}Mn_{0.4}Al_{0.3}$ [43].

The Nominal reaction may be written as

$$LaNi_5 + 3H_2 \leftrightarrow LaNi_5H_6 \qquad (10)$$

$LaNi_5$ has the $CaCu_5$ structure, space group *P6/mmm* [26]; the hexagonal metal lattice is shown in Fig. 4. The crystal structure of $LaNi_5D_7$ has been determined [27, 28] and is illustrated in Fig. 5. There are three types of interstitial D sites: La_2Ni_4 tetrahedra, and Ni_4 tetrahedra. The unit cell is doubled along the *c*-axis because of the formation of a superlattice which is a consequence of long-range correlations between occupied and unoccupied

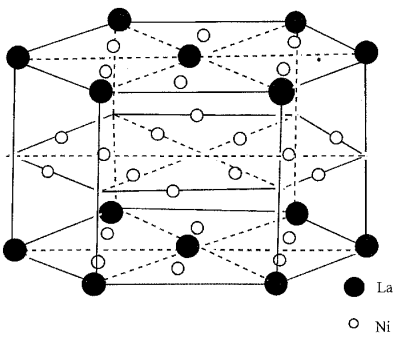


Figure 4. Schematic of hexagonal lattice of $LaNi_5$.

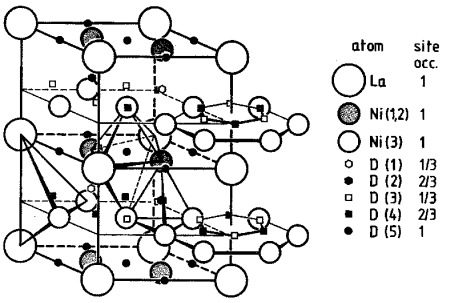


Figure 5. Structure of $LaNi_5D_7$ [27].

Ni_4 tetrahedra.

With reference to rule (3) (Sec. 7.1.3) regarding metal atom mobility, we note that the Gibbs free energies of formation (ΔG_f) at 298 K for $LaNi_5$ and for LaH_2 are about -67 and -171 kJ mol^{-1} respectively. Thus the following disproportionation reaction is highly favored [29]:

$$LaNi_5 + H_2 \rightarrow LaH_2 + 5Ni$$
$$\Delta G_{298\,K} = -104\,kJ\,mol^{-1} \qquad (11)$$

whereas for reaction (10) $\Delta G_{298\,K} \approx 0$, but at low temperatures such disproportionation does not take place. However, disproportionation on the surface of polycrystalline $LaNi_5$ occurs readily at room temperature and constitutes the alloy activation process described in Sec. 7.2.1.

CosMX Exhibit 1008, Page 236 of 633

The kinetics of the formation and decomposition of $LaNi_5$ hydride have been widely studied with just as widely varying results [30]. In most cases the investigations were done using static beds of metal/metal hydride particles in contact with gaseous hydrogen. Such system have inherently poor heat—transport and exchange characteristics and , since reaction rates are high, isothermal conditions are difficult if not impossible to maintain. Consequently the data are difficult to interpret; this is the likely cause of the disparity in reported results. When kinetic experiments were carried out isothermally or nearly so, the kinetics were well described by a shrinking-core model [31, 32]. In this model the rate-limiting process is the solid—state transformation taking place at the interface between of the α and β phases. In hydride formation a growing product layer of β—$LaNi_5H_x$ proceeds inwards from the surface, whereas in hydride decomposition the reaction also proceeds inwards from the surface but now the growing product layer is α—$LaNi_5$, as illustrated in Fig. 6 [33].

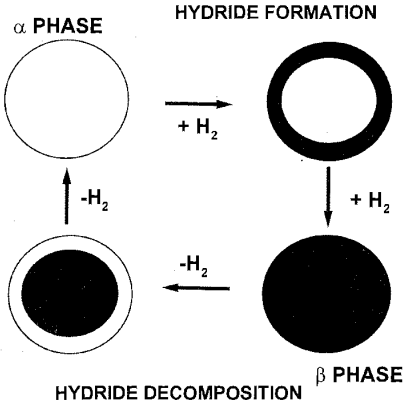


Figure 6. Schematic representation of the reaction paths for hydriding and dehydriding $LaNi_5$ [33].

A particular advantage of the AB_5 hydride family is that the properties of the alloy–hydrogen system can be varied almost at will by substituting, in whole or in part, other metals for La and Ni. For example, mischmetal, when substituted for La in $LaNi_5$, forms a hydride with about the same hydrogen content but much more unstable [34]. Lundin et al. [8] carried out a systematic study of such substitutional alloys and correlated the free energy of formation (plateau region) with the change in the interstitial hole size caused by the substituted metal component. Gruen et al. [7] have taken a similar approach, but rather correlate the cell volume with $\ln P_{plateau}$, as shown in Fig. 7.

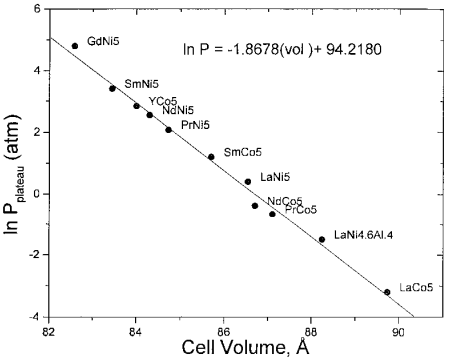


Figure 7. Alloy cell volume vs. ln $P_{plateau}$ for various AB_5 –type hydrides [7].

7.2.2.2 Preparation of AB_5 Electrodes

Electrode behaviour is strongly influenced by alloy microstructure, metal stoichiometry, and composition. Thus, an understanding of the physical metallurgy [35] of a particular system as well as a knowledge of its phase diagram is highly desirable if one wishes to prepare alloys having reproducible properties. There are no phase diagrams for these multicomponent alloys, but those having the AB_5 stoichiometry still

CosMX Exhibit 1008, Page 237 of 633

behave similarly to $LaNi_5$. Percheron-Guegan and Welter have described both laboratory and industrial preparation techniques for many intermetallic hydride formers, particularly emphasizing $LaNi_5$ and its substitutional analogues [36].

All AB_5 alloys are very brittle and are pulverized to fine particles in the hydriding-dehydriding process (see Sec. 7.2.1). Thus electrodes must be designed to accommodate fine powders as the active material. There are several methods of electrode fabrication: Sakai et al [35] pulverize the alloy by subjecting it to several hydrogen absorption-desorption cycles, before coating the resulting particles with Ni by chemical plating. The powder is mixed with a Teflon dispersion to obtain a paste which is finally roller-pressed to a sheet and then hot-pressed to an expanded nickel mesh. The fabrication of a simple paste electrode suitable for laboratory studies is reported by Petrov et al. [37].

7.2.2.3 Effect of Temperature

Ni–MH batteries are currently under consideration for use as power sources for automotive propulsion and thus will be required to operate over a large ambient temperature range. The stated goal of the USABC (US Automotive Battery Consortium) program [38] is to develop a battery which can operate satisfactorily over a range extending from $-30°C$ to $65°C$. However, hydride stability is a logarithmic function of the temperature and must be taken into account when choosing an electrode composition. For example, the equilibrium plateau pressure (decomposition) of $LaNi_5H_x$ at $65°C \approx 10$ atm, much too high for use as a battery electrode. Van't Hoff plots [39] for $LaNi_5H_x$, $MmNi_{3.55}Co_{0.75}Mn_{0.4}Al_{0.3}H_x$ and $Mm*Ni_{3.55}Co_{0.75}Mn_{0.4}Al_{0.3}H_x$ (Mm* = cerium-free mischmetal; see Table 2) are shown in Fig. 8. At 65°C the absorption plateau pressure of $Mm*B_5$ would be 0.5 atm whereas that of MmB_5 is 5.0 atm. Thus, even through both mischmetal electrodes have similar electrochemical properties at room temperature, only the former would be suitable for use at higher temperatures.

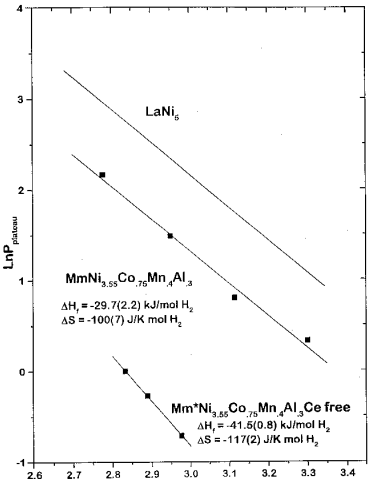


Figure 8. Van't Hoff plots for $LaNi_5H_x$, $MmNi_{3.55}Co_{0.75}Mn_{0.4}Al_{0.3}H_x$, and $Mm*Ni_{3.55}Co_{0.75}Mn_{0.4}Al_{0.3}H_x$ [39].

7.2.3 Electrode Corrosion and Storage Capacity

Deterioration of electrode performance due to corrosion of electrode components is a critical problem. The susceptibility of MH_x electrodes to corrosion is essentially determined by two factors: surface passivation due to the presence of surface oxides or hydroxides, and the molar volume of hydrogen, V_H, in the hydride phase. As pointed out by Willems and Buschow [40], V_H is important since it governs alloy expansion and contraction during the charge–discharge cycle. Large volume changes

CosMX Exhibit 1008, Page 238 of 633

increase the flushing action of the electrolyte through the pores and microcracks of the electrode during each charge–discharge cycle, thereby increasing the rate of contact of the alloy surface with fresh electrolyte and, consequently, the corrosion rate. Thus, when the effect of various substituents upon electrode corrosion is examined the question always arises as to whether an observed change is due to a change in lattice expansion or to a change in surface, e.g., the formation of a corrosion—resistant oxide layer.

Although the partial substitution of Ni by other metals has ameliorated the corrosion problem, it has also resulted in a reduced storage capacity and high alloy costs (because of the incorporation of Co). None of the substituted multicomponent hydrides approaches the storage capacity of $LaNi_5H_x$ because it is reduced by the partial substitution of Ni. Percheron-Guegan et al. [41] noted this for the ternary alloy $LaNi_{5-x}M_x$ (M=Al, Mn, Si, or Cu). Thus, although the cycle life of substituted AB_5 electrodes is greatly extended over that of $LaNi_5$, a severe penalty in storage capacity is exacted for this improvement, as illustrated by the *PC* isotherms in Fig. 3. It is also of interest to note that while $LaNi_5$ exhibits a significant hysteresis effect, $MmNi_{3.55}Co_{0.75}Mn_{0.4}Al_{0.3}$ does not. The small or even complete lack of hysteresis in multicomponent AB_5 hydrides is not unusual, but it is almost always present in less complex systems.

7.2.4 Corrosion and Composition

The long life of MmB_5 battery electrodes raises the question of why such electrodes behave so differently from other more simple formulations. Such differences are very apparent in plots of charge capacity against charge–discharge cycles, as reported by Adzic et al. [42] and shown in Fig.9. Here three different electrodes are compared: Mm(or Mm*)$Ni_{3.55}Co_{0.75}Mn_{0.4}Al_{0.3}$ (Mm* refers to Ce-free mischmetal) and a Co-free electrode $MmNi_{4.3}Mn_{0.4}\cdot Al_{0.3}$. The latter electrode corrodes rapidly and would not be suitable for battery applications. The alloy composition is clearly responsible for the observed behavior, and is discussed in the following sections. The results of these experiments are summarized in Table 3. Although cycle life may vary dramatically, inspection of cycle-life plots reveals a common behaviour which is found in almost all MH_x electrodes.

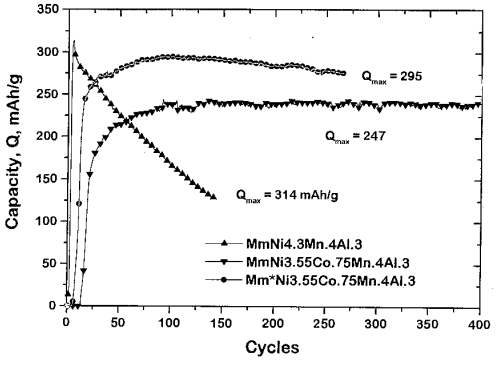


Figure 9. Charge capacity, Q, vs. number of charge-discharge cycles for three mischmetal AB_5 electrodes. Note the high decay rate in charge capacity for Co–free electrode [42].

CosMX Exhibit 1008, Page 239 of 633

There in an initial steep increase in capacity in the first few cycles which comprise the activation process. After activation, a maximum in electrochemical storage capacity, Q_{max}, is reached. This is usually followed by an almost linear decrease in capacity which may be termed capacity decay.

It is defined as the slope of the capacity–cycle curve, i.e., $-\partial Q/\partial \text{cycle}$. In order to elucidate the relationship between corrosion rate and composition it is necessary to determine lattice expansion quantitatively.This requires the determination of V_H, which is listed in Table 4 for a number of alloys.

Table 3. Effect of Co in various MmB_5 electrodes [42]

Alloy	V_H (Å^3)	Q_{max} (mAh g^{-1})	n (H atoms/ unit cell)	$\Delta V/V$ (%)	Corrosion (wt.%/cycle)
$MmNi_{3.55}Co_{0.75}Mn_{0.4}Al_{0.3}$	3.13	247	3.90	14.3	0.001
$Mm^*Ni_{3.55}Co_{0.75}Mn_{0.4}Al_{0.3}$ †	3.05	295	4.64	16.0	0.041
$MmNi_{4.3}Mn_{0.4}Al_{0.3}$	3.51	314	4.96	20.1	0.354
$Mm^*Ni_{4.3}Mn_{0.4}Al_{0.3}$	3.14	314	4.94	17.7	1.029

† Mm*, Ce-free mischmetal

Table 4. Crystallographic parameters and V_H of selected alloys

Composition	a (Å)	c (Å)	Cell vol. (Å^3)	V_H (Å^3)	Ref.
$NdNi_{3.55}Co_{0.75}Mn_{0.4}Al_{0.3}$	4.9992	4.0221	87.05	2.66	[15]
$La_{0.25}Nd_{0.75}Ni_{3.55}Co_{0.75}Mn_{0.4}Al_{0.3}$	5.0138	4.0254	87.63	2.74	[15]
$LaNi_{3.55}Co_{0.75}Mn_{0.4}Al_{0.3}$	5.0642	4.0325	89.56	2.93	[43]
$La_{0.65}Pr_{0.35}Ni_{3.55}Co_{0.75}Mn_{0.4}Al_{0.3}$	5.0368	4.0206	88.33	2.97	[15]
$LaNi_{3.5}Co_{0.75}Mn_{0.4}Al_{0.3}$	5.0699	4.0392	89.91	3.00	[43]
$Mm_{0.3}Mm^*_{0.7}Ni_{3.55}Co_{0.75}Mn_{0.4}Al_{0.3}$	5.0234	4.0434	88.36	3.00	[15]
$LaNi_{3.95}Co_{0.75}Al_{0.3}$	5.0378	4.0107	88.15	3.02	[51]
$MmNi_{3.55}Co_{0.75}Mn_{0.4}Al_{0.3}$ (Ce-free)	5.0318	4.0309	88.38	3.05	[51]
$LaNi_{3.55}Co_{0.75}Mn_{0.4}Al_{0.3}$	5.0615	4.0298	89.40	3.06	[43]
$La_{0.5}Nd_{0.5}Ni_{3.55}Co_{0.75}Mn_{0.4}Al_{0.3}$	5.0315	4.0259	88.26	3.07	[15]
$LaNi_{3.55}Co_{0.75}Mn_{0.3}Al_{0.3}$	5.0662	4.0321	89.70	3.07	[51]
$LaNi_{4.1}Co_{0.2}Mn_{0.4}Al_{0.3}$	5.0609	4.0361	89.52	3.09	[42]
$LaNi_{3.9}Co_{0.4}Mn_{0.4}Al_{0.3}$	5.0629	4.0349	89.57	3.09	[42]
$MmNi_{3.55}Co_{0.75}Mn_{0.4}Al_{0.3}$ †	4.9890	4.0545	87.39	3.10	[43]
$Mm\ Ni_{3.55}Co_{0.75}Mn_{0.4}Al_{0.3}$	4.9626	4.0560	86.50	3.13	[43]
$La_{0.25}Ce_{0.75}Ni_{3.55}Co_{0.75}Mn_{0.4}Al_{0.3}$	4.9538	4.0559	86.19	3.15	[43]
$La_{0.5}Ce_{0.5}Ni_{3.55}Co_{0.75}Mn_{0.4}Al_{0.3}$	4.9934	4.0446	87.33	3.15	[43]
$La_{0.65}Nd_{0.35}Ni_{3.55}Co_{0.75}Mn_{0.4}Al_{0.3}$	5.0324	4.0211	88.19	3.15	[15]
$LaNi_{3.55}Co_{0.75}Mn_{0.14}Al_{0.3}$	5.0509	4.0321	89.08	3.16	[51]
$LaNi_{3.85}Co_{0.75}Mn_{0.38}$	5.0526	4.0195	88.86	3.20	[51]
$La_{0.8}Ce_{0.2}Ni_{3.55}Co_{0.75}Mn_{0.4}Al_{0.3}$	5.0380	4.0416	88.84	3.21	[43]
$MmNi_{3.5}Co_{0.75}Mn_{0.4}Al_{0.3}$	4.9623	4.0456	86.27	3.23	[43]
$LaNi_{4.3}Mn_{0.4}Al_{0.3}$	5.0591	4.0370	89.48	3.26	[42]
$La_{0.65}Ce_{0.35}Ni_{3.55}Co_{0.75}Mn_{0.4}Al_{0.3}$	5.0168	4.0451	88.16	3.24	[43]
$LaNi_{3.85}Co_{0.75}Mn_{0.04}$	5.0494	4.0034	88.39	3.35	[51]
$LaNi_{4.7}Al_{0.3}$	5.0195	4.0076	87.44	3.47	[43]
$MmNi_{4.3}Mn_{0.4}Al_{0.3}$	4.9652	4.0453	86.37	3.51	[42]

† Synthetic mischmetal, i.e., $La_{0.26}Ce_{0.52}Pr_{0.06}Nd_{0.16}$

CosMX Exhibit 1008, Page 240 of 633

In order to determine electrode corrosion quantitatively, Adzic et al. [43], used the following approach. The H content of the charged electrode, expressed as the number of H atoms, n, per formula unit, was calculated from Q_{max} by the Faraday equation, Eq.(12),

$$n = e^- = \frac{3600}{9.65 \times 10^7}(mw)(Q_{max}) \qquad (12)$$

where mw is the molecular weight of the alloy and the units of Q are $mAh\,g^{-1}$. They assumed that after activation the remaining uncorroded alloy in each subsequent charge–discharge cycle is hydrided and dehydrided to the same degree, and that n is constant. The percentage lattice expansion of the unit cell in each electrochemical cycle was calculated by Eq. (13),

Lattice expansion =

$$\frac{\Delta V}{V} = \frac{V_H}{V} n \times 100\ [\%] \qquad (13)$$

where ΔV is the actual volume change of the unit cell in $Å^3$ in each charge or discharge cycle, V is the initial unit cell volume and n is the number of H atoms inserted into the unit cell volume and subsequently discharged.

Finally, the loss of electrochemical capacity is directly proportional to the loss of the AB_5 alloy by oxidation and is readily calculated from Eq.(14).

% wt. loss/cycle =

$$-\frac{\partial Q}{\partial \text{cycle}}(Q_{max})^{-1} \times 100 \qquad (14)$$

The effects of Ce, Co, Al, and Mn upon the properties and performances of $A(NiCoMnAl)_5$ electrodes employing the above equations are discussed in the following sections.

7.2.4.1 Effect of Cerium

The rare earth composition of commercial electrodes is also related to electrode corrosion. This was noted by Sakai et. al. [44], who found that the presence of Nd or Ce inhibited corrosion when substituted in part for La in $La_{1-x}Z_x(NiCoAl)_5$ (Z = Ce or Nd) electrodes. However no explanation for the effect was noted. Willems [22] prepared an electrode of $La_{0.8}Nd_{0.2}Ni_{2.5}Co_{2.4}Si_{0.1}$ which retained 88% of its storage capacity after 400 cycles. He attributed its long cycle life to a low V_H of 2.6 $Å^3$.

The case of cerium is of particular interest. Adzic et al. [43] examined the properties of a homologous series of alloys with a composition corresponding to $La_{1-x}Ce_xNi_{3.55}Co_{0.75}Mn_{0.4}Al_{0.3}$ and measured their comparative performance as battery electrodes. A *PCT* diagram for this system is shown in Fig. 10.

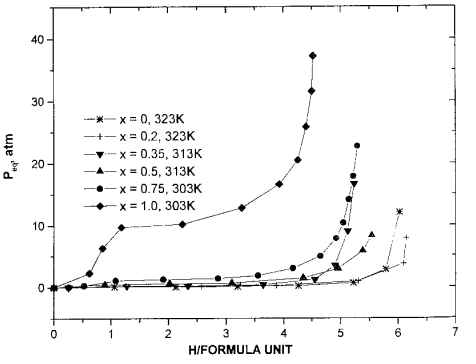


Figure 10. *P–C* isotherms for the $La_{1-x}Ce_xNi_{3.55}Co_{0.75}Mn_{0.4}Al_{0.3}$ – H system [43].

Note that at $x > 0.2$ there is a decrease in the H storage capacity and thermodynamic stability, until at $x = 1$ the decrease in both

CosMX Exhibit 1008, Page 241 of 633

parameters are marked. This reduced stability is not unexpected as the unit cell volume decreases with Ce content (see Fig.7).

Cycle-life plots for the $La_{1-x}Ce_xB_5$ electrodes are illustrated in Fig. 11. The decreased charge capacity in all $La_{1-x}Ce_xB_5$ alloys with x > 0.35 conforms with the shorter and higher plateau pressure of the isotherms depicted in Fig. 10. The extremely low electrochemical capacity of CeB_5 is a consequence of the high dissociation pressure of the hydride phase.

The corrosion rate for the $La_{1-x}Ce_xB_5$ electrodes are listed in Table 5. The results are summarized graphically in Fig. 12 in which lattice expansion, corrosion rate, and H content (n) are plotted against Ce content. The plot clearly shows the anomalous correlation of lattice expansion with corrosion; thus one concludes that the corrosion inhibition stemming from the presence of Ce is due to a surface effect. This conclusion is supported by a previous report that a film of CeO_2 on metal surfaces inhibits corrosion [45]. XAS (X-ray absorption spectroscopy) studies discussed in Sec. 7.4 confirm the corrosion inhibition effect of Ce [46].

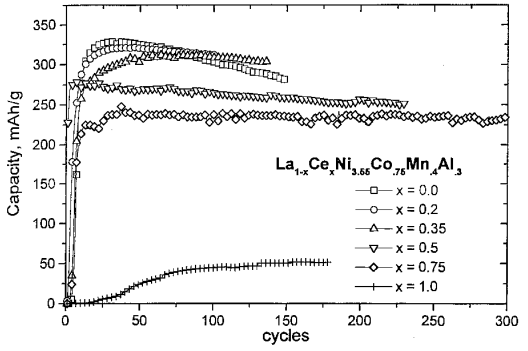


Figure 11. Charge capacity, Q, vs. number of charge–discharge cycles for $La_{1-x}Ce_xNi_{3.55}Co_{0.75}Mn_{0.4}Al_{0.3}$ [43].

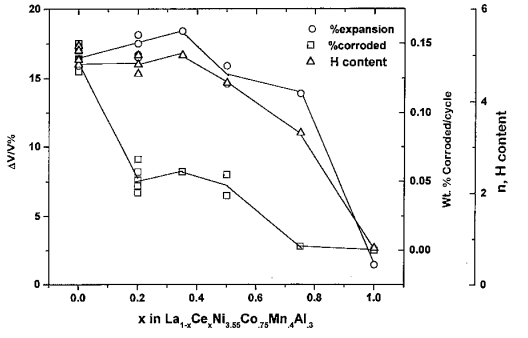


Figure 12. $\Delta V/V$ (%), wt.% corroded/cycle, and H content vs. Ce content, x, in $La_{1-x}Ce_xNi_{3.55}Co_{0.75}Mn_{0.4}Al_{0.3}$ electrodes [43].

CosMX Exhibit 1008, Page 242 of 633

Table 5. Effect of Ce in $La_{1-x}Ce_xCo_{0.75}Mn_{0.4}Al_{0.3}$ electrodes [43]

x	V_H (A^3/atom)	n (H atoms/unit cell)	$\Delta V/V$ (%)	Q_{max} (mAh g^{-1})	Corrosion (wt.% / cycle)
1.0	1.6 *	0.8	1.4625	51	0
0.75	3.15	3.8	13.919	241	0.003
0.5	3.15	4.4	15.917	278	0.04
0.20	3.21	4.8	17.534	305	0.042
0.20	3.21	4.6	16.547	293	0.047
0.50	3.15	4.0	14.634	260	0.054
0.20	3.21	4.6	16.659	293	0.051
0.20	3.21	5.0	18.122	318	0.057
0.35	3.24	5.0	18.376	318	0.057
0.20	3.21	5.0	18.112	318	0.066
0.0	2.99 †	4.8	15.96	305	0.15
0.0	2.99 †	5.2	17.33	331	0.139
0.0	2.99 †	5.1	17.002	325	0.145
$LaNi_{4.7}Al_{0.3}^{\ddagger}$	3.47	4.5	17.943	285	0.291

* α phase
† Average
‡ Included for comparison

7.2.4.2 Effect of Cobalt

Cobalt is invariably present in commercial MH_x battery electrodes. It tends to increase hydride thermodynamic stability and inhibit corrosion. However, it is also expensive and substantially increases battery costs; thus, the substitution of Co by a lower/cost metal is desirable. Willems and Buschow [40] attributed reduced corrosion in $LaNi_{5-x}Co_x$ (x=1–5) to low V_H. Sakai et al. [47] noted that $LaNi_{2.5}Co_{2.5}$ was the most durable of a number of substituted $LaNi_{5-x}Co_x$ alloys but it also had the lowest storage capacity.

The results of a systematic study of the effect of Co in an alloy series corresponding to $LaNi_{4.3-x}Co_xMn_{0.4}Al_{0.3}$ are shown in Fig. 13 and summarized in Table 6 and graphically in Fig. 14. The correlation between expansion and corrosion is rather weak; e.g., even though the H content is unchanged. It is thus likely that corrosion inhibition by Co is also due to a surface effect as with Ce. In this connection Kanda et al. [48] found evidence that Co suppresses the transport of Mn to the surface, where it is readily oxidized, causing rapid electrode deterioration. Recent XAS results also suggest that Co inhibits corrosion by a surface process, by suppressing Ni oxidation [49].

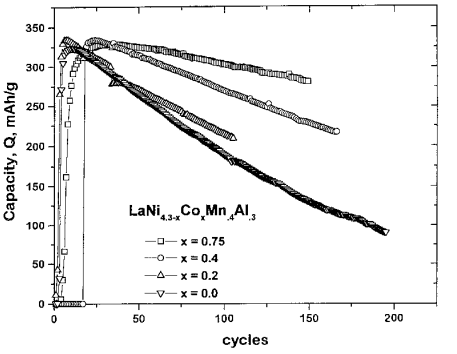


Figure 13. Charge capacity, Q, vs. number of charge–discharge cycles for $LaNi_{4.3-x}Co_xMn_{0.4}Al_{0.2}$ electrodes [42].

7.2.4.3 Effect of Aluminum

Aluminum appears to be present in all commercial AB_5 electrodes. Sakai et al.

CosMX Exhibit 1008, Page 243 of 633

Table 6. Effect of Co in $LaNi_{4.3-x}Co_xMn_{0.4}Al_{0.3}$ electrodes [4]

x	V_H ($Å^3$)	Q_{max} ($mAh\,g^{-1}$)	n (H atoms/ unit cell)	$\Delta V/V$ (%)	Corrosion (wt.% / cycle)
0.75	2.99	330	5.18	17.3	0.139
0.40	3.09	334	5.25	18.1	0.257
0.20	3.09	334	5.25	18.1	0.380
0.0	3.26	324	5.09	18.5	0.485

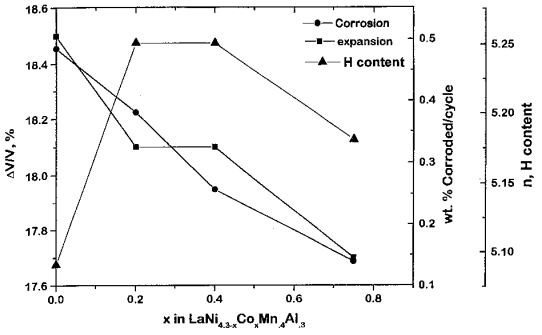


Figure 14. $\Delta V/V$ (%), wt.% corroded/cycle, and H content vs. Co content, x, in $LaNi_{4.3-x}Co_xMn_{0.4}Al_{0.3}$ electrodes [42].

[50] noted that the incorporation of Al in $La(NiCoAl)_5$ alloys substantially reduced electrode corrosion; they attributed this to the formation of protective surface oxides. The corrosion-inhibiting effect of Al is clearly shown in Fig. 15 in which storage capacity is plotted versus cycle life for $LaNi_{3.85-x}Co_{0.75}Mn_{0.4}Al_x$ (x = 0, 0.1, 0.2, 0.3) electrodes [51]; the Al–free electrode corrodes at a greatly increased rate. As illustrated in Table 7 and Fig. 16, the presence of even a small amount of Al substantially decreases V_H and n, and consequently both lattice expansion and corrosion.

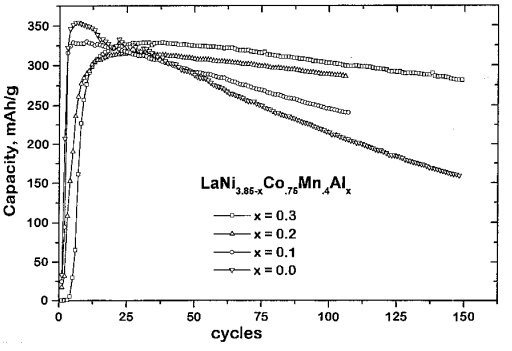


Figure 15. Charge capacity, Q, vs. number of charge–discharge cycles for $LaNi_{3.85-x}Co_{0.75}Mn_{0.4}Al_x$ electrodes [51].

Table 7. Effect of Al in $LaNi_{3.85-x}Co_{0.75}Mn_{0.4}Al_x$ electrodes [51]

x	V_H ($Å^3$)	Q_{max} ($mAh\,g^{-1}$)	n (H atoms/ unit cell)	$\Delta V/V$ (%)	Corrosion (wt.% / cycle)
0.2	3.01	314	4.98	16.66	0.1274
0.3	2.99	330	5.18	17.33	0.1394
0.1	3.01	327	5.22	17.58	0.2905
0.0	3.20	353	5.66	20.39	0.4079
0.0	3.35	366	5.88	22.30	0.4126

CosMX Exhibit 1008, Page 244 of 633

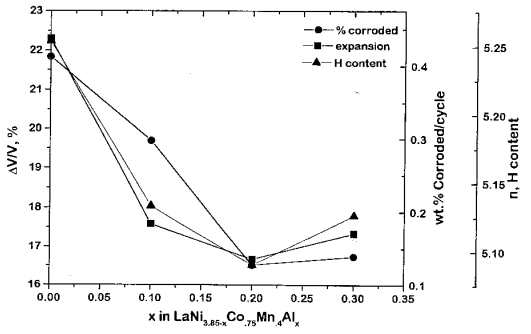


Figure 16. $\Delta V/V$ (%), wt.% corroded/cycle, and H content vs. Al content, x, in $LaNi_{3.85-x}Co_{0.75}Mn_{0.4}Al_x$ electrodes [51].

7.2.4.4 Effect of Manganese

Manganese is also present in most commercial electrodes. In a series of experiments examining the cycle lives of the homologous alloys $LaNi_{5-x}M_x$ (M= Mn, Cu, Al, and Co) Sakai et al. [50] noted that Mn was the least effective. In more complex alloys examined by Adzic et al. [51] the function of Mn is still open to question.

The cyclic behaviour of a series of electrodes of varying Mn content is shown in Fig. 17. It apparently increases V_H (Table 8) slightly and although the correlation between lattice expansion, n, and corrosion rate is fairly strong, they are not a function of Mn content, as shown in Fig. 18.

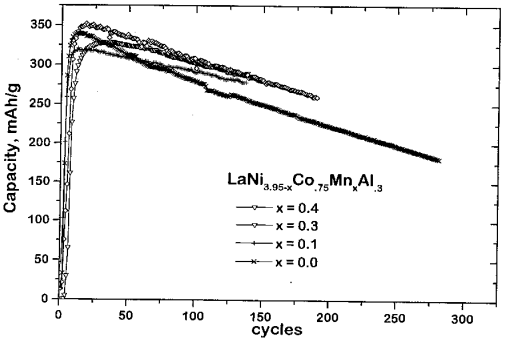


Figure 17. Charge capacity, Q, vs. number of charge–discharge cycles for $LaNi_{3.95-x}Co_{0.75}Mn_xAl_{0.3}$ electrodes [51].

Table 8. Effect of Mn in $LaNi_{3.95-x}Co_{0.75}Mn_xAl_{0.3}$ electrodes

x	V_H ($Å^3$)	Q_{max} ($mAh\,g^{-1}$)	n (H atoms/ unit cell)	$\Delta V/V$ (%)	Corrosion (wt.% / cycle)
0.14	3.16	320	4.87	17.27	0.106
0.40	2.99	330	5.18	17.33	0.1394
0.0	3.02	340	5.37	18.38	0.1676
0.30	3.07	353	5.48	18.75	0.150

CosMX Exhibit 1008, Page 245 of 633

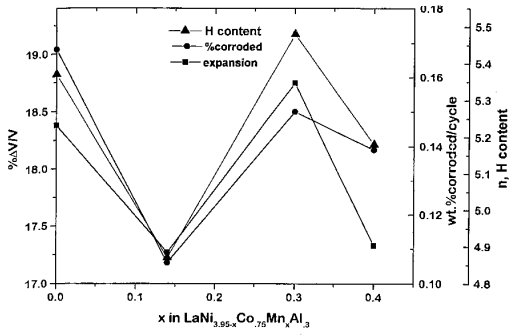


Figure 18. $\Delta V/V$ (%), wt.% corroded/cycle, and H content vs. Al content, x, in $LaNi_{3.95-x}Co_{0.75}Mn_xAl_{0.3}$ electrodes [51].

7.3 AB_2 Hydride Electrodes

The active materials in these electrodes are Laves phase alloys. These have close-packed structures in which the radii of the A and B atoms must lie within a certain range based on a hard—sphere packing model. The ideal ratio r_a / r_b is 1.225 but known Laves phases have ratios ranging from 1.05 to 1.68. There are three structural types: the hexagonal C14 ($MgZn_2$), the cubic C15 ($MgCu_2$), and the hexagonal C36 ($MgNi_2$). The C14 and C15 structures are common and form many hydride phases [52]. However, the alloys used in battery applications are very complicated and may contain as many three distinct bulk phases [53]. Ovshinsky et al. [54] described the properties of a series of alloys containing V, Ti, Zr, Ni, Cr, Co, and Fe in various proportions; they qualitatively discussed how AB_2 alloy properties are influenced by various elemental constituents. Gifford et al. [55] described an experimental EV battery incorporating an AB_2 anode having an energy density of 80 $Wh\,kg^{-1}$. The battery lost 18% of its original charge after 800 cycles at 80% depth of discharge.

PCT diagrams of AB_2 (electrode alloys) /H systems reflect multiphase or nonideal behaviour [54]. This is illustrated in Fig. 19, in which both the equilibrium pressure and the open—circuit equilibrium voltage, E_r are plotted for $Zr_{0.5}Ti_{0.5}V_{0.5}Ni_{1.1}Fe_{0.2}Mn_{0.2}$.

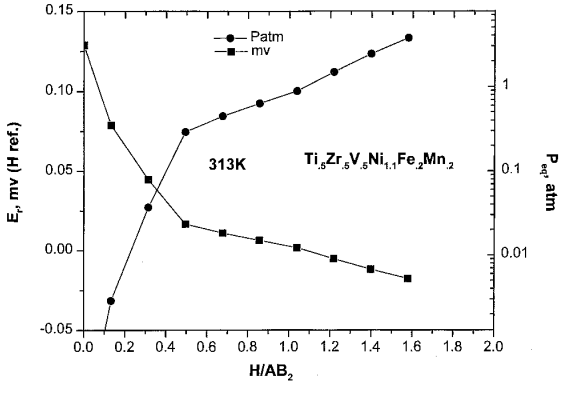


Figure 19. Electrochemical isotherm for $Ti_{0.5}Zr_{0.5}V_{0.5}Ni_{1.1}Fe_{0.2}Mn_{0.2}$. The P_{eq} is calculated from the equilibrium voltage, E_r, by the Nernst equation [56].

CosMX Exhibit 1008, Page 246 of 633

The pressure was calculated from E_r using the Nernst equation [56]. The use of the electrochemical technique is more convenient to measure such equilibrium than the conventional gas/solid method [19] when equilibrium pressures are much less than 1 atm. over a significant portion of the H-content range. The isotherm is highly sloping with no plateau, and reflects nonideal behaviour, i.e., the presence of inhomogeneities, defects, etc. However, unlike applications which involve the storage of hydrogen for subsequent evolution as a gas, battery applications do not require flat, wide plateaus because the pressure is a logarithmic function of the voltage. Of course, if the isotherm is too steep, a portion of the H storage capacity will not be electrochemically accessible, because either the voltage will become too anodic and corrosion will ensue, or the equilibrium H_2 pressure will become excessive.

The cycle lives of several AB_2 electrodes are illustrated in Fig. 20 [56]. In some cases alloys require many charge–discharge cycles to become fully activated; preactivation via direct reaction with H_2 gas is helpful in this regard. Some pertinent properties and results are given in table 9.

It is of interest to note that V_H in the hydride phase is significantly less than in AB_5 hydrides. Consequently, lattice expansion is also significantly reduced. However, the corrosion rate of the electrodes in Table 9 is still appreciable. Indeed, for the electrode with $x = 0.25$ the corrosion rate is very high in spite of a small lattice expansion. Clearly this material is quite sensitive to corrosion and indicates that a moderately high Zr content is necessary to inhibit corrosion by a surface passivation, as suggested by Zuttel et al. [57]

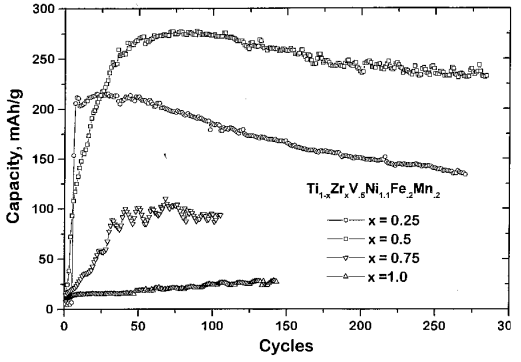


Figure 20. Charge capacity, Q, vs. number of charge–discharge cycles for $Zr_{1-x}Ti_xV_{0.5}Ni_{1.1}Fe_{0.2}Mn_{0.2}$ electrodes [56].

Table 9. Properties of $Ti_{1-x}Zr_xV_{0.5}Ni_{1.1}Fe_{0.2}Mn_{0.2}$ electrodes [56]

x	V_H ($Å^3$)	Q_{max} ($mAh\,g^{-1}$)	n (H atoms/ unit cell)	$\Delta V/V$ (%)	Corrosion (wt.% / cycle)
0.25	1.95	215	5.48	6.45	0.214
0.5	2.76	299	8.12	13.1	0.097
0.5	2.76	278	7.56	12.3	0.083
0.75		95	0.7		0.0
1.0		27	0.2		0.0

* There four formula units in the hexagonal C14 unit cell

CosMX Exhibit 1008, Page 247 of 633

7.4 XAS Studies of Alloy Electrode Materials

The availability of high-intensity, tunable X-rays produced by synchrotron radiation has resulted in the development of new techniques to study both bulk and surface materials properties. XAS methods have been applied both in situ and ex situ to determine electronic and structural characteristics of electrodes and electrode materials [58, 59]. XAS combined with electron-yield techniques can be used to distinguish between surface and bulk properties. In the latter procedure X-rays are used to produce high energy Auger electrons [60] which, because of their limited escape depth ($\approx$150–200 Å), can provide information regarding near surface composition.

The element-specific nature of XAS makes it particularly useful for the study of complex AB_5 and AB_2 metal hydride electrode materials. Mukerjee et al. [46] examined $La_{0.8}Ce_{0.2}Ni_{4.8}Sn_{0.2}$ and $LaNi_{4.8}Sn_{0.2}$ electrodes using XAS in situ. It was determined by analysis of the X-ray absorption near-edge structure (XANES) that the presence of Ce reduced Ni corrosion, a finding which confirmed previous cycle-life experiments [43]. This was done by determining quantitatively the amount of oxidized Ni (assumed to be $Ni(OH)_2$) in cycled electrodes as a function of Ce content. It is interesting that the 001 peak of $\alpha\,Ni(OH)_2$ was weakly observed in an electrode after 500 cycles using conventional X-ray diffraction (XRD). Although this is to be expected, since the nickel hydroxide formed is somewhat amorphous, it illustrates an important advantage of XAS over XRD since the former probes short-range order and thus can provide quantitative information regarding amorphous or partly amorphous materials. Tryk et. al. have similarly examined $LaNi_5$ [61] and $MmNi_{3.5}Co_{0.8}Mn_{0.3}Al_{0.4}$ [62] electrodes; they noted the electronic transitions taking place in the metal lattice as a function of charge, and the strong interaction of absorbed H with Ni. This is not unexpected as hydrogen occupies a Ni tetrahedral site in $LaNi_5H_6$ (Fig. 5).

XAS studies have also been carried out on C14 Laves phase alloys $Ti_{0.5}Zr_{0.5}M_2$ and $Ti_{0.75}Zr_{0.25}M_2$ ($M = V_{0.5}Ni_{1.1}Fe_{0.2}Mn_{0.2}$) [56]. The XANES spectra at the Ni K-edge indicates that, unlike the AB_5 alloys, there is very little interaction between hydrogen and Ni but rather strong interactions with Ti, V, and Zr. The hydrogen is presumably located in tetrahedra that contain large fractions of these three elements, whereas the Ni-rich sites are probably empty. Thus the function of Ni in AB_2 alloys may be primarily to serve as a catalyst for the electrochemical hydriding reactions.

7.5 Summary

This survey presents an overview of the chemistry of metal–hydrogen systems which form hydride phases by the reversible reaction with hydrogen. The discussion then focuses on the AB_5 class and, to a lesser extent, the AB_2 class of metal hydrides, both of which are of interest for battery applications.

Electrode corrosion is the critical problem associated with the use of metal hydride anodes in batteries. The extent of corrosion is essentially determined by two factors: alloy expansion and contraction in the charge–discharge cycle, and chemical surface passivation by the formation of corrosion—resistant oxides or hydroxides.

CosMX Exhibit 1008, Page 248 of 633

Both factors are sensitive to alloy composition, which can be adjusted to produce electrodes having an acceptable cycle life. In AB_5 alloys the effects of Ce, Co, Mn, and Al upon cycle life in commercial AB_5-type electrodes are correlated with lattice expansion and charge capacity. Ce was shown to inhibit corrosion even though lattice expansion increases. Co and Al also inhibit corrosion. XAS results indicate that Ce and Co inhibit corrosion though surface passivation.

There are few systematic guidelines which can be used to predict the properties of AB_2 metal hydride electrodes. Alloy formulation is primarily an empirical process where the composition is designed to provide a bulk hydride-forming phase (or phases) which form, in situ, a corrosion–resistance surface of semipassivating oxide (hydroxide) layers. Lattice expansion is usually reduced relative to the AB_5 hydrides because of a lower V_H. Pressure–composition isotherms of complex AB_2 electrode materials indicate nonideal behaviour.

Finally, it should be noted that while small Ni–MH batteries are now an article of commerce, a major challenge still remains. It is to produce a low-cost MH_x electrode having a long cycle life and a storage capacity of >300 $mAh\,g^{-1}$ which is suitable for use in heavy-duty, long-life batteries such as proposed for electric and hybrid vehicles [38].

Acknowledgement. The author acknowledges the support of the DOE Chemical Science Division and DOE Office of Transportation Technologies under contract number DE-AC02—76CH00016. Further thanks are due to John R. Johnson, Gordana Adzic, and Claire Reilly for proofreading the manuscript and for offering many helpful suggestions.

7.6 References

[1] T. B. Flanagan, W. A. Oates, in *Hydrogen in Intermetallic Compounds* (Ed.: L. Schlapbach), Topics in Applied Pshysics, No. 63, Springer Verlag, New York, **1988**, p. 49.

[2] G. G. Libowitz, The Solid State Chemistry of Binary Metal Hydrides, W. A. Benjamin, New York, **1965**.

[3] W. M. Müller, J. P. Blackledge, G. G. Libowitz (Eds.), *Metal Hydrides*, Academic Press, New York, **1968**.

[4] E. Wicke, H. Brodowsky, H. Zuchner in *Hydrogen in Metals II* (Eds.: G. Alefeld, J. Volkl), Topics in Aplied Physics, No. 28, Springer Verlag, New York, **1978**, p. 73.

[5] A. C. Switendick in *Hydrogen in Metals I* (Eds.: G. Alefeld, J. Volkl), Topics in Aplied Physics, No. 28, Springer Verlag, New York, **1978**, p. 101.

[6] M. Gupta, L. Schlapbach in *Hydrogen in Intermetallic Compounds I* (Ed.: L. Schlapbach), Topics in Aplied Physics, No. 63, Springer Verlag, New York, **1988**, p. 139.

[7] D. N. Gruen, M. H. Mendelsohn, A. E. Dwight, *J. Less-Common Metals* **1979**, *63*, 193.

[8] C. E. Lundin, F. E. Lynch, C. B. Magee, *J. Less-Common Metals* **1977**, *56*, 19.

[9] D. G. Westlake, J. Less-Common Metals **1983**, *91*, 1.

[10] A. C. Switendick, *Z Phys. Chem. N. F.* **1979**, *117*, 89.

[11] J. J. Reilly in *Proc. Int. Symp. On Hydrides for Energy Storage, Geilo, Norway* (Eds.: A. F. Andresen, A. J. Maeland), Pergamon, New York, **1978**, p. 301.

[12] J. J. Reilly, *Z. Phys. Chem. N. F.* **1979**, *117*, 155.

[13] J. J. Reilly, R. H. Wishall, *Inorg. Chem.* **1968**, *7*, 2254.

[14] J. J. Reilly, R.H. Wishall, *Inorg. Chem.* **1974**, *13*, 218.

[15] J. R. Johnson, unpublished data.

[16] Y. Lei, Y. Wu, Q. Yanf, J. Wu, Q. Wang, *Z Phys. Chem.* **1994**, *183*, 379.

[17] M. Tsukahara, K. Takahashi, T. Mishima, H. Miyamura, T. Sakai, N. Kuriyama, I. Uehara, *J. Alloys Compds.* **1995**, *231*, 616.

[18] H. C. Siegman, L. Schlapbach, C. R. Brundle, *Phys. Rev. Lett.* **1978**, *40*, 547.

[19] J. J. Reilly in *Inorganic syntheses* (Ed.: S. L.

CosMX Exhibit 1008, Page 249 of 633

Holt), John Wiley, New York, **1983**, p. 90.

[20] E. W. Justi, H. H. Ewe, H. Stephan, *Energy Conversion* **1973**, *13*, 109.

[21] A. Percheron-Guegan, J. C. Achard, J. Sarradin, G. Bronoel in *Proc. Int. Symp. on Hydrides for Energy Storage, Geilo, Norway* (Eds.: A. F. Andresen, A. J. Maeland), Pergamon, New York, **1978**, p. 485

[22] J. J. G. Willems, Philips *J. Res.* **1984**, 39 (*Suppl. 1*).

[23] M. Ikowa, H. Kawano, I. Matsumoto, N. Yanagihara, European Pattent Application 0271043, 1987; H. Ogawa, M. Ikowa, H. Kawano, I. Matsumoto, *Power Source* **1988**, *12*, 393.

[24] M. Ikoma, S. Hamada, N. Morishita, Y. Hoshina, K. Ohta, T. Kimura, *Proc Symp on Hydrogen and Metal Hydride Batteries* (Eds.: P. D. Bennet, T. Sakai), The electrochemical Society, Pennington, NJ, **1996**, *94–27*, p. 370.

[25] J. H. N. van vucht, F. A. Kuipers, H. C. A. M. Bruning, *Philips Res. Rep.* **1970**, *25*,133.

[26] J. H. Wernick, S. Geller, *Acta Crystallogr.* **1959**, *12*, 662.

[27] P. Thompson, J. J. Reilly, L. M. Corliss, J. M. Hastings, R. Hempelmann, *J. Phys. F: Metal Phys.* **1986**, *16*, 679.

[28] C. Lartique, A. Percheron-Guegan, J. C. Achard, J. L. Soubeyoux, *J. Less-Common Metals* **1985**, *113*, 127.

[29] K. H. J. Buschow, A. R. Medima in *Proc. Int. Symp. Hydrides for Energy Storage, Geilo, Norway* (Eds.: A. F. Andresen, A. J. Maeland), Pergamon, New York, **1978**, p. 235.

[30] P. D. Goodell, P. S. Rudman, *J. Less-Common Metals* **1983**, *89*, 117.

[31] J. J. Reilly, Y. Josephy, J. R. Johnson, *Z. Phys. Chem. N.F.* **1989**, *164*, 1241.

[32] M. Miyamoto, K. Yamaji, Y. Nakata, *J. Less-Common Metals* **1989**, *89*, 111

[33] J. J. Reilly in *Proc. Symp. on Hydrogen STorage Materials, Batteries, and Electrochemistry* (Eds.: D. A. Corrigan, S. Srinivasan), The Electrochemical Society, Pennington, NJ, **1992**, *92–5*, p. 24.

[34] J. J. Reilly, R. H. Wiswall, Jr., *Hydrogen Storage and Purification Systems*, US Atomic Energy Commission, BNL—17136, Brookhaven National Laboratoru, Upton, NY 11973, August **1972**.

[35] T. Sakai, H. Yoshinaga, H. Miyamura, N. Kuriyama, H. Ishikawa, *J. Alloys Compds.* **1992**, *180*, 37.

[36] A. Percheron-Guegan, J. M. Welter in *Hydrogen in Intermetallic Compounds I*, (Ed.: L. Schlapbach), Topics in Applied Physics, No. 63, Springer Verlag, New York, **1988**, p. 11.

[37] K. Petrov, A. A. Rostami, A. Visintin, S. Srinivasan, *J. Electrochem. Soc.* **1994**, *141(7)*, 1747.

[38] W. A. Adams in *Proc. Symp. on Exploratory Research and Development of Batteries for Electric and Hybrid Vehicles* (Eds.: W. A. Adams, A. R. Landgrebe, R. Scrosati), The Electrochemical Society, Pennington, NJ, **1996**, *96–14*, p. 1.

[39] G. D. Adzic, J. R. Johnson, S. Mukerjee, J. McBreen, J. J. Reilly *Meeting Abstracts of the 189th Meeting of the Electrochemical Society, Los Angeles, 1996*, The Electrochemical Society, Pennington, NJ, **1996**, *96–1*, Abstract No. 65.

[40] J. J. G. Willems, K. H. J. Buschow, *J. Less-Common Metals* **1987**, *129*, 13.

[41] M. Latroche, A. Percheron-Guegan, Y. Chabre, J. Bouet, J. Pannetier, E. Ressouche, *J. Alloys Compds.* **1995**, *231*, 537.

[42] G. Adzic, J. R. Johnson, S. Mukerjee, J. McBreen, J. J. Reilly, *J. Alloys Compds.* **1997**, *253-254*, 579

[43] G. Adzic, J. R. Johnson, J. J. Reilly, J. McBreen, S. Mukerjee, M. P. S. Kumar, W. Zhang, S. Srinivasan, *J. Electrochem.* Soc. **1995**, *142*, 3429.

[44] T. Sakai, T. Hazama, H. Miyamura, N. Kuriyama, A. Kato, H. Ishikawa, *J. Less-Common Metals* **1991**, *172–174*, 1175.

[45] A. J. Davenport, H. S. Isaacs, M. W. Kendig, *Corros. Sci.* **1991**, *32(5/6)*, 653.

[46] S. Mukerjee, J. McBreen, J. J. Reilly, J. R. Johnson, G. Adzic, K. Petrov, M. P. S. Kumar, W. Zhang, S. J. Srinivasan *J. Electrochem. Soc.* **1995**, *142(7)*, 2278.

[47] T. Sakai, K. Oguro, H. Miyamura, N. Kuriyama, A. Kato, H. Ishikawa et al., *J. Less-Common Metals* **1990**, *161*, 193.

[48] M. Kanda, M. Yamamoto, K. Kanno, Y. Satoh, H. Hayashida, M. Suzuki, *J. Less-Common Metals* **1987**, *129*, 13.

[49] S. Mukerjee, J. McBreen, G. D. Adzic, J. R. Johnson, J. J. Reilly *Extended Abstracts, National Meeting of the Electrochemical Society, San Antonio, Texas, USA*, Oct. **1996**, *96–2*, Abstract No. 48.

[50] T. Sakai, H. Miyamura, H. Kuriyama, A. Kato, K. Oguro, H. Ishikawa, *J. Less-Common Met-*

CosMX Exhibit 1008, Page 250 of 633

als **1980**, *159*, 127.
[51] G. Adzic, J. R. Johnson, S. Mukerjee, J. McBreen, J. J. Reilly in *Proc. Symp. on Exploratory Research and Development of Batteries for Electric and Hybrid Vehicles* (Eds.: W. A. Adams, A. R. Landgrebe, R. Scrosati), Electrochemical Society, Pennington, NJ, **1996**, *96–14*, p. 189.
[52] D. G. Ivey, D. O. Northwood, *Z. Phys. Chem. N. F.* **1986**, *147*, 191.
[53] J. Huot, E. Akiba, Y. Ishido, *J. Alloys Compds.* **1995**, *231*, 85.
[54] S. R. Ovshinsky, M. A. Fetcenko, J. Ross, *Science* **1993**, *260*, 176
[55] P. R. Gifford, M. A. Fetcenko, S. Venkatesan, D. A. Corrigan, A. Holland, S. K. Dhar, S. R. Ovshinsky, *Proc. Symp. on Hydrogen and Metal Hydride Batteries* (Eds.: P. D. Bennet, T. Sakai), The Electrochemical Society, Pennington, NJ, **1996**, *94–27*, p. 353.
[56] J. R. Johnson, S. Mukerjee, G. D. Adzic, J. J. Reilly, J. McBreen, In situ XAS studies on AB_2 type metal hydride alloys for battery applications. Presented at The International Symposium on Metal Hydrogen Systems; Fundamentals and applications, Les Diablerets, Switzerland, August **1996**
[57] A. Zuttel, F. Meli, L. Schlapbach, *J. Alloys Compds.* **1995**, *231*, 645.
[58] J. McBreen in *Proc. Symp. on Exploratory Research and Development of Batteries for Electric and Hybrid Vehicles* (Eds.: W. A. Adams, A. R. Landgrebe, R. Scrosati), The Electrochemical Society, Pennington, NJ, **1996**, *96–14*, p. 162.
[59] D. A. Scherson, *Interface* **1996**, *5(3)*, 34.
[60] A. N. Mansour, C. A. Melandres, S. J. Poon, Y. He, G. J. Shiflet, *J. Electrochem. Soc.* **1987**, *143*, 219.
[61] D. A. Tryk, I. T. Bae, Y. Hu, S. Kim, M. R. Antonio, D. A. Sherson, *J. Electrochem. Soc.* **1995**, *142(3)*, 824.
[62] D. A. Tryk, I. T. Bae, D. A. Sherson. M. R. Antonio, G. W. Jordan, E. L. Huston, *J. Electrochem. Soc.* **1995**, *142(5)*, L76.

CosMX Exhibit 1008, Page 251 of 633

8 Carbons

K. Kinoshita

8.1 Introduction

Solid carbon materials are available in a variety of crystallographic forms, typically classified as diamond, graphite, and amorphous carbon. More recently another structure of carbon was identified—namely the fullerenes which resemble a soccer ball (C_{60}). In this section, the discussion will focus on graphites and amorphous carbons which are practical materials for use in aqueous batteries.

Carbonaceous materials serve several functions in electrodes and other cell components for aqueous-electrolyte batteries, and these are summarized in Table 1.

Table 1. Application of carbon in aqueous batteries

Battery	Application of carbonaceous material
Lead–acid	Bipolar current collector, electrode additive
Metal/air	Air electrode, electrocatalyst support
Redox flow	Positive electrode, negative electrode substrate, electrocatalyst support, current collector, bipolar separator
Metal hydride/NiOOH	Electrode additive
Hydrogen/NiOOH	Electrode additive, electrocatalyst support
Cd/NiOOH	Electrode additive
Zn/NiOOH	Electrode additive
ZnAgO and Zn/Ag_2O	Electrode additive
Zn/HgO	Electrode additive
Alkaline Zn/MnO_2	Electrode additive
Zinc/carbon (Leclanché cell)	Electrode additive, current collector

Of practical importance is the contribution that is made by carbonaceous materials as an additive to enhance the electronic conductivity of the positive and negative electrodes. In other electrode applications, carbon serves as the electrocatalyst for electrochemical reactions and/or the substrate on which an electrocatalyst is located. In addition, carbonaceous materials are fabricated into solid structures which serve as the bipolar separator or current collector. Clearly, carbon is an important material for aqueous-electrolyte batteries. It would be very difficult to identify a practical alternative to carbon-based materials in many of their battery applications. The attractive

features of carbon in electrochemical applications are its high electrical conductivity, acceptable chemical stability, and low cost. These characteristics are important for the widespread acceptance of carbon in aqueous electrolyte batteries.

8.2 Physicochemical Properties of Carbon Materials

8.2.1 Physical Properties

The crystal structure of graphite and amorphous carbon is illustrated by the schematic representations given in Fig. 1.

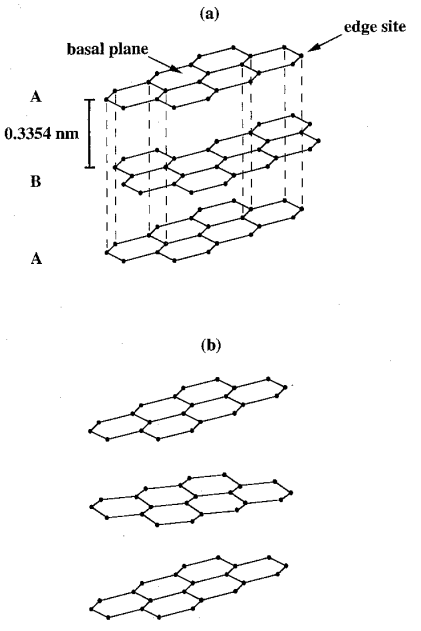


Figure 1. Crystal structure of (a) graphite; (b) amophous carbon.

The structure consists of carbon atoms arranged in hexagonal rings that are stacked in an orderly fashion in graphite (see Fig. 1a). Only weak van der Waals bonds exist between these layer planes. The usual stacking sequence of the carbon layers is ABABA... for hexagonal graphite. The stacking sequence ABCABC... is found less frequently (i.e., in a few percent of the solid) and is called rhombohedral graphite. The $d(0\ 0\ 2)$ interplanar spacing in graphite is 0.3354 nm in the C-axis direction (perpendicular to the layer planes), while the C–C bond distance in the A-axis direction (parallel to the layer planes) is 0.142 nm. It is apparent in Fig. 1(a) that graphite has two distinct surfaces present, the basal plane and the edge sites. Furthermore, the physical properties of graphite are highly anisotropic because of this crystallographic structure. For instance, the electrical conductivity in the direction parallel to the basal plane is about 100 times higher than in the perpendicular direction.

Amorphous carbons (see Fig. 1b) also consist of hexagonal carbon rings, but the number of these rings that constitutes a crystallite is much less than for graphite. In addition there is very little order between the layers. Instead, the layers are rotated with respect to each other but they are parallel to each other (i.e., the material is turbostratic) and there is no three-dimensional ordering. The layer spacing of carbon blacks is typically >0.350 nm, and the crystallite sizes are typically 1.0–2.0 nm for L_a (crystallite size in the direction parallel to the basal plane) and L_c (crystallite size in the direction perpendicular to the basal plane). In contrast, L_a and L_c for graphites can be >100 nm. The surface area of graphite and amorphous carbon can be <10 $m^2\,g^{-1}$ to >1000 $m^2\,g^{-1}$ respectively. The densities of these carbonaceous materials are 2.25 $g\,cm^{-3}$ for graphite and

CosMX Exhibit 1008, Page 253 of 633

usually <1.80 $g\,cm^{-3}$ for amorphous carbon. Further details on the physical properties can be found in the extensive discussion by Kinoshita [1] and in review articles [2–5].

The lattice plane images of carbonaceous materials, which were obtained by high-resolution transmission electron microscopy (HRTEM), are reviewed by Millward and Jefferson [6]. Examples of HRTEM of carbon blacks are presented in Fig. 2 to illustrate the difference in the structure of an amorphous carbon and a graphitized carbon. The electron micrographs show a distinct difference in the structure of the carbon particles. The amorphous carbon (d(0 0 2) spacing of 0.352 nm) shows little evidence for long-range order of the basal planes. On the other hand, the graphitized carbon black (d(0 0 2) spacing of 0.344 nm) has well-defined layer planes that follow the surface contours of the carbon particles. Despite heat treatment at 2700 °C, the d(0 0 2) spacing is much higher than that of graphite, and there are regions in the carbon particles which appear to be amorphous. These observations are typical for carbon blacks which are heat-treated at graphitizing temperatures. The particle size restricts the motion of the layer planes and the stresses that result inhibit the formation of a highly graphitized structure that is similar to that of pure graphite.

A terminology to identify carbons that are graphitizable or those that are none graphitizable by heat treatment has been adopted. Hard carbons are those carbons that are nongraphitizable and are mechanically hard—hence the name In contrast, soft carbons are mechanically soft and can be graphitized. Hard carbons are obtained by carbonizing precursors such as thermosetting polymers (e.g., phenol–formaldehyde resins, furfuryl alcohol, divinylbenzene–styrene copolymer), cellulose, charcoal, and coconut shells. These carbons are usually formed by solid-state transformation during the carbonization steps. One explanation for the inability of hard carbons to form a graphitic structure by heat treatment is the presence of strong sp^3 crosslinking bonds which impede movement and reorientation of the carbon atoms to form the ordered layer structure of graphite. Soft carbons are formed by carbonizing precursors such as petroleum coke, oil, and coal-tar pitch. In these materials the formation of carbon proceeds through an intermediate liquid-like phase (referred to as a mesophase), which facilitates the three-dimensional ordering that is necessary to create a graphite-like struc-

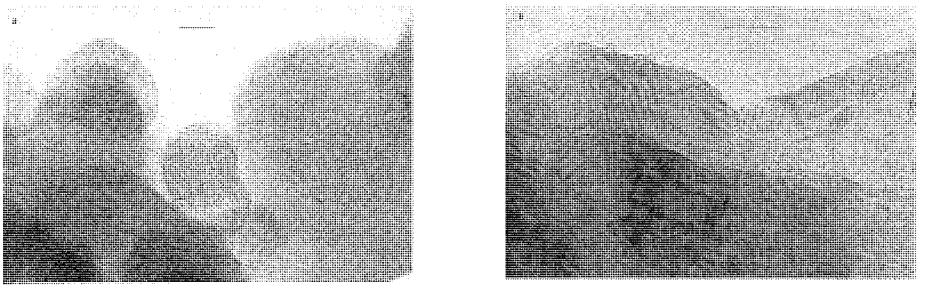


Figure 2. High-resolution transmission electron micrograps of carbon black (Sterling R, Cabot Corp.): (a) as-received; (b) heat-treated at 2700 °C. Scale marker 10 nm.

CosMX Exhibit 1008, Page 254 of 633

ture. Besides the discussion by Kinoshita [1], an extensive review that describes the formation of carbonaceous materials and their physical properties is presented by researchers from Japan [7].

Natural graphite is classified as flake, vein, or microcrystalline (amorphous), depending on the crystallite size and particle shape. Major sources of natural graphite are found in Mexico, China, and Brazil. Flake graphite is anisotropic and has a crystallinity similar to that of single-crystal graphite. One problem with many sources of natural graphite is their ash content (e.g., Fe, Si), which can be as high as 25%. Much of this ash can be removed by leaching in concentrated acid or exposure to halogen gases. Synthetic or artificial graphite is produced by heat treatment of a precursor carbon such as petroleum coke to temperatures in the region of 2800 °C or higher. Solid graphite structures for bipolar separators or electrode substrates for batteries are obtained by extrusion or molding of blended mixtures of petroleum coke and a binder of coal-tar pitch which are heat-treated to graphitization temperatures [8].

A variety of amorphous carbons such as carbon black, active carbon, and glassy carbon is available. With the exception of glassy carbon, these amorphous carbons generally have high surface area, high porosity, and small particle size. Carbon blacks, for example, are available with surface areas that are >1000 $m^2 g^{-1}$, particle size <50 nm, and density much less than the theoretical value for graphite (2.25 $g cm^{-3}$). In addition, the morphology of carbon blacks may resemble individual spheres of about 250 nm diameter (i.e., thermal blacks) or a cluster of fused carbon particles of <50 nm diameter (i.e., furnace blacks). The morphology of carbon black particles has been the subject of much discussion [9–12]. Active carbons are typically granular carbons which are produced by carbonizing materials such as wood (charcoal), coconut and other fruit shells, and low-rank coals. The resulting carbon is activated by treatment with gas (steam activation) or chemical processing [7]. The end product is a carbon material with high surface area (>1000 $m^2 g^{-1}$) and extensive micropores (pore size <2 nm); these properties were analyzed by Kaneko et al. [13]. It is this microporosity that contributes to the high adsorption properties of these carbons.

8.2.2 Chemical Properties

The surface of carbonaceous materials contains numerous chemical complexes that are formed during the manufacturing step by oxidation or introduced during post-treatment. The surface complexes are typically chemisorbed oxygen groups such as carbonyl, carboxyl, lactone, quinone, and phenol (see Fig. 3).

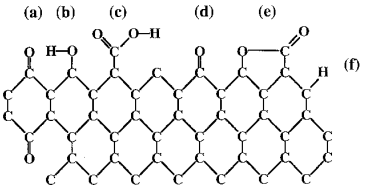


Figure 3. Schematic representation of the common functional groups that are present on carbon: (a) quinone; (b) phenol; (c) carboxyl; (d) carbonyl; (e) lactone; (f) hydrogen.

In addition, carbon–hydrogen bonds are present, particularly in carbonaceous materials obtained by carbonizing polymers at low temperatures, typically <1000 °C. Detailed discussions on the types of surface groups and their surface concentrations are presented by Boehm [14] and Rivin [15].

CosMX Exhibit 1008, Page 255 of 633

These surface groups exhibit different thermal stabilities with the functional groups that contain two oxygen atoms (carboxyl and lactone) desorbing as CO_2, generally at <500 °C. Functional groups that contain one oxygen atom (phenol, quinone) evolve CO at temperatures of about 600 °C and higher. The thermal analysis by Rivin [15] with an oil furnace black (surface area 122 $m^2 g^{-1}$) indicated that surface concentrations of about 1×10^{-10} mol cm^{-2}(CO_2) and 5×10^{-10} mol cm^{-2} (CO) were present. However after oxidation in air for 2 h at 420 °C, the surface concentrations increased by about two and three-fold, respectively, and the surface area increased about 2.5-fold. Hydrogen is frequently found in carbon blacks and other carbonaceous materials. Analysis of carbon blacks indicates that the hydrogen content is in the range 0.01–0.7%. The hydrogen that is bonded to carbon is relatively stable, commencing evolution at about 700 °C and reaching a maximum at about 1100 °C. Other common heteroatoms such as nitrogen and sulfur are also found in carbon. Nitrogen is usually present in minor amounts, but sulfur can be present in high concentrations, >1%, depending on the precursor that is used to manufacture the carbonaceous material. Besides sulfur that is bonded to carbon, other forms such as elemental sulfur, inorganic sulfate, and organosulfur compounds may be present. The carbon–sulfur surface compounds on carbon blacks are relatively stable, but they desorb as H_2S when carbon is heat-treated in H_2 between 500 and 1000 °C.

The surface oxide groups on carbon play a major role in its surface properties; for example, the wettability in aqueous electrolytes, work function, and pH in water are strongly affected by the presence of surface groups on the carbonaceous material. Typically, the wettability of carbon blacks increases as the concentration of surface oxides increases [16]. The pH of an aqueous slurry of carbon decreases as the volatile or oxygen content of the carbon increases [17]. The work function of carbon blacks shows a minimum at a pH near 6 [18].

The physicochemical properties of carbonaceous materials can be altered in a predictable manner by different types of treatments. For example, heat treatment of soft carbons, depending on the temperature, leads to an increase in the crystallite parameters, L_a and L_c and a decrease in the $d(0\ 0\ 2)$ spacing. Besides these physical changes in the carbon material, other properties such as the electrical conductivity and chemical reactivity are changed. A review of the electronic properties of graphite and other types of carbonaceous materials is presented by Spain [3].

8.3 Electrochemical Behavior

8.3.1 Potential

Several significant electrode potentials of interest in aqueous batteries are listed in Table 2; these include the oxidation of carbon, and oxygen evolution/reduction reactions in acid and alkaline electrolytes. For example, for the oxidation of carbon in alkaline electrolyte, E° at 25 °C is -0.780 V vs. SHE or -0.682 V (vs. Hg/HgO reference electrode) in 0.1 mol L^{-1} CO_3^{2-} at pH [14]. Based on the standard potentials for carbon in aqueous electrolytes, it is thermodynamically stable in water and other aqueous solutions at a pH less than about 13, provided no oxidizing agents are present.

CosMX Exhibit 1008, Page 256 of 633

Table 2. Standard potentials for reactions of carbon materials in batteries containing aqueous electrolytes

Electrochemical reaction	Standard potential (V vs. SHE)	Electrolyte
$C + 2H_2O \rightarrow CO_2 + 4H^+ + 4e^-$	0.207	Acid
$C + 6OH^- \rightarrow CO_3^{2-} + 3H_2O + 4e^-$	–0.780	Alkaline
$O_2 + 4H^+ + 4e^- \rightarrow 2H_2O$	1.229	Acid
$O_2 + 2H^+ + 2e^- \rightarrow H_2O_2$	0.682	Acid
$H_2O_2 + 2H^+ + 2e^- \rightarrow 2H_2O$	1.776	Acid
$O_2 + 2H_2O + 4e^- \rightarrow 4OH^-$	0.401	Alkaline
$O_2 + H_2O + 2e^- \rightarrow HO_2^- + OH^-$	–0.076	Alkaline
$HO_2^- + H_2O + 2e^- \rightarrow 3OH^-$	0.878	Alkaline

The typical products that form during oxidation of carbon in acid and alkaline electrolytes are CO_2 and carbonate species, respectively. Additional details of the thermodynamic stability of carbon in aqueous electrolytes, and the electrode potentials for reactions involving carbon, are presented in the review by Randin [19].

The standard oxidation potentials suggest that carbon has a limited stability domain in aqueous electrolytes. As noted in Table 2 the oxidation (corrosion) of carbon should occur at potentials much lower than the reversible potential for oxygen evolution/reduction. To illustrate this point further, take the example of an air electrode (for instance in a metal/air battery) that utilizes carbon. In an acid electrolyte, for instance, a typical potential at which oxygen reduction occurs is about 0.7 V, whereas in alkaline electrolyte the reaction may take place at about 0.1 V. At these operating potentials, the overpotential for carbon oxidation is high in both electrolytes (i.e., 0.5 V in acid and 0.9 V in alkaline electrolytes). Furthermore, the overpotential is much higher in alkaline electrolyte, which suggests that carbon oxidation should be much greater at high pH. In rechargeable alkaline metal/air batteries that utilize carbon in the bifunctional air electrodes, corrosion during charge is a major problem that has not been resolved satisfactorily. The net result is that practical rechargeable metal/air batteries are not available because of their limited cycle life.

8.3.2 Conductive Matrix

Perhaps the first practical application of carbonaceous materials in batteries was demonstrated in 1868 by Georges Leclanché in cells that bear his name [20]. Coarsely ground MnO_2 was mixed with an equal volume of retort carbon to form the positive electrode. Carbonaceous powdered materials such as acetylene black and graphite are commonly used to enhance the conductivity of electrodes in alkaline batteries. The particle morphology plays a significant role, particularly when carbon blacks are used in batteries as an electrode additive to enhance the electronic conductivity. One of the most common carbon blacks which is used as an additive to enhance the electronic conductivity of electrodes that contain metal oxides is acetylene black. A detailed discussion on the desirable properties of acetylene black in Leclanché cells is provided by Bregazzi [21]. A suitable carbon for this application should have characteristics that include: (i) low resistivity in the presence of the electrolyte and active electrode material, (ii) absorption and retention of a significant

CosMX Exhibit 1008, Page 257 of 633

amount of electrolyte without reduction of its capability of mixing with the active material, (iii) compressibility and resiliency in the cell, and (iv) only low contents of impurities. Graphite has higher electrical conductivity than acetylene black but it is not capable of retaining the same amount of electrolyte or demonstrating the same mechanical properties in the cell. Acetylene black has a well-developed chain structure, and it is this characteristic which provides the capability to retain a significant amount of electrolyte. In addition, acetylene black is produced with a low ash content and it does not contain surface groups. The results obtained by Bregazzi [21] indicate that acetylene black is capable of retaining over three times as much electrolyte (cm^{-3} electrolyte/g carbon) as graphite, which has a very low structure. The capacity of Leclanché cells is dependent on the amount and type of carbon black that is used. Generally about 55 vol% carbon black mixed with MnO_2 yields the maximum capacity [22]. This composition agrees closely with the minimum in the electrical resistivity of the electrode mixture.

A carbon rod is used as a current collector for the positive electrode in dry cells. It is made by heating an extruded mixture of carbon (petroleum coke, graphite) and pitch which serves as a binder. A heat treatment at temperatures of about 1100 °C is used to carbonize the pitch and to produce a solid structure with low resistance. For example, Takahashi [23] reported that heat treatment reduced the specific resistance from 1 Ω cm to $3.6\times10^{-3}\Omega$cm and the density increased from 1.7 to 2.02 $g\,cm^{-3}$. Fischer and Wissler [24] derived an experimental relationship [Eq. (1)] between the electrical conductivity, compaction pressure, and properties of graphite powder:

$$\log\rho = K - 0.45\log L_c - 0.4\log d_{50} - 0.54\log p \quad (1)$$

where ρ is the electrical resistivity, K is a constant, L_c is the crystallite size in the direction perpendicular to the basal plane, d_{50} is the mean particle diameter and p is the compaction pressure. This relationship indicates that the electrical resistivity decreases as the crystallite size increases, and with a given average particle size and compaction pressure. When graphite is mixed with MnO_2 in an electrode structure, the conductivity increases with a decrease in the particle size of graphite. In addition, the conductivity increases dramatically when the graphite concentration increases above about 10%.

Another example of the use of a graphite as an additive to improve the electronic conductivity of an electrode can be found in the discussion of the Fe/NiOOH cell developed by Edison in the early 1900s [25]. The positive electrode which contained graphite (20–30% graphite flake) degraded rapidly during charge because of oxidation and swelling. This experience led to the development of electrolytic nickel flakes and eventually to the porous nickel plaque for use in NiOOH electrodes.

Composite structures that consist of carbon particles and a polymer or plastic material are useful for bipolar separators or electrode substrates in aqueous batteries. These structures must be impermeable to the electrolyte and electrochemical reactants or products. Furthermore, they must have acceptable electronic conductivity and mechanical properties. The physicochemical properties of carbon blacks, which are commonly used, have a major effect on the desirable properties of the conductive composite structures. Physicochemical properties such as the surface

CosMX Exhibit 1008, Page 258 of 633

area, structure, and volatile content (oxygen surface groups) influence the electronic conductivity of the composite structure. Typically the electronic conductivity is significantly lower when less than about 30 wt% carbon black is incorporated in the composite structure Carbon blacks with higher surface area, and usually smaller particle size, are desirable because the interparticle distance is shorter and electron tunneling can occur more easily. The structure of carbon blacks is conventionally defined by the amount of adsorption of dibutyl phthalate (DBP); higher adsorption means a higher structure. For example, acetylene black has DBP absorption of 200–250 $cm^3 g^{-1}$ and is a high-structure black, whereas a low structure has a DBP absorption of <100 $cm^3 g^{-1}$. A higher oxygen or volatile content is not desirable because its presence renders the carbon black lèss conductive. Further details are available in the publication by Kinoshita [1].

8.3.3 Electrochemical Properties

A comprehensive review which discusses the surface properties and their role in the electrochemistry of carbon surfaces was written by Leon and Radovic [26]. This review provides a useful complement to the following discussion on the role of carbon in aqueous batteries. Four key parameters that are important for carbonaceous materials in batteries, which were identified by Fischer and Wissler [24], are:

(i) chemical purity
(ii) crystalline structure
(iii) particle size distribution, and
(iv) porosity

These parameters are critical to the operation of alkaline batteries. Evaluation of graphite additives in the positive electrode for Cd/NiOOH cells by Veres and Csath [27] showed that the state of oxidation of graphite and the level of impurities strongly influence the electrode capacity. The capacity of the active material decreased with an increase in the amount of impurities and the degree of oxidation of the graphite.

The studies by Biermann et al. [28] indicate that the carbon blacks used as the conductive matrix in Leclanché cells remain chemically inert, that is, they do not undergo oxidation during storage or discharge of the cell. However, Caudle et al. [29] found evidence that the ion-exchange properties of carbon black, which exist because of the presence of surface redox groups, are responsible for electrochemical interactions with MnO_2. The extent of MnO_2 reduction to MnOOH depends on the carbon black (i.e., furnace black > acetylene black).

8.3.4 Electrochemical Oxidation

In acid electrolytes, carbon is a poor electrocatalyst for oxygen evolution at potentials where carbon corrosion occurs. However, in alkaline electrolytes carbon is sufficiently electrocatalytically active for oxygen evolution to occur simultaneously with carbon corrosion at potentials corresponding to charge conditions for a bifunctional air electrode in metal/air batteries. In this situation, oxygen evolution is the dominant anodic reaction, thus complicating the measurement of carbon corrosion. Ross and co-workers [30] developed experimental techniques to overcome this difficulty. Their results with acetylene black in 30 wt% KOH showed that substantial amounts of CO in addition to CO_2 (carbonate species) and O_2, are

CosMX Exhibit 1008, Page 259 of 633

produced at 550–600 mV (vs. Hg/HgO reference electrode) and temperatures up to 65 °C. Evidence for the formation of an organic species (appearance of a deep reddish-brown color in the solution) was found at 65 °C but the composition was not identified. However, Thiele [31] and Heller [32] concluded that the organic species was probably a humic acid.

The major oxidation reactions of acetylene black in an alkaline electrolyte (30 wt% KOH + 2 wt% LiOH) are strongly dependent on the potential (vs. Hg/HgO) and temperature [30]:

- <500 mV and <50 °C: carbonate formation (CO_2) is the dominant reaction;
- 500–600 mV and <50 °C, carbonate formation and O_2 evolution rates are comparable;
- >600 mV or >60 °C and >450 mV: O_2 evolution and CO formation are the dominant reactions.

Other experiments by Ross and co-workers [30] clearly indicate that the common metal (Co, Ni, Fe, Cr, Ru) oxides that are used for oxygen electrocatalysts also catalyze the oxidation of carbon in alkaline electrolytes.

The surface structure has a strong influence on the corrosion rate of carbon in both acid and alkaline electrolytes. Studies by Kinoshita [33] clearly showed that the specific corrosion rate $mA\,cm^{-2}$ of carbon black in 96 wt% H_3PO_4 at 160 °C was affected by heat treatment. A similar trend in the corrosion rate in alkaline electrolyte was observed by Ross [30c], as shown in Fig. 4. It is evident that the corrosion rates of the nongraphitized carbons are higher than those of the corresponding graphitized carbons. Their study further indicated that some types of carbon blacks (e.g., semi reinforcing furnace blacks) showed a larger decrease in the corrosion rate after graphitization than others that were evaluated. The decrease in the corrosion rate is attributable to the change in the surface microstructure after heat treatment. The surface layers rearrange to form a graphitic structure with basal planes that are exposed to the electrolyte. This surface is more resistant to corrosion than the edge plane sites, and experiments by Ross [30c] indicate that the nongraphitic surface sites, which are capable of adsorbing iodine from solution, are the likely corrosion sites.

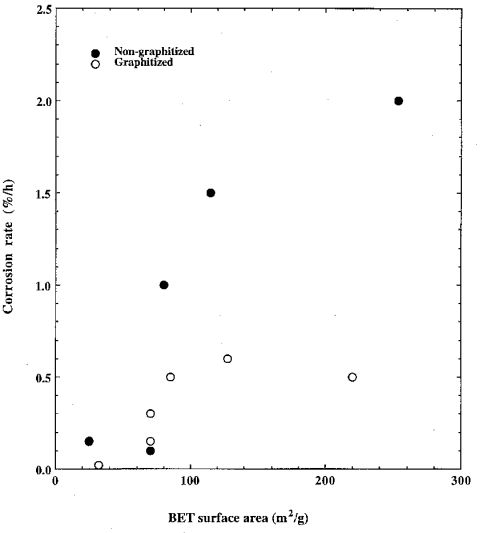


Figure 4. Corrosion of carbon blacks at 550 mV (vs. Hg/HgO) in 35 wt% KOH at 55 °C. From Ross [30c].

8.3.5 Electrocatalysis

Carbon shows reasonable electrocatalytic activity for oxygen reduction in alkaline electrolytes, but it is a relatively poor oxygen electrocatalyst in acid electrolytes. A detailed discussion on the mechanism of

CosMX Exhibit 1008, Page 260 of 633

oxygen reduction and evolution on carbon was presented by Kinoshita [1]. The experimental studies suggest that oxygen reduction in alkaline electrolytes is first order in O_2 concentration. There is evidence that the reaction mechanism is not the same on different carbon electrodes, as illustrated by Eq. (2)–(7) for graphite and carbon black.

Graphite:

$$O_2 \rightarrow O_2(\text{ads}) \tag{2}$$

$$O_2(\text{ads}) + e^- \rightarrow O_2^-(\text{ads})$$
[rate-determining step] (3)

$$2O_2^-(\text{ads}) + H_2O \rightarrow O_2 + HO_2^- + OH^- \tag{4}$$

where O_2^- is a superoxide radical ion.

Carbon black:

$$O_2 + e^- \rightarrow O_2^- \tag{5}$$

$$O_2^- + H_2O \rightarrow HO_2^- + OH$$
[rate-determining step] (6)

$$OH + e^- \rightarrow OH^- \tag{7}$$

The rate and mechanism are different on the basal plane and edge sites of carbon. The reactions involving oxygen are two to three orders of magnitude slower on the basal plane than on the edge sites, because of the weak adsorption of oxygen molecules on the basal plane surface [34].

The overpotentials for oxygen reduction and evolution on carbon-based bifunctional air electrodes for rechargeable Zn/air batteries are reduced by utilizing metal oxide electrocatalysts. Besides enhancing the electrochemical kinetics of the oxygen reactions, the electrocatalysts serve to reduce the overpotential to minimize carbon oxidation during charge (oxygen evolution). An example of the polarization curves for oxygen reduction and evolution on a bifunctional air electrode with an electrocatalyst of cobalt and nickel oxides on a graphitized carbon black is presented in Fig. 5.

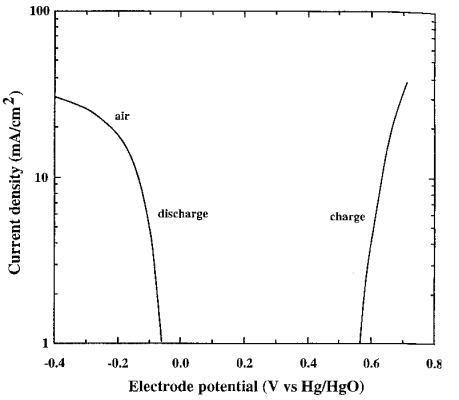


Figure 5. Polarization curves for bifunctional air electrode in 1.5Ah Zn/air cell with 12 KOH at 27 °C. From Ross [35].

These results were obtained in a 1.5Ah Zn/air cell with 12 mol L^{-1} KOH at 27 °C by Ross [35]. The reversible potential for the electrochemical reactions of oxygen is 0.303 V (vs. $Hg/HgO, OH^-$), and the corresponding reversible potential for the oxidation of carbon is $-0.682\,V$ in alkaline electrolyte. Based on these reversible potentials and the polarization curves in Fig. 5, it is apparent that oxygen reduction and evolution occur at high overpotentials. For example, at 10 mA cm^{-2} the electrode potentials for oxygen reduction (discharge) are $-0.130\,V$ in air and 0.638 V for oxygen evolution (charge); these correspond to overpotentials of 0.433 V and 0.335 V, respectively. These results indicate several of the technical problems facing the viability of a rechargeable Zn/air battery

CosMX Exhibit 1008, Page 261 of 633

which utilizes carbon-based bifunctional air electrodes. That is, the overpotentials for the electrochemical oxygen reactions must be reduced to improve energy efficiency, and the potential of the electrode during charge must be lowered to protect the carbon from electrochemical oxidation. As mentioned above, electrocatalysts such as cobalt and nickel oxides enhance the kinetics for the oxygen reactions, but they are also catalysts for carbon oxidation. Thus, the challenge is to identify electrocatalysts which are beneficial for the electrochemical reactions of oxygen, and at the same time do not promote carbon oxidation.

In redox flow batteries such as Zn/Cl_2 and Zn/Br_2, carbon plays a major role in the positive electrode where reactions involving Cl_2 and Br_2 occur. In these types of batteries, graphite is used as the bipolar separator, and a thin layer of high-surface-area carbon serves as an electrocatalyst. Two potential problems with carbon in redox flow batteries are: (i) slow oxidation of carbon and (ii) intercalation of halogen molecules, particularly Br_2 in graphite electrodes. The reversible redox potentials for the Cl_2 and Br_2 reactions [Eq. (8) and (9)]

$$Cl_2 + 2e^- \rightarrow 2Cl^- \qquad (8)$$

$$Br_2 + 2e^- \rightarrow 2Br^- \qquad (9)$$

are 1.358 V and 1.066 V, respectively. These potentials are considerably higher than the reversible potential for the C/H_2O reaction (see Table 2), which suggests that carbon is susceptible to oxidation at the redox potentials for the Cl_2 and Br_2 reactions.

In the Zn/Cl_2 battery, carbon is utilized in both electrodes, serving as a flow-through positive electrode and a substrate for the zinc negative electrode. The requirements are listed below.

Chlorine, flow-through electrode:

- relatively narrow pore size distribution for uniform flow characteristics;
- uniform porosity and permeability for good electrolyte flow distribution;
- low resistivity to minimize *IR* drop in the electrode;
- capability to accept activation treatment;
- no distortion in flowing electrolyte;
- adequate physical strength to permit press-fitting of electrode into the intercell busbar.

Graphite substrate for zinc deposit:

- low surface porosity and fine grain-size for attaining an adherent and uniform zinc deposit;
- low exchange current for hydrogen evolution;
- good physical strength for press-fitting of the electrode into the intercell busbar;
- easily machined into thin electrodes, about 1 mm thick.

Jorne et al. [36] investigated the reactivity of graphites in acidic solutions that are typically used for Zn/Cl_2 cells. The degradation of porous graphite is attributed to oxidation to CO_2. The rate of CO_2 evolution gradually decreased with oxidation time until a steady state was reached. The decline in the CO_2 evolution rate is attributed to the formation of surface oxides on the active sites.

A composite consisting of a mixture of carbon particles (e.g., carbon black or graphite) and a polymer binder such as polyethylene or polypropylene with a surface layer of a carbon-black or carbon-felt

CosMX Exhibit 1008, Page 262 of 633

flow-through structure, serves as the Br_2 electrode in Zn/Br_2 batteries. Because of the low surface area of the carbon–polymer surface, an additional layer of carbon is necessary to obtain higher reaction rates. The mechanical deterioration of graphite–polymer composite electrodes (e.g., 50 wt% high-density polyethylene, 35 wt% graphite, 15 wt% carbon black) in Br_2-containing electrolytes was investigated by Futamata and Takeuchi [37]. The intercalation of Br_2 in graphite and the reaction of Br_2 with polyethylene resulted in mechanical degradation of the composite electrode.

Another type of redox flow battery that utilizes carbon electrodes and soluble reactants involving vanadium compounds in H_2SO_4 is under evaluation [38,39]:

Positive electrode (discharge):

$$VO_2^+ + 2H^+ + e^- \rightarrow VO^{2+} + H_2O \quad (10)$$

Negative electrode (discharge):

$$V^{2+} \rightarrow V^{3+} + e^- \quad (11)$$

Electrodes consisting of carbon-reinforced graphite or carbon fibers were investigated with the redox reactions of soluble vanadium ions. The former material showed evidence for the intercalation of H_2SO_4 at concentrations >5 $mol\,L^{-1}$; however, a similar reaction was not observed with the carbon fibers. Skyllas-Kazacos and coworkers [39] noted that the electrochemical activity of graphite–polymer composite electrodes in the vanadium redox battery was enhanced by a chemical activation treatment involving strong inorganic acids (H_2SO_4, HNO_3). The increase in electrochemical activity is attributed to the increase in the concentration of surface functional groups containing $C-O$ and $C=O$ which could behave as active sites.

Activation by electrochemical or gas-phase oxidation can alter the performance of carbon electrodes for redox reactions. The two major changes that occur to the carbon electrodes as a result of these treatments are an increase in the surface area of the carbon and the formation of surface functional groups on the surface. Jorne and Roayaie [40] reported that electrochemical activation (applying a current density of 33 $mA\,cm^{-2}$ for 5 h in 1.85 N 0.975 $mol\,L^{-1}$ H_2SO_4 at 40 °C) of porous graphite electrodes produced an increase in the surface area of nearly an order of magnitude, and this is mainly responsible for the improved kinetics for the Cl^-/Cl_2 redox reaction. On the other hand, gas-phase oxidation of highly oriented pyrolytic graphite in air at 600 °C is reported to enhance the surface area and form acidic surface oxides which both help to increase the kinetics of the redox reactions involving Cr^{3+}/Cr^{2+} and Fe^{3+}/Fe^{2+} [41].

8.3.6 Intercalation

Highly ordered graphite serves as a host for intercalation of ions such as HSO_4^-, ClO_4^- and BF_4^- in aqueous electrolytes. Graphite intercalation compounds in H_2SO_4 containing HNO_3 have shown some encouraging results [42]. In lead–acid batteries, graphite in the positive electrode is beneficial because the formation of an intercalation compound $C_nHSO_4 \cdot 2.5H_2SO_4$ expands the electrode structure [43]. This expansion increases the porosity and the amount of electrolyte available in the electrode to improve the discharge performance. More recently, carbon has played a pivotal role in the success of Li-ion batteries, serving as the host material for lithium storage in the negative elec-

CosMX Exhibit 1008, Page 263 of 633

trode. In this application, the high electronic conductivity of carbon and its ability to intercalate and/or adsorb lithium ions are critical to the success of the Li-ion battery. A detailed review of carbon in the negative electrode of Li-ion batteries is discussed in Chapter III, Sec. 3.5.

8.4 Concluding Remarks

The element carbon has many desirable characteristics which have prompted its use in aqueous batteries; they include its low cost, acceptable corrosion stability, high electronic conductivity, compatibility with processing conditions used in porous electrode structures, availability in a range of particle sizes and shapes, and reasonable electrochemical activity. It would be difficult to find an alternative material which could match these advantageous features. In this review, the electrochemical behavior of amorphous carbons and graphitic materials is discussed. Carbon can be tailored to meet the electrochemical requirements in many battery applications because of the wide range of properties that are available with its various forms extending from amorphous carbon to graphite.

8.5 References

[1] K. Kinoshita, *Carbon Electrochemical and Physicochemical Properties*, John Wiley, New York, **1988**, p. 20.

[2] W. Hess, C. Herd in *Carbon Black*, 2nd ed. (Eds: J. Donnet, R. Bansal, M. Wang), Marcel Dekker, New York, **1993**, p.89.

[3] I. Spain, in *Chemistry and Physics of Carbon*, Vol. 16 (Eds: P. Walker, P. Thrower], Marcel Dekker, New York, **1981**, p. 119.

[4] P. Delhaés, F. Carmona, in *Chemistry and Physics of Carbon*, Vol. 17 (Eds: P. Walker, P. Thrower), Marcel Dekker, New York, **1981**, p. 89.

[5] E. Dannenberg, in *Kirk-Othmer: Encyclopedia of Chemical Technology*, Vol. 4, John Wiley, New York, **1978**, p. 631.

[6] G. Millward, D. Jefferson, in *Chemistry and Physics of Carbon*, Vol. 14 (Eds: P. Walker, P. Thrower), Marcel Dekker, New York, **1978**, p. 1.

[7] T. Ishikawa, T. Nagaoki (Eds.), in *Recent Carbon Technology Including Carbon & SiC Fibers*, JEC Press, Cleveland, OH, **1983**.

[8] R. Allera, P. Ruopp, *Am. Ceram. Soc. Bull.* **1993**, 72, 99.

[9] (a) A. Medalia, L. Richards, F. Heckman, *J. Coll. Sci.* **1972**, 40, 223; (b) *ibid.* **1971**, 36, 173; (c) *ibid.* **1970**, 32, 115.

[10] (a) W. Hess, L. Ban, G. McDonald, E. Urban *Rubber Chem. Technol*, **1977**, 50, 842; (b) *ibid.* **1973**, 46, 204; (c) *ibid.* **1969**, 42, 1209.

[11] L. Ban, W. Hess in *Petroleum Derived Carbons*, (Eds: M. Deviney, T. O'Grady) ACS Symposium Series, American Chemical Society, Washington, DC, **1969**, p. 358.

[12] F. Ehrburger-Dolle, S. Misono, *Carbon* **1992**, 30, 31.

[13] K. Kaneko, C. Ishii, M. Ruike, H. Kuwabara, *Carbon* **1992**, 30, 1075.

[14] H. Boehm, *Carbon* **1994**, 32, 759.

[15] D. Rivin, *Rubber Chem. Technol* **1971**, 44, 307.

[16] K. Kinoshita, J. Bett, *Carbon* **1975**, 13, 405.

[17] W. Wiegand, *Ind. Eng. Chem.* **1937**, 29, 953.

[18] T. Fabish, D. Schleifer, *Carbon* **1984**, 22, 19.

[19] J.-P. Randin in *Encyclopedia of Electrochemistry of the Elements*, Vol. VII (Ed: A. Bard) Marcel Dekker, New York, **1976**, p. 1.

[20] G.W. Vinal, *Primary Batteries*, John Wiley, New York, **1950**, p. 20.

[21] M. Bregazzi, *Electrochem. Technol.* **1967**, 5, 507.

[22] J. Lahaye, M. Wetterwald, J. Messiet, *J. Appl. Electrochem.* **1984**, 14, 545.

[23] K. Takahashi, *Prog. Batt. Solar Cells* **1980**, 3, 140.

[24] F. Fischer, M. Wissler, in *Battery Material Symposium*, Vol. 1, *Brussels 1983* (Eds: A.Kozawa, M. Nagayama), International Battery Material Association, Cleveland, OH, **1984**, p. 115; *New Mater New Proc.* **1985**, 3,

268.
[25] D. Tuomi: in *Proc. Symp. on History of Battery Technology* (Ed: A. Salkind) The Electrochemical Society, Pennington, NJ, **1987**, p. 21.
[26] L. Leon, L. Radovic in *Chemistry and Physics of Carbon*, Vol. 24 (Ed: P. Thrower) Marcel Dekker, New York, **1994**, p. 213.
[27] A. Veres, G. Csath, *J. Power Sources* **1986**, 18, 305.
[28] J. Biermann, M. Wetterwald, J. Messiet, J. Lahaye, *Electrochim. Acta* **1981**, 26, 1237.
[29] J. Caudle, K. Summer, F. Tye in *Power Sources 6* (Ed: D. Collins), Academic Press, New York, **1977**, p. 447.
[30] (a)P. Ross, N. Staud, H. Sokol, *J Electrochem. Soc.* 1984, 131, **1742** (b) *ibid.* **1986**, 133, 1079; (c) *ibid.* **1988**, 135, 1464; *ibid.* **1989**, 136, 3570.
[31] H. Thiele, *Trans. Faraday Soc.* **1938**, 34, 1033.
[32] H. Heller, *Trans. Electrochem. Soc.* **1945**, 87, 501.
[33] K. Kinoshita in *Proc. Workshop on the Electrochemistry of Carbon* (Eds: S. Sarangapani, J. Akridge, B. Schumm), The Electrochemical Society, Pennington, NJ, **1984**, p. 273.
[34] I. Morcos. E. Yeager, *Electrochim. Acta* **1970**, 15, 953.
[35] P. Ross in *Proc. 21st Intersociety Energy Conversion Engineering Conference*, American Chemical Society, Washington, DC, **1986**, p. 1066.
[36] J. Jorne, E. Roayaie, S. Argade, *J. Electrochem. Soc.* **1988**, 135, 2542.
[37] M. Futamata, T. Takeuchi , *Carbon* **1992**, 30, 1047.
[38] H. Kaneko, K. Nozaki, Y. Wada, T. Aoki, A. Negishi, M. Kamimoto, *Electrochim. Acta* **1991**, 36, 1191.
[39] (a) M. Skyllas-Kazacos, M. Kazacos, S. Zhong, B. Sun *Electrochim. Acta* **1992**, 37, 2459; (b) *J. Electrochem. Soc.* **1989**, 136, 2759; (c) *J. Power Sources* **1991**, 36, 29; (d) *ibid.* **1992**, 39, 1.
[40] J. Jorne, E. Roayaie, *J. Electrochem. Soc.* **1986**, 133, 696.
[41] E. Hollax, D. Cheng, *Carbon* **1985**, 23, 655.
[42] (a) N. Iwashita, H. Shiogama, M. Inagaki, *Synth. Metals* **1995**, 73, 33; (b) M. Inagaki, O. Tanaika, N. Iwashita *ibid.* **1995**, 73, 83; (c) M. Inagaki, N. Iwashita *J. Power Sources* **1994**, 52, 69.
[43] (a) A. Tokunaga, M. Tsubota, K Yonezu, K. Ando, *J. Electrochem. Soc.* **1987**, 134, 525; (b) idem, *ibid.* **1989**, 136, 33.

CosMX Exhibit 1008, Page 265 of 633

9 Separators

Werner Böhnstedt

9.1 General Principles

The separator — the distance-keeping component between the positive and the negative electrode of a galvanic cell — is not directly participating in the electrochemical processes of electricity storage. As a "passive" element it has naturally attracted only little scientific interest; its significance lies in the technical challenge to build batteries ever more compact and long-lasting. A decisive breakthrough could be achieved only in the second half of the 20th century by the development of sufficiently stable synthetic materials. The know-how of the chemical industry in selecting suitable plastics and their processing was combined with the experience of the battery industry regarding the unique conditions of use; an independent separator industry developed which, since the late 1960s, from the combination of these two aspects has given essential impulses to the advancement of batteries.

A comprehensive modern survey of separators for electrochemical power sources exists only in incomplete parts [1–3], and textbooks on batteries treat this important element only as a side aspect [4–11]. This section is an attempt to describe, besides some fundamental aspects, the development history of the battery separator, competing systems of the present day with their advantages and weaknesses, and also future development trends.

9.1.1 Basic Functions of the Separators

Separators serve two primary functions: while having to keep the positive electrode physically apart from the negative in order to prevent any electronic current passing between them, they also have to permit an ionic current with least, possible hindrance. These two opposing requirements are best met by a compromise: a porous nonconductor.

The necessity of electronic insulation — the origin of the term "separator" — has to be met durably, i.e., often over many years within a wide range of temperatures and in a highly aggressive medium. Under these conditions no substance harmful to the electrochemical reactions may be generated.

The unhindered ionic charge transfer requires many open pores of the smallest possible diameter to prevent electronic bridging by deposition of metallic particles floating in the electrolyte. Thus the large number of microscopic pores form immense internal surfaces, which inevitably are increasingly subject to chemical attack.

CosMX Exhibit 1008, Page 266 of 633

Not only the electrolyte, but also the electrodes, directly or indirectly exert a chemical attack, either by an oxidation or reduction potential of the electrode material itself or by the generation of soluble oxidizing or reducing substances.

The requirements for the separator properties are generally lower in primary cells, i.e., in nonrechargeable systems. This results from the lack of problematic phenomena accompanying any charging of a battery, such as recrystallization of active materials or the generation of oxidizing species during overcharge. Within the framework of this chapter, therefore, separators mainly for secondary cells will be described.

In the older battery literature the term "separator" is frequently used very loosely, to include all nonmetallic solid components between the electrodes, such as supporting structures for active materials (tubes, gauntlets, glass mats), spacers, and separators in a narrow sense. In this section, only the last of these, the indispensable separating components in secondary cells, will be termed "separators", distinguished from the others by their microscopically small pores, i.e., with a mean diameter significantly below 0.1 mm.

9.1.2 Characterizing Properties

Some terms and properties common to all separators are defined and discussed below.

9.1.2.1 Backweb, Ribs, and Overall Thickness

Separator backweb refers to the porous separating membrane. It is of uniform thickness and has a macroscopically uniform pore distribution. Only in this way can an overall uniform current density be ensured during the operation of the storage battery, achieving a uniform charging and discharging of the electrodes and thus a maximum utilization of the electrode materials.

The lead–acid battery has a peculiarity: the electrolyte sulfuric acid not only serves as ion conductor (as charge-transport medium), but it actively participates in the electrochemical reaction:

$$Pb + PbO_2 + 2\,H_2SO_4 \leftrightarrow 2\,PbSO_4 + 2\,H_2O \quad (1)$$

During charging at the positive electrode one additional water molecule is consumed per electron converted, which is regenerated during discharging.

In practice the desired electrolyte distribution is achieved by distance–maintaining ribs on the porous backweb; this in addition has the advantage of maintaining a maximum distance between the origin of oxidizing substances located at the positive electrode and the highly porous separating membrane, sensitive due to its large inner surface.

The total or overall thickness thus comprises the backweb thickness and the rib height. For achieving a uniform current distribution the thickness is normally specified very precisely and it is acceptable only within rather narrow tolerances. Besides technical difficulties in the production, this also presents a problem in measurement: since all separator materials are more or less compressible, a specified measuring pressure has to be used. Moreover, the measuring area is also significant; one can easily imagine an extended area touching only the microscopic elevations of the separator, whereas a measuring tip may very well hit "valleys".

CosMX Exhibit 1008, Page 267 of 633

9.1.2.2 Porosity, Pore Size, and Pore Shape

Porosity of a separator is defined as the ratio of void volume to apparent geometric volume. High porosity is desirable for unhindered ionic current flow.

The pores of the separating membrane are to be most uniformly distributed and of minimum size to avoid deposition of metallic particles and thus electronic bridging. One distinguishes between macroporous and microporous separators, the latter having to show pore diameters below 1 micron (μm), i.e., below one-thousandth of a millimeter. Thus the risk of metal particle deposition and subsequent shorting is quite low, since active materials in storage batteries usually have particle diameters of several microns.

However, even these small pores cannot prevent the formation of so-called "microshorts", arising by metal deposition (e.g., dendrites) from the solution phase. The pores of modern separators have a diameter of about 0.1 μm, equal to 100 nm, while metal ions have a diameter of few angstroms, equal to 0.5–1 nm. On an atomic scale even micropores are barn doors!

Micropores are invisible to the naked human eye; thus for outsiders it is always surprising that separators of typically 60 percent porosity (i.e., 60 percent void volume, 40 percent solid material) present the impression of a compact, hole-free, nontransparent sheet.

In a first approximation the average size of pore diameter has no effect on porosity, even though a superficial view leads to other conclusions. A mental experiment may be of assistance: imagine a pore and its outside wall, decrease both to identical scale, then the ratio of void to outside volume remains constant. Of course the requirements as to pore sizes and their uniform distribution increase with decreasing separator backweb thickness. The risk of defects also increases; so-called "pinholes" can originate, e.g., by bubble inclusion within the separator membrane during the production process.

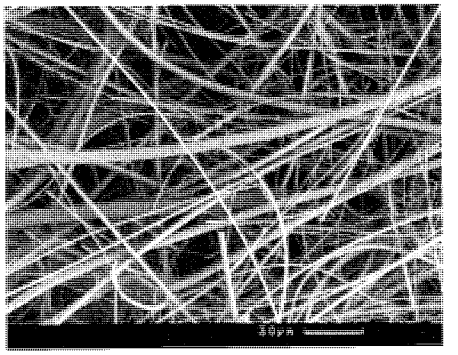


Figure 1. Microfiber glass fleece separator (SEM)

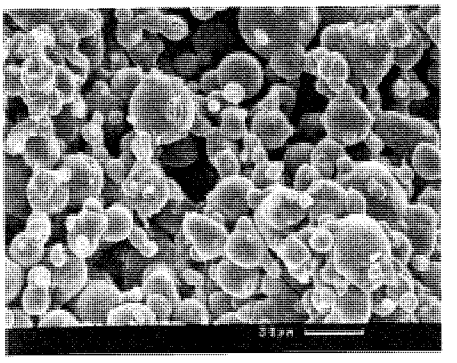


Figure 2. Sintered PVC separator (SEM)

Pores generally are not of a hose-like configuration of constant diameter, in a straight-line direction from one electrode to the other. In practice, separators pores are formed as void between fibers (Fig. 1),

CosMX Exhibit 1008, Page 268 of 633

or spherical bodies in amorphous agglomerates (Fig. 2), thus being very different in their form and size. Statements of any pore diameter are always to be viewed with the above in mind. Figures 1 and 2 represent macroporous systems, whereas Fig. 3 and 4 show microporous separators. It should be noted that the latter figures have a 50-fold larger magnification!

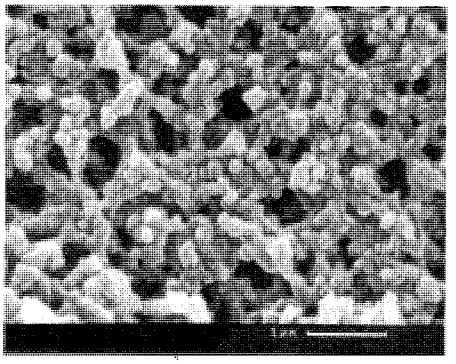


Figure 3. Phenol-formaldehyde resin resorcinol separator (SEM)

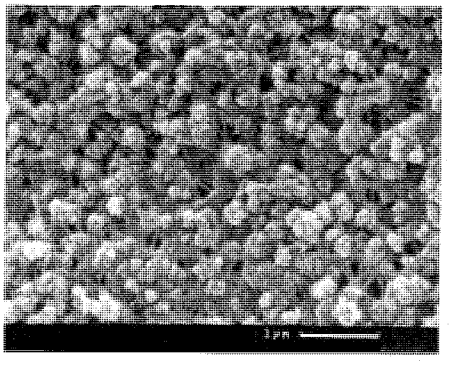


Figure 4. Microporous polyethylene separator (SEM)

The path taken by an ion from one electrode to the other will not be a straight one, as it has to evade the solid structures by making detours. The ratio of the mean actual path in comparison with the direct distance is called the tortuosity factor T. For plastic bodies consisting essentially of spherical, interconnected particles with voids in between, with a porosity of about 60 percent this value is roughly 1.3; for higher porosities it decreases to approach a value of 1.0 at very high porosities.

9.1.2.3 Electrical Resistance

The electrical resistance exerted by a separator on the ionic current is defined as the total resistance of the separator filled with electrolyte minus the resistance of a layer of electrolyte of equal thickness, but without the separator. The separator resistance has to be considered as an increment over the electrolyte resistance.

$$\text{R(separator)} = \text{R(electrolyte+separator)} - \text{R(electrolyte)} \quad (2)$$

Generally,

$$R = \frac{1}{\sigma} \cdot \frac{l}{q} \quad (3)$$

where l is the length of the ion path and q the area of the ionic flow; σ is the specific electrolytic conductivity, the reciprocal of the specific resistance ρ of the electrolyte, and is a temperature-dependent material constant.

The tortuosity factor T of a separator can be expressed by

$$T = \frac{l_s}{d} \quad (4)$$

with l_s the ion path through the separator and d the thickness of the separating layer.

The porosity of the separator is defined as:

CosMX Exhibit 1008, Page 269 of 633

$$P = \frac{\text{void separator volume}}{\text{geometric separator volume}} = \frac{q_s l_s}{qd} \quad (5)$$

with q_s as the "open" area of the separator.

A transformation results in

$$q_s = q \cdot \frac{P}{T}$$

and substitution into Eq. (2) gives :

$$R(\text{separator}) = \frac{1}{\sigma} \cdot \frac{l_s}{q_s} - \frac{1}{\sigma}\frac{d}{q} = \frac{1}{\sigma}\left(dT \cdot \frac{T}{qP}\right) - \frac{d}{q} = \frac{1}{\sigma}\frac{d}{q}\left(\frac{T^2}{P} - 1\right) = R(\text{electrolyte})\left(\frac{T^2}{P} - 1\right)$$

$$R_{sep} = R_{el}\left(\frac{T^2}{P} - 1\right) \quad (6)$$

with $R_{el} = \frac{1}{\sigma} \cdot \frac{d}{q}$

This formula shows the factorial effect of the separator on the electrical resistance; the measured resistance of the electrolyte-filled separator is the (T^2/P) - fold multiple of the electrolyte resistance without the separator; by definition, $T^2/P \geq 1$.

With increasing tortuosity factor T and lower porosity P, R increases sharply. The electrical resistance of a separator is proportional to the thickness d of the membrane and is subject to the same dependence on temperature or concentration as the electrolyte itself.

For sulfuric acid (H_2SO_4) of specific density 1.28 g cm^{-3} at 25 °C, the specific resistance $(1/\sigma)$ is 1.26 Ω cm ; using this value in the Eq. (6) and selecting values typical for polyethylene starter battery separators at d = 0.25 mm, P = 0.6 and T =1.3, the electrical resistance for 1 cm^2 of separators area results in

$$R_{sep} = 1.26\,\Omega\,\text{cm}\,\frac{0.025\,\text{cm}}{1\,\text{cm}^2}\left(\frac{1.3^2}{0.6} - 1\right) = 0.057\,\Omega$$

Usually the electrical resistance of a separator is quoted in relation to area; in the above case it is 57 mΩ cm^2. In order to quote it for other areas, due to the parallel connection of individual separator areas, Kirchhoff's law has to be taken into account:

$$\frac{1}{R_{total}} = \frac{1}{R_1} + \frac{1}{R_2} + \cdots$$

or, as all R_i are equal,

$$R_{total} = \frac{1}{n} R_n$$

Applying this to the above example for an area of 1 in^2 = 6.45 cm^2, the result is R= 8.8 mΩ in^2. Taking an example from SLI battery practice: one cell with six positive and seven negative electrodes of typical 114 mm × 147 mm size with the above separator show a resistance of $28.3 \times 10^{-6}\,\Omega$ at 25°C, or close to $75 \times 10^{-6}\,\Omega$ at –18 °C. For a cold crank current of 320 A and six cells in series in a 12 V battery, the voltage drop due to the separator resistance amounts to ≈ 0.15 V; Fig. 5 shows this correlation.

CosMX Exhibit 1008, Page 270 of 633

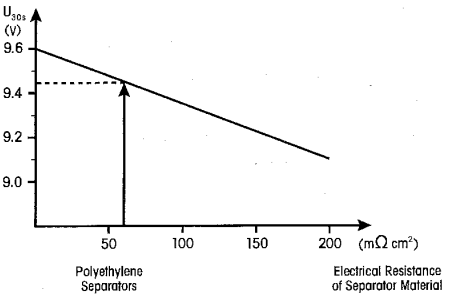


Figure 5. Cold crank voltage as a function of separator electrical resistance *)

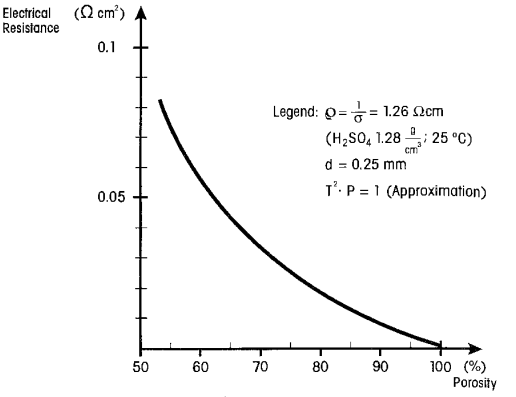


Figure 6. Electrical resistance as a function of porosity *)

The dependence of separator electrical resistance on porosity for the selected SLI battery separator (0.25 mm backweb thickness) and the practical approximation $T^2P = 1$ can be seen in Fig. 6.

Other characterizing separator properties are either application-related or product-specific; they will therefore be discussed with the individual separator types.

9.1.3 Battery and Battery Separator Markets

There are no indications, or only vague ones, of the size of the various battery separator markets in the literature [3]. A rough estimate can be deduced from the sales figures for battery systems by a rule of thumb: the sales value of separators is roughly 2–5% of the sales for the battery producers. Even the data for battery markets are not uniformly gathered, however, and contain considerable uncertainties.

The total sales value for battery systems worldwide in 1997 may amount to US $ 25.5 billion and the sales value for battery separators correspondingly to US $ 600 million; Table 1 gives an estimate of the work battery market, split according to the different battery systems.

Table 1. World battery markets 1998 (US $ million, estimate)

Lead–Acid Batteries		
Automotive Batteries	8200	
Industrial batteries	2300	
VRLA batteries	1000	
Total		11 500
Alkaline Batteries		
Vented	500	
Sealed	2800	
Total		3300
Lithium-ion batteries		1300
Consumer batteries		9400
Total markets		25 500

From this — albeit rather rough — overview, the proportions become clear: around 45 percent of all battery sales worldwide and thus also separator sales worldwide are in lead–acid batteries and

*Reprinted from W. Böhnstedt, Automotive lead/acid battery separators: a global overview, *J. Power Sources*, **1996**, *59*, 45–50, with kind permission from Elsevier Science S.A., Lausanne.

CosMX Exhibit 1008, Page 271 of 633

a further 13 percent in the rechargeable alkaline battery sector. The remaining 40 percent or more is split among the recently introduced lithium-ion batteries as well as a multitude of primary systems in the portable battery sector. This distribution of battery production is not geographically uniform; whereas in Europe and the USA automotive and industrial batteries are in the lead, in the Asia–Pacific area consumer batteries are more strongly represented. In this section separators for mainly those rechargeable batteries which have aqueous electrolyte will be discussed individually, whereas separators for batteries with non-aqueous electrolyte, which have attained a commercial breakthrough in the recent years, will be the subject of a separate chapter.

9.2 Separators for Lead–Acid Storage Batteries

9.2.1 Development History

9.2.1.1 Historical Beginnings

The historical development of the separator and of the lead–acid storage battery are inseparably tied together. When referring to lead–acid batteries today one primarily thinks of starter batteries or forklift traction batteries, but the original applications were quite different.

The very first functioning lead–acid battery was presented by Gaston Planté in 1860: spirally would lead sheets served as electrodes, separated by a layer of felt — the first separator of a lead–acid battery [12]. This assembly in a cylindrical vessel in 10% sulfuric acid had only a low capacity, which prompted Planté to undertake a variety of experiments resulting in many improvements that are still connected with his name.

Until about 1880 the lead–acid battery was exclusively then subject of scientific study. Possible commercial utilization lacked suitable charging processes; secondary cells had to be charged by means of the primary cells already known at that time.

Only with the discovery of the dynamoelectric effect and its rapid commercialization after 1880 did the industrial use of lead–acid storage battery begin. Here the development of pasted plates by Camille Faure was essential for significantly raising the amount of stored energy; they were separated by layers of parchment and felt [13]. These batteries served predominantly for illumination and later — beginning around 1890 — also as stationary batteries for peak power load leveling in power plants. Glass rods frequently sufficed as spacers, or these batteries were even built without separators at all, simplifying the frequent removal of anode mud from the containers.

The development of the tubular plate during the last decennium of the 19th century required oxidation- and acid-stable porous material. Of the natural materials only a few are moderately stable in sulfuric acid: glass, asbestos, rubber, and cellulose. All have been tested, singly or in combination. Asbestos fabrics as tubular material for positive electrodes, textiles for fixing the negative mass, and rubber rods as spacers were in the first batteries for driving electric vehicles, an application becoming popular in that period. These vehicles, however, required increased energy densities, i.e., the electrode distance had to be decreased. After many trials, extruded hard rubber tubes prevailed for the positive electrodes, with finely sawn cross-slits to allow ion migration. At that time the first wooden veneers [14] were used for sepa-

CosMX Exhibit 1008, Page 272 of 633

rating the electrodes — the first separator in the narrow meaning of the word, and for about 60 years the most successful material.

9.2.1.2 Starter Battery Separators

In the competition between the systems (electric motor versus combustion engine) for vehicles, one essential disadvantage of the latter was the tedious and demanding process of starting by muscular power. Only the development of the electric starter by Kettering in 1911, and the battery accompanying it, changed this situation suddenly. It is an irony of history that the starter battery contributed essentially to the downfall of the early electric car. A rapid development of the car industry, and of the battery industry in parallel with this, followed. Wooden veneer became the standard separation of the lead–acid storage battery, be it in double separation as wood veneer with rubber spacers or later as ribbed wood veneer alone, when the electrodes became thinner; thus the required acid supply and also the distance between electrodes decreased in order to increase the energy and power density.

Wood veneers were produced preferentially from Port Orford cedar, primarily domiciled in Oregon (USA). Trials with other types of wood, e.g., with poplar, remained makeshift measures. The preparation of the wood veneer, i.e., the sawing and slicing of the trees, the dissolving of the lignin to achieve porosity, and the almost complete leaching of resins which would otherwise accelerate the corrosion, was quite difficult [15]. Wood veneer separators could be stored and transported only when wet; dry-charged starter batteries could not be built using them. Nevertheless, wood veneers remained the predominant separators until about 1960!

In the meantime another development had decisively altered the outset situation; plastics had been discovered and synthesized, among them also some acid-stable ones such as phenol–formaldehyde resin or poly(vinyl chloride) (PVC). These opened up new possibilities: cellulose papers could be impregnated with phenol–formaldehyde resin solution and thus rendered sufficiently acid-stable, and sintered sheets from PVC powder were developed. Independent separators producers were founded, combining knowledge of the chemical industry with experience of the battery industry and thus accelerating the development process.

During the first trials with synthetic separators around 1940 it had already been observed that some of the desired battery characteristics were affected detrimentally. The cold crank performance decreased and there was a tendency towards increased sulfation and thus shorter battery life. In extended test series, these effects could be traced back to the complete lack of wooden lignin, which had leached from the wooden veneer and interacted with the crystallization process at the negative electrode. By a dedicated addition of lignin sulfonates — so called organic expanders — to the negative mass, not only were these disadvantages removed, but an improvement in performance was even achieved.

Larger vehicles with bigger engines required even higher cold crank performance. In order to meet the resulting requirements for separators with lower electrical resistance, around 1970 the polyethylene separator [16] and more or less at the same time glass separators were developed and introduced. Glass separators are very similar to the cellulosic separators already mentioned; they do not require special machinery for processing and offer a very low

CosMX Exhibit 1008, Page 273 of 633

electrical resistance. They succeeded in the USA in largely displacing sintered PVC and cellulosic separators, before they themselves were supplanted by a completely new technology, polyethylene pocket separation. In Europe this intermediate step — glass separators — did not occur; the transition from PVC or cellulosic leaf separators to the polyethylene pockets proceeded directly, albeit some five or ten years later than in the USA.

The decisive advantage of the polyethylene pocket is its flexibility and sealability as well as its very small pore diameters. In the course of their efforts at efficiency improvement, around 1970 Delco – Remy had designed a completely novel starter battery concept: electrodes of expanded lead strip were to replace cast grids, promising a significant saving in weight and thus in cost. Only lead–calcium alloys proved to be suitable for expansion, which had a tendency, however, towards increased mud shedding during battery operation. Against this the microporous polyethylene separator film, developed by W.R. Grace & Co. in 1966 [16], promised to be a remedy. While the mud could be accommodated by the formation of a three-sided sealed pocket around the electrode, at the same time the micropores eliminated the risk of penetration through the separator. A largely automated starter battery production was the positive result of these developments. The commercial advantages of pocketed starter batteries as well as their technical ones, such as freedom from maintenance, high cold crank power and prolonged battery life, have led to a victorious worldwide advance of this technology [3].

Alternative separator materials such as organic fibers or sintered PVC did not succeed as pocket materials due to their excessive pore size. The pore diameter of 10–20 μm typical for such materials is insufficient to effectively prevent the preferential formation of shorts by mass particles at the folding edge of the pocket.

A completely separate development took place in Japan. Traditionally, very porous positive active materials are used in that country requiring support glass mats to avoid premature capacity loss and shorting in cycling service. Since the introduction of the cellulosic separator a version of this kind has been used in Japan without distance ribs, achieving the total thickness of the separator by means of a thick glass mat instead. Certainly this is an expensive type of separator, but it can be balanced by savings in active material. In Japan, meanwhile, the fleece of organic fibers, which was unsuitable for pocketing, has replaced the impregnated cellulosic sheet. It distinguishes itself by favorable electrical resistance data and good acid and oxidative stability. The transition to microporous polyethylene pockets proceeds more slowly than in the USA or in Europe, because it requires a simultaneous change in formulation of the positive mass.

Starting with the development of sealed lead–acid cells by The Gates Rubber Co. in 1972 [17], this principle of internal oxygen transfer was transferred to starter batteries around 1980. The electrolyte is absorbed in a microfiber glass mat; this has to leave electrolyte-free channels, through which the oxygen generated at the positive electrode can diffuse to the negative, where it is reduced. Thus one has a theoretically maintenance-free battery without any water consumption. Despite additional indisputable advantages such as spill-proofness or flexibility of position in the car, this construction — mostly for reasons of cost — has not yet made a breakthrough in starter battery applications.

After this stroll through history, let us

CosMX Exhibit 1008, Page 274 of 633

consider the current markets, split according separation systems in the various geographic areas (Table 2).

The microporous polyethylene pocket has succeeded worldwide; more than 70 percent of all starter batteries use this form of separation. Whereas in the USA and Western Europe the transition is essentially complete, a similar development in the Asia-Pacific area and Latin America, and in the medium term also in Russia and China, is expected [3].

ages. The batteries in these applications are charged continuously with a low current to counteract self-discharge and to allow discharging at comparably high currents when required. Due to the level of maintenance necessary, these batteries were initially built in an open construction, the required electrolyte reservoir being supplied with wide electrode spacing, frequently without any separators. Later, spacers of hard rubber — initially rods and then corrugated spacers — were used. With the invention

Table 2. Automotive lead–acid battery production 1997 (million kWh, estimate)

	Polyethylene pocket separators	Sintered PVC/ Rubber separators	Cellulosic/ Glass separators	Synth. pulp / GM separators	VRLA SLI Batteries	Total
USA–Canada	56.5	1.2	0.6	–	0.7	59.0
Europe	30.0	11.0	3.4	–	0.1	45.4
Asia–Pacific	16.3	11.4	4.5	9.8	0.3	42.3
Latin America	11.7	0.9	3.9	–	–	16.5
Total (million kWh)	115.4	24.5	12.4	9.8	1.1	163.2
(%)	70.7	15.0	7.6	6.0	0.7	100.0

9.2.1.3 Industrial Battery Separators

Stationary Battery Separators

As already mentioned, at the beginning of the 20th century the electric power supply was still very susceptible to load changes, requiring the use of stationary lead batteries for load leveling. As more powerful generators were developed this application diminished, but from the increasing dependence on general supply of electricity the need for emergency power batteries developed, e.g., for emergency lights. From the start , the telephone systems required huge battery installations in float service, on the one hand as buffer batteries filtering interferences from the alternating current circuits and on the other hand permitting (as least for limited periods) an uninterrupted service during power out of

PVC and their low-cost industrial production process, sintered PVC separators have been used since around 1950 and some are still employed today.

In the second half of the 1960s, at the same time but independently, three basically different plastic separators were developed. One was the polyethylene separator [16] already referred to in starter batteries, used only rarely in stationary batteries, but successful in traction batteries. The others were the microporous phenolic resin separator (DARAK) [18] and a microporous PVC separator [19], both of which became accepted as the standard separation for stationary batteries. They distinguish themselves by high porosity (about 70 percent) and thus very low electrical resistance and very low acid displacement, both important criteria for stationary batteries.

CosMX Exhibit 1008, Page 275 of 633

The desire for maintenance-free service, e.g., in decentralized single emergency lights for panic lighting, around 1960 had led to the development of small, sealed, lead–acid batteries with gelled electrolyte [20 ,21]. An idea that was already known — the gelling of electrolyte — became applicable to the sulfuric acid electrolyte with the industrial availability of silica types of very high surface area. These fumed silicas have an internal surface of, say, 200–300 $m^2 g^{-1}$ and convert sulfuric acid into a thixotropic gel. By vigorous stirring the electrolyte is liquefied and can be filled into the battery cell, where it gels again, rendering it leakproof and serviceable in all positions. Microporous separators, e.g., of phenolic resin or PVC, like the ones referred to above are required for maintaining the spacing and preventing shorts.

However, because of the viscous electrolyte, the charging gases can no longer escape! The application of the principle of sealed nickel–cadmium batteries, known since around 1933 [22], letting the oxygen generated at the positive electrode diffuse to the negative electrode for reduction with partial discharge there, was successful. After an initial water loss, the gel starts to dry out, thereby forming cracks and allowing the oxygen to find a path. Unfortunately this technology is rather costly and therefore can only be justified for special applications.

Uninterrupted power supply for computers, initially only for central units, grew significantly with the introduction of personal computers (PCs): the batteries became smaller and, since they had to be located in offices, had to be in a sealed version, since no aggressive charging gases were permitted to escape. This advanced the breakthrough of the development of so-called recombination or valve-regulated batteries, a version with an absorptive glass mat and an internal oxygen cycle. At about the same time British Telecom phased them out because of the high maintenance, especially the water replenishment required for large stationary batteries with liquid electrolyte, and also started using recombination batteries. The liquid electrolyte is completely absorbed by a microfiber glass fleece, although some channels have to remain free from electrolyte to permit oxygen transfer. The electrolyte absorption occurs on the surface of the microfibers, which — as known — increases steeply with decreasing diameter. Frequently such separators are therefore also characterized by means of their internal surface area ($\sim 1\,m^2 g^{-1}$!). The pore distribution is anisotropic, which is desirable; in the plane between the electrodes — because of the fiber diameters — very small pores are formed effecting a large capillary force, while perpendicular to this plane — due to the high porosity of >90 percent, — pores of 10–20 μm diameter are found, which are necessary to ensure the oxygen transport [23–25]. A number of producers of specialized papers starter to manufacture and to develop these microfiber glass mats further. Fibers below 1 μm in diameter are expensive, and due to their shortness ($\approx$ 1 mm) contribute only little to the tensile strength. Binder may be omitted, however, to achieve good wettability; the addition of longer glass fibers of large diameter is required to improve the processability of such separators. A microfiber content of 20–30 percent has proven sufficient largely to optimize the desired characteristics [26].

The market for sealed stationary batteries has greatly increased since 1980, both by the growth of the PC market as well as by the decentralization of emergency power supplies and telephone ex-

CosMX Exhibit 1008, Page 276 of 633

changes, even though this conversion has not remained undisputed [27]. Table 3 gives an estimate of the present situation; these figures also include small consumer lead–acid batteries, which are constructed similarly. More than 60 percent of all stationary batteries are currently being produced in the sealed version, with the total market growing by roughly 5–10 percent annually.

In Europe, with the economic upswing after 1950, forklifts with batteries came into use — a development which met less

Table 3. World lead–acid stationary and consumer battery production 1997 (million Wh, estimate)

	Polyethylene separators	Phenol-formald.-resorcinol separators	PVC separators	Rubber separators	Microfiber glass mat separators	Total
USA–Canada	620	350	60	120	3900	5 050
Europe	210	1520	510	180	2350	4 770
Asia–Pacific	150	50	420	410	2600	3 630
Latin America	80	40	120	140	100	480
Total (million Wh)	1060	1960	1110	850	8950	13 930
(%)	7.6	14.1	8.0	6.1	64.2	100.0

Traction Battery Separators

Electric road vehicles have been reduced to insignificance, as mentioned already by, vehicles with combustion engines. Another electric vehicle — the electrically driven submarine — presented a continuous challenge to lead–acid battery separator development since the 1930s and 1940s. The wood veneers originally used in electric vehicles proved too difficult to handle, especially if tall cells had to be manufactured. Therefore much intense effort took place to develop the first plastic separators. In this respect the microporous hard rubber separator, still available today in a more advanced version, and a microporous PVC separator (Porvic I) merit special mention [28]. For the latter a molten blend of PVC, plasticizer and starch was rolled into a flat product. In a lengthy process the starch was subsequently leached, leaving voids interconnected through holes in their walls. This resulted in an extremely high porosity (levels of up to 85 percent were reported), but due to a high tortuosity factor of about 1.7 there was also a relatively high electrical resistance.

acceptance in the USA for various reasons, among them low fuel cost. In this application rubber separators and microporous PVC (Porvic I) were finally able to replace wood veneers, until from around 1975 they again met strong competitors in the new separators already mentioned made of phenolic resin (DARAK), PVC, and mainly polyethylene (Daramic). Today this market is dominated by the polyethylene separator, as is shown in Table 4. The annual growth of this market is 2–3 percent, but with large fluctuation based on prevailing economic conditions.

Sealed batteries have made little entry into this market with heavy cycling service, since the lead–calcium alloys required for these versions tend towards premature capacity loss, a phenomenon intensively investigated in recent years and possibly close to a solution.

CosMX Exhibit 1008, Page 277 of 633

Table 4. World lead–acid traction battery production 1997 (million Wh, estimate)

	Polyethylene separators	Phenol–formaldehyde–resorcinol separators	PVC separators	Rubber separators	Microfiber glass mat separators	Total
USA – Canada	4150	80	50	350	150	4 780
Europe	3700	800	1100	950	50	6 600
Asia–Pacific	950	150	500	900	50	2 550
Latin America	20	50	50	100	–	220
Total (million Wh)	8820	1080	1700	2300	250	14 150
(%)	62.3	7.6	12.0	16.3	1.8	100.0

Electrical Vehicle Battery Separators

Although electric vehicles are only a special application for traction batteries, the general interest in them may justify their own separate section.

Electric vehicles are around only in a few surviving niches, electric baggage carts at German railway stations, postal delivery trucks, and milk delivery vans in the UK being the best-known examples. Based on a growing consciousness of decreasing natural resources and especially on the oil crisis around 1970 there were intensive efforts to develop electric propulsion further, but they focused mainly on high-energy battery systems such as sodium/sulfur. The serious difference in energy density between a fuel tank of around 12 000 $Wh\,kg^{-1}$ and the batteries of 30–40 $Wh\,kg^{-1}$ actually available was insurmountable; even when considering all efficiencies involved, there remains a factor in the order of magnitude of 100; the electric vehicle returned to the background. Only since about 1990, prompted by the California Clean Air Act and by considerable research grants from the US Advanced Battery Consortium (USABC) — a joint activity mainly of the three major US car manufacturers — have increased efforts on electric vehicles been resumed. USABC has set the goal so high that lead acid batteries have been put out of the question for this application [29]. This led to an initiative by the lead–acid battery industry and their suppliers to set up the Advanced Lead–Acid Battery Consortium (ALABC) with the goal of fostering development of the lead–acid battery for use in electric vehicles, at least for an interim period until more powerful batteries with higher energy density will become available. Here a series of complex technical problems have to be solved [30]. Of course, such electric vehicle batteries have to be maintenance-free, i.e., of sealed construction; the resulting use of lead–calcium alloys and thus the premature capacity loss have already been touched on.

For the separation of such batteries, gel construction and microfiber glass fleece separators again compete: because of the deep discharge cycles, the gel construction with its lower tendency to acid stratification and to penetration shorts has advantages; for the required power peaks, microfiber glass fleece construction would be the preferred solution. The work on reduction of premature capacity loss with lead–calcium alloys has shown that considerable pressure (e.g., 1 bar) on the positive electrode is able to achieve a significantly better cycle life [31–36]. Pressure on the electrodes produces counter pressure on the separators, which is not unproblematic for both separation systems. New separator developments have been presented with

CosMX Exhibit 1008, Page 278 of 633

the goal of their being only a little deformed even at high pressure despite high porosity, be they of ceramics [37] or highly filled polymer [38]. Because of the power requirements the trend is clearly towards thinner electrodes and thus thinner separators, which should render a microporous pore size structure indispensable.

9.2.2 Separators for Starter Batteries

9.2.2.1 Polyethylene Pocket Separators

Production Process

The term "polyethylene separator" is somewhat misleading, since this separator consists mainly of agglomerates of precipitated silica, held within a network of extremely long-chained, ultrahigh-molecular weight polyethylene molecules. The raw materials, precipitated silica (SiO_2 — about 60 percent), ultrahigh-molecular weight polyethylene (UHMW PE — about 23 percent), a mineral process oil (about 15 percent) –all percentages are relative to the final product– and some processing aids (e.g., antioxidants) together with an additional considerable excess of mineral oil, are mixed intensively and fed into an extruder. Here, by the effects of heat and mechanical shear, a viscous melt is formed which is extruded through a slit die 1 m wide into a sheet 1–2 mm thick which is then formed between the two profiling rolls of a calendar into the desired separator profile. Generally this is characterized by a backweb of about 0.2 mm, which on one side has continuous ribs 0.6–1 mm high in the machine direction at a distance of about 10 mm. At this point the separator material is oil-filled and thus shiny black. In a subsequent step the mineral oil serving as pore-former is largely extracted in a solvent bath [16]. Some producers use trichloroethylene for solvent; it is easy to handle processwise, but as a chlorinated hydrocarbon it carries environmental risks.

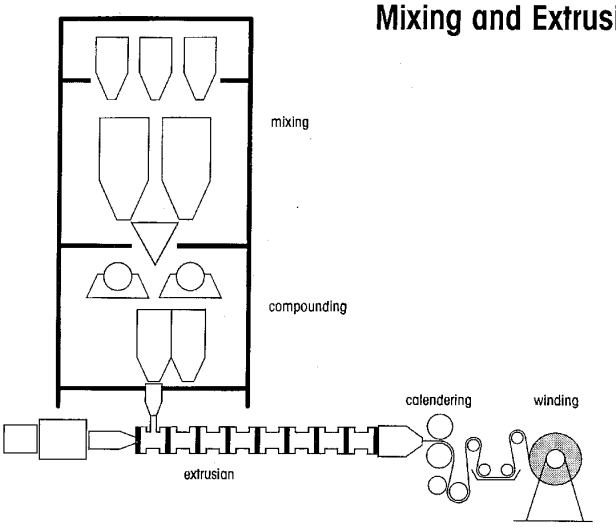


Figure 7. Polyethylene separator production process (I) Mixing and Extrusion

CosMX Exhibit 1008, Page 279 of 633

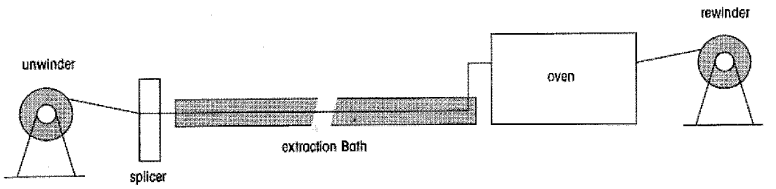


Figure 8. Polyethylene separator production process (II) Extraction

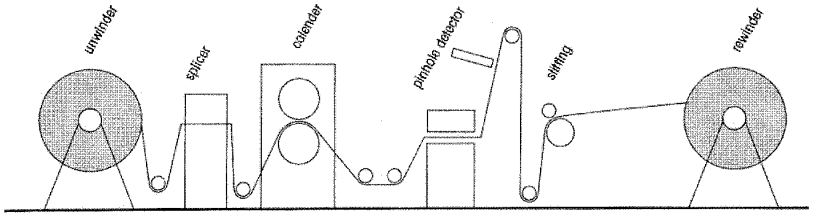


Figure 9. Polyethylene separator production process (III) Slitting

The alternative is hexane, which because of the explosion hazard requires a more expensive type of extractor construction. After the extraction the product is dull gray. The continuos sheet is slit to the final width according to customer requirements, searched by fully automatic detectors for any pinholes, wound into rolls of about 1 m diameter (corresponding to a length of 900–1000 m), and packed for shipping. Such a continuous production process is excellently suited for supervision by modern quality assurance systems, such as statistical process control (SPC). Figures 7–9 give a schematic picture of the production process for microporous polyethylene separators.

Properties

Filled polyethylene separators are the only pocket material that has been able to meet all requirements of a starter battery reliably [39–48]. It is flexible and weldable into three-sided closed pockets, making the previously usual mud room at the bottom of a starter battery redundant; an increase of 8 percent in could crank performance and energy density results (cf. Fig. 10 and 11) [3]. It is microporous, i.e., its pore diameters are significantly below 1 μm, which durably avoids penetration by lead particles. Only in this way has the use of lead–calcium alloys in electrodes, with their increased tendency to shedding, become possible, together with a reduction in water consumption over the life of the battery, allowing today's batteries to be properly called maintenance-free.

The thin backweb, typically 0.2 mm thick with a porosity of 60 percent yields excellent electrical resistance values of $\approx 50\ \mathrm{m}\Omega\ \mathrm{cm}^2$, permitting further optimization of high-performance battery constructions. These require very thin electrodes due to the overproportionally increasing polarization effects at higher current densities and consequently also low distances: most modern versions have separators only 0.6 mm thick. Such narrow spacings enforce microporous separation!

Practical experience has shown poly

CosMX Exhibit 1008, Page 280 of 633

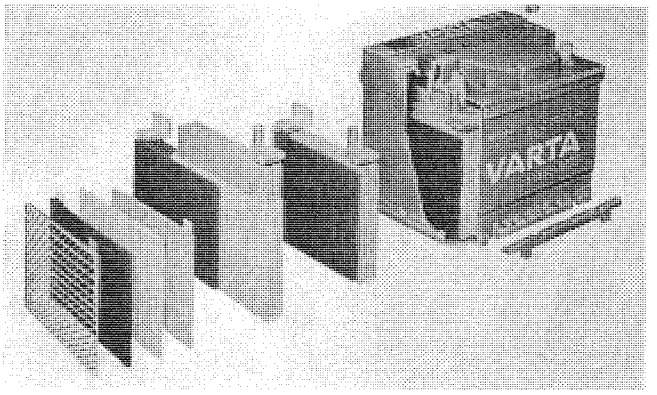


Figure 10. Starter battery with pocketed plates *)

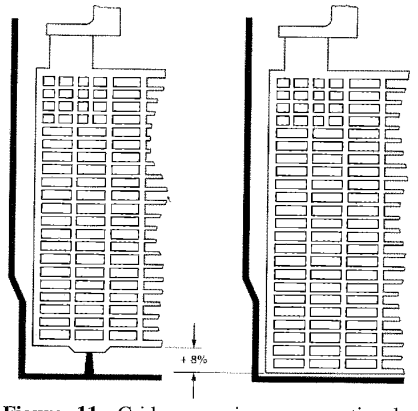


Figure 11. Grid comparison: conventional vs. pocket construction *)
(Courtesy: VARTA Batterie AG)

ethylene pocket separators only in very exceptional cases to be considered as a cause of failure in starter batteries [40, 49–51]. Here it has usually been the case of an atypical application, e.g., a power supply in seasonal use on a boat or long-term deep discharges resulting in penetration shorts from the solution phase. Under extreme temperature conditions, as in the famous Las Vegas taxicab service, the battery life is severely reduced, but again the predominant failure modes are corrosion or worn-out positive electrodes and expander deterioration. One has to concede that under such extreme conditions the separators also approach their limits of stability [40] and less oxidation-stable versions can begin to shorten the battery life. The prevailing cost pressure has led to increasing use of thinner backweb, e.g., 150 μm, in order to reduce raw material costs; this calls for a thorough evaluation of the limitations mentioned above [41].

In this connection the remaining oil in the separator plays an important role. At the first glance, to increase the porosity a total extraction of the oil would be expedient, but certain oil components have been shown to exert a protective action on the polyethylene. Oil content and its distribution, as well as selection of the oil, thus gain particular significance [41, 52–54].

For problem-free processing, high tensile and puncture strengths are desirable. Especially when using expanded metal

*Reprinted from W. Böhnstedt, Automotive lead/acid battery separators: a global overview, *J. Power Sources*, **1996**, *59*, 45–50, with kind permission from Elsevier Science S.A., Lausanne.

CosMX Exhibit 1008, Page 281 of 633

electrodes, sharp edges or points which may puncture the backweb and lead to shorts have to be taken into account. Even though the polyethylene separator is unique in these properties compared with conventional separators, these are considerable differences between the products of various suppliers.

Profiles

The standard profile for microporous pocket separators exhibits continuous longitudinal ribs 10 – 12 mm apart, which determine the total thickness (Fig. 12). The margin area, used later for the welding process, generally has ribs of lower height (Fig. 13) or only a thicker backweb. These measures facilitate the mass distribution in calendering during the production process, and apart from this they protect the particularly exposed edges of the pockets during the life of the battery. One noteworthy version of a profile has recently been presented by providing

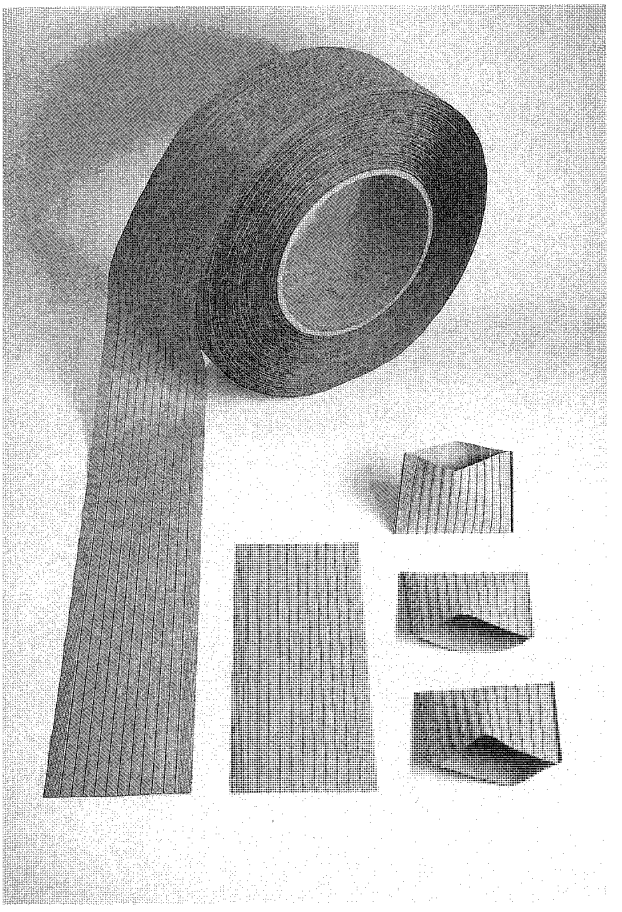


Figure 12. Polyethylene separator: pockets

CosMX Exhibit 1008, Page 282 of 633

cross-ribs within the margin area (Fig. 14) to keep the backweb in this area always at a safe distance from the grid edge of the positive electrode; the oxidizing substances originating there will thus do less damage [55,56]. A similar protection is offered by profiles with a continuous rib pattern, i.e., extending also into the welding zone, be it as narrow vertical ribs or especially as sinusoidal ribs [57].

The narrow tolerances to be maintained for the total separator thickness are tightened even further by the trend towards high-performance batteries with many thin electrodes, and therefore many separators also. One can easily calculate that for, say, ten or more electrodes and an equal number of separators per cell, the permitted tolerances become very small for fitting the electrodes/separators stack into the cell container. With electrodes and separators being produced continuously, i.e., the thickness of consecutive individual pieces all having the same tendency, this means that if they are too thick, the stack does not fit into the cell without great pressure; if they are too thin, there is the danger of the electrode stack suffering in service due to vibration. As one solution, compressible ribs have been proposed [58] with groups of three ribs of which the middle one which is –not back-to-back–, on the opposite side of the backweb, generates a spring effect, balancing the tolerances and fixing the electrode stack within the container by its resilience (Fig. 15).

The desire for cost savings starts with utilization of material. Is the continuous vertical rib necessary? Interrupted rib versions [56] or so-called dimples [47] have been proposed repeatedly, but they have not succeeded because production or proc-

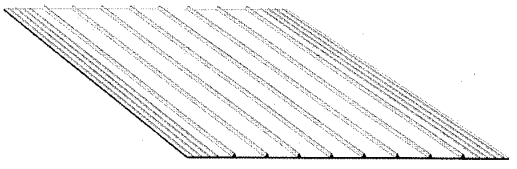


Figure 13. Polyethylene separator: standard profile

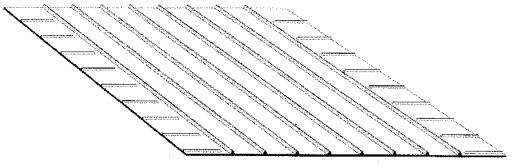


Figure 14. Polyethylene separator: cross-ribs in the margin area

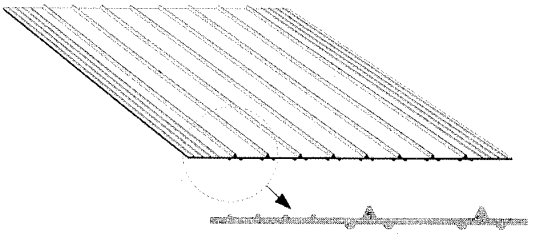


Figure 15. Polyethylene separators: compressible rib design

CosMX Exhibit 1008, Page 283 of 633

essing problems in practice could not be justified by the minor cost advantages.

The trend towards thinner backwebs has already been mentioned several times; it leads to a significant decrease in separator stiffness and thus possibly to processing problems. This loss in stiffness concerns the cross-direction more seriously than the longitudinal one, which is supported essentially by its high vertical ribs [41]. To regain stiffness, additional small longitudinal ribs between the main ones have been proposed (Fig. 16) [47] and for the far more seriously affected cross-stiffness additional flat ribs across the main rib direction can help (Fig. 17) [59]. These enable the cross–stiffness of a backweb of almost twice the thickness to be maintained, without obstructing the escape of charging gases.

The selection of suitable profiles improves the efficiency of processing on pocketing machines. Experience has shown, that even with an optimum machine adjustment, the pocketing material by its profile design and the strict adherence to tolerances contributes essentially to the quantity and quality of the pockets produced.

Product Comparison

Table 5 shows typical values for polyethylene pocket materials; of course, for the various producers [60–65] they vary slightly owing to differences in formulation and process. An exact comparison is also difficult, since not all producers state tolerances respectively clarify their statistical base.

9.2.2.2 Leaf Separators

The term "leaf separator" characterizes the customary stiff version of a starter battery separator that can be inserted individually between the electrodes on automatic stackers, in contrast to pocket separators. This processing requires considerably higher bending stiffness than for pocket separators, calling for thicker backwebs, typically 0.4–0.6 mm (Fig. 18 and 19).

Sintered PVC Separators

The first synthetic separator is still in use today in some geographical areas, for two reasons: this separator is unchallenged in its low raw-material and production costs

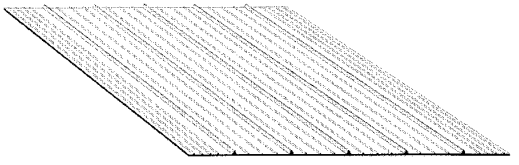


Figure 16. Polyethylene separator: intermediate vertical ribs

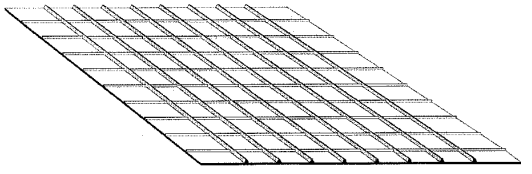


Figure 17. Polyethylene separator: cross-rib design

CosMX Exhibit 1008, Page 284 of 633

Table 5. Microporous polyethylene pocket separators

Brand name	Backweb thickness * (mm)	Electrical resistance ($m\Omega\,cm^2$)	Oil content (%)	Porosity (%)	Puncture strength (N)	Supplier
Daramic II	0.20 – 0.25	60	12 ± 3	60	9	Daramic, Inc [60,61]
Daramic High Performance	0.15 – 0.20	50	12 ± 3	60	11	Daramic, Inc [60,61]
EMARK	0.20 – 0.25	55	12 ± 3	60	6	Entek Int. LLC [62,63]
RhinoHide	0.15	50	13 ± 3	60	6	Entek Int. LLC [62,63]
Junfer PE Separator SLI	0.25	90	13 ± 3	60	n. a. +	Jungfer GmbH & Co. KG [64]

* Other backweb thicknesses upon request n.a.: not available

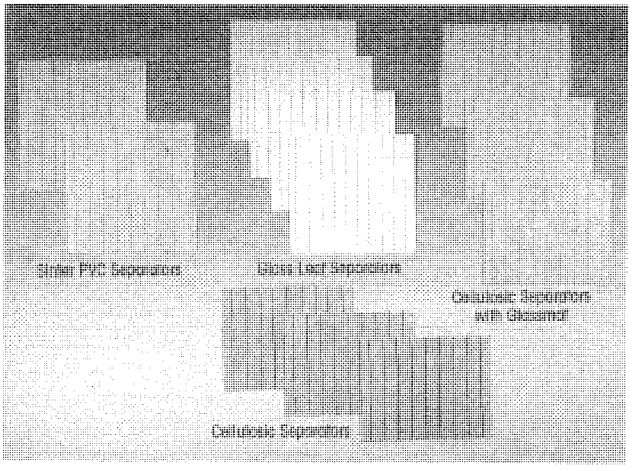


Figure 18. Leaf type separators

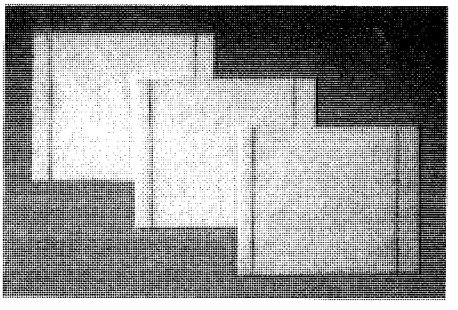


Figure 19. "Japanese separators"

and it shows good stability against oxidation at elevated temperatures and vibrations. However, its processing is difficult and its brittleness leads to higher scrap rates. Tender treatment, preferentially by manual labor, and an increased quality control effort may be justifiable at low labor rates. Sintered PVC separators are thus still widely used in China, India, Russia and some Asia–Pacific countries as well as around the Mediterranean Sea.

CosMX Exhibit 1008, Page 285 of 633

Sintered PVC is not at all one uniform product; large differences in properties and quality are possible. Experience has shown that premium qualities require significantly higher production costs.

The production process is comparatively simple, even though — of course — the respective know-how is also decisive. The equipment for the production of sintered PVC separators is suitable in size and production capacity to be operated on its own by individual, medium-sized, starter battery plants, in contrast to the far larger units required for the production of polyethylene pocket material.

Fine-grained PVC powder is spread onto a flat steel transport belt and by means of a doctor knife brought into the desired profile, i.e., generally quite a thin sheet of 0.3 – 0.6 mm thickness with vertical ribs. While passing through a sintering oven the surface of the PVC grains is just barely molten, causing neighboring particles to stick together (cf. Fig. 2); the remaining void spaces within this spherical packing are the resulting porosity. Finally the product is slit and chopped into the dimensions required. In an alternative version of the process the thin, sintered sheet produced initially is embossed in a second step between heated calender rolls to achieve the requisite total thickness.

Whereas a maximum number of contact points between PVC grains is desired to achieve mechanical stability, this prevents higher porosities. Typical values for porosity are 30 – 35 percent; therefore the electrical resistance is rather high, i.e., 170 $m\Omega\,cm^2$, despite thin 0.3 mm backwebs for top qualities. As mentioned, the range is very wide — even considerably higher electrical resistances are sometimes acceptable, e.g., in areas where cold crank performance is of no significant importance.

Typical pore size distributions result in mean pore diameters of around 15 μm. Even long and intensive efforts did not succeed in decreasing this value decisively in order to enable production of microporous pocketing material resistant to penetration [65, 66]. In practice PVC separators prove themselves in starter batteries in climatically warmer areas, where the battery life is however noticeably reduced because of increased corrosion rates at elevated temperature and vibration due to the road condition. The failure modes are similar for all leaf separator versions; shedding of positive active mass fills the mud room at the bottom of the container and leads to bottom shorts there, unless — which is the normal case — the grids of the positive electrodes are totally corroded beforehand.

In many countries starter batteries are almost 100 percent recycled; PVC separators can cause some problems here [67]. A prior separation of PVC from other battery components, which is quite tedious, would be desirable, because a PVC content decreases the recycling purity of the container polypropylene and makes further processing of this plastic more difficult. Also, any chlorine compounds liberated can form environmentally hazardous products with other substances; the usual remedy is to install costly filter stations, with the residues representing possibly toxic wastes requiring special disposal methods.

Sintered PVC separators are frequently produced only for captive consumption; beyond that there are specialized producers for these separators [64,68,69] and for equipment for their production [64]. The data compiled in Table 6 comprise only premium products of independent producers.

CosMX Exhibit 1008, Page 286 of 633

Table 6. Sintered PVC separators

Brand name	Backweb thickness (mm)	Electrical resistance * ($m\Omega\,cm^2$)	Porosity (%)	Pore size (average) (μm)	Supplier
Accuma PVC	0.20 – 0.30	170	30	30	Accuma S.p.A. [68]
ICS LR type	0.30	170	37	<25	ICS S.p.A. [69]
Jungfer LJF	0.25 – 0.30	170	33	<30	Jungfer Ges.mbh & Co. KG [64]

* Electrical resistance of a separator of 1.3 mm overall thickness

Cellulosic Separators

The closest relative to the wood veneer surprisingly has retained some of its properties, which differentiate these separators from pure synthetic ones: primarily, a positive effect in reducing the water loss in starter batteries [39, 70–72]. This impact tends to decrease as the antimony content in the alloys is lowered, but it still represents an advantage over other leaf separators, unless a microporous pocket is required by the alloy anyway.

A voluminous, highly porous, special paper of cotton linters or other premium α-cellulose fibers is passed through an immersion bath of aqueous phenol–formaldehyde resin solution and dried. A different process combines the production of the paper directly with its impregnation. Common to both processes is the coating of cellulose fibers with a very thin layer of phenol–formaldehyde resin, largely protecting them from acid or oxidative attack. The pore structure of the separator is predetermined by the paper; to increase the porosity further, glass fibers may be mixed in during paper production. In a second step, inside a curing oven the phenolic resin is crosslinked at elevated temperature, and finally ribs of thermoplastic polymers are applied to achieve the desired total thickness. Some versions have the backweb embossed with longitudinal corrugations with plastic coated surfaces for better oxidation stability, since they are placed in the battery directly against the positive electrode. Slitting and chopping processes set the required dimensions for the product. Cellulosic separators show a high porosity (70 – 75 percent) an thus also low electrical resistances (100 – 150 $m\Omega\,cm^2$ according to quality and producer). It is the preferred leaf separator in climatically more moderate areas, where cold crank performance is of importance. The water-loss-reducing properties of the cellulosic separator have made it possible to meet the criteria of the standards for maintenance-free starter batteries, even when using easy-to-cast antimony alloys (1.8 – 2.5 percent).

A thorough study (cf. Ref. [40]) of failure modes in practice has shown that with this form of separation also the cause of failure has not been the separator; the usual failure modes for leaf-type separators, as they have been described for sintered PVC separators, apply here as well.

Table 7 shows typical values for different qualities of cellulosic separators from various producers.

Glass Fiber Leaf Separators

Glass fiber leaf separators in the USA –especially at one large manufacturer– were for over a decade, between 1980 and 1995, an intermediate in the transition from conventional leaf separator to microporous pocket. The web is produced

CosMX Exhibit 1008, Page 287 of 633

Table 7. Cellulosic Separators

Brand name	Backweb thickness (mm)	Electrical resistance ($m\Omega\,cm^2$)	Porosity (%)	Pore size (average) (μm)	Supplier
Armorib-L	0.55	140	70	25	Daramic, Inc. [60]
Darak 101*	0.50	110	75	22	Daramic, Inc. [60]
Axohm A 428	0.60	210	70	20	Iydall Axohm [73]
Axohm A 438+*	0.55	140	75	23	Iydall Axohm [73]

* These types consist of a cellulosic/glass fiber blend paper

from glass fibers of suitable quality (C-glass) and of various diameters (mainly from 3 μm to around 10 μm) on a special paper machine. Even though an impregnation for protecting the fibers is not required, a small quantity of phenolic or acrylate resin is nevertheless applied to achieve the desired bending strength. A thermoplastic rib is added in the usual way. Glass fiber leaf separators distinguish themselves by very high porosity (80 – 85 percent) and very low electrical resistance (65 $m\Omega\ cm^2$). The battery performance meets the expectations: very good cold crank data attract attention, and the water loss is comparable with that of PVC, but exceeds that of cellulosic separators significantly; the separator is not a cause of battery life limitation.

There is at present only one producer of this type of separator left; typical data are shown in Table 8.

Leaf Separators with Attached Glass Mat

Even though this version is not a distinct type of separator, this section is dedicated to it. To all leaf-type separators described, a glass mat can be applied on the side directed towards the positive electrode, which is usually fixed by an adhesive coated onto the ribs (cf. Fig. 18). This raises the cost of the separator and is usually not required for starter batteries used under normal service conditions, but it holds the positive active mass better inside the electrode and thus prevents premature shedding. It is especially important for batteries subject to severe vibrations or encountering frequent deep discharges. Typical applications include construction machinery batteries or the area bordering on cycling applications, such as marine batteries, truck and off-road vehicle batteries, electric lawn mowers, golf carts or other small traction batteries.

"Japanese" Separators

The development of the starter battery in Japan has taken an independent course (see Sec. 9.2.1.2), visibly expressed by the separator's thick glass mat and its lack of spacing ribs (cf. Fig. 19). The cellulosic backweb impregnated with phenolic resin, generally in use until around 1980 and largely identical to the separator of the same type already mentioned has been completely replaced by thin ($\approx$ 0.3 mm) fleece materials made of organic fibers.

Table 8. Glass fiber leaf separators

Brand name	Backweb thickness (mm)	Electrical resistance ($m\Omega\,cm^2$)	Porosity (%)	Pore size (average) (μm)	Supplier
Axohm 10 G +	0.70	65	85	27	Iydall Axohm [73]

CosMX Exhibit 1008, Page 288 of 633

Since the glass mat supplies sufficient stiffness, high backweb thickness was no longer needed! These fleeces are made of organic fibers (polyester and polypropylene, as well as so-called "synthetic pulp", i.e., fibrillated polypropylene) on paper machines.

The basic materials are sufficiently stable in sulfuric acid not to require the expensive phenolic resin impregnation. Traces of adhesive are applied to hold the glass mat in order to achieve the total thickness. This separation system may be expensive to manufacture, a fact certainly largely balanced by savings in positive active mass, but it also has some indisputable advantages.

The electrical resistance, at 60 – 90 $m\Omega\ cm^2$, is astonishingly low, because the backweb is only 0.25 – 0.30 mm thick and the glass mat with its porosity in excess of 90 percent also contributes only little. In some types of construction the low electrical resistance cannot be fully utilized, however, due to a tendency for gas to be trapped within the glass mat.

The oxidative stability is excellent. Direct contact between the glass mat and the positive electrode effects a far lower tendency to shed active mass; thus as a general rule the failure mode is positive grid corrosion.

It is rather difficult to compare constructions differing to such an extent, since in the course of development the standards and also the electric layout of vehicles have been adapted to accommodate to the products available. Table 9 shows typical data for "Japanese" separators. From the above it can be clearly seen that a direct comparison or even an exchange for other leaf separators is almost impossible.

Microfiber Glass Separators

Even though this separation system has not yet entered the starter battery field, it should be discussed here as a possible option for the future.

Microfiber glass fleece mats are typically produced from a blend of 20 – 30 percent glass microfibers <1 μm in diameter, with the balance of the glass fibers thicker (3 – 10 μm) and longer (cf. Fig. 1), on a specialized paper machine (Foudrinier), since this is the only way of achieving the desired tensile strength without binder. The material is supplied in roll form, even though it is normally not processed into pockets, which are not required due to the absence of free electrolyte. The classification here as a leaf separator should be seen in this sense.

The microfiber glass separators have to fill the space between the electrodes completely; the backweb thickness, is thus identical to the total thickness. Due to the high compressibility of such porous glass mats, a standard measuring pressure of 2 kPa or 10 kPa (BCI method) is generally used; during assembly they are compressed

Table 9. Synthetic pulp – glass mat separators ("Japanese" separators)

Brand name	Backweb thickness (mm)	Electrical resistance ($m\Omega\ cm^2$)	Pore size (average) (μm)	Supplier
GSK – CV	0.30	90*	18	GS KASEI KOGYO K.K. [74]
GSK – MS	0.25	30*	23	GS KASEI KOGYO K.K. [74]
GSK – TC	0.25	60*	10	GS KASEI KOGYO K.K. [74]
GSK – SI	0.50	150*	25	GS KASEI KOGYO K.K. [74]

*Electrical resistance without glass mat, which adds approx. 30 $m\Omega\ cm^2$.

CosMX Exhibit 1008, Page 289 of 633

by additional 25 percent of their nominal thickness to make it possible to match the volume changes of the electrodes during charging and discharging; otherwise dry spots could be formed causing performance losses. Characterization of microfiber glass separators by their thickness alone has proven to be ambiguous; therefore the preferred method is by area weight. For a typical separation thickness of 1 mm glass fiber mats of 200 $g\,m^{-2}$ are used. Resulting from the extremely high porosity of more than 90 percent the measured electrical resistance is extremely low, but the difference in the pore spectrum inside the battery due to compression during installation has to be taken into account; moreover, not all pores must be acid-filled, in order not to block the oxygen transfer. The actual electrical resistance "experienced" by the battery is in the order of magnitude of other modern separation systems (50 – 70 $m\Omega\ cm^2$). An excellent description of these relationships exists in the literature [23].

Despite all the efforts over many years to establish this "sealed" construction in starter batteries, field results have been published only sparingly and they have not always been satisfactory. Cold crank results are very good; despite using lead-calcium the cycle life — at least in laboratory tests — has been found to be very good [75], probably due to the mat support of the positive active mass. In the day-to-day practice other influences, such as insufficient recharging and microshorts as a result of deep discharges or valve leaks, appear to lead to premature sulfation of the negative electrode and eventually to capacity deterioration. Improved constructions are continually being presented and tested on a large scale. Besides some open technical questions, the cost structure also has prohibited a wider introduction to date: sturdier containers and more precise electrode geometry, voluminous separators, and reliable valves, an expensive filling process, and last but not least temperature–controlled charging management could only be justified with difficulty in times of cost trimming within the automotive industry.

The range of microfiber glass mat separators offered by the leading producers are presented in Sec. 9.2.3.3 with typical data in connection with their predominant application in sealed stationary batteries.

9.2.2.3 Comparative Evaluation of Starter Battery Separators

The individual starter battery separator systems have been described; here they are evaluated comparatively. There are no standards for evaluating separators! Therefore the comparison will be concentrated primarily on the effects on the performance of the starter battery, with other decisive criteria such as cost structure and effects on productivity indicated.

Cold crank performance, battery life expectancy, and freedom from maintenance are generally co-affected by the separators, whereas ampère-hour capacity remains largely unaffected at a given separator thickness. The properties of the different leaf and pocket separators are compared in Table 10. These typical separator properties (lines 1–4) are reflected in the electrical results of battery tests (lines 5–8). The data presented here are based on the 12 V starter battery standard DIN 43 539–02; tests based on other standards lead to similar results.

The cold crank voltage is directly affected by the separator electrical resistance (cf. Sec. 9.1.2.3; Fig. 5), but to a

CosMX Exhibit 1008, Page 290 of 633

much smaller extent than is normally assumed. Nevertheless the effect of low electrical resistance of the separator is not to be underestimated, since it often presents the only way of meeting the acceptance criteria of high-performance batteries reliably.

The life expectancy of a starter battery, according to DIN 43 539–02, is not affected by the separator. Experience has shown that all batteries with modern standard separators in cycle life tests not only last the required five weeks of cycling, but mostly ten weeks or more. The cause of failure is typically positive grid corrosion — in good agreement with practice [49]. This fact supports this standard, which is supposed to reflect reality, but on an accelerated time scale.

A modification of the test conditions (DIN 43 539-02 E of February, 1980) did prove to show more about the effect of the separator on battery life expectancy. In Fig. 20 the weekly cycling regimes of these two standards are compared. The latter, requiring more discharges at a higher temperature, has been shown to uncover significant differences between the individual types of separators. Macroporous separators with average pore sizes of 10 – 30 μm like PVC, cellulosic, or glass separators, are just meeting the required cycle life. Microporous pocket separators with pore sizes distinctly below 1 μm prevent not only penetration through the separator, but also — because of the pocket — bottom or side shorts, and this to such an extent that even under these aggravated test conditions the separator does not limit the cycle life duration.

Table 10. Comparative evaluation of starter battery separators

		Polyethylene pocket separators	Sintered PVC separators	Cellulosic separators	Cellulosic/glass mix separators	Glass fiber leaf separators
Backweb thickness	(mm)	0.25	0.30	0.55	0.50	0.70
Pore size (average)	(μm)	0.1	15	25	22	27
Acid displacement	($cm^3\,m^{-2}$)	120	210	170	140	110
Electrical resistance	($m\Omega\,cm^2$)	60	160	140	100	65
Test results (DIN 43 539-02) (PbSb 1.6 / PbSb 1.6)						
Cold crank voltage	(V)	9.40	9.20	9.25	9.30	9.35
Cycle life test (weeks)		>10	>10	>10	>10	>10
Accelerated cycle life test (DIN 43 539 E – 1980)	(weeks)	>10	5	6	6	7
Water consumption*	($g\,(Ah)^{-1}$)	2 – 4	4	2	2	4

*504 h overcharge with 14.4 V at 40 °C

Surprisingly the water consumption of a starter battery, provided it contains antimonial alloys, is affected by the separator. Some cellulosic separators as well as specially developed polyethylene separators (e.g., DARAMIC V [76]) are able to decrease the water consumption significantly. The electrochemical processes involved are rather complex and a detailed description is beyond the scope of this chapter. Briefly, the basic principle behind the reduction of water loss by separators is their continuous release of specific organic molecules, e.g., aromatic aldehydes, which

CosMX Exhibit 1008, Page 291 of 633

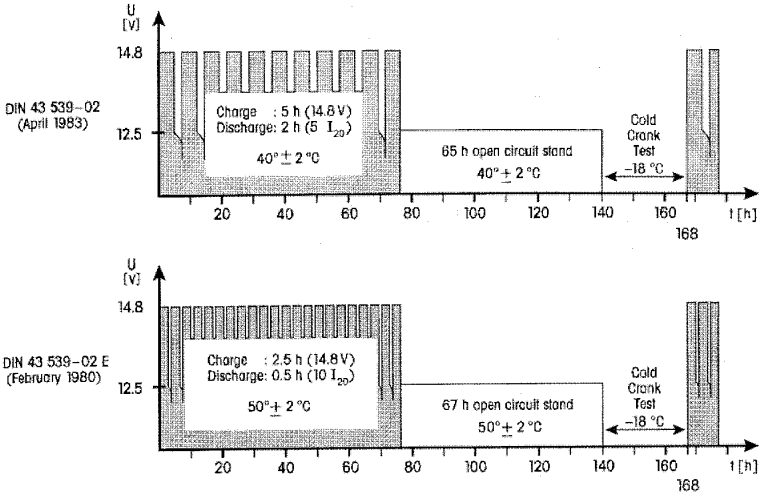


Figure 20. DIN standards: weekly cycling regimes

are selectively adsorbed at antimonial sites of the negative electrode, inhibiting there the catalytic effect of antimony on hydrogen evolution and thus lowering the water consumption [70,71]. The current trend towards low-antimony or lead–calcium alloys — primarily for productivity reasons — reduces the importance of these effects; nevertheless, they remain decisive in many instances.

The above comparative evaluation of starter battery separators refers to moderate ambient temperatures; the standard battery tests are performed at 40 or 50 °C. What happens, however, on going to significantly higher temperatures, such as 60 or 75 °C? This question cannot be answered without considering the alloys used: batteries with antimonial alloys show a water consumption that rises steeply with increasing temperature [40], leaving as the only possibilities for such applications either the hybrid construction, i.e., positive electrode with low-antimony alloy, negative electrode lead–calcium, or even both electrodes lead–calcium.

Because of the increased shedding with these alloys, pure leaf separation is hardly suitable. Separations with supporting glass mats or fleeces as well as microfiber glass mats provide technical advantages, but are expensive and can be justified only in special cases. Also under these conditions of use the microporous polyethylene pocket offers the preferred solution [40]. Lower electrical properties at higher temperatures, especially decreased cold crank duration, are battery-related; the choice of suitable alloys and expanders gains increased importance.

However it has to be conceded that after battery life cycle tests at such temperatures polyethylene separators also reach their limits, although this fact does not yet reflect in failure-mode studies [49], even in locations with extreme ambient temperatures. The tendency towards using ever–thinner backwebs cannot be continued, however, without seeking protective measures. Suitable provisions have to be made espe-

CosMX Exhibit 1008, Page 292 of 633

cially with respect to the separator's oxidative stability at elevated temperature. The leading producers of polyethylene separators have recently presented solutions [41, 47], which even at 150 μm backweb provide for oxidative stability and puncture strength in excess of that for the standard product at 250 μm backweb [41].

Without any doubt the microporous polyethylene pocket will meet all requirements of modern starter batteries for the foreseeable future. Whether and to what extent other constructions, such as valve-regulated lead–acid batteries, other battery systems, or even supercapacitors, will find acceptance, depends — besides the technical aspects — on the emphasis which is placed on the ecological or economical factors.

9.2.3 Separators for Industrial Batteries

9.2.3.1 Separators for Traction Batteries

Traction batteries are the workhorses among batteries; day in, day out they have to perform reliably, i.e., for years they are discharged to about 80 percent by their nominal capacity, typically during an 8h shift of a forklift , and are recharged during the remaining hours of the day. A life of 1500 cycles or five years is taken for granted, with concession regarding the life expectancy only made under extreme condition.

It can be stated generally that requirements for traction battery separators in respect to mechanical properties and chemical stability are considerably higher than for starter battery separators. This is due to the fact that a forklift battery is typically operated for about 40 000 to 50 000 h in charge-discharge service, whereas a starter battery for only about 2000 h. The requirements for electrical resistance are lower because of the typically lower current densities for traction batteries. These differences are of course reflected in the design of modern traction battery separator material.

Polyethylene Separators

A detailed description of the production process and the properties of polyethylene separators can be found in Sec. 9.2.2.1, so only the modifications, which are important for traction battery separators are covered here.

Industrial battery separators are often supplied in cut-piece form, i.e., they have to have a certain stiffness and robustness in order to withstand the assembly into cells, together with electrodes weighing several kilograms without damage. Modern polyethylene traction battery separators have backwebs of about 0.50–0.65 mm, i.e., about three times the backweb thickness of starter battery separators with the respective effect on stiffness, electrical resistance, and also production process line speed. The larger backweb thickness combined with a higher oil content (~ 15–20 percent) gives the separator the required oxidative stability, which to a first approximation is proportional to the product of backweb thickness and its oil percentage. A somewhat lower porosity and thus lower acid availability are the consequences.

The microporosity is also important for this application, in order not to allow shorts through the backweb during battery life. Bottom shorts are avoided by a mud room of sufficient dimensions, and side shorts by plastic edge protectors on the

CosMX Exhibit 1008, Page 293 of 633

frames of the negative electrode. Some manufacturers have switched to using sleeves of polyethylene separator material, rendering an edge protection superfluous. The use of tree-side sealed separator pocket in traction batteries should be avoided, because experience has shown this can lead to increased acid stratification, subsequent sulfation, and thus capacity loss.

The choice of a suitable oil has special importance. Besides beneficial effects of the oil on the oxidative stability of the separator, other consequences have to be considered. From the chemical mixture of which an oil naturally consists, polar substances may migrate into the electrolyte. Being of lower density than the electrolyte, they accumulate on its surface and may interfere for instance with the proper float function of automatic water refilling systems. Some oils which fully meet both of the above requirements have been identified, i.e., they provide sufficient oxidation stability without generating black deposits [53].

An effect similar to the water loss in starter batteries is characterized as top-of-charge performance in traction batteries. Antimony is dissolved from the alloy of the positive electrode, migrates through the electrolyte and is deposited on the negative electrode, where — because of its far lower hydrogen overvoltage than lead — it catalyzes hydrogen evolution, thus reducing the charging voltage at constant current during the overcharge period [77]. From long experience it is known that some separators are able to influence this behavior [78–81]. Many hypotheses have been proposed, examined, and discarded again; for the current status of the discussion reference should be made to the literature [70,71]. Suitable additives, such as uncrosslinked natural rubber [82] or VCA (Voltage Control Additive [83]) allow significant improvement of the top-of-charge performance of batteries, helping polyethylene separators to gain acceptance in the great majority of applications.

Traction batteries are assembled either with pasted and glass mat-wrapped positive electrodes, as is the case predominantly in the USA, or with tubular positive plates, which prevail in Europe. The former electrodes place no particular requirement on the separator profile; vertical ribs on the positive side are standard. The construction with tubular positive electrodes preferably uses a diagonal (Fig. 21) or sinusoidal (Fig. 22) rib pattern. Insufficiently narrowly spaced supporting contact points between tube, rib, and separator backweb have shown the latter to yield to expansion of the negative electrode during cycling. Capacity deterioration by overexpansion and gas trapping result; thus a narrower rib spacing is desirable, but is limited by increased acid displacement. Interrupted ribs or even dotted spacers (dimples) on the backweb are under discussion.

Flexible polyethylene separators have facilitated a novel cell construction: the separator material, supplied in roll form, is wound so that it meanders around electrodes of alternating polarity (Fig. 23), requiring ribs in the cross-machine direction; such profiles are available commercially [60].

Finally, one development results from returning to a basic idea from the dawn of the lead–acid battery, wherein the functions of support for the positive active material and of the separator are combined into one component: the gauntlet separator [84] consisting of a coarsely porous, flexible support structure coated with microporous polyethylene material for separation. The future has to show whether this approach will be able to meet all demands.

CosMX Exhibit 1008, Page 294 of 633

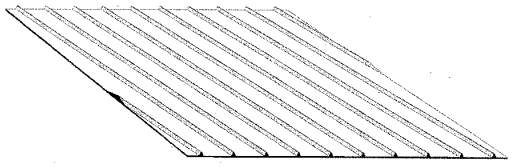


Figure 21 : Polyethylene separator: diagonal industrial battery profile.

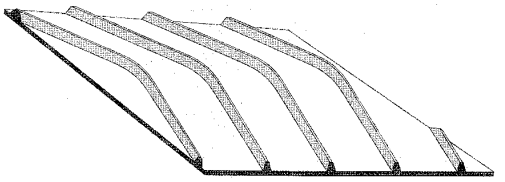


Figure 22 : Polyethylene separator: sinusoidal profile.

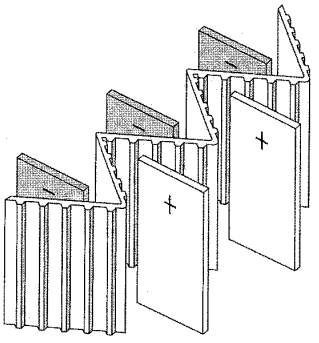


Figure 23: Polyethylene separator: meandering separation

Characteristic data for polyethylene separators in comparison with competing systems are discussed later in this section (Table11).

Rubber Separators

A thin layer of a mix of natural rubber, sulfur, precipitated silica, water, and some additives, such as carbon black and vulcanizing agents, is extruded on a paper support belt, calendered, and vulcanized as a roll in an autoclave under elevated pressure and temperature ($\approx$180 °C). A modified process extrudes and calenders a ribbed profile and crosslinks the rubber separator by irradiation.

Rubber separators have a relatively low porosity ($\approx$50 – 55 percent) and thus high acid displacement and electrical resistance. Furthermore, they are brittle and for this reason difficult to handle in larger sizes. In order to balance this disadvantage, an adjustment to a lower degree of crosslinking has been attempted; the result was a corresponding increase in susceptibility to oxidative attack.

These disadvantages have led to an extensive displacement of rubber separators by polyethylene separators. Nevertheless, a few market segments exist, such as golf cart batteries –which for statistical reasons due to their construction are shown under SLI (starter-lighting-ignition) batteries– and traction batteries in severe heavy-duty service, especially at elevated temperatures, where rubber separators continue to be used. The reason is the top-of-charge behavior of traction batteries referred to above. Rubber separators are able to delay the process of antimony poisoning significantly. Its mechanism is based on uncrosslinked rubber components inhibiting hydrogen evolution [70, 82] in a similar

CosMX Exhibit 1008, Page 295 of 633

manner to that described for the water loss of starter batteries. With a constant-voltage charging regime, this leads to a lower increase in charging current and lower water consumption [80]. A comparative tabulation of rubber separator properties can be found under "Comparative Evaluation of Traction Battery Separators", below in Table 11.

Phenol–Formaldehyde–Resorcinol Separators (DARAK 5000)

An aqueous solution of phenol–formaldehyde resin and resorcinol (~70 vol.% water) is crosslinked by means of organic catalysts [18] at ~95–98 ° C between two continuous Teflon belts. With growing molecular weight the water solubility of the phenolic resin decreases and a phase separation occurs. A three-dimensional phenol resin structure is generated, in the interconnected cavities of which the water accumulates which is evaporated in a subsequent process step, thus generating the porosity of some 70 percent. The Teflon belts mentioned contain grooves, which determine the rib geometry of the separators. Phenolic resin is a duroplast and thus brittle; a polyester fleece is incorporated into the separator backweb during the production process, resulting in a sufficient reinforcing effect. In contrast to the macroporous (phenolic-resin-impregnated) cellulosic separator, the pore size of the present microporous phenolic resin–resorcinol system is determined exclusively by process conditions and not by the reinforcing fleece.

A stiff, microporous separator is formed with a very narrow pore size distribution with an average of 0.5 μm — about 90 percent of all pores being between 0.3 and 0.7 μm in diameter!

The porosity, at 70 percent, is excellent, and it also achieves strikingly good values for acid displacement and electrical resistance for an industrial battery separator ($0.12\ \Omega\,cm^2$).

The stiffness of the duroplast is helpful in counteracting the tendency of the negative active material to expand during cycling, even at larger rib spacing. The prevailing profiles have vertical or diagonal ribs on the positive side and on the negative side a low rib is frequently added for better gas release from the negative electrode.

Further details are given in the systems comparison under "Comparative Evaluation of Traction Battery Separators", below.

Microporous PVC Separators

A mixture of powdered poly(vinyl chloride), cyclohexanone as solvent, silica, and water is extruded and rolled in a calender into a profiled separator material. The solvent is extracted by hot water, which is evaporated in an oven, and a semiflexible, microporous sheet of very high porosity (~ 70 percent) is formed [19]. Further developments up to the 75 percent porosity have been reported [85,86], but these materials suffer increasingly from brittleness. The high porosity results in excellent values for acid displacement and electrical resistance. For profiles, the usual vertical or diagonal ribs on the positive side, and as an option low ribs on the negative side, are available [86].

Comparative Evaluation of the Traction Battery Separators

Which separator properties are important for use in traction batteries ? For this aspect primarily the highly predominant application, namely forklift traction batteries,

CosMX Exhibit 1008, Page 296 of 633

is to be considered: chemical resistance against attacks by acid and oxidation, mechanical stability for problem-free assembly, stiffness to counteract overexpansion of the negative active material, and low acid displacement are particularly desirable. Delay in antimony poisoning, absence or near-absence of oily deposits in the cells, and — last but not least — a low electrical resistance complete the requirement profile.

In Table 11 an attempt is made to include the above criteria in the form of quantitative data or qualitative evaluations.

Table 11. Separators for lead–acid traction batteries

	Polyethylene separators	Rubber separators	Phenol–formaldehyde–resorcinol separators	Microporous PVC separators
Supplier	Daramic, Inc. [60, 61] *	Amerace [87]	Daramic, Inc.[60, 61]	AMER-SIL s.a. [86]
Brand name	DARAMIC Industrial CL	Ace-Sil	DARAK 5000	AMER-SIL Standard
Backweb thickness (mm)	0.6	0.8	0.6	0.5
Pore size (average) (μm)	0.1	0.2	0.5	0.5
Acid displacement ($cm^3\ m^{-2}$)	320	450	235	250
Electrical resistance ($m\Omega\ cm^2$)	280	240	120	200
Initial capacity [+]	+	0	++	++
Handling properties [+]	++	0	+	+
Water consumption [+]	+	++	0	0

*Polyethylene industrial separators are also available from ENTEK International [62].
[+] Ranking: ++ very good, + good, 0 acceptable, – poor.

Polyethylene separators offer the best balanced property spectrum: excellent mechanical and chemical stability as well as good values for acid availability and electrical resistance have established their breakthrough to be the leading traction battery separator. Rubber separators, phenolic resin–resorcinol separators, and microporous PVC separators are more difficult to handle than polyethylene separators; their lack of flexibility does not allow folding into sleeves or use in a meandering assembly; in addition they are more expensive.

Special applications are often governed by different priorities: as already discussed in relation to golf carts, the low water loss and the delay in antimony poisoning in heavy-duty service of a forklift are of eminent importance, with the result that rubber separators remain the preferred product there. Submarine batteries offer a different picture: the number of cycles to be reached is far lower (~ 500) and, due to the slow (~ 100 h) but very deep discharge, the acid availability becomes the decisive criterion, which favors, for example, the phenolic resin–resorcinol separator. Such requirements are already similar to the application in open stationary cells.

9.2.3.2 Separators for Open Stationary Batteries

Stationary batteries serve predominantly as an emergency power supply, i.e., they are on continuous standby in order to be discharged for brief periods and sometimes deeply, up to 100 percent of nominal capacity, in the rare case of need. The following profile of requirements for the separator thus arises: very low electrical resistance, low acid displacement, no leaching of substances harmful to float-

CosMX Exhibit 1008, Page 297 of 633

service, as well as an excellent mechanical and chemical stability, especially against oxidation at continuous overcharge, because such batteries have a life expectancy of 20 – 30 years.

Polyethylene Separators

The production process for polyethylene separators (Sec. 9.2.2.1) as well as the characteristic properties (see Sec. 9.2.2.1 and 9.2.3.1) have already been described in detail above. Deviating therefrom, the desire for low acid displacement has to be added for separators in open stationary batteries. This can be met either by decreasing the backweb thickness or by increasing the porosity; the latter, however, is at the expense of separator stability.

Stationary batteries, moreover, often have transparent containers; historically, probably to allow observation of the electrolyte level or the extent of shedding. Deposits of oily substances accumulating at the electrolyte surface due to their stickiness could gather lead particles and produce an unpleasantly dirty rim, which can be avoided by careful selection of suitable oils [53].

Phenol–Formaldehyde Resin Resorcinol Separators (DARAK 2000/5005)

The production process and the principal properties of this system have been described in detail in the section on traction battery separators (see Sec. 9.2.3.1). The outstanding properties, such as excellent porosity (70 percent) and resulting very low acid displacement and electrical resistance, come into full effect when applied in open stationary batteries. Due to the good inherent stiffness the backweb may even be reduced to 0.4 mm, reducing acid displacement and electrical resistance to low levels that are not achievable by any other system. Furthermore, the phenolic resin–resorcinol separator neither generates any harmful substances nor is it attacked chemically or by oxidation. The sum of these properties has made it the preferred separator for open stationary batteries.

Microporous PVC Separators

Much of the above also holds true for the application of microporous PVC separators (see Sec. 9.2.3.1) in open stationary batteries. Very high porosity and thus low acid displacement and electrical resistance are also offered by this system. The relevant properties are compiled in Table 12.

Since the early days of using PVC separators in stationary batteries, there has been a discussion about the generation of harmful substances: caused by elevated temperatures or other catalytic influences, a release of chloride ions could occur which, oxidized to perchlorate ions, form soluble lead salts resulting in enhanced positive grid corrosion. Since this effect proceeds by self-acceleration, the surrounding conditions such as temperature and the proneness of alloys to corrosion as well as the quality of the PVC have to be taken carefully into account.

Sintered PVC Separators

Sintered PVC separators for open stationary batteries are produced in the same way as the corresponding starter battery version (Sec. 9.2.2.2). Their brittleness and thus difficult processability are disadvantages, as is their relatively low porosity; the concerns about release of chloride ions and subsequent increased corrosion are to be considered here as well. On the other hand,

CosMX Exhibit 1008, Page 298 of 633

they are unrivalled in low cost, even up to extreme overall thickness (up to 5 mm). Since at these thicknesses electrical resistance and acid displacement by the backweb have a relatively low impact, there is a remaining niche for the application of sintered PVC separators.

Comparative Evaluation of Separators for Open Stationary Batteries

Table 12 shows the physicochemical data of separators used in open stationary batteries. Since the emphasis is on low acid displacement, low electrical resistance, and high chemical stability, the phenolic resin–resorcinol separator is understandably the preferred system, even though polyethylene separators, especially at low backweb, are frequently used. For large electrode spacing and consequently high separation thickness, microporous as well as sintered PVC separators also find use.

9.2.3.3 Separators for Valve Regulated Lead–Acid Batteries

Batteries with Absorptive Glass Mat

Valve-regulated lead–acid (VRLA) batteries are frequently also somewhat misleadingly called sealed or recombinant batteries. Their operating principle is — as mentioned already — based on oxygen, which is generated during charging at the positive electrode, able to reach the negative electrode internally, and reduced there again. The negative electrode thus becomes partially discharged, so that it does not enter the overcharge phase, i.e., it does not lead to hydrogen evolution. No water consumption occurs; viewed externally, the total charging current is transformed into heat. For a more detailed description of the system, the literature [7, 23–27, 88–

Table 12. Separators for flooded lead–acid stationary batteries

	Polyethylene separators	Phenol–Formaldehyde–resorcinol Separators	Microporous PVC separators	Sintered PVC separators	Rubber separators
Supplier	Daramic, Inc. [60, 61] *	Daramic, Inc. [60, 61]	AMER-SIL s.a. [86]	Jungfer GmbH [64]	AMERACE Microporous Products [87]
Brand name	DARAMIC Industrial CL	DARAK 5005	AMER-SIL HP	Sintered PVC	Micropor-Sil M3
Backweb thickness (mm)	0.5	0.5	0.5	0.5	0.50
Pore size (average) (μm)	0.1	0.5	0.5	15	0.25
Acid displacement ($cm^3\ m^{-2}$)	280	200	220	350	n. a.
Electrical resistance ($m\Omega\ cm^2$)	240	110	150	300	150
Initial capacity +	0	++	++	0	++
Handling properties +	++	++	+	0	+
Black Deposits +	+	++	++	++	++

* Polyethylene industrial separators are also available from ENTEK International [62].
+ Ranking ++ very good, + good, 0 acceptable, – poor.

CosMX Exhibit 1008, Page 299 of 633

98] should be consulted.

What requirements are placed by this construction on the separator? First, the free mobility of the electrolyte has to be hampered in order to maintain tiny open channels for oxygen transfer from the positive to the negative electrode. One solution to this problem is the use of highly porous microfiber glass mats as separators. This glass mat has to fill the space between the electrodes completely and to absorb a maximum amount of electrolyte. These requirements imply extremely high porosity (>90 percent), large internal surface area, and good wettability, to assure a high absorption for the electrolyte. Starting from a fibrous structure, a large internal surface means a fiber diameter as small as possible: glass fibers of 0.5 μm reach around 3 $m^2 g^{-1}$, whereas 10 μm fibers have only some 0.15 $m^2 g^{-1}$ of surface. The good wettability of glass fibers suffers if binder is used. Of course, the separator has to have long-term resistance against various chemical and electrochemical attack inside a lead–acid battery and its susceptibility increases with the internal surface! It must not generate substances that increase the gassing rate, corrosion, or self-discharge. Finally it has to be mechanically robust enough to be handled during the battery production process. Sharp corners or edges should not be able to penetrate it. This last demand competes, of course, with the desire for the least possible binder content.

These generally defined requirements are met quite comprehensively by microfiber glass fleeces. These are blends of C-glass fibers of various diameter, which are processed in the usual way on a Foudrinier paper machine into a voluminous glass mat. The blending ratio gains special importance since cost aspects have to be balanced against technical properties. The expensive microfibers below 1 μm in diameter (~20–30 percent share) give a large internal surface and the desired pore size distribution, but do not contribute substantially to the mechanical properties. Fibers of significantly larger diameter increase the tensile strength and thus the processability, but tend to break more easily when the glass mat is under compression, which is required to maintain at all times sufficient contact with the electrodes as they respectively contract and expand during charging and discharging.

The conventional requirements of a separator are met fully by microfiber glass mats: the extreme porosity guarantees — in spite of the free volume for oxygen transfer of about 10 vol.% — that acid displacement and also electrical resistance remain very low, even though they are significantly higher (about double [23]) than is indicated by values measured on fully soaked samples. The chemical and oxidative stability is very good. The dimensional stability of absorptive microfiber glass fleeces is a critical parameter. On one hand, during the production of these fleeces the thickness (i.e., weight per unit area and fiber distribution/cloudiness) has to be maintained within narrow limits in order to assure a uniform distribution of electrolyte and subsequently of the depth of discharge at the assembly pressure. On the other hand, the resilience arising from the assembly pressure must not be noticeably reduced by fiber fracture or drying-out.

The small pore size and the uniform distribution result in capillary forces which should allow wicking heights and thus battery heights of up to 30 cm. Due to the cavities required for gas transfer and under the effect of gravity, the electrolyte forms a filling profile, i.e., fewer cavities remain at the bottom than at the top. Therefore with absorptive glass mats a rather flat battery

CosMX Exhibit 1008, Page 300 of 633

construction is preferred. Another reason for this is acid stratification: since the electrolyte is still liquid, and acid of higher density formed for example during charging will diffuse downwards — even at a delayed pace — this may detrimentally affect especially any deep-cycling service. Furthermore, due to the severe acid limitation of such cells during deep discharge, lead sulfate will dissolve increasingly and during recharge — and thus at higher acid density — it is again precipitated and can lead after reduction to microshorts. This effect is partially counteracted by the addition of sodium sulfate to the electrolyte. Nevertheless, sealed batteries with microfiber glass fleece separation are therefore predominantly used in service rarely incurring deep-discharge cycles. A special development, the addition of a low percentage of organic fibers to microfiber glass fleeces [99], allegedly simplifies the acid filling; excess acid is removed simply by dumping. Due to their hydrophobicity the organic fiber facilitate the oxygen transfer and they should suffice to weld such fleeces into pockets. Reports of practical experience have not yet been published.

Developments to produce such absorptive mats totally from organic fibers even go one step further. Only recently success came in achieving a suitable fiber diameter and permanent hydrophilization [100]. Such materials are not yet commercially available, however, and field experience has not been reported as yet.

Table 13 compares the specification data of microfiber glass fleeces from various manufacturers.

Batteries with Gelled Electrolyte

An advanced solution to the problem of decreasing the free mobility of the electrolyte in sealed batteries is its gel formation. By adding some 5–8 wt.% of pyrogenic silica to the electrolyte, a gel structure is formed due to the immense surface area (~200–300 $m^2 g^{-1}$) of such silicas, which fixes the sulfuric acid solution molecules by van der Waals bonds within a lattice. These gels have thixotropic properties; i.e., by mechanical stirring they can be liquefied and used to filled into the

Table 13. Separators for valve-regulated lead–acid batteries (liquid electrolyte)

	Absorptive microfiber glassmat separators * (100 % glass fibers +)					
Supplier	B. Dumas S.A. [101]	Hollingsworth & Vose Co. [102]	Lydall Axohm [73]	Nippon Glass Fiber Co., Ltd. [103]	Technical Fibre Prod. Ltd. [104]	Whatman Int. Ltd. [105]
Brand name	2133 XP	05 series	AXΩMAT	MS type	40101 series	SLA 1250
Thickness at 10 kPa (mm)	1.33	1.35	1.30	1.25	n. a.	1.35
Grammage ($g m^{-2}$)	210	200	200	200	n. a.	200
Tensile strength (N/15 mm)	n. a.	n. a.	7.65	7.5	9.0	11.2
Porosity (%)	94.5	n. a.	> 93	n. a.	> 94	n. a.
Pore size (average) (μm)	5.5	n. a.	7.5	10	n. a.	n. a.

* AMER-SIL s. a. [86] has recently introduced a microfiber glass fleece separator ("AMER-GLASS").
+ Dumas ("Series 6000"), H & V ("Hovosorb II"), Technical Fiber Products ("Polymer Reinforced Sealable Separator "). Nippon Glass Fiber ("MFC") and Whatman also offer products with organic fibers and/or binders.

CosMX Exhibit 1008, Page 301 of 633

battery cells, where they gel again within a few minutes. Initially such batteries suffer some water loss during overcharge. The gel dries to some extent and forms cracks, allowing the oxygen to transfer to the negative electrode where the internal oxygen consumption occurs, which avoids further water loss and gel drying [20,21, 106,107].

Batteries with gelled electrolyte have been shown to require a separator in the conventional sense, to secure spacing of the electrodes as well as to prevent any electronic shorts; the latter is achieved by microporous separators. An additional important criterion is minimal acid displacement, since these batteries — in comparison with batteries with liquid electrolyte — lack the electrolyte volume share taken up by gelling and by the cracks.

Among the separator varieties described, the phenol–formaldehyde–resorcinol separator (DARAK 2000) [60] as well as the microporous PVC separator [86] have proven effective for this construction. For applications without deep discharges, concessions may be made with the respect to porosity and pore sizes of the separator; therefore polyethylene separators or a special version of glass leaf separators with attached glass mat [73] are occasionally used in such cases.

Table 14 compares the most important physicochemical data of separators used in batteries with gelled electrolyte.

9.3 Separators for Alkaline Storage Batteries

9.3.1 General

In acidic electrolytes only lead, because it forms passive layers on the active surfaces, has proven sufficiently chemically stable to produce durable storage batteries. In contrast, in alkaline medium there are several substances basically suitable as electrode materials: nickel hydroxide, silver oxide, and manganese dioxide as positive active materials may be combined with zinc, cadmium, iron, or metal hydrides. In each case potassium hydroxide is the electrolyte, at a concentration — depending on battery systems and application — in the range of 1.15 – 1,45 $g\,cm^{-3}$. Several elec-

Table 14. Separators for valve-regulated lead–acid batteries (gelled electrolyte)

	Phenol–formaldehyde–resorcinol separators	Microporous PVC separators	Glass fiber/ polyester fiber separators	Rubber separators
Supplier	Daramic, Inc. [60, 61]	AMER-SIL s.a. [86]	Lydall Axohm [73]	AMERACE Microporous Products [87]
Brand name	Darak 2003 Ind. with glassmat	DGT 200 HP	Standard D. S. R.	Micropor-Sil
Backweb thickness (mm)	0.3	0.55	0.7	0.4
Porosity [%]	70	71	85	70
Pore size (average) (μm)	0.5	0.2	27.5	0.1
Acid displacement ($cm^3\,m^{-2}$)	145	260	n. a.	n. a.
Electrical resistance ($m\Omega\,cm^2$)	120	160	170	140

CosMX Exhibit 1008, Page 302 of 633

trochemical couples consequently result, which are available in a variety of constructions and sizes, with an even larger variety of separators of course.

For alkaline storage batteries requirements are often demanded exceeding by far those for lead storage batteries. The reason is that the suitable materials for the positive electrode are very expensive (silver oxide, nickel hydroxide) and thus the use of these storage batteries is only justified where requirements as to weight, number of cycles, or temperature range prohibit other solutions. Besides a few standardized versions — mainly for nickel–cadmium batteries — this has led to the existence of a large diversity of constructions for special applications [4–6, 108, 109].

In order to classify this diversity from the viewpoint of the separator, the basic requirements for separators in alkaline cells are discussed below and an attempt at structuring them accordingly is made.

The prime requirements for the separators in alkaline storage batteries are on the one hand to maintain durably the distance between the electrodes, and on the other to permit the ionic current flow in as unhindered a manner as possible. Since the electrolyte participates only indirectly in the electrochemical reactions, and serves mainly as ion-transport medium, no excess of electrolyte is required, i.e., the electrodes can be spaced closely together in order not to suffer unnecessary power loss through additional electrolyte resistance. The separator is generally flat, without ribs. It has to be sufficiently absorbent and it also has to retain the electrolyte by capillary forces. The porosity should be at a maximum to keep the electrical resistance low (see Sec. 9.1.2.3); the pore size is governed by the risk of electronic shorts. For systems where the electrode substance does not dissolve or is only slightly soluble (e.g., nickel hydroxide, cadmium) separators are sufficient, which prevent a deposit of particles of the active materials and subsequent shorting, whereas for electrodes that dissolve (e.g., zinc) effective ion-selective barriers are desirable, delaying the forming of penetration from the solution phase. Positive electrodes (e.g., silver oxide) whose ions are dissolved — even sparingly — and deposited on the negative electrode, form local elements there, and thus increase self-discharge, also require separators with ion-segregating properties. Ion separation means however, pore sizes on an atomic scale; this leads empirically to higher electrical resistance and especially to chemical susceptibility. The optimizations achieved to date towards increasing the service life of alkaline storage batteries are still unsatisfactory; this presents a particular challenge to the further development of separators.

9.3.2 Primary Cells

Primary cells generally do not place high demands on the separator, so these are not covered exhaustively here; the lack of a charging process avoids undesirable electrochemical deposits (e.g., dendrites) as well as generation of oxidizing substances. Thus low-priced, alkali-resistant sheets are used as separators; generally cellulosic papers, fleeces or woven fabrics of polyamide, poly(vinyl alcohol) or polypropylene fibers meet this requirement satisfactorily [4]. It is generally sufficient for them to absorb and retain as much as possible of the electrolyte without decomposition and to be resistant against the substance of the positive electrode under the conditions of use to be expected. The fleeces of organic fibers are also used in alkaline secondary

CosMX Exhibit 1008, Page 303 of 633

cells and will be explained in more detail in that context (cf. Sec. 9.3.5).

9.3.3 Nickel Systems

9.3.3.1 Nickel–Cadmium Batteries

Vented Construction

The first practical alkaline storage batteries were developed in the 1890 – 1910 period by Waldemar Jungner in Sweden and almost simultaneously by Thomas Alva Edison in the USA [10]. These nickel–iron batteries, because of their high self-discharge rates due to iron poisoning of the nickel electrodes, have been replaced almost completely by the nickel–cadmium batteries also developed by W. Jungner. The original construction with so-called pocket plates is still available today, with only little change. The active material powders are held in pockets of perforated (nickel-coated) steel sheets. In the simplest case the pocket electrodes are kept at a spacing of about 1 – 3 mm by PVC rod plates ("ladders"), and occasionally also by extruded PVC ribs or perforated, corrugated PVC spacers, according to the designed electrical power performance. Since, as mentioned, no soluble ions cause any interferences in a nickel–cadmium pocket plate battery, a separator in the narrow sense is not required.

For increased power requirements, electrode constructions have been developed which bring the electronic conductors in closer contact with the active material particles: first, around 1930, the sinter electrode [110], recently in sealed cells largely replaced by the nichel–foam electrode, and then, around 1980, the fiber structure electrode [111]. In order to take full advantage of their increased performance, the electrodes have to be as close together as possible, i.e., a uniformly thin, highly porous separator is required with sufficiently small pores to prevent any penetration even at narrow spacing. For medium electrical performance — i.e., electrode spacings of about 1 mm — ribbed or corrugated sintered PVC separators are used. They largely correspond to the product used in lead–acid batteries and have been described in that context in detail (cf. Sec. 9.2.2.2). This separator is good value, but it is rather brittle and thus difficult to handle, and it has relatively large pores (~ 15 μm).

For higher current loads, especially for sinter electrodes, smaller separator pores are desired; such materials are mostly sensitive, frequently requiring multiple layers performing different duties. Both electrodes are wrapped in a relatively open fleece or woven fabric of polyamide ("nylon") or, if higher temperatures apply, of polypropylene fibers, which provide sufficient electrolyte at the electrode surface to keep the electrical resistance low. Between these an ion-semipermeable membrane, typically regenerated cellulose ("cellophane") [112], serves as a gas barrier to prevent the generated oxygen from reaching the negative electrode. In wet condition, where it swells achieves the desired pore sizes and properties, cellophane is mechanically very sensitive; the aforementioned nylon fleeces offer the required support from both sides.

Better mechanical stability can be expected from irradiated polyethylene or microporous polypropylene ("Celgard") membranes, but these account for increased electrical resistance values.

One version of the microporous, filled polyethylene separator ("PowerSep") [113], which is so successful in the lead–acid battery, is also being tested in nickel–cadmium batteries. This separator is manu-

CosMX Exhibit 1008, Page 304 of 633

dmium batteries. This separator is manufactured largely in the same way and also has similar properties as described in Sec. 9.2.2.1. Of course, silica cannot be used as a filler, but has to be replaced by an alkali-resistant substance, e.g., titanium dioxide. The resulting separator membrane excels, with very small pore sizes and low electrical resistance as well as outstanding mechanical properties. A comprehensive presentation of the different separation materials follows in Sec. 9.3.5.

The microporous or semipermeable separators serve, as explained, to avoid oxygen transfer and thus increased self-discharge. In special cases of severe cycling service without extended stand periods, this oxygen transfer is actually desired, in order to suppress — in addition to constructional means — hydrogen generation and consequently water consumption. Batteries for electric vehicles are such a case, in which freedom from maintenance is the primary goal. As separators, several layers of macroporous fleeces of either polyamide, polyethylene, or polypropylene fibers and blends thereof, as well as spun fleece (melt-blown) of polypropylene, are used. This construction ("partial recombination") is already a transition stage to sealed batteries.

Sealed Construction

The working principle of sealed nickel-cadmium batteries is based on internal oxygen consumption. The negative electrodes have a larger capacity than the positive ones; therefore, during the charging step the latter reach their fully charged status earlier and start to evolve oxygen, which migrates through voids in the electrolyte to the negative electrode to discharge cadmium, which was already charged. As a prerequisite the separator has to be permeable to gaseous oxygen; this is achieved by separator pores being of a specific minimum size and not all of them being filled with electrolyte at the same time, so as to leave some gas channels. For this application the fleeces of polyamide, polyethylene, or polypropylene fibers mentioned above have proven themselves. With their porosity they can absorb sufficient electrolyte, and due to their pore size distribution they can simultaneously bind electrolyte and allow oxygen transfer.

Mechanical strength becomes an important criterion, because wound cells (spiral-type construction), in which a layer of separator material is spirally wound between each two electrodes, are manufactured automatically at very high speed. Melt-blown polypropylene fleeces, with their excellent tensile properties, offer an interesting option. Frequently two layers of the same or different materials are used, to gain increased protection against shorts; for button cells the use of three layers, even, is not unusual. Nevertheless the total thickness of the separation does not exceed 0.2 – 0.3 mm. For higher-temperature applications (up to about 60 °C) polypropylene fleeces are preferred since they offer a better chemical stability, though at lower electrolyte absorption [114].

9.3.3.2 Nickel–Metal Hydride Batteries

Cadmium presents an environmental risk. Since small nickel–cadmium cells are often not separately disposed of, they may enter municipal garbage incinerators. The search for alternative materials for the negative electrode led to metal hydrides, which not only are regarded as environmentally less critical, but also allow higher energy density than cadmium. This is especially important for use in portable equipment, such as cellular phones or lap-

CosMX Exhibit 1008, Page 305 of 633

top computers, where the nickel–metal hydride system is especially successful. Only in applications requiring high current densities are they second to nickel–cadmium. The requirements for the separators are largely identical with those for the sealed nickel–cadmium cells; therefore mostly the same separator materials are used. They are described in Sec. 9.3.5.

9.3.4 Zinc Systems

9.3.4.1 Nickel–Zinc Storage Batteries

Electrochemical systems with zinc as the negative electrode material in alkaline electrolyte promise high energy and power densities. The nickel–zinc storage battery especially is being discussed as a candidate for the power source of electric vehicles, last but not least because zinc — compared with the above-mentioned metal hydrides — is of low cost and available in sufficient quantity. Even though this system has been studied and developed since 1930 [115], no success has yet been achieved in reaching a sufficient number of cycles, so no commercial utilization has resulted; 200 – 300 cycles are still considered to be the limit today; although recently laboratory cells are reported to have reached 600 cycles [116].

The reason for this limited cycle life is the high solubility of the zinc electrode in alkaline electrolyte; the zincate ions formed are deposited again during the subsequent charging in the form of dendrites, i.e., of fernlike crystals. They grow in the direction of the counterelectrode and finally cause shorts.

A remedy could be achieved by a decrease in the zinc solubility in the electrolyte or by suppression of dendrite formation; cadmium–, lead–, or bismuth oxide, as well as calcium hydroxide or aluminum hydroxide have been added to the zinc electrode or the electrolyte for this purpose, but not with longlasting effectiveness.

Thus in this system, in addition to the usual requirements, the separator has the task of delaying penetration for as long as possible. A membrane would be regarded as perfect which lets hydroxyl ions pass, but not the larger zincate ions. This requirements is best met by regenerated cellulose ("cellophane") [10,11], which in swollen condition shows such ion-selective properties but at the same time is also chemically very sensitive and allows only a limited number of cycles; the protective effects of additional fleeces of polyamide or polypropylene have already been taken into account.

Chemically more stable systems with microporous properties, such as streched polypropylene films ("Celgard"), irradiated, coated polyethylene, or filled polyethylene separators ("PowerSep") offer a compromise: smaller pore diameters have been shown to increase the number of cycles to penetration. However, a different failure mode occurs at an earlier stage, namely "shape change" of the negative electrode [117]. If the off-diffusion of zincate ions into the bulk electrolyte is obstructed, e.g., by small separator pores, concentration gradients on the electrode surface cause a shifting of the zinc deposit from the edges towards the center of the electrode [118]. In summary it may be noted that these opposing effects have prevented a breakthrough of the nickel–zinc system, as yet.

9.3.4.2 Zinc–Manganese Dioxide Secondary Cells

This system, known as primary alkaline manganese cells, has been further devel-

CosMX Exhibit 1008, Page 306 of 633

oped since 1975 into secondary cells [119, 120]. The above-mentioned problems of the zinc electrode apply here as well, although safety is assured for these sealed cells by constructional measures. Depending on the depth of discharge, between 20 and 200 cycles can be attained, which may be sufficient for many applications, e.g., as low-cost rechargeable power source for children's toys. The described combination of a few layers of fleece of polyamide or polypropylene fibers with an ion-selective film of regenerated cellulose ("cellophane") is being used as separation to prevent shorting by dendrites. A further development of the separator has been achieved by impregnation of a polyamide fleece with regenerated cellulose in order to obtain a single, stable, ion-semipermeable separator layer.

9.3.4.3 Zinc–Air Batteries

A completely different way has been taken to render zinc–air elements of very high energy density rechargeable for the use in electric vehicles [121]. In the vehicle they are used exclusively as primary cells to be "mechanically" recharged at a central depot. The zinc electrodes are removed from the discharged battery, then they are mechanically crushed, chemically dissolved, and electrolytically deposited again zinc, compacted, and supplied with a separator pocket before being reinstalled in the battery. A woven fabric of polyamide ("nylon") fibers serves a separator, which is sufficient to prevent shorts during discharge.

9.3.4.4 Zinc–Bromine Batteries

Even though zinc–bromine batteries operate with a slightly acidic electrolyte (pH 3), they are discussed here briefly, because they offer another way of escaping the problems of zinc deposition. At this pH value both zinc corrosion as well as the tendency towards dendrite formation are low; the latter, furthermore, is prevented by electrolyte circulation [122]. The separator, besides meeting the usual requirements, has to perform an additional duty: although it must permit the charge transfer of zinc and bromide ions, it should suppress the transfer of dissolved bromine, of polybromide ions, or of the complex phase. Due to mechanical and chemical susceptibility, ion-selective membranes did not prove effective. Microporous polyethylene separators are usually used; in their manufacture and properties they are quite similar to those described in Sec. 9.2.3.1.

9.3.4.5 Zinc–Silver Oxide Storage Batteries

Zinc–silver oxide batteries as primary cells are known both as button cells, e.g., for hearing aids, watches, or cameras, and for military applications, usually as reserve batteries. Since the latter after activation have only a very short life (a few seconds to some minutes), a separation by cellulosic paper is generally sufficient.

Rechargeable zinc–silver oxide batteries have to struggle against the same problems of the zinc electrode which have been described in detail for the nickel–zinc systems. To make matters even worse the silver oxide electrode contributes an additional problem: silver ions — even to a small extent — dissolve, deposit on the negative electrodes, and poison them by forming local corrosion elements and causing self-discharge under hydrogen evolution. In order to prevent this, several layers of semipermeable cellophane membranes are used [123], amongst others. The beneficial effect is caused by a sacrificial

CosMX Exhibit 1008, Page 307 of 633

action: the silver ions migrate through the electrolyte and oxidize (i.e., they thus destroy) cellophane film sites, simultaneously being reduced to metallic silver and thereby becoming less harmful. The life of the cellophane is therefore limited; together with wetting fleeces to prevent also direct contact with the silver oxide electrode, this is fully sufficient for primary cells. For rechargeable batteries, cycle lives of 10–100 cycles are quoted [124,125], depending on type of separation and depth of discharge; in special cases of very shallow discharges of only a few percent, however, 3000 cycles and three years of life have been reported.

Advanced development of ion-selective films has been attempted by radiation grafting of methacrylic acid on polyethylene films, and combination of this with cellophane are also being tested. Polyamide fleece impregnated with regenerated cellulose, is another option for zinc–silver oxide batteries.

Occasionally the zinc electrode is wrapped in a polypropylene fleece filled with inorganic substances, such as potassium titanate, in order to reduce the solubility of zinc since the problem of dendrite growth is aggravated even by the metallization of the cellophane separator due to the aforesaid silver reduction and its promoting the generation of shorts.

After these comments it is understandable that this expensive and life-limited system could succeed only in a few special applications, where the high energy and power density could not be achieved by other systems.

9.3.5 Separators Materials for Alkaline Batteries

In the product range of alkaline power sources each manufacturer has developed for each special application on optimum separation. Generally, however, these consist of the combination of a relatively small variety of proven materials. These are presented here jointly, even if they can hardly be compared with each other. They may be divided into three groups, depending on their application: macroporous wetting fleeces (Table 15), microporous separators (Table 16), and ion-semipermeable membranes (Table 17).

Of all possible manufacturing proceses for macroporous separators to be employed in alkaline batteries, the wet-fleece process using paper machines is the predominant one [130]; it permits a very uniform ("cloud-free") production of such material and the use of different types of fibers as well as of short and very thin fibers, thus achieving a uniform structure of small pores (Table 15).

Whereas PVA fleeces are used only in primary cells polyamide fleeces compete with polyolefin, preferably polypropylene fleeces. The latter are more stable at higher temperatures and do not contribute to electrolyte carbonation, but they wet only after a pretreatment either by fluorination [131] or by coating and crosslinking with hydrophilic substances (e.g., polyacrylic acid [132]) on the surface of the fiber.

Only very recently the production of melt-blown polypropylene fleeces with considerably thinner fiber diameter became possible [100], thus making it possible — a low-cost hydrophilization provided — to achieve attractive properties with regard to small pore size and excellent tensile performance for use in highly automated assembly processes.

Very different microporous separators for alkaline batteries are included in Table 16. The very thin (~25 μm) films of stretched polypropylene ("Celgard") are generally employed in combination with

CosMX Exhibit 1008, Page 308 of 633

Table 15. Nonwoven materials for alkaline batteries

	Wet-laid poly(vinyl alcohol) (PVA) fiber fleece	Wet-laid polyamide (PA) fiber fleece	Wet-laid polyolefin (PP/PE) fiber fleece	Wet-laid grafted polypropylene fiber fleece	Melt-blown grafted polypropylene fiber fleece
Supplier *	C. Freudenberg [126]	C. Freudenberg [126]	C. Freudenberg [126]	Sci MAT Ltd. [127]	Sci MAT Ltd. [127]
Brand name	Viledon FS 2183	Viledon FS 2117	Viledon FS 2123 WI	Sci MAT 700/25	Sci MAT 700/35
Weight + $g\,m^{-2}$	70	70	72	70	60
Thickness(mm)	0.35	0.33	0.26	0.23	0.18
Tensile strength (N/15 mm)	≥ 60	≥ 21	≥ 45	45	45
Air pemeability ($L\,s^{-1}\,m^{-2}$)	450	700	400	n. a.	n. a.
KOH absorption ($g\,m^{-2}$)	≥ 350	≥ 300	150	200	120
Porosity (%)	84	81	71	n. a.	n. a.
Pore size (average) (μm)	36	40	40	20	20
Electrical resistance (KOH) ($m\Omega\,cm^2$)	40	40	70	n. a.	n. a.

* Other suppliers include PGI Nonwovens Chicopee, Inc. [128], Kuraray Co., Ltd. [129] and Hollingsworth and Vose Comp. [102].

+ Representative examples of a variety of weights/thickneses.

Table 16 . Microporous separators for alkaline batteries

	Microporous polypropylene film	Microporous polypropylene film	Microporous filled UHMW polyethylene separator	Sintered PVC separator
Supplier	Hoechst Celanese Corp. [133]	Hoechst Celanese Corp. [133]	Daramic, Inc. [60, 61]	Jungfer gesmbH [64]
Brand name	Celgard 3401	Celgard 3501	PowerSep	Sintered PVC
Thickness (mm)	0.025	0.025	1.3	1.3
Backweb thickness (mm)	0.025	0.025	0.2	0.3
Porosity (%)	38	45	40	33
Pore size (average) (μm)	< 1	< 1	0.2	15
Electrical resistance (KOH) ($m\Omega\,cm^2$)	80	40	200	300

fleeces, while separators of sintered PVC or filled ultrahigh-molecular-weight polyethylene find use also in single separation of alkaline industrial batteries.Their production process corresponds to the analogous version for lead–acid batteries and is described in detail in Sec. 9.2.2.1 and 9.2.2.2 respectively.

As ion – semipermeable membranes, which — despite good permeability to hydroxyl ions — hinder the transfer of zincate and silver ions, essentially only regenerated cellulose is being used in alkaline batteries. In a complex conversion process a pulp of wood cellulose, primarily from eucalyptus trees, is dissolved in caustic solution under reaction with carbon disulfide, to be precipitated as cellulose xan-

CosMX Exhibit 1008, Page 309 of 633

Table 17 . Semipermeable membranes for alkaline batteries

	Regenerated cellulose membrane	Regenerated cellulose membrane	Regenerated cellulose membrane (silver-treated)	Polyamide non-woven impregnated with regenerated cellulose
Supplier	UCB Cellophane Ltd. [134]	Viskase Corp. [135]	Yardney Techn. Prod., Inc. [136]	Viskase Corp. [135]
Brand name	350 POO	SEPRA-CEL	C 19	SEPRA-CEL
Thickness (mm)	0.025	0.025	0.025	0.175
Pore size (nm)	2.5	2.5-5	2.5	n. a.
KOH absorption ($g\,m^{-2}$)	n. a.	60	55	275
Electrical resistance (KOH) ($m\Omega\,cm^2$)	40	n. a.	< 120	90

thate. The xanthate is then dissolved in a sodium hydroxide solution, thickened ("viscose"), then extruded and regenerated with sulfuric acid to cellophane. "Cellophane" was originally a registered trade name and in some countries still is to this day. This material is macromolecular and swells in potassium hydroxide solution forming pores in the order of magnitude of 25 – 50 Å. The molecules are attacked and oxidized by potassium hydroxide, by oxygen, but particularly by silver ions. This process can be slowed down by a pretreatment with silver salt solution [137]: the precipitated silver atoms, by comproportionation with the "dangerous" silver(II)ions, form silver(I)ions, which are less soluble and precipitate on the semipermeable membrane without being able to reach the negative electrode. This prepoisoning contributes additionally, however, to the metal content of the separator.

The development of stable, effectively ion-separating membranes for rechargeable alkaline batteries remains a persistent challenge, in which the separator can provide decisive contributions to the advancement of storage batteries of high power and energy density.

Acknowledgement. I thank many colleagues in the battery industry for critical discussions, for suggestions, and for supplying me with references, as well as Daramic, Inc., Burlington, MA (USA) for the publication permission. My special appreciation goes to Dr. F. Theubert and Mrs. A. Hayen for their untiring assistance in the preparation of the manuscript.

9.4 References

[1] J. J. Lander, *Proc. Symp. on Battery Separators,* The Electrochemical Society, Columbus, OH, **1970**, p. 4.
[2] J.Q. Selsor, *The Battery Man* **1985**, 9.
[3] W. Böhnstedt, *J. Power Sources* **1996**, *59*, 45.
[4] D. Linden (Ed.), *Handbook of Batteries,* 2nd ed., McGraw-Hill, New York, **1995**.
[5] M. Barak, *Electrochemical Power Sources,* The Institution of Electrical Engineers, London/ P. Peregrinus, Stevenage, UK, **1980**.
[6] K. Wiesener, J. Garche, W. Schneider, *Elektrochemische Stromquellen,* Akademie-Verlag, Berlin, **1980**.
[7] D. Berndt, *Maintenance–Free Batteries,* 2nd ed., Research Studies Press Ltd., Taunton, Somerset, England, **1997**.
[8] H. Bode, *Lead–Acid Batteries,* John Wiley, New York, **1977**.
[9] G. W. Vinal, *Storage Batteries,* John Wiley, New York, **1955**.
[10] S. U. Falk, A. J. Salkind, *Alkaline Storage Batteries,* John Wiley, New York, **1969**.
[11] A. Fleischer, J. J. Lander, *Zinc–Silver Oxide Batteries,* John Wiley, New York, **1971**.
[12] R. H. Schallemberg, *Bottled Energy,* American

CosMX Exhibit 1008, Page 310 of 633

Philosophical Society, Memoirs Series, Vol. 148, G. H. Buchanan, Philadelphia, PA, **1982**, p. 27.
[13] R. H. Schallemberg, *Bottled Energy,* American Philosophical Society, Memoirs Series, Vol. 148, G. H. Buchanan, Philadelphia, PA, **1982**, p. 58.
[14] R. H. Schallemberg, *Bottled Energy,* American Philosophical Society, Memoirs Series, Vol. 148, G. H. Buchanan, Philadelphia, PA, **1982**, p. 269.
[15] P. J. Moll, *Die Fabrikation von Bleiakkumulatoren,* 2nd ed., Akademischer Verlag Geest/ Portig K.-G., Leipzig, **1952**, p. 131.
[16] D. W. Larsen, C. L. Kehr, US Patent 3 351 495, **1966**.
[17] D. H. McClelland, J. L. Devitt, US Patent 3 862 861, **1972**.
[18] E. Decker, German Patent 1 279 795, **1965**; US Patent 3 475 355, **1969**.
[19] A. B. Tudor, British Patent 1 183 470, **1966**.
[20] O. Jache, German Patent 1 194 015, **1958**.
[21] O. Jache, German Patent 1 671 693, **1967**.
[22] A. E. Lange, E. Langguth, E. Breuning, A. Dassler, German Patent 674 829, **1933**.
[23] B. Culpin, J. A. Hayman, *Power Sources 11* (Ed.: L. J. Pearce), International Power Sources Symposium Committee, Leatherhead, UK, **1986**, p.45.
[24] K. Peters, *J. Power Sources* **1993**, *42*, 155.
[25] G. C. Zguris, D. W. Klauber, N. L. Lifshutz, *Power Sources 13* (Eds. T. Keily, B. W. Baxter), International Power Sources Symposium Committee, Leatherhead, UK, **1991**, p. 45.
[26] F. J. T. Harris, US Patent 4 465 748, **1982**.
[27] D. Feder, Performance Measurement and Reliability of VRLA Batteries, Paper presented at Battery Council International, 106th Convention (Technical Committee Workshop), San Diego, CA, **1994**.
[28] Pritchett & Gold and E.P.S. Co. Ltd., British Patent 565 022, **1942**.
[29] F. R. Kalhammer, A. Kozawa, C. B. Moyer, B. B. Owens, *Performance and Availability of Batteries for Electric Vehicles*, Report of the Battery Technical Advisory Panel, California Air Resource Board, El Monte, CA, **1995**.
[30] P. T. Moseley, *J. Power Sources* **1997**, *67*, 115.
[31] J. Alzieu, J. Robert, *J. Power Sources* **1984**, *13*, 93.
[32] J. Alzieu, N. Koechlin, J. Robert, *J. Electrochem. Soc.* **1987**, *134*, 1881.
[33] K. Takahashi, M. Tsubota, K. Yonezu, K. Ando, *J. Electrochem. Soc.* **1983**, *130*, 2144.
[34] A. F. Hollenkamp, K. K. Constanti, M. J. Koop, K. McGregor, *J. Power Sources* **1995**, *55*, 269.
[35] A. F. Hollenkamp, *J. Power Sources* **1996**, *59*, 87.
[36] A. F. Hollenkamp, R. H. Newham, *J. Power Sources* **1997**, *67*, 27.
[37] J. L. Stempin, R. L. Steward, D. R. Wexell, European Patent EPO 750 357 A2, **1995**.
[38] W. Böhnstedt, J. Deites, K.Ihmels, J. Ruhoff, German Patent Application DE 197 02 757, **1997**.
[39] W. Böhnstedt, A. Weiß, *J. Power Sources* **1992**, *38*, 103.
[40] W. Böhnstedt, *J. Power Sources* **1993**, *42*, 211.
[41] W. Böhnstedt, *J. Power Sources* **1997**, *67*, 299.
[42] J. W. Reitz, *J. Power Sources* **1987**, *19*, 181.
[43] J. W. Reitz, *J. Power Sources* **1988**, *23*, 109.
[44] M. J. Weighall, *J. Power Sources* **1991**, *34*, 257.
[45] M. J. Weighall, *J. Power Sources* **1992**, *40*, 195.
[46] M. J. Weighall, *J. Power Sources* **1995**, *53*, 273.
[47] M. J. Weighall, 5th European Lead Battery Conference, Barcelona, **1996**.
[48] J. Schneider, *J. Power Sources* **1988**, *23*, 113.
[49] J. Hoover, Failure Modes of Batteries Removed from Service, Paper presented at Batteries Council International, 107th Convention, Orlando, FL, **1995**.
[50] K. Fischer, *LABAT/96 Conference,* Varna, **1996**, p. 171.
[51] J. Kung, *Batteries Int.* **1994**, *1*, 46.
[52] N. Sugarman, German Patent DE 30 04 659, **1979,** British Patent 2 044 516.
[53] H. Bünsch, K. H. Ihmels, F. O. Teubert, German Patent DE 39 28 468, **1989**; European Patent EP 0 425 784.
[54] W. M. Choi, W. Böhnstedt, US Patent 5 384 211, **1983**.
[55] K. Nakano, European Patent EP 0 541 124, **1991**.
[56] D. J. Knauer, US Patent 5 558 952, **1995**.
[57] D. D. O'Rell, N.-J. Lin, G. Gordon, J. H. Gillespie, British Patent GB 2 097 174, **1981**.
[58] W. Böhnstedt, W. Lindenstruth, German Patent DE 38 30 728, **1988**; US Patent 4 927 722.
[59] W. Böhnstedt,, German Patent DE 44 14 723,

CosMX Exhibit 1008, Page 311 of 633

1994; World Patent WO 95/29 508.
[60] Daramic, Inc., Postfach 1509, D-22805 Norderstedt, Germany.
[61] Daramic, Inc., 20 Burlington Mall Road, Burlington, MA 01803, USA.
[62] ENTEK International LLC, P.O. Box 127, 250 North Hansard Avenue, Lebanon, OR, 97355, USA.
[63] ENTEK International Ltd., Mylord Crescent, Camperdown Industrial Estate, Killingworth, Newcastle upon Tyne NE 12 0XG, UK.
[64] Jungfer ges.m.b.h. & Co. KG, A-9181 Feistritz, Austria.
[65] Grace gmbH (unpublished results)
[66] M. Engelmann, H. Kraus, O. Plewan, German Patent DE 43 37 429, **1992**.
[67] R. Müller, The lead market towards the 21st century, Paper presented at EUROBAT Convention, Prague, **1993**.
[68] Accuma S.p.A., Via Medici, 14, I 20052 Monza, Italy.
[69] I.C.S. Industria Composizioni Stampate S.p.A., I – 24040 Canonica d'Adda, Bergamo, Italy.
[70] W. Böhnstedt, C. Radel, F. Scholten, *J. Power Sources* **1987**, *19*, 301.
[71] H. Döring, M. Radwan, H. Dietz, J. Garche, K. Wiesener, *J. Power Sources* **1989**, *28*, 381.
[72] J. Cerný, V. Koudelka, *J. Power Sources* **1990**, *31*, 183.
[73] Axohm Industries S.A., Lydall, Inc., Saint Rivalain, F – 56310 Melrand, France.
[74] GS Kasei Kogyo K.K., Inoguchi Takatsuki-Cho Ikagun, Siga Prefecture, Japan • 529–02.
[75] E. Nann, *J. Power Sources* **1991**, *33*, 93.
[76] C. M. Yaacoub, German Patent DE 39 22 160, **1989**; European Patent EP 0 409 363.
[77] J. L. Dawson, M. I. Gillibrand, J. Wilkinson, *Power Sources 3* (Ed.: D. H. Collins), Oriel Press, Newcastle upon Tyne, UK, **1971**, p. 1.
[78] W. Herrmann, G. Pröbstl, *Z. Elektrochem*, **1957**, *61*, 1154.
[79] E. Zehender, W. Herrmann, H. Leibssle, *Electochim. Acta* **1964**, *9*, 55.
[80] B. S. Goldberg, A. G. Hausser, B. T. Le, *J. Power Sources* **1983**, *10*, 137.
[81] S. L. Paik, G. Terzaghi, *J. Power Sources* **1995**, *53*, 283.
[82] W. Böhnstedt, C. Radel, German Patent DE 41 08 176, **1991**; European Patent EP 0 507 090.
[83] N. I. Palmer, J. L. Rooney, N. Sugarman, German Patent DE 25 20 961, **1974**; British Patent 1 512 997.
[84] W. M. Choi, I. W. Schmidt, US Patent 5 478 677, **1995**.
[85] A. L. Ferreira, H. A. Lingscheidt, *J. Power Sources* **1997**, *67*, 291.
[86] AMER-SIL s.a., Zone Industrielle, L-8287 Kehlen, Luxembourg.
[87] AMERACE Microporous Products, L. P., 596 Industrial Park Road, Piney Flats, TN 37686, USA.
[88] R. F. Nelson, *Power Sources 13* (Eds: T. Keily, B. W. Baxter), International Power Sources Symposium Committee, Leatherhead, UK, **1991**, p. 13.
[89] R. F. Nelson, *J. Power Sources* **1993**, *46*, 159.
[90] D. A. Crouch, Jr., J. W. Reitz, *J. Power Sources* **1990**, *31*, 125.
[91] B. Culpin, *J. Power Sources* **1995**, *53*, 127.
[92] H. Miura, H. Hosono, *J. Power Sources* **1994**, *48*, 233.
[93] G. C. Zguris, *J. Power Sources* **1996**, *59*, 131.
[94] T. V. Nguyen, R. E. White, H. Gu, *J. Electrochem. Soc* **1990**, *137*, 2998.
[95] T. V. Nguyen, R. E. White, *Electrochim. Acta* **1993**, *38*, 935.
[96] D. M. Bernardi, M. K. Carpenter, *J. Electrochem. Soc* **1995**, *142*, 2631.
[97] G. J. May, *J. Power Sources* **1995**, *53*, 111.
[98] G. C. Zguris, F. C. Harmon, Jr., US Patent 5 336 275, **1992**.
[99] J. P. Badger, US Patent 4 908 282, **1987**.
[100] J. Zucker, Application, Inc., US Patent, **1997**, (not yet published).
[101] B. Dumas S.A., P.O. Box 3, Creysse, F – 24100 Bergerac, France.
[102] Hollingsworth & Vose Co., 112 Washington Street, East Walpole, MA 02032, USA.
[103] Nippon Glass Fiber Co., Ltd., 2 Chitose-Cho, Yokkaichi, Mie Prefecture, Japan.
[104] Technical Fibre Products, Burneside Mills, Kendal, Cumbria LA9 6PZ, UK.
[105] Whatman International Ltd. Springfield Mill, James Whatman Way, Maidstone, Kent ME 14 2LE, UK.
[106] H. Tuphorn, *J. Power Sources* **1988**, *23*, 143.
[107] H. Tuphorn, *J. Power Sources* **1993**, *46*, 361.
[108] T. R. Crompton, *Battery Reference Book*, Butterworth, London, **1990**.
[109] H. D. Jaksch, *Batterie-Lexikon*, Pflaum Verlag, München, **1993**.
[110] G. Pfleiderer, F. Spoun, P. Gmelin. K. Ackermann, German Patent 491 498, **1928**.
[111] G. Benczúr-Ürmössy, G. Berger, F. Haschka,

CosMX Exhibit 1008, Page 312 of 633

etz **1983**, *104*, 1098.
[112] T. Danko, Proceedings of the 10th Annual Battery Conference on Applications and Advances, Long Beach, CA, Institute of Electrical and Electronic Engineers (IEEE), New York, **1995**, p. 261.
[113] J. T. Lundquist, Jr., C. B. Lundsager, US Patent 4 287 276, **1979**.
[114] J. Bennett, W. M. Choi, Proceedings of the 10th Annual Battery Conference on Applications and Advances, Long Beach, CA, Institute of Electrical and Electronic Engineers (IEEE), New York, **1995**, p. 265.
[115] J. J. Drumm , British Patent 365 125, **1930**.
[116] D. Coates, E. Ferreira, A. Charkey, Proceedings of the 12th Annual Battery Conference on Applications and Advances, Long Beach, CA, Institute of Electrical and Electronic Engineers (IEEE), New York, **1997**, p. 23.
[117] J. T. Lundquist, Jr., *J. Membr. Sci.* **1983**, *13*,337.
[118] M. Klein, F. McLarnon, Nickel zinc batteries in *Handbook of Batteries*, 2th ed. (Ed.: D. linden), McGraw-Hill, New York, **1995**,p. 29.4.
[119] K. Kordesch, J. Gsellmann, *Power Sources 7* (Ed.: J. Thompson), Academic Press, London, **1979**, p. 557.
[120] K. Kordesch, J. Gsellmann, US Patent 4 384 029, **1983**.
[121] R. Hamlen, Metal/air batteries in *Handbook of Batteries*, 2th ed. (Ed.: D. Linden), McGraw-Hill, New York, **1995**,p. 38.18.
[122] R. J. Bellows, D. J. Eustace, P. Grimes, J. A. Shropshire, H. C. Tsien, A. F. Venero, *Power Sources 7* (Ed.: J. Thompson), Academic Press, London, **1979**, p. 301.
[123] H. André, *Bull. Soc. Franc. Electriciens* **1941**, *6*, 132.
[124] H. L. Lewis, C. Grun, A. Salkind, *Electrochem. Soc. Proc.* **1995**, *14*, 68.
[125] R. Serenyi, J. Kuklinski, D. C. Williams, A. F. Thompson, *Electrochem. Soc. Proc.* **1995**, *14*, 84.
[126] C. Freudenberg, D-69465 Weinheim, Germany (or licensee: Japan Vilene Co., Ltd., Tokyo, Japan).
[127] Sci MAT Ltd., Dorcan 200, Murdock Road, Dorcan, Swindon SN3 5HY, UK.
[128] PGI Nonwovens, Chicopee, Inc., 2351 US Route 130, Dayton, NJ 08810-1004, USA.
[129] Kuraray Co., Ltd., 1-12-39, Umeda, Kita-ku, Osaka 530, Japan.
[130] H. Hoffmann, *Batteries Int.* **1995**, *10*, 44.
[131] R. P. Schwöbel, H. Hoffmann, A. Keil, B. Möller, German Patent DE 195 23 231, **1995**.
[132] R. Singleton , D. Barker, *Batteries Int.* **1996**, *7*, 35.
[133] Hoechst Celanese Corporation, 13800 South Lakes Drive, Charlotte, NC 28273, USA.
[134] UCB Cellophane Ltd., Bath Road, Bridgwater, Somerset TA6 4PA, UK.
[135] Viskase Corp., 6855 W. 65th St., Chicago, IL 60638, USA.
[136] Yardney Technical Products, Inc., 82 Mechanic St., Pawcatuck, CT 06379, USA.
[137]M. Mendelsohn, US Patent 2 816 154, **1957**.

CosMX Exhibit 1008, Page 313 of 633

Part III:
Materials for Alkali Metal Batteries

1 The Structural Stability of Transition Metal Oxide Insertion Electrodes for Lithium Batteries

M. M. Thackeray

1.1 Introduction

The advent of lithium batteries for consumer products such as cameras, flashlights, camcorders, laptop computers and cellular phones was initiated by the development of primary 3.0V lithium/MnO_2 cells and, thereafter, by rechargeable 3.5V lithium-ion cells with lithiated carbon negative electrodes and $LiCoO_2$ positive electrodes. However, despite rapid advances over the past ten years, lithium-ion battery technology has not yet been optimized in terms of battery performance, safety, and cost. From a materials standpoint, intense worldwide R&D efforts are underway to seek superior materials to overcome the current limitations of the technology. As lithium battery technology has progressed, periodic reviews on lithium batteries and on the chemistry of insertion compounds have been written [1–6].

Lithium-ion cells operate during charge and discharge by a mechanism that involves the electrochemical insertion of lithium into, and extraction from, positive and negative electrode host structures. For example, in the well known Li_xC_6 / $Li_{1-x}CoO_2$ system, which is assembled in the discharged state, lithium ions are extracted from the metal oxide structure and inserted into the carbon electrode during charge with a concomitant oxidation of the positive electrode and a reduction of the negative electrode; the reverse process occurs during discharge.

The cycle life of a lithium-ion battery depends on the structural integrity of the insertion electrodes during repeated insertion/extraction of lithium. Lithium insertion/extraction reactions with metal oxide host structures should occur with a minimum displacement of the oxygen array to minimize strain and possible fragmentation of the metal oxide crystals; these processes cause loss of particle-to-particle contact and electronic connection to the external circuit. Furthermore, the metal cations of the host structure should remain on their crystallographic sites; they should not diffuse into the interstitial space of the host and block the pathways that are required for rapid lithium-ion transport. Most transition metal oxide host structures of interest have close-packed oxygen arrays, in which the oxygen array comprises a network of interlinked octahedra and tetrahedra. The metal ions of the host are generally located in octahedral sites. Structures with cubic close-packed arrays tend to be more stable to lithium insertion than hexagonal close-packed structures. In cubic close-packed structures the octahedra share edges with one another, whereas in hex-

agonal close-packed structures neighboring octahedra share either edges or faces. Hexagonal close-packed oxygen arrays, therefore, shear on lithium insertion towards cubic close-packing in response to the electrostatic interactions between the incoming lithium ions and the metal ions on face-shared octahedral sites. Cubic close-packed insertion compounds become saturated with lithium at the rock salt stoichiometry when the total number of cations in the structure equals the number of anions, and when all the octahedral sites are filled and all the tetrahedral sites are empty.

Structural damage can occur if insertion electrodes are overcharged or overdischarged. For example, oxygen loss from an overcharged $Li_{1-x}NiO_2$ electrode lowers the nickel oxidation state and increases the Ni:O ratio; these changes destroy the integrity of the layered structure and reduce its electrochemical properties. If close-packed metal oxide structures are overdischarged, lithiation beyond the rock salt stoichiometry generally results in a displacement reaction at the electrode surface, where two or more phases are formed. These displacement reactions tend to be irreversible at room temperature and, if allowed to occur, will cause a significant capacity loss in the cell. The structural degradation and capacity loss of an insertion electrode can also occur through dissolution of the metal oxide in the electrolyte, the rate of which depends on the oxidation state of the transition metal ions within the host. As a consequence, the extent to which a host electrode structure can tolerate lithium insertion and extraction must be carefully monitored, and restrictions must be carefully placed on the upper and lower voltage limits to ensure optimum cell operation.

Insertion electrodes can, in principle, tolerate minor and subtle phase changes without suffering structural disintegration during cycling. Lithium insertion/extraction reactions are generally accompanied by expansion or contraction of the unit cell parameters; the "breathing" of the host should, ideally, be isotropic rather than anisotropic to reduce crystallographic strain and should, in principle, be kept to a minimum. Phase transitions that are accompanied by major structural changes during lithium insertion (for example, either to the atomic coordinates of the transition metal cations within the host, or to the unit cell parameters) quickly destroy the integrity of the parent electrode and cause a rapid deterioration of both capacity and cycle life.

This review discusses insertion compounds with tunnel structures (i.e., having a one-dimensional interstitial space for lithium-ion transport), layered structures (two-dimensional interstitial space), and framework structures (three-dimensional interstitial space). The discussion is restricted predominantly to crystalline and anhydrous transition metal oxides with close-packed oxygen arrays, whose structures can be determined, with at least a reasonable degree of accuracy, by X-ray or neutron diffraction techniques. The review, therefore, does not cover in any significant detail hydrated materials such as those found in the family of layered manganese oxides (phyllomanganates), e.g., birnessite [7, 8] and rancieite [9], whose structures are often stabilized by large cations such as Na^+ or K^+ [8–10], nor does it treat amorphous materials such as V_2O_5 xerogels [11]. Also outside the scope of the review are metal phosphate and sulfate positive electrodes with NASICON-related (framework) structures [12] as are the "amorphous" tin oxides, currently under consideration as negative electrode materials for lithium-ion batteries [13].

CosMX Exhibit 1008, Page 316 of 633

This review focuses on the structural stability of transition metal oxides to lithium insertion/extraction rather than on their electrochemical performance. The reader should refer to cited publications to access relevant electrochemical data. Because of the vast number of papers on lithium metal oxides that have been published since the 1970s, only a selected list of references has been provided.

1.2 Tunnel Structures: MnO_2 Compounds

The discussion of metal oxide insertion electrodes with tunnel structures has been restricted to manganese dioxides and their derivatives. Many of the MnO_2 derivatives, which have modified structures, show enhanced structural stability to lithium insertion and extraction over their parent compounds. The structures of $a-MnO_2$, $\beta-MnO_2$, $\gamma-MnO_2$, and ramsdellite-MnO_2 are shown in Fig. 1(a–d); the dimensionality of the tunnels in each structure, which is based on the size of an empty octahedron, can be described as (1 × 1) for $\beta-MnO_2$ and (2 × 1) for ramsdellite-MnO_2. $\alpha-MnO_2$ has discrete (2 × 2) and (1 × 1) tunnels, whereas $\gamma-MnO_2$ can be considered as having a structure with intergrown domains of $\beta-MnO_2$ and ramsdellite-MnO_2. These MnO_2 materials are of interest primarily for 3 V Li/MnO_2 batteries.

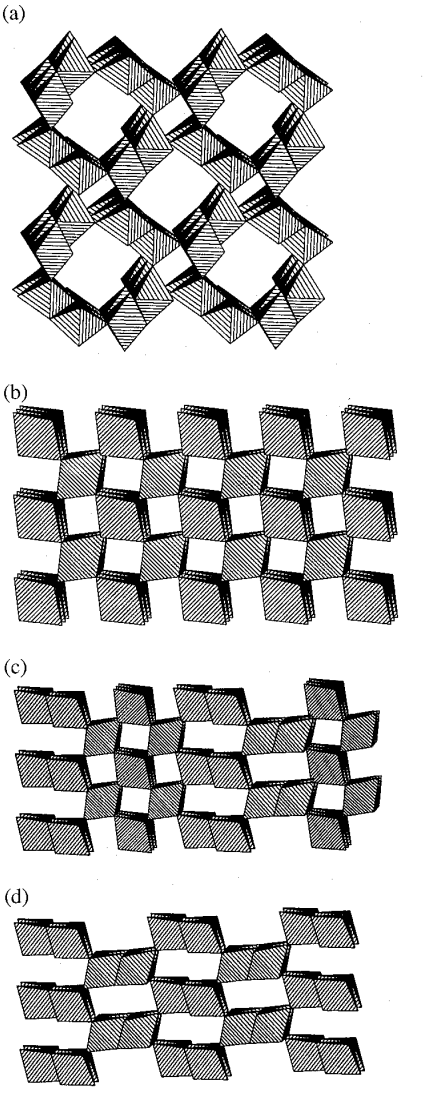


Figure 1. The structures of (a) $\alpha-MnO_2$, (b) $\beta-MnO_2$, $\gamma-MnO_2$, and (d) ramsdellite $-MnO_2$ Hatched regions represent MnO_6 octahedra

1.2.1 $\alpha-MnO_2$

The compound $\alpha-MnO_2$ exists in nature in several mineral forms, such as hollandite ($BaMn_8O_{16}$) and cryptomelane (KMn_8O_{16}). The Ba^{2+} and K^+ cations partially occupy crystallographic sites at the center of the (2 × 2) tunnels. The presence of these large cations led, for many

CosMX Exhibit 1008, Page 317 of 633

years, to the belief that $\alpha - MnO_2$ materials had to be stabilized by foreign cations within the MnO_2 framework. When initially screened for lithium batteries, $\alpha - MnO_2$ compounds were synthesized in the presence of these cations [14]. The electrochemical performance of these $\alpha - MnO_2$ electrodes is limited because the large cations hinder lithium-ion diffusion within the $\alpha - MnO_2$ structure. However, recent research has shown that when $\alpha - MnO_2$ is synthesized from either Li_2MnO_3 [15] or Mn_2O_3 precursors [16], it is possible to fabricate highly crystalline $\alpha - MnO_2$ products without any foreign "stabilizing" cation present in the framework. Neutron diffraction studies indicated that these highly crystalline $\alpha - MnO_2$ materials are stabilized by H_2O molecules in the (2 × 2) channels, and that the water can be removed from the structure at 300 °C without destroying the $\alpha - MnO_2$ framework [15, 17]. However, the pure $\alpha - MnO_2$ structure is not stable to lithium insertion. Electrochemical data have shown that despite an initial high discharge capacity of approximately 200 $mAh\,g^{-1}$, capacity is lost rapidly on subsequent cycling [15, 17]; the capacity stabilizes after reaching 100–120 mAh g^{-1}. The initial capacity loss is believed to be associated with an instability of the (2 × 2) tunnel; structural modifications that occur within the host structure during the initial discharge make it difficult for all the inserted lithium to be extracted from the structure at voltages below 3.8 V [17].

1.2.2 $0.15\,Li_2O \cdot \alpha - MnO_2$

The performance of $\alpha - MnO_2$ electrodes can be significantly improved if $\alpha - MnO_2$ is reacted with LiOH at 300–400 °C [17–20]; these lithia-stabilized $\alpha - MnO_2$ electrodes yield a typical rechargeable capacity of 150 $mAh\,g^{-1}$ or more [18]. For example, the H_2O component in water-stabilized $\alpha - MnO_2$ structures $\alpha - MnO_2 \cdot nH_2O$ $(0.20 \leq n \leq 0.36)$ can be replaced by Li_2O to yield a lithia-stabilized $\alpha - MnO_2$ structure with nominal stoichiometry $0.15\ Li_2O \cdot MnO_2$ (Fig. 2) [17].

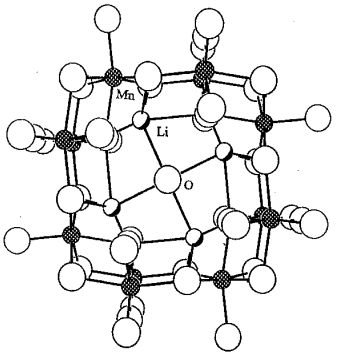


Figure 2. The structure of $0.15\ Li_2O \cdot MnO_2$. The lithium and oxygen sites within the (2 × 2) channel of the $\alpha - MnO_2$ framework are partially occupied.

Alternatively, this structure can be obtained by first dehydrating $\alpha - MnO_2 \cdot nH_2O$, then reacting the dehydrated product with $LiOH \cdot H_2O$ at 275 °C. Note that the oxygen ion from the water or lithia molecule resides at approximately the same crystallographic site as the large Ba^{2+} or K^+ ions in cation-stabilized $\alpha - MnO_2$ structures. More importantly, this oxygen ion partially occupies an anion vacancy in a defect and distorted close-packed oxygen array, thus introducing greater stability to the $\alpha - MnO_2$ structure. The lithium ions of the lithia molecule are coordinated to the oxygen ions of the framework and to the oxygen at the center of the (2 × 2) channel, but are more strongly bound to the walls of the framework (Fig. 2). Because the lithium ions

CosMX Exhibit 1008, Page 318 of 633

only partially occupy their crystallographic sites, additional lithium ions can be accommodated in these sites during electrochemical discharge. Before the electrochemical insertion of lithium, no evidence of lithium-ion occupation of the narrow (1 × 1) channels was detected in lithia-stabilized MnO_2 products.

1.2.3 $\beta - MnO_2$

In the MnO_2 family, the β-polymorph is the most stable. It has a rutile-type structure and tetragonal symmetry (Fig. 1b). The oxygen ions are arranged in a distorted hexagonal close-packed array (in rutile, sometimes referred to as tetragonal close packing [21]). The interstitial space in the $\beta - MnO_2$ structure consists of narrow (1 × 1) channels. Murphy has reported that crystalline $\beta - MnO_2$ can reach a limiting composition of $Li_{0.2}MnO_2$ [22], which corresponds to a low electrochemical capacity of 62 mAh g^{-1}. Crystalline $\beta - MnO_2$ electrodes are, therefore, of little interest as insertion electrodes. Studies have shown that $\beta - MnO_2$ materials with low crystallinity yield an initial capacity greater than 200 mAh g^{-1}, but the charge–discharge reaction is not fully reversible [6, 23]. The irreversibility can perhaps be related to the findings of David and co-workers, who demonstrated that when $\beta - MnO_2$ is extensively lithiated with butyl lithium at 50 °C, the rutile-type structure transforms to the lithiated spinel $Li_2[Mn_2]O_4$, which is not stable to electrochemical cycling [24] (see Sect. 1.4.2).

1.2.4 $\gamma - MnO_2$ and Ramsdellite $-MnO_2$

$\gamma - MnO_2$ is well known as an electrode material. It has been used predominantly in Leclanché and alkaline cells with aqueous electrolytes, but also in primary lithium cells with organic electrolytes. The $\gamma - MnO_2$ structure consists of intergrown domains of $\gamma - MnO_2$ and ramsdellite-MnO_2, a result of de Wolff disorder and micro twinning [25] (Fig. 1c). When synthesized by either chemical or electrolytic techniques, $\gamma - MnO_2$ contains an appreciable amount of water on the surface of the particles and at grain boundaries. For application in lithium cells, $\gamma - MnO_2$ is heated at about 375 °C to remove the water [26]; this process slightly increases the concentration of $\beta - MnO_2$ in the intergrown structure. During electrochemical discharge, lithium is inserted into the ramsdellite-MnO_2 domains. This reaction, which significantly changes the unit cell parameters, is reversible if electrochemical cycling is carried out at low current rates [27, 28]. Greater stability to electrochemical cycling can be achieved by reacting LiOH with $\gamma - MnO_2$ in a 3:7 (or 0.43:1.0) molar ratio at 375–420 °C; the product has been given the acronym "CDMO" (composite dimensional manganese oxide) by Sanyo Corp. [29–31]. The CDMO products have a Li:Mn ratio close to that of Li–Mn–O spinel compounds, which vary between 0.5:1.0 and 0.8:1.0. These products also tend to be two-phase; they consist of lithiated $\gamma - MnO_2$ plus a spinel component [32–34]. The spinel domains that have a cubic close-packed oxygen array are believed to play an important role in stabilizing the composite structure. Because $\gamma - MnO_2$ materials and their lithiated derivatives tend to be poorly crystalline, it has been difficult to determine the exact structural features of lithiated $\gamma - MnO_2$ products. However, with the synthesis of crystalline ramsdellite-MnO_2 products (Fig. 1d), it has been possible to gather

CosMX Exhibit 1008, Page 319 of 633

structural information that accounts for the overall superior structural stability and electrochemical performance of CDMO electrodes [34].

1.2.5 Lithiated Ramsdellite – MnO_2

The structures of ramsdellite-MnO_2 and lithiated products Li_xMnO_2 $(0 \leq x \leq 1)$are shown in Figs. 3(a–c). Chemical lithiation of ramsdellite-MnO_2 with either n-butyl lithium or with lithium iodide causes sever shearing and buckling of the close-packed oxygen planes from a distorted hexagonal close-packed array towards cubic close-packing (Fig. 3 b, c). The lithiation process is accompanied by significant anisotropic changes to the unit cell parameters; at the composition $Li_{0.9}MnO_2$, a expands by 5.6 percent, b`(the direction of shear) expands by 16.5 percent, while c contracts by 1 percent. These changes in lattice parameters increase the unit cell volume by 21.4 percent and are believed to be far too severe for the ramsdellite-MnO_2 electrode to tolerate many deep discharge cycles without structural deterioration.

The structure of the lithiated ramsdellite-MnO_2 product after reaction with LiOH at 300 °C is shown in Fig. 3(d) [6]. The overall ideal reaction, which is similar to that when LiOH is used as a lithiating agent, can be written as:

$$x\mathrm{Li_2O} + \text{ramsdellite} - \mathrm{MnO_2} \rightarrow \mathrm{Li_{2x}MnO_{2+x}}\ (0 \leq x \leq 0.15) \qquad (1)$$

In this case, lithiation of ramsdellite occurs by incorporation of Li_2O into the MnO_2 structure, which is analogous to the situation for the stabilization of $\alpha - MnO_2$ (see Sec. 1.2.2); the reaction does not involve the reduction of the manganese ions. Note also that the stabilizing lithium ions in an ideal $Li_{2x}MnO_{2+x}$ structure cannot be extracted by electrochemical methods because this necessitates an oxidation state for the

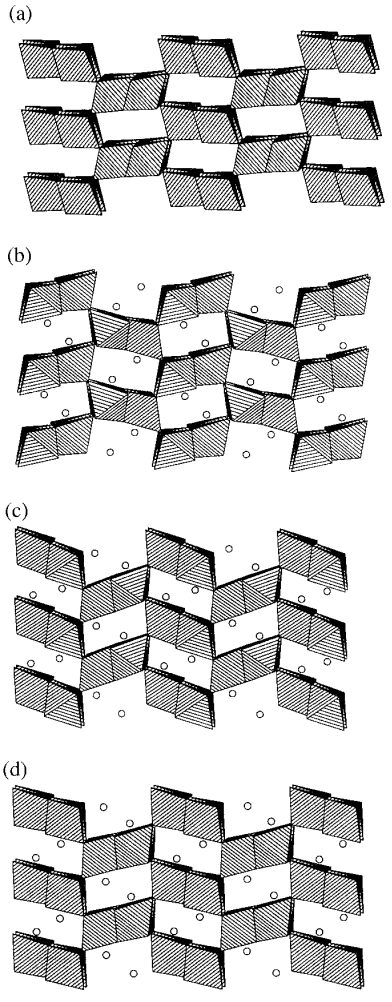


Figure 3. The structures of (a) ramsdellite-MnO_2, (b) $Li_{0.3}MnO_2$, (c) $Li_{0.9}MnO_3$ and, (d) $0.15\ Li_2O \cdot MnO_2$. Hatched regions represent MnO_6 octahedra. The circles show the approximate positions of the lithium ions.

CosMX Exhibit 1008, Page 320 of 633

manganese ions above 4. (In practice, the oxidation state of Mn in the parent ramsdellite-MnO_2 and in lithia-stabilized products is slightly less than 4.) The incorporation of Li_2O into ramsdellite-MnO_2 increases the ratio of cations to anions in the structure. The result is shearing and buckling of the hexagonal close-packed structure and a transformation towards a cubic close-packed structure similar to lithiated ramsdellite-MnO_2 products obtained from reactions with n-butyl lithium or lithium iodide. Because the oxygen array in lithia-stabilized ramsdellite-MnO_2 structures (and by analogy, $\gamma - MnO_2$ structures) is close to cubic close-packing and is not prone to shear, it provides a more stable framework for lithium insertion/extraction reactions than pure ramsdellite-MnO_2 (or $\gamma - MnO_2$).

1.2.6 Orthorhombic $Na_{0.44}MnO_2$

Many lithium–manganese oxides are unstable to electrochemical cycling and transform to a spinel structure. The structure of sodium-stabilized manganese dioxide, $Na_{0.44}MnO_2$, is, therefore, of particular significance because the large stabilizing sodium ions prevent the conversion to spinel. The structure of orthorhombic $Na_{0.44}MnO_2$ is shown in Fig. 4 [35]. Because of the large radius of the Na^+ ion (0. 97 Å), the packing of the oxygen array is severely distorted, providing a tunnel structure with channels of unusual dimensions. This structure consists of columns of edge-sharing square pyramids and sheets of edge-sharing octahedra two and three units in width that run parallel to the c-axis of the unit cell. The structure has two types of tunnel: a large S-shaped one and two identical pentagonally shaped tunnels. The pentagonal tunnels are almost fully occupied by sodium, whereas the four sodium sites in the S-shaped tunnels are partially occupied. The sodium ions can be partially ion-exchanged with lithium to provide an electrode structure with nominal composition $Na_{0.14}Li_{0.30}MnO_2$.

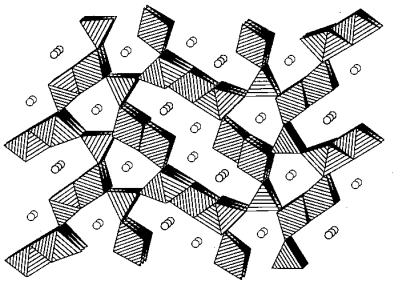


Figure 4. The structure of $Na_{0.44}MnO_2$. Hatched regions represent MnO_6 octahedra and MnO_5 square pyramids. The circles show the positions of the sodium ions (after Ref. [35]).

These electrodes have been evaluated in lithium–polymer cells that operate at 85 °C [35]. Although the electrochemical discharge is not yet fully understood, differential capacity plots have shown evidence of two reversible ordering transitions and a kinetically slow phase transformation.

1.3 Layered-Structures

The best known layered structures that have been exploited in lithium-ion cells have the general formula $LiMO_2$ (M= Co,

CosMX Exhibit 1008, Page 321 of 633

Ni, Mn, V). In the ideal layered $LiMO_2$ structure, the Li^+ and the M^{3+} ions occupy octahedral sites in alternate layers between cubic close packed oxygen layers (Fig. 5).

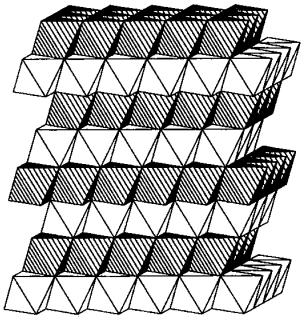


Figure 5. A schematic representation of an ideal layered $LiMO_2$ structure. The layers of shaded and unshaded octahedra are occupied by M and Li ions, respectively.

In reality, because of the difference in the binding energy of the Li^+ and the M^{3+} ions that hold the oxygen layers together, the oxygen array is not ideally close-packed. $LiMO_2$ structures (M=Co, Ni, V) have trigonal symmetry (space group $R\bar{3}m$); the deviation from ideal cubic-close-packing is reflected by the magnitude of the crystallographic *c/a* ratio, which for cubic symmetry is 4.899.

1.3.1 $LiCoO_2$

The compound $LiCoO_2$ is an attractive positive electrode for lithium-ion cells because it has a stable structure which is easy to prepare with the ideal layered configuration (*c*/a ratio = 4.99). At present, $LiCoO_2$ is the preferred positive electrode for lithium-ion cells but it has the disadvantage of being expensive. Another drawback is the instability of extensively delithiated (charged) $Li_{1-x}CoO_2$ electrodes ($x \geq 0.5$), which are prone to oxygen loss in the presence of an organic electrolyte solvent, particularly when cells reach an operating temperature of 50 °C or more.

Since the first investigation by Mizushima et al. in 1980 [36], there have been many detailed studies of the $Li_{1-x}CoO_2$ electrode system [37–41]. At room temperature, the $Li_{1-x}CoO_2$ system shows excellent rechargeability when charged and discharged over the range $0 \leq x \leq 0.5$. Indeed, an all-solid-state Li/lipon/ Li_{1-x} CoO_2 cell ("lipon" refers to a lithium-phosphorus–oxynitride solid electrolyte glass), has achieved more than 40000 cycles without significant capacity loss [42].

$Li_{1-x}CoO_2$ electrodes undergo a reversible phase transition at $x \approx 0.5$, which has been attributed to a change in crystal structure from trigonal to monoclinic symmetry, brought about by the ordering of the lithium ions on discrete crystallographic sites [38, 40]. This transition is accompanied by very small changes in the lattice parameters and occurs without any significant disruption of the CoO_2 sublattice; therefore, this transition would not be expected to cause any significant structural degradation of the electrode during electrochemical cycling [43]. An in-situ X-ray diffraction study of a $Li_{1-x}CoO_2$ electrode during electrochemical removal of lithium demonstrated that it is possible to prepare compositions very close to the end-member CoO_2 (x = 1) [41]. The delithiated phase, which retains its layered character, is believed to be isostructural with hexagonal close-packed CdI_2, in which the stacking of the anion planes is

CosMX Exhibit 1008, Page 322 of 633

ABABAB....etc, rather than ABCAB-CABC....etc, in the parent $LiCoO_2$ compound.

1.3.2 $LiNiO_2$

Although $LiNiO_2$ is cheaper than $LiCoO_2$ and is capable of a rechargeable capacity >130 mAh g^{-1} when charged to 4.2 V, it is difficult to prepare large and reproducible $LiNiO_2$ batches with the ideal layered structure. The product, which has a typical *c/a* ratio of 4.93, often contains a small amount of nickel in the lithium layers, which changes the true composition of the layered structure to a more generalized notation, $Li_{1-y}Ni_{1+y}O_2$ [44–49]. The contamination of the lithium layers with nickel can radically impair the electrochemical activity of the electrode [44, 50]. Electrochemical data (specifically $\delta x / \delta V$ versus V plots) have demonstrated that lithium extraction is accompanied by a series of subtle phase transitions, which are difficult to characterize in detail but are similar to the trigonal-to-monoclinic transition that is observed in $Li_{1-x}CoO_2$ [50, 51]. Nevertheless, the gradual variation of the unit cell parameters of $Li_{1-x}NiO_2$ during lithium extraction/reinsertion is a major reason why it maintains its structural integrity during cycling, at least when the composition is limited to $x_{max} \approx 0.5$ [43]. Accelerated rate calorimetry studies have demonstrated that extensively delithiated $Li_{1-x}NiO_2$ electrodes are less stable than $Li_{1-x}CoO_2$ electrodes in lithium–organic electrolyte cells, an indication that Ni^{4+} ions are reduced more easily than Co^{4+} ions in the cell environment. The structural limitations of $LiNiO_2$ electrodes can be partly overcome by using cobalt-substituted $LiNi_{1-z}Co_zO_2$ structures [44, 52, 53]. Recent data have shown that a rechargeable capacity of approximately 180 mAh g^{-1} can be achieved from electrodes of composition $LiNi_{0.85}Co_{0.15}O_2$ [53]. Other substituents, e.g., Al [54, 55] and Mn [56], have also been used, with limited success, in attempts to increase the sta-bility of layered lithium–nickel–oxide elec-trode structures to electrochemical cycling.

1.3.3 Li–Mn–O Compounds

Several attempts have been made to synthesize a layered $LiMnO_2$ structure, isostructural with that of $LiCoO_2$ [57–61].

1.3.3.1 $LiMnO_2$ from $NaMnO_2$

Recent studies have shown that an anhydrous $LiMnO_2$ compound can be prepared by ion exchange of Li for Na in the layered $\alpha - NaMnO_2$ structure by using LiCl or LiBr in n-hexanol or methanol [59–61]. The $LiMnO_2$ structure has monoclinic symmetry (space group C2/m). The reduction of crystal symmetry from the trigonal ($R\bar{3}m$) symmetry that characterizes $LiCoO_2$ to the monoclinic symmetry of $LiMnO_2$ arises because of crystallographic distortions induced by Jahn–Teller Mn^{3+} ions. Structure analyses have shown that the $LiMnO_2$ products are not ideally layered, and that the Li layers contain between 3 and 9 percent Mn [59–61]. Although almost all the lithium can be extracted from $LiMnO_2$ on an initial charge, the structure is not stable to electrochemical cycling. $LiMnO_2$ products containing 9 percent Mn in the lithium layers deliver very little capacity on the subsequent discharge [59], which is analogous to $LiNiO_2$ and $LiCoO_2$ electrodes that contain a significant

CosMX Exhibit 1008, Page 323 of 633

amount of Ni and Co in the lithium layers [50, 62]. An electrode with 3 percent Mn in the lithium layers provides better rechargeable capacities but develops distinct voltage plateaus at 3 and 4 V on cycling, indicative of a phase transformation of the layered structure to a spinel-like structure [60]. This transformation necessitates the migration of Mn ions into the lithium layers during the electrochemical reaction such that the ratio of Mn in alternate layers in the lithiated $LiMnO_2$ spinel structure (in spinel notation, $Li_2[Mn_2]O_4$) becomes 3:1.

1.3.3.2 $Li_{2-x}MnO_{3-x/2}$ and Lithiated Derivatives

Li_2MnO_3 has a layered structure that may be represented, in $LiMnO_2$ notation, as $Li(Li_{0.33}Mn_{0.67})O_2$; in this structure, alternate cation layers consist of layers of only lithium and layers of lithium and manganese with Li:Mn = 1:2 (Fig. 6a). Li_2MnO_3 is electrochemically inactive. Lithium can neither be inserted into the rock salt structure, because all the octahedral sites are fully occupied, nor easily electrochemically extracted, because the manganese ions are fully oxidized (Mn^{4+}). However, by leaching Li_2O from a Li_2MnO_3 ($Li_2O \cdot MnO_2$) product synthesized at moderately low temperature (400 °C), it is possible to fabricate a layered $Li_{2-x}MnO_{3-x/2}$ ($0<x<2$) compound in which the manganese ions remain in octahedral sites [63]. When x = 1.6 the resulting composition is $Li_{0.4}MnO_{2.2}$, or in layered notation, $Li_{0.36}Mn_{0.91}O_2$ [58]. However, removal of lithia from the Li_2MnO_3 structure causes shearing of the oxygen planes from their slightly distorted cubic close-packed arrangement to yield an oxygen array containing alternate sheets of trigonal prisms and octahedra (Fig. 6b).

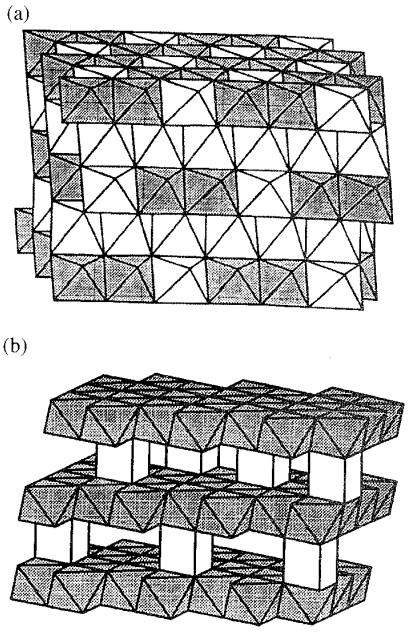


Figure 6. The structures of (a) Li_2MnO_3 and (b) layered MnO_2 derived from (a), showing the sheets of edge-sharing MnO_6 (shaded) and LiO_6 octahedra (unshaded) in (a), and alternate layers of MnO_6 octahedra and trigonal prisms in (b) (after Ref.[6]). The trigonal prisms are believed to be partially occupied by residual lithium ions.

Lithiation of $Li_{0.36}Mn_{0.91}O_2$ with LiI to form $Li_{1.09}Mn_{0.91}O_2$ regenerates the close-packed oxygen array of the parent Li_2MnO_3 structure. Like Li_2MnO_3, $Li_{1.09}Mn_{0.91}O_2$ has the ideal rock salt stoichiometry; the structure differs only in the Li:Mn ratio of the manganese-rich layer and closely approximates the layered structures of $LiCoO_2$ and $LiNiO_2$ (Fig. 5). Electrochemically active Li–Mn–O materials have also been made from Li_2MnO_3 by heating acid-treated samples to 300 °C in air [64, 65]; the heated products are believed to contain domains of both Li_2MnO_3-related and spinel-related structures [6, 63].

CosMX Exhibit 1008, Page 324 of 633

1.3.3.3 Orthorhombic $LiMnO_2$

Orthorhombic $LiMnO_2$ has a rock salt structure with a distorted cubic close-packed oxygen array and is characterized by alternate corrugated layers of lithium and manganese ions (Fig. 7). Although it is sometimes referred to as being a layered structure, the layering is not parallel to the close-packed oxygen planes, thereby differentiating this structure type from the classical layered $LiMnO_2$ compounds (M=Co, Ni, V).

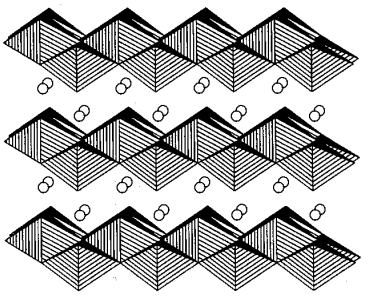


Figure 7. The structure of orthorhombic $LiMnO_2$. Hatched regions represent MnO_6 octahedra. The circles show the positions of the lithium ions.

Orthorhombic $LiMnO_2$ can be synthesized over a wide temperature range, for example, 800–1000 °C, in a conventional solid-state reaction under an inert atmosphere such as argon [66, 67]. It can also be synthesized at lower temperature, for example, 600 °C, by reducing MnO_2 with carbon in the presence of LiOH [68], or at 300–450 °C by reacting $\gamma-MnOOH$ with LiOH under flowing nitrogen [69]. An undisclosed method of preparing $LiMnO_2$ below 100 °C has also been reported [70].

A substantial amount of lithium can be extracted from orthorhombic $LiMnO_2$ between 2.0 and 4.5 V in $Li/LiMnO_2$ cells. The electrochemical de-intercalation of lithium from $LiMnO_2$ samples synthesized at low temperatures can yield an initial (charge) capacity of ~200 mAh g^{-1}, or more [69, 70]. However, the orthorhombic $LiMnO_2$ structure is unstable to delithiation. Powder X-ray diffraction data of cycled cathodes clearly show a transformation to a spinel-type structure [68, 71]; electrochemical data also show that $Li/LiMnO_2$ cells exhibit increasing spinel-like behavior, with the development of characteristic voltage plateaus at 4 V and 3 V as the cells are cycled [68, 72]. In practice, several cycles are necessary to accomplish this transformation. The proposed mechanism is a solid state reaction in which the cooperative displacement of 50 percent of the Mn ions occurs within the close-packed oxygen array to generate the $[Mn_2]O_4$ spinel framework [68].

1.3.4 Orthorhombic $LiFeO_2$

Research on lithium iron oxides has been spearheaded primarily in attempts to find an alternative low-cost electrode material to $LiCoO_2$. An orthorhombic $LiFeO_2$ structure, which is isostructural with orthorhombic $LiMnO_2$ (Fig. 6), has recently been synthesized by reaction of FeOOH with LiOH at moderate temperatures [73]. Like orthorhombic $LiMnO_2$, orthorhombic $LiFeO_2$ is unstable to lithium extraction, but unlike orthorhombic $LiMnO_2$, it does not convert to a stable spinel-type structure. Delithiated $Li_{1-x}FeO_2$ products transform to an "amorphous" phase, which has not yet been characterized. Although $LiFeO_2$ electrodes can be cycled in the voltage range 3.5–1.5V, they deliver relatively low capacities (80–100 mAh g^{-1}) compared to orthorhombic $LiMnO_2$ [73].

CosMX Exhibit 1008, Page 325 of 633

1.3.5 Li–V–O Compounds

1.3.5.1 $LiVO_2$

$LiVO_2$ is isostructural with $LiCoO_2$; it has a *c/a* ratio of 5.20 (space group $R\bar{3}m$) [74]. Unlike $LiCoO_2$ and $LiNiO_2$, $LiVO_2$ is unstable to delithiation; at $x \approx 0.3$ in $Li_{1-x}VO_2$, the vanadium ions become mobile and diffuse from the octahedral sites (3b) of the vanadium layer into octahedral sites (3a) left vacant by the extracted lithium ions. The diffusion of vanadium ions takes place through face-shared tetrahedra linking the octahedra of alternate layers and is believed to occur by a disproportionation reaction in which V^{5+} ions occupy tetrahedral (6c) sites [74, 75]:

$$2V^{4+}{}_{3b,oct} + \square_{6c,tet} \rightarrow V^{5+}{}_{6c,tet} + V^{3+}{}_{3b,oct} + \square_{3b,oct}$$

$$V^{5+}{}_{6c,tet} + V^{3+}{}_{3b,oct} + \square_{3a,oct} \rightarrow \square_{6c,tet} + V^{4+}{}_{3b,oct} + V^{4+}{}_{3a,oct}$$

Overall reaction:

$$2V^{4+}{}_{3b,oct} \rightarrow V^{4+}{}_{3b,oct} + V^{4+}{}_{3a,oct}$$

The disproportionation reaction destroys the layered structure and the two-dimensional pathways for lithium-ion transport. For $x>0.3$, delithiated $Li_{1-x}VO_2$ has a defect rock salt structure without any well-defined pathways for lithium-ion diffusion. It is, therefore, not surprising that the kinetics of lithium-ion transport and overall electrochemical performance of $Li_{1-x}VO_2$ electrodes are significantly reduced by the transformation from a layered to a defect rock salt structure [76]. This transformation is clearly evident from the differences in the relative peak intensities in the X-ray diffraction patterns of the layered and defect rock salt phases [74]. Heat treatment of the partially delithiated compound $Li_{0.5}VO_2$ at 300 °C results in a transformation to the spinel LiV_2O_4 (Sec. 1.4.3) [76–78].

1.3.5.2 $\alpha - V_2O_5$ and its Lithiated Derivatives

Vanadium oxides are attractive candidates as insertion electrodes for lithium batteries because three stable oxidation states (V^{5+}, V^{4+} and V^{3+}) can be accommodated within a close-packed oxygen array. $\alpha - V_2O_5$ has the highest theoretical capacity of the vanadium oxide family (442 mAh g^{-1}); three lithium ions can be inserted into the structure, reaching the rock salt stoichiometry at the composition $Li_3V_2O_5$. During this reaction, the vanadium oxidation state changes from 5 in V_2O_5 to an average of 3.5 in $Li_3V_2O_5$. $\alpha - V_2O_5$ has a layered structure with a distorted close-packed oxygen array in which the vanadium ions are bonded strongly to five oxygen ions, giving them square-pyramidal coordination (Fig. 8a) [79]. Lithium insertion into V_2O_5 forms several $Li_xV_2O_5$ phases ($\alpha, \varepsilon, \delta, \gamma$ and ω phases) as x increases [44]. The α, ε and δ phases are closely related to the parent layered V_2O_5 structure, with x reaching 1 in $\delta - Li_xV_2O_5$ (Fig. 8b) [80]. For the range $0 \le x \le 1$, the reaction is reversible. The incorporation of approximately one additional lithium buckles the V_2O_5 framework ($\gamma - Li_xV_2O_5$, $x \approx 2$, Fig. 8c). Although delithiation of $\gamma - Li_xV_2O_5$ does not regenerate the original $\alpha - V_2O_5$ structure, all the lithium can be removed from the structure if cells are charged to a higher voltage than initially provided [44, 80, 81]. Discharge

CosMX Exhibit 1008, Page 326 of 633

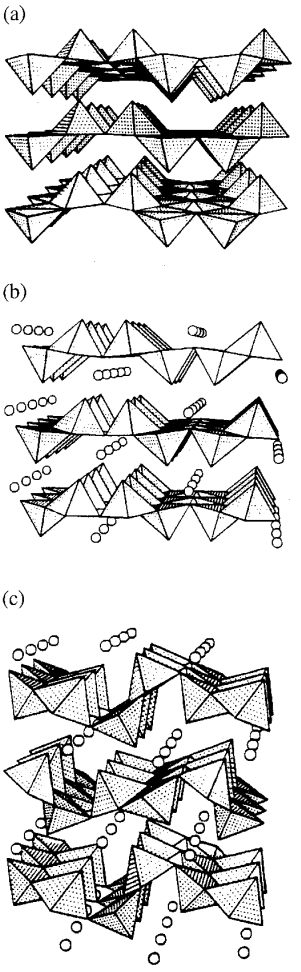


Figure 8. The structures of (a) $\alpha - V_2O_5$, (b) $\delta - Li_xV_2O_5$ ($x \approx 1$), and (c) $\delta - Li_xV_2O_5$ ($x \approx 2$) (after Ref.[44]). Hatched regions represent VO_5 square pyramids.

of $Li_xV_2O_5$ beyond x=2 causes a major structural transformation in which vanadium ions migrate from their original sites into neighboring empty octahedra; the resulting structure, $\omega - Li_3V_2O_5$, has a rock salt structure, with an almost random arrangement of the vanadium ions on the octahedral sites [82]. Lithium extraction from the rock salt phase does not regenerate the layered $Li_xV_2O_5$ structures; rather, by a single-phase reaction, lithium is extracted from the rock salt phase, in which there are no well-defined conduction pathways for the lithium ions. For this reason, removal of lithium from $\omega - Li_3V_2O_5$ is relatively difficult, and it requires high voltages (up to 4 V) to extract most of the lithium from the structure. However, the $\omega - Li_{3-x}V_2O_5$ defect rock salt structure is robust and stable over a wide range of x and can withstand many cycles without degradation.

1.3.5.3 $Li_{1.2}V_3O_8$

The layered structure of $Li_{1.2}V_3O_8$ was first determined by Wadsley in 1956 [83] (Fig. 9a); it has monoclinic symmetry (space group $P2_1/m$).

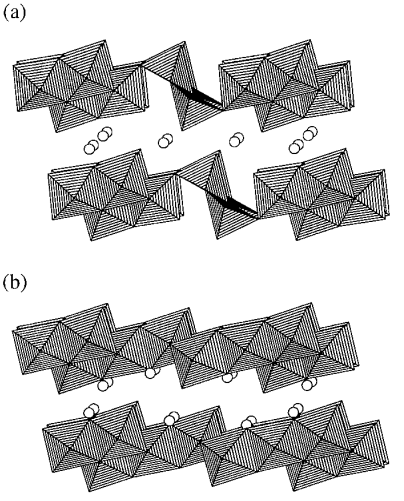


Figure 9. The structures of (a) $Li_{1.2}V_3O_8$ and (b) $Li_4V_3O_8$. Hatched regions represent VO_6 octahedra and VO_5 square pyramids in (a), and VO_6 octahedra in (b). The circles show the positions of the lithium ions.

CosMX Exhibit 1008, Page 327 of 633

$Li_{1.2}V_3O_8$ can be regarded as a lithia-stabilized V_2O_5 compound, with notation $0.4\,Li_2O \cdot V_2O_{5-\delta}$, where = δ = 0.067. In $Li_{1.2}V_3O_8$, the average oxidation state of the vanadium ions is 4.93. A single-crystal structure determination of $Li_{1.2}V_3O_8$ confirmed Wadsley's data that one lithium ion is located on an octahedral site, and that the remaining 0.2 Li^+ is located on a tetrahedral site [84]. A single-crystal structure analysis of the lithiated product $Li_4V_3O_8$, obtained by reaction of $Li_{1.2}V_3O_8$ with an excess of n-butyl lithium, has shown that the V_3O_8 framework remains intact on lithiation, and that the lithium ions all reside in octahedral sites of a defect rock salt structure (Fig. 9b) [84]. A surprising feature of this insertion electrode is that, although the monoclinic unit cell parameters vary anisotropically during lithium insertion to a composition $Li_4V_3O_8$, there is no change in the unit cell volume. Several electrochemical studies of $Li_{1.2}V_3O_8$ compounds with various degrees of crystallinity have been made since 1983 [85–92]. These data have demonstrated that $Li_{1.2}V_3O_8$ undergoes several phase changes on lithiation, and that these transitions are reversible. A recent study of a $Li_{1.2}V_3O_8$ electrode, prepared at 150 °C from a spray-dried xerogel, showed that the layered structure can be electrochemically lithiated to the rock salt composition $Li_5V_3O_8$ in lithium–organic liquid electrolyte cells [91]. The phase changes in $Li_{1.2+x}V_3O_8$ are subtle; they are associated predominantly with the changes in the distribution of the lithium ions in the tetrahedral and octahedral interstitial sites of a stable V_3O_8 sublattice. The stability of the structure to lithium insertion and extraction, and the availability of a two-dimensional interstitial space for lithium-ion transport, have made $Li_{1.2}V_3O_8$ an attractive electrode candidate for rechargeable lithium cells.

1.3.5.4 $Li_{0.6}V_{2-\delta}O_{4-\delta} \cdot H_2O$ and $Li_{0.6}V_{2-\delta}O_{4-\delta}$

Recent advances in fabricating novel metal oxide electrodes have been made by exploiting hydrothermal preparation techniques [93, 94]. An example is $Li_{0.6}V_{2-\delta}O_{4-\delta} \cdot H_2O$, which is prepared by dissolving V_2O_5 in tetramethyl ammonium hydroxide and LiOH, acidified with nitric acid and heated at 200 °C [94].

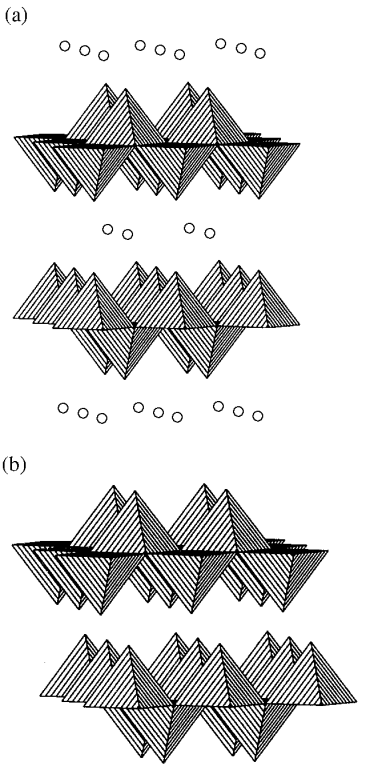


Figure 10. The structures of (a) $Li_{0.6}V_{2-\delta}O_{4-\delta} \cdot H_2O$ and (b) $Li_{0.6}V_{2-\delta}O_{4-\delta}$. Hatched regions represent VO_5 square pyramids. The circles in (a) show the positions of the oxygen ions from the water molecules (adapted from Refs. [91, 92]).

CosMX Exhibit 1008, Page 328 of 633

$Li_{0.6}V_{2-\delta}O_{4-\delta} \cdot H_2O$ has a layered structure in which sheets of VO_5 square pyramids sandwich the water molecules (Fig. 10a). Half of the square pyramids in one sheet point towards one hydrated layer; the other half point in the opposite direction, towards an adjacent layer. Neutron diffraction data have suggested that the lithium ions are distributed over various sites, (i) between the water molecules, (ii) at the base of the VO_5 square pyramids, and (iii) in some vanadium sites. The $Li_{0.6}V_{2-\delta}O_{4-\delta} \cdot H_2O$ structure can be dehydrated; removal of water shifts the sheets of VO_5 square pyramids so that the oxygens at the peak of each pyramid occupy the sites where the water oxygens had resided in the hydrated phase (Fig. 10b). Electrochemical data obtained from anhydrous $Li_{0.6}V_{2-\delta}O_{4-\delta}$ electrodes have shown that all the lithium can be de-intercalated from the structure on an initial charge; on subsequent discharge and charge, 1.4 Li can be inserted into, and removed from, the structure in a reversible manner [94].

1.4 Framework Structures: The Family of Spinel Compounds

Electrode materials with a spinel-type structure, $A[B_2]X_4$, have become the subject of intensive research over the past 10 years. This interest is partly due to the fact that many spinel compounds exist in nature, and are therefore intrinsically stable materials. Furthermore, the family of spinels encompasses a vast number of compositions because it is possible to vary not only the type and valency of the A and B cations within the $A[B_2]X_4$ structure, but also the type and valency of the X anions, which can be a group VIa element (e.g., O, S, Se) or a group VIIa element (e.g., F, Cl or Br) [95–97]. The versatility of the $A[B_2]X_4$ system has allowed the synthesis of many new spinel compounds in the laboratory, particularly by "chimie douce" or "soft chemistry" techniques. The oxo-spinels have received the greatest attention because of their relative ease of synthesis and attractive electrochemical properties. The prototypic compound, is the mineral spinel, $Mg[Al_2]O_4$, which has cubic symmetry Fd3m. The oxygen ions, which form a cubic close-packed array, are located on the 32e sites. The A cations (Mg) reside on the tetrahedral sites (8a) of the structure, and the B cations (Al) on the octahedral sites (16d). The interstitial space of spinel structures contains empty octahedral sites (16c) and tetrahedral sites (48f and 8b).

In the late 1970s, at the time of the oil crisis, transition metal oxides received attention as possible electrodes for high-temperature lithium cells. Of particular significance was the electrochemical performance of iron oxide positive electrodes, such as magnetite (Fe_3O_4, spinel-type structure) [98], hematite ($\alpha - Fe_2O_3$, corundum-type structure) [98], and $LiFeO_2$ (rock salt-type structure) [99] in LiAl/LiCl,KCl/iron oxide cells, which showed good rechargeability at 420 °C [98, 99]. These experiments demonstrated that discharge took place in several discrete steps, each of which was associated with the formation of independent lithium–iron–oxide phases in the positive electrode. These phases were produced during discharge by insertion of lithium ions into, and extrusion of metallic iron from, the close-packed oxygen array. For example, the discharge of magnetite took place through the following reaction sequence:

CosMX Exhibit 1008, Page 329 of 633

$$Li + 2Fe_3O_4 \rightleftharpoons LiFe_5O_8 + Fe \quad (3)$$

$$3Li + LiFe_5O_8 \rightleftharpoons 4LiFeO_2 + Fe \quad (4)$$

$$3Li + 2LiFeO_2 \rightleftharpoons Li_5FeO_4 + Fe \quad (5)$$

$$3Li + Li_5FeO_4 \rightleftharpoons 4Li_2O + Fe \quad (6)$$

Although these displacement reactions were reversible at the operating temperature of the cell, capacity was lost because of the slow dissolution of Li_2O in the molten salt (LiCl, KCl) electrolyte. Nevertheless, these experiments demonstrated the principle that the cubic close-packed oxygen framework remained intact throughout cell discharge and charge, and that the phase transformations occurred by changing the Li:Fe ratio in the close-packed oxygen array and by allowing the lithium and iron ions within the structure to adopt either tetrahedral or octahedral coordination. For example, in Fe_3O_4 (spinel), the iron ions occupy both tetrahedral and octahedral sites; in $LiFeO_2$ (rock salt), the lithium and iron ions occupy all the octahedral sites; and in Li_2O (anti fluorite), the lithium ions occupy all the tetrahedral sites.

When $\alpha - Fe_2O_3$ was used as the positive electrode in high-temperature lithium cells, the introduction of a small amount of lithium into the corundum-type structure caused the hexagonal-close-packed oxygen array to shear irreversibly to cubic-close packing which generated a defect $\gamma - Li_\delta Fe_2O_3$ (spinel-type) structure. Further lithiation resulted in the formation of $LiFe_5O_8$; thereafter, the reaction followed the same sequence as that shown in reactions (4), (5) and (6) [100]. The stability of the spinel structures at elevated temperatures, as well as the ability of the cubic close-packed oxygen array to accommodate lithium at the expense of iron extrusion, prompted a subsequent investigation of the spinels Fe_3O_4 [101], Mn_3O_4 [102, 103] and Co_3O_4 [104], and the corundum-type á $-Fe_2O_3$ [101] in room temperature lithium cells.

1.4.1 Fe_3O_4, Mn_3O_4 and Co_3O_4

Mineral spinels, such as magnetite (Fe_3O_4) and hausmannite (Mn_3O_4), are stable, "gem-like" materials. In principle, a stoichiometric $A[B_2]O_4$ spinel does not have a structure that is favorable for lithium insertion because all the interstitial (empty) octahedra (16c) and tetrahedra (8b and 48f) share at least two faces with the occupied A tetrahedra (8a) or B octahedra (16d). It was therefore surprising to discover that lithium could be inserted into the spinels Fe_3O_4, Mn_3O_4 and Co_3O_4 at room temperature [101–104]. This anomaly was explained by electrochemical data obtained from a Li/Fe_3O_4 cell and by a structure analysis of the lithiated products. These data showed that lithium insertion into the spinel structure was accompanied by the immediate displacement of the A-site cation into a neighboring 16c octahedral site, and that the inserted lithium ions occupied the remaining octahedral sites to generate a rock salt phase $LiFe_3O_4$. For Fe_3O_4, the reaction is:

$$Li + Fe_{8a}[Fe_2]_{16d}O_4 \rightarrow (LiFe)_{16c}[Fe_2]_{16d}O_4 \quad (7)$$

Two important observations were made in this study of magnetite [101]. Firstly, the $[Fe_2]O_4$ spinel framework remained intact during the lithiation process, and secondly, the interstitial space of 8a tetrahedra and 16c octahedra provided a three-

CosMX Exhibit 1008, Page 330 of 633

dimensional percolation pathway for the inserted lithium ions. Similar behavior was observed for Mn_3O_4 and Co_3O_4. For Fe_3O_4 and Co_3O_4, the cubic symmetry of the spinel is maintained on lithiation. By contrast, Mn_3O_4 has tetragonal symmetry with a *c/a* ratio of 1.16. The crystallographic distortion arises because Jahn–Teller (d^4) Mn^{3+} ions reside on the octahedral B sites of the structure. Lithium insertion into Mn_3O_4 lowers the concentration of Mn^{3+} ions on the B sites and, consequently, reduces the extent of the Jahn–Teller distortion. Therefore, in $(LiMn)_{16c}[Mn_{16d}]O_4$ the *c/a* ratio is only 1.05 [102, 103].

Reaction of Fe_3O_4, Mn_3O_4 and Co_3O_4 with an excess of n-butyl lithium results in further lithiation of the oxide particles, but with a concomitant extrusion of very finely divided transition metal from the rock salt structure. Highly lithiated iron oxide particles are pyrophoric if exposed to air [100].

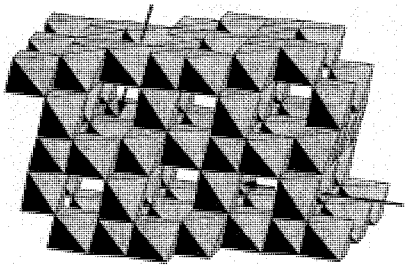


Figure 11. The $[B_2]X_4$ framework of an $A[B]_2X_4$ spinel, e.g. $\lambda-MnO_2$ with three dimensional pathways for lithium-ion transport. (The direction of transport perpendicular to the plane of the paper has not been marked by an arrow).

Unfortunately, Fe_3O_4, Co_3O_4, and Mn_3O_4 are unattractive insertion electrodes because the large and bulky transition metal ions in the interstitial space of the $[B_2]O_4$ spinel framework impede the diffusion of the lithium ions. Recent attention has therefore been placed on the lithium spinels $Li[B_2]O_4$, which provide $[B_2]O_4$ host structures that allow unrestricted diffusion of lithium ions through a three-dimensional network of face-shared 8a–16c–8a–16c–8a etc tetrahedra and octahedra. The structure of the ideal $[B_2]O_4$ framework of an $A[B_2]O_4$ spinel is shown in Fig. 11.

1.4.2 Li–Mn–O Spinels

The lithium spinels, $Li[B_2]O_4$, are particularly attractive electrode materials because they offer the possibility of both lithium insertion (e.g., $Li_{1+x}[Mn_2]O_4$ [102]), and lithium extraction ($Li_{1-x}[Mn_2]O_4$ [105]), thereby extending the working capacity of the electrode. Furthermore, because the oxidation potential of the spinel electrode depends on the metal cation on the octahedral B sites, it is possible to tailor the voltage of a lithium/spinel oxide cell. In the $[B_2]O_4$ spinel framework, the B cations are distributed in alternate layers between the cubic-close packed oxygen planes in a 3:1 ratio. Therefore, enough B cations are available in every layer to provide, on delithiation, a sufficiently high binding energy to impart stability to the close-packed oxygen array. Lithium–manganese–oxide spinels, in particular, have been extensively studied for lithium batteries because they are relatively inexpensive materials, and because they offer a high oxidation potential (3–4 V vs. Li).

The composition of lithium–manganese–oxide spinel electrodes that are of interest for lithium battery applications fall within the $Li[Mn_2]O_4$ – $Li_4Mn_5O_{12}$ – $Li_2[Mn_4]O_9$ tie-triangle of the Li–Mn–O

CosMX Exhibit 1008, Page 331 of 633

phase diagram (Fig. 12) [106–109]. The spinels can be classified according to two broad categories: (i) stoichiometric spinels $Li_{1+x}Mn_{2-x}O_4$ ($0 \leq x \leq 0.33$); (ii) non stoichiometric spinels that can either be "oxygen rich" (e.g., $LiMn_2O_{4+\delta}$ ($0 \leq \delta \leq 0.5$) or, alternatively, $Li_{1-\delta}Mn_{2-2\delta}O_4$ ($0 \leq \delta \leq 0.11$)), or "oxygen-deficient" (e.g., $LiMn_2O_{4-\delta}$ ($0 < \delta \leq 0.14$)).

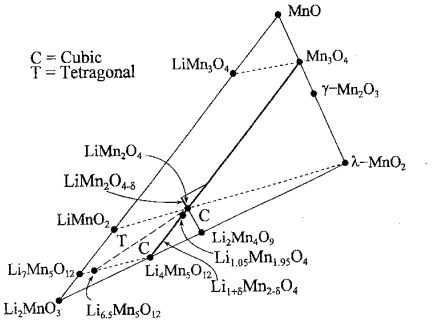


Figure 12. A schematic representation of a section of the Li–Mn–O phase diagram (adapted from Ref. [130]).

1.4.2.1 $Li[Mn_2]O_4$

$Li[Mn_2]O_4$ is an end member of the stoichiometric spinel system $Li_{1+x}Mn_{2-x}O_4$ ($x = 0$); it has cubic symmetry (Fd3m). Lithium insertion into $Li[Mn_2]O_4$ causes a cooperative displacement of the tetrahedral (8a) lithium ions into neighboring octahedral (16c) sites. The inserted Li ions fill the remaining empty octahedral (16c) sites to generate the rock salt composition $Li_2[Mn_2]O_4$ [102]. Mosbah and co-workers have reported that, in $Li_2[Mn_2]O_4$, the lithium ions fill the octahedral 16c sites [110], whereas David and co-workers found evidence that the lithium ions are distributed over both the 16c and tetrahedral 8a sites [111]. Reduction of the manganese ions from the average valency of 3.5 in $Li[Mn_2]O_4$ to 3.0 in $Li_2[Mn_2]O_4$ induces a crystallographic Jahn–Teller (tetragonal) distortion in the spinel structure, which is a consequence of the increased number of Mn^{3+} (d^4) ions on the octahedral 16d sites. The discharge reaction, which progresses from the particle surface into the bulk, occurs at 3 V versus metallic lithium. For the range $1 \leq x \leq 2$ in $Li_x[Mn_2]O_4$, the electrode consists of two phases: lithiated $Li_2[Mn_2]O_4$ spinel particles with tetragonal symmetry on the surface and unlithiated $Li[Mn_2]O_4$ spinel particles with cubic symmetry in the bulk. The Jahn–Teller distortion is severe; it causes a 16 percent increase in the *c/a* ratio, which is sufficient to fracture the spinel particles at the surface [43]. Because of the loss of particle-to-particle contact in the electrode, $Li_x[Mn_2]O_4$ electrodes cannot be effectively used in rechargeable 3 V lithium cells over the range $1 \leq x \leq 2$. This result highlights the importance of designing insertion electrodes that do not undergo major structural distortions during the insertion and extraction of lithium [43]. Lithiation beyond $x = 2$ in $Li_x[Mn_2]O_4$ is possible [112, 113]; reaction of $Li[Mn_2]O_4$ with an excess of n-butyl lithium at 50 °C results in a layered Li_2MnO_2 ($Li_4Mn_2O_4$) structure with a hexagonal close-packed oxygen array and with Mn^{2+} in alternate octahedral-site basal planes; the lithium ions occupy tetrahedral sites in the other basal planes [112]. Removal of lithium from Li_2MnO_2 by chemical treatment regenerates the $[Mn_2]O_4$ spinel framework [6].

By contrast, lithium extraction from the tetrahedral sites in $Li[Mn_2]O_4$, i.e., for $0 < x < 1$ in $Li_x[Mn_2]O_4$, takes place at 4 V, with retention of the cubic symmetry of the spinel structure [105, 114, 120]. It is difficult to extract all the lithium electrochemically from $Li[Mn_2]O_4$, at least at practical voltages, without causing decomposi-

CosMX Exhibit 1008, Page 332 of 633

tion of the highly delithiated $Li_x[Mn_2]O_4$ electrodes in the presence of the organic electrolyte. During extraction, the $Li[Mn_2]O_4$ unit cell volume contracts isotropically by 7 percent, to the composition $Li_{0.27}[Mn_2]O_4$ [114]. A small and subtle phase transition occurs at the composition $Li_{0.5}[Mn_2]O_4$, which is associated with the ordering of lithium on one-half of the 8a tetrahedral sites [103]; the transition is gentle and does not damage the structural integrity of the electrode during cycling.

Prior to the evaluation of $Li[Mn_2]O_4$ as a rechargeable cathode material, the ideal spinel framework $[Mn_2]O_4$, (commonly referred to as $\lambda - MnO_2$, after Hunter) was chemically synthesized by acid digestion of $Li[Mn_2]O_4$ [121]. The formation of $\lambda - MnO_2$ by chemical methods differs from the electrochemical reaction because it dissolves 25 percent of the Mn cations from the original spinel framework:

$$2Li[Mn_2]O_4 \rightarrow 3\lambda - MnO_2 + MnO + Li_2O \quad (8)$$

There are distinct differences in the electrochemical behavior of lithium cells constructed with $\lambda - MnO_2$ electrodes prepared by acid treatment and those containing $Li[Mn_2]O_4$ electrodes [120].Cells with $\lambda - MnO_2$ electrodes show an essentially featureless voltage profile at 4V on the initial discharge; on subsequent cycling, the cells show a profile more consistent with that expected from an $Li[Mn_2]O_4$ electrode.

Although $Li_x[Mn_2]O_4$ appears to have the ideal structure for an insertion electrode in 4V lithium cells, the cells lose capacity slowly when operated over the high voltage range. Several reasons have been given for the capacity fade:

(i) Dissolution of the spinel framework at the end of discharge when the concentration of Mn^{3+} ions is at its highest. Dissolution is believed to occur at the particle surface of the spinel by the disproportionation reaction [6, 43, 107, 122]:

$$2Mn^{3+}_{(solid)} \rightarrow Mn^{4+}_{(solid)} + Mn^{2+}_{(solution)} \quad (9)$$

in which the Mn^{2+} ion is the soluble species.

(ii) The onset of the Jahn–Teller distortion at the end of discharge on the surface of a few particles that may reach an overall composition of $Li_{1+\delta}[Mn_2]O_4$. This occurs because, under dynamic conditions, the system is never in true thermodynamic equilibrium [43, 107]. Even a very small ä would be sufficient to cause structural deterioration because the phase transition from cubic to tetragonal symmetry is first order.

(iii) An instability of highly delithiated (i.e., highly oxidizing) spinel particles in the organic electrolyte at the top of charge [107, 116, 123].

It is possible that all three phenomena contribute to the capacity loss of 4V $Li_x[Mn_2]O_4$ electrodes. Nonetheless, all three can be at least partly circumvented by slightly modifying the composition of the spinel electrode. For example, cell performance can be improved by increasing the amount of lithium in the spinel structure [107, 123, 130] and, in particular, by substituting a small amount of manganese on the B sites with lithium [107], which drives the composition a small way down the stoichiometric spinel tie-line, towards

CosMX Exhibit 1008, Page 333 of 633

$Li_4Mn_5O_{12}$ (Fig. 12). Capacity loss with cycling has been considerably reduced by using $Li_{1+x}Mn_{2-x}O_4$ spinel electrodes with $0.03 \leq x \leq 0.05$ [107, 131]. However, in these materials improved stability of the spinel electrode is gained at the expense of capacity; $Li[Mn_2]O_4$ offers a theoretical capacity of 148 $mAh\,g^{-1}$ at 4V, whereas $Li_{1.05}Mn_{1.95}O_4$ offers 128 $mAh\,g^{-1}$. The manganese ions in these lithium-substituted spinels have an average valency slightly above 3.5; in $Li_{1.05}Mn_{1.95}O_4$, it is 3.56. Therefore, the increased concentration of Mn^{4+} ions in the discharged electrode combats both the disproportionation reaction (point (i) above) and the onset of the Jahn–Teller effect (point (ii)), which would occur only in overdischarged electrodes when the average Mn oxidation state reaches 3.5. Furthermore, fully charged lithium-substituted spinels (i.e., in which all the Mn ions have been oxidized to Mn^{4+}) always contain residual lithium ions, which cannot be extracted from the structure; these residual lithium ions provide additional stability to the spinel and combat the instability at the top of charge (point (iii)). Lithium-substituted spinels, $Li_{1+x}Mn_{2-x}O_4$, are prepared at a lower temperature than $Li[Mn_2]O_4$, because they are less stable to heat treatment [107, 130, 132]. Substitution of some oxygen by fluorine in these lithium-substituted spinels, $Li_{1-x}Mn_{2-x}O_{4-y}F_y$ ($0<y<0.5$) lowers the dissolution rate of manganese in organic electrolytes, which improves the storage performance of cells at elevated temperature (~50 °C) [133, 134]. The substitution of fluorine for oxygen reduces the manganese oxidation state; the amount of lithium in the structure (i.e. the value of x) must therefore be increased slightly to compensate for this effect and to ensure that the average oxidation state of the manganese ions at the end of discharge at 4 V remains marginally above 3.5.

Cations other than lithium (such as the divalent or trivalent cations Mg, Zn, Co, Ni, and Cr) can also be substituted for Mn to stabilize the $Li[Mn_2]O_4$ structure [107, 117, 135–139]. Some cations with an octahedral-site preference (such as Ni^{2+}, Co^{3+}, and Cr^{3+}) are expected to occupy the 16d sites of the spinel with Mn, whereas cations with a strong tetrahedral-site preference (such as Zn^{2+}) are expected to occupy the 8a sites and to dislodge corresponding lithium ions into the 16d sites. In cases where Mn is substituted by transition metal ions (such as Co, Ni, and Cr) that can partake in the electrochemical reaction, voltage plateaus between 4 and 5V have been observed [135, 136].

1.4.2.2 $Li_4Mn_5O_{12}$

The compound $Li_4Mn_5O_{12}$ is an end-member of the stoichiometric $Li_{1+x}Mn_{2-x}O_4$ spinel system (x=0.33). In this structure, one-sixth of the manganese ions in $Li[Mn_2]O_4$ are replaced by lithium; in spinel notation, it is represented as $Li[Mn_{1.67}Li_{0.33}]O_4$ [106]. This substitution requires a charge compensation by the manganese ions. In $Li[Mn_2]O_4$ the average Mn oxidation state is 3.5, whereas in $Li_4Mn_5O_{12}$ it is 4.0. Therefore lithium cannot be electrochemically extracted from $Li_4Mn_5O_{12}$. Lithium insertion into $Li_4Mn_5O_{12}$ occurs at 3V, as in $Li_{1+\delta}[Mn_2]O_4$. However, because the manganese ions in $Li_4Mn_5O_{12}$ are tetravalent, the onset of the Jahn–Teller distortion to tetragonal symmetry occurs only late in the discharge, at the composition $Li_{6.5}Mn_5O_{12}$, when the average Mn oxidation state reaches 3.5 [106]. End of discharge is reached at the rock salt composition $Li_7Mn_5O_{12}$. Moreover, the extent of

CosMX Exhibit 1008, Page 334 of 633

the Jahn–Teller effect is not as severe in $Li_7Mn_5O_{12}$ (c/a=1.106) [106] as it is in $Li_2[Mn_2]O_4$ (c/a= 1.16) [102]. Therefore $Li_4Mn_5O_{12}$ provides a more stable 3 V insertion electrode than $Li[Mn_2]O_4$. This demonstrates that the Li–Mn–O system can be used for designing electrode materials for either 3 V or 4 V lithium batteries. $Li_4Mn_5O_{12}$ has a theoretical capacity of 163 mAh g^{-1}, of which 130–140 mAh g^{-1} can be readily accessed in practice [106]. However, it is difficult to synthesize fully oxidized $Li_4Mn_5O_{12}$ products; they tend to be oxygen-deficient, with the manganese ions having an oxidation state slightly below 4 [106, 108, 140, 141].

1.4.2.3 $Li[Mn_{1.5}Ni_{0.5}]O_4$

Experience with $Li_4Mn_5O_{12}$ showed that 3V Li–Mn–O spinel structures can be stabilized (with respect to lithium insertion/extraction) by cation substitution to increase the manganese oxidation state in fully charged electrodes to Mn^{4+}. This concept was recently extended to the spinel $Li[Mn_{1.5}Ni_{0.5}]O_4$ in which all the manganese ions are tetravalent if the structure is synthesized with Ni^{2+} in the spinel framework [142]. Lithium is inserted into $Li[Mn_{1.5}Ni_{0.5}]O_4$ in a two-phase reaction at 3V until the composition of the final lithiated product reaches the rock salt stoichiometry $Li_2[Mn_{1.5}Ni_{0.5}]O_4$. Despite the fact that lithium insertion causes the average oxidation state of Mn to fall below 3.5, to reach 3.3 in the fully lithiated product, no evidence of a tetragonally distorted phase could be detected [142]. However, unlike $Li_4Mn_5O_{12}$, in which lithium extraction is not possible, lithium can be extracted from $Li[Mn_{1.5}Ni_{0.5}]O_4$ at 4.7V, because it is possible to oxidize Ni^{2+} to Ni^{4+} [137].

1.4.2.4 Oxygen-Rich and Oxygen Deficient Spinels, $LiMn_2O_{4\pm\delta}$

Varying synthesis conditions, particularly the nature of the precursor materials, the temperature, and dwell time, allows one to vary the oxygen content in $LiMn_2O_{4\pm\delta}$ spinels [108, 143–145]. Spinels with an Li:Mn ratio of 1:2 synthesized by solid state reaction of $MnCO_3$ and Li_2CO_3 at moderate temperatures (300–400°C) tend to be oxygen rich; the limiting composition is $Li_2Mn_4O_9$,which is a defect spinel with the cation arrangement $(Li_{0.89}\square_{0.11})_{8a}$ $[Mn_{1.78}\square_{0.22}]O_4$. In $Li_2Mn_4O_9$, all the manganese ions are tetravalent. Lithium insertion into $Li_2Mn_4O_9$ on the initial discharge of Li/$Li_2Mn_4O_9$ cells occurs at 3 V. Subsequent cycling shows processes at 3 V and 4 V, consistent with lithium insertion into, and extraction from, octahedral and tetrahedral sites, respectively [143]. The onset of the Jahn–Teller distortion occurs late in the discharge, at the composition $Li_4Mn_4O_9$, when the average manganese oxidation state reaches 3.5 (c/a= 1.14) [106].

If $Li[Mn_2]O_4$ is heated above ~780 °C, oxygen-deficient spinels $LiMn_2O_{4-\delta}$ ($\delta \leq 0.14$) are produced [132, 144, 145]. The loss of oxygen lowers the manganese oxidation state below 3.5 and triggers a mild Jahn–Teller distortion; the c/a ratio in the tetragonal $LiMn_2O_{4-\delta}$ phase varies between 1.02 and 1.07.

1.4.2.5 Thin-Film $LiMn_2O_4$

When $LiMn_2O_4$ electrodes are deposited as thin films on a platinum substrate, either by electron-beam evaporation or radio-frequency (rf) sputtering, structures are sometimes formed that exhibit unusual electrochemical behavior [146, 147]. Such electrodes have been evaluated in solid-

CosMX Exhibit 1008, Page 335 of 633

state electrochemical cells that employ a metallic lithium anode and a glassy lithium-phosphorus-oxynitride (Lipon) solid electrolyte. The electrolyte is stable to 5.5 V. Li/Lipon/$LiMn_2O_4$ cells show voltage plateaus at 5 V and sometimes at 4.6 V, in addition to the plateaus at 4 V and 3 V that are expected for a standard Li/$Li[Mn_2]O_4$ cell. When the cells are allowed to relax intermittently during discharge and charge, open-circuit voltage measurements have shown that one lithium is inserted into thin-film $LiMn_2O_4$ electrodes at 3V, consistently with standard $Li[Mn_2]O_4$ bulk electrodes. However, major differences in the electrochemical profile are observed when lithium is extracted from thin-film $LiMn_2O_4$ electrodes above 4 V. The unusual electrochemical behavior of these electrodes has been interpreted in terms of a spinel-type structure in which a fraction of the manganese ions are located outside the $[B_2]O_4$ spinel framework [148]. Such a situation could arise if two crystallographically independent spinels, one defined by the conventional spinel notation $Li_{8a}[Mn_2]_{16d}O_4$, and the other by a second, alternative notation $Li_{8b}[Mn_2]_{16c}O_4$, are deposited as an intergrown structure [149]. The fabrication of a spinel intergrowth seems feasible because, during sputter deposition, the $LiMn_2O_4$ product is constructed atom by atom, or fragment by fragment, on the substrate. The presence of Mn on both sets of octahedral sites destabilizes the tetrahedral sites and displaces at least some of the tetrahedral-site lithium ions into neighboring octahedral sites.

Lithium extraction from thin-film $LiMn_2O_4$ electrodes takes place in several stages. It has been proposed that lithium is first extracted from the tetrahedral sites at approximately 4 V. Second, because the manganese ions in these thin-film $LiMn_2O_4$ electrodes appear to be located predominantly on the 16d set of octahedral sites, it is energetically more favorable for the lithium to be extracted first from the 16c set of octahedral sites into a more energetically accessible and less restricted 16c–8a–16c–8a (etc) pathway, rather than the alternative 16d–8b–16d–8b (etc) pathway; this process occurs at 4.6 V. Third, the reaction at 5 V corresponds to the removal of the residual lithium ions from 16d octahedral sites. The electrochemical reactions occurring at 4.6 and 5 V have been proposed to involve the formation of (i) defect-spinel structures that contain Mn^{2+} ions on tetrahedral sites and Mn^{3+} and Mn^{4+} ions on octahedral sites, and ii) defect rock salt structures with only Mn^{3+} and Mn^{4+} ions on octahedral sites [148].

Thin film $LiMn_2O_4$ electrodes produced by rf-sputtering that show both the 4.6 V and 5 V plateaus on the initial charge to 5.3 V do not show these plateaus on the subsequent discharge [148]. Instead, cycling of $Li_xMn_2O_4$ electrodes ($0 \leq x \leq 1$) is characterized by a sloping voltage profile between 5 V and 3 V. This result is consistent with the fact that spinel-type phases containing Mn^{2+} ions are unlikely to be regenerated over this compositional range by insertion of lithium into a defect MnO_2 rock salt structure. The shape of the profile, which is indicative of single-phase reactions associated with the occupation of tetrahedral and octahedral sites, depends on the final distribution of the Mn ions over the 16c and 16d octahedral sites of the MnO_2 phase.

1.4.3 Li–V–O Spinels

1.4.3.1 The Normal Spinel, $Li[V_2]O_4$

$Li[V_2]O_4$ has a spinel structure with the

CosMX Exhibit 1008, Page 336 of 633

ideal distribution of lithium and vanadium on the tetrahedral (8a) and octahedral (16d) sites [150]. However, although the $[V_2]O_4$ spinel framework remains intact on lithiation to the rock salt stoichiometry $Li[V_2]O_4$ [151, 152], it is unstable to delithiation [76, 78]. When approximately one-third of the lithium ions have been extracted from the structure (i.e., when x reaches ~0.3 in $Li_{1-x}V_2O_4$), vanadium ions migrate from the vanadium-rich layer into adjacent ones. This process destroys the $[V_2]O_4$ spinel framework and the ordered three-dimensional pathway for lithium ion transport. The product has a defect rock salt structure, similar to that formed when lithium is removed from layered $LiVO_2$ electrodes [74]. The instability of vanadium oxide structures, which arises because of the inherent ability for V^{4+} to disproportionate into V^{5+} and V^{3+}, poses problems for designing close-packed vanadium oxide materials that will be stable to lithiation and delithiation over a wide compositional range.

1.4.3.2 The Inverse Spinels, V[LiM]O_4 (M=Ni Co)

It is worthwhile to point out that lithium extraction from inverse spinels $V[LiM]O_4$, such as $V[LiNi]O_4$ and $V[LiCo]O_4$ takes place at high voltage, typically between 4 and 5V [153]. Lithium is extracted from the octahedral 16d sites of these spinels with a concomitant oxidation of the divalent nickel or cobalt ions. From a structural point of view, this can be readily understood because lithium must be dislodged from the 16d octahedral sites, which are of low-energy, into neighboring energetically unfavorable 8b tetrahedra, which share all four faces with 16d sites that are occupied by nickel or cobalt and by lithium. Lithium extraction reactions are reversible only for low values of x in $V[Li_{1-x}Co]O_4$; $V[LiNi]O_4$ appears to be unstable to lithium extraction [153].

1.4.4 Li–Co–O Spinels

1.4.4.1 $Li[Co_2]O_4$ and $Li_2Co_2O_4$ (LT-$LiCoO_2$)

When $LiCoO_2$ is prepared at moderate temperature, 400 °C, rather than at 850 °C, the product, often referred to as LT-$LiCoO_2$ (LT= "low temperature"), displays electrochemical properties significantly different from those of the high-temperature layered $LiCoO_2$ analogue [154, 155]. Despite a structural anomaly that makes it difficult to distinguish by X-ray or neutron diffraction techniques between an ideal layered $LiMO_2$ structure and an ideal lithiated spinel $Li_2[M_2]O_4$ structure with cubic close-packed oxygen arrays [156], high-resolution neutron diffraction data have shown that LT-$LiCoO_2$ materials tend to have structures with a cation distribution which is intermediate between that of ideal layered and ideal spinel structures [157–159]. Therefore, LT-$LiCoO_2$ compounds have structures similar to those of layered $LiMnO_2$ compounds [59] and nickel-rich $Li_{1-x}Ni_{1+x}O_2$ compounds [50] in which some Mn or Ni ions reside in the lithium layers. These structures tend to show poor electrochemical behavior, both in terms of delivered capacity and cycle life. LT-$LiCoO_2$ is no exception; although an appreciable amount of lithium can be extracted on the initial charge cycle, the corresponding capacity is not delivered on the subsequent discharge [154, 155]. Electrodes that are derived from nickel-substituted LT-$LiCo_{1-x}Ni_xO_2$ compounds($0< x \leq 0.2$) show a slightly enhanced capacity and structural

CosMX Exhibit 1008, Page 337 of 633

stability on cycling compared to LT-$LiCoO_2$ products [160]. Acid treatment of LT-$LiCoO_2$ generates the ideal spinel $Li[Co_2]O_4$ structure [43], according to the reaction:

$$3LT\text{-}LiCoO_2 \rightarrow Li[Co_2]O_4 + CoO + Li_2O \quad (10)$$

Note that this reaction is similar to that used by Hunter in his preparation of $\lambda - MnO_2$ in acid medium at room temperature [121]:

$$2Li[Mn_2]O_4 \rightarrow 3\ddot{e} - MnO_2 + MnO + Li_2O \quad (11)$$

Electrodes that are prepared from acid-leached LT-$LiCo_{1-x}Ni_xO_2$ compounds ($0 < x \leq 0.2$) show significantly enhanced electrochemical behavior over the parent LT-$LiCo_{1-x}Ni_xO_2$ structure. The improved performance has been attributed to the formation of compounds with a composition and cation arrangement close to the ideal $Li[B_2]O_4$ spinel structure (B = Co, Ni) [62]. These spinel-type structures have cubic symmetry, which is maintained on lithiation; the unit cells expand and contract by only 0.2 percent during lithium insertion and extraction.

1.4.5 Li–Ti–O spinels

Lithium–titanium–oxide spinels provide a relatively low voltage of 1.5V vs. lithium. They are, therefore, of interest as possible negative electrode materials for lithium-ion cells [161–163]; they can be coupled, for example, to $Li[Mn_2]O_4$ (4V vs. Li) to yield a 2.5V lithium-ion cell, or to Li_xMnO_2 (3V vs. Li) to yield a 1.5V lithium-ion cell. Although these cells have a voltage lower than that of commercial $Li_xC/Li_{1-x}CoO_2$ cells (3.5V), they are attractive from a safety point of view because the titanium spinel operates at a potential significantly far away from that of metallic lithium.

1.4.5.1 $Li[Ti_2]O_4$ and $Li_4Ti_5O_{12}$

In a study of titanium oxides, Murphy demonstrated that the spinel $Li[Ti_2]O_4$ can be chemically lithiated to the composition $Li_2[Ti_2]O_4$, but that the $[Ti_2]O_4$ spinel framework is unstable to chemical delithiation [164, 165]. Colbow and coworkers investigated the electrochemical properties of $Li[Ti_2]O_4$ and $Li_4Ti_5O_{12}$ ($Li[Li_{1/3}Ti_{5/3}]O_4$, in spinel notation) in lithium cells. Both materials can accommodate one additional lithium ion per spinel unit to form the rock salt compositions $Li_2[Ti_2]O_4$ and $Li_2[Li_{1/3}Ti_{5/3}]O_4$, respectively [166]. Because lithium insertion is accompanied by a cooperative displacement of the lithium ions from tetrahedral (8a) sites to octahedral (16c) sites, the electrochemical discharge involves a two-phase reaction; the electrode consists of an unreacted spinel phase and the lithiated-spinel (rock salt) phase. The reaction results in a flat voltage plateau at 1.5V. For the $Li[Ti_2]O_4$-to-$Li_2[Ti_2]O_4$ transition, the cubic lattice parameter decreases slightly from 8.416 Å to 8.380 Å, whereas for the transition from $Li_4Ti_5O_{12}$ ($Li[Li_{1/3}Ti_{5/3}]O_4$) to $Li_7Ti_5O_{12}$ ($Li_2[Li_{1/3}Ti_{5/3}]O_4$), the cubic lattice parameter increases from 8.36 to 8.37Å [164, 165]. $Li_4Ti_5O_{12}$ has been the preferred electrode material because it is much easier to synthesize than $Li[Ti_2]O_4$.

Although $Li[Ti_2]O_4$ and $Li_4Ti_5O_{12}$ have low theoretical capacities (161 and 175 mAh g^{-1}, respectively), they have excellent structural properties for an insertion electrode. The spinel structures are excep-

CosMX Exhibit 1008, Page 338 of 633

tionally stable to lithiation/delithiation; the stability can be attributed to the retention of the cubic $[Li_xTi_{2-x}]O_4$ (x=0 or 1/3) spinel framework and to the minimal isotropic expansion and contraction (<1 percent) of the unit cell that occurs during discharge and charge [43].

1.5 Concluding Remarks

The research that has been undertaken on numerous transition metal oxide electrode structures for lithium batteries has clearly demonstrated that the long-term performance of insertion electrodes is critically dependent on the structural stability of the transition metal oxide to lithium insertion and extraction. Much progress has been made in identifying the most promising materials, and in developing methods to tailor both composition and structure to improve their stability to long-term electrochemical cycling. Most of the current knowledge comes from crystalline materials, from which important structural information has been gathered. Many more improvements in the quality and performance of electrode materials can be expected in the future. Materials that have not yet been thoroughly exploited are those with composite structures and those with "low crystallinity" or short range order. From a materials standpoint, they could provide a direction which may lead to the further improvement of the electrochemical and physical properties of metal oxide insertion electrodes, for example, higher rechargeable capacities and greater tolerance to deep discharge and charge reactions.

Acknowledgments. Dr. M. F. Mansuetto is thanked for his assistance with the computer drawings of the various structures. Support from the U.S. Department of Energys Advanced Battery Research Program, Chemical Sciences Division, Office of Basic Energy Sciences, is gratefully acknowledged.

1.6 References

[1] G. Pistoia (Ed.), *Lithium Batteries, New Materials, Developments and Perspectives* Industrial Chemistry Library, Volume 5, Elsevier, Amsterdam, **1994**.

[2] S. Megahed, B. Scrosati, *J. Power Sources* **1994**, *51*, 79.

[3] D. W. Murphy, *Adv. Synth. React. Solids*, **1991**, *1*, 237.

[4] T. A. Hewston, B.L. Chamberland, *J.Phys. Chem. Solids* **1987**, *48*, 97.

[5] M. S. Whittingham, *Prog. Solid State Chem.* **1978**, *12*, 41.

[6] M. M. Thackeray, *Prog. Batt. and Batt. Mater.* **1995**, *14*, 1.

[7] P. Strobel, C. Mouget, *Mater. Res. Bull.* **1993**, *28*, 93.

[8] F. le Cras, S. Rohs, M. Ann, P.Strobel, *J. Power Sources* **1995**, *54*, 319.

[9] F. le Roux, D. Guyomard, Y. Piffard, *Solid State Ionics* **1995**, *80*, 307.

[10] R. Chen, P. Zavalij, M. S. Whittingham, *Chem. Mater.* **1996**, *8*, 1275.

[11] H.-K. Park, W. H. Smyrl, M. D. Ward, *J. Electrochem.* Soc. **1995**, *142*, 1068.

[12] K. S. Nanjundaswamy, A. K. Padhi, J. B. Goodenough, S. Okada, H.Ohtsuka, H. Arai, J.Yamaki, *Solid State Ionics*, **1996**, *92*, 1.

[13] Y. Idota, M. Mishima, Y. Miyaki, T. Kubota, T. Miyasaka, Fuji Photo Film Co., Ltd, Canadian Patent Application 2 134 052, **1995**.

[14] T. Ohzuku, M. Kitagawa, K. Sawai, T. Hirai, *J. Electrochem.* Soc. **1991**, *138*, 360.

[15] M. H. Rossouw, D. C. Liles, M. M. Thackeray, W.I.F. David, S. Hull, *Mater. Res. Bull.* **1992**, *27*, 221.

[16] M. H. Rossouw, D. C. Liles, M. M. Thackeray, *Prog. Batt. Batt Mater.* **1995**, *15*, 8.

[17] C. S. Johnson, D. W. Dees, M. F. Mansuetto, M. M. Thackeray, D. R. Vissers, D. Argyriou, C.-K. Loong, L. Christensen, *J. Power Sources*, **1997**, *68*, 570.

[18] M. A. Humbert, P. Biensan, M. Broussely, A. Lecerf, A. Dollé, H. Ladhily, *J. Power Sources*

CosMX Exhibit 1008, Page 339 of 633

1993, *43-44*, 681.
[19] P. Botkowitz, P. Deniard, M. Tournoux, R. Brec, *J. Power Sources* **1993**, *43–44*, 657.
[20] P. Botkowitz, R. Brec, P. Deniard, M. Tournoux, G.Burr, *Mol. Cryst. Liq. Cryst.* **1994**, *244*, 233.
[21] W.I.F. David, P. G. Bruce, J. B. Goodenough, *J. Solid State Chem.* **1983**, *50*, 235.
[22] D. W. Murphy, F. J. Di Salvo, J. N. Carides, J. V. Waszczak, *Mater. Res. Bull.* **1978**, *13*, 1395.
[23] M. M. Thackeray, A. de Kock, L. A. de Picciotto, G. Pistoia, J. *Power Sources* **1989**, *26*, 355.
[24] W.I.F. David, M. M. Thackeray, P. G. Bruce, J. B. Goodenough, *Mater. Res. Bull.* **1984**, *19*, 99.
[25] Y. Chabre, J. Pannetier, *Prog. Solid State Chem.* **1995**, *23*, 1.
[26] H. Ikeda, S. Narukawa, *J. Power Sources* **1983**, *9*, 329.
[27] T. Ohzuku, M. Kitagawa, T. Hirai, *J. Electrochem. Soc.* **1989**, *136*, 3169.
[28] T. Ohzuku, M. Kitagawa, T. Hirai, *J. Electrochem. Soc.* **1990**, *137*, 40.
[29] T. Nohma, T. Saito, N. Furukawa, H. Ikeda, *J. Power Sources* **1989**, *26*, 389.
[30] T. Nohma, Y. Yamamoto, K. Nishio, I. Nakane, N. Furukawa, J. *Power Sources* **1990**, *32*, 373 .
[31] T. Nohma, Y. Yamamoto, I. Nakane, N. Furukawa, *J. Power Sources* **1992**, *39*, 51.
[32] M. M. Thackeray, M. H. Rossouw, A. de Kock, A. P. de la Harpe, R. J. Gummow, K.Pearce, D. C.Liles, *J. Power Sources* **1993**, *43–44*, 289.
[33] Y. Shao, S. Hackney, *Ext. Abstr. 189th Electrochem. Soc. Meeting, Los Angeles, (5–10 May)* **1996**, p. 58.
[34] M. M. Thackeray, M. H. Rossouw, R. J. Gummow, D. C. Liles, K. Pearce, A. de Kock, W.I.F. David, S. Hull, *Electrochim. Acta* **1993**, *38*, 1259.
[35] M. M. Doeff, T. J. Richardson, L. Kepley, *J. Electrochem. Soc.* **1996**, *143*, 2507.
[36] K. Mizushima, P. C. Jones, P. J. Wiseman, J. B. Goodenough, *Mater. Res. Bull.* **1980**, *15*, 783.
[37] T. Ohzuku, A. Ueda, N. Nagayama, Y. Iwakoshi, H. Komori, *Electrochim. Acta* **1993**, *38*, 1159.
[38] T. Ohzuku, A. Ueda, *J. Electrochem. Soc.* **1994**, *141*, 2972.
[39] T. Ohzuku, A. Ueda, *Solid State Ionics* **1994**, *69*, 201.
[40] J. N. Reimers, J. R. Dahn, *J. Electrochem. Soc.* **1992**, *139*, 2091.
[41] G. G. Amatucci, J. M. Tarascon, L. C. Klein, *J.Electrochem. Soc.* **1996**, *143*, 1114.
[42] J. B. Bates, personal communication, **1996**.
[43] M. M. Thackeray, *J. Electrochem. Soc.* **1995**, *142*, 2558.
[44] C. Delmas in Ref. [1], p. 457.
[45] J. B. Goodenough, D. G. Wickham, W.J. Croft, *J. Phys. Chem. Solids* **1958**, *5*, 107.
[46] A. Rougier, P. Gravereau, C. Delmas, *J. Electrochem. Soc.* **1996**, *143*, 1168.
[47] H. Arai, S. Okada, H. Ohtsuka, M. Ichimura, J. Yamaki, *Solid State Ionics* **1995**, *80*, 261.
[48] G. Dutta, A. Manthiram, J. B. Goodenough, J.-C. Grenier, *J. Solid State Chem.* **1992**, *96*, 123.
[49] J. Morales, C. Prez-Vicente, J. L. Tirado, *Mater. Res. Bull.*, **1990**, *25*, 623.
[50] T. Ohzuku, A. Ueda, M. Nagayama, *J. Electrochem. Soc.* **1993**, *140*, 1862.
[51] W. Li, J. N. Reimers, J. R. Dahn, *Solid State Ionics* **1993**, *67*, 123.
[52] T. Ohzuku in Ref. [1], p. 239.
[53] W. Li, J. C. Currie, *J. Electrochem. Soc.* **1997**, *144*, 2773.
[54] T. Ohzuku, A. Ueda, M. Kouguchi, *J. Electrochem. Soc.* **1995**, *142*, 4033.
[55] Q. Zhong, U. von Sacken, *J. Power Sources* **1995**, *43–44*, 221.
[56] E. Rossen, C.D.W. Jones, J. R. Dahn, *Solid State Ionics* **1992**, *57*, 311.
[57] T. Ohzuku, H. Fukuda, T. Hirai, *Chem. Express* **1987**, *2*, 543.
[58] M. H. Rossouw, D. C. Liles, M.M. Thackeray, *J. Solid State Chem.* **1993**, *104*, 464.
[59] A. R. Armstrong, P. G. Bruce, *Nature (London)* **1996**, *381*, 499.
[60] C. Delmas, F. Capitaine, *Ext. Abstr. II-B-33, 8th Int. Meeting on Lithium Batteries, Nagoya, Japan, June 16–21*, **1996**, p. 470.
[61] F. Capitaine, P. Gravereau, C. Delmas, *Solid State Ionics* **1996**, *89*, 197.
[62] R. J. Gummow, M. M. Thackeray, *J. Electrochem. Soc.* **1993**, *140*, 3365.
[63] M. H. Rossouw, M. M. Thackeray, *Mater. Res. Bull.* **1991**, *26*, 463.
[64] F. Lubin, PhD Thesis, Institut National des Sciences Appliquées de Rennes, France, **1991**.
[65] F. Lubin, A. Lecerf, M. Broussely, J. Labat, *J. Power Sources* **1991**, *34*, 161.
[66] R. Hoppe, G. Brachtel, M. Jansen, *Z. Anorg.*

CosMX Exhibit 1008, Page 340 of 633

Allg. Chem. **1975**, *417*, 1.
[67] I. J. Davidson, R. S. McMillan, J. J. Murray, J. E. Greedan, *J. Power Sources* **1995**, *54*, 232.
[68] R. J. Gummow, D. C. Liles, M. M. Thackeray, *Mater. Res. Bull.* **1993**, *28*, 1249.
[69] T. Ohzuku, A. Ueda, T. Hirai, *Chem. Express* **1992**, *7*, 193.
[70] I. Koetschau, M. N. Richard, J. R. Dahn, J. B. Soupart, J. C. Rousche, J. *Electrochem. Soc.* **1995**, *142*, 2906.
[71] J. N. Reimers, E. W. Fuller, E. Rossen, J. R. Dahn, *J. Electrochem. Soc.* **1993**, *140*, 3396.
[72] R. J. Gummow, M. M. Thackeray, *J. Electrochem. Soc.* **1994**, *141*, 1178.
[73] R. Kanno, T. Shirane, Y. Kawamoto, Y. Takeda, M. Takano, M. Ohashu, Y. Yamaguchi, *J.Electrochem. Soc.* **1996**, *143*, 2435.
[74] L. A. de Picciotto, M. M. Thackeray, W. David, P. G. Bruce, J. B. Goodenough, *Mater. Res. Bull.* **1984**, *19*, 1497.
[75] L. A. de Picciotto, M. M. Thackeray, W. David, P. G. Bruce, J. B. Goodenough, *J. Solid State Chem.* **1987**, *67*, 285.
[76] L. A. de Picciotto, M. M. Thackeray, G. Pistoia, *Solid State Ionics* **1988**, *28-30*, 1364.
[77] L. A. de Picciotto, M. M. Thackeray, *Mater. Res. Bull.* **1985**, *20*, 187.
[78] L. A. de Picciotto, M. M. Thackeray, *Solid State Ionics* **1986**, *18–19*, 773.
[79] R. Enjalbert, J. Galy, *Acta Crystallogr.*, **1986**, *Sect.C42*, 1467.
[80] J. M. Cocciantelli, J. P. Doumerc, M. Pouchard, M. Broussely, J. Labat, *J. Power Sources* **1991**, *34*, 103.
[81] J. M. Cocciantelli, M. Ménétrier, C. Delmas, J. P. Doumerc, M. Pouchard, P. Hagenmuller, *Solid State Ionics* **1992**, *50*, 99.
[82] C. Delmas, S. Brthes, M. Ménétrier, *J. Power Sources* **1991**, *34*, 113.
[83] A.D. Wadsley, *Acta Crystallogr.*, **1957**, *10*, 261.
[84] L. A. de Picciotto, K. T. Adendorff, D. C. Liles, M. M. Thackeray, *Solid State Ionics* **1993**, *62*, 297.
[85] D. W. Murphy, P. A. Christian, F. J. di Salvo, J. N. Carides, J. V. Waszczak, *J. Electrochem. Soc.* **1981**, *128*, 2053.
[86] S. Panero, M. Pasquali, G. Pistoia, *J. Electrochem. Soc.* **1983**, *130*, 1225.
[87] G. Pistoia, S. Panero, M. Tocci, R. V. Moshtev, V. Manev, *Solid State Ionics* **1984**, *13*, 311.
[88] G. Pistoia, M. Pasquali, M. Tocci, R. V. Moshtev, V. Manev, *J. Electrochem. Soc.* **1985**, *132*, 281.
[89] G. Pistoia, M. Pasquali, G. Wang, L. Li, *J. Electrochem. Soc.* **1990**, *137*, 2365.
[90] V. Manev, A. Momchilov, A. Nassalevska, G. Pistoia, M. Pasquali, *J. Power Sources* **1995**, *54*, 501.
[91] K. West, B. Zachau-Christiansen, S. Skaarup, Y. Saidi, J. Barker, I. I. Olsen, R. Pynenburg, R. Koksbang, *J. Electrochem. Soc.* **1996**, *143*, 820.
[92] J. Kawakita, T. Miura, T. Kishi, *Ext. Abstr. II-B-61, 8th Int. Meeting on Lithium Batteries, Nagoya, Japan, June 16-21* **1996.**
[93] T. Chirayil, P. Zavalij, M. S. Whittingham, *Solid State Ionics* **1996**, *84*, 163.
[94] T. Chirayil, P. Zavalij, M. S. Whittingham, *J. Electrochem. Soc.* **1996**, *143*, L193.
[95] A. F. Wells, *Structural Inorganic Chemistry*, 4th ed., Clarendon Press, Oxford **1975**, p. 489.
[96] R. J. Hill, J. R. Craig, G. V. Gibbs, *Phys. Chem. Miner.* **1979**, *4*, 317.
[97] M. M. Thackeray, J. B. Goodenough, US Patent 4 507 371, **1985**.
[98] M. M. Thackeray, J. Coetzer, *Mater. Res. Bull.* **1981**, *16*, 591.
[99] N. A. Godshall, I. D. Raistrick, R. A. Huggins, *Mater. Res. Bull.* **1980**, *15*, 561.
[100] M. M. Thackeray, W. David, J. B. Goodenough, *J. Solid State Chem.* **1984**, *55*, 280.
[101] M. M. Thackeray, W. David, J. B. Goodenough, *Mater. Res. Bull.* **1982**, *17*, 785.
[102] M. M. Thackeray, W. David, P.G. Bruce, J. B. Goodenough, *Mater. Res. Bull.* **1983**, *18*, 461.
[103] J. B. Goodenough, M. M. Thackeray, W. David, P. G. Bruce, *Rev. Chim. Miner.* **1984**, *231*, 435.
[104] M. M. Thackeray, S. D. Baker, K. T. Adendorff, J. B. Goodenough, *Solid State Ionics* **1985**, *17*, 175.
[105] M. M. Thackeray, P. J. Johnson, L. A. de Picciotto, P. G. Bruce, J. B. Goodenough, *Mater. Res. Bull.* **1984**, *19*, 179.
[106] M. M. Thackeray, A. de Kock, M. H. Rossouw, D. C. Liles, R. Bittihn, D. Hoge, *J.Electrochem. Soc.* **1992**, *139*, 3643.
[107] R. J Gummow, A. De Kock, M. M. Thackeray, *Solid State Ionics* **1994**, *69*, 59.
[108] C. Masquelier, M. Tabuchi, K. Ado, R. Kanno, Y. Kobayashi, Y. Maki, O. Nakamura, J.B.Goodenough, *J. Solid State Chem.* **1996**, *123*, 255.
[109] P. Strobel, F. Le Cras, M. Anne, *J. Solid State*

CosMX Exhibit 1008, Page 341 of 633

Chem. **1996**, *124*, 83.
[110] A. Mosbah, A. Verbaere, M. Tournoux, *Mater. Res. Bull.* **1983**, *18*, 1375.
[111] W. David, M. M. Thackeray, L. A de Picciotto, J. B. Goodenough, *J. Solid State Chem.* **1987**, *67*, 316.
[112] W. David, J. B. Goodenough, M. M. Thackeray, M G S R. Thomas, *Rev. Chim. Minér.* **1983**, *20*, 636.
[113] R. Koksbang, J. Barker, M. Y. Saidi, K. West, B. Zachau-Christiansen, S. Skaarup, *Solid State Ionics* **1996**, *83*, 151.
[114] T. Ohzuku, M. Kitagawa, T. Hirai, *J. Electrochem. Soc.* **1990**, *137*, 769.
[115] J. M. Tarascon, E. Wang, F. K. Shokoohi, W. R. McKinnon, S. Colson, *J. Electrochem. Soc.* **1991**, *138*, 2859.
[116] D. Guyomard, J. M. Tarascon, *J. Electrochem. Soc.* **1992**, *139*, 937.
[117] A. Momchilov, V. Manev, A. Nassalevska, A. Kozawa, *J. Power Sources* **1993**, *41*, 305.
[118] G. Pistoia, D. Zane, Y. Zhang, *J. Electrochem. Soc.* **1995**, *142*, 2551.
[119] V. Manev, W. Ebner, *Ext. Abstr. FRI-02, 8th Int. Meeting on Lithium Batteries, Nagoya, Japan, June 16–21*, **1996**, p.146.
[120] M. Y. Saidi, J. Barker, R. Koksbang, *Electrochim. Acta* **1996**, *41*, 199.
[121] J. C. Hunter, *J. Solid State Chem.* **1981**, *39*, 142.
[122] D. H. YJang, Y. J. Shin, S.M. Oh, *J. Electrochem. Soc.* **1996**, *143*, 2204.
[123] D. Guyomard, J. M. Tarascon, *Solid State Ionics* **1994**, *69*, 222.
[124] J. M. Tarascon, D. Guyomard, *J. Electrochem. Soc.* **1991**, *138*, 2864.
[125] Y. Xia, H. Takeshige, H. Noguchi, M. Yoshio, *J. Power Sources* **1995**, *56*, 61.
[126] Y. Xia, H. Noguchi, M. Yoshio, *J. Solid State Chem.* **1995**, *119*, 216.
[127] Y. Gao, J. R. Dahn, *J. Electrochem. Soc.* **1996**, *143*, 100.
[128] Y. Gao, J. R. Dahn, *Solid State Ionics* **1996**, *84*, 33.
[129] Y. Xia, M. Yoshio, *J. Electrochem. Soc.* **1996**, *143*, 825.
[130] Y. Gao, J. R. Dahn, *J. Electrochem. Soc.* **1996**, *143*, 1783.
[131] M. M. Thackeray, R. J. Gummow, US Patent 5 316 872, **1995**.
[132] M. M. Thackeray, M.F. Mansuetto, D.W. Dees, D.R. Vissers, *Mater. Res. Bull.* **1996**, *31*, 133.
[133] G.G. Amatucci, I.Plitz, D.Larcher, A.Blyr, J.Shelburne, J.M.Tarascon, *Ext. Abstr. No. 84, 191st Electrochem. Soc. Meeting, Montreal*, p.97 (4–9 May), **1997**
[134] G.G. Amatucci, I.Plitz, J.Shelburne, J.M.Tarascon, *Ext. Abstr. No. 85, 191st Electrochem. Soc. Meeting, Montreal*, p.98 (4–9 May), **1997**
[135] R. Bittihn, R. Herr, D. Hoge, *J. Power Sources* **1993**, *43–44*, 223.
[136] C. Sigala, D. Guyomard, A. Verbaere, Y. Piffard, M. Tournoux, *Solid State Ionics* **1995**, 81.
[137] Q. Zhong, A. Bonakdarpour, M. Zhang, Y. Gao, J. R. Dahn, *J. Electrochem. Soc.* **1997**, *144*, 205.
[138] Y. Gao, K. Myrtle, M. Zhang, J. N. Reimers, J. R. Dahn, *Phys. Rev.* **1996**, *54 (24)*, 1.
[139] M. Wakihara, *Ext. Abstr. THU-10, 8th Int. Meeting on Lithium Batteries, Nagoya, Japan, June 16–21*, **1996**, p.136.
[140] M. M. Thackeray, A. de Kock, *Mater. Res. Bull.* **1993**, *28*, 1041.
[141] T. Takada, H. Hayakawa, E. Akiba, *J. Solid State Chem.* **1995**, *115*, 420.
[142] K. Amine, H. Tukamoto, H. Yasuda, Y. Fujita, *J. Electrochem. Soc.* **1996**, *143*, 1607.
[143] A. de Kock, M. H. Rossouw, L. A. de Picciotto, M. M. Thackeray, W. David, S. Hull, *Mater. Res. Bull.* **1990**, *25*, 657.
[144] J. M. Tarascon, W. R. McKinnon, F. Coowar, T. N. Bowmer, G. Amatucci, D. Guyomard, *J. Electrochem. Soc.* **1994**, *141*, 1421.
[145] A. Yamada, K. Miura, K. Hinokuma, M. Tanaka, *J. Electrochem. Soc.* **1995**, *142*, 2149.
[146] J. B. Bates, D. Lubben, N. J. Dudney, F. X. Hart, *J. Electrochem. Soc.* **1995**, *142*, L149.
[147] J. B. Bates, D. Lubben, N. J. Dudney, R. A. Zuhr, *Proc. Symp. Electrochem. Soc.* **1995**, *95–22*, 215.
[148] M. M. Thackeray, M. F. Mansuetto, J. B. Bates, *J. Power Sources* **1997**, *68*, 153.
[149] M. M. Thackeray, *J. Electrochem. Soc.* **1997**, *144*, L100.
[150] L. A. de Picciotto, M. M. Thackeray, *Mater. Res. Bull.* **1985**, *20*, 187.
[151] L. Guohua, S. Sakuma, H. Ikuta, T. Uchida, M. Wakihara, G. Hetong, *Denki Kagaku* **1996**, *64*, 202.
[152] G. Pistoia, M. Pasquali, L. A. de Picciotto, M. M. Thackeray, *Solid State Ionics* **1988**, *28*, 879.
[153] G T.-K. Fey, W. Li, J. R. Dahn, *J. Electro-*

CosMX Exhibit 1008, Page 342 of 633

chem. Soc. **1994**, *141*, 2279.
[154] R. J. Gummow, M. M. Thackeray, W. David, S. Hull, *Mater. Res. Bull.* **1992**, *27*, 327.
[155] E. Rossen, J. N. Reimers, J. R. Dahn, *Solid State Ionics* **1993** , *62*, 53.
[156] J. N. Reimers, W. Li, E. Rossen, J. R. Dahn, *Mater. Res. Soc. Symp. Proc.* **1993**, *293*, 3.
[157] R. J. Gummow, D. C. Liles, M. M. Thackeray, *Mater. Res. Bull.* **1993**, *28*, 235.
[158] R. J. Gummow, D. C. Liles, M. M. Thackeray, W. David, *Mater. Res. Bull.* **1993**, *28*, 1177.
[159] B. Garcia, P. Barboux, F. Ribot, A. Kahn-Harari, L. Mazerolles, N. Baffier, *Solid State Ionics* **1995**, *80*, 111.
[160] R. J. Gummow, M. M. Thackeray, *Solid State Ionics* **1992**, *53–56*, 681.
[161] E. Ferg, R. J. Gummow, A. de Kock, M. M. Thackeray, *J. Electrochem. Soc.* **1994**, *141*, L147 .
[162] T. Ohzuku, A. Ueda, N. Yamamoto, Y. Iwakoshi, *J. Power Sources* **1995**, *54*, 99.
[163] T. Ohzuku, A. Ueda, N. Yamamoto, *J. Electrochem. Soc.* **1995**, *142* , 1431.
[164] D. W. Murphy, M. Greenblatt, S. M. Zahurak, R. J. Cava, J. V. Waszczak, G.W. Hull, R.S. Hutton, *Rev. Chim. Minér.* **1982**, *19*, 441.
[165] D. W. Murphy, R. J. Cava, S. M. Zahurak, A. Santoro, *Solid State Ionics* **1983**, *9-10*, 413.
[166] K. M. Colbow, J. R. Dahn, R. R. Haering, *J. Power Sources* **1989** , *26*, 397.

CosMX Exhibit 1008, Page 343 of 633

2 Overcharge-Protected Oxide Cathodes

Tsutomu Ohzuku

2.1 Introduction

Lithium-ion batteries consisting of two insertion materials have been of interest among electrochemists and battery researchers because of their capability of operating thousands of cycles safely while retaining a high-energy lithium technology [1]. One of the characteristic features of lithium-ion batteries is flexibility in cell design. One can choose a suitable voltage together with a cell capacity by selecting insertion materials for the positive and negative electrodes. The materials are usually lithiated transition metal (di)oxides [2] for the positive electrodes and carbons [3, 4] for the negative electrodes in order to obtain a high cell voltage and consequently to make batteries with a high energy density. Organic electrolytes are usual in commercially available lithium-ion batteries for cordless telephones, laptop computers, and other electronic devices. Moreover, recent demands for high-volume lithium-ion batteries with high energy and power densities for electric vehicles are stimulating materials research for lithium-ion batteries worldwide on a large scale.

The goal in this section is to show the possibility of material design based on an insertion scheme for lithium-ion batteries. In Sec. 2.2 candidate materials for advanced lithium batteries will be reviewed. Specific problems in designing high-volume, high energy density lithium-ion batteries will be discussed in Sec. 2.3 with emphasis on nonaqueous electrochemistry. Solid-state redox reaction of lithium nickelate, which is one of the most attractive insertion materials, will be described in detail and the difficult problems in applying this material to lithium-ion batteries will be specified in Sec. 2.4. The thermal behavior of insertion materials with an organic electrolyte for positive electrodes in conditions where the materials are electrochemically oxidized (or in a charged state) will be described and the haystack-type reaction associated with thermal runaway will be considered in Sec. 2.5. In Sec. 2.6 and 2.7 an innovative insertion material, $LiAl_{1/4}Ni_{3/4}O_2$, will be highlighted [5, 6]; this is one of the achievements of basic research on the solid-state electrochemistry of insertion materials for advanced lithium batteries.

2.2 Candidate Materials for Advanced Lithium Batteries

In this section candidate materials for the positive electrodes of lithium-ion batteries

are reviewed briefly. This battery concept has already been described previously [1, 2].

Materials that have been examined for positive electrodes have included $LiCoO_2$ [7, 8], $LiNiO_2$ [9, 10] (more generally $LiCo_yNi_{1-y}O_2$ [11–13] ($0 \leq y \leq 1$)), $LiMnO_4$ [14–16] (or $Li[Li_y\ Mn_{2-y}]O_4$, assuming a spinel formulation [17, 18], and $LiMnO_2$ [19, 20]. The research on $LiCoO_2$ is more advanced than that on the other materials, and lithium-ion cells consisting of $LiCoO_2$ and carbonaceous material have already been fabricated and used as power sources in small or moderate sizes for electronic devices [21, 22].

The reactions of these insertion materials, except for $LiMnO_2$ [19, 20], consist of electron and lithium-ion insertion into, or extraction from, each matrix without the destruction of its core structure; this is called a topotactic reaction. A series of $LiCo_yNi_{1-y}O_2$ ($0 \leq y \leq 1$)) and $Li[Li_yMn_{2-y}]O_2$ ($0 \leq y < 1/3$)) shows an operating voltage above 3.5V with respect to a lithium electrode.

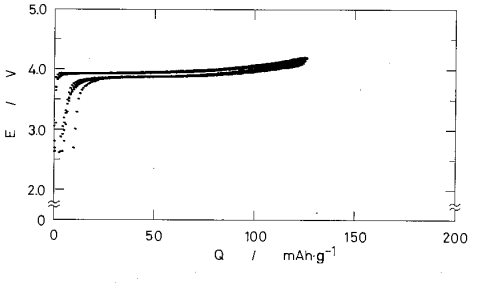


Figure 1. Charge and discharge curves of an $Li/LiCoO_2$ cell at a rate of 0.17 mA cm^{-2} at 30 °C. The cell was discharged to 2.5V, after a constant-capacity charge at 125 mAh g^{-1} based on weight of $LiCoO_2$.

Figure 1 shows the charge and discharge curves of an $Li/LiCoO_2$ cell. When the $Li/LiCoO_2$ cell is cycled over the limited composition range $0< x < 0.5$ in $Li_{1-x}CoO_2$, rechargeability and also retention of capacity are good. However, the rechargeable capacity fades rapidly for deep charge and discharge cycles, i.e., for $x > 0.5$ in $Li_{1-x}CoO_2$ [8]. Therefore, the maximum rechargeable capacity of $LiCoO_2$ is about 125 $mAhg^{-1}$ based on weight of $LiCoO_2$ when this material is applied to long-life lithium secondary batteries.

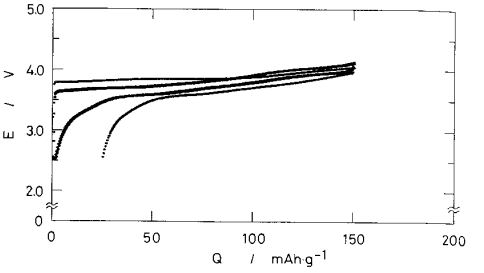


Figure 2. Charge and discharge curves of an $Li/LiNiO_2$ cell at a rate of 0.17 mA cm^{-2} at 30 °C. The cell was discharged to 2.5V, after a constant-capacity charge at 150 mAh g^{-1} based on weight of $LiNiO_2$.

$LiNiO_2$ has a higher rechargeable capacity than $LiCoO_2$, as shown in Fig. 2, although the preparation of battery-active $LiNiO_2$ is more difficult than that of $LiCoO_2$ [9, 10]. The Li/NiO_2 cell usually exhibits rechargeable capacities of more than 150 mAh g^{-1} based on weight of $LiNiO_2$. When the charge-end voltage of an $Li/LiNiO_2$ cell is accurately controlled below 4.2 V (typically 4.1 V), a maximum rechargeable capacity of about 200 mAh g^{-1} is obtainable with retention of the appropriate cycle life [10]. However, accurate regulation of the charge-end voltage below 4.2 V versus Li is very difficult, or almost impossible, for lithium-ion bat-

CosMX Exhibit 1008, Page 345 of 633

tery applications unless an auxiliary lithium electrode is properly placed in the cell.

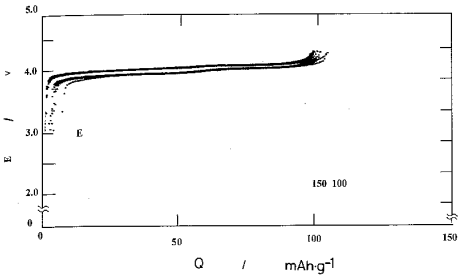


Figure 3. Charge and discharge curves of an $Li/Li[Li_{0.1}Mn_{1.9}]O_4$ cell cycled at voltages between 3.0 and 4.4V at a rate of 0.1 mA cm^{-2} at 30 °C. To describe the composition of an Li–Mn–O ternary phase a defect-spinel formulation was assumed.

Figure 3 shows the charge and discharge curves of an $Li/Li[Li_{0.1}Mn_{1.9}]O_4$ cell [18]. Its composition is described assuming a defect-spinel formulation. Stoichiometric spinel-type $LiMn_2O_4$ is difficult to prepare because of the nonstoichiometric nature of the Li–Mn–O ternary phases. Although stoichiometric $LiMn_2O_4$ exhibits the highest capacity among $Li[Li_yMn_{2-y}]O_4$ materials at 4 V its rechargeable capacity fades rapidly. Conversely, nonstoichiometric $Li[Li_yMn_{2-y}]O_4$ (normally $0 < y < 0.33$ in the assumed defect-spinel formulation) shows excellent rechargeability compared with stoichiometric $LiMn_2O_4$ although the rechargeable capacity decreases monotonically as y in $Li[Li_yMn_{2-y}]O_4$ increases, indicating that a tradeoff relationship exists between cyclability and rechargeable capacity when these materials are applied to lithium-ion batteries [18]. A rechargeable capacity of 100–110 mAh g^{-1} based on the sample weight is easily attained when $Li[Li_yMn_{2-y}]O_4$, with $y \cong 0.1$ is used. However, it is very difficult to attain a higher capacity than this while retaining the high-voltage character at 4 V.

Table 1 summarizes the rechargeable capacities, average operating voltages, and energy densities for $LiCoO_2$, $LiCo_{1/2}Ni_{1/2}O_2$, $LiNiO_2$, and $Li[Li_{0.1}Mn_{1.9}]O_4$. In calculating energy densities, the negative electrode material is assumed to be lithium metal. As shown in Table 1, $Li[Li_yMn_{2-y}]O_4$ shows the highest operating voltage among the insertion materials described above for lithium-ion batteries while its rechargeable capacity is about 100 mAh g^{-1}. Conversely, $LiNiO_2$ shows the largest rechargeable capacity but the lowest operating voltage among the samples listed in Table 1. Consequently, the energy density of an $Li/LiNiO_2$ cell works out to be the highest value , i.e., about 700 Wh kg^{-1}, which is almost twice that of an $Li/Li[Li_{0.1}Mn_{1.9}]O_4$ cell.

Table 1. Theoretical capacities, rechargeable capacities, average operating voltages, and energy densities of secondary lithium batteries with insertion materials

Material	Theoretical capacity mAh g^{-1}	Experimental rechargeable capacity (maximum degree of oxidation) mAh g^{-1}	Average operating voltage (V)	Energy density (Wh kg^{-1})
$LiCoO_2$	274	125 ($Li_{0.55}CoO_2$)	3.9	450
$LiCo_{1/2}Ni_{1/2}O_2$	274	170 ($Li_{0.4}Co_{1/2}Ni_{1/2}O_2$)	3.8	600
$LiNiO_2$	275	200 ($Li_{0.25}NiO_2$)	3.7	700
$Li[Li_{0.1}Mn_{1.9}]O_4$	106	100 $Li_{0.3}[Li_{0.1}Mn_{1.9}]O_4$	4.0	400

CosMX Exhibit 1008, Page 346 of 633

2.3 Specific Problems in Designing High–Volume, High–Energy, Reliable Lithium–Ion Batteries

In designing lithium-ion batteries, the following 20 behaviour requirements must be considered from the start of the research :

(1) high specific capacity in both $Ah\,cm^{-3}$ and $Ah\,g^{-1}$;
(2) high operating voltage for positive electrode materials;
(3) low operating voltage for negative electrode materials;
(4) excellent rechargeability;
(5) easy connection of batteries in series and/or parallel;
(6) high discharge rate capability;
(7) quick charging capability;
(8) resistance against overcharging;
(9) capacity recovery even after (over) discharging to zero voltage;
(10) safe, stable, reliable cell chemistry in closed cells;
(11) long cycle life;
(12) low self-discharge rate even at high temperature;
(13) low internal cell resistance capable of high-rate discharge and charge;
(14) low cell temperature even at high rate;
(15) low materials cost;
(16) state-of-charge indication capability;
(17) capability to predict of cycle life remaining;
(18) capability to predict and forewarn of eventual cell failure;
(19) low toxicity of materials (environmental friendliness); and
(20) recyclability of the materials in battery waste.

These are general requirements for both aqueous and nonaqueous batteries. Nonaqueous batteries normally exhibit a high-voltage character, because the thermodynamic limitation of water (1.23 V decomposition voltage at room temperature) is eliminated, leading to high energy density batteries. However, nonaqueous lithium batteries, including current lithium-ion batteries, are quite difficult to connect in series because of the lack of solvent cycling in a cell but their operating voltage is two or three times higher than that aqueous batteries, corresponding to two or three aqueous batteries connected in series. The absence of solvent cycling in a closed cell containing strong oxidizing and reducing agents in close proximity to organic electrolyte may cause other problems which we have not met in aqueous batteries. As will be discussed later, there is a tradeoff relationship between "high-energy and high-power density" and "safety", even when the batteries are properly designed and fabricated.

Of these requirements (1) – (4) relating to the energy density and requirements (8) and (10) associated with safety are most important behavior criteria for insertion materials for lithium-ion batteries, even in basic research.

2.4 Reaction Mechanism of $Li_{1-x}NiO_2$ and Its Thermal Behaviour with Organic Electrolyte

As was described in Sec. 2.2, $LiNiO_2$ is one of the most attractive materials for lithium-ion batteries. The reaction mechanism of $LiNiO_2$ ($R3m$; a = 2.88 Å and c = 14.19 Å in a hexagonal setting) is al-

CosMX Exhibit 1008, Page 347 of 633

ready known to be a topotactic reaction consisting of three single-phase reactions for $0 < x < 0.75$ in $Li_{1-x}NiO_2$, i.e., a rhombohedral phase for $0 < x < 1/4$, a monoclinic phase for $1/4 < x < 0.55$, and a rhombohedral phase for $0.55 < x < 0.75$, and a two-phase reaction for $0.75 < x < 1$ [10]. This can be better illustrated as a change in the interlayer distance between NiO_2 sheets as a function of x in $Li_{1-x}NiO_2$, as shown in Fig. 4.

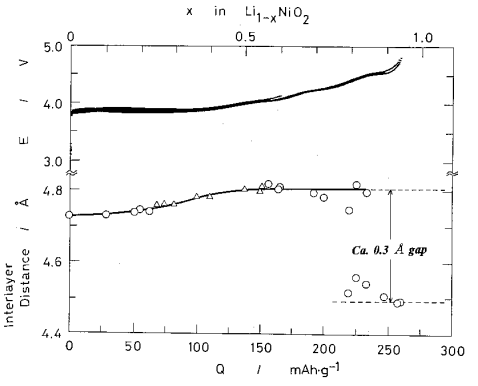


Figure 4. Change in interlayer distance between NiO_2 sheets upon charge for an Li/$LiNiO_2$ cell. The gap (shrinkage) of ca.0.3 Å in the interlayer distance is associated with the formation of nickel dioxide ($\square NiO_2$) for $0.75 < x < 1$ in $Li_{1-x}NiO_2$.

During the oxidation of $LiNiO_2$ the interlayer distance between NiO_2 sheets expands almost continuously from 4.73 Å to 4.80 Å as x approaches 0.5, where it levels off until x exceeds 0.75. Rechargeability of this single-phase region ($0 < x < 0.75$) is good. However, further oxidation induces a shrinkage of ca. 0.3 Å in the interlayer distance, so that the rechargeability in the two-phase region for $0.75 < x < 1$ is not expected to be good. The shrinkage is associated with the formation of nickel dioxide ($R3m$; $a = 2.81$ Å and $c = 13.47$ Å in a hexagonal setting) which is formed above 4.2 V against a lithium electrode [10]. Therefore, it is necessary to set the charge-end voltage slightly below 4.2 V (typically 4.1 V) versus a lithium electrode, not the terminal voltage of a lithium-ion cell, when a cycle life more than 1000 is needed. The need for accurate regulation of the charge-end voltage prevents widespread use of $LiNiO_2$ for lithium-ion batteries.

The thermal behavior of $Li_{1-x}NiO_2$ in relation to safety is another key factor when in considering materials for lithium-ion batteries. $LiNiO_2$ is stable even when it is heated with an organic electrolyte. However, partially or fully oxidized $LiNiO_2$ is quite active toward organic electrolyte oxidation and this reaction is exothermic.

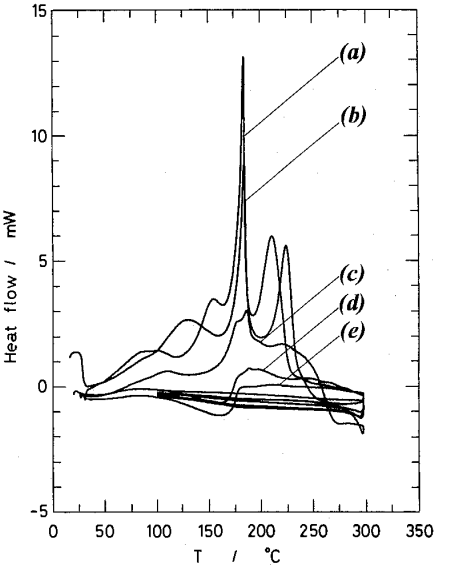


Figure 5. DSC curves for (a) $\square_{0.85}Li_{0.15}NiO_2$ (0.0232g), (b) $\square_{3/4}Li_{1/4}NiO_2$ (0.0235g), (c) $\square_{1/2}Li_{1/2}NiO_2$ (0.0266g), (d) $\square_{1/4}Li_{3/4}NiO_2$ (0.0226g), and (e) $LiNiO_2$ (0.0241g). The weights listed above in parentheses contained the electrolyte ($1 mol\,L^{-1}$ $LiClO_4$ – propylene carbonate). The heating and cooling rates were both 5 °C min^{-1}.

CosMX Exhibit 1008, Page 348 of 633

Figure 5 shows an example of the results of differential scanning calorimetry (DSC) measurements of $Li_{1-x}NiO_2$ prepared by electrochemical oxidation of $LiNiO_2$. In preparing the samples for DSC measurements, a compressed $LiNiO_2$ pellet was oxidized electrochemically in 1mol L^{-1} $LiClO_4$ dissolved in propylene carbonate solution and the sample containing the electrolyte was sealed in an aluminum cell. As can be seen in Fig. 5, $LiNiO_2$ and $□_{1/4}Li_{3/4}NiO_2$ are stable even when they are heated with the electrolyte. $□_{1/2}Li_{1/2}NiO_2$ shows some exothermic peaks around 180 °C, but they seem to be mild at this stage. An endothermic signal at temperatures between 100 and 180 °C is due to the decomposition of propylene carbonate. However, when $□_{3/4}Li_{1/4}NiO_2$ or $□_{0.85}Li_{0.15}NiO_2$ (the fully charged state of $LiNiO_2$ under these experimental conditions) is heated at a rate of 5 °C min^{-1}, exothermic signals in heat flow in the milliwatt range were observed until the decomposition reaction of the sample was completed at about 250 °C. The exothermic signals increase as the temperature rises, and then increase rapidly at about 160 °C; then a rapid increase and decrease in the DSC signals form a spike at 185 °C which indicates an electrolyte oxidation (exothermic) and a decomposition (endothermic) reaction of $□_{3/4}Li_{1/4}NiO_2$ or $□_{0.85}Li_{0.15}NiO_2$ releasing oxygen, the onset temperature of which is 185 °C, as confirmed by thermogravimetry and X-ray deffraction (XRD). Figure 6 shows thermogravimetric (TG) curves for the thermal decomposition of $□_{0.85}Li_{0.15}NiO_2$ in air. To prepare for TG curve measurement, the sample was washed with dimethoxyethane (DME) and tetrahydrofuran (THF) in order to remove the electrolyte as far as possible. A rapid change in weight at about 200 °C is due to the decomposition of nickel dioxide, releasing oxygen. The observed weight loss is 15.8 weight percent, which is approximately consistent with the calculated value of 17.6 weight percent assuming that nickel dioxide (formula weight = FW = 90.7) is decomposed to nickel monoxide (FW = 74.7) releasing oxygen. Figure 7 shows the XRD results for the thermal decomposition of nickel dioxide ($□_{0.85}Li_{0.15}NiO_2$, in fact). When nickel dioxide is heated at 100 °C in air, some change in XRD patterns is observed although a core structure remains, as shown in Fig. 7 (c). Higher heating temperatures than 100 °C result in destruction of the structure, forming nickel monoxide (*Fm3m*; a = 4.16 Å). Although the decomposition reaction releasing oxygen is endothermic, the overall reaction turns out to be exothermic, if the oxygen meets reducing agents such as lithiated (high-area) carbons.

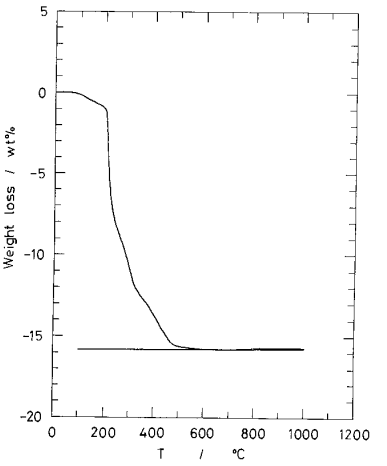


Figure 6. Thermogravimetric curves for $□_{0.85}Li_{0.15}NiO_2$ in air. The heating and cooling rates were 5 $^0Cmin^{-1}$. The sample was prepared by electrochemical oxidation of $LiNiO_2$ without addition of conductive binder to 4.8V using an $Li/LiNiO_2$ cell, washed with DME and THF, and dried under vacuum at room temperature.

CosMX Exhibit 1008, Page 349 of 633

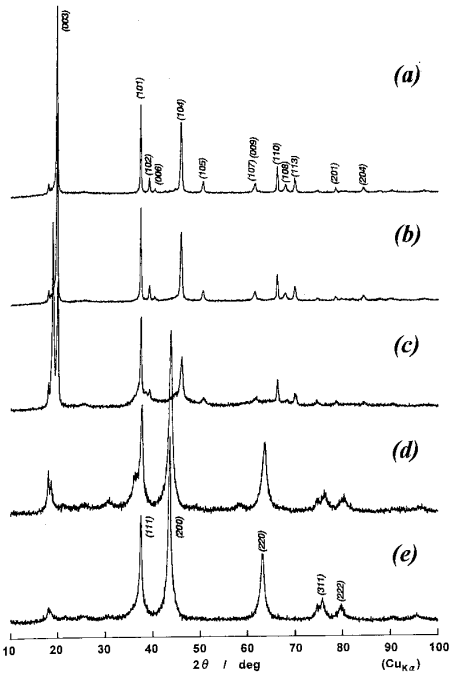


Figure 7. X-ray diffraction patterns of (a) NiO_2 ($\square_{0.85}Li_{0.15}NiO_2$, in fact), (b) NiO_2 washed with DME and THF, and the samples after heating at (c) 100 °C, (d) 200 °C, and (e) 300 °C. XRD examinations were performed at room temperature.

2.5 Possible Haystack-Type Reaction Associated with Thermal Runaway in a Closed Reaction Vessel

As can be seen in Fig. 5, exothermic reactions observed even at room temperature for $Li_{1-x}NiO_2$, especially with $x > 0.75$, with an organic electrolyte may give some problems in designing high-volume lithium-ion batteries with $LiNiO_2$. In this section a possible haystack-type reaction, or "clock reaction", associated with thermal runaway is described briefly in order to give some basis for considering insertion materials for advanced lithium batteries from a quite different angle.

Imagine a closed reaction vessel in which an exothermic reaction proceeds at room temperature at a finite rate. Although the temperature in the reaction vessel is initially the same as room temperature, it rises gradually until the rate of heat generation due to the exothermic chemical reaction is equal to the rate of heat escape from the reaction vessel surface. However, if a thermal balance is not established for such a chemical reaction, the reaction rate is accelerated by self–heating as the temperature rises, leading to thermal runaway. The temperature change in a reaction vessel is represented by Eq. (1),

$$C_p\rho(dT/dt) = QcA\exp(-E/RT) - \chi(S/V)(T-T_a) \quad (1)$$

where C_p is the heat capacity of the reaction vessel, and ρ is the density. Q is the reaction exothermicity, c is the concentration of reactant, and $A\exp(-E/RT)$ is a reaction rate constant. The first term on the right-hand side is the rate of heat evolution due to exothermic chemical reaction, and the second term is heat dissipation from the surface of the reaction vessel, where χ is the heat transfer coefficient, S/V is the ratio of surface area to volume, and T_a is the ambient temperature. Eq. (1) demonstrates that the thermal design of the reaction vessels (i.e., lithium-ion batteries) is very important in considering safe large-volume lithium-ion batteries if any exothermic chemical reaction proceeds in them.

Another problem is the delayed action involved in thermal runaway, which makes

CosMX Exhibit 1008, Page 350 of 633

it difficult to predict or forewarn when such runaway will take place; i.e., one cannot tell whether it will happen one day, one week, or one year after a clock reaction is switched on in a reaction vessel. This is better illustrated in Fig. 8.

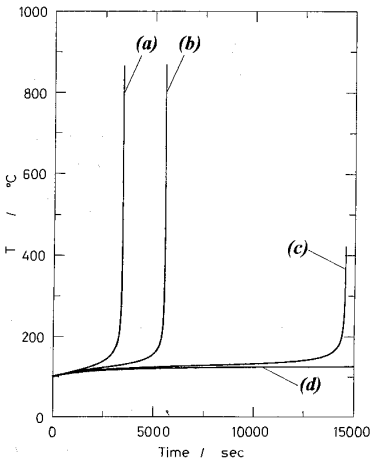


Figure 8. Clock or haystack-type reaction associated with thermal runaway derived from self-heating due to exothermic reactions in a closed vessel. Parameters :
(a) $c = 0.01$, $S/V = 0.5$, $T_a = 100$ °C;
(b) $c = 0.02$, $S/V = 1.0$, $T_a = 100$ °C;
(c) $c = 0.01$, $S/V = 1.0$, $T_a = 101$ °C;
(d) $c = 0.01$, $S/V = 1.0$, $T_a = 100$ °C, with $A' = 10^7$, $E = 4.927 \times 10^4$, and $B = 1.363 \times 10^{-3}$ in Eq.(2).

To show the delayed action effect in thermal runaway, Eq. (1) is rewritten as

$$(dT/dt) = A'c\exp(-E/RT) - \\ -B(S/V)(T - T_a) \qquad (2)$$

and we assume values which may not be useful in practice. As seen in Fig. 8, cells with a larger volume (smaller S/V value), higher ambient temperature, or higher capacity (larger c value) give an earlier thermal runaway event. To avoid thermal runaway, critical values exist for the nominal capacity, cell size, operating temperature, depth of charge relative to the charge-end voltage at which the cells are held potentiostatically, and the cell chemistry under consideration. It is worth noting that a lithium-ion battery with organic electrolyte is not immune to incidents, even with state-of-the-art safety technologies such as internal fusing, overpressure disconnection devices with safety venting inside the cells, and so forth, if a clock reaction is possible in the cell chemistry. The absence of exothermic reactions in the cell chemistry is the ideal situation for a high-volume lithium-ion battery.

2.6 Characteristic Features of Solid-State Redox Reactions in $Li_{1-x}NiO_2$

As described above, $LiNiO_2$ is an attractive material for lithium-ion batteries. However, it is difficult to operate high-volume lithium-ion batteries consisting of $LiNiO_2$ and (natural) graphite (or other negative electrode materials) safely for thousands of cycles. The difficulty is associated with the formation of nickel dioxide, so that it is hopeless to cope with this problem in a usual manner. However, it may be possible using a characteristic feature of the solid-state redox reaction of $LiNiO_2$.

According to our analytical results on the solid-state redox reaction of $LiNiO_2$ based on the phenomenological expression for solid-state redox potentials of insertion electrodes [23], the reaction consists of three redox systems characterized by potentials of 4.23, 3.93, and 3.63V with re-

CosMX Exhibit 1008, Page 351 of 633

spect to a lithium electrode. The reaction is formally represented by Eqns. (3)–(5).

$$\square NiO_2 + 0.25Li \rightarrow \square_{3/4}Li_{1/4}NiO_2 \quad (3)$$

$$\square_{3/4}Li_{1/4}NiO_2 + 0.5Li \rightarrow \square_{1/4}Li_{3/4}NiO_2 \quad (4)$$

$$\square_{1/4}Li_{3/4}NiO_2 + 0.25Li \rightarrow LiNiO_2 \quad (5)$$

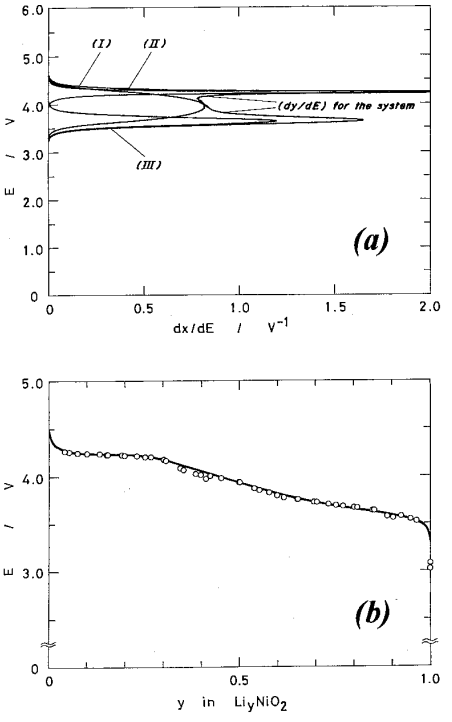


Figure 9. Variation of E with the electrochemical density of states (dx/dE) for the solid-state redox reaction of $LiNiO_2$. The system described by (dy/dE), which is the sum of the (dx/dE) values, is characterized by three redox systems. (b) Comparison of the observed (O) and calculated $E(y)$ curves for the reaction $\square NiO_2 + yLi \rightarrow Li_yNiO_2$. The E versus y curve was obtained by integrating (dy/dE) in (a) with respect to E from infinity to E.

Figure 9 shows the analytical results represented by the electrode potential (E) versus (dx/dE) curves and the comparison between the observed and calculated potential curves. Since (dx/dE) indicates the charge density capable of being stored or delivered at the potential $E(x)$, we call (dx/dE) the electrochemical density of states. Derivation of the phenomenological equations characterizing solid-state redox reactions with emphasis on the electrochemical density of states is beyond the scope of this section, so for brevity systems I, II, and III approximately correspond to Eqs. (3), (4), and (5), respectively [23]. Since the undesirable reaction is given by Eq. (3) (or system I in Fig. 9), we thus find a possible solution as to the formation of nickel dioxide which prevents us from making high-volume lithium-ion batteries with $LiNiO_2$.

A possible way of erasing system I in Fig. 9 is to design materials having an electron sink (or source) limiting capacity [2, 5, 24] using characteristic features of solid-state redox reactions in $LiNiO_2$. We can expect the elimination of system I in Fig. 9 by substituting nickel for other inactive species. If this speculation is correct, the redox level for system I goes to infinity while the approximate redox levels for systems II and III are retained. The inactive species that we selected in view of their structural inorganic chemistry are aluminum and gallium, because $LiAlO_2$ and $LiGaO_2$ are isostructural with $LiNiO_2$ and both species seem to be inactive (the redox potential of the tetravalent/trivalent state is infinity on the usual electrochemical scale). Of these, we examined lithium aluminate intensively because of its availability, light weight, and lack of toxicity. Therefore, our target material is $LiAl_{1/4}Ni_{3/4}O_2$, which is a solid solution of $LiNiO_2$ ($R3m$; a = 2.88 Å and

CosMX Exhibit 1008, Page 352 of 633

c = 14.19 Å). and $\alpha-LiAlO_2$ ($R\bar{3}m$; a = 2.80 Å and c = 14.23 Å) We expect the topotactic reaction represented by Eq. (6),

$$LiAl_{1/4}Ni_{3/4}O_2 \rightarrow \square_{3/4}LiAl_{1/4}Ni_{3/4}O_2 + 0.75Li \quad (6)$$

where □ denotes the vacant octahedral sites in a cubic close-packed oxygen array. The fully charged species is $\square_{3/4}Li_{1/4}\ NiO_2$, which is expected to be an insulator having an interlayer distance of about 4.8 Å if the Ni^{4+} ions are in their low-spin states ($t_{2g}^6e_g^0$ in O_h symmetry) and also to resistant to electrolyte oxidation.

2.7 Synthesis and Characterization of the Solid Solution of $LiNiO_2$ and α - $LiAlO_2$

Preparation of a single phase, comprising $\alpha-$, $\beta-$, or $\gamma-LiAlO_2$, was investigated initially using combinations of Al_2O_3 or $Al(OH)_3$ and $LiOH$, Li_2CO_3, or $LiNO_3$ at several temperatures in air, before deciding on the conditions in which to prepare $LiAl_{1/4}Ni_{3/4}O_2$. After several trials, a single phase of $\alpha-LiAlO_2$ ($R3m$: a = 2.80 Å, c = 14.23 Å in a hexagonal setting) was obtained by heating a reaction mixture of $Al(OH)_3$ and $LiNO_3$ (or Li_2CO_3) at 650 °C and then at 750 °C for 20h in air. When we substituted $\alpha-Al_2O_3$ for $Al(OH)_3$, hardly any single phase of $\alpha-LiAlO_2$ was obtained. Any combination with $LiOH$ did not give a single phase of $\alpha-LiAlO_2$. $\beta-$ $LiAlO_2$ ($Pna2_1$: a =5.28 Å b = 6.31 Å, c = 4.91 Å) was obtained by heating $Al(OH)_3$ (or Al_2O_3)` with excess $LiOH$ at 500 °C for 4h in air, washing the reaction product with distilled water, and then heating it at 400 °C in air. At temperatures above 850 °C both $\alpha-LiAlO_2$ and $\beta-LiAlO_2$ were converted to $\gamma-$ $LiAlO_2$ ($P4_12_12$: a = 5.18 Å, c =6.28 Å). Since the reaction conditions required to prepare $\alpha-LiAlO_2$ were almost the same as those to prepare $LiNiO_2$ [10], we examined intesively the conditions for preparations of $LiAl_{1/4}Ni_{3/4}O_2$ using a reaction mixture of $LiNO_3$, $Al(OH)_3$, and $NiCO_3$, and we have succeeded in making a solid solution of $\alpha-LiAlO_2$ and $LiNiO_2$.

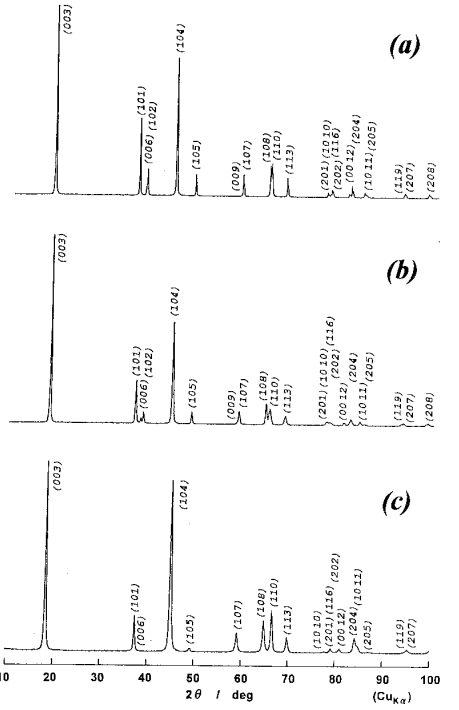


Figure 10. X-ray diffraction patterns of (a) $LiNiO_2$ ($R3m$; a = 2.88 Å, c =14.19 Å in a hexagonal setting); (b) $LiAl_{1/4}Ni_{3/4}O_2$ ($R3m$; a = 2.86 Å, c =14.24 Å); and (c) $\alpha-LiAlO_2$ ($R3m$; a = 2.80 Å, c =14.23 Å).

CosMX Exhibit 1008, Page 353 of 633

Figure 10 shows the X-ray diffraction pattern of $LiAl_{1/4}Ni_{3/4}O_2$ in comparison with those of $LiNiO_2$ and $\alpha-LiAlO_2$. The *a*-axis dimension of $LiAl_{1/4}Ni_{3/4}O_2$ is 2.86 Å, which is a quarter-point between 2.88 Å for $LiNiO_2$ and 2.80 Å for $\alpha-LiAlO_2$. This suggests a homogeneous distribution of aluminum ions at nickel sites in $LiNiO_2$. The unit cell parameters for $LiAl_{1/4}Ni_{3/4}O_2$ were determined to be a = 2.86 Å and c = 14.24 Å in a hexagonal setting by a least-squares method using 15 diffraction lines. In analyzing the structure, we assumed a space group *R*3*m* in which trivalent aluminum and trivalent nickel ions were randomly distributed at the octahedral 3(a) sites with an occupancy of 1/4 for aluminum and 3/4 for nickel. The lithium ions were located at the octahedral 3(b) sites, and oxygen ions at the 6(c) sites, and we obtained an oxygen positional parameter of 0.262.

Thus we have succeeded in preparing the target material of $LiAl_{1/4}Ni_{3/4}O_2$ (*R*3*m*), which is a solid solution of $\alpha-LiAlO_2$ and $LiNiO_2$ (*R*3*m*) in a ratio of 1:3.

2.8 An Innovative $LiAl_{1/4}Ni_{3/4}O_2$ Insertion Material for Lithium-Ion Batteries

Figure 11 shows the charge and discharge curves of $Li/LiAl_{1/4}Ni_{3/4}O_2$ cells. To plot the curves, the cells were charged at a constant capacity of 100, 125, or 150 mAh g^{-1} at a rate of 0.17 mA cm^{-2} and then discharged to 2.5 V. As shown in Fig. 11, $LiAl_{1/4}Ni_{3/4}O_2$ gives almost the same operating voltages as $LiNiO_2$. Coulombic efficiency during charge and discharge is ca. 99 percent under these experimental conditions.

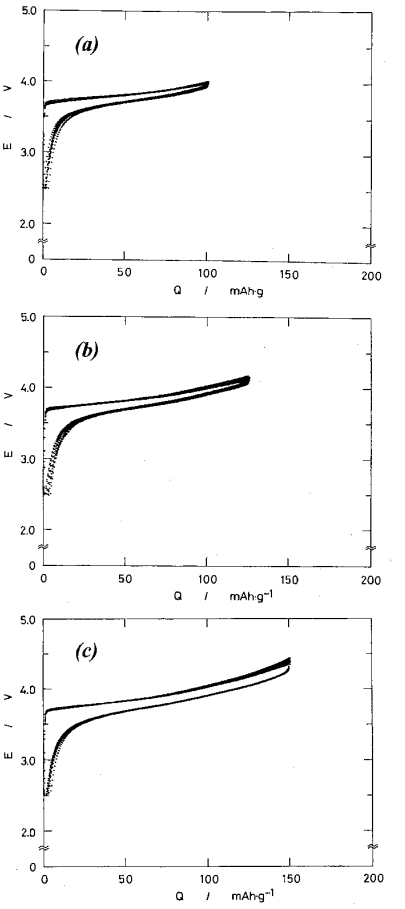


Figure 11. Charge and discharge curves of $Li/LiAl_{1/4}Ni_{3/4}O_2$ cells at a rate of 0.17 mA cm^{-2} at 30 °C. The cell was charged at a constant capacity of (a) 100 mAh g^{-1}, (b)125 mAh g^{-1}, or (c) 150 mAh g^{-1} based on weight of $LiAl_{1/4}Ni_{3/4}O_2$, then discharged to 2.5 V.

The X-ray diffraction examinations of $Li_{1-x}Al_{1/4}Ni_{3/4}O_2$ indicate that the reaction proceeds topotactically in a single phase over the entire range, called a single-phase reactions, as shown in Fig. 12. Gen-

CosMX Exhibit 1008, Page 354 of 633

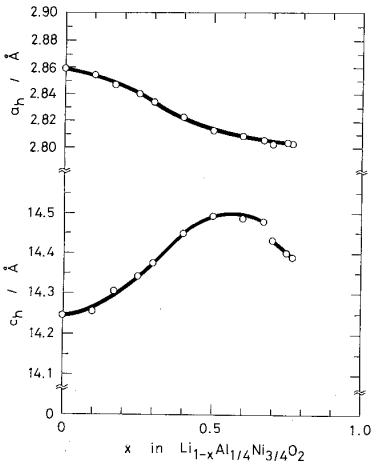


Figure 12. Charge in lattice parameters of $Li_{1-x}Al_{1/4}Ni_{3/4}O_2$ on charge, for $Li/LiAl_{1/4}Ni_{3/4}O_2$ cells.

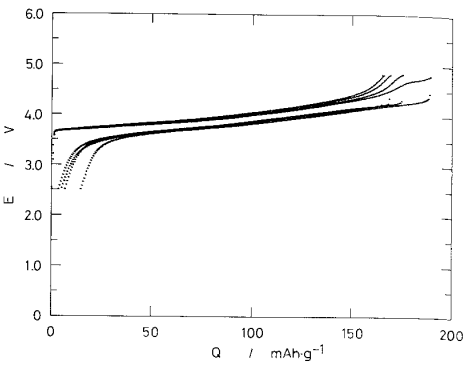


Figure 13. Charge and discharge curves of an $Li/LiAl_{1/4}Ni_{3/4}O_2$ cell operated in voltages between 2.5 and 4.8V at a rate of 0.17 mA cm^{-2} at 30 °C.

eral observations, such as the shrinkage in the *a*-axis dimension to 2.80 Å and the increase in the *c*-axis dimension up to 14.5 Å as x increases (oxidation of $LiAl_{1/4}Ni_{3/4}O_2$), are the same as those for $LiCoO_2$, $LiNiO_2$, or $LiNi_{1/2}Co_{1/2}O_2$. A dramatic change in the *c*-axis dimension to below 14.0 Å is usually observed in the range $0.75 < x < 1$ for these materials. This gives a limitation in applying these materials to lithium-ion batteries, as was discussed in Sec.2.4, i.e., accurate regulation of the charge-end voltage is necessary to prevent overcharging. However, such a dramatic change in the *c*-axis dimension (below 14.0 Å) is not observed for $Li_{1-x}Al_{1/4}Ni_{3/4}O_2$; it remains above 14.3 Å even for a fully charged state. A fully charged state of $LiAl_{1/4}Ni_{3/4}O_2$ is obtained by constant-current charge to 4.9 V or constant-voltage charge at 4.50 V. Figure 13 shows the constant-current charge and discharge curves of an $Li/LiAl_{1/4}Ni_{3/4}O_2$ cell operated at voltages between 2.5 and 4.8 V at a rate of 0.17 mA cm^{-2}. Almost steady charge and discharge curves are obtained under stringent conditions in terms of charge end-voltage using a normal electrolyte (1mol L^{-1} $LiClO_4$ dissolved in propylene carbonate in this case). This is due to the formation of $\square_{3/4}Li_{1/4}Al_{1/4}Ni_{3/4}O_2$ insulating material, which behaves like an ideally polarizable electrode, leading to resistance to overcharging.

Figure 14 shows the results of the DSC measurements of partially or fully charged $LiAl_{1/4}Ni_{3/4}O_2$ prepared by electrochemical oxidation in lithium cells. Experimental conditions were the same as those for $Li_{1-x}NiO_2$ in Fig. 5. In order to facilitate comparison between $Li_{1-x}NiO_2$ and $Li_{1-x}Al_{1/4}Ni_{3/4}O_2$ we have presented DSC results on the same scale on both the vertical and horizontal axes. The DSC results for $Li_{1-x}Al_{1/4}Ni_{3/4}O_2$ indicate that the exothermic reactions are remarkably suppressed by substituting aluminum for nickel in $LiNiO_2$. A noticeable exothermic peak cannot be seen, even for a fully charged state of $LiAl_{1/4}Ni_{3/4}O_2$. Therefore, such mild thermal behavior will not lead to thermal runaway derived from haystack-type or clock reactions in closed cells as discussed in Sec.2.5.

CosMX Exhibit 1008, Page 355 of 633

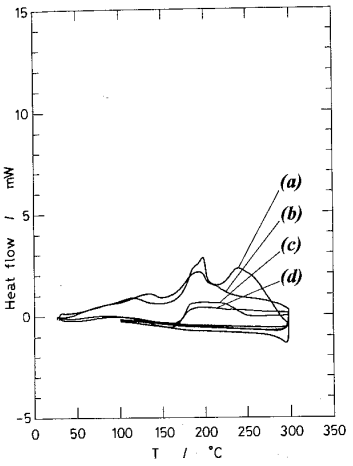


Figure 14. DSC curves for
(a) $\square_{0.69}Al_{1/4}Ni_{3/4}O_2$ (0.0205g),
(b) $\square_{1/2}Li_{1/2}Al_{1/4}Ni_{3/4}O_2$ (0.0205g),
(c) $\square_{1/4}Li_{3/4}Al_{1/4}Ni_{3/4}O_2$ (0.0201g), and
(d) $LiAl_{1/4}Ni_{3/4}O_2$ (0.0209g). The weights listed above in parentheses contained the electrolyte. The heating and cooling rates were both 5 °C min^{-1}.

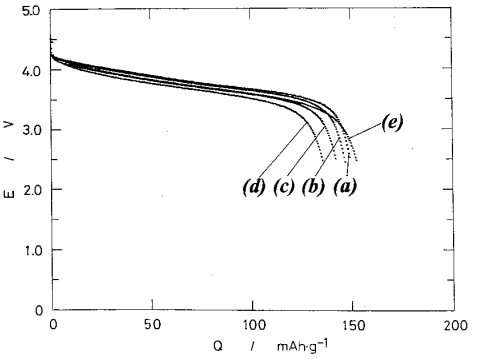


Figure 15. Effect of constant-voltage charging at 4.5 V after the 31st cycle for an $Li/LiAl_{1/4}Ni_{3/4}O_2$ cell upon the discharge capacity (shown in (e)). Capacity fading observed during continuous constant-curent charge and discharge at voltages between 2.5 and 4.5 V as the (a) 5th, (b) 10th, (c) 20th, and (d) 30th discharge curves.

The charging mode usually applied to lithium-ion batteries is constant-current charge up to certain terminal voltage followed by constant-voltage charge at that voltage for certain period of time. In order to examine whether or not such a charging mode can be applied to our system, an $Li/LiAl_{1/4}Ni_{3/4}O_2$ cell was charged at a constant current of $0.17\,mA\,cm^{-2}$ up to 4.5 V, then at a constant voltage of 4.5 V for 12h, and then discharged to 2.5 V. Figure 15 shows the discharge curves of an $Li/LiAl_{1/4}Ni_{3/4}O_2$ cell after a constant-current charge to 4.5 V (5th, 10th, 20th, and 30th) or a constant-voltage charge at 4.5 V for 12h following a constant-current charge up to 4.5 V (32nd). As shown in Fig. 15, a constant voltage of 4.5 V can be used in charging this cell. Such a capability of high-voltage charging is a unique characteristic of $LiAl_{1/4}Ni_{3/4}O_2$.

2.9 Concluding Remarks

In this sections, reasons why it is difficult to make high-volume, high energy density, lithium-ion batteries that may be cycled safely for thousands of cycles, have been described along with the main factors affecting cell failure, the key behavior to be considered when selecting materials or designing lithium-ion batteries, and whether or not material design based on an insertion scheme is possible for reliable lithium-ion batteries to be developed from basic research results.

One insertion material that has been obtained deductively from basic research results is $LiAl_{1/4}Ni_{3/4}O_2$, which is a solid solution of $\alpha - LiAlO_2$ and $LiNiO_2$. On charge, this material is oxidized to $\square_{1/4}Li_{1/4}Al_{1/4}Ni_{3/4}O_2$, in which lithium ions are available but no electrons can be removed (electron-sink (or source)-limiting capacity); it is an insulator be-

cause the matrix consists of tetravalent nickel ions in their low-spin state and trivalent aluminum ions, resulting in resistance to overcharging. The overall reaction is represented by Eq. (7),

$$LiAl_{1/4}Ni_{3/4} \rightarrow 0.75Li + \square_{3/4}Li_{1/4}Al_{1/4}Ni_{3/4}O_2 \quad (7)$$

giving a theoretical capacity of $224\,mAh\,g^{-1}$ while the high-voltage character of $LiNiO_2$ is retained owing to the characteristic features of a solid-state redox reaction. Although the current $LiAl_{1/4}Ni_{3/4}O_2$ shows slightly more polarization character than $LiCoO_2$, $LiNiO_2$, or $LiCo_{1/4}Ni_{3/4}O_2$, with a rechargeable capacity of about $150\,mAh\,g^{-1}$ based on the sample weight, we are expecting $200\,mAh\,g^{-1}$ of rechargeable capacity out of $224\,mAh\,g^{-1}$ of theoretical capacity with a smaller polarization than $LiCoO_2$ or $LiCo_{1/4}Ni_{3/4}O_2$ by improving the processing methods for preparing the samples and electrodes. Such approaches are still under way in our laboratory. We believe that the combination of $LiAl_{1/4}Ni_{3/4}O_2$ ($R3m$) and natural graphite is most attractive system for reliable high-energy, high-volume, lithium-ion batteries.

Acknowledgments. In describing our ideas we have refered mostly to our own work. However, throughout our research we owe much to other workers through literature that spans a generation, and all are worthy of credit. We also thank the former graduate students Dr. Atsushi Ueda, Mr. Masatoshi Nagayama (M. S.), Mr. Masaru Kouguchi (M. S.), and Mr. Takayuki Yanagawa (M. S.), for their devotion to basic research on solid-state electrochemistry, and thank Mr. Masato Iwanaga, graduate student of Osaka City University, for his help in making the Figures.

2.10 References

[1] See, for examples : a) *Lithium Batteries* (Ed.: G. Pistoia), Elsevier, Amsterdam, **1993**; b) *Extended Abstracts, 8th Int. Meeting on Lithium Batteries, Nagoya, Japan,* June 16–21, **1996.**

[2] T. Ohzuku, A. Ueda, *Solid State Ionics* **1994,** *69*,201.

[3] J. R. Dahn, A. K. Sleigh, H. Shi, B. M. Way, W. J. Weydanz, J. N. Reimers, Q. Zhong, U.von Sacken, in *Lithium Batteries* (Eds.: G. Pistoia), Elsevier, Amsterdam, **1993,** ch.1.

[4] K. Sawai, Y. Iwakoshi, T. Ohzuku, *Solid State Ionics* **1994,***69*, 273.

[5] T. Ohzuku, A. Ueda, M. Kouguchi, *J. Electrochem.Soc.* **1995**, *142*, 4033.

[6] T. Ohzuku, T. Yanagawa, M. Kouguchi, A. Ueda, *J. Power Sources* **1997**, *68*, 131.

[7] K. Mizushima, P. C. Jones, P. J. Wiseman, J. B. Goodenough, *Mater.Res.Bull* **1980**, *15*, 2972.

[8] T. Ohzuku, A. Ueda, *J. Electrochem.Soc* **1994**, *141, 2972.*

[9] J. R. Dahn, U.von Sacken, M. W. Juzkow, H. Al-Janaby, *J. Electrochem. Soc* **1991,** *138*, 2207.

[10] T. Ohzuku, A. Ueda, M. Nagayama, *J. Electrochem.Soc* **1993**, *140*, 1862.

[11] T. Ohzuku, H. Komori, K. Sawai, T. Hirai, *Chem. Express* **1990**, *5*, 737.

[12] T. Ohzuku, A. Ueda, M. Nagayama, Y. Iwakoshi, H. Komori, *Electrochim. Acta* **1993**, *38*, 1159.

[13] A. Ueda, T. Ohzuku, *J. Electrochem Soc.* **1994**, *141*, 2010.

[14] M. M. Thackeray, P. J. Johnson, L. A.de Picciotto, P. G. Bruce, J. B. Goodenough, *Mater.Res.Bull.* **1984**, *19*, 179.

[15] T. Ohzuku, M. Kitagawa, T. Hirai, *J. Electrochem.Soc.* **1990**, *137*, 769.

[16] J. M. Tarascon, D. Guyomard, G. L. Baker, *J. Power Sources* **1993**, *43–44*, 689.

[17] A. Yamada, *J. Solid State Chem.* **1996**, *122*, 160.

[18] T. Ohzuku, S. Kitano, M. Iwanaga, H. Matsuno, A. Ueda, *J. Power Sources* **1997**, *68*, 646.

[19] T. Ohzuku, A. Ueda, T. Hirai, *Chem. Express* **1992**, *7*, 193.

[20] J. N. Reimers, E. W. Fuller, E. Rossen, J. R. Dahn, *J. Elecrochem. Soc.* **1993,** *140*, 3396.

CosMX Exhibit 1008, Page 357 of 633

[21] K. Sekai, H. Azuma, A. Omaru, S. Fujita, H. Imoto, T. Endo, K. Yamada, Y. Nizhi, S. Mashito, M. Yokogawa, *J. Power Sources* **1993**, *43–44*, 241.

[22] J. Yamaura, Y. Ozaki, A. Morita, A. Ohta, *J. Power Sources* **1993**, *43–44*, 241.

[23] T. Ohzuku, A. Ueda, *J. Electrochem.Soc.* **1997**, *144*, 2780.

[24] T. Ohzuku, A. Ueda, N. Yamamoto, *J. Electrochem.Soc.* **1995**, *142*, 1431.

CosMX Exhibit 1008, Page 358 of 633

3 Rechargeable Lithium Anodes

Jun-ichi Yamaki and Shin-ichi Tobishima

3.1 Introduction

The need to increase the energy density of rechargeable cells has become more urgent as a result of the recent rapid development of new applications, such as electric vehicles, load leveling and various types of portable equipment, including personal computers, cellular phones and camcorders. Moreover, a lithium metal anode is an attractive way of delivering the high energy density from such cells. The lithium-metal anode has a very large theoretical capacity of 3860 mAh g^{-1}, in contrast to the value of 372 mAh g^{-1} for an LiC_6 carbon anode. This high energy encourages an attempt to realize a practical lithium-metal anode cell.

Primary lithium-metal cells, including cylindrical and coin-type cells, have been manufactured as high-energy cells since 1973 (Panasonic, Li / polyfluorocarbon cell). In addition, several small rechargeable coin-type cells have appeared on the market (cell-capacity < 100 mAh), which are generally categorized as lithium cells. These small rechargeable cells do not employ pure lithium metal as their anode, but have anodes of lithium-metal alloys (Table 1). The cells with lithium-ion inserted compounds have been commercialized more recently (Table 2). In spite of their lower energy density, these alternative anodes are used because pure lithium tends to be deposited on the anode in dendrite form when the cell is charged. These dendrites may cause an internal short as well as a decrease in lithium-cycling efficiency.

The alternative alloy anodes which exhibit good cycle life in coin cells (Table 1) are not applied to cylindrical cells. This is because they are brittle and these alloy anodes turn into fine particles after cycling when the anode is spirally wound in the cylindrical cell. Cylindrical rechargeable lithium-metal cells, such as AA-size cells, are not yet commercially available. Several prototype AA cells with pure lithium anodes have been developed since late 1980

Table 1. Commercially available rechargeable coin-type cells with lithium-metal alloys

Anode	Cathode	Cell voltage (V)	Main application	Manufacturer
Pb–Cd–Bi–Sn(–Li)	Carbon	3	Memory backup	Panasonic
Li–Al	c- V_2O_5	3	Memory backup	Panasonic
Li–Al–Mn	$Li_2MnO_3 + \gamma - \beta$ - MnO_2	3	Memory backup	Sanyo
Li–Al	Polyaniline	3	Memory backup	Seiko/Bridgestone

CosMX Exhibit 1008, Page 359 of 633

Table 2. Commercially available rechargeable coin-type cells with lithium-ion inserted anodes

Anode	Cathode	Cell voltage (V)	Main application	Manufacturer
$Li_xNb_2O_5$	c- V_2O_5	1.5	Watches	Panasonic
Li_xTiO_2	Li_xMnO_2	1.5	Watches	Panasonic
Carbon(–Li)	c- V_2O_5	3	Memory backup	Toshiba
polyacenic semiconductor(–Li)	polyacenic semiconductor(–Li)	2	Memory backup	Kanebo

Table 3. Prototype AA-size rechargeable lithium-metal cells

Cathode	Voltage (V)	Weight (g)	Capacity (Ah)	Energy (Wh)	Energy density (Wh kg^{-1})+	(Wh L^{-1})+	Cycle life**	Organization
$NbSe_3$	2	20.5	1.1	2.2	107	293	200–400	ATT
TiS_2	2.1	15.6	1.0	2.1	135	280	200–250	Duracel
Li_xMnO_2	2.8	16.3	0.7	2.0	125	267	200–400	Sony
Li_xMnO_2	2.8	17	0.75	2.1	124	280	100–250	Tadiran
MoS_2*	1.8	22	0.8	1.4	64	187	200	Moli Energy
a- V_2O_5	2.3	18	0.9	2.0	110	267	150–300	NTT

* B-type cell, + Assumed cell volume=7.5 cm^3, ** 100 percent depth of discharge; cycle life depends on cycling current.

(Table 3). However, their cycle life depends on the discharge and charge currents. This problem results from the low cycling efficiency of lithium anodes. Another big problem is the safety of lithium-metal cells. One of the reasons for their poor thermal stability is the high reactivity and low melting point (180 °C) of lithium.

Nippon Telegraph and Telephone Corporation (NTT) has developed a prototype AA-size lithium-metal anode cell [1] with an amorphous V_2O_5 cathode. The energy of this cell is 2 Wh, which is higher than the value of 1.8 Wh for a lithium-ion cell with an $LiCoO_2$ cathode (The estimated value for an AA-size lithium-metal cell with an $LiCoO_2$ cathode is about 3 Wh). However, this metal-anode cell has a cycle life of 150 cycles and its thermal stability is 130 °C at a high discharge rate. At a low discharge rate, it has a cycle life of 50 cycles and its thermal stability is 125 °C. These values are poor compared with lithium-ion cells, whose corresponding values are 500 cycles and above 130 °C. This poor performance is explained mainly by the characteristics of the lithium-metal anode, and specifically its low cycling efficiency.

Many studies have been undertaken with a view to improving lithium anode performance to obtain a practical cell. This section will describe recent progress in the study of lithium-metal anodes and the cells. Sections 3.2 to 3.7 describe studies on the surface of uncycled lithium and of lithium coupled with electrolytes, methods for measuring the cycling efficiency of lithium, the morphology of deposited lithium, the mechanism of lithium deposition and dissolution, the amount of dead lithium, the improvement of cycling efficiency, and alternatives to the lithium-metal anode. Section 3.8 describes the safety of rechargeable lithium-metal cells.

CosMX Exhibit 1008, Page 360 of 633

3.2 Surface of Uncycled Lithium Foil

Lithium foil is commercially available. Its surface is covered with a "native film" consisting of various lithium compounds [$LiOH, Li_2O, Li_3N$, (Li_2O-CO_2) adduct, or Li_2CO_3]. These compounds are produced by the reaction of lithium with O_2, H_2O, CO_2, or N_2. These compounds can be detected by electron spectroscopy for chemical analysis (ESCA) [2]. As mentioned below, the surface film is closely related to the cycling efficiency.

Lithium foil is made by extruding a lithium ingot through a slit. A study of the influence of the extrusion atmosphere on the kind of native film produced showed that lithium covered with Li_2CO_3 is superior both in terms of storage and discharge because of its stability and because a lithium anode has a low impedance [3, 4].

3.3 Surface of Lithium Coupled With Electrolytes

Lithium metal is chemically very active and reacts thermodynamically with any organic electrolyte. However, in practice, lithium metal can be dissolved and deposited electrochemically in some organic electrolytes [5]. It is generally believed that a protective film is formed on the lithium anode which prevents further reaction [6, 7]. This film strongly affects the lithium cycling efficiency.

According to the solid electrolyte interphase (SEI) model presented by Peled [8], the reaction products of the lithium and the electrolyte form a thin protective film on the lithium anode. This film is a lithium-ion conductor and an electronic insulator, whose nature prevents any further chemical reaction. Aurbach et al. and many other research workers have tried to identify the chemical products composing the protection film [9–20] using Fourier transform infrared spectroscopy (FTIR), X-ray photoelectron spectroscopy (XPS) and Raman spectroscopy. The protective films differ depending on the kind of electrolyte, and mainly consist of Li_2CO_3, LiX (X: Halogen), ROLi and ROCOOLi (R: Hydrocarbon). $LiAsF_6$ solute forms some As compounds as the protective films. Ethylene carbonate (EC) and propylene carbonate (PC) are electrolyte solvents with very similar chemical structures but providing different lithium cycling efficiencies. Aurbach et al. have reported differences between the lithium surface films in EC or PC, namely that $CH_3CH(OCO_2Li)$ CH_2OCO_2Li and $(CH_2OCO_2Li)_2$ are detected in the lithium surface film with dry PC and EC, respectively [21].

The reaction of the electrolyte with lithium and the resulting film properties affect the cycle life of the lithium cell. Shen et al. [22] have examined the stability (reactivity) of the electrolytes by open-circuit storage tests for the Li/TiS_2 cell system by microcalorimetry and AC impedance spectroscopy. They used tetrahydrofuran (THF)-and 2-methyl-THF (2Me THF)-based electrolyte, with additives such as 2-methylfuran (2MeF), EC, PC, and 3-methylsulfolane (3MeS), and $LiAsF_6$ as the solute. The heat output of the cells on open circuit for a day (short-term reactivity) or a year (long-term reactivity) is lower for EC/2Me THF than for 2MeTHF or PC/2MeTHF. Also, the cell with EC/2MeTHF has a lower SEI resistivity of 51 $\Omega\,cm^2$ than that with

CosMX Exhibit 1008, Page 361 of 633

2MeTHF (119 $\Omega\,cm^2$) or PC/2MeTHF (214 $\Omega\,cm^2$). The cycle life increases with decreases in heat output and resistivity. They indicate that these measurements are effective in determining electrolyte stability.

3.4 Cycling Efficiency of Lithium Anode

3.4.1 Measurement Methods

Lithium deposited on an anode during a charge is chemically active and reacts with organic electrolytes after deposition. Then, the lithium is consumed during cycling. The cycling efficiency (percent) of a lithium anode (Eff) is basically defined by Eq. (1) [23], where Q_p is the amount of electricity needed to plate lithium and Q_s is the amount of electricity needed to strip all the plated lithium. As Eff is less than 100 percent, an excess of lithium is included in a practical rechargeable cell to compensate for the consumed lithium.

$$\text{Eff} = 100 \times Q_s / Q_p \tag{1}$$

The figure of merit (FOM) for lithium cycling efficiency [24] also is often used to evaluate the cyclability of a lithium cell. The FOM is defined as the number of cycles completed by one atom of lithium before it becomes electrochemically inactive. Equation (2) is derived from the above definition.

$$\text{FOM} = \frac{\text{sum of each discharge capacity to the end of cycle life}}{\text{capacity of lithium anode cell}} \tag{2}$$

We can calculate the FOM from Eff, using Eq. (3) [25].

$$\text{FOM} = \frac{1}{1 - \text{Eff}/100} \tag{3}$$

The value of Eff is affected by many experimental conditions other than the electrolyte and anode materials. The experimental conditions include such factors as the cell configuration, electrode orientation, electrode surface area, working electrode substrate, charge–discharge currents, charge quantity, and amount of electrolyte.

When Al, Pt, Ni, or Cu is used as the substrate of lithium plating with 1 mol L^{-1} $LiClO_4$–PC/1,2-dimethoxyethane (DME), Eff decreases in the order is Al > Pt > Ni > Cu [26]. Lithium is easily alloyed electrochemically with many metals [27]; the Eff values measured in these experiments could include those of lithium alloys.

Lithium cycling on a lithium substrate (Li-on-Li cycling) is another frequently used Li half-cell test [28], in which an excess of lithium (Q_{ex} is plated on a metal working electrode, and then constant-capacity cycling (Q_{ps}); Q_{ps} is smaller than Q_{ex}) is continued until all the excess lithium is consumed. The FOM can be evaluated as shown in Eq.(4).

$$\text{FOM} = \frac{(\text{cycling life}) \times Q_{ps}}{Q_{ex}} \tag{4}$$

The influence of the amounts of lithium deposited in Li-on-Li cycling have been examined by Foos et al. [29]. They used a cell (I) with a Q_{ex} of 3.4 C cm^{-2} and a Q_{ps} of 1.1 C cm^{-2} and a cell (II) with a Q_{ex} of 18–23 C cm^{-2} and a Q_{ps} of 5–10 C cm^{-2} with $LiAsF_6$–THF based electrolytes. The cell (II) experiment provides

CosMX Exhibit 1008, Page 362 of 633

a more predictable result for the cycle life of the Li/TiS_2 full cell because minimizes the effect of trace impurities.

3.4.2 Reasons for The Decrease in Lithium Cycling Efficiency

The reason why lithium cycling efficiency is not 100 percent are generally considered to be as follows;

(1) Lithium is consumed by reaction with the electrolyte which forms a protective film [6]. During the deposition and stripping of lithium, the surface shape changes and a fresh lithium surface is formed, with a new protection film on it; lithium is consumed in the process.
(2) Lithium is isolated in a protective film [8]. During the deposition of lithium, the protective film may be heated locally by ion transport in the film itself. As a result of this local heating, part of the protective film (SEI) becomes an electronic conductor, and therefore lithium metal is deposited in the film. If local heating does not occur during stripping, the isolated lithium becomes electrochemically inactive.
(3) Deposited lithium is isolated from the base anode [30, 31]. When a cell is charged, lithium is deposited on the lithium substrate of the anode. Sometimes, the plated lithium is not flat but fiber-like. When the cell is discharged, the lithium anode dissolves, and sometimes the fiber-like lithium is cut and becomes isolated from the anode substrate [31]. This isolated lithium is called "dead lithium", and it is electochemically inactive but chemically active. During cycling, this dead lithium accumulates on the anode.

We believe that (3) is the main reason for the low cycling efficiency. The thermal stability of lithium-metal cells decreases with cycling [30] and the dead lithium may be the cause of this reduction. This indicates that the cycling efficiency is strongly affected by the morphology of the lithium surface.

3.5 Morphology of Deposited Lithium

There have been many reports on the morphology of the lithium that is electrochemically deposited in various kinds of organic electrolyte [32–39].

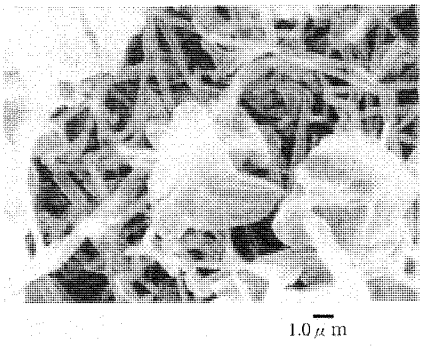


Figure 1. Morphology of lithium deposited on stainless steel, 3 $mA\,cm^{-2}$, 3 $mAh\,cm^{-2}$, 1.5 $mol\,L^{-1}$ $LiAsF_6$ – EC/2MeTHF (1:1), v/v.

Figure 1 shows a typical lithium deposition morphology. Here, the lithium is deposited on stainless steel at 3 mA cm^{-2} for 1 h with 1.5 mol L^{-1} $LiAsF_6$–EC/2MeTHF (1:1, v/v).

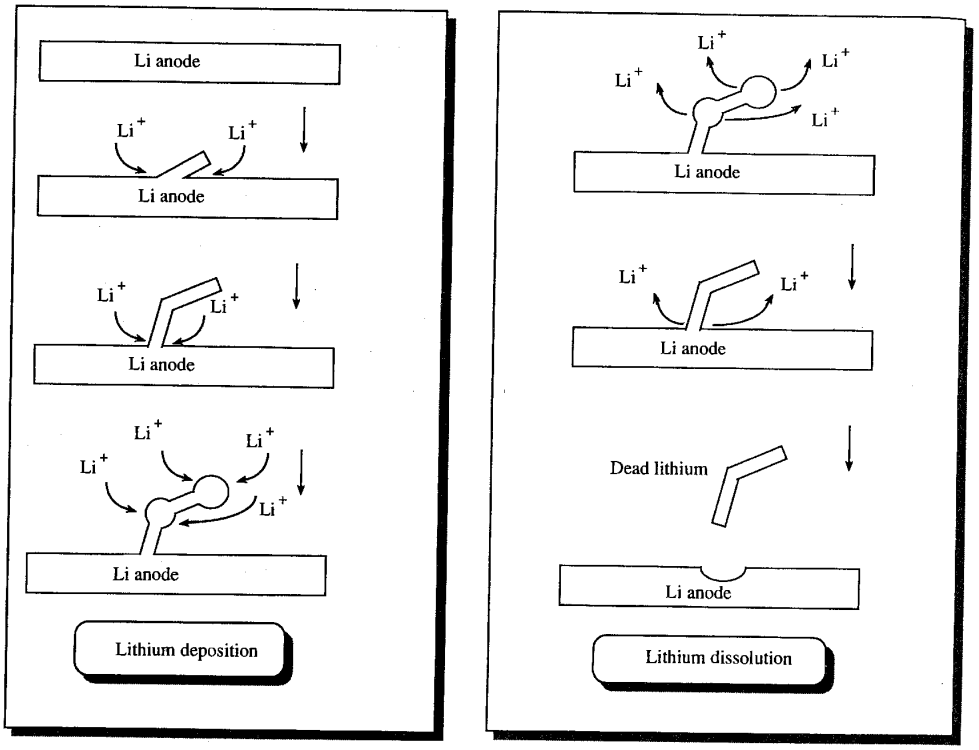


Figure 2. A possible mechanism for lithium deposition (left) based on dissolution (right) lithium morphology observations in $LiAsF_6$ – EC/2MeTHF electrolyte.

Koshina et al. have reported that there are three kinds of morphology [40]: dendritic, granular and mossy. Mossy lithium is formed when the deposition current is small and the salt concentration is high. This mossy lithium provides a high cycling efficiency.

A possible mechanism for lithium deposition based on our observations of lithium morphology in $LiAsF_6$–EC/2MeTHF electrolyte is described below [31]. Figure 2 (left-hand panel) shows our image of the mechanism.

(1) Lihium is deposited on a lithium anode under the protective film without serious damage to the film.
(2) The deposition points on the lithium electrode are the points at which the protective film has a higher lithium-ion conductivity. One example of these deposition points are the pits on the lithium anode caused by discharge. Crystalline defects and the grain boundaries in lithium may also initiate deposition.
(3) As lithium does not deposit uniformly for the reason mentioned above, mechanical stress is created in the lithium electrode under the protective film.
(4) The stress causes lithium-atom trans-

CosMX Exhibit 1008, Page 364 of 633

port, which means that deformation of the lithium occurs to release the stress in it. The lithium transport is not free but is conditioned by a force created by lithium surface tension (including the surface tension caused by the protective film) at a curved surface, and it may also be affected by crystalline defects and grain boundaries.

(5) The protective film is broken in certain places on the lithium surface by the stress. Fiber-like lithium grows, like an extrusion of lithium, through these broken holes in the film. If the deposition current is small enough and the stress is therefore small, the protective film will probably not break. In this case, the deposited lithium may be particle-like or amorphous.

(6) After the fiber-like lithium has grown, lithium is still deposited on the lithium substrate that is not at the tip of the fiber-like lithium. If the deposition continues for a long time, the lithium electrode becomes covered with long, fiber-like lithium. In this situation, lithium-ion transport in the electrolyte to the lithium electrode surface is hindered by the fiber-like lithium. Then, lithium begins to be deposited on the tip and on kinks of the fiber-like lithium, where there are crystalline defects. The morphology of the deposited lithium is particle-like or amorphous. As there are many kinks, the current density of the lithium deposition becomes very low. This low current density may create particle-like, rather than fiber-like, lithium. Thus the morphology of the lithium as a whole becomes mushroom-like [31].

The dissolution process of plated lithium may be the reverse of the plating process (Fig. 2, right-hand panel). At first, the particle-like lithium on the kinks is dissolved. Then, the fiber-like lithium at the base is dissolved. During this process, fiber-like lithium is sometimes cut from the lithium substrate and become dead lithium. There is a large amount of dead lithium when the diameter of the fiber-like lithium is small under conditions of high-rate and/or low-temperature deposition, because the whiskers are easily cut.

A microelectrode has been used by Uchida et al. to study lithium deposition in order to minimize the effect of solution resistance [41]. They used a Pt electrode (10–30 μm in diameter) to measure the lithium-ion diffusion coefficient in 1 mol L^{-1} $LiClO_4$/PC electrolyte. The diffusion coefficient was 4.7×10^{-6} $cm^2\ s^{-1}$ at 25 °C.

The lithium morphology at the beginning of the deposition was measured by in-situ atomic force microscopy (AFM) [42]. When lithium was deposited at 0.6 C cm^2, small particles 200–1000 nm in size were deposited on the thin lines and grain boundaries in $LiClO_4$–PC. Lump-like growth was observed in $LiAsF_6$–PC along the line.

An electrochemical quartz crystal microbalance (EQCM or QCM) can be used to estimate the surface roughness of deposited lithium [43].

3.6 The Amount of Dead Lithium and Cell Performance

From our experimental results [44], the FOM at a low discharge rate is considerably smaller than that at a high discharge rate. The influence of the discharge rate on

CosMX Exhibit 1008, Page 365 of 633

the specific surface area of a lithium anode was examined [44] using the Brunauer–Emmett–Teller (BET) equation. The surface area (26 $m^2 g^{-1}$) for low-rate discharge cycles (0.2 mA cm^{-2}) is double that (13 $m^2 g^{-1}$) for high–rate discharge cycles (3.0 mA cm^{-2}). In addition, the surface area increases with an increase in cycle number. The surface area after the sixth discharge at a low discharge rate was 30 times larger than that before cycling (1 $m^2 g^{-1}$). The main reason for the increase in the lithium surface area is considered to be the accumulation of dead lithium on the anode surface.

There are four possible ways of explaining [45] why a higher current discharge creates a smaller amount of dead lithium.

(1) When the discharge current is high, delocalized pits (small in size but large in number) are formed on a native lithium anode. As a lithium is deposited on these pits, the local charge current density becomes low when the discharge current is high, producing thicker fiber-like lithium that is not easily cut to form dead lithium.
(2) When the discharge current is large, delocalized pits formed in the anode are shallow, so the deposited lithium whiskers can easily emerge from the pits and stack pressure can be applied to them, as mentioned in Sec.3.7.3.
(3) Isolated lithium near the anode becomes a local cell because of stray current. As the stray current is high when the cell discharge current is high, lithium recombination occurs easily at a high discharge current [46].
(4) When the discharge current is high, transport of lithium ions becomes difficult and stripping occurs from the particle-like lithium on the tip and on the kinks of the fiber-like lithium. In this case, the fiber-like lithium rarely breaks and the efficiency increases.

3.7 Improvement in the Cycling Efficiency of a Lithium Anode

There have been many attempts to improve the cycling efficiency of lithium anodes. We describe some of them below, by discussing electrolytes, electrolyte additives, the stack pressure on the electrode, composite anodes, and alternatives to the lithium-metal anode anode.

3.7.1 Electrolytes

Lithium cycling efficiency depends on the electrolyte solutions used. A mixture of EC and 2MeTHF with $LiAsF_6$ as the solute exhibits a high lithium cycling efficiency of 97.2 percent (FOM=35.7) as revealed by a Li-on-Li half-cell test with 10^{-2} S cm^{-1} conductivity at 25 °C [47, 48]. A Li/a-$V_2O_5 - P_2O_5$ coin-type cell with $LiAsF_6$–EC/2MeTHF has a FOM of 28.2, while cells with 2MeTHF or EC/PC (1:1) have FOMs of 9.4 and 14.8, respectively [48]. Lithium cycling efficiency is strongly influenced by impurities in electrolytes. The relationship between total impurity and the FOM of Li in $LiAsF_6$–EC/2MeTHF has been examined [49]. The FOM for EC/2MeTHF increases with decreases in both water and organic impurities. The influence of the impurity depends on the electrolyte system used.

Hayashi et al. [50] investigated the electrolyte materials and their compositions with various carbonates and ethers as

CosMX Exhibit 1008, Page 366 of 633

solvents, in relation to the cycling efficiency of a lithium-metal anode, using cells with a $LiMn_{1.9}Co_{0.1}O_4$ cathode (Fig.3). As electrolyte solvents, they used four carbonates (PC, EC, dimethyl carbonate (DMC), and diethyl carbonate (DEC))and two ethers (DME and 1, 2-diethoxyethane (DEE)). Of the electrolytes used here, 1.0 mol L^{-1} $LiPF_6$–EC/DMC (1:4) provided a high FOM of around 60 and a long cycle life of about 1200 cycles until the discharge capacity became less than 80 percent of the initial capacity.

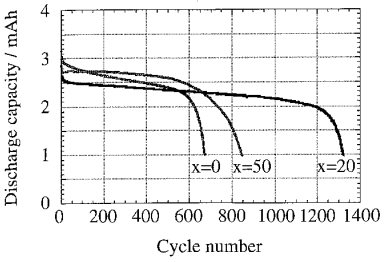


Figure 3. Charge–discharge cycling characteristics of an Li/$LiMn_{1.9}Co_{0.1}O_4$ coin–type cell (thickness 2 mm, diameter 23 mm). Charge: 4.3 V, 1 mA cm^{-2} ; discharge: 3.3 V, 3 mA cm^{-2} ; 1 mol L^{-1} $LiPF_6$ – EC/DMC (x:100–x).

3-Propylsydnone (3-PSD) was proposed as a new solvent by Sasaki et al. [51]. The cycling efficiency of lithium on a Ni electrode of the ternary mixed-solvent electrolyte of 3-PSD, 2MeTHF and 2, 5-dimethyltetrahydrofuran with $LiPF_6$ was about 60 percent, and it was stable with cycling.

An ether, such as 2MeTHF, has the effect of raising the FOM. When an AA Li/a–V_2O_5–P_2O_5 cell with an $LiAsF_6$–EC/PC electrolyte is cycled with a low discharge current of 60 mA (0.1 C discharge rate), the cell shows a shunting tendency (a partial internal short) near the end of its cycle life [52]. However, the addition of 2MeTHF to EC/PC causes the soft shorting to decrease dramatically.

Another influence that electrolyte materials have on the cycle life of a practical lithium cell results from the evolution of gas as a result of solvent reduction by lithium. For example, EC and PC give rise to [53] evolution of ethylene and propylene gas, respectively. In a practical sealed-structure cell, the existence of gas causes irregular lithium deposition. This is because the gas acts as an electronic insulator and lithium is not deposited on an anode surface where gas has been absorbed. As a result, the lithium cycling efficiency is reduced and shunting occurs.

3.7.2 Electrolyte Additives

There have been many studies with the goal of improving lithium cycling efficiency by the use of electrolyte additives. These additives can be classified into three types:

(a) stable additives which cover the lithium to limit any chemical reaction between the electrolyte and lithium;
(b) additives which modify the state of solvation of lithium ions;
(c) reactive additives used to make a better protective film.

Some of the studies on additives based on this classification will now be described.

3.7.2.1 Stable Additives Limiting Chemical Reaction Between the Electrolyte and Lithium

Besenhard et al. [54] studied ways to protect lithium anodes from corrosion by adding saturated hydrocarbons to electro-

CosMX Exhibit 1008, Page 367 of 633

lytes. They considered saturated hydrocarbons to be chemically stable, and thus able to delay the irreversible reduction of organic electrolytes by lithium. They found that the deposited lithium was particle-shaped when *cis-* or *trans*-decalin was added to $LiClO_4$–PC electrolyte. Although there was no change in the cycling efficiency, the long-term storage characteristics improved.

Naoi and co-workers [55], with a QCM, studied lithium deposition and dissolution processes in the presence of polymer surfactants in an attempt to obtain the uniform current distribution at the electrode surface and hence smooth surface morphology of the deposited lithium. The polymer surfactants they used were polyethyleneglycol dimethyl ether (molecular weight≈446), or a copolymer of dimethylsilicone (ca. 25 wt%) and propylene oxide (ca. 75 wt%) (molecular weight≈3000) in $LiClO_4$–EC/DMC (3:2, v/v).

Yoshio and co-workers [56, 57] tried using aromatic compounds of benzene, toluene or 4, 4-dipyridyl as additives and found them to be effective.

Later, Saito et al. [58] studied anodes with a layered structure consisting of Li/ protective film/additive/protective film/Li/ protective film/additive/ –. They made the anode by dropping the additive on a lithium sheet, folding the lithium sheet, and then compressing the folded lithium with an oil press. They repeated this process more than ten times. The FOM in $LiAsF_6$–EC/2MeTHF electrolyte was 7.41, 13.5, and 37.0 for a lithium anode without additives, a lithium anode with toluene in the electrolyte, and a layered-structure lithium anode containing toluene, respectively.

3.7.2.2 Additives Modifying the State of Solvation of Lithium Ions

Compounds which produce a complex with Li^+ ions have been investigated. The compounds examined were *N,N,N′,N′*–tetramethylethylenediamine (TMEDA), ethylenediamine, crown ethers, cryptand [211], diglyme, triglyme, tetraglyme, ethylenediamine tetraacetic acid (EDTA) and EDTA-Li^+n (n=1, 2, 3) complexes [59]. The cycling efficiency was improved by adding TMEDA, but the other additives did not show distinct effects.

3.7.2.3 Reactive Additives Used to Make a Better Protective Film

The effect of "precursors" was examined by Brummer et al. [69] with the aim of producing a thin and Li^+-ion conductive film which was impermeable to solvent molecules. As precursors, they tested CS_2, $PSCl_3$, $PSBr_3$, $POBr_3$, $PNBr_2$, $POCl_3$, CH_3SO_2, $MoOCl_4$, $VOCl_2$, CO_2, N_2O, and SO_2 with 1 mol L^{-1} $LiClO_4$–PC. The concentration of additive ranged from 0.01 to 0.36 mol L^{-1}. A maximum efficiency of 85.1 percent was obtained by the addition 0.01 mol L^{-1} $POCl_3$, where the base electrolyte without any additive showed an average efficiency of 40 percent. However, without additives, 1 mol L^{-1} $LiAsF_6$–PC has an efficiency of 85.2 percent and the addition of $POCl_3$ to $LiAsF_6$ provides 75.8 percent efficiency. These results indicate that the use of $LiAsF_6$ provides a better film for cycling Li than those formed by the precursors. However, we believe that it is still worth attempting to find new precursors.

Also, the influence of adding O_2, N_2, Ar, or CO_2 to $LiAsF_6$–THF on lithium cycling efficiency has been examined [64].

CosMX Exhibit 1008, Page 368 of 633

Lithium was cycled on an Ni electrode with Q_p=1.125 C cm^{-2} and cycling currents of 5 mA cm^{-2}. Oxygen and N_2 helped to maintain the cycle life relative to Ar, while CO_2 and ungassified electrolyte did not. The addition of O_2 showed the highest lithium cycling efficiency which resulted from the formation of an Li_2O film. However, the lithium cycling efficiency rapidly degraded beyond the ten cycle. On the basis of these results, Dominey et al. [65] examined the effect of adding KOH to ether-based electrolytes such as THF, 2MeTHF, or 1, 3-dioxolane. They showed that the presence of the hydroxide modifies the surface film formation. The anode-related heat output was reduced three-to four-fold in cyclic-ether electrolytes containing approximately 100 ppm of OH^-. The Li/TiS_2 cell with THF to which 2MeF, KOH, and 12-crown-4 had been added has been reported to show excellent cycling efficiency. Further improvement in the lithium deposition morphology is still required, however. $LiAsF_6$–2MeTHF has a good cycling efficiency. Abraham et al. [66] showed that the high cycling efficiency is caused by 2MeF, which is naturally contained in 2MeTHF as in impurity.

Quinoneimine dyes, aromatic nitro compounds, and triphenylmethane compounds have been studied [70]. These compounds are highly reactive with lithium. If the lithium cell includes these compounds as the cathode, it will exhibit cell voltages of 2–3 V. The cycling efficiency was improved by adding quinoneimine dyes. However, this effect depends on the charge capacity and the duration of charge–discharge cycling. The effect of hexamethylphosphoric triamide (HMPA) has also been examined. HMPA has an extremely high solvation power for cations whose donor number (DN) is 38 [71]. A unique characteristic of HMPA is that it produces solvated electrons in contact with alkali metals when there is a large excess of HMPA. A lithium cycling efficiency of 86.6 percent was obtained by the addition of 0.5 vol.% HMPA to 1 mol L^{-1} $LiClO_4$–PC, which exhibits 67.0 percent efficiency [72]. In addition, Li cells with an organic cathode, Fe phthalocyanine (FePc), containing 1 mol L^{-1} $LiClO_4$–PC with HMPA (0.5–10 vol.%) completed 80–240 cycles, whereas a cell without PC completed only 55 cycles [72] (Table 4).

Table 4. Influence of HMPA addition on cycle life of Li/Fe-phthalocyanine (FePc) cell*

HMPA(vol.%)	Cycle life
0.5	240
1.0	220
10.0	80
No additives	55

*Electrolyte = 2 mol Li^{-1} $LiClO_4$–PC; charge–discharge currents = 0.3 mA cm^{-2}; cycling capacity =200 mAh g^{-1} (4.3 Li/FePc).

Carbon dioxide has been proposed as an additive to improve the performance of lithium batteries [60]. Aurbach et al. [61] studied the film formed on lithium in electrolytes saturated with CO_2, and using in situ FTIR found that Li_2CO_3 is a major surface species. This means that the formation of a stable Li_2CO_3 film on the lithium surface may improve cyclability [62]. Osaka and co-workers [63] also studied the dependence of the lithium efficiency on the plating substrate in $LiClO_4$–PC. The addition of CO_2 resulted in an increase in the efficiency when the substrate was Ni or Ti, but no effect was observed with Ag or Cu substrates.

Tekehara and co-workers [67] tried to modify the native film of lithium by an acid–base reaction. HF, HI, H_3PO_4, and HCl were selected as acids, because of the

CosMX Exhibit 1008, Page 369 of 633

possibility of their reacting with the Li_2CO_3, LiOH, and Li_2O which compose the lithium native film, resulting in the formation of LiA (HA=acid). LiF was observed, by XPS, in the film treaded with HF. HF treatment changed the deposition morphology from dendritic to particle-like in $LiPF_6$–PC electrolyte. XPS showed that after HF treatment the lithium surface was composed of two layers (LiF and Li_2O), whereas the native surface was composed of three layers (Li_2CO_3, LiOH, and Li_2O). The impedance of the lithium was reduced by this treatment. The cycling efficiencies [68] in $LiPF_6$–PC were 57 and 70 percent for as-received and HF-treated lithium, respectively. We have also confirmed the above results reported by Takehara et al. Figures 4 and 5 show our results, which reveal that HF treatment changed the deposition morphology from dendritic to particle-like in $LiPF_6$–PC electrolyte.

Sulfur is known to be easily reducible in nonaqueous solvents and its reduction products exist at various levels of reduction of polysulfide radical anions ($S_n^{\bullet -}$) and dianions (S_m^{2-}) [73]. Recently Besenhard and co-workers [74] have examined the effect of the addition of polysulfide to $LiClO_4$–PC. Lithium is cycled on an Ni substrate with Q_p=2.7 C cm^{-2} and cycling currents of 1 mA cm^{-2}. The cycling efficiency in PC with polysulfide is higher than that without an additive. The lithium deposition morphology is compact and smooth in PC with added polysulfide, whereas it is dendritic in PC alone.

Matsuda and co-workers [75, 76] examined LiI, SnI_2, AlI_3 and 2MeF (2-methylfuran) as additives in $LiClO_4$–PC or $LiClO_4$–PC/DMC electrolyte. They measured the cycling efficiency of lithium on an Ni electrode. All the additives increased the efficiency; the best additive was a combination of AlI_3 and 2MeF. They attributed the improvement to the formation of Li–Al alloy on the surface by AlI_3, or a more protective film formed by 2MeF.

We have examined the effects of adding metal chloride (MCl_x; CuCl, $CuCl_2$, $AlCl_3$, and $NiCl_2$) on the lithium cycling efficiency in 1 mol L^{-1} $LiClO_4$–PC. The results are shown in Table 5.

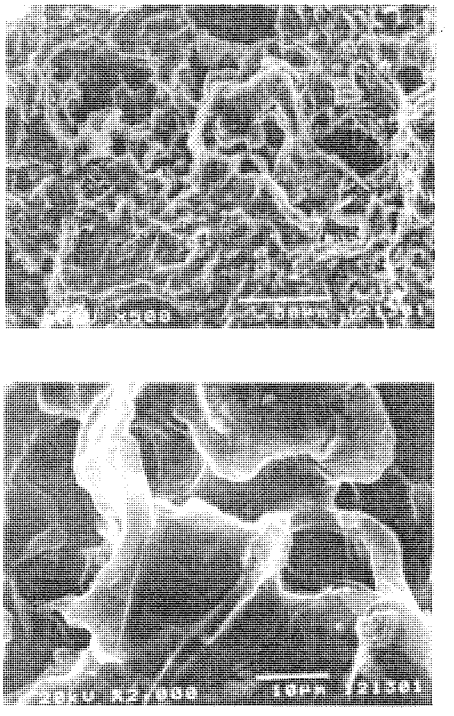
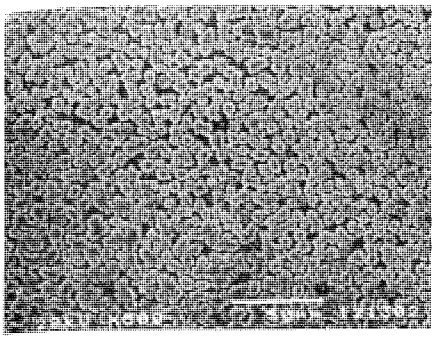


Figure 4. Morphology of deposited lithium on lithium, after five cycles with 1 mA cm^{-2}, 2 mAh cm^{-2} in 1 mol L^{-1} $LiPF_6$ – PC.

These compounds may reduce the reactivity of lithium and make the lithium deposition morphology smoother as a result of the spontaneous electrochemical alloy formation during the charging of lithium on the anode. The lithium was plated on

CosMX Exhibit 1008, Page 370 of 633



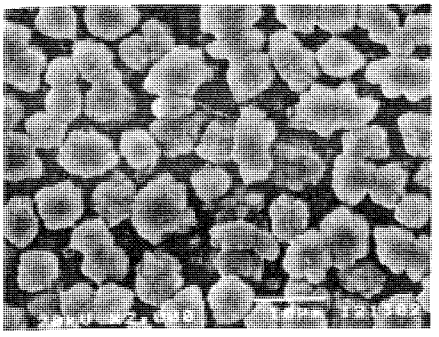


Figure 5. Morphology of deposited lithium on lithium after immersion of lithium in 1 mol L^{-1} $LiPF_6$ – PC with HF (3 vol. %) for three days: five cycles with 1 mAh cm^{-2} in 1 mol L^{-1} $LiPF_6$ – PC.

the Pt working electrode with Q_p=0.6 C cm^{-2} at 0.5 mA cm^{-2}. The lithium cycling efficiency was improved by addition of metal chlorides. The cycling efficiencies were in the order Al > Ni > Cu. β-Li–Al was detected by X-ray diffraction in the surface of the lithium anode after charge–discharge cycling.

3.7.3 Stack Pressure on Electrodes

Wilkinson et al. [77] examined the effect of stack pressure on the lithium turnover (FOM for lithium cycling efficiency) in Li/MoS_2 prismatic cells containing 1 mol L^{-1} $LiAsF_6$–PC. The cycle life for spirally wound AA-size Li/MoS_2 cells showed that when the electrode assembly is housed tightly in the cell the cycle life is better than with loosely housed cells.

FOMs were also measured [78] for coin-type cells with an amorphous V_2O_5–P_2O_5 cathode and a lithium anode 20 μm thick. $LiAsF_6$–EC/2MeTHF electrolyte had an FOM of 80 at 125 kg cm^{-2}, which was almost four times the value without compression. An SEM image of lithium deposited under stack pressure showed that it was densely packed, which reduces the amount of lithium that was isolated from the anode substrate, resulting in a high cycling efficiency.

Table 5. Lithium cycling efficiency on Pt in 1 mol L^{-1} $LiClO_4$ –PC with 0.1 mol L^{-1} metal halides added.*

Metal halide	Eff, 10**(%)	Electrochemical alloying efficiency of metals with lithium [27]
$AlCl_3$	91.2	92
CuCl	88.7	42
$NiCl_2$	84.8	50
$CuCl_2$	72.0	–
No additives	65.0	–

*Cycling current=0.5 mA cm^{-2}, plating capacity=0.6 C cm^{-2}.
**Eff, 10=average cycling efficiency from 1st to the 10th cycle.

CosMX Exhibit 1008, Page 371 of 633

3.7.4 Composite Lithium Anode

Desjardins and MacLean [79] studied a composite of lithium and Li_3N named "Linode". Their research cell showed improvements in cycle life, shelf life, and electrode morphology after cycling.

A lithium anode mixed with conductive particles of Cu or Ni was studied by Saito et al.; they obtained an improvement in the cycling efficiency (Fig.6) [80]. Their idea is based on the recombination of dead lithium and formation of many active sites for deposition.

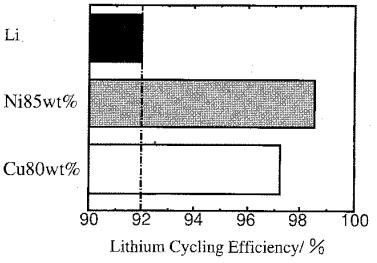


Figure 6. Lithium cycling efficiency of composite lithium anodes in an Li/a $-V_2O_5$ coin-type cell (thickness 2 mm, diameter 23 mm) with 1.5 mol L^{-1} $LiAsF_6$ – EC/2MeTHF.

We believe that the advantage of these composite anodes is that they result in a uniform lithium deposition at the boundaries of two components that may improve the cycling efficiency.

3.7.5. Influence of Cathode on Lithium Surface Film

It is generally considered that the lithium surface film is produced by a reaction between the lithium and the electrolyte materials. However, by XPS we have detected vanadium on a lithium anode surface cycled for Li/a-$V_2O_5-P_2O_5$ cells with EC-based electrolytes [81]. Vanadium comes from the partially dissolved discharge product, $Li_xV_2O_5$, in the electrolyte. Then, with a Li/a-V_2O_5 cell, the cathode also affects the chemical composition of the surface film [81].

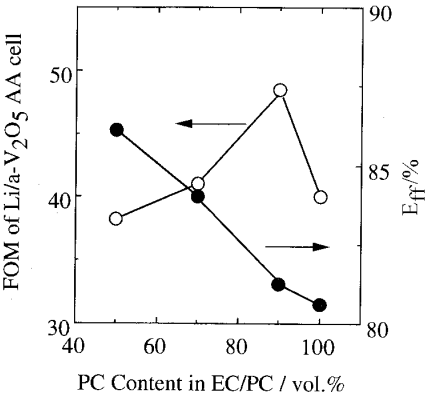


Figure 7. Relationship between FOM of AA cells, lithium cycling efficiency (Eff) on stainless steel, and PC content in 1 mol L^{-1} – $LiAsF_6$ – EC/PC.

Figure 7 shows the FOM of an AA cell and the PC content in EC/PC binary mixed-solvent electrolytes. With an increase in PC content, the lithium cycling efficiency (Eff) obtained with Li cycling on a stainless steel substrate increases. However, the FOM of the AA cell reaches its maximum value at EC/PC=1:9 [82]. This result arises from the interaction between EC and the a-$V_2O_5-P_2O_5$ cathode.

3.7.6. An Alternative to the Lithium-Metal Anode (Lithium-Ion Inserted Anodes)

Recently, lithium-ion inserted compounds have been investigated as new anodes. These compounds have the possibility of

CosMX Exhibit 1008, Page 372 of 633

exhibiting a larger energy density than carbon materials and have anode properties similar to those of lithium metal.

Nishijima et al. [83] reported that lithium ternary nitrides of Li_3FeN_2, Li_7MnN_4, and $Li_{2.5}Co_{05}N$ perform as anodes. These materials exhibit a specific capacity of 200–480 mAh^{-1} g, which is as high as that of carbon. Shodai et al. have found that the capacity of the $Li_{3-x}Co_xN$ (x=0.2–0.6) system can be increased substantially by extracting lithium ions from the matrix. $Li_{2.6}Co_{0.4}N$ exhibits a high specific capacity of 760 mAh g^{-1} in the 0–1.4 V vs. Li/Li^+ range. Shodai et al. [84] also described the performance of an $Li_{1.6}Co_{0.4}N/LiNiO_2$ lithium-ion cell, which was designed so that the $Li_{1.6}Co_{0.4}N$ anode operated at 0–1.0 V and the $LiNiO_2$ cathode operated at 4.2–3.5 V vs. Li/Li^+. This cell shows a good reversibility of more than 150 cycles.

Idota et al. have demonstrated [85] that amorphous material based on tin oxide has capacities of 800 mAh g^{-1} and 3200 mAh cm^{-3}, which are respectively two and four times higher than those of carbon. An 18 650-size cell with an $LiCoO_2$ cathode has a capacity of 1850 mAh, which is higher than the value of 1350 mAh for the commercial cells.

Sigala et al. [86] also examined Li_xMVO_4 (M = Zn, Co, Ni, Cd) as anode materials. The best compounds (M = Zn, Ni) deliver capacities of about 700 mAh g^{-1} after 200 cycles. The search for new anode compounds will prove to be a fruitful area in the future.

3.8 Safety of Rechargeable Lithium Metal Cells

We have developed a prototype AA-size cell which consists of an amorphous (a-) $V_2O_5-P_2O_5$ (95:5, molar ratio) cathode and a lithium anode (Li/a-V_2O_5 cell) [1]. In this section, we describe safety test results for AA Li/a-V_2O_5 cells. The AA cell we fabricated has a pressure vent, a Polyswitch (PS, Raychem Co., thermal and current fuse) and is composed of a spirally wound cathode sheet, a metallic Li-based anode sheet and a polyethylene (PE) separator [87].

The basic considerations regarding the cell safety and the test results are described briefly below.

3.8.1. Considerations Regarding Cell Safety

The basic problem in regard to the safety of rechargeable metal cells is how to manage the heat generated in a cell when it is abused. The temperature of a cell is determined by the balance between the amount of heat generated in the cell and the heat dissipated outside the cell. Heat is generated in a cell by thermal decomposition and /or the reaction of materials in the cell, as listed below:

(1) by a reaction between an electrolyte and an anode;
(2) by the thermal decomposition of an electrolyte.
(3) by a reaction between an electrolyte and a cathode;
(4) by the thermal decomposition of an anode;
(5) by the thermal decomposition of an cathode;
(6) by an entropy change in a cathode active material (and an anode inactive material);
(7) by current passing through a cell with electric resistance.

When a cell is heated by some trigger (for

CosMX Exhibit 1008, Page 373 of 633

example, an internal short, application of a high current, or overcharge), heat will be generated if the cell temperature is high enough to cause decomposition and/or a reaction. This situation leads to the thermal runaway of the cell. In the worst case, the cell ignites. If the additional heat generation is small, the cell temperature does not increase so much, and the cell is safer.

3.8.2. Safety Test Results

3.8.2.1 External Short

We experienced no safety problems during the external short tests because of the Polyswitch inside the cell. We confirmed that even if the Polyswitch fails to operate, the short-circuit current stops flowing before thermal runaway occurs because the micropores are closed by the polyethylene separator, which melts at 125 °C ("separator shutdown").

3.8.2.2 Overcharge

In the overcharge tests we carried out, there was no fire or explosion. The cell impedance increased suddenly in every test. This was due to the oxidation of the electrolyte with a low charging current, or to the separator melting with a high charging current. In practical applications, an electronic device should be used to provide overcharge protection and ensure complete safety.

3.8.2.3 Nail Penetration

The nail penetration test is very important and is considered to simulate an internal short in a cell. No electronic device can protect against an internal short, so the cell itself should pass this test. Our cell did not ignite or explode.

3.8.2.4 Crush

The cell should also be able to survive a crush test because an electronic device cannot provide protection in this case either. Our test cell remained safe in crush tests, both with a bar and with a flat plate.

3.8.2.5 Heating

The heating test is carried out by increasing the temperature at a rate of 5 °C min^{-1} and then holding it constant at least until the maximum cell temperature induced by the internal exothermic reactions starts to decrease. If the thermal stability decreases after cycling, we have to be careful when estimating the safety. The thermal stability of our cell is defined by the maximum temperature at which it can be ensured that no fire will occur. For our cell, this is 130 °C before cycling. The thermal stability limit becomes even higher after cycling. These results are considered to be closely related to the increase in the thermal stability of a lithium anode with an increase in the number of charge–discharge cycles as the result of the formation of a special lithium surface film containing vanadium.

3.9 Conclusion

It is worthwhile attempting to develop a rechargeable lithium metal anode. This anode should have a high lithium cycling efficiency and be very safe. These properties can be realized by reducing the dead lithium. Practical levels of lithium cycling efficiency and safety could be achieved

simultaneously by the same technical breakthrough. This will be realized by a wholehearted effort to develop a method of anode construction a new electrolyte and a new cell structure. Another interesting area of study is the investigation of new anode materials whose energy density is as close as possible as to that of pure lithium metal.

3.10 References

[1] Y. Sakurai, S. Sugihara, M. Shibata, J. Yamaki, *NTT ev* **1995**, *7*, 60.

[2] S. P. S. Yen, D. Dhen, R. P. Vansquéz, F. J. Grunthaner, R. B. Somoano, *J. Electrochem. Soc.* **1981**, *128*, 1434.

[3] S. Hirayama, H. Hiraga, K. Otsuka, N. Ikeda, M. Sasaki, *Extended Abstracts of the 34th Battery Symposium in Japan*, **1993**, Abstract No. 1AOb.

[4] N. Yamamoto, K. Saito, T. Ishibashi, M. Honjo, T. Fujieda, S. Higuchi, *Extended Abstracts of the 34th Battery Symposium in Japan*, **1993**, Abstract No.

[5] W. R. Harris, Ph. D. Thesis, University of California, Berkeley, **1958**.

[6] A. N. Dey, *Extended Abstracts of Electrochemical Society Meeting*, Atlantic City, USA, **1970**, Abstract No.

[7] R. D. Rauh, S. B. Brummer, *Electrochim. Acta.* **1977**, *22*, 75.

[8] E. Peled, *J. Electrochem. Soc.* **1979**, *126*, 2047.

[9] A. N. Dey, *Thin Solid Films* **1977**, *43*, 131.

[10] G. Nazri, R. H. Muller, *J. Electrochem. Soc.* **1985**, *132*, 2050.

[11] D. Aurbach, M. L. Daroux, P. W. Faguy, E. Yeager, *J. Electrochem. Soc.* **1987**, *134*, 1611.

[12] K. M. Abraham, S. M. Chaudhri, *J. Electrochem. Soc.* **1986**, *133*, 1307.

[13] J. L. Goldman, R. M. Mank, J. H. Young, V. R. Koch, *J. Electrochem. Soc.* **1980**, *127*, 1461.

[14] D. Aurbach, M. L. Daroux, P. W. Faguy, E. Yeager, *J. Electrochem. Soc.* **1986**, *135*, 1307.

[15] M. Odziemkowski, M. Krell, D. E. Irish, *J. Electrochem. Soc.* **1992**, *139*, 3052.

[16] S. P. S. Yen, D. Shen, R. P. Vasquez, F. J. Grunthaner, R. B. Samoano, *J. Electrochem. Soc.* **1981**, *128*, 1434.

[17] D. Aurbach, *J. Electrochem. Soc.* **1989**, *136*, 1606.

[18] D. Aurbach, O. Youngman, Y. Gofer, A. Meitav, *Electrochim. Acta* **1990**, *35*, 625.

[19] Y. E. Ely, D. Aurbach, *Proc. Symp. High Power Ambient Temperature Lithium Batteries*, The Electrochemical Society, **1992**, p. 157.

[20] T. Itoh, T. Nishina, T. Matsue, I. Uchida, *Extended Abstracts of the 36th Battery Symposium in Japan*, **1995**, Abstract No.

[21] D. Aurbach, A. Zaban, Y. Gofer, Y. E. Ely, I. Weissman, O. Chusid, O. Abramson, *J. Power Sources*, **1995**, *54*, 76.

[22] D. H. Shen, S. Subbarao, F. Deligiannis, G. Halpert, *Proc. Symp. Materials and Processes for Lithium Batteries*, The Electrochemical Society, **1989**, p. 223.

[23] R. Selim, P. Bro, *J. Electrochem. Soc.* **1974**, *121*, 1457.

[24] a) L. P. Klemann and G. H. Newman, *Proc. Symp. Lithium Batteries*, Battery Division, The Electrochemical Society, **1981**, *81–4*, p. 189; b) K. M. Abraham, J. L. Goldman, D. L. Natwig, *J. Electrochem. Soc.* **1982**, *129*, 2404.

[25] J. Yamaki, M. Arakawa, S. Tobishima, T. Hirai, *Proc. Symp. Lithium Batteries*, Battery Division, The Electrochemical Society, **1987**, *87–1*, p. 266.

[26] S. Tobishima, J. Yamaki, A. Yamaji, T. Okada, *J. Power Sources* **1984**, *13*, 261.

[27] A. N. Dey, *J. Electrochem. Soc.* **1971**, *118*, 1547.

[28] D. Rauh, T. F. Reise, S. B. Brummer, *J. Electrochem. Soc.* **1983**, *130*, 101.

[29] J. S. Foos, V. Meltz, L. M. Rembetsy, *Extended Abstarcts of Electrochemical Society Fall Meeting*, **1984**, Abstract No.

[30] F. C. Laman, K. Brandt, *J. Power Sources* **1988**, *24*, 195.

[31] a) I. Yoshimatsu, T. Hirai, J. Yamaki, *J. Electrochem. Soc.* **1988**, 135, 2422; b) M. Arakawa, S. Tobishima, Y. Nemoto, M. Ichimura, J. Yamaki, *J. Power Sources* **1993**, *43–44*, 27.

[32] K. Kanamura, S. Shiraishi, Z. Takehara, *J. Electrochem. Soc.* **1994**, *141*, L108.

[33] J. O. Besenhard, G. Eichinger, *J. Electroanal. Chem* **1976**, *68*, 1.

[34] S. Tobishima, J. Yamaki, A. Yamaji, T. Okada, J. *Power Sources* **1984**, *13*, 261.

CosMX Exhibit 1008, Page 375 of 633

[35] S. Tobishima, T. Okada, *Electrochim. Acta* **1985**, *30*, 1715.
[36] S. Tobishima, T. Okada, *J. Appl. Electrochem.* **1985**, *15*, 317.
[37] S. Tobishima, J. Yamaki, T. Okada, *DENKI KAGAKU* **1985**, *53*, 173.
[38] T. Hirai, I. Yoshimatsu, J. Yamaki *J. Electrochem. Soc.* **1994**, *141*, 611.
[39] C. Fringant, A. Tranchant, R. Messina, *Electrochim. Acta* **1995**, *40*, 513.
[40] H. Koshina, N. Eda, A. Morita, *Extended Abstracts of the 30th Battery Symposium in Japan* **1995**, Abstract No.
[41] I. Uchida, X. Wang, T. Nishina, *Extended Abstracts of the 35th Battery Symposium in Japan* **1994**, Abstract No.
[42] K. Morigaki, N. Kabuto, K. Yoshino, A. Ohta, *Extended Abstracts of the 35th Battery Symposium in Japan* **1994**, Abstract No.
[43] M. Mori, Y. Shinagawa, T. Suzuki, K. Naoi, *Extended Abstracts of the 36th Battery Symposium in Japan* **1995**, Abstract No.
[44] K. Saito, M. Arakawa, S. Tobishima, J. Yamaki, *DENKI KAGAKU* **1994**, *62*, 888.
[45] S. Hirayama, H. Hiraga, K. Otsuka, N. Ikeda, M. Sasaki, *'Extended Abstracts of the 34th Battery Symposium in Japan* **1993**, Abstract No. 1A0b.
[46] M. Arakawa, S. Tobishima, Y. Nemoto, M. Ichimura, J. Yamaki, *J. Power Sources* **1993**, *43–44*, 27.
[47] M. Arakawa, S. Tobishima, T. Hirai, J. Yamaki, *J. Electrochem. Soc.* **1986**, *133*, 1527.
[48] S. Tobishima, M. Arakawa, T. Hirai, J. Yamaki, *J. Power Sources* **1987**, *20*, 293.
[49] M. Arakawa, S. Tobishima, T. Hirai, J. Yamaki, *Extended Abstracts Spring Meeting of the Electrochemical Society of Japan* **1986**, Abstract No.
[50] K. Hayashi, S. Tobishima, J. Yamaki, *Extended Abstracts of '95 Asian Conference on Electrochemistry*, **1995**, Abstract No.
[51] Y. Sasaki, H. Kaido, H. Ohashi, T. Minato, M. Handa, N. Chiba, *Extended Abstracts of the 34th Battery Symposium in Japan* **1993**, Abstract No.
[52] S. Tobishima, K. Hayashi, K. Saito, T. Shodai, J. Yamaki, *Electrochim. Acta* **1997**, *42*, 119.
[53] J. A. Stiles, D. T. Fouchard, *Proc. Symp. Primary and Secondary Ambient Temperature Lithium Batteries*, The Electrochemical Society, **1988**, *Vol.* PV-88, p. 422.
[54] J. O. Besenhard, J. Guertler, P. Komenda, *J. Power Sources* **1987**, *20*, 253.
[55] M. Mori, Y. Kakuta, K. Naoi, D. F. Auteux, *Extended Abstracts of the 37th Battery Symposium in Japan*, **1996**, Abstract No.
[56] M. Yoshio, H. Nakamura, K. Isono, S. Itoh, K. Holzleithner, *Progr. Batt. Solar Cells* **1988**, *7*, 271.
[57] C. Wang, H. Nakamura, M. Yoshio, *Extended Abstracts of the 37th Battery Symposium in Japan*, **1996**, Abstract No.
[58] K. Saito, Y. Nemoto, S. Tobishima, J. Yamaki, *Extended Abstracts of the 36th Battery Symposium in Japan*, **1995**, Abstract No.
[59] S. Tobishima, M. Arakawa, K. Hayashi, J. Yamaki, *Extended Abstracts of the 34th Battery Symposium in Japan*, **1993**, Abstract No.
[60] M. Salomon, *J. Power Sources* **1989**, *9*, 26.
[61] D. Aurbach, O. Chusid (Youngman), *J. Electrochem. Soc.* **1993**, *140*, L155.
[62] T. Osaka, T. Momma, T. Tajima, Y. Matsumoto, *DENKI KAGAKU* **1994**, *62*, 451.
[63] Y. Matsumoto, Y. Uchida, T. Momma, T. Osaka, *Extended Abstracts of the 36th Battery Symposium in Japan*, **1995**, Abstract No.
[64] V. R. Koch, J. H. Young, *J. Electrochem. Soc.* **1978**, *125*, 1371.
[65] L. A. Dominey, J. L. Goldman, V. R. Koch, *Proc. Symp. Materials and Processes for Lithium Batteries*, The Electrochemical Society, **1989**, p. 213.
[66] K. M. Abraham, J. S. Foos, J. L. Goldman, *J. Electrochem. Soc.* **1984**, *131*, 2197.
[67] S. Shiraishi, K. Kanamura, Z. Takehara, *Extended Abstracts of the 34th Battery Symposium in Japan*, **1993**, Abstract No.
[68] S. Shiraishi, K. Kanamura, Z. Takehara, *Extended Abstracts of the 35th Battery Symposium in Japan*, **1994**, Abstract No.
[69] S. B. Brummer, V. R. Koch, R. D. Rauh, *Materials for Advanced Batteries*, Eds: D. W. Murphy, J. Broadhead, B. C. H. Steel, Plenum Press, New York, **1980**, p. 123.
[70] S. Tobishima, T. Okada, *J. Appl. Electrochem.* **1985**, *15*, 901.
[71] V. Gutman, *The Donor–Acceptor Approach To Molecular Interactions*, Plenum Press, New York, **1978**, ch. 3.
[72] S. Okada, S. Tobishima, J. Yamaki, *Extended Abstracts of Spring Meeting of Electrochemical Society of Japan*, **1987**, D132.
[73] S. Tobishima, H. Yamamoto, S. Nishi, M. Matsuda, *Extended Abstracts of Fall Meeting*

CosMX Exhibit 1008, Page 376 of 633

of Electrochemical Society of Japan, **1978**, Abstract No. 1J25.

[74] M. W. Wagner, C. Liebenow, J. O. Besenhard, *Extended Abstracts of 8th Int. Meeting on Lithium Batteries*, **1996**, Abstract No. I B12.

[75] M. Ishikawa, S. Yoshitake, M. Morita, Y. Matsuda, *J. Electrochem. Soc.* **1994**, *141*, L159.

[76] U. Uraoka, M. Ishikawa, K. Kishi, M. Morita, Y. Matsuda, *Extended Abstracts of the 37th Battery Symposium of Japan*, **1996**, Abstract No. 1A29.

[77] D. P. Wilkinson, H. Blom, K. Brandt, D. Wainwright, *J. Power Sources* **1991**, *36*, 517.

[78] T. Hirai, I. Yoshimatsu, J. Yamaki, *J. Electrochem. Soc.* **1994**, *141*, 611.

[79] C. D. Desjardins, G. K. MacLean, *Extended Abstracts of the Electrochemical Society Meeting, Hollywood, Florida, USA*, **1989**, Abstract No. 52.

[80] K. Saito, M. Arakawa, S. Tobishima, J. Yamaki, *Extended Abstracts of the Electrochemical Society Meeting, Reno, Nevada, USA*, **1995**, Abstract No. 14.

[81] M. Arakawa, Y. Nemoto, S. Tobishima, M. Ichimura, J. Yamaki, *J. Power Sources* **1993**, *43–44*, 517.

[82] S. Tobishima, K. Hayashi, Y. Nemoto, J. Yamaki, *Denki Kagaku* **1996**, *64*, 1000.

[83] M. Nishijima, N. Tadokoro, N. Imanishi, Y. Takeda, O. Yamamoto, *Extended Abstracts of 61th Electrochemical Society Meeting of Japan*, **1996**, Abstract No.

[84] T. Shodai, S. Okada, S. Tobishima, J. Yamaki, *Extended Abstracts of 8th Int. Meeting on Lithium Batteries*, **1996**, Abstract No. IA18.

[85] Y. Idota, Y. Mineo, A. Matsufuji, T. Miyasaka, *Abstracts of 96 IBA Fall Semin Tokyo, Oct. 22*, **1996**, Abstract No. 1.

[86] C. Sigala, A. L. La Salle, D. Guyomard, Y. Piffard, *Extended Abstracts of 8th Int. Meeting on Lithium Batteries*, **1996**, Abstract No. II B63.

[87] S. Tobishima, Y. Sakurai, J. Yamaki, *Extended Abstracts of 8th Int. Meeting on Lithium Batteries*, **1996**, Abstract No. IC17.

CosMX Exhibit 1008, Page 377 of 633

4 Lithium Alloy Anodes

Robert A. Huggins

4.1 Introduction

The interest in ever-higher energy content has caused the development of cells with relatively high voltages to receive much attention in the lithium battery research community in recent years. This has led to the exploration of a number of positive electrode materials that operate at potentials of about 4 V, or even more, positive of the potential of elemental lithium.

However, this is only part of the story, for the voltage of a cell is determined by the difference between the potentials of the negative and positive electrodes. The highest voltages are obtained by the use of elemental lithium in the negative electrode. The use of negative electrode reactants with lithium activities of less than unity results in electrodes with more positive potentials, thus reducing the cell voltage.

The voltage is only one of the important parameters of batteries, and other considerations also are often important in practical systems. One that has received increasing attention in recent years is the question of safety. Batteries that store large amounts of energy can be very dangerous if that energy is suddenly released, and there have been a number of accidents involving lithium batteries. It is now recognized that these safety problems generally relate to phenomena at the negative electrode. Local heating to high temperatures, especially above the melting point of lithium when elemental lithium is used, can lead to serious disasters.

In addition, the cycling behaviour of lithium cells is often limited by negative electrode problems. These may include gradually increasing impedance, which is observed as decreasing output voltage. In some cases there is a macroscopic shape change. If elemental lithium is used (below its melting point), there may be dendrite growth, or a tendency for filamentary or whisker formation. This may lead to disconnection and electrical isolation of active material, resulting in loss of capacity. It may also result in potentially dangerous electrical shorting between electrodes.

Whereas there had been a significant amount of work on the properties of lithium alloys in the research community for a number of years, this alternative did not receive much attention in the commercial world until about 1990, when Sony began producing batteries with lithium–carbon negative electrodes. Since then, there has been a large amount of work on the preparation, structure, and properties of various carbons in lithium cells.

Another aspect is now beginning to receive attention, also on the basis of commercial development rather than arising

directly from activities in the public research community. This is the development by Fuji Photo Film Co. of the use of materials based upon tin oxide as negative electrodes. As will be discussed later, this involves the formation of alloys by the in-situ conversion of the oxide.

4.2 Problems with the Rechargeability of Elemental Electrodes

In the case of an electrochemical cell with a negative electrode consisting of an elemental metal, the process of recharging is apparently very simple, for it merely involves the electrodeposition of the metal. There are problems, however.

One of these is the "shape change" phenomenon, in which the location of the electrodeposit is not the same as that of the discharge (deplating) process. Thus, upon cycling, the electrode metal is preferentially transferred to new locations. For the most part, this is a problem of current distribution and hydrodynamics rather than being a materials issue, therefore it will not be discussed further here.

A second type of problem relates to the inherent instability of a flat interface upon electrodeposition [1]. This is analogous to the problems of the interfaceevolution during electropolishing and the morphology development during the growth of an oxide layer upon a solid solution alloy, problems that were discussed by Wagner [2, 3] some time ago.

Another analogous situation is present during the crystallization of the solute phase from liquid metal solutions. This leads to the production of protuberances upon the growth interface, which gradually become exaggerated, and then develop into dendrites. A general characteristic of dendrites is a tree-and-branches type of morphology, which often has very distinct geometric and crystallographic characteristics, due to the orientation dependence of surface energy or growth velocity. The current distribution near the front of a protrusion develops a three-dimensional (3-D) character, leading to faster growth than the main electrodes surface, where the mass transport is essentially, one-dimensional (1-D). In relatively low-concentration solutions, this leads to a runaway type of process, so that the dendrites consume most of the solute and grow farther and farther ahead of the main, or bulk, interface.

A third type of problem, that is often mistakenly confused with dendrite formation, is due to the presence of a reaction-product layer upon the growth interface if the electrode and electrolyte are not stable in the presence of each other. This leads to filamentary or hairy growth, and the deposit often appears to have a spongy character. During a subsequent discharge step the filaments often become disconnected from the underlying metal, so that they cannot participate in the electrochemical reaction, and the rechargeable capacity of the electrode is reduced.

This is a common problem when using elemental lithium negative electrodes in contact with electrolytes containing organic cationic groups, regardless of whether the electrolyte is an organic liquid or a polymer [4].

In order to achieve good rechargeability, one has to maintain a consistent geometry on both the macro and micro scales, and to avoid electrical disconnection of the electroactive species.

CosMX Exhibit 1008, Page 379 of 633

4.3 Lithium Alloys as an Alternative

Attention has been given for some time to the use of lithium alloys as an alternative to elemental lithium. Groups working on batteries with molten salt electrolytes that operate at temperatures of 400–450 °C, well above the melting point of lithium, were especially interested in this possibility. Two major directions evolved. One involved the use of lithium–aluminium alloys [5, 6], whereas another was concerned with lithium–silicon alloys [7–9].

Whereas this approach can avoid the problems related to lithium melting, as well as the others mentioned above, there are always at least two disadvantages related to the use of alloys. Because they reduce the activity of the lithium, they necessarily reduce the cell voltage. In addition, the presence of additional species that are not directly involved in the electrochemical reaction always brings additional weight, and generally, volume. Thus the maximum theoretical values of the specific energy and the energy density are always reduced in comparison with what might be attained with pure lithium.

In practical cases, however, the excess weight and volume due to the use of alloys may not be very far from those required with pure lithium electrodes, for one generally has to operate with a large amount of excess lithium in rechargeable cells in order to make up for the capacity loss related to the filament growth problem upon cycling.

Lithium alloys have been used for a number of years in the high–temperature "thermal batteries" that are produced commercially for military purposes. These devices are designed to be stored for long periods at ambient temperatures before use, where their self-discharge kinetic behavior is very slow. They must be heated to elevated temperatures when their energy output is desired. An example is the Li alloy/FeS_2 battery system that employs a molten chloride electrolyte. In order to operate, the temperature must be raised to above the melting point of the electrolyte. This type of cell typically uses either Li–Si or Li–Al alloys in the negative electrode.

The first use of lithium alloys as negative electrodes in commercial batteries to operate at ambient temperatures was the employment of Wood's metal alloys in lithium-conducting button-type cells by Matsushita in Japan. Development work on the use of these alloys started in 1983 [10], and they became commercially available somewhat later.

It was also shown in 1983 [11] that lithium can be reversibly inserted into graphite at room temperatures when a polymeric electrolyte is used. Prior experiments with liquid electrolytes were unsuccessful due to co-intercalation of species from the organic electrolytes that were used at that time. This problem has been subsequently solved by the use of other electrolytes.

There has been a large amount of work on the development of graphites and related carbon-containing materials for use as negative electrode materials in lithium batteries in recent years, due in large part to the successful development by Sony of commercial rechargeable batteries containing negative electrodes based upon materials of this family.

Lithium–carbon materials are, in principle, no different from other lithium-containing alloys. However, since this topic is treated in more detail in Chapter III, Sec. 5, only a few points will be briefly discussed here.

One is that the behavior of these materials is very dependent upon the details of

CosMX Exhibit 1008, Page 380 of 633

both the nanostructure and the microstructure. Therefore, the composition as well as thermal and mechanical treatments play especially important roles in determining the resulting thermodynamic and kinetic properties. Materials with a more graphitic structure have more negative potentials, whereas those with less well-organized structures typically operate over much wider potential ranges, resulting in a cell voltage that is both lower and more dependent on the state-of-charge.

Another important consideration in the use of carbonaceous materials as negative electrodes in lithium cells is the common observation of a considerable loss of capacity during the first charge–discharge cycle due to irreversible lithium absorption into the structure. This has the distinct disadvantage that it requires an additional amount of lithium to be initially present in the cell. If this irreversible lithium is supplied by the positive electrode, this means that an extra amount of the positive electrode reactant material must be put into the cell during its fabrication. As the positive electrode reactant materials often have relatively low specific capacities, e.g., around $140\,mAh\,g^{-1}$, this irreversible capacity in the negative electrode leads to a requirement for an appreciable amount of extra material weight and volume in the total cell.

There are some other matters that should be considered when comparing metallic lithium alloys with the lithium-carbons. The specific volume of some of the metallic alloys can be considerably lower than that of the carbonaceous materials. As will be seen later, it is possible by selection among the metallic materials to find good kinetics and electrode potentials that are sufficiently far from that of pure lithium for there to be a much lower possibility of the potentially dangerous formation of dendrites or filamentary deposits under rapid recharge conditions.

It has been shown that there is a significant advantage in the use of very small particles in cases in which there is a substantial change in specific volume upon charging and discharging electrode reactants [12]. Since the absolute magnitude of the local dimensional changes is proportional to the particle size, smaller particles lead to fewer problems with the decrepitation, or "crumbling" of electrode microstructure that often leads to loss of electrical contact, and thus capacity loss, as well as macroscopic dimensional problems.

4.4 Alloys Formed in Situ from Convertible Oxides

A renewed interest in noncarbonaceous lithium alloy electrodes arose recently as the result of the announcement by Fuji Photo Film Co. of the development of a new generation of lithium batteries based upon the use of an amorphous tin-based composite oxide in the negative electrode [13]. It is claimed that these electrodes have a volumetric capacity of 3200, $Ah\,L^{-1}$ which is four times that commonly achieved with carbonaceous negative electrodes, and a specific capacity of 800, $mAh\,g^{-1}$ twice that generally found in carbon-containing negative electrodes.

According to the public announcement a new company, Fujifilm Celltec Co., has been formed to produce products based upon this approach. It was reported that some 200 patents have been applied for in this connection. Unfortunately, there is little yet available in the standard literature concerning these matters. To date, there are only references to some of the patents [14–17]. However, what must be happen-

CosMX Exhibit 1008, Page 381 of 633

ing seems rather obvious.

If, as an example, we make the assumption that the electrode initially has the composition SnO, if we introduce lithium into it there will be a displacement reaction in which Li_2O will be formed at the expense of the SnO due to the difference in the values of their Gibbs free energies of formation ($-562.1\,kJ\,mol^{-1}$ for Li_2O and $-256.8\,kJ\,mol^{-1}$ in the case of SnO). This is equivalent to a driving force of 1.58 V. The other product will be elemental Sn, and as additional Li is brought into the electrode this will react further to form the various Li-Sn alloys that are discussed in some detail later in this section. This simplified picture is consistent with what has been found in experiments of this general type [18].

4.5 Thermodynamic Basis for Electrode Potentials and Capacities under Conditions in which Complete Equilibrium can be Assumed

The general thermodynamic treatment of binary systems which involve the incorporation of an electroactive species into a solid alloy electrode under the assumption of complete equilibrium was presented by Weppner and Huggins [19–21]. Under these conditions the Gibbs Phase Rule specifies that the electrochemical potential varies with composition in the single-phase regions of a binary phase diagram, and is composition-independent in two-phase regions if the temperature and total pressure are kept constant.

Thus the variations of the electrode potential during discharge and charge, as well as the phases present and the charge capacity of the electrode, directly reflect the thermodynamic of the alloy system.

A series of experiments have been undertaken to evaluate the relevant thermodynamic properties of a number of binary lithium alloy systems. The early work was directed towards determination of their behavior at about 400 °C because of interest in their potential use as components in molten salt batteries operating in that general temperature range. Data for a number of binary lithium alloy systems at about 400 °C are presented in Table 1. These were mostly obtained by the use of an experimental arrangement employing the LiCl–KCl eutectic molten salt as a lithium-conducting electrolyte.

Table 1. Plateau potentials and composition ranges of some binary lithium alloys Li_yM at 400 °C.

Voltage vs. Li	M	Range of y	Reference
0.047	Si	3.25–4.4	[37]
0.058	Cd	1.65–2.33	[29]
0.080	In	2.08–2.67	[49]
0.089	Pb	3.8–4.4	[50]
0.091	Ga	1.53–1.93	[51]
0.122	Ga	1.28–1.48	[51]
0.145	In	1.74–1.92	[49]
0.156	Si	2.67–3.25	[37]
0.170	Sn	3.5–4.4	[38]
0.237	Pb	3.0–3.5	[50]
0.271	Pb	2.67–3.0	[50]
0.283	Si	2–2.67	[37]
0.283	Sn	2.6–3.5	[38]
0.300	Al	0.08–0.9	[35]
0.332	Si	0–2	[37]
0.373	Cd	0.33–0.45	[29]
0.375	Pb	1.1–2.67	[50]
0.387	Sn	2.5–2.6	[38]
0.430	Sn	2.33–2.5	[38]
0.455	Sn	1.0–2.33	[38]
0.495	In	1.2–0.86	[49]
0.507	Pb	0–1.0	[50]
0.558	Cd	0.12–0.21	[29]
0.565	Ga	0.15–0.82	[51]
0.570	Sn	0.57–1.0	[38]
0.750	Bi	1.0–2.82	[21]
0.875	Sb	2.0–3.0	[21]
0.910	Sb	0–2.0	[21]

CosMX Exhibit 1008, Page 382 of 633

It was shown some time ago that one can also use a similar thermodynamic approach to explain and/or predict the composition dependence of the potential of electrodes in ternary systems [22–25]. This followed from the development of the analysis methodology for the determination of the stability windows of electrolyte phases in ternary systems [26]. In these cases, one uses isothermal sections of ternary phase diagrams, the so-called Gibbs triangles, upon which to plot compositions. In ternary systems, the Gibbs Phase Rule tells us that three-phase equilibria will have composition-independent intensive properties, i.e., activities and potentials. Thus compositional ranges that span three-phase regions will lead to potential plateaus at constant temperature and pressure.

Estimated data on a number of ternary lithium systems theoretically investigated as extensions of the Li–Si binary system are included in Table 2. Also included are comparable data for the binary Li–Si alloy that is currently being used in commercial thermal batteries.

This thermodynamically based methodology provides predictions of the lithium capacities in addition to the electrode potentials of the various three-phase equilibria under conditions of complete equilibrium. This information is included as the last column in Table 2, in terms of the number of moles of lithium per kilogram total alloy weight.

From a practical standpoint, the most useful compositions would be those with quite negative potentials, so as to give high cell voltages, that also have large capacities for lithium. However, it must be recognized that the materials with the most negative potentials, and thus the highest lithium activities, will be the most reactive, and thus will be more difficult to handle than those whose potentials are somewhat farther from that of pure lithium.

As recently pointed out [25], several of these ternary systems appear to have po-

Table 2. Estimated data relating to lithium–silicon-based ternary systems at 400 °C.

System	Starting composition	Phases in equilibrium	Voltage (mV) vs. Li	Li (mol/kg^{-1})
Li–Si–Mo	Mo_5Si_3	$Mo_5Si_3 - Mo_3Si - Li_{22}Si_5$	3	9.7
Li–Si–Ca	CaSi	$CaSi - Ca_2Si - Li_{22}Si_5$	13	26.4
Li–Si–Mn	Mn_3Si	$Mn_3Si - Mn - Li_{22}Si_5$	43	19.7
Li–Si–Mn	Mn_5Si_3	$Mn_5Si_3 - Mn_3Si - Li_{13}Si_4$	45	11.1
Li–Si–Mg	Mg_2Si	$Mg_2Si - Mg - Li_{13}Si_4$	60	32.7
Li–Si–Mo	$MoSi_2$	$MoSi_2 - Mo_5Si_3 - Li_{13}Si_4$	120	24.8
Li–Si–Cr	Cr_5Si_{13}	$Cr_5Si_{13} - Cr_3Si - Li_{13}Si_4$	138	11.6
Li–Si	Li_7Si_3	$Li_7Si_3 - Li_{13}Si_4$	158	18.1
Li–Si–Mn	MnSi	$MnSi - Mn_5Si_3 - Li_7Si_{13}$	163	10.4
Li–Si–Ti	TiSi	$TiSi - Ti_5Si_3 - Li_7Si_3$	182	11.3
Li–Si–Nb	$NbSi_2$	$NbSi_2 - Nb_5Si_3 - Li_7Si_3$	184	19.0
Li–Si–V	VSi_2	$VSi_2 - V_5Si_3 - Li_7Si_3$	191	25.2
Li–Si–Cr	CrSi	$CrSi - Cr_5Si_3 - Li_7Si_3$	205	10.8
Li–Si–Ta	$TaSi_2$	$TaSi_2 - Ta_5Si_3 - Li_7Si_3$	211	12.6
Li–Si–Cr	$CrSi_2$	$CrSi_2 - CrSi - Li_7Si_3$	223	18.8
Li–Si–Ni	Ni_7Si_{13}	$Li_7Si_{13} - NiSi - Li_{12}Si_7$	316	12.1

CosMX Exhibit 1008, Page 383 of 633

tentials and capacities that should make them quite interesting for practical applications. Li–Si ternary systems with Mg, Ca, and Mo seem especially interesting from the standpoint of their potentials and capacities. As an example, if one assumes that a positive electrode is used that has a potential 2.0 V positive of elemental lithium, and a capacity of 1 mol of lithium per 60 g of active component, these negative electrode materials provide a maximum theoretical specific energy of 574, 544, and 502 $Wh\,kg^{-1}$, respectively, whereas the binary Li–Si alloy currently used in thermal batteries would have a maximum value of 428 $Wh\,kg^{-1}$. Confirmatory experimental information on the Li–Mg–Si system [27] was recently presented [28].

4.6 Crystallographic Aspects and the Possibility of Selective Equilibrium

If we look at the mechanistic and crystallographic aspects of the operation of polycomponent electrodes, we see that the incorporation of electroactive species such as lithium into a crystalline electrode can occur in two basic ways. In the examples discussed above, and in which complete equilibrium is assumed, the introduction of the guest species can either involve a simple change in the composition of an existing phase by solid solution, or it can result in the formation of new phases with different crystal structures from that of the initial host material. When the identity and/or amounts of phases present in the electrode change, the process is described as a reconstitution reaction. That is, the microstructure is reconstituted.

In the simple case of a reconstitution reaction in which the incorporation of additional electroactive species occurs by the nucleation and growth of a new phase, the relative amount of this new phase with a higher solute content increases. If the initial phase and the new phase are in local equilibrium, the respective compositions at their joint interface do not change with the extent of the reaction. The amounts of the phases, determined by the motion of the interfaces between these phases, are related to the lengths of the two-phase constant-potential plateaus in binary systems, and of the three-phase constant-potential plateaus in ternary systems, and these, in turn, are determined by the extent of the corresponding regions in the relevant phase diagrams.

In many systems, both single-phase and polyphase behaviors are found in different composition ranges. Intermediate, as well as terminal, phases often have been found to have quite wide ranges of composition. Examples are the broad Zintl phases found in several of the binary lithium systems studied by Wen [29].

The second way in which an electroactive species such as lithium can be incorporated into the structure of an electrode is by a topotactic insertion reaction. In this case the guest species is relatively mobile and enters the crystal structure of the host phase so that no significant change in the structural configuration of the host lattice occurs.

Thus the result is the formation of a single-phase solid solution. The insertion of additional guest species involves only a change in the overall (and thus also the local) composition of the solid solution, rather than the formation of additional phases.

From a thermodynamic viewpoint, there is selective, rather than complete, equilibrium under conditions in which this type of reaction occurs. We can assume

CosMX Exhibit 1008, Page 384 of 633

equilibrium in the sublattice of the mobile solute species, but not in the host substructure, as strong bonding makes atomic rearrangements relatively sluggish in that part of the crystal structure.

In general, equilibrium within the guest species sublattice results in their being randomly arranged among the various interstitial locations within the host structure. There are, however, a number of cases, in which the guest species are distributed among their possible sites within the host structure in an ordered, rather than random, manner. There can be different sets of these ordered sites, each having the thermodynamic characteristics of a separate phase. Thus, as the concentration of guest species is changed, such materials can appear thermodynamically to go through a series of phase changes, even though the host structure is relatively stable. This type of behavior was demonstrated for the case of lithium insertion into a potassium tungsten oxide [30].

The thermodynamic properties of topotactic insertion reaction materials with selective equilibrium are quite different from those of materials in which complete equilibrium can be assumed, and reconstitution reactions take place. Instead of flat plateaus related to polyphase equilibria, the composition-dependence of the potential generally has a flat S-type form.

Under near-equilibrium conditions the shape of this curve is related to two contributions, the compositional dependence of the configurational entropy of the guest ions, and the contribution to the chemical potential from the electron gas [31].

The configurational entropy of the mobile guest ions, assuming random mixing and a concentration x, residing in x° lattice sites of equal energy, is

$$S = -R\ln[x/(x^0 - x)] \qquad (1)$$

There is also a small contribution from thermal entropy, but this can be neglected.

If we can assume that the electrode material is a good metal, and the electronic gas is fully degenerate, the chemical potential of the electrons is given by the Fermi level, E_F, which can be written as

$$E_F = [\text{Constant}][(x)^{2/3}/m^*] \qquad (2)$$

where m^* is the effective mass of the electrons.

4.7 Kinetic Aspects

In addition to the questions of the potentials and capacities of electrodes, which are essentially thermodynamic considerations, practical utilization of alloys as electrodes also requires attractive kinetic properties.

The primary question is the rate at which the mobile guest species can be added to, or deleted from, the host microstructure. In many situations the critical problem is the transport within a particular phase under the influence of gradients in chemical composition, rather than kinetic phenomena at the electrolyte/electrode interface. In this case, the governing parameter is the chemical diffusion coefficient of the mobile species, which relates to transport in a chemical concentration gradient.

Diffusion has often been measured in metals by the use of radioactive tracers. The resulting parameter, D_T, is related to the self-diffusion coefficient by a correlation factor f that is dependent upon the details of the crystal structure and jump geometry. The relation between D_T and the self-diffusion coefficient D_{self} is thus simply

$$D_T = D_{self} * f \qquad (3)$$

CosMX Exhibit 1008, Page 385 of 633

Whereas in many metals with relatively simple and isotropic crystal structures the parameter f has values between 0.5 and 1, it can have much more extreme values in materials in which the mobile species move through much less isotropic structures with 1-D or two-dimensional (2-D) channels, as is often the case with insertion reaction electrode materials. As a result, radiotracer experiments can provide misleading information about self-diffusion kinetics in such cases.

More importantly, the chemical diffusion coefficient D_{chem}, instead of D_{self}, is the parameter that is relevant to the behavior of electrode materials. They are related by

$$D_{chem} = D_{self} * W \quad (4)$$

where W is an enhancement factor. This is sometimes called the "thermodynamic factor", and can be written as

$$W = \mathrm{dln}a_i/\mathrm{dln}c_i \quad (5)$$

in which a_i and c_i are the activity and concentration of the neutral mobile species i, respectively. Experimental data have shown that the value of W can be very large in some cases. An example is the phase Li_3Sb, in which it has a value of 70000 at 360 °C [32].

It is thus much better to measure the chemical diffusion coefficient directly. Descriptions of electrochemical methods for doing this, as well as the relevant theoretical background, can be found in the literature [33, 34]. Available data on the chemical diffusion coefficient in a number of lithium alloys are included in Table 3.

Table 3. Data on chemical diffusion in lithium alloy phases.

Composition		Max. D_{chem} (cm^2s^{-1})	Max. W	Temp. (°C)	Reference
Nominal	Range (%Li)				
LiAl	16.4	$1.2*10^{-4}$	70	415	[34, 35]
Li_3Sb	0.05	$7.0*10^{-5}$	70000	360	[32]
Li_3Bi	1.37	$2.0*10^{-4}$	370	380	[52]
$Li_{12}Si_7$	0.54	$8.1*10^{-5}$	160	415	[37]
Li_7Si_3	3.0	$4.4*10^{-5}$	111	415	[37]
$Li_{13}Si_4$	1.0	$9.3*10^{-5}$	325	415	[37]
$Li_{22}Si_5$	0.4	$7.2*10^{-5}$	232	415	[37]
LiSn	1.9	$4.1*10^{-6}$	185	415	[39]
Li_7Sn_3	0.5	$4.1*10^{-5}$	110	415	[39]
Li_5Sn_2	1.0	$5.9*10^{-5}$	99	415	[39]
$Li_{13}Sn_5$	0.5	$7.6*10^{-4}$	1150	415	[39]
Li_7Sn_2	1.4	$7.8*10^{-5}$	196	415	[39]
$Li_{22}Sn_5$	1.2	$1.9*10^{-4}$	335	415	[39]
LiGa	22.0	$6.8*10^{-5}$	56	415	[51]
LiIn	33.0	$4.0*10^{-5}$	52	415	[49]
LiCd	63.0	$3.0*10^{-6}$	7	415	[29]

CosMX Exhibit 1008, Page 386 of 633

4.8 Examples of Lithium Alloy Systems

4.8.1 Lithium–Aluminium System

Because of the interest in its use in elevated-temperature molten salt electrolyte batteries, one of the first binary alloy systems studied in detail was the lithium–aluminium system. As shown in Fig. 1, the potential–composition behavior shows a long plateau between the lithium-saturated terminal solid solution and the intermediate β phase "LiAl", and a shorter one between the composition limits of the β and γ phases, as well as composition-dependent values in the single-phase regions [35]. This is as expected for a binary system with complete equilibrium. The potential of the first plateau varies linearly with temperature, as shown in Fig. 2.

Chemical diffusion in the β phase determines the kinetic behavior of these electrodes when lithium is added, so this was investigated in detail using four different electrochemical techniques [34, 35]. It was found that chemical diffusion is remarkably fast in this phase, and that the activation energy attains very low values on the lithium-poor side of the composition range. These data are shown in Fig. 3.

In addition to this work on the β phase, both the thermodynamic and kinetic properties of the terminal solid-solution region, which extends to about 9 atom% lithium at 423 °C, were also investigated in detail [36].

4.8.2 Lithium–Silicon System

The lithium–silicon system has also been of interest for use in the negative electrodes of elevated-temperature molten salt electrolyte lithium batteries. A composition containing 44 wt.% Li, where Li/Si=3.18, has been used in commercial

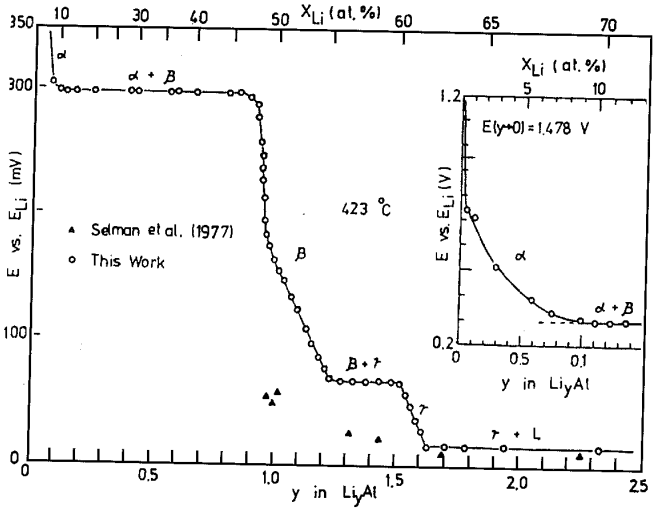


Figure 1. Potential vs. composition in Li–Al system at 423 °C [35].

CosMX Exhibit 1008, Page 387 of 633

thermal batteries developed for military purposes.

Experiments have been performed to study both the thermodynamic and kinetic properties of compositions in this system [37], and the composition dependence of the equilibrium potential at 415 °C is shown in Fig. 4. It is seen that the commercial electrode composition sits upon a two-phase plateau at a potential 158mV positive of pure lithium. As lithium is removed the overall composition will first follow that plateau. The potential will then become more positive as it traverses the other plateaus at 288 and 332mV versus lithium, in order.

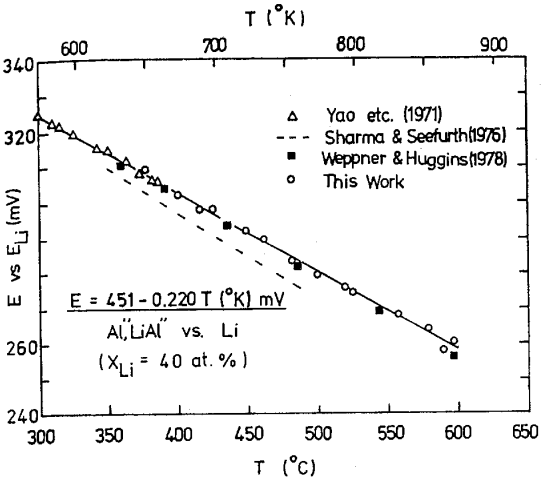


Figure 2. Temperature dependence of the potential of the Al/"LiAl" plateau [35].

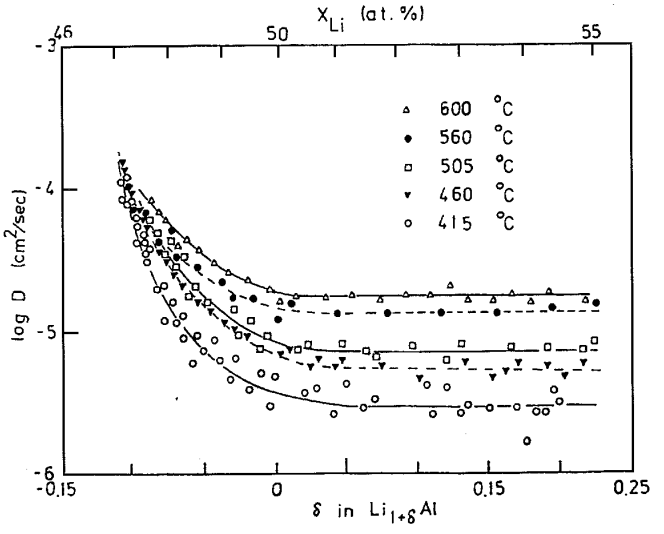


Figure 3. Variation of the chemical diffusion coefficient with composition in the "LiAl" phase at different temperatures [35].

CosMX Exhibit 1008, Page 388 of 633

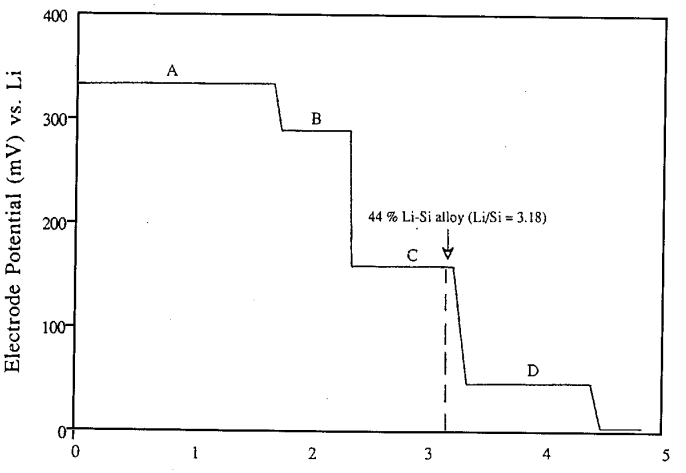


Figure 4. Potential vs. composition in the Li–Si system at 415 °C [37].

As a result, the cell voltage will decrease during the discharge, regardless of the behavior of the positive electrode.

4.8.3 Lithium–Tin System

The lithium–tin binary system is somewhat more complicated, as there are six intermediate phases, as shown in the phase diagram in Fig. 5. A thorough study of the thermodynamic properties of this system was undertaken [38]. The composition dependence of the potential at 415 °C is shown in Fig. 6.

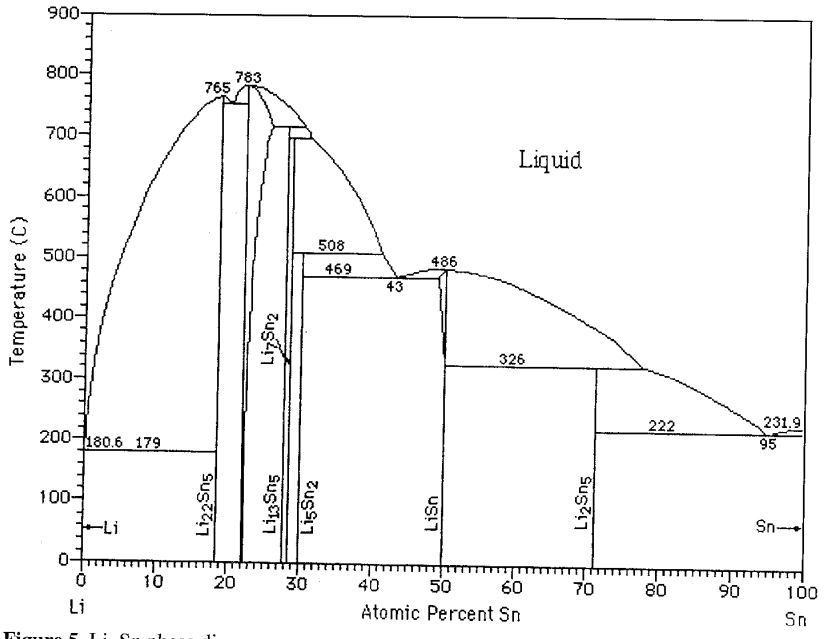


Figure 5. Li–Sn phase diagram.

CosMX Exhibit 1008, Page 389 of 633

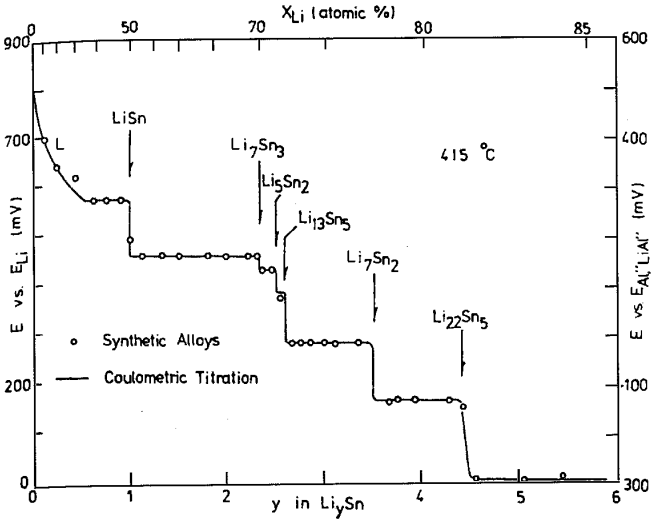


Figure 6. Potential vs. composition in the Li–Sn system at 415 °C [38].

Measurements were also made of the potential–composition behavior, as well as the chemical diffusion coefficient, and its composition dependence, in each of the intermediate phases in the Li–Sn system at 415 °C [39].

It was found that chemical diffusion is reasonably fast in all of the intermediate phases in this system. The self-diffusion coefficients are all high and of the same order of magnitude. However, due to its large value of thermodynamic enhancement factor W, the chemical diffusion coefficient in the phase $Li_{13}Sn_5$ is extremely high, approaching $10^{-8}cm^2s^{-1}$, which is about two orders of magnitude higher than that in typical liquids. These data are included in Table 3.

4.9 Lithium Alloys at Lower Temperatures

A smaller number of binary lithium systems have also been investigated at lower temperatures. This has involved measurements using $LiNO_3-KNO_3$ molten salts at about 150 °C [40], as well as experiments with organic solvent-based electrolytes at ambient temperatures [41, 42]. Data on these are included in Table 4.

Table 4. Plateau potentials and composition ranges of lithium alloys Li_yM at 25 °C.

Voltage vs. Li	M	Range of y	Reference
0.005	Zn	1–1.5	[42]
0.055	Cd	1.5–2.9	[42]
0.157	Zn	0.67–1	[42]
0.219	Zn	0.5–0.67	[42]
0.256	Zn	0.4–0.5	[42]
0.292	Pb	3.2–4.5	[42]
0.352	Cd	0.3–0.6	[42]
0.374	Pb	3.0–3.2	[42]
0.380	Sn	3.5–4.4	[41]
0.420	Sn	2.6–3.5	[41]
0.449	Pb	1–3.0	[42]
0.485	Sn	2.33–2.63	[41]
0.530	Sn	0.7–2.33	[41]
0.601	Pb	0–1	[42]
0.660	Sn	0.4–0.7	[41]
0.680	Cd	0–0.3	[42]
0.810	Bi	1–3	[41]
0.828	Bi	0–1	[41]
0.948	Sb	2–3	[41]
0.956	Sb	1–2	[41]

CosMX Exhibit 1008, Page 390 of 633

The lithium–tinsystem has been investigated room temperature and the influence of temperature upon the composition dependence of the potential is shown in Fig. 7. It is seen that five constant potential plateaus are found at 25 °C. Their potentials are listed in Table 4. It was also shown that the kinetics on the longest plateau, from $x = 0.8$ to 2 in Li_xSn, are quite favorable, even at quite high currents (see Fig. 8).

The composition dependence of the potential of the $Li_{4.4}Sn$ phase was determined, as shown in Fig. 9.

The chemical diffusion coefficient in that phase was also evaluated and found to

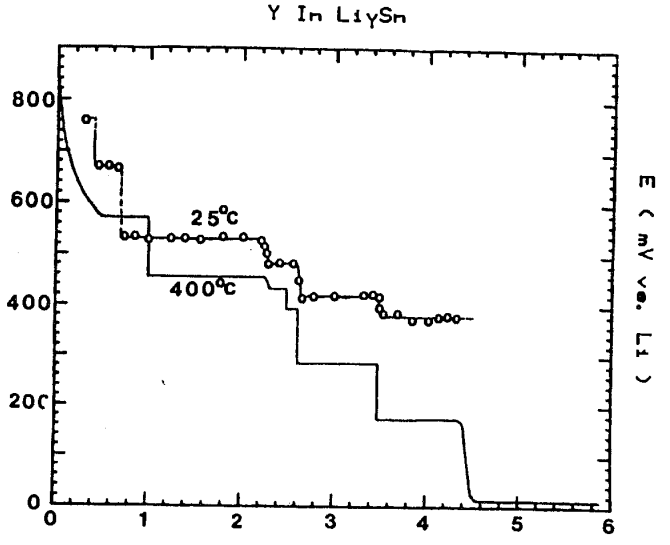


Figure 7. Potential vs. composition in the Li–Sn system at 25 °C compared with data at 400 °C [41].

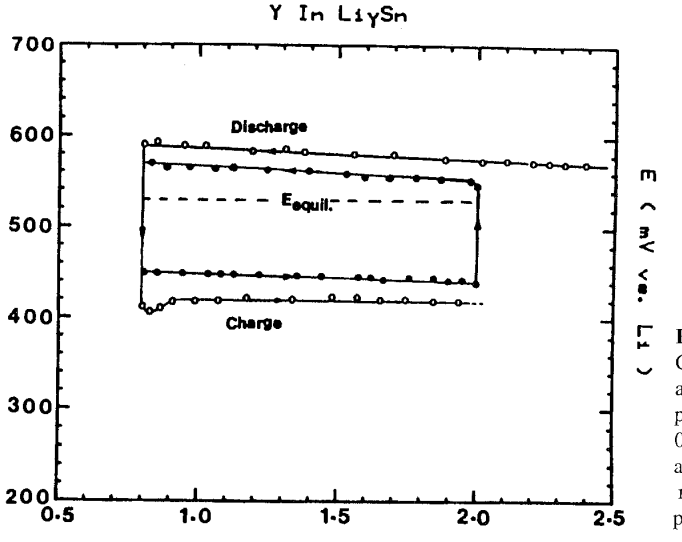


Figure 8. Charge–discharge Curves for Li_xSn (x=0.8 to 2.5) at ambient temperature. Solid points are at a current density of 0.24 $mAcm^{-2}$, and open points at a current density of 0.5 $mAcm^{-2}$. The equilibrium potential is also shown [41].

CosMX Exhibit 1008, Page 391 of 633

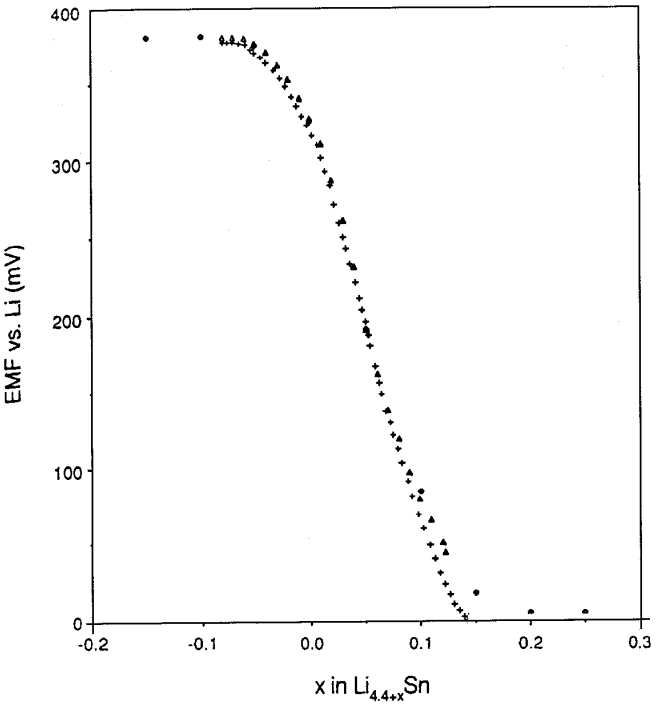


Figure 9. Potential vs. composition in the $Li_{4.4}Sn$ phase at ambient temperature [43]

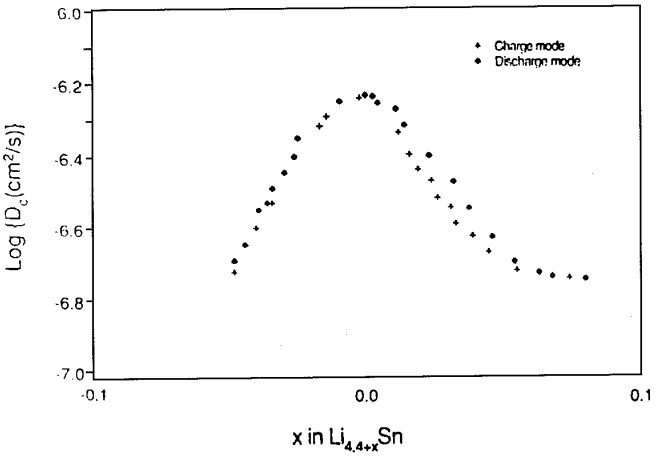


Figure 10. Composition dependence of the chemical diffusion coefficient in the $Li_{4.4}Sn$ phase at ambient temperature [43].

CosMX Exhibit 1008, Page 392 of 633

be quite high, as can be seen in Fig. 10 [43]. The chemical diffusion coefficient was also measured in two other Li–Sn phases; these data are all included in Table 5.

Comparable information on the Li–Bi and Li–Sb systems was also obtained, and their room-temperature potentials are also included in Table 4. The temperature dependence of the potentials of the different two-phase plateaus is shown in Fig. 11.

This work was extended to the investigation of the Li–Zn, Li–Cd, and Li–Pb alloy systems [42, 43]. The potentials of the various plateaus found in these systems are included in Table 4, and are summarized in Fig. 12.

Table 5. Chemical diffusion data for lithium–tin phases at 25 °C.

Phase	Volts vs. Li	D_{chem} (cm^2s^{-1})
$Li_{0.7}Sn$	0.560	$(6–8)*10^{-8}$
$Li_{2.33}Sn$	0.520	$(3–5)*10^{-7}$
$Li_{4.4}Sn$	0.0–0.380	$(1.8–5.9)*10^{-7}$

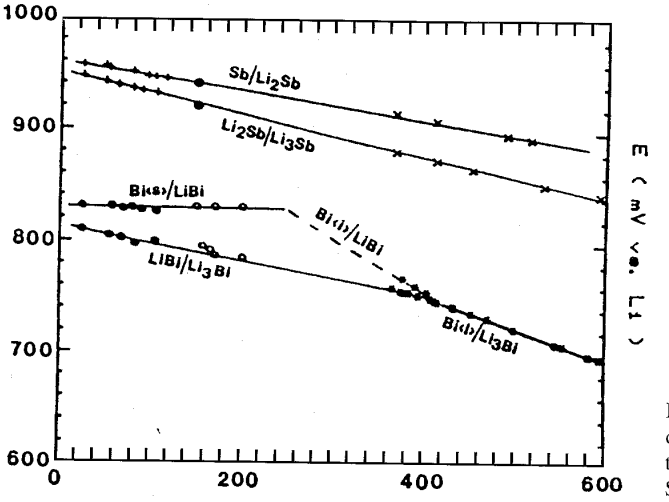


Figure 11. Temperature dependence of the potential of the two-phase plateaus in the Li–Sb and Li–Bi systems [41].

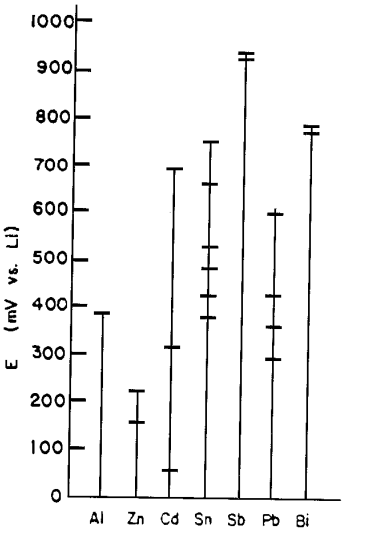


Figure 12. Plateau potentials of seven lithium alloy systems at ambient temperature [42].

4.10 The Mixed-Conductor Matrix Concept

In order to achieve appreciable macroscopic current densities while maintaining

CosMX Exhibit 1008, Page 393 of 633

low local microscopic charge and particle flux densities, many battery electrodes that are used in conjunction with liquid electrolytes are produced with porous microstructures containing very fine particles of the solid reactant materials. This porous structure of high reactant surface area is permeated with the electrolyte.

This porous fine-particle approach has several characteristic disadvantages, among which are difficulties in producing uniform and reproducible microstructures, and limited mechanical strength when the structure is highly porous. In addition, these systems often suffer Ostwald ripening, sintering, or other time-dependent changes in both microstructure and properties during cyclic operation.

A quite different approach was introduced in the early 1980s [44–46], in which a dense solid electrode is fabricated which has a composite microstructure in which particles of the reactant phase are finely dispersed within a solid, electronically conducting matrix in which the electroactive species is also mobile. There is thus a large internal reactant/mixed-conductor matrix interfacial area. The electroactive species is transported through the solid matrix to this interfacial region, where it undergoes the chemical part of the electrode reaction. Since the matrix material is also an electronic conductor, it can also act as the electrode's current collector. The electrochemical part of the reaction takes place on the outer surface of the composite electrode.

When such an electrode is discharged by removal of the electroactive species, the residual particles of the reactant phase remain as relics in the microstructure. This provides fixed permanent locations for the reaction to take place during following cycles, when the electroactive species again enters the structure. Thus this type of configuration can provide a mechanism for the achievement of true microstructural reversibility.

In order for this concept to be applicable, the matrix and the reactant phase must be thermodynamically stable in contact with each other. One can evaluate this possibility if one has information about the relevant phase diagram — which typically involves a ternary system — as well as the titration curves of the component binary systems. In a ternary system, the two materials must lie at corners of the same constant-potential tie-triangle in the relevant isothermal ternary phase diagram in order to not interact. The potential of the tie-triangle determines the electrode reaction potential, of course.

An additional requirement is that the reactant material must have two phases present in the tie-triangle, but the matrix phase only one. This is another way of saying that the stability window of the matrix phase must span the reaction potential, but that the binary titration curve of the reactant material must have a plateau at the tie-triangle potential. It has been shown that one can evaluate the possibility that these conditions are met from knowledge of the binary titration curves, without having to perform a large number of ternary experiments.

The kinetic requirements for a successful application of this concept are readily understandable. The primary issue is the rate at which the electroactive species can reach the matrix/reactant interfaces. The critical parameter is the chemical diffusion coefficient of the electroactive species in the matrix phase. This can be determined by various techniques, as discussed above.

The first example that was demonstrated was the use of the phase with the nominal composition $Li_{13}Sn_5$ as the matrix, in conjunction with reactant phases

CosMX Exhibit 1008, Page 394 of 633

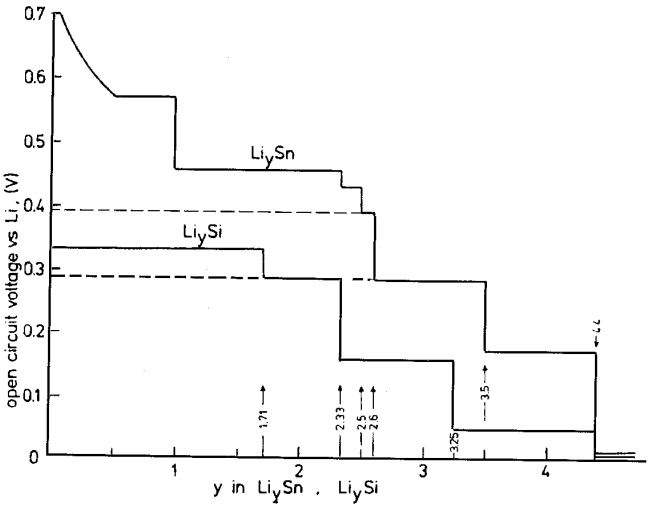


Figure 13. Composition dependence of the potential in the Li–Sn and Li–Si systems at 415 °C [44].

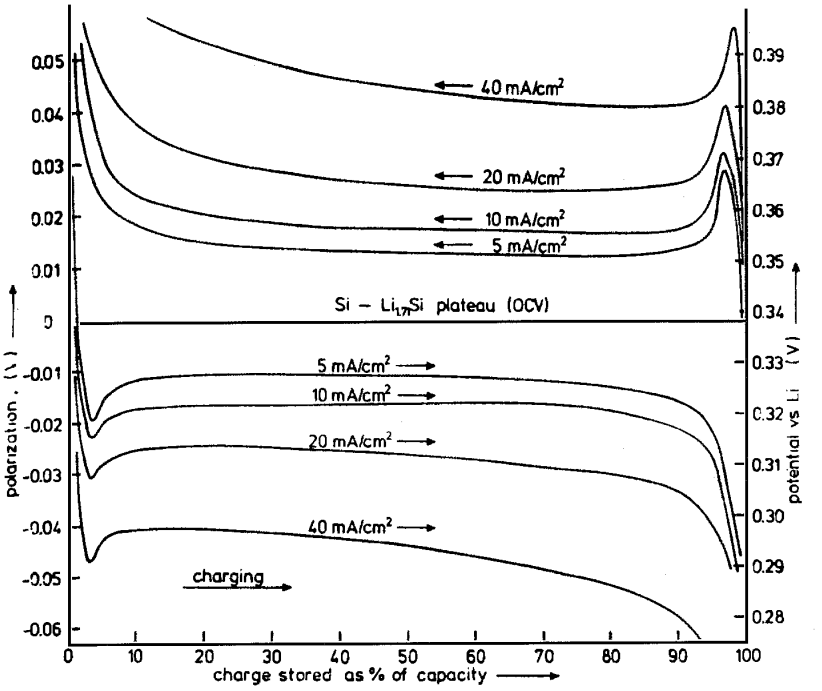
in the lithium–silicon system at temperatures near 400 °C. This is an especially favorable case, due to the high chemical diffusion coefficient or lithium in the $Li_{13}Sn_5$ phase.

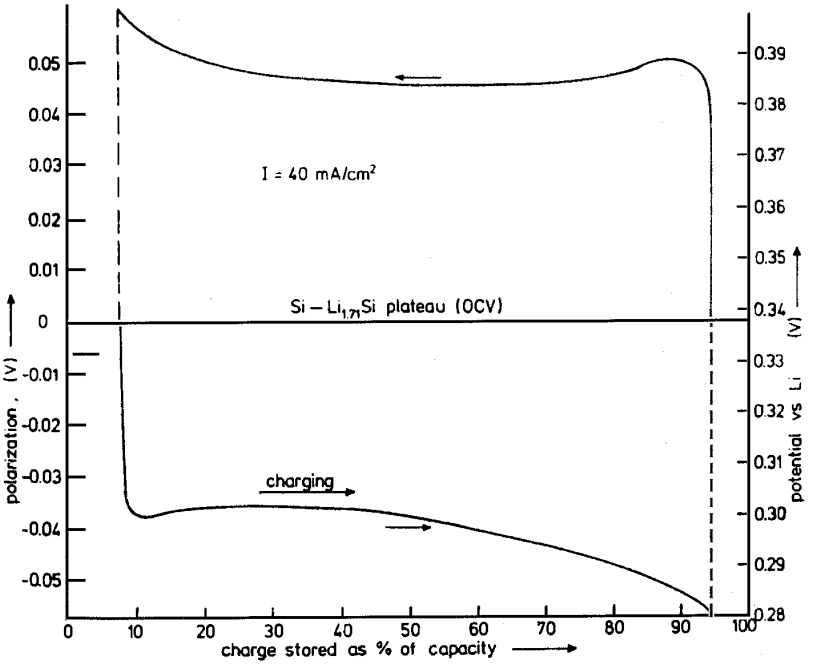
The relation between the potential–composition data for these two systems under equilibrium conditions is shown in Fig. 13. It is seen that the phase $Li_{2.6}Sn$ ($Li_{13}Sn_5$) is stable over a potential range that includes the upper two-phase reconstitution reaction plateau in the lithium–silicon system. Therefore, lithium can react with Si to form the phase $Li_{1.7}Si$ ($Li_{12}Si_7$) inside an all-solid composite electrode containing the $Li_{2.6}Sn$ phase, which acts as a lithium transporting, but electrochemically inert, matrix. Figure 14 shows the relatively small polarization that was observed during the charge and discharge of this electrode, even at relatively high current densities. It is seen that there is a potential overshoot due to the free energy involved in the nucleation of a new second phase if the reaction goes to completion in each direction. On the other hand, if the composition is not driven quite so far, this nucleation-related potential overshoot does not appear.

This concept has also been demonstrated at ambient temperature in the case of the Li–Sn–Cd system [47, 48]. The composition-de-pendences of the potentials in the two binary systems at ambient temperatures are shown in Fig. 15, and the calculated phase stability diagram for this ternary system is shown in Fig. 16. It was shown that the phase $Li_{4.4}Sn$, which has fast chemical diffusion for lithium, is stable at the potentials of two of the Li–Cd reconstitution reaction plateaus, and therefore can be used as a matrix phase.

Figure 14. Charge–discharge curves for the upper plateau in the Li_xSi system inside a matrix of the $Li_{2.6}Sn$ → phase at 415 °C. The upper panel shows the effect of current density, whereas the lower panel shows that the potential overshoot related to the nucleation of the second phase is mostly eliminated if the electrode is not cycled to the ends of the plateau [44].

CosMX Exhibit 1008, Page 395 of 633





CosMX Exhibit 1008, Page 396 of 633

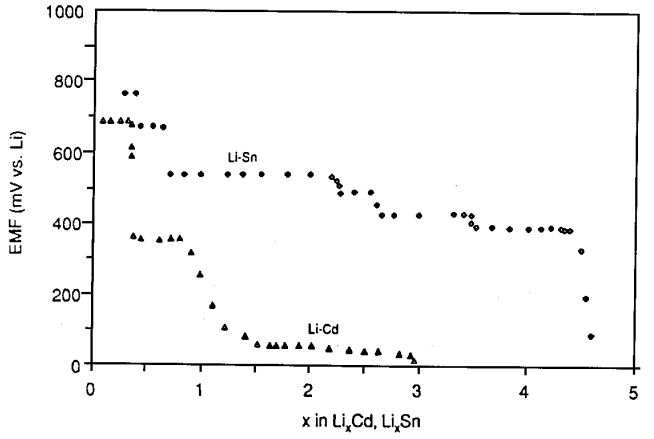


Figure 15. Potential vs. composition for the Li–Sn and Li–Cd systems at ambient temperature [48].

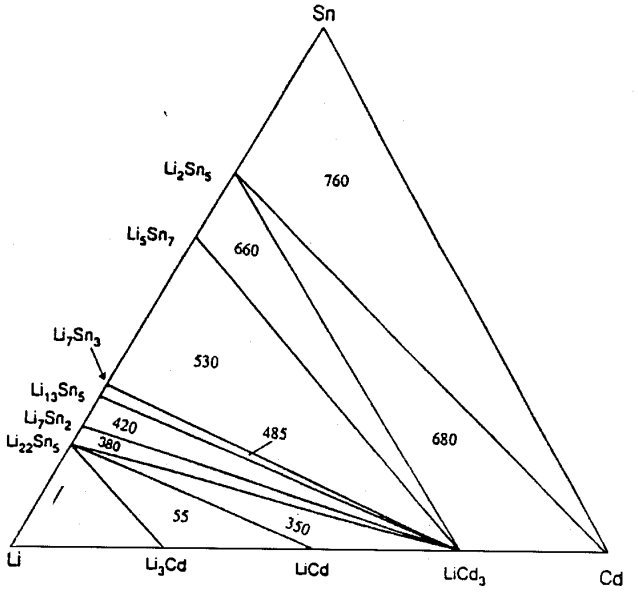


Figure 16. Calculated isothermal Li–Cd–Sn ternary phase stability diagram at ambient temperature [48].

The behavior of this composite electrode, in which Li reacts with the Cd phases inside of the Li–Sn phase, is shown in Fig. 17.

In order to achieve good reversibility, the composite electrode microstructure must have the ability to acommodate any volume changes that might result from the reaction that takes place internally. This can be taken care of by clever microstructural design and alloy fabrication techniques.

CosMX Exhibit 1008, Page 397 of 633

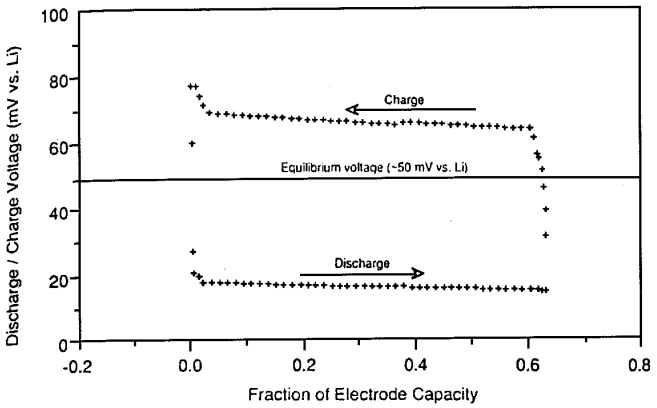


Figure 17. Sixth charge–discharge curve of a composite Li–Sn/Li–Cd electrode at a current density of 0.1 $mA\,cm^{-2}$ at ambient temperature [48].

4.11 Solid Electrolyte Matrix Electrode Structures

In solid-state systems it is often advantageous to have some of the electrolyte material mixed in with the reactant. There are two general advantages that result from doing this. One is that the contact area between the electrolyte phase and the electrode phase (the electrochemical interface) is greatly increased. The other is that the presence of the electrolyte material changes the thermal expansion characteristics of the electrode structure so as to be closer to that of the pure electrolyte. By doing so, the stresses that arise as the result of a difference in the expansion coefficients of the two adjacent phases that can use mechanical separation of the interface are reduced.

It is interesting to note that the recently announced Fujifilm development of convertible oxide electrodes results in the formation of a microstructure containing fine dispersions of both Li–Sn alloys and Li_2O. The latter is known to be a lithium-transporting solid electrolyte. Thus these electrodes can be thought of as having a composite microstructure with an electrolyte as well as the reactant phase.

4.12 What About the Future ?

The recent development of the convertible oxide materials at Fuji Photo Film Co. will surely cause much more attention to be given to alternative lithium alloy negative electrode materials in the near future from both scientific and technological standpoints. This work has shown that it may pay not only to consider different known materials, but also to think about various strategies that might be used to form attractive materials in situ inside the electrochemical cell.

4.13 References

[1] R.A Huggins, D. Elwell, *J. Crystal Growth*, **1977**, *37*, 159.

[2] C. Wagner, *J. Electrochem. Soc.*, **1954**, *101*, 225.

CosMX Exhibit 1008, Page 398 of 633

[3] C. Wagner, *J. Electrochem. Soc.*, **1956**, *103*, 571.
[4] G. Deublein, R.A. Huggins, *Solid State Ionics*, **1986**, *18/19*, 1110.
[5] N.P. Yao, L.A. Heredy, R.C. Saunders, *J. Electrochem. Soc.*, **1971**, *118*, 1039.
[6] E.C. Gay, *J. Electrochem. Soc.*, **1976**, *123*, 1591.
[7] S.C. Lai, *J. Electrochem. Soc.*, **1976**, *123*, 1196.
[8] R.A. Sharma, R.N. Seefurth, *J. Electrochem. Soc.*, **1976**, *123*, 1763.
[9] R.N. Seefurth, R.A. Sharma, *J. Electrochem. Soc.*, **1977**, *124*, 1207.
[10] H. Ogawa in *Proc. 2nd Int. Meeting on Lithium Batteries*, Elsevier Sequoia, S. A. Lausanne, **1984**, p. 259.
[11] R. Yazami, P. Touzain, *J. Power Sources*, **1983**, *9*, 365.
[12] J.O. Besenhard, J. Yang, M. Winter, *J. Power Sources*, **1997**, *68*, 87.
[13] Internet: http://www.fujifilm.co.jp/eng/news_e/nr079.html, **1996**.
[14] T. Kubota, M. Tanaka, Jpn. Kokai Tokkyo Koho, JP 94-55614940325, **1994**.
[15] E. Funatsu, Jpn. Kokai Tokkyo Koho, JP 94-2592940114, **1994**.
[16] Y. Idota, M. Nishima, Y. Miyaki, T. Kubota, T. Miyasaka, European Patent Application EP 651450 A1 950503, **1996**.
[17] Y. Idota, M. Nishima, Y. Miyaki, T. Kubota, T. Miyasaka, Canadian Patent Application 21134053, **1994**.
[18] I.A. Courtney, J.R. Dahn, *J. Electrochem. Soc.*, **1997**, *144*, 2045.
[19] W. Weppner, R. A. Huggins in *Proc. Symposium on Electrode Materials and Processes for Energy Conversion and Storage*, Ed.: J.D.E. McIntyre, S. Srinivasan, F. G. Will, The Electrochemical Society, Pennington, NJ, **1977**, p. 833.
[20] W. Weppner, R.A. Huggins, *Z. Phys. Chem. N.F.*, **1977**, *108*, 105.
[21] W. Weppner, R.A. Huggins, *J. Electrochem. Soc.*, **1978**, *125*, 7.
[22] C.M. Luedecke, J.P. Doench, R.A. Huggins in *Proc. Symp on High Temperature Materials Chemistry* (Eds.: Z.A. Munir, D. Cubicciotti), The Electrochemical Society, Pennington, NJ, **1983**, p. 105.
[23] J.P. Doench, R.A. Huggins in *Proc. Symp on High Temperature Materials Chemistry* (Eds.: Z.A. Munir, D. Cubicciotti), The Electrochemical Society, Pennington, NJ, **1983**, p. 115.
[24] A. Anani, R.A. Huggins in *Proc. Symp. on Primary and Secondary Ambient Temperature Lithium Batteries* (Eds.: J.-P. Gabano, Z. Takehara, P. Bro), The Electrochemical Society, Pennington, NJ, **1988**, p. 635.
[25] A. Anani, R.A. Huggins, *J. Power Sources*, **1992**, *38*, 351.
[26] R.A. Huggins in *Fast Ion Transport in Solids* (Eds.: P. Vashishta, J.N. Mundy, G.K. Shenoy), North-Holland, Amsterdam, **1979**, p. 53.
[27] R.A. Huggins, A.A. Anani, US patent 4950566, August 21, **1990**.
[28] A. Anani, R.A. Huggins, *J. Power Sources*, **1992**, *38*, 363.
[29] C.J. Wen, Ph.D. Dissertation, Stanford University, **1980**.
[30] I.D. Raistrick, R.A. Huggins, *Mater. Res. Bull.*, **1983**, *18*, 337.
[31] I.D. Raistrick, A.J. Mark, R.A. Huggins, *Solid State Ionics*, **1981**, *5*, 351.
[32] W. Weppner, R.A. Huggins, *J. Electrochem. Soc.*, **1977**, *124*, 1569.
[33] W. Weppner, R.A. Huggins in *Annu. Rev. Mater. Sci.*, **1978**, 269.
[34] C.J. Wen C. Ho, B. A. Boukamp, I. D. Raistrick, W. Weppner, R. A. Huggins, *Int. Metals Rev.*, **1981**, *5*, 253.
[35] C.J. Wen B. A. Boukamp, R. A. Huggins, W. Weppner, *J. Electrochem. Soc.*, **1979**, *126*, 2258.
[36] C.J. Wen W. Weppner, B. A. Boukamp, R. A. Huggins, *Met. Trans. B.*, **1980**, *11*, 131.
[37] C.J. Wen, R.A. Huggins, *J. Solid State Chem.*, **1981**, *37*, 271.
[38] C.J. Wen, R.A. Huggins, *J. Electrochem. Soc.*, **1981**, *128*, 1181.
[39] C.J. Wen, R.A. Huggins, *J. Solid State Chem.*, **1980**, *35*, 376.
[40] J.P. Doench, R.A. Huggins, *J. Electrochem. Soc.*, **1982**, *129*, 341.
[41] J. Wang, I.D. Raistrick, R.A. Huggins, *J. Electrochem. Soc.*, **1986**, *133*, 457.
[42] J. Wang, P. King, R.A. Huggins, *Solid State Ionics*, **1986**, *20*, 185.
[43] A. Anani, S. Crouch-Baker, R.A. Huggins, *Proc. Symp on Lithium Batteries* (ed. A.N. Dey), The Electrochemical Society, Pennington NJ, **1987**, p.365.
[44] B.A. Boukamp, G.C. Lesh, R.A. Huggins, *J. Electrochem. Soc.*, **1981**, *128*, 725.

CosMX Exhibit 1008, Page 399 of 633

[45] B.A. Boukamp, G.C. Lesh, R.A. Huggins in *Proc. Symp on Lithium Batteries* (Ed. H.V. Venkatasetty), The Electrochemical Society, Pennington NJ, **1981**, p.467.

[46] R.A Huggins, B.A. Boukamp, US Patent 4436796, **1984**.

[47] A. Anani, S. Crouch-Baker, R.A. Huggins in *Proc. Symp on Lithium Batteries* (Ed. A.N. Dey), The Electrochemical Society, Pennington NJ, **1987**, p.382.

[48] A. Anani, S. Crouch-Baker, R.A. Huggins, *J. Electrochem. Soc.*, **1988**, *135*, 2103.

[49] C.J. Wen, R.A. Huggins, *Mater. Res. Bull.*, **1980**, *15*, 1225.

[50] M.L. Saboungi J. J. Marr, K. Anderson, D. R. Vissers, *J. Electrochem. Soc.*, **1979**, *126*, 322.

[51] C.J. Wen, R.A. Huggins, *J. Electrochem. Soc.*, **1981**, *128*, 1636.

[52] W. Weppner, R.A. Huggins, *J. Solid State Chem.*, **1977**, *22*, 297.

CosMX Exhibit 1008, Page 400 of 633

5 Lithiated Carbons

Martin Winter and Jürgen Otto Besenhard

5.1 Introduction

The rapid proliferation of new technologies, such as portable consumer electronics and electric vehicles, has generated the need for batteries that provide both high energy density and multiple rechargeability. In order to accomplish such high energy density batteries, the use of electrode materials with high charge-storage capacity is inevitable. Considering thermodynamic reasons for the selection of an anode material, light metals M, such as Li, Na, K, or Mg, are favored as they combine outstanding negative standard redox potentials with low equivalent weights. However, a realization of batteries using these metals as active anode materials is in most cases not possible because the strong reducing power of the metals results in a spontaneous reaction in contact with an electrolyte.

Among the light metals M, only metallic lithium shows a chemical and electrochemical behavior which favors its use in high energy-density batteries [1, 2]. In suitable nonaqueous electrolytes "passivating" films of Li^+-containing electrolyte decomposition products, spontaneously formed upon immersion in the electrolyte, protect the lithium surfaces. These films act as a "sieve", being selectively permeable to the electrochemically active charge carrier, the Li^+ cation, but impermeable to any other electrolyte component that would react with lithium, i.e., they behave as an electronically insulating solid electrolyte interphase (SEI) [3–5].

The composition, structure, and formation process of the SEI on metallic lithium depend on the nature of the electrolyte. The variety of possible electrolyte components makes this topic very complex; it is reviewed by Peled, Golodnitsky, and Penciner in Chapter III, Sec.6 of this handbook. The types and properties of liquid nonaqueous electrolytes, that are commonly used in lithium cells are reviewed by Barthel and Gores in Chapter III, Sec.7.

The observation of the kinetic stability of lithium in a number of nonaqueous electrolytes was the foundation of the research on "lithium batteries" in the 1950s, and the commercialization of primary (not rechargeable) lithium batteries followed quickly in the late 1960s and early 1970s [2, 6–12]. Today, primary metallic lithium systems have found a variety of applications, e.g., military, consumer and medical, and commercial interest is still growing. However, apart from the rechargeable Li/MnO_2 cell commercialized by Tadiran (Israel) [13–15], the commercial breakthrough of rechargeable secondary batteries based on metallic lithium anodes has not been achieved so far. Upon recharge of

the anode lithium plating occurs simultaneously with lithium corrosion and "passivation" (i.e., formation of SEI). Thus, lithium is deposited as highly dispersed, highly reactive metal particles. These dendrites are covered with SEI films and therefore are partially electrochemically inactive. This reduces the efficiency of the lithium deposition/ dissolution process. Moreover, the dendrites grow to filaments upon cycling, which may short-circuit, overheat the cell locally, and cause a disastrous thermal runaway due to the low melting point of Li (~180 °C) [10, 16–19]. In contrast, the lithium insertion materials used for the cathode exhibited sufficient cycleability and safety.

Beginning in the early 1980s [20, 21] metallic lithium was replaced by lithium insertion materials having a lower standard redox potential than the positive insertion electrode; this resulted in a "Li-ion" or "rocking-chair" cell with both negative and positive electrodes capable of reversible lithium insertion (see recommended papers and review papers [7, 10, 22–28]). Various insertion materials have been proposed for the anode of rechargeable lithium batteries, e.g., transition metal oxides and chalcogenides, carbons, lithium alloys, lithium transition metal nitrides, and several polymers. In general, both the specific charges and the charge densities of lithium insertion materials are theoretically lower than those of metallic lithium, because the use of an electrochemically inactive lithium insertion host is associated with additional weight and volume (Fig. 1). However, as the lithium is stored in the host in ionic and not in atomic form, the packing densities and thus the charge densities of several lithium insertion materials, e.g., Sn (Fig. 1) and others [29] are close to those of Li. Considering, moreover, that in practical cases the cycling efficiency of metallic lithium is ≤ 99 percent, one has to employ a large excess of lithium [10, 19, 30, 31] to reach a reasonable cycle life. Therefore, the practical specific charge and the charge density of a secondary lithium metal electrode are much lower than the theoretical values, almost in the same order as those of graphite. (More information on the properties of the metallic lithium anode are given in Chapter III, Sec.3.)

From a thermodynamic point of view, apart from charge density and specific charge, the redox potential of lithium insertion into/removal from the electrode materials has to be considered also. For instance, the redox potential of many Li alloys is between ~0.3 and ~1.0 V vs. Li/Li^+, whereas it is only ~0.1 V vs. Li/Li^+ for lithiated graphite (Fig. 2). From the point of view of energy density, the use of anodes with highly negative potential, yielding high cell voltages, would be advantageous. However, the materials with the potential closest to that of metallic lithium may be the most reactive (although

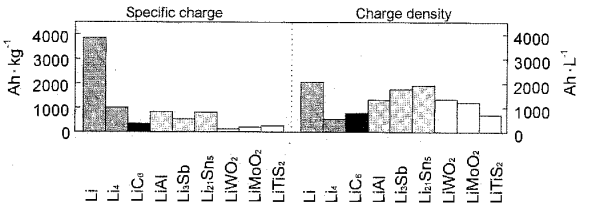


Figure 1. Specific charges and charge densities of several lithiated anode materials for lithium batteries, calculated by using data from Refs. [10, 32–35]. Li_4 denotes a fourfold excess of lithium, which is necessary to attain a sufficient cycle life.

CosMX Exhibit 1008, Page 402 of 633

due to kinetic effects they are not necessarily so) and thus they can cause safety problems as well as handling difficulties. This will be discussed further in the following section of this chapter.

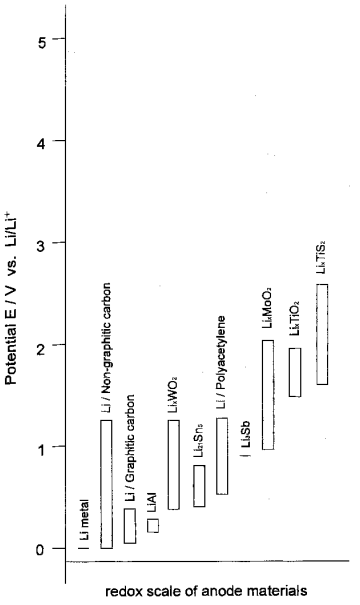


Figure 2. Redox potentials for lithium insertion into/removal from several anode materials for lithium cells.

5.1.1 Why Lithiated Carbons?

Among the mentioned lithium insertion materials above lithiated carbons (Li_xC_n) are considered to be the most promising at present. Carbonaceous materials exhibit higher lithium storage capacities and more negative redox potentials versus the cathode than polymers, metal oxides, or chalcogenides. Furthermore, they show long-term cycling performance superior to Li alloys due to their better dimensional stability. In addition, most carbons suitable as anodes for lithium ion cells are cheap and abundant compared with the other materials.

Though considerable safety improvements were the major driving force for the introduction of lithiated carbons into rechargeable lithium cells, it has to be kept in mind that the lithium activity of lithium-rich carbons is similar to that of metallic lithium. Thus the redox potential vs. Li/Li^+ is quite close to 0 V (Fig. 2) and the reactivity is high. Additionally, the particle size of Li_xC_n in practical electrodes is only in the order of 10 µm, i.e., the reactive surface area is large. Moreover, ex situ investigations after cycling have shown that cycling of graphite electrodes increases the specific surface area of Li_xC_n by a factor of five [36]. Recent differential scanning calorimetry studies on polymer-bonded lithiated carbons reveal that the SEI films degrade at temperatures of approx. 120-140 °C, then undergo a reaction with the electrolyte *and* the binder material at temperatures above 200 °C. The degradation reactions are proportional to the surface area of the carbon [37], and furthermore can be expected to depend on the SEI films formed, i.e., the electrolytes used. The tendency of the SEI film to peel off the carbon anode is assumed to be suppressed (the adherence between carbon and SEI is supposed to be improved) by proper surface pre–treatment of the carbon [38].

However, the reaction rate of Li_xC_n depends on the lithium concentration at the surface of the carbon particles, which is limited by the rather slow transport kinetics of lithium from the bulk to the surface [17–19, 39]. As the melting point of metallic lithium is low (~180 °C) there is some risk of melting of lithium under abuse conditions such as short-circuiting, followed by a sudden breakdown of the SEI and a violent reaction of liquid lithium

CosMX Exhibit 1008, Page 403 of 633

with the other cell components. In contrast, there is no melting of lithiated carbons.

5.1.2 Electrochemical Formation of Lithiated Carbons

The electroinsertion reaction of mobile lithium ions into a solid carbon host proceeds according to the general reaction scheme

$$Li_xC_n \underset{\text{charge}}{\overset{\text{discharge}}{\rightleftharpoons}} xLi^+ + xe^- + C_n \quad (1)$$

During electrochemical reduction (charge) of the carbon host, lithium cations from the electrolyte penetrate into the carbon and form a lithiated carbon Li_xC_n. The corresponding negative charges are accepted by the carbon host lattice. As for any other electrochemical insertion process, the prerequisite for the formation of lithiated carbons is a host material that exhibits mixed (electronic and ionic) conductance.

The reversibility of this so-called "intercalation" reaction can be checked by subsequent electrochemical oxidation (discharge) of Li_xC_n, i.e., the de-intercalation of Li^+. The term "intercalation" is regarded as a special case of "intercalation". Its use implies the restricting condition that a layer of guest ions slides between the sheets of a layered host matrix, while the host broadly retains its structural integrity. These prerequisites are, for instance, fulfilled for the insertion of lithium ions in graphite. In most cases, however, a strict differentiation between insertion and intercalation is a formal question and both terms are used inter-changeably. Following historical conventions, the terms "intercalation" and "lithium/carbon intercalation compounds" will be used in this review, even though only a small fraction of layered structure units may be present in a specific carbon material (see also [2, 6]).

5.2 Graphitic and Non-Graphitic Carbons

The electrochemical performance of lithiated carbons depends basically on the electrolyte, the parent carbonaceous material, and the interaction between the two (see also Chapter III, Sec.6). As far as the lithium intercalation process is concerned, interactions with the electrolyte, which limit the suitability of an electrolyte system, will be discussed in Secs. 5.2.2.3, 5.2.3 and 5.2.4 of this chapter. First, several properties of the carbonaceous materials will be described.

The quality and quantity of sites which are capable of *reversible* lithium accommodation depend in a complex manner on the crystallinity, the texture, the (micro)structure, and the (micro)morphology of the carbonaceous host material [7, 19, 22, 40–57]. The type of carbon determines the current/potential characteristics of the electrochemical intercalation reaction and also potential side-reactions. Carbonaceous materials suitable for lithium intercalation are commercially available in many types and qualities [19, 43, 58–61]. Many exotic carbons have been specially synthesized on a laboratory scale by pyrolysis of various precursors, e.g., carbons with a remarkably high lithium storage capacity (see Secs. 5.2.4 and 5.2.5), and tailored carbons, which were prepared by the use of inorganic templates [62, 63]. It has to be emphasized that the assumed suitability of a carbonaceous material for a lithium intercalation host depends strongly on the method of its evaluation and quite a few

CosMX Exhibit 1008, Page 404 of 633

carbons may have been rejected as anode materials due to an inadequate evaluation method. As a consequence, sometimes the classification of a carbon as "good" or "poor" anode material can be only preliminary. For instance, though in principle electrochemical intercalation in graphite was already observed in the mid-1970s [64, 65], it took about 15 years for an appropriate electrolyte allowing the highly reversible operation of a graphite anode to be found [66].

5.2.1 Carbons: Classification, Synthesis, and Structures

Because of the variety of available carbons, a classification is inevitable. Most carbonaceous materials which are capable of reversible lithium intercalation can be classified roughly as graphitic and non-graphitic (disordered).

Graphitic carbons basically comprise "graphene layer" is formed. Van der Waals forces provide a weak cohesion of the graphene layers leading to the well-known *layered* graphite structure. From a strictly crystallographic point of view the term "graphite" is, however, only applicable for carbons having a layered lattice structure with a perfect stacking order of graphene layers, either the prevalent AB (hexagonal graphite, Fig. 3) or the less common ABC (rhombohedral graphite). Due to the small amount of required energy for transformation of AB into ABC stacking (and vice versa), perfectly stacked graphite crystals are not readily available. For instance, typically about 5 percent of the graphene layers in natural graphite are arranged rhombohedrally. Therefore, the term "graphite" is often used regardless of stacking order.

The actual structure of practical carbonaceous materials deviates more or less from the ideal graphite structure. Even number of structural defects. Moreover,

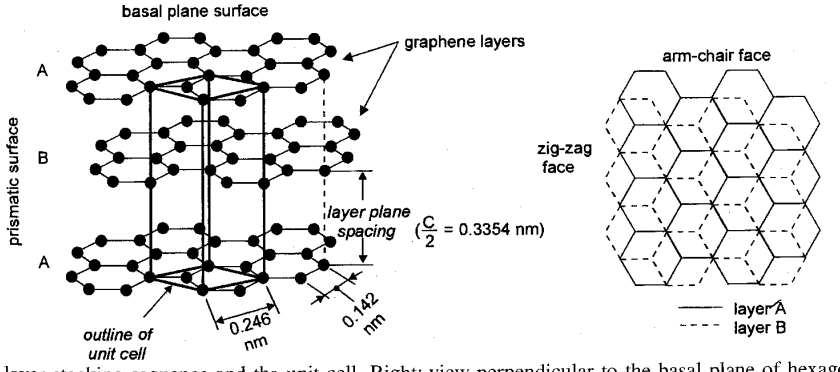


Figure 3. Left: schematic drawing of the crystal structure of hexagonal graphite showing the AB graphene layer stacking sequence and the unit cell. Right: view perpendicular to the basal plane of hexagonal graphite. Prismatic surfaces can be subdivided into armchair and zig-zag faces. Modified and redrawn from Ref. [2].

sp^2 - hybridized carbon atoms which are arranged in a planar hexagonal ("honeycomb-like") network such that a so-called highly ordered graphites typically have a carbonaceous materials consisting of aggregates of graphite crystallites are called

CosMX Exhibit 1008, Page 405 of 633

graphites as well. For instance, the terms "natural" graphite, "artificial" or "synthetic" graphite, and "pyrolytic" graphite are commonly used, although the materials are polycrystalline [67]. The crystallites may vary considerably in size, ranging from the order of nanometers to micrometers. In some carbons, the aggregates are large and relatively free of defects, e.g., in highly oriented pyrolytic graphite (HOPG). Furthermore, texture effects can be observed as the crystallites may be differently oriented to each other. In addition to essentially graphitic crystallites, carbons may also include crystallites containing carbon layers (or packages of stacked carbon layers) with significant, randomly distributed misfits and misorientation angles of the stacked segments to each other (turbostratic orientation or turbostratic disorder [68]). The latter disorder can be identified from a nonuniform, and on average increased interlayer spacing compared with to graphite [67, 69].

When the disorder in the structure becomes more dominant among the crystallites, the carbonaceous material can no longer be considered graphitic but must be regarded as a non-graphitic carbon. For carbon samples that contain both characteristic graphitic *and* non-graphitic structure units, the classification in graphitic and non-graphitic types can be somehow arbitrary and in many cases is only made for the sake of convenience.

In the case of non-graphitic (disordered) carbons, most of the carbon atoms are arranged in a planar hexagonal network, too. Though layered structure segments are probable, there is actually no far-reaching crystallographic order in the *c*-direction. The structure of these carbons is characterized by amorphous areas embedding and partially crosslinking more graphitic (layered) structure segments [70–72] (Fig. 4). The number and the size of the areas vary, and depend both on the precursor material and on the manufacturing process, e.g., on the manufacturing temperature and pressure. Using a simple model [19, 43] the complex X-ray deffraction (XRD) patterns of non-graphitic carbons can be correlated with the probability of finding unorganized (randomly oriented and amorphous) and organized (layered) areas. As a result the lithium storage capacity of a specific non-graphitic carbon material can be predicted approximately.

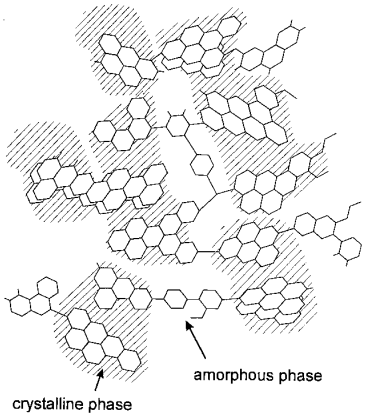


Figure 4. Schematic drawing of a non-graphitic (disordered) carbon [2].

Most non-graphitic carbons are prepared by pyrolysis of organic polymer or hydrocarbon precursors at temperatures below ~1500 °C. Further heat treatment of most non-graphitic carbons at temperatures from ~1500 to ~3000 °C makes it possible to distinguish between two different types of carbons.

Graphitizing carbons develop the graphite structure continuously during the heating process. The carbon layers are mobile enough to form graphite-like crystallites as crosslinking between the layers is weak. Non-graphitizing carbons exhibit no

CosMX Exhibit 1008, Page 406 of 633

true development of the graphite structure, not even at high temperatures (2500–3000 °C), since the carbon layers are immobilized by strong crosslinking. Since non-graphitizing carbons are mechanically harder than graphitizing ones, it is common to divide the non-graphitic carbons into "soft" and "hard" carbons [70]. The precursors and—at least to some extent—the preparation and assumed structure of the hard carbons resemble those of glassy carbon [73, 74]. Franklin [70] reported that, compared with graphitizing carbons, non-graphitizing carbons exhibit a considerably more extensive fine-structure porosity (nanoporosity). Models for only partially graphitizing carbons are also discussed [70, 75].

The mobility of the carbon structure units, which determines the degree of microstructural ordering as well as the texture of the carbonaceous material, depends on the state of aggregation of the intermediate phase during pyrolysis, which can be solid, liquid or gaseous [72]. Non-graphitizing carbons are usually products of solid-phase pyrolysis whereas graphitizing carbons are commonly produced by liquid- or gas-phase pyrolysis. Examples of products of solid-phase pyrolysis are chars and glassy (vitreous) carbon, which are produced from crosslinked polymers. Because of small crystal size and a high structural disorder of the polymers, the ability of these carbons to graphitize is low. Pyrolysis of thermally stabilized polyacrylonitrile or pitch, which are the precursors for carbon fibers, also yields solid intermediate phases, but stretching of the fibrous material during the manufacturing process produces an ordered microstructure [72]. The synthesis of petroleum coke, which is the most important raw material for the manufacture of carbons and graphites, is an example of liquid-phase pyrolysis. Petroleum coke is produced by the pyrolysis of petroleum pitch, which is the residue from the distillation of petroleum fractions. Cokes are also products from pyrolysis of coal tar pitch and aromatic hydrocarbons at 300–500 °C. Carbon black, pyrocarbon and carbon films are examples of gas-phase pyrolysis products, i.e., products of thermal cracking of gaseous hydrocarbon compounds which are deposited as carbon on a substrate [67, 72].

The ability to graphitize also depends on the pre-ordering and pre-texture of the respective precursor. For example, the graphitization ability is higher (i) if the precursor material comprises highly condensed aromatic hydrocarbons which can be considered to have a graphene-like structure, and (ii) if neighboring graphene layers or graphitic crystallites are suitably orientated to each other.

Apart from manifold structures, carbons can have various shapes, forms, and textures, including powders with different particle size distributions, foams, whiskers, foils, felts, papers, fibers [76, 77], spherical particles [76] such as mesocarbon microbeads (MCMB's) [78], etc. Comprehensive overviews are given, for example in [67, 71, 72]. Further information on the synthesis and structures of carbonaceous materials can be found in [67, 70, 72, 75, 79]. Details of the surface composition and surface chemistry of carbons are reviewed in Chapter II, Sec. 8, and in Chapter III, Sec. 6, of this handbook. Some aspects of surface chemistry of lithiated carbons will also be discussed in Sec. 5.2.2.3.

CosMX Exhibit 1008, Page 407 of 633

5.2.2 Lithiated Graphitic Carbons (Li_xC_n)

5.2.2.1 In-Plane Structures

The first lithiated graphitic carbons (lithium–graphite intercalation compounds, abbreviated as Li–GIC's), (Li_xC_n), were obtained by chemical synthesis in the mid-1950s. [80, 81]. At ambient pressure, a maximum lithium content of one Li guest atom per six carbon host atoms can be reached for highly crystalline graphite ($n \geq 6$ in LiC_n or $x \leq 1$ in Li_xC_6). The intercalation reaction proceeds via the prismatic surfaces (armchair and zig-zag faces). Through the basal plane intercalation is possible at defect sites only. During intercalation the stacking order of the graphene layers shifts to AA. Thus, two neighboring graphene layers in LiC_6 directly face each other (Fig. 5a). The energetically favored AA stacking sequence of LiC_6 has been proved by ab-initio studies [82]. Due to the hosted lithium the interlayer distance between the graphene layers increases moderately (10.3 percent has been calculated for LiC_6 [35, 83]). The stacking order of the lithium interlayers is αα (a Li - C_6 - Li - C_6 - Li chain exists along the *c*-axis) [84, 85]. In LiC_6 the lithium is distributed in-plane in such a manner that the occupation of the nearest-neighbor sites is avoided (Fig. 5b).

A higher lithium in-plane density by occupation of nearest neighbor sites is obtained in the phases $LiC_2 - LiC_4$, i.e., x = 2–3 in Li_xC_6, which are prepared chemically from graphitic carbon under high pressure (~60 kbar) and high temperature (~300 °C) conditions [44, 86–89]. The close Li–Li distance in LiC_2 (Fig. 5c) results in a higher chemical activity of lithium than that of lithium metal (Li–Li bond lenght (20°C) = 0.304 nm [34]). Under ambient conditions LiC_2 decomposes slowly via various metastable intermediate Li/C phases to LiC_6 and metallic lithium [44, 88]. A preliminary study of the electrochemical behavior of LiC_2 can be found in Ref. [44]. For more comprehensive details on the chemical synthesis of Li_xC_6 see the literature [42, 44, 81, 90-92]. Selected general reviews on graphite intercalation compounds are cited in Ref. [6].

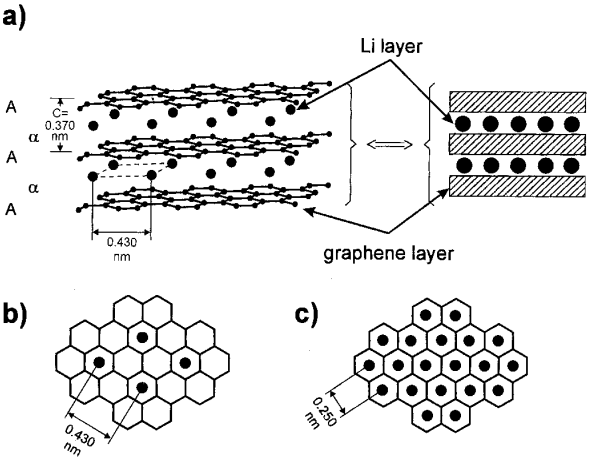


Figure 5. Structure of LiC_6. (a) Left: schematic drawing showing the AA layer stacking sequence and the αα interlayer ordering of the intercalated lithium. Right: Simplified representation [2]. (b) In-plane distribution of Li in LiC_6. (c) In-plane distribution of Li in LiC_2.

CosMX Exhibit 1008, Page 408 of 633

5.2.2.2 Stage Formation

A general feature of intercalation into graphite is the formation of a periodic array of unoccupied layer gaps at low concentrations of guest species, called stage formation [80, 81, 92–98]. This stepwise process can be described by the stage index s which is equal to the number of graphene layers between two nearest-guest layers. Staging is a thermodynamic phenomenon related to the energy required to (constant current) reduction (= charge) of graphite to LiC_6 corresponding to a lithium storage capacity of $372\,Ah\,kg^{-1}$ with respect to the graphite mass (compare Fig. 1, where the lithium storage capacities are given with respect to the lithiated hosts, i.e., $339\,Ah\,kg^{-1}$ for LiC_6). The plateaus arising during reduction in the curve indicate two-phase regions (coexistence of two phases) [99, 100]. Under potentiodynamic control (linear potential sweep voltammetry) the two-phase regions are indicated by

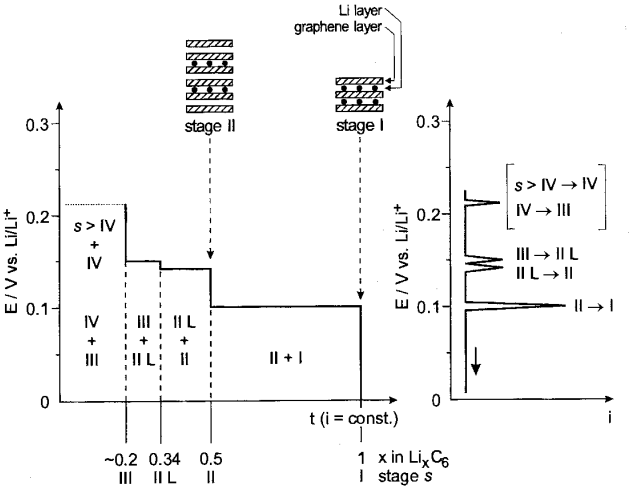


Figure 6. Simplified scheme showing the stage formation during electrochemical formation of lithiated graphite. Left: schematic galvanostatic curve. Right: schematic voltammetric curve. Prepared with data from [92, 100, 104, 105, 110]. For a more detailed discussion, see text.

"open" the van der Waals gap between two graphene layers for the guests entering the hosts. The repulsive coulombic interactions between the guest ions are less effective. As a consequence, only a few (but highly occupied) van der Waals gaps are energetically favored over a random distribution of guests.

Staging phenomena as well as the degree of intercalation can be easily observed during the electrochemical reduction of carbons in Li^+-containing electrolytes. Figure 6 (left) shows a schematic potential/composition curve for the galvanostatic current peaks (Fig. 6, right). Apart from the stage s = I, other binary phases corresponding to the stages s = IV, III, II L, and II (which can also be obtained by chemical synthesis [80, 81, 94, 95, 99, 101–103]) were identified by electrochemical experiments and confirmed by X-ray diffraction [35, 99, 100, 102–106] and Raman spectroscopy [107, 108]. Stages higher than s = IV were reported, too [100, 108–111]. However, there are some discrepancies in the reported literature concerning the staging process, in particular regarding stages s>II. This is discussed in ref. [112].

CosMX Exhibit 1008, Page 409 of 633

The splitting of the second stage into two, $s = II$ (x=0.5 in Li_xC_6) and $s = II\,L$ (x=0.33 in Li_xC_6), is due to different lithium packing densities. It disappears at temperatures below ~10 °C [100]. At temperatures above 700 °C Li_xC_6 ($0.5 \le x \le 1$) is transformed into lithium carbide Li_2C_2 and carbon [96, 113].

Commercial graphites can contain a considerable proportion of rhombohedral structure units. It has been reported that lithium intercalation mechanisms and storage capabilities are similar for both rhombohedral and hexagonal graphite structures [59, 61]. However, the preparation of graphite with a higher proportion of rhombohedrally structured graphene planes and its use as anode material is claimed in a patent [114]. Lithiated graphites can also be prepared from a KC_8 precursor, either (i) chemically by ion exchange reactions [115] or (ii) electrochemically after de-intercalation of potassium [116, 117].

5.2.2.3 Reversible and Irreversible Specific Charge

Experimental constant current charge/ discharge curves for Li^+ intercalation/de-intercalation into/out of graphite clearly prove the staging phenomenon (Fig. 7). Nevertheless, there are no sharp discontinuities between the two-phase regions because (i) the packing density of Li_xC_6 varies slightly (a phase width exists), and (ii) various types of overpotentials cause plateau-sloping in galvanostatic measurements (and peak-broadening in voltammetric measurements). Theoretically, Li^+ intercalation into carbons is fully reversible. In the practical charge/discharge curve, however, the charge consumed in the first cycle significantly exceeds the theoretical specific charge of 372 Ah kg^{-1} for the first stage LiC_6 first stage (Fig. 7). The subsequent de-intercalation of Li^+ recovers only ~80–95 percent of this charge. In the second and subsequent cycles, then, the charge consumption for the Li^+ intercalation half-cycle is lower and the charge recovery is close to 100 percent.

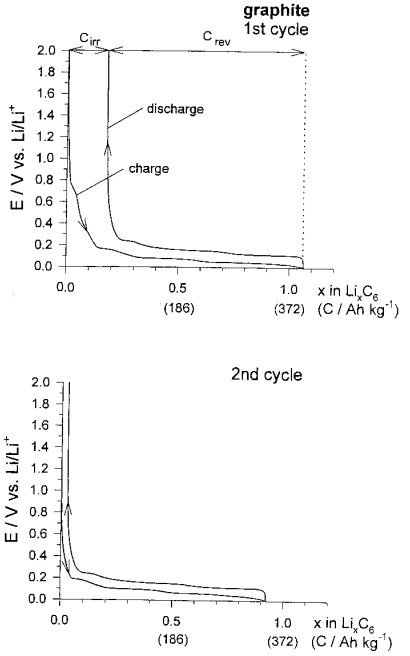


Figure 7. First- and second- cycle constant-current charge/discharge curves of graphite Timrex® KS44 in $LiN(SO_2CF_3)_2$ /ethylene carbonate/dimethyl carbonate as the electrolyte (C_{irr} =irreversible specific charge; C_{rev} =reversible specific charge) [2].

The excess charge consumed in the first cycle is generally ascribed to SEI formation and corrosion-like reactions of Li_xC_6 [19, 66, 118–120]. Like metallic lithium and Li-rich Li alloys, lithiated graphites, and more generally lithiated carbons are thermodynamically unstable in all known electrolytes, and therefore the surfaces which are exposed to the electrolyte have to be kinetically protected by SEI films (see Chapter III, Sec.6). Neverthe-

CosMX Exhibit 1008, Page 410 of 633

less, there are significant differences in the film formation processes between metallic lithium and lithiated carbons. Simplified, these differences are as follows: Film formation on metallic Li takes place upon contact with the electrolyte. Various electrolyte components decompose spontaneously with low selectivity and some of the decomposition products form the film. When the film grows, the activity of the metallic lithium electrode versus the electrolyte decreases because of an increasing I R drop in the film. At this stage the electrolyte reduction processes become more and more selective as the number of electrolyte components which are still sensitive to reduction versus the (now partially electronically "passivated") lithium electrode is limited. In contrast, film formation on carbonaceous hosts takes place as a charge–consuming side reaction in the first few Li^+ intercalation / de-intercalation cycles, especially during the first reduction of the carbon host material. In this case, the electrolyte components which are least stable towards reduction are the first to react selectively. As a result, in the case of metallic lithium the decomposition products of electrolyte components which are highly sensitive to reduction will be accumulated in the *external* film regions near the electrolyte solution, whereas in the case of lithiated carbons the *internal* film regions near the carbon surface will contain more decomposition products stemming from these electrolyte components. Moreover, as a consequence of the differences in the reduction behavior, dissimilar intermediate reduction products may be formed, which can initiate different decomposition mechanisms of the electrolyte. From the viewpoint of the above considerations, it should be emphasized that chemically prepared lithiated carbons, that are exposed to the electrolyte behave similarly to metallic lithium (and not similarly to lithiated carbons which have been prepared electrochemically, e.g., Fig. 7) regarding film formation.

Finally, regarding long-term cycling of metallic lithium and of lithiated carbon, respectively, and its influence on the SEI: the surface of a metallic lithium electrode is periodically renewed during cycling, causing irreversible formation of a "new" SEI in each cycle. Unless the lithium electrode becomes electrochemically inactive due to passivation, this process can be repeated until the lithium and / or the electrolyte are completely consumed. In contrast, the surface of the lithiated carbon electrode is passivated by the SEI throughout the cycling process.

Since film formation on Li_xC_6 is associated with the irreversible consumption of material (lithium and electrolyte), the corresponding charge loss is frequently called "irreversible specific charge" or "irreversible capacity". Reversible lithium intercalation, on the other hand, is called "reversible specific charge" or "reversible capacity". The losses have to be minimized because the losses of charge and of lithium are detrimental to the specific energy of the whole cell and, moreover, increase the material expenses because of the necessary excess of costly cathode material which is the lithium source in a lithium-ion cell after cell assembly.

The extent of the irreversible charge losses due to film formation depends to a first approximation on the surface area of the lithiated carbon which is wetted by the electrolyte [36, 66, 120–124]. Electrode manufacturing parameters influencing the pore size distribution within the electrode [36, 121, 124, 125] and the coverage of the individual particles by a binder [124, 126] have an additional influence on the carbon electrode surface exposed to the electro-

CosMX Exhibit 1008, Page 411 of 633

lyte. These and other technical aspects which are important in this respect are reviewed in recent papers [2, 6].

Besides the irreversible charge loss caused by electrolyte decomposition, several authors claim that the following reactions are also responsible for (additional) irreversible charge losses:

(i) irreversible reduction of impurities such as H_2O or O_2 on the carbon surface
(ii) reduction of "surface complexes" such as "surface oxides" at the prismatic surfaces of carbon, and
(iii) irreversible lithium incorporation into the carbon matrix ("formation of residue compounds" [127–129], e.g., by irreversible reduction of "internal surface groups" at prismatic surfaces of domain boundaries in polycrystalline carbons).

In order to improve the electrochemical performance with respect to lower irreversible capacity losses, several attempts have been made to modify the carbon surface. Here the work of Peled's [38, 130–132] and Takamura's groups [133–138] deserves mention. A more detailed discussion can be found Chapter III, Sec. 6.

5.2.3 Li_xC_6 vs. $Li_x(solv)_yC_n$

Apart from reactions with the electrolyte at the carbon surface, the irreversible specific charge is furthermore strongly affected by the possible co-intercalation of polar solvent molecules between the graphene layers of highly graphitic matrices [139]. This so-called "solvated intercalation reaction" depends (i) on the crystallinity and the morphology of the parent carbonaceous material, which will be discussed in Sec. 5.2.4, and (ii) on the composition of the electrolyte, which is discussed in this section.

Whereas the electrochemical decomposition of propylene carbonate (PC) on graphite electrodes at potentials between ~1 and ~0.8 V vs. Li/Li^+ was already reported in 1970 [140], it took about four years to find out that this reaction is accompanied by a partially reversible electrochemical intercalation of solvated lithium ions, $Li^+(solv)_y$, into the graphite host [64]. In general, the intercalation of Li^+ (and other alkali-metal) ions from electrolytes with organic donor solvents into fairly crystalline graphitic carbons quite often yields solvated (ternary) lithiated graphites, $Li_x(solv)_yC_n$ (Fig. 8) [7, 24, 26, 65, 66, 141–146].

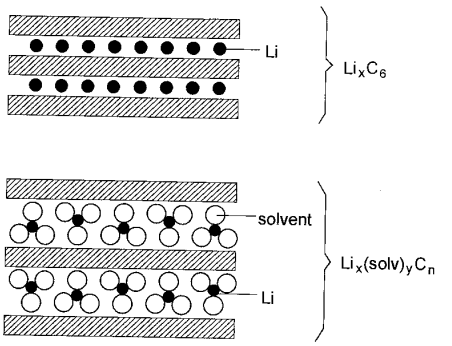


Figure 8. Schematic drawing of binary (Li_xC_n) and ternary [$Li_x(solv)_yC_n$] lithiated graphites. Modified and redrawn from Ref. [26].

The co-intercalation of the large solvent molecules is associated with extreme expansion of the graphite matrix (typically in the region above ~100 percent), frequently leading to exfoliation of graphene layers, and mechanical disintegration of the electrode. In the "best" case reduction of charge storage capabilities, and in the worst case complete electrode destruction, are the typical results of this reaction.

CosMX Exhibit 1008, Page 412 of 633

As long as the content of lithium in the graphitic carbon is low ($x \leq 0.33$ in Li_xC_6), the ternary lithiated graphites are thermodynamically favored over the corresponding binary lithiated graphites Li_xC_6. Hence, the potentials of their electrochemical formation are more positive than those for the formation of the corresponding compound Li_xC_6. At this stage of Li^+ intercalation the coulombic interaction between the lithium guest layer (Li^+) and the balancing negative charge distributed over the graphene layers (C_n^-) is weak, and space to accommodate large solvent molecules is still available [24, 26, 147, 148]. As a further result of the low coulombic interactions the mobility of the intercalants is high and therefore the guest distribution among the interlayer spaces is incommensurable or random. By contrast, the lithium guests in the binary phase LiC_6 form a commensurable structure, i.e., they are organized according to the honeycomb "raster" of the graphene layers [92]. The solvated GICs are thermodynamically unstable with respect to the reduction of the co intercalated solvent molecules [139]. The kinetically controlled reduction depends on the type of co-intercalated solvent. It is slow for, e.g., dimethyl sulfoxide, where even staging of solvated GICs can be observed [141, 149], but very much faster e.g., for PC [64, 140, 150–154], where the electrochemical intercalation followed by fast decomposition of the intercalated $Li^+(solv)_y$ can be misunderstood as simple electrolyte decomposition. Anyway, the reduction of $Li^+(solv)_y$ inside the graphite is associated with an increase of irreversible losses of charge and of material.

Both effects resulting from solvent co-intercalation, the mechanical destruction and the higher irreversible specific charge losses, seriously complicate the operation of graphitic anode materials. Since ternary lithiated carbons are thermodynamically favored at low lithium concentrations in the graphite, i.e., at the beginning of intercalation, kinetic measures have to be applied to prevent, or at least suppress, solvent co-intercalation. This can be accomplished by using electrolyte components that form effectively protecting SEI films on the external graphite surfaces in the very early stages of the first reduction, at potentials which are positive relative to the potentials of a significant formation of $Li_x(solv)_yC_n$. The first [66], and for a long time the only, effective solvent in this respect seemed to be ethylene carbonate (EC) [139, 155, 156]. Since the viscosity of electrolytes based on pure EC is rather high, mixtures of EC with low viscosity solvents such as dimethyl carbonate (DMC) and diethyl carbonate (DEC) are widely used [157–162]. Several papers, which report on investigations and applications of these electrolyte blends, are compiled in recent reviews [2, 6].

Although the formation of binary lithium/graphite intercalation compounds prevails in EC–based electrolytes, many investigations indicate a mechanism of film formation in which solvated lithiated graphites also participate. Film formation in the first cycle during the first reduction of the host material due to electrolyte decomposition is not a simple surface reaction but a rather complex three-dimensional process, taking place basically at a potential of ~1 to ~0.8 V vs. Li/Li^+ (Fig. 7, top). In-situ dilatometric [155], scanning tunneling microscopy (STM) [163, 164], and Raman [108] methods indicate a (fairly large) expansion of the graphite host corresponding to the (intermediate) formation of $Li_x(solv)_yC_n$ at those potentials. The reduction of $Li_x(solv)_y$ on parts of the *internal* sur-

CosMX Exhibit 1008, Page 413 of 633

faces *between* the graphene layers results in an "extra" film, which penetrates into the bulk of the graphite host (Fig. 9). Correspondingly "extra" irreversible charge losses are observed [155]. Several other investigations indicate that the film-formation process on graphite can be even more complex [109, 163–166].

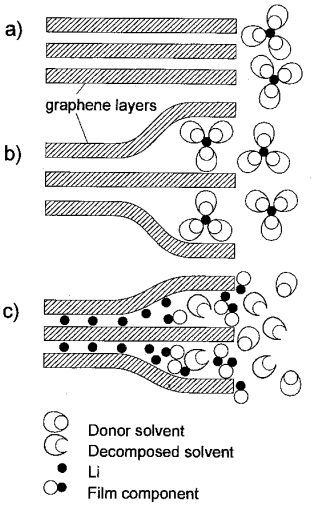


Figure 9. Schematic model of the film-formation mechanism on/in graphite: (a) the situation before reaction; (b) formation of ternary lithiated graphite $Li_x(solv)_yC_n$, (c) film formation due to decomposition of $Li_x(solv)_y$. Prepared with data from Ref. [155].

As in analogy to unsolvated intercalation reactions, solvent co–intercalation takes place via the prismatic surfaces only, not only the total external surface area but also the ratio between the prismatic and basal surfaces affects the irreversible charge loss [120]. This is in good agreement with the observations of Imanishi et al. [167, 168], who found that the tendency for PC co-intercalation into graphitized carbon fibers depends on the fiber texture. Carbon fibers in which the graphite packages are concentrically arranged expose a smaller amount of prismatic surfaces to the electrolyte, i.e., they are less sensitive to solvent co-intercalation, than fibers with a radial texture.

To take into account the effect of the thickness of the respective graphite flake on the formation of $Li_x(solv)_yC_n$ several simple models have been suggested recently [120]. The intercalation of all kinds of species into graphite generally requires energy to expand the gaps between the graphene layers held together by van der Waals forces. Firstly, the "expansion energy" (related to the threshold intercalation potential) depends on the mechanical flexibility of those graphene layers that are deformed by the intercalation process. The average "expansion energy" increases with the thickness of the graphite flake, or more precisely with the number of adjacent graphene layers on both sides of a particular gap. Therefore, intercalation typically starts close to the basal planes of the flake, in the gaps adjacent to the end basal plane. Then the intercalation progresses towards internal layer gaps.

Secondly, the "expansion energy" increases with the size of the guest species. Intercalation of large solvated lithium ions into the outer van der Waals gaps produces a considerable deformation (bending) of the outer graphene layers. Further intercalation into the internal gaps increases the bending angles of the outer graphene layers. However, when the outer graphene layers can not be bend anymore, the intercalation of solvated lithium into the internal van der Waals gaps is hintered. In conclusion, the graphite particle thickness effect should be particularly regarded for the intercalation of solvated lithium ions (Fig. 10 and 120, 169). This means, furthermore, that it should be possible to diminish some expansion due to solvent co-intercalation by sufficient external pressure on the elec-

CosMX Exhibit 1008, Page 414 of 633

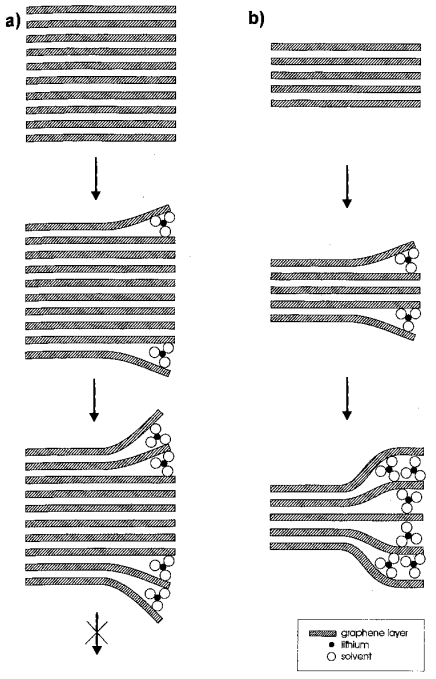


Figure 10. Schematic model showing the influence of the thickness of a graphite flake on the extent of co-intercalation of solvent molecules in the internal van der Waals gaps of graphite. (a) Thick graphite flakes; (b) thin graphite flakes. Prepared with data from Ref. [169].

trode, e.g., by close packing of the electrodes in the cell.

Thirdly, strong solvent co-intercalation, in particular into *internal* van der Waals gaps, can only be expected for kinetically stable ternary compounds $Li_x(solv)_yC_n$. For example, comparison of DMC and DEC with dimethoxyethane (DME), shows that the kinetic stability of $Li_x(DME)_yC_n$ can be considered much higher than that of $Li_x(DMC)_yC_n$ and $Li_x(DEC)_yC_n$ {and of course $Li_x(EC)_yC_n$} [169]. With EC/DME, solvent co-intercalation proceeds on a macroscopic scale, i.e., the external van der Waals gaps and some internal ones can participate in the solvent co-intercalation reaction. When DMC or DEC is used as co-solvent, solvent co-intercalation can be expected to take place at the more external gaps only. Instrumentation such as STM with which it is possible to investigate the edge of a basal plane surface can still detect a local expansion [163, 164], whereas instrumentation providing information on a macroscopic scale, such as dilatometry [155] or XRD, cannot.

Numerous research activities have focused on the improvement of the protective films and the suppression of solvent co-intercalation. Beside ethylene carbonate, significant improvements have been achieved with other film-forming electrolyte components such as CO_2 [156, 169-177], N_2O [170, 177], SO_2 [155, 169, 177-179], S_x^{2-} [170, 177, 180, 181], ethyl propyl carbonate [182], ethyl methyl carbonate [183, 184], and other asymmetric alkyl methyl carbonates [185], vinylpropylene carbonate [186], ethylene sulfite [187], *S,S*-dialkyl dithiocarbonates [188], vinylene carbonate [189], and chloroethylene carbonate [190-194] (which evolves CO_2 during reduction [195]). In many cases the suppression of solvent co-intercalation is due to the fact that the electrolyte components form effective SEI films already at potential which are positive relative to the potentials of solvent co-intercalation. An excess of DMC or DEC in the electrolyte inhibits PC co-intercalation into graphite, too [183].

Furthermore, the molecular size of the Li^+-solvating solvents may affect the tendency for solvent co-intercalation. Crown ethers [19, 152-154, 196, 197] and other bulky electrolyte additives [196] are assumed to coordinate Li^+ ions in solution in such a way that solvent co-intercalation is suppressed. The electrochemical formation of binary lithiated graphites Li_xC_6 was also reported for the reduction

CosMX Exhibit 1008, Page 415 of 633

of graphite in electrolytes containing high-molecular-mass polymers as solvent. The claimed lithium intercalation, however, proceeds in a potential region where usually solvated lithiated graphites appear [42, 44, 198, 199] (for comparison, see Ref. [200]).

Graphitic anodes which have been "pre-filmed" in an electrolyte "A" containing effective film-forming components before they are used in a different electrolyte "B" with less effective film-forming properties show lower irreversible charge losses and/or a decreased tendency to solvent co-intercalation [155, 201, 202]. However, sufficient insolubility of the pre-formed films in the electrolyte "B" is required to ascertain long-term operation of the anode.

5.2.4 Lithiated Non-graphitic Carbons

The use of non-graphitic (disordered) carbons as anode materials in lithium ion cell is highly attractive for two reasons:

1. The crosslinking between the graphene layers (or packages of graphene layers) by sp^3-hybridized carbon atoms (Fig. 4) mechanically suppresses the formation of solvated lithiated graphites, $Li_x(solv)_yC_n$, [19, 26, 66, 155]. As a result the gap between the layers cannot expand very much, and thus there is not enough space for the solvent to co-intercalate. Moreover, these carbons have the advantage that they can operate in EC-free electrolytes. Consequently, the first practically applicable lithiated carbon anodes [203, 204] were based on these non-graphitic carbons and not on graphitic materials. Furthermore, the use of composite carbonaceous materials comprising a "core" of graphite and a protective "shell" of non-graphitic carbon is an alternative to inhibit the solvent co-intercalation reaction in graphite [205–208].
2. In comparison with graphite, non-graphitic carbons can provide additional sites for lithium accommodation. As a result, they show a higher capability of reversible lithium storage than graphites, i.e., stoichiometries of $x>1$ in Li_xC_6 are possible.

The latter, so-called "high specific charge" or "high capacity", carbons have received considerable attention in recent research and development. Usually they are synthesized at rather low temperatures, ranging from ~500 to ~1000 °C, and can exhibit reversible specific charges from ~400 to ~ $2000\,Ah\,kg^{-1}$ (x = ~1.2 to ~5 in Li_xC_6), depending on the heat treatment, the organic precursor, and the electrolyte [209, 210]. Such materials have been known since the late 1980s, when non-graphitic carbons with specific charges of up to ~ $500\,Ah\,kg^{-1}$ were synthesized [203]. When lithium is stored in the carbon bulk, one can suppose that a higher specific charge (in $Ah\,kg^{-1}$) requires a correspondingly higher volume (i.e., lower density) of the carbonaceous matrix to accommodate the lithium. As a consequence, the charge densities (in $Ah\,L^{-1}$) of the high-specific-charge carbons should be comparable with those of graphite. Several models have been suggested to explain the high specific charge of these lithiated carbons. This may be because the variety of precursor materials and of manufacturing processes leads to carbonaceous host materials with various structures and compositions.

Yazami et al. [42,211–215] proposed the formation of nondendritic metallic

CosMX Exhibit 1008, Page 416 of 633

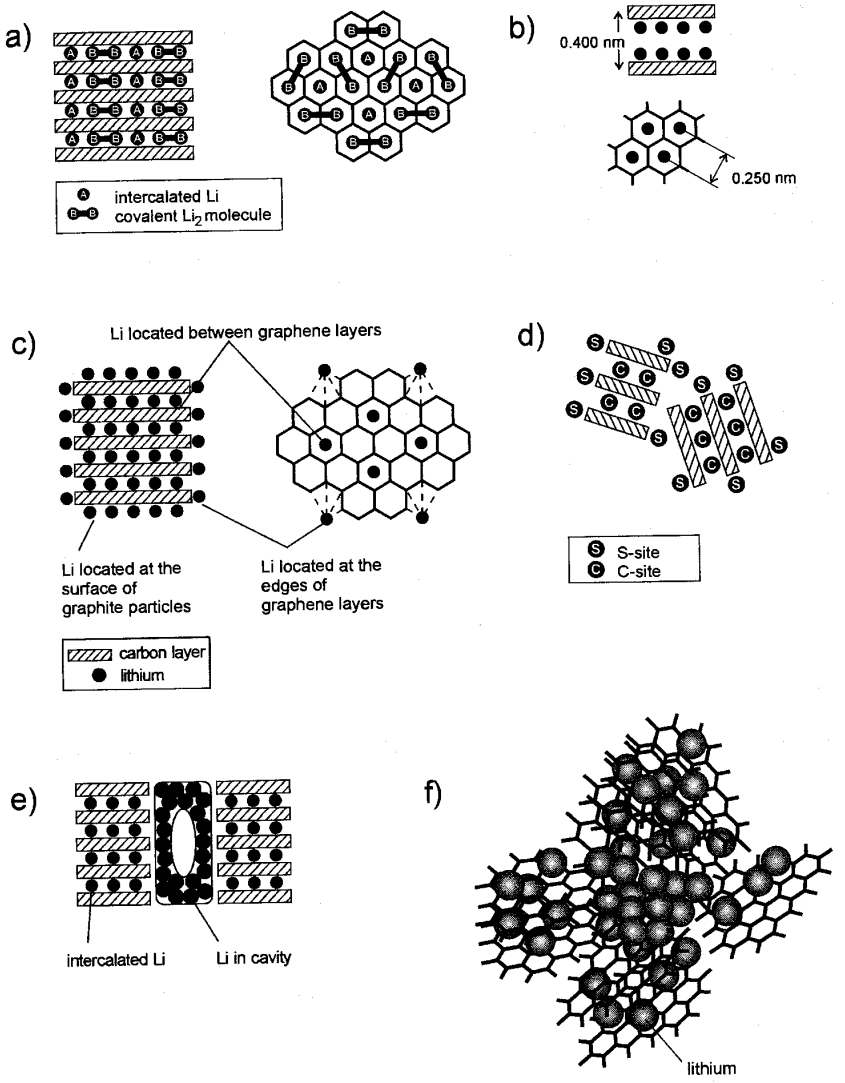


Figure 11. Schematic drawing of some mechanisms for reversible lithium storage in "high-specific-charge" lithiated carbons as proposed in Refs. (a) [216], (b) [218], (c) [224], (d) [230], (e) [41], and (f) [238]. The latter figure has been reproduced with kind permission of Kureha Chemical Industry Co., Ltd.

11a). lithium multilayers on external graphene sheets and surfaces. Peled et al. [130, 131] suggested that the extra charge gained by mild oxidation of graphite is attributed to the accommodation of lithium at the prismatic surfaces (Fig. 3) between two adjacent crystallites, and in the vicinity of defects. Sato et al. [216, 217] sug-

CosMX Exhibit 1008, Page 417 of 633

gested that lithium molecules occupy nearest-neighbor sites in intercalated carbons Yata's and Yamabe's groups discussed the possibility of the formation of LiC_2 in carbons with high a interlayer spacing of ~0.400nm (graphite: 0.335nm) for their "polyacenic semiconductor" (Fig. 11b) [218–223]. In Refs. [224–229] it is assumed that carbons with a small particle size can store a considerable amount of lithium on graphite edges and surfaces in addition to the lithium located between the graphene layers (Fig. 11c). The existence of different "Li storage sites" (Fig. 11d) was discussed in Refs. [230–232], too. Others [41, 233–236] proposed that additional lithium can be accommodated in nanocavities which are present in the carbon at temperatures below ~800 °C [237] (Fig. 11e). Kureha Chemical Industry Co. proposes a cluster-like storage of lithium in pores where the electrolyte solvent cannot enter (Fig. 11f). This carbon, so-called "Carbotron P " [238] or "pseudo isotropic carbon (PIC)" [239], was used in the second generation of Sony's lithium-ion cell [240].

The probabilities of the models have been discusses rather controversially [51, 52, 241–243]. There are various attempts by several researchers (in particular, Dahn's group [51, 52, 244–249]) to interpret the behavior of the high-specific-charge carbons systematically. Many graphitizing (soft) and nongraphitizing (hard) carbons which were prepared below approximately 800–900 °C and which show very high specific charges, exhibit a hysteresis [51, 52, 219, 246, 247]: the lithium intercalation occurs close to 0 V vs. Li/Li^+ whereas the lithium de-intercalation occurs at much more positive potentials (Fig. 12, bottom). The potential hysteresis seems to be proportional to the hydrogen content in the carbon. The ratio of hydrogen to carbon (*i*) in the material is high when a substantial amount of hydrogen is present during manufacture, either because hydrogen is already incorporated in the precursor material and/or because manufacture takes place under an H_2 atmosphere, and (ii) when the manufacturing temperature has been so low that hydrogen has not been removed yet. It has been suggested that lithium is bound near H-terminated edge carbon atoms, which induces a partial bond change at the carbon from sp^2 - to sp^3 -hybridization [247]. This bond change requires energy for both the intercalation and removal of lithium, leading to the observed potential hysteresis (Fig. 12, top) [250].

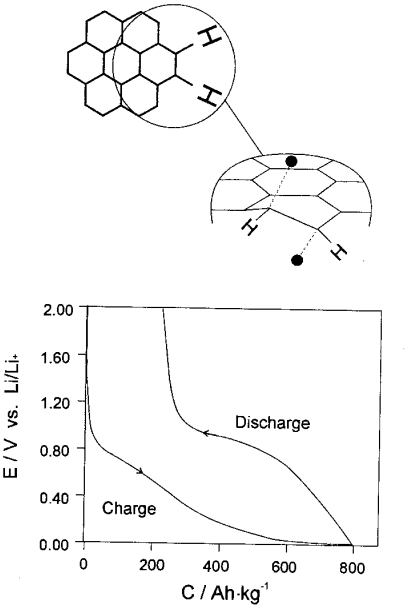


Figure 12. Top: Schematic model showing the mechanism of lithium storage in hydrogen containing carbons as proposed in Ref. [247]. Below: Schematic charge/discharge curve of a hydrogen containing carbon.

Serious drawbacks of the carbons which are prepared at temperatures below ~800–

CosMX Exhibit 1008, Page 418 of 633

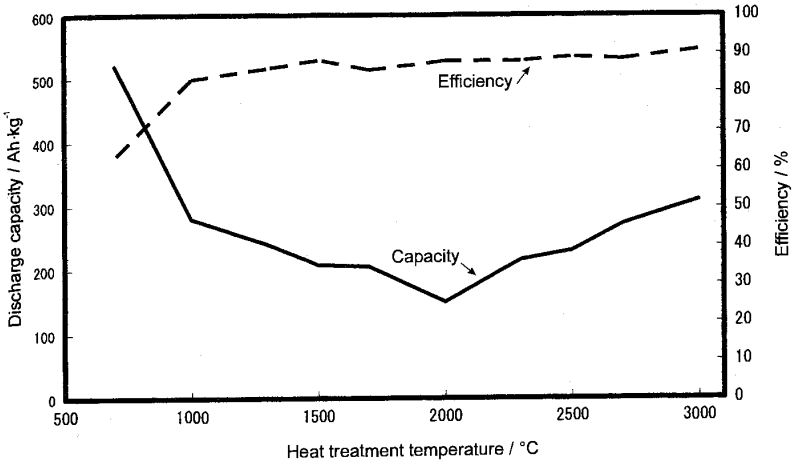


Figure 13. First cycle discharge capacities (——) and charge/discharge efficiencies (- - -) of a soft (graphitizing) carbon { Melblon® carbon fibers (MPCF)} at different heat-treatment temperatures. Reproduced with kind permission of Petoca, Ltd. [253].

900 °C, and which exhibit hysteresis, are their very low charge/discharge efficiencies (Fig. 13) and their low cycle lives [253]. With increasing temperature the hydrogen is removed. The specific charges achieved after the removal of hydrogen depend on the structure of the carbonaceous material, whether it is a soft (graphitizing) or a hard (nongraphitizing) carbon [48, 52, 233, 234, 247, 254–259].

Around or above ~1000 °C the graphitizing (soft) carbons develop a structure with "wrinkled" and "buckled" structure segments (see Fig. 4). This structure offers fewer sites for lithium intercalation than graphite [7, 19, 24, 43]. In addition, crosslinking of carbon sheets in disordered carbons hampers the shift to AA stacking, which is necessary for the accommodation of a greater amount of lithium into graphitic sites [260–262]. Correspondingly, rather low specific charges are observed (x in Li_xC_6 is typically between ~0.5 and ~0.7) in soft carbons such as turbostratic carbons [19, 43, 48, 118, 260–262] and more disordered carbons like] and more disordered carbons like cokes [19, 43, 48, 263–273] and certain carbon blacks [267, 274–276]. On the other hand the charge/discharge efficiency increases with the temperature during heat treatment (Fig. 13). A type of soft carbon has been used in the first generation of Sony's lithium-ion cell [240].

Figure 14 shows the first Li^+ intercalation / de-intercalation cycle of a coke electrode. The potential profile differs from that of graphite, in the sense that the reversible intercalation of Li^+ begins at a potential above 1 V vs. Li/Li^+, and the curve slopes without distinguishable plateaus. This behavior is a consequence of the disordered structure providing electronically and geometrically nonequivalent sites, whereas for a particular intercalation stage in highly crystalline graphite the sites are basically equivalent [19, 26]. With increasing temperature soft carbons develop more graphitic structure segments. The sites for lithium storage which were formerly determined by the disordered struc-

CosMX Exhibit 1008, Page 419 of 633

ture (see above) change to graphitic sites, where lithium resides in the van der Waals gaps between ordered graphene layers. Finally, at ~3000 °C, the structure and the specific charge (Fig. 13) of graphite are achieved. The probability of finding disor

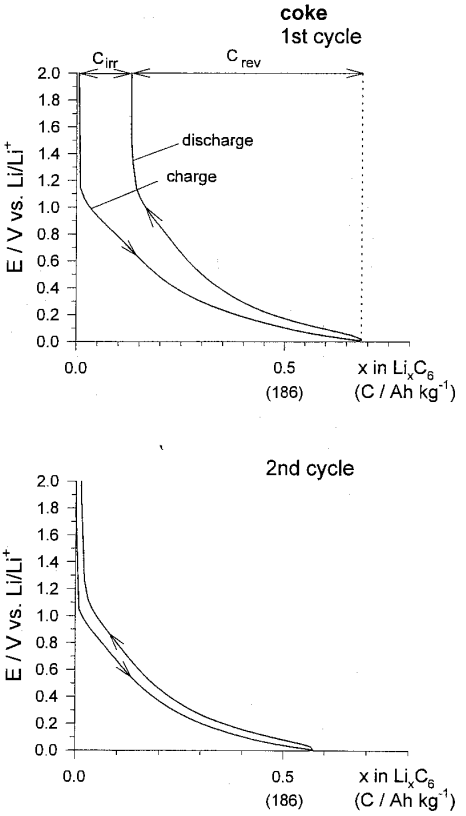


Figure 14. First- and second- cycle constant-current charge/discharge curves of coke (Conoco) in $LiN(SO_2CF_3)_2$ / ethylene carbonate / dimethyl carbonate as the electrolyte (C_{irr} =irreversible specific charge; C_{rev} = reversible specific charge) [2].

dered and ordered (graphitic) structure segments for soft carbons obtained at temperatures between ~1000 °C and ~3000 °C has been intensively discussed in a model developed by Dahn's group [19, 43], who correlated the measured XRD data with the experimental lithium storage capacity of a specific carbon material.

In contrast to soft carbons, many non-graphitizing (hard) carbons obtained at temperatures of ~1000 °C show a high specific charge with little hysteresis (several hundreds of $Ah\,kg^{-1}$)which can be reached only at a very low potential of a few millvolts vs. Li/Li$^+$ (Fig. 15 and 16, bottom). Compared with graphitic carbons and cokes, which show volume expansions and contractions in the range of ~10 percent during lithium intercalation and de-intercalation, the hard carbons are claimed not to be subject to dimensional changes during lithium uptake and removal because of the high separation ~0.380 nm between neighboring carbon layers [240]. In order to explain the high capability of lithium storage in non-graphitizing carbons, Dahn et al. [51, 244, 248, 249, 277, 278] suggested that lithium is "adsorbed" on both sides of single graphene layer sheets which are arranged like a "house of cards" [248] or like "falling cards" [249] (Fig. 16, top). The "falling cards" model is the advanced form of the "house of cards" model and also takes into account the storage of lithium in micropores. The accumulation of lithium in the micropores is in line with other mechanisms proposing the storage of lithium clusters or agglomerates in specific carbon "spaces" [238–240]. Both the pore size and the pore openings should be small to avoid the reaction of stored lithium with the electrolyte [52, 244, 277, 279]. The proportion of nanopores in the carbons can be expected to increase with the cross–linking density of the precursor material [229, 237, 280]. Recent studies on a hard carbon prepared at 1000 °C reveal that the sizes of the single layers as well as the sizes of the pores are in the range of 1 nm [281]. In addition to microporosity, microtexture should be considered, too [280].

CosMX Exhibit 1008, Page 420 of 633

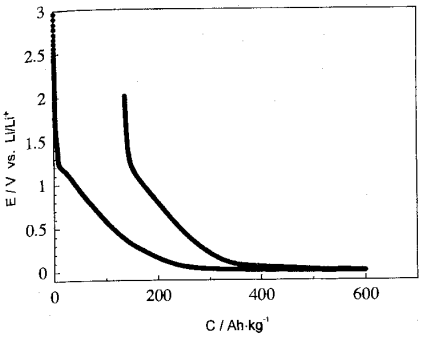


Figure 15. First- cycle constant-current charge/discharge curve of hard carbon ("Carbotron P"). The figure has been reproduced with kind permission of Kureha Chemical Industry Co., Ltd. [238].

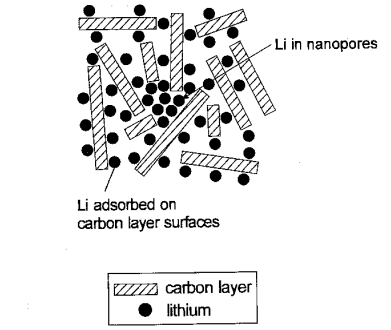


Figure 16. Top: schematic model showing the mechanism of lithium storage in hard (nongraphitizing) carbons as proposed in Refs.[248, 249]. Below: Schematic charge/discharge curve of hard carbon.

In conclusion, a large fraction of single-layer sheets and nanopores is beneficial for the lithium storage capabilities of hard carbons. On the other hand, heat treatment, above 1000 °C, leads to drastically increased irreversible specific charges of hard carbons [256, 282]. This may be related to the burn-off of material which causes the opening of the nanopores. Electrolyte can penetrate in and the sites in the pore are no longer available for lithium storage. In this respect, it should be noted that the sensibleness of nanoporous hard carbons towards strong heat might be a difficulty for surface treatment processes typically involving higher temperatures.

Finally, it should be emphasized that the models proposed above for lithium storage in nongraphitic carbons are based on a limited number of experiments made with a limited number of carbonaceous materials. This means that carbons may be synthesized which do not belong to any of the above categories, i.e., hydrogen-containing carbon, soft or hard carbon, etc. For example, it was reported that milling [283] or strong burn-off [256, 182] of hard carbons in air alters the cgarge/discharge curve completely, as these carbons show hysteresis, too. The change in electrochemical behaviour may due to the introduction of hydrogen - and/or oxygen - containing surface groups Others report a lithium storage mechanism for hard carbons prepared at 1000 °C, which considers lithium intercalated between turbostratically disordered graphene layers and lithium accommodation in amorphous hydrogen-containing carbon regions [284]. In recent work much effort has been invested in the evaluation of carbons prepared from inexpensive and abundant precursors [245, 248, 249, 285, 286].

Although the high specific charge carbons exhibit a multiple of the specific charge that is severafold that of graphite, there are still some problems to solve:

CosMX Exhibit 1008, Page 421 of 633

1. In many cases extremely high irreversible specific charges were observed [45, 51, 52, 218, 220, 230, 233, 244, 287, 288], occasionally also at higher cycle numbers [52, 230, 287–289]. The irreversible capacities can be correlated with the formation of the SEI [52, 233, 244, 287, 290]. However, an "irreversible lithium incorporation" into the carbon is discussed, too. [230, 290, 291]. In analogy to graphites (Sec. 5.2.2.3) this irreversible reaction can be related to the reaction with surface groups on the carbon. In comparison with highly graphitic carbons with a relatively low number of surface groups, the large fraction of (internal and external) heteroatoms in the non-graphitic carbons, such as hydrogen and oxygen, can bind irreversibly a considerable amount of lithium during reduction of the carbon and thus increase the irreversible specific charge losses. Anyway, any charge losses have to be compensated by an excess of cathode material, as lithium-ion cells are assembled in the discharged state. Therefore, the specific charges calculated for the masses of *both* anode *and* cathode material put in the cell can be about the same for graphitic (with low irreversible charge losses) and high-specific-charge carbons (with high irreversible charge losses).
2. Carbons exhibiting hysteresis show poor cycling performance, and can be discharged only in a broad potential region of about 1–2 V (Fig. 13) [41, 51, 52, 218–220, 234–236, 244, 277, 278, 287]. As a result, the energy efficiency of a lithium-ion cell is reduced.
3. The end-of-charge potential of non-graphitic carbons, either hydrogen-containing carbons (Fig. 12) or cokes (Fig. 14), but in particular of hard carbons treated at 1000 °C (Fig. 15 and 16, bottom) must be chosen very close to 0 V vs. Li/Li^+ in order to obtain the full specific charge available. The narrow "safety zone" separating this from the potential where metallic lithium is deposited on the carbon surface might give rise to some safety problems for these carbons, in particular if fast charging is required. In some cases [52, 244, 277, 278] the electrode was indeed charged to potentials below 0 V vs. Li/Li^+ to achieve the high specific charge.

In contrast, there is a difference of approximately 0.1 V between the potential of graphitic LiC_6 and the potential of lithium deposition (Fig. 7). This might be why–apart from Sony and Hitachi Maxell–many battery companies, for example, Sanyo [292–294], Nikkiso [295, 296], Matsushita/Panasonic [297], Moli Energy Ltd. [298], Varta [299] and A&T [300, 301], use graphitic anodes in their prototype or already-commercialized lithium-ion cells. Even Sony is said to use graphitic carbon in their newest generation of lithium ion cells. Moreover, there is a search for carbons which combine both high specific charge and graphite-like charge/discharge potential characteristics [302].

5.2.5 Lithiated Carbons Containing Heteroatoms

Depending on the precursor and the heat-treatment temperature, the carbonaceous materials discussed so far contain heteroatoms in addition to the prevailing carbon atoms. Even highly crystalline graphite is saturated with heteroatoms at dislocations in the crystallites and at the edges

CosMX Exhibit 1008, Page 422 of 633

of the graphene layers (prismatic surfaces), which are supposed to affect the formation of residue compounds and the (electro)chemistry at the electrode/electrolyte interface. Substantial amounts of heteroatoms, such as hydrogen, are furthermore believed to change the bulk electrochemical properties of the host material, such as reversible specific charge (see previous section). From this point of view the influence of other "noncarbonaceous" elements is of great interest. The pyrolysis of precursor materials containing (i) carbon atoms together with (various) heteroatoms and/or (ii) combining a "carbon precursor" with "heteroatom precursors" can result in a variety of new anode materials with interesting properties. Several aspects are reviewed briefly in this section.

Boron is assumed to act as an electron acceptor in a carbon host and thus to cause a shift of the intercalation potential to more positive values and an increase in the reversible capacity because there are more electronic sites [19, 43, 303–306]. This can enable a more rapid charging process. Nitrogen presumably functions as an electron donor and should therefore have the opposite effect on the reversible capacity and the intercalation potential [19, 307]. Contrarily, others [308] report that nitrogen-containing carbons can provide high specific charges of $\sim 500\,\mathrm{Ah\,kg^{-1}}$. Whereas the higher lithium storage capability of the above B- and N-containing anode materials is explained by different electronic properties of the host [19, 304], the high specific charge of phosphorus-doped carbons [309–314] is discussed on the basis of steric effects [309, 310]. Anyway, in analogy to "pure" carbonaceous hosts, the influence of structure should be considered as well. Other substituted carbons, such as layered B / C / N materials [315–321] and C_xS [308], have been intensively evaluated, too.

Recently, several results obtained with high-specific-charge lithium storage materials derived from (composite) silicon containing precursors have been published [322–328]. In addition to silicon and carbon these materials can contain a substantial proportion of hydrogen and oxygen, which can lead to a large variety of compositions [323, 324]. Very high specific charges of up to $770\,\mathrm{Ah\,kg^{-1}}$ can be reached, which seem to depend on the Si content in the matrix [324, 325]. However, these materials usually exhibit strong potential hysteresis and large irreversible specific charges ($>150\,\mathrm{Ah\,kg^{-1}}$). The interactions of the various heteroatoms with each other and with the carbon neighbors seem to be quite complex and have not been entirely clarified. Also, the nature of the lithium insertion mechanism is not certain yet. In particular, it seems not to be clear if the higher lithium storage capacity is due to the presence of Si or simply due to structural effects and/or the presence of other heteroatoms. However, in earlier papers it was speculated that composite carbon/silicon insertion materials exhibit high reversible capacities because of the high lithium alloying capacity of silicon in addition to the lithium incorporation proceeding independently in disordered carbon regions [329, 330]. Furthermore, in analogy to carbonaceous materials, manufacturing parameters such as the pyrolysis temperature, have to be considered [327]. For further details, in particular regarding the synthesis and preparation of the materials discussed in this section, see the literature [2, 6, 19, 43, 331, 332].

5.2.6 Lithiated Fullerenes

Fullerenes C_{60} and C_{70} have been evaluated for use as anode materials by several

CosMX Exhibit 1008, Page 423 of 633

groups [333–338]. A maximum reversible capacity corresponding to the approximate stoichiometry Li_2C_{60} (x=0.2 in Li_xC_6) is available [333, 336], but is not sufficient for application in high energydensity batteries. Moreover, fullerenes show some solubility in nonaqueous organic electrolytes [339].

5.3 Lithiated Carbons vs. Competing Anode Materials

Despite the fact that currently commercialized lithium-ion cells basically contain anode materials based on lithiated carbons, there are still strong interests in replacing the carbon by other anode materials which show better electrochemical performance in terms of irreversible and reversible specific charges. Hence, recently proposed anode materials with specific charges higher than those of graphites and hard carbons have attracted significant interest. In particular, a lithium-ion cell with the trademark Stalion announced by Fujifilm Celltec Co. [340] has found considerable publicity, because it can provide a higher energy density and specific energy than "conventional" lithium ion cells (Fig. 17). The improved performance is due to the replacement of the carbon anode by an "amorphous tin-based composite oxide (abbreviated TCO or ATCO)" The TCO combines both (i) a promising cycle life [340, 341] and (ii) a high specific charge ($>600\,Ah\,kg^{-1}$, Fig. 18) and charge density ($>2200\,Ah\,L^{-1}$) [342, 343].

The TCO is synthesized from SnO, B_2O_3, $Sn_2P_2O_7$, Al_2O_3, and other precursors. The nature of the insertion mechanism of lithium into the Fuji material has been considered by several groups [29, 344–347]. To date it is quite clear that the lithium is not simply inserted into the TCO as in the case of the dioxides of the transition metals Mo [32, 348], W [21, 32, 349–353], and Ti [354–356]. Fujifilm Celltec claims that only the Sn(II) compounds in the composite oxide form the electrochemically active centers for Li insertion, whereas the oxides of B, P, or Al are electrochemically inactive. In order to explain the high specific charge, a mechanism is

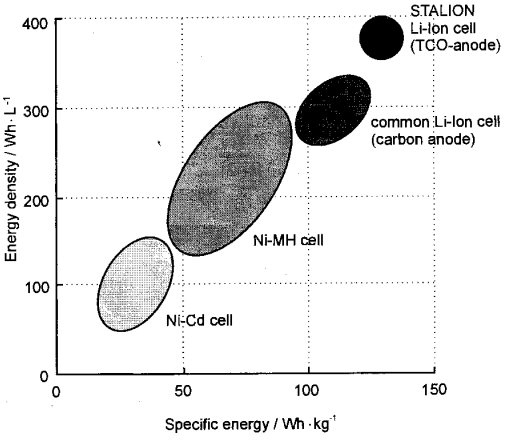


Figure 17. Specific energies and energy densities of rechargeable cells. Prepared from data kindly provided by Fujifilm Celltech Co., Ltd. [342].

CosMX Exhibit 1008, Page 424 of 633

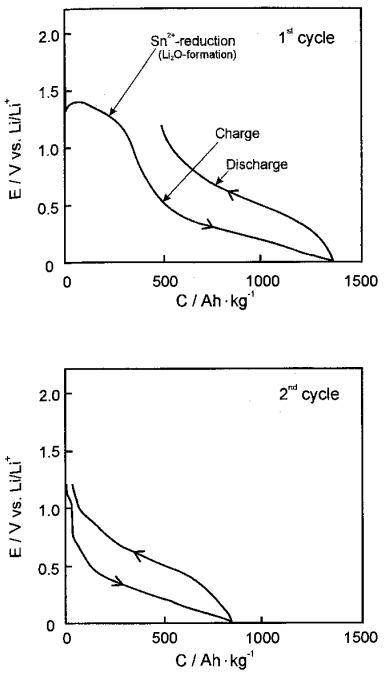


Figure 18. First- and second- cycle constant current charge/discharge curves of a tin composite oxide (TCO) electrode. Prepared by using data kindly provided by Fujifilm Celltech Co., Ltd. [342].

suggested in which the tin oxide reacts to Li_2O and metallic Sn [29, 344–347]. This reaction is associated with large charge losses due to the irreversible formation of Li_2O during the first charge (Fig. 18). In a second step the Sn then alloys with lithium reversibly. Though Fuji Cellec Co. has stopped its R&D activities on the TCO recently, the idea that the high specific charge of the TCO is due to the alloying of metallic tin has led to a revival of research and development of Li alloys and related materials [138, 345–347, 357–359].

The good cycling stability of the tin in TCO is quite unusual, because the electrochemical cycling of Li_xSn and also of other Li alloy electrodes is commonly associated with large volume changes in the order of 100–300 percent (Fig. 19) [2, 7, 22, 24, 26, 360–362]. Moreover, lithium alloys Li_xM have a highly ionic character ("Zintl-Phases", $Li_x^{x+}M^{x-}$). For this reason they are usually fairly brittle. Mechanical stresses related to the volume changes induce a rapid decay in mechanical properties and, finally, a "pulverization" of the electrode (see Chapter III, Sec. 4). In the TCO, however, the Sn is finely distributed within the matrix of the oxides of B, P, and Al. The matrix compounds have glass-forming properties, form a network, and thus stabilize the composite microstructure during charge/discharge cycling [343]. The strategy for the improvement of cycle life by using a composite comprising an (amorphous) lithium insertion material and a network-former follows the ideas reported in Refs. [352, 363–368].

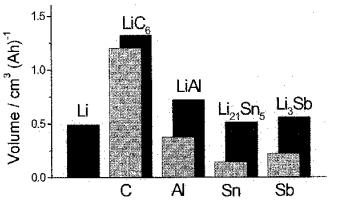


Figure 19. The volumes of several anode materials for lithium ion cells before (gray) and after (black) lithiation.

A strategy to counteract the mechanical degradation of Lialloys without incurring the irreversible lithium losses due to the formation of considerable amounts of Li_2O during the first reduction of the TCO has been suggested alternatively [29, 369]. Using thin layers of materials of small particle size or small grainsize ("submicro" or "nano"materials), relatively large dimensional changes in the crystallites (~100 percent) do not cause particle cracking, as the absolute changes in particle dimensions are small. For instance, small particle size,

CosMX Exhibit 1008, Page 425 of 633

submicro-structured multiphase matrices, such as Sn/SnSb alloys, show a significant improvement in the cycling performance compared with coarse particles of (single phase) metallic tin (Fig. 20). The multiphase composition is favorable for the cycling behavior of the electrode as it allows the more reactive domains of the matrix (SnSb) to expand in the neighborhood of as-yet unreacted and ductile material (Sn) in the first charging (alloying) step [29, 369–371].

Carbons containing dispersed silver [205, 372–374] also show good cycling behavior. Independently of the alloying of lithium with the metal, lithium intercalation into the carbon takes place. Apart from carbons and metal phases, novel oxides such as Li_xMVO_4 (M = Co, Cd, Ni, Zn; $1<x\leq 8$) [375] or $MnV_2O_{6+\delta}$ ($0<\delta\leq 1$) [376] have been proposed as anode materials. Furthermore, lithium/transition metal nitrides $Li_xM_yN_z$ with M = Co, Fe, Mn [377–381] with high specific charge of up to $760\,Ah\,kg^{-1}$ are reviewed intensively in Ref. [112]. Other anode materials for rechargeable lithium batteries with special applications are surveyed in Chapter 1, Sec. 2.5 and Chapter 3, Sec. 1.4.5.

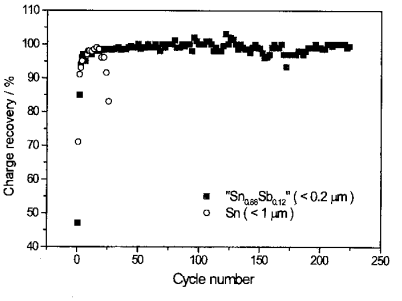


Figure 20. Cycling behavior of Sn+SnSb powder (analytical composition "$Sn_{0.88}Sb_{0.12}$"; particle size <0.2µm) and Sn powder (particle size <1µm) in $1\,mol\,L^{-1}$ $LiClO_4$/propylene carbonate as electrolyte. Constant time charge with a charge input of 1.6 Li/M (~$360\,Ah\,kg^{-1}$); potential-controlled discharge with a cut-off of 1.6 V vs. Li/Li^+. $i_c = i_d = 0.3$. $mA\,cm^{-2}$ Prepared with data from Ref. [371].

5.4 Summary

Lithiated carbons are the state-of-the-art anode materials for rechargeable lithium batteries. An immense number of carbon materials has been evaluated and many more will be tested in the future. Since R&D on lithium-ion cells began in 1985 [240] the specific energy increased continuously because carbons with ever-higher specific charge were used. Until now, graphite and hard carbons have been prefered. At present, the graphitic materials seem to be winning *this* race. However, future trends are directed towards materials which show still-higher specific charges and charge densities while having reduced irreversible specific charges. In this respect, attention should be paid to alternative anode materials, for example Li alloys and related materials, because their specific charges and charge densities can exceed by far those of graphite. Moreover, several important features such as electrode manufacturing technologies, composite anode materials, appropriate bulk material and surface pre-treatments, and safety aspects, which have not been comprehensively reviewed here, will have a great influence on the future selection of anode materials for rechargeable lithium batteries.

Acknowledgments. The authors are grateful to Professor Tsutomu Takamura, Petoca Ltd., for several personal communications and for his support in gathering some of the data presented in this section. The companies and academic organizations who provided data and literature presented and cited in this work are gratefully acknowledged. We thank M. Wachtler and G. H. Wrodnigg for careful reading of

CosMX Exhibit 1008, Page 426 of 633

this manuscript and for additional technical support. This work was partially supported by the Austrian Science Fund (FWF) in the "Electroactive Materials" special research program.

5.5 References

[1] J. O. Besenhard, M. Winter, *Pure App. Chem.*, **1998**, *70*, 603.

[2] M. Winter, J. O. Besenhard, M.E. Spahr, P. Novák, *Adv. Mater.*, **1998**, *10*, 725.

[3] E. Peled, in *Lithium Batteries* (Ed.: J.-P. Gabano), Academic Press, London, **1983**, Ch. 3.

[4] E. Peled, in *Rechargeable Lithium and Lithium-Ion Batteries* (Eds.: S. Megahed, B. Barnett, L. Xie), The Electrochemical Society, Pennington, NJ, **1995**, PV 94 28, +p 1.

[5] E. Peled, D. Golodnitzky, G. Ardel, *J. Electrochem. Soc.* **1997**, *144*, L208.

[6] M. Winter, J. O. Besenhard, *in Lithium Ion Batteries* (Eds.: M. Wakihara, O. Yamamoto), Kodansha/Wiley–VCH, Tokyo, Weinheim **1998**, Ch. 6.

[7] J. O. Besenhard, in *Progress in Intercalation Research* (Eds.: W. Müller-Warmuth, R. Schöllhorn), Kluwer, Dordrecht, **1994**, p. 457.

[8] D. Linden (Ed.), *Handbook of Batteries and Solar Cells*, McGraw-Hill, New York **1984**.

[9] D. Linden (Ed.), *Handbook of Batteries*, McGraw-Hill, New York, **1995**.

[10] K. Brandt, *Solid State Ionics* **1994**, *69*, 173.

[11] J. O. Besenhard, G. Eichinger, *J. Electroanal. Chem.* **1976**, *68*, 1.

[12] G. Eichinger, J. O. Besenhard, *J. Electroanal. Chem.* **1976**, *72*, 1.

[13] P. Dan, E. Mengeritsky, Y. Geronov, D. Aurbach, *J. Power Sources* **1995**, *54*, 143.

[14] P. Dan, E. Mengeritsky, D. Aurbach, I. Weissman, E. Zinigrad, *J. Power Sources* **1997**, *68*, 443.

[15] E. Mengeritsky, P. Dan, I. Weissman, A. Zaban, D. Aurbach, *J. Electrochem. Soc.* **1996**, *143*, 2110.

[16] S. C. Levy, P. Bro, *Battery Hazards and Accident Prevention*, Plenum Press, New York, **1994**.

[17] U. von Sacken, E. Nodwell, A. Sundher, J. R. Dahn, *Solid State Ionics* **1994**, *69*, 284.

[18] D. Fouchard, L. Xie, W. Ebner, S. Megahed, in *Rechargeable Lithium and Lithium-Ion Batteries* (Eds.: S. Megahed, B. Barnett, L. Xie), The Electrochemical Society, Pennington, NJ, **1995**, PV 94-28, p. 349.

[19] J. R. Dahn, A. K. Sleigh, H. Shi, B. M. Way, W. J. Weydanz, J. N. Reimers, Q. Zhong, U. von Sacken, in *Lithium Batteries, New Materials, Developments and Perspectives* (Ed.: G. Pistoia), Elsevier, Amsterdam **1994**, p. 1.

[20] M. B. Armand, in *Materials for Advanced Batteries* (Eds.: D. W. Murphy, J. Broadhead, B. C. H. Steele), Plenum Press, New York. **1980**, p. 145.

[21] B. Scrosati, *J. Electrochem. Soc.* **1992**, *139*, 2776.

[22] D. Fauteux, R. Koksbang, *J. Appl. Electrochem.* **1993**, *23*, 1.

[23] S. Megahed, B. Scrosati, *J. Power Sources* **1994**, *51*, 79.

[24] J. O. Besenhard, in *Soft Chemistry Routes to New Materials* (Eds.: J. Rouxel, M. Tournoux, R. Brec), Materials Science Volumes 152–153, Trans-Tech Publications, Switzerland, **1994**, p. 13.

[25] S. Basu, US Patent 4423125, **1983**.

[26] J. O. Besenhard, M. Winter, *2. Ulmer Elektrochemische Tage, Ladungsspeicherung in der Doppelschicht* (Ed.: W. Schmickler), Universitätsverlag Ulm, **1995**, p. 47.

[27] T. Nagaura, in *Progress in Batteries and Solar Cells*, Vol. 10 (Eds: JEC Press Inc. and IBA Inc.), JEC Press, Brunswick, OH, **1991**, p. 218.

[28] T. Nagaura, K. Tozawa, in *Progress in Batteries and Solar Cells*, Vol. 9 (Eds.: JEC Press Inc. and IBA Inc.), JEC Press, Brunswick, OH, **1990**, p. 209.

[29] J. O. Besenhard, J. Yang, M. Winter, *J. Power Sources* **1997**, *68–69*, 87.

[30] K. Brandt, *J. Power Sources* **1995**, *54*, 151.

[31] K. Brandt, F. J. Kruger, *Batteries Int.* **1993** July, 24.

[32] M. S. Whittingham, *Prog. Solid State Chem.* **1978**, *12*, 41.

[33] R. Nesper, *Prog. Solid State Chem.* **1990**, *20*, 1.

[34] R. C. Weast (Ed.) *Handbook of Chemistry and Physics*, 68th ed., CRC Press, Boca Raton, FL, **1987**.

[35] D. Billaud, E. McRae, A. Hérold, *Mater. Res. Bull.* **1979**, *14*, 857.

[36] V. Manev, I. Naidenov, B. Puresheva, G. Pistoia, *J. Power Sources* **1995**, *57*, 133.

CosMX Exhibit 1008, Page 427 of 633

[37] A. Du Pasquier, F. Disma, T. Bowmer, A.S. Gozdz, G. Amatucci, J.-M. Tarascon, *J. Electrochem. Soc.* **1998**, *145*, 472.
[38] C. Menachem, D. Golodnitzky, E. Peled, in *Batteries for Portable Applications and Electric Vehicles* (Eds.: C. F. Holmes, A. R. Landgrebe), The Electrochemical Society, Pennington, NJ, **1997**, PV97-18, p. 95.
[39] Lithiated carbons are mostly multiphase systems. Hence, the determination of chemical diffusion coefficients for Li^+ causes experimental problems because the propagation of a reaction front has to be considered.
[40] K. Sawai, Y. Iwakoshi, T. Ohzuku, *Solid State Ionics* **1994**, *69*, 273.
[41] A. Mabuchi, *Tanso* **1994**, *165*, 298.
[42] R. Yazami, M. Z. A. Munshi, in *Handbook of Solid State Batteries and Capacitors* (Ed.: M. Z. A. Munshi), World Scientific, Singapore, **1995**, p. 425.
[43] J. R. Dahn, A. K. Sleigh, H. Shi, J. N. Reimers, Q. Zhong, B. M. Way, *Electrochim. Acta*, **1993**, *38*, 1179.
[44] R. Yazami, in *Lithium Batteries, New Materials, Developments and Perspectives* (Ed.: G. Pistoia), Elsèvier, Amsterdam, **1994**, p. 49.
[45] O. Yamamoto, Y. Takeda, N. Imanishi, R. Kanno, in *New Sealed Rechargeable Batteries and Supercapacitors* (Eds.: B. M. Barnett, E. Dowgiallo, G. Halpert, Y. Matsuda, Z. Takehara), The Electrochemical Society, Pennington, NJ, **1993**, PV 93-23, p. 302.
[46] R. Yazami, D. Guérard, *J. Power Sources* 1993, *43–44*, 39.
[47] N. Takami, A. Satoh, M. Hara, T. Ohsaki, *J. Electrochem. Soc.* **1995**, *142*, 371.
[48] A. Satoh, N. Takami, T. Ohsaki, *Solid State Ionics* **1995**, *80*, 291.
[49] M. Endo, J. Nakamura, A. Emori, Y. Sasabe, K. Takeuchi, M. Inagaki, *Mol. Cryst. Liq. Cryst.* **1994**, *245*, 171.
[50] R. Yazami, K. Zhaghib, M. Deschamps, *Mol. Cryst. Liq. Cryst.* **1994**, *245*, 165.
[51] T. Zheng, J. S. Xue, J. R. Dahn, *Chem. Mater.* **1996**, *8*, 389.
[52] T. Zheng, Y. Liu, E. W. Fuller, S. Tseng, U. von Sacken, J. R. Dahn, *J. Electrochem. Soc.* **1995**, *142*, 2581.
[53] O. Yamamoto, N. Imanishi, Y. Takeda, H. Kashiwagi, *J. Power Sources* **1995**, *54*, 72.
[54] G. Li, R. Xue, L. Chen, Y. Huang, *J. Power Sources* **1995**, *54*, 271.
[55] J. Yamaura, Y. Ohzaki, A. Morita, A. Ohta, *J. Power Sources* **1993**, *43–44*, 233.
[56] G. Li, Z. Lu, B. Huang, H. Huang, R. Xue, L. Chen, *Solid State Ionics* **1995**, *81*, 15.
[57] N. Takami, A. Sato, T. Ohsaki, in *Lithium Batteries* (Eds.: S. Surampudi, V. R. Koch), The Electrochemical Society, Pennington, NJ, **1993**, PV *93–24*, p. 44.
[58] T. D. Tran, J. H. Feikert, X. Song, K. Kinoshita, *J. Electrochem. Soc.* **1995**, *142*, 3297.
[59] H. Shi, J. Barker, M. Y. Saiidi, R. Koksbang, L. Morris, *J. Power Sources* **1997**, *68*, 291.
[60] S. Miura, H. Nakamura, M. Yoshio, in *Progress in Batteries and Battery Materials*, Vol. 12 (Eds: ITE–JEC Press Inc. and IBA Inc.), JEC Press, Brunswick, OH, **1993**, p. 115.
[61] H. Shi, J. Barker, M. Y. Saidi, R. Koksbang, *J. Electrochem. Soc.* **1996**, *143*, 3466.
[62] R. E. Winans, K. A. Carrado, *J. Power Sources* **1995**, *54*, 11.
[63] G. Sandi, R. E. Winans, K. A. Carrado, *J. Electrochem. Soc.* **1996**, *143*, L95.
[64] J. O. Besenhard, H. P. Fritz, *J. Electroanal. Chem.* **1974**, *53*, 329.
[65] J. O. Besenhard, *Carbon* **1976**, *14*, 111.
[66] R. Fong, U. von Sacken, J. R. Dahn, *J. Electrochem. Soc.* **1990**, *137*, 2009.
[67] H. O. Pierson, *Handbook of Carbon, Graphite, Diamond and Fullerenes*, Noyes Publications, Mill Road, Park Ridge, NJ, **1993**, p. 43.
[68] B. E. Warren, *Phys. Rev.* **1941**, *59*, 693.
[69] R. E. Franklin, *Acta Crystallogr.* **1951**, *4*, 253.
[70] R. E. Franklin, *Proc. R. Soc. London Ser. A*, **1951**, *209*, 196.
[71] K. Kinoshita, *Carbon, Electrochemical and Physicochemical Properties*, Wiley, New York, **1987**.
[72] O. Vohler, F. von Sturm, E. Wege, H. von Kienle, M. Voll, P. Kleinschmitt, in *Ullmann's Encyclopedia of Industrial Chemistry* (Executive Ed.: W. Gerhartz), 5th ed., VCH, Weinheim, **1986**, Volume 5A, p. 95.
[73] G. M. Jenkins, K. Kawamura, *Polymeric Carbons, Carbon Fibre, Glass and Char*, Cambridge University Press, Cambridge, UK, **1976**.
[74] R. Dübgen, G. Popp, *Z. Werkstofftech.* **1984**, *15*, 331.
[75] H. Marsh, *Introduction to Carbon Science*, Butterworth, London , **1989.**
[76] M. Inagaki, *Solid State Ionics* **1996**, *86–88*, 833.
[77] W. Ruland, *Adv. Mater.* **1990**, *2*, 528.
[78] Y. Nakagawa, Osaka Gas Chemicals Co., Ltd.,

CosMX Exhibit 1008, Page 428 of 633

personal communication.
[79] B. T. Kelly, *Physics of Graphite*, Applied Science, Englewood, NJ, **1981**.
[80] A. Hérold, *Bull. Soc. Chim. Fr.* **1955**, *187*, 999.
[81] A. Hérold, in *Chemical Physics of Intercalation,* NATO ASI Series (Eds.: A. P. Legrand, S. Flandrois), Plenum Press, New York, **1987**, Vol. B172, p. 3.
[82] C. Hartwigsen, W. Witschel, E. Spohr, *Ber. Bunsenges. Phys. Chem.* **1997**, *101*, 859.
[83] X. Y. Song, K. Kinoshita, T. D. Tran, *J. Electrochem. Soc.* **1996**, *143*, L120.
[84] R. Moret, in *Intercalation in Layered Materials,* NATO ASI Series (Ed.: M. S. Dresselhaus), Plenum Press, New York, **1986**, Vol. B148, p. 185.
[85] J. Rossat-Mignod, D. Fruchart, M. J. Moran, J. W. Milliken, J. E. Fisher, *Synth. Met.* **1980**, *2*, 143.
[86] V. V. Avdev, V. A. Nalimova, K. N. Semenenko, *High Press. Res.* **1990**, *6*, 11.
[87] D. Guerard, V. A. Nalimova, in *Solid State Ionics IV* (Eds.: G.-A. Nazri, J.-M. Tarascon, M. Schreiber), Mater Res. Soc. Symp. Proc. Vol. 369, **1995,** p. 155.
[88] V. A. Nalimova, G. Guerard, M. Lelaurain, O. V. Fateev, *Carbon* **1995**, *33*, 177.
[89] V. A. Nalimova, C. Bindra, J. E. Fisher, *Solid State Commun.* **1996**, *97*, 583.
[90] R. Yazami, A. Cherigui, V. A. Nalimova, D. Guerard, in *Lithium Batteries* (Eds.: S. Surampudi, V. R. Koch), The Electrochemical Society, Pennington, NJ, **1993**, PV 93–24, p. 379.
[91] Y. Mizutani, T. Abe, K. Ikeda, E. Ihara, M. Asano, T. Harada, M. Inaba, Z. Ogumi, *Carbon* **1997**, *35*, 61.
[92] J. O. Besenhard, H. P. Fritz, *Angew. Chem. Int. Ed. Engl.* **1983**, *95*, 950.
[93] W. Rüdorff, U. Hofmann, *Z. Anorg. Allg. Chem.* **1938**, *238*, 1.
[94] N. Daumas, A. Hérold, *C. R. Acad. Sci. Paris* Ser.C **1969**, *268*, 373.
[95] N. Daumas, A. Hérold, *Bull. Soc. Chim.* **1971**, *5*, 1598.
[96] L. B. Ebert, *Annu. Rev. Mater. Sci.* Fr. **1976**, *6*, 181.
[97] W. Rüdorff, in *Advances in Inorganic Chemistry and Radiochemistry* (Eds.: H. J. Emèleus, A. G. Sharpe), Academic Press, New York **1959**, Vol. 1, p. 223.
[98] R. Schlögl, in *Progress in Intercalation Research* (Eds.: W. Müller-Warmuth, R. Schöllhorn), Kluwer, Dordrecht, **1994**, p. 83.
[99] J. E. Fisher, in *Chemical Physics of Intercalation,* NATO ASI Series (Eds.: A. P. Legrand, S. Flandrois), Plenum Press, New York, **1987**, Vol. B172, p. 59.
[100] J. R. Dahn, *Phys. Rev. B* **1991**, *44*, 9170.
[101] M. Bagouin, D. Guerard, A. Hérold, *C. R. Acad. Sci. Paris*, Ser. C, **1966**, *262*, 557.
[102] D. Guerard, A. Hérold, *Carbon* **1975**, *13*, 337.
[103] P. Pfluger, V. Geiser, S. Stolz, H.-J. Güntherodt, *Synth. Met.* **1981**, *3*, 27.
[104] D. Billaud, F. X. Henry, P. Willmann, *Mater. Res. Bull.* **1993**, *28*, 477.
[105] D. Billaud, F. Henry, P. Willmann, *Mol. Cryst. Liq. Cryst.* **1994**, *245*, 159.
[106] A. H. Whitehead, K. Edström, N. Rao, J. R. Owen, *J. Power Sources* **1996**, *63*, 41.
[107] M. Inaba, H. Yoshida, Z. Ogumi, T. Abe, Y. Mizutani, M. Asano, *J. Electrochem. Soc.* **1995**, *142*, 20.
[108] W. Huang, R. Frech, *J. Electrochem. Soc.* **1998**, *145*, 765.
[109] S. Mori, H. Asahina, H. Suzuki, A. Yonei, E. Yasukawa, *J. Power Sources* **1997**, *68*, 59.
[110] T. Ohzuku, Y. Iwakoshi, K. Sawai, *J. Electrochem. Soc.* **1993**, *140*, 2490.
[111] During the first charge the SEI layers on the surface of the graphite electrode are not fully developed. Moreover, there is a strong tendency to co-intercalate solvent molecules at low lithium concentrations in graphite. Thus, particularly in the first charge the Li-GICs, which correspond to high stage numbers, might be insufficiently protected from a reaction with the electrolyte and the intercalated lithium is irreversibly consumed for the formation of films between the graphene layers (see Sec. 5.2.3).
[112] N. Imanishi, Y. Takeda, O. Yamamoto, in *Lithium Ion Batteries* (Eds.: M. Wakihara, O. Yamamoto), Kodansha/Wiley-VCH, Tokyo, Weinheim, **1998**, Ch. 5.
[113] V. V. Avdeev, A. P. Savchenko, L. A. Monyakina, I. V. Nikol'skaya, A. V. Khvostov, *J. Phys. Chem. Solid* **1996**, *57*, 947.
[114] S. Flandrois, A. Fevrier, P. Biensan, B. Simon, US Patent *5, 554, 462,* **1996**.
[115] Y. V. Isaev, N. D. Lemenko, L. V. Gumileva, A. G. Buyanovskaya, Y. N. Novikov, E. Stumpp, *Carbon* **1997**, *35*, 563.
[116] R. Tossici, M. Berrettoni, R. Marassi, B. Scosati, *J. Electrochem. Soc.* **1996**, *143*, L65.
[117] R. Tossici, M. Berrettoni, M. Rosolen, R.

CosMX Exhibit 1008, Page 429 of 633

Marassi, B. Scosati, *J. Electrochem. Soc.* **1997**, *144*, 186.
[118] K. Yokoyama, N. Nagawa, in *New Sealed Rechargeable Batteries and Supercapacitors* (Eds.: B. M. Barnett, E. Dowgiallo, G. Halpert, Y. Matsuda, Z. Takehara), The Electrochemical Society, Pennington, NJ, **1993**, PV 93-23, p. 270.
[119] R. Kanno, Y. Kawamoto, Y. Takeda, S. Ohashi, N. Imanishi, O. Yamamoto, *J. Electrochem. Soc.* **1992**, *139*, 3397.
[120] M. Winter, P. Novák, A. Monnier, *J. Electrochem. Soc.*, **1998**, *145*, 428.
[121] V. Manev, I. Naidenov, B. Puresheva, G. Pistoia, *J. Power Sources* **1995**, *57*, 211.
[122] R. Imhof, P. Novák, in *Batteries for Portable Applications and Electric Vehicles* (Eds.: C. F. Holmes, A. R. Landgrebe), The Electrochemical Society, Pennington, NJ, **1997**, PV97-18, p. 313.
[123] R. Imhof, P. Novák, *J. Electrochem. Soc.* **1998**, *145*, 1081.
[124] P. Novák, W. Scheifele, M. Winter, O. Haas, *J. Power Sources* **1997**, *68*, 267.
[125] J. M. Rosolen, F. Decker, *J. Electrochem. Soc.* **1996**, *143*, 2417.
[126] K. A. Hirasawa, K. Nishioka, T. Sato, S. Yamaguchi, S. Mori, *J. Power Sources* **1997**, *69*, 97.
[127] R. Bittihn, R. Herr, D. Hoge, *J. Power Sources* **1993**, *43–44*, 409.
[128] G. R. Hennig, *Prog. Inorg. Chem.* **1959**, *1*, 125.
[129] J. G. Hooley, *Chem. Phys. Carbon* **1969**, *5*, 321.
[130] E. Peled, C. Menachem, D. Bar-Tow, A. Melman, *J. Electrochem . Soc.* **1996**, *143*, L4.
[131] C. Menachem, E. Peled, L. Burstein, Y. Rosenberg, *J. Power Sources* **1997**, *68*, 277.
[132] D. Bar-Tow, E. Peled, L. Burstein, in *Batteries for Portable Applications and Electric Vehicles* (Eds.: C. F. Holmes, A. R. Landgrebe), The Electrochemical Society, Pennington, NJ, **1997**, PV97-18, p. 324.
[133] T. Takamura, H. Awano, T. Ura, Y. Ikezawa, *Anal. Sci. Technol.* **1995**, *8*, 583.
[134] M. Kikuchi, Y. Ikezawa, T. Takamura, *J. Electroanal. Chem.* **1995**, *396*, 451.
[135] T. Takamura, M. Kikuchi, J. Ebana, M. Nagashima, Y. Ikezawa, in *New Sealed Rechargeable Batteries and Supercapacitors* (Eds.: B. M. Barnett, E. Dowgiallo, G. Halpert, Y. Matsuda, Z. Takehara), The Electrochemical Society, Pennington, NJ, **1993**, PV 93 23, p. 229.
[136] T. Takamura, M. Kikuchi, Y. Ikezawa, in *Rechargeable Lithium and Lithium-Ion Batteries* (Eds.: S. Megahed, B. Barnett, L. Xie), The Electrochemical Society, Pennington, NJ, **1995**, PV 94-28, p. 213.
[137] T. Takamura, H. Awano, T. Ura, K. Sumiya, *J. Power Sources* **1997**, *68*, 114.
[138] K. Sumiya, K. Sekine, T. Takamura, in *Batteries for Portable Applications and Electric Vehicles* (Eds.: C. F. Holmes, A. R. Landgrebe), The Electrochemical Society, Pennington, NJ, **1997**, PV97-18, p. 523.
[139] M. Winter, J. O. Besenhard, P. Novák, *GDCh Monographie* **1996**, *3*, 438.
[140] A. N. Dey, B. P. Sullivan, *J. Electrochem. Soc.* **1970**, *117*, 222.
[141] J. O. Besenhard, H. Möhwald, J. J. Nickl, *Carbon* **1980**, *18*, 399.
[142] M. Rose, C. Nacchache, J. Golé, *C.R. Acad. Sci. Paris*, Ser. C, 1968, *266*, 421.
[143] Co-Minh-Duc, M. Rose, J.-P. Pascault, *C.R. Acad. Sci. Paris*, Ser. C, **1970**, *270*, 569.
[144] F. Beguin, R. Setton, A. Hamwi, P. Touzain, *Mater. Sci. Eng.* **1979**, *40*, 167.
[145] J. O. Besenhard, H. Witty, H.-F. Klein, *Carbon* **1984**, *22*, 98.
[146] J. O. Besenhard, H.-F. Klein, H. Möhwald, J. J. Nickl, *Synth. Met.* **1981**, *4*, 51.
[147] J. O. Besenhard, I. Kain, H.-F. Klein, H. Möhwald, H. Witty, in *Intercalated Graphite* (Eds.: M. S. Dresselhaus, G. Dresselhaus, J. E. Fischer, M. J. Moran), North-Holland, New York, **1983**, p. 221.
[148] B. Marcus, P. Touzain, *J. Solid State Chem.* **1988**, *77*, 223.
[149] P. Schoderböck, H. P. Boehm, *Synth. Met.* **1991**, *44*, 239.
[150] M. Arakawa, J. Yamaki, *J. Electroanal. Chem.* **1987**, *219*, 273.
[151] G. Eichinger, *J. Electroanal. Chem.* **1976**, *74*, 183.
[152] Z. X. Shu, R. S. McMillan, J. J. Murray, *J. Electrochem. Soc.* **1993**, *140*, 922.
[153] Z. X. Shu, R. S. McMillan, J. J. Murray, *J. Electrochem. Soc.* **1993**, *140*, L101.
[154] Z. X. Shu, R. S. McMillan, J. J. Murray, in *New Sealed Rechargeable Batteries and Supercapacitors* (Eds.: B. M. Barnett, E. Dowgiallo, G. Halpert, Y. Matsuda, Z. Takehara), The Electrochemical Society, Pennington, NJ, **1993**, PV 93-23, p. 238.
[155] J. O. Besenhard, M. Winter, J. Yang, W. Bib-

CosMX Exhibit 1008, Page 430 of 633

eracher, *J. Power Sources* **1995**, *54*, 228.
[156] D. Aurbach, Y. Ein-Eli, O. Chusid, Y. Carmeli, M. Babai, H. Yamin, *J. Electrochem. Soc.* **1994**, *141*, 603.
[157] D. Guyomard, J. M. Tarascon, *J. Power Sources* **1995**, *54*, 92.
[158] D. Guyomard, J. M. Tarascon, *Solid State Ionics* **1994**, *69*, 222.
[159] D. Guyomard, J. M. Tarascon, US Patent 5, 192, 629 **1993**.
[160] D. Aurbach, B. Markovsky, A. Shechter, Y. Ein-Eli, H. Cohen, *J. Electrochem. Soc.* **1996**, *143*, 3809
[161] D. Aurbach, A. Zaban, A. Schechter, Y. Ein-Eli, E. Zinigrad, B. Markovsky, *J. Electrochem. Soc.* **1995**, *142*, 2873.
[162] A. Ohta, H. Koshina, H. Okuno, H. Murai, *J. Power Sources* **1995**, *54*, 6.
[163] M. Inaba, Z. Siroma, A. Funabiki, Z. Ogumi, *Langmuir* **1996**, *12*, 1535.
[164] M. Inaba, Z. Siroma, Y. Kawadate, A. Funabiki, Z. Ogumi, *J. Power Sources* **1997**, *68*, 221.
[165] K. A. Hirasawa, T. Sato, H. Asahina, S. Yamaguchi, S. Mori, *J. Electrochem. Soc.* **1997**, *144*, L81.
[166] D. Aurbach, Y. Ein-Eli, *J. Electrochem. Soc.* **1995**, *142*, 1746.
[167] N. Imanishi, H. Kashiwagi, T. Ichikawa, Y. Takeda, O. Yamamoto, M. Inagaki, *J. Electrochem. Soc.* **1993**, *140*, 315.
[168] N. Imanishi, H. Kashiwagi, Y. Takeda, O. Yamamoto, M. Inagaki, in *High Power, Ambient Temperature Lithium Batteries* (Eds.: S. Megahed, B. Barnett, L. Xie), The Electrochemical Society, Pennington, NJ, **1992**, PV 92-15, p. 80.
[169] M. Winter, Doctoral Thesis, University of Münster, Germany, **1995**.
[170] J. O. Besenhard, M. W. Wagner, M. Winter, A. D. Jannakoudakis, P. D. Jannakoudakis, E. Theodoridou, *J. Power Sources* **1993**, *43–44*, 413.
[171] Y. Ein-Eli, B.Markovsky, D. Aurbach, Y. Carmeli, H. Yamin, S. Luski, *Electrochim. Acta* **1994**, *39*, 2559.
[172] D. Aurbach, Y. Ein-Eli, B. Markovsky, A. Zaban, S. Lusky, Y. Carmeli, H. Yamin, *J. Electrochem. Soc.* **1995**, *142*, 2882.
[173] J. O. Besenhard, P. Castella, M. W. Wagner, *Mater. Sci. Forum* **1992**, *91–93*, 647.
[174] B. Simon, J. P. Boeuve, M. Broussely, *J. Power Sources* **1993**, *43–44*, 65.
[175] O. Chusid, Y. Ein-Eli, D. Aurbach, *J. Power Sources* **1993**, *43–44*, 47.
[176] J. O. Besenhard, M. Winter, J. Yang, *International Workshop on Advanced Batteries (Lithium Batteries)*, Osaka, **1995**, p. 129.
[177] M. Winter, Diploma Thesis, University of Münster, Germany, **1993**.
[178] Y. Ein-Eli, S. R. Thomas, V.R. Koch, *J. Electrochem. Soc.* **1997**, *144*, 1159.
[179] Y. Ein-Eli, S. R. Thomas, V.R. Koch, *J. Electrochem. Soc.* **1997**, *144*, L195.
[180] M. W. Wagner, C. Liebenow, J. O. Besenhard, *J. Power Sources* **1997**, *68*, 328.
[181] M. W. Wagner, J. O. Besenhard, C. Liebenow, in *Batteries for Portable Applications and Electric Vehicles* (Eds.: C. F. Holmes, A. R. Landgrebe), The Electrochemical Society, Pennington, NJ, **1997**, PV97-18, p. 26.
[182] Y. Ein-Eli, S. McDevitt, D. Aurbach, B. Markovsky, A. Schechter, *J. Electrochem. Soc.* **1997**, *144*, L180.
[183] H. Nakamura, H. Komatsu, M. Yoshio, *J. Power Sources*, **1996**, *62*, 219.
[184] Y. Ein-Eli, S. R. Thomas, V. Koch, D. Aurbach, B. Markovsky, A. Schechter, *J. Electrochem. Soc.* **1996**, *143*, L273.
[185] Y. Ein-Eli, S. F. McDevitt, R. Laura, *J. Electrochem. Soc.* **1998**, *145*, L1.
[186] C. Jehoulet, P. Biensan, J. M. Bodet, M. Broussely, C. Moteau, C. Tessier- Lescourret, in *Batteries for Portable Applications and Electric Vehicles* (Eds.: C. F. Holmes, A. R. Landgrebe), The Electrochemical Society, Pennington, NJ, **1997**, PV97-18, p. 974.
[187] G. H. Wrodnigg, J. O. Besenhard, M. Winter, Subm. HCD to *Electrochemical and Solid-State Letters*
[188] Y. Ein-Eli, S. F. McDevitt, *J. Solid State Electrochem.* **1997**, *1*, 227.
[189] Y. Naruse, S. Fujita, A. Omaru, US Patent 5, *714*, 281, **1998**.
[190] Z. X. Shu, R. S. McMillan, J. J. Murray, *J. Electrochem. Soc.* **1995**, *142*, L161.
[191] Z. X. Shu, R. S. McMillan, J. J. Murray, in *Rechargeable Lithium and Lithium-Ion Batteries* (Eds.: S. Megahed, B. M. Barnett, L. Xie), The Electrochemical Society, Pennington, NJ, **1995**, PV 94-28, p. 431.
[192] Z. X. Shu, R. S. McMillan, J. J. Murray, I. J. Davidson, *J. Electrochem. Soc.* **1996**, *143*, 2230.
[193] Z. X. Shu, R. S. McMillan, and J. J. Murray, US Patent 5, 529, 859, **1996**.

CosMX Exhibit 1008, Page 431 of 633

[194] Z. X. Shu, R. S. McMillan, and J. J. Murray, *US* Patent 5, 571, 635, **1996**.
[195] M. Winter, P. Novàk, *J. Electrochem. Soc.* **1998**, *145*, L27.
[196] D. P. Wilkinson, J. R. Dahn, US Patent 5, 130, 211, **1992**.
[197] Y. B. Roh, K. Tada, T. Kawai, H. Araki, K. Yoshino, M. Takase, T. Suzuki, *Synth. Met.* **1995**, *69*, 601.
[198] R. Yazami, P. Touzain, *J. Power Sources* **1995**, *9*, 365.
[199] R. Yazami, D. Guerard, *J. Power Sources* **1993**, *43–44*, 65.
[200] S. Lemont, D. Billaud, *J. Power Sources* **1995**, *54*, 340.
[201] D. Billaud, A. Naji, P. Willmann, *J. Chem. Soc., Chem. Commun*. **1995**, 1867.
[202] A. Naji, J. Ghanbaja, P. Willmann, D. Billaud, *Carbon* **1997**, *35*, 845.
[203] R. Kanno, Y. Takeda, T. Ichikawa, K. Nakanishi, O. Yamamoto, *J. Power Sources* **1989**, *26*, 535.
[204] M. Mohri, N. Yanagisawa, Y. Tajima, H. Tanaka, T. Mitate, S. Nakajima, M. Yoshida, Y. Yoshimoto, T. Suzuki, H. Wada, *J. Power Sources* **1989**, *26*, 545.
[205] H. Momose, A. Funahashi, J. Aragane, K. Matsui, S. Yoshitake, I. Mitsuishi, H. Awata, T. Iwahori, in *Batteries for Portable Applications and Electric Vehicles* (Eds.: C. F. Holmes, A. R. Landgrebe), The Electrochemical Society, Pennington, NJ, **1997**, PV97-18, p. 376.
[206] X. Shu, L. D. Schmidt, W. H. Smyrl, in *Rechargeable Lithium and Lithium-Ion Batteries* (Eds.: S. Megahed, B. Barnett, L. Xie), The Electrochemical Society, Pennington, NJ, **1995**, PV 94-28, p. 196.
[207] I. Kuribayashi, M. Yokoyama, M. Yamashita, *J. Power Sources* **1995**, *54*, 1.
[208] H. Kurokawa, T. Maeda, N. Nakanishi, T. Nohma, K. Nishio, *8th Int. Meeting on Lithium Batteries,* Nagoya, **1996**, Ext. Abstr.p. 222.
[209] Carbons chemically pre-lithiated before the production of the electrode can exhibit specific charges grater than 400 $Ahkg^{-1}$, too [210].
[210] R. Yazami, M. Moreau, US Patent No. 5543021, **1996**.
[211] R. Yazami, M. Deschamps, in *Advances in Porous Materials* (Eds.: S. Komarneni, D. M. Smith, J. S. Beck), Mater. Res. Soc. Symp. Proc., No. 369, Materials Research Society, **1995**, p. 165.
[212] R. Yazami, M. Deschamps, *J. Power Sources* **1995**, *54*, 411.
[213] R. Yazami, M. Deschamps, in *Rechargeable Lithium and Lithium-Ion Batteries* (Eds.: S. Megahed, B. Barnett, L. Xie), The Electrochemical Society, Pennington, NJ, **1995**, PV 94-28, p. 183.
[214] M. Deschamps, R. Yazami, *J. Power Sources* **1997**, *68*, 236.
[215] R. Yazami, M. Deschamps, in *Progress in Batteries and Battery Materials,* Vol. 15 (Eds: ITE-JEC Press Inc./IBA Inc.), JEC Press, Brunswick, OH, **1996**, p. 161.
[216] K. Sato, M. Noguchi, A. Demachi, N. Oki, M. Endo, *Science* **1994**, *264*, 556.
[217] K. Sato, M. Noguchi, A. Demachi, N. Oki, M. Endo, Y. Sasabe, *Int. Workshop on Advanced Batteries (Lithium Batteries),* Osaka, **1995**, p. 219.
[218] S. Yata, H. Kinoshita, M. Komori, N. Ando, T. Kashiwamura, T. Harada, K. Tanaka, T. Yamabe, *Synth. Met.* **1994**, *62*, 153.
[219] S. Yata, K. Sakurai, T. Osaki, Y. Inoue, K. Yamaguchi, *Synth. Met.* **1990**, *33*, 177.
[220] S. Yata, Y. Hato, H. Kinoshita, N. Ando, A. Anekawa, T. Hashimoto, M. Yamaguchi, K. Tanaka, T. Yamabe, *Synth. Met.* **1995**, *73*, 273.
[221] S. Yata, *Int. Workshop on Advanced Batteries (Lithium Batteries),* Osaka, **1995**, p. 204.
[222] S. Yata, H. Kinoshita, M. Komori, N. Ando, T. Kashiwamura, T. Harada, K. Tanaka, and T. Yamabe, in *New Sealed Rechargeable Batteries and Supercapacitors* (Eds: B. M. Barnett, E. Dowgiallo, G. Halpert, Y. Matsuda), The Electrochemical Society, Pennington, NJ, **1993**, PV 93-23, p. 502.
[223] S. Yata, *Denki Kakagu* **1997**, *9*, 65.
[224] S. Wang, Y. Matsumura, T. Maeda, *Synth. Met.* **1995**, *71*, 1759.
[225] Y. Matsumura, S. Wang, J. Mondori, *Carbon* **1995**, *33*, 1457.
[226] Y. Matsumura, S. Wang, T. Kasuh, T. Maeda, *Synth. Met.* **1995**, *71*, 1755.
[227] Y. Matsumura, S. Wang, K. Shinohara, T. Maeda, *Synth. Met.* **1995**, *71*, 1757.
[228] W. S. Li, L. C. Jiang, G. Y. Xie, X. Jiang, *J. Power Sources* **1996**, *58*, 235.
[229] H. Xiang, S. Fang, Y. Jiang, *J. Electrochem. Soc.* **1997**, *144*, L187.
[230] Y. Mori, T. Iriyama, T. Hashimoto, S. Yamazaki, F. Kawakami, H. Shiroki, T. Yamabe, *J. Power Sources* **1995**, *56*, 205.

CosMX Exhibit 1008, Page 432 of 633

[231] Y. Mori, T. Iriyama, T. Hashimoto, S. Yamazaki, F. Kawakami, H. Shiroki, *Int. Workshop on Advanced Batteries (Lithium Batteries)*, Osaka, **1995**, p. 199.
[232] N. Takami, A. Satoh, T. Ohsaka, M. Kanda, *Electrochim. Acta* **1997**, *42*, 2537.
[233] H. Fujimoto, A. Mabuchi, K. Tokumitsu, T. Kasuh, *J. Power Sources* **1995**, *54*, 440.
[234] A. Mabuchi, H. Fujimoto, K. Tokumitsu, T. Kasuh, *J. Electrochem. Soc.* **1995**, *142*, 1041.
[235] K. Tokumitsu, A. Mabuchi, H. Fujimoto, T. Kasuh, *J. Power Sources* **1995**, *54*, 444.
[236] K. Tokumitsu, A. Mabuchi, T. Kasuh, H. Fujimoto, 8th *Int. Meeting on Lithium Batteries*, Nagoya, **1996**, Ext. Abstr. No. 212.
[237] K. Tokumitsu, A. Mabuchi, H. Fujimoto, T. Kasuh, *J. Electrochem. Soc* **1996**, *143*, 2235.
[238] S. Morimoto, Kureha Chemical Industry Co., Ltd., personal communication.
[239] A. Nagai, M. Ishikawa, J. Masuko, N. Sonobe, H. Chuman, T. Iwasaki, *Mater. Res. Soc. Symp. Proc.*, *Vol.* 393, **1995**, 339.
[240] Y. Nishi, in *Lithium Ion Batteries* (Eds.: M. Wakihara, O. Yamamoto), Kodansha/Wiley–VCH, Tokyo, Weinheim, **1998**, Ch. 8.
[241] L. B. Ebert, *Carbon* **1996**, *34*, 671.
[242] J. R. Dahn, T. Zheng, Y. Liu, J. S. Xue, *Science* **1995**, *270*, 590.
[243] P. Zhou, P. Papanek, C. Bindra, R. Lee, J. E. Fischer, *J. Power Sources* **1997**, *68*, 297.
[244] J. S. Xue, J. R. Dahn, *J. Electrochem. Soc.* **1995**, *142*, 3668.
[245] J. R. Dahn, J. S. Xue, W. Xing, A. M. Wilson, A. Gibaud, *8th Int. Meeting on Lithium Batteries*, Ext. Abstr. Nagoya **1996**, p. 89.
[246] T. Zheng, J. R. Dahn, *J. Power Sources* **1997**, *68*, 201.
[247] T. Zheng, W. R. McKinnon, J. R. Dahn, *J. Electrochem. Soc.* **1996**, *143*, 2137.
[248] W. Xing, J. S. Xue, T. Zheng, A. Gibaud, J. R. Dahn, *J. Electrochem. Soc.* **1996**, *143*, 3482.
[249] J. R. Dahn, W. Xing, Y. Gao, *Carbon* **1997**, *35*, 825.
[250] Other explanations for the increase in specific charge obtained by using hydrogen-containing carbons and for the observation of potential hysteresis were suggested in Refs. [251, 252].
[251] S. Wang, Y. Zhang, L. Yang, Q. Liu, *Solid State Ionics* 1996, *86–88*, 919.
[252] N. Takami, A. Satoh, T. Ohsaki, M. Kanda, *J. Electrochem. Soc.* **1998**, *145*, 478.
[253] T. Takamura, T. Tamaki, Petoca Ltd., personal communication.
[254] A. Satoh, N. Takami, T. Ohsaki, M. Kanda, in *Rechargeable Lithium and Lithium-Ion Batteries* (Eds.: S. Megahed, B. Barnett, L. Xie), The Electrochemical Society, Pennington, NJ, **1995**, PV 94-28, p. 143.
[255] K. Tatsumi, A. Mabuchi, N. Iwashita, H. Sakaebe, H. Shioyama, H. Fujimoto, S. Higuchi, in *Batteries and Fuel Cells for Stationary and Electric Vehicle Applications* (Eds: A. R. Landgrebe, Z. Takehara) Electrochemical Society, Pennington, NJ, **1993**, PV 93-8, p. 64.
[256] A. Mabuchi, H. Fujimoto, K. Tokumitsu, T. Kasuh, *J. Electrochem. Soc.* **1995**, *142*, 3049.
[257] K. Tokumitsu, A. Mabuchi, H. Fujimoto, T. Kasuh, in *Rechargeable Lithium and Lithium-Ion Batteries* (Eds.: S. Megahed, B. Barnett, L. Xie), The Electrochemical Society, Pennington, NJ, **1995**, PV 94-28, p. 136.
[258] K. Tatsumi, T. Akai, T. Imamura, K. Zaghib, N. Iwashita, S. Higuchi, Y. Sawda, *J. Electrochem. Soc.* **1996**, *143*, 1923.
[259] K. Tatsumi, N. Iwashita, H. Sakaebe, H. Shioyama, S. Higuchi, A. Mabuchi, H. Fujimoto, *J. Electrochem. Soc.* **1995**, *142*, 716.
[260] T. Zheng, J. R. Dahn, *Synth. Met.* **1995**, *73*, 1.
[261] T. Zheng, J. R. Dahn, *Phys. Rev. B* **1996**, *53*, 3061.
[262] T. Zheng, J. N. Reimers, J. R. Dahn, *Phys. Rev. B* **1995**, *51*, 734.
[263] W. Qiu, R. Zhou, L. Yang, Q. Liu, *Solid State Ionics* **1996**, *86–88*, 903.
[264] M. Jean, C. Desnoyer, A. Tranchant, R. Messina, *J. Electrochem. Soc.* **1995**, *142*, 2122.
[265] R. V. Moshtev, P. Zlatilova, B. Puresheva, V. Manev, *J. Power Sources* **1995**, *56*, 137.
[266] J. M. Chen, C. Y. Yao, C. H. Cheng, W. M. Hurng, T. H. Kao, *J. Power Sources* **1995**, *54*, 494.
[267] A. K. Sleigh, U. von Sacken, *Solid State Ionics* **1992**, *57*, 99.
[268] S. Ma, J. Li, X. Jing, F. Wang, *Solid State Ionics* **1996**, *86–88*, 911.
[269] R. Alcántara, J. M. Jiminéz-Mateos, P. Lavela, J. Morales, J. L. Tirado, *Mater. Sci. Eng.* **1996**, *B39*, 216.
[270] R. Kostecki, T. Tran, X. Song, K. Kinoshita, F. McLarnon, *J. Electrochem. Soc.* **1997**, *144*, 3111.
[271] M. Jean, A. Tranchant, R. Messina, *J. Electrochem. Soc.* **1996**, *143*, 391.
[272] M. Jean, A. Chausse, R. Messina, *J. Power Sources* **1997**, *68*, 232.

CosMX Exhibit 1008, Page 433 of 633

[273] N. R. Avery, K. J. Black, *J. Power Sources* **1997**, *68*, 191.
[274] K. Takei, N. Terada, K. Kumai, T. Iwahori, T. Uwai, T. Miura, *J. Power Sources* **1995**, *55*, 191.
[275] K. Takei, K. Kumai, Y. Kobayashi, H. Miyashiro, T. Iwahori, T. Uwai, T. Miura, *J. Power Sources* **1995**, *54*, 171.
[276] K. Takei, K. Kumai, T. Iwahori, T. Uwai, M. Furusyo, *Denki Kakagu* **1993**, *4*, 421.
[277] Y. Liu, J. S. Xue, T. Zheng, J. R. Dahn, *Carbon* **1996**, *34*, 193.
[278] T. Zheng, Q. Zhong, J. R. Dahn, *J. Electrochem. Soc.* **1995**, *142*, L211.
[279] H. Ago, K. Tanaka, T. Yamabe, T. Miyoshi, K. Takegoshi, T. Terao, S. Yata, Y. Hato, S. Nagaura, N. Ando, *Carbon* **1997**, *12*, 1781.
[280] N. Sonobe, T. Iwasaki, J. Masuko, US Patent No. 5, 527, 643, **1996**.
[281] P. Zhou, P. Papanek, R. Lee, J. E. Fisher, W. A. Kamitakahara, *J. Electrochem. Soc. 1997*, *144*, 1744.
[282] H. Iomoto, A. Omaru, A. Azuma, Y. Nishi, in *Lithium Batteries* (Eds.: S. Surampudi, V. R. Koch), The Electrochemical Society, Pennington, NJ, **1993**, PV 93-24, p. 9.
[283] W. Xing, R. A. Dunlap, J. R. Dahn, *J. Electrochem. Soc.* **1998**, *145*, 62.
[284] Y. Dai, Y. wang, V. Eshkenazi, E. Peled, S. G. Greenbaum, *J. Electrochem. Soc.* **1998**, *145*, 1179.
[285] W. Xing, J. S. Xue, J. R. Dahn, *J. Electrochem. Soc.* **1996**, *143*, 3046.
[286] T. Zheng, W. Xing, J. R. Dahn, *Carbon* **1996**, *34*, 1501.
[287] H. Imoto, M. Nagamine, Y. Nishi, in *Rechargeable Lithium and Lithium-Ion Batteries* (Eds.: S. Megahed, B. Barnett, L. Xie), The Electrochemical Society, Pennington, NJ, **1995**, PV 93-24, p. 43.
[288] M. Alamgir, Q. Zuo, K. M. Abraham, *J. Electrochem. Soc.* **1994**, *141*, L143.
[289] T. Iijima, K. Suzuki, Y. Matsuda, *Synth. Met.*. **1995**, *73*, 9.
[290] Y. Matsumura, S. Wang, J. Mondori, *J. Electrochem. Soc.* **1995**, *142*, 2914.
[291] Y. Jung, M. C. Suh, H. Lee, M. Kim, S. Lee, S. C. Shim, J. Kwak, *J. Electrochem. Soc.* **1997**, *144*, 4279.
[292] K. Nishio, Sanyo Electric Co., Ltd., personal communication.
[293] K. Nishio, M. Fujimoto, Y. Shoji, R. Ohshita, T. Nohma, K. Moriwaki, S. Narukawa, T. Saito, *8th Int. Meeting on Lithium Batteries*, Nagoya, **1996**, Ext. Abstr. p. 93.
[294] H. Kurokawa, T. Nohma, M. Fujimoto, T. Maeda, K. Nishio, T. Saito, *International Workshop on Advanced Batteries (Lithium Batteries)*, Osaka, **1995**, p. 332.
[295] H. Abe, *Nikkiso Co., Ltd.*, personal communication.
[296] K. Zaghib, K. Tatsumi, H. Abe, T. Ohsaki, Y. Sawada, S. Higuchi, *J. Electrochem. Soc.* **1998**, *145*, p. 210.
[297] *JEC Battery Newsletter*, JEC Press, Brunswick OH, **1994**, Vol. 5, p. 32.
[298] *JEC Battery Newsletter*, JEC Press, Brunswick, OH, **1994**, Vol. 5, p. 33.
[299] U. Koehler, F. J. Kruger, J. Kuempers, M. Maul, E. Niggemann, *Varta Special Report*, December **1997**, p. 7.
[300] N. Takami, A. Satoh, M. Hara, T. Ohsaki, *J. Electrochem. Soc.* **1995**, *142*, 2564.
[301] A. Satoh, Toshiba Corp., personal communication.
[302] T. Kasuh, A. Mabuchi, K. Tokumitsu, H. Fujimoto, *J. Power Sources* **1997**, *68, 99*.
[303] J. R. Dahn, J. N. Reimers, A. K. Sleigh, T. Tiedje, *Phys. Rev.* B **1992**, *45*, 3773.
[304] B. M. Way, J. R. Dahn, *J. Electrochem. Soc.* **1994**, *141*, 907.
[305] T. Tamaki, M. Tamaki, *8th Int. Meeting on Lithium Batteries*, Nagoya, **1996**, Ext. Abstr. p. 216.
[306] B. M. Way, J. R. Dahn, T. Tiedje, K. Myrtle, M. Kasrai, *Phys. Rev.* B **1992**, *46*, 1697.
[307] W. J. Weydanz, B. M. Way, T. van Buuren, J. R. Dahn, *J. Electrochem. Soc.* **1994**, *141*, 900.
[308] S. Ito, T. Murata, M. Hasegawa, Y. Bito, Y. Toyoguchi, *J. Power Sources* **1997**, *68*, 245.
[309] T. D Tran, J. H. Feikert, S. T. Mayer, X. Song, K. Kinoshita, in *Rechargeable Lithium and Lithium-Ion Batteries* (Eds.: S. Megahed, B. Barnett, L. Xie), The Electrochemical Society, Pennington, NJ, **1995**, PV 94-28, p. 110.
[310] H. H. Schönfelder, K. Kitoh, H. Nemoto, *J. Power Sources* **1997**, *68*, 258.
[311] T. D. Tran, S. T. Mayer, R. W. Pekala, in *Advances in Porous Materials* (Eds.: S. Komarneni, D. M. Smith, J. S. Beck), Mater. Res. Soc. Symp. Proc., Vol. 369, **1995**, p. 449.
[312] Q. Zhong, U. v. Sacken, *8th Int. Meeting on Lithium Batteries*, Nagoya **1996**, Ext. Abstr. p. 202.
[313] A. Omaru, H. Azuma, M. Aoki, A. Kita, Y. Nishi, *in Lithium Batteries* (Eds.: S. Suram-

CosMX Exhibit 1008, Page 434 of 633

pudi, V. R. Koch), The Electrochemical Society, Pennington, NJ, **1993**, PV 93-24, p. 21.
[314] R. L. Morrison, US Patent 5, 558, 954, **1996**.
[315] Y. Matsuda, M. Ishikawa, T. Nakamura, M. Morita, S. Tsujioka, T. Kawashima, in *Rechargeable Lithium and Lithium-Ion Batteries* (Eds.: S. Megahed, B. Barnett, L. Xie), The Electrochemical Society, Pennington, NJ, **1995**, PV 94-28, p. 85.
[316] M. Morita, T. Hanada, H. Tsotsumi, Y. Matsuda, M. Kawaguchi, *J. Electrochem. Soc.* **1992**, *139*, 1227.
[317] Y. Matsuda, M. Morita, T. Hanada, M. Kawaguchi, *J. Power Sources* **1993**, *43–44*, 75.
[318] M. Ishikawa, T. Nakamura, M. Morita, Y. Matsuda, S. Tsujioka, T. Kawashima, *J. Power Sources* **1995**, *55*, 127.
[319] M. Ishikawa, T. Nakamura, M. Morita, Y. Matsuda, M. Kawaguchi, *Denki Kakagu*, **1994**, *62*, 897.
[320] M. Morita, T. Hanada, H. Tsutsumi, Y. Matsuda, in *High Power, Ambient Temperature Lithium Batteries* (Eds.: W. D. Clark, G. Halpert), The Electrochemical Society, Pennington, NJ, **1992**, PV 92-15, p. 101.
[321] M. Ishikawa, M. Morita, T. Hanada, Y. Matsuda, M. Kawaguchi, *Denki Kakagu*, **1993**, *61*, 1395.
[322] A. M. Wilson, J. N. Reimers, E. W. Fuller, J. R. Dahn, *Solid State Ionics* **1995**, *74*, 249.
[323] A. M. Wilson, G. Zank, K. Eguchi, W. Xing, J. R. Dahn, *J. Power Sources* **1997**, *68*, 195.
[324] W. Xing, A. M. Wilson, K. Eguchi, G. Zank, J. R. Dahn, *J. Electrochem. Soc.* **1997**, *144*, 2410.
[325] A. M. Wilson, G. Zank, K. Eguchi, W. Xing, B. Yates, J. R. Dahn, *Chem. Mater.* **1997**, *9*, 2139.
[326] J. S. Xue, K. Myrtle, J. R. Dahn, *J. Electrochem. Soc.* **1995**, *142*, 2927.
[327] R. A. Guidotti, B. J. Johnson, *Proceedings of the 37th Power Sources Conference*, Cherry Hill, NJ, **1996**, p. 219.
[328] W. Xing, A. M. Wilson, G. Zank, J. R. Dahn, *Solid State Ionics* **1997**, *93*, 239.
[329] A. M. Wilson, J. R. Dahn, *J. Electrochem Soc.* **1995**, *142*, 326.
[330] A. M. Wilson, J. R. Dahn, in *Rechargeable Lithium and Lithium-Ion Batteries* (Eds.: S. Megahed, B. Barnett, L. Xie), The Electrochemical Society, Pennington NJ, **1995**, PV 94-28, p. 158.
[331] R. Riedel, *Adv. Mater.* **1994**, *6*, 549.
[332] M. Kawaguchi, *Adv. Mater.* **1997**, *9*, 615.
[333] S. Lemont, J. Ghanbaja, D. Billaud, *Mol. Cryst. Liq. Cryst.* **1994**, *244*, 203.
[334] L. Firlej, A. Zahab, F. Brocard, P. Bernier, *Synth. Met.* **1995**, *70*, 1373.
[335] W. Zho, H. Huang, Y. Li, R. Xue, Y. Huang, Z. Zhao, L. Chen, *7th Int. Meeting on Lithium Batteries*, Boston, **1994**, Ext. Abstr. p. 278.
[336] R. Yazami, A. Cherigui, *7th Int. Meeting on Lithium Batteries*, Boston, **1994**, Ext. Abstr. p. 255.
[337] R. Yazami, A. Cherigui, V. A. Nalimova, D. Guerard, in *Lithium Batteries* (Eds.: S. Surampudi, V. R. Koch), The Electrochemical Society, Pennington, NJ, **1993**, PV 93-24, p. 1.
[338] W. A. Kamitakahara, *J. Phys. Chem. Solids* **1996**, *57*, 671.
[339] B. Soucaze-Guillous, W. Kutner, M. T. Jones, K. M. Kadish, *J. Electrochem. Soc.* **1996**, *143*, 550.
[340] *Nippon Denki Shinbun*, March 11, **1996**.
[341] Y. Idota, Y. Mineo, A. Matsufuji, T. Miyasaka, *Denki Kakagu* **1997**, *65*, 717.
[342] Y. Idota, Fujifilm Celltech Co. Ltd., personal communication.
[343] Y. Idota, T. Kubota, A. Matsufuji, Y. Maekawa, T. Miyasaka, *Science* **1997**, *276*, 1395.
[344] M. Székely, B. Eid, E. Caillot, M. Herlem, A. Etcheberry, C. Mathieu, B. Fahys, *J. Electroanal. Chem.* **1995**, *391*, 69.
[345] R. A. Huggins, in *Batteries for Portable Applications and Electric Vehicles* (Eds.: C. F. Holmes, A. R. Landgrebe), The Electrochemical Society, Pennington, NJ, **1997**, PV 97-18, p. 1.
[346] T. Brousse, R. Retoux, U. Herterich, D. M. Schleich, in *Batteries for Portable Applications and Electric Vehicles* (Eds.: C. F. Holmes, A. R. Landgrebe), The Electrochemical Society, Pennington, NJ, **1997**, PV 97-18, p. 34.
[347] I. A. Courtney, J. R. Dahn, *J. Electrochem Soc.* **1997**, *144*, 2045.
[348] J. J. Auborn, Y. L. Barberio, *J. Electrochem. Soc.* **1987**, *134*, 638.
[349] B. Di Pietro, M. Patriarca, B. Scrosati, *J. Power Sources* **1982**, *8*, 289.
[350] B. Di Pietro, M. Patriarca, B. Scrosati, *Synth. Met.* **1982**, *5*, 1.
[351] S. Morzilli, B. Scrosati, F. Sgarlata, *Electrochim. Acta* **1985**, *30*, 1271.
[352] T. Shodai, Y. Sakurai, S. Okada, in *Recharge-*

CosMX Exhibit 1008, Page 435 of 633

able Lithium and Lithium-Ion Batteries (Eds.: S. Megahed, B. Barnett, L. Xie), The Electrochemical Society, Pennington, NJ, **1995**, PV 94-28, p. 224.

[353] K. M. Abraham, D. M. Pasquariello, E. B. Willstaedt, G. F. McAndrews, in *Primary and Secondary Ambient Temperature Lithium Batteries* (Eds.: J.-P. Gabano, Z. Takehara, P. Bro), The Electrochemical Society, Pennington, NJ, **1988**, PV 88-6, p. 669.

[354] S. Y. Huang, L. Kavan, I. Exnar, M. Grätzel, *J. Electrochem. Soc.* **1995**, *142*, L142.

[355] M. Grätzel, *Chem. Tech.* **1995**, *67*, 1300.

[356] L. Kavan, M. Grätzel, J. Rathousky, A. Zukal, *J. Electrochem. Soc.* **1995**, *142*, 394.

[357] K. Sekine, T. Shimoyamada, R. Takagi, K. Sumiya, T. Takamura, in *Batteries for Portable Applications and Electric Vehicles* (Eds.: C. F. Holmes, A. R. Landgrebe), The Electrochemical Society, Pennington, NJ, **1997**, PV97-18, p. 92.

[358] T. Brousse, R. Retoux, U. Herterich, D. M. Schleich, *J. Electrochem. Soc.*, **1998**, *145*, 1.

[359] W. Liu, X. Huang, Z. Wang, H. Li, L. Chen, *J. Electrochem. Soc.*, **1998**, *145*, 59.

[360] J. O. Besenhard, M. Hess, P. Komenda, *Solid State Ionics* **1990**, *40–41*, 525.

[361] H. H. Landoldt, R. Börnstein, *Structure Data of the Elements and Intermetallic Phases*, Vol. 6, Springer Verlag, Berlin, **1971**.

[362] E. Zintl, G. Bauer, *Z. Physik. Chem.* **1933**, (B)*20*, 245.

[363] Y. Sakurai, S. Okada, J. Yamaki, T. Okada, *J. Power Sources* **1987**, *20*, 173.

[364] T. Pagnier, M. Fouletier, J. L. Souquet, *Solid State Ionics* **1983**, *9/10*, 649.

[365] Y. Sakurai, J. Yamaki, *J. Electrochem. Soc.* **1985**, *132*, 512.

[366] M. Arakawa, S. Tobishima, T. Hirai, J. Yamaki, *J. Electrochem. Soc.* **1986**, *133*, 1527.

[367] S. Tobishima, M. Arakawa, T. Hirai, J. Yamaki, *J. Power Sources* **1987**, *20*, 293.

[368] Y. Sakurai, J. Yamaki, *J. Electrochem. Soc.* **1988**, *135*, 791.

[369] J. Yang, M. Winter, J. O. Besenhard, *Solid State Ionics* **1996**, *90*, 281.

[370] J. Yang, J. O. Besenhard, M. Winter, in *Batteries for Portable Applications and Electric Vehicles* (Eds.: C. F. Holmes, A. R. Landgrebe), The Electrochemical Society, Pennington, NJ, **1997**, PV 97-18, p. 350.

[371] M. Winter, J. O. Besenhard, J. H. Albering, J. Yang, M. Wachtler, *Prog. Batteries Batt. Mater.* 1998, in press.

[372] J. Aragane, K. Matsui, H. Andoh, S. Suzuki, H. Fukada, H. Ikeya, K. Kitaba, R. Ishikawa, *J. Power Sources* **1997**, *68*, 13.

[373] K. Nishimura, H. Honbo, S. Takeuchi, T. Horiba, M. Oda, M. Koseki, Y. Muranaka, Y. Kozono, H. Miyadera, *J. Power Sources* **1997**, *68*, 436.

[374] H. Momose, H. Honbo, S. Takeuchi, K. Nishimura, T. Horiba, Y. Muranaka, Y. Kozono, H. Miyadera, *J. Power Sources* **1997**, *68*, 208.

[375] D. Guyomard, C. Sigala, A. Le Gal La Salle, Y. Piffard, *J. Power Sources* **1997**, *68*, 692.

[376] Y. Piffard, F. Leroux, D. Guyomard, J.-L. Mansot, M. Tournoux, *J. Power Sources* **1997**, *68*, 698.

[377] T. Shodai, S. Okada, S. Tobishima, J. Yamaki, *J. Power Sources* **1997**, *68*, 515.

[378] M. Nishijima, T. Kagohashi, M. Imanishi, Y. Takeda, O. Yamamoto, S. Kondo, *Solid State Ionics* **1996**, *83*, 107.

[379] O. Yamamoto, Y. Takeda, N. Imanishi, *Int. Workshop on Advanced Batteries (Lithium Batteries)*, Osaka, **1995**, p. 189.

[380] M. Nishijima, T. Kagohashi, Y. Takeda, N. Imanishi, O. Yamamoto, *J. Power Sources* **1997**, *68*, 510.

[381] M. Nishijima, *Denki Kakagu* **1997**, *65*, 711.

CosMX Exhibit 1008, Page 436 of 633

6 The Anode/Electrolyte Interface

E. Peled, D. Golodnitsky and J. Penciner

6.1 Introduction

The anode/electrolyte interphase plays a key role in lithium—metal, lithium-alloy, lithium-ion, and any other alkali-metal and alkaline—earth batteries. In primary batteries it determines the safety, self—discharge (shelf life), power capability, low-temperature performance, and faradaic efficiency. In secondary batteries it determines, in addition, the faradaic efficiency on charge, the cycle life, the morphology of lithium deposits, and the irreversible capacity loss (Q_{IR}) for the first charge cycle of lithium-ion batteries. As its importance is well recognized in the scientific community, special sessions are devoted to it in battery-related meetings such as the International Meetings on Lithium Batteries (IMLBs) International Symposia on Polymer Electrolytes (ISPEs), and in others including meetings of the Electrochemical Society (ECS), the Battery Symposium in Japan, and the Materials Research Society (MRS).

The alkali-metal/electrolyte interphase was named [1] the "solid-electrolyte interphase" (SEI). A good SEI must have the following properties:

(1) electronic transference numbers $t_e = 0$, i.e., it must be an electronic resistor, in order to avoid SEI thickening leading to a high internal resistance, self-discharge and low faradaic efficiency (ε_f);
(2) cation transference number $t_+ = 1$, to eliminate concentration polarization and to ease the lithium-deposition process;
(3) high conductivity to reduce overvoltage;
(4) in the case of the rechargeable lithium battery, uniform morphology and chemical composition for homogeneous current distribution;
(5) good adhesion to the anode;
(6) mechanical strength and flexibility.

The early literature (until 1982) is summarized in Refs. [1] and [2]. Hundreds of papers have been published since then (most of them in since 1994) and it is impossible to summarize all of them here. The Proceedings of the conferences mentioned above are good, sources of recent developments though sometimes incomplete. Since the early 1980s new systems have been introduced. The most important of these are lithium-ion batteries (which have lithiated carbonaceous anodes) and polymer-electrolyte batteries. Until 1991 very little was published on the Li/polymer-electrolyte interface [3, 4]. The application of the SEI model to Li–PE batteries is ad-

dressed in Refs. [5] and [6].

Film-forming chemical reactions and the chemical composition of the film formed on lithium in nonaqueous aprotic liquid electrolytes are reviewed by Dominey [7]. SEI formation on carbon and graphite anodes in liquid electrolytes has been reviewed by Dahn et al. [8]. In addition to the evolution of new systems, new techniques have recently been adapted to the study of the electrode surface and the chemical and physical properties of the SEI. The most important of these are X-ray photoelectron spectroscopy (XPS), SEM, X-ray diffraction (XRD), Raman spectroscopy, scanning tunneling microscopy (STM), energy-dispersive X-ray spectroscopy (EDS), FTIR, NMR, EPR, calorimetry, DSC, TGA, use of quartz-crystal microbalance (QCMB) and atomic force microscopy (AFM).

It is now well established that in lithium batteries (including lithium-ion batteries) containing either liquid or polymer electrolytes, the anode is always covered by a passivating layer called the SEI. However, the chemical and electrochemical formation reactions and properties of this layer are as yet not well understood. In this section we discuss the electrode surface and SEI characterizations, film formation reactions (chemical and electrochemical), and other phenomena taking place at the lithium or lithium-alloy anode, and at the Li_xC_6 anode/electrolyte interface in both liquid and polymer-electrolyte batteries. We focus on the lithium anode but the theoretical considerations are common to all alkali-metal anodes. We address also the initial electrochemical formation steps of the SEI, the role of the solvated-electron rate constant in the selection of SEI-building materials (precursors), and the correlation between SEI properties and battery quality and performance.

6.2 SEI Formation Chemical Composition, and Morphology

6.2.1 SEI Formation Processes

Alkali and alkaline-earth metals have the most negative standard reduction potentials; these potentials are (at least in ammonia, amines, and ethers) more negative than that of the solvated-electron electrode. As a result, alkali metals (M) dissolve in these highly purified solvents [9, 12] following reactions (1) and (2) to give the well-known blue solutions of solvated electrons.

$$M^0 - e \rightarrow M^+_{solv} \quad (1)$$

$$e(M) \rightarrow e^-_{solv} \quad (2)$$

These reactions proceed to equilibrium when the potential of the solvated-electron electrode equals that of the alkali metal [13]:

$$E^0_M \frac{RT}{F} \ln a_{M^+} = E_{e^-} - \frac{RT}{F} \ln a_{e^-} \quad (3)$$

were E^0_x is the standard potential of the X electrode and a_x is the activity of X. In ammonia the difference between E^0_M and E^0_e is a few hundred millivolts, so the equilibrium concentration of e^-_{solv} is in the range of several millimoles per liter.

This dissolution process takes place in many solvents to an extent governed by Eq. (3). Solvated electrons can be formed in all solvents by many means. Their kinetics is best studied with the use of pulse radiolysis.

Practical primary or secondary alkali-

CosMX Exhibit 1008, Page 438 of 633

metal or alkaline-earth batteries can be made only if the dissolution of the anode by reactions (1) and (2) (and by other corrosion reactions) can be stopped. Since e^-_{solv} attacks both the electrolyte and the cathode, the electrolyte must be designed to contain at least one material that reacts rapidly with lithium (or with the alkali-metal anode) to form an insoluble solid/electrolyte interphase (the SEI). On inert electrodes, the SEI is formed by reduction of the electrolyte. This type of electrode (completely covered by SEI), was named [1, 2] the "SEI electrode".

In this paper we shall discuss four types of SEI electrodes:

(1) inert metal covered by SEI (e.g., anode current collectors or battery case connected to the anode;
(2) freshly cut lithium immersed in the electrolyte or lithium plated (deposited) in the electrolyte;
(3) lithium covered with native oxide film as received from the manufacturer;
(4) carbonaceous and alloy anodes.

$$C_3O_3H_4 \xrightarrow{e^-} (C_3O_3H_4)^- \xrightarrow[2Li^+]{e^-} Li_2CO_3 + CH_2 = CH_2$$

$$2[(C_3O_3H_4)^-] \longrightarrow {}^-OCO_2CH_2CH_2CH_2CH_2OCO_2 \xrightarrow{2Li^+}$$

$$LiOCO_2CH_2CH_2CH_2CH_2OCO_2Li$$

$$CH_2 = CH_2 \xrightarrow{e^-} H_2\dot{C} - CH_2^- \xrightarrow{CH_2=CH_2} [CH_2 - CH2]_n$$

$$AsF_6^- + 3Li^+ \xrightarrow{2e^-} 3LiF + AsF_3 \xrightarrow[3Li^+]{3e^-} 6LiF + As^0$$

$$\frac{1}{2}O_2 + 2Li^+ \xrightarrow{2e^-} Li_2O$$

$$H_2O + Li^+ \xrightarrow{e^-} LiOH + \frac{1}{2}H_2$$

$$BF_4^- + 4Li \xrightarrow{3e^-} B^0 + 4LiF$$

$$PF_6^- + H_2O \longrightarrow HF + PF + OH^-$$

$$Li + HF \longrightarrow LiF + \frac{1}{2}H_2$$

$$Li_2CO_3 + 2HF \longrightarrow 2LiF + H_2CO_3$$

$$LiOH + HF \longrightarrow LiF + H_2O$$

$$Li_2O + 2HF \longrightarrow 2LiF + H_2O$$

Figure 1. Electrolyte decomposition reactions.

CosMX Exhibit 1008, Page 439 of 633

When an inert metal (or any electronic conductor) is negatively polarized in the electrolyte (typically from 3 V versus the lithium reference electrode (LiRE) to 0 V versus LiRE), the following reactions take place at different potentials and at varying rates, depending on E^0, on concentration, and on i_0 for each of the following electrochemically active materials: (1) solvents, (2) anions of the salts, and (3) impurities such as H_2O, O_2, HF, CO_2 etc. (Fig. 1). Some of the products, especially at more positive potentials, may be soluble and diffuse away from the electrode, while others will precipitate on the surface of the electrode to form the SEI. At potentials lower than a few hundred millivolts, solvated electrons will be formed. These will also react with impurities, solvents and salts (e^-_{sol} scavengers) to produce similar products. The lifetime τ, ($\tau = 0.69K_e[S]$; K_e = rate constant; [S]=scavenger concentration) of solvated electrons in battery-related electrolytes is expected to be in the range of $10^{-4} - 10^{-10}$s (for more details see Sec. 6.2.3). Schematics of these processes can be seen in Fig. 5 in Sec. 6.3.2, which deals with SEI formation on carbonaceous electrodes. When the thickness of the SEI is larger than the tunneling range of electrons, or when the electric field in the SEI is smaller than that for dielectric breakdown (typically at a thickness of 2–5nm), the electrons cease flowing through the SEI and lithium deposition at the electrode/SEI interface begins [1, 2].

The charge needed to complete the formation of the SEI (about 10^{-3} mAh cm^{-2} [8, 14]) increases with the real surface area of the electrode and decreases with increase in the current density and with decrease in the electrode potential (below the SEI potential). In practice, it may take from less than a second to some hours to build an SEI 2–5nm thick. When lithium is cut while immersed in the electrolyte, the SEI forms almost instantaneously (in less than 1ms [15,16]). On continuous plating of lithium through the SEI during battery charge, some electrolyte is consumed in each charge cycle in a break-and-repair process of the SEI [1, 2] and this results in a faradaic efficiency lower than 1. When a battery is made with commercial lithium foil, the foil is covered with a native surface film. The composition of this surface film depends on the environment to which the lithium is exposed. It consists of Li_2O, LiOH, Li_2CO_3, Li_3N, and other impurities. When this type of lithium is immersed in the electrolyte, the native surface film may react with the solvent, salts, and impurities to form an SEI, whose composition may differ from that of electrodeposited lithium in the same electrolyte. The formation of SEI on carbonaceous anodes is discussed in Sec. 6.3.

6.2.2 Chemical Composition and Morphology of the SEI

6.2.2.1 Ether-Based Liquid Electrolytes

Fresh lithium surface

Little work has been done on bare lithium metal that is well defined and free of surface film [15–24]. Odziemkowski and Irish [15] showed that for carefully purified $LiAsF_6$ tetrahydrofuran (THF) and 2-methyltetrahydrofuran 2Me-THF electrolytes the exchange-current density and corrosion potential on the lithium surface immediately after cutting in situ, are primarily determined by two reactions: anodic dissolution of lithium, and cathodic reduc-

CosMX Exhibit 1008, Page 440 of 633

tion of the AsF_6^- anion by bare lithium metal. The SEI was formed in less than 1ms. As pointed out by Holding et al. [17], the reduction of AsF_6^-, PF_6^-, BF_4^- and ClO_4^- is thermodynamically favored. All of the electrolytes investigated [15, 16] were unstable with respect to bare lithium metal. The most unstable system was lithium hexafluoroarsenate in THF and 2Me-THF [16]. Odziemkowski and Irish [15] concluded that in THF, 2Me-THF and PC, electrochemical reduction of the anion AsF_6^- overshadows any possible solvent—reduction reaction. It was also pointed out by Campbell et al. [18], who observed that films on lithium surfaces are formed in most cases by electrochemical reduction of the electrolyte anions. One of the main products detected in $LiAsF_6$/THF electrolyte by in-situ and ex-situ Raman microscopy [15] was a polytetrahydrofurane (PTHF). The polymerization reaction is determined by: (1) the ratio of the concentration of nucleophilic impurities like H_2O, O_2, etc., to the concentration of the pentavalent Lewis acid AsF_5, and (2) the ratio of the volume of the electrolyte to the active surface area of the lithium electrode. In contrast to THF, 2Me-THF does not polymerize. However, the brown film formed on lithium was observed in both electrolytes. It was found that the film decomposes to arsenious oxide, when exposed to air, moisture, and heat, and may not be polymeric [19]. The surface film formed in imide-based electrolytes was found to be a better electronic conductor and more permeable to an oxidizer. Thus it is suggested that the SEI in Li imide electrolytes is less compact than in $LiClO_4$, $LiBF_4$, and $LiPF_6$ electrolytes regardless of the type and purity of solvent. It also was noted that the SEI in $LiBF_4$/THF electrolyte was the most water-sensitive [15].

According to the depth profile of lithium passivated in $LiAsF_6$ / dimethoxyethane (DME), the SEI has a bilayer structure containing lithium methoxide, LiOH, Li_2O, and LiF [21]. The oxide–hydroxide layer is close to the lithium surface and there are solvent-reduction species in the outer part of the film. The thickness of the surface film formed on lithium freshly immersed in $LiAsF_6$/DME solutions is of the order of 100 Å.

Kanamura et al. [22] thoroughly studied the chemical composition of surface films of lithium deposited on a nickel substrate in γ—butyrolactone (γ-BL) and tetrahydrofurane electrolytes, containing various salts, such as $LiClO_4$, $LiAsF_6$, $LiBF_4$, and $LiPF_6$. They found, with the use of XPS, that the outer and inner layers of the surface film covering lithium in $LiClO_4$/γ-BL involve LiOH or possibly some Li_2CO_3 and Li_2O as the main products. Chlorine and oxygen were produced uniformly over the entire region of the surface film. The authors suggested that the hydrocarbon observed in the C 1s spectrum is due not only to a hydrocarbon contaminant but also to organic compounds incorporated in the surface film. The chemical composition and the depth profile of the surface film formed in $LiAsF_6$ + γ-BL and $LiBF_4$ + γ-BL electrolytes are very similar to what is observed in the case of $LiClO_4$-based electrolyte. The only difference is the type of the lithium halide present. LiF is formed by the acid–base reaction between basic lithium compounds (LiOH, Li_2CO_3, and Li_2O) and HF, which is present as a contaminant in the electrolyte or as a product of the reaction of Li with $LiAsF_6$ ions. However, the reaction products of BF_4^- ions were not present in the surface film. The Li 1s spectra of $LiPF_6$ + γ-BL electrolyte were completely different from those observed for

CosMX Exhibit 1008, Page 441 of 633

the other γ-BL electrolytes [22]. The surface film consists of LiF as the main component of the outer layer the inner layer is mainly Li_2O. All the spectra of electrochemically deposited lithium in $LiClO_4$ + γ-BL containing 5×10^{-3} mol L^{-1} HF were very similar to those of $LiPF_6$ + γ-BL electrolyte. The same results were obtained with other electrolyte salts [21] and propylene carbonate (PC) based electrolytes (see Sec. 6.2.2.2).

The XPS data of the surface film on lithium deposited in $LiClO_4$ + THF before etching show that the outer surface film consists of LiOH, Li_2CO_3, LiCl, and organic compounds [21]. The depth profiles of the surface in THF were similar to those obtained in γ-BL, but the distribution of LiOH and Li_2O was slightly different. The surface film obtained in $LiClO_4$ + THF probably has a thicker mixed LiOH + Li_2CO_3 layer than that obtained in $LiClO_4$ + γ-BL [21].

The chemical species in the surface film of lithium deposited in $LiBF_4$ + THF electrolyte are not very different from those in $LiBF_4$ + γ-BL. However, more LiF and other fluoride compounds are formed and chemical species including elemental boron were also observed in the B 1s spectra. This means that BF_4^- ion reacts quite strongly with lithium during electrochemical deposition in THF electrolyte. According to the depth profile, the surface film comprises mainly a mixture of LiF, LiOH and Li_2CO_3 [22]. The carbon content in $LiAsF_6$ + γ-BL was greater than that in $LiAsF_6$ + THF.

Lithium covered by native film

The formation of a native surface film on lithium is unavoidable. It arises from storage and laboratory handling of the lithium metal in the gaseous atmosphere of the dry box, and from the immediate reaction taking place after immersion of lithium electrodes in an electrolyte. The outer part of the native film, which was analyzed by XPS [23], consists of Li_2CO_3 or LiOH and the inner part is Li_2O. X-ray microanalysis of lithium electrodes, covered by native film and treated in fluorine—containing salts such as $LiAsF_6$, $LiBF_4$, $LiPF_6$, Li imide and Li triflate dissolved in THF, always shows fluorine, oxygen, and carbon peaks, which are characterized by different relative intensities [20].

Among many polar aprotic solvents, including ethers, BL, PC, and ethylene carbonate (EC), methyl formate (MF) seems to be the most reactive towards lithium. It is reduced to lithium formate as a major product which precipitates on the lithium surface and passivates it [24]. The presence of trace amounts of the two expected contaminants, water and methanol, in MF solutions does not affect the surface chemistry. CO_2 in MF causes the formation of a passive film containing both lithium formate and lithium carbonate.

6.2.2.2 Carbonate-Based Liquid Electrolyte

Fresh lithium surface

The structure and composition of the lithium surface layers in carbonate-based electrolytes have been studied extensively by many investigators [19-37]. High reactivity of propylene carbonate (PC) to the bare lithium metal is expected, since its reduction on an ideal polarizable electrode takes place at much more positive potentials compared with THF and 2Me-THF [18]. Thevenin and Muller [29] found that the surface layer in $LiClO_4$/PC electrolyte is a mixture of solid Li_2CO_3 and a

CosMX Exhibit 1008, Page 442 of 633

polymer they suggested is $P(PO)_xLiClO_4$. Aurbach and Zaban [25] have proposed that the lithium surface deposited on a nickel electrode in any of several electrolytes is covered with Li_2CO_3, LiOH, Li_2O, LiOR, $LiOCO_2R$ (R= hydrocarbon), and lithium halide. Kanamura et al. [26] showed that LiF is a final product of the reduction of electrolytes that contain HF as a contaminant. When a small amount of HF is added to PC containing $1.0\,mol\,L^{-1}$ $LiClO_4$, lithium deposited on a nickel substrate is covered with a thin LiF/Li_2O surface film. Without the addition of HF, the surface of electrodeposited lithium is covered with a thick film (mainly LiOH and Li_2O). Using in-situ X-ray diffraction, Nazri and Muller [30] identified two peaks on the lithium surface during its cathodic deposition on a nickel substrate in $1.5\,mol\,L^{-1}$ $LiClO_4$/PC electrolyte. The broad peak at low diffraction angle (20°) is characteristic of polymer compounds; the second sharp peak is attributed to lithium carbonate.

Lithium covered by native film

Aurbach and Zaban [25] used special methods to study the lithium (covered by native film)/electrolyte interphase formed in uncontaminated PC solutions. They found the interphase to be mainly a matrix of Li alkylcarbonate (probably of the type $CH_3CH(OCO_2Li)CH_2OCO_2Li$), containing salt-reduction products and trace Li_2CO_3. Lithium carbonate is formed by the reaction of $ROCO_2Li$ with traces of water unavoidably present in solutions. They also suggested the possibility of Li_2CO_3 formation by further reduction of Li alkylcarbonate species close to the lithium surface. FTIR spectra obtained from lithium electrodes stored in PC/LiBr solutions show the formation of Li alkyl carbonates ($ROCO_2Li$) and Li_2CO_3, which are the major surface species formed on lithium in PC [20]. It was shown that in the presence of LiI, PC was reduced to $ROCO_2Li$ and propylene. In Li imide/PC electrolytes these products were not dominant. On lithium surfaces stored in Li imide and Li triflate, both fluorine- and sulfur—containing compounds are present. The surface concentration of sulfur in Li-triflate-based solutions was higher than in Li-imide/PC electrolytes. When the solution contains CO_2, the main surface species is lithium carbonate. In PC-based electrolytes, $LiPF_6$, $LiBF_4$, $LiSO_3CF_3$, and $LiN(SO_2CF_3)_2$ were found to be more reactive towards lithium than were $LiClO_4$ and $LiAsF_6$ [20]. Aurbach and Gofer [31] investigated the formation of SEI in mixtures of carbonate- and ether-based solvents, such as PC/THF, PC/2Me-THF, DME/PC, EC/THF, EC/dioxolane and EC/PC, containing $LiClO_4$ or $LiAsF_6$. They found that lithium electrodes treated in $LiAsF_6$/PC/THF solutions are covered by a surface film containing carbon, oxygen, and fluorine. Both PC and THF contribute to the buildup of surface films, but the F and As peaks in pure THF were much higher. This indicates that the addition of reactive PC to the ether decreases salt reduction by competing with it, and the film becomes more organic in nature, containing less LIF. In the case of EC/PC or EC/ether mixtures, the reduction of EC by lithium seems to be the dominant process, followed by the formation of lithium alkylcarbonates (derivatives of ethylene glycol) [31]. It was suggested [34] that in mixed organic solvent systems, the solvent having higher donicity tends to coordinate preferentially with Li^+ ion and consequently to react at the Li-electrode / electrolyte interface. Matsuda and coworkers [35, 36] showed that some cyclic

CosMX Exhibit 1008, Page 443 of 633

compounds containing heteroatoms and conjugated double bonds, such as 2-methylthiophene (2MeTp), 2-methylfuran (2MeF), and aromatic compounds like benzene are very effective in electrolyte solutions for rechargeable lithium batteries. On the basis of AC-impedance measurements it was estimated that the reaction between lithium and 2MeTp or 2MeF would result in a thick SEI of uniform composition [36]. Tobishima et al. [37] showed that the addition of 2Me-THF improves the cycle life of the Li/EC–PC/V_2O_5–P_2O_5 cell. The interaction between the cathode and electrolyte leads to the formation of a film containing vanadium on the lithium anode surface. Mori et al. [38], using a quartz-crystal microbalance, demonstrated the smooth surface morphology and almost constant thickness of the lithium film in EC/dimethyl carbonate (DMC) solutions in the presence of surfactants like polyethylene glycol dimethyl ether, and a mixture of dimethyl siloxane and propylene oxide. The morphological properties of the surface layers formed on the lithium electrode (covered by native film) in sulfolane-based electrolytes (SFLs) have been investigated [42]. It was found that the surface layers are essentially homogeneous and consist mainly of waxy degradation material in which some long white microcrystals are present.

Matsuda and co-workers [39-41] proposed the addition of some inorganic ions, such as Mg^{2+}, Zn^{2+}, In^{3+}, Ga^{3+}, Al^{3+},and Sn^{2+}, to PC-based electrolytes in order to improve cycle life. They observed the formation of thin layers of Li/M alloys on the electrode surface during the cathodic deposition of lithium on charge–discharge cycling. The resulting films suppress the dendritic deposition of lithium [40, 41]. The Li/Al layer exhibited low and stable resistance in the electrolyte, but the resistance of the Li/Sn layer was relatively high and unstable.

6.2.2.3 Polymer (PE), Composite Polymer (CPE), and Gelled Electrolytes

It seems clear that in polymer electrolytes, especially in the gel types, lithium-passivation phenomena are similar to those commonly occurring in liquid electrolytes. The crucial role played by the nature and composition of the PE in controlling electron transfer has been described by several authors [3–6, 43–45]. It is postulated that at least two separate competitive reactions occur simultaneously to form the passive layer. The first is the reaction of lithium with contaminants. The second reaction is that of lithium metal with salt. The passivation film appears to consist mainly of Li_2O and/or LiOH [46]. Chabagno [47] observed that polyethylene oxide (PEO) and LiF will not form a complex. LIF is therefore insoluble and will remain at the interface between the lithium electrode and the polymer electrolyte. In one publication [48] polyethylene glycol dimethyl ether (PEGDME) (molecular weight MW=400) was chosen as a model system for the investigation of the process of passivation of lithium in contact with polymer electrolytes. The authors showed that SEI formation was apparently complete in just 2–3 min. The increase in the SEI resistance (R_{SEI}) over hours and days is apparently due to the relaxation of the initially formed passivation films or to the continuation of the reaction at a much slower rate. Results obtained with PEGDME electrolytes containing different salts showed that the formation of LiF as a result of the reduction of anions like AsF_6^- or $CF_3SO_3^-$ plays a key role in the lithium passivation mechanism [48].

Finely divided ceramic powders, which

CosMX Exhibit 1008, Page 444 of 633

have a high affinity for water and other impurities, were initially added in order to improve the mechanical and electrical properties of LiX–PEO polymer electrolytes [53–55]. However, today there is considerable experimental evidence for higher stability of lithium/composite polymer electrolyte (CPE) interfaces as compared with pure PEs [49–52]. On the basis of standard free energies of reactions of lithium with ceramic fillers, such as CaO, MgO, Al_2O_3 and SiO_2, it was concluded [56] that lithium passivation is unlikely to occur when lithium is in contact with either CaO or MgO. However, passivation is possible in the case of Al_2O_3 and SiO_2. It was shown that the interfacial stability can be significantly enhanced by decreasing the ceramic particle size to the scale of nanometers [56, 57]. The mechanism of the processes leading to improved stability is not well understood and some explanations include scavenging effects and screening of the electrode with the ceramic phase [56].

The morphology of lithium deposits from 1–3 mol L^{-1} $LiClO_4$–EC/PC–ethylene oxide (EO)/ propylene oxide (PO) copolymer electrolytes was investigated [58]. It was found that, as the weight ratio of host polymer to liquid electrolyte increased, fewer lithium dendrites were formed, with no dendrites found in electrolytes containing more than 30 percent w/w host polymer. The authors emphasized that good contact between the polymer and lithium is also of great importance for the suppression of dendrites. Direct in-situ observation of lithium dendritic growth in Li imide $P(EO)_{20}$ polymer electrolyte [59] shows that dendrites grow at a rate close to that of anionic drift.

6.2.3 Reactivity of e^-_{sol} with Electrolyte Components – a Tool for the Selection of Electrolyte Materials

As mentioned in Sec. 6.2.1, solvated electrons may take part in the early stage of SEI formation and during break-and-repair healing processes during lithium plating and stripping. It is most important that the formation and the healing of the SEI, especially on graphite, in the first intercalation step be a very fast reaction, and that the SEI-building materials have extremely low solubility. The best SEI materials seem to be LiF, Li_2CO_3 and Li_2O. They are insoluble in most of the lithium–battery organic-based electrolytes, and LiF and Li_2O are thermodynamically stable with respect to lithium metal and are cationic conductors. LiOR (R is an organic residue), Li_2S, LiCl, and LiBr are suitable materials for some electrolytes. Li_2O cannot serve as the sole SEI material; because of its low equivalent volume, it cannot supply sufficient corrosion protection for a metallic lithium anode. In practice, it is mixed with LiF or covered by a second layer of LiF, Li_2CO_3, semicarbonates, polyolefins, or mixtures of these. The electrolyte must be designed to contain one or more SEI precursors having high E^0 and high exchange-current density (i_0) for reduction (electron scavengers such as CO_2, ethylene carbonate (EC), and $LiAsF_6$) where the reduction products are appropriate SEI-building materials [60]. However, the data bank of i_0 for such reactions is limited. The determination of practical i_0 values for the electrolyte components (solvents, salts, and impurities) is a difficult task for two reasons: (1) the electrodes must be solid—mercury cannot be used; (2) the electrode is passivated during the cathodic sweep. It is therefore

CosMX Exhibit 1008, Page 445 of 633

suggested that the data bank be used for the bimolecular rate constant (k_e) for the reaction:

$$e^-_{aq} + S \rightarrow product \qquad (4)$$

where e^-_{aq} is a hydrated electron and S is an electron scavenger and a candidate material for a lithium-battery electrolyte. This data bank has information on more than 1500 materials [61, 62]. The reactivity of materials towards e^-_{aq} (in aqueous solutions) is expected to be quite close to that for e^-_{sol} in organic solutions, at least in most simple cases. For example, the rate constants measured for the reaction of solvated electrons in methanol, ethanol, and water with H^+, O_2, $C_6H_5CH_2Cl$, and $C_{10}H_8$ are about the same, i.e., no solvent effect is observed [63]. Another factor which must be taken into account is that, in some cases, the heterogeneous reaction at the electrode and the homogeneous reaction in the solution may yield different products.

According to the Marcus theory [64] for outer-sphere reactions, there is good correlation between the heterogeneous (electrode) and homogeneous (solution) rate constants. This is the theoretical basis for the proposed use of hydrated-electron rate constants (k_e) as a criterion for the reactivity of an electrolyte component towards lithium or any electrode at lithium potential. Table 1 shows rate-constant values for selected materials that are relevant to SEI formation and to lithium batteries. Although many important materials are missing (such as PC, EC, diethyl carbonate (DEC), $LiPF_6$, etc.), much can be learned from a careful study of this table (and its sources).

The first factor to take into account is that rate constants higher than 10^{10} $L\,mol^{-1}\,s^{-1}$ relate to diffusion-controlled reactions, i.e., reactions which have almost zero energy of activation and are therefore controlled by the diffusion of the reactants. These reactions are expected to proceed very quickly at the lithium electrode potential. Therefore SEI precursors should be

Table 1. A compilation of specific bimolecular rate constants (k_e) for the reaction of hydrated electrons with Li battery related materials [61, 62]

Reactant	pH	Rate constant, k_e at 15-25 °C ($Lmol^{-1}s^{-1}$)
AsF_6^-	7	9×10^9
BF_4^-	5.8	$<2.3\times10^5$
CO_2	7	7.7×10^9
CO_3^{2-}		$<3.9\times10^6$
ClO_4		$<10^6$
CrO_4^{2-}	13	5.4×10^{10}
H^+		2.5×10^{10}
HF		6×10^7
MnO_4^-	7	4.4×10^{10}
NO_3^-		8.2×10^9
O_2	7	1.9×10^9
$H_2PO_4^-$	6.7	7.7×10^6
SO_4^{2-}	7	$<10^6$
$S_2O_8^{2-}$	7	1×10^{10}
SF_6	7	1.6×10^{10}
Acetone	7	6×10^9
Acetonitrile		4×10^7
Acetophenone		2.4×10^{10}
Acrylamide		2.2×10^{10}
Acrylate ion	9.2	5.3×10^9
Acrylonitrile		1.3×10^{10}
Carbon disulfide		3.1×10^{10}
Cyclopentanone		7.4×10^9
Ethyl acrylate	11	8.7×10^9
Cyclohexene	11	$<10^6$
Diethyl ether		$<10^7$
Dimethyl fumarate	9.2	3.3×10^{10}
Dimethyl oxalate		2×10^{10}
Ethyl acetate	6.5	5.9×10^7
Furane	8	3×10^6
Propylene glycol carbonate [$CH_3CH(CH_2)OCOO$]		7.2×10^7
Naphthalene	11	5.4×10^9
Styrene	12.7	1.1×10^{10}
α, α, α-Trifluorotoluene	11	1.8×10^9

CosMX Exhibit 1008, Page 446 of 633

chosen from this group, or at least from the group having rate constants higher than 10^9 L mol^{-1} s^{-1}. On the other hand, "inert" electrolyte components, which are chosen because of their very slow reaction with lithium (or with the Li_xC_6 anode) must be taken from the group that has the smallest rate constant—preferably smaller than 10^7 (or even 10^5) L mol^{-1} s^{-1}—for example, ethers. The reactions of strong oxidants like O_2, CrO_4^{2-}, MnO_4^-, and $S_2O_8^{2-}$ are diffusion-controlled. AsF_6^- and CO_2, which are good SEI precursors [15, 16, 24, 25] have values of k_e that approach those for diffusion-controlled reactions. There is good correlation between the SEI composition and the reactivity of electrolyte components towards e_{aq}^-.For example, LiF and As–F–O species are found in the SEI formed in electrolytes containing $LiAsF_6$ [7, 22, 26–28]. Also, when CO_2 is added to the electrolyte, more Li_2CO_3 is found in the SEI [20, 24]. EC is so far the best SEI-forming precursor; we attribute this to its high i_0, although this still needs to be proved. On the other hand BF_4^- and ClO_4^- are much less reactive towards e_{aq}^- ($k_e < 10^6$) and LiCl and B^0 are rarely found in the SEI in ã-BL solutions [20–22]. However, in ether-based solutions containing $LiBF_4^-$, B^0 was found in the SEI [22, 23]. In some cases, BF_4^- electrolytes contain some HF (or hydrolyze to yield HF) which reacts with lithium or with Li_2O, LiOH, or Li_2CO_3 and covers the anode with LiF [26]. Esters such as ethyl acetate and semicarbonates like propylene glycol carbonate have moderate rate constants (10^7–10^8 L mol^{-1} s^{-1}). This suggests that semicarbonate is not stable with respect to lithium and that the part of the SEI which is close to the lithium (or the Li_xC_6) anode cannot consist of semicarbonate as already reported [26–28, 65]. In the solid phase, Li_2CO_3 is thermodynamically unstable with respect to lithium (i.e., ÄG for the reaction: $4Li(s) + Li_2CO_3(s) \rightarrow 3Li_2O(s) + C(s)$ is negative). As a result, the Li_2CO_3 particles at the Li/SEI (or Li_xC_6/SEI) interface are expected to be reduced to $Li_2O + C$. The equivalent volumes of both LiF and Li_2O are too small (9.84 and 7.43mL, respectively) to provide adequate corrosion protection for lithium metal (the equivalent volume of lithium is 12.98mL). Thus a second layer of Li_2CO_3 (equivalent volume, 17.5mL) or other organic materials is required to cover the first layer in order to provide this protection. XPS measurements [22, 26] show that the part of the SEI which is closer to the lithium or carbon electrode is rich in Li_2O and low in Li_2CO_3. The carbon may further react to form lithium intercalation compounds–Li_xC_6 (see also Sec. 6.5.2).

A problem associated with the use of organic-carbonate-based electrolytes is gas evolution during the formation of the SEI (or during cycling of cells with lithium-metal anodes). A possible way to overcome this problem is to consider the use of reactive e_{sol}^- scavengers not based on organic carbonates, such as SF_6, trifluorotoluene, etc., which may form an LiF-based SEI instead of an Li_2CO_3-based SEI. We recently found [60] that.the addition to DEC of dimethyl oxalate (DMO), which is an excellent e_{sol}^- scavenger, enables cycling graphite in 1.2 mol L^{-1} $LiAsF_6$/DMO—DEC (1:2).

6.3 SEI Formation on Carbonaceous Electrodes

Carbonaceous materials such as various types of soft and hard carbons and graphites are currently the focus of greatest

CosMX Exhibit 1008, Page 447 of 633

interest in the field of battery technology. Lithium-ion batteries with this type of anode show excellent performance in terms of cycle life, energy density, power density, and charge rate. For this reason, these anodes deserve special attention.

6.3.1 Surface Structure and Chemistry of Carbon and Graphite

The physicochemical properties of carbon are highly dependent on its surface structure and chemical composition [66—68]. The type and content of surface species, particle shape and size, pore-size distribution, BET surface area and pore-opening are of critical importance in the use of carbons as anode material. These properties have a major influence on Q_{IR}, reversible capacity Q_R, and the rate capability and safety of the battery. The surface chemical composition depends on the raw materials (carbon precursors), the production process, and the history of the carbon. Surface groups containing H, O, S, N, P, halogens, and other elements have been identified on carbon blacks [66, 67]. There is also ash on the surface of carbon and this typically contains Ca, Si, Fe, Al, and V. Ash and acidic oxides enhance the adsorption of the more polar compounds and electrolytes [66].

The basic building block of carbon is a planar sheet of carbon atoms arranged in a honeycomb structure (called graphene or basal plane). These carbon sheets are stacked in an ordered or disordered manner to form crystallites. Each crystallite has two different edge sites (Fig. 2): the armchair and zig-zag sites. In graphite and other ordered carbons, these edge sites are actually the crystallite planes, while in disordered soft and hard carbons these sites, as a result of turbostratic disorder, may not

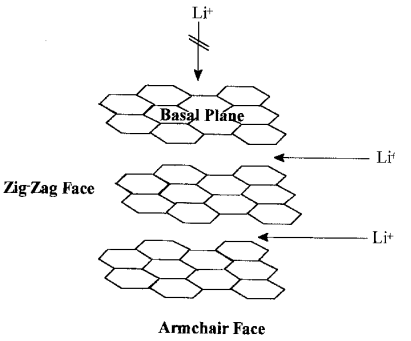


Figure 2. The faces of carbon crystallite.

form large planes (i.e., the crystallite dimensions parallel and perpendicular to the basal plane, l_a and l_c, are in the nanometer range). The reactivity of carbon atoms at the edge sites (and near lattice defects and foreign atoms) is much higher than that of carbon atoms in the basal planes [66–68]. Consequently, the physical and chemical properties of carbon vary with the basal-plane to edge-plane area ratio. The surface area of carbon powders varies over a wide range from less than a few square meters per gram for large-particle graphite powders to more than 1000 $m^2 g^{-1}$ for high-surface-area carbons. As a result, the content of surface groups or heteroatoms, measured as the ratio of foreign atoms to C, varies from nearly zero up to 1:5 in the case of hydrogen [66–68].

Carbons may have closed and open pores with a large variety of dimensions from a few Ångstroms to several microns. In terms of structure, the pores in active carbons are divided into three basic classes [66, 69]: macropores, transitional pores, and micropores. Pores are formed during the production of carbon (pyrolysis of its precursors), or can be formed by other means such as oxidation by O_2, air, CO_2, or H_2O [66]. According to Dubinin's

CosMX Exhibit 1008, Page 448 of 633

classification [66, 69], the radius of a macropore is in the range 500–20000 Å, and its surface area can vary from 0.5 to $2 m^2 g^{-1}$. Transitional pores have an effective radius between 16 and 2000 Å and they can contribute a BET surface area of 20–70 $m^2 g^{-1}$. The effective radius of micropores is less than 20 Å and can constitute 95 percent of the total specific BET area. The pore structure has the following pattern: the macropores open out to the external surface of the particle, transitional pores branch off from macropores, and micropores, in turn, branch off from the transitional pores.

Surface species can be present at edge sites inside open and closed pores, and not only on the external surface of the carbon particles. Some pores have very narrow openings and are not accessible to battery electrolyte (solvents or salt), but may be permeable to oxygen and water [70, 71]. Other pores are completely closed and not permeable even to helium. The edge atoms in these closed pores are actually radicals and are said to have a "dangling" bond [68]. These pores are responsible for "extra" reversible capacity of disordered carbons [70] and oxidized graphite [72–75]. The surface oxygen species are by far the most important group, influencing the physicochemical properties such as wettability, catalysis, and electrical and chemical bonding to other materials [66–68]. A schematic representation of surface oxygen species that are believed [67] to be present on the carbon surface is given in Fig. 3. The formation processes and properties of these species are reviewed and widely discussed by Kinoshita and Cookson [66, 67].

It is common practice to classify the surface oxides as basic, neutral, and acidic [66, 67]. Acidic surface oxides (carboxylic groups) are formed when the carbon is ex

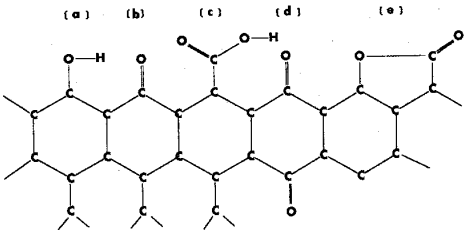


Figure 3. Schematic representation of the oxygen functional groups on the carbon surface: (a) phenol; (b) carbonyl; (c) carboxyl; (d) quinone; (e) lactone [2].

posed to oxygen at temperatures between 200 and 500 °C or by the action of aqueous oxidizing solutions. They start to decompose under vacuum (or inert atmosphere) at about 250 °C and in general are completely desorbed at above 800 °C. The basic surface oxides are formed when the carbon surface is freed of all surface compounds by heating in vacuum or inert atmosphere (above 1200 °C) and then exposed to air or O_2 after cooling [66, 67]. The neutral surface oxides are formed by the irreversible adsorption of oxygen on unsaturated sites [67] to form a –C–O–O–C– bond. These oxides are more stable than the acidic surface oxides and begin to decompose to CO_2 only at 500–600 °C [67]. When graphite or carbon powders are vacuum heated, CO_2, CO, and H_2 begin to desorb at 100, 200–300 and 700 °C respectively, and decomposition is complete at 700, 1000 and > 1200 °C (sometimes 1600 °C) respectively [67]. Acidic groups can be titrated by alkali hydroxides, barium hydroxide, and carbonates, whereas basic groups are titrated by HCl and other acids [66, 67]. Various spectroscopic techniques have been used to characterize surface species [66, 67]; these include IR, FTIR, XPS, Raman, and EPR.

CosMX Exhibit 1008, Page 449 of 633

6.3.2 The First Intercalation Step in Carbonaceous Anodes

The first 1.5 charge–discharge cycles of lithium/carbon cells are presented in Fig. 4 for both graphite (b) and petroleum coke (a) [71]. In both cases, the first intercalation capacity is larger than the first deintercalation capacity.

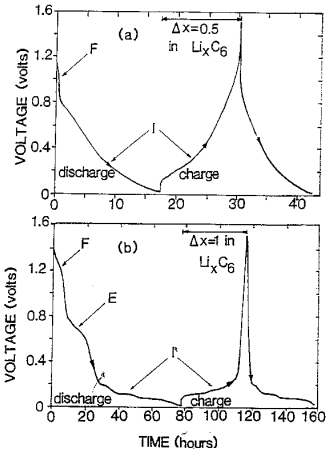


Figure 4. (a) The first 1.5 cycles of a lithium/petroleum coke cell; (b) the first 1.5 cycles of a lithium/graphite cell [11].

This difference is the irreversible capacity loss (Q_{IR}). Dahn and co-workers [71] were the first to correlate Q_{IR} with the capacity required for the formation of the SEI. They found that Q_{IR} is proportional to the specific surface area of the carbon electrode and, assuming the formation of an Li_2CO_3 film, calculated an SEI thickness of 45±5 Å on the carbon particles, consistent with the barrier thickness needed to prevent electron tunneling [1, 2]. They concluded [71] that when all the available surface area is coated with a film of the decomposition products, further decomposition ceases.

In general, lithium-ion batteries are assembled in the discharged state. That is, the cathode, for example Li_1CoO_2, is filly intercalated by lithium, while the anode (carbon) is completely empty (not charged by lithium). In the first charge the anode is polarized in the negative direction (electrons are inserted into the carbon) and lithium cations leave the cathode, enter the solution, and are inserted into the carbon anode. This first charge process is very complex. On the basis of many reports it is presented schematically [6, 74, 76] in Fig. 5. The reactions presented in Fig. 5 are also discussed in Sec. 6.2.1, 6.2.2 and 6.3.5.

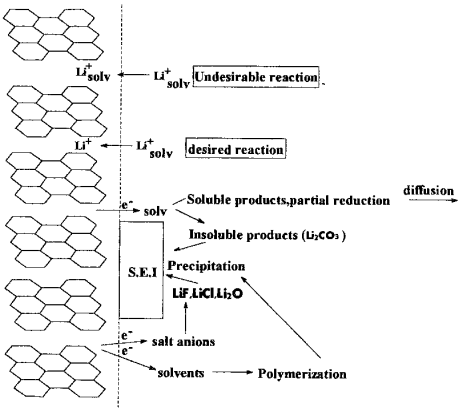


Figure 5. The complexity of the first intercalation process into graphite (after Refs. [6, 25].

At the electrode surface there is competition among many reduction reactions, the rates of which depend on i_0 and overpotential η for each process. Both i_0 and η depend on the concentration of the electroactive materials (and on the catalytic properties of the carbon surface). However, the chemical composition of the SEI is also influenced by the solubility of the reduction products. As a result, the voltage at

CosMX Exhibit 1008, Page 450 of 633

which the SEI is formed (V_{SEI}) depends on the type of carbon, the catalytic properties of its surface (ash content, type of crystallographic plane, basal to edge planes ratio), temperature, concentrations and types of solvents, salts and impurities, and current density. For lithium-ion battery electrolytes, V_{SEI} is typically in the range 1.7–0.5 V (Table 2) vs. LiRE, but it continues to form down to 0 V. In some cases, ε_F is less than 100 percent in the first few cycles [77]. This means that the completion of SEI formation may take several charge–discharge cycles. Table 2 shows that V_{SEI} depends on the reactivity of the electrolyte components towards e^-_{aq}; this reactivity correlates with i_0 In the case of reactive components like AsF_6^-, CO_2, and EC, V_{SEI} moves to more positive values, while for more kinetically stable (lower-k_e,) substances like ClO_4^- (and probably PF_6^- and imide), V_{SEI} approaches the Li/Li^+ potential, i.e., η is higher. It has been reported [73] that if the first intercalation of graphite is not completed (to 0 V vs. LiRE) the performance of the graphite anode (as characterized in Li/Li_xC_6 cells) suffers, i.e., x is smaller and there is a higher rate of carbon capacity degradation.

Table 2. Correlation between k_e and V_{SEI}

Reference	V^*_{SEI} (V)	k^+_e ($L\,mol^{-1}\,s^{-1}$)	Material	Carbon type	Electrolyte
[120]	0.8	$<10^6$	ClO_4^-	Graphite fibers	$LiClO_4$/EC–DEC
[77]	0.8	$<10^6$	ClO_4^-	Nat. graphite	$LiClO_4$/EC–DEC
[78]	0.8	$<10^6$	ClO_4^-	Graphite	$LiClO_4$/EC–PC
[117]	1.0	$<10^6$	ClO_4^-	Graphite	$LiClO_4$/EC
		$10^{10}-10^{9\mp}$	EC		
[118]	0.65		PF_6^-	Graphite	$LiPF_6$/EC–DEC
[118]	0.7		PF_6^-	Graphite fibers	$LiPF_6$/EC–DEC
[81]	0.6	9×10^9	AsF_6^-	Graphite	$LiAsF_6$/PC, 12-crown-4
[81]	1.7	9×10^9	AsF_6^-	Pet. coke	$LiAsF_6$/MF–CO_2
		7.7×10^9	CO_2		
[82]	1.3	9×10^9	AsF_6^-	Acetylene black	$LiAsF_6$/MF–CO_2
		7.7×10^9	CO_2		
[82]	1.33	9×10^9	AsF_6^-	Graphite	$LiAsF_6$/MF–CO_2
		7.7×10^9	CO_2		
[67]	1.2	9×10^9	AsF_6^-	Graphite	$LiAsF_6$/EC–DEC
[122]	1.2	9×10^9	AsF_6^-	Graphite fibers	$LiAsF_6$/EC–DEC
[122]	1.25	9×10^9	AsF_6^-	Graphite	$LiAsF_6$/1,3-dioxolane–EC
[122]	1.2	9×10^9	AsF_6^-	Graphite	$LiAsF_6$/1,3-dioxolane
[122]	1.5	9×10^9	AsF_6^-	Carbon DB40R	$LiAsF_6$/1,3-dioxolane
[79]	1.2	9×10^9	AsF_6^-	Graphite	$LiAsF_6$/EC–PC
[79]	1.1	9×10^9	AsF_6^-	Pet. coke	$LiAsF_6$/EC–DEC
[119]	0.75		$N(CF_3SO_2)_2^-$	Graphite	$LiN(CF_3SO_2)_2$/PC–EC, 12-crown-4
[108]	2.7	$10^{10\wp}$	SO_2	Graphite	$LiAsF_6$/MF or PC+SO_2
[87]	2.7	$10^{10\wp}$	SO_2	Carbon fiber	LiBr/AN+SO_2

* Vs. LiRE (or Li/Li^+), V peak in dQ/dV curve or inflection point in V vs. Q curves.
\+ From Table 1.
$\mp$ Assumed tto be similar to that of other esters (like dimethyl oxalate) in Table 1.
$\wp$ Assumed to equal that of O_2.

CosMX Exhibit 1008, Page 451 of 633

In both graphite and disordered carbons, lithium begins to intercalate in parallel with the formation of the SEI. In the case of disordered carbons, this, in general, does not constitute a problem, as the lithium intercalates as the naked ion, leaving its solvation sheath in the electrolyte. However, in the case of graphite, lithium can intercalate together with some of its solvation molecules, and this leads to the exfoliation of the graphite. Exfoliation may be enhanced in cases where the reduction of the solvated molecules produces gas (Fig. 1) [71, 78, 79]. In most organic electrolytes this problem is very severe, and the result is complete destruction of the structure of the graphite and almost zero reversible capacity. The only practical electrolyte known today for graphite-anode cells is based on ethylene carbonate (EC) [80]. It was reported that graphite can also be cycled with reasonable stability in dioxolane-based electrolytes [81, 82], and in other high-molecular-weight ethers such as 2Me-THF, dimethyl THF, and 1-methoxybutane [83].

Recently, there have been several very important reports by the groups of Ogumi [84, 85], Farrington [72], Yamaguchi [86], and Besenhard [87], who used STM, AFM and dilatometry to study the early stages of intercalation into highly oriented pyrolytic graphite (HOPG). Ogumi et al. [84, 85], using STM, found that in $1\,mol\,L^{-1}$ $LiClO_4$/EC–DC, a hill-like structure of about 1nm height appeared on the HOPG surface (near a step) at 0.95 V vs. Li/Li^+, and then changed at 0.75 V to an irregular blister-like feature with a maximum height of about 20 nm (see Fig. 6).

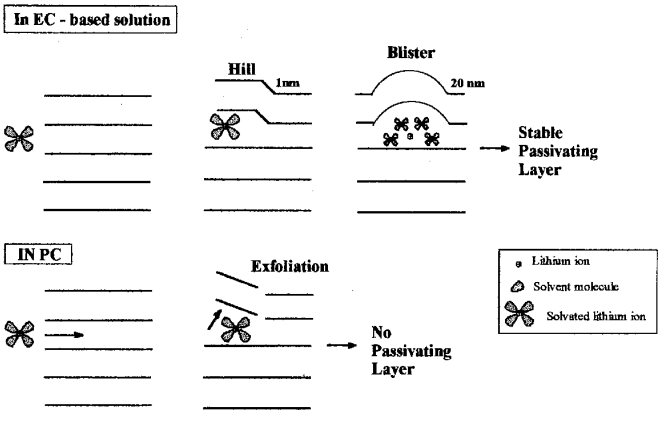


Figure 6. Early stages of intercalation into HOPG: above, in EC-based electrolyte; below, in PC-based electrolyte [4, 5].

These morphological changes (hill and blister formation) were attributed to the intercalation of solvated lithium ion into graphite interlayers and to the accumulation of its decomposition products (some of them gases), respectively. On the other hand, rapid exfoliation and rupturing of graphite layers were observed in $1\,mol\,L^{-1}$ $LiClO_4$ / PC electrolyte (Fig. 6), a process which was considered to be responsible for the continuing solvent decomposition when graphite is charged in PC-based electrolytes. This showed that, even in EC-based electrolytes, some degree of solvent co-intercalation exists but does not prevent formation of a stable SEI. It is clear that

CosMX Exhibit 1008, Page 452 of 633

this phenomenon of co-intercalation must be minimized in practical graphite-anode lithium-ion batteries.

Using dilatometry in parallel with cyclic voltammetry (CV) measurements in $1\,mol\,L^{-1}$ $LiClO_4$ EC–1,2-dimethoxyethane (DME), Besenhard et al. [87] found that over the voltage range of about 0.8–0.3 V (vs. Li/Li^+), the HOPG crystal expands by up to 150 percent. Some of this expansion seems to be reversible, as up to 50 percent contraction due to partial de-intercalation of solvated lithium cations was observed on the return step of the CV. It was concluded [87] that film formation occurs via chemical reduction of a solvated graphite intercalation compound (GIC) and that the permselective film (SEI) in fact penetrates into the bulk of the HOPG. It is important to repeat the tests conducted by Besenhard et al. [87] in other EC-based electrolytes in order to determine the severity of this phenomenon.

Chu et al. [72] and Yamaguchi [86] ran AFM measurements on the basal plane of HOPG in $1\,mol\,L^{-1}$ $LiClO_4$/EC–DMC (1:1) at various potentials versus the Li/Li^+ electrode. It was found that at 1.45 V some material begins to form in the vicinity of a step on the basal plane. When the voltage is reduced to 1.17 V, this material expands and becomes about 100 nm thick. Below 0.9 V it covers the basal plane. It seems to be a soft material as the AFM tip drags it. This is in agreement with findings on the formation of polymers as one of the major constituents of the film [15, 30, 76, 89]. It has been found that the addition of crown ethers suppress the co-intercalation of solvated lithium into the graphite [8, 78, 81]. It was concluded that crown ethers are too large to be intercalated into the graphite layers. The solvated lithium ion in EC or PC is a large cation (not much smaller than the crown ether), containing four to five solvent molecules [88]. It is suggested that the intercalation of $Li(solv)_n^+$ follows a step in which it loses some of its solvated molecules and is adsorbed on the surface of the carbons, losing some of its charge:

$$Li(solv)_n^{+1} \rightarrow Li(solv)_{n-m}^{+(1-\partial)} + m(solv) \quad (5)$$

This pattern is similar to that for the formation process of ad-atoms in metal plating [90].

The smaller ion may intercalate faster into the graphite galleries. Reaction (5) may be the rate-determining step for the solvent co-intercalation process, and if so, molecules that form large and stable solvated lithium cations will have a smaller tendency for co-intercalation into the graphite.

In conclusion, it seems that solvents appropriate for lithium-ion batteries employing a graphite anode must have high solvation energy, high E^0, and high i_0 for reduction in order to slow the co-intercalation of the solvated ion, and to enhance the formation of the SEI at the most positive potential (far from the Li/Li^+ potential).

Another phenomenon which has practical importance, especially for large prismatic cells, is gas production during the first charge [91, 92]. There are two sources of gas: (1) the reduction of the electrolyte with the formation of methane or ethane, CO, and hydrogen; (2) replacement of gases adsorbed on the carbon by SEI-building materials during the formation of the SEI. Gases such as H_2, O_2, CO_2, N_2, and small organic molecules are released from the micropores of the carbon. The second source of gases is very significant in the use of disordered carbons but less important when graphite-like carbons are being used.

CosMX Exhibit 1008, Page 453 of 633

It was concluded [93, 94] that, on long cycling of the lithium-ion battery, the passivating layer on the carbon anode becomes thicker and more resistive, and is responsible, in part, for capacity loss.

6.3.3 Parameters Affecting Q_{IR}

It has been shown [8, 74, 76] that Q_{IR} is consumed mainly in the building of the SEI. However, for a variety of carbons and graphites, Q_{IR} may have other sources [6, 74] (Eq. (6):

$$Q_{IR} = Q_{SEI} + Q_{SP} + Q_U + Q_T \qquad (6)$$

where Q_{SEI} is the capacity needed for the formation of the SEI, Q_U is the unused capacity under specified experimental conditions (it is usable at low rates and high potentials), Q_{SP} is the capacity associated with the formation of soluble reduction products [6, 74], and Q_T is the capacity associated with the trapping of lithium inside the structure of the carbon, generally as a result of irreversible reaction with heteroatoms present on the inner surface of closed pores [70].

Q_{IR} depends on the electrolyte type (solvent and salts), the impurity level of the carbon and the electrolyte, the real surface area of the carbon including inner pores which the electrolyte can enter, the surface morphology, and the chemical composition of the carbon. It typically decreases in the order: powders > microbeads > fibers. Impurities such as acids and alcohols, water, or heavy metals may contaminate the SEI, causing side-reactions [1, 2] such as hydrogen evolution and electrolyte reduction; this results in larger Q_{IR} values [95, 96].

Since in many publications the impurity level in the carbons and electrolytes is not specified, it is difficult to correlate Q_{IR} reliably with the type of solvent or salt. However, it seems that in cases where the electrolyte reduction products are Li_2CO_3 and LiF (as in the cases when EC, CO_2, and fluorinated anions are used), Q_{IR} is lowest. We believe that controlled reduction-induced formation of nonconducting polymers (polyolefins) [6, 74] also suppresses Q_{IR}. Polymers have been reported to form on Li_xC_6 and on lithium in several electrolytes [15, 30, 89, 97].

One of the most important factors affecting Q_{SEI} [76, 78, 87] is graphite-anode exfoliation, as a result of intercalation of solvated lithium ions. Factors that are reported to decrease Q_{IR} are: increasing the EC content in organic carbonates or dioxolane solutions [98, 99]; addition of CO_2 [31, 87, 99] or crown ethers [8, 71, 78]; and increasing the current density [73] (this also lowers Q_{SE} [14] as a result of decrease in Q_{SP}).

Q_{SEI} is expected to depend, on the morphology of the carbon and should increase with the ratio of cross-sectional plane area to basal-plane area. This is suggested in view of the recent findings of Besenhard et al. [87], who reported on the penetration of the passivating layer into the graphite galleries through the cross-section planes, and Peled and co-workers [121], who found that the thickness of the SEI at the cross-sectional planes is greater than that at the basal plane (of an HOPG crystal).

Xing and Dahn recently reported [70] that Q_{IR} for disordered carbon and MCMB 2800 can be markedly reduced from about 180 and 30 $mAh\,g^{-1}$ to less than 50 and 10 $mAh\,g^{-1}$ respectively, when the carbon anode and cell assembly are made in an inert atmosphere and never come in contact with air. This indicates that these carbons contain nanopores that

CosMX Exhibit 1008, Page 454 of 633

are not accessible to the electrolyte but are permeable to O_2, CO_2, and H_2O. The absorption of these gases appears to be the dominant cause of the irreversible capacity [70]. The peaks at about 0.7 and 0.3 V vs. Li/Li^+ in dQ/dV curves are assigned to electrolyte reduction and reactions with COH and COOH groups respectively.

It is not clear why Q_{IR} is twice as large [6, 76, 96] (or more) in polymer electrolytes than it is in liquid electrolytes. This may result from larger Q_{SP} and larger Q_{SEI} due to partial exfoliation.

6.3.4 Graphite Modification by Mild Oxidation and Chemically Bonded (CB) SEI

We recently found [6,73–76] that mild air oxidation (burnoff) of two synthetic graphites and NG7 (natural graphite). improves their performance in Li/Li_xC_6 cells. The reversible capacity of the graphite (Q_R) increased (up to $405\,mAh\,g^{-1}$ at 4–11 percent burnoff), its irreversible capacity (Q_{IR}) was generally lower and the degradation rate of the Li_xC_6 electrode (in three different electrolytes) was much lower. STM images of these modified graphites show nanochannels having openings ranging from a few nanometers up to tens of nanometers (Fig. 7). It was suggested that these nanochannels are formed at the zig-zag and armchair faces between two adjacent crystallites and in the vicinity of defects and impurities. Performance improvement was attributed to the formation of SEIs chemically bonded to the surface carboxylic and oxide groups at the zig-zag and armchair faces (Fig. 8), better wetting by the electrolyte, and accommodation of extra lithium at the zig-zag, armchair, and other edge sites and nanovoids. This graphite modification,

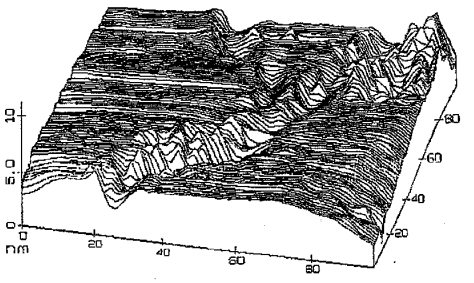


Figure 7. An STM image of an oxidized R-LibaD Lonza graphite (3 percent burnoff, 500 °C, 7.5 h) [25].

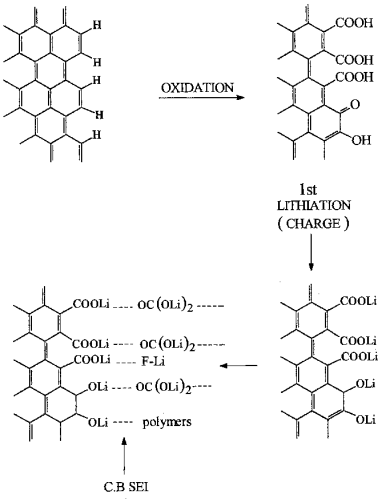


Figure 8. The formation of a chemically bonded SEI at the zig-zag and armchair faces (schematic presentation of an organic carbonate-based electrolyte) [25].

following mild burnoff, was found to make the Li_xC_6 electrode performance more reproducible and less sensitive to electrolyte impurities. The increase in capacity at 4–11 percent burnoff of NG7 was found to be associated with the formation of less than 1 percent void volume. XPS studies showed [75] that the surface atomic oxygen concentration of NG7 has a broad minimum at 4–22 percent burnoff (Fig. 9).

CosMX Exhibit 1008, Page 455 of 633

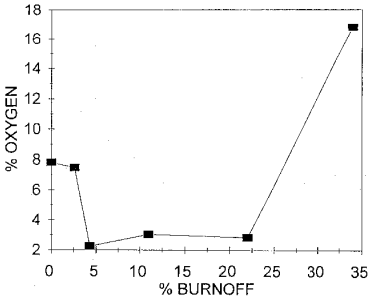


Figure 9. Effect of burnoff on surface oxygen content; natural graphite NG7 [39].

The oxygen peak maximum shifted monotonically with burnoff time, rising from 531.05 eV for pristine NG7 to 534.0 eV for a 34 percent burnoff sample. The analysis of XPS spectra by curve fitting is presented in Table 3.

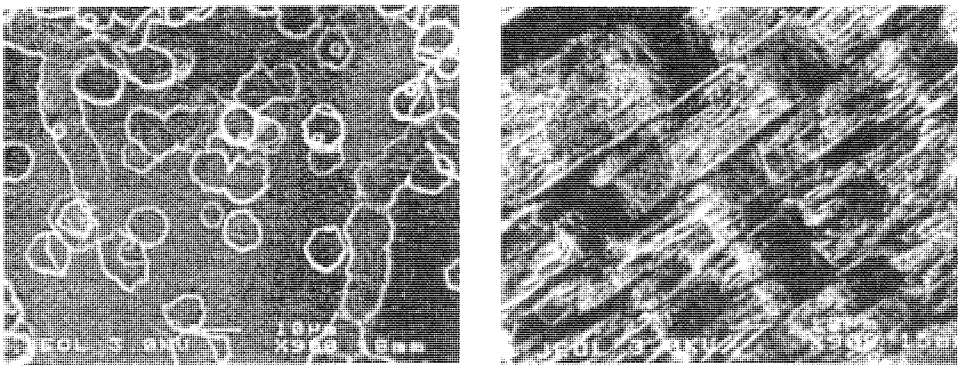
It can be seen that pristine NG7 surface contains mostly (53 percent) aromatic carbon, about 20 percent each of CH and COH groups—only 4.8 percent of CO groups, and no COOH groups. The 34 percent burnt sample consists of mostly CO groups (33 percent), C–OH groups (26.6 percent) and 8.9 percent of COOH groups.

It was recently found [100] that chemical oxidation of graphite powder by strong oxidizing agents such as ammonium peroxysulfate and hot concentrated nitric acid gave similar results, i.e., it suppresses Q_{IR} and enhances Q_R to 410–430 $mA\,hg^{-1}$. Following this wet oxidation, carboxyl groups were identified on the surface of the graphite. Takamura et al. found that heat treatment at 700 °C in the presence of acetylene black improved the performance of the graphite-fiber anode [101]. HOPG was used as a model electrode for studying separately the oxidation processes taking place on the basal and on the edge planes [121]. The mechanism of oxidation of the basal plane and that of the cross-section are entirely different (Fig. 10). Oxygen content on the cross-section rises with oxidation, while that on the basal plane drops from about 10 to 1 percent. This may correlate with the decrease in the ratio of edge planes to basal planes due to selective burning of the edge planes.

Table 3. Binding energies and fitting parameters of the C 1s curves for the pristine and 34 percent burnt samples [75]

Peak no.	Sample	Peak position (eV)	Peak shift (eV)	FWHM (eV)	Percentage of total	Peak assignment
1	Pristine	281.48	2.8	1.5	5.2	Hydrocarbons
	34%	281.5	2.6	1.6	4.1	
2	Pristine	283.0	1.3	2.1	15.4	Hydrocarbons
	34%	283.0	1.1	1.8	7	
3	Pristine	0	0.68	53	5.2	Aromatic carbon, C–C
	34%	0	0.63	13.4	4.1	
4	Pristine	285.2	0.9	2.1	19.5	C–OH
	34%	284.9	0.8	1.9	26.6	
5	Pristine	286.9	2.6	2.1	4.8	C = O
	34%	286.7	2.6	1.9	33.1	
6	Pristine	–	–	–	–	
	34%	288.2	4.1	1.9	8.9	O = C –OH
7	Pristine	290.2	5.9	2.2	2.1	Shake-up
	34%	290.1	6.0	2.2	6.8	Satellite

CosMX Exhibit 1008, Page 456 of 633



(a) (b)

Figure 10. SEM micrographs of HOPG after burning at 650 °C; magnification, ×900 . (a) basal plane 2 percent burnoff; (b) cross-section 4 percent burnoff [10].

6.3.5 Chemical Composition and Morphology of the SEI

6.3.5.1 Carbons and Graphites

The chemical composition of the SEI formed on carbonaceous anodes is, in general, similar to that formed on metallic lithium or inert electrodes. However some differences are expected as a result of the variety of chemical compositions and morphologies of carbon surfaces, each of which can affect the i_0 value for the various reduction reactions differently. Another factor, when dealing with graphite, is solvent co-intercalation. Assuming Li_2CO_3 to be a major SEI building material, the thickness of the SEI was estimated to be about 45 Å [71].

The anodic behavior of carbon materials, such as acetylene black, activated carbon, and vapor-grown carbon fiber, in $LiClO_4$/PC solution was studied by Yamamoto et al. [102]. Irreversible reactions, including gas evolution and disintegration, were mainly observed on that part of the surface occupied by the edge planes of the graphite. XRD measurements indicated that these reactions were the decomposition of the electrolyte, leading to the formation of Li_2CO_3. The surface reactions on the carbon-fiber electrodes in LiX/PC–DME solution have been investigated by XRD, XPS and differential scanning calormetry–thermogravimetric analysis (DSC–TGA) methods [103]. According to this work, the reaction during the first charge, which includes solvent co-intercalation, can proceed by more than two mechanisms, with different kinetics. The mechanism was found to depend on the electrolyte composition and discharge-current density. Aurbach and co-workers [81, 82] carried out an extensive electrochemical and spectroscopic study of carbon electrodes in lithium-battery systems. The carbons investigated included carbon black, graphite and carbon fibers. The solvents MF, PC, EC, THF, DME, 1,3-dioxolane, and their mixtures were used. The salts tested were $LiClO_4$, $LiAsF_6$, and $LiBF_4$. It was found that the first charging of carbon with lithium is accompanied by irreversible solvent and salt reduction and this is followed by coating of

CosMX Exhibit 1008, Page 457 of 633

the carbon surface with passivating films. These films are similar in their chemical structure to those formed on lithium in the same solutions. Thus, PC is reduced on carbon to $ROCO_2Li$, ethers are reduced to alkoxides, MF to lithium formate. $LiAsF_6$ is reduced to LiF and AsF_3, and further to insoluble Li_xAsF_y (Fig. 1). IR spectra of graphite-EPDM electrodes cycled in $LiClO_4$–MF solution seem to prove the existence of $LiClO_3$, $LiClO_2$ or LiClO. CO_2 reacts with Li_xC_6 to form Li_2CO_2 (and probably CO). Because of the high surface area of graphite particles as compared with the lithium–metal electrode, the role of contaminants, such as HF in $LiPF_6$-and $LiBF_4$-based electrolytes, is much less pronounced [104]. Disordered or graphitized carbons with turbostratic structure were shown to be less sensitive to the solution composition Aurbach and coworkers [81, 82] emphasized that the most important aspect of the optimization of lithium-ion batteries is the modification of the surface chemistry of carbon by the proper electrolyte additives (e.g., CO_2, crown ethers) which form better passivating layers and/or prevent solvent intercalation. The beneficial effect of inorganic additives, such as CO_2, N_2O, S_x^{2-} etc., on the formation of SEI on carbons was also emphasized by Besenhard et al. [105]. Tibbets et al. [106] showed that oxidative pretreatment of vapor-grown carbon fibers (VGCFs) can reduce the capacity of SEI building in $LiClO_4$/PC electrolyte by an order of magnitude. Their experiments confirm the idea that air etching removes the more active carbon atoms — those capable of decomposing the electrolyte — and completely alters the fiber morphology.

Ein-Eli et al. [107] showed that the use of SO_2 as an additive to $LiAsF_6$/MF or $LiAsF_6$/PC–DEC–DMC solutions offers the advantage of forming fully developed passive films on graphite at a potential much higher (2.7 V vs. Li/Li^+) than that of electrolyte reduction (<2 V vs. Li/Li^+) or of lithium intercalation (0.3 to 0 V vs. Li/Li^+). They claimed that the major surface species are organic lithium alkylcarbonates ($ROCO_2Li$) and inorganic lithium salts (Li_xAsF_y, Li_2CO_3, Li_2S O_2O_4, Li_2SO_3, $Li_2S_2O_5$, and Li_2S). The predominating surface reactions in $LiAsF_6$/MF–EC electrolytes contaminated with water [108] result in the formation of insoluble lithium alkylcarbonates, Li_2O and LiOH (Fig. 1). EDX analysis of the surface film formed on mesocarbon-derived carbon fibers in $LiBF_4$/EC–PC–DME solution [109] indicated that the film is composed of C, F, B, and O. SEM measurements showed that the lithiated carbon fibers cohere as a result of the formation of a passivating film [109]. An unstable passivating layer on petroleum coke in Li triflate/EC–PC–DMC, followed by interaction between the electrolyte and the intercalated lithium was observed by Jean et al. [110]. The increased stability of lithium–carbon electrodes in EC-containing electrolytes [87] was related to inorganic films formed via secondary chemical decomposition of electrochemically formed EC–graphite-intercalation compounds. Using cyclic voltammetry, Inaba et al. [84] found that for graphite electrodes, an EC–DEC solvent mixture is preferred over EC–DME with respect to the formation of a stable passivating film. When graphite electrodes are charged in PC-based solutions, the solvent decomposes at about 1 V, and this makes SEI formation difficult. It was shown [77] that $LiBF_4$ is more reactive than $LiPF_6$ towards an Li_xC_6 anode. A lithium-ion battery based on $LiPF_6$/EC-DEC (7:3) electrolyte [111] underwent more than 300 stable charge–discharge

CosMX Exhibit 1008, Page 458 of 633

cycles. However an increase of cell resistance from 1.5 to $3.5\,k\Omega cm^2$ was observed on cycling, and this was attributed to the decomposition of electrolyte.

Lithium intercalation into graphite was studied by Morita et al. [112], who used XRD and electrochemical quartz-crystal-microbalance techniques. The XRD pattern of the graphite electrode after cathodic polarization in $LiClO_4$/EC–DMC solution shows a spectrum that is more complicated than that for an electrode polarized in EC–PC mixture. The diffraction angles observed do not correspond exactly to the values expected from any idealized stage structure of Li_xC_6. Changes in the resonance frequency of the graphite-coated quartz crystal showed that the cathodic intercalation of lithium is accompanied by electrochemical decomposition of the electrolyte The mass change per coulomb over the potential range of 0.0–0.2 V vs. Li/Li^+ was higher in EC–DMC than in EC–PC, indicating different surface reactions.

Lithium carbonate and hydrocarbon were identified in XPS spectra of graphite electrodes after the first cycle in $LiPF_6$/EC–DMC electrolyte [104]. Electrochemical QCMB experiments in $LiAsF_6$/EC–DEC solution [99] clearly indicated the formation of a surface film at about 1.5 V vs. (Li/Li^+). However the values of mass accumulation per mole of electrons transferred (m.p.e), calculated for the surface species, were smaller than those of the expected surface compounds (mainly $(CH_2OCO_2Li)_2$). This was attributed to the low stability of the SEI and its partial dissolution.

6.3.5.2 HOPG

HOPG was used as a model electrode to study separately the formation of the SEI on the basal and cross-section planes [121]. The cross-section planes of HOPG consist of both zig-zag and armchair planes. Carbon atoms on these two planes are considered to be much more active than carbon atoms on the basal plane [66, 68, 74, 75]. There are therefore, expected to be different SEI compositions on these planes.

Table 4. XPS measurements of HOPG after one cycle in $1.2\,mol\,L^{-1}$ $LiAsF_6$/EC–DEC electrolyte

Element	Cross-section(%)	Basal(%)
C	40.27	63.51
O	23.40	17.16
F	14.46	4.71
Li	19.52	12.10
As	2.35	0.87

Table 4 presents the SEI elemental composition on both basal and cross section planes as measured by XPS, after forming in $1.2\,mol\,L^{-1}$ $LiAsF_6$/EC:DEC (1:2). For light atoms, the XPS detection depth is about five to ten atomic layers, so Table 4 reflects the composition of the SEI which was exposed to the electrolyte. It is clear that the SEI on the cross section is rich in inorganic components (Li, F, O, As), while that on the basal plane is rich in carbon compounds. Detailed analysis of the XPS spectra for C, O, As, F, and Li at different sputtering times, together with atomic accounting, leads [121] to the formation of an estimated depth profile for the SEI materials (Fig. 11). As the vacuum in the XPS instrument is about 10^{-10} Torr, it was concluded that the hydrocarbons found in the SEI are actually polymers (polyolefins). We believe that the hydrocarbons reported by Takehara to be present in the SEI lithium [26–28] are also polymers (for the same reason). This conclusion is in agree of ment with a number of authors [6, 15, 30, 74, 89, 97] who reported on the

CosMX Exhibit 1008, Page 459 of 633

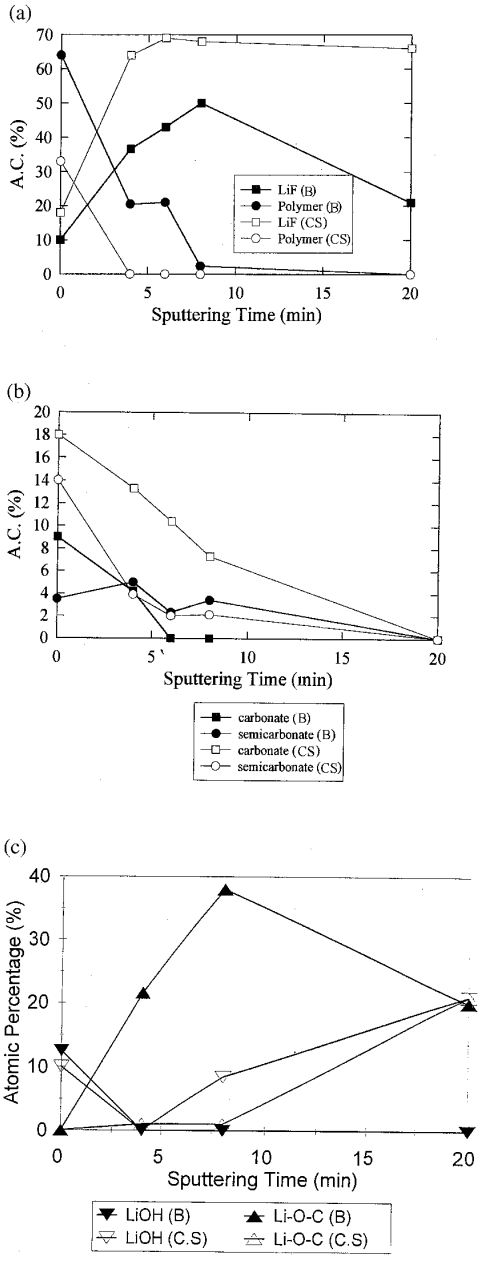


Figure 11. Depth profile of estimated SEI composition on the basal (B) and cross section (CS) plane of HOPG, 1.2 mol L^{-1} $LiAsF_6$ / EC–DEC (1:2) (Chapter III Sec. 2).

formation of polymers on the surface of lithium or lithium amalgam. It was concluded [121] that at the basal plane reduction of the solvents is more pronounced, and this causes the surface of the SEI to contain about 60 percent polymers, while at the cross-section the SEI is formed by the reduction products of the salt anion (AsF_6^-). The thickness of the SEI on the cross-section planes is larger than that on the basal plane. This is in agreement with Besenhard's [87] conclusion that the film penetrates into the graphite galleries as a result of co-intercalation of solvent molecules. Additional support for this is our finding of much carbonate material on the cross section plane (after 8min of sputtering), but none on the basal plane (Fig. 11). The bulk of the SEI on both planes consists mainly of LiF (60–80 percent) and carbonates (more carbonates on the cross-section planes) (Fig. 11) [121]. The SEI composition is in agreement with thermodynamics: at the carbon/SEI interphase we found fully reduced anions (Fig. 11) [121], such as Li_2O, LiF, and As, whereas on the solution side we found partially reduced materials: semicarbonates, polymers, AsO_x, and AsF_3 (as well as LiF). The cross-section SEI contains very few Li–O–C groups, but on the basal plane they constitute up to 40 percent of the surface. The cross-section SEI has a very strong As XPS peak at 48 eV which is absent from the basal plane (it may be assigned to some AsO_xF_y compounds). Considering the sputtering depth profiles, it must be noted that the sputtering yield is not the same for all materials; organic and thermally unstable materials may have higher sputtering rates. These findings are in agreement with EDS measurements of the SEI on NG7 formed in the same electrolyte [122]. The SEI on the basal plane of a single graphite flake consists of less F, As, and O when

CosMX Exhibit 1008, Page 460 of 633

compared with the content of a large sample area (200 μm × 200 μm) which contains both basal and cross-section planes. The SEI on oxidized HOPG seems to be thinner [122] than that on pristine HOPG.

6.3.6 SEI Formation on Alloys

The processes taking place in the first intercalation of lithium into an alloy anode in a lithium-ion battery assembled in the discharged state are expected to be very similar to those in a disordered-carbon anode. The intercalation of lithium into the alloy proceeds in parallel with the reduction of the electrolytes and the building of the SEI. However, because of the dependence of i_0 on the catalytic nature of the alloy, the chemical composition and the morphology of the SEI may vary from alloy to alloy. A problem unique to lithium-alloy anodes is the high degree of expansion and contraction during charge-discharge cycles. This may result in shorter cycle life and lower faradaic efficiency as a result of the formation of cracks in both the alloy and the SEI. Therefore, in this case the flexibility of the SEI is highly important. Besenhard et al. [114] recently showed that when thin alloy layers are used, a longer cycle life can be achieved. Yoshio et al. [115] applied for a patent which covers tin oxide-based materials which on the first intercalation are likely to turn into lithium-tin alloys [116]. It seems that lithium alloys in the form of (probably disordered) small particles may be potential candidates for high-capacity anodes (as a replacement for carbon anodes) in lithium-ion batteries.

6.4 Models for SEI Electrodes

6.4.1 Liquid Electrolytes

In the first papers dealing with SEI electrodes it was suggested that the passivating layer consists of one or two layers [1, 2]. The first one (the SEI) is thin and compact; the second (if it exists), on top of the SEI, is a more porous, or structurally open, layer that suppresses the mass transport of ions in the electrolyte filling the pores of this layer.

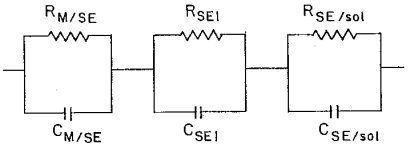


Figure 12. Equivalent circuit for the SEI electrode [1, 2].

According to this model, the SEI is made of ordered or disordered crystals that are thermodynamically stable with respect to lithium. The grain boundaries (parallel to the current lines) of these crystals make a significant contribution to the conduction of ions in the SEI [1, 2]. It was suggested that the equivalent circuit for the SEI consists of three parallel *RC* circuits in series combination (Fig. 12). Later, Thevenin and Muller [29] suggested several modifications to the SEI model:

(1) the polymer electrolyte interphase (PEI) model, in which the lithium in PC electrolyte is covered with a PEI which consists of a mixture of Li_2CO_3, $P(PO)_x$ and, $LiClO_4$, where $P(PO)_x$ is polypropylene

CosMX Exhibit 1008, Page 461 of 633

oxide, formed by reduction-induced polymerization of PC

(2) the solid–polymer-layer (SPL) model, where the surface layer is assumed to consist of solid compounds dispersed in the polymer electrolyte;

(3) the compact-stratified-layer (CSL) model, in which the surface layer is assumed to consist of two sublayers; the first layer on the electrode surface is the SEI, while the second layer is either the SEI or the PEI.

The first two models are irrelevant to lithium-battery systems since the PEIs are not thermodynamically stable with respect to lithium. Perchlorate (and other anions but not halides) were found to be reduced to LiCl [15, 16, 22–27]. It is commonly accepted that in lithium batteries the anode is covered by SEI which consists of thermodynamically stable anions (such as O^{2-}, S^{2-}, halides). Recently, Aurbach and Zaban [25] suggested an SEI which consists of five different consecutive layers. They represented this model by a series of five parallel *RC* circuits representing the capacitance and resistance of each layer. Some of these layers have a thickness of only a few ångstroms, a fact which makes it difficult to assign physical properties such as dielectric constant ε, ionic conductivity, energy of activation, etc. In addition, between each two adjacent layers there is an interface which must be represented by another *RC* circuit. Thus a model which consists of three different layers with two interfaces seems to be more appropriate to their AC data.

It is well known today that the SEI on both lithium and carbonaceous electrodes consists of many different materials including LiF, Li_2CO_3, $LiCO_2R$, Li_2O, lithium alkoxides, nonconductive polymers, and more. These materials form simultaneously and precipitate on the electrode as a mosaic of microphases [5, 6]. These phases may, under certain conditions, form separate layers, but in general it is more appropriate to treat them as heteropolymicrophases. We believe that Fig. 13(a) is the most accurate representation of the SEI.

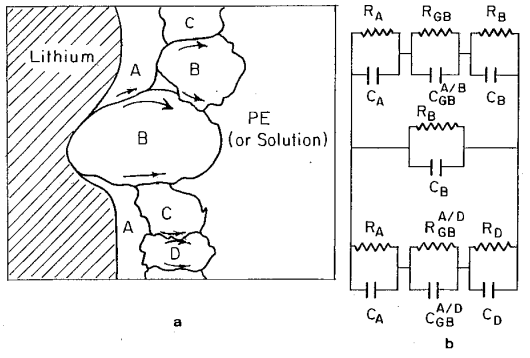


Figure 13. Schematic presentation of a small segment of polyheteromicrophase SEI (a) and its equivalent circuit (b):A, native oxide film; B, LiF or LiCl; C, non conducting polymer; D, Li_2CO_3 or $LiCO_3R$; GB, grain boundary. R_A, R_B, R_D, ionic resistance of microphase A, B, D. $R_{GB}^{A/B}, R_{GB}^{A/D}$ charge-transfer resistances at the grain boundary of A to B or A to D, respectively. C_A, C_B, C_D SEI capacitance for each of the particles A to D. $C_{GB}^{A/B}, C_{GB}^{A/D}$, grain boundary (dl) capacitance for A/B and A/D interfaces.

CosMX Exhibit 1008, Page 462 of 633

The equivalent circuit of a section of this SEI is presented in Fig. 13(b). It was recently found [123, 124] that at temperatures lower than 90 °C, the grain-boundary resistance of composite polymer electrolytes and composite solid electrolytes based on LiI–Al_2O_3 is many times larger than their ionic resistance. At 30 °C R_{GB} is several orders of magnitude larger than R_B (the ionic resistance) and for 100 μm-thick CPE foils or LiI–Al_2O_3 pellets it reaches [125] 10^5–$10^6\,\Omega cm^2$ (depending on CPE composition).

A value of R_{GB} for an SEI 10nm thick can be estimated from its values for CPE and CSE by assuming that these solid electrolytes consist of nanometer-sized particles. Thus the expected value for R_{GB} at 30 °C for a 10nm SEI is in the range $10–100\,\Omega cm^2$, i.e., it cannot be neglected. In some cases it may be larger than the ionic (bulk) resistance of the SEI. This calculation leads us to the conclusion that R_{GB} and C_{GB} must be included in the equivalent circuits of the SEI, for both metallic lithium and for Li_xC_6 electrodes. The equivalent circuit for a mosaic-type SEI electrode is extremely complex and must be represented by a very large number of series and parallel distributions of parallel *RC* elements (Fig. 13b). Since the exact composition, size, and distribution of these particles are generally unknown, we prefer to make the following approximations [5, 6]: the contributions R_B of all particles (in the same sublayer) are combined in one term— the apparent SEI ionic resistance, R_{SEI} — and the values R_{GB} of all the particles in the same sublayer are combined into another term— the apparent R_{GB} of the sublayer [125]. The same is done for C_{SEI} and C_{GB}, and the result is the equivalent circuit shown in Fig. 14 representing a two-sublayer (SL) SEI [125]. $C_{E/SE}$, $C_{1/2}$, and $C_{SE/sol}$ are the double-layer capacitances between, respectively, the following pairs of phases: electrode/solid electrolyte, sublayer-1/sublayer-2, and solid electrolyte/solution (or battery electrolyte). R_{CT1}, $R_{1/2}$, R_{CT2} are the charge-transfer resistance between the pairs of phases mentioned above. *W* represents the Warburg impedance on the solution side of the SEI electrode.

In many cases, the Nyquist plot for SEI electrodes consists of only one, almost perfect, semicircle whose diameter increases with storage time (and a Warburg section at low frequencies). For these cases the following can be concluded: the SEI consists of only one sublayer, R_{CT1}, R_{GB} and $R_{CT2} << R_{SEI}$; C_{GB}, $C_{SE/sol}$, and $C_{E/SE} >> C_{SEI}$. Under these conditions the SEI can be represented by a single *RC* element–R_{SEI} and C_{SEI} (and the Warburg element). In other cases, aside from the Warburg section, the Nyquist plot can consist of two semicircles [126, 128, 142], many semicircles [20, 25, 128], or a shallow arc [127]. For these cases, the equivalent circuit of Fig. 14 or a similar one should be considered.

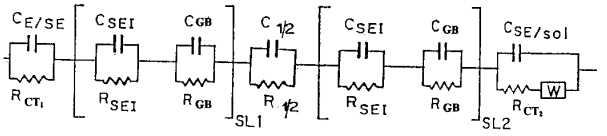


Figure14. Equivalent circuit for two sublayer polyheteromicrophase SEI (for notation, see text) [125].

CosMX Exhibit 1008, Page 463 of 633

6.4.2 Polymer Electrolytes

The major differences between polymer and liquid electrolytes result from the physical stiffness of the PE. PEs are either hard-to-soft solids, or a combination of solid and molten in phases equilibrium. As a result, wetting and contact problems are to be expected at the Li/PE interface. In addition, the replacement of the native oxide layer covering the lithium, under the PE and its impurities.

Figure 15 [6] schematically represents the Li/PE interphase. Solid PEs have a rough surface, so when they are in contact with lithium, some spikes, like "2" in Fig. 15, penetrate the oxide layer and the lithium metal, and a fresh SEI is formed at the Li/PE interface. In other parts of the interface, softer contacts between the PE and lithium are formed ("1" and "3" in Fig. 15). Here the fresh SEI forms on the native

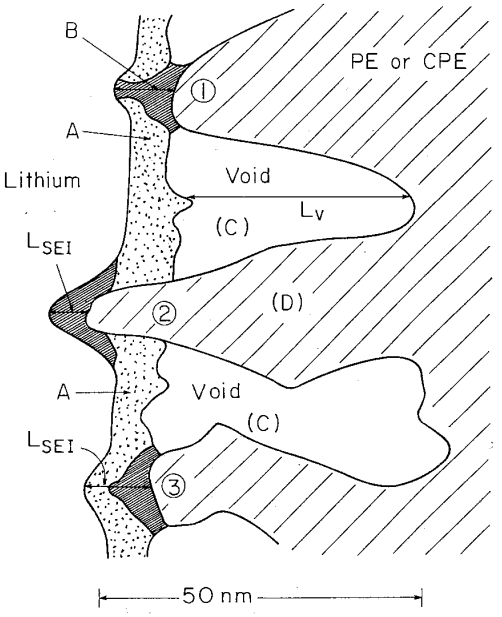


Figure 15. Schematic presentation of the Li/Pe interphase [5, 6]; A, native oxide film; B, freshly formed SEI; C, void; D, PE (solid)

OCV conditions, by a newly formed SEI is expected to be a slow process. The SEI is necessary in PE systems in order to prevent the entry of solvated electrons to the electrolyte and to minimize the direct reaction between the lithium anode and the electrolyte. SEI-free Li/PE batteries are not practical. The SEI cannot be a pure polymer, but must consist of thermodynamically stable inorganic reduction products of oxide layer or, as a result of the retreat of lithium during its corrosion, the native oxide layer breaks and the gap is filled by a fresh SEI ("1" in Fig. 15). The net result is that only a fraction (θ) of the lithium surface is in intimate contact with the PE. The situation in composite solid electrolytes (CPEs) is more severe because of their greater stiffness. This complex morphology of the Li/PE and Li/CPE inter-

CosMX Exhibit 1008, Page 464 of 633

faces causes difficulties in measuring SEI and PE properties such as conductivity and energy of activation for conduction, and also in the interpretation of the results. As θ changes with temperature, stack pressure, the preparation process for the PE, and the morphology of the native lithium surface film, there is often disagreement between measurements taken in different laboratories for the same PE.

For simplicity we assume here that $R_{GB} = 0$ and there is only one sublayer in the SEI. In this case, the SEI resistance (R_{SEI}) is given by $R_{SEI} = R^0_{SEI}/\theta$ where R^0_{SEI} is the value for $\theta = 1$. The SEI capacitance (C_{SEI}) is given, to a first approximation, by $C_{SEI} = \theta C^0_{SEI}$ where C^0_{SEI} is the capacitance for $\theta = 1$.

For $\theta = 1$ the apparent thickness of the SEI (L^0_{SEI}) can be calculated from Eq. (7),

$$L^0_{SEI} = \frac{\varepsilon\varepsilon_0 A}{C^0_{SEI}} \tag{7}$$

where A is the electrode area, ε is the dielectric constant of the SEI and ε_0 is the dielectric constant of a vacuum. Substituting the experimental C_{SEI} values gives $L_{SEI} = L^0_{SEI}/\theta$. However, it is difficult to determine both θ and L^0_{SEI} simultaneously.

At temperatures above or near the eutectic temperature of the polymer phase, C_{SEI} values are typically in the range of 0.1–2 $\mu F cm^{-2}$ [5]. However, for stiff CPEs or below this temperature, C_{SEI} can be as low as $0.001\,\mu F cm^{-2}$ (Fig. 16). When a CPE is cooled from 100 °C to 50 °C, the C_{SEI} falls by a factor of 2–3, and on reheating to 100 °C it returns to its previous value. This is an indication of void formation at the Li/CPE interface. As a result, the apparent energy of activation for ionic conduction in the SEI cannot be calculated from Arrhenius plots of $1/R_{SEI}$ but rather from Arrhenius plots of σ_{SEI}

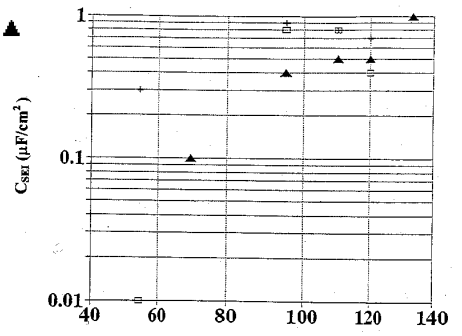


Figure 16. Temperature dependence of C_{SEI} in Li/CPE cell [5]. LiI/P(EO)$_n$ –9% Al_2O_3: 1, (+) n=9,; 2, (□) n=2.5; 3, (▲) n=6.

(the apparent conductivity of the SEI), which to a first approximation, does not depend on θ. This approximation is based on the assumption that the heights of the voids (L_V in Fig. 15) are much greater than the thickness of the SEI:

$$\sigma_{SEI} = (L/R)_{SEI} = ((\varepsilon_0 \varepsilon A/RC^0\theta))_{SEI} = \varepsilon_0 \varepsilon A/C^0_{SEI}R^0_{SEI} \tag{8}$$

Similar contact problems are expected at the PE/carbon interface, where the wetting of the carbon by the PE is of crucial importance [128, 129].

6.4.3 Effect of Electrolyte Composition on SEI Properties

6.4.3.1 Lithium Electrode

The properties of SEI electrodes, the growth rate of the SEI, the mechanism of dissolution and deposition, and the effects of various factors on SEI conductivity have been addressed elsewhere [1, 2]; space limitations do not permit their repetition here.

CosMX Exhibit 1008, Page 465 of 633

A comparison of the SEI properties on bare lithium in four electrolytes, $LiClO_4$/PC, $LiClO_4$/PC–DME, $LiAsF_6$/EC–2Me-THF, and $LiAsF_6$/THF–2Me-THF, was made by Montesperelli et al. [32] using impedance spectroscopy. The resistance of the passivation film in $LiAsF_6$-based solutions was found to be twice as large as in $LiClO_4$ electrolyte after 10 days of storage. High values of R_{film} (~45 Ωcm^2) in THF-containing electrolyte were explained by the high reactivity of this solvent towards lithium, followed by the formation of a thick (~220 Å) surface film . The impedance spectra of the lithium electrode in $LiPF_6$ electrolyte were analyzed by Takami and Ohsaki [126]. The two semicircles in the impedance spectra have been interpreted as resulting from two kinds of passivating film. The formation of the first film is considered to be closely related to decomposition of the PF_6^- anion, which should lead to a thick outer passivation film, probably consisting of LiF [22]. It was found that the most effective solvent for decreasing the film resistance is an EC–2Me-THF mixed solvent. This may result from enrichment of the SEI with Li_2CO_3. It was found [22] that the SEI in $LiPF_6/\gamma$-BL electrolyte is much thinner than those formed in $LiAsF_6$, $LiClO_4$, and $LiBF_4/\gamma$-BL-based electrolytes. The SEI thickness was found to be less than a few tens of Ångstroms in $LiPF_6/\gamma$-BL, while for other electrolytes it exceeds 200 Å. Moreover, the film formed in the $LiPF_6$-containing electrolyte was very uniform and sufficiently compact. The thickness of the lithium surface layer in a lithium perchlorate/propylene carbonate solution, calculated from the apparent resistance according to the CSL interface model, was found to increase exponentially with storage time from 100 to 1000 Å [29]. The values are in good agreement with those deduced from ellipsometric measurements [33].

The order of the interfacial resistance of the SEI on lithium covered by native film in 1 mol L^{-1} LiX/PC solutions was determined by Aurbach and Zaban [20; 25] from Nyquist plots. For the different salts, the order of R_{SEI} was: $LiPF_6$ >> $LiBF_4$ > $LiSO_3CF_3$ >> $LiAsF_6$ > $LiN(SO_2CF_3)_2$ > LiBr, $LiClO_4$ [20]. The values for $LiPF_6$/PC and $LiN(SO_2CF_3)_2$/PC were about 800 and 23 Ωcm^2, respectively. The resistivity of the film was found to be directly proportional to the salt concentration, and the presence of CO_2 in solutions considerably reduced the interfacial resistance.

In PC-based electrolytes, inorganic ions like Mg^{2+}, Zn^{2+}, In^{3+}, and Ga^{3+} form thin layers of lithium alloys at the electrode surface during cathodic deposition of lithium, and the resulting thin films suppress the dendritic deposition of lithium that causes the lowering of the coulombic efficiencies in the charge–discharge cycles [36, 39–41]. The Li–Sn electrode shows the greatest increase in interfacial resistance with immersion time and has a double–layer capacitance–C_{dl}, between 0.03 and 0.08 mF [39]. The most stable and lowest interfacial resistance (80–100 Ù cm^2) was observed with the Li–3 percent (w/w) Al alloy electrode. The SEI resistance decreased in the order: no additive>LiI>SnI_2>AlI_3 ≅ AlI_3–2MeF. For systems containing AlI_3 in particular, the film resistance was low (5Ω), almost constant, and independent of the cycle number.

The interfacial phenomena in LiX/PE systems were studied extensively by Scrosati and co-workers [3, 53, 130]. They found that the high-frequency semicircle in the impedance spectrum of $LiClO_4$/$P(EO)_8$ electrolyte (EO = ethylene oxide),

CosMX Exhibit 1008, Page 466 of 633

which is attributed to the interfacial resistance, is often irregularly shaped and seems to contain an additional arc. The authors suggested that this impedance response is based on more than one relaxation phenomenon. The resistance of the passivation film was found to increase continuously upon storage, reaching a value three orders of magnitude higher than the initial resistance ($10^5\,\Omega$). In some cases, film growth leads to the blocking of lithium ion-transport and to the almost complete inactivity of the polymer cell. The progressive decay of capacitance from 0.65 to 0.5 μF in the initial stage of film evolution during 100 h of storage was associated with the increase of film thickness. Hiratani et al. [131] postulated that the interfacial–impedance semicircle in the lithium/solid electrolyte system corresponds to two main processes: the ionic conduction of the interphase film and the charge-transfer process ($Li^+ + e \rightarrow Li$). The increase of interfacial resistance throughout the temperature cycle (heating–cooling) was time-independent and explained by a reduction in the contact area. This is in good agreement with other results [5, 6]. A study was made of the passivation of metallic lithium in contact with poly(ethylene oxide)-based polymer electrolytes as a function of the nature and concentration of the salt ($LiClO_4$, $LiCF_3SO_3$, $LiAsF_6$, LiI), time, temperature, and current density [46, 47]. The $LiCF_3SO_3$ $P(EO)_n$, based electrolytes, with $\infty > n > 4$, show similar behavior, where the increase in R_{SEI} is proportional to the growth of the film with time. However, at low salt concentrations for single-phase PE composition, the apparent activation energy of ionic conduction in SEI ($E_{A,SEI}$) did not exceed 0.65 eV, while at high salt concentrations ($n<20$) for the two-phase electrolyte, $E_{A,SEI}$ rose to 0.78 eV. Sloop and Lerner [132] showed that SEI formation can be affected by treatment of the cross–linked polymer, poly–[oxymethylene oligo(oxyethylene)] (PEM) with an alkylating agent. Cross–linked films of PEM do not form a stable interface with lithium; however, upon treatment with methyl iodide, R_{SEI} stabilizes at 2000 $\Omega\,cm^{-1}$. Such an SEI is characterized by low conductivity, from 10^{-12} to 10^{-8} $\Omega^{-1}cm^2$, which is linear over the temperature range of 25–85 °C.

Composite polymer electrolytes (CPEs), containing various inorganic fillers, show a trend of impedance behavior quantitatively similar to that of pure LiX–PEO electrolytes. However, the growth rate of the passive film and the capacitance changes were found to be considerably lower in CPEs. Addition of $LiAlO_2$ [130], Al_2O_3, MgO, SiO_2 [50, 53, 49, 133], Li_3N, or zeolite [134] improves SEI stability. Kumar et al. [51] reported suppression of the charge-transfer resistance by a factor of three when glass powder (composition: $0.4\,B_2O_3$, $4Li_2O$, $0.2Li_2SO_4$) was added to the $LiBF_4/P(EO)_n$ electrolyte. It was shown [135] that glass–polymer, composite (GPC) electrolytes, prepared by mixing and grinding 87 percent (v/v), of $0.56Li_2S$, $0.19B_2S_3$, 0.25 LiI glass powder with 13 percent (v/v) Li imide/$P(EO)_6$, appear to be stable with respect to lithium and Li_xC_6 electrodes, since the interfacial impedances are relatively constant (60 and 30 Ω, respectively) at 70 °C for up to 375 h. The lithium/polymer electrolyte interface is extremely sensitive to the amount of water absorbed in the $LiClO_4$/ poly[oxymethylene-oligo(oxyethylene)] electrolyte [136].

An extensive study of the fundamental processes taking place in Li/CPE inter-

CosMX Exhibit 1008, Page 467 of 633

phases and the properties of the SEI was made by Peled and co-workers [5, 6, 49, 125, 137, 138]. It was found that the use of a thermodynamically stable anion like I^- or Br^- and fine Al_2O_3 or MgO powders resulted in very stable Li/CPE (n>3) and Li/CSE ($n \leq 3$) interphases. The maximum value of R_{SEI} in LiI/P(EO)$_9$P(MMA)$_{0.5}$EC$_1$ 9 percent Al_2O_3 or MgO electrolytes was $8\,\Omega cm^2$ at 120 °C. The apparent thickness (L_{SEI}) of the SEI did not exceed 120 Å, and remained constant or decreased slightly during 1800 h of storage at 120 °C. The SEI conductivity in some cases was stable and in others decreased with storage at elevated temperatures. This was explained by composition changes or recrystallization of the SEI particles to yield a more ordered and less conductive film, as found previously [1, 2] for nonaqueous solutions. In another test, an Li/CPE/Li cell was stored for over 3000 h with almost no change in R_{SEI}. At temperatures above or near the eutectic temperature of the polymer electrolyte, C_{SEI} values were in the range 0.1–2 $\mu F cm^{-2}$. However, below this temperature or for CSEs, which are stiffer than CPEs, the SEI capacitance could be as low as $0.001\,\mu F cm^{-2}$. The conductivity of the SEI (σ_{SEI}) was found to be three to four orders of magnitude lower than that of the CPE and did not change much with the salt concentration [5]. The replacement of Al_2O_3 by MgO, or LiI by LiBr, had little effect on σ_{SEI}. However, both changes result in a severe decrease in C_{SEI}, probably due to the stiffness of these CPEs. The apparent energy for ionic conduction in the SEI measured at 130 °C > T > 60 °C was found to be 7–11 $kcal mol^{-1}$. The addition of copolymers such as poly(butyl acrylate) (PBA) and poly(methyl acrylate) (PMA) and the variation of the EO:Li ratio from 6:1 to 10:1 were found to have some effect on the SEI properties. In general, C_{SEI} increases and R_{SEI} decreases with increasing organic content of the CPE. The stiffer CPE, which contained PBA, had the highest SEI resistance (due to low θ values), and the lowest conductivity.

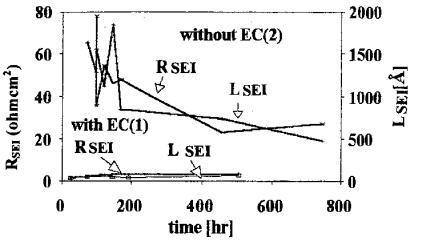


Figure 17. Effect of EC on the apparent thickness and stability of SEI [6]. CPE composition:
(1) LiI/P(EO)$_9$P(MMA)$_{0.5}$(EC)$_2$ + 6%(v/v)Al_2O_3
(2) LiI/P(EO)$_9$P(MMA)$_{0.5}$ + 6%(v/v)Al_2O_3

Figure 17 presents the effect of EC and PEGMDE on the Li/CPE interphase. The addition of EC was followed by a decrease by one order of magnitude in R_{SEI} and L_{SEI}. Both R_{SEI} and L_{SEI} were stable for over 500 h of storage at 120 °C. Similar behavior was observed in CPEs containing PEGDME with a molecular weight of 500 and 2000. High SEI stability was achieved in these electrolytes for 1200 h of storage. The positive effect of plasticizers may result from better wetting of the lithium metal by the PE, i.e., an increase in the contact area. In addition, the formation of a thin and stable SEI composed mainly of lithium carbonate is expected in CPE containing EC.

The interfacial properties of gel electrolytes containing ethylene carbonate immobilized in a polyacrylonitrile (PAN) matrix with a lithium (bis)trifluoromethane sulfonimide (LiTFSI) salt have been studied [139]. SEI stability appeared to be strongly dependent on the LiTFSI concentration. A minimum value of R_{SEI} of about 1000 Ωcm^2 was obtained after 200h

CosMX Exhibit 1008, Page 468 of 633

of storage of an electrolyte containing 14 percent salt. This value was doubled after 1000 h of storage; however, for 9 and 18 percent LiTFSI electrolytes, a sixfold increase of R_{SEI} was observed. The increase of interfacial resistance in poly(methyl methacrylate) (PMMA) gel electrolyte with storage time was described by Osaka et al. [140]. Croce et al. [130] emphasized that the passivation of lithium in $LiClO_4$ PC/EC–PAN electrolytes is very severe and induces the growth at the interface of a layer having a resistance orders of magnitude higher than the bulk resistance of the electrolyte itself. Fan and Fedkiw [52] found that in gel-like composite electrolytes, based on fumed silica, PEGDME (polyethylene oxide, PEO, oligomer), and Li imide or Li triflate, the interfacial stability and conductivity are significantly improved by the addition (10 or 20 percent) of fumed-silica R805 (Degussa). Nagasubramanian and Boone [141] found that saturated cyclic compounds with functional groups decrease the interfacial impedance of $LiPF_6$–PVDF EC/PC gel electrolyte, especially at low temperature.

6.4.3.2 Li_xC_6 Electrode

Since this is a new field, little has been published on the Li_xC_6/electrolyte interface. However, there is much similarity between the SEIs on lithium and on Li_xC_6 electrodes. The mechanism of formation of the passivation film at the interface between lithiated carbon and a liquid or polymer electrolyte was studied by AC impedance [128, 142]. Two semicircles observed in AC-impedance spectra of $LiAsF_6$/EC–2Me-THF electrolytes at 0.8 V vs. Li/Li^+ [142] were attributed to the formation of a surface film during the first charge cycle. However, in the cases of $LiClO_4$ or $LiBF_4$/EC–PC–DME (dimethoxyethane), only one high-frequency distorted semicircle was found in the impedance spectra [128]. Yazami et al. [128] explained the complicated arc shape by surface-film formation followed by electrode gassing during the decomposition of the electrolyte. This phenomenon is less pronounced in Li triflate, Li imide and lithium hexafluorophosphate. However, we believe that the depressed high—frequency arc may be due to the overlapping of two, or even more, arcs and may be associated with grain-boundary resistance in the SEI (see Sec.6.4.1 and 6.4.2). In another investigation [142] it was found that the interfacial resistance of graphite electrodes in $LiPF_6$ and $LiBF_4$/EC–DMC solutions is about one order of magnitude higher than that of $LiAsF_6$-based electrolytes and increases considerably upon storage. This is explained by different surface chemistry, namely by the increased resistance of a passive film containing LiF.

Yazami et al. [128, 129] studied the mechanism of electrolyte reduction on the carbon electrode in polymer electrolytes. Carbonaceous materials, such as cokes from coal pitch and spherical mesophase and synthetic and natural graphites, were used. The change in R_{film} with composition on Li_xC_6 electrodes was studied for three ranges of x in an Li/POE–LiX/carbon cell [128]. The first step in the lithium intercalation ($0<x<0.5$) is characterized by a sharp increase in R_{film} and is attributed to the formation of a bond between lithiated coke and POE. Such intercalated lithium is irreversible in the 1.5–0.5 V range. In the second step, ($\Delta x \sim 1$), lithium intercalates mainly into the coke and the film does not grow significantly, so a slow increase in R_{film} is observed. In the third step, excess lithium is formed on the surface of the coke, and this induces a further increase in the film thickness and its resistance.

CosMX Exhibit 1008, Page 469 of 633

6.5 Summary and Conclusions

The anode/electrolyte interphase (the SEI) plays a key role in lithium-metal, lithium-alloy and lithium-ion batteries. Close to the lithium side, it consists of fully reduced (thermodynamically stable) anions such as F^-, O^{2-}, S^{2-}, and other elements such as As, B, C (or their lithiated compounds). The equivalent volumes of both LiF and Li_2O are too small (9.84 and 7.43mL, respectively) to provide adequate corrosion protection for lithium metal. Thus a second layer of Li_2CO_3 (equivalent volume, 17.5mL) or other organic materials is required to cover the first layer in order to provide this protection. The outer part of the SEI (near the solution) consists of partially reduced materials such as polyolefins, poly-THF, Li_2CO_3, $LiRCO_3$, ROLi, LiOH, and LiF, LiCl, Li_2O, etc. Often, polymers are the major constituent of the outer part of the SEI. It has been shown that the rate constants of the reactions of solvated electrons with electrolyte and solvent components (and impurities) are a good measure of the stability of these substances towards lithium. Use of the rate constants (k_e) for these reactions is suggested as a tool for the selection of electrolyte components. Good correlation was found between k_e and SEI formation voltage and composition.

The SEI is formed by parallel and competing reduction reactions and its composition thus depends on i_0, η, and the concentrations of each of the electroactive materials. For carbon anodes, i_0 also depends on the surface properties of the electrode (ash content, surface chemistry, and surface morphology). Thus, SEI composition on the basal plane is different from that on the cross—section planes. Mild oxidation of graphite was found to improve anode performance. Improvement was attributed to the formation of an SEI chemically bonded to the surface carboxylic and oxide groups at the zig-zag and armchair faces, better wetting by the electrolyte, and accommodation of extra lithium at the zig-zag, armchair, and other edge sites and nanovoids. Since the SEI consists of a mosaic of heteropolymicrophases, its equivalent circuit is extremely complex and must be represented by a very large number of series and parallel distributions of *RC* elements representing bulk ionic conductivity and grain boundary phenomena aside from the Warburg element. In some cases it can be reduced to simpler equivalent circuits.

In lithium-ion batteries, with carbonaceous anodes, Q_{IR} can be lowered by decreasing the true surface area of the carbon, using pure carbon and electrolyte, applying high current density at the beginning of the first charge, and using appropriate electrolyte combinations.

Today we have some understanding of the first lithium intercalation step into carbon and of the processes taking place on the lithium metal anode. A combination of a variety of analytical tools including dilatometry, STM, AFM, XPS, EDS, SEM, XRD, QCMB, FTIR, NMR, EPR, Raman spectroscopy, and DSC is needed in order to understand better the processes occurring at the anode/electrolyte interphase. This understanding is crucial for the development of safer and better lithium-based batteries.

CosMX Exhibit 1008, Page 470 of 633

6.6 References

[1] E. Peled, *J. Electrochem. Soc.* **1979**, *126*, 2047.

[2] E. Peled in *Lithium Batteries* (Ed: J.P. Gabano), Academic Press, **1983**, p. 43.

[3] B. Scrosati in *Polymer Electrolyte Reviews—1*, (Eds: J.R. MacCallum, C.A. Vincent), Elsevier Applied Science, London **1987**, p.315.

[4] F.M. Gray, *Solid Polymer Electrolytes*, VCH, Weinheim, **1991**, ch. 10, p.215.

[5] E. Peled, D. Golodnitsky, G. Ardel, V. Eshkenazy, *Electrochim. Acta* **1995**, *40*, 2197.

[6] B. Peled, D. Golodnitsky, G. Ardel, C. Menachem, D. Bar-Tow, V. Eshkenazy, *Mater. Res. Soc. Symp.* **1995**, *393*, 209.

[7] L.A. Dominey in *Lithium Batteries, New Materials, Development and Perspectives* (Ed.: G. Pistoia), Elsevier, New York, **1994**, p. 137.

[8] J.R. Dahn et al. in *Lithium Batteries, New Materials, Development and Perspectives* (Ed.: G. Pistoia), Elsevier, New York, **1994** p.22.

[9] C.K. Mann in *Electroanalytical Chemistry* (Ed.: A.J. Bard), Vol. 3, Marcel Dekker, New York, **1969**.

[10] J. Jortner, N.R. Kestner, (Eds.), *Electrons in Fluids*, Springer-Verlag Berlin, **1973**.

[11] Y. Arima, S. Aoyagui, *Israel J. Chem.* **1979**, *18*, 81.

[12] M. Yoshio, N. Ishibashi, *J. Appl. Electrochem.*, **1973**, *3*, 321.

[13] S. Makishima, *J. Facult. Eng., Tokyo Univ.* **1938**, *21*, 115.

[14] E. Peled, H. Yamin, *Power Sources* (Ed.: S. Thompson), Academic Press, New York, **1981**, p. 101.

[15] M. Odziemkowski and D.E. Irish, *J. Electrochem. Soc.* **1994**, *140(6)*, 1546.

[16] M. Odziemkowski, D.E. Irish, *J. Electrochem. Soc.* **1992**, 139,363.

[17] A.D. Holding, D. Pletcher, R.V.H. Jones, *Electrochim. Acta* **1989**, *34*, 1529.

[18] S.A. Campbell, C. Bowes, R.S. McMillan, *J. Electroanal. Chem.* **1990**, *284*,195.

[19] M. Odziemkowski, M. Krell, D.E. Irish, *J. Electrochem. Soc.* **1992**, *139*, 3063.

[20] D. Aurbach, I. Weissman, A. Zaban, O. Chuzid (Youngman), *Electrochim. Acta* **1994**, *39*, 51.

[21] D. Aurbach, M. Daroux, G. McDougal, E.B. Yeager, *J. Electroanal. Chem.* **1993**, *358*, 63.

[22] K. Kanamura, H. Tamura, S. Shiraishi, Z.-i. Takehara, *J. Electroanal. Chem.* **1995**, *394*, 49.

[23] K. Kanamura, S. Shiraishi, Z.-i. Takehara, *Chem. Let.* **1995**, 209.

[24] Y.E. Ely, D. Aurbach, *Langmuir* **1992**, *8*, 1845.

[25] D. Aurbach, A.Zaban, *J. Electroanal. Chem.* **1993**, *348*, 155.

[26] K. Kanamura, S. Shiraishi, Z.-i. Takehara, *J. Electrochem. Soc.* **1996**, *143(7)*, 2187.

[27] K. Kanamura, S. Shiraishi, Z.-i. Takehara, *J. Electrochem. Soc.* **1994**, *141(9)*, L108–L110.

[28] K. Kanamura, H. Tamura, Z. Takehara, *J. Electroanal. Cherm.* **1992**, *333*, 127.

[29] J.G. Thevenin, R.H. Muller, *J. Electrochem. Soc.* **1987**, *134(2)*, 273.

[30] G. Nazri, R.H. Muller, *J. Electrochem. Soc.* **1985**, *132(6)*, 1385.

[31] D. Aurbach, Y. Gofer, *J. Electrochem. Soc.* **1991**, *138(12)*, 3529.

[32] G. Montesperelli, P. Nunziante, M. Pasquali, G. Pistoia, *Solid State Ionics* **1990**, *37*, 149.

[33] F. Schwager, Y. Geronov, R.H. Muller, *J. Electrochem. Soc.* **1985**, *132*, 285.

[34] Y. Matsuda in *Electrochemistry in Transition* (Eds: O.J. Murphy, S. Srinivasan, B.E. Conway), Plenum, New York, **1992**, ch. 14.

[35] M. Morita, S. Aoki, Y. Matsuda, *Electrochim. Acta* **1992**, *37(1)*, 119.

[36] Y. Matsuda, *J. Power Sources* **1993**, *43*, 1.

[37] S. Tobishima, K. Hayashi, Y. Nemoto, J. Yamaki, *37th Battery Symposium, Japan, Tokyo*, **1996**.

[38] M. Mori, Y. Kakuta, K. Naoi, D. Fauteux, *37th Battery Symposium, Japan, Tokyo*, **1996**.

[39] Y. Matsuda, M. Ishikawa, S. Yoshitake, M. Morita, *J. Power Sources* **1995**, *54*, 301.

[40] M. Ishikawa, S. Yoshitake, M. Morita, Y. Matsuda, *J. Electrochem. Soc.* **1994**, *141(12)*, L159.

[41] M. Ishikawa, K.-Y. Otani, M. Morita, Y. Matsuda, *Electrochim. Acta* **1996**, *41(7/8)*, 1253.

[42] Y. Uraoka, M. Ishikawa, K. Kishi, M. Morita, Y. Matsuda, *37th Battery Symposium, Japan, Tokyo*, **1996**.

[43] D. Fauteux, *J. Electrochem. Soc.* **1988**, *135(9)*, 2231.

[44] Z. Takehara, Z. Ogumi, Y. Uchimoto, E. Endo, *Proc. Symp. on High Power, Ambient Temperature Lithium Batteries, Phoenix, AZ*, **1991**, p. 176.

CosMX Exhibit 1008, Page 471 of 633

[45] R. Xue, H. Huang, M. Menetrier, L. Chen, *J. Power Sources* **1993**, *44*, 431.
[46] D. Fauteux, *Solid State Ionics* **1985**, *17*, 133.
[47] J.M. Chabagno, Thesis, INP—Grenoble, **1980**.
[48] Jun J. Xu, G.C. Farrington, *Abstr. Electrochemical Soc. Meeting, San Antonio, TX, October*, **1996**, p. 74.
[49] D. Golodnitsky, G. Ardel, E. Peled, *Solid State Ionics* **1996**, *85*, 231.
[50] W.T. Krawiec, J.P. Fellner, E.P. Giannelis, L.G. Scanlon in *Diffusion and Defect Data, Part B [Solid State Phenomena]*, **1994**, *39*, 175.
[51] B. Kumar, J.D. Schaffer, N. Munichandraiah, L.G. Scanlon, *J. Power Sources* **1994**, *47*, 63.
[52] J. Fan,P.S. Fedkiw, *Abstr. 190th Electrochemical Soc. Meeting, San Antonio, TX*, **1996**, Vol. 96-2, p. 89.
[53] B. Scrosati, *J. Elecrochem. Soc.* **1990**, *136*, 2774.
[54] F. Capuano, F. Croce, B. Scrosati, *J. Electrochem. Soc.* **1991**, *138*,1918.
[55] F. Croce, B. Scrosati, *J. Power Sources* **1993**, *43–44*, 9.
[56] B. Kumar, L.G. Scanlon, *Proc. 36th Power Sources Conference, Cherry Hill, NJ*, **1994**, 236.
[57] G. Nagasubramanian, A.I. Attia, G. Halpert, E. Peled, *Solid State Ionics* **1993**, *67*, 51.
[58] T. Matsui, K.Takeyama, *Electrochim. Acta* **1995**, *40(13–14)*, 2165.
[59] C. Brissot, M. Rosso, J.-N. Chazalviel, *Electrochim. Acta* **1996**, *43(10-11)*, 1569.
[60] E. Peled, D. Golodnitsky, *Abstr. 192nd Electrochem. Soc. Meeting, Paris*, **1997**.
[61] M. Anbar, P. Neta, *Int. J. Appl. Radiat. Isotopes* **1967**, *18*, 493.
[62] G.V. Buxton, C.L. Greenstock, W.P. Helman, A.B. Ross, *J. Phys. Chem. Ref. Data* **1988**, *17(2)*, 513.
[63] M.S. Matheson, L.M. Dorfman, *Pulse Radiolysis*, MIT Press, Cambridge MA **1969**, p. 173.
[64] R.A. Marcus, *Electrochim. Acta* **1968**, *13*, 995.
[65] V.R. Koch, *J. Electrochem. Soc.* **1979**, *126*, 181.
[66] J.T. Cookson in *Carbon Adsorption Handbook* (Eds.: P.N. Cheremisinoff, F. Ellerbush), Ann Arbor Science, Ann Arbor, MI, **1978**, p. 241.
[67] K. Kinoshita, *Carbon, Electrochemical and Physicochemical Properties*, Wiley–Interscience, New York,**1987**.
[68] H.P. Pierson, *Handbook of Carbon, Graphite, Diamond and Fullerenes*, Noyes, Park Ridge, NJ, **1993**.
[69] M.M. Dubinin, *Chemistry and Physics of Carbon* (Ed.: P.L. Walker, Jr.), Marcel Dekker, New York, **1966**, ch. 2, p. 251.
[70] W. Xing, J.R. Dahn, *Abstr. 190th Electrochemical Soc. Meeting, San Antonio, TX*, **1996**, Vol. 96-2, p. 1055.
[71] R. Fong, U.V. Sacken, J.R. Dahn, *J. Electrochem. Soc.* **1990**, *137*, 2009.
[72] A.C. Chu, J.X. Josefowicz, J.E. Fischer, G.C. Farrington, *Abstr. 190th Electrochemical Soc. Meeting, San Antonio, TX*, **1996**, Vol. 96-2, p. 1062.
[73] C. Menachem, E. Peled, L. Burstein, *Proc. 37th Power Sources Conference, Cherry Hill, NJ*, **1996**, p. 208.
[74] E. Peled, C. Menachem, D. Bar-Tow, A. Melman, *J. Electrochem. Soc.* **1996**, *143*, L4.
[75] C. Menachem, E. Peled, L. Burstein, Y. Rosenberg, *Abstr. 8th Int. Meeting on Li Batteries, Nagoya, Japan*, **1996**, p. 224; idem, *J. Power Sources*, *68*, 277.
[76] E. Peled in *Rechargeable Lithium and Lithium-Ion Batteries*, (Eds.: S. Megahed, B.M. Barnett, Xie), The Electrochemical Society, Pennington, NJ, **1995**, Vol. 94-28, p. 1.
[77] K. Zaghib, K. Tatsumi, H. Abe, H. Sakaebi, S. Higuchi, T. Ohsaki, Y. Sawada, *Proc. Electro chemical Soc. Meeting, San Fransisco*, **1994**, Vol. 94-1, Abs. 581
[78] Z.X. Shu, R.S. McMillan, J. Murray, *J. Electrochem. Soc.* **1993**, *140*, 992.
[79] M. Arakawa, J. Yamaki, T. Okada, *J. Electrochem. Soc.* **1984**, *131(11)*, 2605.
[80] B.A. Johnson, R.E.Write, *Abstr. 190th Electrochemical Soc. Meeting, San Antonio, TX*, **1996**, Vol. 96-2, p. 170.
[81] D. Aurbach, Y. Ein-Eli, O. Chusid, Y. Carmeli, M. Babai, H. Yamin, *J. Electrochem. Soc.* **1994**, *141*, 603.
[82] O. Chusid, Y. Ein-Eli, D. Aurbach, *J. Power Sources*, **1993**, *43*, 47.
[83] T. Abe, Y. Mizutani, K. Ikada, M. Inaba, Z. Ogumi, *37th Battery Symposium, Japan, Tokyo*, **1996**, p. 53.
[84] M. Inaba, Z. Siroma, Y. Kawatate, A. Funabiki, Z. Ogumi, *J. Power Sources* **1997**, *68*, 221.
[85] Z. Ogumi, M. Inaba, Z. Siroma, Y. Kawatate, A. Funabiki, *Abstr. 190th Electrochemical Soc. Meeting, San Antonio, TX*, **1996**, Vol. 96-2, p. 1045.

CosMX Exhibit 1008, Page 472 of 633

[86] S. Yamaguchi, K.A. Hirasawa, S. Mori, *37th Battery Symposium, Japan*, **1996**, p. 49.
[87] J.O. Besenhard, M. Winter, J. Yang, W. Biberacher, *J. Power Sources* **1995**, *54*, 228.
[88] R. Blint, *Proc. Symp. on Lithium Batteries* (Eds.: N. Doddapaneni, A.R. Langrebe), The Electrochemical Society, Pennington, NJ, **1994**, Vol. 94-4, p. 1.
[89] E. Peled, D. Bar-Tow, V. Eshkenazy, *37th Battery Symposium, Japan, Tokyo*, **1996**, Abstr. no. 3I02.
[90] J.O.M. Bockris, A.K.N. Reddy, *Modern Electrochemistry*, Plenum Press, New York, **1970**, p. 1176.
[91] M. Fujimoto, Y. Kida, T. Nohma, M. Takahashi, K. Nishio, T. Saito, *J. Power Sources* **1996**, *63*, 127.
[92] H. Yoshida, T. Fukunaga, T. Hazama, M. Terasaki, M. Mizutani, M. Yamachi, *Abstr. 8th Int. Meeting on Li Batteries, Nagoya, Japan*, **1996**, p. 252.
[93] K. Tanaka, M. Itabashi, M. Aoki, S. Hiraka, M. Kataoka, S. Fujita, K. Sekai, K. Ozawa, *184th Electrochemical Soc. Meeting, New Orleans*, **1993**, Vol. 93-2 , Abstr. no. 21.
[94] C.K. Huang, M. Smart, E. Davies, R. Cortez, S. Surampudi, *Abstr. 190th Electrochemical Soc. Meeting, San Antonio, TX*, **1996**, Vol. 96-2, p. 171.
[95] E. Peled, D. Bar-Tow, A. Melman, E. Gerenrot, Y. Lavi, Y. Rosenberg, *Proc. Symp. on Lithium Batteries*, The Electrochemical Society, Penninton, NJ, **1994**, Vol. 94-4, p. 177.
[96] K. Zaghib, Y. Choquette, A. Guerbi, M. Simoneau, A. Belanger, M. Gauthier, *Abstr. 8th Int. Meeting on Li Batteries, Nagoya, Japan*, **1996**, p. 298.
[97] I. Endo, private communication.
[98] D. Guyomard, J.M. Tarascon, US Patent 5192629, **1993**.
[99] C.K. Huang, S. Surampudi, D.H. Shen, G.Halpert, *Abstr. 184th Electrochemical Soc. Meeting, San Antonio, TX*, **1993**, Vol. 93-2, p. 26.
[100] Y. Ein-Eli, V.R. Koch, *J. Electrochem.Soc.* **1997**, *144*, 2968.
[101] T. Takamura, M. Kikuchi, Y. Ikezawa in *Rechargeable Lithium-Ion Batteries* (Eds.: S. Megahed, B.M. Barnett, L. Xie), the Electrochemical Society, Pennington, NJ, **1995**, Vol. 94-28, p. 213.
[102] O. Yamamoto, Y. Takeda, N. Imanishi, *Proc. Electrochem. Soc. Meeting, Honolulu*, **1993**.
[103] R. Kanno, Y. Kawamoto, Y. Takeda, S. Ohashi, N. Imanishi, O. Yamamoto, *J. Electrochem. Soc* **1992**, *139(12)*, 3397.
[104] H. Momose, H. Honbo, S. Takeuchi, K. Nishimura, T. Horiba, Y. Muranaka, Y. Kozono, H. Miadera, *Abstr. 8th Int. Meeting on Li Batteries, Nagoya, Japan*, **1996**, p. 172.
[105] J.O. Besenhard, M.W. Wagner, M. Winter, A.D. Jannakoudakis, P.D. Jannakoudakis, E. Theodoridou, *J. Power Sources* **1993**, *43/44*, 413.
[106] G.G. Tibbets, G.-A. Nazri, B.J. Howie, *Abstr. 190th Electrochemical Soc. Meeting, San Antonio, TX*, **1996**, Vol. 96-2, p. 117.
[107] Y. Ein-Eli, S.R. Thomas, V.R. Koch, *J. Electrochem. Soc.* **1996**, *143(9)*, L195.
[108] Y. Ein-Eli, S.R. Thomas, V.R.Koch, *Abstr. 190th Electrochemical Soc. Meeting, San Antonio, TX*, **1996**, Vol. 96-2, p. 1046.
[109] K. Zaghib, R. Yazami, M. Broussly, *Abstr. 8th Int. Meeting on Li Batteries, Nagoya, Japan*, **1996**, p. 192.
[110] M. Jean, A. Chausse, R. Messina, *Abstr. 8th Int. Meeting on Li Batteries, Nagoya, Japan*, **1996**, p. 186.
[111] T. Tada, H. Yoshida, E. Yagasaki, K. Hanafusa, G. Tanaka, *Ext. Abstr. 36th Battery Symp. Japan, Kyoto, Japan*, **1995**, p. 195.
[112] M. Morita, T. Ichimura, M. Ishikawa, Y. Matsuda, *J. Electrochem. Soc.* **1996**, *143(2)*, L26.
[113] D. Aurbach, A. Zaban, M. Moshkovich, *Abstr. 8th Int. Meeting on Li Batteries, Nagoya, Japan*, **1996**, p. 246.
[114] J.O. Besenhard, J. Yang, M. Winter, *Abstr. 8th Int. Meeting on Li Batteries, Nagoya, Japan*, **1996**, p. 96.
[115] I. Yoshio, M. Masayuki, M. Yukio, K. Tadahiko, M. Tsutomu, European Patent Application 94116643-1, October 21, **1994**.
[116] I.A. Courtney, A.M. Wilson, W. Xing, J.R. Dahn, *Abstr. 190th Electrochemical Soc. Meeting, San Antonio, TX*, **1996**, Vol. 96-2, Paper no. 66.
[117] D. Billaud, A. Naji, P. Willmann, *J. Chem. Soc. Chem. Commun.* **1995**, 1867.
[118] N. Takami, A. Satah, M. Hara, T. Ohsaki. *J. Electrochem. Soc* **1995**, *142*, 8.
[119] J.R. Dahn, *Phys. Rev. B*, **1991**, *44*, 17.
[120] K. Tatsumi, K. Zaghib, Y. Sawada, *J. Electrochem. Soc.* **1995**, *142*, 1090.
[121] D. Bar-Tow, E. Peled, L. Burstein, *Abstr. 190th Electrochemical Soc. Meeting, San Antonio, TX*, **1996**, Vol. 96-2, Paper. no. 1028.

CosMX Exhibit 1008, Page 473 of 633

[122] D. Bar-Tow, C. Menachem, E. Peled, unpublished results
[123] G. Ardel, D. Golodnitsky, E. Strauss, E. Peled, *Proc. 37th Power Sources Conference (ARL), NJ*, **1996**, p. 283.
[124] G. Ardel, D. Golodnitsky, E. Strauss, E. Peled, *Abstr. 190th Electrochemical Soc. Meeting, San Antonio, TX*, **1996**, Vol. 96-2, Paper no. 104a.
[125] G. Ardel, D. Golodnitsky, E. Peled, *J. Electrochem. Soc.* **1997**, *144(8)*, L208.
[126] N. Takami, T. Ohsaki, *J. Electrochem. Soc.* **1992**, *139(7)*, 1849.
[127] S. Fouache-Ayoub, M. Garreau, P.V.S.S. Prabhu, J. Thevenin, *J. Electrochem. Soc.* **1990**, *137(6)*, 1659.
[128] R. Yazami, M. Deschamps, S. Genies, J.C. Frison, J. Ledran, *Abstr. 8th Int. Meeting on Li Batteries, Nagoya, Japan*, **1996**, p. 107.
[129] R. Yazami, M. Deschamps, *Abstr. 8th Int. Meeting on Li Batteries, Nagoya, Japan*, **1996**, p. 190.
[130] F. Croce, S. Panero, S. Passerini, B. Scrosati, *Electrochim. Acta* **1994**, *39(2)*, 255.
[131] M. Hiratani, K. Miyauchi, T. Kudo, *Solid State Ionics* **1988**, *28–30*, 1431.
[132] S.E. Sloop, M.M. Lerner, *Solid State Ionics* **1996**, *85*, 251.
[133] E. Peled, D. Golodnitsky, C. Menachem, G. Ardel, *Abstr. 7th Int. Meeting on Lithium Batteries, Boston*, **1994**, Paper no. 21.
[134] N. Munichandraiah, L.G. Scanlon, R.A. Marsh, B. Kumar, A.K. Sircar, *Applied Electrochemistry* **1995**, *25(9)*, 857.
[135] J. Cho, M. Liu, *Abstr. Electrochemical Soc. Meeting,San Antonio, TX*, **1996**, Vol. 96-2, Paper no.104.
[136] I.M. Ismail, U. Kadiroglu, N. D. Gray, J.R. Owen, *Abstr. Electrochemical Soc. Meeting, San Antonio, TX*, **1996**, Vol. 96-2, 84.
[137] E. Peled, D. Golodnitsky, C. Menachem, G. Ardel, Y. Lavi, *The Electrochemical Society Fall Meeting, New Orleans*, **1993**, Vol. 93-2, Abstr. no. 504.
[138] E. Peled, D. Golodnitsky, G. Ardel, J. Lang, Y. Lavi, *Proc. 11th Int. Sem. on Primary and Secondary Battery Technology and Applications*, Eds.:S.P. Wolsky, N. Marincic, Florida, **1994.**
[139] A.du Pasquier, C. Sarrazin, X. Andrieu, J.-F. Fauvarque, *Abstr. 190th Electrochemical Soc. Meeting, San Antonio, Tx*, **1996**, Vol. 96-2, Paper no. 82.
[140] T. Osaka, T. Momma, H. Ito, *Abstr. Electrochemical Soc. Meeting, San Antonio, TX*, **1996**, Vol. 96-2, Paper no. 87.
[141] G. Nagasubramanian,D.R. Boone, *Abstr. 190th Electrochemical Soc. Meeting, San Antonio, TX*, **1996**, Vol. 96-2, Paper no. 166.
[142] D. Aurbach, B. Markovsky, A. Shechter, *Abstr. 190th Electrochemical Soc. Meeting, San Antonio, TX*, **1996**, Vol. 96-2, Paper no. 164.

CosMX Exhibit 1008, Page 474 of 633

7 Liquid Nonaqueous Electrolytes

Josef Barthel and H.J. Gores

7.1 Introduction

This section reports on the current state of knowledge on nonaqueous electrolytes for lithium batteries and lithium-ion batteries. The term "electrolyte" in the current text refers to an ion-conducting solution which consists of a solvent S and a salt, here generally a lithium salt. Often 1:1-salts of the LiX type are preferred for reasons given below; only a few 1:2-salts Li_2X have attained some importance for batteries, and 1:3-salts Li_3X are not in use.

Chemists prefer to use the term electrolyte for the salt itself, in contrast to the above definition of the term. According to their use, the liquid ion-conductor is called an electrolyte solution.

In the tradition of previous reviews [1–22], this section addresses various aspects of nonaqueous electrolytes, including intrinsic properties, such as local structures caused by ion–ion and ion–solvent interactions; and bulk properties, such as ionic conductivity, viscosity, and electrochemical stability (voltage window), and their relationships to intrinsic properties.

In comparison with aqueous electrolytes, liquid nonaqueous electrolytes offer larger liquid ranges, down to below -150 °C [23] and up to above 300 °C [24], voltage windows up to more than 5 V, (see Sec. 7.4.1), a large range of acid–base properties, and often a better solubility for many materials, electrolytes and nonelectrolytes, better compatibility with electrode materials, and increased chemical stability of the solution. Their drawbacks are lower conductivity, higher costs, flammability, and environmental problems.

In comparison with solid electrolytes, (Sec. 9), liquid nonaqueous electrolytes generally show better leveling capabilities for temperature and concentration discontinuities, maintenance of a permanent interfacial contact at electrodes, allowance for small volume changes, often larger electrochemical windows, and higher conductivity. Typical advantages of solid electrolytes are exclusive cationic or anionic conductivity, no need for separators, no gassing and leakage problems, resistance to mechanical stresses, and ease of cell assembly.

Room-temperature molten salts are a relatively new subgroup of liquid nonaqueous electrolytes. They share their advantages and disadvantages. Unfortunately, until now, no useful room-temperature molten salt based on lithium cations has been available.

Polymer electrolytes (Sec. 8), especially those which have been developed recently, combine several advantages of both types of electrolytes. They share sev-

eral properties with nonaqueous electrolytes, because they are made of a salt and an ion-solvating polymer with or without additional solvent.

The ideal nonaqueous electrolyte for practical batteries would possess the following properties:

- high conductivity of about 3×10^{-3} to $2\times10^{-2}\,\mathrm{S\,cm^{-1}}$ over a wide temperature range [9],
- large electrochemical window, at least 1.5–3.5 V [9] for lithium batteries and more than 4.5 V for lithium-ion cells with high-voltage cathodes,
- large usable liquid range, typically –40 °C to 70 °C [9],
- low vapor pressure,
- low temperature coefficient of viscosity,
- good solvating properties for ions,
- good chemical and thermal stability,
- low toxicity,
- easy biodegradability, and
- low price.

Of course these requirements cannot be fulfilled simultaneously. For example, a low vapor pressure of the liquid electrolyte is obtained only by using more viscous dipolar aprotic solvents such as propylene carbonate, but high solvent viscosity generally entails a low conductivity. Nevertheless, a large number of useful solvents and electrolytes is available, allowing a sufficiently good approximation to an ideal electrolyte.

7.2 Components of the Liquid Electrolyte

7.2.1 The Solvents

Solvents can be classified [15] according to bulk properties, such as

- permittivity ε,
- viscosity η,
- empirical solvent parameters representing their acid–base properties and their polarizability,
- chemical categories referring to the functional group of the molecule (esters, ethers, ketones, and so on),

or molecular properties such as

- dipole moment μ,
- polarizability α,
- van der Waals volumes and radii or related size parameters,
- the electrostatic factor (EF=$\varepsilon\mu$).

Empirical solvent parameters are determined by thermodynamic or spectroscopic experiments which yield parameters representing:

- the ability of solvents to interact with acceptors such as protons, other cations or Lewis acids (e.g., BF_3, $SbCl_5$) as reflected by Gutmann's donor number (DN) [25–28] or Kamlet and Taft's β-scale [29–32],
- the ability of solvents to interact with donors such as anions or Lewis bases, as reflected by Dimroth and Reichart's ET(30) scale [33, 34], Mayer, et al. acceptor number (AN) [35], or Kamlet and Taft's α-scale [32, 36],
- the polarity of a solvent and the po-

CosMX Exhibit 1008, Page 476 of 633

larizability of solvent molecules expressed with the help of the solvatochromic parameter π^* of Kamlet et al. [29, 37–40].

Based on previous classifications and according to criteria discussed in Ref. [15], we have extended the classification of solvents into eight classes:

(1) amphiprotic hydroxilic solvents, typical examples of wild are the alcohols;
(2) amphiprotic protogenic solvents, e.g., carboxylic acids;
(3) protophilic H-bond donor solvents, e.g., amines;
(4) dipolar aprotic protophilic solvents, e.g., pyridine;
(5) dipolar aprotic protophobic solvents, e.g., esters;
(6) low-permittivity electron-donor solvents, e.g., ethers;
(7) low-polarity solvents of high polarizability, e.g., benzene; and
(8) inert solvents, e.g., alkanes and perfluoroalkanes.

Because of the reactivity of lithium or lithium intercalated in carbon, protic solvents cannot be used in lithium batteries because hydrogen would be formed according to Eq. (1).

$$RH + Li \rightarrow Li^+ + R^- + \frac{1}{2}H_2, \qquad (1)$$

Hence, it is mainly solvents of the classes 5–8 that are suitable for lithium batteries, but only under condition that they are electrochemically stable with lithium and cathode materials. A recently reported exception is *n*-butylamine [41], a solvent of class 3, because reaction (1) does not take place.

Table 1 shows various solvents (in alphabetical order) used in lithium batteries. The table contains the names of the solvents, their acronyms, the liquid range represented by melting (Θ_m,°C) and boiling points (Θ_m,°C), and the physical properties at 25 °C unless otherwise noted, permittivity ε, viscosity η/(cP), and density ρ/(kg L^{-1}). The data are taken from Ref. [15], where the original literature is cited, or from more recent references given in the table.

It must be stressed that addition of salts often greatly extends the solvent range, due to freezing-point depression and an increase in boiling point. This effect can be increased further by the use of mixed solvents. For example, the fusion point of EC is 36.35 °C and that of DMC is 4.6 °C [42] (0.5 °C [76]). The 1:1 mixture of both solvents containing 1 mol L^{-1} $LiAsF_6$ freezes at −19.7 °C, that containing 1 mol L^{-1} lithium bis(trifluoromethylsulfonyl)imide, $Li[N(SO_2CF_3)_2]$, freezes at about −29.0 °C, whereas the mixture containing 1 mol L^{-1} lithium tris(trifluoromethylsulfonyl) methide, $Li[C(SO_2CF_3)_3]$, is liquid in the range down to −30 °C.

Table 2 shows the empirical solvent parameters for the same solvents as Table 1. They are taken from Refs. [15], [29], [35], or [27] and the literature cited therein.

An inspection of Tables 1 and 2 shows that appropriate solvents for lithium batteries mainly belong to classes 6 and 7 and include cyclic (EC, PC) and open-chain (DMC, MEC, DEC, MPC) esters and ethers (DIOX, DME, THF) as well as inorganic sulfur compounds (SO_2, $SOCl_2$). These sulfur compounds are mainly used as liquid cathode materials, simultaneously serving as solvents (SO_2Cl_2, $SOCl_2$) or cosolvents (SO_2) in primary or secondary lithium batteries. Recent developments of solvents include

CosMX Exhibit 1008, Page 477 of 633

methane sulfonyl chloride (MSC) [43], boric acid esters of glycol such as 1,3-propylene glycol boric ester (BEG-1) [45], ethylene sulfite (ES) [46], ethyl methyl carbonate, (EMC), and methyl propyl carbonate (MPC) [151].

The increase of the liquid range of binary mixtures based on a polar (e.g., EC) and a nonpolar component (e.g., DMC) by salt addition reflects the association of the electrolyte. Large freezing-point depressions are obtained in EC-rich mixtures whereas DMC-rich mixtures yield only small depressions. As a consequence, the minima of the eutectic phase diagrams shift to higher EC contents. For example, EC/DMC mixtures show an eutectic point at a molar ratio of EC of $x_{EC} = 0.348$ at $-7.76\,°C$. The minimum of the ternary mixture EC/DMC/$LiPF_6$ is obtained at $-16.04\,°C$ and $x_{EC} = 0.476$ [72].

Table 1. Physical properties of solvents for lithium batteries

Solvent	Acronym	θ_m/°C	θ_b/°C	ε	η/(cP)	(kg L^{-1})	Ref.
Acetonitrile	AN	−48.835	81.60	35.95	0.341	0.77675	
n-Butylamine	*n*-BU	−49.1	77.4	4.88 (20 °C)	0.681	0.7385	[41]
γ-Butyrolactone	GBL	−43.53	204	39.1	1.7315	1.1242	
Diethyl carbonate	DEC	−43.0	126.8	2.8059	0.7529	0.96928	[42]
Dimethoxyethane	DME	−58	84.50	7.075	0.407	0.86122	
Dimethyl carbonate	DMC	4.6	90	3.1075	0.5902	1.06316	[42]
Dimethyl sulfoxide	DMSO	18.54	189	46.5	1.992	1.0955	
1,3-Dioxolane	DIOX	−97.22	76.5		0.6 (20 °C)	1.0647 (20 °C)	
Ethylene carbonate	EC	36.5	238	90.36 (40 °C)	1.9 (40 °C)	1.3214 (40 °C)	
Ethyl methyl carbonate	EMC			2.4	0.65	1.0070	[137]
				2.958	0.6893	1.00621	[42]
Methane sulfonyl chloride	MSC	−50	160				[43]
Methyl acetate	MA	−98.05	56.868	6.68	0.364	0.9279	
Methyl formate	MF	−99.0	31.75	8.5 (20 °C)	0.328	0.9664	
3-Methyl-2-Oxazolidinone	3Me2OX	15.9	74-75 (<1Torr)	77.5	2.450	1.1702	
2-methyltetrahydrofuran	2-Me-THF	−137.2	79.9	6.75		0.8540 (20 °C)	
Propylene carbonate	PC	−54.53	242	64.95	2.512	1.1996	
Sulfolane	TMS, SL	28.45	287.3	43.30 (30 °C)	10.287 (30 °C)	1.2619 (30 °C)	
Sulfur dioxide		−75.46	-10.01	15.6 (0 °C)	0.4285 (0 °C)	1.46 (−10°C)	
Sulfuryl chloride		−54.1	69.4	11.5	0.674	1.657	
Tetrahydrofuran	THF	−108.5	65.965	7.43	0.459	0.8819	
Thionyl chloride		−104.5	77	8.675	0.603	1.629	

CosMX Exhibit 1008, Page 478 of 633

Table 2. Empirical solvent parameters

Solvent	Acronym	DN	ET(30)	AN	α	β	π^*
Acetonitrile	AN	14.1	46.0	18.9	0.19	0.31	0.75
γ-Butyrolactone	GBL			(18.6)	0.00	0.49	0.87
Diethyl carbonate	DEC						
Dimethoxy ethane	DME		38.2	10.2	0.00	0.41	0.53
Dimethyl carbonate	DMC	15.1†				0.00	0.38
Dimethyl sulfoxide	DMSO	29.8	45.0	19.3	0.00	0.76	1.00
Ethylene carbonate	EC	16.4					
Methyl acetate	MA	16.5	40.0		0.00	0.42	0.60
Methyl formate	MF				0.00	0.37	0.62
2-Methyltetrahydrofuran	2-Me-THF		36.5				
Propylene carbonate	PC	15.1	46.6	18.3	0.00	0.40	(0.83)
Sulfolane	SL	14.8	44.0	19.2	0.00		0.98
Tetrahydrofuran	THF	20.0	37.4	8.0	0.00	0.55	0.58

† Ref. [44]

7.2.2 The Salts

The main requirements for a suitable lithium salt are:

- intrinsic thermal stability,
- high oxidation limit of the anion (electrochemical stability),
- low reduction limit of the anion,
- good solubility of the salt in appropriate solvents,
- chemical stability with the solvent,
- high conductivity of its solutions,
- low molecular weight,
- low cost.

Unfortunately, the requirements cannot be fulfilled by a single salt, because they are partially contradicting. For example, the last two requirements would be best fulfilled with simple halides such as LiF or LiCl. However, their solubility in every suitable solvent is low, due to their high lattice energies. In addition, these salts show strong ion–ion interaction forces, even in solvents of high permittivity.

The first electrolytes used for primary lithium cells [47, 48] were based on lithium salts with coordinatively saturated molecular anions, such as ClO_4^-, and anions based on Lewis acids XF_n as well as the corresponding Lewis base F^-, e.g., BF_4^-, AsF_6^-, and PF_6^-. These salts used until now in primary lithium cells [49] are not easily oxidized or reduced at the electrodes, and therefore are the preferred anions of supporting lithium or tetraalkylammonium salts for electrochemical studies.

Some problems associated with the use of these anions have stimulated the search for substitutes [6], especially for rechargeable lithium cells.

- Lithium perchlorate solutions are thermally unstable and show explosion risks, especially in ethers [50, 51],
- Lithium hexafluorophosphate is thermally unstable in the solid state [52], where it decomposes at about 30 °C [53]. In solvents and solvates it is more stable. Decomposition begins in the range from 80 °C [53] to about 130 °C [13], yielding scarcely soluble LiF and the Lewis acid PF_5 which in turn initiates polymerization of cyclic

ethers and degrades the solution, if this process is not inhibited by additives. Due to their outstanding stability to oxidation and high conductivities, $LiPF_6$ solutions in organic carbonates are still used in rechargeable lithium-ion cells.

- Lithium hexafluoroarsenate is thermally stable [54, 55] but shows environmental risks due to possible degradation products [56–58], even though it is itself not very toxic. Its LD 50 value is similar to that of lithium perchlorate [55]. Just like lithium hexafluorophosphate, it can initiate the polymerization of cyclic ethers. Polymerization may be inhibited by tertiary amines [59], or 2-methylfuran [60], yielding highly stable electrolytes.
- Lithium tetrafluoroborate yields only poorly conducting solutions with all solvents. It is unstable [61] and also leads to polymerization with cyclic ethers initiated by the corresponding Lewis base BF_3.

All anions are thermodynamically unstable with lithium, e.g., $LiAsF_6$ generates about $1600\ kJ\ mol^{-1}$ heat upon reduction with lithium metal [6].

More recently considered candidates are large molecular anions with delocalized anionic charge, which offer low lattice energies, relatively small ion–ion interaction, and hence sufficient solubility and relatively large conductivity. Delocalization of the charge is achieved by electron-with drawing substituents such as –F or $-CF_3$. Furthermore, these anions show a good electrochemical stability to oxidation. In contrast to Lewis acid-based salts they are chemically more stable with various solvents and often also show excellent thermal stability.

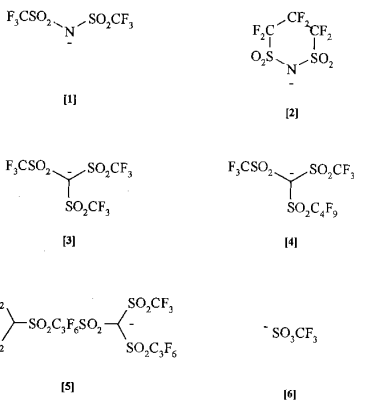


Figure 1. Some selected imides, methides, and the triflate.

The first anions developed especially for lithium batteries were:

- the triflate $CF_3SO_3^-$, (Fig. 1, [6]), available from the 3M Company [6] and used in primary lithium batteries,
- other perfluoroalkyl or perfluoroaryl sulfonates [6],
- the closoboranes, such as $B_{10}Cl_{10}^{2-}$ and $B_{12}Cl_{12}^{2-}$ [62], and
- alkyl- or arylborates such as BMe_4^- or $B(Ph)_4^-$ [63] and their fluorinated analogues [64] which exhibit a superior stability versus oxidation when compared with non fluorinated anions.

The latest developments include:

- lithium bis (trifluoromethylsulfonyl) imide, $Li[N(SO_2CF_3)_2]$ [65–71] commercially available from the 3M company [6], also called lithium "imide" and abbreviated LiIm (Fig. 1, [1]), the related cyclic imide $Li[N(SO_2(CF_2)_4(SO_2)]$ [71], and $Li[N(SO_2)(CF_2)_n(SO)_2]$, n=1–3, synthesized by

CosMX Exhibit 1008, Page 480 of 633

Sartori et al. [72]; cf. Fig. 1, [2] for n=3 (for synthesis and structure of potassium and rubidium salts of the cyclic imides with n=1 and n=2, see Ref. [73]),

- lithium tris(trifluoromethylsulfonyl) methide $Li[C(SO_2CF_3)_3]$, invented by Covalent Associates, in short lithium methide or LiMe [74–77] (cf. Fig. 1, [3]), the asymmetric methide $Li[C(SO_2CF_3)_2(SO_2C_4F_9)]$, (Fig. 1, [4]), and the bismethide $Li_2[C_2(SO_2CF_3)_4(S_2O_4C_3F_6)]$, in short LiBisMe, (Fig. 1, [5, 224], synthesized by Sartori et al. [72]),
- the tetrakis[4 - (fluoromethyl) phenyl] borate invented by EXXON,
- the tetrakis[3, 5 - bis(trifluoromethyl) phenyl]borate synthesized by Kita et al. [78] , and
- the family of chelatoborates developed in our laboratory [79–83, 225], see Fig. 2.

These chelatoborates are synthesized by reactions of aromatic diols (e.g., pyrocatechol), hydroxycarboxylic acids (e.g., salicylic acid), or other aromatic OH-containing compounds, including heterocycles, boric acid, and lithium hydroxide, or they are obtained by transesterification of alkylborates such as lithium methoxyborate with the help of diols. The new salts include:

(1) derivatives of pyrocatechol and fluorinated analogues, $Li[BC_6H_{4-x}F_xO_2]$ (x=0, 1, 4), i.e., lithium bis[1,2-benzenediolato(2–)-O,O'] borate (Fig. 2, [7]) lithium bis[3 fluoro-1,2- benzenediolato(2–)-O,O']borate, and lithium bis[tetrafluoro-1,2-benzenediolato (2–) -O,O']borate (Fig. 2, [8]),

(2) derivatives of other aromatic diols, lithium bis[2,3-naphthalenediolato - O,O']borate (Fig. 2, [9]) and lithium bis [2, 2' - biphenyldiolato (2–)-O,O'] (Fig. 2, [10]),

(3) derivatives of aromatic hydroxyacids, lithium bis[salicylato(2–)] borate (Fig. 2, [11]), lithium bis[2-olato - 1 - benzenesulfonato(2–)] borate, and the fluorinated sulfborate lithium bis[5-fluoro - 2 - olato - 1-benzenesulfonato (2-)] borate (Fig. 2, [12])

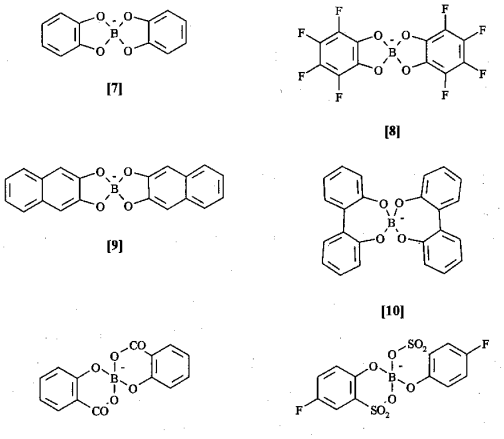


Figure 2. Some chelatoborates.

CosMX Exhibit 1008, Page 481 of 633

They show high thermal stability; for example the decomposition temperature of lithium bis[2,2'-biphenyldiolato(2–)O,O'] borate is 270 °C [80].

7.2.3 Purification of Electrolytes

Purification of solvents and salts is essential for reliable electrochemical studies and measurements. A water content of 20ppm already corresponds to a 10^{-3} mol L^{-1} solution. This is in the concentration range of dilute solutions used in conductivity studies for the determination of association constants (see Sec.7.3.2). Traces of water may affect chemical equilibria and therefore act on specific conductivities and limiting ion conductivities. For example, addition of 30 ppm water to a 2×10^{-4} mol L^{-1} solution of $LiBF_4$ in THF at 15 °C increases its conductivity by 4.4 percent (precision of measurements about 0.02 percent); 380 ppm water causes an increase by 51.7 percent; see Fig. 3 [20].

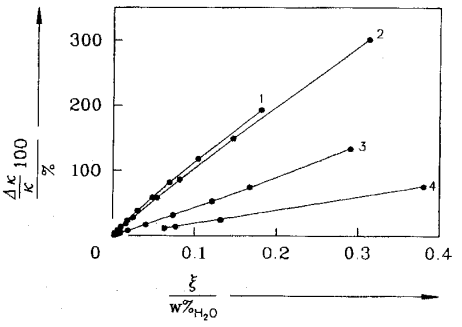


Figure 3. Conductivity increase caused by traces of water. From top to bottom: $LiCl_4$/THF (1), $LiClO_4$ /THF/DME, x_{DME} =0.16 (2); $LiClO_4$ /THF/DME, x_{DME} (3); $LiClO_4$ DME, (4).

For electrode reactions at corroding electrodes the purity requirements are even more stringent; a water content of 2×10^{-2} ppm suffices to produce a monolayer of LiOH on a lithium surface of 1 cm^2 in contact with 1 cm^3 electrolyte [1]. However, despite good purification procedures [84–86], equipment, and purity control, even recent publications are based on materials used "as received" without (at least) purity control. As a consequence, results disagree among various authors.

Another essential which must be considered in order to obtain reliable measurements is the storage of purified solvents and salts in high-vacuum glassware, equipped with joints and vents under an inert gas, which for studies on lithium generally is purified argon. Often the preparation of the electrolyte requires both slow addition of the salt and cooling, because the dissolution of lithium salts may be highly exothermic, entailing the decomposition of noncooled components.

Finally, recrystallization and dehydration of lithium salts deserve mention. Generally, lithium salts are highly hygroscopic and often strongly hydrated. For example, the equilibrium temperature for the dehydration process of $LiClO_4$ is 136 °C. Salts, even those which are not thermally stable, are often dried below the equilibrium temperature for dehydration of the lithium ion and temperatures which are too low are compensated by reduced pressure and long drying periods at elevated temperatures. Possible side reactions such as the hydrolysis of the anion and the formation of LiOH are not taken into account. A common way to bypass these problems is to use dried organic solvents with low boiling points for recrystallization and to desolvate the solvated salt obtained in vacuum, under continuous weight control, to constant weight.

CosMX Exhibit 1008, Page 482 of 633

7.3 Intrinsic Properties

In the last two decades experimental evidence has been gathered showing that the intrinsic properties of the electrolytes determine both bulk properties of the solution and the reactivity of the solutes at the electrodes. Examples covering various aspects of this field are given in Ref. [16]. Intrinsic properties may be described with the help of local structures caused by ion–ion, ion–solvent, and solvent–solvent interactions. An efficient description of the properties of electrolyte solutions up to salt concentrations significantly larger than 1 mol kg^{-1} is based on the chemical model of electrolytes.

7.3.1 Chemical Models of Electrolytes

Chemical models of electrolytes take into account local structures of the solution due to the interactions of ions and solvent molecules. The underlying information stems from spectroscopic, kinetic, and electrochemical experiments, as well as from dielectric relaxation spectroscopy. The postulated structures include ion pairs, higher ion aggregates, and solvated and selectively solvated ions.

The formation of these structures is represented with the help of chemical equilibria. The equilibrium constants can be determined consistently with the help of experimental methods.

The association of solvated ions can be described by the overall equilibrium reaction

$$C_s^+ + A_s^- \Leftrightarrow IP_s \tag{2}$$

where C_s^+ is the solvated cation, A_s^- is the solvated anion, and IP_s is a solvated ion pair. The association constant $K_A^{(c)}$ is given by the relationship

$$K_A^{(c)} = \frac{(1-\alpha)y_{IP}}{\alpha^2 c y_{\pm}'^2} \tag{3}$$

where $K_A^{(c)}$ is the association constant in the molarity scale, α is the degree of dissociation, y_{IP} is the activity coefficient of the ion pair, $y_{\pm}'$ is the mean activity coefficient of the free ions, and c is thesalt concentration.

According to Eigen and Tamm [87,88], ion-pair formation proceeds stepwise, starting from separated solvated ions which form a solvent-separated ion pair $[C^+SSA^-]^0$, followed by a solvent-shared ion pair $[C^+SA^-]^0$ and finally a contact ion pair, $[C^+A^-]^0$ [Eqs. (4)–(6)]. All these species are solvated. The types of ion pair formed depend on the relative strength of the interaction of the involved species.

$$[C^+ \cdot nS]^+ + [A^- \cdot mS] \rightleftharpoons [C^+SSA^-]^0 + [(n+m)-2]S \tag{4}$$

$$[C^+SSA^-]^0 \rightleftharpoons [C^+SA^-]^0 + S \tag{5}$$

$$[C^+SA^-]^0 \rightleftharpoons [C^+A^-]^0 + S \tag{6}$$

7.3.2 Ion-Pair Association Constants

The commonly used method for the determination of association constants is by conductivity measurements on symmetrical electrolytes at low salt concentrations. The evaluation may advantageously be based on the low-concentration chemical model (lcCM), which is a Hamiltonian model at the McMillan–Mayer level including short-range nonelectrostatic interactions of cations and anions [89]. It is a feature of the lcCM that the association constants do not depend on the physical

CosMX Exhibit 1008, Page 483 of 633

properties of the electrolyte used for their determination. Association constants of the same electrolyte at approximately equal concentration ranges of the salt, when determined from thermodynamic properties (heat of dilution, EMF, vapor pressure) or spectroscopic properties (IR, Raman, NMR, microwave), are consistent with those from conductivity measurements [16], [90–92].

Conductivity measurements yield molar conductivities Λ ($S\,cm^2\,mol^{-1}$) at salt concentration c (mol L^{-1}). A set of data pairs (Λ_i, c_i), is evaluated with the help of non linear fits of equations [89,93,94] consisting of the conductivity equation, Eq. (7), the expression for the association constant, Eq. (3), and an equation for the activity coefficient of the free ions in the solution, Eq.(8); the activity coefficient of the ion pair is neglected at low concentrations.

given in Table 3. The coefficients are given in their usual form showing the relaxation (S_1, E_1, σ_1, σ_3) and electrophoretic (S_2, E_2, σ_2, σ_4) effects of conductivity.

$$S = S_1\Lambda_0 + S_2 \tag{9}$$

$$E = E_1\Lambda_0 - 2E_2 \tag{10}$$

$$J_1 = \sigma_1\Lambda_0 + \sigma_2 \tag{11}$$

$$J_2 = \sigma_3\Lambda_0 + \sigma_4 \tag{12}$$

R is the distance parameter, defining the upper limit of ion association. For spherical ions forming contact ion pairs it is simply the sum of the crystallographic radii of the ions $a = a_+ + a_-$, for solvent-shared and solvent-separated ion pairs it equals $a + s$ or $a + 2s$ respectively, where s is

Table 3. Coefficients S, E', J_1 and J_2 for lcCM evaluations based on the non developed Fuoss–Hsia conductivity equation [96].

$S_1 = 0.82043\times10^6\, z^3(\varepsilon T)^{-3/2}$ and $S_2 = 82.484\times10^{-5}\, z^2(\varepsilon T)^{-1/2}\eta^{-1}$
$E_1 = 2.94227\times10^{12}\, z^6(\varepsilon T)^{-3}$ and $E_2 = 0.433204\times10^3\, z^5(\varepsilon T)^{-2}\eta^{-1}$
$\sigma_1 = 2E_1\{(2h^2+2h-1)h^{-3} + 0.9074\} + \{\ln(0.50290\times10^{12}\, z(\varepsilon T)^{-1/2}R)\}$
$\sigma_2 = E_2\{35/3h + 2/h^2 - 2.0689 - 4\ln(0.50290\times10^{12}\, z(\varepsilon T)^{-1/2}R)\}$
$\sigma_3 = E_1(0.6094 + 4.4748/h + 3.8284/h^2)(0.50290\times10^{12}\, z(\varepsilon T)^{-1/2}R)$
$\sigma_4 = E_2(-1.3693 + 34/3h - 2/h^2)(0.50290\times10^{12}\, z(\varepsilon T)^{-1/2}R)$
where $h = 16.709\times10^{-6}\, z^2(\varepsilon T)^{-1}R^{-1}$ and $z = z_+ + |z_-|$

$$\Lambda/\alpha = {}_0 - S(\alpha c)^{1/2} + E'\alpha c\ln(\alpha c) + J_1(R)\,\alpha c + J_2(R)(\alpha c)^{3/2} \tag{7}$$

$$\ln y'_{\pm} = -\frac{\kappa_D q_B}{1+\kappa_D R} \tag{8}$$

In Eq. (7) Λ_0 is the limiting molar conductivity at infinite dilution and α is the degree of dissociation. A revised set of coefficients S, E', J_1, and J_2 of Eq. (7) for lcCM evaluations [95] based on the Fuoss–Hsia conductivity equation [96] is

the length of an orientated solvent molecule. For molecular ions the determination of the distance parameters a and R is more complicated; the distances must be taken from experimental determinations or semiempirical quantum-mechanical calculations as shown in Ref. [97]. For 1: 1 salts the Debye parameter κ_D and Bjerrum parameter q_B are given by the relationships

$$\kappa_D^2 = \frac{2e_0^2\alpha c N_A}{\varepsilon_0\varepsilon k_B T}\times10^3 \tag{13}$$

CosMX Exhibit 1008, Page 484 of 633

$$q_B = \frac{e_0^2}{8\pi\varepsilon_0 \varepsilon k_B T} \tag{14}$$

were e_0 is the elementary charge, ε_0 is permittivity of vacuum, and k_B is Boltzmann's constant.

The association constant of the lcCM counts all paired states of oppositely charged ions in the range a<r<R as ion pairs.

$$K_A^{(c)} = \frac{1-\alpha}{\alpha^2 c y_\pm'^2} = 4000\,\pi N_A \cdot \int_a^R r^2 \exp\left[\frac{2q_B}{r}\right] \exp\left\{-\frac{W_{ij}^*}{kT}\right\} dr \tag{15}$$

In Eq. (15) $2q_B/r$ is the coulombic part of the mean force potential, and W_{ij}^* is the noncoulombic part. The earlier association constants of Fuoss, Prue, and Bjerrum are special cases of this general chemical model [15]. The importance of noncoulombic interactions is proved [16] by:

- significantly different K_A values for isodielectric solvents, especially when they belong to different solvent classes,
- studies of electrolytes with mixed solvents, and
- different temperature dependencies of K_A for alkali metal halides and tetraalkylammonium halides in protic and aprotic solvents [98,99].

For weakly and moderately associated electrolytes, $10 < K_A < 10^4$, no problem generally occurs in obtaining reliable values for K_A and Λ_0 from conductivity measurements. Strong association, however, as known for many salts in the solvent class 6, often entails unrealistic Λ_0 values and K_A values. This is a problem of data analysis caused by the large extrapolation of very small Λ_i values at the lowest concentration of a run when compared with the expected Λ_0 value. Improved estimates for Λ_0 are obtained with the help of the Walden rule at constant temperature T, if Λ_0 is known for the electrolyte in another solvent (2) where a small association constant does not prohibit its determination and, η is known for both solvents (1,2):

$$\left\{\frac{\Lambda_0^{(1)}}{\Lambda_0^{(2)}} = \frac{\eta^{(2)}}{\eta^{(1)}}\right\}_T \tag{16}$$

Thereafter Λ_0 is fixed in the subsequent fitting procedure and reliable K_A and R values are obtained.

If the temperature dependence of conductivity is known in a given solvent, an estimate of an unknown Λ_0 at higher temperatures may be obtained which is much better than that measurable at lower temperatures with the help of the Walden rule:

$$\frac{\Lambda_0^{(T_1)}}{\Lambda_0^{(T_2)}} = \frac{\eta^{(T_2)}}{\eta^{(T_1)}} \tag{17}$$

This procedure is especially useful when the temperature coefficient of viscosity is small and the temperature coefficient of the association constant is large.

Solvents of class 6 generally show this behavior. At low temperatures, say T_1, both quantities K_A and Λ_0 are small and they can be determined with the help of the conductivity equation, Eq. (7). Equation (17) is then used to estimate Λ_0 values at other temperatures T_2.

CosMX Exhibit 1008, Page 485 of 633

Table 4. Molar conductivities of $LiBF_4$ in DME at zero concentration and their standard deviations at 25 °C according to different methods

Method	Λ_0 / S cm^2 mol^{-1}	$\sigma_0(\Lambda_0)$ / S cm^2 mol^{-1}
Eq. (7), Eq. (17)	139.3	± 2.2
Eq.(16)	140	± 10
Eq.(7)	63.2	± 4.3

Table 4 shows that the results obtained with this procedure for $LiBF_4$ in DME at 25 °C are significantly more precise than those obtained from use of Eq. (16). The. direct evaluation of the data, by Eq. (7) [100].

7.3.3 Triple-Ion Association Constants

7.3.3.1 Bilateral Triple-Ion Formation

Conductivity curves (Λ versus $c^{1/2}$) of salts in solvents of low–permittivity commonly show a weakly temperature–dependent minimum around 0.02 mol L^{-1} followed by a strongly temperature-dependent maximum at about 1 mol L^{-1}. According to Fuoss and Kraus [101,102] the increase of conductivity behind the minimum is due to the formation of new charge carriers from the ion pairs. They assume that coulombic forces suffice to form bilateral cationic $[C^+A^-C^+]_S^+$ and anionic $[A^-C^+A^-]_S^-$ triple ions in solvents of low–permittivity (ε <15) if the ions have approximately equal radii.

The conductivity functions of such electrolytes can be evaluated at the level of limiting laws with the help of Eq. (18), permitting the determination of the triple-ion–constant K_T and the ion-pair association constant K_A.

$$g(c)\Lambda\sqrt{c} = \frac{\Lambda_0}{\sqrt{K_A}} + \frac{K_T}{\sqrt{K_A}}\lambda_0 c\left(1-\frac{\Lambda}{\Lambda_0}\right) \qquad (18)$$

$$g(c) = y_\pm^{-1}\left\{1 - S\Lambda_0^{3/2}\sqrt{\Lambda c}\left(1-\frac{\Lambda}{\Lambda_0}\right)^{1/2}\right\}^{-1} \qquad (19)$$

The experimentally noionic accessible limiting conductivities $\lambda_0 = \lambda_0^+ = \lambda_0^-$ of the triple ion must be estimated with consideration of ion sizes yielding $\lambda_0^T = \Lambda_0/3$ [101,102] or $2\Lambda_0/3$ [103], with preference for the latter value.

Ion-pair association constants K_A determined with the set of conductivity equations (7)–(15) agree with those obtained from Eq. (18) and (19) [100]. Salomon and Uchiyama have shown that it is also possible to extend the directly Fuoss–Hsia equation to include triple-ion formation [104].

7.3.3.2 Unilateral Triple-Ion Formation.

In contrast to bilateral triple-ion formation, unilateral triple-ion formation may also occur in solvents of high permittivity, when ion-pair association is increased by noncoulombic specific ion–ion interactions in solvents of low basicity such as PC or AN. Exclusive formation of anionic triple-ions $[A^-C^+A^-]_S^-$, is observed in these solvents when large organic molecular anions A_S^- interact with small cations such as Li^+ or H^+. For example, in contrast to lithium acetate in DMSO [97], where ion association is moderate, ion association as well as unilateral triple-ion formation is observed in the solvent PC [105] due to the much lower basicity of this solvent, (see Table 2)

Acording to Wooster [106,107], conductivity measurements can be evaluated

CosMX Exhibit 1008, Page 486 of 633

at the level of limiting laws with the conductivity equation

$$[g(c)\Lambda]^2 c\left[1-\frac{\Lambda}{\Lambda_0}\right]^{-1} = \frac{\Lambda_0^2}{K_A}+\frac{K_T}{K_A}c\left[2\Lambda_0\lambda_0-\Lambda_0^2\right]\left[1-\frac{\Lambda}{\Lambda_0}\right] \quad (20)$$

Despite the results from various experiments such as transference number measurements, polarographic studies, spectroscopic measurements, and dielectric relaxation studies in addition to conductivity measurements, unilateral triple–ions remain a matter of debate. For experimental examples and other hypotheses for the interpretation of conductance minima the reader is referred to Ref. [15] and the literature cited there.

The investigation of ion-aggregate formation based on conductivity studies can be extended to quadruple-ion formation [108–111], which is thought to be the reason for the conductivity maximum and the subsequent decrease of conductivity.

However, in our opinion the interdependence of up to four aggregation constants in addition to uncertainties in the determination of the limiting conductivity and activity coefficients makes their determination with recent equations [110] increasingly unsure.

Table 5 contains a selection of ion-pair association constants, triple ion formation constants, and limiting conductivities for various electrolytes which have been studied in connection with the optimization of battery electrolytes. It shows

- low limiting conductivities and low association constants of electrolytes based on solvents of high permittivity and high viscosity, e.g., PC;
- high limiting conductivities and high association constants for low-permittivity solvents with low viscosities;
- rather small association constants and moderate limiting conductivities for electrolytes based on a mixture of both solvent types;
- association constants of the lithium salts strongly depending on the radius of the anion and its ability to delocalize its charge
- association constants decreasing strongly with decreasing temperature; and
- association constants decreasing by the substitution of a proton of the anion $Li[B(C_6H_4O_2)_2]$ by fluorine, entailing increased charge delocalization.

The last point has been studied more quantitatively for the electrolyte $LiO_2CCH_xF_y$ (x+y=3) / DMSO [97,105]. Semiempirical quantum-mechanical calculations with the help of MOPAC [143] show that the mean electron density at the oxygen atoms q(O) decreases for these acetates by about 0.1 unit with increasing fluorine content of the anion [97]. As a consequence:

- Ion association constants decrease by a factor of about 50.
- The logarithm of the association constant is linearly correlated to the mean charge density of oxygen atoms obtained from MNDO calculations, $q(O)_{MNDO}$ (Fig. 4), showing that the decrease in association is governed only by decreasing electrostatic interaction. This finding is supported by

CosMX Exhibit 1008, Page 487 of 633

Table 5. Association constants, triple ion formation constants and limiting conductivities of some lithium electrolytes.

Solvent	Salt	K_A / (L^{-1} mol^{-1})	K_T / (L^{-1} mol^{-1})	Λ_0 / S cm^2 mol^{-1}	Ref.
AN	LiMe	5.99	–	144.46	[75]
DMC	$LiAsF_6$	8.9×10^{11}	445	97.4	[112]
DMC	$LiClO_4$	8.6×10^{12}	418	115.7	[112]
DME	$Li[B(C_6H_3FO_2)_2]$	0.77×10^{6}	–	108.37	[82]
DME	$Li[B(C_6H_4O_2)_2]$	4.23×10^{6}	–	108.37	[82]
DME	$LiBF_4$	24×10^{6}	30.8	139.3	[100]
DME	$LiClO_4$	3.6×10^{6}	31.3	143.1	[113]
DME	$LiPF_6$	1.9×10^{5}	27.1	135.1	[113]
DME	$LiAsF_6$	12.6×10^{4}	21.8	143.7	[113]
DME	$LiSbF_6$	10.8×10^{4}	22.9	136.7	[113]
DME	$LiBPh_4$	2.6×10^{4}	11.5	104.9	[113]
DME*	$Li[B(C_6H_3FO_2)_2]$	4.58×10^{4}	–	36.60	[82]
DME*	$Li[B(C_6H_4O_2)_2]$	2.13×10^{5}	–	36.60	[82]
DME*	$LiBF_4$	0.56×10^{6}	14.9	46.45	[100]
MA	$LiAsF_6$	9.4×10^{5}	70.7	155.7	[10, 114]
MA	$LiClO_4$	7.8×10^{7}	38	186.3	[10, 114]
MF	$LiAsF_6$	4.38×10^{4}	69.1	168.4	[115]
MF	$LiClO_4$	6.54×10^{5}	22.0	157.0	[115]
MF	LiIm	2.34×10^{4}	20.1	131.489	[115]
2Me-THF	$LiClO_4$	1.8×10^{8}	33	144	[116]
MTHF+	$LiClO_4$	7.2×10^{6}	7	61	[116]
PC	$Li[B(C_6H_3FO_2)_2]$	4.08	–	19.093	[82]
PC	$Li[B(C_6H_4O_2)_2]$	14.24	–	19.297	[82]
PC	$LiAsF_6$	0	–	27.30	[117]
PC	$LiBF_4$	4.4	–	30.14	[117]
PC	$LiC_4F_9SO_3$	11.3	–	21.49	[117]
PC	$LiCF_3SO_3$	13.2	–	26.68	[117]
PC	$LiClO_4$	0.1	–	28.60	[117]
PC	LiIm	0	–	22.02	[117]
PC	LiMe	1.24	–	20.20	[75]
PC	$LiPF_6$	0	–	27.32	[117]
PC/DME‡	$LiBF_4$	40.1	–	66.11	[212]
PC/DME‡	$LiCF_3SO_3$	59.4	–	63.57	[212]
PC/DME‡	$LiClO_4$	20.0	–	65.02	[212]
PC/DME‡	LiIm	16.0	–	60.54	[212]
PC/DME‡	$LiPF_6$	16.7	–	64.73	[212]
PC/DME‡	$LiPF_6$	26.9	–	45.63	[212]
PC/DME‡	$LiBF_4$	119.0	–	47.20	[212]
PC/DME‡	$LiCF_3SO_3$	59.4	–	63.57	[212]
PC/DME‡	$LiClO_4$	47.7	–	45.97	[212]
PC/DME‡	LiIm	25.3	–	41.78	[212]
THF	$LiClO_4$	4.8×10^{7}	153	–	[118]
THF	$LiClO_4$	3.7×10^{7}	34		[113]
THF	$LiAsF_6$	5.3×10^{5}	35		[113]
THF	$LiSbF_6$	2.7×10^{5}	40.8		[113]
THF	$LiBPh_4$	2.2×10^{4}	16.5		[113]

* –45°C

+ –43°C

‡ Equimolar mixtures

CosMX Exhibit 1008, Page 488 of 633

linear plots of $\ln(K_A)$ versus $(1/r^+)$ for alkali metal acetates with cationic radius r^+ in DMSO.

- The ratio of association constants for pairs of salts, 4.2 for (y=0)/(y=1), 3.1 for (y=1)/(y=2), and 3.7 for (y=2)/(y=3) is scarcely temperature-dependent.

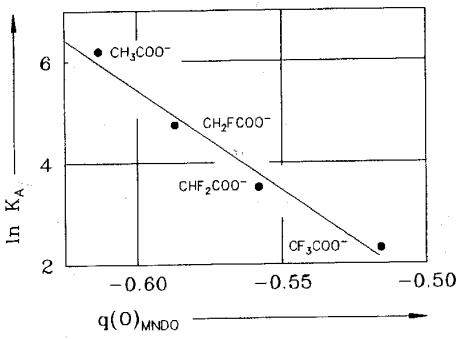


Figure 4. Linear correlation of $\ln K_A$ vs. mean charge density of oxygen atoms, $q(O)_{MNDO}$, for $LiO_2CCH_xF_y$, $x + y = 3$/DMSO.

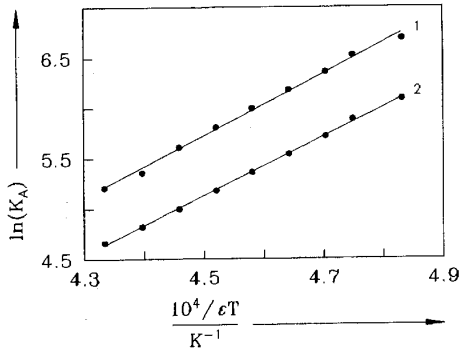


Figure 5. Plot $\ln K_A$ vs. $(1/\varepsilon T)$ for $Li[B(C_6H_4O_2)_2]$ (1) and $Li[B(C_6H_3FO_2)_2]$ (2) in DME.

Figure 5 shows the results obtained for $Li[B(C_6H_4O_2)_2]$ and $Li[B(C_6H_3FO_2)_2]$ in DME where the plot $\ln K_A = f(1/\varepsilon T)$ yields two parallel lines. Again, the ratio (5.5) of association constants is nearly independent of temperature. Distance parameters as determined from the slopes are approximately equal, showing that fluorination scarcely affects the radius of the anion [81].

7.3.3.3 Selective Solvation of Ions and Competition Between Solvation and Ion Association.

Counterions and solvent molecules compete for a place in the vicinity of every ion. The relative strength of interaction and the space available in the neighborhood of the ion determine which species are formed.

In mixed solvent systems the difference in the solvating abilities of solvent molecules S_1 and S_2 causes a selective solvation of cations and anions [119,120].

$$\begin{aligned} &C^+ \cdot nS_1 + A^- \cdot mS_1 + xS_2 \rightleftharpoons \\ &C^+ \cdot (n-y)S_1(x-k)S_2 + \\ &A^- \cdot (m-z)S_1 kS_2 + (y+z)S_1 \end{aligned} \qquad (21)$$

Selective solvation of the cations and anions takes place if the molar fraction x_{S_1} of the solvent S_1 differs from that in the vicinity of the ions:

$$\frac{(n-y)}{(x-k)+(n-y)} \neq \frac{(m-z)}{(m-z)+k} \neq x_{S_1} \qquad (22)$$

If S_1 is a weak base (low DN) and S_2 is a strong base, cations are selectively solvated by S_2; conversely, if S_1 is a good acceptor (high AN) it will preferentially solvate the anion. As a consequence, the Stokes radii of ions generally change with the composition of a binary solvent.

Addition of strongly solvating ligands L to electrolytes with high ion-pair associa-

CosMX Exhibit 1008, Page 489 of 633

tion constants entails a series of selective solvation reactions:

$$C_s^+ + L \rightleftharpoons [C^+L]_s^+ \quad (23)$$

$$C_s^+ + L \rightleftharpoons [C^+L_2]_s^+ \quad (24)$$

$$A_s^- + L \rightleftharpoons [A^-L]_s^- \quad (25)$$

$$[C^+A^-]_s^0 + L \rightleftharpoons [C^+LA^-]_s^0 \quad (26)$$

shifting the equilibria of Eq. (4)–(6) in the direction of the solvated free ions. As a consequence, the properties of the electrolyte change; for example, the addition of small amounts of ligands to a solution entails large conductivity increases of up to more than 100 percent [121]. Conductivity measurements in solvents of very low permittivityare therefore strongly affected by traces of water, which acts as a ligand (cf. Sec. 7.2.3 and Ref. [20]).

The pioneering work of Gilkerson and co-workers [122–130] and Huyskens and colleagues [131,132] allows the determination of the corresponding equilibrium constants from conductivity measurements. If all equilibria, Eq. (4)–(6), are involved, the association constants of an electrolyte without (K_A^0) and with (K_A) addition of the ligand at concentration c_L of the ligand L are given by the relationship [132]

$$\frac{K_A^0}{K_A} = \frac{(1+K_1^+c_L+K_2^+c_L^{\,2})(1+K_1^-c_L)}{(1+K_Pc_L)} \quad (27)$$

where K_1^+ refers to the Eq. (23) equilibrium, K_2^+ to Eq. (24), K_1^- to Eq. (25), and K_P to Eq. (26). Studies of this type are very time consuming because many series of conductivity measurements must be performed, as K_A^0 and $K_A(c_L)$ are needed along with their appertaining limiting values of conductivity with and without added ligand.

At low salt concentrations and very high association constants, the ratio of association constants can be approximated by

$$\frac{K_A^0}{K_A} = \left(\frac{\Lambda_L}{\Lambda}\right)^2\left(\frac{1-\Lambda\Lambda_0^{-1}}{1-(\Lambda_0^L)^{-1}}\right) = R_G\frac{1-\Lambda\Lambda_0^{-1}}{1-(\Lambda_0^L)^{-1}} \approx R_G \approx \left(\frac{\kappa_L}{\kappa}\right)^2 \quad (28)$$

when neglecting the difference in molar ionic conductivities due to selective Li^+-ion solvation. Λ_0^L and Λ_L are the limiting molar conductivity and the molar conductivity at finite concentration in presence of the ligand; Λ_0 and Λ are the limiting value and the value at finite concentration before addition of ligand.

Salomon and co-workers investigated the role of ligands known to offer cavities with diameters matching the radius of the lithium ion, e.g., 15-crown-5 or the cryptand [222] 12–crown-4 (12C4) and derivatives such as 1-aza-12-crown-4 (1-A 12C4) and 1-benzoaza-12-crown-4 (1-BA-12C4) for various battery electrolytes at moderate concentrations [133–136,217].

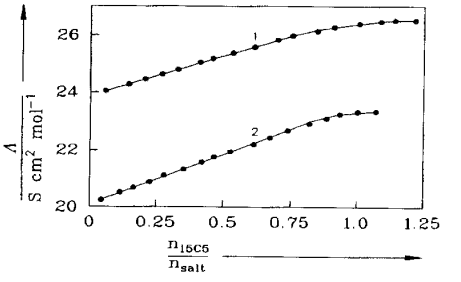


Figure 6. Conductivity increase of $LiBF_4$ (1) and $LiSO_3CF_3$ (2) solutions in PC/5-crown-5 mixtures, as obtained by titration. Adapted from Ref. [135].

CosMX Exhibit 1008, Page 490 of 633

The conductometric titration shown in Fig. 6 (adapted from Ref. [135]) exhibits the expected conductivity increase for $LiBF_4$ and $LiSO_3CF_3$ solutions in PC / 5-crown-5 mixtures at 25 °C, i.e., for salts which are known to be strongly associated despite the relatively high permittivity of the solvent.

It is worth mentioning that single-ion conductivities of lithium ions and anions at infinite dilution, and transference numbers of ligand–solvated lithium ions estimated therefrom, increase due to the replacement of more than one (generally four) solvent molecules. Table 6 demonstrates this beneficial feature.

Table 6. Single-ion conductivities of solvated lithium ions and anions at 25 °C in PC at infinite dilution [13]

Cation	λ_+^0 / Scm^2mol^{-1}	Anion	λ_-^0 / Scm^2mol^{-1}
$Li^+ \cdot n$PC	7.86	ClO_4^-	18.89
$Li^+ \cdot$12C4	10.02	BF_4^-	20.71
Li^+1–A–12C4	10.25	$CF_3SO_3^-$	16.41
Li^+1–BA–12C4	11.99	Im^-	14.9
$Li^+ \cdot$12C5	10.50	Me^-	12.4

7.4 Bulk Properties

7.4.1 Electrochemical Stability Range

The electrochemical stability range determines the usefulness of nonaqueous electrolytes for electrochemical studies as well as for applications. It indicates the absence of electrochemical oxidation or reduction of solvent or ions, and of faradaic current when an external voltage is applied at the electrodes.

The electrochemical stability range covers potentials from the anodic limit E_{ox} to the cathodic limit E_{Red}. Electrochemical investigations on solutes can be performed in this range which is also called the voltage window in analogy to spectroscopy. Generally the electrochemical stability range is established by cyclic voltammetry (CV) or linear-sweep voltammetry. It depends on experimental conditions, the scan rate v ($mV\,s^{-1}$) and the arbitrarily chosen current density i_0 ($mA\,cm^{-2}$) for the onset of the electrochemical process. Unfortunately no generally accepted conditions for CV experiments exist; scan rates range from 2 to $100\,mV\,s^{-1}$ and onset current densities vary from 0.01 to $3\,mA\,cm^{-2}$ (see Ref. [137], and the literature cited therein). Furthermore, many investigations have been performed with a saturated calomel electrode and without investigation of the reaction products by potentiostatic electrolysis. Therefore unknown liquid-junction potentials and insufficient knowledge of electrode reactions must be taken into account in addition to differing experimental conditions for the interpretation of such data.

However, even if electrolytes have sufficiently large voltage windows, their components may not be stable (at least kinetically) with lithium metal; for example, acetonitrile shows very large voltage windows with various salts, but is polymerized at deposited lithium if this reaction is not suppressed by additives, such as SO_2 which forms a protective ionically conductive layer on the lithium surface. Nonetheless, electrochemical stability ranges from CV experiments may be used to choose useful electrolytes.

According to Ue et al. [141] the anodic

CosMX Exhibit 1008, Page 491 of 633

stability sequence of solvents is DME (5.1) < THF, DIOX (5.2) < EC (6.2) < AN (6.3) < MA (6.4) < PC (6.6) < DMC, DEC, EMC (6.7) < glutaronitrile GLN (8.3), where the figures in parentheses are the limiting anodic oxidation potentials (V) vs. Li/Li^+.

It is worth mentioning that the use of microelectrodes allows the investigation of the electrochemical stability range of solvents without addition of a salt [138]. These studies make it possible to discriminate between chemical and electrochemical reactions at the electrodes. For example, THF is not reduced at potentials down to −2V vs. Li, but oxidized already at +4V vs. Li, whereas PC is stable up to 5 V but already reduced at potentials of less than 1 V vs. Li.

The use of liquid salts, based on anodically stable cations such as 1,2-dimethyl-3-propylimidazolium (Dmpi) without added solvent, allows the investigation of the electrochemical stability of anions [75].

Table 7. Electrochemical stability ranges or anodic stability limits of several nonaqueous electrolytes

Solvent	Salt, $c.(\mathrm{mol\,L^{-1}})$	E_{Red} / V	E_{ox} / V	E_{REF}	E_W	$V/(\mathrm{mV\,s^{-1}})$, $i/(\mathrm{mA\,cm^{-2}})$	Refs.
2Me-THF	$LiAsF_6$, 1.0		4.15	Li/Li^+	GC[3]	100, 0.1	[67]
2Me-THF	$LiAsF_6$, 1.0		4.32	Li/Li^+	Pt	50, 1	[039]
2Me-THF	LiIm, 1.0		4.0	Li/Li^+	GC	100, 0.1	[67]
AN	Et_4NBF_4, 0.65	−2.8	+3.3	SCE	GC	5, 1	[137]
BEG-1/EC	–	–	>5.8		Pt	10	[45]
DIOX	$LiAsF_6$, 1.5		3.60	Li/Li^+	Pt	50, 1	[139]
DIOX	LiIm, 1.0		4.2	Li/Li^+	GC	100, 0.1	[67]
DIOX	$LiPF_6$, 1.0		3.50	Li/Li^+	Pt	50, 1[5]	[139]
DIOX[1]	$LiB(C_5F_6)_4$		4.40	Li/Li^+	Pt	50, 1	[139]
DIOX[1]	$LiB(CH_3)_4$		2.85	Li/Li^+	Pt	50, 1	[139]
DIOX[1]	$LiB(Ph)_4$		3.53	Li/Li^+	Pt	50, 1	[139]
EC,DMC,MF	LiMe		4.3	Li/Li^+	Al	5, 0.01	[76]
EC,DMC,MF	LiMe		4.3	Li/Li^+	GC	5, 0.058	[76]
EC,DMC,MF	LiMe		4.3	Li/Li^+	Pt	5, 0.068	[76]
EC/TMS (1:1)	Et_4NBF_4, 0.5	−2.6	+2.1	SCE	GC	0.05, 0.5	[140]
EC/TMS (1:1)	Et_4NClO_4, 0.5	−2.6	+1.9	SCE	GC	0.05, 0.5	[140]
EC/TMS (1:1)	Et_4NPF_6, 0.5	−2.8	+2.4	SCE	GC	0.05, 0.5	[140]
GBL	Et_4NBF_4, 0.65	−3.0	+5.2	SCE	GC	5, 1	[137]
MSC	$LiAlCl_4$		4.5	Li/Li^+			[43]
MSC	LiIm		5.5	Li/Li^+			[43]
n-Bu	LiIm, LiTri or $LiNO_3$, 1	−1.0	+3.5	Ag/Ag^+	Pt	–	[41]
No solvent	$DmpiAsF_6$		5.10±0.02	Li/Li^+	Pt, 80°C	20, 1	[75]
No solvent	DmpiMe		5.35±0.02	Li/Li^+	Pt, 80°C	20, 1	[75]
No solvent	$DmpiPF_6$		5.003±0.02	Li/Li^+	Pt, 80°C	20, 1	[75]
No solvent	DmpiIm		5.13±0.02	Li/Li^+	Pt, 80°C	20, 1	[75]
PC	Et_4NBF_4, 0.65	−3.0	+3.6	SCE	GC	5, 1	[137]
PC	Et_4NBF_4 0.65	−3.7	+2.8	Ag/Ag^+[8]	GC	5, 1	[141]
PC	Et_4NPF_6, 0.65	−3.0	+3.6	SCE	GC	5, 1	[137]
PC	Et_4NAsF_6, 0.65	−3.8	+3.0	Ag/Ag^+[8]	GC	5, 1	[141]
PC	$LiOSO_2C_4F_9$		6.02	Li/Li^+	Pt	50,–	[78]
PC	$LiOSO_2C_8F_{17}$		6.51	Li/Li^+	Pt	50,–	[78]
PC	$LiOSO_2CF_3$		4.76	Li/Li^+	Pt	50,–	[78]

CosMX Exhibit 1008, Page 492 of 633

PC	$Li[B(C_6H_3FO_2)_2]$, 0.9 mol kg^{-1}		3.7	Li/Li^+	Au	$20, 0+\varepsilon$[7]	[82]
PC	$Li[B(C_6H_4O_2)_2]$,1.1 mol kg^{-1}		3.6	Li/Li^+	Au	$20, 0+\varepsilon$	[82]
PC	$Li[B(C_6H_4O_2)_2]$, 0.4 mol kg^{-1}		4.0	Li/Li^+	Au	$20, 0+\varepsilon$	[82]
PC	$Li[B(C_7H_4O_3)_2]$, 0.775 mol kg^{-1}	0.62 to 0.67	4.5	Li/Li^+	Au	$20, 0+\varepsilon$	[80]
PC	$LiB[C_5H_3(CF_3)_2]_4$		5.07	Li/Li^+	Pt	50, 0.5	[78]
PC	$LiClO_4$	−2.2	+2.3	Ag/Ag^+	Pt		[142]
PC	$LiClO_4$, 0.65	−3.0	+3.1	SCE	GC	5, 1	[137]
PC	$LiSO_3CF_3$, 0.65	−3.0	+3.1	SCE	GC	5, 1	[137]
PC	$Et_4NSO_3CF_3$, 0.65	−3.8	+2.2	Ag/Ag^+[8]	GC	5, 1	[141]
PC	$Et_4NSO_3C_4F_9$, 0.65	−3.7	+2.5	Ag/Ag^+[8]	GC	5, 1	[141]
PC	Et_4NIm, 0.65	−3.8	+2.5	Ag/Ag^+[8]	GC	5, 1	[141]
PC	$Et_4NB[C_6F_5]_4$, 0.65	−3.3	+1.4	Ag/Ag^+[8]	GC	5, 1	[141]
PC	$Et_4NB[C_6H_5]_4$, 0.65	−3.9	+0.2	Ag/Ag^+[8]	GC	5, 1	[141]
PC	Et_4NSbF_6, 0.65	−3.7	+3.3	Ag/Ag^+[8]	GC	5, 1	[141]
PC	No electrolyte	<1	+5	Li/Li^+ (1 mol L^{-1})	Pt micro[4]	0.2, –	[138]
THF	$LiAsF_6$, 1.0		4.25	Li/Li^+	GC	100, 0.1	[67]
THF	LiIm, 0.5		4.4	Li/Li^+	GC	100, 0.1	[67]
THF	No electrolyte	<−2	4	Li/Li^+ (1 mol L^{-1})	Pt micro	0.2, –	[138]
TMS	Et_4NBF_4,0.65	−3.1	+3.3	SCE	GC	5, 1	[137]
TMS	LiIm, 1.0M		4.5	Li/Li^+	GC	100, 0.1	[67]

(1) or DIOX–DME, salt concentration 0.6–2 mol L^{-1}.
(2) Dmpi is the cation1,2-dimethyl-3-propylimidazolium.
(3) GC is the glassy carbon electrode.
(4) Pt-micro refers to platinum microelectrodes.
(5) Assigned as oxidation voltage, the anodic stability limit is slightly lower.
(6) Values from different reference electrodes, can be converted to the NHE scale or any other scale by referring to their reduction potentials versus the NHE-electrode or other reference electrodes, and correlation of the activity of the electroactive cation. Reduction potentials are: SCE 0.2412V; Ag/AgCl - 0.197V; Li/Li^+ - 2.962V. For example: E(SCE)=*E*(NHE) - 0.2412V.
(7) $0+\varepsilon$ refers to the onset of the decomposition where the current starts to deviate from zero.
(8) Double junction reference electrode.

Table 7 lists the electrochemical windows or the anodic stability limits of several nonaqueous electrolytes, or their anodic stabilty, the reference electrodes R_{REF} used, the working electrode material E_W, the experimental conditions, and the references. It shows the following features:

- Nonaqueous electrolytes may offer very large voltage windows, up to more than 8 V.
- New electrolytes, especially those based on carbonates show anodic stability ranges of more than 5 V vs. Li/Li^+ and even reaching 6.5 V, sufficiently high for application with high-voltage cathodes.
- Ethers are oxidized at much lower potentials than carbonates.
- Comparison of stability limits of low-temperature molten salts and lithium salts with a common anion shows the influence of the solvent, which limits the anodic stability range of solutions based on LiMe or LiIm. The 1,2-dimethyl-3-propylimidazolium methide

CosMX Exhibit 1008, Page 493 of 633

or imide exceed 5 V vs. Li at their anodic limit, whereas LiMe or LiIm solutions in EC/DMC reach only 4.3 V [75,76].

- Working electrode materials have an appreciable effect on the oxidation potentials and the resulting current densities (see also Ref. [139]).
- Substitution of anions by electron-withdrawing substituents, such as F or CF_3, increases the anodic stability of anions [78,82,139]; Figure7 shows an example.
- The anodic stability of anions on glassy carbon is the following order: $BR_4^- < ClO_4^- < Tri^- < Im^- < Me^- < SO_3C_4F_9^- < BF_4^- < AsF_6^- < SbF_6^-$ [141].

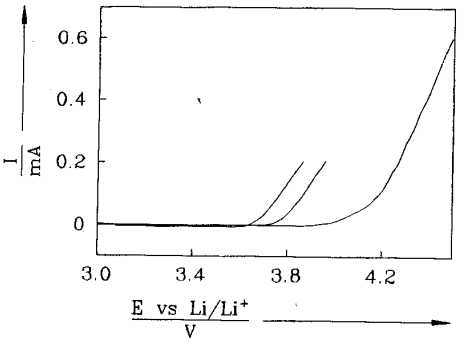


Figure 7. Anodic stability limits of lithium benzenediolatoborates, $Li[B(C_6H_{4-x}F_xO_2)_2]$, in PC. From left to right: x=0, 1, 4 as obtained from CVs at gold electrodes [82].

The last remark deserves a more quantitative explanation. Horowitz et al. [64] have shown that useful correlations are obtained between the oxidation voltages of the anion and the averaged Hammett σ-function or Ingold and Taft's σ^*-function of the substituents around a boron atom. Both empirical functions reflect the electron-withdrawing ability of the substituent group. Hammett's averaged σ^*-values are obtained from the dissociation constants of *meta*-substituted benzoic acids, and σ^*-values are obtained from comparative rates of acid and alkaline ester hydrolysis; for details see Ref. [64].

The slope of the linear correlation oxidation potential at $1 mA cm^{-2}$ at platinum electrodes versus the averaged Hammett σ^*-function (E_{ox} vs.σ^*) is about 1 V per averaged σ^*-value. Using this result, a comparison with results from the ionization of carboxylic acids is possible which shows that the effect of a given electron-withdrawing group is twice as large for the free energy of oxidation as for the free energy of ionization of carboxylic acids. Horowitz et al. [64] explain this result by the larger separation of groups from the oxygen atoms of the carboxylate group when compared with their (smaller) distance from the boron atom, and better solvation of anions in water when compared with the solvents of low permittivity in their study.

A more recent but closely related explanation of the shift of oxidation potentials by electron-withdrawing substituents is based on results of semiempirical quantum-mechanical calculations [143–146]. Methods such as MNDO, AM1, or PM3 are used to yield the energy of the highest occupied molecular orbital of the anion, E_{HOMO}. Correlations of E_{ox} with $-E_{HOMO}$ are linear for a given set of compounds of similar structure. Anodic stability limits E_{ox} of vinyl compounds, for example, are linearly correlated with their E_{HOMO} values with a slope of $1 eV V^{-1}$ [147]. For alkyl- and arylborates, however, a much larger value of $3 eV V^{-1}$ is obtained [78], in accordance with our value for the chelatoborates $Li[B(C_6H_{4-x}F_xO_2)_2]$ (x=0, x=1, and x=4; points 1 – 3 in Fig.8 and lithium bis[2, 3 – naphthalenediolato (2 -) -O,O']borate, $Li[B(O_2C_{10}H_6)_2]$ (point 4

CosMX Exhibit 1008, Page 494 of 633

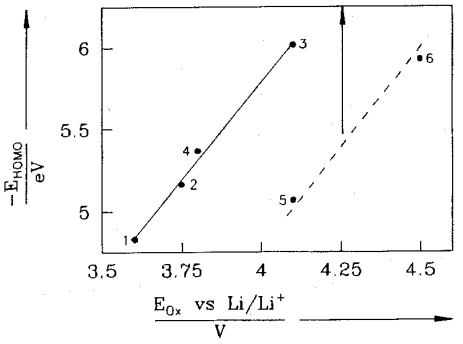


Figure 8. Linear correlation of HOMO<O energies and anodic oxidation limits of lithium borates Li[B(C_6 $H_{4-x}F_xO_2)_2$], x=0 (1), x=1 (2), and x=4 (3); Li[B($O_2C_{10}H_6)_2$] (4); lithium bis[salicylato (2-)]borate (6); and lithium bis [2,2' - biphenyldiolato (2 -) -O,O']borate (5).

[82] in Fig. 8), showing that the underlying oxidation mechanisms are closely related.

There is a difference in the behavior of benzenediolatoborate and naphthalenediolatoborate solutions on the one hand, and lithium bis[2,2' -biphenyldiolato(2-)-O,O'] borate (point 5 in fig. 8) lithium bis[salicylato (2-)]borate (point 6) or benzenediolatoborate/phenolate mixed solutions on the other (Fig.8). This can be tentatively explained by the assumption of different decomposition mechanisms due to different structures, which entail the formation of soluble colored quinones from benzenediolatoborate anions and lithium-ion conducting films from solutions of the latter compounds (points 5 and 6) [80]. The assumption of a different mechanism and the formation of a lithium-ion conducting, electronically insulating film is supported by

- the shift of the linear correlation of the values for the highest occupied molecular orbital E_{HOMO} with anodic decomposition voltages E_{ox}, of about $-3\,eV\,V^{-1}$, to higher oxidation potentials by about 1 eV (see Fig.8).
- the same effects obtained with lithium phenolate or dilithium 2,2' -biphenyldiolate-based solutions [80].
- anodic polymer formation from phenols yielding polyphenoxide as already postulated and proved by Bruno et al. [148];
- different CV data in the region of the anodic decomposition.

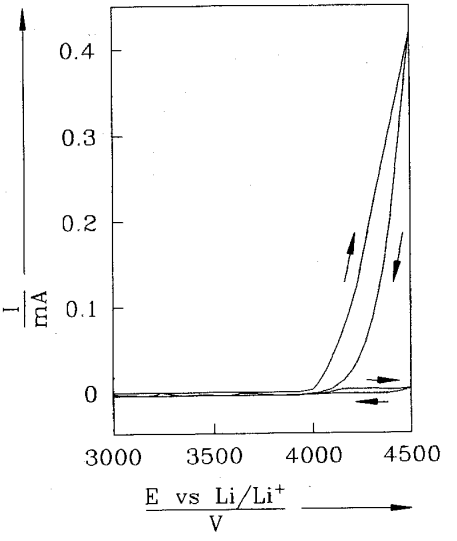


Figure 9. CV of 0.2 mol kg^{-1} lithium bis[2,2' -biphenyldiolato(2-)-O,O']borate solution in PC at a stainless steel electrode, area 0.5 cm^{-2}, showing the passivation of the electrode.

Figure 9 shows the first and second cycle of a cyclic voltammogram of a 0.2 molal (mol kg^{-1}) solution of lithium bis[2,2' biphenyldiolato(2-)-*O,O'*]borate in PC at a stainless steel electrode. The sweep covers the potential range from open circuit potential E_R versus a lithium reference electrode up to 4500 mV versus Li and back to E_R. The first cycle shows

CosMX Exhibit 1008, Page 495 of 633

an anodic decomposition of the anion at about 4.1 V versus Li, as obtained from the linear extrapolation of the increasing oxidation current. Upon decreasing the potential the current is lower, showing the beginning of a passivation of the electrode which clearly is complete on the second cycle, where the current is zero up to 4.5 V versus Li. The same behavior is obtained at gold electrodes.

Subsequent deposition and dissolution of lithium at the anodically passivated electrode by CV in the range −1000 mV to 6000 mV versus Li was successful, showing that the passivating film at the electrode is only impermeable for the anions, but not for lithium ions; however, the amount of lithium deposited decreases, with cycle number.

Upon an increase of the anodic reverse potential finally up to 8 V versus Li the cyclic voltammogran corresponding to Fig. 9 remains unchanged, showing that the passivating layer at the electrode also protects the solvents (PC and DME) from being oxidized. Subsequent deposition and dissolution of lithium at the passivated electrodes remains possible when the electrode is passivated but the cycling efficiency decreases.

CV of solutions of lithium bis[salicylato(2-)]borate in PC shows mainly the same oxidation behavior as with lithium bis[2,2′ biphenyldiolato(2-)-O,O′] borate, i.e., electrode (stainless steel or Au) passivation. The anodic oxidation limit is the highest of all borates investigated by us so far, namely 4.5 V versus Li. However, in contrast to lithium bis[2,2′-biphenyldiolato(2-)-*O,O*′]borate based solutions, lithium deposition and dissolution without previous protective film formation by oxidation of the anion is not possible, as the anion itself is probably reduced at potentials of 620–670 mV versus Li, where a continuously decreasing cathodic peak is observed in the cyclic voltammograms.

Small amounts of lithium phenolate or dilithium-2,2′ biphenyldiolate, whose anodic decomposition starts at about 3.2 V versus Li and thus before anodic decomposition of the borates begins, prevent the anodic decomposition of benzenediolatoborate anions in PC. The behavior of the solution is then determined by the additive.

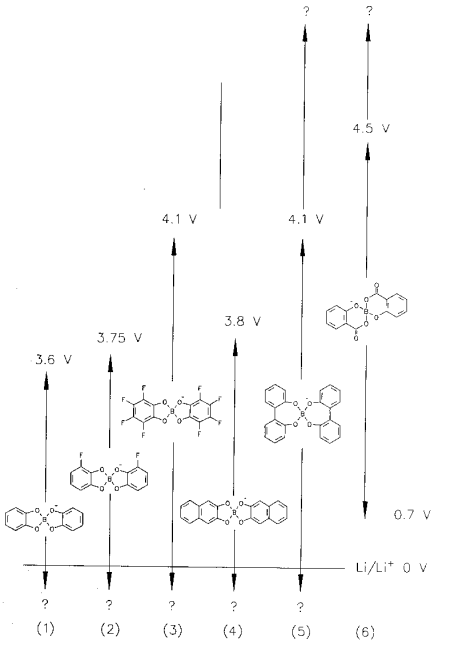


Figure 10. Stability limits of lithium chelatoborates; for details see the text.

Figure 10 shows the voltage windows of chelatoborates. The question mark (?) indicates the formation of lithium-ion conducting films, preventing the electrolyte from decomposition; the numbers refer to the compounds mentioned in this section of the text.

CosMX Exhibit 1008, Page 496 of 633

7.4.2 Chemical Stability of Electrolytes with Lithium and Lithiated Carbon

Unfortunately, both lithium and the lithiated carbons used as the anode in lithium ion batteries (Li_xC_6, $1 \geq x \geq 0$) are thermodynamically unstable relative to solvent molecules containing polar bonds such as C–O, C–N, or C–S, and to many anions of lithium salts, solvent or salt impurities (such as water, carbon dioxide, or nitrogen), and intentionally added traces of reactive substances (additives) .

For example, the reaction enthalpy for the reduction of PC proceeding at lithium amalgam to form propylene gas and lithium carbonate is estimated to be $-141\,kcal\,(mol\,PC)^{-1}$ [149]. PC is reduced at noble-metal electrodes at potentials below 1.5 V vs. Li, and yields lithium alkyl carbonates when lithium salts are the supporting electrolytes. Reduction occurs at 0.7–0.8 V vs. Li with Bu_4NClO_4 as supporting electrolyte [150].

Kinetic stability of lithium and the lithiated carbons results from film formation which yields protective layers on lithium or on the surfaces of carbonaceous materials, able to conduct lithium ions and to prevent the electrolyte from continuously being reduced: film formation at the Li/PC interphase by the reductive decomposition of PC or EC/DMC yielding alkylcarbonates passivates lithium, in contrast to the situation with DEC where lithium is dissolved to form lithium ethylcarbonate [149]. EMC is superior to DMC as a single solvent, due to better surface film properties at the carbon electrode [151]. However, the quality of films can be increased further by using the mixed solvent EMC/EC, in contrast to the recently proposed solvent methyl propyl carbonate (MPC) which may be used as a single solvent [152].

Passivating films, which are formed in less than a second on the surface when lithium is exposed to a suitable solution determine [153]

- the quality of passivation,
- the electrode kinetics of lithium deposition (intercalation),
- dissolution by the resistivity of the lithium/solution interphase,
- its uniformity and thickness,
- the roughness of the lithium metal surface, and hence
- the current distribution.

It is interesting to note that even some gases (O_2,SO_2,N_2) at low pressures form thin primaryfilms in fast reactions [154-156].

Passivating films may change their chemical composition after their formation due to reactions with water or carbon dioxide; lithium alkylcarbonates react with traces of water to yield lithium carbonate (see Table 8).

Likewise carbonaceous materials, when polarized to potentials of less than 2 V vs. Li, intercalate lithium with or without inclusion of solvent molecules. Solvent molecules may then be reduced or polymerized and yield reaction products in the electrolyte, in the carbonaceous material, or at the surface [157–162]. Therefore different electrolyte solutions show widely varying irreversible capacities for the first intercalation–deintercalation cycle for carbon [163]. For example, using $1.0\,mol\,L^{-1}$ LiIm PC/EC, 1087 $mAh\,g^{-1}$ is obtained, but only 108 $mAh\,g^{-1}$ for $1.0\,mol\,L^{-1}$ LiIm EC/DEC at synthetic graphite, showing that (nonprotected) PC is the less suited of the two solvents. The use of a nondisclosed electrolyte with PC as the cosolvent and $LiClO_4$ as the salt reduces the capacity loss due to the reduction of PC

CosMX Exhibit 1008, Page 497 of 633

Table 8. Composition of surface films at lithium and lithiated carbons

Solid phase(s) /electrode(s)	Liquid phase/ electrolyte	Method	Species	Res.
Li/TiS_2	2Me - THF/$LiAsF_6$	XPS	$LiAs(OR)_xF_{6-x}$, $-(As-O-)_n$, As_0	[165]
Li/TiS_2	2Me - THF/$LiAsF_6$	EDS, ESCA, FTIR	As, F, C, O, S (elements);–OH,–CH–, -CF,–AsF (groups);ROLi, AsF_3, As_2O_3, LiF, As^0, $(-As-O-)_n$,	[166]
Li	2Me - THF, EC/$LiAsF_6$ THF, EC/$LiAsF_6$ EC/$LiAsF_6$	FTIR	$ROCO_2Li$	[188]
Li	2Me - THF, EC, or THF, EC, or EC	FTIR	$ROCO_2Li$, Li_2CO_3 (ageing)	[188]
Li/TiS_2	3 - Me - SL/$LiAsF_6$	XPS, FTIR	LiF, Li_2O, RSO_2Li, R'SLi, RS, R'S, RSO, $(-As-S-)_n$ R = $-(CH_2)_2CH(CH_3)CH_2-$; R'= $(CH_2=C(CH_3)(CH_2)_2-)$	[167]
Li	DEC/$LiClO_4$	FTIR, XPS	$ROCO_2Li$, ROLi, Li_2CO_3	[168]
Li	DEC/$LiPF_6$	FTIR, XPS	LiF, Li_2O	[168]
Li	DIOX, LiMe or LiIm or $LiAsF_6$	FTIR (ex situ)	Li_2CO_3, $ROCO_2Li$, ROLi, LiO_2CH (LiMe and $LiAsF_6$ only), reaction products from LiIm; NS, S = O, CF bonds Li_xAsF_y from $LiAsF_6$	[169]
Li	DIOX, $LiAsF_6$	FTIR (in situ)	ROLi, LiO_2CH, Li_xAsF_y from $LiAsF_6$	[169]
Li	DIOX, LiIm	FTIR (in situ)	ROLi, LiO_2CH; S - O - N, S_2O - N, S - O, CF_3, C - S, C - F (from anion)	[169]
Li	DIOX, LiMe	FTIR (in situ)	ROLi , LiO_2CH; S - O, C - S, C - F (from anion)	[169]
Li	DIOX/$LiClO_4$	FTIR, ESCA	LiOR, LiCl, $LiOCH_2OCH_2CH_3$,polymers	[170]
Li	DIOX(H_2O)/$LiClO_4$	FTIR	LiOR, LiOH	[171]
Pt	DIOX, LiOH(H_2O)/ $LiClO_4$	FTIR	LiOR, LiCl, no LiOH	[171]
Pt(0.3VvsLi)	DME/$LiAsF_6$	FTIR (in situ)	ROLi	[187]
Li	DME, PC / $LiClO_4$	FTIR (in situ)	$ROCO_2Li$ (PC), ROLi (DME)	[172]
Graphite, KS44, Lonza	EC, DEC/$LiAsF_6$, or $LiClO_4$	FTIR	$(LiO_2COCH_2)_2$ (from EC), Li_2CO_3 (traces)	[200]
Graphite, Lonza, KS	EC/ DMC, $LiAsF_6$, LiIm, $LiPF_6$, $LiBF_4$	FTIR, XPS, XRD, SEM	Main product $(CH_2OCO_2Li)_2$	[192]
Graphite, KS44, Lonza	EC, DEC/$LiBF_4$	FTIR	Small carbonate content, B–F	[200]
Graphite, KS44, Lonza	EC, DEC/$LiPF_6$	FTIR	Few $(LiO_2COCH_2)_2$ (from EC), Li_2CO_3 in contrast to Li electrodes	[200]
Graphite, KS44, Lonza	EC, DEC, $p(CO_2)$ = 6 atm/$LiAsF_6$	FTIR	Few $(LiO_2COCH_2)_2$ (from EC), Li_2CO_3	[200]
Ag, Au, Pt	GBL (H_2O)/$LiClO_4$	FTIR	LiOH, $HO(CH_2)_3CO_2Li$	[173]
Ag, Au, Pt	GBL (O_2) / $LiClO_4$	FTIR	$LiO(CH_2)_3CO_2Li$, Li_2O, $LiO(CH_2)_3(C=O)O_2Li$	[173]
Pt(0.3VvsLi)	GBL / $LiClO_4$	FTIR (in situ)	RCO_2Li	[187]
Ag, Au	GBL / $LiClO_4$	FTIR	$LiO_2C(CH_2)_2CH_3$, β-ketoestedianion	[173]
Li	MPC / $LiAsF_6$	FTIR	$ROCO_2Li$, CH_3OLi, C_3H_7OLi, Li_2CO_3 on storage	[152]
Graphite, KS-6	MPC / $LiAsF_6$	FTIR	$ROCO_2Li$, Li_2CO_3	[152]
Li	PC / LiBr	FTIR, ESCA	$ROCO_2Li$, Li_2CO_3 (traces, from water?)	[174]
Pt(0.3VvsLi)	PC / $LiAsF_6$	FTIR (in situ)	$ROCO_2Li$	[187]
Li	PC / $LiClO_4$	XPS	Li_2CO_3, LiCl, $LiClO_4$, Li_2O, LiOH	[175]
Li	PC / $LiClO_4$	XRD	Li_2CO_3, LiCl, $LiClO_4$ in polymers	[176,177]

CosMX Exhibit 1008, Page 498 of 633

Li	PC / $LiClO_4$	XRD, AES, EL	Li_2O dense,bottom; Li_2CO_3 in polymers,top.	[178]
Pt(0.3VvsLi)	PC / $LiClO_4$	FTIR (in situ)	$ROCO_2Li$	[187]
Li	PC / $LiAsF_6$	FTIR	$ROCO_2Li$	[188]
Li	PC / $LiAsF_6$	XPS	LiOH, Li_2CO_3, Li_2O , (a little LiF) (native film); no N compounds	[179]
Li	PC / $LiClO_4$	XPS	LiOH, Li_2CO_3, Li_2O , (a little LiCl) (native film); no N compounds	[179]
Li	PC /$LiPF_6$	XPS	mainly LiF	[179]
Li	PC /$LiBF_4$	XPS	mainly LiF	[179]
Li	PC / $LiClO_4$	XPS	LiCl, Li_2CO_3, Li_2O, LiOH	[180]
Li	PC (H_2O) / $LiClO_4$	FTIR (in situ)	$ROCO_2Li$, Li_2CO_3 (from water)	[187]
Li	PC, EC, DME /$LiAsF_6$	SNIFTIR, EMIRS	$ROCO_2Li$, Li_2CO_3 , peroxides, ketals	[181]
Li	PC / $LiAsF_6$	FTIR, XPS, IR	alkyl carbonates, Li_2CO_3 (from water), LiF	[149]
Li	PC, LiTri	FTIR, XPS, IR	alkyl carbonates, Li_2CO_3 (from water), LiF	[149]
Li	PC, THF / $LiAsF_6$	FTIR, ESCA	R'OLi (THF) , $ROCO_2Li$ (PC) , LiF , As	[188,172]
Li	PC, $LiClO_4$	FTIR, XPS, IR	alkyl carbonates, Li_2CO_3 (from water), LiCl	[149]
Li	PC / LiTri, LiIm	FTIR, ESCA	mainly salt reaction products, Li_2O , (Li_3N from LiIm only), –(C–F),–(CF_3),–(C–S)–, –(C–O)– , sulfone (SO_2) , (sulfone amide SO_2 –N , LiIm only), and a little $ROCO_2Li$, Li_2CO_3 (S > F , PC only; less with LiIm)	[174]
Li	PC / LiTri, LiIm, CO_2	FTIR, ESCA	Li_2CO_3 (main compound)	[174]
Li	SO_2	EA, IR,XPS	$Li_2S_2O_4$, Li_2S , Li_2SO_3 , $Li_2S_2O_5$, $Li_2S_nO_6$	[182, 183]
Li, discharged	SO_2, AN / $LiAsF_6$	XPS	Li_2SO_3 , As_2O_3 , F(40%), C(32%), O(16%), S(3%)	[184]
Graphite, SAFT	SO_2, PC / $LiAsF_6$	FTIR	$ROCO_2Li$, $LiO_2COCH_2O(OCO_2Li)CHCH_3$, Li_2CO_3 , $Li_2S_2O_4$, Li_xAsF_y , Li_2SO_3 , $Li_2S_2O_5$, Li_2S	[201]
Li	THF / $LiAsF_6$	FTIR, EDAX	ROLi , traces of Li_2CO_3 and $ROCO_2Li$ (from CO_2 and H_2O contamination), LiF , Li_xAsF_y , As^0, but no –(As–O)–	[195]
Li	THF / $LiAsF_6$	IR, EA, ESCA	As_2O_3 , LiF	[185]
Pt	THF / $LiClO_4$	Viscometry	Living polymers, $M \approx 2 \times 10^5$ g mol^{-1}	[186]
Li	THF / LiTri, LiIm	FTIR, ESCA	sulfone amide SO_- – N (LiIm only), (CF_3) , Li_2O ,(O,C > F,S)	[174]

R refers to different alkyl groups; for examples, see Eqs. (39)–(50).

to 120 mAh g^{-1}; the electrolyte $LiClO_4$/ PC/EC/12 – crown – 4 reduces it further to 84 mAh g^{-1}, but yields lower reversible capacities [164].

Table 8 shows results obtained from the application of various bulk and surface analysis methods to lithium metal at rest or after cyclization experiments, as well as at inert and carbon electrodes after cathodic polarization. The analytical methods include elemental analysis, X-ray photoelectron spectroscopy (XPS or ESCA), energy-dispersive analysis of X-rays (X-ray microanalysis) (EDAX), various types of Fourier transform infrared spectroscopy (FTIR), Auger electron spectroscopy (AES), ellipsometry (E), electromodulated infrared reflectance spectroscopy (EMIRS), subtractively normalized interfacial Fourier transform infrared spectroscopy (SNIFTIRS), gas chromatography (GC), IR spectroscopy, and X-ray diffraction (XRD).

The underlying chemistry is rather complicated [202]. It depends on the history of the electrode (cycling, storage,

CosMX Exhibit 1008, Page 499 of 633

etc.), the presence of impurities, the anions of lithium salts, the solvents, etc. As a consequence, reaction mechanisms of the heterogeneous and homogeneous reactions which depend on the morphology of the films and the solubility of reaction products are scarcely known.

In addition, ex situ techniques suffer from possible contamination and subsequent reactions which may change the original composition of the film. For example, alkoxides obtained from ethers react with CO_2 to yield alkylcarbonates [187], and these can react with traces of water yielding Li_2CO_3 [188–190]. Similarly, native films [15] formed at the lithium electrode may be converted to yield secondary reaction products; for example, in $LiClO_4$/PC or $LiAsF_6$/PC the native film consisting of LiOH, Li_2CO_3, and Li_2O is quite stable and scarcely reacts with the electrolyte, whereas in $LiBF_4$ or $LiPF_6$/PC it forms mainly LiF [179].

In electrolytes based on solvent mixtures both solvent compounds may react to form films of scarcely soluble materials. PC/THF mixtures yield alkoxides and alkylcarbonates [188]; EC/ether blends mainly yield alkylcarbonates, which are thought to be the reason for smaller lithium loss during cycling [188]. PC based electrolytes with $LiAsF_6$ and $LiClO_4$ form films containing alkylcarbonates which allow the access of other molecules, such as ethers, reacting more slowly with lithium. No alkylcarbonates are assumed to be formed in $LiPF_6$/PC, but only nonspecified adsorbates which are believed to be responsible for the reduced dentritic lithium growth during deposition [191].

When salts are more reactive with lithium than solvent, such as LiTri and LiIm in PC [174] or LiIm and LiMe in DIOX (where LiIm is more reactive then LiMe [169]), their reduction components dominate the film and its behavior. For $LiAsF_6$ and $LiClO_4$ in PC [174] or $LiAsF_6$ in DIOX or other ethers [169], the situation is reversed.

The product $(CH_2OCO_2Li)_2$ seems to form very efficient films on carbon electrodes, where lithium can be cycled close to its optimal capacity hundreds of times in EC/DMC-based solutions of $LiAsF_6$, LiIm, or $LiPF_6$ [199].

In contrast to DEC/$LiClO_4$ solutions, where typical reaction products of carbonate solvents including alkyl carbonates, alkoxides, and Li_2CO_3 are formed at the lithium surface, DEC/$LiPF_6$ solutions yield LiF and Li_2O only [168].

These and other examples from Table 8 show the importance of the anions in film formation.

The following reactions proposed by Aurbach and co-workers are examples of the reductive decomposition reactions of anions with lithium [199, 169]:

$$\mathrm{LiIm} + n\mathrm{e}^- + n\mathrm{Li}^+ \rightarrow \mathrm{Li_3N} + \mathrm{Li_2S_2O_4} + \mathrm{LiF} + \mathrm{Li}_y\mathrm{C_2F}_x \tag{29}$$

$$\mathrm{LiIm} + 2\mathrm{e}^- + 2\mathrm{Li}^+ \rightarrow \mathrm{Li_2NSO_2CF_3} + \mathrm{LiSO_2CF_3} \tag{30}$$

$$\mathrm{Li_2S_2O_4} + 4\mathrm{e}^- + 4\mathrm{Li}^+ \rightarrow \mathrm{Li_2SO_3} + \mathrm{Li_2S} + \mathrm{Li_2O} \tag{31}$$

$$\mathrm{LiMe} + n\mathrm{e}^- + n\mathrm{Li}^+ \rightarrow \frac{1}{2}\mathrm{Li_2S_2O_4} + \mathrm{mLiF} + \frac{1}{2}\mathrm{Li}_y\mathrm{C_2F}_x + \mathrm{Li_2C(SO_2CF_3)_2} \tag{32}$$

$$\mathrm{LiMe} + 2\mathrm{e}^- + 2\mathrm{Li}^+ \rightarrow \mathrm{Li_2C(SO_2CF_3)_2} + \mathrm{LiSO_2CF_3} \tag{33}$$

CosMX Exhibit 1008, Page 500 of 633

$$LiAsF_6 + 2e^- + 2Li^+ \rightarrow 3LiF + AsF_3 \quad (34)$$

$$AsF_3 + 2xLi^+ + 2xe^- \rightarrow Li_xAsF_{3-x} + xLiF \quad (35)$$

$$PF_6^- + 2e^- + 3Li^+ \rightarrow 3LiF + PF_3 \quad (36)$$

$$BF_4^- + xe^- + xLi^+ \rightarrow yLiF + Li_{x-y}BF_{4-y} \quad (37)$$

The decomposition reactions of the preferred organic carbonate solvents are [152,192]:

$$PC + 2e^- + 2Li^+ \rightarrow Li_2CO_3(s) + CH_3CH=CH_2(g) \quad (38)$$

$$2PC + 2e^- \rightarrow CH_3CH(OCO_2^-)CH_2OCO_2^- + CH_3CH=CH_2(g) \quad (39)$$

$$2PC + 2e^- + 2Li \rightarrow CH_3CH(OCO_2Li)CH_2OCO_2Li(s) + CH_3CH=CH_2(g) \quad (40)$$

$$2EC + 2e^- + 2Li \rightarrow (CH_2OCO_2Li)_2(s) + CH_2=CH_2(g) \quad (41)$$

$$2DMC + 2e^- + 2Li \rightarrow CH_3OCO_2Li(s) + CH_3CH_3(g) \quad (42)$$

$$2ROCO_2Li + H_2O \rightarrow Li_2CO_3(s) + ROH + CO_2 \quad (43)$$

$$EMC + e^- + Li^+ \rightarrow CH_3OCO \cdot CH_3CH_2OLi \quad (44)$$

$$EMC + e^- + Li^+ \rightarrow CH_3CH_2OCO \cdot CH_3OLi \quad (45)$$

$$EMC + e^- + Li^+ \rightarrow CH_3OCO_2Li + CH_3CH_2 \cdot \quad (46)$$

MPC reacts in a similar way, Eqs. (44)–(46), see Ref. [151].

Alkyl ($R\cdot$) and acyl ($ROCO\cdot$) radicals react according to:

$$R\cdot + e^- + Li^+ \rightarrow RLi \quad (47)$$

$$ROCO\cdot + e^- + Li^+ \rightarrow ROLi + CO \quad (48)$$

where ROLi may react with EMC yielding ethers or other alkoxides and carboxylate anions. Li_2CO_3 is formed in two ways:

$$ROCO_2Li + e^- + Li+ \rightarrow R\cdot + Li_2CO_3 \quad (49)$$

$$2ROCO_2Li + H_2O \rightarrow CO_2 + 2ROH + Li_2CO_3 \quad (50)$$

CosMX Exhibit 1008, Page 501 of 633

Different reaction rates of all the reactive components with lithium yield surface films of different quality for cycling lithium; additives can be used which modify the surface films to highly conductive lithium films, protecting the components of the electrolyte from further decomposition. There are many successful examples of this approach in the open and patent literature both for lithium anodes and more recently also for lithiated carbon electrodes. Typical additives include 2-methylfuran and KOH in DIOX- or THF-based solutions [193], [194], MF in 2-Me-THF (THF, low content) [195], CO_2 in PC [196, 197] DMC or EC at lithium electrodes [198, 199], and CO_2 [200] or SO_2 [201] at lithiated carbon electrodes. Traces of reactive compounds which show beneficial effects in lithium cycling may also be formed in purification procedures. Thus, aluminum oxide, which is used as a drying agent, increases the cycling efficiency due to a partial decomposition of alkylcarbonates entailing the formation of CO_2 [199].

Carbon dioxide as additive improves the behavior of $(LiO_2COCH_2)_2$ films formed above intercalation potentials in EC/DEC-based electrolytes due to increased formation of Li_2CO_3 [200]. It is interesting to note that SO_2 reduction occurs at quite high potentials, before the reduction of other electrolyte components; films contain inorganic and organic lithium salts [201].

The superiority of $LiAsF_6$ in ether based solvents (2-Me-THF, THF, MeF) at lithium electrodes is an example of the formation of useful protecting films (As, Li_3As, Li_xAsF_y) allowing uniform lithium deposition [195]. According to Aurbach and co-workers, $LiAsF_6$/2-Me-THF is a highly suitable electrolyte for rechargeable lithium batteries. However, as 2-Me-THF is one of the least reactive solvents, it is sensitive to contamination [202].

It is interesting to note that, in addition to the chemical composition of surface films at lithium anodes, another possibility is available for increasing the cycleability, i.e., changing the morphology of the deposited lithium by adding surfactants to the electrolyte. For example addition of lithium perfluorooctanesulfonate or the corresponding tetraalkylammonium salt doubles or trebles the mean number of achievable deposition–dissolution cycles with $LiClO_4$/PC -based solutions [203]. Addition of HF to electrolytes results in a combined action, both improving the morphology of the deposited lithium and changing the composition of the surface films [204]. In order to suppress lithium dendrite formation during deposition, the chemical reaction rates of surface materials must be greater than the electrochemical deposition rate of lithium. Chemical reactions of surface materials with HF include [204]:

$$Li_2CO_3 + 2HF \rightarrow 2LiF + H_2CO_3 \quad (51)$$

$$LiOH + HF \rightarrow LiF + H_2O \quad (52)$$

$$Li_2O + 2\,HF \rightarrow 2LiF + H_2O \quad (53)$$

$$LiOR + HF \rightarrow LiF + ROH \quad (54)$$

$$LiOCO_2R + HF \rightarrow LiF + ROH + CO_2 \quad (55)$$

$$2Li + 2\,HF \rightarrow 2LiF + H_2 \quad (56)$$

A new measurement technique, in-situ atomic force microscopy combined with XPS and scanning Auger electron microscopy and continuous argon sputtering, recently revealed that the films are not uni-

CosMX Exhibit 1008, Page 502 of 633

form. Nanostructures, consisting of grain boundaries, ridge lines and flat areas, at the lithium surface have an important role in controlling the morphology of lithium electrodeposition [180].

7.4.3 Conductivity of Concentrated Solutions

7.4.3.1 Introduction

Conductivities κ of electrolytes are related to molar conductivities Λ, ion conductivities λ_i and ionic mobilities u_i by Eq. (57) and (58),

$$\kappa = \Lambda n_e c \tag{57}$$

$$\Lambda = \lambda_+ + \lambda_- = F(u_+ + u_-) \tag{58}$$

where F is the Faraday constant, n_e is the electrochemical valence

$$n_e = \nu_+ z_+ = |\nu_- z_-| \tag{59}$$

of a binary salt with anionic and cationic charges z_- and z_+, and stoichiometric coefficients ν_- and ν_+.

The most spectacular feature of a conductivity–concentration function is its maximum, attained for every electrolyte if the solubility of the salt is sufficiently high. For electrolytes which do not show strong ion association, the maxima can be understood on the basis of the defining equation of specific conductivity at the maximum [205], yielding

$$d\kappa = n_e(\Lambda dc + c d\Lambda) \tag{60}$$

The maxima are the consequence of two competing effects:

- ionic mobilities decreasing with increasing concentration of the salt, and
- increasing ionic charge densities.

For attempts in the literature to rationalize the maximum, with reference to solvation, ion association, or viscosity of the electrolyte, see Ref. [15].

The search for a suitable electrolyte requires comprehensive studies. It is necessary to measure the conductivities of electrolytes with various solvents, solvent mixtures, and anions over the accessible concentration range of the salts, and to cover a sufficiently large temperature range and the whole composition range of the binary (or ternary) solvent mixture. Figure 11 shows, as an example, the conductivity plot of $LiAsF_6$/GBL as a function of temperature and molality.

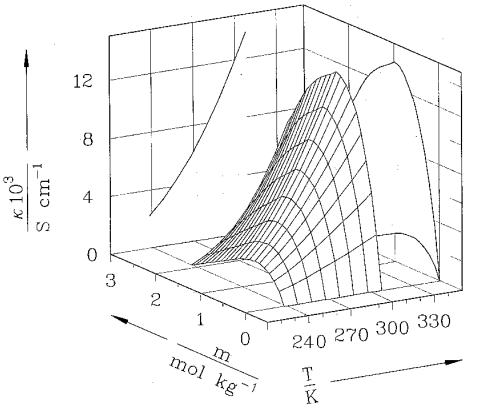


Figure 11. Conductivities of $LiAsF_6$ in GBL.

In the literature measurements are often given at only $1\,mol\,kg^{-1}$ or $1\,mol\,L^{-1}$ for some salts in various single or mixed solvents. These are not suitable for rationalizing results, because the conductivity maxima depend on the type of ions, solvent, solvent composition, and temperature.

CosMX Exhibit 1008, Page 503 of 633

Results from conductivity measurements can be advantageously evaluated for every temperature and solvent composition using the nonlinear fit [206]

$$K = K_{max}\left(\frac{m}{\mu}\right)^{a} \exp\left[b(m-\mu)^2\right] - \frac{a}{\mu}(m-\mu) \quad (61)$$

in order to obtain the maximum conductivity κ_{max} attained at the concentration μ of the electrolyte; a and b are empirical parameters without physical meaning. For a discussion of Eq. (61), see Refs. [16, 81, 207]. For an example showing the fit of conductance data of $LiBF_4$/GBL, see Fig. 12.

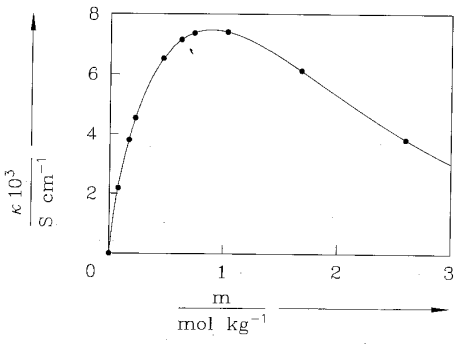


Figure 12. Fit of conductivity dat5a of $LiBF_4$/GBL at 25 °C.

Recent developments of the chemical model of electrolyte solutions permit the extension of the validity range of transport equations up to high concentrations ($c >> 1\,mol\,L^{-1}$) and permit the representation of the conductivity maximum K_{max} in the framework of the mean spherical approximation (MSA) theory with the help of association constant K_A and ionic distance parameter a, see Ref. [87] and the literature quoted there in.

7.4.3.2 Conductivity-Determining Parameters

The intrinsic properties of an electrolyte evaluated at low concentrations of the salt and from the viscosity and permittivity of the solvent also determine the conductivity of concentrated solutions. Various systems were studied to check this approach. The investigated parameters and effects were:

(1) the dynamic viscosity η or the fluidity $\phi(=\eta^{-1})$ of the solvent, and its temperature dependence;
(2) the radii of the ions;
(3) the solvation of cations and anions, as accessible from Stokes radii R_i of the ions;
(4) the association constant of the salt;
(5) the role of selective solvation; and
(6) the competition of solvation and association.

The main problem in the study of the role of these parameters in electrolyte conductivity is their interdependence. A change in composition of a binary solvent changes viscosity, along with the permittivity, ion–ion association, and ion solvation, which may be preferential for one of the two solvents and therefore also changes the Stokes radii of the ions.

7.4.3.3 The Role of Solvent Viscosity, Ionic Radii, and Solvation

For simple salts the influence of parameters (1)–(3) can be studied separately by the investigation of series of salts with a common anion or cation in a solvent of high dielectric permittivity. However, high solvent permittivity is only a necessary, but not a sufficient, condition for complete dissociation. High permittivity of the solvents does not prevent ions from associating, if these ions interact specifically

CosMX Exhibit 1008, Page 504 of 633

and the solvent possesses a poor basicity (DN). Lithium fluoroacetates in PC [105] show association constants of about $10^4 L\,mol^{-1}$ which are of the order of many lithium salts with large anions in DME.

The results of an investigation performed upon various salts in PC [207] or MeOH [15] can be summarized as follows. Both the maximum conductivity K_{max} and the appertaining concentration μ are determined by the viscosity and ionic radii (nonsolvated ions) or Stokes radii (solvated ions), meaning that electrolytes show a Stokes–Walden behavior, entailing

- linear plots of κ_{max} versus $1/r_+$ for tetraalkylammonium hexafluorophosphates at every temperature,
- linear plots of κ_{max} versus μ at every temperature, and
- κ_{max} decreasing versus μ, both at decreasing temperature and at decreasing viscosity of the solvent [207].

Analysis of the activation energies of charge transport as a function of temperature and concentration shows that a type of corresponding state is attained at concentration μ characterized by constant critical energies of activation for a given temperature. Electrolytes based on salts with small nonsolvated ions or small Stokes radii attain high μ and κ_{max} values, whereas those based on large ions attain only small μ and κ_{max} values.

Many recent examples show the importance of ionic radii and solvation in the conductivity of concentrated solutions. Suffice it to refer to three examples from the literature.

Binary mixtures of dipolar aprotic solvents of sufficiently high permittivity such as BC, PC, EC, and AN, show Stokes-Walden behavior [208] [209]. For Bu_4NBr in AN/PC in the temperature range $75\,°C > \theta > -35\,°C$ a linear correlation κ_{max} (μ) is found [209], independent of temperature and solvent composition. The use of high-permittivity solvents belonging to the same class suppresses the effects due to strong selective solvation or changing association.

In SL/glyme (1:1) mixtures with glymes of different chain length $(CH_3(C_2H_4O)_nCH_3, n = 1,2,3,4)$ Dudley et al. [210] obtained for $1\,mol\,kg^{-1}$ $LiAsF_6$ a linear relation of specific conductivity and fluidity ϕ, (see Fig. 13).

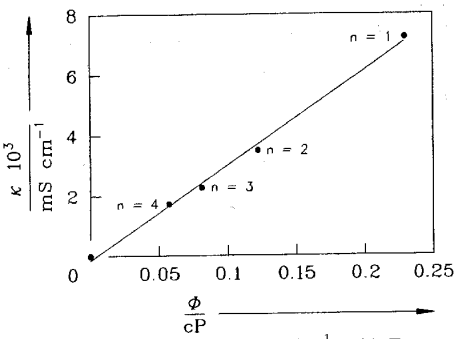


Figure 13. Conductivity of 1 $mol\,L^{-1}$ $LiAsF_6$ versus fluidity in SL/glyme mixtures, adapted from Ref. [210]; for details see the text.

Table 9. Ionic radii and ionic limiting molar conductivities of some anions in PC at 25°C, taken from Ref. [211]

Ion	r/(nm)	λ^0 ($S\,cm^2\,mol^{-1}$)
Ph_4B^-	0.419	8.52
Me^-	0.375	11.80
$C_4F_9SO_3^-$	0.339	13.03
Im^-	0.325	14.40
PF_6^-	0.254	17.86
AsF_6^-	0.260	17.58
Tri^-	0.270	16.89
ClO_4^-	0.237	18.93
BF_4^-	0.229	20.43

Radii of anions of lithium salts and limiting molar conductivities in solvents of

CosMX Exhibit 1008, Page 505 of 633

high permittivity such as PC are linearly correlated, the slope corresponding approximately to perfect slip [211]. Table 9 shows these parameters for PC at 25 °C.

7.4.3.4 The Role of Ion Association

In contrast to points (1)–(3) of discussion, the effect of ion association on the conductivity of concentrated solutions is proven only with difficulty. Previously published reviews refer mainly to the permittivity of the solvent or quote some theoretical expressions for association constants which only take permittivity and distance parameters into account. Ue and Mori [212] in a recent publication tried a multiple linear regression based Eq. (62)

$$\Lambda_c = C_\Lambda \Lambda_0 + C_K K_A \qquad (62)$$

for an investigation on the role of ionic mobility represented by limiting conductivity Λ_0 and association characterized by association constant K_A. C_Λ and C_K are regression coefficients and Λ_c is the calculated conductivity. For seven lithium salts in two pure solvents (PC/GBL) and two equimolar mixtures (PC/DMC, PC/EMC) they obtained a fairly good straight line of calculated and measured conductivities (slope ~1, intercept ~0). The authors concluded that ion association has a stronger influence than the ion–mobility effects on conductivities at high concentrations. Unfortunately the K_A range covered by this investigation was rather small; the largest K_A value was less than 300 $L\,mol^{-1}$.

Fluorination of anions of lithium salts offers a possibility for a study of the influence of ion association on the maxima of conductivity, because fluorination of large molecular anions only slightly affects the anionic radius and all other conductivity determining effects (1–3, 5, 6) are eliminated or constant within a series of lithium salts in a given solvent.

The chelatoborates $LiB(C_6H_{4-x}F_xO_2)_2$ (x = 0, 1, 4) are sufficiently soluble in various solvents and yield chemically stable solutions. Figure 14 shows the results of conductivity measurements at concentrations of about 1 mol L^{-1} in DME solvent, showing that a conductivity increase of about 440 percent at 35 °C and of about 240 percent at −45 °C can be obtained with increasing fluorination of the salt.

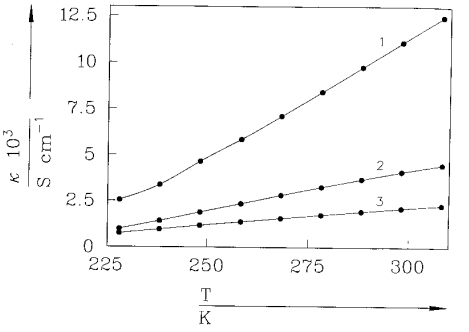


Figure 14. Conductivities of chelaborates Li[B($O_2C_6F_4$)] (1), Li[B($O_2C_6H_3F$)] (2), and Li[B($O_2C_6H_4$)] (3) in DME at molalities 1,239 mol kg^{-1}, and 0.9940 mol kg^{-1}, respectively.

The main conclusions from this study are that the electron-drawing fluorine substituent produces a decrease in the association constant by a factor of about 3 for PC-based solutions and of 5.5 for solutions in DME [81] (cf. also Fig. 5). The consequence is an increase in the maximum of conductivity by about 30 percent (PC) and about 80 percent (DME).

7.4.3.5 Effects of Selective Solvation and Competition Between Solvation and Ion Association

It has been shown in Sec. 7.3.3.3 how the addition of strong ligands to electrolytes

CosMX Exhibit 1008, Page 506 of 633

can decrease their association constants, due to the displacement of the anion by ligands in the vicinity of cations or the displacement of the cation by a ligand which selectively solvates anions. This conductivity-increasing effect can be utilized for technical electrolytes.

Only very few examples exist in the open literature showing this effect and its importance for intercalation of concentrated electrolytes [213–217]. The reason for this might be the high price of several very effective ligands and their potential ability to co-intercalate with lithium into cathode materials, entailing the disintegration of the material. Examples are known where solvents are co-intercalated into carbon anodes [218]. However, suitable ligands can prevent co-intercalation of solvents. The addition of 12-C-4 to $LiClO_4$/PC or to other carbonate-based electrolytes entails better cycling efficiencies of TiS_2 cathodes and Li_xC_6 anodes [6], cf. also Sec. 7.4.2.

A prerequisite condition for the increase in conductivity being caused by added ligands is a high association constant of the salt in the absence of added ligand. If the association constant is low, as it is for AN-based solutions, a decrease of conductivity may occur, because the Stokes radius of the solvated Li^+ ion is increased by ligands with molecular diameters larger than that of AN, entailing lower cation mobility [214].

An example by Olmstead [213] illustrates a limitation in the use of this effect for technical applications. Figure 15 shows a large conductivity increase at low concentrations upon addition of the ligand hexamethyltriethylenetetramine (HMTT) to LiI/DIOX which, however, decreases at increasing salt concentration in the technically interesting concentration range.

A similar example is given by Whitney

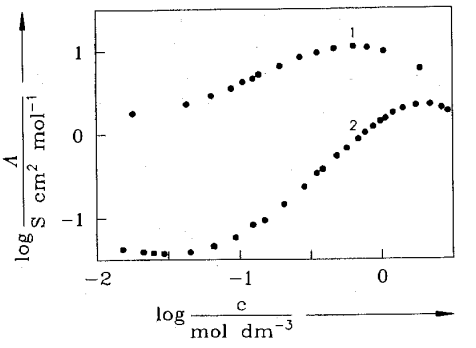


Figure 15. Conductivity of LiI/DIOX/HMTT (1) and LiI/DIOX mixtures (2. Adapted from Ref. [213]).

et al. [219], who have shown that addition of 1, 1, 4, 7, 7 –pentamethyldiethylene triamine (PMDT) even produces sufficiently conductive solutions of lithium salts in toluene, where the lithium salts are scarcely soluble.

A new approach is based on ligands which displace cations in ion pairs, instead of solvating cations, by anion solvation. This is made possible by the strong interaction of the anions with aza-ether compounds [220]. Electron-withdrawing substituents such as CF_3SO_2- make the local charge at the nitrogen positive, so that these compounds become effective ligands for anions. Anion complexation has been proven by conductivity and NEXAFS measurements.

A 0.2 $mol\,L^{-1}$ LiCl/THF solution possesses only very low conductivity of $1.6\times10^{-6}\,S\,cm^{-1}$. Addition of $N(CH_2CH_2NR_2)_3$ ($R = CF_3SO_2$ short nomenclature M6R) yields an increase in conductivity by three orders of magnitude to $1.7\times10^{-3}\,S\,cm^{-1}$. This approach is seemingly especially useful for battery electrolytes, because the transference number of the lithium ion is increased. Conceptually this approach is similar to the use of lith-

CosMX Exhibit 1008, Page 507 of 633

ium salts with large anions or the immobilization of anions at polymer backbones.

7.4.3.6 Optimization of Conductivity

There are three strategies to increase the conductivity of an electrolyte:

- the mixed-solvent approach;
- the addition of ligands, selectively solvating cations, or anions; and
- the modification of anions by the introduction of electron–withdrawing substituents.

The mixed-solvent approach is a compromise, based on mixed solvents of moderate permittivity and moderate viscosity. The following example illustrates that.

Solvents which are kinetically stable with lithium show either high viscosity and high permittivity, or low viscosity and low permittivity. The diminution of high viscosity of solvents such as PC or EC is accomplished by the addition of low-viscosity solvents such as DME or DMC. As a consequence solvent permittivity is also lowered. However, by adjusting solvent composition in such a way that ion association remains unimportant, a conductivity increase of more than 100 percent at ambient temperatures and of about 1000 percent at low temperatures can be obtained [221].

Optimum compositions may be planned with the help of plots of κ_{max} versus solvent composition, where κ_{max} increases with increasing amounts of the low-viscosity component, reaching its maximum at $\overset{*}{\kappa}_{max}$, and then decreases again in accordance with increasing association of the electrolyte [221]. For this approach, many examples exist[15].

Table 10 shows a collection of typical battery electrolytes, their conductivities at various temperatures, the concentration of the salt, and references. More examples can be found in Ref. [15] and the literature cited therein

Table10. Conductivities of various lithium ion containing liquid electrolytes

Solvent	Composition	Salt	K or K_{max} / ms cm^{-1}	μ (or m or c)(*)	θ /°C	Ref.
BEG-1/EC	1:2 (w/w)	$LiClO_4$	6.2	1*m*	25	[45]
BEG-1/EC	1:2 (w/w)	LiIm	3.2	1*m*	25	[45]
BEG-1/EC	1:2 (w/w)	LiTri	0.19	1*m*	25	[45]
DEC	–	$LiAsF_6$	5	1.5M	25	[10]
DIOX	–	LiIm	6.9	2.0M	25	[67]
DMC	–	$LiAsF_6$	11	1.9M	25	[10]
DME	–	$Li[B(C_6F_4O_2)_2]$	11.074	0.994 *m*	25	[82]
DME	–	$Li[B(C_6F_4O_2)_2]$	2.551	0.994 *m*	–45	[82]
EC/DMC	50vol.%	$LiAsF_6$	11	1 M	25	[76]
EC/DMC	50vol.%	$LiAsF_6$	18	1 M	55	[76]
EC/DMC	50vol.%	$LiAsF_6$	0.26	1 M	–30	[76]
EC/DMC	50vol.%	$LiPF_6$	11.984	0.899*m*	25	[72]
EC/DMC	50vol.%	LiTri	2.994	0.674*m*	25	[72]
EC/DMC	50vol.%	LiIm	9	1 M	25	[76]
EC/DMC	50vol.%	LiIm	9.615	0.866*m*	25	[72]
EC/DMC	50vol.%	LiIm	14	1 M	55	[76]

CosMX Exhibit 1008, Page 508 of 633

EC/DMC	50vol.%	LiIm	0.34	1 M	−30	[76]
EC/DMC	50vol.%	LiMe	7.1	1 M	25	[76]
EC/DMC	50vol.%	LiMe	7.596	0.704*m*	25	[72]
EC/DMC	50vol.%	LiMe	11	1 M	55	[76]
EC/DMC	50vol.%	LiMe	1.1	1 M	−30	[76]
EC/DMC	50vol.%	LiBisMe	6.379	0.314*m*	25	[72]
EC/MF	3:1 (v/v)	$LiAsF_6$	14.5	1M	22	[222]
EC/MF	1:1 (v/v)	$LiAsF_6$	24.2	1M	22	[222]
EC/MF	1:3 (v/v)	$LiAsF_6$	25.3	1M	22	[222]
EC/MF	3:1 (v/v)	LiMe	8.4	1M	22	[222]
EC/MF	1:3 (v/v)	LiMe	17.6	1M	22	[222]
EC/MF	3:1 (v/v)	$LiAsF_6$	4.5	1M	−10	[222]
EC/MF	1:1 (v/v)	$LiAsF_6$	13.2	1M	−10	[222]
EC/MF	1:3 (v/v)	$LiAsF_6$	16.5	1M	−10	[222]
EC/MF	3:1 (v/v)	LiMe	2.1	1M	−10	[222]
EC/MF	1:3 (v/v)	LiMe	11.0	1M	−10	[222]
EC/MF	1:1 (v/v)	$LiAsF_6$	5.6	1M	−40	[222]
EC/MF	1:3 (v/v)	$LiAsF_6$	8.4	1M	−40	[222]
EC/MF	1:3 (v/v)	LiMe	5.4	1M	−40	[222]
EC/DEC	50vol.%	LiMe	5.372	0.658*m*	25	[72]
EC/DEC	50vol.%	$LiBi_sMe$	4.385	0.292*m*	25	[72]
EC/DMC/MF	33.3vol.% each	LiMe	12	1 M	25	[76]
EC/DMC/MF	33.3vol.% each	LiMe	18	1 M	55	[76]
EC/DMC/MF	33.3vol.% each	LiMe	3.5	1 M	−30	[76]
MA		$LiAsF_6$	26	2M	25	[10]
MF		$LiAsF_6$	43	2.0*m*	25	[223]
MF		$LiAsF_6$	47	2.1M	25	[10]
MF/DEC	50wt% MF	$LiAsF_6$	21	1.9M	25	[10]
MF/DMC	47wt% MF	$LiAsF_6$	26	1.9M	25	[10]
MF/NM	90wt% MF	$LiAsF_6$	47	2M	25	[223]
MSC		$LiAlCl_4$	13	1.5M	25	[43]
2-Me-THF	-	LiIm	2.2	1.5M	25	[67]
n-BU		LiTri	3	μ	20	[41]
n-BU		$LiNO_3$	2.2	μ	20	[41]
n-BU		LiIm	4	μ	25	[41]
THF	-	LiIm	9.4	1.5M	25	[67]

(*) Concentration at the maximum of conductivity: *m*, molality (mol kg^{-1}); M, molarity (mol L^{-1})

7.5 References

[1] R. Jasinsky, *High-Energy Batteries*, Plenum, New York, **1967**.

[2] J. O. Besenhard, G. Eichinger, *J. Electroanal. Chem. Interfacial Electrochem.* **1976**, *68*, 1.

[3] R. Jasinsky in *Advances in Electrochemistry and Electrochemical Engineering*, Vol. 7, (Eds.: P. Delahay, P. C. W. Tobias), Interscience, New York, **1970**, p. 77.

[4] R. Herr, *Electrochim. Acta* **1990**, 35, 1257.

[5] G. E. Blomgren in *Lithium Batteries* (Ed.: J.-P. Gabano), Academic Press, London, **1983**, ch.

CosMX Exhibit 1008, Page 509 of 633

2.
[6] L. A. Dominey in *Lithium Batteries. New Materials, Developments and Perspectives* (Ed.: G. Pistoia), Elsevier, Amsterdam, **1994**, ch. 4.
[7] K. M. Abraham in *Lithium. Current Application in Science, Medicine and Technology* (Ed.: R. O. Bach), Wiley, New York, **1985**, ch. 11.
[8] K. M. Abraham, *Electrochim. Acta* **1993**, *38*, 1233.
[9] K. M. Abraham in *Rechargeable Lithium Batteries* (Eds.: S. Subbarao, V. R. Koch, B. B. Owens, W. H. Smyrl), The Electrochemical Society Proceeding Series, PV 90-5, The Electrochemical Society, Pennington, NJ **1990**, p.1.
[10] M. Salomon, *J. Power Sources* **1989**, *26*, 9.
[11] M. Salomon, *Proc. 4th Int. Rechargeable Battery Sem.* (Eds.: S. Wolsky, N. Marincic), Ansum Enterprises, Boca Raton, FL, **1992**.
[12] M. Ishikawa, S. Q. Wen, Y. Matsuda, *J. Power Sources* **1993**, *45*, 229.
[13] M. Salomon, B. Scrosati, *Gazz. Chim. Ital.* **1996**, *126*, 415.
[14] L. Xie, D. Fouchard, S. Megahed, *Mater. Res. Soc. Symp. Proc.* **1995**, *393*, 285.
[15] J. Barthel, H. J. Gores in *Chemistry of Nonaqueous Electrolyte Solutions. Current Progress* (Eds.: G. Mamontov, A. I. Popov), VCH, New York, **1994**, ch. 1.
[16] J. Barthel, H. J. Gores, G. Schmeer, R. Wachter, *Top. Curr. Chem.* **1983**, *111*, 33.
[17] H. J. Gores, J. M. G. Barthel, *Pure Appl. Chem.* **1995**, *67*, 919.
[18] J. Barthel, H. J. Gores, *Pure Appl. Chem.* **1985**, *57*, 1071.
[19] J. Barthel, R. Wachter, H. J. Gores in *Modern Aspects of Electrochemistry*, Vol. 13 (Eds.: B. E Conway, J. O'M. Bockris), Plenum, New York, **1979**, ch. 1.
[20] J. Barthel, R. Buchner, H. J. Gores, DECHEMA *Monographien*, **1991**, *124*, 65.
[21] H. J. Gores, J. Barthel, *Naturwiss enschaften* **1983**, *70*, 495.
[22] D. H. Doughty, *SAMPE J.* **1996**, *32*, 75
[23] S. Ching, J. T. McDevitt, S. R. Peck, R. W. Murray, *J. Electrochem. Soc.* **1991**, *138*, 2308.
[24] G. Geblewicz, R. J. Potter, D. J. Schifrin, *T ans. Inst. Met. Finish* **1986**, *64*, 134.
[25] V. Gutmann, E. Wychera, *Inorg. Nucl. Chem. Lett.* **1966**, *2*, 257.
[26] V. Gutmann, G. Resch, W. Linert, *Coord. Chem. Rev.* **1982**, *43*, 133.
[27] Y. Marcus, *Ion Solvation*, Wiley, Chichester, **1985**.
[28] Y. Marcus, *J. Solution Chem.* **1984**, *13*, 599.
[29] M. J. Kamlet, J. L. M. Abboud, M. H. Abraham, R. W. Taft, *J. Org. Chem.* **1983** *48*, 2877.
[30] M. J. Kamlet, R. W. Taft, *J. Am. Chem. Soc.* **1976**, *98*, 377.
[31] R. W. Taft, N. J. Pienta, M. J. Kamlet, E. M. Arnett, *J. Org. Chem.* **1981**, *46*, 661.
[32] M. J. Kamlet, M. E. Jones, R. W. Taft, J. L. Abboud, *J. Chem. Soc., Perkin Trans. 2*, **1979**, 342.
[33] C. Reichardt, *Solvent and Solvent Effects in Organic Chemistry*, 2nd. ed., VCH, Weinheim, **1988**.
[34] C. Reichardt, *Pure Appl. Chem.* **1982**, *54*, 1867.
[35] U. Mayer, V. Gutmann, W. Gerger, *Monatsh. Chem.* **1975**, *106*, 1235.
[36] J. L. M. Abboud, R. W. Taft, *J. Phys. Chem.* **1979**, *83*, 412.
[37] M. J. Kamlet, R. M. Doherty, J. L. M. Abboud, M. H. Abraham, R. W. Taft, *J. Pharm. Sci.* **1986**, *75*, 338.
[38] M. J. Kamlet, R. M. Doherty, M. H. Abraham, R.W. Taft, *Quant. Struct.–Act. Relat.* **1988**, *7*, 71.
[39] M. J. Kamlet, J. L. Abboud, R.W. Taft, *J. Am. Chem. Soc.* **1977**, *99*, 6027.
[40] M. J. Kamlet, R. W. Taft, *J. Org. Chem.* **1982**, *47*, 1734.
[41] G. Herlem, B. Fahys, M. Székely, E. Sutter, C. Mathieu, M. Herlem, J.-F. Penneau, *Electrochim. Acta* **1996**, 41, 2753.
[42] J. Barthel, H.J. Gores, E. Carl, E.Y. Menzel, R.Meyer. *J. Chem. Eng. Data*, to be published
[43] K. Xu, N. D. Day, C. A. Angell, *J. Electrochem. Soc.* **1996**, *143*, L 209.
[44] S. Hahn, W. M. Miller, R. N. Lichtenthaler, J. M. Prausnitz, *J. Solution Chem.* **1985**, *14*, 129.
[45] S. S. Zhang C. A. Angell, *J. Electrochem. Soc.* **1996**, *143*, 4047.
[46] G. H. Wrodnigg, L. H. Lie, B. Evers, I. Schneider, J. O. Besenhard, M. Winter, R. Blyth, M. Ramsey, F. Netzer, Jahrestagung der GDCh—FG Angewandte Elektrochemie, Wien, Sept. 24–26, **1997**
[47] D. Linden (Ed.), *Handbook of Batteries and Fuel Cells.* McGraw Hill, New York, **1984**.
[48] H. V. Venkatasetty (Ed.), *Lithium Battery Technology*, The Electrochemical Society, Bloomington Wiley, New York, **1984**.
[49] D. Linden, (Ed.), *Handbook of Batteries*, 2nd ed., McGraw Hill, New York, **1995**.

CosMX Exhibit 1008, Page 510 of 633

[50] R. Jasinsky, S. Carroll, *J. Electrochem. Soc.* **1970**, 117, 218.
[51] G. H. Newman, R. W. Francis, L. H. Gaines, B. M. L. Rao, *J. Electrochem. Soc*, **1980**, *127*, 2025.
[52] T. C. Ehlert, M.-M. Hsia, *J. Chem. Eng. Data* **1972**, *17*, 18.
[53] J. R. Waason, D. K. Hoffmann in *Proc. Symp. on Power Sources for Biomedical Implantable Applications and Ambient Temperature Lithium Batteries* (Eds.: B. G. Owens, N. Margalit), The Electrochemical Society Proceeding Series, PV 80-4, The Electrochemical Society, Princeton, NJ, **1980**, p.309.
[54] E. W. Lawless, C. J. W. Wiegand, Y. Mizumoto, C. Weis, *Inorg. Chem.* **1971**, *10*, 1084.
[55] R. C. Cannon, C. C. Stone, R. A. Wiesboeck in *Proc. Symp. on Power Sources for Biomedical Implantable Applications and Ambient Temperature Lithium Batteries* (Eds.: B. G. Owens, N. Margalit), The Electrochemical Society Proceeding Series, PV 80-4, The Electrochemical Society, Princeton, NJ **1980**, p. 321.
[56] V. R. Koch, *J. Electrochem. Soc*, **1979**, *126*, 181.
[57] R. B. Somoano, B. J. Carter, D. Shen, S. P. S. Yen, *J. Power Sources* **1985**, *14*, 53.
[58] M. M. Archuleta, *J. Power Sources* **1995**, *54*, 138.
[59] Y. Gofer, M. Ben-Zion, D. Aurbach, *J. Power Sources* **1992**, *39*, 163.
[60] J. L. Goldman, L. A. Dominey, V. R. Koch, *J. Power Sources* **1989**, *26*, 519.
[61] V. N. Plakhotnik, V. B. Tul'chinskii, V. K. Steba, Russ. *J. Inorg. Chem.* **1976**, *21*, 451.
[62] J. W. Johnson, J. F. Brody, *J. Electrochem. Soc.* **1982**, *129*, 2213.
[63] L. P. Klemann, G. H. Newman, *J. Electrochem. Soc.* **1981**, *128*, 13.
[64] H. R. Horowitz, J. I. Haberman, L. P. Klemann, G. H. J. Newman, E. L. Stogryn, T. A. Whitney in *Lithium Batteries* (Ed.: H. V. Venkatasetty), The Electrochemical Society Proceeding Series, PV 81-4, The Electrochemical Society, Princeton, NJ, **1981**, p. 131.
[65] M. Armand, F. Moursli, French Patent FR 2527602; *Chem. Abstr.* **1985**, *100*, 195112.
[66] M. Armand, M. Gauthier, D. Muller, French patent FR 2606217; *Chem. Abstr.* **1989**, *110*, 98805,.
[67] L. A. Dominey, J. L. Goldman, V. R. Koch , C. Nanjundiah in *Rechargeable Lithium Batteries* (Eds.: S. Subbarao, V. R. Koch, B. B. Owens, W. H. Smyrl), The Electrochemical Society Proceeding Series, PV 90-5 The Electrochemical Society, Pennington, NJ, **1990**, p. 56.
[68] L. Turowsky, K. Seppelt, *Inorg. Chem.* **1988**, *27*, 2135.
[69] J. Foropoulos, Jr., D. D. Des Marteau, *Inorg. Chem.* **1984**, *23*, 3720.
[70] M. B. Armand, W. Gorecki, R Adréani in *Second International Symposium on Polymer Electrolytes* (Ed.: B. Scrosati), Elsevier, London, **1990**, p.91.
[71] A. Webber, *J. Electrochem. Soc.* **1991**, *138*, 2586.
[72] J. Barthel, H. J. Gores in *C,DCh Monographien*, 12, Frankfurt 1998, p. 185.
[73] R. Jüschke, G. Henkel, P. Sartori, *Z. Naturforsch, B* **1997**, *52*, 359.
[74] L. A. Dominey, V. R. Koch, T. J. Blakeley, *Electrochim. Acta* **1992**, *37*, 1551.
[75] F. Croce, A. D'Aprano, C. Nanjundiah, V. R. Koch, C. W. Walker, M. Salomon, J. *Electrochem. Soc.* **1996**, *143*, 154.
[76] C. W. Walker, Jr., J. D. Cox, M. Salomon, *J. Electrochem. Soc.* **1996**, *143*, L80.
[77] L. A. Dominey, US Patent, PCT Int. Appl. WO 9202966; *Chem. Abstr.* **1992**, *117*, 93735.
[78] F. Kita, A. Kawakami, T. Sonoda, H. Kobayashi in *New Sealed Rechargeable Batteries and Supercapacitors* (Eds.: B. M. Barnett, E. Dowgiallo, G. Halpert, Y. Matsuda, Z.-I. Takehara), The Electrochemical Society Proceeding Series, PV 93-23, The Electrochemical Society, Pennington, NJ. **1993**, p. 321.
[79] J. Barthel, M. Wühr, R. Buestrich, H. J. Gores, *J. Electrochem. Soc.* **1995**, *142*, 2527.
[80] J. Barthel, R. Buestrich, H. J. Gores, M. Schmidt, M. Wühr, *J. Electrochem. Soc.* **1997**, *144*, 3866
[81] J. Barthel, E. Carl, R. Buestrich, H. J. Gores, *J. Electrochem. Soc.* **1996**, *143*, 3565.
[82] J. Barthel, R. Buestrich, E. Carl, H. J. Gores, *J. Electrochem. Soc.* **1996**, *143*, 3572
[83] J. Barthel, M. Schmidt, H. J. Gores, *J. Electrochem. Soc.*, **1998**, *145*, L17.
[84] J. A. Riddick, W. B. Bunger, T. K. Sakano, *Organic Solvents. Physical Properties and Methods of Purification, 4th ed., Techniques of Chemistry*, Vol. II (Sen. Ed.: A. Weissberger), Wiley, New York, **1986**.
[85] J. F. Coetzee (Ed.), *Recommended Methods for Purification of Solvents and Tests for Impurities*, Pergamon, Oxford, **1982**.
[86] D. D. Perrin, W. L. F. Armarego, D. R. Perrin,

CosMX Exhibit 1008, Page 511 of 633

Purification of Laboratory Chemicals, 3rd ed., Pergamon, Oxford, **1988**.
[87] J. Barthel, H. Krienke, and W. Kunz, *Physical Chemistry of Electrolyte Solutions. Modern Aspects*. Steirkopff, Darmstadt; Springer **1998**.
[88] M. Eigen, K. Tamm, *Z. Elektrochem.* **1962**, *66*, 107.
[89] J. Barthel, Ber. Bunsenges. *Phys. Chem.* **1979**, *83*, 252.
[90] J. Barthel, H. Popp, *Anal. Chim. Acta* **1992**, *265*, 259.
[91] J. Barthel in *The Role of Data in Scientific Progress* (Ed.: P. S. Glaeser), North-Holland, Amsterdam, **1985**, p. 337.
[92] J. Barthel in *Phase Equilibria and Fluid Properties in the Chemical Industry*, Vol. 2, DECHEMA, Frankfurt a. M., **1980**, p. 497.
[93] J. Barthel, *Ionen in nichtwäßrigen Lösungen*, Steinkopff, Darmstadt, **1976**.
[94] J. C. Justice in *Comprehensive Treatise of Electrochemistry* (Eds.: B. E. Conway, J. O'M. Bockris, E. Yeager), Vol. 5, Plenum, New York, **1983**, p. 223.
[95] J. Barthel, R. Neueder in *Electrolyte Data Collection* (Ed.: G. Kreysa), Chemistry Data Series, Vol. XII, Part 1, DECHEMA, Frankfurt, **1992**.
[96] R.M. Fuoss, H.-L. Hsia, *Proc. Nat. Acad. Sci. U.S.A.* **1967**, *57*, 1550.
[97] J. Barthel, H. J. Gores, L. Kraml, *J. Phys. Chem.* **1996**, *100*, 1283.
[98] J. Barthel, M. Krell, L. Iberl, F. Feuerlein, *J. Electroanal. Chem. Interfacial Electrochem.* **1986**, *214*, 485.
[99] J. Barthel, L. Iberl, J. Rossmaier, H. J. Gores, B. Kaukal, *J. Solution Chem.* **1990**, *19*, 321.
[100] J. Barthel, R. Gerber, H. J. Gores, *Ber. Bunsenges. Phys. Chem.* **1984**, *88*, 616.
[101] R. M. Fuoss, F. Accascina, *Electrolytic Conductance*, Interscience, New York, **1959**.
[102] R. M. Fuoss, C. A. Kraus, *J. Am. Chem. Soc.* **1933**, *55*, 2387.
[103] S. Boileau, P. Hemery, *Electrochim. Acta* **1976**, *21*, 647.
[104] M. Salomon, M. C. Uchiyama, *J. Solution Chem.* **1987**, *16*, 21.
[105] J. Barthel, L. Kraml, H. J. Gores, *J. Phys. Chem.* **1996**, 105, 3671.
[106] C. B. Wooster, *J. Am. Chem. Soc.* **1937**, *59*, 377.
[107] C. B. Wooster, *J. Am. Chem. Soc.* **1938**, *60*, 1609.
[108] M. Hojo, Y. Miyauchi, I. Nakatani, T. Mizobuchi, Y. Imai, *Chem. Lett.* **1990**, 1035.
[109] M. Hojo, Y. Miyauchi, Y. Imai, *Bull. Chem. Soc. Jpn.* **1990**, *63*, 3288.
[110] Y. Miyauchi, M. Hojo, H. Moriyama, Y. Imai, *Faraday Discuss. Chem. Soc.* **1992**, *88*, 3175.
[111] H. C. Wang, P. Hemmes, *J. Am. Chem. Soc.* **1973**, *95*, 5119.
[112] M. Delsignore, H. Farber, S. Petrucci, *J. Phys. Chem.* **1985**, *89*, 4968.
[113] J. Barthel, R. Gerber, H. J. Gores, J. Solution Chem.,to be published.
[114] M. Salomon, M. Uchiyama, M. Xu, S. Petrucci, *J. Phys. Chem.* **1989**, *93*, 4374.
[115] M. Salomon, *J. Solution Chem.* **1993**, *22*, 715.
[116] H. Maaser, M. Xu., P. Hemmes, S. Petrucci, *J. Phys. Chem.* **1987**, *91*, 3047.
[117] M. Ue, *Denki Kagaku*, **1994**, *62*, 620.
[118] H. Farber, S. Petrucci, *J. Phys. Chem.* **1975**, *79*, 1221.
[119] H. Schneider, *Electrochim. Acta* **1976**, *21*, 711.
[120] H. Strehlow, W. Knoche, H. Schneider, *Ber. Bunsenges. Phys. Chem.* **1973**, *77*, 760.
[121] H. B. Flora II, W. R. Gilkerson, *J. Phys. Chem.* **1973**, *77*, 1421.
[122] H. W. Aitken, W. R. Gilkerson, *J. Am. Chem. Soc.* **1973**, *95*, 8551.
[123] W. R. Gilkerson, E. K. Ralph III, *J. Am. Chem. Soc.* **1965**, *87*, 175.
[124] E. K. Ralph III, W. R. Gilkerson, *J. Am. Chem. Soc.* **1964**, *86*, 4783.
[125] W. R. Gilkerson, J. B. Ezell, *J. Am. Chem. Soc.* **1965**, *87*, 3812.
[126] M. D. Jackson, W. R. Gilkerson, *J. Am. Chem. Soc.* **1979**, *101*, 328.
[127] J. B. Ezell, W. R. Gilkerson, *J. Phys. Chem.* **1968**, *72*, 144.
[128] H. B. Flora II, W. R. Gilkerson, *J. Am. Chem. Soc.* **1970**, *92*, 3273.
[129] J. B. Ezell, W. R. Gilkerson, *J. Am. Chem. Soc.* **1966**, *88*, 3486.
[130] H. B. Flora II, W. R. Gilkerson, *J. Phys. Chem.* **1976**, *80*, 679.
[131] P. Huyskens, *Ind. Chim. Belge* **1972**, *37*, 553.
[132] J. Macau, L. Lamberts, P. Huyskens, *Bull. Soc. Chim. Fr.* **1971**, *7*, 2387.
[133] M. Salomon and G. T. Hefter, *Pure Appl. Chem.* **1993**, *65*,1533.
[134] A. D'Aprano, M. Salomon, V. Mauro, *J. Solution Chem.* **1995**, *24*, 685.
[135] A. F. Danil. de Namor, M. A. Llosa Tanco, M. Salomon, J. C. Y. Ng, *J. Phys. Chem.* **1994**, *98*, 11796

CosMX Exhibit 1008, Page 512 of 633

[136] M. Salomon, *J. Electroanal. Chem. Interfacial Electrochem.* **1993**, *355*, 265.
[137] M. Ue, K. Ida, S. Mori, *J. Electrochemical Soc.* **1994**, *141*, 2989.
[138] S. A. Campbell, C. Bowes, R. S. McMillan, *J Electroanal. Chem.* **1990**, *284*, 195.
[139] H. H. Horowitz, J. I. Habermann, L. P. Klemann, G. H. Newman, E. L. Strogryn, T. A. Whitney in *Lithium Batteries* (Ed.: H. V. Venkatasetty), The Electrochemical Society Proceeding Series Vol. 81-4, The Electrochemical Society, Pennington, NJ, **1981**, p. 131.
[140] M. Morita, M. Goto, Y. Matsuda, *J. Appl. Electrochem.* **1992**, *22*, 901.
[141] M. Ue, M. Takeda, M. Takehara, S. Mori, *J. Electrochemical Soc.* **1997**, *144*, 2685.
[142] C. K. Mann, *Nonaqueous Solvents for Electrochemical Use in Electroanalytical Chemistry* (Ed.: A. J. Bard), Dekker, New York, **1969**, p. 57
[143] J. J. P. Stewart, *MOPAC: A General Molecular Orbital Package*, Frank J. Seiler Research Laboratory, Colorado Springs, CO, **1987**.
[144] J. J. P Stewart in *Reviews in Computational Chemistry*, Vol. 1, (Eds.: K. B. Lipkowitz, D. B. Boyd), VCH, New York, **1990**, p. 45.
[145] J. J. P Stewart, *J. Comput.-Aided Mol. Des.* **1990** *4*, 1.
[146] M. C. Zerner in *Reviews in Computational Chemistry*, Vol. 2 (Eds.: K. B. Lipkowitz, D. B. Boyd), VCH, New York, **1991**, p. 313.
[147] H. Yilmaz, E. Yurtsever, L. Toppare, *J. Electroanal. Chem.* **1989**, *261*, 105.
[148] F. Bruno, M. C. Pham, J. E. Dubois, *Electrochim. Acta* **1977**, *22*, 451
[149] D. Aurbach, M. L. Daroux, P. W. Faguy, E. Yeager, *J. Electrochem. Soc.* **1987**, *134*, 1611.
[150] D. Aurbach, M. Daroux, P. Faguy, E. Yeager, *J. Electroanal. Chem. Interfacial Electrochem.* **1991**, *297*, 225.
[151] Y. Ein-Ely, S. F. McDevitt, D. Aurbach, B.Markovsky, A. Schechter, *J. Electrochem. Soc.* **1997**, *144*, L180.
[152] Y. Ein-Ely, S. R. Thomas, V. R. Koch, D. Aurbach, A. Schechter, B.Markovsky, *J. Electrochem. Soc.* **1996**, *143*, L273.
[153] M. Odziemkowski, D. E. Irish, *Proc. 35th Int. Power Sources Symp.*, **1992**, 174.
[154] J. R. Hoenigman, R. G. Keil in *Lithium. Current Application in Science, Medicine and Technology* (Ed.: R. O. Bach) Wiley, New York **1985**, p. 233.
[155] J. R. Hoenigman, R. G. Keil, *Appl. Surf. Sci* **1984**, *18*, 207.
[156] K. W. Nebesny, K. Zavadil, B. Burrow, R. Armstrong, *Surf. Sci.* **1985**, *162*, 292.
[157] E. Peled, in *Rechargeable Lithium and Lithium Ion Batteries* (Eds.: S. Megahead, B. M. Barnett, L. Xie), The Electrochemical Society Proceeding Series, PV 94-28, The Electrochemical Society, Pennington, NJ, **1995**, p. 1.
[158] E. Peled, C. Menachem, D. Bar-Tow, A. Melman, *J. Electrochem. Soc.* **1996**, *143*, L4.
[159] M. Jean, C. Desnoyer, A. Tranchant, R. Messina, *J. Electrochem. Soc.* **1995**, *142*, 2122.
[160] O. Chusid, Y. Ein-Ely, D. Aurbach, M. Babai, Y. Carmeli, *J. Power Sources*, **1993**, *43*, 47.
[161] D. Aurbach, Y. Ein-Ely, O. Chusid, Y. Carmeli, M. Babai, H. Yamin, *J. Electrochem. Soc.* **1994**, *141*, 603.
[162] M. Jean, A. Tranchant, R. Messina, *J. Electrochem. Soc.* **1996**, *143*, 391.
[163] S. Megahed, W. Ebner, *J. Power Sources* **1995**, *54*, 155.
[164] Z. X. Shu, R. S. McMillan, J. J. Murray, in *Rechargeable Lithium and Lithium Ion Batteries* (Eds.: S. Megahead, B. M. Barnett, L. Xie), The Electrochemical Society, Proceeding Series, PV 94-28, The Electrochemical Society, Pennington, NJ, **1995**, p. 431.
[165] R. Somoano, B. J. Carter, S. Subba Rao, D. Shen, *Proc. 20th Intersoc. Energy Convers. Eng. Conf.* **1985**, Vol. 2, p. 2.43.
[166] D. H. Shen, S. Subbaro, B. J. Nakamuro, S. P. S. Yen, C. P. Bankston, G. Halpert in *Primary and Secondary Ambient Temperature Lithium Batteries* (Eds.: J. P. Gabano, Z. Takehara, B. Bro), The Electrochemical Society Proceeding Series, PV 88-6, The Electrochemical Society, **1988**, p. 409.
[167] S. P. S. Yen, D. H. Shen, R. P. Vasquez, B. J. Carter R. B. Somoano in *Lithium Batteries* (Ed.: A. N. Dey), The Electrochemical Society Proceeding Series, PV 84-1, The Electrochemical Society, Pennington, NJ, **1984**, p. 403.
[168] K. Kanamura, H. Takezawa, S. Shiraishi, Z.-I. Takehara, *J. Electrochem. Soc.* **1997**, *144*, 1900.
[169] D. Aurbach, O. Chusid, I. Weissman, P.Dan, *Electrochim. Acta* **1996**, *41*, 747.
[170] D. Aurbach, O. Youngman, Y. Gofer, A. Meitav, *Electrochim. Acta*, **1990**, *35*, 625.
[171] D. Aurbach, O. Youngman P. Dan, *Electro-*

CosMX Exhibit 1008, Page 513 of 633

chim. Acta **1990**, *35*, 639.
[172] D. Aurbach, Y. Gofer, E. Goren in *Primary and Secondary Lithium Batteries* (Eds.: K. M. Abraham, M. Salomon), The Electrochemical Society Proceeding Series, PV 91-3, The Electrochemical Society, Pennington, NJ, **1991**, p. 247.
[173] D. Aurbach, *J. Electrochem Soc.* **1989**, *136*, 906.
[174] D. Aurbach, I. Weissman, A. Zaban, O. Chusid (Youngman), *Electrochim. Acta* **1994**, *39*, 51.
[175] J. P. Contour, A. Salesse, M. Froment, M. Garreau, J. Thevenin, D. Warin, *J. Microsc. Spectrosc. Electron.* **1979**, *4*, 483.
[176] M. Froment, M. Garreau, J. Thevenin, D. Warin, *J. Microsc. Spectrosc. Electron.* **1979**, *4*, 111.
[177] I. Epelboin, M. Froment, M. Garreau, J. Thevenin, D. Warin, *J. Electrochem Soc.* **1980**, *127*, 2100.
[178] G. Nazri, R. H. Muller, *J. Electrochem Soc.* **1985**, *132*, 1385.
[179] K. Kanamura, H. Tamura, Z.- I. Takehara, *J. Electroanal. Chem. Interfacial Electrochem.* **1992**, *333*, 127.
[180] K.-I. Morigaki, N. Kabuto, K. Yoshino, A. Ohta, *Power Sources* **1995**, *15*, 267.
[181] S. Barusseau, B. Beden, M. Broussely, F. Perton, *J. Power Sources* **1995**, *54*, 296.
[182] K. M. Abraham, L. Pitts, *J. Electrochem. Soc.* **1983**, *130*, 1618.
[183] K. M. Abraham, S. M. Chaudri, *J. Electrochem. Soc.* **1986**, *133*, 1307.
[184] C. R. Anderson, S. D. James, W. P. Kilroy, R. N. Lee, *Appl. Surf. Sci.*, **1981**, *9*, 388.
[185] V. R. Koch, *J. Electrochem. Soc.* **1979**, *126*, 181.
[186] A. N. Dey, E. J. Rudd, *J. Electrochem Soc.* **1974**, *121*, 1294.
[187] E. Goren, O. Chusid, D. Aurbach, *J. Electrochem. Soc.* **1991**, *138*, L6.
[188] D. Aurbach, Y. Gofer, *J. Electrochem. Soc.* **1991**, *138*, 3529.
[189] D. Aurbach, M. L. Daroux, P. W. Faguy, E. B. Yeager, *J. Electrochem. Soc.* **1987**, *134*, 1611.
[190] D. Aurbach, M. L Daroux, P. W. Faguy, E. B. Yeager, *J. Electrochem. Soc.* **1988**, *135*, 1863.
[191] S. Fujita, A. Yasuda, Y. Nishi in *Primary and Secondary Lithium Batteries* (Eds.: K. M. Abraham, M. Salomon), The Electrochemical Society Proceeding Series, PV 91-3, The Electrochemical Society, Pennington, NJ, **1991**, p. 262.
[192] D. Aurbach, Y. Ein-Ely, A. Zaban, *J. Electrochem. Soc.* **1994**, *141*, L1.
[193] L. A. Dominey, J. L. Goldman, V. R. Koch, C. Nanjundiah in *Rechargeable Lithium Batteries* (Eds.: S. Subbarao, V. R. Koch, B. B. Owens, W. H. Smyrl), The Electrochemical Society Proceeding Series, PV 90-5, The Electrochemical Society, Pennington, NJ, **1990**, p. 56.
[194] L. A. Dominey, J. L. Goldman, V. R. Koch, D. Shen, S. Subbarao, C. K. Huang, G. Halpert, F. Deligiannis in *Primary and Secondary Lithium Batteries* (Eds.: K. M. Abraham, M. Salomon) The Electrochemical Society Proceeding Series PV 91-3, The Electrochemical Society, Pennington, NJ, **1991**, p. 293.
[195] D. Aurbach, A. Zaban, Y. Gofer, O. Abramson, M. Ben-Zion, *J. Electrochem. Soc.* **1995**, *142*, 687.
[196] T. Osaka, T. Momma, T. Tajima,Y. Matsumoto, *J. Electrochem. Soc.* **1995**, *142*, 1057.
[197] T. Momma, Y. Matsumoto, T. Osaka,, *J. Mater Res. Soc. Symp. Proc.* **1995**, *393*, 221.
[198] E. Plichta, S. Slane, M. Uchiyama, M. Salomon, D. Chua, W. B. Ebner, H. W. Lin, *J. Electrochem. Soc.* **1989**, *136*, 1865.
[199] D. Aurbach, Y. Gofer, M. Ben-Zion, P.Aped, *J. Electroanal .Chem.* **1992**, *339*, 451.
[200] D. Aurbach, Y. Ein-Ely, B.Markovsky, A. Zaban, S. Luski, Y. Carmeli, H. Yamin, *J. Electrochem. Soc.* **1995**, *142*, 2883.
[201] Y. Ein-Ely, S. R. Thomas, V. R. Koch, *J. Electrochem. Soc.* **1996**, *143*, L195.
[202] D. Aurbach, A. Zaban, Y. Gofer, Y. Ein Ely, I. Weissman, O. Chusid, O. Abramson, *J. Power Sources* **1995**, *54*, 76.
[203] A. Tudela Ribes, P. Beaunier, P. Willmann, D. Lemordant, *J. Power Sources* **1996**, *58*, 189.
[204] K. Kanamura, S. Shiraishi, Z.-I. Takehara, J. Electroanal. *J. Electrochem. Soc.* **1996**, *143*, 2187.
[205] J. Molenat, *J. Chim. Phys. Phys.–Chim. Biol.* **1969**, *66*, 825.
[206] J. F. Casteel, E. S. Amis, *J. Chem. Eng. Data* **1972** *17*, 55.
[207] J. Barthel, H. J. Gores, G. Schmeer, *Ber. Bunsenges Phys. Chem.* **1979**, *83*, 911.
[208] J. Barthel, H. Graml, T. Neumeier, R. Neueder, V. K. Syal, in preparation.
[209] J. Barthel, H. Graml, R. Neueder, P. Turq, O. Bernard, *Curr. Top. Solution Chem.* **1994**, *1*, 223.
[210] J. T. Dudley, D. P. Wilkinson, G. Thomas, R.

CosMX Exhibit 1008, Page 514 of 633

LeVae, S. Woo, H. Blom, C. Horvath, M. W. Juzkow, B. Denis, P. Juric, P. Aghakian, J. R. Dahn, *J. Power Sources* **1991**, *35*, 59.
[211] M. Ue, *J. Electrochem. Soc.* **1996**, *143*, L271.
[212] M. Ue, S. Mori in *Rechargeable Lithium and Lithium-Ion Batteries* (Eds.: S. Megahead, B. M. Barnett, L. Xie), The Electrochemical Society Proceeding Series, PV 94-28, The Electrochemical Society, Pennington, NJ, **1995**, p.440.
[213] W. N. Olmstead in *Proc. Lithium Batteries* (Ed. H. V. Venkatasetty), The Electrochemical Society Proceeding Series, PV 81-4, The Electrochemical Society, Princeton, NJ, **1981**, p. 144.
[214] I. A. Angres, S. D. James in *Proc. Symp. on Power Sources for Biomedical Implantable Applications and Ambient Temperature Lithium Batteries* (Eds.: B. G. Owens, N. Margalit), The Electrochemical Society Proceeding Series, PV 80-4, The Electrochemical Society, Princeton, NJ, **1980**, p. 332.
[215] S.-I. Tobishima, A. Yamaji, *J. Power Sources* **1984**, *12*, 53.
[216] M. Morita, H. Hayashida, Y. Matsuda, *J. Electrochem. Soc.* **1987**, *134*, 2107.
[217] M. Salomon, *J. Solution Chem.* **1990**, *19*, 1225.
[218] P. Atkins, G. T. Hefter, P. Singh, *J. Power Sources* **1991**, *36*, 17.
[219] T. A. Whitney, D. L. Foster, US Patent 4, 670, 363, **1987**; *Chem. Abstr.* **1987**, *107*, 80996.
[220] H. S. Lee, X. Q. Yang, J. McBreen, L. S. Choi, Y. Okamoto in *Rechargeable Lithium and Lithium-Ion Batteries*, (Eds.: S. Megahead, B. M. Barnett, L. Xie), The Electrochemical Society Proceeding Series, PV 94-28, Pennington, NJ, **1995**, p. 452.
[221] H. J. Gores, J. Barthel, *J. Solution Chem.* **1980**, *9*, 939.
[222] Y. Ein-Ely, S. R. Thomas, R. Chadha, T. J. Blakley, V. R. Koch, *J. Electrochem. Soc.* **1997**, *144*, 823.
[223] M. Uchiyama, S. Slane, E. Plichta, M. Salomon, *J. Power Sources* **1987**, *20*, 279.
[224] R. Jüschke, G. Henkel, P. Sartori, *Z. Naturforsch.* **1998**, *135*, 53b.
[225] M. Handa, S. Fukuda, Y. Sasaki, *J. Electrochem. Soc.* **1997**, *144*, L235.

CosMX Exhibit 1008, Page 515 of 633

8 Polymer Electrolytes

Fiona Gray and Michel Armand

8.1 Introduction

Ionically conducting solid materials display numerous advantages over their liquid counterparts, ranging practical consideration, such as leakage, to structural factors, such as ease of miniaturization. Polymer ionics was a relative late comer to the field of solid-state ionics but it was realized as early as 1973 that thin-film polymers would have significant potential in all-solid-state electrochemical cells [1]. Although the complexing ability of oligoethers had been known for some time , Wright and co-workers were the first to measure the ionic conductivity of poly(ethylene oxide)–salt complexes [2]. The significance of this was overlooked for some time [3], but once these new polymer–salt complexes had been endorsed as solid electrolytes there followed a rapid growth in research programs devoted largely to simple polyether–salt systems. Polymer-electrolyte-based lithium battery technology was initiated in North America and Europe as early as 1980. Uneven plating (dendritic) and safety problems associated with lithium-metal anodes has hindered commercialization of any lithium secondary battery with liquid electrolytes and the discovery that, under the right condition, non-uniform lithium dendrite growth could be minimized or even suppressed in solvent-free polymer electrolyte cells [4] added to the enthusiasm. Although many important technological advances have been made in the development of electrochemical cells employing a lithium anode, it is recent developments in lithium insertion solid-state anodes that has led to some conviction amongst the industrial community. A number of companies are known to be developing lithium-ion-based polymer-electrolyte batteries, but disclosure of results in the open literature is still limited.

The term "polymer electrolyte" can be applied to a broad family of ion-conducting materials:

(1) A system comprising a salt dissolved in a high-molecular-weight polar polymer matrix.
(2) A gel electrolyte, formed by dissolving a salt in a polar liquid and adding an inactive polymeric material to give the material mechanical stability.
(3) A plasticized electrolyte, usually obtained by the addition of small amounts of a liquid of high dielectric constant to a solving polymer electrolyte in order to enhance its conductivity.
(4) An "ionic rubber" comprising a low-temperature molten salt mixture and a small amount of high-molecular-

weight polymer. On a structural level, these electrolytes have some factors in common with gel electrolytes. They were first reported in the literature in 1993 [5] and are in the early stages of development.

(5) A membrane ionomer, in particular a polyelectrolyte with an inert backbone such as Nafion®. They require a plasticizer (typically water) to achieve good conductivity levels and are associated primarily, in their proton-conducting form, with solid polymer-electrolyte fuel cells.

The focus has largely been on polyether-based solvent-free systems for lithium rechargeable batteries. They are simple to prepare and their fundamental physical and electrical properties are almost unique, making them interesting materials for a broad range of fundamental research studies. More recently, studies have been initiated on multivalent cation-based systems with possible implication for, amongst other things, calcium- and zinc-based electrochemical cells [6,7]. Despite the superior ionic conductivities that can be achieved with plasticized systems, they have not had the same level of attention mainly because they share many properties and drawbacks of the liquid component, including those encountered in cells containing metallic lithium electrodes.

Figure 1 shows the temperature variation of the ionic conductivities for several polymer-electrolyte systems. At room temperature they are typically 100 to 1000 times less than those exhibited by a liquid or the best ceramic- or glass-based electrolytes [6,8]. Although higher conductivities are preferable, 100-fold or 1000-fold increases are not essential, as a thin-film electrochemical cell configuration can largely compensate for these lower values. Less favorable is the tendency for ion association and low cationic relative mobility (a property shared with aprotic liquids, as opposed to ceramic or glassy electrolytes) in polyether-based materials. These fun-

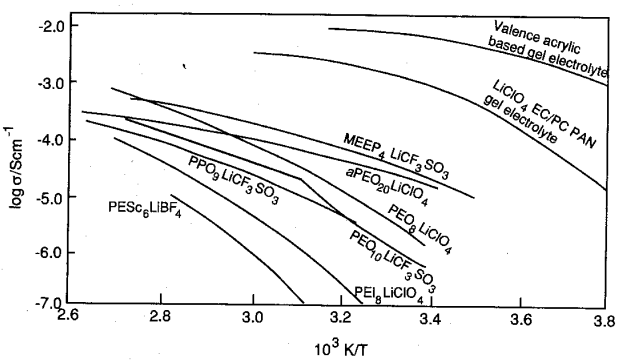


Figure 1. Temperature variation of the conductivity for a cross-section of polymer electrolytes. PESc, poly (ethylene succinate); PEO, poly(ethylene oxide); PPO, poly(propylene oxide); PEI, poly(ethyleneimine); MEEP, poly(methoxyethoxy-ethoxyphosphazene); *a*PEO, amorphous methoxy-linked PEO; PAN, polyacrylonitrile; PC, propylene carbonate; EC, ethylene carbonate.

CosMX Exhibit 1008, Page 517 of 633

damental properties can affect cell performance and must influence the design of new polymeric electrolytes to make them competitive as battery materials.

8.2 Solvent-Free Polymer Electrolytes

8.2.1 Technology

The first report of the performance of small-scale polyether-based batteries came in 1983. The choice of salt necessitated operation at 120 °C, which contributed to the severe decline in capacity and restricted operation to only 50 cycles. Improved cell performance and working temperature were achieved in the first instance by altering the salt and the intercalation cathode. Once the principle of a polymer-electrolyte secondary battery was established, the level of commercial interest remained. The advent of stringent environmental laws, however, have led to government-backed R&D efforts, such as in North America with the United States Advanced Battery Consortium (USABC) and in Japan with the national ten-year research programme involving the Lithium Battery Energy Storage Technology Research Association (LIBES). On a more fundamental level, the timing of developments in realistic alternatives to lithium-metal anodes has also been fortuitous. Because of perceived limitations in the use of polyether-based solvent-free electrolytes, commercial interest has largely focused on lithium-ion electrodes with gel-type electrolytes, at least for small (< 10 Wh) devices. No alternative lithium source anode materials are available, however, to replace lithium metal without sacrificing anode capacity, cell voltage, and consequently energy density. For this reason, a number of commercially based programs are dedicated to the development of "dry" electrolyte–lithium metel anode technology.

The major investor in the development of "dry" electrolyte technology has been Hydro-Québec, a Canadian electricity utility, in partnership with various groups and companies since 1980 (Elf-Aquitaine, Yuasa, 3M). A large proportion of the work being carried out at present by the present consortium is funded by USABC. Much of the improvement in performance of cells under trial in the 1980s and early 1990s can be attributed to modifications to the poly(ethylene oxide) (PEO)–salt polymer electrolyte. Development of amorphous modified polyethers and new plasticized anions permits operation at 60 °C and below, higher bulk conductivities, and much improved lithium-ion transport. New materials, still under development, are hoped to improve rate capability, operating temperature, and cycle life. Generally, the cycling efficiency of cells is very good [9]. Cells can be fully discharged for over 500 cycle at moderate temperatures. Those able to operate at ambient temperatures are capable of deep discharge cycling for at least 700 cycles. Impressive long-term monitoring of self-discharge characteristics make polymer-electrolyte standby batteries with exceptionally long shelf-like look an attractive proposition; over a six-year testing period, the self-discharge rates were found to be < 3 percent per year at 80 °C, < 2 percent per year at 60 °C and 0 percent per year at 40 °C.

During the 1990s, lithium polymer cells have been scaled up to a size of 10 Wh, and assessment of their performance of continues. Test cells show a 1000-fold scale-up to have little effect on cell cycling

CosMX Exhibit 1008, Page 518 of 633

performance. Recent (1994) test cells, operating at 60 °C, confirm 100 percent Ah efficiency and > 85 percent energy efficiency between charge and discharge over the first nine cycles [10]. Despite progress in terms of the number of cycles, operating temperature, and energy density which make these batteries closer to fulfilling all the requirements for commercial exploitation, the technology has yet to be demonstrated at full scale; cost optimization must also be favorable.

8.2.2 The Fundamentals of a Polymer Electrolyte

The solvation enthalpy of a salt in a polymer matrix is influenced by the lattice energy of the salt, the strength of interaction between polymer coordinating group and cation, and the electrostatic interaction between the dissolved ions. Polyethers, polyesters, polyimines, and polythioethers have strong coordinating groups along the chain and can dissolve a wide variety of salts responding to specific criteria. In low-molecular-weight solvents, solvation of the cation depends mainly on the number of molecules that pack around it. In higher-molecular-weight polymers, the chain must wrap around the cation without excessive strain. Taking polyethers as an example, $-(CH_2CH_2O)_n-$ provides just the right spacing for maximum solvation but $-(CH_2O)_n-$ and $-(CH_2CH_2CH_2O)_n-$ are much weaker solvents. In terms of the acid–base interactions between solvet and solute molecules, with each solvent being classified as hard or soft [11], the strongest interactions occur by hard–hard or soft–soft matches. The strongest solvation in a polyether is with a hard cation, e.g., Li^+, Na^+, Mg^{2+}, Ca^{2+}. The ranking of best donors for hard Lewis acids follows the relative value of the negative charge on the heteroatom:

$$-\ddot{O}- > -\ddot{N}H- >> -\ddot{S}- \qquad (1)$$

PEO is found to be an ideal solvent for alkali-metal, alkaline-earth metal, transition-metal, lanthanide, and rare-earth metal cations. Its solvating properties parallel those of water, since water and ethers have very similar donicites and polarizabilities. Unlike water, ethers are unable to solvate the anion, which consequently plays an important role in polyether polymer-electrolyte formation.

Both entropy and enthalpy change has to be considered when dissolving a salt in any solvent. Dissolution can lead to either a positive or negative overall entropy change. In polymer electrolytes, a negative entropy of dissolution is common and can be an important consideration at higher temperatures. This effect arises because the dielectric constant of the solvent polymer (solid or liquid) is usually low (e.g., for PEO, ~5–10) and ion association will reduce the dissociation effect in the entropy. Experimentally, there is widespread evidence for ion association in polymer electrolytes [12]. These ion pairs or higher aggregates may be contact or solvent-separated species. In general, high salt concentrations are likely to favor contact ion pairs (or aggregates). In long-chain polyethers, steric factors also need to be considered. To avoid polymer chain strain, the ion's coordination sphere may not be saturated, making it easy for empty sites around the cation to be occupied by anions. This would lead to the formation of contact ionic clusters, even at low salt concentrations. Experimentally, however, it can be difficult to make a specific identification of species present [8, 13, 14].

In solvents lacking hydrogen-bonding

CosMX Exhibit 1008, Page 519 of 633

ability (low acceptor number), anion stability depends on charge dispersion. Large anions with delocalized charge require little solvation. Salts of singly charged polyatomic anions such as in $LiCF_3SO_3$ or $LiClO_4$ will dissolve easily in polyethers. These salts also tend to have low lattice energies. Salts containing monatomic anions may be soluble in polyethers, provided they are large and polarizable, e.g., I^-, Br^-. Some theoretically suitable anions for polymer electrolytes are ClO_4^-, $CF_3SO_3^-$, $(CF_3SO_2)_2N^-$, BF_4^-, BPh_4^-, AsF_6^-, PF_6^- SCN^-, I^-. However, coordination anions like AsF_6^- are sources of Lewis acids, particularly when associated with lithium, and are capable of inducing polymer chain scission. A choice of ClO_4^- with associated dangers restricts its commercial use, while $CF_3SO_3^-$ complexes have a very unfavorable phase diagram [8], restricting its application to amorphous polymer hosts.

Noncoordination anions with extensive charge delocalization have been very succesful in enhancing the performance of dry polymer electrolytes. Examples of these are given in Table 1.

The major breakthrough has been with bis(trifuoromethanesulfonyl)imido, (TFSI) [15 – 17]. The size and conformation of the imide anion in the polymer complex results in the chains being forced apart [18], reducing their ability to pack into a regular structure, and thus lowering the melting point of the crystalline phase. This is accompanied by a several-fold increase in conductivity. The charge delocalization concept has been extended to carbon analogues, $(CF_3SO_2)_2CRH$ [19, 20], but electrochemical instability and synthetic problems have limited progress to date [21].

8.2.3 Conductivity, Structure, and Morphology

Ion motion in polymer hosts is facilitated by low barriers to bond rotation; this makes $-(CH_2CH_2O)_n-$, $-(CH_2CH_2(CH_3)O)_n-$, and $-(CH_2CH_2NH)_n-$ favorable units to incorporate in a polymer electrolyte. Commercially available high-molecular-weight PEO is the most extensively studied host. It melts ~65 °C and is approximately 85% crystalline. NMR studies have shown beyond doubt that ion transport occurs predominantly through the amorphous phase [22], making a totally amorphous polymer host or a knowledge of the structure and morphology of PEO systems essential. Poly(propylene oxide), PPO, is completely amorphous when, as in the commercial product, the arrangement of the methyl groups along the chain is practically random, preventing the polymer from crystallizing. The steric effects of the methyl group, however, adversely affect polymer–cation interactions and conductivity [23, 24]. PPO may have few advantages as a practical material, but it is used extensively experimentally where a simple, amorphous host material is an essential requirement.

Phase diagrams have been constructed

Table 1. Some imide ions and carbanions used in salts to enhance polymer electrolyte conductivity and reduce crystallinity

Name	Acronym	Structure	Reference
Bis(trifluoromethanesulfonyl)imido	TFSI	$[N(CF_3SO_2)_2]^-$	[15]
(Methoxypropyltrifluormethanesulfonyl)amino	MPSA	$[(CF_3SO_2)N(CH_2)_3OCH_3]^-$	[20]
Bis(trifluoromethanesulfonyl)methyl	TFSM	$[(CF_3SO_2)_2CH]^-$	[19]

CosMX Exhibit 1008, Page 520 of 633

for numerous polymer electrolytes [6, 8, 25–27]. For systems containing small monovalent cations, e.g., Li^+, the stoichiometric complex is $P(EO_3)MX$, while for larger cations, e.g., K^+, NH_4^-, the equivalent complex is $P(EO_4)MX$. Phases that are even richer in salt are known to exist [26–29]. Some salts also from a 6:1 complex, a consequence of anionic symmetry and/or ion size [30]. A eutectic exists between the most dilute complex and PEO. When this complex is $P(EO_3)MX$, the eutectic's melting temperature and composition are close to those of PEO itself. This accounts for the unfavorable PEO–$LiCF_3SO_3$ phase diagram. When a 6:1 complex is the most dilute present, the eutectic composition is much more concentrated and the melting temperature is depressed. This reduces the severity of constraints on PEO–$LiClO_4$ systems. The thèrmal properties of PEO–$LiN(CF_3SO_2)_2$ have been studied in some detail [26, 27, 31] and a partial phase diagram is shown in Fig. 2.

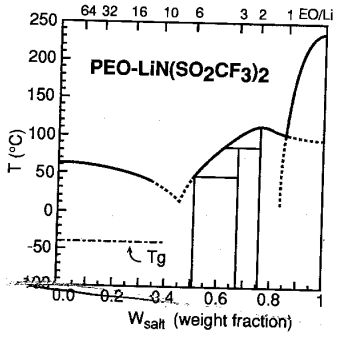


Figure 2. Phase diagram for PEO–$LiN(CF_3SO_3)_2$ showing the eutectic equilibrum between PEO ($M_w = 4\times10^6$) ant the 6:1 (salt wt. Fraction 0.52) intermediate compound. Compiled from C. Labrèche, I. Lévesque, J. Prud'homme, *Macromolecule* **1996**, *29*, 7795 and S. Lascaud, M. Perrier, A. Vallee, S. Besner, J. Prud'homme, M. Armand, *Macromolecules* **1994**, *27*, 7469.

Like PEO–$LiClO_4$, a 6:1 crystalline compound is formed but, in this instance, the weakened interactions between polymer chains [18] contributes to the lowest melting point for any PEO–salt crystalline complex. A eutectic with composition O:Li = 11:1 forms, provided the PEO molecular chain length is beyond the entanglement threshold [31]. For lower molecular weights, the 6:1 compound dose not crystallize in the presence of excess PEO and a crystallinity gap exists over the range 6:1 < O:Li < 12:1 [26].

8.2.4 Second-Generation Polymer Electrolytes

The main advantage of PEO as a host is that it is chemically and electrochemically stable since it contains only strong unstrained C–O, C–C, and C–H bonds. The disadvantage is the inherent crystallinity, and considerable effort has gone into synthesizing all-amorphous polymer hosts. Unfortunately, with the bulk conductivity as the prime motivator, many amorphous polymer hosts incorporate organic functional groups which limit their practical application. Detailed accounts of many of the hosts synthesized have been reviewed [8, 32–36].

Random copolymers are similar to PEO but when the regular helical structure of the chains is demolished, the crystallinity is also destroyed. One of the simplest and most successful amorphous host polymers is an oxyethylene– oxymethylene structure in which medium length but statistically variable EO units are interspersed with methylene oxide groups. First described in 1990 [37], *a*PEO has the general structure

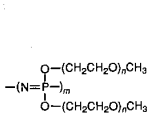
$$-[-(OCH_2CH_2)_mOCH_2-]_n-$$
$$m = 5-10$$

CosMX Exhibit 1008, Page 521 of 633

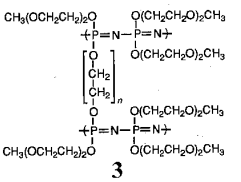
and can be easily synthesized in a range of molar masses up to ~100000. All systems are fully amorphous at and above room temperature. A copolymer similar to *a*PEO includes dimethylsiloxy units rather than methylene oxide groups [38]. Polydimethylsiloxane has a low T_g which helps to optimize ionic conductivity by enhancing polymer chain flexibility. Other quasi-random systems include ethylene oxide–propylene oxide copolymers [39].

Comb-branched copolymer and block copolymer architectures are similar in that they are generally based on short polyether chains supported in some manner to give the material its mechanical stability. Success has been variable in attempts to exploit the unique properties of ABA block copolymers and optimize conductivity and mechanical strength [40–42]. For most comb-branched systems, the ether chain length, the nature of the salt, and the salt concentration affect the formation or otherwise of a crystalline complex and, in general, conductivities comparable with or higher than those of PEO analogues can be achieved. The backbone of a comb-branched system may be of high T_g, (e.g., polymethacrylate, polyitaconate [43–45]) to enhance mechanical stability or of low T_g (polyphosphazene, polydimethylsiloxane [46, 47]) to favor flexibility and bulk conductivity. The most succesful of the latter materials is poly(methoxyethoxyethoxyphosphazene), known as MEEP (**2**). Dimensional stability is poor but this can be enhanced without seriously impairing conductivity by judiciously crosslinking the material or branching the side chains [48]; **3** represents a PEO-crosslinked MEEP network.

Both radiation and chemical crosslinking can produce amorphous, mechanically stable networks. Radiation crosslinking has a practical advantage in that polymer electrolyte films can be fashioned to the desired thickness or shape, and even incorporated into a device before crosslinking. Chemical crosslinking often introduces undesirable functional groups which may offer few advantages from a practical viewpoint but can be a very useful route to the simple preparation of network for fundamental studies [33, 49–51].



2

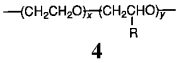


3

One of the major drawbacks to many promising copolymers is their unsatisfactory electrochemical stability. Carbonyl groups which feature in many of the backbone/chain linking groups are likely to cause stability concerns. Likewise, urethane, alcohol, and siloxane functions are sensitive to lithium metal. With this in mind, a recent trend has been to find synthetic routes to amorphous structures with

- a high –OCCO– density
- electrochemically unstable groups excluded, and
- functions to enable crosslinking for mechanical stability.

The first of such materials was reported in 1990 [52] and was based on the general structure **4**.

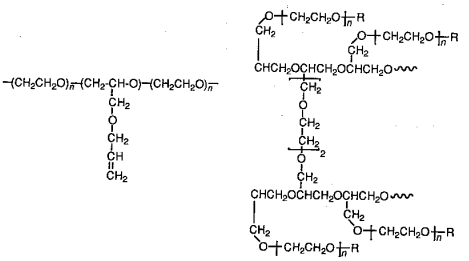


4

The side group R is an ether of varying chain length and end group. Crosslinked networks can easily be prepared by incorporating unsaturated centers. A number of network structures of varying complexity

CosMX Exhibit 1008, Page 522 of 633

have since been prepared [41, 53–55]; **5** and **6** are two examples [40, 54, 56].



5 **6**

5 is an electrochemically stable copolymer with an unsaturated center in a side group which can be radiation-crosslinked to give a mechanically and electrochemically stable network, and **6** PEO-crosslinked network.

It is noteworthy that the crosslinkable $CH_2=C(CH_2-)_2$ moieties linking the EO units are based on the same principle as *a*PEO. In addition to their crystallinity-breaking effect, these groups have a reactive double bond. Depending on salt concentration, side-chain length, and crosslink density, room-temperature conductivities in the range $10^{-4}-10^{-5}$ S cm^{-1} can be achieved. All these materials exhibit very good electrochemical stability for both oxidation and reduction, with the electrolyte stable up to at least 3.9 V vs, Li/Li^+.

8.2.5 Structure and Ionic Motion

Much success in determining crystal structures has been achieved through high-quality powder X-ray data of polycrystalline powders [57]. Structures which have been elucidated include $P(EO)_3LiCF_3SO_3$, $P(EO)_3NaClO_4$, $P(EO)_4KSCN$, $P(EO)_4RbSCN$, $P(EO)_4NH_4SCN$, and $P(EO)_3LiN(SO_3CF_3)_2$ [18,58]. All crystal structures show the cations (with radii ranging from Li^+ (0.76 Å) to Rb^+ (1.52 Å)) located within the PEO helix as shown in Fig. 3.

Many features are common to all polymer electrolytes. The helical conformation

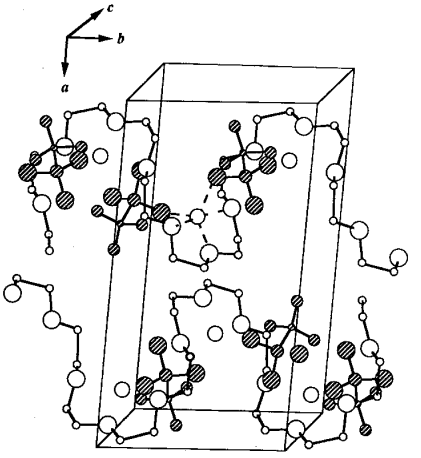


Figure 3. $PEO_3LiCF_3SO_3$ crystal structure viewed along the *c* axis. $CF_3SO_3^-$ groups are shared. Coordination around one Li^+ ion is shown by broken lines. Reprinted with permission from P. Lightfoot, M. A. Meltha and P. G. Bruce, *Science* **1993**, *262*, 883. Copyright 1993 American Association for the Advancement of Science.

of PEO is retained, but with a different pitch. Each turn of the helix contains one cation coordinated by oxygen atoms from the polymer chain. The number of coordinating ether oxygens per cation increases from 3 (Li^+) to 5 (Rb^+). Each cation is coordinated by two triflate anions which bridge neighboring cations. Most importantly, it is found that each chain forms an isolated one-dimensional coordination complex. Cation and anions do *not* bridge chains. Spectroscopic studies of $P(EO)_3LiCF_3SO_3$ have recently identified the anion as essentially a $[Li_2CF_3SO_3]^+$ species which forms part

CosMX Exhibit 1008, Page 523 of 633

of an extended ionic chain, $\ldots Li^+ \ldots CF_3SO_3^- \ldots Li^+ \ldots$, a similar arrangement to that in Fig. 3 [59]. This structure is maintained on heating through the melting transition at 180 °C and beyond. One can only speculate at this stage on the implication for the ion-transport mechanism according to which a predominance of interchain cation movement used to be assumed (Fig. 4).

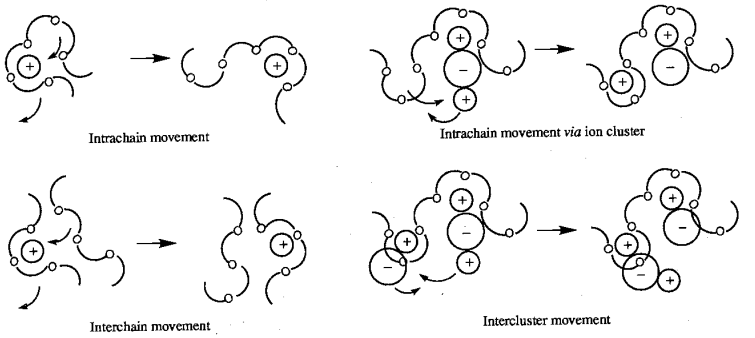


Figure 4. Two representations (on the left) of cation motion in a polymer electrolyte assisted by polymer chain motion only, and two (on the right) showing cation motion taking account of ionic cluster contributions.

Polymer dynamics studies also point to intrachain, not interchain, crosslinking being primarily responsible for increasing T_g at high salt concentration [60]. Long-range ion transport requires the movement of ions from chain to chain but it may be also possible for chain dynamics to facilitate ion hopping between vacant sites along the polymer helix. The relative importance of intrachain coordination in ion transport may vary with salt concentration and its overall importance has yet to be addressed.

8.2.6 Mechanisms of Ionic Motion

The importance of polymer segmental motion in ion transport has already been referred to. Although classical Arrhenius theory remains the best approach for describing ion motion in solid electrolytes, in polymer electrolytes the typical curvature of the log σ vs. $1/T$ plot is usually described in terms of T_g-based laws such as the Vogel–Tamman–Fulcher (VTF) [61] and Williams–Landel–Ferry (WLF) [62] equations. These approaches and other more sophisticated description of ion motion in a polymer matrix have been extensively reviewed [6, 8, 63].

The form of the VTF equation normally used to fit the thermal dependence of the ionic conductivity is:

$$\sigma = \sigma_0 \exp\left[\frac{-B}{(T - T_0)}\right] \qquad (2)$$

T_0 is a reference temperature which can be identified with T_g, and although the constant B is not related to any simple activation process, it has dimensions of energy. This form of the equation is derived by assuming an electrolyte to be fully dissociated in the solvent, so it can be related to the diffusion coefficient through the Stokes–Einstein equation. It suggests that thermal motion above T_0 contributes to relaxation and transport processes and that

CosMX Exhibit 1008, Page 524 of 633

for low T_g, faster motion and faster relaxation should be observed. In polymer electrolytes, the assumption is that ions are transported by the semi random motion of short polymer segments, providing free volume into which the ion can diffuse under the influence of an electric field. Figure 4 shows this type of motion schematically. The model is very much an over simplification as it does not consider effects such as ion–ion interactions and their contribution to the conductivity mechanism.

The WLF approach is a general extension of the VTF treatment to characterize relaxation processes in amorphous systems. Any temperature-dependent mechanical relaxation process, R, can be expressed in terms of a universal scaling law:

$$\log\left[\frac{R(T)}{R(T_{ref})}\right] = \log(a_T) = -\frac{C_1(T-T_{ref})}{(C_2+T-T_{ref})} \quad (3)$$

T_{ref} is a reference temperature, a_T is known as the shift factor and C_1 and C_2 are constants which may be obtained experimentally. The two equations are identical if $C_1C_2 = B$ and $C_2 = (T_{ref} - T_0)$. Although T_{ref} is arbitrary, it is often taken to be 50 K above T_g, allowing master curves to be drawn as a function of $(T - T_g)$. Extensive measurements of shift factors for PEO-based networks do reveal expected correlations [33]. The universality of the relationship [Eq. (3)] was believed to be due to a dependence of relaxation rates on free volume. Regardless of how accurate a given set of measurements is, and although the constants C_1 and C_2 may be given significance in terms of free-volume theory, there is nothing to connect the system's behavior to free-volume behavior [63, 64]. Often the fit of the temperature variation of the conductivity is good but, equally, there are many instances when it is not. A free-volume model is unsatisfactory here as it does not relate directly to a microscopic picture and therefore does not predict straighforwardly how variables such as ion size, polarizability, ion pairing, solvation strength, ion concentration, polymer structure, or chain length will affect the conduction process. Also, ion motion in an electric field makes a substantial contribution to mobility; ions are not merely pushed along by the segmental motion of the polymer. Such are the difficulties of interpreting the measured temperature dependence of the conductivity simply and straightforwardly.

More detailed theoretical approaches which have merit are the configurational entropy model of Gibbs et al. [65, 66] and dynamic bond percolation (DBP) theory [67], a microscopic model specifically adapted by Ratner and co-workers to describe long-range ion transport in polymer electrolytes.

In the former, WLF-type behavior is again analyzed but in terms of configuration entropy and not volume. Transport is modeled on group cooperative rearrangements of the polymer chain rather than a void-to-void jumping mechanism. The model is built upon some realistic arguments concerning relaxation processes and availability of states and also introduces kinetic ideas. When kinetic effects are taken into account in a free-volume-based transport treatment, the results very much resemble the configuration entropy model [68]. The reason, however, why free-volume ideas appear to work so well for polymer electrolytes may to the close correlation between volume and enthalpy or entropy [69].

DBP theory provides the simplest model which includes information on local mechanistic processes, and involves ion

CosMX Exhibit 1008, Page 525 of 633

hopping between sites on a continually renewing lattice (not static as for a solid electrolyte). The configuration is continually changing, with sites moving with respect to each other. Hopping probabilities readjust their values on a time scale which is determined by the polymer motion. This theory has the advantage of allowing different particle subsets (anions, cations, etc.) to be treated individually by taking chemical interactions into consideration.

There is experimental evidence to suggest that anion and cation diffusion can have different mechanisms [70]. The temperature variation of the diffusion coefficients of ^{31}P and ^{7}Li in aPEO – $LiPF_6$ shows quite different trends. The ^{31}P diffusion coefficients follow a VTF-type dependence at all concentration and are always significantly faster that those of Li^+-based species. Anions do not form strong bonds with the polymer hosts so their transport is likely to depend principally on the rate of polymer rearrangements. Such a mechanism may be described in terms of configurational entropy or free-volume theories, both of which predict a VTF-like temperature dependence. ^{7}Li diffusion shows a change in the ion-diffusion mechanism from a process controlled by VTF kinetics to a thermally activated mechanism as salt concentration is increased. Ionic conductivity for the cation appears to be an average of two distinct processes, with an ion-hopping mechanism predominating at high salt concentrations.

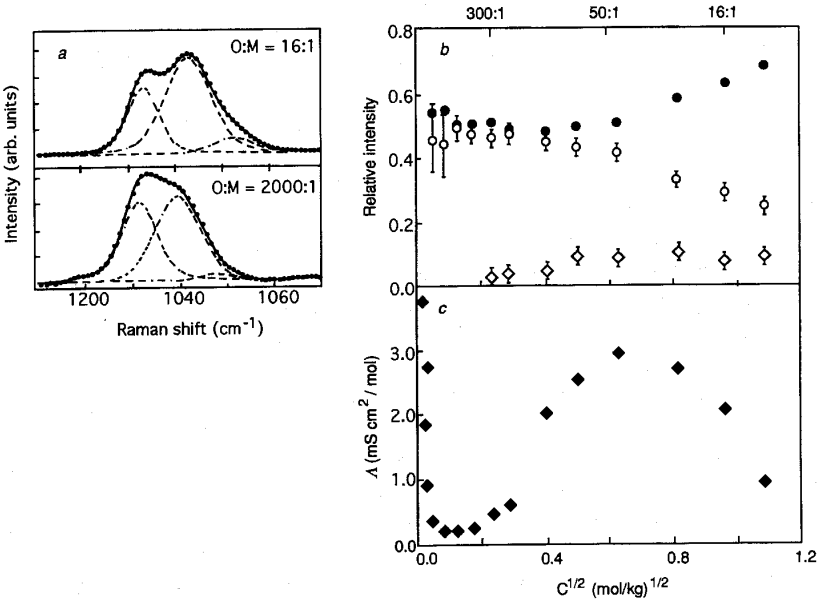


Figure 5. (a) The (A_1, SO_3) anion symmetric streching mode of poly(propylene glycol)–$LiCF_3SO_3$ for O:M ratios of 2000:1 and 6:1. Solid symbols represent experimental data after subtraction of the spectrum correponding to the pure polymer. Solid curves represent a three-component fit. Broken curves represent the individual fitted components. (b) Relative Raman intensities of the fitted profiles for the (A_1, SO_3) anion mode for this system, plotted against square root of the salt concentration:○, solvated ions;●, ion pairs;◆, triple ions. (c) The molar conductivity of the same system at 293 K. Adapted from A. Ferry, P. Jacobsson, L. M. Torell, *Electrochim. Acta* **1995**, *40*, 2369 and F. M. Gray, *Solid State Ionics* **1990**, *40/41*, 637.

CosMX Exhibit 1008, Page 526 of 633

8.2.7 An Analysis of Ionic Species

For a salt MX dissolved in a polymer host solvent, the formation of neutral ion pairs, $[MX]^0$, leads to a drop in the concentration of charge carriers. Larger aggregates may also exist in some media and although they may be charged, e.g. $[M_2X]^+$ or $[MX_2]^-$, their mobilities will be impaired by size in comparison with free ions, which again adversely affects conductivity. The nature of the anionic species is of course of paramount importance for the type of speciation. Both spectral and molar conductivity studies reveal marked change in the type and concentration of species involved in charge transport as salt concentration changes [71,72]. Figure 5 compares these data.

At salt concentration below those shown in Fig. 5, molar conductivity behavior has been identified with the formation of electrically neutral ion pairs [8]. Between concentration of 0.01 and ~0.1 mol L^{-1} (up to an O:M ratio of ~50:1) the molar conductivity rises and this can be explained by the formation of mobile charged clusters such as triple ions, a progressive dissociation of ion pairs, or a combination of both. Up to O:M $\cong$ 50:1, however, spectral data indicate very little change in the species concentrations and this may instead indicate an enhancement in ionic mobility. With charge separation <5 Å and polymer motion restricted by ion coordination, an anion-assisted (Grotthus-like) transport mechanism could be envisaged as Eq. (4) and (5).

$$XM + X^- + X^- \leftrightarrow X^- + MX \quad (4)$$

$$OM + X^- \leftrightarrow O + MX \quad (5)$$

8.2.8 Cation-Transport Properties

The mobility of lithium ions in cells based on cation intercalation reactions in clearly a crucial factor in terms of fast and/or deep discharge, energy density, and cycle number. This is especially true for polymer electrolytes. There are numerous techniques available to measure transport

Table 2. Techniques for measuring transport/transferene numbers in polymer electrolytes, and the range of values encontered

Name	Polymer matrix	Concentration range	t_+/T_+	Reference
Tubandt–Hittorf	$(PEO)_x - LiCF_3SO_3^*$	242:1 – 8:1	0.2 – 0.4	[79]
	$(PEO)_x - LiClO_4^*$	242:1 – 8:1	0.2 – 0.4	[79]
	$PEO - LiClO_4$	8:1	0.06	[80]
Concentration cell	$Polym - LiClO_4^\dagger$	80:1 – 8:1	0.3	[81, 82]
	$Polym - LiCF_3SO_3^\dagger$	80:1 – 8:1	0.6	[83]
	$PEO - NaCF_3SO_3$	160:1 – 8:1	0.3 – 0.45	[83]
Radiotracer	PEO – NaI	8:1	0.36	[74]
	PEO – NaSCN	8:1	0.38	[84]
PFG NMR	$PEO - LiCF_3SO_3$	20:1 – 6:1	0.4 – 0.5	[85]
	$PEO - LiClO_4$	20:1 – 8:1	0.3	[86]
	$PEO - Li(CF_3SO_2)N$	30:1 – 6:1	0.25 – 0.3	[76]
DC polarization	$PEO - LiClO_4$	100:1 – 8:1‡	0.2 – 0.3‡	[87, 88]
	$PEO - LiCF_3SO_3$	100:1 – 8:1‡	0.45 – 0.6‡	[73, 89, 90]

* $(PEO)_x$, crosslinked network.
† (Polym), various polymers.
‡ Current fraction.

CosMX Exhibit 1008, Page 527 of 633

properties, including:

- Group 1: Tubandt–Hittorf; concentration cell techniques;
- Group 2: Radiotracer; pulsed field gradient NMR measurements (PFG NMR);
- Group 3: DC polarization; AC impedance methods.

For a fully dissociated salt, all techniques should give the same values of transport number, t_i. Transference number measurements are appropriate for electrolytes containing associated species and any technique within one of the three groups will give a similar response, but values of T_i across the groups may vary.

Table 2 gives an indication of the considerable variation and disagreement concerning the measured values of transference numbers in polymer electrolytes. Diffusion techniques such as PFG NMR measure the flux of both charged and electrically neutral species. If a high concentration of *mobile* ion pairs or higher neutral aggregates is present, a neutral pseudo-transport number of ~0.5 is predicted [73] and indeed, similarities have been observed between cationic and anionic diffusion coefficients [74, 75]. More realistic diffusion coefficient and transport measurements should be available from PEO–$LiN(CF_3SO_2)_2$, as ionization is maximized through extensive delocalization of the negative charge [76–78]. The resulting Li^+ transport number of only 0.3 implies extensive anion mobility.

For DC polarization studies, the ratio of steady-state to initial current is not the transport number but determines the "limiting current fraction", the maximum fraction of the initial current which may be maintained at steady-state (in the absence of interfractional resistances). Variations observed in this parameter with salt concentration and temperature must result from changes in the state of the electrolyte and are compatible with changes in ionic species contributing to the steady-state current. These may include mobile neutral species [73].

Of all the techniques, it is those of Group 1 that are likely to give the most realistic data, simply because they measure transport of charged species only. They are not the easiest experimental techniques to perform on polymeric systems and this probably explains why so few studies have been undertaken. The experimental difficulties associated with the Tubandt–Hittorf method are in maintaining nonadherent thin-film compartments. One way is to use crosslinked films [79], while an alternative has been to use a redesigned Hittorf cell [80]. Although very succesful experimentally, the latter has analytical problems. Likewise, emf measurements can be performed with relative ease [81, 82]; it is the necessary determination of activity coefficients that is difficult.

Some cations are too strongly attached to the polymer chains to move independently and are effectively immobilized. Electron donicities of the oxygen in water and ethers are very similar. By comparing the kinetics of solvent exchange around the cation with data known for ligand exchange of ions in aqueous solutions, a ligand exchange rate threshold value of $\sim 10^{-8}$ s^{-1} is found to separate the mobile from the immobile cations in PEO [91]. Notably, Mg^{2+} is immobile ($<10^{-8}$ s^{-1}) whereas Hg^{2+} ($>10^{-8}$ s^{-1}) has a transference number close to that of alkali metals, despite carrying a higher charge [92, 93]. In order to extend mobility to effectively immobile cations, a vehicular mechanism has been examined whereby the metal cation is incorporated as part of an anionic

CosMX Exhibit 1008, Page 528 of 633

complex [7, 94]. If $ZnCl_2$, for example, is co-dissolved with CsCl, which does not itself dissolve in PEO, highly conductive homogeneous electrolytes result with very fast zinc-stripping/plating kinetics.

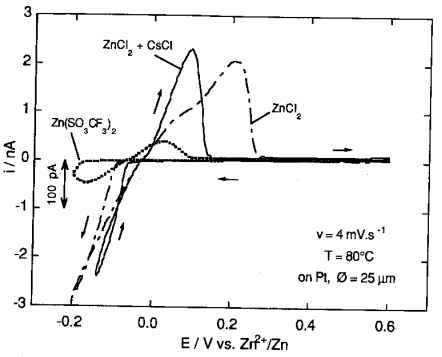


Figure 6. Voltammetry at microelectrode of different zinc derivates in PEO; the CsCl adduct corresponds to $P(EO)_9(ZnCl_2)_{0.8} \cdot CsCl$. For the triflate derivative, the current is magnified by a factor of 10. Reprinted from D. Baril, C. Michot, M. Armand, *Solid State Ionics* **1997**, *94*, 35, Copyright 1997, with kind permission of Elsevier Science—NL, Sara Burgerhartstraat 25, 1055 KV Amsterdam, The Netherlands.

Figure 6 compares voltammograms for $P(EO)_9(ZnCl_2)_{0.8} \cdot CsCl$ which contains a mixture of $ZnCl_3^-$ and $ZnCl_4^{2-}$ and for a zinc triflate derivative [95]. The metal desposition process can be written as Eq. (6),

$$4ZnCl_3^- + 2e^- \Leftrightarrow Zn^0 + 3ZnCl_4^{2-} \quad (6)$$

involving downfield migration of the halide-rich complex and upfield concentration diffusion of the three-coordinated species [96]. The transport of zinc as a complex ionic species is much faster than in the form of the dissociated salt $Zn(CF_3SO_3)_2$. Provided there is sufficient dissociation and properly designed ligands then, in principle, highly conducting polymer electrolytes can be formed for any cation.

Dissociation can be improved by using anions with highly delocalized charge but cation mobility is still undesirably low. A new approach to polymer electrolyte design which could enhance cation mobility is thr formation of ionic rubbers. The aim is to produce a material which combines the advantages of a superionic glass (decoupled cation motion) and the macroscopic rubbery properties of a polymer electrolyte [5, 97–100]. The polymer need only be present as a small percentage of the total electrolyte to impart flexibility to the system. Complexing lithium chlorosulfonate with aluminum chloride to give a mixed anion, $[AlCl_3 - SO_3Cl]^-$, produces a material with a room-temperature conductivity better than 10^{-3} S cm^{-1} and a 4.0 V electrochemical window. $LiAlCl_4$ (T_g = –39 °C) is also being investigated as a potential electrolyte component. In combination with complexes of $Li(CF_3SO_2)_2N$ and $AlCl_3$, ambient conductivities range from 10^{-4} to 10^{-5} S cm^{-1} [100]. Simpler imides like dichlorosulfonimide and fluorochlorosulfonimide enhance the conductivity further. Again, these systems exhibit a wide electrochemical stability window ~5 V.

8.3 Hybrid Electrolytes

The polymer electrolytes discussed so far suffer from a number of disadvantages. Firstly, they exhibit low conductivities in comparison with liquid or solid (crystalline or glassy) electrolytes at or below room temperature. The best all-amorphous systems have conductivities less than 10^{-4} S cm^{-1} at room temperature. These ambient

CosMX Exhibit 1008, Page 529 of 633

temperature conductivities may be insufficient in some cases for the power required by a lithium battery. Secondly, the interfacial impedances present at both the lithium anode (passivation) and composite cathode (passivation, contact) are in addition to the ohmic losses in the electrolyte. Thirdly, the lowness of cation transference number, although similar to the values in liquid systems, is a major issue since the total conductivity is lower and could limit the use of solvent-free polymer electrolytes except in the form of extremely thin films or above room temperature.

One way of addressing these issues has been to form polymer hybrid electrolytes [101]. These generally consist of a polymeric component and either (a) a liquid phase, (b) another polymer, conducting or nonconducting, (c) a solid ceramic or glassy component, (d) a combination of these. Many hybrid systems, particularly those containing a liquid component, have not been viable for practical lithium-metal-based electrochemical cells until now. Despite their superior conducting properties, the addition of a liquid component reintroduces the undesirable physical and electrochemical properties of a liquid-based electrolyte: mechanical instability, solvent combustibility, severe interfacial reactions, and the tendency for lithium dendrites to form on cell cycling. Lithium-ion or "rocking-chair" batteries do not use lithium metal, making gel-type materials much more attractive. This is reflected in the growing commercial interest in polymer electrolyte batteries as well as more fundamental studies of ternary systems.

8.3.1 Gel Electrolytes

Gel electrolytes are attractive alternatives to the dry electrolytes, particularly with respect to higher, more practical, ionic conductivities. Two distinct methods can be used to achieve macroscopic immobilization of the liquid solvent: increase the viscosity of the liquid electrolyte by adding a soluble polymer, e.g., PEO, poly(methyl methacrylate) (PMMA), polyacrylonitrile (PAN), poly(vinylidene fluoride) (PVdF), etc. [32, 34]; or load the liquid electrolyte into a microscopous matrix, e.g., porous polyethylene [102, 103].

The solidity of gel electrolytes results from chain entanglements. At high temperatures they flow like liquids, but on cooling they show a small increase in the shear modulus at temperatures well above T_g. This is the liquid-to-rubber transition. The values of shear modulus and viscosity for rubbery solids are considerably lower than those for glass forming liquids at an equivalent structural relaxation time. The local or microscopic viscosity relaxation time of the rubbery material, which is reflected in the T_g, obeys a VTF equation with a pre-exponential factor equivalent to that for small-molecule liquids. Above the liquid-to-rubber transition, the VTF equation is also obeyed but the pre-exponential term for viscosity is much larger than is typical for small-molecule liquids and is dependent on the polymer molecular weight.

Addition of a plasticizing solvent to a polymer–salt system modifies the electrolyte by lowering the T_g through an isothermal increase in the system's configurational entropy and this consequently increases the mobility of all particles. A suitable choice of organic solvent can lead to very high conductivities (10^{-3}–10^{-2} S cm^{-1}) while still retaining the rubbery character of the material. The challenge is to find the right combination of components to give high ionic conductivity, chemical stability, and a wide voltage win-

CosMX Exhibit 1008, Page 530 of 633

dow, and to be able to resist steady stresses over a practical temperature range.

Gel electrolytes based on polystyrene, poly(vinyl chloride), poly(vinyl alcohol), PAN and PVdF, various salts, and high-dielectric-constant solvents have been investigated since the early 1980s [34, 104–106]. The polymer imparts mechanical stability; solvating power is not a requirement. Conductivity is critically affected by the physical properties of the solvent, such as the viscosity, mobility, and dielectric constant, and by the concentration of salt in the electrolyte. A high dielectric constant increases the level of salt dissociation, whereas low viscosities lead to high ionic mobility. The main role of small molecules is therefore to plasticize the host polymer, improving flexibility and segmental motion, and to solvate the cation (or the anion in some instances), which reduces ion–ion interactions.

PAN-based systems have been the focus of much recent interest. Although the polymer is assumed to be nonsolvating, NMR studies [107] suggest that there may be some competition (albeit small) for solvation between the polymer and plasticizing solvent in PAN-based gel electrolytes. This makes for a rather complex ion-transport mechanism. Probing on a microscopic level, such as through ^{7}Li NMR [107], shows that the polymer can impart a strong influence on ionic conductivity, even on short-range ionic motion, and that impedance of ionic motion can be correlated with T_g. IR spectroscopic studies of "kinks" in the log σ vs. $1/T$ plots observed when PAN or PVdF is added to a liquid electrolyte with relatively high concentrations of salt show that it is not related to changes in mechanical properties but are believed to result from direct ion–polymer interactions or changes in the ability of the low-molecular-weight solvent (high or low dielectric constant) to solvate the salt as a result of the presence of the polymer. Increasingly, the influence of interactions between components of the gel electrolytes is being scrutinized [108, 109]. With regard to safety, the Sony Corporation [110] have investigated PAN gels and claim that, given the right combination of polymer/salt/solvent, gels can have remarkably high conductivities (~3 × 10^{-3} S cm^{-1}) and electrochemical stability (>4.5 V), and exhibit superior thermal stability (and hence safety), in comparison with other gels and liquid solvents. This thermal stability is said to result from cyclization experienced by PAN at high temperatures.

The role of plasticizers in ion–ion interactions may not be straightforward either, judging by IR data on plasticized $(PEO)_9LiCF_3SO_3$ [108]. Propylene carbonate (PC) reduces ion association but a large percentage by weight is required to achieve this. The material becomes more amorphous at room temperature as a result of preferential interaction of PC with pure PEO in the heterogeneous system to form conducting pathways. Despite PC being a good solvent for the salt, at least 50 wt. % is required before any significant interaction is detected.

The conductivity of gelled electrolytes is determined primarily by the liquid and salt components. High liquid content, of the order of 40 percent, is required to attain conductivities comparable with those of the corresponding liquid electrolyte. At these liquid loading levels there is often insufficient mechanical strength, and although this effect may not be noticeable on 1–2 cm^2 laboratory cells, it is certainly evident on scale-up [111]. Polymer blends such as PEO–MEEP are much more mechanically stable than MEEP itself and more conductive than PEO but there is little overall improvement of the room tem-

CosMX Exhibit 1008, Page 531 of 633

perature conductivity, even when they are complexed with plasticizing salts [112]. A novel approach to mechanically stable, highly conducting electrolytes is to use a dual-phase electrolyte (DPE) made up of two different polymers, one a supporting latex, the other a latex containing polar units which are fused together [113, 114]. An example is a styrene–butadiene rubber (SBR) fused with an acrylonitrile–butadiene rubber (NBR). When immersed in a lithium salt solution, only the polar phase takes up solvent to form ion-conducing pathways while the nonpolar phase imparts mechanical strength. Alternatively, a core–shell latex can be synthesized by polymerizing a nonpolar monomer (e.g., polybutadiene) in a fine dispersion of a polar polymer (e.g., poly(vinylpyrrolidone). A polar polymer shell forms around the stabilizing nonpolar core. The latex particles collapse on removal of the dispersion medium, causing the cores to fuse partially, and once again the polar phase takes up electrolyte solution to form ion-conducting pathways [114]. Figure 7 shows a schematic of DPE electrolytes. Above a percolation threshold of ~15 wt. % NBR, an NBR/SBR matrix containing 1 $\mathrm{mol\,L^{-1}}$ $LiClO_4$ in γ-butyrolactone exhibits a conductivity of $\sim 10^{-3}$ S $\mathrm{cm^{-1}}$.

PC and EC are compatible with a wide range of salts and polymers and are commonly used in gel electrolytes. They have high dielectric constants and consequently high conductivities can be achieved using relatively low concentrations of plasticizer, which minimizes the reduction in mechanical stability. They are, however, much more aggressive towards lithium metal than ethers such as cyclic polyethers (monocyclic crown ethers, bicyclic cryptands), which are also very effective at reducing ion association. They are more complexing for alkali-metal ions than their linear counterparts, and better able to shield the cation from anion. Their strong complexing ability, however, causes some concern with respect to desolvation kinetics at the interface. Whereas crown ethers provide incomplete shielding [115], bicyclic cryptand complexing agents are much more effective; unfortunately, steric hindrance effects ultimately lead to cryptand–cation complex precipitation. Reducing ion association through cation complexation is

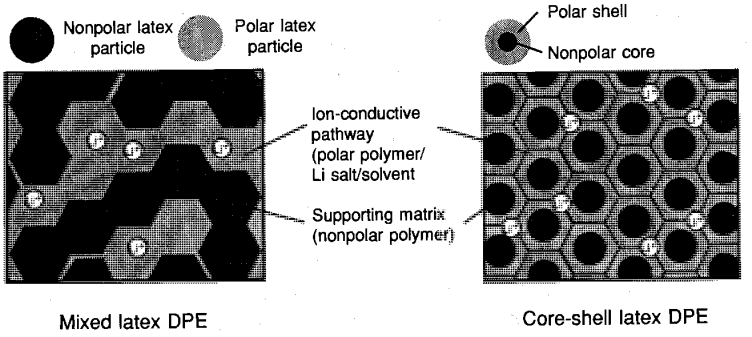
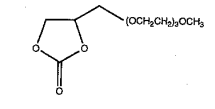


Figure 7. Structures of dual-phase polymer electrolytes. Reprinted from T. Ichino, M. Matsumoto, Y. Takeshita, J. S. Rutt, S. Nishi, *Electrochim. Acta, 40*, 2265–2268, Copyright 1995, with kind permission of Elsevier Science Ltd. The Boulevard, Langford Lane, Kindlington OX5 1GB, UK.

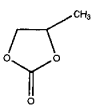
CosMX Exhibit 1008, Page 532 of 633

also likely to result in increased anion mobility which from a practical viewpoint, is not a desirable outcome.

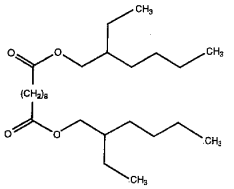
Tetraalkylsulfamides, known to be stable towards reducing agents [116], may also be less aggressive plasticizers in lithium-based electrochemical cells [117]. The conductivity enhancement brought about by addition of tertaethylsulfamide is only half that produced by PC in PEO–$LiN(CF_3SO_2)_2$ on a weight basis [31]. The difference is thought to be due to the small T_g depression it produces, suggesting it is less competitive for cation solvation than PC. Results for other tetraalkylsulfamides with higher dielectric constants are more promising. A new generation of plasticizers are being developed for their plasticizing properties and ability to enhance ion-pair dissociation. A modified carbonate (MC) (**7**) is effectively PC (**8**) with the $-CH_3$ 'group substituted by three ethylene oxide units [118].



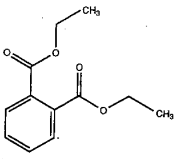
7 Modified carbonate



8 Propylene carbonate



9 Dioctyl sebacate
(bis(2-ethylhexyl) sebacate)



10 Diethyl phthalate

MC has a much stronger influence on ion-pair dissociation than PC. The EO units on MC coordinate cations which have been dissociated by the carbonate group, and prevent cation association with the anion. It is thought that, whereas conventional plasticizers like PC create fast ion-conduction pathways through the plasticizer, MC increases the ionic conductivity throughout the entire system. PEO–$LiCF_3SO_3$ plasticized with 50 percent MC results in a conductivity an order of magnitude higher than if PC were used, and two orders higher than PEO–$LiCF_3SO_3$ itself. Dioctyl sebacate (DOS, **9**) and diethyl phthalate (DEP, **10**) [119] have similarities to MC: the two ester linkages provide multiple oxygen sites for cation coordination. The primary effect of adding these two solvents to PEO–$LiCF_3SO_3$ is to reduce low-temperature crystallinity, and a plasticizing salt is required to have any marked effect on conductivity.

8.3.2 Batteries

The majority of electrochemical cells to have been constructed are based on PEO, PAN, or PVdF [101]. Recently, the Yuasa Corporation have commercialized solid polymer electrolyte batteries, primarily for use in devices such as smart cards, ID cards, etc. To date, the batteries which have been manufactured and marketed are primary lithium batteries based on a plasticized polymer electrolyte, but a similar secondary battery is expected [120].

With regard to rechargeable cells, a number of laboratory studies have assessed the applicability of the rocking-chair concept to PAN–EC/PC electrolytes with various anode/cathode electrode couples [121–123]. Performance studies on cells of the type Li^0 | PAN–EC/PC-based electrolyte | $LiMn_2O_y$ and carbon | PAN–EC/PC-based electrolyte | $LiNiO_2$ show some capacity decline with cycling [121]. For cells with a lithium anode, the capacity decay can be attributed mainly to passivation and loss of lithium by its reaction with

CosMX Exhibit 1008, Page 533 of 633

the electrolyte. A carbon/$LiNiO_2$ cell retains 85 percent of the initial discharge capacity after >300 cycles. Reversibility can be improved by replacing carbon with TiS_2 [122]. The reduction in capacity results from a rise in internal impedance, possibly associated with a reduction of the electrolyte on carbon. Other factors such as solvent cointercalation, which in known to contribute to the decline in capacity of similar organic liquid-electrolyte-based cells, could also be involved.

The preparation and properties of a novel, commercially viable Li-ion battery based on a gel electrolyte has recently been disclosed by Bellcore (USA) [124]. The technology has, to date, been licensed to six companies and full commercial production is imminent. The polymer membrane is a copolymer based on PVdF copolymerized with hexafluoropropylene (HFP). HFP helps to decrease the crystallinity of the PVdF component, enhancing its ability to absorb liquid. Optimizing the liquid absorption ability, mechanical strength, and processability requires optimized amorphous/crystalline-phase distribution. The PVdF–HFP membrane can absorb plasticizer up to 200 percent of its original volume, especially when a pore former (fumed silica) is added. The liquid electrolyte is typically a solution of $LiPF_6$ in 2:1 ethylene carbonate: dimethyl carbonate. A graphite carbon anode is used in conjunction with a lithium manganese oxide cathode. Cell assembly is crucial to the final cell performance. After the cell laminate has been processed, the membrane processing plasticizer is extracted and replaced by the electrolyte solution, to activate the membrane. Conductivities of over 1 mS cm^{-1} are achieved. Table 3 compares this battery's key characteristics with those of other technologies.

Valence Technology are now advancing towards commercializing a lithium rechargeable battery based on the Bellcore technology allthough other efforts have focused on a new gelled system [125–127]. This electrolyte is a radiation-cross-linked polymer formed from a mixture of liquid prepolymer compounds, typically PEO-based acrylates, which have crosslinkable unsaturated centres, a radiation-inert ionically conducting liquid (e.g., PC, 2-methyltetrahydrofuran) and a lithium salt. Following parent patent claims, the conductivity measurements are interpreted in terms of little or no contribution from the polymer network to the conducting phase, but there are in fact some interactions which aid suppression of salt precipitation from the electrolyte and of eletrolyte solidification. The degree of interaction depends on the nature and ratio of the individual components.

Table 3. Typical performance characteristics of various rechargeable battery technologies

Technology	Energy density		Cell voltage (V)	Self discharge per month at 20 °C (%)	Cycles to 80 of rated capacity and 100% DOD*
	(Wh kg^{-1})	(Wh L^{-1})			
Ni – Cd	30–55	100–150	1.3	>15	>1000
Ni – MH	50–80	155–185	1.25	>20	500
Lithium-ion (liquid electrolyte)	90–120	225–350	3.0–3.6	~8	>1000
Li-polymer (estimated)	70–120	100–170	2.5–3.2	<0.1	200–500
Bellcore plastic Li-ion battery	110†	200–280	3.0–3.8	<10	>1000

*DOD , depth of discharge
† Excluding pactaging

CosMX Exhibit 1008, Page 534 of 633

8.3.3 Enhancing Cation Mobility

Polymer electrolytes are not single-ion conductors; in fact, the bulk conductivity is due primarily to anion mobility. Electrochemical devices are therefore susceptible to resistance due to buildup of high or low salt concentration at the interfaces during charging. In order to promote higher cation mobility, two obvious approaches may be considered: immobilize the anion, or promote anionic coordination. Polyelectrolytes are clear candidates because the polymer backbones contain covalently bonded ionizing groups. They have been investigated as potential solvent-free polymer electrolytes but they do not show the flexibility or conductivity suitable for this purpose. One exception is a polyelectrolyte containing covalenty bonded perfluorosulfonated anions, the polyelectrolyte equivalent of the triflate anion [128]. The strong acidity of these groups ensures dissociation of the lithium ion from the chain, similar to that of triflate and substantially greater than that provided by nonfluorinated sulfonates, but an order of magnitude less than that achievable with imide-based free salts. Conductivities of $\sim 10^{-5}$ S cm^{-1} at 50 °C can be obtained. Reports of the preparation of polymerizable anions based of the carbon equivalent of the plasticizing imide, $-C(CF_3SO_2)_2-$, proved to be unfounded [21]. In the case of polyelectrolytes also, a plasticizer significantly improved the ionic conductivity. Spectroscopic data suggest that the plasticizer coordinates with the cation, reducing ion association with the immobilized anions. It also provides a locally mobile coordination environment which promotes ion motion. The reduction in ion association appears to more than compensate for the reduction in cation mobility brought about by solvation [129].

A second approach to promoting high cationic transport is to choose a molecular solvent which has the ability to interact with anions than cations. A number of electron deficient borates such as

$$F_2BO-CH_2CH_2CH_2-OBF_2$$

are presently under consideration by Angell and co-workers [100, 130]. Lee and co-workers have prepared a new family of anion receptors based on linear or cyclic substituted aza-ether compounds [131]. The nitrogen is positively charged when CF_3SO_2- groups are substituted into the aza-ethers. The degree of complexation, ionic conductivity and stability depends on the structure of the compound and anion size.

8.3.4 Mixed-Phase Electrolytes

Polymer electrolytes may offer flexibility and superior interfacial contacts, but some ceramic or glassy electrolytes have higher conductivities, a high cation transference number and generally better thermodynamic stability towards lithium and other alkali metals. Introducing ceramic powder, in particular those of nanometer grain size, into a polymer electrolyte has an interesting effect on their conductivity and interfacial properties. A useful review of these so-called mixed-phase electrolytes, or nanocomposites, has been given by Kumar and Scanlon [132]. Some examples of mixed-phase electrolytes are listed in Table 4.

Addition of both ion-conducting and inert ceramics enhances the conductivity of a polymer electrolyte. This increase is attributed to an increase in volume fraction of the amorphous phase [133–136]. No

CosMX Exhibit 1008, Page 535 of 633

Table 4. Components of some mixed-phase electrolytes which have been investigated

Ceramic	Polymer electrolyte
Li_3N	PEO – $LiCF_3SO_3$
γ – $LiAlO_2$	PEO – $LiClO_4$
α – $LiAlO_2$	PEO – $LiClO_4$
Nasicon	PEO – NaI
α – Al_2O_3	PEO – $LiClO_4$
β''–Al_2O_3	PEO – NaI
θ – Al_2O_3	PEO – NaI
SiO_2	PEO – NaI
Zeolite, $[(Al_2O_3)_{12}(SiO_2)_{12}]$	PEO – $LiBF_4$
$1.2Li_2S{\cdot}1.6LiI{\cdot}B_2S_3$	Polyethylene

significant effect on the conductivity is observed for a composite containing amorphous polymer. Grain size, phase boundary resistance, phase composition, and T_g are all contributing factors and make the analysis of ion transport very complex. Figure 8 shows experimental data on heat of fusion (degree of crystallinity), T_g and conductivity for a PEO $-LiBF_4$ – zeolite mixed-phase electrolyte. In this instance the opposing mechanisms, heat of fusion and T_g, tend to cancel each other out, leaving the conductivity relativity unchanged. In other instances, the conductivity can rise modestly despite a large change in the value of T_g. This implies that another more significant factor contributes to conductivity enhancement and may be associated with the generation of polymer–ceramic grain boundaries [132]. Lithium-containing ceramics such as Li_3N and $LiAlO_2$ may give rise to more defect-rich grain boundaries that inert ceramics like SiO_2. The grain boundaries could serve as channels for the conducting ions. Solids exhibiting high ionic conductivity possess conduction channels that allow fast ion transport with low activation energy. Polymer-ceramic grain boundaries may provide similar structures. This could account for smaller grain size effecting more significant conductivity enhancement. Nanometer-size grains can produce conductivities an order of magnitude higher than micrometer-size grains [137]. The trend is now towards composites with reactive components, e.g., $LiAlO_2$, which participate in the conduction process, rather than inert materials such as SiO_2.

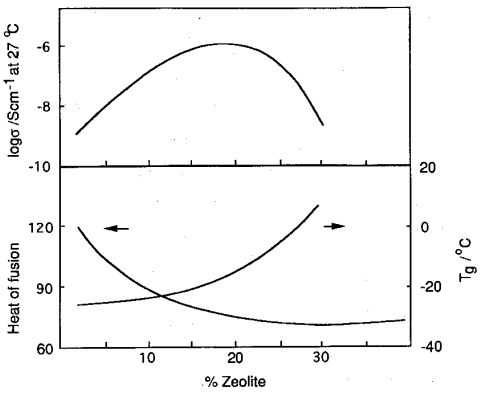


Figure 8. Effect on conductivity, heat of fusion (degree of crystallinity), and T_g of adding zeolite to PEO – $LiBF_4$. Adapted from B. kumar, L. G. Scanlon, *J. Power Sources* **1994**, *52*, 261.

Mixed-phase electrolytes comprising ceramics such as finely dispersed $\gamma - LiAlO_2$ or zeolite ($[(Al_2O_3)_{12}(SiO_2)_{12}]$) and a PEO electrolyte have superior lithium–polymer electrolyte interfacial stability [136, 137]. Nanosize particles suppress the growth of resistive layers much more effectively than microsize particles. This effect may be caused by the layer itself being disrupted, possibly by a scavenging effect of the ceramic powder [138]. The mechanism by which ceramic or glass powders can render the interface more stable is not fully understood. One answer may lie in the reactivity and free energy of the passivation reaction. It would be expected that the reaction leading to Li_2O at an $Li - SiO_2$ interface would

CosMX Exhibit 1008, Page 536 of 633

proceed more readily than at an $Li - Al_2O_3$ one ($\Delta G \sim 0$). Alternatively, if the passivation reaction results in the formation of a highly conducting product such as Li_2N, then the high conductivity may facilitate ion transport through the passivating layer. The outcome can also be explained by a reduction in contact between lithium and the polymer electrolyte. The grain size would be an important consideration for stability; smaller grains dispersed in the polymer are more effective at shielding the electrolyte. Above a threshold in the volume fraction, the solid is likely to form an insulating layer between lithium and electrolyte, impeding electrode reactions. Some experimental observations for composites with high ceramic content tend to support this. Prototype rechargeable cells have utilized Al_2O_3 in the electrolyte to impart mechanical stability and help achieve low and stable interfacial resistances. As I^- does not react with lithium metal, the interface is more stable and passivation can largely be eliminated. Li–PEO–LiI/alumina composite– FeS_2 cells operate at 100–140 °C [139]. They are salt-rich with O:M=3:1–2:1 and have a t_+ of about 1.

8.4 Looking to the Future

Research and development into polymer electrolyte battery systems continues, yet many unsolved and controversial issues, particularly relating to the inadequate understanding and control of ion dissociation and the relative mobilities of the ions, remain. Modern computational resources now allow the structures of complex systems such as polymer electrolytes to be simulated and evaluated. Computer simulation have the potential to contribute significantly to the understanding of these issues and give insight into the structural makeup of polymer electrolytes. Much of the work in this field is still in its early stages but realistic prediction can be made from many models [6].

As to technology, materials development has come a long way from the early dry polymer electrolyte batteries of the early 1980s and the first gel-based system of the mid 1980s. Commercialization of the first small batteries is imminent but it is power sources for electric vehicles which are the environmental necessity. The stakes are high: polymer electrolyte technology must compete with other developing lithium battery technologies over the next ten years and prove themselves in terms of key electrochemical cell characteristics, as well as processing and manufacturability on a commercial scale.

8.5 References

[1] M. B. Armand in *Fast Ion Transport in Solids* (Ed.: W. Van Gool), North Holland, Amsterdam, **1973**, p. 665.

[2] D. E. Fenton, J. M. Parker, P. V. Wright, *Polymer* **1973**, *14*, 589.

[3] M. B. Armand, J. M. Chabagno, M. Duclot, *Second International Meeting on Solid Electrolytes, St. Andrews, Scotland, Sept. 20–22*, **1978**.

[4] M. Gauthier, A. Belanger, B. Kapfer, G. Vassort in *Polymer Electrolyte Reviews 2* (Eds.: J. R. MacCallum, C. A. Vincent), Elsevier, London **1989**, p. 285.

[5] C. A. Angell, C. Liu, E. Sanchez, *Nature London* **1993**, *362*, 137.

[6] F. M. Gray, *Polymer Electrolytes*, RSC Materials Monographs (Series Ed.: J. A. Connor), Royal Society of Chemistry, Cambridge, UK, **1997**.

[7] D. Baril, Y. Chabre, M. B. Armand, *J. Elec-*

CosMX Exhibit 1008, Page 537 of 633

trochem. Soc. **1993**, *140*, 2687.
[8] F. M. Gray, *Solid Polymer Electrolytes, Fundamentals and Technological Applications*, VCH, New York, **1991**.
[9] A. Bélanger, M. Gauthier, M. Robitaille, R. Bellemare in *Second International Symposium on Polymer Electrolytes* (Ed.: B. Scrosati), Elsevier, London, **1990**, p. 347.
[10] M. Gauthier, A. Bélanger, P. Bouchard, B. Kapfer, S. Ricard, G. Vassort, M. Armand, J. Y. Sanchez, L. Krause, *J. Power Sources* **1995**, *54*, 163.
[11] R. G. Pearson, *J. Am. Chem. Soc.* **1963**, *85*, 97.
[12] G. G. Cameron, M. D. Ingram in *Polymer Electrolyte Reviews 2* (Eds.: J. R. MacCallum, C. A. Vincent), Elsevier, London, **1989**, p. 157.
[13] F. M. Gray, *Solid State Ionics* **1990**, *40/41*, 637.
[14] L. M. Torell, S. Schantz in *Polymer Electrolyte Reviews 2* (Eds.: J. R. MacCallum, C. A. Vincent) Elsevier, London, **1989**, p. 1.
[15] M. Armand, W. Gorecki, R. Andréani in *Second International Symposium on Polymer Electrolytes* (Ed.: B. Scrosati), Elsevier, London, **1990**, p. 91.
[16] L. A. Dominey, V. R. Koch, T. J. Blakely, *Electrochim. Acta* **1992**, *37*, 1551.
[17] D. Benrabah, D. Baril, J.-Y. Sanchez, M. Armand, G. G. Gard, *J. Chem. Soc., Faraday Trans,* **1993**, *89*, 355.
[18] Y. G. Andreev, P. Lightfoot, P. G. Bruce, *J. Chem. Soc., Chem. Commun.* **1996**, 2169.
[19] D. Benrabah, J.-Y. Sanchez, M. Armand, *Solid State Ionics* **1993**, *60*, 87.
[20] D. Benrabah, J.-Y. Sanchez, D. Deroo, M. Armand, *Solid State Ionics* **1994**, *70–71*, 157.
[21] M. Armand, *Solid State Ionics* **1996**, *89*, 5.
[22] W. Gorecki, M. Minier, M. B. Armand, J. M. Chabagno, P. Rigaud, *Solid State Ionics* **1983**, *11*, 91.
[23] J. M. G. Cowie, S. H. Cree, *Annu. Rev. Phys. Chem.,* **1989**, *40*, 85.
[24] R. Frech, J. Manning, D. Teeters, B. E. Black, *Solid State Ionics* **1988**, *28–30*, 954.
[25] D. Fauteux in *Polymer Electrolyte Reviews 2* (Eds.: J. R. MacCallum, C. A. Vincent), Elsevier, London, **1989**, p. 121.
[26] A. Vallée, S. Besner, J. Prud'homme, *Electrochim. Acta* **1992**, *37(9)*, 1579.
[27] S. Lascaud, M. Perrier, A. Vallée, S. Besner, J. Prud'homme, M. Armand, *Maromolecules* **1994**, *27*, 7469.
[28] S. M. Zahurak, M. L. Kaplan, E. A. Rietman, D. W. Murray, R. J. Cava, *Maromolecules* **1989**, *26*, 503.
[29] P. W. M. Jacobs, J. W. Lorimer, A. Russer, M. Wasiucionek, *J. Power Sources* **1989**, *26*, 503.
[30] M. Armand, M. Gauthier in *High Conductivity Solid Ionic Conductors* (Ed.: T. Takahashi), World Scientific, Singapore, **1989**, p. 114.
[31] C. Labrèche, I. Lévesque, J. Prud'homme, *Maromolecules* **1996**, *29*, 7795.
[32] J. M. G. Cowie in *Polymer Electrolyte Reviews 1* (Eds.: J. R. MacCallum, C. A. Vincent), Elsevier, London, **1987**, p. 69.
[33] H. Cheradame, J. F. LeNest in *Polymer Electrolyte Reviews 1* (Eds.: J. R. MacCallum, C. A. Vincent), Elsevier, London, **1987**, p. 103.
[34] F. M. Gray in *Polymer Electrolyte Reviews 1* (Eds.: J. R. MacCallum, C. A. Vincent), Elsevier, London, **1987**, p. 139.
[35] C. A. Vincent, *Prog. Solid State Chem.* **1987**, *17*, 145.
[36] D. F. Shriver, P. G. Bruce in *Solid State Electrochemistry* (Ed.: P. G. Bruce), Cambridge University Press, **1995**, p. 95.
[37] D. J. Wilson, C. V. Nicholas, R. H. Mobbs, C. Booth, *Br. Polymer J.* **1990**, *22*, 129.
[38] K. Nagoka, H. Naruse, I. Shinohara, M. Watanabe, *J. Polym. Sci., Polym. Lett.* **1990**, *22*, 659.
[39] X. Andrieu, J. F. Fauvarque, A. Goux, T. Hamaide, R. M'Hamdi, T. Vicedo, *Electrochim. Acta* **1995**, *40*, 2295.
[40] F. Alloin, J.-Y. Sanchez, M. Armand, *Solid State Ionics* **1993**, *60*, 3.
[41] F. Alloin, J.-Y. Sanchez, M. Armand, *Electrochim.Acta* **1992**, *37*, 1729.
[42] F. M. Gray, J. R. MacCallum, C. A. Vincent, J. R. M. Giles, *Macromolecules* **1988**, *21*, 392.
[43] D. W. Xia, J. Smid, *J. Poly. Sci., Polym. Lett. Ed.* **1984**, *22*, 617.
[44] J. M. G. Cowie, A. C. S. Martin, *Polymer Commun.* **1985**, *26*, 298.
[45] J. M. G. Cowie, R. Ferguson, *J. Polym. Sci. Polym. Phys. Ed.* **1985**, *23*, 2181.
[46] J. S. Tonge, D. F. Shriver, *J. Electrochem. Soc.* **1987**, *134*, 269.
[47] I. M. Khan, Y. Yuan, D. Fish, E. Wu, J. Smid, *Macromolecules* **1989**, *21*, 2684.
[48] L. Gao, D. MacDonald, *J. Electrochem. Soc.* **1997**, *144(4)*, 1174.
[49] A. Killis, J. F. LeNest, H. Cheradame, A. Gandini, *Macromol. Chem.* **1982**, *183*, 2835.
[50] J. R. M. Giles, M. P. Greenhall, *Poly. Com-*

CosMX Exhibit 1008, Page 538 of 633

mun. **1987**, *27*, 360.
[51] A. Bouridah, F. Dalard, D. Deroo, H. Cheradame, J. F. LeNest, *Solid State Ionics* **1985**, *15*, 233.
[52] M. Armand, M. Duval, E. Harvey, D. Muller, French Patent 8 309 886.
[53] D. J. H. Ballard, P. Cheshire, T. S. Mann, J. E. Przeworski, *Macromolecules* **1990**, *23*, 1256.
[54] (a) F. Alloin, J.–Y. Sanchez, *Electrochim. Acta* 1995, *40*, 2276.
[55] L. Marchese, M. Andrei, A. Roggero, S. Passerini, P. Prosperi, B. Scrosati, *Electrochim. Acta* **1992**, *37*, 1559.
[56] F. Alloin, J.–Y. Sanchez, M. Armand, *J. Power Sources* **1995**, *54*, 34.
[57] P. Lightfoot, M. A. Mehta, P. G. Bruce, *Science* **1993**, *262*, 883.
[58] P. G. Bruce, *Electrochim. Acta* **1995**, *40*, 2077.
[59] R. Frech, S. Chintapalli, P. G. Bruce, C. A. Vincent, *J. Chem. Soc.,Chem. Commun.* **1997**, 157.
[60] I. M. Ward, N. Boden, J. Cruickshank, S. A. Leng, *Electrochim. Acta* **1995**, *40*, 2071.
[61] (a) H. Vogel, *Phys. Z.* **1921**, *22*, 645; (b) G. Tamman, W. Hesse, *Z. Anorg. Allg. Chem.* **1926**, *156*, 245; (c) G. S. Fulcher, *J. Am. Ceram. Soc.* **1925**, *8*, 339.
[62] M. L. Williams, R. F. Landel, J. D. Ferry, *J. Am. Chem. Soc.* **1955**, *77*, 3701.
[63] M. A. Ratner in *Polymer Electrolyte Reviews 1* (Eds.: J. R. MacCallum, C. A. Vincent), Elsevier Applied Science, London, **1987**, p. 173.
[64] M. H. Cohen, D. Turnbull, *J. Chem. Phys.* **1959**, *31*, 1164.
[65] J. H. Gibbs, E. A. di Marzio, *J. Chem. Phys.* **1958**, *28*, 373.
[66] G. Adams, J. H. Gibbs, *J. Chem. Phys.* **1965**, *43*, 139.
[67] M. A. Ratner, D. F. Shriver, *Chem. Rev.* **1988**, *88*, 109.
[68] M. H. Cohen, G. S. Grest, *Phys. Rev. B* **1979**, *20*, 1077.
[69] E. Williams, C. A. Angell, *J. Polym. Sci., Polym. Lett. Ed.* **1973**, *11*, 383.
[70] S. Arumugam, J. Shi, D. P. Tunstall, C. A. Vincent, *J. Phys. C* **1993**, *5*, 153.
[71] F. M. Gray, *Solid State Ionics* **1990**, *40/41*, 637.
[72] A. Ferry, P. Jacobsson, L. M. Torell, *Electrochim. Acta* **1995**, *40*, 2369.
[73] P. G. Bruce, C. A. Vincent, *Faraday Discuss. Chem. Soc.* **1989**, *88*, 43.
[74] A. V. Chadwick, M. R. Worboys in *Polymer Electrolyte Reviews 1* (Eds.: J. R. MacCallum, C. A. Vincent), Elsevier Applied Science, London, **1987**, p. 275.
[75] G. Xu, *Solid State Ionics* **1992**, *50*, 345.
[76] W. Gorecki, M. Jeannin, E. Belorizky, C. Roux, M. Armand, *Eur. J. Phys. Condensed Matter* **1995**, *7*, 6823.
[77] S. Lascaud, M. Perrier, A Vallée, S. Besner, J. Prud'homme, M. Armand, *Macromolecules* **1994**, *27*, 7469.
[78] A. Johnsson, A. Gogoll, J. Tegenfeld, *Polymer* **1996**, *37(8)*, 1387.
[79] M. Levêque, J. F. Le Nest, A. Gandini, H. Cheradame, *J. Power Sources* **1985**, *14*, 1018.
[80] P. G. Bruce, M. T. Hardgrave, C. A. Vincent, *Solid State Ionics* **1992**, *53/56*, 1087.
[81] A. Bouridah, F. Dalard, D. Deroo, M. B. Armand, *Solid State Ionics* **1986**, *18/19*, 287.
[82] A. Bouridah, F. Dalard, D. Deroo, M. B. Armand, *J. Appl. Electrochem.* **1987**, *17*, 625.
[83] Y. Ma, M. Doyle, T. F. Fuller, M. M. Doeff, L. D. De Jonghe, J. Newman, *J. Electrochem. Soc.* **1990**, *142*, 3465.
[84] C. Bridges, A. V. Chadwick, M. R. Worboys, *Br. Poly. J.* **1988**, *20*, 207.
[85] S. E. Lindsay, D. H. Whitmore, W. P. Halperin, J. M. Torkelson, *Polym. Prepr.* **1989**, *301*, 442.
[86] W. Gorecki, P. Donoso, C. Berthier, M. Mali, J. Roos, D. Brinkmann, M. B. Armand, *Solid State Ionics* **1988**, *28–30*, 1018.
[87] J. Evans, C. A. Vincent, P. G. Bruce, *Polymer* **1987**, *28*, 2324.
[88] P. G. Bruce, J. Evans, C. A. Vincent, *Solid State Ionics* **1988**, *28–30*, 918.
[89] P. G. Bruce, C. A. Vincent, *Solid State Ionics* **1990**, *40–41*, 607.
[90] P. G. Bruce, *Synth. Met.* **1991**, *45*, 267.
[91] M. Eigen, *Pure Appli. Chem.* **1963**, *6*, 97.
[92] J. Shi, C. A. Vincent, *Solid State Ionics* **1993**, *60*, 11.
[93] P. G. Bruce, F. Krok, C. A. Vincent, *Solid State Ionics* **1988**, *27*, 81.
[94] S. Atchia, J. P. Petit, J. Y. Sanchez, M. Armand, D. Deroo, *Electrochim. Acta* **1992**, *32*, 1599.
[95] J. MacBreen, X. Q. Yang, H. S. Lee, K. Okamoto, *J. Electrochem. Soc.* **1996**, *143*, 3198.
[96] D. Baril, C. Michot, M. Armand, *Solid State Ionics* **1997**, *94*, 35.
[97] S. Lascaud, M. Perrier, A. Vallée, S. Besner, J. Prud'homme, M. Armand, *Macromolecules*

CosMX Exhibit 1008, Page 539 of 633

1994, *27*, 7469.
[98] C. A. Angell, J. Fan, C. Liu, Q. Lu, E. Sanchez, K. Xu, *Solid State Ionics* **1994**, *69*, 343.
[99] K. Xu, C. A. Angell, *Electrochim. Acta* **1995**, *40*, 2401.
[100] C. A. Angell, K. Xu, S. S. Zhang, M. Videa, *Solid State Ionics* **1996**, *86–88*, 17.
[101] R. Koksbang, I. I. Olsen, D. Shackle, *Solid State Ionics* **1994**, *69*, 320.
[102] T. Itoh, K. Saeki, K. Kohno, K. Koseki, *J. Electrochem. Soc.* **1989**, *136*, 3551.
[103] K. Koseki, K. Saeki, T. Itoh, Co Qui Juan, O. Yamamoto in *Second International Symposium on Polymer elctrolytes* (Ed.: B. Scrosati), Elsevier, London, **1990**, p. 197.
[104] G. G. Cameron, M. D. Ingram, K. Sarmouk, *Europ. Polym. J.* **1990**, *26*, 1097.
[105] G. Feuillade, P. Perche, *J. Appl. Electrochem.* **1975**, *5*, 63.
[106] M. Watanabe, M. Kamba, H. Matsuda, K. Tsunemi, K. Misoguchi, E. Tsuchida, I. Shinohara, *J. Polym. Sci., Polym. Phys. Ed.* **1981**, *13*, 9.
[107] F. Croce, S. D. Brown, S. G. Greenbaum, S. M. Slane, M. Salomon, *Chem. Mater.* **1993**, *5*, 1268.
[108] R. Frech, S. Chintapalli, *Solid State Ionics* **1996**, *85*, 61.
[109] J. P. Southall, H. V. St. A. Hubbard, S. F. Johnston, V. Rogers, G. R. Davies, J. E. McIntyre, I. M. Ward, *Solid State Ionics* **1996**, *85*, 51.
[110] H. Akashi, K. Tanaka, K. Sekai, *5th International Symposium on Polymer Electrolytes, Uppsala, Sweden, August* **1996**, Poster P-10.
[111] R. Koksbang, I. I. Olsen, P. E. Tønder, N. Knudsen, D. Fauteux, *J. Appl. Electrochem.* **1991**, *21*, 301.
[112] H. Hong, C. Liquan, H. Xueje, X. Rongjian, *Electrochim. Acta* **1992**, *37*, 1671.
[113] M. Matsumoto, J. S. Rutt, S. Nishi, *J. Electrochem. Soc.* 1995, *142*, 3052.
[114] T. Ichino, M. Matsumoto, Y. Takeshita, J. S. Rutt, S. Nishi, *Electrochim. Acta.* 1995, *40*, 2265.
[115] K. E. Doan, B. J. Heyen, M. A. Ratner, D. F. Shriver, *Chem. Mater.* **1990**, *2*, 539.
[116] H. G. Richley, J. Farkas, *J. Org. Chem.* **1987**, *52*, 479.
[117] M. Armand, M. Gauthier, D. Muller, European Patent 87 402 441.7, **1997**.
[118] X. Q. Yang, H. S. Lee, L. Hanson, J. McBreen, Y. Okamoto, *J. Power Sources* **1995**, *54*, 198.
[119] C. W. Walker, M. Salomon, *J. Electrochem. Soc* **1993**, *140*, 3409.
[120] K. Murata, *Electrochim. Acta* **1995**, *40*, 2177.
[121] M. Alamgir, K. M. Abraham, *J. Power Sources* **1995**, *54*, 40.
[122] B. Scrosati, *Prog. Batteries Battery Mater.* **1994**, *13*, 363.
[123] K. M. Abraham, M. Alamgir, *J. Power Sources* **1993**, *43–44*, 195.
[124] J.–M. Tarascon, A. S. Gozdz, C. Schmutz, F. Shokoohi, P. C. Warren, *Solid State Ionics* **1996**, *86–88*, 49.
[125] M. Lee, D. Shackle, G. Schwab, US Patent 4 830 939, **1989**.
[126] D. Shackle, M. Lee, US Patent 5 037 712, **1991**.
[127] D. Shackle, D. Fauteux, J. S. Lundsgaard, US Patent 4 997 732, **1990**.
[128] D. Benrabah, S. Sylla, F. Alloin, J.–Y. Sanchez, M. Armand, *Electrochim. Acta* **1995**, *40*, 2259.
[129] K. E. Doan, M. A. Ratner, D. F. Shriver, *Chem. Mater.* **1991**, *3*, 418.
[130] S. S. Zhang, C. A. Angell, *J. Electrochem. Soc.* **1998**, in press.
[131] H. S. Lee, X. Q. Yang, J. McBreen, L. S. Choi, Y. Okamoto, *J. Electrochem. Soc.* **1996**, *143*, 3825.
[132] B. Kumar, L. G. Scanlon, *J. Power Sources* **1994**, *52*, 261.
[133] J. Plocharski, W. Wieczorek, *Solid State Ionics* **1988**, *28–30*, 979.
[134] J. Plocharski, W. Wieczorek, J. Przyluski, K. such, *Appl. Phys. A* **1989**, *49*, 55.
[135] F. Croce, F. Bonino, S. Panero, B. Scrosati, *Phil. Mag. B* **1989**, *59*, 161.
[136] F. Croce, B. Scrosati, *J. Power Sources* **1993**, *43–44*, 9.
[137] W. Krawiec, L. G. Scanlon, J. P. Fellner, R. A. Vaia, S. Vasudevan, E. P. Giannelis, *J. Power Sources* **1995**, *54*, 310.
[138] F. Croce, F. Gerace, B. Scrosati, *Proceedings of the 35th International Power Sources Symposium, Cherry Hill, NJ*, **1992**, p. 267.
[139] E. Peled, D. Goldonitsky, G. Ardel, J. Lang, Y. Lavi, *J. Power Sources* **1995**, *54*, 496.

CosMX Exhibit 1008, Page 540 of 633

9 Solid Electrolytes

P. Birke and W. Weppner

9.1 Introduction

By the end of the 19th century, E. Warburg had already recognized that some solid compounds are practically pure ionic conductors [1, 2]. With the discovery of a rapidly increasing number of such solid electrolytes during the early 20th century, the field of solid–state electrochemistry was born [3]. However, rapid progress has only been achieved during the last 30 years by the discovery of many solid electrolytes with high ionic conductivities at room temperature and high chemical stabilities; this has caused a strong interest in technological applications of these materials [4]. At the same time, the oxygen ion conducting, stabilized, cubic ZrO_2 solid electrolyte was developed into a commercially successful mass product for automobiles known as λ-probe and a separator for solid oxide fuel cells which recently provided current densities as high as $2\,A\,cm^{-2}$ at elevated temperatures. Sodium–β/β''-alumina became used simultaneously as a solid electrolyte and as a separator in advanced sodium/sulfur and sodium/nickel chloride ("zebra") batteries [5, 6].

Currently, there is great interest in the application of solid electrolytes for high-performance secondary lithium batteries because of the high electrical, chemical, and mechanical stability of many lithium compounds. These advantages have already led to their practical application in pacemaker batteries which provide high energy densities and extraordinarily high reliability [7]. The power density is quite low in this case, however. Most efforts are at present directed toward improving this property for advanced lithium batteries.

Progress in the development of solid electrolytes is also being achieved from advances in several other fields of technology such as fuel and electrolysis cells, thermoelectric converters, electrochromic devices, and sensors for many chemical and physical quantities.

Fabrication techniques, especially the preparation of thin films of functional materials, have made major progress in recent years. Thin-film solid electrolytes in the range of several nanometers up to several micrometers have been prepared successfully. The most important reason for the development of thin–film electrolytes is the reduction in the ionic resistance, but there is also the advantage of the formation of amorphous materials with stoichiometries which cannot be achieved by conventional techniques of forming crystalline compounds. It has often been observed that thin-film electrolytes produced by vacuum evaporation or sputtering provide a struc-

ture, morphology, or composition which is different from that obtained by employing common thermal annealing processes.

9.2 Fundamental Aspects of Solid Electrolytes

9.2.1 Structural Defects

Ionic transport in solids originates from the atomic disorder in real crystals compared with ideal crystal lattices. The most important defects of this kind are:

(1) vacancies, i.e., missing ions such as $V_A^{\cdot}$ in the case of positively charged ions A^+; and
(2) interstitial ions, i.e., additional ions such as $A_i^{\cdot}$ between the ideal lattice sites.

These defects may be present in some structures and materials in such large numbers that a large fraction of a specific type of ion is disordered. The ions are distributed over several sites that are energetically nearly equivalent. This is the most important case for practically useful solid electrolytes, namely "structural disorder". Examples are α-AgI [8], Ag_4RbI_5 [9], and β-alumina [10]. In view of the large number of available sites and the low activation enthalpy for the hopping process of the ions from one site to another, high ionic conductivities may be achieved even at ambient or slightly increased temperatures. The observed conductivities are comparable with those of common liquid electrolytes and are in the same range as the electronic conductivity of semiconductors.

Figures 1–6 show the structures of some

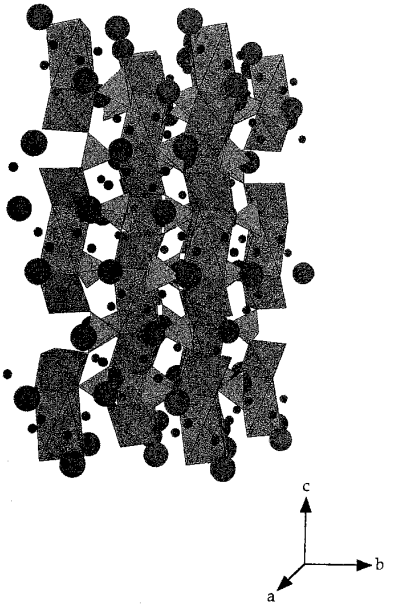


Figure 1. Schematic representation of the NASICON structure. The SiO_4 and PO_4 tetrahedra are indicated by light blue, the ZrO_6 octahedra by darkblue and the NaO_6 octahedra by green. The sodium ions are depicted by the red circles. The different radii represent the probability of lattice site occupation: large radius 67 percent, small radius 1.1 percent. The Si/P ratio is 0.683:0.317. The *a*, *b*, and *c* axes are indicated.

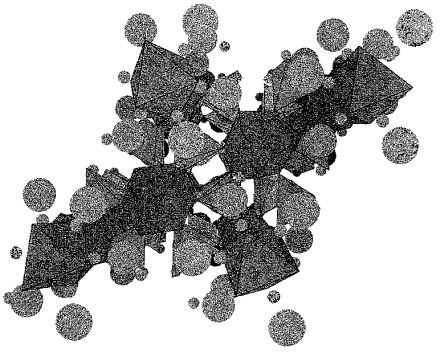


Figure 2. Rotation of the NASICON structure represented in Fig. 1 by 90°. For clearer representation of the structural aspects, the sodium ions are indicated by yellow.

CosMX Exhibit 1008, Page 542 of 633

prominent electrolytes for battery applications. The NASICON structure is represented in Fig. 1 and 2. The SiO_4 and PO_4 tetrahedra are indicated by the light-blue color. These share edges with the dark-blue ZrO_6 octahedra which are corner-sharing with the green NaO_6 octahedra. The sodium ions are located between the tetrahedra and octahedra and are shown as red circles in Fig. 1. These mobile ions are distributed over several sites. The differences in the probability of lattice site occupation is indicated by the radii of the circles; 67 percent of the sites indicated by the large circles are occupied, in contrast to only 1.1 percent of the lattice sites of the small circles. The ratio of $SiO_4 : PO_4$ tetrahedra is 0.683:0.317. Figure 2 shows the structure rotated through 90°, which illustrates better the conducting paths of the sodium ions, as indicated by yellow circles.

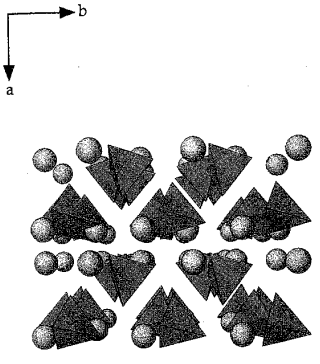


Figure 3. Schematic representation of the lithium-ion conductor $LiAlCl_4$. The $AlCl_4^-$ may be considered as tetrahedral anions, as indicated by green. The lithium ions are located between them.

The structure of $LiAlCl_4$ is shown in Fig. 3. $AlCl_4^-$ is represented by the green tetrahedra; the lithium ions (gray circles) are mobile between them, along various pathways. The large size of the $AlCl_4^-$ anions leads to low electrostatic interaction with the lithium ions which therefore allows high conductivities. The channels for ionic transport are made more clearly visible by a rotation of the structure (Fig. 4).

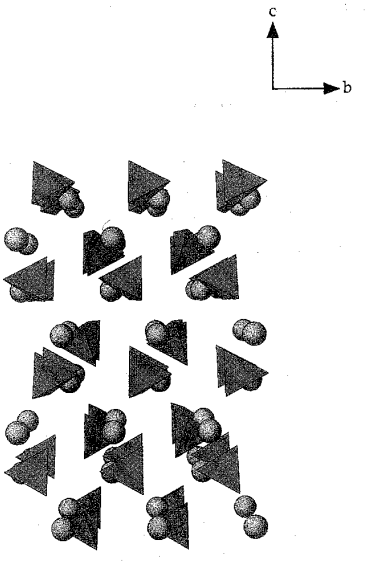


Figure 4. Rotation of the structure of $LiAlCl_4$ compared with Fig. 3, as indicated by the *b* and *c* axes for clearer representation of the diffusion paths of the lithium ions.

The structure of β-alumina is shown in Fig. 5. The aluminum and oxygen ions (green and red, respectively) form spinel blocks. The mobile sodium ions (blue) are located in layers between them. The spinel blocks are connected to each other by oxygen ion bridges within the conducting layer.

The structure of the perovskite-type lithium ion conductor $Li_{0.29}La_{0.57}TiO_3$ is represented in Fig. 6. The small gray circles depict the lithium ions, the big gray circles the lanthanum ions. These are randomly distributed over the A sites: 14 per-

CosMX Exhibit 1008, Page 543 of 633

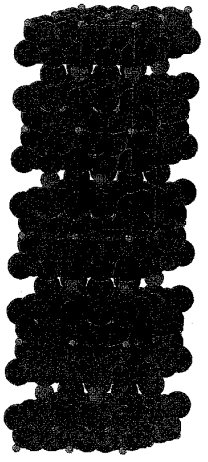


Figure 5. Schematic representation of the β-alumina structure. The aluminum (green) and oxygen (red) ions form spinel blocks which are separated from each other by oxygen bridges. The mobile sodium ions (blue) are located in the layer. The unit cell is indicated.

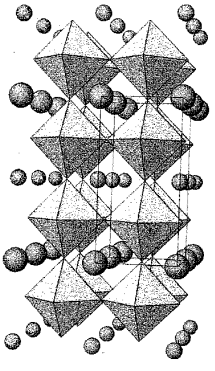


Figure 6. Structure of the perovskite-type lithium-ion conductor $Li_{0.29}La_{0.57}TiO_3$. The lithium ions (small, gray) and the lanthanum ions (large, gray) are randomly distributed over the A sites, of which 14 percent are vacancies, enabling the lithium ions to be mobile. Titanium forms TiO_6 octahedra, as shown in yellow. The unit cell is indicated.

cent of vacancies occur on the La and Li sites, which provides the possibility for the lithium ions to move by a vacancy mechanism. The titanium forms TiO_6 octahedra which are represented in yellow.

Point defects are always present in every material in thermodynamic equilibrium. Considering the formation of n vacancies, the increase in configuration entropy is determined by the number of different possible ways of taking n atoms out of the crystal comprising N atoms in total. This number, c_N^n, is given by

$$c_N^n = \frac{N!}{n!(N-n)!} \tag{1}$$

considering that the exchange of two vacancies or interstitial ions of the same type does not result in a new configuration. According to Boltzmann's equation, the increase in entropy is accordingly

$$\Delta S = k \ln \frac{N!}{n!(N-n)!} \tag{2}$$

If the energy of formation of a vacancy is U (which should include all entropy contributions other than the configurational entropy), the change in the free energy F at constant temperature is given by

$$\Delta F = nU - T\Delta S \tag{3}$$

In thermodynamic equilibrium, the free energy has a minimum. Accordingly, F does not change with the number of introduced vacancies n. Feeding Eq. (2) into Eq. (3) results in the following equilibrium concentration of vacancies:

$$n = N \exp(-U/kT) \tag{4}$$

An Arrhenius-type relationship is obtained, with a slope determined by the energy of formation of the defects.

CosMX Exhibit 1008, Page 544 of 633

At a given ideal composition, two or more types of defects are always present in every compound. The dominant combinations of defects depend on the type of material. The most prominent examples are named after Frenkel and Schottky. Ions or atoms leave their regular lattice sites and are displaced to an interstitial site or move to the surface simultaneously with other ions or atoms, respectively, in order to balance the charge and local composition. Silver halides show dominant Frenkel disorder, whereas alkali halides show mostly Schottky defects.

The formation of the combination of defects may be described as a chemical reaction and thermodynamic equilibrium conditions may be applied. The chemical notations of Kröger–Vink, Schottky, and defect structure elements (DSEs) are used [3, 11]. The chemical reactions have to balance the chemical species, lattice sites, and charges. An unoccupied lattice site is considered to be a chemical species (V); it is quite common that specific crystal structures are only found in the presence of a certain number of vacancies [12]. The Kröger-Vink notation makes use of the chemical element followed by the lattice site of this element as subscript and the charge relative to the ideal undisturbed lattice as superscript. An example is the formation of interstitial metal M ions and metal M ion vacancies, e.g., in silver halides:

$$M_M + V_i = V_M^{\cdot} + M_i^{\cdot} \quad \text{(Kröger-Vink)} \qquad (5)$$

This notation by Kröger-Vink is very intuitive. However, the laws of thermodynamic equilibrium may not be applied to these symbols because the elements are not independent of each other as required by thermodynamics. For example the formation of the interstitial metal ion $M_i^{\cdot}$ requires the simultaneous disappearance of an interstitial vacancy V_i. Accordingly, one has to consider combinations of Kröger-Vink elements which result from the rearrangement of Eq. (5):

$$O = \left(V_M^{\cdot} - M_M\right) + \left(M_i^{\cdot} - V_i\right) \qquad (6)$$

The expressions in parantheses may be varied independently. These correspond to the Schottky building units. In the latest notation, interstitials are indicated by the chemical elements without any subscript, and vacancies are indicated by the missing chemical element between two vertical lines. Equations (5) or (6) then read:

$$O = |M|^{\cdot} + M^{\cdot} \quad \text{(Schottky)} \qquad (7)$$

Thermodynamic equilibrium laws are applicable to the Schottky building units. However, there is a loss in intuition. In view of that conflict, the DSEs [11] make use of Kröger-Vink structural elements with the meaning of Schottky building units. This conversion is easily achieved by omitting all ideal lattice elements such as M on M sites, M_M, and interstitial vacancies, V_i. This reads, for the example of Eqs. (5)–(7),

$$O = V_M^{\cdot} + M_i^{\cdot} \quad \text{(DSE)} \qquad (8)$$

The DSEs thus combine the advantages of both descriptions — Kröger-Vink and Schottky.

The equilibrium concentration of defects is obtained by applying the law of mass action to Eq. (7) or (8). This leads in the case of Frenkel disorder to

$$[V_M^{\cdot}][M_i^{\cdot}] = K_1 \qquad (9)$$

Concentrations are indicated by square brackets. Commonly, concentrations rather

CosMX Exhibit 1008, Page 545 of 633

than activities may be used because of small numbers of defects. An analogous treatment of Schottky defects leads to

$$[V_M^{'}][V_X^{\cdot}] = K_2 \tag{10}$$

in the case of singly-charged M cations and X anions. In addition, thermodynamic equilibrium holds for the concentrations of electrons and holes,

$$[e^{'}][h^{\cdot}] = K_3 \tag{11}$$

Furthermore, equilibria hold for ions and electrons. In every case, the Gibbs energy of the defect reaction has to provide a minimum for the equilibrium concentrations:

$$(\Delta G)_{p,T} = 0 \tag{12}$$

It is a common situation for the composition of a compound to be changed. This happens especially in the case of an exchange of atoms with a gaseous environment, e.g., for the exchange of oxygen with an oxide. In the case of solid electrolytes for batteries, this process also occurs by the exchange of the mobile atom with the electrode, because of the chemical equilibration of both phases. This change in the concentration of one of the species generally has an effect on the electronic concentration and accordingly on the electronic leakage current. The ionic defects are commonly predominant in highly structurally disordered ionic conductors. Therefore, the relative changes in the concentrations of the ionic defects are negligible compared with the relative changes in the number of electronic species. The relationship between the partial pressure or the activity of the exchangeable component and the concentration of electrons or holes is derived from the incorporation reaction. This reaction reads, in Kröger-Vink notation for oxygen and lithium,

$$\frac{1}{2}O_2(g) + V_O^{\cdot\cdot} + 2e^{'} = 0_O \tag{13}$$

$$\mathrm{Li(electrode)} + V_{Li}^{'} = Li_{Li} + e^{'} \tag{14}$$

for a material with divalent oxygen vacancies and monovalent lithium vacancies, respectively. Application of the law of mass action results in

$$p_{O_2}^{1/2}[V_O^{\cdot\cdot}][e^{'}] = K_4 \tag{15}$$

and

$$\frac{a_{Li}(\mathrm{electrode})[V_{Li}^{'}]}{[e^{'}]} = K_5 \tag{16}$$

If the material is highly disordered, i.e., $V_O^{\cdot\cdot}$ and $V_{Li}^{'}$ are approximately constant, Eqs. (15) and (16) read

$$[e^{'}] = K_4^{'} p_{O_2}^{-1/4} \tag{17}$$

and

$$[e^{'}] = K_5^{'} a_{Li}(\mathrm{electrode}) \tag{18}$$

From Eq. (18) the concentration of electrons, and according to Eq. (11) the concentration of holes also, depend on the lithium activity of the electrode phases with which the electrolyte is in contact. Since anode and cathode have quite different lithium activities, the electronic concentration may vary to a large extent and an ionically conducting material may readily turn into an electronic conductor.

In the case of a less disordered structure, the defect concentrations vary ac-

CosMX Exhibit 1008, Page 546 of 633

cording to the electronic concentration and are related to each other by the electroneutrality condition, e.g.,

$$2\left[V_O^{\cdot\cdot}\right]=\left[e'\right] \tag{19}$$

and

$$\left[V_{Li}'\right]=\left[h^{\cdot}\right] \tag{20}$$

Feeding Eqs. (19) and (20) into Eqs. (15) and (16), and taking into account Eq. (11), yields

$$\left[e'\right]=K_4''\ p_{O_2}^{-1/6} \tag{21}$$

and

$$\left[e'\right]=K_5''\ a_{Li(electrode)}^{1/2} \tag{22}$$

The experimental determination of the relationship between the electronic concentration and the partial pressure or activity of a component is commonly the best method to determine the type of disorder in a material.

9.2.2 Migration and Diffusion of Charge Carriers in Solids

The most important driving forces for the motion of ionic defects and electrons in solids are the migration in an electric field and the diffusion under the influence of a chemical potential gradient. Other forces, such as magnetic fields and temperature gradients, are commonly much less important in battery-type applications. It is assumed that the fluxes under the influence of an electric field and a concentration gradient are linearly superimposed, which leads to the gradient of the electrochemical potential

$$\eta_i = \mu_i + z_i q \varphi \tag{23}$$

as the general driving force, where μ_i, z_i, q and φ are the chemical potential, charge number, elementary charge, and electrostatic potential, respectively.

The flux by diffusion is described by the diffusivity D_i and the migration by the conductivity σ_i. The conductivity is proportional to the product of the mobility and the concentration of the mobile species. The diffusivity and mobility are related by the Nernst–Einstein relation [3]. The flux is in general given by

$$j_i = -\frac{\sigma_i}{z_i^2 q^2}\,\mathrm{grad}\eta_i \tag{24}$$

with

$$\sigma_i = c_i b_i z_i^2 q^2 = c_i u_i |z_i| q = \frac{c_i D_i z_i^2 q^2}{kT} \tag{25}$$

The partial flux density j_i is related to the partial electric current density i_i by

$$j_i = \frac{i_i}{z_i q} \tag{26}$$

Depending on the majority charge carriers, quite different driving forces and fluxes apply for the ions and electrons in solid electrolytes and electrodes. The highly concentrated, predominantly mobile species are transferred in an electric field, whereas the minority charge carriers are moved by diffusion. The solid electrolyte therefore carries the mobile ions according to Ohm's law and the electronic charge carriers according to Fick's law. The

CosMX Exhibit 1008, Page 547 of 633

electrodes carry the ions toward the interfaces with the electrolytes by diffusion.

It is important to realize that the migration in an electric field depends on the magnitude of the concentration of the charged species, whereas the diffusion process depends only on the concentration gradient, but not on the concentration itself. Accordingly, the mobility rather than the concentration of electrons and holes has to be small in practically useful solid electrolytes. This has been confirmed for several compounds which have been investigated in this regard so far [13].

In the predominantly electronically conducting electrodes it is the chemical diffusion of the ions which controls the electrical current of the galvanic cell. This includes the internal electric field which is built up by the simultaneous motion of ions and electrons to establish charge neutrality [14]:

$$i_i = \frac{c_i z_i q \tilde{D}}{kT} \mathrm{grad} c_i \qquad (27)$$

The chemical diffusion coefficient $\tilde{D}$ is the product of the diffusivity of the ions D_i and the Wagner factor $\partial \ln a_{i^x} / \partial \ln c_{i^x}$ [3],

$$\tilde{D} = D_i \frac{\partial \ln a_{i^x}}{\partial \ln c_{i^x}} \qquad (28)$$

where a_{i^x} indicates the activity of the neutral mobile component i. The variation of $\ln a_{i^x}$ is the sum of the variations of $\ln a_i$ and $\ln a_e$. Therefore, large Wagner factors may be achieved in the case of low concentrations of electrons which results in large variations of $\ln c_e$. For predominant electronic conductivity it is necessary for the mobilities of the electrons to be rather high. This is commonly observed in the case of semiconducting compounds, which are therefore ideal electrode materials and should be favored over metallic conducting electrodes. The slightly higher ohmic resistances of the electrodes are commonly negligible compared with the resistance of the electrolyte.

It should be kept in mind that all transport processes in electrolytes and electrodes have to be described in general by irreversible thermodynamics. The equations given above hold only in the case that asymmetric Onsager coefficients are negligible and the fluxes of different species are independent of each other. This should not be confused with chemical diffusion processes in which the interaction is caused by the formation of internal electric fields. Enhancements of the diffusion of ions in electrode materials by a factor of up to 70000 were observed in the case of Li_3Sb [15].

Ionic transport in solid electrolytes and electrodes may also be treated by the statistical process of successive jumps between the various accessible sites of the lattice. For random motion in a three-dimensional isotropic crystal, the diffusivity is related to the jump distance r and the jump frequency ν by [3]:

$$D_i = \tfrac{1}{6} \nu r^2 \qquad (29)$$

This relationship makes it possible to calculate the maximum ionic conductivity of solid electrolytes. Assuming that the mobile ions are moving with thermal velocity v without resting and oscillating at any lattice site, this results in a jump frequency

$$\nu = \frac{v}{r} = 3.4 \times 10^{12} \mathrm{s}^{-1} \qquad (30)$$

CosMX Exhibit 1008, Page 548 of 633

for a jump distance of 1 Å at 300 °C, and according to Eq. (29) in a diffusivity

$$D_{max} = 5.6 \times 10^{-5}\ cm^2\ s^{-1} \quad (300\,°C, r = 1Å) \tag{31}$$

Making use of Eq. (25), the maximum conductivity of a solid electrolyte with monovalent mobile species is given by

$$\sigma_{max} = 2.8\,\Omega^{-1}\,cm^{-1} \quad (300\,°C, r = 1\,Å, z_i = 1) \tag{32}$$

The experimental value for AgI is $1.97\,\Omega^{-1}cm^{-1}$ [16, 3], which indicates that the silver ions in AgI are mobile with nearly a thermal velocity. Considerably higher ionic transport rates are even possible in electrodes, by chemical diffusion under the influence of internal electric fields. For Ag_2S at 200 °C, a chemical diffusion coefficient of $0.4\,cm^2s^{-1}$, which is as high as in gases, has been measured [17].

9.3 Applicable Solid Electrolytes for Batteries

9.3.1 General Aspects

Generally, solid electrolytes for battery applications require high ionic conductivities and wide ranges of appropriate thermodynamic stability.

Though solid electrolytes for multivalent ions offer the advantage of a larger charge transfer, their conductivities are much lower than those of monovalent ions at ambient temperature because of a higher activation enthalpy for the ionic motion caused by strong electrostatic interactions between the lattice and the multivalent ions. Besides the charge, there is a strong correlation between the mobility and the ionic radius of the mobile ions. Both aspects are illustrated by looking at the various β- and β''-aluminas, as presented in Fig. 7.

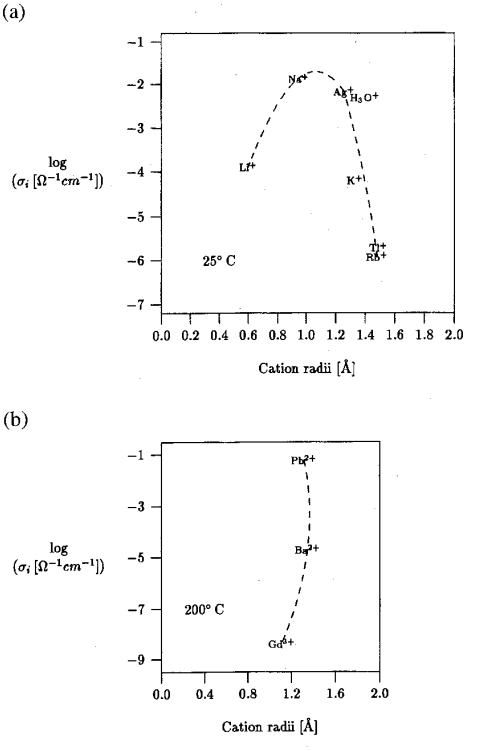


Figure 7. Ionic conductivities for various monovalent (a) and multivalent (b) ions in β and β''-alumina single crystals in the direction of the conduction plane [4, 19].

The ionic conductivity for various ions in the β/β''-alumina structure along the conduction planes shows a maximum for an optimum size of the ions. It should be neither too small nor too big to fit the available pathways in the lattice [8].

CosMX Exhibit 1008, Page 549 of 633

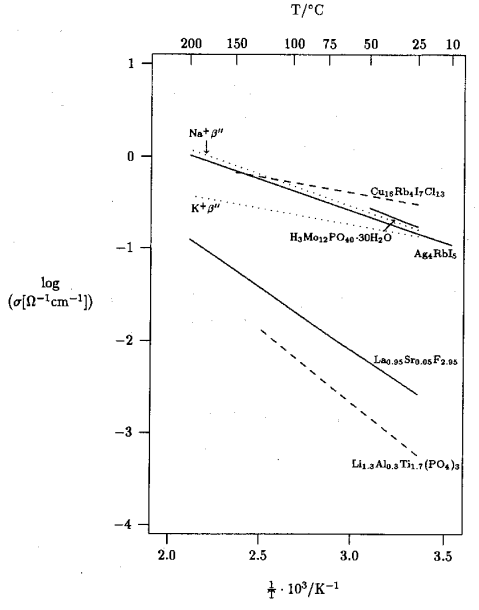


Figure 8. Arrhenius diagram for various fast ion conductors. For each indicated monovalent mobile ion, the given ionic conductors are the fastest ones known (Na^+, $Na^+-\beta''$-Al_2O_3; Cu^+, $Cu_{16}Rb_4I_7Cl_{13}$; K^+, $K^+-\beta''$-Al_2O_3; H^+, $H_3Mo_{12}PO_{40}\cdot 30H_2O$; Ag^+, Ag_4RbI_5; F^-, $La_{0.95}Sr_{0.05}F_{2.95}$; Li^+, $Li_{1.3}Al_{0.3}Ti_{1.7}(PO_4)_3$) [4].

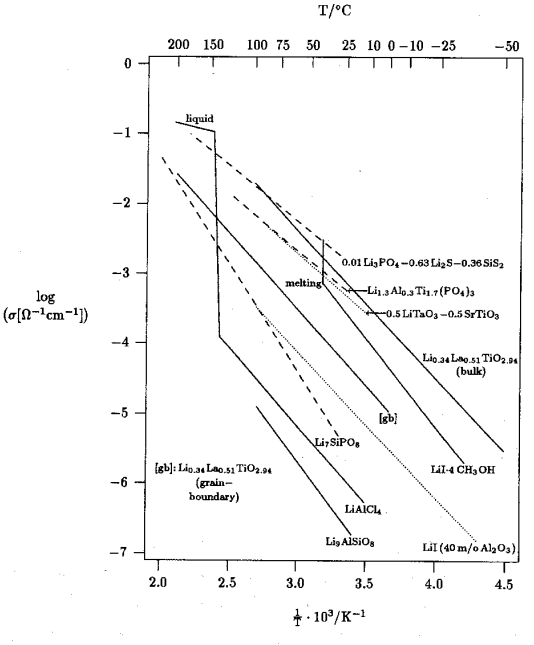


Figure 9. Compilation of the solid ionic conductors known at present. For references see Table 1.

CosMX Exhibit 1008, Page 550 of 633

Table 1. Conductivities, activation enthalpies, and other aspects of fast lithium-ion solid conductors

Solid electrolyte	σ 25 °C (Scm^{-1})	E_A (eV)	Remarks	Ref.
$0.01Li_3PO_4 - 0.63Li_2S - 0.36SiS_2$	1.6×10^{-3} (total)	0.30(1) (total) <200 °C	Glass prepared by liquid–nitrogen quenching and twin-roller quenching	[47]
$Li_{1.3}Al_{0.3}Ti_{1.7}(PO_4)_3$	7×10^{-4} (total)	0.35 (total) <150 °C	Cold-pressed samples, sintering temperature 980–1000 °C	[19]
$0.5LiTaO_3 - 0.5SrTiO_3$	5×10^{-4} (bulk)	0.33 (bulk) ≤ 150 °C	Cold-pressed samples, sintering temperature 1350–1400 °C	[48]
$Li_{0.34}La_{0.51}TiO_{2.94}$	10^{-3} (bulk) 7.5×10^{-5} (grain-b.)	0.40 (bulk) 0.42 (grain-b.) <100 °C	Cold-pressed samples, sintering temperature 1200 °C	[24, 25]
$LiI\cdot4CH_3OH$	2.2×10^{-4} (total)	0.51 (total) below melting point	Very convenient preparation by dissolving LiI in $4CH_3OH$	[49]
Li (40 m/o Al_2O_3)	10^{-5} (total)	0.43 (total) –40 to 100 °C	Composite	[34]
$LiAlCl_4$	1×10^{-6} (total)	0.47 (total) below melting point	Moisture–sensitive	[50]
Li_7SiPO_8	3.7×10^{-6} (total)	0.52 (total)	Hot-pressed at 1000 °C, insensitive to moisture, stable at high lithium activities	[51]
Li_9AlSiO_8	2.3×10^{-7} (total)	0.55 (total)	Cold pressed samples, sintering temperature 900 °C, stability range vs. lithium 0–5.4 V	[52]

Another way of looking at high ionic conductivities of solid electrolytes is to consider the activation enthalpy as illustrated in Fig. 8. Generally, the activation enthalpy is strongly correlated with the room-temperature ionic conductivity: the higher the room–temperature ionic conductivity, the lower the activation enthalpy. The straight lines in the Arrhenius diagram intersect at about the same value with the $\log\sigma$ axis at $1/T = 0$. At infinitely high temperatures all attempts of the ions to jump become successful and compounds have the same jump frequency within about two orders of magnitude. Accordingly, for the construction of high–temperature batteries quite different materials are applicable than for ambient-

CosMX Exhibit 1008, Page 551 of 633

temperature devices. Thermodynamic stability aspects are more important than fast kinetics at high temperatures, whereas a low activation energy is required rather than thermodynamic stability at low temperatures.

9.3.2 Lithium-, Sodium-, and Potassium-Ion Conductors

Quite a large variety of interesting fast lithium-ion solid conductors is now known, as compiled in Fig. 9 and Table 1. In the case of sodium- and potassium-ion conductors only the β/β''-alumina family, and for sodium the NASICON structure, were considered for practical application, due to the high ionic conductivities of these materials which are unmatched by any other sodium- or potassium-ion conductor. However, for β/β''-alumina, NASICON and structurally related ionic conductors, the ionic conductivities and activation enthalpies are quite dependent on the preparation routes. Therefore, only the order of magnitude of ionic conductivities and activation energies of practically useful sodium- and potassium-ion conductors are compiled in Fig. 10. $NaAlCl_4$ is included because of the importance of this material in the "zebra" battery.

For lithium, counterparts structurally related to the sodium– and potassium–β/β''-aluminas and NASICON with similar high ionic conductivities were not found, possibly because of the small ionic radius of lithium. Therefore, much intensive work has been done on developing lithium-ion solid conductors during recent years, in view of the interest in high-energy-density batteries.

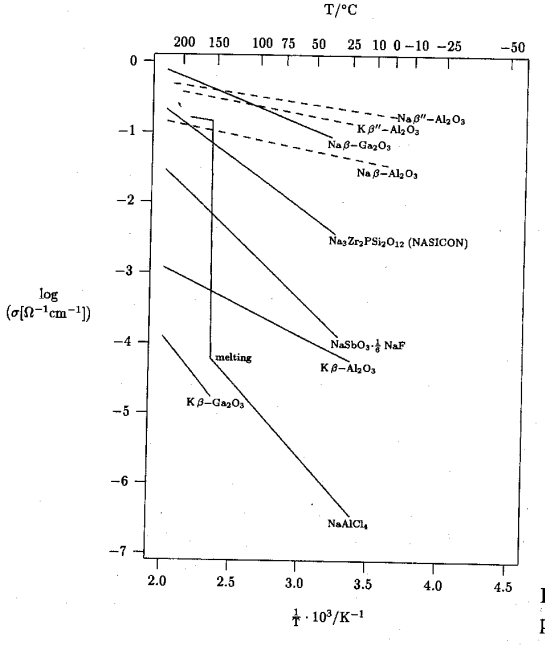


Figure 10. Practically useful solid sodium-and potassium-ion conductors [4, 20].

CosMX Exhibit 1008, Page 552 of 633

Generally, the interpretation and reliability of published experimental data for solid electrolytes should be regarded with care. The most important experimental methods are presented in Sec. 9.6.

9.3.3 Capacity and Energy Density Aspects

In spite of the extraordinarily high ionic conductivity of silver- and copper-ion conductors, these materials suffer from their low capacity and energy density. In addition, only a few positive electrode materials have been found until now.

Some fluorine-ion conductors exhibit high ionic conductivities, even at room temperature [4], which are not equaled by other halide-ion conductors. However, there is a lack of known electrode materials. Further research on this topic is very worthwhile.

Apart from applications in sensors [21, 22], divalent-ion conductors, e.g., for Mg^{2+} ions, are of great interest for thin film batteries which may be incorporated into microelectronics as memory backups and into other applications. For these batteries high volumetric specific energy densities rather than high current densities are required, and thin films offer in addition a major decrease in the total ionic resistance.

Most of the recent research focuses on proton, lithium, sodium and potassium batteries. This is not only for the reasons discussed above. The availability of a large variety of electrodes also plays an important role. Furthermore, high voltages rather than high currents are favorable from a practical point of view.

In the case of potassium, a large number of very fast ion conductors [4] and very fast insertion/extraction materials, such as the potassium hexacyanoferrates, are known. Therefore, potassium batteries may provide one of the best compromises with regard to fast kinetics, high capacities, and high energy densities.

9.4 Design Aspects of Solid Electrolytes

Four major aspects should be taken into consideration for the design of suitable solid electrolytes:

- optimizing the lattice structure spatially and energetically to improve the number and mobility of ionic defects,
- developing synthesis routes which lead to materials of amorphous or polycrystalline structure with high overall conductivity,
- optimizing the stability range to prevent chemical reactions with the electrodes, and
- optimizing the electrolytic domain with negligible electronic conduction over the activity range employed.

The best-known and most instructive example for the first aspect is the design of the fast sodium ion conducting electrolyte NASICON by Goodenough [23]: high ionic mobility requires the existence of interconnected spaces of partially occupied lattice sites having nearly identical site-occupation energies, since the activation energy for an ion jump from one site to another must be small for fast ion transport. Therefore, the "bottlenecks", whether shared faces or shared edges, must be sufficiently open. Since only a few binary solid electrolytes exhibit a random cation distribution at elevated temperatures providing very fast ion conduction, e.g., α-

CosMX Exhibit 1008, Page 553 of 633

AgI above 149 °C, the design of multinary compounds by adding cations or anions to form a suitable sublattice for fast ionic motion is necessary.

The second aspect–improving the total ionic conductivity by the synthesis route—is illustrated by two recently discovered solid electrolytes which exhibit high Li^+ bulk conductivities of the order of $10^{-3}\,Scm^{-1}$. $Li_{0.34}La_{0.51}TiO_{2.94}$ [24], which has a defect perovskite type structure, shows a bulk Li^+ conductivity of $10^{-3}\,Scm^{-1}$, but a total Li^+ conductivity of only $2–7\times10^{-5}\,Scm^{-1}$ [25]. $Li_{1.3}Al_{0.3}Ti_{1.7}(PO_4)_3$, with a NASICON-type structure, provides a bulk Li^+ conductivity of $3\times10^{-3}\,Scm^{-1}$ and a total Li^+ conductivity of $7\times10^{-4}\,Scm^{-1}$ [19]. In the case of the latter compound, liquid–phase sintering was applied successfully by adding a second phase ($LiBO_2 + LiF$) at the grain boundaries [26].

However, in the case of the perovskite even the application of sintering temperatures as high as 1200 °C did not result in a higher overall ionic conductivity. Since the total ionic conductivity is two orders of magnitude lower than the bulk conductivity in polycrystalline $Li_{0.34}La_{0.51}TiO_{2.94}$, an improvement by way of the preparation route is necessary rather than changes in the lattice by the addition of dopants.

The third aspect, the stability range of solid electrolytes, is of special concern for alkaline-ion conductors since only a few compounds show thermodynamic stability with, e.g., elemental lithium. Designing solid electrolytes by considering thermodynamic stability did lead to very interesting compounds and the discovery of promising new solid electrolytes such as the lithium nitride halides [27]. However, since solid-state reactions may proceed very slowly at low temperature, metastability of the solid electrolyte in combination with the electrodes is sufficient for many applications.

Low electronic conductivity of solid electrolytes over the entire activity range employed in batteries requires slow mobilities of the electrons or holes rather than low concentrations. A small number is readily increased percentage wise by changes in the activity of the mobile component or in the impurity content. Solid electrolytes may therefore be considered to be materials with low electronic conductivities because of low electronic mobilities [27]. Considering this aspect one may recognize that lithium is readily mobile in $Li_{0.34}La_{0.51}TiO_{2.94}$ due to the large number of defects. At voltages lower than about 2 V versus elemental Li, however, the overlap of the lanthanum and titanium orbitals provides high electronic concentrations and neutral lithium may be exchanged. In contrast, the band structure of the NASICON-type structure of $Li_{1.3}Al_{0.3}Ti_{1.7}(PO_4)_3$, with three sites that are energetically nearly equivalent for the Li^+ ions does not provide the electrons.

Traditionally, the chemical stability of the electrode/electrolyte interface and its electronic properties have not been given as much consideration as structural aspects of solid electrolytes, in spite of the fact that the proper operation of a battery often depends more on the interface than on the solid electrolyte. Because of the high ionic conductivity in the electrolyte and the high electronic conductivity in the electrode, the voltage falls completely within a very narrow region at the electrolyte/electrode interface.

Some further important aspects for the design of solid electrolytes and solid electrodes for battery-type applications are the following:

CosMX Exhibit 1008, Page 554 of 633

- *Electronic conductivity of thin-film solid electrolytes.* Besides having low electronic transference numbers, it is essential for thin films of the order of 1 μm that the magnitude of the electronic resistance is low in order to prevent self-discharge of the battery. For this reason, specific electronic resistances in the range of 10^{12}–10^{14} Ωcm are required for thin-film solid electrolytes. Often the color may be a valuable indication of the electronic conductivity. In this regard, solid electrolytes should preferably be transparent white [20].
- *Improvement of the ionic current by fast transport in the electrodes.* High electronic mobility and low electronic concentration favor fast chemical diffusion in electrodes by building up high internal electric fields [14]. This effect enhances the diffusion of ions toward and away from the solid electrolyte and allows the establishment of high current densities for the battery.
- *Debye length in solid electrolytes.* The Debye length L_D describes the shielding of an electric field by the charge carriers. The electrostatic potential drops to 1/e of its value within L_D. In contrast to diluted media with small concentrations of ions, such as liquid electrolytes, solid electrolytes have very small Debye lengths. One can easily estimate that this value is in the region of one atomic layer. This means that, the formation of an ionically blocking reaction product at the interface would make a battery behave like a capacitor. However, the formation of a good ionic or mixed conducting product at the interface, which is stable with both the electrode and the electrolyte, is not necessarily a problem and may even improve the contact between the two phases. An example is the formation of Ag_3SI between AgI (electrolyte) and Ag_2S (electrode) in a solid-state galvanic silver cell.
- *Contacts.* Usually, good mechanical contacts to a solid are best accomplished by a liquid. Examples are the sodium/sulfur and the "zebra" batteries where the solid electrolyte acts as a separator between two liquid phases. In the case of the zebra battery [6], an auxiliary electrolyte, $NaAlCl_4$ (which is liquid at the operating temperature of the battery), is employed to provide the contact between the solid sodium electrolyte, Na/β″ alumina, and the positive electrode, $NiCl_2$. It is especially difficult to prepare all-solid state batteries–except possibly thin-film batteries–with good contacts because of differences in the thermal expansion coefficients of the different materials and because the application of high temperatures may result in undesirable side reactions including the evaporation of alkaline oxides. Employment of binders may minimize the mechanical contact problem but may increase the electrical resistance and may lead to slow reactions with the organic component of the binder.
- *One-layer systems.* One-layer systems might easily overcome most of the above-mentioned problems. Such materials show predominantly ionic conduction in the as-prepared state but behave as electrodes in that the concentration of the mobile component is increased and decreased by the charging process in the vicinity of the two electronic leads.

CosMX Exhibit 1008, Page 555 of 633

9.5 Preparation of Solid Electrolytes

9.5.1 Monolithic Samples

A commonly inexpensive way to prepare solid electrolytes is the formation of monolithic samples. Depending on the required phases and final compounds, a large variety of preparation methods are known. These methods usually provide polycrystalline materials.

9.5.1.1 Solid-State Reactions

The starting materials for solid-state reactions are the oxides, hydroxides, sulfates, carbonates, etc. of the various cations of the final product. The drawback of the method is the need for intimate mixing, which is commonly achieved by powder milling. Normally, no smaller grain size than 1μm can be obtained. This always causes problems when solid electrolytes are prepared which contain ions with extremely low diffusion coefficients, even at relatively high temperatures beyond 1000 °C. If ZrO_2 is doped with Y_2O_3, Fe_2O_3, or other compounds to improve the temperature stability or to change the electrical properties, mixing on the atomic scale is rather desirable and can best be accomplished by wet chemical methods discussed below. Oxides with slow cationic diffusion coefficients such as ZrO_2 and SiO_2, are preferably incorporated into organic precursors, as in the case of the sol–gel technique which is also mentioned below.

9.5.1.2 The Pechini Method

The Pechini method was originally developed for preparing lead and alkaline-earth titanates and niobates, and combinations thereof, by way of resin intermediates [29]. On ignition of the resin the organic portion is removed, leaving the selected composition of mixed oxides chemically combined. The oxides are then sintered into dense ceramic bodies. This method is also applicable to solid electrolytes, allowing a very intimate mixture of the starting materials.

9.5.1.3 Wet Chemical Methods

Generally, wet chemical methods require the availability of compounds which are soluble in water or in another solvent. The dissolution in a solvent allows intimate mixture on an atomic or molecular scale. However, it has to be ensured that no compound precipitates before the others when the solvent is evaporated, or else insoluble products are formed. The importance of wet chemical methods lies in the possibility of simple upscaling to industrial needs.

The co-precipitation technique starts with an aqueous solution of nitrates, carbonates, chlorides, oxychlorides, etc., which is added to a pH-controlled solution of NH_4OH, allowing the hydroxides to precipitate immediately. This method requires water-soluble precursors and insoluble hydroxides as a final product. The hydroxides are filtered and rinsed with water when chlorides are employed as starting materials and chlorine is not desired in the final product. After drying the filtrate, it is calcined and sintered. This method is being applied very successfully for oxygen-ion conducting zirconia ceramics [30].

The precipitation step may be replaced by spray drying of a homogeneously stirred solution of, e.g., nitrates [31], or by spraying the precursors into a very hot flame at about 1500–2200 °C. This method is called flame pyrolysis.

CosMX Exhibit 1008, Page 556 of 633

The sol–gel method also benefits from intimate mixture on the molecular level. This process may be divided into two categories:

(1) water-based processes starting from an aqueous solution of a metal salt; and
(2) alcohol-based processes starting from a metal alkoxide.

In the water-based process the first step is the formation of a sol. This step is accomplished by the hydrolysis of the metal cations:

$$M^{n+} + nH_2O \rightarrow m(OH)_n + nH^+ \quad (33)$$

In most cases, this reaction is driven to the right by the addition of a base. The sol is a dispersion of solid particles in a liquid phase, where the particles are small enough to remain suspended for indefinite periods of time by Brownian motion. The sol can be prepared either by condensation, when sol particles are generated by the slow controlled nucleation and growth of crystals at elevated temperatures, or by rapid hydrolysis of the metal salt at room temperature with an excess of a base to form a gelantinous precipitate. In either case, the final state is a sol stabilized by a positively charged surface at pH≈3. The gelation is accomplished either by removal of the water (dehydration gelation) or by increasing the pH (alkaline gelation).

The alcohol-based process involves reactions with metal alkoxides. The reactions are hydrolysis,

$$M(OR)_4 + nH_2O \rightarrow M(OR)_{4-n}(OH)_n + nHOR \quad (34)$$

and condensation

$$2M(OR)_{4-n}(OH)_n \rightarrow M(OR)_{4-n}((OH)_{n-1})_2O + H_2O \quad (35)$$

In this case, there is no distinct sol formation process but rather simultaneous hydrolysis and condensation reactions proceed to form a gel.

Employing silicon alkoxides, the hydrolysis has to be catalyzed by the addition of an acid or a base, and an excess of water is often used. Employing zirconium alkoxides, the hydrolysis reaction proceeds much faster than the condensation so that the product is obtained as a precipitate rather than a gel.

9.5.1.4. Combustion Synthesis and Explosion Methods

The glycine nitrate process [32] is an example of a combustion synthesis method to prepare oxide ceramic powders. A precursor is prepared by combining glycine with metal nitrates in their appropriate stoichiometric ratios in an aqueous solution. The precursor is heated to evaporate excess water, which yields a viscous liquid. Further heating to about 180 °C causes the precursor liquid to become auto-ignited. Combustion is rapid and self-sustaining, with flame temperatures ranging from 1100 to 1450 °C. The resulting powders exhibit surface areas in the range of several tens of square meters per gram. Parameters such as compositional uniformity, residual carbon levels, and particle size depend on the organic compound in the precursor, where the glycinenitrate may be replaced by carboxylate azides for example. While this combustion method makes it possible to prepare a large variety of solid electrolytes, the explosion method [33] results in amorphous lithium conducting solid

CosMX Exhibit 1008, Page 557 of 633

electrolytes of the multinary system Li:Al:Ti:Ge:P:O:C. Perfect ball-shaped glasses without any microcracks are obtained by vitrification.

9.5.1.5 Composites

Dispersing a dielectric substance such as Al_2O_3 in LiI [34] enhances the ionic conductivity of LiI about two orders of magnitude. The smaller the particle size of the dielectrics, the larger is the effect. This phenomenon is explained on the basis that the space-charge layer consists of V'_{Li} or Li_i generated at the interface between the ionic conductor (LiI) and the dielectric material (Al_2O_3) [35].

9.5.1.6 Sintering Processes

The important quantity for practical applications is the total ionic conductivity, which is the sum of bulk and grain boundary ionic conductivity. While the bulk ionic conductivity is a structural property, the total ionic conductivity depends to a large degree on the sintering process and the grain size of the polycrystalline material. In the case of alkaline-ion solid conductors, the high volatility of the alkaline oxides Me_2O (Me=Li, Na, K, Rb, Cs) commonly does not allow high sintering temperatures, i.e., above 900 °C. Therefore it is often difficult to obtain dense sintered ceramics and to compensate for the alkaline oxide loss if high sintering temperatures are required. Hot-pressing, adding excess amounts of Me_2O, and covering the sample with powder of the same material which is disregarded after the sintering process are ways to overcome this problem. This should be taken into consideration when total conductivities of alkaline and other ion conductors are compared.

9.5.2 Thick Film Solid Electrolytes

9.5.2.1 Screen Printing

The screen-printing method employs stencils which are high mesh sieves with impermeable areas where no print is wanted. The precursors are printed using a roller. In the case of solid electrolytes, the precursors may be prepared by employing a very fine powder to which organic solvents are added to obtain a good "green print". These solvents are then evaporated by heating. To get a high-quality solid-electrolyte thick film, different glasses may be added to the precursor as very fine powders. These glasses act as flux additives during the firing process. This method requires a substrate for the solid electrolyte, which in the case of a battery is one of the electrodes. An example is the combination of NASICON with Na_xCoO_2 to prepare a solid–state sodium battery. These two materials may withstand firing temperatures in the region of 700 °C without reacting with each other. The present challenge is the development of a suitable glass solder.

With the screen-printing method, films with thicknesses in the region of several tens of micrometers are usually obtained.

9.5.2.2 Tape Casting

The tape-casting method makes possible the fabrication of films in the region of several hundred micrometers thick. The mechanical strength allows the use of such a solid electrolyte as the structural element for devices such as the high-temperature solid oxide fuel cell in which zirconia-based solid electrolytes are employed both as electrolyte and as mechanical separator of the electrodes.

CosMX Exhibit 1008, Page 558 of 633

The challenge of the tape-casting method is the preparation of the green tape, which is made by mixing the extremely fine electrolyte powder with organic solvents. The mixture is pasted onto a glass plate or polymer film with homogeneous thickness, with a doctor blade. After the highly volatile solvent is evaporated, the green tape is peeled off and fired to evaporate the less volatile organic ingredients and to sinter the ceramic material. To obtain flat thick films without any bending it is often necessary to apply some pressure during the firing process.

In solid-state batteries, it is extremely favorable to use the solid electrolyte for mechanical support. Despite the larger thickness, which lowers the relative amount for active material in the battery, the advantages are the absence of pinholes of the solid electrolyte, high electronic resistance, and simple multistack fabrication, since the individual cells may be contacted by their electronically conducting current collectors.

9.5.3 Thin Film Solid Electrolytes

Thin-film solid electrolytes in the range of 1μm have the advantage that the material which is inactive for energy storage is minimized and the resistance of the solid electrolyte film is drastically decreased for geometrical reasons. This allows the application of a large variety of solid electrolytes which exhibit quite poor ionic conductivity but high thermodynamic stability. The most important thin-film preparation methods for solid electrolytes are briefly summarized below.

9.5.3.1 Sputtering

Reactive radio frequency sputtering makes it possible to prepare amorphous solid electrolytes with a glassy structure. Due to this structure some solid electrolytes show a distinct enhancement in their ionic conductivity which is commonly explained by an expanded structure allowing the ions to migrate more easily. An example is the lithium-ion conducting $LiNbO_3$ where the ionic conductivity in a glassy sample is enhanced several orders of magnitude at room temperature compared with crystalline $LiNbO_3$ samples [36]. In addition, compounds may be formed by sputtering which cannot be prepared by conventional chemical reactions; an example is $LiAlF_4$ [37]. Due to the relatively high energy, in the range of several electronvolts, of the neutral particles which hit the substrate, dense and pinhole-free films are easily obtained. However, if the energy is too high, some kind of atomic peening may occur causing severe mechanical stress in the films. Since sputtering is a well established method in the semiconductor industry, the application of the method for the preparation of solid electrolytes is considered to be feasible also.

Direct-current sputtering is not generally applicable for the preparation of thin-film solid electrolytes since these compounds are electronic insulators. The target surface would be charged with the same polarity as that of the ions in the plasma, and the sputtering plasma would rapidly break down.

9.5.3.2 Evaporation

In comparison with sputtering, the energy of the particles which arrive at the substrate is one order of magnitude lower. This may favor the formation of pinholes,

CosMX Exhibit 1008, Page 559 of 633

but also more expanded atomic structures, which may enhance the ionic conductivity. As in the case of sputtering, a process of metastable thermodynamics is established, providing amorphous films or unusual stoichiometries. A distinct advantage of evaporation is the simplicity of covering large areas and the employment of powders or granules instead of expensive targets. Since it is known for elements such as carbon that evaporation favors an orientation of structurally layered materials prependicular and not parallel to the electrodes as in the case of sputtering, solid electrolytes with layered structures, in particular, are good candidates for evaporation rather than sputtering.

9.5.3.3 Spin-On Coating and Spray Pyrolysis

The distinct advantage of spin-on coating is the low cost of this method. A thin film is prepared by spinning a liquid on a fast–rotating substrate, then it undergoes a sintering process. However, precursors are often toxic and may not be available for several elements. In addition, the spinning and sintering process may have to be repeated several times to obtain sufficient film thickness. Furthermore, the sintering step may cause problems due to reactions with the electrodes and cracks in the electrolyte film.

In spray pyrolysis, very fine droplets are sprayed onto a heated substrate. The limitations of this process are the same as for spin-on coating. The same is often the case for preparing solid electrolytes by chemical vapor deposition (CVD) processes, which in addition are more expensive, and the precursors are often very toxic.

9.6 Experimental Techniques for the Determination of the Properties of Solid Electrolytes

For the application of solid electrolytes in batteries it is essential to characterize the materials carefully. These measurements may be easily misleading and are often incorrectly interpreted. It is therefore vital that the correct arrangements and procedures are applied.

9.6.1 Partial Ionic Conductivity

9.6.1.1 Direct-Current (DC) Measurements

In most cases of practically useful ionic conductors one may assume a very large concentration of mobile ionic defects. As a result, the chemical potential of the mobile ions may be regarded as being essentially constant within the material. Thus, any ionic transport in such a material must be predominantly due to the influence of an internal electrostatic potential gradient,

$$i_{\text{ion(electrolyte)}} = -\sigma_{\text{ion}} \frac{\partial \varphi}{\partial x} \qquad (36)$$

Accordingly, the ionic conductivity in an electrolyte with negligible electronic conduction ($i_{\text{ion}} \approx i_{\text{total}}$) may be determined by Ohm's law, provided that unpolarizable electrodes are employed. To overcome this limitation, separate voltage probes in the shape of identical electronic leads connected to the electrolyte at positions separated by a distance L may be employed (four-probe technique [38]). Under these

CosMX Exhibit 1008, Page 560 of 633

conditions, the ionic conductivity is

$$\sigma_{\text{ion}} = -\frac{iL}{E}, \tag{37}$$

where E is the voltage drop between the probes and i the current density.

An alternative method to overcome the polarization is impedance analysis which is discussed below. However, because of problems of misinterpretation of impedance analysis plots, it is always desirable to obtain confirmation by DC-measurements, desireable with good contacts at the electrode/electrolyte interface. Depending on the ductility of the solid electrodes and the electrolyte, the difference in the current measured by the two–electrode technique may vary between sputtered and spring–loaded electrodes by more than one order of magnitude. In the case of alkaline electrolytes, especially, the limited stability range at high alkaline activities may require the application of an auxiliary electrolyte. This additional electrolyte has to have high ionic conductivity and has to provide good contact in order to minimize its contribution to the current. Therefore, liquid electrolytes are often suitable. A simple technique is the use of blotting paper as a carrier for the liquid electrolyte. Some skill is required, however, to obtain the appropriate grade of wetting. Another way to overcome the problem is the application of lithium compounds or alloys such as Li_3Sb and Li_3Bi, which show high lithium diffusion.

9.6.1.2 Impedance Analysis

Impedance analysis overcomes polarization problems by employing alternating currents in the frequency range from 10^{-2} to 10^{+6} Hz [39]. Only in the case of sufficiently high disorder, the ionic conductivity is practically independent of the activity.

Normally, the impedance plots are fitted to an often-complex equivalent circuit. Mathematically, this means searching for a global solution in R^n. However, problems arise if a complicated equivalent circuit is found which does not allow physical interpretation. Therefore, it is preferable to run a wide variety of experiments with different samples rather than trying to fit in detail the results of a single measurement in order to analyze the resulting impedance plots.

In the complex impedance plot three minima are attributed to conductivities. In the order of appearance with decreasing frequency, these are the bulk ionic resistance, in polycrystalline materials the bulk + grain boundary ionic resistance (e.g. in ZrO_2), and the total electrical resistance including interfaces and electronic contributions. These minima may be degenerate, and may overlap. To attribute these minima to the appropriate physical properties, the following parameters should be varied: the sample geometry, the sintering conditions, the morphology (e.g., by rapid quenching to obtain a glass), and the type and annealing process of the contacts and the electronic leads connecting the sample to the impedance analyzer.

For a careful comparison and interpretation it is necessary to ensure the reproducibility and to choose the same scale on the ordinate and the abscissa.

9.6.1.3 Determination of the Activation Energy

The relationship between the ionic conductivity σ_i and the temperature T can either be derived from the diffusivity D or the mobility u assuming Arrhenius-type behavior:

CosMX Exhibit 1008, Page 561 of 633

$$D = D_0 \exp\left(-\frac{E_a}{kT}\right) \tag{38}$$

$$u = u_0 \exp\left(-\frac{E_a'}{kT}\right) \tag{39}$$

D and u are related by the Nernst–Einstein relationship. The conductivity σ is given by Eq. (25).

The following two well known relationships are obtained from Eqs. (38) and (39):

$$\sigma_i T = (\sigma T)_0 \exp(-HE_a/kT) \tag{40}$$

$$\sigma_i = \sigma_0 \exp(-HE_a/kT) \tag{41}$$

where $(\sigma T)_0$ and σ_0 are constants.

For reasons of simplicity, σ_i versus $1/T$ plots are more commonly used than $\sigma_i T$ versus $1/T$ relationship. The differences in the straight line characteristics of the Arrhenius plots is mostly negligible.

An example of the determination of activation enthalpies is shown in Figs. 11 and 12. A valuable indication for associating the correct minimum with the ionic conductivity is the migration effect of the minimum with the temperature (Fig. 11) and the linear dependence in the $\sigma_i T$ versus $1/T$ plot (Fig. 12). However, the linearity may be disturbed by phase transitions, crystallization processes, chemical reactions with the electrodes, or the influence of the electronic leads.

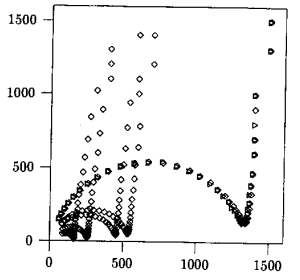


Figure 11. Temperature dependence (from the right to the left 26, 38, 41, 50, and 56 °C) of an as-sputtered lithium-ion conducting $Li_{3\pm x}PO_{4\pm y}N_z$ thin film, 5 Hz–13 MHz, 26 °C, Li_3PO_4 target, 99.9 percent sputtering gas N_2, N_2 flow rate 10 sccm, target–substrate distance 5 cm, sputtering time 3 h, presputtering time 30 min, sputtering pressure 20 mTorr, applied power 100 W, no additional substrate heating or cooling, film thickness ≈1μm,≈ 200 nm Pt/Rh (90:10, w/w) current collectors. Reproducibiliy is indicated by ◇, ▷.

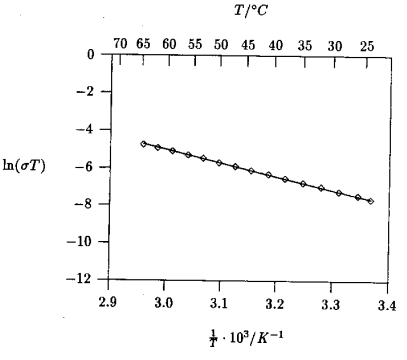


Figure 12. Arrhenius plot obtained from the thin-film measurement of Fig. 11 with additional data.

9.6.2 Partial Electronic Conductivity

The proportionality constant between the current and the electrochemical potential gradient is controlled by the partial electrical conductivity σ_n

$$i_n = -\frac{\sigma_n}{z_n q}\frac{\partial \eta_n}{\partial x} = -\frac{\sigma_n}{z_n q}\left(\frac{\partial \mu_n}{\partial x} + z_n q \frac{\partial \varphi}{\partial x}\right) \tag{42}$$

For electronic species (electrons and holes), which may be considered to be sufficiently diluted in an electrolyte, the con-

CosMX Exhibit 1008, Page 562 of 633

centration gradient rather than the electrostatic potential gradient is the more important driving force. Since the minority electronic properties of solid electrolytes may vary considerably with changes in the composition it is essential to study the minority charge-carrier transport as a function of the activity of the mobile component. The current of the electronic charge carriers with ionically blocking electrodes follows Fick's law (see Sec. 9.6.2.2).

9.6.2.1 Determination of the Transference Number

The electrolyte is sandwiched between two electrodes which have different but precisely known chemical potentials for the electroactive species. Since no overall current is allowed to pass the external electric circuit (i.e., $\sum_n i_n = 0$), integration of Eq. (24), making use of Eqs. (25) and (19), over the thickness of the electrolyte yields

$$E = \frac{1}{q}\sum_{\text{ions}}\frac{1}{z_n}\int_{\text{electrolyte}} t_n \mathrm{d}\mu_n \qquad (43)$$

for the difference in the electrochemical potentials of the electrons between the two electrodes where μ_n is the chemical potential of the neutral mobile species n [40]. The transference number t_n of the species n may be determined as a function of its activity from the change in the cell voltage with the variation of the chemical potential of the neutral component n at one electrode while all other chemical potentials are held constant. Differentation of Eq. (43) using μ_n^r as the upper limit of the integral yields

$$t_n\left(\mu_n^r\right) = -z_n q \frac{\partial E}{\partial \mu_n^r} \qquad (44)$$

9.6.2.2 The Hebb–Wagner Method

The partial electronic conductivity of solid electrolytes may be measured by using ionically blocking electrodes in the steady state (Hebb–Wagner technique [40, 41]). Employing a chemically inert electronically conducting material (e.g., Ta for the lithium electrolyte $Li_4SiO_4 \cdot Li_5AlO_4$) no ions will pass through the electrolyte when a voltage is applied, so that the mobile ions tend to be depleted at the inert electrode. The electrode on the other side has to fix the chemical potential. If the electrolyte has a large degree of disorder, Eq. (42) indicates that no gradient in the electrostatic potential may exist within the sample since the ionic current is zero. Then, steady-state transport of electrons and holes is only due to a concentration gradient [42], which is uniform if the diffusion coefficient does not depend on the concentration.

$$j_{\mathrm{e,h}} = -D_{\mathrm{e,h}}\frac{\mathrm{d}c_{\mathrm{e,h}}}{\mathrm{d}x} \qquad (45)$$

where the subscripts e,h denotes electrones and holes. The difference in the right and left hand electronic concentration may be replaced by an expression which includes the applied voltage E according to the balance of electrical and chemical energy for the transfer of electrons and holes in the absence of an electrical field:

$$E = -\frac{1}{q}\left(\mu_{\mathrm{e}}^{\mathrm{rev}} - \mu_{\mathrm{e}}^{\mathrm{block}}\right) = -\frac{kT}{q}\ln\frac{c_{\mathrm{e}}^{\mathrm{rev}}}{c_{\mathrm{e}}^{\mathrm{block}}} \qquad (46)$$

where superscripts rev, block denote the reversible and ionically blocking elec-

CosMX Exhibit 1008, Page 563 of 633

trodes, respectively. Substitution into Eq. (45) yields the following *I–E* relationship

$$|I_{e,h}| = \frac{S}{l}\frac{kT}{f}\left[\frac{\sigma_e^{ref}\left(1-\exp\left(-Ef/kT\right)\right)+}{\sigma_h^{ref}\left(\exp\left(Ef/kT\right)-1\right)}\right] \quad (47)$$

where l, f and S are the thickness of the sample, elementary charge and electrode area, respectively. For cationic conductors a plateau in current is observed as a function of the applied voltage for hole conductors, and an exponential increase in current for excess electron conductors. The applied voltage reduces the activity of the mobile component at the blocking electrode; and accordingly, the electronic concentration may increase indefinitely without any further major change of the slope with the hole concentration.

When performing a Hebb–Wagner polarization experiment one has to take the following aspects into careful consideration:

(1) Depending on the sample geometry, the resulting currents may be in the pico- and subpico-ampere range. It is essential either to change the sample geometry or to make sure that the experimental setup resolves these small currents.
(2) The *I–E* plots may be extended to higher voltages in order to obtain the decomposition voltage of the sample.
(3) The temperature dependence of the *I–E* plots gives important information about the electrolyte, and also opens up the possibility of extrapolating the electronic properties to lower and higher temperatures.

9.6.2.3 Mobility of Electrons and Holes

The conductivity is proportional to the product of the diffusivity and the concentration. To separate these two contributions, the voltage relaxation [43] and the charge-transfer technique [50] may be employed to obtain separately the diffusivity and concentration, respectively.

For the voltage relaxation method the same cell arrangement may be used as for the DC polarization measurements. Assuming that the diffusion coefficients are independent of concentration and the concentrations are sufficiently small to replace the activity of the electrons, linear concentration profiles will be established for the electronic species. For reasons of charge compensation a corresponding gradient in the chemical composition of the compound must be present. If the applied voltage is switched off, a relaxation of the cell voltage is observed, as shown schematically in Fig. 13. Microscopically this is caused by the diffusion of electrons and holes coupled with an equivalent transport of ions until a homogeneous composition is reached. Because of the large conductivity

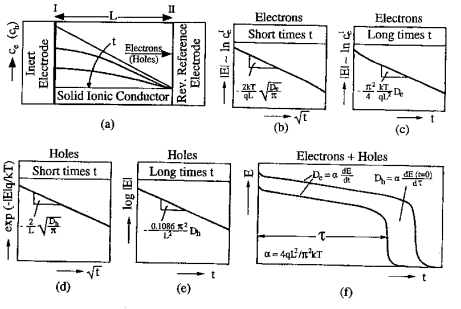


Figure 13. Voltage relaxation method for the determination of the diffusion coefficients (mobilities) of electrons and holes in solid electrolytes. The various possibilities for calculating the diffusion coefficients D_e and D_h from the behavior over short ($t \ll L^2/D_{e,h}$) and long ($t \gg L^2/D_{e,h}$) times are indicated; $c_{e,h}$ is the concentration of the electrons and holes respectively, q is the elementary charge, k is the Boltzmann constant and T is the absolute temperature.

CosMX Exhibit 1008, Page 564 of 633

of the ions, the diffusion coefficient of electrons and holes can be determined if the movement of these species is the rate-determining step. Figure 13 summarizes the technique.

9.6.2.4 Concentration of Electrons and Holes

The charge-transfer technique [45] is an electrochemical method for determination of the concentrations of electronic species. As in the case of DC polarization and voltage relaxation methods, asymmetric cells with ionically blocking electrodes and reversible reference electrodes are employed. A concentration profile of the electronic species is gradually generated with time. The corresponding number of electrons and holes delivered to the ionic conductor can be evaluated from the total charge transfer during the transient period. To eliminate the charge consumed to build up the double layer capacities, experiments with at least two different sample lengths have to be carried out, as illustrated schematically in Fig. 14.

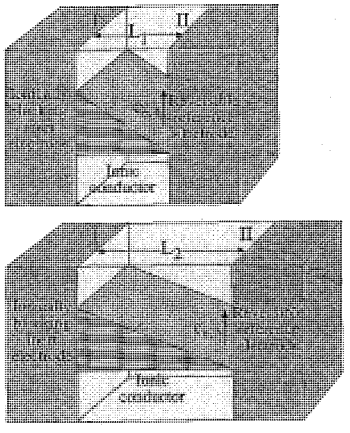


Figure 14. Charge-transfer technique for measurement of the concentration of electrons or holes in solid electrolytes. Two samples of different length are polarized by the same voltage.

The applied voltage determines the difference in the electrochemical potential of the electrons or the ratio of the concentrations of the electronic species on both sides of the electrolyte:

$$E = \frac{kT}{q} \ln \frac{c_e^r}{c_e^l} = -\frac{kT}{q} \frac{c_h^r}{c_h^l} \tag{48}$$

The difference in the charge transfers in the two experiments (ΔQ) is given by the difference in the areas of the two triangles in Fig. 14:

$$\Delta Q = \frac{q}{2}(V_2 - V_1)c_{e,h}^r \left[\exp\left(\frac{E_2 q}{kT}\right) - \exp\left(\frac{E_1 q}{kT}\right)\right] \tag{49}$$

V_1 and V_2 are the two sample volumes, E_1 and E_2 are the two voltages applied to the two samples and q is the elementary charge.

9.6.3 Stability Window

According to the Gibbs phase rule, the activities of all components in an N-component system do not vary in spite of changes in the relative amounts of the various phases if temperature and pressure are kept constant. Drawing a straight line in an N-component phase diagram from the composition of the sample toward the corner of the mobile component A, the adjacent multiphase regions above and below the electrolyte phase determine the maximum and the minimum activity at which the electrolyte is decomposed. Employing the determinant method [45], the corresponding plateau voltages E of N-

CosMX Exhibit 1008, Page 565 of 633

$$E = \frac{1}{z_A F d} \sum_{i=1}^{N} (-1)^{i+k} d_{ik} \; G_f^0\left(A_{\alpha i} B_{\beta i} C_{\gamma i} D_{\delta i} \ldots\right) \; i = 1,2,3,\ldots \tag{50}$$

phase regions in an N–component phase diagram can be calculated to be with reference to the pure component A. Here d and d_{ik} are the determinant and minor (explained below), and ΔG_f is the free enthalpy of formation of the compound $A_{\alpha i} B_{\beta i} C_{\gamma i} D_{\delta i} \ldots$ under standard conditions. The minor d_{ik} is derived from the determinant d formed from the stoichiometric numbers of all components by omitting the ith row and the kth column:

$$d = \begin{vmatrix} \alpha_1 & \beta_1 & \gamma_1 & \delta_1 & \cdots \\ \alpha_2 & \beta_2 & \gamma_2 & \delta_2 & \cdots \\ \alpha_3 & \beta_3 & \gamma_3 & \delta_3 & \cdots \\ \alpha_4 & \beta_4 & \gamma_4 & \delta_4 & \cdots \\ \vdots & \vdots & \vdots & \vdots & \end{vmatrix} \tag{51}$$

One practical problem of the determinant method is the common unavailability of thermodynamic data and phase diagrams for multiphase compounds. For practical applications, an estimate obtained from data for binary compounds of the multinary system may be useful.

In practice, for a ternary system, the decomposition voltage of the solid electrolyte may be readily measured with the help of a galvanic cell which makes use of the solid electrolyte under investigation and the adjacent equilibrium phase in the phase diagram as an electrode. A convenient technique is the formation of these phases electrochemically by decomposition of the electrolyte. The sample is polarized between a reversible electrode and an inert electrode such as Pt or Mo in the case of a lithium ion conductor, in the same direction as in polarization experiments. The decomposition causes a sharp linear increase in the direct current.

9.6.4 Determination of the Ionics Conduction Mechanism and Related Types of Defects

Densities determined by pycnometric methods may be compared with those determined by X-ray diffraction. The pycnometric density is dependent on the presence of vacancies or interstitials, being lower or higher, respectively [46].

The type of disorder may be determined by conductivity measurements of electronic and ionic defects as a function of the activity of the neutral mobile component [3]. The data are commonly plotted as Brouwer diagrams of the logarithm of the concentration of all species as a function of the logarithm of the activity of the neutral mobile component. The slope is fitted to the assumption of a specific defect-type model.

Extended X-ray absorption fine structure (EXAFS) measurements based on the photoeffect caused by collision of an inner shell electron with an X-ray photon of sufficient energy may also be used. The spectrum, starting from the absorption edge, exhibits a sinusoidal fine structure caused by interferences between the outgoing and the backscattered waves of the photoelectron which is the product of the collision. Since the intensity of the backscattering decreases rapidly over the distances to the next neighbor atoms, information about the chemical surroundings of the excited atom can be deduced.

Other suitable methods include inelastic or diffuse X-ray and neutron scattering.

CosMX Exhibit 1008, Page 566 of 633

These methods also provide information about the nearest-neighbor surroundings of the atoms.

Acknowledgment. The authors thank S. Scharner for his support in preparing Figs. 1–6, showing the crystal structures of fast ion conductors.

9.7 References

[1] E. Warburg, *Wiedemann. Ann. Phys.* **1884** *21*, 622.

[2] E. Warburg, F. Tegetmeyer, *Wiedemann. Ann. Phys.*, **1888,** *32*, 455.

[3] H. Rickert, *Solid State Electrochemistry; An Introduction,* Springer-Verlag, Berlin, **1982**.

[4] T. Kudo, K. Fueki, *Solid State Ionics,* VCH, Weinheim, **1990**.

[5] S. Mennicke, in *Solid State Ionics* (Eds.: M. Balkanski et al.), Elsevier Science Oxford, **1992**, p. 3.

[6] H. Boehm, Chap. IV, Sec. 1, this handbook

[7] B. B. Owens, in *Fast Ion Transport in Solids* (Eds.: B. Scrosati et al.), Kluwer Academic Press, Dordrecht, **1993**, p. 259.

[8] L. W. Strock, *Z. Phys. Chem.* **1934** *B25*, 441

[9] J. N. Bradley, P. D. Green, *Trans. Faraday Soc.* **1966**, *62*, 2069.

[10] a)Y.-F. Y. Yao, J. T. Kummer, *J. Inorg. Nucl. Chem.* **1937**, *29*, 2453; b) C. A. Beevers, M. A. Ross, *Z. Kristallogr.* **1937**, *97*, 59.

[11] W. Weppner, *J. Solid State Chem.* **1977**, *20*, 305.

[12] P. Hartwig, W. Weppner, W. Wichelhaus, A. Rabenau, *Angew. Chem.* **1980**, *92*, 72; *Angew. Chem. Int. Ed. Engl.* **1980**, *19*, 74.

[13] W. Weppner, *Z. Naturforsch. A,* **1976**, *31*, 1336.

[14] W. Weppner in: *Fast Ion Transport in Solids* (Eds.: B. Scrosati et al.), Kluwer Academic Press., Dordrecht, **1993**, p. 9.

[15] W. Weppner, R. A. Huggins, *J. Solid State Chem.* **1977**, *22*, 297.

[16] A. Kvist, A. M. Josefson, *Z. Naturforsch. A* **1968**, *23*, 625.

[17] W. F. Chu, H. Rickert, W. Weppner, in *Fast Ion Transport in Solids; Solid State Batteries and Devices* (Ed.: W. van Gool.), North-Holland, Amsterdam/Elsevier, New York, **1973**, p. 181.

[18] W. H. Flygare, R. A. Huggins, *J. Phys. Chem. Solids* **1973**, *34*, 1199.

[19] H. Aono, E. Sugimoto, Y. Sadaoka, N. Imanaka, G. Adachi, *J. Electrochem. Soc.* **1990**, *137*, 1023.

[20] W. Weppner, R. A. Huggins, *Phys. Lett.* **1976**, *58A*, 245.

[21] S. Ikeda, S. Kato, K. Nomura, K. Ito, H. Einaga and S. Saito, Y. Fujita, *Solid State Ionics* **1994**, *70/71*, 569.

[22] S. Ikeda, T. Kondo, S. Kato, K. Ito, K. Nomura, Y. Fujita, *Solid State Ionics* **1995**, *79*, 354.

[23] J. B. Goodenough, Y.-P. Hong, J. A. Kafalas, *Mater Res. Bull.* **1976**, *11*, 203.

[24] a) H. Kawai, J. Kuwano, *J. Electrochem. Soc.* **1994**, *141*, L78; b) Y. Inamuga, L. Chen, M. Itho, T. Nakamura, *Solid State Ionics* **1994**, *70/71*, 196;

[25] Y. Inaguma, C. Liquan, M. Itho, T. Nakamura, *Solid State Commun.* **1993**, *86*, 689.

[26] P. Birke, S. Döring, S. Scharner, W. Weppner, Paper presented on the 192th Meeting of the Electrochemical Society, Paris, France, **1997**, to be published in *Proc. Ionic and Mixed Conducting Ceramics III.*

[27] W. Weppner, in *Solid State Microbatteries* (Eds: J. R. Akridge, M. Balkanski), Plenum, New York, **1990**, p. 371.

[28] L. Heyne, in *Fast Ion Transport in Solids; Solid State Batteries and Devices* (Ed.: W. van Gool), Elsevier, New York, **1973**, p. 123.

[29] M. P. Pechini, US Patent 3330697, **1967**.

[30] P. Kountouros, *Ph.D. Thesis*, Stuttgart, **1993**.

[31] Kountouros, R. Förthmann, A. Naoumidis, G. Stochniol, E. Syskakis, *Ionics* **1995**, *1*, 40.

[32] L. A. Chick, R. D. Pederson, G. D. Mauphin, J. L. Bates, L. E. Thomas, G. J. Exarhos, *Mater. Lett.* **1990**, *10*, 6.

[33] N. Imanaka, T. Shimizu, G. Adachi, *Solid State Ionics* **1993**, *62*, 167.

[34] C. C. Liang, *J. Electrochem. Soc.* **1973**, *120*, 1289.

[35] a) J. B. Wagner, *Mater. Res. Bull.* **1980**, *15*, 1691; b) N. J. Dudney, in *Solid State Ionics* (Eds: G. Nazri et al.), Materials Research Society, Pittsburgh, PA, **1989**, p. 611.

[36] A. M. Glass et al., *J. Appl. Phys.* **1978**, *49*, 4808.

[37] T. Oi, K. Miyauchi, *Mater. Res. Bull.* **1981**,

CosMX Exhibit 1008, Page 567 of 633

16, 1281.
[38] F. Kohlrausch, *Praktische Physik 2*, Teubner, Stuttgart, **1968**, p. 284.
[39] J. R. Macdonald, *Impedance Spectroscopy*, John Wiley, New York, **1987**.
[40] C. Wagner, Proc. *7th Meeting CITCE*, Lindau, Butterworth, London, **1957**, p. 361.
[41] M. Hebb, *J. Chem. Phys.* **1952**, *20*, 185.
[42] W. Weppner, *Z. Naturforsch. A.* **1976**, *32a*, 753.
[43] W. Weppner, *Electrochim. Acta* **1977**, *22*, 721.
[44] W. Weppner, R. A. Huggins, *Ann. Rev. Mater. Sci.* **1978**, *8*, 269.
[45] Chen Li-chuan, W. Weppner, *Naturwissenschaften* **1978**, *65*, 595.
[46] C. Wagner, *Naturwissenschaften* **1943**, *31*, 265.
[47] N. Aotani, K. Iwamoto, K. Takada, S. Kondo, *Solid State Ionics* **1994**, *68*, 35.
[48] Y. Inaguma, Y. Matsui, Y.-J. Shan, M. Itho, T. Nakamura, *Solid State Ionics* **1995**, *79*, 91.
[49] B. Schoch, E. Hartmann and W. Weppner, *Solid State Ionics* **1986**, *18/19*, 529.
[50] W. Weppner and R. A. Huggins, *J. Electrochem. Soc.* **1977**, *124*, 35.
[51] Y.-W. Hu, I. D. Raistrick and R. A. Huggins, *J. Electrochem. Soc.* **1977**, *124*, 1240.
[52] B. J. Neudecker, W. Weppner, *J. Electrochem. Soc.* **1996**, *143*, 2198.

CosMX Exhibit 1008, Page 568 of 633

10 Separators for Lithium-Ion Batteries

R. Spotnitz

10.1 Introduction

Traditionally, battery separators have been used as spacers to prevent electronic contact but to allow ion transport between the positive and negative electrodes. The development of tough, thin, microporous separators made practical the use of resistive, organic electrolytes in high-rate cells while maximizing the volumetric energy density of batteries. Today, with thin (e.g. 25 μm thick) microporous separators and spirally wound cells, nonaqueous batteries achieve discharge rates able to power camera flashbulbs. With the advent of rechargeable, high-energy, lithium-ion batteries, battery makers now use battery separators as thermal fuses to provide some measure of short-circuit and overcharge protection.

Battery makers sometimes view separators with disdain; the separator is needed but does not actively contribute to battery operation. Consequently, very little work (relative to that on electrode materials and electrolytes) is directed towards characterizing separators. In fact, development efforts are under way to displace microporous membranes as battery separators and instead to use gel electrolytes or polymer electrolytes. Polymer electrolytes, in particular, promise enhanced safety by eliminating flammable organic solvents and higher energy density through reduced separator thickness.

This section reviews the state-of-the-art in battery separator technology for lithium-ion cells, with a focus on separators for spirally wound batteries; in particular, button cells are not considered.

Note that a review of battery separators for lithium-ion cells was recently published [1] in Japanese.

10.2 How a Battery Separator is Used

The requirements for a battery separator can best be understood in the context of how the separator is used. The conventional process (Fig. 1) for making spirally wound cells involves threading the separator (a) through a winding pin (b).

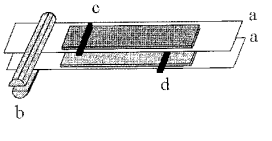


Figure 1. Schematic of components for making spirally wound batteries.

The electrodes (c and d) are interspaced between the two layers of separator, and the layers are wound as tightly as possible to ensure good interfacial contact.

During winding, tension is applied through the separator. The separator must have sufficient strength in the machine direction so that it does not break under the stress of winding. Also, the separator must not yield and reduce in width, or else the electrodes may contact each other. Tension in the separator is used to bend the electrodes during winding. Again, the separator must be strong enough not to break or puncture; this is a common cause for short circuits in wound cells [2]. During winding, small pieces of electrode materials can come off and be forced into the separator by the winding tension. The separator must not puncture, or else the battery will be shorted. Typically, electrode materials use particulates on the order of 10 μm in diameter, so the separator must be thick enough not to be penetrated by the roughness of the particles.

Once wound, the separator is cut and the loose end taped to the spiral. The spiral is pushed off the winding pin and inserted into a can. The can is filled with electrolyte and the separator must be wetted quickly by the electrolyte so that the header (or cover) can be installed in the next processing step.

Once in an operational battery, the separator should be physically and chemically stable to the electrochemical environment inside the cell. The separator should prevent migration of particles between electrodes, so the effective pore size should be less than 1 μm. Typically, a Li-ion battery might be used at a C rate, which corresponds to 1–3 $mA\,cm^{-2}$, depending on electrode area; the electrical resistivity of the separator should not limit battery performance under any conditions.

Underwriters Laboratories (UL) requires that consumer batteries pass a number of safety tests [3]. UL requires that a battery withstand a short circuit without fire or explosion. A positive temperature coefficient (PTC) device [4] is used for external short-circuit protection. The resistance of a PTC placed in series with the cell increases by orders of magnitude at high currents and resulting high temperatures. However, in the case of an internal short, e.g., if the positive tab comes lose and contacts the interior of the negative metal can, the separator could act as a fuse. That is, the impedance of the separator increases by two to three orders of magnitude due to an increase in cell temperature.

UL also requires overcharge testing. Here the PTC may not be activated by the low currents used in charging and thermal runaway might be prevented by fusing of the separator [5].

10.3 Microporous Separator Materials

Currently, all commercially available, spirally wound lithium-ion cells use microporous polyolefin separators. In particular, separators are made from polyethylene, polypropylene, or some combination of the two. Polyolefins provide excellent mechanical properties and chemical stability at a reasonable cost. A number of manufacturers produce microporous polyolefin separators (Table 1.)

Nonwoven materials have not been able to compete with microporous films, most probably because of the difficulty in mak ing thin (25 μm) nonwovens with acceptable physical properties (for example,

CosMX Exhibit 1008, Page 570 of 633

Table 1. Commercially available microporous membrane materials used as separators in lithium-ion batteries.

Manufacturer	Materials
Hoechst Celanese Corp.	Celgard ® membranes made of polypropylene, polyethylene, and combinations
Tonen Corp.	Setela ® membranes made of polyethylene
Asahi Chemical Industries	HiPore ® membranes made of polyethylene
Mitsubishi	Exepol membranes made of polyethylene
Ube Industries Ltd.	Polypropylene membranes
Pall RAI	Polyethylene membranes

gauge uniformity, puncture strength). However, nonwovens are used in button cells and bobbin cells when thicker separators and low discharge rates are acceptable.

The processes for manufacturing microporous membranes can be broadly divided into wet processes and dry processes. Both processes usually employ one or more orientation steps to impart porosity and/or increase tensile strength. Figure 2 shows scanning electron micrographs of surfaces of separators made by each process.

Wet processes involve mixing a hydrocarbon liquid or some other low-molecular -weight substance with a polyolefin resin, heating and melting the mixture, extruding the melt into a sheet, orientating the sheet either in the machine direction or biaxially, and then extracting the liquid with a volatile solvent [6–8].

Dry processes involve melting a polyolefin resin, extruding it into a film, thermal annealing, orientation at a low temperature to form micropore initiators, and then orientation at a high temperature to form micropores [9, 10]. The dry process involves no solvent handling, and therefore is inherently simpler than the wet process. The dry process involves only virgin polyolefin resins and so presents little possibility of battery contamination.

Separators made by the dry process are available from Hoechst Celanese Corporation and Ube. The Celgard ® microporous

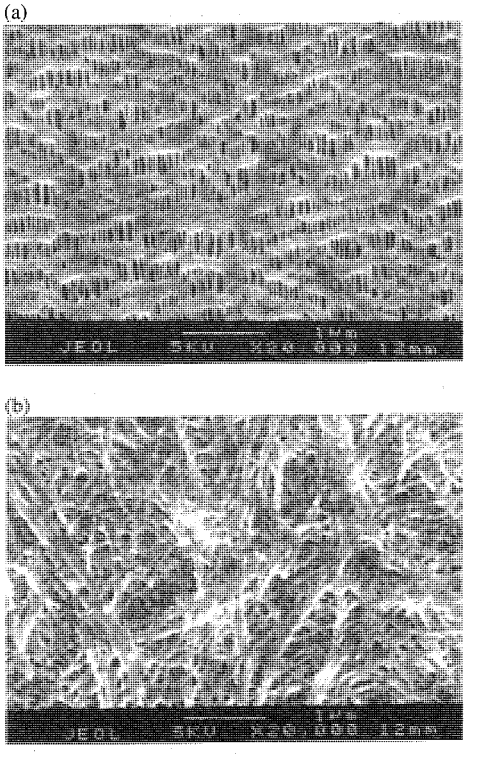


Figure 2. Scanning electron micrographs of surfaces of microporous membranes made by wet and dry processes.: (a) Setela® microporous membrane (net process); (b) Celgard® microporous membrane (dry process).

materials made by Hoechst Celanese Cor poration are the best-characterized battery separators. Bierenbam et al. [11] describe the process, physical, and chemical properties, and end-use applications. The pre-

CosMX Exhibit 1008, Page 571 of 633

cursor polymeric films are characterized by scanning tunneling microscopy, atomic force microscopy, and field emission scanning electron microscopy [12]. The membrane pore structure is studied by high-contrast transmission electron microscopy and high-resolution scanning electron imaging [13]. This work shows the pores are grouped into rows (see Fig. 2b) and the structure is uniform throughout the bulk, except for a thin surface layer (about 0.5 μm thick) which exhibits a slightly smaller pore size than the interior. Fleming and Taskier [14] describe the use of Celgard microporous membranes as battery separators. Hoffman et al. [15] present a comparison of polypropylene (PP) and polyethylene (PE) Celgard microporous materials. Callahan [16] discuss a number of novel uses of Celgard membranes. Callahan and co-workers [17] characterize Celgard membranes by scanning electron microscopy image analysis, mercury porosimetry, air permeability, and electrical resistivity, and later characterize the puncture strength and temperature/impedance data for Celgard membranes [18,19]. Spotnitz et al. [20] report short-circuit behavior in simulated, spirally-wound cells, as well as impedance/temperature behavior and thermomechanical properties.

Yu et al. [21] found that a trilayer structure of PP/PE/PP Celgard ® microporous membranes provided exceptional puncture strength. In addition, the low-melting PE layer (135 °C) can act as a thermal fuse while the higher-melting PP (165 °C) layers provide physical integrity. The concept of using separators consisting of distinct layers, one of which could act as a fuse, is due to Lundquist et al. [22]. One or more layers provide mechanical strength while another layer serves as a fuse. The fuse layer melts and loses porosity at elevated temperature, which effectively stops current flow between electrodes [23]; the other layers do not melt and continue to provide mechanical integrity after the fuse layer has melted. Figure 3 shows a cross-sectional view of a PP/PE/PP trilayer separator before and after exposure to a simulated short circuit [20]. The inner polyethylene layer has lost porosity after melting caused by Joule heating in the cell.

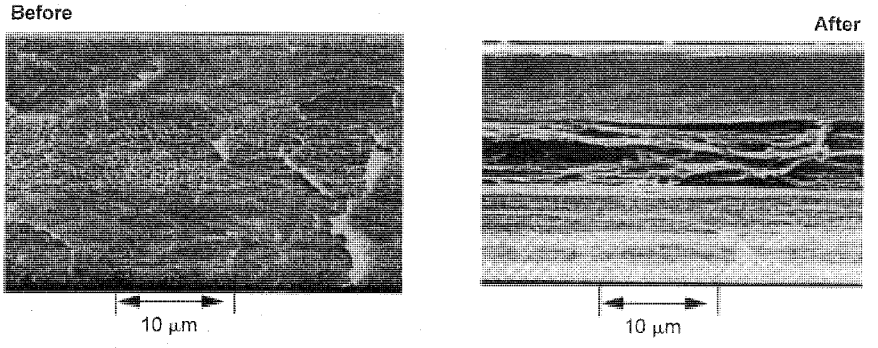


Figure 3. Cross-sectional views of PP/PE/PP trilayer separator before and after exposure to short-circuit conditions.

CosMX Exhibit 1008, Page 572 of 633

Recently, Nitto Denko has patented a single-layer separator made from a PE/PP blend by the dry stretch process [24]. According to the patent, the separator has microporous regions of PE and PP. On heating in an oven, the impedance of the separator increases near the melting point of PE and the impedance remains high until beyond the melting point of PP. However, battery performance data have not been presented.

The wet process is used by a number of companies to make separators containing ultra-high-molecular-weight polyethylene (UHMWPE). The Setela ® membranes made by Tonen are an example; a scanning electron micrograph is shown in Fig. 2(a) of a Setela ® membrane. Because of high viscosity, neat UHMWPE cannot be extruded continuously. Thus, the thin UHMWPE membranes useful for lithium-ion batteries can only be made by the wet process. The use of UHMWPE gives exceptional mechanical properties as well as some degree of melt integrity. Typically, UHMWPE membranes made by the wet process undergo biaxial orientation, followed by extraction. A drawback of the biaxial orientation is that the separator tends to shrink in both machine and transverse directions on heating.

10.4 Gel Electrolyte Separators

The liquid electrolytes used in lithium batteries can be gelled by addition of a polymer [25] or fumed silica [26], or by cross linking of a dissolved monomer [27]. Depending on the mechanical properties, gelled electrolytes can be used as separators, or supported by a conventional [27] or unconventional [28] separator. The incentive for gelling the electrolyte is to eliminate the possibility of electrolyte leakage and provide good adhesion to the electrodes. Good adhesion between the electrodes and electrolyte separator ensures good interfacial contact. A conventional spirally wound cell relies on compression of the wind and a tight fit in a metal can to maintain good interfacial contact. Batteries with gelled electrolytes can be placed in metallized plastic bags, this allows construction of batteries with customized shapes.

Gozdz et al. (of Bellcore) [25] recognized that poly (vinylidene difluoride): hexafluoropropylene (PVDF:HFP) copolymers could form gels with organic solvents and developed an entire battery based on this concept. Typically, the gel separator is 50μm thick and comprises 60wt. % polymer. In the "Bellcore" process the separator is laminated to the electrodes under pressure at elevated temperature. The use of the PVDF:HFP gelling agent increases the resistivity of the electrolyte by about five times which limits the rate capability of such batteries.

Abraham et al. [27] suggested the use of polyacrylamide gels supported in microporous membranes. This approach might provide the packaging advantages of gel electrolytes (that is, metallized plastic bags can be used) with the handling advantages of microporous membranes. However, the resistance of these supported membranes is unacceptably high.

Dasgupta and Jacobs [29] patented a concept of using a gel layer in combination with a microporous membrane. The gel layer acts as an adhesive bridge between separator and electrodes, just as in the flat pack Zn/MnO_2 cell [30]. The microporous membrane (for example, Celgard ® membrane) provides excellent mechanical

CosMX Exhibit 1008, Page 573 of 633

properties and the micropores hold liquid electrolyte by capillary action. This approach solves the problem of high resistance associated with supporting gel electrolytes in a microporous membrane. The electrode/separator composites can still be packaged in metallized plastic bags.

10.5 Polymer Electrolytes

Since the realization in the early 1980s that poly (ethylene oxide) could serve as a lithium-ion conductor in lithium batteries, there has been continued interest in polymer electrolyte batteries. Conceptually, the electrolyte layer could be made very thin (5 μm) and so provide higher energy density. Fauteux et al. [31] have recently reviewed the present state of polymer electrolyte technology. To summarize here briefly, a polymer electrolyte with acceptable conductivity, mechanical properties, and electrochemical stability has yet to be developed. Yuasa and HQ have announced they will introduce a primary Li / MnO_2 cell based on a "plasticized" polymer electrolyte and are working to develop lithium-ion cells; at the latest report [32] their cell allows discharge at 0.3 C and a 200–300 cycle life.

10.6 Characterization of Separators

The key properties of separators are summarized in Table 2. Table 3 gives some typical values for Celgard ® membranes.

Currently, 25 μm is the most widely

Table 2. Summary of key properties of separators and how they are measured

Property	How measured
Permeability	Electrical resistivity, voltage drop, air flow
Porosity	Calculated from dimensions, basis wt., and skeletal density
Pore size	Image analysis, Hg porometry
Thickness	Micrometer
Chemical composition	Atomic absorption, differential scanning calorimetry, others
Thermal stability	Hot electrical resistivity, thermal–mechanical analysis
Mechanical strength	Tensile properties, puncture strength

Table 3. Typical properties of some Celgard ® microporous membranes.

	Celgard ® 2400	Celgard ® 2300
Structure	1 layer, PP	3 layers, PP/PE/PP
Thickness (μm)	25	25
Porosity (%)	38	38
Gurley air permeability (sin^2)	35	25
Puncture strength (g)	380	480

CosMX Exhibit 1008, Page 574 of 633

used thickness for lithium ion battery separators. Single layers can be made as thin as $7\,\mu m$ or as thick as $40\,\mu m$. The thicker the separator, the greater the mechanical strength and the lower the probability of punctures during cell assembly, but the smaller the amount of active materials that can be placed in the can. The uniformity of thickness is important so that the jellyroll (that is, the spirally wound electrodes and separator) will fit into a can.

The mechanical strength of a separator is characterized in terms of tensile properties and puncture strength. Tensile strength measurements (e.g., Young's modulus, 2 percent offset strength, elongation at break, stress at break) can be made by standard procedures. The tensile properties are dependent on the manufacturing process. Uniaxially oriented films have high strength in only one direction, whereas biaxially oriented films are strong in both machine and transverse directions. Although intuitively one might expect biaxially oriented films to be preferred over uniaxially oriented films, in practice biaxial orientation provides no advantage. In fact, biaxial orientation tends to introduce transverse-direction shrinkage. This shrinkage, at elevated temperatures, can allow electrodes to contact each other. Uniaxially oriented films exhibit no tendency to shrink in the transverse direction at elevated temperatures.

More recently, puncture strength (the weight required on a given needle to puncture a given separator) [19] has been used to indicate the tendency of separators to allow short circuits during battery assembly. Note that the puncture strength requirement for lithium-ion batteries is higher than for lithium-foil batteries, because the separator must contend with two rough surfaces.

Porosity is important for high permeability (see below) and also for providing a reservoir of electrolyte in the cell. It is usually calculated from the skeletal density, basis weight, and dimensions of the material and so may not reflect the accessible porosity of the material.

Ideally, separators would present no resistance to ion transport. In practice, some resistance must be tolerated. Still, the resistance of the separator is usually insignificant relative to the transport limitations in the electrodes. Separator permeability is typically characterized by air permeability. The Gurley number expresses the time required for a specific amount of air to pass through a specific area of separator under a specific pressure (e.g., 10 mL through $1\,in^2\,(6.45\,cm^2)$ at 2.3 cm Hg). This measurement depends on porosity, pore size, thickness, and tortuosity according to Eq. (1) [17]:

$$t_{Gur} = 5.18 \cdot 10^{-3}[\tau^2 L/\varepsilon d] \qquad (1)$$

where t_{Gur} = Gurley number obtained by experiment (sin^2), τ = tortuosity, L = thickness of the membrane (cm), ε = porosity of the membrane (fraction), and d = diameter of the pores (cm).

The Gurley number is used to characterize membranes because the measurement is accurate and easy to make, and deviations from specified values are a good indication of problems. A higher Gurley value than specified can indicate the membrane has surface damage; a lower value than specified can indicate pinholes.

The electrical resistivity (ER) is a more comprehensive measure of permeability than the Gurley number (air permeability), in that the measurement can be carried out in the actual electrolyte solution. Thus, the measurement reflects the compatibility of the separator with the electrolyte (e.g., the

CosMX Exhibit 1008, Page 575 of 633

value of the electrical resistivity will reflect pores that are nonwetting). The magnitude of the electrical resistivity can be used to estimate ohmic losses in a cell. Unfortunately, ER is significantly more difficult to measure than air permeability. Battery makers may find evaluating the electrical performance of a spirally wound cell made with dummy electrodes and a particular separator an efficient means of measuring ER [33].

In theory, the resistivity of a membrane, $R_m(\text{ohm cm}^2)$, can be expressed as:

$$R_m = \rho\tau^2 L / \varepsilon d \qquad (2)$$

where ρ (ohmcm) is the resistivity of the electrolyte. Note that ER does not depend on pore size. Callahan [17] combined Eqs. (1) and (2) to relate ER with Gurley:

$$R_m = (\rho d / 5.18 \cdot 10^{-3}) t_{Gur} \qquad (3)$$

and experimentally verified this relation for Celgard ® membranes.

An excellent review of experimental techniques for measuring electrical resistivity in aqueous solutions is available [34]. Separators used in nonaqueous systems can be characterized by wetting them with a surfactant and measuring the electrical resistivity in an aqueous solution. Then the resistivity in a nonaqueous membrane can be estimated from Eq. (2).

The "hot-ER" test refers to measuring the impedance of a separator while the temperature is linearly increased; this technique was first used by Laman et al. [5]. Figure 4 shows actual measurements for some Celgard ® membranes [20]. The single-layer materials exhibit a sharp rise in impedance near their respective melting points; the impedance goes back down after a maximum value has been reached.

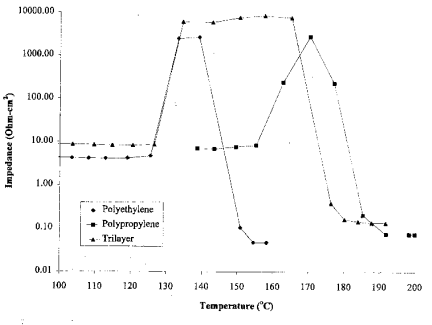


Figure 4. Impedance versus temperature behavior of Celgard® microporous membranes.

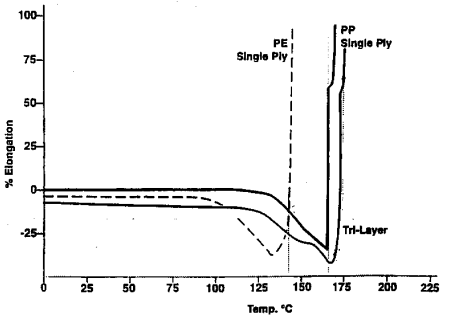


Figure 5. Thermal-mechanical analysis of Celgard® microporous membranes.

With a multilayer polypropylene/ polyethylene separator, the impedance rise occurs near the melting point of polyethylene (135 °C), and stays high till just past the melting point of polypropylene (165 °C). The rise in impedance corresponds to a collapse in pore structure due to melting of the separator. Laman et al. [5] suggested that at least a thousand-fold increase in impedance is necessary for the separator to stop thermal runaway in a battery. The drop in impedance corresponds to opening of the separator due to coalescence of the polymer, and/or to penetration of the separator by the electrodes; this phenomenon is referred to as a loss in "melt integrity".

CosMX Exhibit 1008, Page 576 of 633

The "hot-ER" test seems fairly reliable in indicating the temperature at which the impedance rises, but shows some variability in characterizing the subsequent drop in impedance.

Thermal–mechanical analysis (TMA) has proven a more reproducible measure of melt integrity [20]. The TMA test involves measuring the shape change of a separator under load while the temperature is linearly increased. Typically, separators show some shrinkage, then start to elongate, and finally break (see Fig. 5).

The simulated short-circuit test was developed to characterize the response of the separator to a short circuit without the complications of battery electrodes. The separator was spirally wound between lithium foils and placed in an AA-size can. To avoid lithium dendrite formation, an alternating voltage was applied to the cell. The cell current and can temperature were monitored. Figure 6 shows the behavior of Celgard ® membranes.

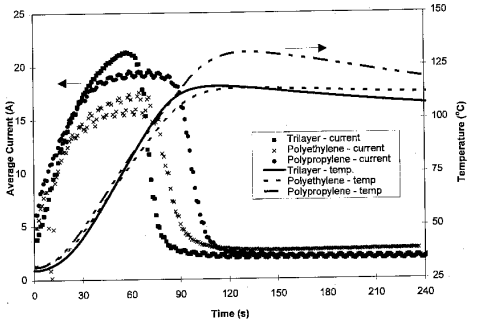


Figure 6. Simulated short-circuit of Celgard® microporous membrnes.

With a polypropylene separator, the can temperature reached 125 °C, but with polyethylene or polypropylene / polyethylene laminate separators the can temperature was held to about 115 °C. The vents burst in the cells with the polypropylene separator, but not in the other cells.

Short-circuit tests with lithium-ion batteries have been reported recently [35]. This work shows that the separator provides "shutdown" when the battery is subjected to an external short circuit with the PTC bypassed. The large increase in impedance of the separator is attributed to the temperature rise in the battery.

10.7 Mathematical Modeling of Separators

Very little work has been done in this area. Even electrolyte transport has not been well characterized for multicomponent electrolyte systems. Multicomponent electrochemical transport theory [36] has not been applied to transport in lithium-ion electrolytes, even though these electrolytes consist of a blend of solvents. It is easy to imagine that ions are preferentially solvated and ion transport causes changes in solvent composition near the electrodes. Still, even the most sophisticated mathematical models [37] model transport as a binary salt.

Tye [38] explained that separator tortuosity is a key property determining the transient response of a separator (and batteries are used in a non steady-state mode); steady-state electrical measurements do not reflect the influence of tortuosity. He recommended that the *distribution of tortuosity* in separators be considered; some pores may have less tortuous paths than others. He showed mathematically that separators with identical average tortuosities and porosities can be distinguished by their unsteady-state behavior if they have different distributions of tortuosity.

CosMX Exhibit 1008, Page 577 of 633

Mao and White developed a mathematical model for discharge of an Li/TiS_2 cell [39]. Their model predicts that increasing the thickness of the separator from 25 to 100 μm decreases discharge capacity from 95 percent to about 90 percent; further increasing separator thickness to 200 μm reduced discharge capacity to 75 percent. These theoretical results indicate that conventional separators (25–37 μm thick) do not significantly limit mass transfer of lithium.

Doyle et al. [40] used a mathematical model to examine the effect of separator thickness for the PVDF:HFP gel electrolyte system and found that decreasing separator thickness below 52 μm caused only a minor decrease in ohmic drop across the cell. The voltage drops in the electrodes were much more significant. They state that their model predictions were confirmed experimentally.

10.8 Conclusions

Microporous separators have been developed from simple microporous films to complex multilayer structures to meet the increasing demands of high-energy nonaqueous batteries. Separators are now used to provide an electronically insulating, ionically conductive spacer between electrodes, high ionic impedance at elevated temperature, and good adhesion to the electrodes. Separator materials now have sufficient permeability not is limit the electrical performance of batteries, and excellent mechanical properties for use with high-speed, automated winding machines.

10.9 References

[1] H. Shirai, R. Spotnitz, *Lithium Ion Secondary Battery–Materials and Applications* (Eds.: Yoshio, Kozawa), Nikkan Kogyo Shin-bun, **1996** p. 91. In Japanese.

[2] M. Ellis, *Batteries Int.* **1995**, 56.

[3] *Outline of Investigation for Household and Commercial Batteries*, Subject 2054, Underwriters Laboratories, Inc. September 7, **1993**.

[4] M. Stoessl, *PCIM Magazine* **1993,** *6*.

[5] R.C. Laman, M. A. Gee, J. Denovan, *J. Electrochem. Soc.*, **1993,** *140*, L51.

[6] K. Takita, K. Kono, T. Takashima, K. Okamoto, US Patent 5051183, **1991**.

[7] T. Fujii, K. Handa, K. Watanabe, H. Nakanishi, Y. Usami, K. Sugiura, European Patent Application 0603500A1, **1994**.

[8] K. Yagi, A. Hashimoto, H. Mantoku, European Patent Application 0683196A2, **1995**.

[9] R.B. Isaacson, H. S. Bierenbaum, US Patent 3558764, **1971**.

[10] E. Kamei, Y. Shimomura, US Patent 4563317, **1986**.

[11] H.S. Bierenbaum, RB. Isaacson, M.L. Druin, S. G. Plovan, *Ind. Eng. Chem., Prod. Res. Dev.*, **1974,** *13*, 2.

[12] T. Sarada, L.C. Sawyer, M.I. Ostler, *J. of Membr. Sci.*, **1983,** *15*, 97.

[13] R.T. Chen, C.K. Saw, M.G. Jamieson, T. R. Aversa, R.W. Callahan, *J. Appl. Polym. Sci.*, **1994,** *53*, 471.

[14] R. Fleming, H. Taskier, *Prog. Batt. Solar Cells*, **1990,** *9*, 58.

[15] D. Hoffman, H. Fisher, E. Langford, C. Dwiggins, *Prog. Batt. Solar Cells*, **1990,** *9*, 48.

[16] R. W. Callahan, *AIChE Symp. Ser.* **1988,** *84*, *261*, p. 54.

[17] R. W. Callahan, K. V. Nguyen, J. G. McLean, J. Propst, D. K. Hoffman, *10th International Seminar on Primary and Secondary Battery Technology and Application*, March 1–4, **1993**.

[18] R. Callahan, C. Dwiggins, H. Fisher, M. Geiger, D. Hoffman, W. Yu, K. Abraham, M. Jillson, T. Nguyen, *Extended Abstracts and Program Spring Meeting of Electrochemical Society, Boston*, **1994,** p. 72.

[19] M. Geiger, R. Callahan, C. Dwiggins, H. Fisher, D. Hoffman, W. Yu, K. Abraham, M. Jillson, T. Nguyen, *11th International Seminar on Primary and Secondary Battery Technol-*

CosMX Exhibit 1008, Page 578 of 633

ogy and Applications,**1994**.
[20] R. Spotnitz, M. Ferebee, R. Callahan, K. Nguyen, W.-C. Yu, M. Geiger, C. Dwiggins, H. Fisher, D. Hoffman, *12th International Seminar on Primary and Secondary Battery Technology and Applications*,**1995**.
[21] W.-C. Yu, R. W. Callahan, C. F. Dwiggins, H. M. Fisher, M. W. Geiger, W. J. Schell, *North America Membrane Society Conference, Breckenridge, CO*, **1994**.
[22] J.T. Lundquist, C. B. Lundsager, N. I. Palmer, H. J. Troffkin, US Patent 4650730, **1987;** US Patent 4731304, **1988**.
[23] D. Zuckerbrod, R. T. Giovannoni, K.R. Grossman, *Proc. 34th Int. Power Sources Symposium*, **1990**, p. 172.
[24] H. Higuchi, K. Matsushita, M. Ezoe, T. Shinomura, US Patent 5385777, **1995**.
[25] A.S. Gozdz, C.N. Schmutz, J.-M. Tarascon, P. C. Warren, US Patent 5456000, **1995**.
[26] G. Eichinger and M. Fabian, *8th Int. Meeting on Lithium Batteries, PostConference,* **1996**.
[27] K.M. Abraham, M. Alamgir, D.K. Hoffman, *J. Electrochem. Soc.*, *142*, *3*, **1995**.
[28] J. Kejha, S. Hope, US Patent 5521023, **1996**.
[29] S. Dasgupta, J.K. Jacobs, US 5437692, **1995**.
[30] S.M. Bloom, C.K. Chiklis, G.F. Kinsman, US Patent 4172319, **1979**.
[31] D. Fauteux, A. Massucco, M. McLin, M. van Buren, J. Shi, Electrochim. Acta, **1995,** *40, (13–14)*, 2185.
[32] S. Izuchi, K. Takeuchi, *8th Int. Meeting on Lithium Batteries, Nagoya, Japan,* **1996**.
[33] J.W. Marple, US Patent 5290414, **1994**.
[34] J.J. Lander, R. D. Weaver, A.J. Salkind, J.J. Kelley in *Characteristics of Separators for Alkaline Silver Oxide Zinc Secondary Batteries. Screening Methods* (Eds.: J.E. Cooper, A. Fleischer), NASA Technical Report NAS 5-2860, **1964**.
[35] K. Kate, K. Takano, K. Nozaki, Y. Saito, A. Negishi, K. Kanari, *8th Int. Meeting on Lithium Batteries, Nagoya, Japan,* **1996**.
[36] D.D. Frey, T. Wong, *Chem.Eng. Commun* ,**1989**, *75*, 195.
[37] T. F. Fuller, M. Doyle, J. Newman, *J. Electrochem. Soc.*, **1994,** *141,* 982.
[38] F. L. Tye, *J. Power Sources*, **1983,** *9,* 89.
[39] Z. Mao, R. E. White, *J. Power Sources*, **1993,** *43–44,* 181.
[40] M. Doyle, J. Newman, A.S. Gozdz, C.N. Schmutz, J.-M. Tarascon, *J. Electrochem. Soc.*, **1996,** *143*, 1890.

CosMX Exhibit 1008, Page 579 of 633

11 Materials for High Temperature Batteries

H. Böhm

11.1 Introduction

The California Air Resource Board (CARB) regulation have provided a powerful driving force for the development of zero-emission vehicles (ZEV). This legislation provides a unique opportunity for the development of advanced batteries. The sodium / nickel chloride (ZEBRA) and sodium /sulfur advanced high-temperature batteries have been regarded as viable options for ZEV. These battery systems achieve the required energy density to give marketable vehicles. Battery energy densities of approximately 100 $Wh\,kg^{-1}$ are required to give vehicles urban range of 150 km , and power densities of 150 $W\,kg^{-1}$ are needed to give acceptable acceleration and hill climbing ability. ZEBRA batteries and Na/S batteries have already demonstrated in cars that they can give vehicles adequate performance. The ZEBRA ($Na/NiCl_2$) battery, especially, has reached a live record which no other battery system has achieved: more than 110000 km driving in about three years with no cell exchange or other maintenance.

Besides the two battery systems, a third high temperature system has been under development for a long time: lithium aluminum iron sulfide ($LiAl/FeS_2$) [1]. This battery system has the potential of high performance (200 $Wh\,kg^{-1}$ and 400 $W\,kg^{-1}$) and works with a lithium aluminum alloy as negative electrode, iron disulfide as positive electrode, and a molten electrolyte consisting of LiCl , LiBr and KBr . This molten electrolyte is soaked into a matrix which consists of either MgO or boron nitride. The operating temperature of the $LiAl/FeS_2$ battery is very high: 400–450 °C. This high temperature, together with the molten electrolyte, causes many material problems. This is one reason why this battery system is still in the research stage; major efforts will be necessary to commercialize this system and bring $LiAl/FeS_2$ batteries into cars for fleet demonstration.

Recently the development of Na/S batteries for car applications has been abandoned; only Na/S batteries for stationary applications (load leveling) are still under development in Japan. Among the high-temperature batteries, the ZEBRA battery is the only system at present which is being commercialized for car applications.

Because of the less advanced status of the lithium aluminum/iron sulfide battery, only the ZEBRA battery and the Na/S battery are described in this section.

11.2 The ZEBRA System

The ZEBRA battery is a high-energy battery based on a cell with electrodes of sodium and metal chloride. The ZEBRA system was first described by Coetzer in 1986 [2].

A series of solid transition-metal chlorides can be used as positive electrodes in cells with sodium as the negative electrode. The various metal chlorides form electrochemical pairs with sodium showing different emf values (Table 1).

Table 1. Electrochemical pairs formed by sodium and metal chlorides.

Cell	Emf(V)	Temperature(°C)
$Na/NiCl_2$	2.58	300
$Na/FeCl_2$	2.35	250
$Na/CoCl_2$	2.52	300
$Na/CuCl_2$	2.34	290
$Na/CrCl_2$	2.04	300

11.2.1 The ZEBRA Cell

Nickel chloride is preferred and ZEBRA batteries are based today on nickel chloride and sodium. According to the very simple cell reaction

$$2Na + NiCl_2 \leftrightarrow Ni + 2NaCl \qquad (1)$$

the sodium reacts with nickel chloride to form salt and nickel. The reaction is reversed during charging.

This cell reaction necessitates a sodium-ion-conductive electrolyte. At present, the best and most stable sodium ion conductor is β''–alumina. This electrolyte has sufficient high sodium ion conductivity at temperatures of about 300 °C. The β''–alumina electrolyte is normally designed as a tube closed at one end with a negative electrode on the outside and the positive electrode inside the tube. The positive electrode, which consists of nickel chloride, nickel, and salt, throughout the reaction is incorporated in a nickel powder matrix and has a nickel current collector. The positive electrode is solid, as well as the ceramic electrolyte; therefore the solid electrode must be made to work together with the solid electrolyte, so that cell reactions can proceed. This is achieved by using a second electrolyte, sodium aluminum chloride, which is molten at the operating temperature. The $NaAlCl_4$ melt, which is also a sodium ion conductor, penetrates the total volume of the positive electrode and assures the utilization of the total mass of the positive material. Both electrolytes, the β''–alumina as well as the melt, do not participate in the normal cell reaction but serve as sodium ion conductors only.

The β''–alumina tube inserted in a steel cell case which forms the negative terminal. The space between the ceramic tube and the cell case is the sodium compartment.

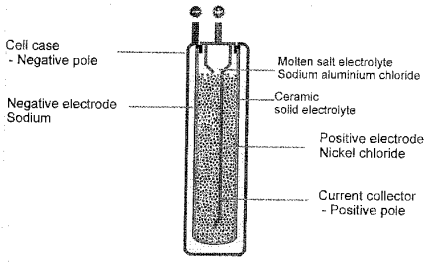


Figure 1. ZEBRA cell ($Na / NiCl_2$ – cell).

The cell is hermetically sealed. This is performed by a glass connection from the β''–alumina ceramic tube to a ring of α–alumina. Metal parts are connected to the α–alumina by thermocompression bonding and the metal parts are either con-

CosMX Exhibit 1008, Page 581 of 633

nected to the cell case or to the positive nickel current collector by welding. Figure 1 gives a schematic view of a cell.

The manufacture of the cells is simple because the cells are assembled in the fully discharged state. A discharged cell only contains nickel and salt, both in the positive electrode compartment. During manufacture the β''–alumina ceramic which is glassed to the α–alumina ring with the metal parts is pushed into the cell case and the outer metal part of the α–ring is welded to the cell case. Only nickel powder and salt are filled in through the inner ring-shaped part and the melt is added as second electrolyte. The cell is closed by welding to finalize the manufacture. Any handling of sodium can be avoided during this process, so the process is very simple. The sodium is formed electrochemically in the negative electrode compartment between the ceramic and cell case during the first charge of the cell.

11.2.2 Properties of ZEBRA Cells

ZEBRA cells have a high open-circuit voltage (OCV) of 2.58 V at 300 °C. The temperature dependency of the OCV is shown in Fig. 2.

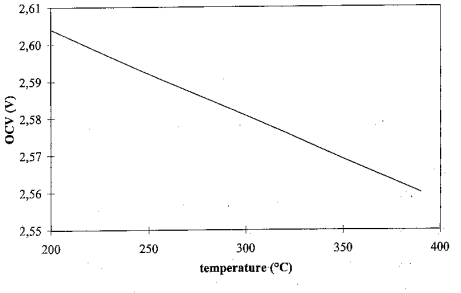


Figure 2. Open-circuit voltage of the Zebra cell versus temperature.

Table 2. Theoretical energy densities of batteries

Battery type	Energy density ($Wh\,kg^{-1}$)
Lead-acid	161
Ni/Cd	208
Na/S	760
ZEBRA ($Na/NiCl_2$)	796

The thermoneutral potential is 2.72 V; this means that during charging at voltage below this value ZEBRA cells will be cooled thermodynamically.

The theoretical energy density of the ZEBRA system (sodium and nickel chloride) exhibits the high value of 796 $Wh\,kg^{-1}$. Table 2 shows a comparison of the theoretical energy densities between the ZEBRA system and other battery systems. The practical energy density of ZEBRA batteries remains high in spite of applying two electrolytes and a sophisticated battery box. The practical value for the battery energy density is close to 100 $Wh\,kg^{-1}$ [3–5].

The second electrolyte, the melt of sodium aluminum chloride, provides another advantage for the ZEBRA system. This second electrolyte makes the system tolerant to overcharge and overdischarge. In the overcharge reaction $NaAlCl_4$ reacts with nickel to form sodium, nickel chloride, and $AlCl_3$:

$$Ni + 2NaAlCl_4 \leftrightarrow 2Na + 2AlCl_3 + NiCl_2 \qquad (2)$$

This reaction will take place after total consumption of the salt in the cell. The emf of this reaction amounts to 3.05 V.

When all the nickel chloride has been discharged, the remaining sodium will react with sodium aluminum chloride to form sodium chloride and aluminum:

$$3Na + NaAlCl_4 \leftrightarrow 4NaCl + Al \qquad (3)$$

CosMX Exhibit 1008, Page 582 of 633

This overdischarge reaction can proceed as long sodium is available. To build the overdischarge capacity into the cell, the cells will be constructed with an addition of some aluminum powder which reacts first according to Eq. (3). The sodium formed during this reaction provides the overdischarge capability of the cell [6]. The situation is schematically shown in Fig. 3.

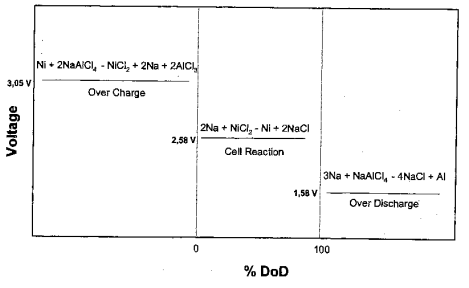


Figure 3. Overcharge and overdischarge reactions of the ZEBRA cell

The molten salt, sodium aluminum chloride, fulfills two other tasks in the cell system. The ceramic electrolyte β''–alumina is sensitive to high-current spots. The inner surface of the ceramic electrolyte tube is completely covered with molten salt, leading to uniform current distribution over the ceramic surface. This uniform current flow is one reason for the excellent cycle life of ZEBRA batteries.

The molten salt electrolyte also contributes to the safety behavior of ZEBRA cells. The large amount of energy stored in a 700 g cell, which means about 30 kWh in a 300 kg battery, is not released suddenly as heat as be expected in a system with liquid electrodes such as the sodium sulfur cell. In the case of accidental destruction of ZEBRA cells, the sodium will react mainly with the molten salt, forming Al sponge and NaCl. –The diffusion of the $NaAlCl_4$ melt to the reaction zone of the chemical reaction is the rate-determining step which controls the release of heat.

11.2.3 Internal Resistance of ZEBRA Cells

The power of the ZEBRA cell depends on the resistance of the cell during discharge. The resistance of the ZEBRA cell rises with increasing depth of discharge (DOD). There is a contribution to the resistance from the fixed values of the solid metal components and of the β''–alumina solid electrolyte. The variable parts of the resistance are the sodium electrode and the positive electrode. The increase in internal resistance during discharge is almost entirely due to the positive electrode, as can be seen from Fig. 4.

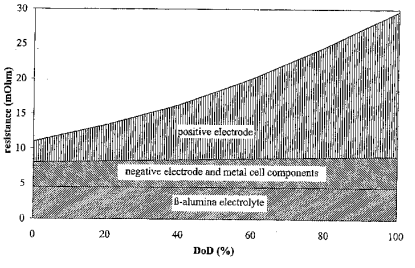


Figure 4. Contributions to the internal resistance of a ZEBRA cell.

The reason for this increase can be found in the way the positive electrode operates. During charge as well as during discharge the reaction always starts from a point which represents the lowest internal cell resistance. This is at the inner surface of the β''–alumina and a reaction front moves through the positive electrode during charge and discharge. This has been shown by examination of the positive electrodes from cells at different states of

CosMX Exhibit 1008, Page 583 of 633

charge [7]. At this boundary nickel chloride is converted to nickel and sodium chloride during the discharge reaction. Behind the reaction front the current is carried by sodium ions migrating through the molten sodium aluminum chloride. Between the reaction front and the current collector in the middle of the cell, the current is carried by electronic conduction by the nickel matrix. The ionic conductivity of $NaAlCl_4$ is much lower than the electronic conductivity of nickel and as the distance between the β"–alumina surface and the reaction front increases, the resistance of the positive electrode also increases.

The ZEBRA cell shows the similar behavior during the charging reaction, in which the nickel is converted to nickel chloride within the reaction front. During the charging reaction the reaction front also moves from the β"–alumina into the positive electrode.

The reduction of the internal resistance of the cell can obviously be achieved by two measures:

(a) increase of the surface of the β"–alumina and
(b) reduction of the thickness of the positive electrode,

keeping the mass of the electrode constant. This has been realized by changing the cross-sectional shape of the ceramic electrolyte from a round tube to a cruciform shape (Fig. 5). This ceramic is called a monolith tube; the main features of this monolith are the four lobes. This result in a positive electrode which is approximately 10 mm thick. At 80 percent DOD the reaction front is only 5 mm away from the β"–alumina surface, compared with 8 mm in the round slim line cell. Moreover, the surface area of the monolith β"–alumina electrolyte is 50 percent greater and this will reduce the resistance contribution of the ceramic. In this way the monolith shape improves the contributions of both the fixed- and the variable-resistance parts. The comparison of the resistances of the slim line cell and the monolith is shown in Fig. 6 [8].

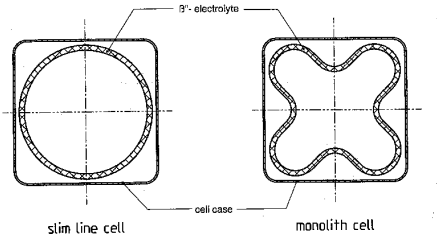


Figure 5. Cross section of various β"–Al_2O_3 electrolytes.

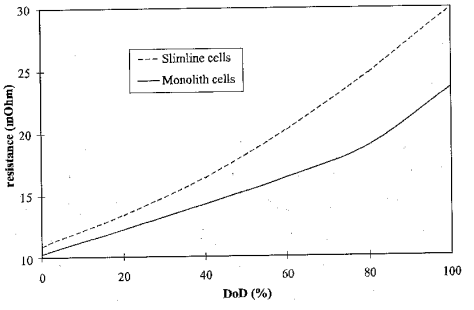


Figure 6. Comparison of internal resistance of cells with different β"–Al_2O_3 electrolyte geometries.

11.2.4 The ZEBRA Battery

The ZEBRA cells are connected in series to obtain the demanded voltages, and chains of these cells are connected in parallel to obtain the capacity which is requested. At present there is a request from the car companies to obtain battery voltages close to 300 V, which means that about 110–120 cells will be connected in series in one string. The capacity of one

CosMX Exhibit 1008, Page 584 of 633

cell is 30 Ah (line slim) or 32 Ah (monolith), so two or three strings will be connected in parallel in order to build a 20 or 30 kWh battery. The cell pack has to be operated at temperatures of about 300 °C; it is therefore enclosed in a battery housing which is vacuum-isolated (Fig. 7).

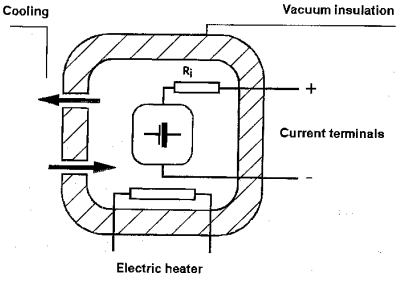


Figure 7. ZEBRA battery (schematically).

This ensures that the outer surface of the battery housing remains cold and the heat loss of the battery is low. Inside the battery a heating and cooling system is installed. An electrical heater will increase the inside temperature to operating temperature after the battery starts to operate. Normally the battery will be kept at this operating temperature unless the operation is to be interrupted for several weeks. During heavy-duty operation the temperature of the battery rises, due to the internal resistance losses. The ZEBRA battery has a very wide operating temperature window, of 270—350 °C. For normal city driving this temperature range is large enough for no cooling in operation to be necessary, but in heavy-duty cycling a cooling system must keep the operating temperature of the battery within the limit [9]. For the ZEBRA battery air cooling and oil cooling systems have been developed: the oil cooling system has a cooling power about five to eight times greater than that of the air cooling.

The operation of the battery is controlled by a battery controller, which is the brain of the battery and ensures that the battery always stays within the operating limits.

The performance of the ZEBRA battery system is shown in Table 3;

Table 3. Data for ZEBRA batteries (including peripheral equipment)

	Z5	Z11
Open-circuit voltage (V)	283	301
Capacity (Ah)	64	96
Energy content kWh	17.8	29
Peak power at $\frac{2}{3}$ OCV, 80 percent DOD, 30 s (kW)	31.5	50.2
Weight (kg)	210	335
Energy density ($Wh\,kg^{-1}$)	85	87
Power density ($W\,kg^{-1}$)	150	150

The values given in the table do not relate to the ZEBRA battery itself but to the complete system, including all peripheral equipment such as the electronic control system, the main circuit breakers of the car, and the oil cooling system with pumps, heat exchangers and oil storage vessel. Figure 8 shows the power density of a ZEBRA battery system vs. DOD for different operating temperatures. The ZEBRA battery has a high power density in the fully charged state of 220 $W\,kg^{-1}$. In the nearly discharged state at 80 percent DOD 150 $W\,kg^{-1}$ were still being achieved.

The battery system has reached more than 1700 cycles in life cycle tests. The calendar life of the /zebra battery has been proven to be close to five years in a continuing life test. In practical operation in cars the ZEBRA battery exceeded 110000 km within a three year period. This excellent result proves the ZEBRA battery to be a reliable system.

There are some other advantageous properties to be mentioned: the nameplate capacity of a battery can be fully discharged.

CosMX Exhibit 1008, Page 585 of 633

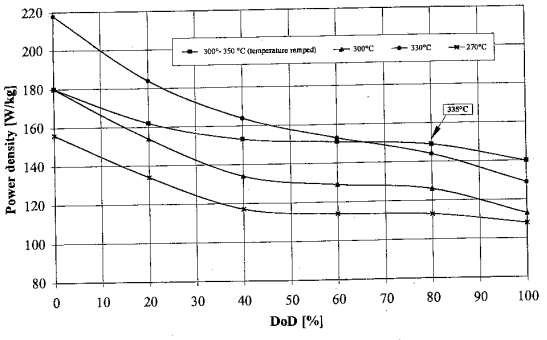


Figure 8. Power density of ZEBRA batteries during discharge.

The battery is maintenance-free and the battery housing is completely sealed by welding. In the case of the failure of one cell in a cell string, the failed cell shorts itself, which means the battery can be operated further even cell failures occur. The reason for this behavior is that in the case of cell failures the ceramic breaks and the sodium reacts with $NaAlCl_4$ forming of a sponge of Al, which builds up in the cell between the cell case and the positive current collector. Freeze/thaw cycles have no adverse effect on the cells, and batteries will not fail by cooling down.

The safety of the ZEBRA battery has been proven extensively by abuse testing: overheating, overcharging, short-circuiting of battery terminals and of cell groups, crash tests on the battery itself by dropping it at 50 $km\,h^{-1}$ onto a pole or spike, and crash tests of cars with built-in ZEBRA batteries at 50 $km\,h^{-1}$ [10]. The results of abuse testing prove the ZEBRA battery to be a safe battery system.

11.3 The Sodium Sulfur Battery

11.3.1 The Na/S System [11]

In 1967 Kummer and Weber of the Ford Motor Company described the sodium/sulfur system as a new secondary battery. At almost the same time Levine and Brown published a paper on a similar system, differing only using in the sodium-conductive electrolyte.

In the Na/S system the sulfur can react with sodium yielding various reaction products, i.e. sodium polysulfides with a composition ranging from Na_2S to Na_2S_5. Because of the violent chemical reaction between sodium and sulfur, the two reactants have to be separated by a solid electrolyte which must be a sodium-ion conductor. β''–Alumina is used at present as the electrolyte material because of its high sodium-ion conductivity.

β''–alumina develops a good conductivity only at temperatures of above 300 °C. On the other hand sodium, sulfur and the polysulfides are solids at room temperature and therefore they cannot be used as solids to form a high-performance cell. From the phase diagram (Fig. 9) it can be seen that the different polysulfide compounds have melting points between 200 and 300 °C. Therefore the normal operating temperature of sodium/sulfur cells and batteries has been selected to be in the range of 300-350 °C. The phase diagram further shows that in order to avoid precipitation of solids the discharge reaction is normally terminated at the composition of Na_2S_3. In polysulfide melts containing

CosMX Exhibit 1008, Page 586 of 633

between 78 and 100 wt.% sulfur, two immiscible liquids are formed: a sulfur-rich phase which is in fact almost pure sulfur and an ionically conducting melt of composition $Na_2S_{5.2}$.

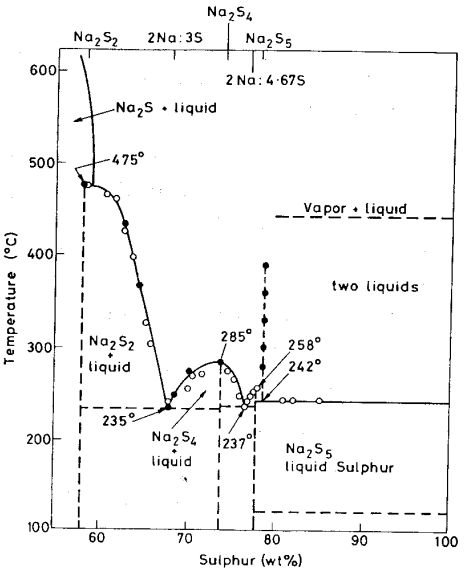


Figure 9. Phase diagram of the Na_2S/S. Reproduced with permission of Chapman and Hall, London.

During discharge the emf of the sodium/sulfur system reflects the changing composition of the melt, starting with sulfur and passing through various compounds until the formation of Na_2S_3. As long as the two phases are present the emf remains constant, but between the compositions $Na_2S_{5.2}$ and $Na_2S_{2.7}$ the emf declines steadily. Beyond the composition $Na_2S_{2.7}$, solid Na_2S_2 is formed during discharge and the composition of Na_2S_x in the liquid is fixed. In this region the emf also remains constant (Fig. 10). According to the conditions given by the phase diagram, the cell reaction of the sodium/sulfur cell is written as follows:

$$2Na + 3S \leftrightarrow Na_2S_3 \quad (4)$$

The theoretical specific energy based on this reaction is calculated as 760 $Wh\,kg^{-1}$.

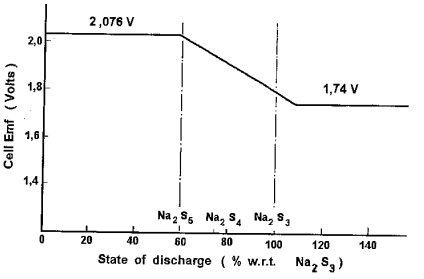


Figure 10. Emf of an Na/S cell at 350 °C versus DOD. Reproduced with permission of Chapman and Hall, London.

11.3.2 The Na/S Cell

The sodium and the sulfur, both contained in closed compartments, are separated by a ceramic electrolyte which is conductive for sodium ions but an insulator for electrons. The ceramic β''–alumina is used as the electrolyte, as mentioned above. The open circuit voltage depends on the depth of discharge and varies from 2.08 to 1.78 V. The operating temperature of a sodium/sulfur cell must be above 285 °C in order to avoid solidification of the reaction product, sodium polysulfide. This would increase the internal resistance of the cell and can result in cell failures. During charging and discharging the internal resistance is nearly constant, but at the end of the charging process a steep increase of the internal resistance occurs. This resistance increase is used to identify the end of charge. The cell reaction is completely reversible, with no side reactions, which means the coulometric efficiency is 100 percent.

Sodium/sulfur cells are cylindrical. In

CosMX Exhibit 1008, Page 587 of 633

addition to sodium, sulfur, and β''–alumina, the cell contains a carbon felt in the sulfur compartment which serves as an electronic conductor in the electrically isolating sulfur. On the sodium side a metal foil is attached to the ceramic in order to provide a capillary gap and this gap ensures the wicking of the sodium over the full surface of the electrolyte. The metal part also servers as current collector in the sodium compartment.

Several cell designs have been developed in the past. The main features are either a central sodium or a central sulfur electrode. Another feature is the length of the cells, which determines their capacity. During the last ten years the cell with central sodium electrode has normally been used. For safety reasons the sodium is encapsulated in a metal container which is fitted into the ceramic tube in such a way that the capillary gap for sodium wicking is directly formed. On the underside of the sodium container there is a small hole which restricts the sodium flow. The capacity of such cells varies from 10 Ah (PB cell from Silent Power) to 45 Ah (ABB) [12]. These cells are mainly used for mobile applications in cars but are also suitable for stationary applications. In Japan much larger cells are being developed (300—600 Ah) which will be used in stationary applications for load leveling [49]. One condition necessary for introducing small cells was introduction of small seals which have no impact on energy density and power density. On the other hand it was shown that the reliability of cells can be improved by using a short electrolyte length. Such a cell is presented in Fig. 11. The closed end of the electrolyte is an active as the lateral surface area, thereby utilizing to the fullest extent the electrolyte surface area. The nominal rating of the PB cell is 20 Wh (10 Ah).

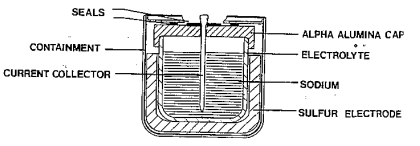


Figure 11. Design of an Na/S cell.

The small-cell approach has been described as having many advantages in battery design [13]:

- Potential for very high cell and battery reliability (small electrolyte shapes have fewer defects; small cells offer maintenance-free batteries by providing a multiplicity of parallel paths);
- High power and energy densities;
- Improved battery safety as result of a high degree of multipartitioning of the reactive materials;
- Flexibility to satisfy a wide range of applications;
- Great tolerance to thermal and mechanical shock.

It has also to be mentioned, however, that the larger number of cells in a battery will increase the cost. Compared with the large cells which are very sensitive against freeze/thaw cycles, the small PB cells have survived around 150 thermal cycles between room temperature and 350 °C, suggesting that the system can stand occasional cool-down without detriment to reliability [14].

The ratio between length and diameter of the PB cells was about 1:1. For application in cars, more powerful cells have been requested. Recently it was reported [15] that the ratio of length to diameter was increased to 2:1 without changing the mass of sodium or sulfur, i.e., the surface area of the β''–alumina was increased but the capacity of the cells remained unchanged. This results in higher power and energy densities (Table 4).

CosMX Exhibit 1008, Page 588 of 633

Table 4. Comparison between Mk4 and Mk6 batteries from Silent Power

	Mk4 battery	Mk6 battery
Dimensions (mm)	760×600 ×353	728×635 ×365
Open-circuit voltage (V)	149	182
Capacity (Ah)	150	160
Energy content kWh	21	28.8
Peak power at $\frac{2}{3}$OCV and 80 percent DOD (kW)	27.4	59.3
Weight (kg)	245	247
Energy density ($Wh\,kg^{-1}$)	88	117
Energy density ($Wh\,L^{-1}$)	134	171
Power density ($W\,kg^{-1}$)	112	240
Power density ($W\,L^{-1}$)	170	353

11.3.3 The Na/S Battery

The sodium/sulfur cells are interconnected in a parallel—series network. Sodium / sulfur cells have the disadvantage of failing in a high-resistance mode, i.e., any series-connected cell strings are interrupted and the battery fails. ABB therefore tried to install short-circuit elements on top of the cells which should short the cell in the case of a failure. Silent Power overcome the high-resistance problem of failing cells by a network of small 10 Ah cells. Cells are stacked four high, and connected in series to form a string. The four cell strings are separated electrically but close-packed and connected to upper and lower bus plates which provide parallel connections of the 8 V unit and supply physical integrity. The four-cell string approach to battery design has been validated in test ranging from small networks of four strings to 32 strings in parallel. A cell failure in a string simply results in charge of the three remaining cells in the string by parallel strings. One of the three cells then develops the high effective resistance characteristic of the top of charge of the sodium/sulfur cell, preventing further current flow. The string is then inoperable during the remaining duty life of the battery. Two series banks of 60 cells (15 parallel four-cell strings) forms a battery, which identifies the minimal effect of cell failure on capacity and resistance [14,16].

The operating temperature of 300–350 °C of the Na/S battery necessitates a thermal enclosure for the cell pack. The thermal insulation used in the battery enclosure must satisfy several criteria, depending on the vehicle application. Important factors are cost, volume, weight, load-bearing properties, and long-term thermal performance. Non evacuated insulation material is too bulky for vehicle applications. Evacuated insulation is required to meet volumetric constraints imposed by the vehicle design. Evacuated insulation offers reduced heat losses compared with non evacuated insulation material but poses special problems associated with a need to maintain a low pressure within the insulation space for long periods. In order to keep the vacuum over a long period, the quality of the battery box welds must be extremely good. Sometimes therefore, chemical getter materials – capable of absorbing gases left within the insulation after assembly and also gases entering the system subsequently through small leaks – have been employed. Two insulation materials have been favored for the application in thermal enclosures of Na/S batteries: microporous insulating materials and compressed glass fiber boards. All together heat loss and temperature variations within the enclosure must be kept to a minimum, yet outlets must be provided for main current-carrying terminals and instrumentation channels.

The thermal management of the battery necessitates heaters and cooling devices together with temperature sensors. Both oil

CosMX Exhibit 1008, Page 589 of 633

cooling and air cooling have been applied to sodium/sulfur batteries.

The disadvantage of the heat loss which is caused by the high operating temperature is compensated by the advantage that the sodium/sulfur battery can be operated independently of the ambient temperature, which can vary from –40 to +50 °C.

An electronic management system has been applied which controls all functions of the battery for its operation. Batteries with about 30 kWh have been built for car applications. Due to the permanently increasing demands of the car industry, the performance of the batteries has been improved significantly. As an example, the data of two Silent Power batteries, the old type Mk4 and the recent type Mk6, are compared in Table 4.

11.3.4 Corrosion-Resistant Materials for Sodium/Sulfur Cells

A prerequisite of long-life sodium/sulfur batteries is that the cells contain suitable corrosion-resistant materials which withstand the aggressively corrosive environment of this high—temperature system. Stackpool and Maclachlan have reported on investigations in this field [17]. The components in an Na/S cell are required to be corrosion-resistant towards sodium, sulfur and especially sodium polysulphides. Four cell components suffer particularly in the Na/S environment: the glass seal, the anode seal, the cathode seal, and the current collector (in central sodium arrangements, the cell case).

11.3.4.1 Glass Seal

The glass seal mainly shows corrosion problems relating to the thermodynamic stability of the glass at the sodium interface. In order to be ionically insulating , the glass should not include significant quantities of sodium oxide, and therefore it is also stable towards sulfur. Additionally, the sealing glass thermal expansion coefficient should be such that the glass is in compression at the cell operating temperature of about 300—350 °C. Employing the above criteria, mixed alkaline-earth—aluminum borate glasses have been identified as a viable solution. Such glasses have been operated satisfactorily in cells with lifetimes extending to about five years.

11.3.4.2 Cathode and Anode Seal

Besides the necessity for corrosion resistance in seals, seal stresses generated during thermal cycling must not fracture the bond interfaces. The anode as well as the cathode seals in sodium/sulfur cells consist of ceramic-to-metal thermocompression bonds between metal components and the α–alumina header. Thermocompression bonds are formed by heating the components in an evacuated chamber and applying a load under these conditions. Elemental diffusion occurs at the conducting interfaces. Such seals have typical leak rates of 10^{-10} l s^{-1}. Intermetallics are also formed during the actual bonding operation. The life-timing factor of the seals is the growth of intermetallics when they are held at the cell operating temperature for prolonged periods of time. The growth of thicker intermetallic layers can seriously reduce seal strength owing to corrosive attack of the compounds formed in the intermetallic layers.

For the cathode seal material, there is a criterion that the thermal expansion coefficient of the metal component must be lower than that of the α–alumina header. A nickel–cobalt–iron alloy (NiloK) with a

CosMX Exhibit 1008, Page 590 of 633

thermal expansion of $6.1x10^{-6}\,°C^{-1}$ was identified as a suitable material. This showed a stability of the bond for more than about four years at 330 °C.

The anode seal which closes the sodium compartment is a nickel—chromium alloy (Inconel 600). The application of Inconel 600 minimizes the growth of thick intermetallics and it was shown that seals of this material have been operated for over three years. Contrarily to Inconel, the application of mild steel as the anode seal material gave a life of only 6000 h due to gross intermetallic growth which caused sodium attack of this intermetallic layer in the mild steel.

11.3.4.3 Current Collector for the Sulfur Electrode

The main criteria for the selection of the current collector material in a central sulfur cell or for the cell case material in a central sodium cell are corrosion resistance to sulfur and sodium polysulfides, good electrical conductivity, and low costs. This cost argument has led to coated materials which have been compared with nickel—chromium alloys (Inconel 600).

The high resistivity of Inconel 600 ($110x10^{-8}\,\Omega m$) demanded the application of this material as a composite with a central aluminum core. The aluminum was totally enclosed in Inconel 600 so that the Inconel was only exposed to sulfur and polysulfides. In a test over more than three years, cells with a composite current collector of this kind suffered from a high capacity decline. Post-test analysis showed that Inconel sustained polysulfide attack with the formation of a duplex nickel and chromium sulfide layer on the current collector surface.

Aluminum itself cannot be used as a current collector or cell case material due to the formation of a high-resistivity aluminum sulfide layer. Therefore a surface protection has to be applied which necessitates a corrosion-resistant but electrically conductive coating. Good results have been obtained with aluminum coated with a layer of nichrome and covered by a secondary protective coating of carbon, which formed a tightly adherent, corrosion-resistant, outer layer. Post-mortem examination after four years of operation showed that such a current collector had been largely unaffected by the very aggressive environment.

11.4 Components for High-Temperature Batteries

11.4.1 The Ceramic Electrolyte β''–Alumina

The electrolyte β''–alumina has already been described in Chapter III, Sec. 9. This section relates to additional information on the manufacture of β''–alumina and its application and behavior in high-temperature batteries (ZEBRA and Na/S).

There are a number of oxides known to belong to the β–alumina group, which may be subdivided into those members containing a two-fold screw axis and those containing a three-fold screw axis. The arche types of the two subgroups are designated β–alumina and β''–alumina respectively, and there are fundamental differences between the properties of the two forms. The β–alumina group of oxides is characterized by structures composed of alternating slabs of close-packed oxides and layers of low atom density containing mobile sodium cations. The close-packed oxide slabs accommodate small metal ca-

CosMX Exhibit 1008, Page 591 of 633

tions (typically Al^{3+}). The β and β''–alumina structures are described by Moseley [18]. Both β and β''–alumina posses structures which are highly defective in the sodium-containing zones.

The β–alumina structures are remarkable not only for their ionic conductivities but also for the versatility in isomorphous replacement. There is little of the structure of $(Na_2S)_{1+x} \cdot 11Al_2O_3$ which cannot be substituted, at least in part, by an alternative ion. MgO and Li_2O are preferred additives to β–alumina in order to obtain good ionic conduction with no electronic contribution.

Reliable thermodynamic and phase diagram data are only available for undoped β–alumina. Even for the binary system, the stoichiometry range of the material and the intervention of the metastable β''–phase pose problems for experimental determination. The β''–phase, formed at around 1100 °C, disproportionates to β–alumina and $\delta - NaAlO_2$ when the temperature is raised to 1550 °C. β''–Alumina is in fact metastable in the absence of dopants. The presence of MgO or Li_2O dopants modifies the phase stability profoundly. The phase diagram for the system Na_2O/Al_2O_3 shows the β–alumina region (Fig. 12); the hatched region corresponds to the coexistence of β- and β''–alumina.

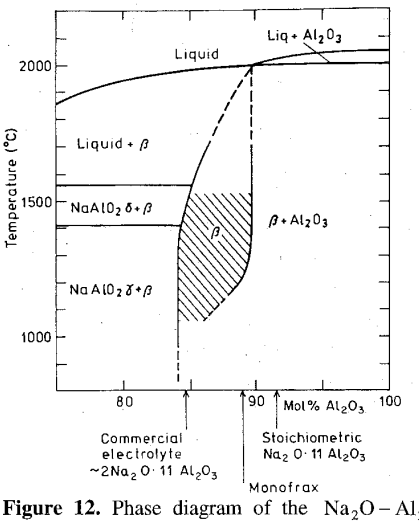


Figure 12. Phase diagram of the $Na_2O - Al_2O_3$ system. Hatching indicates the coexistence of β– and β''–Al_2O_3. Reproduced with permission of Champan and Hall, London.

11.4.1.1 Doping of β'' - Al_2O_3

From the two main subgroups of β–alumina, $\beta - Al_2O_3$ and $\beta'' - Al_2O_3$, the $\beta'' - Al_2O_3$ is the preferred phase for battery applications due to its higher conductivity. The formation of β''–alumina compared to β–alumina depends on the preparation route as well as on the starting materials. The synthesis of $\beta'' - Al_2O_3$ from an $\alpha - Al_2O_3$ precursor has the disadvantage that the two-phase mixture of $\beta - Al_2O_3$ and $\beta'' - Al_2O_3$ is formed by the reconstructive transformation of the hexagonal close-packed oxygen lattice of $\alpha - Al_2O_3$ to the cubic close-packed stacking sequence of the oxygen ions in the spinel blocks in β–alumina. When β''–alumina compositions based on reactive α–aluminas are heated to 1200 °C, phase conversions to β–aluminas is complete with a ratio of β'' to β of approximately 40:60. The β''–alumina will decompose above 1500 °C to β–alumina. Therefore spinel formers, such as Li_2O or MgO, are added to the raw materials. Due to the dopants the level of β''–alumina increases with increasing temperature above 1200 °C, so that a fully dense artifact of β''–alumina could be obtained by sinteting at 1600 °C.

11.4.1.2 Manufacture of β''–Alumina Electrolyte Tubes

The manufacture of $\beta'' - Al_2O_3$ tubes for

CosMX Exhibit 1008, Page 592 of 633

batteries should result in a product with the properties of high sintered density, fine closed porosity, low electrical resistivity, good mechanical strength , and close dimensions. The formation of β''–alumina electrolyte depends on the starting materials as well as on the production process itself. Different starting materials necessitate different production routes. Some key requirements which strongly influence the production process must be mentioned:

- Careful control of chemical composition and purity of starting materials
- Homogeneous mixing of the constituents
- Careful attention to detail in the forming process
- Accurate control of the sintering process
- Development of suitable quality-control procedures

The difficulty of obtaining pure β''–material for the electrolyte has been tackled in many production processes worked out in the past. Unless precautions are taken, sintering of α–alumina-derived β''–alumina compositions invariably results in the duplex microstructure and a low-strength ceramic. Therefore a balance has to be struck between conductivity and strength. The problem arises because the conversion from β–alumina to β''–alumina is slow compared with a rapid densification and grain growth. Barrow and Duncan have classified the process into four main routes [19]:

(1) Rapid firing followed by a subsequent anneal. This process relies on sintering quickly before any grain growth can occur, and then an anneal at a lower temperature where little growth can occur, to aid conversion from β–alumina to β''–alumina.

(2) To-peak firing. With this process time is allowed on either side of the first, lower, temperature peak, so that on approaching the final temperature the β''–alumina content is higher than during a normal "straight-trough" firing. The cooldown of 170—200 °C after the first peak controls the duplex microstructure of β''–alumina, maximizing the strength when the material is reactively sintered in a single firing operation. The extra energy involved in the two-peak firing increases the degree of conversion to low-resistivity β''–alumina and increases the crystal size of the matrix while the growth of large individual β''–alumina crystals is restricted.

(3) Zeta process. This process improves the mixing and uses the ξ-spinel $LiAl_5O_8$ as a spinel-former additive. In doing this the proportion of β''–alumina at 1260 °C is increased to 65 percent.

(4) Seeding. This process relies on addition of approximately 2 percent of β''–alumina seeds to powders, which increases the amount of β''–alumina formed.

The results of development work on processes indicate that the two main methods of preventing the duplex microstructure from forming appear to be fast-firing, or increasing the amount of β''–alumina at low temperatures. Based on these results, Duncan et al. [20] and Zyl et al. [21] have described production processes starting from aluminum oxy–hydroxides or aluminum hydroxides as precursors for the synthesis of the solid electrolyte β''–alumina. Duncan et al. described an alumina precursor which substitutes in part or wholly for α–alumina in an established

CosMX Exhibit 1008, Page 593 of 633

slurry solution spray-drying process. As precursors, hydrothermal boehmite, "Cera" hydrate, has been used. A calcination step is important at the beginning of the process. Boehmite was used both in the as-received condition and after calcination. The effect of the calcination temperature on the fired properties of β''-alumina can be seen in Table 5.

Table 5. Effect of calcination temperature of "Cera" hydrate on the fired properties of β''-alumina

Temperature (°C)	Na_2O (wt%)	Li_2O (wt%)	β''-alumina (%)	Density ($g\,cm^{-3}$)
0	9.3	0.72	96	3.17
560	9.3	0.7	96	3.20
640	9.0	0.7	99	3.20
700	9.2	0.7	95	3.21
790	9.2	0.7	95	3.18
925	9.0	0.7	96	3.19
1050	8.7	0.66	93	ND*

*ND, Not determined

A comparison of boehmite with other raw materials is included in Table 6. In this table the soda and lithia contents of compositions based on a range of raw materials and the resultant properties are detailed. The level of β''-alumina was always higher with the hydrate-type raw material; the hydrothermally prepared raw materials gave the highest content of β''-alumina.

Van Zyl et al. described the starting materials boehmite, pseudoboehmite, bayerite, and gibbsite. In contrast to the distinct two- phase mixture of $\beta-Al_2O_3$ and $\beta''-Al_2O_3$ which results from the reaction of $\alpha-Al_2O_3$ with Li_2CO_3 and Na_2CO_3, van Zyl et al. found that a single-phase $\beta''-Al_2O_3$ product can be prepared from boehmite and bayerite and that an intergrown $\beta/\beta''-Al_2O_3$ product is formed from gibbsite and pseudoboehmite. The transition aluminas, which can be derived from the hydroxy-aluminas boehmite and bayerite, are characterized by a regular cubic close-packed oxygen-ion array. The lithium ions play a critical role in stabilizing the overall cubic close-packed oxygen framework of this solid electrolyte. By contrast, the hydroxy-aluminas pseudoboehmite and gibbsite, which form transition aluminas with an irregular oxygen-ion stacking sequence, produce intergrown $\beta-Al_2O_3$ and $\beta''-Al_2O_3$ products. The formation of the intergrown product is attributed to the inability of the Li^+ ions to diffuse uniformly through the negatively charged alumina framework that has both hexagonal close-packed and cubic close-packed character.

The overall manufacturing process of β''-alumina tubes can be subdivided into the production stages powder preparation,

Table 6. Properties of β''-aluminas derived from aluminum oxide from various sources

Raw material	Na_2O (wt%)	Li_2O (wt%)	β''-Alumina %		Fired density ($g\,cm^{-3}$)	Strength by Bortz ring test ($MN\,m^{-2}$)
			1200 °C 6 min	1617 °C 20 min		
Alcoa A16SG	8.9	0.65	41	76	3.20	173
Two-peak firing	8.9	0.65	41	84	3.22	190
BACO gibbsite	9.2	0.64	56	85	3.15	ND
BACO Bacasol 2 (colloidal boehmite)	9.3	0.70	I*	88	3.14	163
Kaiser Versal B (hydrothermal bayerite)	9.4	0.74	83	94	3.20	231
Boehmite (BACO "Cera" hydrate)	9.3	0.72	ND	96	3.17	260
Boehmite (calcined at 700 °C)	9.1	0.65	92	98	3.19	260

CosMX Exhibit 1008, Page 594 of 633

forming, and sintering. The main production routes are shown in Fig. 13. The powder preparation includes mainly milling , spray drying, and calcination steps. These are described in detail by Duncan et al. [22].

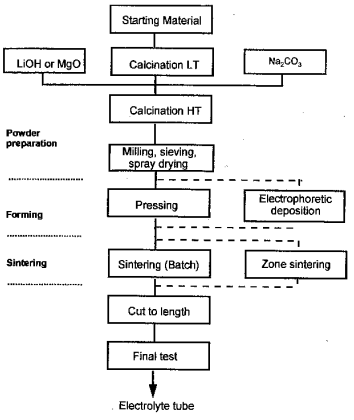


Figure 13. Manufacturing routes of β''–Al_2O_3 electrolytes.

As forming processes, slip casting, extrusion, isostatic pressing and electrophoretic forming have been applied. There are some advantages to isostatic pressing:

- No binder or a minimal amount, needs to be added to the powder to impart strength to the compact.
- The compact has a high strength and can be handled easily immediately it is from the mold.
- The parameters of isostatic pressing can be adapted to the character of the powder.
- Dry-bag pressing is know as well-suited mass production method.

The electrolytes for ZEBRA batteries at AEG Anglo Batteries as well as for the NaS batteries at ABB are manufactured by the isostatic method. In contrast to this, Silent Power used electrophoretic deposition as the forming method for their sodium/sulfur batteries. Heavens showed that with precise control of forming conditions it is possible to obtain good microstructural control in β''–Al_2O_3 ceramics but he admitted that this electrophoretic forming can be difficult to achieve under production conditions [23]. Improvements in control of grain growth can be achieved by the addition of zirconia as a second phase in order to effect transformation toughening. The zirconia phase is well dispersed, with 80 percent retained in the tetragonal form, and substantial increases in both strength and fracture toughness are obtained, with no adverse influence on the electrical properties of the ceramic.

Sintering is a most difficult process to control and potentially the most expensive operation involved in the fabrication of β''–alumina electrolyte tubing. Two sintering techniques have been described: batch sintering and continuous sintering. In batch sintering the tubes are normally sintered in a free—standing vertical position and an encapsulation tube is placed over the electrolyte. The encapsulation keeps a sodium-rich atmosphere around the β–alumina tube. Heating rates between 70 and 200 $°Ch^{-1}$ and top temperatures of around 1600 °C have been applied. The grain size is strongly dependant on the maximum temperature and the hold time.

The continuous sintering is mainly a zone sintering process in which the electrolyte tube is passed rapidly through the hot zone at about 1700 °C. This hot zone is small (about 60 mm); in zone sintering, no encapsulation devices are employed. The sodium oxide vapor pressure in the furnace is apparently controlled by the tubes themselves. Due to the short residence time in the hot zone, the problem of soda loss on evaporation can be circumvented. A detailed description of β''–alumina sintering is given by Duncan et al. [22].

CosMX Exhibit 1008, Page 595 of 633

11.4.1.3 Properties of β''-Alumina Tubes

Life and reliability data of β''-alumina tubes have been reported by Barow[24]. Table 7 includes the dimensions and physical properties of β''-alumina tubes, and Table 8 shows the resistivity of β''-alumina tubes at 300 and 350 °C. The resistivity at 350 °C reported by Heavens [25] is somewhat lower. The resistivity of β''-alumina remains nearly constant even when zirconia is added (Fig. 14).

Table 7. Dimensions and physical properties of β''-alumina tubes (laboratory-made)

Strength ($MN\,m^{-2}$)	219.0
Density ($g\,cm^{-3}$)	3.22
Wall thickness (mm)	1.65
Internal diameter (mm)	29.30
External diameter (mm)	32.60
Dome thickness (mm)	2.00

Table 8. Resistivity of β''-alumina tubes

	300 °C	350 °C
Axial resistivity (ohm·cm)	6.35	4.46
Radial resistivity (ohm·cm)	7.7	5.8

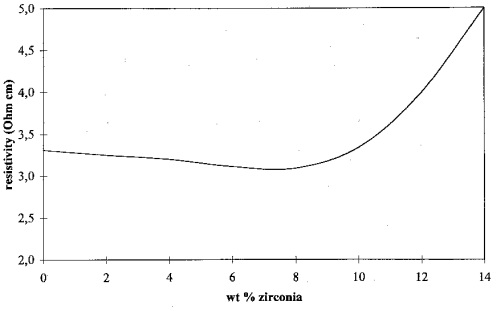


Figure 14. Resistivity of β''-alumina doped with zirconia.

The preparation method also influences the resistivity of β''-alumina tubes. Bugden and Duncan [26] showed that the resistivity of tubes made from spray-dried powder is lower ($4.3\,\Omega cm$) than that of tubes of vacuum-dried powder (5.5 Ωcm).

Compared with the ionic conductivity of β''-alumina tubes, the electronic conductivity is negligible. The electronic resistivity was found to be $10^9\,\Omega$cm at 300 °C and $7\times10^3\,\Omega$cm at 1000 °C [27].

11.4.1.4 Stability of β-Alumina and β''-Alumina

The chemical stability of the β species has been investigated in sulfur/sodium polysulfide melt [28] and in sodium/$FeCl_2$ cells [29]. In regard to its chemical stability β/β''-alumina is unique as a solid electrolyte. It is reasonable to expect that β/β''-alumina ceramic will equilibrate rapidly in sodium by absorbing Na_2O. In molten sulfur, Na_2O is abstracted from the conduction planes so that the Na_2O comes into equilibrium with the melt, without the β/β''-alumina structure being affected.

Thermodynamic data suggest that β-alumina is stable in sulfur and that Na_2O-rich β''-alumina maybe unstable to some degree. In the latter event, depletion of Na_2O from β''-alumina according to Eq. (5) would result in a surface layer resistant to further corrosion. A significant corrosion reaction does occur be-

CosMX Exhibit 1008, Page 596 of 633

tween sulfur and $NaAlO_2$ but, even at this high Na_2O activity, passivation occurs within a few days. Concentration of up to 1 percent $NaAlO_2$ can occur in sintered β/β''–alumina ceramic and it is probably advisable to minimize this by ensuring complete conversion to β''–alumina during the sintering process.

$$Na_2O \cdot yAl_2O_3 + 4zS \rightarrow 3z/4Na_2S_5 + z/4Na_2SO_4 + (1-z)Na_2O \cdot yAl_2O_3 \quad (5)$$

The investigation of the stability of β–alumina in ZEBRA cells, which always contain some iron, showed an increase of resistance under certain extreme conditions of temperature (370 °C) and of voltage. This is related to the interaction of the β–alumina with iron and it was shown that iron enters β–alumina in the presence of an electric field when current is passing, if the cell is deliberately overheated. However, it was found that only the β–phase but not the β''–phase was modified by the incursion of iron. The resistance of the iron-doped regions was high. It was shown that the addition of NaF inhibits access of the iron to the β''–alumina ceramic. By doping practical cells these difficulties have now been overcome and lifetime experiments show that the stability of β''–alumina electrolytes are excellent in ZEBRA cells.

11.4.2 The Second Electrolyte $NaAlCl_4$ and the $NaCl-AlCl_3$ System

The properties of the molten electrolyte sodium aluminum chloride influence the performance and the behavior of the ZEBRA cell.

11.4.2.1 Phase Diagram

The electrolyte $NaAlCl_4$ is prepared by reaction of salt with $AlCl_3$. Therefore the phase diagram of the system $NaCl-AlCl_3$ is of fundamental interest. The system was studied several times earlier in the 20th century, but Levin et al. investigated it again in 1974 [30]. The phase diagram resulting from these studies is shown in Fig. 15

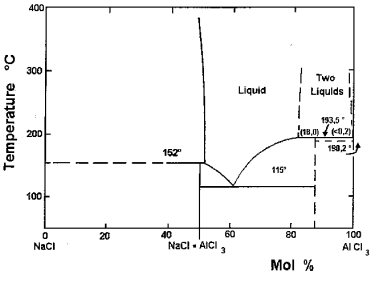


Figure 15. Phase diagram of the $NaCl-AlCl_3$ system.

It was confirmed that the system contains one intermediate compound, $NaAlCl_4$ with an incongruent melting point of 153 ± 0.5 °C. Additionally, an $NaAlCl_4-AlCl_3$ eutectic exists at 61.4 mol% $AlCl_3$. Further it was found the two-liquid region above 80 percent $AlCl_3$ is present at a temperature of 191.3 °C. The region of liquid immiscibilty extends from 80.25 to 99.6 mol% $AlCl_3$. The ZEBRA cell works with the intermediate compound $NaAlCl_4$ with 50 mol% $AlCl_3$ and 50 mol% NaCl and at temperatures well above 250 °C. In this region only the molten $NaAlCl_4$ is present in the system. This composition will vary slightly, e.g., in case of overcharge when $AlCl_3$ formation occurs. Under these circumstances $AlCl_3$ is dissolved in the $NaAlCl_4$ melt, which represents the liquid phase in the diagram.

CosMX Exhibit 1008, Page 597 of 633

11.4.2.2 Vapor Pressure

Another important parameter is the vapor pressure of the melt system at operating temperature, and above when the cell is overheated. The vapor pressure of the system $NaCl-AlCl_3$ was investigated by Dewing [31], who found that both $AlCl_3$ and $NaAlCl_4$ could be evaporated. The vapor pressures for mixtures with 49.5 mol% $AlCl_3$ are shown in Fig. 16. It was found that from a melt with 50 mol% $AlCl_3$, distillates obtained above 550 °C contained significant quantities of sodium. This was explained by the evaporation of $NaAlCl_4$. Melts with more than 50 mol% $AlCl_3$ showed that no volatile sodium compounds were present in the gas phase.

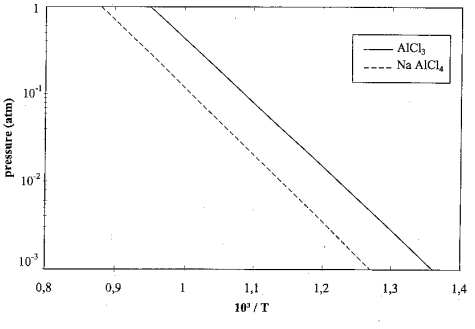


Figure 16. Vapor pressure versus temperature of a $NaCl-AlCl_3$ mixture with 49.5 mol% $AlCl_3$.

Morozov and Morozov [32] have also investigated the temperature dependence of the pressure and composition of the vapors and confirmed that the vapors contain aluminum chloride as well as sodium tetrachloroaluminate. This could be shown experimentally by condensing the vapors which occurred in two zones. In a temperature range from 600 to 800 °C the pressures of $AlCl_3$ and $NaAlCl_4$ over sodium tetrachloroaluminate are quite similar; they rise from about 10 mm Hg at 600 °C to about 130 mmHg at 800 °C. Over mixtures which are NaCl–rich (i.e., $AlCl_3$ 25mol%, NaCl 75 mol%) the partial pressure of $AlCl_3$ becomes significantly less than for the pure tetrachloroaluminate. The vapor pressure of $AlCl_3$ amounts at 790 °C to 14.9 mm Hg and that of $NaAlCl_4$ to 56.6 mm Hg.

In the discharged state of ZEBRA batteries NaCl is formed in the positive electrode, which is beside the $NaAlCl_4$. In abuse experiments, e.g., overheating , less volatile material will be released in the discharged state compared with the charged state where no NaCl is present. This is due to the lower vapor pressure of mixtures with increased NaCl content.

11.4.2.3 Density

For the calculation of free volume inside the cell, which is essential for the design of a ZEBRA cell to keep internal pressure low for safety reasons, the density of molten $NaAlCl_4$ over the full temperature range between 160 and 600 °C should be known. Berg et al. [33] have compared these values with the literature. The densities are compiled in Table 9.

Table 9. Density of molten $NaAlCl_4$

Temperature (°C)	Density (gcm^{-3})
165.6	1.7091
195.4	1.6805
200.0	1.675
245.3	1.6413
299.8	1.5996
409.0	1.5171
511.5	1.4399
594.2	1.3810

11.4.2.4 Viscosity

The viscosity of the $NaCl-AlCl_3$ melt system was investigated near the $NaAlCl_4$ region by Cleaver and Koronaios

CosMX Exhibit 1008, Page 598 of 633

[34]. The viscosity η can be described by the function

$$\ln\eta = a + b/T + c(x - 0.5) \qquad (6)$$

where a,b, and c are constants, T the absolute temperature and x the concentration of $AlCl_3$. The results of the measurements show a strong dependence on the temperature; the values for $x = 0.502$ are included in Table 10.

Table 10. Viscosity, η, of $NaCl - AlCl_3$ melt system

Molar fraction, x_{AlCl_3}	Temperature, $t(°C)$	$\eta(mPas)$
0.4893	350	0.980
0.4925	300	1.247
0.4954	250	1.631
0.502	250	1.672
	275	1.454
	300	1.265
	325	1.111
	350	0.986
	400	0.858
0.525	250	1.734
0.532	250	1.676
	275	1.438
0.587	275	1.580
	300	1.403

With increasing content of $AlCl_3$ the viscosity increases.

11.4.2.5 Dissociation

It is assumed that $NaAlCl_4$ is dissociated into sodium and tetrachloroaluminate ions. Torsi and Mamantov [35] have investigated a further dissociation of the tetrachloroaluminate ion in molten sodium chloroaluminates by potentiometric studies. For the 50:50 mol% composition of $NaCl - AlCl_3$ the principal anion is $AlCl_4^-$. In acidic melts it was assumed that the reaction $AlCl_3 + AlCl_4^- \leftrightarrow Al_2Cl_7^-$ is quantitative. More important is the concentration of chloride ions in $NaAlCl_4$ saturated with $NaCl$, i.e. the solubility of $NaCl$. Figure 17 shows the solubility of $NaCl$ versus the temperature of the $NaAlCl_4$ melt.

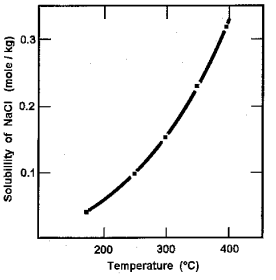


Figure 17. Solubility of NaCl in $NaAlCl_4$ melt versus temperature.

11.4.2.6 Ionic Conductivity

The most interesting parameter of the $NaCl - AlCl_3$ system is its conductivity at the operating temperature. It was found by Howie and Macmillan [36] that the conductivity χ can be described by Eq. (7),

$$\chi = (A_0 + B_0T) - (A_1 + B_1T)W + (A_2 + B_2T)W^2 \qquad (7)$$

where W is the content (wt.%) of $NaCl$ and $A_0, A_1, A_2, B_0, B_1, B_2$ are constants. Measurements to confirm this equation were taken only in the region 160–200 °C and over the range of composition between 15 and 30 wt.% of sodium chloride. It was stated that χ depends firstly on the temperature and secondly on the concentration of sodium chloride.

The ionic conductivity of alkali-metal chloroaluminates was also investigated by Weppner and Huggins [37] but also only in the temperature range between room temperature and just above the melting point. At room temperature the ionic conductivity

CosMX Exhibit 1008, Page 599 of 633

of $NaAlCl_4$ was found to be 3.5×10^{-7} $\Omega^{-1}cm^{-1}$. With increasing temperature the ionic conductivity also increases and after melting the melts showed the expected high conductivities in the range 10^{-1}–1 $\Omega^{-1}cm^{-1}$.This is about 10^3 to10^4 times higher than in the solid state before melting. It was stated that $NaAlCl_4$ is practically a pure ionic conductor. Because of its size the $AlCl_4^-$ ions are assumed to be relatively immobile. The conductivity may therefore be attributed to the motion of the sodium ion.

Janz et al. compiled the specific conductance values in the temperature range from 460 to 540 K (187 to 267 °C) [38]. With a decreasing NaCl content compared with $NaAlCl_4$ (the melt becomes acidic) the conductance also decreases. Table 11 contains the conductance values.

Table 11. Conductance of NaCl – $AlCl_3$ melts ($\Omega^{-1}cm^{-1}$)

Temperature, T(K)	NaCl(mol%)		
	50	49.2	42.2
460	0.462	0.453	0.309
470	0.490	0.477	0.329
480	0.517	0.501	0.348
490	0.544	0.525	0.368
500	0.572	0.549	0.387
510	0.599	0.573	0.406
520	0.626	0.598	0.426
530	0.654	0.622	0.445
540	0.681	0.646	0.465

11.4.2.7 Solubility of Nickel Chloride in Sodium Aluminum Chloride

The solubility of nickel chloride in the molten electrolyte is of interest because high solubilities of nickel chloride will cause capacity loss over the lifetime. Dissolved nickel chloride will not be contacted by the electronically conductive backbone nickel and cannot participate in the discharge reaction. Therefore it is essential that the nickel chloride is formed on nickel grains and will remain there until it is discharged to nickel. Macmillan and Cleaver have investigated the solubility of nickel chloride in $NaAlCl_4$ saturated with sodium chloride [39]. This system is normally present in ZEBRA cells. Only in the fully charged state all the NaCl is converted to nickel chloride and sodium. In this case the solubility of nickel chloride in $NaAlCl_4$ is relevant. It was found that the solubility of $NiCl_2$ will fall if the concentration of NaCl in $NaAlCl_4$ is reduced. A minimum in solubility of $NiCl_2$ is observed when the ratio $AlCl_3$:NaCl is exactly 1:1 ($NaAlCl_4$). This occurs in the fully charged state of the ZEBRA system. Table 12 shows the solubility of $NiCl_2$ in NaCl–saturated $NaAlCl_4$ in the range 200–400 °C. It can be seen that, under the conditions applied, $NiCl_2$ is around two orders of magnitude less soluble than NaCl in $NaAlCl_4$. In Macmillan and Cleaver's model it is assumed that $NiCl_2$ dissolves as a complex, $NiCl_4^{2-}$. Form the table it can also be seen that the solubility of $NiCl_2$ as well as of NaCl increases with increasing temperature.

Table 12. Solubility of $NiCl_2$ and NaCl in NaCl-saturated

Temperature, t(°C)	Solubility (mol kg^{-1})	
	$NiCl_2$	NaCl
200	$(2.34-2.95)\times10^{-4}$	0.05
250	$(6.31-7.41)\times10^{-4}$	0.09
300	$(1.20-1.51)\times10^{-3}$	0.15
350	$(2.14-2.75)\times10^{-3}$	0.22
400	$(4.18-5.30)\times10^{-3}$	0.32

The dissolution of $AlCl_3$ in the $NaAlCl_4$ melt makes the melt acidic. The acidic-base concept has been discussed by Blander et al. [40]. An acidic melt influences the solubility of the nickel chloride in the ZEBRA cell: the solubility of the nickel chloride increases.

CosMX Exhibit 1008, Page 600 of 633

11.4.3 Nickel Chloride $NiCl_2$ [41] and the $NiCl_2$–NaCl System

11.4.3.1 Relevant Properties of $NiCl_2$

Relevant properties of $NiCl_2$ are listed in Tables 13-16.

11.4.3.2 $NiCl_2$–NaCl System

In the ZEBRA cell system about 30 percent of the nickel metal is converted to $NiCl_2$ during charging. During charging as well as during discharging both components, NaCl and $NiCl_2$, are present in the positive electrode material. Therefore the phase diagram for the $NiCl_2$–NaCl system will apply (Fig. 18). The phase diagram $NiCl_2$–NaCl published by Bolshakov and Fedovov [42] shows that within the possible temperature range of operation (160–400 °C) two phases exist in equilibrium; this has been confirmed in practice both by X-ray diffraction of partially charged cathodes and by accurate coulometric titrations. Above the two-phase region of NaCl and $NiCl_2$ eutectic composition exists at a temperature of 570 °C.

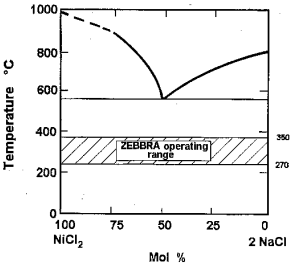


Figure 18. Phase diagram of the NaCl – $NiCl_2$ system. The stipled area is the operating region of the ZEBRA cell.

Table13. Properties of $NiCl_2$

Free energy of formation, ΔG°_{298}	$-65.1\ kcal\,mol^{-1}$
Heat of formation, Q	$75.5\ kcal\,mol^{-1}$
Crystal form	Pseudocubic rhombohedron
Colour	Light to dark yellow
Density at 25 °C	$3.544\ g\,cm^{-3}$
Melting point	1009 °C
Heat of fusion	$18.47\ kcal\,mol^{-1}$
Sublimation temperature, T_s	1241 K (730 Torr)
Heat of sublimation, L_s	$53.81\ kcal\,mol^{-1}$ (1 atm)

Table 14. Vapor pressure of $NiCl_2$

T(K)	973	993	1010	1025	1056
t(°C)	700	720	737	752	783
p(Torr)	1.59	3.04	4.94	6.66	13.29

Table 15. Enthalpy of $NiCl_2$

T(K)	400	500	600	700	800	900	1000
$H_T - H_{298}\ (cal\,mol^{-1})$	1800	3650	5545	7465	9400	11360	13350

Table 16. Pressure of dissociation p_{Cl_2} for the reaction $NiCl_2 \rightarrow Ni + Cl_2$

t(°C)	300	350	450	500	550
$\log(p_{Cl_2})$	−19.59	−17.47	−14.10	−12.74	−11.71

CosMX Exhibit 1008, Page 601 of 633

11.4.4 Materials for Thermal Insulation

Batteries with a high operating temperature, of about 300 °C, require high-efficiency insulating jackets to maintain the temperature within an acceptable range. Especially in non operating periods, the battery should not cool down. It was requested that batteries should keep their operating temperature window for at lest four days. This requires heat loss rates of less than 200 W for a 40 kWh battery.
The thermal insulation has also to fulfill the further requirements of:

- Stability to atmospheric pressure after evacuation;
- Stability to acceleration forces;
- Low density (i.e. low weight);
- Stability at temperatures up to 800 °C; and
- Low cost.

To limit the thickness of the insulation, and thus the battery volume, the battery insulation is usually maintained at a vacuum of 10^{-3} mbar or less. This makes possible the use of jackets that are only15–30 mm thick.

The factors that must be controlled for efficient insulation are the amounts of heat transferred by radiation, by conduction through the solid structure, and by conduction through the residual gases.

The heat loss by radiation increases with increasing temperatures, being proportional to T^4. This means there is a steep increase with increasing temperature. It was found that about 50 percent of heat loss of a battery is caused by radiation. In order to reduce the transmission of radiation through the thermal insulating material, opacifiers are added to the insulating material.

The heat conductivity in solids occurs via phonons. This conductivity is ideal in single crystals and is considerably reduced in porous solids, by one to two orders of magnitude. Therefore thermal insulation materials are built up of small particles which should touch each other at only a few points. This effect is of course enhanced by a low density of the material.

The conduction through residual gases can be reduced by the application of porous structures. The convection within a single pore is minimal if pore sizes are small. In small pores the temperature difference at the walls of the pore are negligible and no convection occurs. The convection is further reduced by the evacuation of the thermal insulating material.

In order to control the three factors determining heat transfer, much effort has been spent on developing vacuum insulation for high—temperature batteries involving the use of microporous powders pressed to boards, glass fiber boards, or multifoil insulation.

11.4.4.1 Multifoil Insulation

Nelson et al. have described a variable-pressure insulating jacket for high-temperature batteries [43]. In this case the multifoil insulation is combined with flooding with hydrogen released from a hydrogen-gathering alloy operating in the range 50–250 °C. This flooding with hydrogen provides cooling, because of the good thermal conductivity of hydrogen gas. In the insulating mode the hydrogen is absorbed in the getter; in the conducting mode the hydrogen is released by increasing the temperature of the getter. The rate of heat loss through multifoil insulation 1.5 cm thick could be varied by a factor of about 500. The multifoil insulation was built up of alternating layers of aluminum

CosMX Exhibit 1008, Page 602 of 633

foil 7.6 μm thick and of glass paper foil 80 μm thick. This approach requires cylindrical batteries around which about 60 layers have been wrapped.

The disadvantages of multifoil insulation jackets are the high compresibility (about 20 percent under atmospheric pressure), the low residual gas pressure necessary after evacuation (less than 10^3 mbar), and the high cost.

11.4.4.2 Glass Fiber Boards

Glass fiber boards are manufactured from glass microfibers with a diameter of less than 1 μm, by pressing into plates [44]. The heat treatment at 500 °C after the pressing ensures the stability of the shape. The boards have a low compressibility (about 5 percent). This will be obtained by adjusting the density of the boards to $0.3\,g\,cm^{-3}$.

Glass fiber board consisting of a borosilicate glass shows a thermal conductivity under pressure which is dependent on the temperature (Table 17). There is a natural concern about the safety of any fiber material which has the potential to give off particles which can be inhaled. In a report on health risks with microglass fibers [45], it was stated that glass fibers may cause skin, eye, and upper respiratory tract irritation but do not cause cancer or diseases like asbestos. It was found that the fine fibers will dissolve slowly but steadily in bodily fluids and will be more readily cleared from the lung.

11.4.4.3 Microporous Insulation

Microporous insulation materials consist mainly of highly dispersed silica with a particle size of only 5–30 nm. The highly dispersed silica powder is pressed to plates, which receive heat treatment up to 800 °C, after which the plates are self-supporting and possess a micropore structure with pore diameter of 0.1 μm. The addition of opacifiers to the highly dispersed silica starting material reduces the loss of heat by radiation. The dates for such insulation boards are shown in Table 18.

Table 17. Glass fiber board thermal insulating material

Composition	Borosilicate glass fibers
Density ($g\,cm^{-3}$)	0.201
Specific thermal conductivity at 1 bar ($W\,m^{-1}\,K^{-1}$)	
50 °C	0.035
100 °C	0.040
150 °C	0.046
200 °C	0.050
250 °C	0.053
300 °C	0.058
350 °C	0.062
400 °C	0.066
500 °C	0.075
Max. continuous operating temperature (°C)	500

Table 18. Microporous powder pressed to platens as a thermal insulating material

Composition (%)	
SiO_2	65.4
FeO	14.8
TiO_2	16.3
Al_2O_3	2.3
Density ($g\,cm^{-3}$)	0.25–0.35
Specific thermal conductivity at 1 bar ($W\,m^{-1}\,K^{-1}$)	
20 °C	0.02
200 °C	0.021
450 °C	0.025
Max. operating temperature (°C)	
Continuous	850
Short-term	950
Strength at 10 % compression $N\,mm^{-2}$	1–3
Specific heat capacity ($J\,kg^{-1}\,K^{-1}$)	1050

CosMX Exhibit 1008, Page 603 of 633

11.4.4.4 Comparison of Thermal Insulation Materials

Other thermal insulation materials are known besides the three described above. These materials are compared in Table 19, which shows that the thermal conductivity can be reduced by a factor of 2–4 by evacuation; in the evacuated state it is below $10\,mW\,m^{-1}\,K^{-1}$ for all materials. The lowest conductivity is shown for foil insulations, but this requires an extremely low pressure of 10^{-5} mbar which is difficult to obtain in practical applications which ought to last for ten years.

Microporous insulation represents a good compromise; its thermal conductivity reaches 4–8 $mW\,m^{-1}\,K^{-1}$ in a pressure range of only 0.1–1 mbar. Another advantage is its maximum operating temperature of 800–900 °C. This ensures the stability of the insulating layer around the battery, even in abuse situations.

11.4.5 Data for Cell Materials

11.4.5.1 Nickel [46]

The relevant properties of nickel are listed in Tables 20–22. It should also be noted that the specific resistance of nickel, ρ, is 9.0 μΩcm at 20 °C; its temperature coefficient $\alpha(K^{-1})$ is given by Eq. (8):

$$\alpha = (1/\rho)\cdot(d\rho/dt) = 0.0069\,K^{-1} \quad (8)$$

between 0 and 100 °C

Table 19. Comparison of thermal insulating materials

Material	Thermal conductivity ($mW\,m^{-1}\,K^{-1}$)	Max. allowed pressure (mbar)	Thermal conductivity at 1 bar ($mW\,m^{-1}\,K^{-1}$)	Density ($g\,cm^{-3}$)	Max. operating temperature (°C)
Glass fiber boards	2.5	10^{-3}	28	0.25–.35	500
Ceramic fiber boards	4–9	$5\times10^{-3}-10^{-2}$	32–50	0.2–0.4	900–1200
Microporous powder					
Boards	4–8	0.1–1	20–22	0.2–0.4	800–900
Micro glass balls	9–10	$<10^{-4}$	20–25	0.11–0.12	500
Aerogel powder	2	$<10^{-2}$	22–25	0.03–0.3	450
Foil insulation	1	$10^{-5}-10^{-3}$	26–50	–	<500
Polyurethane foam (comparison)	–	–	20–22	0.025–0.035	100

Table 20. Thermal expansion of nickel

t(°C)	28	85.4	140.5	199.4	252.1
$(\Delta l/l_0)\times10^{+}$	3.59	11.047	18.604	27.393	35.299
t(°C)	279.2	308	346	370.6	413
$(\Delta l/l_0)\times10^{+}$	39.657	44.528	50.893	55.299	62.153

Table 21. Enthalpy and heat capacity of nickel

T(K)	298.15	400	500	600	700	800
Enthalpy, $H^\circ - H^\circ_{298}$ ($cal\,mol^{-1}$)	0	662	1373	2165	2940	3690
Heat capacity, C_p ($cal\,mol^{-1}\,K^{-1}$)	6.23	6.76	7.47	8.37	7.35	7.44

CosMX Exhibit 1008, Page 604 of 633

1.4.5.2 Liquid Sodium [47]

Tables 23–26 show the variation with temperature of some relevant physical properties of liquid sodium.

1.4.5.3 NaCl [48]

Sodium chloride has a density, D, of 2.168 $g\,cm^{-3}$ (at 0 °C), which depends on temperature according to Eq. (9), where t is the temperature in °C.

$$D = 2.168 - 1.267 \times 10^{-4} t - 1.754 \times 10^{-7} t^2 \quad (9)$$

The dependence of other relevant properties upon temperature is summarized in Tables 27–29.

1.4.5.4 Sulfur and Sodium Polysulfides

An extended set of data is compiled in [11].

Table 22. Thermal conductivity of nickel

T(°C)	100	200	300	400	500
Thermal conductivity, λ($cal\,cm^{-1}\,K^{-1}\,s^{-1}$)	0.198	0.175	0.152	0.142	0.148

Table 23. Density, D, of liquid sodium

t(°C)	97.83	150	200	300	400	500	600
D($g\,cm^{-3}$)	0.9270	0.9152	0.9037	0.8805	0.8570	0.8331	0.8089

Table 24. Thermal conductivity, λ, of liquid sodium

t(°C)	200	300	400	500	600
λ($Wcm^{-1}K^{-1}$)	0.815	0.757	0.712	0.668	0.631

Table 25. Enthalpy, $H^\circ - H_0^\circ$, and heat capacity, C_p, of liquid sodium

T(K)	370.98	400	500	600	700
$H^\circ - H_0^\circ$($cal\,mol^{-1}$)	2680	2899.2	3640.4	4363.4	5065.2
C_p($cal\,mol^{-1}K^{-1}$)	7.62	7.52	7.32	7.10	6.96

Table 26. Specific resistance, ρ, of liquid sodium

t(°C)	100	150	200	250	300	350	400
ρ(μΩ cm)	9.44	11.1	12.9	14.78	16.78	18.92	21.12

Table 27. Linear thermal expansion coefficient, α, of sodium chloride

t(°C)	30	116	195	288	351	400
α($10^{-6}K^{-1}$)	32.2	34.2	35.9	38.1	39.5	40.6

Table 28. Thermal conductivity, λ, of sodium chloride

T(K)	273	340	380	420	460
$\lambda \times 10^3$($cal\,cm^{-1}\,K^{-1}\,s^{-1}$)	18.2	15.8	13.6	11.0	9.6

Table 29. Heat capacity, C_p, of sodium chloride

T(K)	300	350	400	450	500	550	600	650
C_p($cal\,mol^{-1}\,K^{-1}$)	12.0	12.26	12.5	12.69	12.88	13.07	13.26	13.45

CosMX Exhibit 1008, Page 605 of 633

1.5 References

[1] T.D. Kaun, L. Redey, P.A. Nelson, *Proc. IECEC* **1987**, 1085.

[2] J. Coetzer, *J. Power Sources* **1986**, *18*, 377.

[3] R.J. Bones, D.A. Teagle, S.D. Brooker, F.L. Cullen, *J. Electrochem. Soc.* **1989**, *136*, 1274.

[4] A.R. Tilley, R.J. Wedlake, *Electric Vehicle Dev.* **1987**, *6* ,119.

[5] H. Böhm, G. Beyermann, *ÖZE* **1993**, *46* , 468.

[6] R.J. Wedlake, J. Coetzer, I.L. Vlok, *Proc. Int. Power Sources Symp.* **1988**, paper 41.

[7] N.D. Nicholson, D.S. Demott, R. Hutchings, *Proc. Int. Power Sources Symp.* **1988**, paper 39.

[8] J. Coetzer, J.L. Sudworth, *Proc 13th Int. Electric Vehicle Symp.* **1996**, *I*, 637.

[9] H. Böhm, G. Gutmann, *Proc. 13th Int. Electric Vehicle Symp.* **1996**, *II*, 701.

[10] H. Böhm, J.L. Sudworth, *Elektrische Straßenfahrzeuge im Stadtverkehr der Zukunft* **1993**, *B163*, 125.

[11] J.L. Sudworth, A.R. Tilley (Eds.), *The Sodium Sulfur Battery*, Chapman and Hall, London, **1985**.

[12] H. Birnbreier, *VDI Berichte* **1987**, *652*, 201.

[13] W. Auxer, *Proc. 8th Electric Vehicle Symp.* **1988**.

[14] J.W. Jones, *Proc. Beta Battery Workshop VII*, EPRI, Palo Alto, **1988**, p. 13-1.

[15] F.H. Klein, *Proc. Batterien und Batteriemanagement, Haus der Technik, Essen, Feb. 21/21* **1995**.

[16] P.J. Bindin, A. Leadbetter, J. Molyneux, *Proc. Beta Battery Workshop VII*, EPRI, Palo Alto, **1988**, 49-1.

[17] M.F. Stackpool,S. MacLachlan, *Electric Vehicle Dev.*, **1989**, *8* ,30.

[18] P.T. Moseley in Ref. [11],

[19] P. Barow, J.H. Duncan, *Proc. Beta Battery Workshop VII*, EPRI, Palo Alto, **1988**, p. 16-1.

[20] J.H. Duncan, P. Barrow, P.Y. Brown, *Br. Ceram. Proc.* **1989**, *41*.

[21] A. van Zyl, M.M. Thackeray, G.K. Duncan, A.I. Kingon, *Mater. Res. Bull.* **1993**, *28*, 145.

[22] J.H. Duncan, R.S. Gordon, R.W. Powers, R.J. Bones, in Ref [11].

[23] S.N. Heavens, *Br. Ceram. Proc.* **1986**, *38*, 119.

[24] P. Barrow, *Proc. Beta Batterry Workshop VII*, EPRI, Palo Alto, **1988**, p. 36-1.

[25] S.N. Heavens, *J. Mater. Sci.* **1988**, *23*, 3515.

[26] W.G. Budgen, J.H. Duncan, *Science of Ceramics* **1977**, *9*, 348.

[27] M. Steinbrück, *Proc. 28th IECEC* **1993**, *1*, 1799.

[28] R.S. Gordon, S.N. Heavens, A.V. Virkas, N. Weber, *Proc. Beta Battery Workshop VIII*, EPRI, Palo Alto, **1990/1991**, p. 24-1.

[29] P.T. Moseley, R.J. Bones, D.A. Teagle, B.A. Bellamy, R.W.M. Hawes, *J. Electrochem. Soc.* **1989**, *136*, 1361.

[30] E.M. Levin, J.F. Kinney, R.D. Wells, J.T. Benedict, *J.Res. Nat. Bur. St.* **1974**, *78A*, 505.

[31] E.W. Dewing, *J.Am. Chem. Soc.* **1955**, *77*, 2639.

[32] A.I. Morozov, I.S. Morozov, *Russ. J. Inorg. Chem.* **1973**, *18*, 520.

[33] R.W. Berg, H.A. Hjuler, N.J. Bjerrum, *J. Chem. Eng. Data* **1983**, *28*, 251.

[34] B. Cleaver, P. Koronaios, *J.Chem. Eng. Data* **1994.**

[35] G. Torsi, G. Mamantov, *Inorg. Chem.* **1971**, *10*, 1900.

[36] R.C. Howie, D.C. Macmillan, *J. Inorg. Nucl. Chem.* **1971**, *33*, 3681.

[37] W. Weppner, R.A. Huggins, *Phys. Lett.* **1976**, *58A*, 245.

[38] G.J. Janz, R.P.T. Tomkins, C.B. Allen, J.R. Downey, G.L. Gardner, K. Krebs, S.K. Singer, *J. Phys. Chem. Ref. Data* **1975**, *4*, 871.

[39] M.G. Macmillan, B. Cleaver, *J. Chem. Soc., Faraday Trans.* **1993**, *89*, 3817.

[40] M. Blander, Z. Nagy, M. Saboungi, *Proc. Molten Salt Chem. Technol.* **1983**, 366.

[41] *Gmelin Nickel* **1966**, *57*, B2.

[42] K.A. Bolshakov, P.I. Fedevov, *Russ. J. Inorg. Chem., Engl Transl.* **1960**, 224.

[43] P.A. Nelson, A.A. Chilenskas, R.F. Malecha, *Proc. IECEC* **1992**, *3*.57.

[44] W.Fischer, Report of Ministry of Research and Technology BMFT 86-059, 1986, p. 166.

[45] R.A.Versen, *Batteries Int.* **1993**, 60.

[46] *Gmelin Nickel* **1967**, *57(AII)*, No. 1.

[47] *Gmelin Natrium* **1965**, *21* (Suplement), No. 2.

[48] *Gmelin Natrium* **1973**, *21* (Suplement), No. 6.

[49] E. Kodama, A. Okuno, F. Kiuchi, Y. Kurashima, T. Mima, K. Mori, *Proc. EESAT '98*, Chester 16-18.6.1998, **1998**.

CosMX Exhibit 1008, Page 606 of 633

List of Symbols and Abbreviations

Symbol	Designation	Chapter
a	activity	III.9
a	constant	IV.1
a	crystal unit cell dimension	II.1/7, III.1/3
a	empirical parameter	III.7
a	sum of ionic radii $a_+ + a_-$	III.7
a_+, a_-	crystallographic radius of anions, cations	III.7
a_0	crystal unit cell dimension	II.3
a_{H^+}, a_{H_2}	activity (effective concentration) of H^+, H_2	II.4
a_i	activity of neutral mobile species i	III.4/9
a_i^x	activity of neutral mobile species i	III.9
a_{M^+}, a_{e^-}	activity of M^+,e^-	III.6
a_T	shift factor	III.8
a_X	activity of X	II.7, III.6
A	electroda area	III.6
A	specified constant	II.7
A'	constant	III.2
b	constant	IV.1
b	crystal unit cell dimension	II.1, III.1
b	empirical parameter	III.7
b_0	crystal unit cell dimension	II.3
B	constant	II.7, III.2, III.8
c	concentration	II.7, III.7
c	constant	IV.1
c	crystal unit cell dimension	II.1/7, III.1
c_0	crystal unit cell dimension	II.3
c_e	concentration of electrons	III.9
c_i	concentration of ith compound reacting at electrode	I.1
c_i	concentration of neutral mobile species i	III.4
c_{i^x}	concentration of neutral mobile species i	III.9
c_L	concentration of ligand L	III.7
c_N^n	number of ways of taking n atoms of crystal comprising N atoms	III.9
C	disharge rate	I.1
C	electrical capacitance	III.6
C	intercept on $\ln P_{H2} - 1/T$ graph	II.7

C_1, C_2	constants	III.8
C_A, C_B, C_D	SEI capacitance for each particle A, B, D	III.6
C_{dl}	grain-boundary capacitance	III.6
$C_{GB}^{A/B}, C_{GB}^{C/D}$	grain-boundary (dl) capacitance for A/B, C/D interface	III.6
C_{I12}	double-layer capacitance between sublayers 1 and 2	III.6
C_P	heat capacity	
C_{SEI}	double-layer capacitance between electrode/solid electrolyte phases; SEI capacitance	III.6
C_{SEI}^0	SEI capacitance for $\theta = 1$	III.6
$C_{SE/sol}$	double-layer capacitance	III.6
C_K, C_λ	between solid electrolyte/solution or battery electrolyte phases	III.7
d	crystal interplanar distance	I.2, II.8
d	diameter of separator membrane pores	III.10
d	thickness of separator layer	II.9
d_{50}	mean particle diameter	II.8
d_{cor}	corrosion penetration depth	II.4
$d_{(h,k,l)}$	distance between planes?	II.1
d_{ik}	Minor derived from determinant d by omitting ith row and kth column	III.9
D	density	IV.1
D	diffusivity	III.9
$\tilde{D}$	chemical diffusion coefficient	III.9
D_{chem}	chemical diffusion coefficient	III.4
D_i	diffusivity of ions i	III.9
D_{self}	self-diffusion coefficient	III.4
D_T	diffusion coefficient by radioactive tracers	III.4
e	elementary charge	I.1
e_0	elementary charge	III.7
$[e']$	concentration of electrons	III.9
E	activation energy	III.2
E'	coefficient for lcCM evaluations	III.7
E	voltage drop between probes; plateau voltage in N-component phase diagram	III.9
E^o	equilibrium potential of H_2 evolution in lead-acid cell	II.4
E^o	standard electrode potential (vs. Hg/HgO)	II.8
E^o	standard electrode potential of MnO_2	II.2
$E^o_{e^-}$	equilibrium potential of the M^+ electrode	III.6
$E^o_{M^+}$	equilibrium potential of the M^+ electrode	III.6
$E^o_{O_2}$	decomposition voltage of water	II.4
$E^{o,s}$	standard equilibrum potential	II.4
$E^{o,s}_{H^+}$	electrochemical potential of standard fydrogen electrode	II.4

CosMX Exhibit 1008, Page 608 of 633

E_a	activation energy	III.9
$E_{A,SEI}$	apparent activation energy of ionic conduction in SEI	III.6
E_F	fermi level of electrons	III.4
E_{HOMO}	energy of the HOMO	III.7
E_i, E_m	initial, middle potential of MnO_2	II.2
E_{ox}	anidic potential limit to stability range	III.7
E_r	open-circuit equilibrum voltage	III.7
E_R	open-circuit potential	III.7
E_{Red}	cathidic potential limit to stability range	III.7
Eff	cycling efficiency of lithium anode	III.3
f	charging factor, $1/q_{Ah}$	I.1
f	correlation factor relating D_T and D_{self}	III.4
f_{H_2}	fugacity of hydrogen	II.7
F	Faraday constant	I.1,II.2/4, III.7/9
FOM	figure of merit	II.3
[h]	concentration of holes	III.9
hkl	Miller indices for reflections	II.1
H°	standard enthalpy	IV.1
H_{solid}	concentration of hydrogen in metal	II.7
i	current density	III.9
i	hydrogen/carbon (H/C) ratio	III.5
i_0	current density for onset of electrochemical process	III.7
i_0	exchange current density	III.6
i_{cor}	corrosion current	II.4
i_i	partial electric current density due to species *i*	III.9
i	current supplied by electrochemical cell	I.1
I	current density	I.1
j_0	exhange current density	I.1
j_i	partial flux density due to species *i*	III.9
j_{limit}	maximum current density	I.1
J_1, J_2	Coefficients for lcCM evaluations	III.7
k	Bolzmann constant	III.9
k_B	Bolzmann constant	III.7
K	constant	II.8
K	equilibrum constant	II.7,III.9
K	integration constant	I.1
K_A	association constants of electrolyte with ligand added	III.7
K_A, $K_A^{(C)}$	association constants for solvated ions	III.7

CosMX Exhibit 1008, Page 609 of 633

K_A^0	association constants of electrolyte without ligand	III.7
$K_D^{(T)}$		
K_e	bimolecular rate constant for hydrated electrons	III.6
K_s	Sievert's constant	II.7
l	length of ion path	II.9
l_a	crystallite dimension parallel to basal plane	III.6
l_c	crystallite dimension perpendicular to basal plane	III.6
l_s	length of ion path through separator	II.9
L	distance between probes	III.9
L	membrane thickness	III.10
L_a	crystalline dimension parallel to basal plane	II.8
L_c	crystallite dimension perpendicular to basal plane	I.2, II.8
L_D	Debye length	III.9
L_{SEI}, L_{SEI}^0	apparent thickness of the SEI	III.6
L_V	height of void in PE or CPE	III.6
m	active mass of electrode	I.1
m	parameter in general formula for $\gamma - MnO_2$	II.1
m^*	effective mass of electrons	III.4
mw	molecular weight of alloy in electrode	III.4
M	molar mass of active anode material	I.1
M_w	molecular weight	III.8
n	number of atoms removed from crystal	III.9
n	number of H atoms per formula unit of charged electrode;	II.7
n	number of moles of electrons exchanged at anode	I.1
n	parameter in general formula for $\gamma - MnO_2$	II.2
n_e	electrochemical valence	III.7
N	number of atoms in crystal; number of phases	III.9
N_A	Avogadro constant	I.1, III.7
p	comparison pressure	II.8
p	gas pressure	I.1, III.9
p_{H_2}	H_2 pressure	II.4
P	power delivered by electrochemical cell	I.1
P_r	probability of occurrence of ruitile-like slabs in crystal structure of $\gamma/\varepsilon - MnO_2$	II.1
$P_{r,r}$	probability that a ruitile-like layer is followed by a similar one in $\gamma/\varepsilon - MnO_2$	II.1
$P_{r,R}$	probability that a ruitile-like layer is followed by a ramsdellite-like one in $\gamma/\varepsilon - MnO_2$	II.1
P_R	probability of occurrence of ramsdellite-like building blocks in $\gamma/\varepsilon - MnO_2$	II.1
P_s	power density of electrochemical cell	I.1

CosMX Exhibit 1008, Page 610 of 633

P	pressure	II.7
P	porosity of separator	II.9
P_{eq}	quilibrium H_2 pressure	II.7
$P_{plateau}$	plateau pressure	II.7
q	area of ionic current flow	II.9
q	elementary charge	III.9
q_{Ah}	coulometric efficiency of a battery	I.1
q_B	Bjerrum parameter	III.7
$q(O)$	mean electron density at O atom	III.7
q_{Wh}	energy efficiency of a battery	I.1
Q	charge capacity	II.7
Q	quantity of electricity (electric charge)	I.1
Q	reaction exothermicity	III.2
Q_{charge}	charge necessary to load an accuulator	I.1
$Q_{discharge}$	charge released during discharge of an accumulator	I.1
Q_{ex}	charge necessary to strip all excess lithium from anode	III.3
Q_{IR}	irreversible capacitance loss	III.6
Q_{max}	charge capacity maximum	II.7
Q_p	charge necessary to plate lithium (anode)	III.3
Q_{ps}	charge consumed by constant-capacity cycling of lithium ($Q_{ps} < Q_{ex}$)	III.3
Q_R	reversible capacitance loss	III.6
Q_s	charge necessary to strip all plated lithium from anode	III.3
Q_{SEI}	capacitance needed for formation of the SEI	III.6
Q_{sp}	capacity associated with formation of soluble reduction products	III.6
Q_T	capacity associated with trapping of Li inside the structure of the carbon	III.6
Q_u	unused capacitance	III.6
r	jump distance	III.9
r_a , r_b	radius of atom a, b	II.7
R	distance parameter defining upper limit of ion association	III.7
R	electrical resistance	II.9, III.6/9
R	universal gas constant	I,1, II.2/4/7, III.9
R_{CT1}	charge-tranfer resistance between electrode and solid electrolyte phase	III.6
R_{CT2}	charge-tranfer resistance between electrode and solution phase	III.6
R_{el}	electrical resistance of electrolyte	II.9
R_{film}	resistance of film	III.6
R_{GB}	grain-boundary resistance	III.6
R_i	internal resistance of cell	I.1

CosMX Exhibit 1008, Page 611 of 633

R_i	Stokes radius of ions	III.7
R_{I12}	charge-tranfer resistance between sublayers 1 and 2	III.6
R_{SEI}	electrical resistance of the SEI; apparent SEI ionic resistance	III.6
R^0_{SEI}	R_{SEI} *for* $\theta = 1$	III.6
R_{sep}	electrical resistance of separator	II.9
$R_{SE/sol}$	double-layer resistance between solid electrolyte/solution or battery electrolyte phases	III.6
s	stage index	III.5
s	length of oriented solvent molecule	III.7
S	surface area of reaction vessel	III.2
S	configurational entropy	III.4
S	coefficient for PcCM evaluations	III.7
t	temperature (°C)	IV.1
t	time	I.1
t_+	transport coefficient for cation	III.6/8
t_e	electronic transport coefficient	III.6
t_{Gur}	Gurley number obtained experimentally	III.10
t_i	ionic transport number	III.8
T	absolute temperature	I.1, II.4/7, III.2/7/9, IV/1
T	temperature (°C)	III.6
T	tortuosity factor	II.9
T_0	reference temperature	III.8
T_a	ambient temperature	III.8
T_g	glass temperature	III.8
T_i	ionic transference number	III.8
T_{ref}	reference temperature	III.8
u	mobility	III.9
u_i	ionic mobility	III.7
U	energy of formation of vacancy	III.9
U	terminal voltage measured between poles	I.1
U_{charge}	average terminal voltage during charge	I.1
$U_{discharge}$	average terminal voltage during discharge	I.1
v	thermal velocity of mobile ions	III.9
v	voltammetry scan rate	III.7
V	initial unit cell volume	II.7
V	voltage of electrochemical cell	III.1
V	volume of reaction vessel	III.2
V_H	molar volume of hydrogen	II.7
V_{SEI}	voltage at which the SEI is formed	III.6

CosMX Exhibit 1008, Page 612 of 633

W	enhancement factor or "thermodynamic factor"	III.4
W	reversible reaction heat of electrochemical cell	I.1
W	Warburg impedance on solution side of SEI electrode	III.6
W_{ij}^{*}	noncoulombic part of mean force potencial	III.7
x	concentration of mobile guest ions	III.4
x	fraction of Mn^{4+} ions missing in Mn sublattice of MnO_2; fraction of O per formula unit in $\gamma - MnO_2$	II.1
x	concentration of $AlCl_3$	IV.1
x^0	number of lattice sites occupied by mobile guest ions	III.4
x_{S1}	molar fraction of solvent S_1	III.7
y	fraction of Mn^{4+} ions replaced by Mn^{3+} in Mn sublattice of MnO_2	II.1
$y'_{+/-}$	mean activity coefficient of free ions	III.7
y_{IP}	activity coefficient of ion pair	III.7
z	number of electrons exchanged at anode	I.1
z	$z_+ + \|z-\|$	III.7
z_+, z_-	cationic and anionic charges	III.7
z_i	charge number of species i	III.9
α	degree of association of solvated ions	III.7
α	polarizability	III.7
α	temperature coefficient of specific resistance	IV.1
β	crystallographic angle	II.1
Δd	difference between theoretical and observed distance d	II.1
ΔF	charge in free energy	II.2, III.9
ΔG	reaction free energy	I.1
ΔG	change in Gibbs free energy	III.6/8
ΔG_f	Gibbs free energy of formation	II.7
ΔH	reaction enthalpy	I.1, II.7
ΔH_f	enthalpy of formation	II.7
ΔS	reaction entropy, or change in entropy	I.1, II.7, III.9
ΔV	actual volume change of unit cell	?
$\Delta\varepsilon_0$	nonequilibrum cell voltage	I.1
$\Delta\varepsilon_{00}$	equilibrum cell voltage	I.1
$\Delta\varepsilon_{real}$	real potential	I.1
ε	dielectric constant of SEI	III.6
ε	dielectric permittivity	III.7
ε	porosity of membrane	III.10

CosMX Exhibit 1008, Page 613 of 633

ε_0	dielectric constant of vacuum	III.6/7
ε_{00}	standard electrode potential	I.1
$\varepsilon_{\mathrm{I}}, \varepsilon_{\mathrm{II}}$	potentials for half-cells	I.1
ε_{f}	faradaic efficiancy	III.6
η	overpotential	I.1, III.6
η	polarization	II.4
η	dynamic viscosity	III.7, IV.1
η_{i}	concentration polarization due to charge transfer at the solution-solid interface	II.2
η_{i}	electrochemical potential gradient of species *i*	III.9
η_{T}	total concentration polarization	II.2
$\eta_{\mathrm{c}}(\Delta\mathrm{pH})$	concentration polarization due to pH change of electrolyte pores	II.2
$\eta(\Delta\mathrm{pH})$	concentration polarization due to pH change	II.2
θ	Bragg angle	I.2, II.3
θ	fraction of Li surface in contact with polymer	III.6
Θ_{b}	boiling point	III.7
Θ_{m}	melting point	III.7
K	specific conductivity of electrolyte	I.1
K	conductivity of electrolyte	III.7
K_{D}	Debye parameter	III.7
$K_{\max}$	maximum conductivity	III.7
$K_{\max}$ *	maximum $K_{\max}$ in optimum solvent composition	III.7
λ	thermal conductivity	IV.1
λ_i	ionic conductivity	III.7
λ_+^0	anionic conductivity at infinite dilution	III.7
Λ	molar conductivity at finite concentration	III.7
Λ	limiting molar conductivity at infinite dilution	III.7
Λ_{c}	calculated conductivity	III.7
Λ_{L}	molar conductivity of electrolyte in presence of ligand	III.7
$\Lambda_{0\ldots}$	limiting molar conductivity of electrolyte in presence of ligand	III.7
μ	dipole moment	III.7
μ	concentration of electrolyte	III.7
μ_i	chemical potential of *i*th substance in cell reaction	I.1
μ_i	chemical potential of species *i*	III.9
μ_n	chemical potential of neutral mobile species *n*	III.9
ν	jump frequency	III.9
ν_-, ν_+	anionic and cationic stoichiometric coeffitients	?
ν_i	stoichiometric fector of *i*th subsance nvolved in gross cell reaction	I.1

CosMX Exhibit 1008, Page 614 of 633

π^*	solvatochromic parameter	III.7
ρ	density	III.2/7
ρ	specific resistance, electrical resistivity	I.1, II.8, III.10
σ_i	conductivity of species *i*	III.7/9
σ_n	partial electrical conductivity	III.9
σ_{SEI}	apparent conductivity of the SEI	III.6
ϕ	fluidity of solvent	III.7
ϕ	electrostatic potential	III.9
τ	tortuosity	III.10
χ	heat transfer coefficient	III.2
χ	ionic conductivity	IV.1

CosMX Exhibit 1008, Page 615 of 633

Abbreviation	Explanation
AES	Anger electron spectroscopy
AFM	atomic force microscopy
ALABC	Advanced Lead Acid Battery Consortium
BEG-1	propylene glycol boric ester
BET	Brunauer-Emmett-Teller
CARB	Califomia Air Resource Board
CDMO	composite dimensional manganese oxide
CMD	chemically prepared manganese dioxides
C-MEP	*n,n*-chloromethyl Me-pyrrolidiniumbromide
CPE	composite polymer electrolyte
CSL	compact-stratified layer
CV	cyclic voltammetry
DBP	dynamic bond percolation
DEC	diethylcarbonate
DEE	diethoxyethane
DEP	diethyl phthalate
DMC	dimethylcarbonate
DME	dimethoxyethane
DMO	dimethyl oxalate
Dmpi	I ,2 -dimethyl-3 -propylimidazolium
DN	donor number
DOD	depth of discharge
DOS	dioctyl sebacate
DPE	dual-phase electrolyte
dpg	diphenylglyoxime
DSE	defect structure element
E	ellipsometry
EC	ethylene carbonate
ECQM	electrochemical quartz crystal microbalance
ECS	Electrochemical Society
EDAX	energy dispersive analysis of X-rays
EDS	energy dispersive X-ray spectroscopy
EDTA	ethylene diamine tetraacetic acid
EMC	ethyl methyl carbonate
EMD	electrolytically prepared manganese dioxide
EMIRS	electro-modulated infrared reflectance spectroscopy
EO	ethylene oxide
ER	electrical resistivity
ES	ethylene sulfite
ESCA	electron spectroscopy for chemical analysis
EXAFS	extended X-ray absorption fine structure
FTIR	Fourier transform infrared spectroscopy
GC	gas chromatography
GIC	graphite intercalation compound
HFP	hexafluoropropylene

CosMX Exhibit 1008, Page 616 of 633

HMPA	hexamethylphosphoric triamide
HMTT	hexamethyltriethylenetetramine
HOPG	highly oriented pyrolytic graphite
HRTEM	high-resolution transmission electron microscopy
IMLB	International Meetings on Li Batteries
ISPE	International Symposium on Polymer Electrolytes
lcCM	low concentration chemical model
LGH	linear-graphite hybride
LIBES	Lithium Battery Energy Storage Technology Research Association
LiRE	lithium reference electrode
MC	modified carbonate
MCMB	mesocarbon microbeads
MEEP	poly(*bis*-(methoxy-ethoxy-ethoxy))phosphazene
MeHy	metal-hydride
MEM	*N*-methyl *N* -ethyl morpholinium
MEP	*N*-methyl *N*-ethyl pyrrolidinium
Mm	mischmetal
MPC	methyl propyl carbonate
MRS	Materials Research Society
MSC	methane sulfonyl chloride
NBR	acrylnitrile-butadiene rubber
NHE	normal hydrogen electrode
NTT	Nippon Telegraph and Telephone Corporation
OCV	open circuit voltage
OEM	Original Equipment Manufacturing
PAM	primary alkaline manganese dioxide
PAN	polyacrylonitrile
PAS	polyacenic semiconductor
PC	propylene carbonate
PE	polymer electrolyte
PEGDME	poly(ethylene glycol dimethyl ether)
PEI	poly(ethylene imine)
PEI	polymer-electrolyte interphase
PEO	poly(ethylen oxide)
PESc	poly(ethylene succinate)
PIC	pseudo isotropic carbon
PMDT	1,1,4,7,7-pentamethyldiethylenetriamine
PMMA	polymethyl methacrylate
PO	propylene oxide
PPO	poly(propylene oxide)
PSD	propylsydonone
PTC	positive temperature coefficient
PTC	pressure temperature composition
PTHF	polytetrahydrofurane
PVC	poly(vinyl chloride)
PVDF	polyvinylidene difluoride

CosMX Exhibit 1008, Page 617 of 633

QCMB	quartz crystal microbalance
RAM	rechargeable alkaline manganese dioxide-zinc
SBR	styrene-butadiene rubber
SEI	solid electrolyte interphase
SEM	scanning electron microscopy
SERS	surface enhanced Raman spectroscopy
SFL	sulfolane-based electrolyte
SHE	standard hydrogen electrode
SLI	starter-light-ignition
SNIFTIRS	subtractively normalized interfacial Fourier transform infrared spectroscopy
SPC	statisticalprocess control
SPL	solid-polymer layer
STM	scanning tunneling microscopy
TCDD	tetrachloro dibenzodioxine
TCO	tin based composite oxide
TFSI	bis(trifluoromethanesulfonyl)imide
TG	thermal gravimetric
TGA	thermogravimetric analysis
THF	tetrahydrofuran
TMA	thermal-mechanical analysis
TMA	trimesic acid
TMEDA	tetramethylethylenediamine
UHMWPE	ultrahigh-molecular weight polyethylene
UL	Underwriters Laboratories
USABC	US Advanced Battery Consortium
VCA	Voltage Control Additive
VGCF	vapor-grown carbon fibers
VRLA	valve regulated lead acid batteries
VTF	Vogel-Tamman-Fulcher
WLF	Williams-Landel-Ferry
XANES	X-ray absorption near edge structure
XAS	X-ray absorption structure
XPS	X-ray photoelectron spectros copy
XRD	X-ray diffraction
ZEV	Zero Emission Vehicles

CosMX Exhibit 1008, Page 618 of 633

Index

AA size cells 114
AB_2 hydride electrodes 225 ff
AB_5 electrodes, MH_x–Ni batteries 214 f
absorptive glass mats 278
acceptor number, polymer electrolytes 502
accumulators 1
acetone 428
acetonitrile 460 f
acetylene black
– carbons 236 ff
– manganese oxides 120
– solid/electolyte interface (SEI) 433
acidic environment, lead oxides 155
acidic primaries, zinc electrodes 200
acidic solution, hydrogen 5
acidic surface oxides 431
acrylate ion, SEI 428
acrylate resins, separators 267
acrylonitrile butadiene rubber (NBR) 515
activation energy, solid electrolytes 545
activation enthalpies, solid electrolytes 535
active mass 7
active materials
– bromine 177 ff
– lead oxides 163 ff
additives
– carbon 231
– electrolytes 346 f
– lithium-ion batteries 57
– nickel hydroxides 136
– separators 273, 285 f
aerogel powder 589
ageing effects, lead oxides 172 ff
agglomerates, separators 248
aggregates
– lithiated carbons 388
– polymer electrolytes 502
aggregation states, bromine storage 184, 188
aliphatic ammonium polybromide complexes 181
alkali metal electrolyte interphase 419
alkaline batteries, separators 281 ff, 287
alkaline cells, EMD 131
alkaline gelation, solid electrolytes 541
alkaline low cost reusables 203
alkaline manganese batteries 19 f
alkaline primaries, zinc electrodes 200
alkaline storage batteries, zinc electrodes 202
alkaline(zinc) manganese cell 17
alkylcarbonates 425
alkylborates 476
alloy activation, MH_x–Ni batteries 214
alloy electrode materials 227
alloys, SEI 443
β/β-alumina structures, solid electrolytes 533 ff
β"-alumina 578
– sodium sulfur battery 571
– ZEBRA 566
aluminum 196
aluminum effect, MH_x–Ni batteries 222
aluminum hydroxide 285
ammonium polybromide complexes 180
amorphous carbons 231
amorphous tin-based composite oxide (ATCO) 406
annealing
– β"-alumina 578
– nickel metal hydride batteries 31
anode electrolyte interface 419–456
anode reaction
– Li–$(CF)_n$ 38
– Li–MnO_2 32
– MnOOH 20
anode seal, sodium sulfur battery 575
anodes, metallic negatives 195 ff
anodes advances, market 70
antimony alloys, separators 266
antimony free effect, lead oxides 173
applications
– Li–MnO_2 35
– RAM 74
– solid electrolytes 533 ff
aprotic solvents 424 f, 487
aqueous batteries 16, 231
argon purification 464
aromatic ammonium polybromide complexes 181
Arrhenius relation, solid electrolytes 528, 546
arsenium salts, bromine storage 179
artificial graphite 388
assessment criteria 13 ff
association constants, liquid electrolytes 470
average particle size, EMD 126
Avogadro constant 6

backweb, separators 246 f, 258, 267
barium, manganese oxides 94
Barton process 166
basic functions, separators 245 ff
basic sulfates, lead oxides 156
basic surface oxides, SEI 431
battery definitions 1
battery performances, lithium-ion 54
battery types, metallic negatives 195
bayerite, HT batteries 579
benzene compounds addition, Li anodes 348
benzenediolatoborate solutions 477
bilateral triple ion formation 468
bimolecular rate constants, hydrated electrons 428
binary systems 368 ff
bipolar electrodes 177
birnessite 100 f
Bjerrum parameter, liquid electrolytes 466
boards 589
bobbin structure, Li–MnO_2 34
boehmite 579
boiling point, liquid electrolytes 459
Bragg reflections, manganese dioxide 85
Braunstein 85
bromine storage materials 177–194
Brouwer diagrams 550
Brownian motion, solid electrolytes 541
brucite structure 135 f, 138
Brunauer–Emmet–Teller equation 346
bulk properties, liquid electrolytes 458 ff, 473 ff
burnoff, graphite modification 437
buserite, layer structures 100, 107
Butler–Volmer equation 13
butylamine 460 f
butyrolactone 460 f

cadmium 2, 196
cadmium oxides, separator additives 285
calcination temperature, β"-alumina 579
calcium hydroxides, separator additives 285
capacity 6
– AA-size cells 114
– lithium alloys 363
– lithium batteries 325, 339
– nickel metal hydride batteries 30, 217
– solid electrolytes 537
capacity deterioration, separators 273
capacity loss
– intercalation 432
– lead oxides 172
carbanions, polymer electrolytes 503
carbon blacks 232 ff
carbon classification 387
carbon dioxide addition 349, 484
carbon host 386
carbon monoxide formation 239
carbon precursors, SEI 430
carbonaceous electrodes 421, 429 ff
carbonaceous materials 361, 385
– liquid electrolytes 479
carbonate-based liquid electrolytes 424
carbonate formation 239
carbonates, liquid electrolytes 475
carbonates addition, Li anodes 341, 347 f
carbons 231–244
– hard 53
– lithiated 383–418
– lithium-ion batteries 50
– SEI 439 f
carbonyl 234, 431
Carbotron P 400
carboxyl 234
carboxylate azides 541
carboxylic groups 431
card house model, lithiated carbons 402
cathode influences, lithium surface film 352
cathode reaction
– Li-$(CF)_n$ 38
– Li–MnO_2 32
– MnOOH 19
cathode seal, sodium sulfur battery 575
cathodes, markets 71
cation mobility 518
cation stabilization 312
cavities, EMD 125
Celgard membranes 284 f, 555
cell construction 20
cell data, nickel 589
cell parameters, various 6
cell performance, dead lithium 345 ff
cell safety, Li anodes 353 f
cell stack, bromine 177
cell voltage
– equilibrium 8 f
– hydrogen/oxygen fuel cell 12
– lithium alloys 359
cellophane, separators 283 f
cells, electrochemical 1 ff, 6
cellulosic separators 252, 266
ceramic electrolytes
– β"-alumina 576
– polymer 519
– ZEBRA 568
ceramic fiber boards 589
cerium effect, MH_x–Ni batteries 220
Chabre–Pannetier model 91
chalcophanite 100 f
charge
– characteristic line 15
– ir/reversible 392
charge capacity, MH_x–Ni batteries 221
charge carriers 8
– solid electrolytes 531
charge characteristic, nickel cadmium batteries 24
charge cycle, bromine storage 188
charge/discharge characteristics
– graphite 52
– lead oxides 159, 164

CosMX Exhibit 1008, Page 620 of 633

charge preservation, lead oxides 171
charge transfer complexes, bromine storage 179
charge transfer overpotential 12 f
charge transfer technique 549
charging 7
– RAM 77 f
chelatoborates 463
chemical attack, separators 245
chemical compositions
– EMD 123 ff
– SEI 420 ff, 439 ff
– separators 557
chemical crosslinking, polymer electrolytes 505
chemical elements, battery categories 195
chemical manganese dioxide (CMD) 113 ff
chemical models, liquid electrolytes 465
chemical properties
– AB_5 hydrides 215
– carbon/graphite 233 ff, 430 f
– lead oxides 156
– nickel hydroxides 137 ff
chemical stability, liquid electrolytes 479
chemical stabilization, bromine storage 179
chemically bonded SEI 437
chloride electrolytes, lithium alloys 361
chlorine electrode, carbons 241
chloromethyl *N*-methylpyrrolidinium bromide (MEP) 182
closed pores 124, 430
closed reaction vessel, thermal runaway 329
cloud free production, separators 287
clusters, polymer electrolytes 507
cobalt additives, nickel hydroxides 136
cobalt effect, MH_x–Ni batteries 219, 222
coin cells, Li anodes 339
coin type batteries, Li–MnO_2 34
coke materials 50
cold crank voltage 250 f, 269
combustion synthesis, solid electrolytes 541
compact stratified layer (CSL) 444
complexation, bromines 181
composite dimensional manganese oxide (CDMO) 40 f, 297
composite Li anodes 352
composite polymers, SEI 426
composite solid electrolyte (CPE) 446, 542
composite structures, carbons 237
compositions
– lithium alloys 371
– MH_x–Ni batteries 218 f
– separators 557
concentrated solutions, conductivites 485
concentration cell, polymer electrolytes 510
concentration dependence, equilibrium cell voltage 9 f
condensation, solid electrolytes 541
conductance, sodium aluminum chloride 585
conductive matrix, carbons 236 f
conductivity
– bromine storage 184 ff
– carbons 231
– concentrated solutions 485
– lead oxides 154
– liquid electrolytes 458, 466, 490
– polybromides 178
– polymer electrolytes 503
– SEI 419
– sodium aluminum chloride 584
– solid electrolytes 526, 539
– specific 3
conductivity determination 544
conductor, electronic 2
consumer batteries 19
– market 68
contacts, solid electrolytes 539
container formation, lead oxides 168
conversion, EMD to LiMnO4 129
convertible oxides, lithium alloys 362
copper 1 f
coronadite, tunnel structures 87, 94
corrosion
– carbons 236
– lead oxides 161, 170
– Li anodes 347
– lithiated carbons 384, 392
– MH_x–Ni batteries 213, 217 f
– nickel hydroxides 135
– sodium sulfur battery 575
– zinc 20
corrosion reserve, long-life batteries 170
corrugation, separators 266
coulometric efficiency 15
countercations, ammonium polybromide complexes 180
crimp sealed batteries, Li-MnO_2 33
crosslinking
– chemical 505
– graphene layers 398
crush test 354
crystal structures
– carbons 232 f
– polymer electrolytes 506
crystalline defects, lithium 344
crystallinity, carbon/graphite 50 f
crystallization overpotential 13
crystallographic data
– manganese oxides 87
– MH_x–Ni batteries 219
crystallography 365
cubic close packing 47
cubic packed arrays 293
curing, lead oxides 167
current collector, sulfur electrode 576
current–voltage diagram 14
cycle life 16
– Li anodes 339
– oxide cathodes 324
cycle life test, separators 270
cycles, nickel hydroxides 135
cyclic ethers, lithium-ion batteries 57

CosMX Exhibit 1008, Page 621 of 633

cyclic voltammogram, $LiMn_2O_4$ 131
cycling behavior
– coke materials 51
– Li–Al alloy electrodes 41
– lithiated carbons 385, 393
– lithium alloys 359
cycling efficiency 340, 342 ff, 346 ff
cyclopentanone 428
cylindrical batteries, Li–MnO_2 34
cylindrical sodium/sulfur cell 572

Daniell element 1 ff
DARAK 254 ff, 275 ff
DARAMIC 270
De Wolff model, manganese oxides 89
dead lithium 344 ff
Debye length
– liquid electrolytes 466
– solid electrolytes 539
decalin addition, Li anodes 348
decomposition
– carbonate solvents 483
– SEI 421
– thermal 353
defect structure elements (DSE) 529
defects
– lithium 344
– solid electrolytes 526 ff, 550 f
degradation
– carbons 241
– lithiated carbons 385
dehydration gelation, solid electrolytes 541
dehydriding, MH_x–Ni batteries 216
delocalized pits, dead lithium 346
dendrites
– Li anodes 339
– lithium alloys 360
– separators 247, 285
dendritic lithium 344
density
– electron 2
– lead corrosion products 170
– lead oxides 156
– sodium aluminum chloride 583
density of states, MH electrodes 212
deplating, lithium alloys 360
deposited lithium, morphology 343 f
depth of discharge (DOD) 41, 204
design, solid electrolytes 537
deterioration, graphite–polymer composites 242
diamond 231
diethyl carbonates
– Li anodes 347
– lithiated carbons 395
diffusion
– bromine storage 187
– lithium alloys 366
– solid electrolytes 531, 540
diffusion overpotential 13
dimethyl carbonates
– Li anodes 347
– lithiated carbons 395
– solvents 460 f
dimethyloxyethane (DME) 423
dimethylsulfate 460 f
dimples, separators 262
Dimroth–Reichert ET(30) scale 458
DIN standards, separators 271
diol derivatives 463
dipole moment, liquid electrolytes 458
direct current measurements, solid electrolytes 544
direct current polarization 510
direct current sputtering 543
discharge characteristics 14 f
– alkaline manganese cell 21
– EMD alkaline cells 131
– Li–Al–CDMO cell 43
– Li–MnO_2 33
– lithium nickel oxides 48
– manganese dioxide 114
– MH alloy electrodes 28
– nickel cadmium battery 24
– RAM 75
discharge modification, EMD/$Bi(OH)_3$ 115
discharge process, lithium alloys 360
discharge tests 120 f
discharging 1, 6 ff
disorder model, manganese oxides 89 f
disordered carbon 388, 434
disorders
– solid electrolytes 550
– structural 526
dispersion, solid electrolytes 542
displacement reactions, insertion materials 308
dissociation, sodium aluminum chloride 584
dissolution 2
– polymer electrolytes 502
– spinel framework 311
divinylbenzene styrene copolymer 233
donor/acceptor interactions 180
donor numbers, liquid electrolytes 458
doping, β"-alumina 577
dry cells 19
– manganese oxides 113
dry charged negative plates, lead oxides 172
dry electrolyte technology 501
dry processes, separators 555
duplex microstructure, β"-alumina 578
dynamic bonded percolation (DBP) theory 508

effective ion selective barriers, separators 282
effective volume, EMD 124, 127
electrical vehicle batteries
– lithium 73
– separators 257
electrocatalysis 239 f
electrochemical cells, fundamentals 1 ff
electrochemical formation, lithiated carbons 386

CosMX Exhibit 1008, Page 622 of 633

electrochemical power sources 1 ff
electrochemical properties
– AB_5 hydrides 215
– carbons 235 ff
– EMD 115 ff
electrochemical reactions, nickel hydroxides 145 ff
electrochemical series, metals 4
electrochemical stability, electrolytes 473 f
electrochemical window 458
electrochemistry, manganese oxides 113–133
electrode additives, carbons 231
electrode corrosion 227
– MH_x–Ni batteries 217
electrode potentials
– carbons 235 f
– lithium alloys 363
electrode reactions
– equilibrium 7 ff
– nickel cadmium batteries 22
– nickel MH batteries 26
electrodes 2 ff, 47 ff
– bromine 177
– nickel hydroxides 136 ff
electrolyte additives 347 f
electrolyte composition 447
electrolyte coupling 341
electrolyte solution 3
electrolyte solvents 341
electrolytes
– ether-based 422
– Li anodes 346 f
– lithium alloys 361
– markets 71
– nonaqueous liquid 457–497
electrolytic manganese dioxide (EMD) 113 ff
electron concentrations, solid electrolytes 549
electron density 2
electron mobility 548
electronic conductivity, partial 546
electronic conductor 2
electronic properties, MH electrodes 212
electronic shorts, separators 282
electropolishing, lithium alloys 360
electrostatic factor, liquid electrolytes 458
energy, specific 6, 16
energy density 16
– Li-MnO_2 33
– rechargeable cells 406
– solid electrolytes 537
– ZEBRA 567
energy efficiency 15
enhancement factor, lithium alloys 367
enhancing cation mobility 518
enthalpy 9
– hydrogen formation 162
– MH electrodes 211
– nickel 589
entropy 9
– lead oxides 162
equilibrium cell voltage 8 f
equilibrium conditions, lithium alloys 363
equilibrium potentials, lead oxides 159
equlilibrum electrode processes 7 ff
ether-based liquid electolytes 422
ethers
– Li anodes 347
– liquid electrolytes 475
– lithium-ion batteries 57
ethylene carbonates 460 f
– Li anodes 341, 347
– lithiated carbons 395
– lithium-ion batteries 57
– SEI 424 ff
N-ethylmorpholinium bromide 182
evaporation
– bromine storage 190
– solid electrolytes 525, 543
expansion energy, lithiated carbons 396
explosion methods, solid electrolytes 541
extended X-ray absorption fine structure measurment 550
external chargers, RAM 77
external short safety test 354
extraction
– PE separators 259
– TM oxide insertion 293
extraction materials, solid electrolytes 537
extrusion, PE separators 258

falling cards model 402
Faraday law 6
fast ion conduction, solid electrolytes 534
fast transport, electrodes 539
feitknechtite, reduced manganese oxides 108
Fermi level
– lithium alloys 366
– MH electrodes 212
fiber like lithium 345
Fick law 531
figure of merit (FOM), Li anodes 342
film compositions, liquid electrolytes 480
film properties
– Li anodes 341
– lithiated carbons 393
– SEI 420 f
firing techniques 578
Fischer–Wissler relation 237
flow through electrode, carbons 241
foams, nickel hydroxide electrodes 136
foil insulation 589
foils, lithium 341
framework structures, insertion materials 294, 307 ff
freezing point depression, liquid electrolytes 459
Frenkel defects, solid electrolytes 529
fresh lithium surface, SEI 422 ff
fuel cells 2
fullerenes 405

CosMX Exhibit 1008, Page 623 of 633

functional groups, SEI 431
fundamentals, solid electrolytes 526 ff
Fuoss–Hsia conductivity equation 466
furanes 428
furfuryl alkohol 233
fusion heat, polymer electrolytes 519

galvanic cells 1 ff
– separators 245
gassing
– SEI 435
– separators 279
gel electrolytes 255, 280, 499 f, 513
– SEI 426
– separators 557 ff
gel zones, lead oxides 172
gem like materials 308
Gibbs phase rule
– lithium alloys 363
– solid electrolytes 549
Gibbs–Helmholtz equation 8, 11
gibbsite, HT batteries 579
Giovanoli arrangements 103 f
glass fiber boards 588
glass fiber leaf separators 266
glass fleece separators 247
glass mats
– absorptive 278
– leaf separators 267
glass seal 575
glass separators 252
glassy carbon 234, 389
global competition, primary/secondary batteries 63–83
glycine nitrate 541
grain boundaries
– Li anodes 344
– polymer–ceramic 519
granty, specific 123
granular lithium 344
graphene layers 395
graphite intercalation, bromine storage 179
graphite modification, mild oxidation 437
graphites 231, 386 ff
– lithium-ion batteries 50 f
– SEI 439 f
gravity, specific 125
gray oxide 165
green print, solid electrolytes 542
grid corrosion, lead oxides 161
grids
– lead-acid batteries 165
– pocket construction 260, 265
groutite, reduced manganese oxides 108
growth interface proturberances 360
Gurley number, separators 559
Gutman donor number, liquid electrolytes 458

half cell test 342
half cells 4
halogens, ammonium polybromide complexes 180
hard carbon 53, 233 f, 389, 402
hard sphere packing model 225
hausmannite 108, 308
haystack reaction, oxide cathodes 323, 329
heat capacity, nickel 589
heat loss
– Joule effect 13
– sodium sulfur battery 575
heat treatment, carbons 233 f
heating, lithium alloys 359
heating test 354
Hebb–Wagner method, solid electrolytes 547
Henry law, lead oxides 158
heteroatoms
– lithiated carbons 404
– polymer electrolytes 502
heterocyclic ammonium polybromide complexes 181
hexamethylphosphoric triamide (HMPA) addition 349
high capacity carbons 398
high resolution electron microscopy, MnO_2 85
high temperature batteries 565–591
high volume lithium batteries 326
highly oriented pyrolytic graphite (HOPG) 434 ff, 441
historical remarks
– RAM batteries 73
– separators 251
holes, solid electrolytes 548
hollandite 87, 94 f
honeycomp like networks 387, 395
host structures, insertion materials 293
hybrid electrolytes 512 ff
hydriding, MH_x–Ni batteries 216
hydrocarbons addition, Li anodes 347
hydrogen 2
– acidic solution 5
hydrogen absorbing alloys, nickel systems 26
hydrogen activities, lead oxides 159
hydrogen bonds, carbons 234
hydrogen metal systems 209
hydrogen oxidation
– lead oxides 161
– nickel hydrogens 148
hydrogen/oxygen fuel cell 12
hydrolysis, solid electrolytes 541
hydrophilization, separators 280 f, 288
hydrous nickel oxides 137 f
hydroxyl groups, separators 285

imide ions, polymer electrolytes 503
impedance
– internal 21
– separators 560
impedance analysis 545
in-plane structures, lithiated carbons 390

CosMX Exhibit 1008, Page 624 of 633

industrial battery separators 254, 272
inert electrodes, SEI 421
inert solvents, liquid electrolytes 459
insertion materials 293–321
– lithiated carbons 384
– lithium alloys 366
– oxide cathodes 323 ff
– solid electrolytes 537
insulation, thermal 587
intercalation
– carbonaceous anodes 432 f
– carbons 242 ff
– lithiated carbons 386, 390 f
intercluster movement, polymer electrolytes 507
interfaces
– anode/electrode 419–456
– $Ni(OH)_2$/NiOOH couple 147
interlayer spacing, lithiated carbons 399
internal chargers, RAM 77
internal resistance 12 f
– ZEBRA 568
interstitial ions, solid electrolytes 526
interstitial space, insertion materials 294
intrinsic properties, liquid electrolytes 465 f
inverse spinels, insertion materials 315
ion association
– liquid electrolytes 488
– polymer electrolytes 500
ion conducting solutions 457 f
ion-excharger resins, bromine storage 179
ion pair association, liquid electrolytes 465 f
ion pair contacts, polymer electrolytes 502
ion solvation, selective 471
ion sulfates 4
ionic charge transfer, separators 245
ionic conduction
– solid electrolytes 550 f
– partial 544
– sodium aluminum chloride 584
ionic mobilities, concentrated solutions 485
ionic motion, polymer electrolytes 506 f
ionic radii, solvents 486
ionic rubber, polymer electrolytes 499 f
IR spectroscopy 139
iron, metallic negatives 197
irreversible specific charge 392
isotherm, MH electrodes 210

Jahn–Teller distortions 309 ff
Japanese separators 264, 267
Joule effect, heat losses 13
jump frequency, solid electrolytes 532
Jungner nickel cadmium batteries 22

Kamlet scale 458
kinetics, lithium alloys 366 ff
kinks, lithium deposition 345
Kröger–Vink notation 529
kryptomelane, tunnel structures 87, 94
Kugelhaufen model, lead oxides 173

lactone 431
ladders, separators 283
lambda probe, solid electrolytes 525
$LaNi_5$, MH_x–Ni batteries 213 ff
laser sealed batteries, Li–MnO_2 33
lattice constants 100
lattice planes, carbons 233
lattice sites, solid electrolytes 526, 537
Laves phases
– AB_2 hydride electrodes 227
– MH_x–Ni batteries 213
layered structures
– insertion materials 294, 300 ff
– lithiated carbons 387
– manganese oxides 98 ff
layers
– graphene 395
– lead oxides 164 ff
– lithium alloys 360
– Nernst 13
– nickel hydroxides 138
– SEI 444
– separators 554
lead
– manganese oxides 94
– metallic negatives 197
lead accumulator 2
lead–acid accumulator 16 f
lead–acid batteries 70, 153
lead–acid storage batteries 251 ff
α-lead dioxide 155
β-lead dioxide 155
lead oxides, separator additives 285
lead oxides/dioxides 153–175
lead/oxygen compounds 154 ff
leaf separators 263 f
leakage resistance, Li-MnO_2 33
Leclanché cell 14, 19, 63 f, 85, 236
Lewis acids/bases 458
Li–Co–O spinels, insertion materials 315
Li–LGH–vanadium oxide batteries, secondary 45
Li–Mn–O compounds 301
Li–Mn–O spinels 309 f
Li–Ti–O spinels 316
Li–V–O compounds 304
Li–V–O spinels 314
$LiCoO_2$, layered structures 300
lifetime
– cycles 16
– starter batteries 270
line broadening, manganese oxides 91
$LiNiO_2$, layered structures 301
linking, series/parallel 1
liquid electrolytes
– nonaqueous 457–497
– SEI 424 ff, 443 f

CosMX Exhibit 1008, Page 625 of 633

liquid sodium 590
litharge 153 ff
lithiated carbons 383–418
lithiated ramsdellite MnO_2 298
lithiophorite 100 f
lithium, metallic negatives 198
lithium alloy anodes 359–381
lithium aluminum system 361, 368
lithium anodes, rechargeable 339–357
lithium batteries 2, 19
– advanced 323
– high energy 326
– primary 31 ff
– secondary 40 ff
– TM oxide insertion 293–321
lithium carbon batteries, secondary 45
lithium carbon materials 361
lithium carbon monofluoride batteries 38 f
lithium electrodes 447
lithium hexafluoroarsenate 462
lithium hexafluorophosphate 461
lithium-ion batteries 47 ff
lithium-ion conductors 536 f
lithium-ion inserted anodes 352
lithium-ion metal oxide system 17
lithium iron aluminum sulfide, HT batteries 565 ff
lithium manganese dioxide batteries
– primary 32 f
– secondary 40 f
lithium manganese oxides, EMD 130 f
lithium oxides, layered structures 303
lithium perchlorate solutions 461
lithium polyacene batteries, secondary 45
lithium polyaniline batteries 44
lithium primary market 67
lithium silicon system 361, 368
lithium tetrafluoroborate 462
lithium thionyl chloride batteries 39
lithium–tin system 370
lithium vanadium oxide batteries, secondary 44
load characteristics, Li–MnO_2 37
low temperatures
– lithium alloys 371
– lithium spinels 315
– MH electrodes 212
lump structures, lead oxides 163

magnesium, metallic negatives 198
magnetite 308
maintenance free batteries 259
manganese dioxide 85–112
manganese effect, MH_x–Ni batteries 224
manganese oxides
– electrochemistry 113–133
– reduced 107 ff
manganite 108
manjiroite, tunnel structures 87, 94
manufacture, β"-alumina electrolyte tubes 577
manufacturing process, PE separators 258
margin area, separators 261
markets 65 f
– separators 250
mass, active 7
massicot, lead oxides 154
mathematical modeling, separators 561 f
matrix electrode structures 379
mats, nickel hydroxide electrodes 136
maximum admissible concentration, bromine storage 191
mechanistics 1–17
melt impregnation method, EMD 129
melting point
– Li anodes 340
– lithium alloys 359
membrane ionomers 500
membranes, separators 555
mesocarbon microbeads, lithiated carbons 389
metal additives 41
metal anodes, lithium secondary batteries 56 f
metal halides addition, Li anodes 351
metal hydride electrodes 209–230
metal hydride nickel batteries 212 ff
metal ion potential 8
metallic negatives 195–208
methyl acetate 460 f
methyl formate
– SEI 424
– solvents 460 f
N-methylpyrrolidinium bromide (MEP) 182
microfiber glass separators 247, 256, 268
micropores, separators 247
microporous insulation 588
microporous phenolic resin separator DARAK 254
microporous PVC separators 275 ff
microporous separator materials 554 ff
microporous separators, alkine batteries 288
microshorts, separators 247
migration, solid electrolytes 531
mild oxidation, graphite modification 437
milling, lead oxides 165
minium, lead oxides 155
mischmetal 27
mischmetal compositions, MH_x–Ni batteries 213
mixed conductor matrix concept, lithium alloys 374 ff
mixed phase electrolytes 518
mixing
– pasted plates 166
– PE separators 258
MnO_2 compounds 295
– α-MnO_2 94 f, 295
– β-MnO_2 86 f, 295
– γ-MnO_2 89, 295
– δ-MnO_2 103
– ε-MnO_2 89
Mn_3O_8 98 f
MnOOH compounds 108 f
– α-MnOOH 108 f
– β-MnOOH 109

CosMX Exhibit 1008, Page 626 of 633

– γ-MnOOH 108 f
– δ-MnOOH 109
mobility, solid electrolytes 531
model compounds, nickel hydroxide electrodes 143
molecular properties, liquid electrolytes 458 f
molecular weight, lead oxides 156, 164
molten blends, PVC 256
molten salt electrolytes 457 f
– ZEBRA 568
monolithic samples, solid electrolytes 540 f
monovalent ions 7
morphology
– deposited lithium 343 f
– polymer electrolytes 503
– SEI 420 ff, 439 f
mossy lithium 344
multifoil insulation 587

Na-S system/battery 571, 574
nail penetration, safety tests 354
naphthalene 428
naphthalene diolatoborate solutions 477
NASICON
– insertion materials 294
– solid electrolytes 526 ff, 536 f, 542
native films, Li covered 424
natural graphite 51 f, 234, 388
natural rubber 273
near neighbor environment, manganese dioxide 86
"negalytes", zinc bromine batteries 206
negative electrodes 50 f
– charge preservation 171
Nernst equation 9 f, 13, 157
Nernst–Einstein relation 531, 546
neutron diffraction
– manganese dioxide 85
– nickel hydroxides 137
$Ni(OH)_2$/NiOOH couple reactions 145 ff
α-$Ni(OH)_2$ 135 f, 139 f
β-$Ni(OH)_2$ 137 f
β-NiOOH 135 f, 142
γ-NiOOH 143
nickel, cell data 589
nickel cadmium accumulator 16 f
nickel cadmium batteries 21 ff, 69
– separators 283 f
nickel chloride, HT batteries 585 f
nickel hydroxides 135–151
nickel MH accumulator 16 f
nickel MH batteries 26 ff, 69
– separators 284
nickel oxidation state 148
nickel systems 2
– separators 283 f
nickel-zinc storage batteries 285 f
nickel/cadmium cell 2
nickel/cadmium system 14
niobium oxide–vanadium oxide batteries 46
nomenclature
– manganese oxides 95
– metallic negatives 195
nonaqueous batteries 16
nonaqueous electrolytes, liquid 457–497
nongraphitic carbons, lithiated 398
nonporous manganese dioxide (NMD) 119 f
nonstoichiometric spinels, insertion materials 310
nonstoichiometric phases, lead oxides 156
nonwoven separators, alkine batteries 288
normal hydrogen electrode (NHE) 5
nucleation, lithium alloys 376
nylon, separators 283
Nyquist plot 445

octahedra structure, manganese dioxide 86
Ohm's law, solid electrolytes 531, 544
oil content, separators 260, 272
one-layer system, solid electrolytes 539
Onsager coefficients, solid electrolytes 532
open circuit voltage (OCV)
– manganese dioxide 119 f
– oxide layers 171
– ZEBRA 567
– zinc anodes 199
open pores 430
open stationary batteries, separators 276 ff
operating temperature
– bromine 178
– sodium–sulfur battery 574
operating voltage, Li-ion batteries 326
organic electrolytes, thermal behavior 326 f
original equipment manufactering, zinc electrodes 205
original manufacturer (OEM) markets 68
orthorhombic Na–Mn–O systems 299
overall reaction
– Li-$(CF)_n$ 38
– Li-MnO_2 32
– MnOOH 20
– $Ni(OH)_2$/NiOOH couple 145 f
– nickel metal hydride batteries 26
– zinc/copper 4
overall thickness, separators 246 f
overcharge, safety test 354
overcharge protection, oxide cathodes 323–337
overcharge reactions 15
– ZEBRA 568
overcharging, container formation 168
overpotentials
– carbons 240
– half-cells 12 f
oxidation
– carbons 236 f
– lead 158 f
oxidation half cell 4
oxidation stability, separators 266
oxide cathodes, overcharge protected 323–337
oxide layer disintegration OCV 171

CosMX Exhibit 1008, Page 627 of 633

oxygen 2
oxygen bridges 528
oxygen evolution
– carbons 239
– lead oxides 161
– nickel hydroxides 148
oxygen groups
– carbons 234
– SEI 431
oxygen rich/deficient spinels 310

p-n-junction, $Ni(OH)_2$/NiOOH couple 147
parallel linking 1
parasitic reaction, $Ni(OH)_2$/NiOOH couple 145
particle size, carbons 238
passivated films, liquid electrolytes 479
passivating layers 420 f
passivation
– lead by oxides 169 ff
– lithiated carbons 383
– zinc 5
pasted plates, lead oxides 165 ff
Pechini method 540
Peled model 341
Peltier effect 10
penetration rates, grid corrosion 170
perchloric acid, lead oxides 164
percolation pathway, insertion materials 309
performances, RAM 74
permeability
– lithiated carbons 383
– separators 557 f
– liquid electrolytes 458, 467
perovskite lithium-ion conductor 527
petroleum coke
– lithium-ion batteries 50
– SEI 440
PFG-NMR, polymer electrolytes 510
phase behavior
– lithium alloys 365
– sodium aluminum chloride 582
phase boundaries 7
phases, metal hydride 209 f
phenol
– carbons 234
– SEI 431
phenol formaldehyde resins
– carbons 233
– separators 252
phenol formaldehyde resorcinol separators 248, 256, 275 ff
phenolic resin, separators 267
phophonium salts 179
phosphoric acid 173
phyllomanganates
– buserite type 107
– insertion materials 294
– layer structures 103
physical properties
– bromine storage 184 ff
– carbons 232 ff
– EMD 123 ff
– lead oxides 156
– nickel chloride 586
– separators 557
– solvents 460
– ZEBRA 567
physiological aspects, bromine storage 189
Pisarzhevski–Walden equation 187
pit, dead lithium 346
pitch coke, lithium-ion batteries 50
Planté battery 153, 251
plastic coated surfaces 266
plasticized electrolytes 499 f, 514
plateau voltage, solid electrolytes 549
plates
– lead oxides 164 f
– starter battery separators 260
pocket plates, nickel systems 283
pocket separators 258 ff
point defects, solid electrolytes 528
polarizability, liquid electrolytes 458
polarizations, manganese dioxide 118 ff
polyacene, lithium-ion batteries 54
polyacene semiconductors, lithiated carbons 399
polyamide fibers, separators 283
polybromine phases 177
polyethylene foam 589
poly(ethylene oxide) salt 501
polyethylene pocket separators 258 f, 264, 270
polyethylene separators 248, 252, 256, 272, 277, 284
polymer electrode interphase (PEI) 443 f
polymer electrolytes 457 f, 499-523
– SEI 446 f
– separators 557
polymers
– SEI 426
– thermosetting 233
poly(methoxyethoxyethoxyphosphazene) (MEEP) 505
polymetric matrix, bromine storage 179
polypropylene, separators 283, 561
polystyrene, polymer electrolytes 514
polytetrahydrofuran (PTHF), SEI 423
poly(vinyl alcohol)
– polymer electrolytes 514
– separators 283
poly(vinyl chloride)
– polymer electrolytes 514
– separators 247, 252, 256, 263 f, 277
pores
– carbon/graphite 430
– EMD 124, 127
– separators 247, 557
porosity
– carbons 238
– nickel cadmium batteries 25
– separators 247, 557
"posilytes", zinc bromine batteries 206

positive active materials 177 ff
positive electrode materials 47 f
positive temperature coefficient (PTC) 554
potassium 94
potassium hexacyanoferrates 537
potassium ion conductors 536 f
potentials
– carbons 235 ff
– lithium alloys 371
Pourbaix diagrams
– lead oxides 157
– nickel hydroxides 146
power packs 79
power sources 1 ff
PowerSep 285
PP/PE/PP trilayer separators 556
practical batteries 19–61
precipitation, solid electrolytes 540
precursors
– carbons 233
– Li anodes 348
premature capacity loss, lead oxides 172
pressure dependence
– equilibrium cell voltage 11 f
– MH electrodes 210
primary cells 1, 282
primary systems 17
prismatic nickel MH battery 29
pristine, CBSEI 438
profiles
– PE separators 274
– pocket separators 261
propylene carbonate
– Li anodes 341, 347
– solvents 460 f
protective films 341 ff, 348
proturberances, lithium alloys 360
pseudo isotropic carbon (PIC) 400
pseudoboehmite, HT batteries 579
psilomelane, tunnel structures 96
pulse discharge characteristics, Li–MnO_2 37
purification, liquid electrolytes 464
purity, carbons 238
pycnometric method 550
pyridinium salts, bromine storage 179
pyroaurite type nickel hydroxides 144 f
pyrocatechol derivatives 463
pyrochroite 108 f
pyrolusite 86
pyrolytic graphite 388
pyrophoricity 309

quartz crystal microbalance (QCM) 345
quaternary ammonium polybromide complexes 180
quenching
– nickel metal hydride batteries 31
– solid electrolytes 535
quinone
– carbons 234
– SEI 431
quinoneimine dyes addition, Li anodes 349

radiation crosslinking 505
radiation heat loss 587
radiotracer technique 510
RAM, metallic negatives 204
Raman spectroscopy, nickel hydroxides 139
ramsdellite, tunnel structures 87 f
ramsdellite MnO_2, insertion materials 297
rapid firing, β"-alumina 578
rapid quenching, nickel metal hydride batteries 31
rare-earth elements, MH_x–Ni batteries 213
rare-earth nickel type alloys 27
reaction free energy 8 f
reaction overpotential 13
reaction product layers, lithium alloys 360
reactive radio frequency sputtering 543
rechargeability 1
– lithium alloys 360
– secondary lithium batteries 325
rechargeable batteries
– alkaline MnO_2–Zn (RAM) 73
– EMD 129
– market 68, 72
rechargeable lithium anodes 339–357
recombination batteries 255
recrystallization, active materials 246
recycling
– bromine storage 189 f
– Li-ion batteries 326
redox flow batteries, carbons 241
redox pairs 4
redox potential 8
– negative 383
redox systems, manganese dioxide in KOH 118
reduced manganese oxides 107 ff
reduction half cell 4
reduction process 3
residual compounds, lithiated carbons 394
resins, separators 267
resistance
– electrolyte 3
– internal 12 f, 326
– lead oxides 156
– separators 248 f
resistivity
– bromine storage 184
– electrical 124
– separators 559
reversible specific charge 392
rhombohedral graphite 232
ribs, separators 246 f, 262
romanechite 87, 96
rubbers
– polymer electrolytes 499 f, 515
– separators 256, 273 f, 281
Rubel batteries 19
Ruetschi model 91

CosMX Exhibit 1008, Page 629 of 633

safety
– bromine storage 189
– Li anodes 353 f
– lithiated carbons 385
– lithium alloy anodes 359
– RAM 81
safety vent, nickel cadmium batteries 23
salt bridge 4
salt electrolytes, molten 361
salts
– ion conducting solutions 457 f
– ZEBRA 568
salts classification 461 f
Schottky defects 529
Schottky junction 147 f
screen printing, solid electrolytes 542
sealed cell
– sodium sulfur battery 575
– ZEBRA 566
sealed construction, nickel systems 284
sealed lead–acid batteries 278
sealed nickel–cadmium batteries 22, 255
sealing systems, Li–MnO_2 34
second generation polymer electrolytes 504 f
secondary cells 1
secondary systems 17
seeding, β"-alumina 578
SEI electrode models 443 ff
SEI formation 420 ff
self-diffusion, lithium alloys 366
self-discharge
– bromine 178
– lead oxides 161
– Li-ion batteries 326
– nickel hydroxides 146
– RAM 76
– separators 279, 284
separators 245–292
– lithium batteries 553–563
– markets 72
– shutdown 354
– solutions 3
– zinc electrodes 206
series linking 1
Setela membrane 555
shape change, lithium alloys 360
shapes, Li–MnO_2 34
shedding
– lead oxides 172
– separators 265
shorts, safety tests 354
shrinkage, separators 558
shrinking core model, MH_x–Ni batteries 216
Sievert constant 210
silicon alkoxydes, solid electrolytes 541
Sinsteden battery 153
sintered nickel cadmium batteries 25
sintered PVC separators 247, 263 f, 270, 277
sintering
– β"-alumina 578
– solid electrolytes 535, 542
slitting, PE separators 259
sodium
– liquid 590
– manganese oxides 94
sodium aluminum chloride 582 f
sodium chloride 590
sodium ion conductors 536 f
sodium nickel chloride batteries 525, 565
sodium polysulfides 590
sodium sulfur batteries 525, 571 f
– advanced high temperature 565
sodium β/β"-alumina, solid electrolytes 525
soft carbon 233 f, 389, 402
soft positive, lead oxides 172
sol-gel method, solid electrolytes 541
solar panel charging 79
solid electrolyte interphase (SEI) 341, 383, 392, 419–456
solid electrolyte matrix electrode structure 379
solid electrolytes 457 f, 525–552
solid matrix, bromine storage 179
solid polymer layer (SPL) 444
solid solutions, oxide cathodes 332
solid-state chemistry, nickel hydroxides 137 ff
solid-state reactions, solid electrolytes 540
solid-state redox reactions, oxide cathodes 330
solubility
– manganese in KOH 117
– sodium aluminum chloride 585
soluble salts 3
solutions
– alkaline 19 f
– electolytes 457 f
solvachromic parameter, liquid electrolytes 459
solvation
– additives 348
– liquid electrolytes 486
– SEI 420
– selective 471
solvent-free polymer electrolytes 501 ff
solvents
– Li anodes 347 f
– liquid electrolytes 458 f
– lithiated carbons 395
– lithium-ion batteries 57 f
specifications
– EMD 124
– Li–$(CF)_n$ 38 f
– Li–MnO_2 36
– lithium-ion batteries 55 f
spin-on coating, solid electrolytes 544
spinel block, solid electrolytes 528
spinel compounds
– insertion materials 307 ff
– Mn_3O_4/γ-Mn_2O_3 109
spiral structure, Li–MnO_2 34
spirally wound batteries, separators 553
spray drying, solid electrolytes 540
spray pyrolysis 544

CosMX Exhibit 1008, Page 630 of 633

sputtering
– insertion materials 314
– solid electrolytes 525, 543
stability
– β/β"-alumina 581
– carbons 235
– Li anodes 340
– liquid electrolytes 458, 473 f, 479
– separators 557
– solid electrolytes 537
– transition metal oxide insertion 293–321
stability window 549
stack pressure, Li anodes 346 f, 351 f
stacking sequence
– carbons 232
– lithiated carbons 387, 390
stage formation, lithiated carbons 391
stainless steel, Li deposition 343
standard potentials 6
– carbons 235 f
– hydrogen/oxygen fuel cell 12
– lead oxides 160
– MnO_2 in KOH 118
standard profiles, separators 262
starter battery separators 252 f, 258 f
starter light ignition (SLI) batteries 2
stationary battery separators 254
statistical process control (SPC), separators 259
stoichiometric factors 9 f
stoichiometric spinels, insertion materials 310
Stokes–Einstein equation 507
storage capacity, MH_x–Ni batteries 217
storage characteristics
– Li–Al–CDMO cell 43
– Li–MnO_2 33
storage life, nickel cadmium batteries 25
storage materials, bromine 177–194
storage sites, lithium 400
storage temperature, manganese dioxide 116
stripping, dead lithium 346
structural chemistry, manganese dioxide 85–112
structural damage, insertion materials 294
structural defects, solid electrolytes 526 ff
structural stability, TM oxide insertion 293–321
structures
– carbons 238
– $LaNi_5D_7$ 215
– polymer electrolytes 503, 506
styrene butadiene rubber (SBR) 515
styrenes, SEI 428
sulfates 4, 156
sulfolane 460 f
sulfonium salts, bromine storage 179
sulfur, cell data 590
sulfur addition, Li anodes 350
sulfuric acids, lead oxides 156
sulfuryl chloride 460 f
surface areas
– EMD 124
– lead oxides 164
surface complexes, lithiated carbons 394
surface condition, manganese dioxide 115
surface films
– Li anodes 352
– SEI 422 ff
surface films compositions 480
surface groups, carbons 235
surface structures, carbon/graphite 430 f
surface tension, lithium 345
surface treatments, separators 266
surfaces
– lithium foil 341
– membranes 555
suspension impregnation method, nickel hydroxides 136
synthesis routes, solid electrolytes 537
synthetic graphite 388
synthetic separators 252, 268

Tafel equation 13
Taft scales 458
tank formation, lead oxides 167
tape casting, solid electrolytes 542
Teflon belts, separators 275
teflonized acetylene black (TAB) 120
temperature dependence
– equilibrium cell voltage 10 f
– Li–MnO_2 37
– lithiated carbons 385
– lithium alloys 371 f
– MH_x–Ni batteries 217
– RAM 76
tenside like ammonium polybromide complexes 181
tension, separators 554
terminal voltage 5, 14
ternary system
– lithium–silicon 364
– composition voltage 550
tetraalkylsulfamides, polymer electrolytes 516
tetrahydrofuran (THF)
– SEI 422
– solvents 460 f
thermal batteries, lithium alloys 361
thermal decomposition, Li anodes 353
thermal expansion, nickel 589
thermal insulation 587
thermal mechanical analysis (TMA) 561
thermal runaway, closed reaction vessel 329
thermal shock, sodium sulfur battery 573
thermal stability
– carbons 235
– separators 557
thermodynamic factor, lithium alloys 367
thermodynamic treatment, lithium alloys 363
thermodynamics 1–17
– lead oxides 156 ff
– MH electrodes 209 ff
– $Ni(OH)_2$/NiOOH couple 145 f
thermosetting polymers, carbons 233

CosMX Exhibit 1008, Page 631 of 633

thick-film solid electrolytes 542 f
thickness
– graphite flakes 396
– separators 246 f, 557
thin-film electrolytes 525
– solid 543 f
thin films, insertion materials 313
tin-based composite oxide (TCO) 406
tin influence, lead oxides 173
titanium oxide manganese oxide battery 46
to peak firing, β"-alumina 578
todorokite, tunnel structures 87, 96 f
topotactic insertion, lithium alloys 366
tortuosity, separators 248 f, 559 ff
toxicity
– Li-ion batteries 326
– liquid electrolytes 458
traction batteries 256, 272, 275
transference number
– polymer electrolytes 510
– SEI 419
– solid electrolytes 547
transition metal oxide insertion, lithium battery 293–321
triple ion association, liquid electrolytes 468
Tubandt–Hittorf technique 510
tubes, β"-alumina 581
tubular plates, lead oxides 168
tunnel structures
– insertion materials 294 f
– manganese dioxide 86 ff

ultra-high-molecular-weight PE (UHMWPE) 258, 557
unilateral triple ion formation 468
urotropin bromine adducts 179

vacancies, solid electrolytes 526
vacancy model, manganese oxides 91
vacuum evaporation, solid electrolytes 525
valve-regulated batteries 255
valve-regulated lead–acid batteries 280
van der Waals bonds
– carbons 232
– lithiated carbons 387
van t'Hoff equation, MH electrodes 210, 217
vapor grown carbon fibers, SEI 440
vapor pressure
– bromine/ammonium salts 182
– liquid electrolytes 458
– sodium aluminum chloride 583
vented construction, nickel systems 283
vinyl compounds, liquid electrolytes 476
viscose 289
viscosity
– bromine storage 186
– liquid electrolytes 458
– sodium aluminum chloride 583
– solvents 486
vitreous carbon 389
vitrification, solid electrolytes 542
Vogel–Tamman–Fulcher equations (VTF) 507
voltage
– equilibrium 8 f
– terminal 5
voltage relaxation method 548
voltage windows, liquid electrolytes 473

Wagner factor 532
water decompositon, lead oxides 157
water loss, separators 273
welding, separators 261
wet chemical method, solid electrolytes 540
wet oxidation 438
wet processes, separators 555
Williams–Landel–Ferry equations (WLF) 507
De Wolff model, manganese oxides 89
wood veneers 252
woven fabrics 283

X-ray diffraction
– manganese dioxide 85
– solid electrolytes 550

z-valent ions 7
ZEBRA batteries 525, 569 f
ZEBRA system/cell 566 ff
zero emission vehicle 565
zeta process, β-alumina 578
zinc 1 f
– metallic negatives 199
zinc additives, nickel hydroxides 136
zinc air batteries 67, 286
zinc carbon cell 63
zinc carbon system 17
zinc corrosion/passivation 20
zinc deposit, carbons 241
zinc flow batteries
– bromine 177
– electrodes 205
zinc systems/batteries, separators 285 ff

CosMX Exhibit 1008, Page 632 of 633

WILEY-VCH

Jürgen O. Besenhard (Ed.)

Handbook of Battery Materials

Batteries are finding applications in an increasing range of every-day products: walkmen, mobile phones and electric cars need very different battery types.

Each of these battery systems consists of very different types of materials. Improvement of these materials is an important issue in modern materials science and electro-chemistry.

This handbook gives a concise survey of the materials used in modern battery technology. The physico-chemical fundamentals are treated as are the environmental and recycling aspects. It is a profound reference source for anyone working in the research and development of new battery systems, regardless whether chemist, physicist, or engineer.

ISBN 3-527-29469-4

